

# **ANNUAL REPORT OF NATIONAL INSTITUTE FOR FUSION SCIENCE**

**April 2005–March 2006**

**November 2006**

**NATIONAL INSTITUTE FOR FUSION SCIENCE**

Address : Oroshi-cho, Toki-shi, Gifu-ken 509-5292, JAPAN

Phone : +81-572-58-2222

Facsimile : +81-572-58-2601

Homepage on internet : URL = <http://www.nifs.ac.jp/>

### **Editorial Board**

Kobayashi, M., Murakami, I., Muroga, T., Narihara, K., Toda, S., Namba, C.

<Editorial Office Staff> Kohmoto, Y., Hashimoto, K.

Inquiries about copyright should be addressed to the Research Information Center,  
National Institute for Fusion Science, Oroshi-cho, Toki-shi, Gifu-ken 509-5292 Japan.  
E-mail: [bunken@nifs.ac.jp](mailto:bunken@nifs.ac.jp)

#### **<Notice about photocopying>**

In order to photocopy any work from this publication, you or your organization must obtain permission from the following organization which has been delegated for copyright for clearance by the copyright owner of this publication.

#### Except in the USA

Japan Academic Association for Copyright Clearance (JAACC)  
6-41 Akasaka 9-chome, Minato-ku, Tokyo 107-0052 Japan  
Phone: 81-3-3475-5618 FAX: 81-3-3475-5619 E-mail: [jaacc@mtd.biglobe.ne.jp](mailto:jaacc@mtd.biglobe.ne.jp)

#### In the USA

Copyright Clearance Center, Inc.  
222 Rosewood Drive, Danvers, MA 01923 USA  
Phone: 1-978-750-8400 FAX: 1-978-646-8600



## Contents

I.	National Institute for Fusion Science in April 2005 – March 2006.....	1
II.	Research Activities .....	3
1.	Large Helical Device (LHD) Project .....	3
1-1.	LHD Experiment .....	3
(1)	Overview of LHD Experiment .....	3
(2)	LHD Physics Experiments .....	5
§1.	Superdense Plasma in LHD .....	5
§2.	Super Dense Core Plasma (location of IDB) .....	6
§3.	Super Dense Core Plasma (high beta).....	7
§4.	Particle Balance Study in the LHD .....	8
§5.	Long-Duration Sustainability of Pellet Fueled High Performance Plasma .....	9
§6.	Observation of Slow Transition between Two Transport Branches with Different Temperature Dependence in LHD.....	10
§7.	Effect of Elongation on Transport in ECH Plasma.....	11
§8.	Radial Structure of Edge Transport Barrier in Inward-Shifted Configuration of LHD .....	12
§9.	Effects of Applied Resonant Helical-Field Perturbations on ETB Formation .....	13
§10.	Observation of Radial Structure of Edge MHD Modes in LHD Plasmas with L-H Transition.....	14
§11.	H-mode-Like Discharges and ELM-Like Activities under the Presence of $\nu/2\pi=1$ at Ergodic Layer in LHD.....	15
§12.	Comparison of Confinement Degradation in High Density and Particle Transport between Tokamak and Helical Devices.....	16
§13.	Comparison of Experimental Transport Coefficients and Prediction by the Resistive g-Mode Theory .....	17
§14.	High $W_p$ Experiment .....	18
§15.	Effect of Island Size on High- $T_e$ Transition during Core-Localized ECH....	19
§16.	Common Features of Core Electron-Root Confinement (CERC) in Helical Plasmas .....	20
§17.	Direct Observation of Inward Electron Flux Being Blocked in the Large Helical Device.....	21
§18.	Configuration Effects on Particle Transport in LHD .....	22
§19.	Electron Transport Dynamics in LHD Core Plasmas .....	23
§20.	Study of Nonlocal Electron Heat Transport on the High Temperature Plasmas of LHD .....	24
§21.	Observation of Spontaneous Toroidal Flow in LHD .....	25
§22.	Configuration Effects on Turbulence Transport in LHD .....	26
§23.	Observation of Fluctuation Generated by Energetic Particles and Electrons Using Microwave Reflectometer .....	27
§24.	Microwave Imaging Reflectometry in LHD .....	28
§25.	High-Beta Experiments in LHD.....	29
§26.	Effect of Resonant Magnetic Field on low- $m$ Mode in LHD.....	30
§27.	On the Reconstruction in LHD High Beta Plasmas .....	31
§28.	Two-Dimensional Structure of the MHD Instabilities and Its Non-Linear Evolution in the Large Helical Device.....	32
§29.	Effect of Separatrix Geometry on Transport and MHD.....	33

§30.	Minor Collapse of Current-Carrying Plasma in LHD.....	34
§31.	Control of Magnetic Shear by Neutral Beam Injection in LHD.....	35
§32.	Observation of Localized Oscillations at $m/n = 2/1$ Rational Surface during Counter Neutral Beam Injection.....	36
§33.	Particle Orbit Analysis in High Beta Plasma of LHD.....	37
§34.	Plasma Collapse Phenomenon in Ctr-NBI Heating Plasma with the Magnetic Configuration of $B_q=200\%$ .....	38
§35.	Zeeman Spectroscopy with Tomographic Analysis.....	39
§36.	High-Resolution Measurements of $H\alpha$ Spectral Line Profiles in LHD Steady State Plasmas.....	40
§37.	Application of Visible Bremsstrahlung to a Density Monitor in Steady State Fusion Reactor.....	41
§38.	Estimation of the Particle Confinement Time of the Helium Ash in LHD...	42
§39.	Achievement of 1.6 GJ Input in Steady State Operation in LHD.....	43
§40.	Long Pulse Discharge of MW-ICRF Heated Plasma.....	44
§41.	Density, ICRF Power and Pulse Length Operated in Steady State Experiment in the 9th Cycle Experiment.....	45
§42.	Mechanism of Magnetic Axis Sweeping Divertor.....	46
§43.	Characteristics of Impurity Content in Long-Duration Discharges with Magnetic Axis Sweeping.....	47
§44.	Distribution of Divertor Temperature after Long Pulse Operation Using ICRF Heating in 9th Cycle Experiment.....	48
§45.	Wall Recycling Study Using Pulsed Gas Puffing during a Long Duration Discharge in LHD.....	49
§46.	Instantaneous ECH Injection for ICRF Heated Long Pulse Plasma Discharge.....	50
§47.	Optimization of Magnetic Configuration and Polarization for Long Pulse Plasma Sustainment with ECH.....	51
§48.	Density Limit Study in LHD.....	52
§49.	The Highest Density Achieved in LHD.....	53
§50.	Divertor Transport Study of LHD.....	54
§51.	Simulation of Sheet-Shaped Lithium Beam Probe Performance for Two-Dimensional Edge Plasma Measurement.....	55
§52.	Analyses of the Effect of a Closed Divertor Configuration on the Density Profile of the Neutral Hydrogen Molecules in the LHD Divertor.....	56
§53.	Analyses of the Polarization Resolved H-alpha Spectra in Various Magnetic Configurations in LHD.....	57
§54.	Development of Pellet Ablation Model Considering the Effect of the Plasma Shielding.....	58
§55.	Application of Tomographic Imaging to Photodiode Arrays in LHD.....	59
§56.	Imaging of Radiation from TESPEL Injected into a Magnetic Island in LHD.....	60
§57.	Laser Calibration of the Infrared Imaging Video Bolometer.....	61
§58.	LHD Gauge by External Coil Currents.....	62
§59.	Study on Generation Mechanism of Particles in LHD.....	63
§60.	Erosion of Plasma Facing Materials by Charge Exchange Neutrals.....	64
§61.	The Effect of Argon and Helium Glow Discharge Cleaning on Boronized Surface in LHD.....	65
§62.	Toroidal Uniformity of Boronized Wall During 8 <sup>th</sup> Experimental Campaign.....	66
§63.	Study on Hydrogen Retention and Its Existing State in Boron Film Exposed to Hydrogen Glow Discharges.....	67

§64.	Ion Cyclotron Conditioning with Strong Magnetic Field in LHD .....	68
§65.	Recent Progress on High Ion Temperature Experiment in the LHD .....	69
§66.	Ion Temperature Rise in Electron-ITB Plasmas Formed with Combination of ECH and NBI.....	70
§67.	Effect of Ripple Trapped Electrons on Neutral Beam Driven Current in LHD.....	71
§68.	Fraction of Neutral Beam with Different Energies Measured by the Beam Emission Diagnostic.....	72
§69.	Plasma Sustainment by the ICRF Mode Conversion Heating .....	73
§70.	Experiment of Wave-Particle Interaction by Use of Second Harmonic ICRF Heating and NBI.....	74
§71.	Excitation of High Frequency Fluctuations and Their Effects on High Energy Ions in LHD .....	75
§72.	Study on Electron Bernstein Wave Heating in High Density Regime.....	76
§73.	Excitation of Electron Bernstein Wave via O-X-B Mode Conversion Process in the Over-Dense Plasma on LHD .....	77
§74.	Variation of EBW and X-Mode Absorption Profile with Changing the Electron Density .....	78
§75.	Analysis of Plasma Current Driven by Electron Cyclotron Waves .....	79
§76.	Electron Cyclotron Current Drive Using 2O-port Antenna .....	80
§77.	Ray-Tracing for Electron Cyclotron Waves Propagating Obliquely with Respect to Magnetic Field Lines.....	81
§78.	Study on Production of Energetic Ions in ECH/ECCD Plasmas in LHD .....	82
§79.	Stray Radiation Behavior Measured at Different Locations in the LHD Vacuum Vessel.....	83
(3)	LHD Device Engineering Experiments.....	84
§1.	Influence of Magnetic Hysteresis on Quench-Voltage Detection in Large Superconducting Magnets.....	85
§2.	Optimization of the Distribution of Mass Flow in the Helium Cooling System of the LHD.....	86
§3.	Monitoring and State Estimation of the LHD Coil .....	87
§4.	Open-Loop Excitation and Electrical Parameter Estimation of LHD Superconducting Coils .....	88
§5.	Strain Measurement of Cryogenic Support Structure of LHD.....	89
§6.	Upgrading Program of LHD Helical Coils by Subcooling .....	90
1-2.	Device Engineering and Cooperative Development Research.....	91
(1)	Physics and Engineering of LHD Torus System.....	91
§1.	Improvement of Compact Torus Injector for Fuelling LHD .....	92
§2.	Hydrogen Retention in Vanadium Alloy Exposed to Hydrogen Plasma.....	93
(2)	Applied Superconductivity and Cryogenics.....	94
§1.	Studies on the Thermo-Mechanical Strength Characteristics of Single Crystal RE High $T_c$ Bulk Superconductors .....	96
§2.	Design and Optimization of High $T_c$ Superconductors for Current Lead Application.....	97
§3.	Effect of the Superheating on Heat Transfer in Two-Dimensional Channels in He II .....	98
§4.	Feasibility Study on SMES Systems Using Stress-Minimized Helical Coils .....	99
§5.	Basic Studies of Electric Properties of Polymeric Silver(I) Complexes at Low Temperature .....	100
§6.	Study on Long Loops with Long Time Constants in Cable-in-Conduit Superconductors .....	101

§7.	Reliability of Cryogenic Composite Electrical Insulation for LHD .....	102
§8.	Evaluation of Electrical Insulation Properties of Superconducting Coils.....	103
§9.	Study on Cryogenic Characteristics of Advanced Uni-Polar Power Electronics Devices and Their Application to High Efficiency AC/DC Converter.....	104
§10.	Fundamental Study on Application of Magnetic Levitation Using YBCO Bulk Superconductor to Fusion Research .....	105
§11.	Standardization of the Fabrication and the Operation Technologies for Large Scale Superconducting and Cryogenic Systems .....	106
§12.	Development of a New Conductor Controlled the Twist Angle to Improve the Performance of LTS Coils.....	107
§13.	Basic Study on Oxide Superconductors for Nuclear Fusion Reactor .....	108
§14.	A Co-axial Pulse Tube Current Lead Development .....	109
§15.	“ <i>Cryodielectrics</i> ” – Electrical Insulation of Superconducting Power Equipment Based on Partial Discharge Measurements .....	110
§16.	Validation of the High Performance Conduction-Cooled Prototype LTS Pulse Coil for UPS-SME.....	111
§17.	Improvement in Cryogenic Stability of the Model Coil of the LHD Helical Coil with Lower Temperatures.....	112
§18.	Power Saving Trial of Helium Compressors for the LHD Cryogenic System .....	113
§19.	Cryogenic Stability of LTS/HTS Hybrid Superconductors .....	114
§20.	Operation Test of 100kW Class DEMO SMES .....	115
§21.	Dynamic Simulation of a Large Cryogenic Plant .....	116
§22.	Design Optimization of Bi2212 HTS Tubular Bulk with Conical Shape for Current Lead .....	117
§23.	Preliminary Cool-Down Tests of the Cryogenic Target for the FIREX Project .....	118
§24.	Experimental and Numerical Studies on Heat and Mass Flow of He II through Porous Media .....	119
§25.	Effect of Shielding Currents on Current Decay Behaviors in HTS Coils.....	120
§26.	Development of HTS Loops for Long-Time Plasma Diamagnetic Measurements .....	121
§27.	Stability of NbTi/Cu CICC with Artificial Non-Uniform Current Distribution .....	122
§28.	Cryogenic Stability of LTS/HTS Hybrid Superconductors .....	123
§29.	Summary of Fifteenth International Toki Conference (ITC-15).....	124
(3)	RF Heating Technologies .....	125
§1.	Development of an Evacuated Transmission Line with $\phi 88.9$ Diameter Waveguides for ECH .....	126
§2.	Evaluation of Transmission Efficiency by Power Measurement Using a Compact Portable Dummy-Load.....	127
§3.	Moment Analysis of Power Profiles Radiated from Corrugated Waveguides of ECH Transmission Lines .....	128
§4.	Installation and Operation of New 84GHz Gyrotron System .....	129
§5.	Study on High Energy Particles Escaped from LHD Using Lost Ion Probe .....	130
§6.	Sparks from Inner Side of Torus during ICRF Long Pulse Heating.....	131
§7.	Improvement of Real-Time Impedance Matching System for the ICRF Long Pulse Heating .....	132
§8.	Workshop on Generation, Application and Measurement of High Power Millimeter Waves.....	133

(4) High Energy Beam Technology .....	134
§1. Performance of Neutral Beam Injection Systems in the 9th Campaign.....	135
§2. Spectra of H $\alpha$ Lines and Cs Lines from the Negative Ion Sources during NB Injection .....	136
§3. Operation Start of Diagnostic Neutral Beam Injection in LHD.....	137
§4. Development of Positive Ion Sources for a Perpendicular Neutral Beam Injector (I) –Development of Plasma Generator– .....	138
§5. Development of Positive Ion Sources for a Perpendicular Neutral Beam Injector (II) –Development of Acceleration Grid System– .....	139
§6. Proton Ratio and Beam Divergence Measurement of Diagnostic Neutral Beam .....	140
§7. Development of RF Plasma Source for Negative Ion NBI.....	141
§8. Development of High Power Multi-Antenna rf Ion Source.....	142
§9. Development of a High Intensity He $^{-}$ Beam Source for Fusion-Produced Alpha Particle Measurement .....	143
(5) Diagnostic Systems .....	144
§1. Raman and Rayleigh Calibrations of the LHD YAG Thomson Scattering.....	145
§2. Development of Multichannel Ultrashort Pulsed Radar Reflectometer for Electron Density Profile Measurement .....	146
§3. Application of Ultrashort-Pulse Reflectometer to LHD.....	147
§4. Developments of Millimeter-Wave Diagnostic Simulator .....	148
§5. Potential Measurement by 6 MeV Heavy Ion Beam Probe on LHD.....	149
§6. Calibration of Tandem Energy Analyzer of Heavy Ion Beam Probe on LHD.....	150
§7. Development and Optimization of New Negative Ion Source for a Heavy Ion Beam Probe.....	151
§8. Development of a Compact Au $^{-}$ Source for Local Electric Potential Measurement of a LHD Plasma .....	152
§9. Estimation Method of Impurity Transport by Means of Pulse-Height Analyzer in LHD .....	153
§10. Initial Experiment on the Tracer-Encapsulated Cryogenic Pellet (TECPEL) Injection into LHD Plasmas.....	154
§11. Identification of Micro-Turbulence in LHD from 2d Phase Contrast Imaging .....	155
§12. Application of Precise Phase Detector for Density Profile and Fluctuation Measurements Using CO $_2$ Imaging Heterodyne Interferometer on LHD.....	156
§13. New Calibration Method of Magnetic Measurements Based on the MHD Equilibrium with the Ergodic Region .....	157
§14. Effect of Net Toroidal Current on Measurement of Diamagnetic Beta Value in Heliotron Plasma .....	158
§15. Progress on Temporally and Radially Resolved Charge Exchange Diagnostics of Fast Ions on LHD.....	159
§16. Progress of a New Two Color FIR Laser Interferometer.....	160
§17. Design of the Diverter Interferometer Combined with ECA Measurement on LHD.....	161
§18. Bench Testing of New Polarimeter with Use of Si Photo Elastic Modulator for 57 & 48 $\mu$ m Laser.....	162
§19. Development of the Interface to the Magnetic Force Line and Magnetic Surface Visualization Program .....	163
§20. The Next-Generation Technology of Data Acquisition and Analysis Environment for Fusion Experiments .....	164

§21.	On the Construction of Databases of Experiment Data .....	165
§22.	Framework Remodeling of LABCOM Data Acquisition System for the Next-Generation “LABCOM/X” Project.....	166
§23.	Higher Harmonic Electron Cyclotron Emission Diagnostics .....	167
§24.	Measurement of Soft X-Ray Emission from LHD Plasma.....	168
§25.	Study of High-Performance Array Antennas for Millimeter-Wave Imaging Array .....	169
§26.	Poloidal Polarimetry for ITER .....	170
§27.	Research and Development of an Extremely Compact Fusion Neutron Source by Spherically Converging Ion Beams .....	171
§28.	Two Dimensional Ion Temperature and Velocity Measurements by Use of Visible Light Tomography Technique.....	172
§29.	Development of Diode Laser Absorption Spectroscopy for Diagnostics of Hydrogen Atoms at the $n=2$ State .....	173
1-3.	Theoretical Study .....	174
§1.	Development and Application of HINT2 to Helical System Plasmas .....	176
§2.	Theoretical Considerations of Doublet-Like Configuration in LHD .....	177
§3.	Development of Multi-Scale MHD Simulation Scheme .....	178
§4.	Multi-Scale MHD Simulation of LHD Plasma .....	179
§5.	On the 2nd Stability of Ballooning Modes in the Standard LHD Configuration.....	180
§6.	Self-Sustained Annihilation of Magnetic Islands in Helical Plasmas.....	181
§7.	Nonlinear Dynamics of an ELM Crash in Spherical Tokamak .....	182
§8.	Theoretical Study of Structure of Electric Field and Transport Dynamics.....	183
§9.	Accessibility to a Two-Dimensionally Steep Structure of the Electric Field in Tokamak H-mode .....	184
§10.	Simulation Study of Neoclassical Transport and GAM Oscillation .....	185
§11.	Development of Neoclassical Transport Code Using the $\delta f$ Method.....	186
§12.	Strike Points of High Energy Particles on the LID Head in LHD .....	187
§13.	Set of Model Equations for the Analysis of the Resistive Drift Wave Turbulence in Cylindrical Plasmas .....	188
§14.	Linear Analysis of the Resistive Drift Wave Instability in Cylindrical Plasmas.....	189
§15.	Nonlocal Stability Analysis of Microinstabilities in Inhomogeneous Plasmas.....	190
§16.	Multiple Eigenmodes of Geodesic Acoustic Mode in Collisionless Plasmas.....	191
§17.	Critical Gradients for Short Wavelength Ion Temperature Gradient Instability in Toroidal Plasmas.....	192
§18.	Kinetic Ballooning Mode in $s-\alpha$ Tokamak .....	193
§19.	Effects of Trapped Particles on Residual Zonal Flows in Helical Systems .....	194
§20.	Collisionless Damping of Zonal Flows in Helical Systems.....	195
§21.	Simulations of Electron Bernstein Waves and Zonal Flow Damping in Helical Systems.....	196
§22.	Zonal Flows, Geodesic Acoustic Modes and Geodesic Transfer in the H-1 Helic .....	197
§23.	Hollow Density Profile in LHD .....	198
§24.	On the Basis of Statistical Theory of Strong Turbulence in Inhomogeneous Plasmas .....	199
§25.	On the Bicoherence Analysis of Plasma Turbulence .....	200



§26.	Energy Partition between Fluctuations and Zonal Flows .....	201
§27.	Impact of Turbulence Spreading on Subcritical Turbulence in Inhomogeneous Plasmas .....	202
§28.	Transport Coefficient Induced by Drift Wave Turbulence Screened by Zonal Flows.....	203
§29.	Zonal Flows in Plasma – A Review .....	204
§30.	Probability Density Functions and Structure of Singularities in Non-Dissipative Fields in MHD and NS Turbulences.....	205
§31.	Investigation on the Application of the Plasma-Sheath Having Charged-Dust Grains.....	206
§32.	Equilibrium of Electrostatic Torus Plasma – Ion Temperature Effect.....	207
§33.	Steady State Operation of a Field-Reversed Configuration Plasma by NBI.....	208
§34.	Development of Reactor Design Aid Tool Using Virtual Reality Technology.....	209
1-4.	LHD Project Research Collaboration .....	210
§1.	Experiment on Charge Separation and Direct Energy Conversion Using a Slanted CUSP Field.....	211
§2.	Optimization of Phase Velocity of Traveling Wave in a TWDEC Simulator .....	212
§3.	Fast Power Control Capability of Large-Scale Travelling Wave Direct Energy Conversion.....	213
§4.	Effects of Non-Axisymmetric Magnetic Field on Characteristics of Non-Neutral Plasma .....	214
§5.	Development of High Beta Plasma Formation Using ICRF High Harmonic Fast Wave.....	215
§6.	Experimental Study of Compatibility of a Transport Barrier and Energetic Ion Confinement .....	216
§7.	Study of the Fueling Pellet Transportation in the Guiding Tube .....	217
§8.	Performance of Remote Steering Antenna in Anti-Symmetric and Symmetric Directions.....	218
§9.	Production Mechanism of D <sup>-</sup> Ions and Evaluation of D <sup>-</sup> Ion Current Extraction .....	219
§10.	Development of Continuously Size-Controllable Pellet Injector.....	220
§11.	Chaos Control of Fluctuations Caused by Flute Instability in ECR Plasma .....	221
§12.	Water Vapor Absorption for 48-, 57-, and 119- $\mu$ m Far-Infrared Laser Wavelength .....	222
§13.	Dynamics of Hydrogen Atoms and Molecule in the Periphery Plasma Studied by Means of Polarization Separated Spectra .....	223
§14.	Spectroscopy and Atomic Modeling of EUV Light from LHD Plasmas.....	224
§15.	Development of Wide Band and Compact X-Ray Spectrometer.....	225
§16.	Measurement of the Non-Parallel Flow Velocity Using a Mach Probe in Divertor-Simulating Weakly Magnetized Plasmas (NIFS04KOAB009) .....	226
§17.	Improvement of Plasma Performance by Strong ECH with High Power Gyrotron .....	227
§18.	Formation Mechanism and Transport of Dust Particles in the Divertor Plasmas.....	228
§19.	Development of Integrated Simulation Code for Helical Plasma Experiments.....	229
§20.	Study on Effects of Bending Strain to Critical Current Characteristics of Nb <sub>3</sub> Al CIC Conductors.....	230

§21.	14MeV-Neutron Beam Induced Change in Characteristics of Materials for Superconducting Magnets under 4.5 K .....	231
§22.	Development of New High Field and High Current Density Superconductors for Fusion Devices.....	232
§23.	Suitability of Boron-Titanium as First Wall Material.....	233
§24.	Measurement of the Negative Ion and Control of Recombination Plasma in the LHD Divertor .....	234
§25.	Kinetics of Hydrogen Isotopes at Surfaces and Bulks of Plasma Facing Materials Based on Group 5 Metals .....	235
§26.	Heat Removal Enhancement of Plasma-Facing Components by Using Nano-Particle Porous Layer Method.....	236
§27.	Investigation of Tritium Behavior and Tracability in In-Vessel Systems of LHD during D-D Burning.....	237
§28.	Assessment Study on Biological Effects of Radiation in LHD .....	238
§29.	Study on Environmental Behavior of Tritium .....	239
§30.	Experimental Study on Liquid Lithium Flow for IFMIF Target .....	240
§31.	Integrated Experimental Process Study for Removal of Tritium and Impurities from Liquid Lithium .....	241
§32.	Optimized Thermo-Mechanical Design of High Intensity Neutron Source Test Cell for Material Irradiation .....	242
§33.	Application of Advanced High Temperature Superconductors for Fusion Plasma Experimental Devices.....	243
§34.	Effects of Simultaneous Helium Irradiation on Hydrogen Behavior in Plasma Facing Materials .....	244
§35.	Development of Current Leads Combined with the Pulse-Tube Cryocooler .....	245
2.	Collaboration on Fusion Engineering .....	246
(1)	Fusion Engineering Studies .....	246
§1.	Development of the Fracture Toughness Test Method by Round Bar with Circumferential Notch.....	247
§2.	Retention and Desorption of Deuterium in Model Alloys of Ferritic Steel.....	248
§3.	Development of Reduced Activation Ferritic Steels with Improved Heat Resistance and Elemental Property Characterization for High Efficiency Water-Cooled Blankets .....	249
§4.	Small Specimen Test Techniques for IFMIF .....	250
§5.	Study on Radiation Induced Precipitates in Vanadium Alloys.....	251
§6.	Thermal Creep Mechanism of NIFS-Heat2 Alloys by Using Pressurized Creep Tubes .....	252
§7.	The Microstructure of Laser Welded V-4Cr-4Ti Alloy after Neutron Irradiation.....	253
§8.	Radiation Resistance and Mechanical Properties of Solution and Dispersion Hardened Vanadium Alloys with Fine Grains of High Purity Matrix .....	254
§9.	Development of Joint Technique of SiC/SiC Composites.....	255
§10.	Summary of Key Element Technology Verification and Preparation for Engineering Validation of Intense Neutron Source .....	256
§11.	Joining and Heat Load Test of Tungsten Divertor.....	257
§12.	Synthetic Evaluation of Ultra-Fine Grained, Nano-Particle Dispersed Tungsten Alloys as Plasma Facing Materials .....	258
§13.	Influence of Heating Rate on Subcooled Flow Boiling Critical Heat Flux in a Short Vertical Tube .....	259



§14.	Basic Study on Self-Healing of $\text{Er}_2\text{O}_3$ Coating for Vanadium-Lithium Blanket System.....	260
§15.	Investigation of Issues in Neutronics Evaluations for Advanced Liquid Blanket Systems .....	261
§16.	Examination of Irradiation Damage in Electrical Insulating Coating Using Ion Beam Irradiation .....	262
§17.	Development of Multi Layer Wall Channel to Reduce MHD Pressure Drop.....	263
§18.	Overall Characterization of High Purity Reference Vanadium Alloys NIFS-HEATs.....	264
§19.	Cryogenic Fatigue Delamination Growth in Material Systems for Superconducting Fusion Magnets .....	265
§20.	Thermal and Mechanical Properties of Composite Materials for Superconducting Coils .....	266
§21.	Development of V-Ti and V-Ti-Ta Superconducting Wires .....	267
§22.	Development of Low Activation Compound Superconducting Wires for Fusion Reactor .....	268
§23.	Large-Sized Cylindrical Superconductor Composed with Ni Meshes for a Current Lead.....	269
§24.	Effect of Test Equipment Configuration on Interlaminar Shear Fracture and Strength of Glass Fiber Reinforced Plastics.....	270
§25.	Transmutation of High-Level Wastes in a FLiBe-Cooled Spherical-Tokamak Reactor.....	271
(2)	Helical Reactor Design.....	272
§1.	Reactor Size Optimization of LHD-Type Reactor FFHR2m.....	273
§2.	Study on Position of Magnets and Supports for Heliotron-type Reactors ....	274
§3.	Study of the Fusion Power Rise-Up, Steady State, and Shutdown Scenarios in Helical Reactors.....	275
§4.	Development of a System Code for a Helical Fusion Reactor.....	276
§5.	Design Study of Indirect Cooling Superconducting Magnet for the Helical Reactor.....	277
§6.	Analysis of Tritium Fluoride Behavior and Recovery of Tritium in a Molten Salt Flibe Blanket .....	278
§7.	Feasibility of Helium Gas Turbine System for Molten Salt Blanket .....	279
§8.	Research on the First Wall Cooling Technique in a Flibe Liquid Blanket System .....	280
§9.	Heat Transfer Between Pebbles Considering Large Temperature Gradient Inside Pebble .....	281
§10.	Study on Heat Transfer Region for Fluid System in a Liquid Blanket.....	282
§11.	Design Study of the Electrical Power System for FFHR .....	283
§12.	Study on Vapor Shielding Effects under High Temperature and Particles for Nuclear Fusion Reactor .....	284
§13.	Burning Criteria for $\text{D}-^3\text{He}$ Reactor .....	285
(3)	Fusion Reactor System and Safety .....	286
§1.	Studies of Interaction between Cooling Pipe Materials and Tritium, and Their Chemical Behaviors.....	287
§2.	Advancement of Water-Hydrogen Chemical Exchange Apparatus by Introducing Trickle Bed Reactor.....	288
§3.	Development of Advanced Catalyst for Isotope Exchange Reaction Quantification of Reaction Rate .....	289
§4.	Development of High-Power Adsorbents for Hydrogen Isotope Separation by Pressure Swing Adsorption Method .....	290

§5.	Study on Polymer Membrane Type Dehumidifier for Tritium Removal.....	291
3.	CHS Experiments.....	292
§1.	Reheat Mode Discharges in Search of Attainable High Stored Energy of CHS .....	293
§2.	Observation of Overdense Plasma Heating by ECH Due to O-X-B Mode Conversion in CHS .....	294
§3.	First Observation of High Density Edge Transport Barrier Formation during Reheat Mode of Helical Plasma on CHS.....	295
§4.	Confinement of High Density Edge Transport Barrier during Reheat Mode on CHS.....	296
§5.	Comparison between Magnetic Configuration and Rotational Transform Profile during ETB formation on CHS.....	297
§6.	Edge Pedestal Structure Measured with CXS at a Horizontally Elongated Cross Section.....	298
§7.	Study of an Edge Transport Barrier by Langmuir Probes in the Compact Helical System .....	299
§8.	Impurity Measurements for Edge Transport Barrier Discharges in the Compact Helical System.....	300
§9.	Radial Phase Shift of the EHO Measured Using Beam Emission Spectroscopy in ETB Discharge in CHS (NIFS02KZPD003).....	301
§10.	HCN Laser Scattering Measurement of ETB-Formed Plasmas in CHS.....	302
§11.	Neutral Particle Transport in CHS Edge Region .....	303
§12.	Ion Internal Transport Barrier in CHS .....	304
§13.	Effect of Magnetic Configuration on Confinement Improvement of CHS Plasmas.....	305
§14.	Spectrograph of Electric Field Fluctuation in Toroidal Helical Plasma .....	306
§15.	The Density Profile Measurement with Heavy Ion Beam Probe System on CHS.....	307
§16.	Reconstruction Method of Local Density Fluctuation Spectrum with a Heavy Ion Beam Probe .....	308
§17.	Fluctuation Measurement of High Density Plasma using HIBP with Rb Ion Beam .....	309
§18.	Observation of Nonlinear Interaction between Coherent and Turbulent Magnetic Fluctuations on CHS .....	310
§19.	Measurements of Electron Density Fluctuations in CHS Plasmas by Using YAG Laser Imaging Method.....	311
§20.	Up-Down Asymmetry of the Plasma in the Ergodic Layer of CHS .....	312
§21.	Design and Initial Operation of Lost Fast-Ion Probe Based on Thin Faraday Films in CHS .....	313
§22.	Measurement of Energetic Ion Profile by Calorimetric Method.....	314
§23.	Formation of Peaked Density Profile in Dimensionally Similar Low Temperature Plasmas at Very Low Toroidal Magnetic Field on CHS .....	315
§24.	Measurement of Power Deposition Profile by Heating Power Modulation of 2.45 GHz Microwaves in CHS .....	316
§25.	Intermittent Transport of Particle and Heat in Scrape-Off Layer of Limiter and Divertor Configurations of CHS.....	317
§26.	Electron Heating and Plasma Production by Whistler Wave and Microwave Discharges in Low Toroidal Field .....	318
§27.	Radial Electric Field Control by Electron Injection in CHS.....	319
§28.	Study on the Mechanism of Collisionless Inward Penetration of Electrons via Stochastic Magnetic Region and Experimental Investigation of Energetic Electron Trap in Helical Magnetic Surface .....	320

§29.	Cotton-Mouton Polarimeter with the Use of HCN Laser .....	321
§30.	Installation of New 54.5 GHz Gyrotron to ECH System in CHS.....	322
§31.	Change of Effective Anode Area in Neutral Beam Injector for Compact Helical System .....	323
§32.	CHS Data Acquisition and Analysis System .....	324
4.	Basic Research and Development.....	325
§1.	High Density Plasma Experiment HYPER-I .....	326
§2.	Radial Force Balance in Plasma Hole and Anomalous ExB Drift Solution .....	327
§3.	Measurements of Neutral-Gas Flow in High-Density Plasma Using a Tunable Laser Diode .....	328
§4.	Measurement of Rotational Flow Velocity Using Laser-Induced Fluorescence Spectroscopy .....	329
§5.	Plasma Flow Measurement using Facing-Double Probe .....	330
§6.	Coefficient of Ion Sensitive Probe for Ion Temperature Measurement .....	331
§7.	Excited Atomic Processes as Fundamental Researches for New Plasma Diagnostic .....	332
§8.	Study of the Excitation Processes in Electron-Ion Collisions.....	333
§9.	Isotope Effect on Charge Transfer by Slow Lithium Ions from Hydrogen Molecules .....	334
§10.	Measurement of EUV Out-of-Band Spectra in Laser Produced Sn Plasmas.....	335
§11.	Theoretical and Experimental Studies on the Contribution of Wave-Particle Interactions to Radial Transport in a Strongly Magnetized Non-neutral Plasma.....	336
§12.	Study on Spatio-Temporal Structure of Bistable Density Transition .....	337
§13.	Basic Process of Solid Hydrogen Ablation by Means of Pellet Injection Apparatus with Changeable Size .....	338
§14.	Production of Ions and Radicals in H <sub>2</sub> ECR Plasma with Controlled Electron Temperature.....	339
§15.	Plasma-Quenching Efficiency of Molecular Gas Inclusion on Temperature of Ar Induction Thermal Plasmas.....	340
§16.	High Efficiency RF Induction Plasma Generation.....	341
§17.	Experimental Study of Current Drive Using Nernst Effect .....	342
§18.	Particle Reflections of Low Energy Light Ions from a Polycrystalline W Surface.....	343
§19.	Experimental Study of Plasma Loaded Cyclotron Resonance Maser Using TPD-II Machine at NIFS .....	344
§20.	Effects of $1/\nu$ Ripple Diffusions on the Parallel Viscosity and Bootstrap Current.....	345
5.	Theory and Computer Simulation Project.....	346
§1.	Axisymmetric Toroidal Equilibrium with Flow in an Extended MHD Model .....	348
§2.	Properties of Ballooning Modes in the Planar Axis Heliotron Configurations with a Large Shafranov Shift.....	349
§3.	The 2nd Stability of Ballooning Modes in the Inward-shifted LHD Configurations.....	350
§4.	Nonlinear Evolution of 3D MHD Instability in LHD.....	351
§5.	MPI Parallelization of MEGA Code for Helical Plasmas.....	352
§6.	Nonlinear MHD Effects on the Alfvén Eigenmode Evolution .....	353
§7.	Simulations of Alfvén Eigenmodes with an Extended Ohm's Law .....	354
§8.	Motion of Ablation Cloud in Torus Plasmas .....	355

§9.	Nonlinear Three Dimensional Simulation of Current-Driven Resistive Wall Mode.....	356
§10.	Multi-Scale-Nonlinear Interactions among Micro-Turbulence, Magnetic Islands, and Zonal Flows.....	357
§11.	Extension of Gyrokinetic-Vlasov Simulation for Helical Systems.....	358
§12.	Releasing of Spherical Conducting Dust Particle from Plasma-Facing Wall under Biased Potential.....	359
§13.	Effect of Gravity on Releasing of Spherical Conductive Dust Particle from Plasma-Facing Wall .....	360
§14.	Electrostatic Potential due to Induced Charge of Spherical Dust in Non-Uniform Electric Field .....	361
§15.	Rate Coefficient of Electron Impact Ionization for Electron Truncated Maxwellian Distribution – Single Electron Temperature – .....	362
§16.	Rate Coefficient of Electron Impact Ionization for Electron Truncated Maxwellian Distribution – Double Electron Temperature –.....	363
§17.	Core-SOL-Divertor Model Based on JT-60U Recycling Database and Application to EAST Operation Space .....	364
§18.	Self-Consistent Computation of Radiation Transfer in Edge Plasmas Based on Collisional Radiative Model and Neutral Transport Model.....	365
§19.	Three-Dimensional Particle-in-Cell Simulation of Blob Transport.....	366
§20.	Edge Plasma Simulation for Stellarator System with 2D Transport Code UEDGE .....	367
§21.	Integrated Simulations for Fast Ignition with Cone-Guided Targets.....	368
§22.	Formation of Non-Maxwellian Distribution and Its Role in Collisionless Driven Reconnection.....	369
§23.	Improved Upstream Boundary Condition for PASMO .....	370
§24.	Mass Ratio Dependence of Drift Kink Instability in the Current Sheet .....	371
§25.	Development of 3D MHD Simulation Code for Magnetic Reconnection in an Open System .....	372
§26.	Real-Time Earth Magnetosphere Simulator with 3-Dimensional MHD Code .....	373
§27.	Simulation of Interplanetary Shock Wave Caused by CME on August 25, 2001 .....	374
§28.	Three-Dimensional Simulation Study of Flux Rope Dynamics in the Solar Corona.....	375
§29.	Jet Formation Driven by Magnetic Bridges between Ergosphere and Disk Around Rapidly Rotating Black Hole .....	376
§30.	Analysis of the Energy Transfer in NS and MHD Turbulence by Using Massive DNS .....	377
§31.	Multifractal Characterization of L- and H-mode Plasma Edge Turbulence.....	378
§32.	A Signature of Wave Collapse in the GNLS Model of Plasma Turbulence.....	379
§33.	Low-Frequency Instabilities Due to Flow Velocity Shear in Magnetized Plasmas.....	380
§34.	Molecular Dynamics Simulation for Structure Formation of a Single Polymer Chain in Solution: Local Orientational Correlation .....	381
§35.	Three Processes of the Reaction between a Hydrogen Atom and Graphene .....	382
§36.	Quantum Nernst Effect.....	383
§37.	A Complementary Fluid Method in $\delta f$ Particle Simulation .....	384

§38.	A Primal Coarse-Projective Integration Scheme in Multi-Scale Plasma Dynamics.....	385
§39.	Orthonormal Divergence-Free Wavelet Analysis of Nonlinear Interactions in a Rolling-Up Vortex Sheet.....	386
§40.	A Glassless Stereo-Type Visualization System for 3D MHD Real-Time Earth's Magnetosphere Simulator.....	387
§41.	Construction of Seamlessly Integrated System between Virtual Environment and Numerical Simulation Environment.....	388
6.	Personal Interchange Joint Research Program.....	389
§1.	Electron Bernstein Wave Heating by Long Wavelength Microwave in a Spherical Tokamak and a Helical Device .....	392
§2.	Assessment on Fusion Energy Development from the Socio-Economic Viewpoint.....	393
§3.	Ion Heating and Acceleration in a Supersonic Plasma .....	394
§4.	Higher-Harmonic Oscillation of Peniotron .....	395
§5.	Clarification on Cooling Mechanism of Stirling Type Pulse Tube Cryocooler.....	396
§6.	Study on Various Atomic Processes of Impurity Highly Charged Ions by Versatile Ion Sources .....	397
§7.	Study on Purification and Compatibility of Structural Materials with Molten Salt Breeder .....	398
§8.	Analysis of $J_c$ Properties in High Magnetic Fields for Low Activation Superconducting Wires .....	399
§9.	Experimental and Theoretical Studies of Startup Methods for Spherical Tokamak Plasmas.....	400
§10.	Advanced Large-Scale Simulation on Fusion Plasmas by Using the Earth Simulator .....	401
§11.	Heating and Current Drive Experiments on the TST-2 Spherical Tokamak.....	402
§12.	Degradation of Nb <sub>3</sub> Sn Superconducting Cable Due to Mechanical Stress .....	403
§13.	Magnetic Island Effect on Radial Particle Flux in TU-Heliac.....	404
§14.	ECH Plasma Experiments with an Internal Coil Device Mini-RT .....	405
7.	Collaborations Using Super SINET .....	406
§1.	Reconstruction of the Network for Collaboration using Super-SINET .....	408
8.	Fusion Science Archives .....	409
§1.	NIFS Fusion Science Archives Database and Studies on the Problems Related to Its Disclosure .....	410
§2.	Complementary Study of Nuclear Fusion Archiving by Means of Oral History .....	411
§3.	The Role of Inter-University Institute for Nuclear Fusion Research in Early Period.....	412
§4.	Archival Studies on the Nuclear Fusion Research from Chronological Aspect.....	413
§5.	Research on History of Fusion and Plasma Research Devices .....	414
§6.	The Chronology on the International Exchange of Nuclear Fusion Study .....	415
§7.	US-Japan Workshop on Fusion Science Archives .....	416
9.	Coordination Research Center .....	417
§1.	Helium Ash Removal by Moving-Surface PFCs .....	419
§2.	How to Product, Use, and Export Photovoltaic Power in Developing Countries .....	420

§3.	Development of Cryogenic Foam Target with Guide Cone for FIREX-I ....	421
§4.	Activities on ITER Collaboration .....	422
§5.	3D Edge Transport Analysis of ITER Start-Up Configuration for Limiter Power Load Assessment .....	423
§6.	Microwave Heating of Water, Ice and Salt Solution: Molecular Dynamics Study .....	424
§7.	Destruction of an Intense Laser-Irradiated Fullerene Molecule: Ab initio (First-Principle) Molecular Dynamics Study .....	425
§8.	Ab initio Molecular Dynamics Study of Graphite Erosion and Formation of Hydrocarbon Molecules by Absorption of Many Hydrogen Atoms .....	426
§9.	Experimental Analysis for Thermally Non-Equilibrium State Under Microwave Irradiations: A Greener Process for Steel Making .....	427
§10.	Observation of the Temperature-Jump of the Sample during Microwave Iron Making.....	428
§11.	Carbon Ion Emission Lines during Radiation Collapse in LHD.....	429
§12.	EUV Spectra of Xe Ions Measured from LHD for Study of High Z Ion Emission.....	430
§13.	Identification of Resonance Excitation Double-Autoionization of Li-like Iodine Ions.....	431
§14.	Dielectronic Recombination Rate Coefficients to Excited States of Mg-like Fe and Dielectronic Satellite Lines .....	432
§15.	Recommended Data on Proton-Ion Collision Rate Coefficients for Fe X – Fe XV and Fe XVII – Fe XXIII Ions .....	433
§16.	Evaluation of Electron Impact Excitation Rate Coefficients for Fe M-shell Ions .....	434
§17.	Development of a Collisional-Radiative Model of Oxygen Ions for Plasma Diagnostics .....	435
§18.	Analysis of CV Spectral Lines and the Emitting Location in LHD Plasma .....	436
§19.	Cluster of Mono-Vacancy and Hydrogen Atoms in Ferritic Iron.....	437
§20.	Temperature Effect on Charge Transfer and Ionization in Collisions of H <sup>+</sup> Ions with Hydrocarbon Molecules.....	438
§21.	LHD Simulated Experiment for Solar Non-Equilibrium Plasmas and Development of Its Spectroscopic Diagnostic Tools .....	439
§22.	Plasma Diagnostics of Fe Ion Spectra for Solar-B and LHD.....	440
§23.	Network of Atomic and Molecular Database Related the Processing Plasmas.....	441
§24.	Atomic and Molecular Data Compilation and Update of the NIFS Databases for Molecular Targets .....	442
§25.	New System of Differential Cross Section Databases .....	443
§26.	Study of Evolutional Data Collecting System for the Atomic and Molecular Databases .....	444
§27.	Private Tutoring Academy KENZAIJUKU Started.....	445
§28.	EUV Spectra by Xe <sup>q+</sup> + Xe Charge Transfer .....	446
10.	Fusion Engineering Research Center .....	447
§1.	Neutronics for Li/Vanadium-alloy and Flibe/Vanadium-alloy Blanket Systems .....	449
§2.	Development of 3-D Neutronics Calculation System for Helical Reactor Design .....	450
§3.	Fabrication of Erbium Oxide Coatings by Arc-Source Plasma Deposition Device for Vanadium-Lithium Blanket System.....	451



§4.	The Structural Stability and Growth Process of $\text{Er}_2\text{O}_3$ In-situ Coating on V-4Cr-4Ti.....	452
§5.	Activation Experiment with D-T Neutrons on Materials Relevant to Liquid Blankets .....	453
§6.	Impurity Behavior in V-4Cr-4Ti-Y Alloys Produced by Levitation Melting .....	454
§7.	Creep Property of NIFS-Heat-2 Alloy Strengthened by Precipitation and Cold Rolling .....	455
§8.	Temperature Effect on Strain Hardening and Fracture Mode of JLF-1 Steel under Static Plastic Deformation .....	456
§9.	Compatibility of Low Activation Ferritic Steels with Liquid Lithium .....	457
§10.	Irradiation Effect of 14 MeV Neutron on Interlaminar Shear Strength of Glass Fiber Reinforced Plastics .....	458
§11.	Annealing Effect on Microstructure and Superconductivity of V-based Laves Phase Compound Wires through a RHQ Process.....	459
11.	Safety and Environmental Research Center .....	460
§1.	Measurement Error of Radiation Monitoring by Means of an Electronic Dosimeter .....	461
§2.	Design of an Integrating Type Neutron Dose Monitor .....	462
§3.	Sensitivity of TLD and RPLD to Cosmic Ray Hard Component Measured in Ogoya Tunnel.....	463
§4.	Consideration of Measuring Tritium Concentration in Air Using Gas Chromatograph.....	464
§5.	Chemical Reaction Equation of Water Vapor Decomposition on a Zirconium-Nickel Alloy.....	465
§6.	Performance Test of Direct Immersion Method to Detect Tritium in Concrete .....	466
§7.	Theoretical Expressions for Removing Tritium from Exhaust Gas.....	467
§8.	Characteristics of Honeycomb Catalysts for Oxidation of Tritiated Hydrogen and Methane Gases .....	468
§9.	Entrainment Behavior of Activated Dust in Accidental Event .....	469
§10.	Development of Exhaust Gas and Effluent Liquid Treatment System for LHD.....	470
§11.	Development of Proportional Counter to Measure Tritium in Atmospheric Air.....	471
§12.	Environmental Atmospheric Tritium Monitoring with Discriminate Sampling of Different Chemical Forms .....	472
§13.	A Simplified Method for Tritium Measurement in the Environmental Water Samples .....	473
§14.	Field Measurement in Hi-Level Multiple Source EM Environment .....	474
§15.	Measurements of Static and Variable Magnetic Fields in a Large Plasma Experimental Facility .....	475
12.	Computer and Information Network Center .....	476
13.	Bidirectional Collaborative Research Program.....	480
§1.	Study of Potential Confinement Mechanism via Plasma Visualization Technology.....	481
§2.	Study of Impurity Ion Radiation Intensity in the GAMMA 10 Plasma.....	482
§3.	ICRF Wave Excitation and Propagation in the GAMMA 10 Tandem Mirror .....	483
§4.	Development of High Performance Antennas for Electron Heating in GAMMA 10.....	484

§5.	Propagation and Radiation of Cyclotron Waves and Excitation of Fluctuations Due to High Power Plug ECRH.....	485
§6.	ICRF Heating and Ion Acceleration at the Open End in GAMMA 10.....	486
§7.	Plasma Polarization Spectroscopy on GAMMA10 Tandem Mirror Plasma .....	487
§8.	Excitation of RF Waves in GAMMA 10 and in the Local Magnetic Mirror Configuration on LHD.....	488
§9.	Comprehensive Study of Relationship between Electron Distributions and Performances of Microwave and Mirror Devices .....	489
§10.	Study of Radial Transport of Bounce Ions by Use of a Lithium Beam Probe Method .....	490
§11.	Cross Correlation Measurement between Density and Potential Fluctuations in a Tandem Mirror for the Purpose of Radial Transport Control.....	491
§12.	Analysis of Neutral Particle Transport and Recycling Behavior in Open Magnetic Field Configuration Plasmas .....	492
§13.	Progress in Potential Formation and Radial-Transport-Barrier Production for Turbulence Suppression and Improved Confinement in GAMMA 10 .....	493
§14.	Initial Results of CUSPDEC Applied to the GAMMA 10 Tandem Mirror .....	494
§15.	Effects of Non-Axisymmetric Magnetic Field on Characteristics of Axisymmetric Cusp DEC.....	495
§16.	The Observation of the Negative Toroidal Current in Heliotron-J .....	496
§17.	ICRF Heating Experiment in Heliotron J.....	497
§18.	Hard X-Ray Diagnostic by Use of CdTe Detector in Heliotron J.....	498
§19.	Evaluation of Boozer Coordinates Based on the Field Line Tracing Approach .....	499
§20.	Study of Neutral Hydrogen Atom and Impurity Behaviors in Heliotron J III-2 .....	500
§21.	Optimization of Helical System Concept.....	501
§22.	Study of Peripheral Plasma in Heliotron J Using Fast Camera .....	502
§23.	Study on Neutral Particle Transport in Non-Axisymmetric Helical Plasmas.....	503
§24.	Study on Tritium Behavior in Liquid Blanket System of Laser Inertial Fusion Reactor .....	504
§25.	Aerosol Formation and its Effects on the Chamber Wall Lifetime and Operation of IFE Power Reactors .....	505
§26.	Surface Wave Structure of Vertical Liquid Film Flow with Artificial Oscillation .....	506
§27.	X-ray Penumbral Imaging for Laser-Produced Plasma –Uniformly Redundant Penumbral Array– .....	507
§28.	Design Study on Foam-Cryogenic Targets by Integrated Simulations.....	508
§29.	Natural Diamond Detector for Neutron and $\gamma$ -ray Measurements in Laser Fusion Experiments.....	509
§30.	Development of Gas Gun for Target Injection in Laser-Fusion Reactor.....	510
§31.	Preliminary Study of Chamber Engineering for Fast Ignition Laser Fusion Reactor .....	511
§32.	IFE Reactor Chamber Wall Ablations with Intense Particle and Laser Beams.....	512



§33.	Establishment of Material Database Including High Temperature Irradiation Effect and Material Design of SiC/SiC Composites for Inertial Fusion Dry Wall Chamber.....	513
§34.	Development of Coil Gun for Fast Ignition .....	514
§35.	Researches on Compression and Heating of Cryogenic Target and Related Physics .....	515
§36.	X-ray Imaging in Fast Ignition Fusion Experiments —An ICA based Poisson-Noise Reduction Algorithm—.....	516
§37.	Neutral Particle Behavior in the Edge Plasma of TRIAM-1M Tokamak Measured Using Zeeman Spectroscopy (NIFS04KUTR001).....	517
§38.	Start-Up and Sustainment of Spherical Tokamak by ECH/ECCD .....	518
§39.	Experimental Study of Compact Plasma Wall Interaction Experimental Device (CPD) .....	519
§40.	Modeling of Global Particle Balance and Plasma-Surface Interactions in TRIAM-1M .....	520
§41.	Active Control Over Wall Recycling in a Spherical Tokamak: CPD by a Moving-Surface PFC .....	521
§42.	Compact Toroid Injection into Spherical Tokamak Plasmas in the Small PWI Device .....	522
§43.	Generation of Runaway Electrons by Electron Cyclotron Wave Heating during Current Disruption of TRIAM-1M Tokamak.....	523
§44.	Design Study of Long-Pulse NBI for the Plasma Boundary Dynamics Experimental Device.....	524
§45.	Development of Two-Dimensional Lithium Beam Probe for Edge Density Measurement in CPD.....	525
§46.	Integration of PWI Experiments, Diagnostics, Simulation and Modeling in Steady State Plasma .....	526
§47.	Current Drive and Heating Experiments using RF/mm-Waves on the TRIAM-1M Tokamak.....	527
§48.	Dust Measurement in TRIAM-1M using Fast Camera.....	528
§49.	Neutral Particle Transport in Steady-State Torus Plasmas .....	529
§50.	Construction and Development of Long Term Sustained Spherical Tokamak “QUEST” in Kyushu University.....	530
§51.	Development of an Ion Beam Source for a Low Voltage / High Current Neutral Beam Injector .....	531
§52.	Organization of the All-Japan ST Research Group.....	532
14.	Public Relations Office .....	533
15.	Research Information Office .....	534
III.	International Collaboration .....	535
1.	US – Japan (Universities) Fusion Cooperation Program .....	537
2.	TEXTOR Collaboration .....	540
3.	International Collaboration on Helical Fusion Research — IEA Stellarator Agreement —.....	542
4.	JSPS-CAS Core-University Program on Plasma and Nuclear Fusion.....	558
IV.	Department of Engineering and Technical Services.....	564
V.	Department of Administration .....	577
APPENDIX 1.	Organization of the Institute.....	580
APPENDIX 2.	Members of Committees .....	581
APPENDIX 3.	List of Staff .....	582
APPENDIX 4.	List of Publications I (NIFS Series).....	589
APPENDIX 5.	List of Publications II (Journals, etc.) .....	591
Author Index	.....	606

How to Reach National Institute for Fusion Science.....	615
---	-----

# **I. National Institute for Fusion Science in April 2005 – March 2006**

This annual report summarizes the research activities at NIFS between April 2005 and March 2006. NIFS is pursuing the integration of science and technology to realize a fusion power plant. The systematization of plasma physics, and research and development of reactor relevant engineering are key elements in our strategy. NIFS has been exploiting its role as an inter-university research organization and executing a variety of excellent collaborating studies together with universities and research institutes abroad as well as in Japan.

The main missions of NIFS are (i) the experimental study of toroidal plasma confinement using LHD and (ii) theoretical research and computer simulations for the study of the complex state and nonlinear dynamics such as those seen in high temperature plasmas. These major projects are accompanied by unique supporting research. Advanced engineering and fusion reactor design studies are strongly promoted.

The LHD is a heliotron type device with an intrinsic divertor. It is the largest superconducting fusion device in the world. The major goal of the LHD experiment is to demonstrate the high performance of helical plasmas in a reactor relevant plasma regime. Thorough exploration should lead to the establishment of not only a prospect for a helical fusion reactor but also to a comprehensive understanding of toroidal plasmas. We completed the 9th experimental campaign in FY2005. Diversified studies in LHD have elucidated the broad scope of steady-state high temperature plasmas.

The plasma parameters as well as physical understanding have been progressing steadily since the beginning. The most highlighted achievement in the last experimental campaign in FY2005 is the discovery of Super-Dense-Core plasma operation accompanied by an *Internal Diffusion Barrier*. A synergetic effect of highly efficient pumping by means of the Local Island Divertor and core fueling by repetitive pellet injection generates the SDC mode with a central density of  $5 \times 10^{20} \text{m}^{-3}$ . A steep gradient in the density profile is formed by a drastic improvement in particle transport, i.e., IDB. This observation has been done by Prof. N.Ohyabu and A.Komori, and their colleagues, which is exploring high density and low temperature reactor core concept operation with more than  $5 \times 10^{20} \text{m}^{-3}$  and less than 10keV. This finding has an important meaning equivalent or more important than that of H-mode by Prof. F.Wagner in 1982. It has been said that a helical plasma has an advantage of high density operation and the discovery of the IDB emphasizes this advantage much more than expected. Long pulse operation by means of ion cyclotron resonant heating (ICRH) has shown progress. The pulse length has been prolonged to close to one hour (precisely 3268 s) with a heating power of 500 kW. The total input energy for this discharge reached 1.6 GJ which is a world record in magnetic confinement experiments. High beta discharges also have been advanced by exploration of aspect-ratio control and consequently a beta of 4.5 % has been achieved.

LHD produced about 10,000 plasma discharges in FY2005. This high availability of experimental opportunities has indicated a large potential to enable a variety of approaches for scientific research, which is not limited to fusion science in a narrow sense. These activities are made possible by the reliable operation of the superconducting facility. Much effort to improve the cryogenic stability has led to the successful R&D results of the pool-boiling of helium by the sub-cooling modification. A consequent upgrade of the helical coil cooling system is scheduled in 2006 as one of the performance improvement plans of LHD.

A satellite experimental project, CHS, has been shut down as of fiscal year 2005. CHS has completed its unique role while leaving many important achievements with regard to internal transport barrier, zonal flow, H-mode, etc. Innovative results from CHS will be

extended by LHD in a more advanced manner.


Simulation studies in NIFS are organized towards the exploration of “Simulation Science” while remaining founded in the large-scale simulation of fusion plasmas such as LHD. With the progress of computer performance, the paradigm shift of methodology is progressing from the classical scheme of reduction to the elements, to the integration of various interconnecting physics with different time-space scales. This methodology promises to lead to an understanding of the whole structure of natural phenomena. On the way from macro to micro scales, for example, the properties of equilibria with micro-scale effects such as the Hall term, pressure anisotropy, electron inertia, and wave-particle interaction are investigated, in order to understand the basis of extended MHD and consider the closure problems of fluid equations. This is the successful output of the numerical multi-layer re-normalization. Besides sophisticated studies on magnetic fusion plasmas, a variety of theoretical and simulation studies including inertia fusion plasmas, astronomical plasmas and molecular dynamics have progressed steadily.

The fusion engineering research center has extended the advanced key-technology for a blanket system, low activation materials and superconducting magnet systems. These activities are closely related to a design study on the Force Free Helical Reactor. The properties of Flibe and vanadium alloys are being intensively investigated.

A variety of coordinated research is managed by the coordinated research center. The three major activities are coordinated research with industries and with other institutions in NINS, and an atomic and molecular database. These activities can be the seeds and rhizomes for interdisciplinary evolution originating from fusion science.

These research activities are integrated into three kinds of collaborating frameworks with their own distinguishing features. The framework of general collaboration research covers a wide spectrum of studies on fusion. The Large Helical Device (LHD) program collaboration research has facilitated participation in the LHD project based on the achievements in universities. The bilateral coordinated collaboration research promotes mutual interaction on an equal footing with annexed research institutes of the universities. More than 400 collaborating studies have been implemented during the covered period. In conjunction with the logistics to methodically support these three kinds of collaboration frameworks, the environment and infrastructure for efficient collaboration is being improved continuously.

Lastly, NIFS conducts several international collaboration programs, such as the US-Japan Fusion Cooperation Program, TEXTOR Collaboration and International Collaboration on Helical Research based on the IEA agreement. NIFS plays an important role as a COE in fusion science on a worldwide scale.



Osamu Motojima  
Director-General  
National Institute for Fusion Science

## II. Research Activities

### 1. Large Helical Device (LHD) Project

#### 1-1. LHD Experiment

##### (1) Overview of LHD Experiment

During the 9<sup>th</sup> campaign, we have made significant progress in three areas, a discovery of an improved confinement mode (super dense core plasma mode), a long pulse discharge with nearly an hour duration and achievement of the average beta of 4.5 %. We discovered the new improved confinement mode, the **Super Dense Core (SDC)** mode in diverted discharges in the Large Helical Device (LHD). A **SDC** plasma develops naturally in LHD as a peaked, high density profile is generated by multiple pellet injections from the outside mid-plane as illustrated in Fig.1-a. The density and temperature profiles are shown in Fig. 1-b for a typical SDC discharge ( $R_{ax}=3.75$  m,  $B = 2.64$  T,  $P$  (NBI power input) = 10 MW). They are measured by a Thomson scattering diagnostic along  $R$ , the major radius, in the poloidal plane, where the plasma is horizontally elongated (Fig. 1-a). A core region with electron densities  $\sim 4.5 \times 10^{20} \text{ m}^{-3}$  and temperatures  $\sim 0.85$  keV is maintained by an **Internal Diffusion Barrier (IDB)** located at normalized minor radius  $\rho \sim 0.5$ . The SDC discharges exhibit the highest fusion plasma performance achieved so far on LHD,  $n_0 \tau_E T_0 \sim 4.4 \times 10^{19} \text{ keV m}^{-3} \text{ s}$ , despite a  $\sim 40$  % reduction in effective confinement volume (due to the LID) from standard HD discharges.

The radial width of the IDB is  $\sim 0.1$  m ( $\Delta \rho \sim 0.2$ ). Inside the SDC region, the density and temperature gradients are small. The temperature gradient in the outer region is determined by anomalous thermal diffusivity. We find that the observed  $T_e(0)$  and edge  $T_e$  gradient increase with  $P/n_{edge}$ . And thus lowering  $n_{edge}$  leads to higher edge  $\nabla T_e$  and  $T_e(0)$ . The density gradient outside the IDB behaves as usual with  $n \sim 6 \times 10^{19} \text{ m}^{-3}$  at the last closed flux surface ( $\rho = 1$ ). After the termination of a sequence of pellet injection,  $n(0)$  decays slowly with a time constant of  $\sim 1$  s for the  $B = 2.64$  T case, indicating that the diffusion coefficient in the IDB is a very small value, less than  $\sim 0.02 \text{ m}^2 \text{ s}^{-1}$ .

SDC plasma does not appear in discharges fueled by gas puffing alone because edge recycling results in a flat or slightly hollow density profile. The use of the LID increases

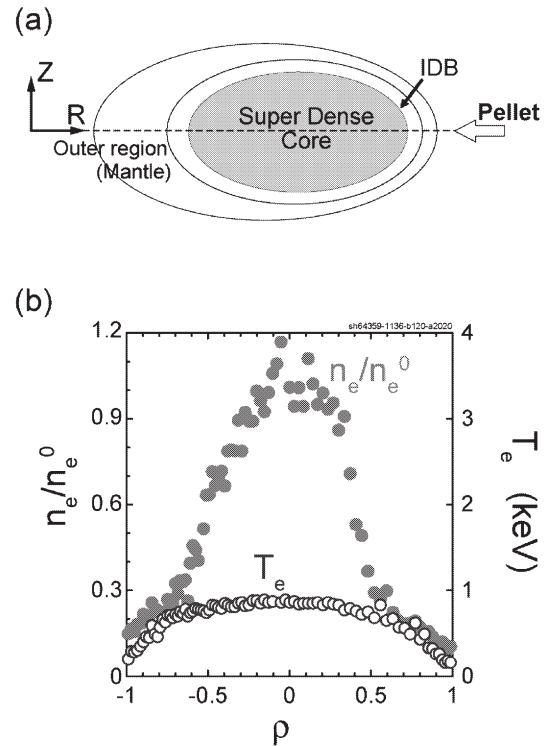


Fig.1 (a) Illustration of the Super Dense Core plasma configuration (b) Density and temperature profiles of an SDC discharge with  $R_{ax} = 3.75$  m are depicted. The density normalization factor  $n^0 = 4.5 \times 10^{20} \text{ m}^{-3}$ ,  $P = 10$  MW.

the pumping of edge-recycled particles and maintains a low edge density and hence high edge electron temperature gradients. In a helical device, the average density is limited by the so called Sudo scaling. It is believed that the edge density is actually what is limited. If so, the core density can be very high for the peaked profile case such as shown in Fig.1-b. Indeed the core density in the SDC discharge is three times the average density predicted by the Sudo scaling.

Steady state plasma operation experiment was carried out as one of the mission in the 9th cycle experimental campaign. The longest plasma discharge was obtained at the



last shot of the campaign. The discharge duration was 54 minutes and 28 seconds. The total injected heating energy reached 1.6 GJ. The time evolutions of the plasma parameters are shown in Fig.2. The plasma was mainly sustained by an ICRF heating of 380 kW in average power and an ECH power of 110 kW was injected as an assist. Sparks were observed in the vacuum vessel during the long pulse discharge. Intensive sparks causes the plasma collapse and correlate with the ICRF power. Then, the long plasma discharge was realized by the fine control of the ICRF power with monitoring the sparks. Helium plasma mixed with the hydrogen minority ions was used for the minority heating of the ICRF heating scheme. A line-averaged electron density was  $0.4 \times 10^{19} \text{ m}^{-3}$  and the central ion and electron temperatures were about 1 keV. The operation method of the magnetic axis sweep was adopted to scatter the heat load on the divertor plates. The temperatures at the divertor plates saturated during the discharge and the maximum temperature increase was less than 300 °C. The discharge was terminated by influx of iron impurity and thus the most critical issue for achievement of further longer pulse discharge is to overcome the problem caused by the heavy impurity influx.

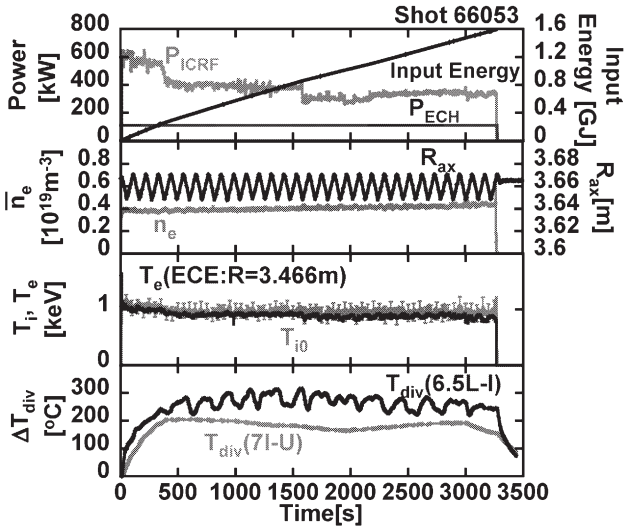


Fig. 2. Time evolution of plasma parameters in the long pulse plasma discharge. An injected heating energy of 1.6 GJ was achieved.

In LHD, the production of high beta plasma has progressed successfully with increasing heating power of neutral beam. In recent experiments, a scan of plasma-aspect-ratio,  $A_p$ , was mainly performed from 6.3 to 8.3 to investigate the configurational dependence of MHD characteristics of high-beta plasmas. An increment of  $A_p$  causes an increase in the central rotational transform and reduces the Shafranov shift. Large  $A_p$  is favorable for a heating efficiency and a transport because the outward shift

of the magnetic axis leads to an increase in a helical ripple loss of particles. It is also suitable for raising an equilibrium beta-limit. However, a reduction of the plasma shift restricts spontaneous formation of magnetic well, and an increment of  $A_p$  reduces magnetic shear. Consequently, violation of MHD stability is concerned. The survey of the optimum operation provided the highest  $\langle \beta_{\text{dia}} \rangle$  value of 4.5 % at  $A_p = 6.6$ , and achieved  $\langle \beta_{\text{dia}} \rangle$  gradually decreases with an increment of  $A_p$ .

Figure 1 shows the typical discharge with  $\langle \beta_{\text{dia}} \rangle = 4.5\%$  in the  $A_p = 6.6$  configuration. The plasma with  $\langle \beta_{\text{dia}} \rangle > 4\%$  was maintained for  $10\tau_E$  or more. Shafranov shift  $\Delta a_{\text{eff}}$  is around 0.2, which is much smaller than equilibrium beta-limit. Peripheral MHD activities, which are dominantly observed in the high-beta regime, are enhanced, whereas  $m/n = 1/1$ ,  $2/3$  and  $1/2$  modes were suppressed and/or intermittently behaved when the  $\langle \beta_{\text{dia}} \rangle$  exceeds around 4 %. Although the  $m/n = 2/5$  mode where the resonance is located near plasma edge remained in the beta range over 4%, the amplitude on the resonance is relatively small compared with other modes. This tendency has been well observed in the high-beta regime and then profile flattening in the vicinity of the resonances occurs

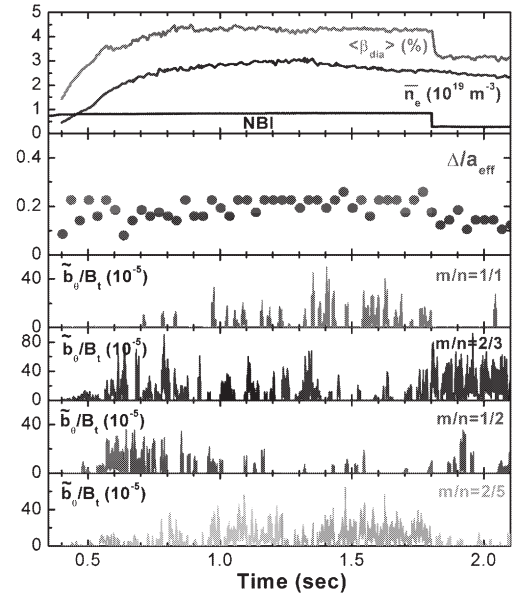


Fig.3 Typical MHD activities in high-beta discharges in  $A_p = 6.6$  configuration.

(Komori, A.)

## (2) LHD Physics Experiments

### §1. Superdense Plasma in LHD

Morisaki, T., Masuzaki, S., Kobayashi, M., Ohyabu, N., Komori, A.

In reduced recycling discharges using a Local Island Divertor (LID) in the Large Helical Device (LHD), a stable superdense plasma develops spontaneously when a series of pellets are injected.<sup>1)</sup> Figure 1 represents the time evolution of the discharge. Oscillations in the wave form correspond to each pellet injection. A core region with  $\sim 4.5 \times 10^{20} \text{ m}^{-3}$  and temperature of 0.85 keV is maintained by an Internal Diffusion Barrier (IDB), as shown in Fig.2 with closed circles. The density gradient at the IDB ( $r/a \sim 0.6$ ) is very high, and the particle confinement time in the core region is  $\sim 300 \text{ ms}$ . The temperature profile inside the IDB ( $r/a < 0.6$ ) is flat, on the other hand, its gradient in the outer region is steep. Because of the increase in the central pressure, a large, stabilizing Shafranov shift is observed. In the discharge shown in Fig.2, the shift is about 0.3 m. The critical ingredients for IDB formation are a strongly pumped divertor to reduce edge recycling, and multiple pellet injection to ensure strong central fueling. Low density in the outer region helps to raise the edge temperature gradient there and hence the core temperature. Gas puffing results in broad, flat or slightly inverted density profiles, and does not lead to formation of a superdense plasma. In that sense, for the strong pumping, it does not take an LID to reduce the edge recycling. If a conventional Helical divertor (HD) has sufficient pumping capability, similar discharges can be achieved in the HD configuration. The electron density and temperature profiles depicted in Fig.2 with open circles are observed in the HD configuration under exhaustive wall conditioning. It is found that two profiles with different divertor configurations represent almost the same shapes and values. This result suggests that the closed HD configuration with baffles is effective to realize superdense plasma.

Although use of the island divertor reduces the confinement volume by  $\sim 30 \%$  from its nominal value, superdense LID discharges exhibit the highest performance ( $n_0 T_0 \tau_E = 4.4 \times 10^{19} \text{ m}^{-3} \cdot \text{keV} \cdot \text{s}$ ) obtained so far in LHD. These plasmas provide unique opportunities for exploration of high-beta MHD stability in heliotron/stellarator configurations, and may extrapolate to a novel scenario for fusion ignition at very high density and relatively low temperature.

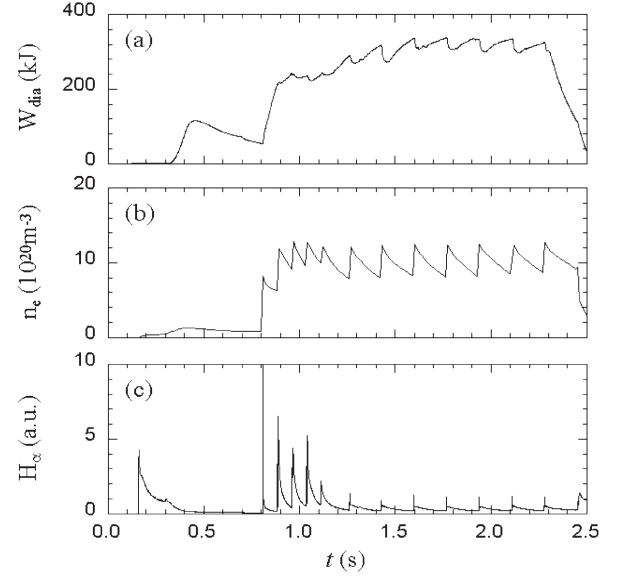


Fig. 1. Time evolutions of (a) stored energy  $W_{\text{dia}}$ , (b) line averaged density  $n_e$  and (c)  $H_\alpha$  emission in superdense LID discharge.

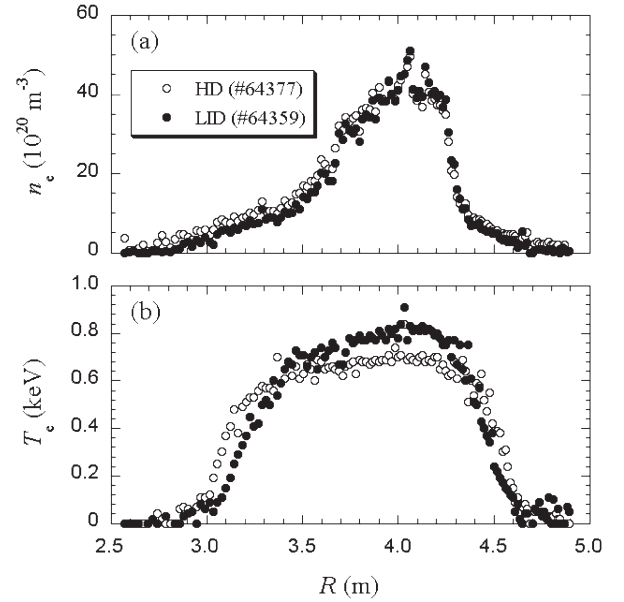


Fig. 2. Radial profiles of (a) electron density and (b) temperature. Open and closed circles represent helical divertor (HD) and local island divertor (LID) configurations, respectively.

### References

- 1) Morisaki, T. et al.: Fusion Sci. Technol. **50**, (2006) Aug.

## §2. Super Dense Core Plasma (location of IDB)

Ohyabu, N., Morisaki, T., Masuzaki, S., Kobayashi, M., Komori, A.

During a sequence of many LID discharges, the wall conditioning take place and thus the wall pumping capability is enhanced. SDC plasmas with somewhat lower temperatures can then be obtained even without the LID. For longer pulse operation in the SDC mode, however, active pumping by the divertor is essential. Figure 2-a (the previous page SDC-I) shows that with continuous pellet injection at intervals of  $\sim 160$  ms and  $\Delta N = 1 \times 10^{21}$  particles, we have successfully maintained a quasi-steady-state SDC operation for nearly 0.6 s. In Fig. 2-b, the density profiles just before and after pellet injection ( $t = 1600$  ms, 1620 ms) are depicted. The pellet particles are fueled in the region where  $\nabla n$  is high, not in the central region ( $3.65 \text{ m} < R < 4.05 \text{ m}$ ). Somehow the temperature and plasma pressure (product of the density and temperature) drops by 20 % in the central region. As indicated by the diamagnetic signal ( $W_p$ ), the change in pressure is small, except the central region. Perturbations by the pellets on the temperature and density profiles can be reduced by optimizing the pellet size for particular discharge conditions.

SDC plasma performance depends on the configuration ( $R_{ax}$ ). This is partly because of geometry effects. The NBI tangency radius is 3.70 m; thus, the power deposited in the core ( $\rho < 0.5$ ) for  $R_{ax} = 3.65$  m is substantially lower than that for  $R_{ax} = 3.75$  m. Pellet fuelling is more effective for larger  $R_{ax}$  because the pellets are injected from the outside and

therefore a higher fraction of the pellet particles is deposited in a larger outward shifted core than in a smaller inward shifted core region.

The minor radial extent of the SDC is determined by the IDB foot (jump in  $\nabla n$ ) location ( $R_{foot}$ ), and increases with  $R_{ax}$  and  $\beta$ . The rotational transform profiles for finite  $\langle \beta \rangle = 0.66\%$  and  $1.2\%$  equilibria are plotted as a function of  $R$  ( $\rho$ ) for the configuration with  $R_{ax} = 3.75$  m [Fig.1-a (b)] to show a large Shafranov shift of the configuration. There exist two distinct regions, separated by the  $R_{sp}$  radius, which is defined as illustrated in Fig.1-c (with enough negative shear in the inner region, it is nearly the same as the zero shear radius ( $R_{zs}$ )). Inside this radius ( $R_{sp}$ ), the rotational transform profile has modest negative shear, or nearly zero for low beta cases. In the outer region (outside this location), the shear is large positive.  $R_{sp}$  is qualitatively insensitive to the shape of pressure profile,  $p(r)$ , for fixed average beta. Figure 1-d shows  $R_{sp}$  (calculated for the pressure profiles similar to the observed ones) and  $R_{foot}$  as a function of the average beta for three different configurations ( $R_{ax} = 3.65$  m, 3.75 m, 3.85 m). The IDB foot point falls close to  $R_{sp}$  in the rotational transform. The difference between  $R_{sp}$  and  $R_{foot}$  is found to be less than  $\sim 0.1$  m.

The “standard” configuration ( $R_{ax} = 3.75$  m) with  $\beta(0) = 4.4\%$ , and the IDB foot at  $\rho = 0.55$  yields an SDC with optimum performance. For the outward shifted configuration ( $R_{ax} = 3.85$  m), the SDC grows with increasing  $\beta$  and the IDB foot is close to the last closed surface at  $\beta = 1.38\%$ . For the inward shifted case ( $R_{ax} = 3.65$  m), the SDC is smaller, with the IDB foot at  $\rho = 0.45$  and  $\langle \beta \rangle = 0.5\%$ . The “super dense” effect is weaker in the present experiments so far.

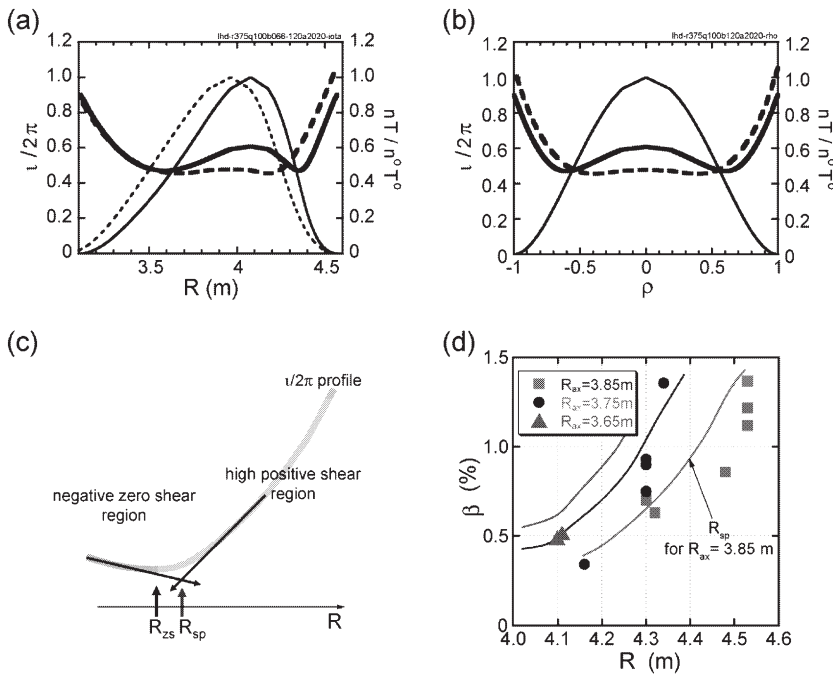


Figure 1. (a) Calculated rotational transform profiles with average  $\beta$ s of 0.66 % (the dotted lines) and 1.20 % (the solid lines). Pressure profile shape is  $(1-\rho^2)^2$  for both cases. Pressure and  $u/2\pi$  are plotted in terms of  $R$ . (b) Pressure and  $u/2\pi$  are plotted in terms of  $\rho$ . (c) Definition of  $R_{sp}$ . (d) With increasing  $\beta$  and  $R_{ax}$ , the foot location of the IDB ( $R_{foot}$ ) increases. The red, blue and green curves are  $R_{sp}$  for  $R_{ax} = 3.85, 3.75, 3.65$  m, respectively.



### §3. Super Dense Core Plasma (high beta)

Ohyabu, N., Morisaki, T., Masuzaki, S., Kobayashi, M., Komori, A.

In order to study the MHD properties of the SDC plasmas, we have made an attempt to achieve higher  $\beta$  at  $B = 1.5$  T. The maximum  $\beta$  value so far is  $\langle\beta\rangle = 1.4\%$  ( $\beta(0) = 5.1\%$ ). We do not see any detrimental MHD activities such as a sawtooth crash or ELM, as seen in case of tokamak improvement modes. The time evolution of the SDC plasma (see Figure 1-a) shows that the SDC forms at 600 ms. After terminating the pellet injection ( $t = 700$  ms), the stored plasma energy and hence  $\langle\beta\rangle$  increases for 100 ms and reach the maximum. It is similar to the “reheat event”, in which temperature rise occurs after gas puff is turned off. The SDC reheat is significantly drastic. During this phase, the NBI power is fixed. Fig. 1-b show a clear, significant change of the helical plasma equilibrium, i.e., the magnetic axis of the plasma moves outwards significantly (a large Shafranov shift). At  $t = 703$  ms, the temperature and density profiles are those of the typical SDC mode, shown in Fig. 1-c. The temperature starts to increase except for the outer region ( $R > 4.45$  m,  $R < 3.25$  m)[Fig. 1-b] and the profile at  $t = 736$  ms, maintains the SDC type profile. Because of lower field, the central density decay rate is much higher without pellet core fueling and thus the central density decreases by 25 % at  $t = 836$  ms. During this evolution, the temperature nearly triples, a significant improvement of the confinement,

The temperature gradients both in the core and outer regions also increase, deviating from the typical SDC profile, i.e., flat core profile. What causes the above evolution remain unclear. We note that the density profile beyond  $\rho = 0.8$  at  $t = 703$  ms is substantially higher than those at later times and thus termination of the pellets may cause a reduction in the density there, which in turn leads to higher temperature and confinement enhancement. There may be also responsible some kinds of MHD effects, as it discussed below.

The ideal MHD stability of these configurations has been examined by using the 3-D COBRA stability code. The core region inside the zero-shear radius has direct access to second stability, i.e., the stability margin increases with  $\beta$ . Outside the zero shear radius, the plasma becomes unstable to ballooning modes at  $\beta$ , much higher than the present experimental value. Of course, resistive versions of the modes are expected to appear at lower  $\beta$ . These results suggest that MHD effects may play a role in formation of the SDC and may also provide a useful mechanism to constrain the plasma pressure in the outer region. It is interesting to note that high density discharge similar to the SDC has been observed in the tokamak experiments despite significant difference in the MHD properties.

These results suggest a novel fusion ignition scenario in which an SDC is used to operate at very high density and relatively low temperature. Such a scheme is particularly attractive for helical devices because (a) they do not require current drive (which is the most effective at low density), and (b) operation at high collisionality reduces the effect of the helical ripple diffusion regime.

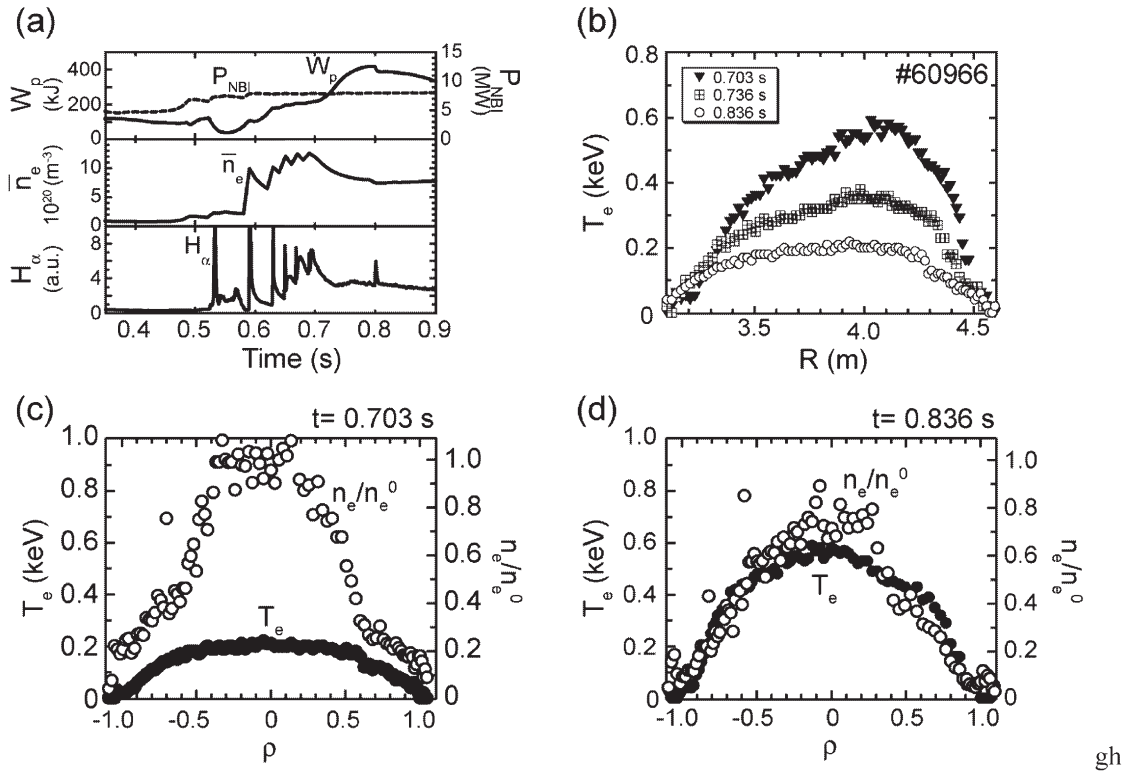


Figure 1. (a) Time evolution of  $\beta$  discharge with a “reheat” event from  $t = 700$  ms. (b) Time evolution of the temperature profile ( $t = 703, 736, 836$  ms). (c) The density and temperature profiles just before termination of the pellet injection ( $t = 703$  ms). (d) The profiles near the peak of the  $W_p$  (stored energy) ( $t = 836$  ms).  $n^0 = 3.3 \times 10^{20} m^{-3}$

## §4. Particle Balance Study in the LHD

Masuzaki, S.

Achieving an effective particle control using a divertor system is a crucial issue in fusion experiment. Particle balance studies are necessary for understanding neutral particle behavior, and are also important from the viewpoint of tritium inventory in vacuum vessel for next step fusion devices. In the Large Helical Device (LHD), plasma experiments with an intrinsic helical divertor (HD [1]) and a local island divertor (LID [2]) have been performed, respectively. The HD is an open divertor at this stage, and the LID is a closed divertor equipping baffle structure and pump-system. In the LID configuration, most particles from the core are well guided by the outer-separatrix of  $m/n=1/1$  island to the closed divertor module located locally in a toroidal section.

In the LHD, the total in-vessel area and volume of vacuum vessel are about  $700\text{m}^2$  and  $210\text{m}^3$ , respectively, and the plasma volume is about  $30\text{m}^3$ . The effective pumping speed of the main pump-system is about  $400\text{m}^3/\text{s}$  and  $200\text{m}^3/\text{s}$  in the HD and LID configuration, respectively [3]. In the LID pump system, the effective pumping speed is about  $200\text{m}^3/\text{s}$ . First wall consists of a number of stain-less steel (SS) tiles, and HD and LID divertor plates are made of isotropic graphite and carbon fiber composite (CFC), respectively. The area ratio of carbon plates to SS tiles is about 10%. Neutral gas pressure is measured by an ASDEX-type fast ionization gauge (FIG) and a cold cathode gauge installed on a torus inboard-side port and an entrance of the pump-system, respectively.

Significant difference in neutral particle behavior has been observed in the two divertor configurations. Figure 1(a) shows the time evolution of the particle balance during and after the discharges with the HD and the LID configurations. In these discharges, fuelling was conducted by ice-pellet injection. In the HD case, the total amount of ionized and evacuated particles is about 25% of the amount of input particles during the discharge. After the termination of the discharge, neutral pressure in the vacuum vessel increases for the recombination of plasma particles and desorption from plasma facing components [4], though the pressure rise is not so large, and about 80% of fuelled particles remain in the vacuum vessel even at the start of next discharge. Therefore the discharge history strongly affects the density control [4]. In contrast to the HD case in Fig.1(a), the total amount of ionized and evacuated particles during a discharge is about 70% of the fuelled particles in the LID case. The total evacuated particles are over 80% during and after a discharge.

It has been found that the pumping efficiency of the LID depends on the LID head position. Figure 1(b) shows the pumping efficiency of the LID for the different head positions ( $R_{\text{head}}$ ).  $R_{\text{head}}=4.18\text{m}$  is the optimum head position for  $R_{\text{ax}}=3.75\text{m}$  configuration, and the pumping efficiency is almost 100%.  $R_{\text{head}}=4.24\text{m}$  case, the outer-separatrix connects to near the head's edge, and the efficiency is about 60%. It is also indicated in Fig.1(b) that the efficiency is about 20% in the HD case.

The difference in the neutral particle behavior between the HD case and the LID case is considered to be related to the mechanisms of the particle retention. Charge-exchange particle implantation to the first wall is a possible cause of the particle retention [4]. In the LID configuration, neutral pressure in vacuum vessel is relatively low comparing with that in the HD case, and the charge exchange particle flux could be smaller than that in the HD case. Particles can be retained by a co-deposition process. The material probe analysis revealed that the surface of the first wall is covered with thin carbon and boron layer in LHD, and the thermal desorption spectroscopic analysis shows that retained hydrogen in the wall is the order of  $10^{21}$ - $10^{22}$  atoms/ $\text{m}^2$

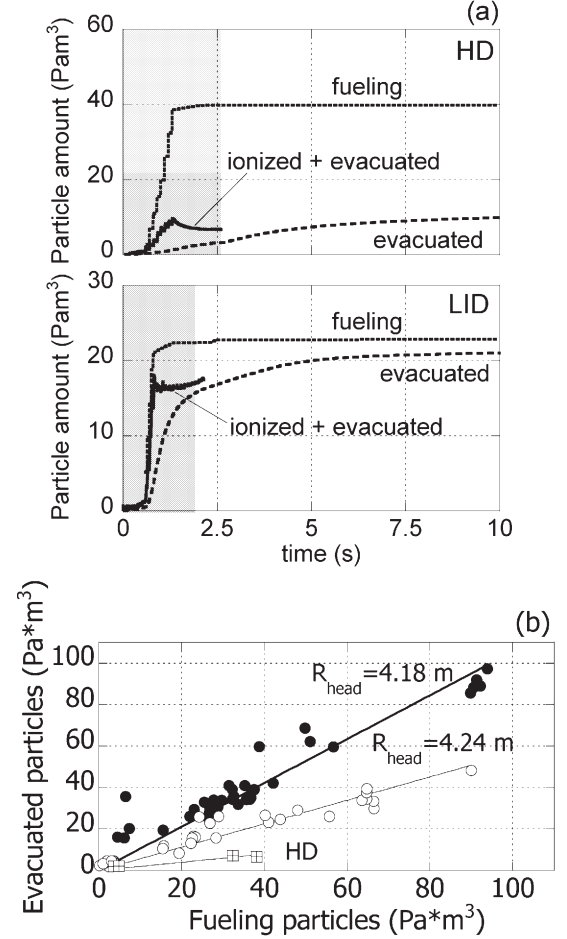


Fig. 1: (a) Time evolutions of time integrated particle amounts during pellet fuelled discharges under the HD and LID configurations. The gray colored regions indicate the discharge durations. In both discharges, the maximum line averaged density is  $\sim 2 \times 10^{20} \text{m}^{-3}$ . (b) Evacuated particles number as a function of fueled particles number.  $R_{\text{head}}$  is the radial head position, and 'HD' means the helical divertor configuration.

[5]. This number is the same order as the averaged areal density of retained hydrogen after an experimental day with the HD configuration [4]. In the LID configuration, particle flux to the helical divertor plates is so small [2] that the carbon amount released by physical and chemical sputtering is small. Therefore, particle amount retained by co-deposition process in vacuum vessel is considered to be smaller than that in the HD case. The temperature of plasma facing components can be another cause of the difference in neutral particle behavior between the two cases. The typical divertor plates' temperature is over 1000K in the LID case, and is less than 600K for the HD case. The first wall temperature is less than 370K. The temperature of LID divertor plates is enough high to desorb particles, though the HD divertor plates and first wall temperatures are too low to particle desorption.

### References

- [1] S.Masuzaki et al., Nucl. Fusion, **42** (2002) 750.
- [2] A.Komori et al., Nucl. Fusion, **45** (2005) 837.
- [3] N.Suzuki, "Measurement of pumping speed of vacuum pumping system in the LHD", in this Annual Reports.
- [4] M.Kobayashi et al, J. Nucl. Mater., **350** (2006) 40.
- [5] Y.Nobuta et al., J. Nucl. Mater., **329-333** (2004) 800.

## §5. Long-Duration Sustainability of Pellet Fueled High Performance Plasma

Sakamoto, R., Yamada, H., Hoshino, M.

For the purpose of investigating fueling issues towards the steady state operation, we have been performed long duration discharge with newly-installed pellet injection timing control system, which is capable of controlling a plasma density in real time.

Fig. 1 shows temporal evolution in a repetitive pellet refueling discharge. Pellets were continuously injected from  $t = 0.4$  s with density control and only pellet injection was employed to build-up plasma density. The reference value of line averaged electron density ( $n_e$ ) was set to  $0.7 \times 10^{20} \text{ m}^{-3}$  during discharge. At the build-up phase ( $t < 0.2$  s), pellet was injected with maximum frequency, 10 Hz. After reaching  $0.7 \times 10^{20} \text{ m}^{-3}$ , the pellet injection interval has gotten longer (0.6 - 0.7 S) to keep  $0.7 \times 10^{20} \text{ m}^{-3}$  at the pellet injection timing. The important point to note is that the local measurements at plasma center such as  $T_e(0)$ ,  $T_i(0)$  and  $n_e(0)$ , and the plasma stored energy,  $W_p$  are maintained virtually constant in spite of pellet sequence. This quasi-stationary phase can be continued until the end of the neutral beam heating ( $t = 10.3$  s).

The electron density profiles just before and after pellet injection at  $t = 6.158$  s and difference between these profiles ( $\Delta n_e$ ) are shown in Fig. 2 (a). The pellet is ablated until about half radius and an obvious hollow density profile, which have density peak at  $\rho = 0.6$ , is formed just after pellet injection. The hollow profile is gradually relaxed and returns back to the original profile. Even in the density profile relaxation phase after pellet injection, the central density  $n_e(0)$  is maintained virtually constant in spite of significant changes of the  $n_e(0.6)$  as shown in Fig. 2 (b).

In order to estimate the diffusion coefficient, these density profile change was fitted using following equation.

$$\frac{\partial n}{\partial t} = -\frac{1}{r} \frac{\partial}{\partial r} (r\Gamma) + S = -\frac{1}{r} \frac{\partial}{\partial r} \left( r \left( -D \frac{\partial n}{\partial r} + nV \right) \right) + S \approx D \frac{\partial^2 n}{\partial r^2} + \frac{D}{r} \frac{\partial n}{\partial r} + S$$

The assumptions made in the above derivation are that the particle source,  $S$  is defined as  $\Delta n_e$ , convection velocity,  $V$  is negligible small and diffusion coefficient  $D$  is constant in terms of time and radial distribution. Assuming  $D = 0.05 \text{ m}^2/\text{s}$ , the calculated density change adequately corresponds with the measurements as shown by solid lines in Fig. 2 (b). Thus we see that the inward diffusion due to inversed density gradient supply particle constantly to the plasma center suppressing a density perturbation in the core region despite a lack of inward pinch velocity. And constant central density;  $n_e(0)$  is sustained quasi-stationary during pellet sequence. In these repetitive pellets refueled discharge, a confinement

index, which is normalized by International Stellarator Scaling (ISS95), is 1.4 despite the high density operation. The confinement property is equal to peaked density profile plasma, which is transiently attained by deep pellet penetration experiments. However, we should not overlook that the increase of pellet firing interval, which is necessary to keep constant density, due to increase of the density decay time,  $\tau_{\text{decay}}$  after pellet ablation, which is obtained by curve fitting with an exponential function,  $\text{Cexp}\{-t/\tau_{\text{decay}}\}$ , as shown in Fig. 3. This tendency is caused by increase of boundary density while keeping constant line averaged electron density during quasi-stationary phase as shown by  $n_e(0.9)$  in Fig. 1 and it have liner correlation with neutral density ( $n_0$ ). Another point to observe is that the plasma stored energy,  $W_p$  is gradually continued decline with increasing the boundary density and neutral density. It is speculated that the plasma stored energy, namely, plasma confinement property is respond to neutral pressure through the boundary plasma density.

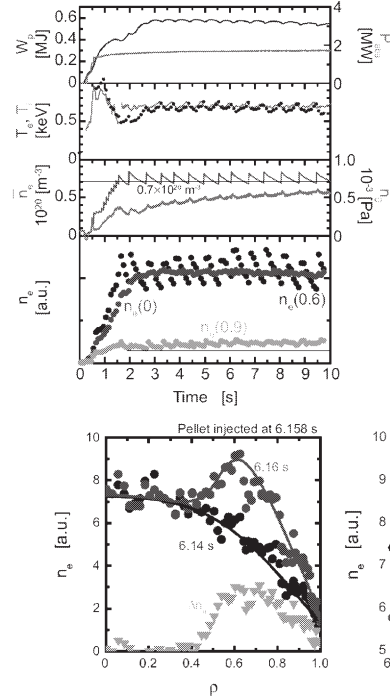


Fig. 1 The temporal evolution of the key parameters in a repetitive pellet refueled discharge. The pellet firing interval is automatically controlled in real time to keep  $0.7 \times 10^{20} \text{ m}^{-3}$  at the pellet injection timing.

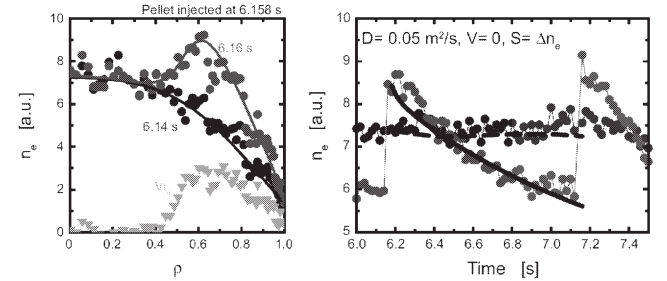


Fig. 2. Comparison between measurement and simple diffusion calculation. The circles and lines denote the measurements and calculation results, respectively. (a) Measured and calculated density profiles change in the density profile relaxation phase after pellet injection. (b) Local electron density evolution at  $\rho = 0$  and  $\rho = 0.6$ .

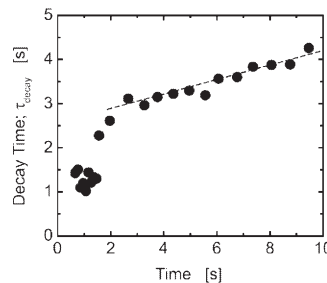


Fig. 3. The change of density decay time in the density profile relaxation phase after pellet injection.



## §6. Observation of Slow Transition between Two Transport Branches with Different Temperature Dependence in LHD

Ida, K., Inagaki, S., Sakamoto, R., Tanaka, K., Itoh, K.

A new slow transition process for energy transport in magnetically confined plasmas is reported. The slow transition is characterized by the change between two meta-stable transport conditions characterized by a weak and a strong electron temperature  $T_e$  dependence of normalized heat flux. These two branches are found to merge at the critical  $T_e$  gradient. In meta-stable transport, the derivative of normalized heat flux to the  $T_e$  gradient,  $d(Q_e/n_e)/d(-dT_e/dr)$ , is positive, while it becomes negative during the transition phase. The time for the transition increases as the normalized  $T_e$  gradient is increased and exceeds the transport time scale characterized by the global energy confinement time.

In order to study the  $T_e$  and  $T_e$  gradient dependence of electron heat transport, the normalized heat flux is scanned by changing the electron density using repetitive pellets in the Large Helical Device (LHD). There are clear phases characterized by the sign of the time derivative of the  $T_e$  gradients as indicated by phases I, II, III, IV. Both  $T_e$  and the  $T_e$  gradient increase in time as the electron density decreases in phases II and IV, which is a normal characteristic of heat transport in plasma. However, in phases I and III, the  $T_e$  gradients decrease even with the increase of  $T_e$ . The change in the time derivative of the  $T_e$  gradient is abrupt (less than 0.01 sec) and its value is roughly constant in time for each phase as -6.6 keV/m/s (in phase I), 2.2 keV/m/s (in phase II), -2.7 keV/m/s (in phase III) and 0.6 keV/m/s (in phase IV). This observation clearly demonstrates that the transition phase between the two meta-stable states is characterized by the change in the time derivative of the  $T_e$  gradient.

Figure 1(a) shows the normalized heat as a function of  $T_e$  and the  $T_e$  gradient in the weak  $T_e$  dependence branch (phase II) and in the strong  $T_e$  dependence branch (phase IV) after the pellets (12 pellets in series) are injected into the plasmas with different densities. The experimental data in phase II shows that the normalized heat flux gradually increases as the  $T_e$  and  $T_e$  gradient are increased, while that in the phase IV shows a sharp increase of the normalized heat flux. It is noted that all the experimental data points of the 12 events are connected and located along curves (data points in phase II are on a weak  $T_e$  dependence curve and data points in phase IV on a strong  $T_e$  dependence curve). The data points in the transition phase (Phase III) are scattered between the weak and the strong  $T_e$  dependence curves. When the plasma is on one of the branches, both  $T_e$  and the  $T_e$  gradient are uniquely determined for the given normalized heat flux, while they are not uniquely determined during the transition phase.

In order to investigate quantitatively the dependence of the normalized heat flux on the  $T_e$  and  $T_e$

gradient dependence, the normalized heat flux is given by  $Q_e/n_e = cT_e^\alpha (dT_e/dr)^\beta$  where  $\alpha$  and  $\beta$  are the  $T_e$  and  $T_e$  gradient dependence parameters, respectively. The difference between the  $Q_e/n_e$  measured and  $Q_e/n_e$  calculated with the parameters  $(\alpha, \beta)$  are investigated in a wide range of  $Q_e/n_e$  for these two branches. Figure 1(b) and 1(c) show the contours of the square of differences between the normalized heat flux measured and that calculated,  $\chi^2 = [Q_e/n_e - cT_e^\alpha (dT_e/dr)^\beta]^2$ , for various values of  $(\alpha, \beta)$  in the weak and strong  $T_e$  dependence branches. The  $T_e$  dependence parameter  $\alpha$  is 0.44 (-0.23, +0.25) for the weak  $T_e$  dependence transport branch and 1.4 (-0.4, +0.3) for the strong  $T_e$  dependence transport branch, while the  $T_e$  gradient dependence parameter,  $\beta$  is close to unity; 0.86 (-0.25, +0.25) and 1.1 (-0.2, +0.27) for the weak and the strong  $T_e$  dependence branches, respectively.

### Reference

[1] K.Ida et al., Phys Rev Lett **96** 125006 (2006)

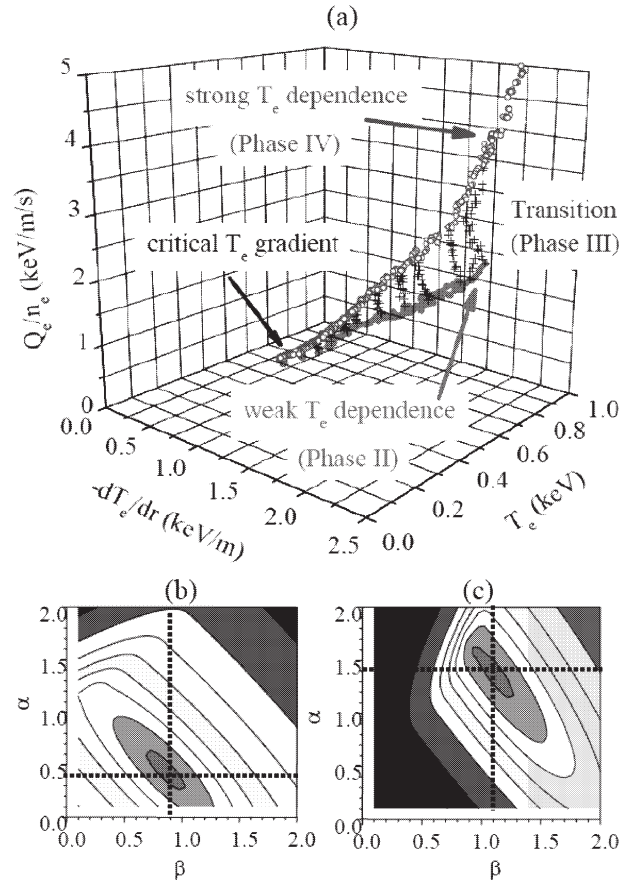


Fig.1. (a) Heat flux normalized by electron density as a function of electron temperature  $T_e$  and temperature gradient in the weak  $T_e$  dependence branch (phase II), in the transition period (phase III) and in the strong  $T_e$  dependence branch (phase IV) and the contours of the difference between the normalized heat flux measured and that calculated with the model of  $cT_e^\alpha (dT_e/dr)^\beta$  with various values of  $(\alpha, \beta)$  for (b) the weak  $T_e$  dependence branch (phase II) and (c) the strong  $T_e$  dependence branch (phase IV) at  $\rho = 0.65$ .

## §7. Effect of Elongation on Transport in ECH Plasma

Yamada, H., Yokoyama, M., Murakami, S.

Exploration of the effect of magnetic configuration on confinement is prerequisite for optimization of a helical system. Geometrical optimization for the neoclassical transport has been demonstrated in NBI plasmas on LHD [1]. Also, the anomalous transport has been suppressed as well in the neoclassical optimized configuration [2]. In these configuration studies, the position of the magnetic axis is the key control parameter. Large flexibility of the coil system of LHD enables us another configuration scan, that is plasma elongation. Although the plasma elongation scan for NBI heated plasmas have been already reported [1], ECH plasmas which are located in deep collisionless regime have not been studied yet. In the 9th experimental campaign, plasma elongation scan was conducted for ECH plasmas.

Plasma elongation has been controlled by the quadrupole field and scanned in the range between  $\kappa=0.8$  and 1.1. Here elongation is defined by the toroidal averaged value since the elliptic surface rotates along the toroidal angle. The magnetic field is fixed at 1.5 T, which provides centrally well focused ECH deposition.

Energy confinement times have the maximum performance at  $\kappa=1$  and degrades in both prolate ( $\kappa>1$ ) and oblate ( $\kappa<1$ ) directions. These trends agree with the observation in NBI heated plasmas.

Then, two dimensionally similar discharges with different elongation have been compared to clarify the elongation effect on heat transport. The line averaged density is controlled at  $1 \times 10^{19} \text{m}^{-3}$  and electron temperature is also controlled to be the same in two case with  $\kappa=0.8$  and 1.0 (see Fig.1). Since the case with  $\kappa=1$  shows the better confinement, the heating power is 0.93MW for  $\kappa=0.8$  and 0.35MW for  $\kappa=1$ . The plasma parameters except for the elongation are similar to each other, therefore, representative non dimensional physical parameters such as normalized gyro-radius  $\rho^*$ , collisionality  $\nu^*$ , and beta are also similar to each other.

Figure 2 shows the ratio of the electron heat diffusivity of these two cases. Since the plasma parameters of these two cases are the same, the deviation of this ratio from 1 can be attributed to the remained difference, i.e., elongation. Corresponding to the global confinement nature, local heat diffusivity in the experiment shown in a solid curve indicates enhancement of heat transport in the case with  $\kappa=0.8$  by a factor of 2 to 3. A dotted line is the prediction from neoclassical theory. These two curves are close to each other, which suggests the neoclassical transport may make the difference in heat transport. However, this is not the case. Figure 3 shows the heat diffusivity profile. The fat solid curve is the experimental value in the case with  $\kappa=0.8$  and the dotted fat curve is the corresponding neoclassical prediction. The experimental

value is significantly larger than the neoclassical value, which indicates heat transport is anomalous even for the case with  $\kappa=0.8$ . Therefore, this is another example that configuration effect on anomalous transport is correlated or accidentally happens to coincide with nature of neoclassical transport [2].

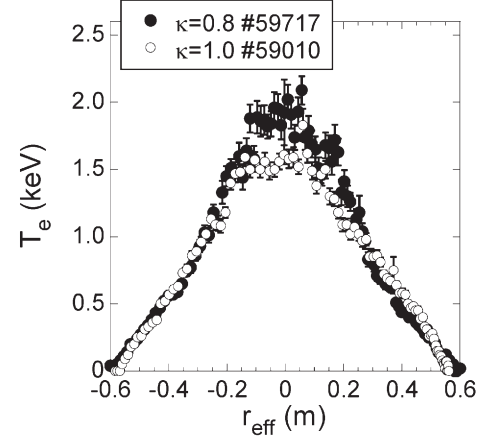


Fig.1 Electron temperature profiles in discharges with different elongation.

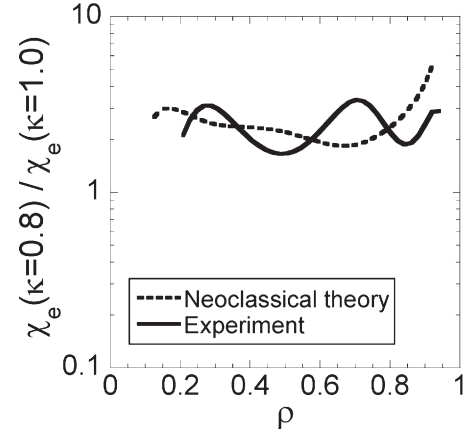


Fig.2 Ratio of heat diffusivity of two discharges with different elongation

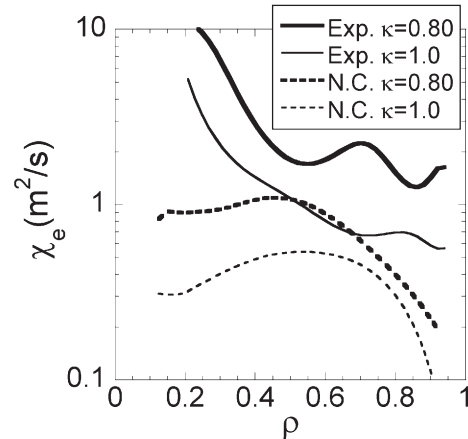


Fig.3 Experimental and neoclassical heat diffusivity.

### References

- [1] H.Yamada et al., Plasma Phys. Control. Fusion **43**, A55 (2001)
- [2] H.Yamada et al., Nucl. Fusion **45**, 1684 (2005)

## §8. Radial Structure of Edge Transport Barrier in Inward-Shifted Configuration of LHD

Toi, K.,

Watanabe, F.,<sup>1)</sup>

Ohdachi, S., Narihara, K., Morisaki, T., Ida, K., Masuzaki, S., Miyazawa, K., Morita, S., Sakakibara, S., Tanaka, K., Tokuzawa, T., Watanabe, K.W., Yoshinuma, M., LHD Experimental Group

<sup>1)</sup> Dep. Energy Sci. and Engineering, Nagoya Univ., Japan

In the magnetic configuration of LHD, H-modes were first achieved in high beta plasmas of  $\langle\beta_{\text{dia}}\rangle > 1.5\%$  where  $\langle\beta_{\text{dia}}\rangle$  is the volume averaged beta value evaluated by diamagnetic measurement assuming the volume of the vacuum field [1,2]. In these high beta H-modes, however, ETB formation immediately leads to excitation of edge MHD modes after short quiescent phase ( $\sim 10\text{ms}$ ). The edge region where ETB is formed is in magnetic hill and is susceptible of ideal or resistive interchange instabilities. Excited edge MHD modes have the following mode structures as  $m/n=2/3, 1/2, 2/5$  and so on, of which rational surfaces reside very close to LCFS or in the ergodic layer[3]. Recently, ETB was also achieved in medium beta regime of  $\langle\beta_{\text{dia}}\rangle \sim 0.9\%$  (Fig.5) [4]. In this case,  $\langle\beta_{\text{dia}}\rangle$  increases in a quiescent phase for  $\sim 120\text{ms}$  without suffering intense edge MHD modes.

In some H-mode plasmas, the pedestal structure was observed in electron temperature profile [2]. The ETB zone extends into ergodic layer outside the last closed flux surface (LCFS) defined in the vacuum field. Moreover, ETB region is deformed by the presence of  $m/n=2/3$  island related to edge MHD mode and has a plateau region. The radial profile of the rise in electron temperature across the transition indicates that the ETB or “pedestal” width averaged over the magnetic surface is fairly large ( $\sim 10\text{ cm}$ ) for the averaged minor radius of  $64\text{ cm}$ , and is much larger than the poloidal ion gyro-radius for proton at ETB ( $\sim 0.8\text{ cm}$ ), where  $T_i \sim T_e (=0.1\text{ keV})$  is assumed and  $B_t=0.75\text{ T}$ . Most of ETB plasmas in LHD exhibit strong density rise near the edge, having almost fixed gradient of electron temperature there. Figure 1 shows the radial profiles of electron density and temperature just before and after the transition at low toroidal field ( $B_t=0.75\text{ T}$ ). It should be noted that the shape of electron density profile in the H-phase is hollow and does not have a typical “pedestal” shape. The terminology “ETB” may be suitable to express the edge structure of density profile, instead of “pedestal”. This figure clearly indicates that ETB zone extends into ergodic layer defined in the vacuum field. The width of ETB defined by the distance between the plasma boundary determined from electron temperature profile and the layer where the density rise reaches the maximum is evaluated to be  $\sim 14\text{ cm}$  at  $B_t=0.75\text{ T}$ . For ETB plasmas in LHD, the dependence of the ETB width on the toroidal field strength was investigated by scanning  $B_t$  from  $0.5\text{ T}$  to  $1.5\text{ T}$  on the condition that the rotational transform at ETB is fixed, that is, poloidal field strength is simply proportional to  $B_t$ . The ETB width has no clear dependence on  $B_t$ , as shown in

Fig.2. In tokamak H-mode plasmas, the width is often compared with poloidal ion gyro-radius through a scan of the toroidal field strength and/or plasma current. In this Bt-scan, the electron temperature at ETB remains almost same around  $T_e \sim 0.1\text{ keV}$ . In ETB region of LHD,  $T_i \sim T_e$  will be satisfied due to relatively high collisionality. The ETB width in LHD is much larger than poloidal ion gyro-radius. Above-mentioned fairly wide width of ETB may be caused by a long penetration length of neutrals. The other cause for thus expanded width of ETB may be ELM activities and/or edge MHD modes. These causes are not yet investigated systematically. The data of ETB width would supplement the database on the pedestal width in tokamak H-mode plasmas and contribute to understanding a dominant mechanism to determine the ETB width.

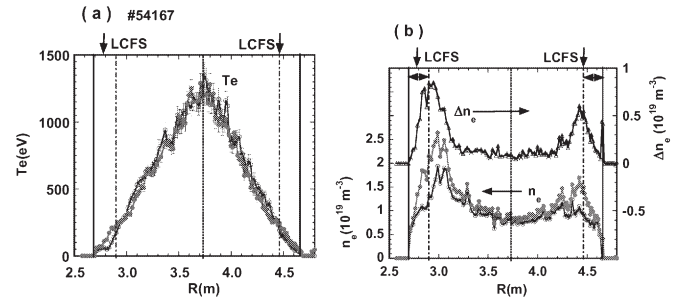


Fig.1 (a) Radial profiles of electron temperature just before (open circle) and after (solid circle) the L-H transition in the configuration of  $R_{\text{ax}}=3.6\text{ m}$  and  $\gamma=1.22$  at  $B_t=0.75\text{ T}$ . (b) Change of electron density profile and radial profile of the increment of electron density  $\Delta n_e$  across the transition.

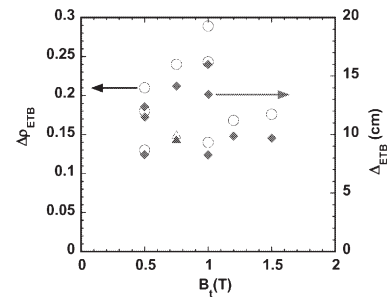


Fig.2 Dependence of ETB width on the toroidal field strength. Solid and open symbols respectively indicate the ETB width  $\Delta_{\text{ETB}}$  and the width normalized by the averaged minor plasma radius  $\Delta p_{\text{ETB}}$ . Triangles correspond to the width derived from electron temperature profile and the others from electron density profile.

- [1] K. Toi, S. Ohdachi, S. Yamamoto et al., Nucl. Fusion **44**, 217 (2004).
- [2] K. Toi, S. Ohdachi, S. Yamamoto et al., Phys. Plasmas **12**, 020701 1 (2005)
- [3] F. Watanabe, K. Toi, S. Ohdachi et al, Plasma Phys. Control. Fusion **48**, A201 (2006).
- [4] K. Toi, F. Watanabe, S. Ohdachi et al., Plasma Phys. Control. Fusion **48**, A295 (2006).



## §9. Effects of Applied Resonant Helical-Field Perturbations on ETB Formation

Toi, K.,

Watanabe, F.,<sup>1)</sup>

Ohdachi, S., Narihara, K., Morisaki, T., Ida, K., Masuzaki, S., Miyazawa, K., Morita, S., Sakakibara, S., Tanaka, K., Tokuzawa, T., Watanabe, K.W., Yoshinuma, M., LHD Experimental Group

<sup>1)</sup> Dep. Energy Sci. and Engineering, Nagoya Univ., Japan

The local island divertor (LID) coils can generate helical field perturbations resonate with the rational surface of  $\iota/2\pi=1$  near the edge in LHD [1]. The Poicare plot of field structure is shown in Fig.1 for the case that the LID field is applied to expand the  $m/n=1/1$  magnetic island. In this magnetic configuration, ergodic layer exists outside the sizable  $m/n=1/1$  magnetic island.

In a shot shown in Fig.2(a) where the line averaged electron density was ramped up by gas puffing, the L-H transition occurred at  $\langle n_e \rangle \sim 2 \times 10^{19} \text{ m}^{-3}$  and  $\langle \beta_{\text{dia}} \rangle \sim 1.8\%$  [2,3]. In this shot, small LID field was applied to diminish  $m/n=1/1$  magnetic island induced by small error field and the electron temperature profile did not have any obvious island structures near the edge. When strong LID field was applied to expand the size of  $m/n=1/1$  magnetic island near the edge as shown in Fig.1, the transition was triggered at the lower electron density ( $\sim 1.3 \times 10^{19} \text{ m}^{-3}$ ) (Fig.2 (b)) [3]. The ETB was formed outside the island separatrix which slightly moves outward from the location calculated in the vacuum field due to finite beta effect, and extends in the ergodic layer, as shown in Fig.2(c). In this case, formation of modest electron temperature pedestal may be caused by the transition at lower electron density which was realized by application of strong field perturbations. However, the sizable  $m/n=1/1$  island degrades core plasma confinement and leads to the decline of  $\langle \beta_{\text{dia}} \rangle$ . A reason why the transition is triggered at lower  $\langle n_e \rangle$  in the case with a sizable  $m/n=1/1$  island is not clarified yet. This is left for an interesting and important issue in future. It should be noted that if the  $\langle n_e \rangle$  dependence in the ITER scaling law of power threshold is taken into account, the threshold power normalized  $\langle n_e \rangle^{0.64}$  increases slightly with the increase in the LID coil current.

As seen from Fig.2(b), ELM like activities in  $H\alpha$  emission were clearly suppressed by application of large LID field. Moreover, amplitude of coherent  $m/n=2/3$  edge MHD mode was also suppressed. The cause of suppression of ELM like  $H\alpha$  fluctuations and  $m/n=2/3$  edge MHD mode may be caused by slight reduction of the pressure gradient at the rational surface  $\iota/2\pi=3/2$  due to expansion of sizable magnetic island. In this experimental campaign, steep pressure gradient region moves outward, but it does not excite other edge

MHD modes such as  $m/n=1/2$  of which rational surface resides in further outer edge.

- [1] A. Komori et al., Proc. 15th IAEA Conf. Plasma Phys. Control. Fusion Res. (seville, 1994) Vol.2 (Vienna, IAEA)p773.
- [2] K. Toi, S. Ohdachi, S. Yamamoto et al., Phys. Plasmas **12**, 020701 1 (2005)
- [3] K. Toi, F. Watanabe, S. Ohdachi et al., Plasma Phys. Control. Fusion **48**, A295 (2006).
- [4] J.A. Snipes and ITPA Conf. and H-mode Threshold Database working Group, 19<sup>th</sup> IAEA Fusion Energy Conf., Lyon, 2002, paper No. CT/P-04

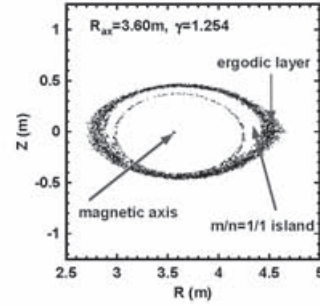


Fig.1 Poincare plot of the field topology in the case that the LID field is applied to expand  $m/n=1/1$  magnetic island near the edge.

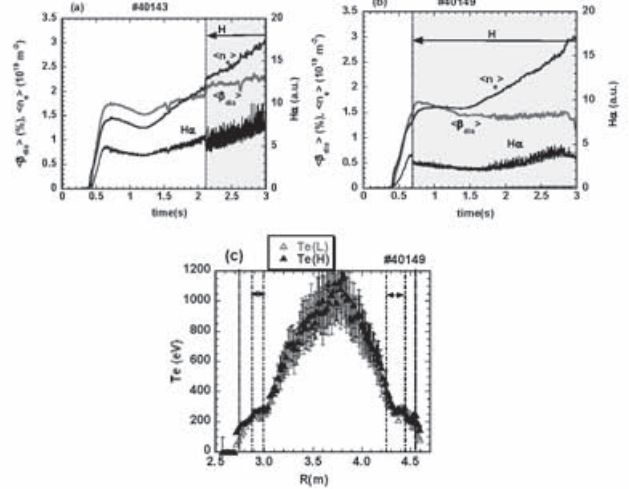


Fig.2(a) Time evolution of  $H\alpha$  emission,  $\langle \beta_{\text{dia}} \rangle$  and line averaged electron density  $\langle n_e \rangle$  in an ETB plasma where  $m/n=1/1$  magnetic island is diminished with small LID field. (b) Time evolution of an ETB plasma in the case that the island was expanded by excessive LID field. (c) Radial profiles of electron temperature just before ( $t=0.669 \text{ s}$ ) and after ( $t=0.769 \text{ s}$ ) the transition in the shot shown in Fig. (b). Dotted vertical lines indicate LCFS in the vacuum field. Two zones defined with a horizontal arrow and two vertical dash-and-dot lines correspond to the expanded  $m/n=1/1$  island region generated in the vacuum field.

## §10. Observation of Radial Structure of Edge MHD Modes in LHD Plasmas with L-H Transition

Watanabe, F. (Dep. Energy Eng. Sci., Nagoya Univ.), Toi, K., Ohdachi, S., Sakakibara, S., Watanabe, K.Y., Morita, S., Narihara, K., Tanaka, K., Yamazaki, K.

In the LHD, edge coherent MHD modes such as  $m/n = 2/3$  or  $1/2$  ( $m, n$ : poloidal and toroidal mode numbers), of which the rational surface is located in the plasma edge region of the magnetic hill, are strongly enhanced after L-H transition [1-3]. The excitation of these edge MHD modes degrades the confinement obviously, and stops a further rise in the plasma stored energy by the transition. Accordingly, it is important to clarify the characteristics of these MHD modes and to stabilize them. For this purpose, seven sets of soft x-ray (SX) detector arrays which consist of 20-channel PIN photodiodes were installed inside the vacuum vessel in vertically elongated sections of the LHD. We have used these arrays in order to measure the radial structure of edge MHD modes and studied the global stability of the ETB region.

Figure 1 shows a typical example of an NBI heated plasma with an L-H transition. In this discharge, an L-H transition takes place at  $t \sim 1.69$ s. As seen from the time evolutions of  $W_p$  and  $dW_p/dt$ , rapidly increases with the transition, but quickly saturates in  $\sim 20$  ms. In the saturation phase of  $W_p$ , the  $m/n = 1/2$  edge coherent mode is clearly enhanced, where the SX fluctuation amplitude,  $\delta I_{sx}$ , of the edge coherent modes was extracted using the FFT filter technique. In contrast, the edge coherent mode with  $m/n = 2/3$  mode is suppressed across the transition. The time behaviours of these edge coherent modes sensitively depend on the location with steep pressure gradient.

Figures 2(a, b) show the radial profiles of the SX fluctuation amplitude,  $\delta I_{sx}$ , and the normalized fluctuation amplitude,  $\delta I_{sx}/I_{sx}$ , where these SX fluctuations have a high coherence with the  $m/n = 2/3$  and  $1/2$  magnetic fluctuations. It should be noted that the  $\delta I_{sx}/I_{sx}$  does not necessarily correspond to an eigenfunction of the edge MHD mode, because of the path integral effect. In addition, the numbers of humps in the profile of  $\delta I_{sx}/I_{sx}$  are caused by the path integral effect in the SX emission measurement, and depend on the mode number  $m$ . The intensity of SX fluctuation will have a peak when two O-point regions or X-point regions in a magnetic island related to the edge MHD mode are aligned along the line of sight of an SX detector. It will be the minimum when O-point region and the X-point region are simultaneously aligned. The shape of the radial profiles of  $\delta I_{sx}$  can be interpreted qualitatively by the above simple consideration. The peaks of the fluctuation amplitude,  $\delta I_{sx}/I_{sx}$ , in the low and high field sides (inboard and outboard sides of the torus) are almost comparable. So far, a strong ballooning character is not recognizable. This is also consistent because low  $m$  interchange modes do not exhibit a ballooning character [4]. The phase difference among SX channels is also shown in Figs. 2(c, d). The derived phase relation indicates the ‘even’ or ‘odd’ character of the  $m$ -number, that is, the phase difference between the SX channels at the inboard

and outboard plasma edges is  $\sim 2\pi$  ( $\sim \pi$ ) for an even (odd)  $m$ -number. The phase differences for  $m/n = 2/3$  and  $1/2$  modes are consistent with the  $m$ -number determined using the magnetic probe arrays.

In NBI heated plasmas with an L-H transition in the LHD, we have measured the radial structure of edge MHD modes using an SX detector array, the rational surfaces of which were located near or just outside the LCFS defined by the vacuum magnetic surfaces. These radial structures of the edge MHD modes depend on the  $m$ -number. In this experimental ETB study, the fluctuation amplitude ( $\delta I_{sx}$ ) of  $m/n = 1/2$  rapidly grows across an L-H transition, and leads to quick saturation of the stored energy in a short time, accompanied by  $H_\alpha$  spikes which are similar to ELMs.

### Reference

- 1) Toi, K. *et al.*, Nucl. Fusion **44**, 217 (2004).
- 2) Toi, K. *et al.*, Phys. Plasma **12**, 020701-1 (2005).
- 3) Watanabe, F. *et al.*, Plasma Phys. Control. Fusion **48** A201-A208 (2006).
- 4) Nakajima, N., Phys. Plasmas **3**, 4556 (1996).

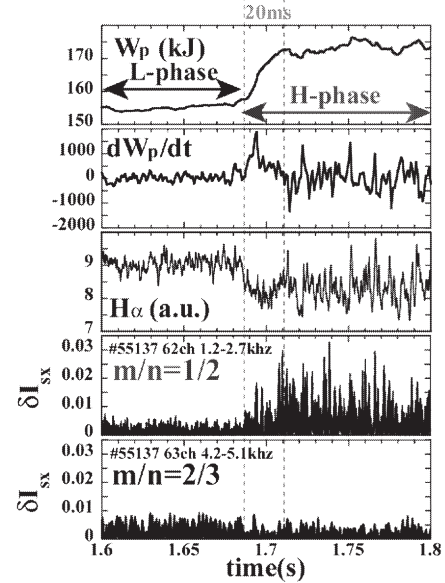


Fig. 1 Time evolutions of an L-H transition plasma at  $B_t = -1.0$ T,  $R_{ax} = 3.6$ m,  $\gamma = 1.20$ .

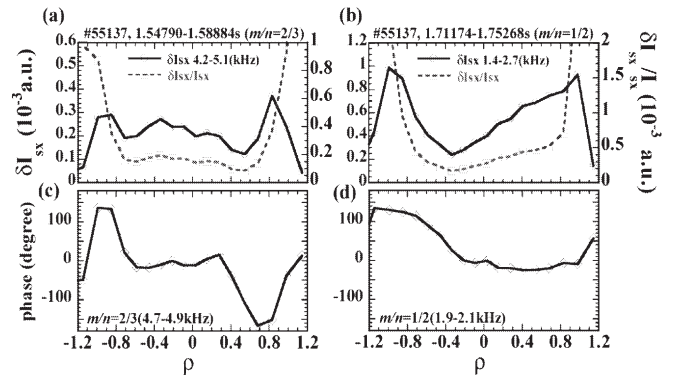


Fig. 2 (a, b) Radial profiles of SX fluctuation amplitude ( $\delta I_{sx}$ ) and normalized SX fluctuation amplitude ( $\delta I_{sx}/I_{sx}$ ) of  $m/n = 2/3$  and  $1/2$  coherent modes. (c, d) Phase difference among SX channels for these modes.



## §11. H-mode-Like Discharges and ELM-Like Activities under the Presence of $\iota/2\pi=1$ at Ergodic Layer in LHD

Morita, S., Morisaki, T., Tanaka, K., Masuzaki, S., Goto, M., Sakakibara, S., Watanabe, K.Y.

Shifting the  $R_{ax}$  outwardly, the profile of rotational transform becomes flat and the edge rotational transform at  $\rho=1$ ,  $\iota/2\pi(a)$ , becomes small with decreasing the edge magnetic shear (see Fig.1). Then, the values of  $\iota/2\pi(a)$  are below unity at  $R_{ax} \geq 3.90\text{m}$ . The H-mode-like discharge with ELM-like activity has been observed in LHD at outwardly shifted configuration where  $\iota/2\pi=1$  exists inside the edge ergodic layer.

A typical waveform of the H-mode-like discharge is shown in Fig.2. The H-mode-like transition is triggered by changing the NBI power input at  $t=1.25\text{s}$ . After turning off the beam line, the  $H\alpha$  emission quickly drops and the density gradually rises, showing a clear turning point. ELM-like bursts appear in the  $H\alpha$  signal. Similar bursts are also observed in an electrostatic probe on the divertor plate ( $I_{is}$ ) and a magnetic probe ( $db/dt$ ). Reduction of the magnetic fluctuation is also seen after the H-mode-like transition. No clear mode numbers are observed on the ELM-like bursts from the magnetic probe measurement. This H-mode-like feature, however, disappears after turning off the second NBI at  $t=2.1\text{s}$ . It strongly suggests that a relatively narrow power window exists for keeping the H-mode-like phase.

Pressure profiles in the ergodic layer measured with YAG laser Thomson diagnostics are plotted in Fig.3. The data are obtained at  $t=1.225\text{s}$  before transition (open circles) and  $t=1.625\text{s}$  after transition (solid circles) in the same discharge shown in Fig.2. The position of  $\iota/2\pi=1$  surface is indicated by a vertical dashed line and the LCFS position is  $R=4.560\text{m}$  shown by a vertical solid line. The edge pressure rapidly increases near  $\iota/2\pi=1$  position and it is seen that a steeper pressure gradient is formed after the transition, although the edge  $T_e$  decreases after the transition because of density increase.

Temporal behaviors of three chord-integrated densities from the edge region are traced in Fig.4(a)-(c). The ergodic layer becomes thick at the inboard side, then, the signals of (a) and (b) show the information only from the ergodic layer. A relatively high density exists even in the middle of the ergodic layer of  $R=3.399\text{m}$  where the  $L_c$  is roughly  $100\text{m}$ . A high density is not formed at a region of  $L_c < 10\text{m}$ . Precise measurement was also done to investigate the relation between the  $\iota/2\pi=1$  position and the density bursts position using a multichannel  $\text{CO}_2$  interferometer with a spatial resolution of  $1\text{cm}$ . It is seen that the amplitude of the density bursts become the largest at  $\iota/2\pi=1$  position.

The edge rotational transform in vacuum is used at present. Taking into account the plasma pressure, the edge rotational transform profile seems to be modified, based on a modification of chaotic magnetic field structure

of the ergodic layer. A detailed discussion has to be made for the modification.

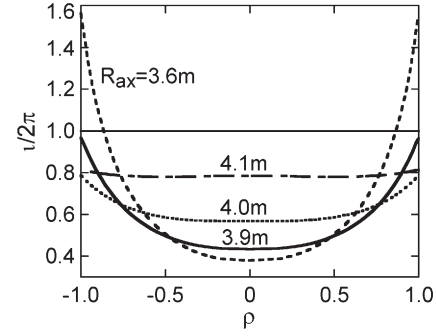


Fig. 1 Rotational transform as a parameter of  $R_{ax}$ .

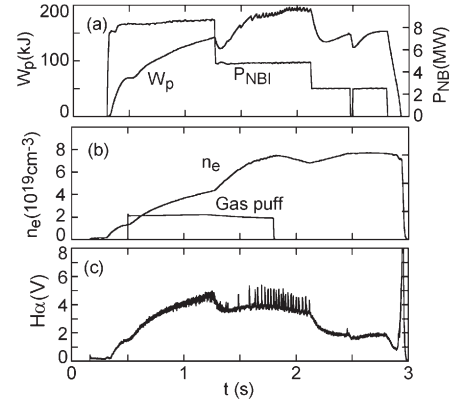


Fig. 2 H-mode-like discharge with ELM-like bursts.

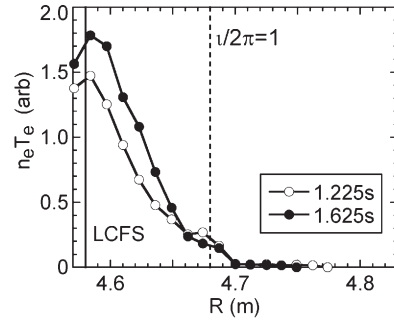


Fig. 3 Edge pressure profile before and after transition.

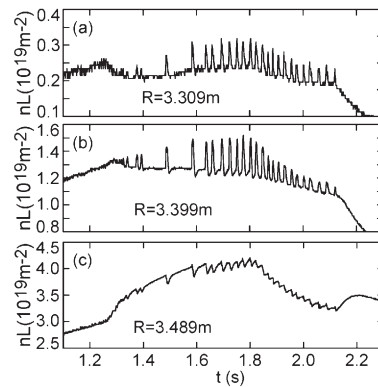


Fig. 4 Edge density behaviors during ELM-like bursts.

### References

- 1) Morita, S. et al., PPCF **48** (2006) A269.

## §12. Comparison of Confinement Degradation in High Density and Particle Transport between Tokamak and Helical Devices

Takenaga, H., Urano, H., Fujita, T. (JAEA), Muraoka, K. (Chubu University), Tanaka, K., Yamada, H.

A comparative study between tokamak and helical plasmas is beneficial for understanding both common physics in toroidal system and unique physics depending on each magnetic configuration. In the past two FYs, confinement degradation at high density observed in JT-60U was compared with that in LHD. In the LHD plasmas, the confinement degradation at high density was also observed at  $R_{ax}=3.6$  m as in JT-60U ELMY H-mode plasmas. At  $R_{ax}=3.75$  m, the confinement degradation was gradual compared with that at  $R_{ax}=3.6$  m, although the confinement was lower at  $R_{ax}=3.75$  m than at  $R_{ax}=3.6$  m in the low density region. In this FY, difference of the density profile, which could influence the confinement, between tokamak and helical devices was focused. The particle transport can be expressed by a sum of neoclassical and turbulence transport and each transport can be divided into diagonal (diffusive) and off-diagonal (convective) terms. The diagonal term is generally dominated by turbulence transport in both tokamak and helical devices. The dominant transport for the off-diagonal term was discussed here.

The density profile was compared in the JT-60U ELMY H-mode plasmas ( $I_p=1.0$  MA,  $B_T=2-2.1$  T,  $P_{NB}=8-10$  MW) and the LHD plasmas ( $B_T=1.5, 2.8$  T) at various  $R_{ax}$  (3.5-3.9 m). In this report, the peaking factor of the density profile was defined as the ratio of the electron density at  $r/a=0.2$  to that at  $r/a=0.8$ . In the JT-60U ELMY H-mode plasmas, the density peaking factor tends to decrease with increasing the electron density at  $r/a=0.5$  as shown in Fig. 1 (a). In ASDEX-U and JET plasmas, the density peaking factor increased with decreasing an effective collisionality ( $\nu_{eff}$ ) defined as the ratio of electron-ion collision frequency to the curvature drift frequency<sup>1),2)</sup>. The curvature drift frequency of  $\omega_{De}=2k_{\perp}\rho_s c_s/R$  provides an estimate of the

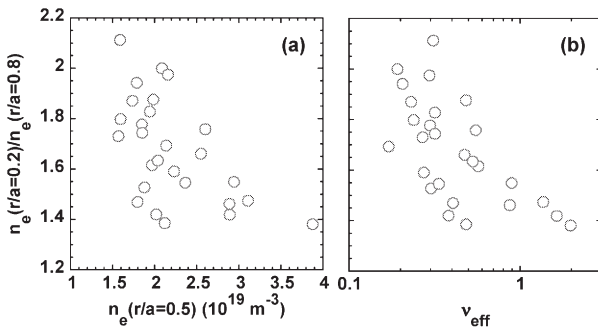


Fig. 1 Density peaking factor as functions of (a) the electron density at  $r/a=0.5$  and (b) the effective collisionality in the JT-60U ELMY H-mode plasmas.

growth rate of the most unstable mode for drift wave instabilities such as ion temperature gradient (ITG) mode and trapped electron mode (TEM). As shown in Fig. 1 (b), the same tendency as observed in ASDEX-U and JET was also observed in JT-60U, indicating that the off-diagonal term is determined by turbulence transport such as ITG and/or TEM. Here,  $k_{\perp}\rho_s = \sqrt{0.1}$  was used for the estimation of  $\nu_{eff}$ .

In the LHD plasmas, the density peaking factor was smaller than unity (hollow density profile) for a part of the data at  $R_{ax}=3.6$  m and for all data at  $R_{ax}=3.75$  and 3.9 m. The density peaking factor increased (the hollowness decreased) with increasing the electron density at  $r/a=0.5$ . This tendency can be qualitatively explained by increase in neoclassical off-diagonal term in  $1/\nu$  regime for the helical system. On the other hand, the peaked density profile was observed at  $R_{ax}=3.5$  m. The density peaking factor tends to decrease with increasing the electron density at  $r/a=0.5$  as well as in JT-60U. The off-diagonal term could be affected by the turbulence transport at  $R_{ax}=3.5$  m similar to tokamak plasmas. At  $R_{ax}=3.6$  m, various density profiles were observed from hollow to peaked one. The data in the range of the electron density at  $r/a=0.5$  of  $1.2-1.6 \times 10^{19} \text{ m}^{-3}$  are plotted as a function of the central electron temperature. The density peaking factor decreased with increasing the central electron temperature and was separated for different  $B_T$ . This result might indicate that the dominant transport for the off-diagonal term changes depending on the  $\nu$  regimes.

The dependence of the upper boundary for the density peaking factor on the electron density in the LHD plasmas at  $R_{ax}=3.5-3.6$  m was similar as that in the JT-60U ELMY H-mode plasmas. In these LHD plasmas, the confinement degradation at high density was strong as well as in the JT-60U ELMY H-mode plasmas. These results might indicate common physics between tokamak and helical devices.

### References

- 1) Angioni, G. et al., : Phys. Rev. Lett, 90 (2003) 205003.
- 2) Weisen, H. et al., : Nucl. Fusion 45 (2005) L1.

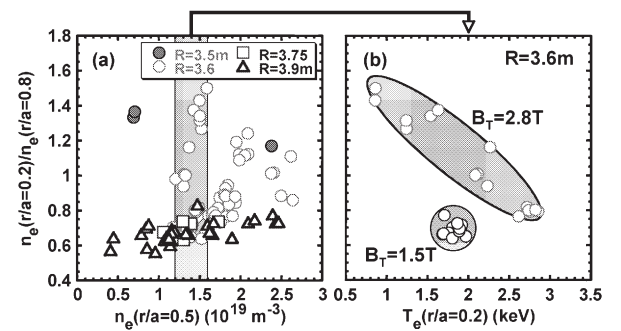


Fig. 2 Density peaking factor as functions of (a) the electron density at  $r/a=0.5$  and (b) the central electron temperature ( $r/a=0.2$ ) in the range of  $n_e(r/a=0.5)=1.2-1.6 \times 10^{19} \text{ m}^{-3}$  for the LHD plasmas.

### §13. Comparison of Experimental Transport Coefficients and Prediction by the Resistive g-Mode Theory

Funaba, H., Watanabe, K.Y., Sakakibara, S.,  
LHD Experimental Group

From the results of the local transport analysis of LHD plasmas in the configuration of  $R_{ax} = 3.6$  and  $\gamma = 1.22$ , it is found that the ratio of the effective transport coefficients to the gyro-reduced Bohm type transport coefficients,  $\chi^{eff}/\chi_e^{GRB}$ , at the peripheral region ( $\rho \sim 0.9$ ) increases in the high  $\beta$  regime. Here,  $\chi^{eff} = (\chi_e^{exp} + \chi_i^{exp})/2$  and  $\chi_e^{exp}$  and  $\chi_i^{exp}$  are the experimental thermal diffusivities of electrons and ions, respectively. They are evaluated by using the one-dimensional transport code for helical plasmas, PROCTR<sup>1)</sup>. On the other hand, the dependence of  $\chi^{eff}/\chi_e^{GRB}$  on the volume averaged  $\beta$ ,  $\langle\beta\rangle$ , is weak around  $\rho \sim 0.5$ . It is considered that the gradual degradation of global confinement against ISS95 with  $\beta$  seems to be mainly caused by the increment in the local transport at the peripheral region.

As one of the causes of this degradation, effects of the resistive pressure-gradient-driven turbulence (g-mode, GMT) on the peripheral transport are studied by comparing the experimental results with the theoretical resistive g-mode transport coefficients. The transport coefficient for electrons and ions by the resistive g-mode,  $\chi_e^{GMT}$  and  $\chi_i^{GMT}$ , are calculated by the equations shown in the references 2) and 3). The theoretical prediction of  $\chi_i^{GMT}$  is smaller than that of  $\chi_e^{GMT}$  by almost one order. However, their dependences on  $\langle\beta\rangle$  are similar. The calculation results show that  $\chi_e^{GMT}$  increases abruptly in the range of  $\langle\beta\rangle < 1.5\%$  and the increment in  $\chi_e^{GMT}$  becomes small at  $\langle\beta\rangle > 1.5\%$ . The ratio of  $\chi^{eff}/\chi_e^{GMT}$  at  $\rho = 0.9$  is shown in figure 1(a). In the range of  $\langle\beta\rangle < 1.0\%$ ,  $\chi^{eff}/\chi_e^{GMT} > 1$ . This result shows that the effect of the resistive g-mode is small in this range. When  $\langle\beta\rangle$  exceeds 1%,  $\chi^{eff}/\chi_e^{GMT}$  becomes almost constant. Therefore, the resistive g-mode is a possible candidate for one of the causes of the degradation in the peripheral region.

On the other hand,  $\chi^{eff}/\chi_e^{GMT}$  at  $\rho = 0.5$  is shown in figure 1(b). In the high  $\beta$  regime,  $\chi_e^{GMT}$  is extremely small since the magnetic well is formed around  $\rho = 0.5$ . The values of  $\chi^{eff}/\chi_e^{GMT}$  are scattered in the range of  $\langle\beta\rangle < 1.5\%$ . In the range of  $\langle\beta\rangle < 1.5\%$ , the scattering of  $\frac{\partial\beta}{\partial\rho}$  is small. The scattering in  $\chi^{eff}/\chi_e^{GMT}$  may be due to the difference of the density and temperature dependence between  $\chi^{GRB}$

and  $\chi_e^{GMT}$ . When  $T_e$  becomes high,  $\chi_e^{GMT}$  tends to become small through  $S$ , while  $\chi^{GRB}$  has the dependence of  $T_e^{3/2}$ . Here,  $S = \tau_R/\tau_{hp}$ , is the magnetic Reynolds number where  $\tau_R$  is the resistive skin time and  $\tau_{hp}$  is the poloidal Alfvén time. From these results, it seems that  $\chi^{eff}/\chi_e^{GMT}$  is not related with  $\langle\beta\rangle$  at  $\rho \sim 0.5$ .

From the comparison results of the transport coefficients which are theoretically estimated by the resistive g-mode model and the experimental  $\chi^{eff}$ , it is found that their dependences on  $\langle\beta\rangle$  in the high  $\beta$  regime are similar. This shows that the resistive g-mode can be considered to be one of the causes of the degradation of global confinement in the high  $\beta$  regime.

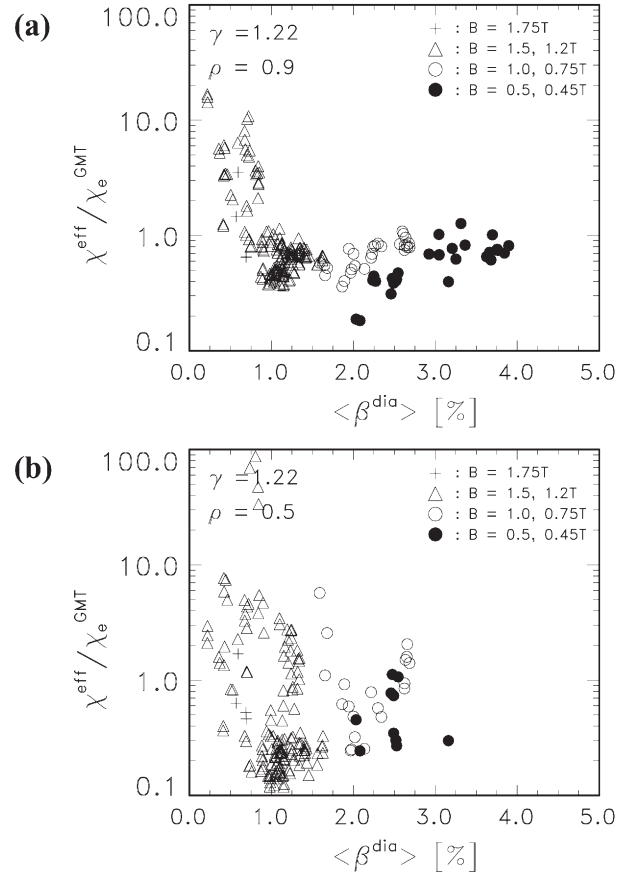


Fig. 1. Dependences of the effective transport coefficients normalized by the resistive g-mode on  $\langle\beta\rangle$  ( $\gamma = 1.22$ ).

(a)  $\chi^{eff}/\chi_e^{GMT}$  at  $\rho = 0.9$ , (b)  $\chi^{eff}/\chi_e^{GMT}$  at  $\rho = 0.5$ .

#### References

- 1) H.C. Howe, ORNL/TM-11521,(1990).
- 2) B.A. Carreras, L. Garcia and P.H. Diamond, Phys. Fluids, **30**, 1388 (1987).
- 3) B.A. Carreras and P.H. Diamond, Phys. Fluids B, **1**, 1011 (1989).

## §14. High $W_p$ Experiment

Nagayama, Y., Sakamoto, R., Narihara, K.

The diamagnetic energy ( $W_p$ ) is the energy confined in the plasma, and it represents overall performance of a plasma confinement device. So far, the record  $W_p$  (1.31 MJ) was obtained in the case of  $R_{ax}=3.6$  m. In this case, the plasma volume is large and the neoclassical transport is reduced. This shot (#47919) is referred as  $R_{ax}=3.6$ m in Figs. 1-3 in this report. In the 9<sup>th</sup> campaign, the pipe-gun type and the repetitive  $H_2$  ice pellet injectors have been significantly improved, and the 40 kV, 3 MW NBI for diagnostics (NBI#4) has been installed.

Figure 1 shows the obtained  $W_p$  versus  $R_{ax}$ . New record (1.37 MJ) is obtained in the case of  $R_{ax}=3.65$  m. Fig. 2 shows time evolution of  $n_{e0}$ ,  $T_{e0}$  and  $W_p$ . In the high  $W_p$  experiment, 8 larger ice pellets are injected from the pipe gun with 30 – 50 ms interval, then small ice pellets are injected repetitively. After the large pellet injection, the  $T_e$  grows as the  $n_e$  is decreased, so that the  $W_p$  is increased. This phenomenon is called “reheat”.

In the previous campaigns, the ice pellets are injected in plasma with lower heating power in order to evaporate limited number of pellets should in the core plasma. In this experiment, most NBI is injected during pellet injection since the pellet becomes bigger. Since the pulse length of NBI#4 is limited, NBI#4 is injected in the reheat phase.

Fig. 3 shows the radial profiles of  $n_e$  and  $T_e$  measured by the Thomson scattering. The value of  $n_e$  is normalized by the FIR laser interferometer at  $t=0.5$  sec and the unit may be close to  $10^{19} \text{ m}^{-3}$ . Although still some systematic error may be remained in the  $n_e$  profile, we can observe a peaked  $n_e$  profile in the case of  $R_{ax}=3.75$  m. In the smaller  $R_{ax}$  cases, the  $n_e$  profile is rather flat. Interestingly, in any cases, we can observe a small step in the  $n_e$  profile at  $R=4.25$  m, where the  $iota=1$  surface is located.

The plasma confinement should be improved to obtain much higher  $W_p$ . The  $n_e$  profile control may be a key.

The small step in the  $n_e$  profile might be a sign of the confinement improvement.

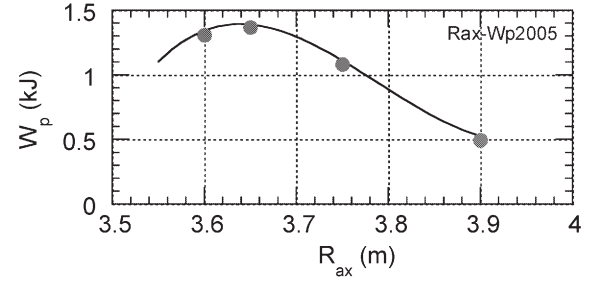


Fig. 1 Obtained  $W_p$  vs. the radius of the magnetic axis.

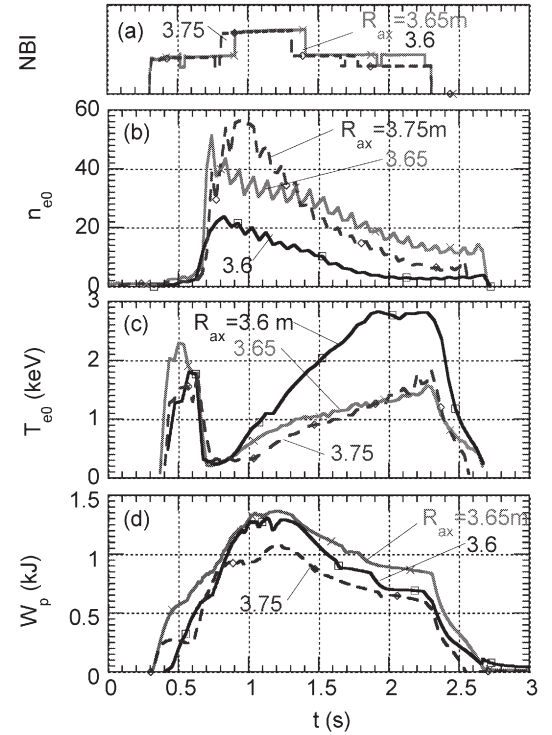


Fig. 2 Time evolution of (a) NBI, (b)  $T_{e0}$ , (c)  $n_{e0}$ , (d)  $W_p$  in high  $W_p$  plasmas.

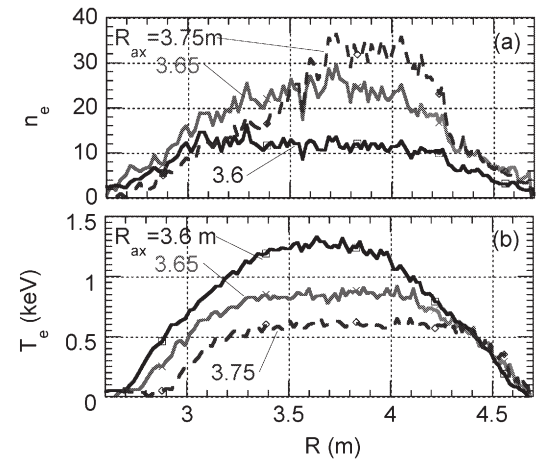


Fig. 3 Radial profile of (a)  $T_e$ , (b)  $n_e$  in high  $W_p$  plasmas.



## §15. Effect of Island Size on High- $T_e$ Transition during Core-Localized ECH

Shimozuma, T., Kubo, S., Inagaki, S., Yoshimura, Y., Igami, H., Notake, T., Mutoh, T.

In LHD, a transition to the high-electron-temperature state is observed with an electron internal transport barrier (ITB). It is characterized by a high central electron temperature up to 10 keV and steep temperature gradient around  $\rho$  (normalized minor radius)  $\simeq 0.3^{(1)}$ . During the additional ECH, two different kinds of improved confinement were observed. The appearance of those states depends on the injection direction of NBI. Heat transport analyses by using MECH clarified that the structure of the ITB existed only in the counter-injected NBI sustained plasmas. There is a threshold ECH power for the transition to the high- $T_e$  state. A triggering mechanism of the transition is possibly related to the magnetic field structure such as existence of low-order rational surfaces and islands in the plasma core<sup>2)</sup>. We have been studying the effect of the existence and size of  $m/n=2/1$  islands on the high- $T_e$  transition in the plasma core.

The experiments were performed at the magnetic configuration with  $B = 2.829\text{T}$  and the magnetic axis of  $R_{ax} = 3.5\text{m}$ . Figure 1 shows the effect of the island-canceling magnetic field by the external perturbation coils on the counter-NBI target plasma during an additional ECH injection (a) with the natural island (without the island-canceling field) and (b) with reducing the island size (with the island-canceling field). Calculated results of flux surfaces with natural islands show that the maximum width of the  $2/1$  island is reduced from 58 mm to 29 mm by the application of the island canceling field produced by the perturbation coil currents used in the experiment. Time variations of the temperature gradients at several minor radii are plotted in the figures. These temperature gradients were determined from fifth-order polynomial fitted temperature data, which were measured by 20-channel Electron Cyclotron Emission (ECE) diagnostic. The rapid and significant increase of the temperature gradient inside  $\rho \simeq 0.3$  is found in existence of the natural island after the additional ECH power of 82.7GHz. The rapid decrease of the gradient, or flattening of the temperature is also observed at  $\rho = 0.4$  and  $0.5$ . On the other hand, a slow and little increase during the additional ECH pulse is found for the plasma with the reduced island size. This experimental evidence assures that the existence of the  $2/1$  island is a candidate for the triggering and driving mechanism of high- $T_e$  transition, which may be induced by the radial electric field bifurcation.

In the 9th experimental campaign, experiments were performed to clarify the effect of the island size on the

high- $T_e$  transition. Three cases were compared; reduced  $2/1$  island (calculated size  $\simeq 29\text{mm}$ ), natural island (size  $\simeq 59\text{mm}$ ) and enlarged island (size  $\simeq 83\text{mm}$ ). In Fig. 2, the central electron temperature increase ( $\rho = 0.1$ ) is plotted as a function of the density normalized ECH power,  $P_{\text{ECH}}/n_e$ . In these experiments, a power threshold for the transition was not clearly observed in the case with natural islands around  $P_{\text{ECH}}/n_e \simeq 1.4$ . Instead, there are small jumps of the temperature between  $P_{\text{ECH}}/n_e \simeq 0.2$  and  $0.4$ . The effect of the island size is noticed around  $P_{\text{ECH}}/n_e \simeq 1.5$ . There is an optimum island size to achieve quick  $T_e$  increase. The central temperature increase, however, seems to be prevented by a flattening of the temperature profile with too large island. A precise investigation of the island size optimization is a future work.

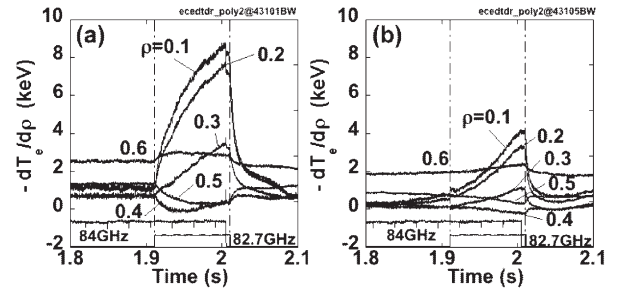


Fig. 1: Effect of island reducing field on high- $T_e$  transition in the Counter-NBI sustained plasma with additional ECH. Time variations of the electron temperature gradient at several radial positions are shown for with natural island in (a) and for with reduced natural island in (b).

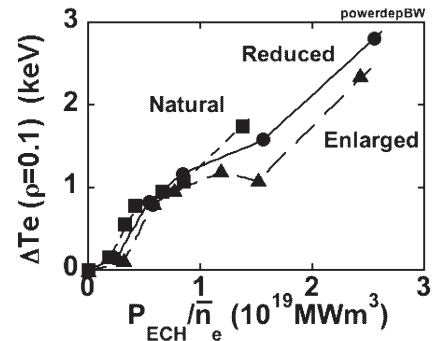


Fig. 2: Central electron temperature increase is plotted as a function of the density normalized ECH power for reduced, natural and enlarged  $2/1$  islands

### References

- 1) T. Shimozuma, *et al*, Plasma Phys. Control. Fusion **45** (2003) 1183.
- 2) T. Shimozuma, *et al*, Nucl. Fusion **45** (2005) 1396.

## §16. Common Features of Core Electron-Root Confinement (CERC) in Helical Plasmas

Yokoyama, M.,

Maaßberg, H.\*, Ida, K., Castejon, F.\*\*, Estrada, T.\*\*, Fujisawa, A., Minami, T., Shimozuma, T., Takeiri, Y., Tribaldos, V.\*\*, Beidler, C.D.\*, Dinklage, A.\*, Murakami, S.\*\*\*, Yamada, H.

\*Max-Planck Institut für Plasmaphysik, Greifswald, Germany

\*\*Laboratorio Nacional de Fusión, CIEMAT-FUSION, Spain

\*\*\*Dep. Nuclear Engineering, Kyoto Univ., Japan

The improvement of core heat confinement has been realized in a wide range of helical devices with central ECH power deposition (alone or in combination with NBI). Peaked electron temperature ( $T_e$ ) profiles and strongly positive radial electric fields ( $E_r$ ) in the core region have been observed commonly in CHS (dubbed neoclassical (NC) internal transport barrier [N-ITB]) [e.g.1], LHD (electron ITB) [e.g.2], TJ-II (Enhanced Heat Confinement (EHC) or electron ITB) [e.g.3] and W7-AS (electron-root feature [e.g.4]).  $T_e$  has exceeded 10 keV in LHD and reached 6 keV in W7-AS with this improvement. The formation of strong positive  $E_r$  is required within NC theory to satisfy the ambipolarity condition. This “electron-root” feature exists only in low-collisionality helical plasmas in which the electrons make a transition from the  $1/\nu$  regime for small  $E_r$  to the  $\nu^{1/2}$  or  $\nu$  regime for larger  $E_r$ . Density and ECH power thresholds for this improved confinement have been recognized associated with this transition of  $E_r$ . Core electron heat diffusivity is reduced significantly compared to its NC level with  $E_r=0$ . This improved core confinement, referred collectively as “Core Electron-Root Confinement (CERC)”, has signatures quite different than those of tokamak ITBs [e.g.7]. The contribution of additional convective electron flux ( $\Gamma_{e,con}$ ) driven by strong ECH has also been revealed, illustrating the configuration dependence of the ECH power threshold [4].

The collisionality regime and the ECH power threshold for CERC are expected to vary depending on the magnetic configuration as well as the heating scenario [8] since the NC fluxes and ECH-driven  $\Gamma_{e,con}$  (by heated trapped electrons) are both influenced by magnetic-field topology. Experiments in a wide range of helical plasmas provide an opportunity for investigating this issue. The accumulation of CERC discharges and related theoretical analyses has led to the initiation of “International Stellarator Profile DataBase (ISPDB)” as an extension of the ongoing

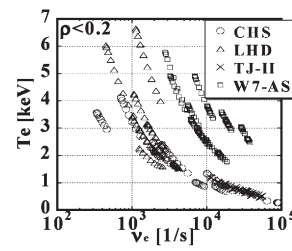


Fig.1. Parameter regime ( $T_e$  and  $v_e$  for  $\rho < 0.2$ ) of CERC in the four devices.

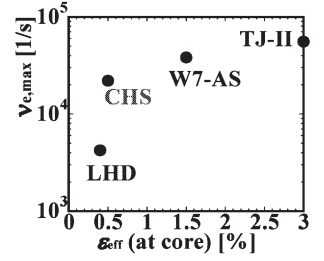


Fig.2.  $v_{e,max}$  versus  $\epsilon_{eff}$  at the core region in the four devices.

research within the International Stellarator Confinement DataBase activity [9]. The collisionality regime for CERC in four devices is compared in Fig. 2, where the electron collisionality,  $v_e$ , in  $\rho < 0.2$  is shown. The data at  $v_e \sim 10^5$  [1/s] in CHS are for non-CERC plasma. The four clusters for W7-AS are due changes in the density. The data points for CHS and LHD are found at smaller  $v_e$  than those of TJ-II and W7-AS. CERC discharges in TJ-II appear in the regime where CHS has not yet achieved CERC. The maximum  $v_e$ ,  $v_{e,max}$ , (from Fig. 1) for CERC is plotted in Fig. 2 as a function of the effective ripple (a measure of the ripple-transport level),  $\epsilon_{eff}$ , at the core region. The trend that the larger  $\epsilon_{eff}$  the higher  $v_{e,max}$  can be recognized. It is worthwhile summarizing CERC discharges with  $v_{e,max}$  since the collisionality has been recognized to be the responsible parameter for transition to the electron root [10]. The trend in Fig. 2 can be understood by the change of the ripple-transport level providing the bifurcation nature of  $E_r$ . It has been confirmed, so far, that, in W7-AS, larger  $\Gamma_{e,con}$  (comparable to the NC electron flux ( $\Gamma_{e,NC}$ ) in ion-root regime, which is contrast to that in LHD where it is at the most 30 % of  $\Gamma_{e,NC}$ ) and higher ECH power density are reasons for higher  $v_{e,max}$ .

The ISPDB activity has allowed us to perform comparative studies of CERC discharges in different devices. It has been recognized that larger  $\epsilon_{eff}$  and  $\Gamma_{e,con}$  help achieving CERC at higher collisionality.

### References

- [1] A.Fujisawa et al., Phys. Rev. Lett. **82** (1999) 2669.
- [2] K.Ida et al., Phys. Rev. Lett. **91** (2003) 085003.
- [3] F.Castejon et al., Nucl. Fusion **42** (2002) 271.
- [4] H.Maaßberg et al., Phys. Plasmas **7** (2000) 295.
- [5] A.Fujisawa, Plasma Phys. Control. Fusion **45** (2003) R1.
- [6] M.Yokoyama et al., submitted to Fusion Sci. Tech. (2005).
- [7] K.Ida et al., Plasma Phys. Control Fusion **46** (2004) A45.
- [8] M.Romé et al., Plasma Phys. Control. Fusion **48** (2006) 353.
- [9] H.Yamada et al., Nucl. Fusion **45** (2005) 1684.
- [10] K.Ida et al., Nucl. Fusion **45** (2005) 391.



## §17. Direct Observation of Inward Electron Flux Being Blocked in the Large Helical Device

Narihara, K., LHD Experimental Group

We analyzed particle transport phenomenon caused by a pellet injection into the Large Helical Device [1].

The plasma (#56112) that we present here was created by ECH in a vacuum magnetic configuration with the magnetic axis at 3.6 m and field intensity 2.75T, heated by 1.3MW NBI, and fueled by a repetitive solid hydrogen pellets. A multi-channel Thomson scattering system measured how the electron temperature ( $T_e$ ) and density ( $n_e$ ) profiles evolve in response to the NBI and pellet injection (PI). Figure 1 shows eight successive snap-shots measured every 0.1s. Before the PI,  $T_e$ -profile shape was a triangle and  $n_e$ -profile shape was a shallow hollow. Pellets entered around 2.45s. Just after the PI,  $n_e$ -profile became a deep hollow shape like a head of a cat. The  $T_e$ -profile just after the PI shrunk a little but soon restored the initial triangle shape. It seems that the  $n_e$ -perturbation caused by the PI did not propagate into the core region. To see this more clearly, we over-plot  $n_e$ -profiles between two PIs in Fig. 2. One can see that particles diffusing into the core region were almost blocked up to the surface intersecting at  $R=3.2$  m and 4.0 m. Only a small amount of particles ( $<10\%$ ) entered the core region just after the PI and resided there for a longer time, thus boosting the background profile as a whole. Except this small increase, the  $n_e$ -profile resumed almost the same shape as before the PI.

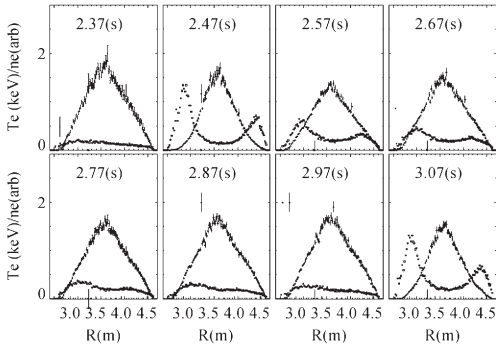


Fig.1  $T_e$  (triangle) and  $n_e$  (hollow) profiles every 0.1s. Pellet entered at 2.45s. The  $n_e$  lies in  $10^{19} \text{ m}^{-3}$  range.

We examine the above blocking phenomenon somewhat quantitatively. Assuming the usual form of the particle flux  $\Gamma = -D\nabla n_e + Vn_e$  with assumed diffusion coefficient  $D$  and convection velocity  $V$ , we follow the left-side  $n_e$ -profile after 2.47s (2<sup>nd</sup> frame) by solving  $A\partial n_e/\partial t = \partial(A\Gamma)/\partial \rho$ , where  $\rho$  is a minor radius and  $A(\rho)$  is the area of the flux surface. Here we drop the source term, since at 2.47s, 20 ms after PI, the injected hydrogen atoms were almost completely ionized and hence the particle source localized at the plasma edge had no influence for the evolution of the *perturbed*  $n_e$ -profile. The most simple model of  $(D, V) = (\text{constant}, 0)$  hardly reproduces the observed  $n_e$ -profile evolution. As shown in Fig. 3(A), the

fit with  $D=0.5 \text{ m}^2/\text{s}$  inevitably accompanies an in-going  $n_e$ -perturbation. This inward propagation is hindered by deliberately lowering the  $D$  in the inner region, which mimics an internal transport barrier (ITB) as shown in Figure 3(B).

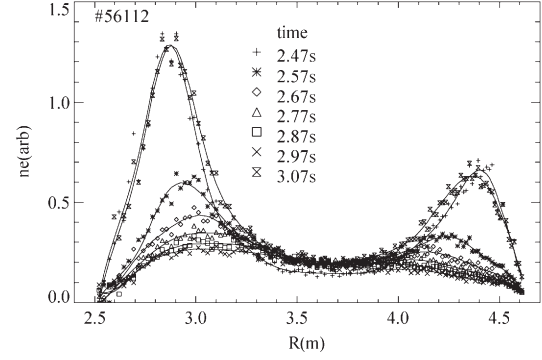


Fig. 2. Evolution of  $n_e$ -profile between two pellet-injections.

One can better reproduce the observation by choosing a two-valued  $(D, V)$  combination:

$D = 0.5 \text{ m}^2/\text{s}$ ,  $V = 0 \text{ m/s}$  in the outer region

$D = 0.05 \text{ m}^2/\text{s}$ ,  $V = 1.5 \text{ m/s}$  in the inner region

as shown in Fig. 3(C). Here the boundary between the inner- and outer-regions is guessed to be at  $R=3.0$  m and 4.2 m, which are marked by the vertical lines.

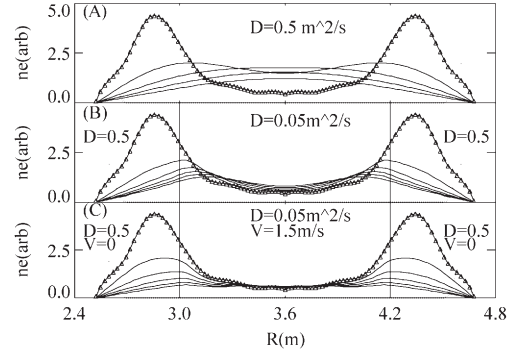


Fig. 3. Calculated  $n_e$ -profile evolutions every 0.1 s after a pellet injection: for (A) uniform  $D=0.5 \text{ m}^2/\text{s}$ ; (B) an 'ITB' with 10-times insulation; (C) the 'ITB' plus an outward convection. The right side of each figure is reflection of the left with plane of symmetry at  $R=3.6$  m. The dotted triangles at the edges are the estimated source profile.

In considering the bi-directional property of the diffusion process, we could guess from the present result that the core region can hold plasma a longer time once plenty of particles are introduced inside by some means.

[1] Narihara, K., *et al*, Plasma and Fusion Research: Rapid Communications 1, 023 (2006).

## §18. Configuration Effects on Particle Transport in LHD

Tanaka, K., Michael, C.A. (JSPS fellow), Kawahata, K.

The particle transport was investigated using density modulation for three different magnetic configurations, represented by the magnetic axis position in vacuum ( $R_{ax}$ ) of 3.6, 3.75 and 3.9m [1]. Figure 1 shows the change of the  $T_e$  and  $n_e$  profiles at three different  $R_{ax}$ . The heating power was adjusted to maintain almost identical electron temperature profiles. In a previous study [2], it was found that for constant density, the electron temperature and its gradient are key parameters for controlling particle diffusion and convection respectively. Despite this, as shown in Fig. 1(b), the achieved density profiles are rather different for almost identical  $T_e$  profile. The average density is almost the same for  $R_{ax} = 3.6$  and 3.75m, but the density profile is more hollow for  $R_{ax} = 3.75$ m. The achieved density was lower for  $R_{ax} = 3.9$  m compared with other configurations under almost identical particle fuelling.

Figure 2 shows parameter dependence of  $D$  and  $V$ . The electron temperature and  $-\text{grad } T_e/T_e$  are averaged over  $0.4 < \rho < 0.7$  for the core and  $0.7 < \rho < 1.0$  for the edge. As shown in Fig.2 (a), (b), positive  $T_e$  dependencies are observed in all configurations. For more outward shifted configurations, the diffusion coefficient becomes larger at the same  $T_e$  both in the core and edge region. The temperature dependence also varies with  $B_t$ . Stronger  $D_{edge}$  variation with  $T_e$  at lower  $B_t$  was observed at  $R_{ax}=3.6$ m.

A positive dependence of  $V_{core}$  on  $-\text{grad } T_e/T_e$  is observed for all configurations as shown in Fig.2(c). As shown in Fig. 1(d), the edge convection velocity is proportional to  $-\text{grad } T_e/T_e$  at  $R_{ax}=3.6$ m and 3.75m, and also reverses direction from inward to outward with increasing  $-\text{grad } T_e/T_e$ . However, at  $R_{ax}=3.9$ m,  $V_{edge}$  does not change dramatically. Each graph in Fig. 2 appears to show an offset linear trend, with a different offset for each configuration.

Figure 3 shows comparisons of  $D$  and  $V$  with neoclassical values and their dependence on the normalized collision frequency ( $\nu_h^*$ ), which is normalized by the collision frequency of boundary between plateau and  $1/\nu$  regime. As  $\nu_h^*$  is decreased, the experimental  $D_{core}$  increases, and the neoclassical value of  $D_{core}$  becomes closer to the experimental value as shown in Fig.3 (a). However, the experimental  $D_{core}$  is around one order magnitude larger than neoclassical even in the  $1/\nu$  regime ( $\nu_h^* < 1$ ). The difference between the experimental and neoclassical  $D_{edge}$  values is larger. For all values of collisionality, the experimental value of  $D_{edge}$  is more than one order magnitude larger than the neoclassical one.

As shown in Fig. 3(a), the experimental  $V_{core}$  is comparable with neoclassical for all values of  $\nu_h^*$ . Although, at  $R_{ax}=3.6$ m,  $B_t=2.8$ T,  $V_{core}$  from experiments at higher  $\nu_h^*$  is directed inward contrary to neoclassical prediction, which is directed outward. Generally, both

experimental and neoclassical  $V_{core}$  almost agree within experimental error.

### Reference

- 1) Tanaka, K., et al., to be published Fusion Science and Technology
- 2) Tanaka, K., et al., Nucl. Fusion 46 (2006) 110–122

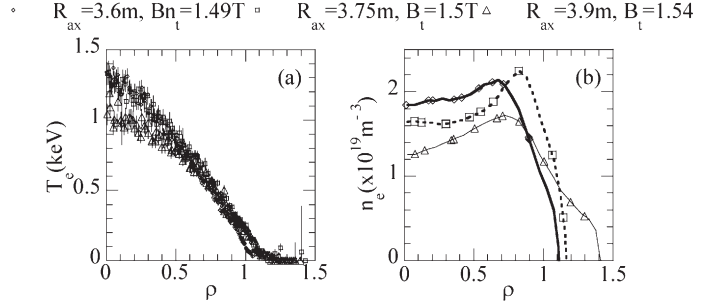


Fig. 1. (a)  $T_e$  and (b)  $n_e$  profiles of three different configurations

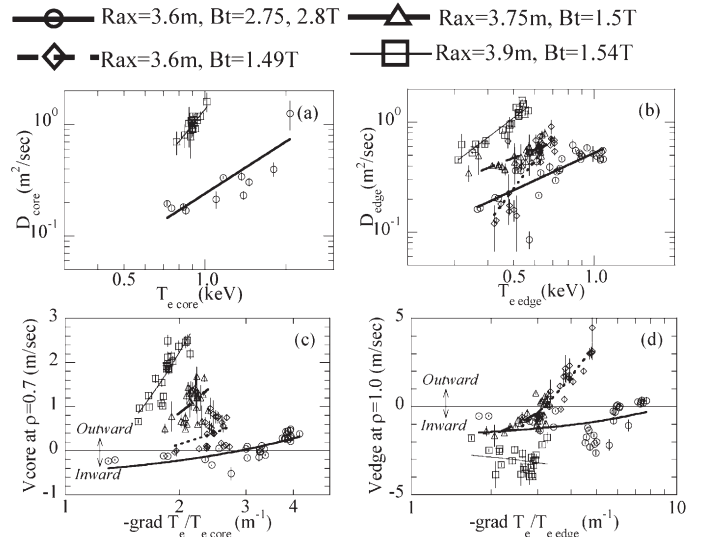


Fig.2 Parameter dependence of  $D$  and  $V$  (a)  $T_e$  dependence of  $D_{core}$ , and (b)  $D_{edge}$ ,  $-\text{grad } T_e/T_e$  dependence of (c)  $V_{core}$  and (d)  $V_{edge}$

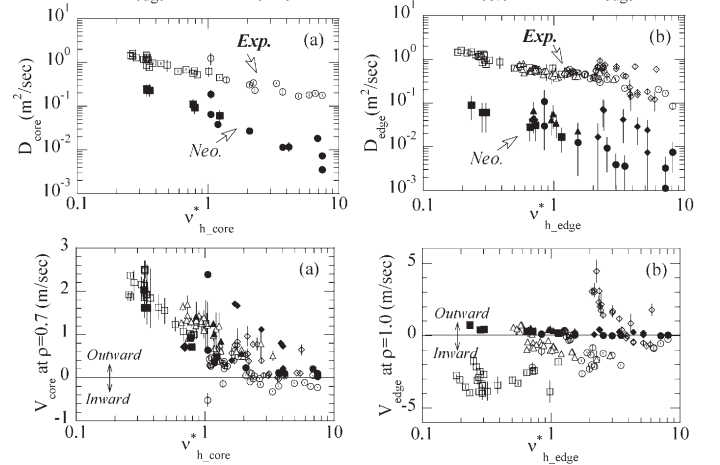


Fig.3 Comparison with neoclassical estimation (a)  $D_{core}$ , (b)  $D_{edge}$ , (c)  $V_{core}$  and (d)  $V_{edge}$ . Symbols are same as in Fig.2 Coloured symbols indicates neoclassical estimation.

## §19. Electron Transport Dynamics in LHD Core Plasmas

Inagaki, S., Nagayama, Y., Kawahata, K.

The observed dynamics has different time and space scales. Plasma transport is dominated by turbulence, and thus the exhibited time and space scales of transport dynamics is considered to be resulted from the turbulence-transport interactions. To achieving a predictive capability of turbulence transport, therefore, understanding of the dynamics is crucial.

An spontaneous electron ITB (eITB) formation and a non-local electron temperature,  $T_e$ , rise have been observed in the Large Helical Device (LHD), which has negative magnetic shear and is free of net current. Neutral beams with a power of 2-4 MW are injected to initiate and sustain the plasma. The fundamental and the second harmonics of ECH is added with a power of 0.5-1 MW. Figure 1(a) shows a typical time evolution of  $T_e$  at the spontaneous eITB formation. A decrease in the density triggers an eITB formation in LHD. Electron ITB formation event propagates core to edge and then stopped near the low order rational surface ( $m/n = 2/1$ ) as well as in tokamaks. The time scale of the ITB event propagation is 50 ms and is comparable to the energy confinement time of this

discharge.

A typical  $T_e$  response to the edge cooling in LHD by a tracer encapsulated solid pellet (TESPEL) injection is shown in Fig. 1(b). Although the TESPEL affects only on the edge plasma, a sudden rise of  $T_e$  takes place in the central region ( $\rho \leq 0.4$ ). Unlike the ITB formation, the plasma starts to go back to normal condition 30 ms after TESPEL injection as in tokamaks. Radial propagation of  $T_e$  rise is unclear because it takes place almost simultaneously in the core region ( $\rho \leq 0.4$ ).

The spontaneous eITB formation and the non-local  $T_e$  rise takes place in the low- $n_e$  and high- $T_e$  (low collisionality) regime in LHD. The critical density for non-local  $T_e$  rise ( $1.5 \times 10^{19} \text{ m}^{-3}$ ) is 2-3 times larger than that for eITB formation ( $0.6 \times 10^{19} \text{ m}^{-3}$ ). The  $T_e$  changes discontinuously at the critical value. On the other hand, an increase in  $T_e$  induced by TESPEL injection gradually increases with decrease in the density. Although two phenomena are observed similar experimental conditions, physical mechanisms are considered to be quite different qualitatively. The time and space scales of two phenomena are quite different. The spontaneous eITB formation in LHD is characterized by narrow in radial region and slow in propagation time scale. On the other hand, the non-local  $T_e$  rise is characterized by wide in radial region and fast in propagation time scale.

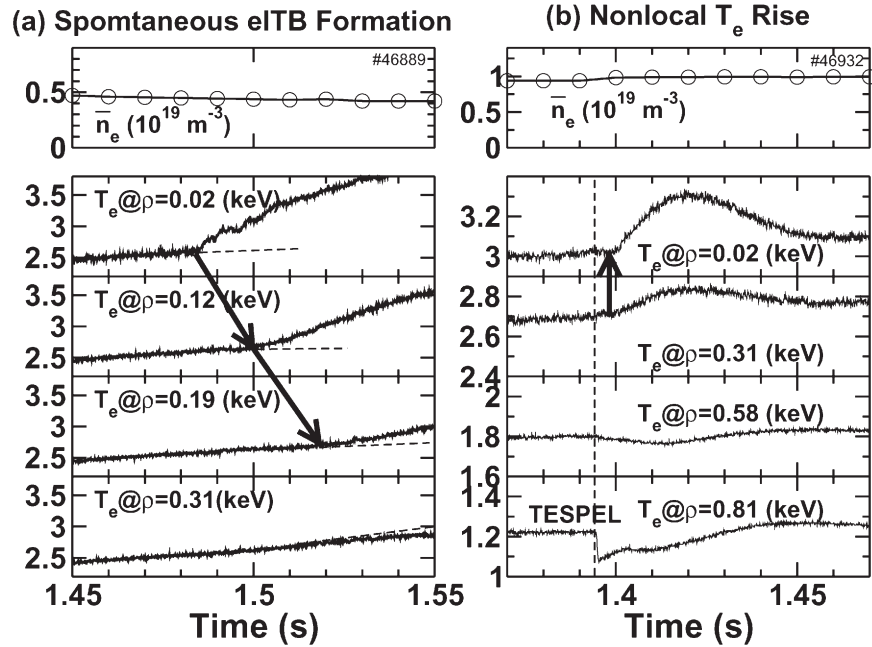


Fig. 1: Typical time evolutions of line-averaged density and electron temperature at different radii in LHD plasmas with (a) the spontaneous ITB formation and (b) the non-local  $T_e$  rise (a major radius at the magnetic axis of 3.5 m, an averaged minor radius of 0.56 m and a magnetic field at the axis of 2.829 T).

## §20. Study of Nonlocal Electron Heat Transport on the High Temperature Plasmas of LHD

Tamura, N., Inagaki, S., Tokuzawa, T., Tanaka, K., Michael, C., Sakakibara, S., Shimozuma, T., Kubo, S., Itoh, K., Kalinina, D.V., Sudo, S., Nagayama, Y., Kawahata, K.

In order to achieve a reliable predictive capability for well-controlled fusion plasmas, a definitive understanding of turbulent transport is highly required. The recent study of turbulent transport suggests the importance of an edge-core interaction and coupling in the nonlocal response observed in many tokamaks and helical systems. The recent edge cooling experiment in the LHD shows the nonlocal electron temperature  $T_e$  rise invoked by the rapid cooling of the edge plasma. Nonlocal transport phenomenon in helical device would be very useful to obtain a comprehensive understanding of the turbulent transport in magnetically confined toroidal devices, since the helical devices are free of net-current and have different magnetic shear from that of tokamaks. Figure 1 shows a typical result of the peripheral cooling experiment by a TESPEL injection. Within the time displayed in Fig. 1, the plasma is heated continuously by co-NBI (injected power  $\sim 2$  MW) and ECH (injected power  $\sim 1.7$  MW). Since the power of the neutral beam mainly goes into the electrons due to its high acceleration energy ( $\sim 140$  keV), the electron heat transport is the dominant thermal loss channel. The TESPEL penetration depth is around  $\rho \sim 0.8$ . A significant rise of the core  $T_e$  in response to the edge cooling can be immediately recognized in Fig. 1. During the rising phase of the core  $T_e$ , neither density peaking nor significant change in low- $m$  MHD modes are observed. As shown in Fig. 1, the discrepancy between the  $T_e$  measured and that simulated, which is obtained by solving the perturbed heat transport equation with a simple diffusion model, is quite noticeable in the core ( $\rho < 0.6$ ) region. Even with the model based on the assumption that heat flux has a strong non-linear dependence on  $T_e$  and/or  $T_e$  gradient cannot reproduce the cold pulse propagation with inversion of polarity. A transient analysis of electron heat transport indicates an abrupt reduction of electron heat diffusivity takes place with no change in local parameters in the region of interest. Therefore the sudden rise in the core  $T_e$  invoked by the edge cooling in the LHD can be caused by a nonlocal effect. In the LHD, the nonlocal  $T_e$  rise is observed in various plasmas. For example, the observation of nonlocal  $T_e$  rise in a plasma heated only with ECH (i.e. net-current free plasma) can completely rule out the contribution of the toroidal plasma current as a reason for the non-local  $T_e$  rise.

The interaction of turbulence over long distance (nonlocality of the turbulence) has been studied as a possible candidate for the nonlocal behavior in the electron heat transport. Microturbulence theory predicts two candidates for the electron transport, ETG and TEM modes. Based on a simple mixing length estimate, an ETG driven electron heat diffusivity is generally much lower than an ITG/TEM driven one. Thus the ETG turbulence might be ruled out of the candidates of the nonlocal  $T_e$  rise. The nonlocal transport observed in the ECH plasma, which has the weakly driven ion heat channel, may suggest that ITG turbulence also could be ruled out. The TEM modes are generally coupled to ITG modes and are

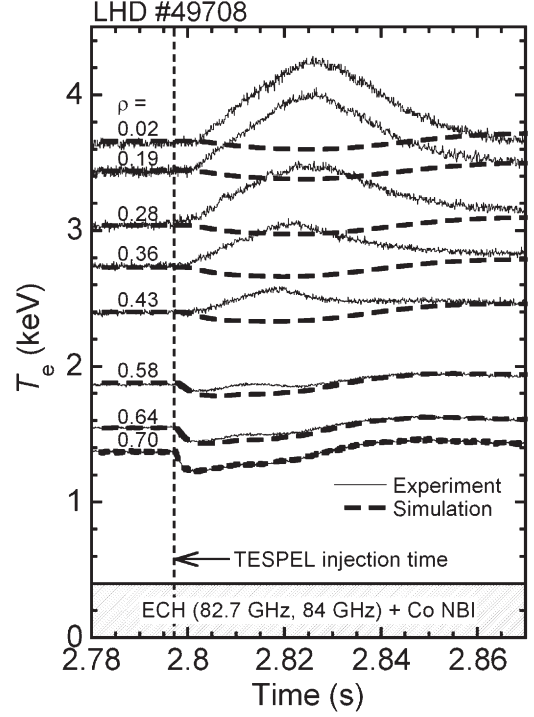


Fig. 1. Time evolution of the measured electron temperature (solid line) at different normalized minor radii. The simulated temperature (broken line) is also plotted. The TESPEL injection time is indicated as the vertical dashed line.

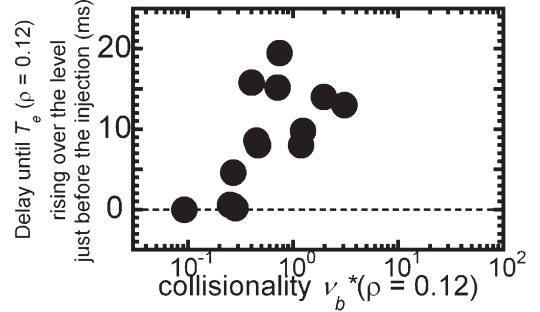


Fig. 2. The delay until the  $T_e$  rise over the level just before the TESPEL injection as a function of the collisionality  $\nu_b^*$ .

stabilized in high collisionality regimes. Thus it is important to study a dependence of the nonlocal transport on the collisionality. In the low density (low collisionality) plasma, the core  $T_e$  rise takes place almost as soon as the TESPEL penetrates. However, when the  $n_e$  increases, the delay of the core  $T_e$  rise appears. (e.g. at  $\rho = 0.12$ ,  $\sim 5$  ms delayed at a line averaged density of  $0.94 \times 10^{19} \text{ m}^{-3}$ ) It should be noted here that even with a delayed onset time of nonlocal  $T_e$  rise, the time of the  $T_e$  rise in the core region still has kind of a spatial uniformity. The amplitude of the core  $T_e$  rise decreases with increasing  $n_e$  as well as in tokamaks. Figure 2 shows the delay until the  $T_e$  ( $\rho = 0.12$ ) rise over the level just before the TESPEL injection as a function of collisionality  $\nu_b^*$ , which is electron collisionality obtained at  $\rho = 0.12$  normalized by bounce frequency of banana orbit. The low collisionality ( $\nu_b^* < 1$ ) is favorable for a strong nonlocal effect producing. In the high collisionality regime, the nonlocal  $T_e$  rise is never observed. Therefore the TEM turbulence may play an important role in the nonlocal transport phenomenon.



## §21. Observation of Spontaneous Toroidal Flow in LHD

Yoshinuma, M., Ida, K.

A moderate velocity shear of plasma flow is considered to play an important role to suppress turbulence and reduce transport, although a large velocity shear causes Kelvin-Helmholtz instabilities. Thus the measurement of radial profiles of flow velocity is important in the study of plasma confinement. Because the toroidal flow is coupled with poloidal flow through viscosity tensor, the toroidal flow determined by not only toroidal momentum driven by NBI and momentum transport but also by toroidal forces driven by poloidal flow and radial electric field through viscosity tensor. The profiles of toroidal flow velocity are measured with charge exchange spectroscopy (CXS) with tangential view using the emission from carbon impurity (CVI).

The magnetic field strength is 2.75T and the major radius of the magnetic axis is  $R_{ax}=3.6\text{m}$  in this experiment. The plasma is produced initially by electron cyclotron heating with hydrogen gas and sustained with tangentially injected n-NBI with negative ion source and perpendicularly injected p-NBI with positive ion source. The line averaged electron density and central electron temperature is  $1.6 \times 10^{19}\text{m}^{-3}$  and 2.5 keV, respectively. The n-NBI is also used to control the momentum injection in tangential direction which drives the toroidal flow directly, while the p-NBI is used as a probe beam for CXS as well as the ion heating.

Figure 1 shows the radial profiles of the toroidal flow velocity in the plasma with co-injected and counter-injected NBI. The differences in toroidal flow velocity between these two discharges are considered to be the toroidal flow driven by momentum injection from n-NBI. The toroidal flow driven by the n-NBI is localized near the plasma center ( $\rho < 0.4$ ) because the beam deposition profile is peaked at the plasma center and the toroidal viscosity, which plays as a drag of toroidal flow, significantly increases towards the plasma edge. The toroidal flow in the counter direction is observed off the plasma center ( $\rho > 0.4$ ) even in the plasma with co-injection. Because the magnitude of this counter rotation does not depend on the direction of n-NBI injected, the toroidal flow is considered to be a spontaneous toroidal rotation driven by the coupling between toroidal and poloidal flow through viscosity tensor. Figure 2 shows the radial profiles of radial electric field in the plasma similar to that plotted in Fig.1. The positive radial electric field is observed in the plasma with both the co-injected and counter-injected of NBI. In helical plasma the positive radial electric field drives spontaneous toroidal flow in the counter direction due to viscosity tensor because the plasma tends to flow along the minimum gradient B direction, which is in contrast to the fact that the positive radial electric field drives spontaneous rotation in the co-direction.

In summary, the toroidal flow observed in LHD is dominated by the toroidal flow driven by NBI near the plasma center, while it is dominated by the spontaneous

toroidal flow outer region of the plasma. The spontaneous toroidal flow observed is in the counter direction when the radial electric field is positive in the electron root plasmas. This result is consistent with the experimental results in CHS[1] and considered to be common characteristics in Heliotron plasma, where the pitch angle of minimum gradient B is always larger than the pitch angle of magnetic field averaged in magnetic flux surface.

### Reference

- 1) Ida, K., et.al., Phys.Rev.Lett **86**, (2001) 3040.

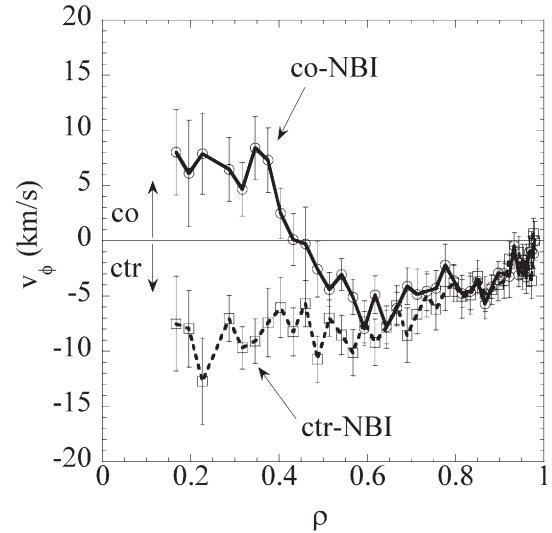


Fig. 1. Radial profiles of toroidal flow velocity in the plasma with co-injected and counter-injected NBI. Positive (negative) toroidal flow corresponds to the toroidal flow parallel (anti-parallel) to the equivalent toroidal plasma current which produces the poloidal magnetic field due to the external current in helical coils.

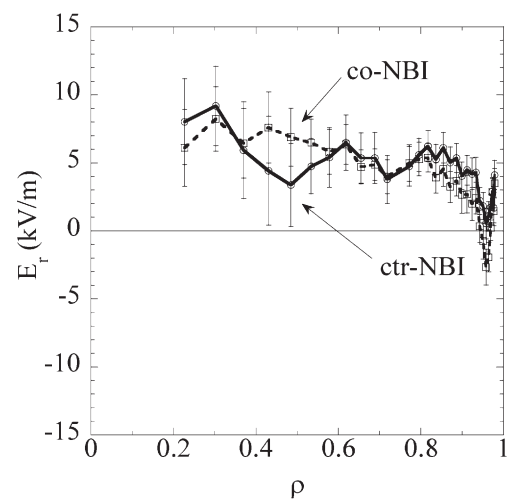


Fig. 2. Radial profiles of radial electric field in the plasma similar to that plotted in Fig.1.

## §22. Configuration Effects on Turbulence Transport in LHD

Tanaka, K., Michael, C.A. (JSPS fellow),  
Vyacheslavov, L.N. (Budker Institute of Nuclear Physics), Sanin, A.L. (Budker Institute of Nuclear Physics), Yamagishi, O., Kawahata, K.

The characteristics of the particle transport are studied from density modulation experiments in LHD[1]. The roles of fluctuations are investigated from the turbulence measurements by using a two dimensional phase contrast interferometer (2D-PCI) [2,3]. These studies are done under three different magnetic configurations. The experimental values of particle diffusion coefficients ( $D$ ) and particle convection velocities ( $V$ ) are compared with neoclassical prediction. The value of  $D$  is anomalously large and both in core and edge in whole configuration and core convection velocities were comparable with neoclassical estimation in the present experimental regime. The three kind of fluctuation, whose existing region, propagation direction, peak wave number is different, are observed. Low  $k$  ( $\sim 0.4\text{mm}^{-1}$ ) are localized in core ( $\rho < 0.8$ ), and higher  $k$  ( $\sim 0.8\text{mm}^{-1}$ ) are localized in edge ( $\rho > 0.8$ ). Edge high  $k$  components consist of two components. One is propagating to the electron diamagnetic direction and the other to the ion diamagnetic direction in laboratory frame.

As shown in Fig.1, the fluctuation level of edge ion diamagnetic components increases with  $D_{\text{edge}}$  in the all configurations, although the edge electron diamagnetic components do not show such a clear dependence on  $D_{\text{edge}}$ . This strongly suggests edge ion diamagnetic components play role on edge diffusion. Figure 2 (a) (b) shows density and fluctuation profiles. At more outward shifted configuration, where edge diffusion becomes larger, fluctuation amplitude becomes larger under similar averaged density. However, the growth rate does not vary very much, although diffusion and fluctuation changes clearly. Especially, growth rate is not smallest at  $R_{\text{ax}}=3.6\text{m}$ , whose fluctuation amplitude and  $D_{\text{edge}}$  are the smallest. One of the possible interpretation is reduction of growth rate or stabilize due to the  $E_r$  shearing rate ( $\omega_{E_r}$ ). Figure 2 (d) shows  $\gamma_{\text{ITG}} - \omega_{E_r}$ . The  $E_r$  shearing rate was calculated with  $E_r$  from GSRAKE code. The value of  $\gamma_{\text{ITG}} - \omega_{E_r}$  becomes smaller at  $R_{\text{ax}}=3.6\text{m}$  suggesting stronger  $\omega_{E_r}$  help to reduce fluctuation. However, more detail systematic study is required to conclude the identification of the edge ion diamagnetic components and the mechanism of reduced fluctuation at  $R_{\text{ax}}=3.6\text{m}$ .

### Reference

- 1) Tanaka, K., et al., to be published Fusion Science and Technology
- 2) Sanin, A.L., et al., Rev. Sci. Instrum. 75, (2004) 3439
- 3) Michael, C.A., to be published Rev. Sci. Instrum.

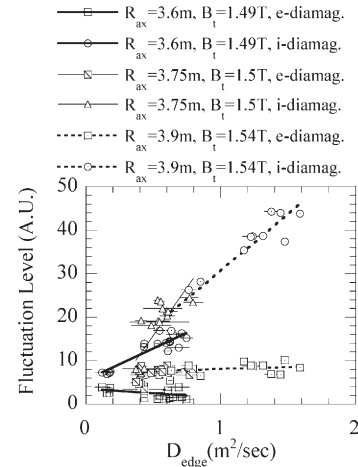


Fig.1 Relation of  $D_{\text{edge}}$  and edge fluctuation level for three different configurations

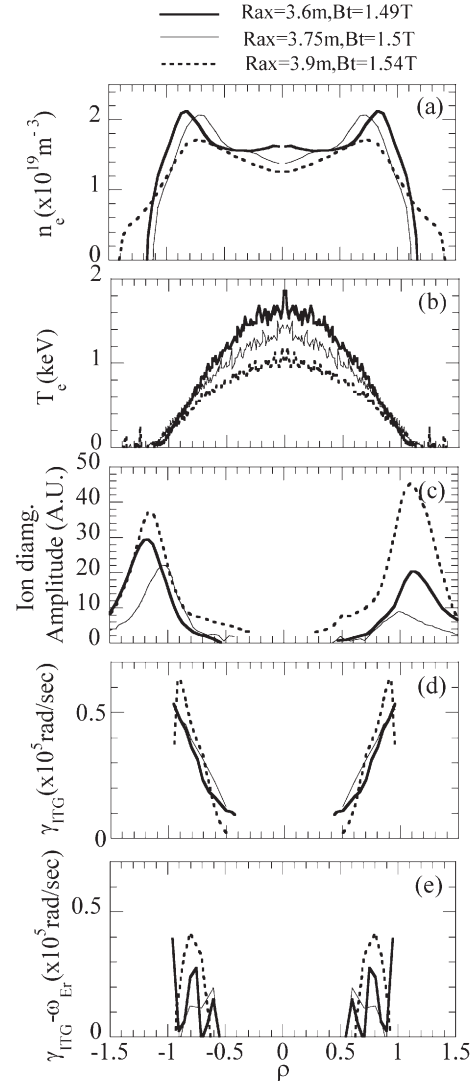


Fig.2 (a)  $n_e$ , (b)  $T_e$  profile, (c) Fluctuation amplitude profile (d) ITG growth rate and (e) ITG growth rate subtracted  $E_r$  shearing rate.  $D_{\text{edge}}=0.18, 0.42, 0.57\text{m}^2/\text{sec}$  at  $R_{\text{ax}} = 3.6, 3.75, 3.9\text{m}$  respectively.



### §23. Observation of Fluctuation Generated by Energetic Particles and Electrons Using Microwave Reflectometer

Tokuzawa, T., Osakabe, M., Sakakibara, S., Toi, K., Muto, S., Shimozuma, T., Kawahata, K.

Two reflectometer systems are utilized for fluctuation measurements. Using the extraordinary polarized wave, we can measure the corresponding value to the combined fluctuation with the electron density and the magnetic field in the plasma core region.

One system has 4 channels of fixed frequencies of 78, 72, 68, and 65 GHz. This system is very convenient to observe MHD phenomena such as energetic particle driven Alfvén eigenmodes. Another system is consisted by a VCO which is the frequency changeable source. The source frequency is swept full range (26 – 40GHz) every 200ms and the number of the stair step is 20. Each time of the launching frequency is 10ms and data sampling rate is 1 $\mu$ s, then the data point is 10,000 and the frequency resolution is 100Hz. It is also enough to observe the MHD phenomena such as TAE. Figure 1 shows the frequency spectrum of the frequency fixed 78GHz reflectometer signal. In this plasma condition that the axial magnetic field strength is 1.0 T and the averaged electron density is under  $0.5 \times 10^{19} \text{ m}^{-3}$ , there is no cut-off layer of 78GHz and this system is operated as an interferometer mode. We can see several continuous coherent frequency components. Figure 2 shows the radial profile of the fluctuation strength of the frequency swept reflectometer signal during  $t=4.0\text{--}4.8\text{s}$  (4 periods). It can be obtained that the frequency component around 200kHz is large near at  $\rho=0.8$  and the other component around 150kHz is localized in the plasma core. Here the meaning of the data points which are located under  $\rho=0$  is that these frequency waves are not reflected from the plasma and they are come back from the opposite wall.

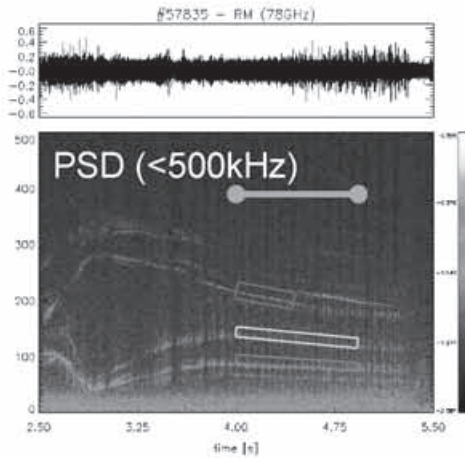


Fig. 1. Frequency spectrum of interferometer mode CW Reflectometer.

Non-thermal electrons have been seen to leads the energy quench in several tokamaks. Also, in LHD it is observed that the high power ECH generates the high energy electrons measured by HX-NPA. In such discharges, the fluctuation with coherent spectra of around 10 kHz is observed in reflectometer signal as shown in Fig. 2. Here an additional ECH is injected after 0.75s. The characteristics of this phenomenon need the future study.

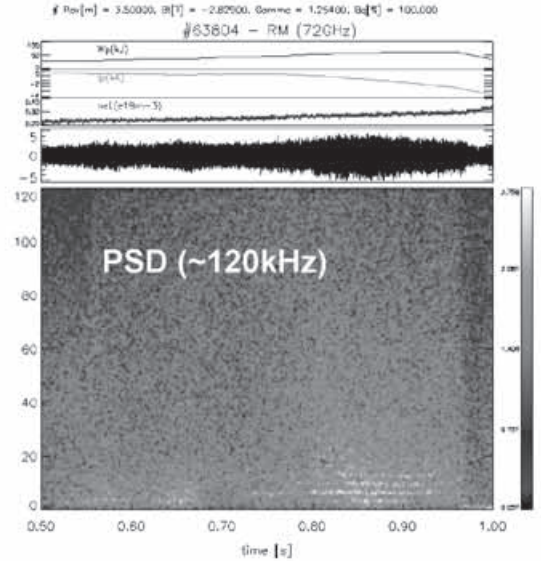


Fig. 3. Temporal evolution of frequency spectrum of 72 GHz reflectometer signal.

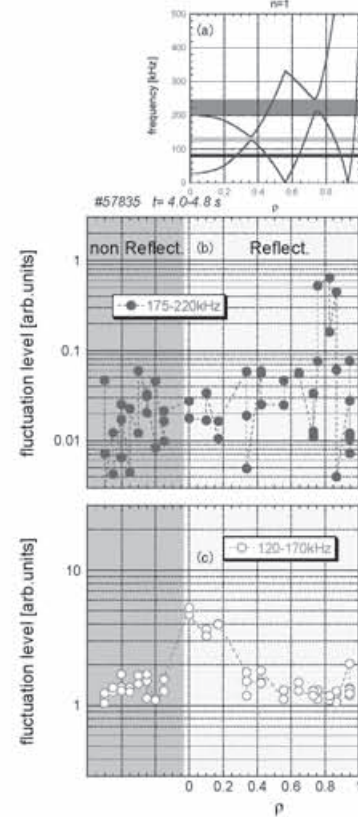


Fig.2. (a) Shear Alfvén spectra for  $n=1$  and Radial profile of the fluctuation component of FM-CW reflectometer in the range that (b) 175-220 kHz and (c) 120-170kHz.

## §24. Microwave Imaging Reflectometry in LHD

Yamaguchi, S., Nagayama, Y., Pavlichenko, R., Inagaki, S., Kogi, Y., Mase, A. (KASTEC, Kyushu Univ.)

The microwave reflectometry is a radar technique for the measurement of the electron density profiles and fluctuations by probing the density-dependent cutoff layer in the plasma. A multi-channel reflectometry system equipped with an imaging optical system has been developed to the microwave imaging reflectometry (MIR) [1, 2]. It has a potential to obtain the 2-D/3-D image of the MHD turbulences and instabilities with excellent time and spatial resolutions. The MIR system is under development in the Large Helical Device (LHD).

Figure 1(a) shows the schematic of the MIR system of LHD. The illumination beams of 66 and 69 GHz are launched from the port 4-O to the plasma center, and they are reflected at the right-hand cutoff layer in the peripheral plasma. Since the cutoff layer of X-mode is less bent and the wavelength of X-mode is shorter than O-mode, the X-mode illumination is utilized in LHD. The reflected beams are focused by the imaging optical system, and the reflected power is measured by the 6-channels heterodyne receiver. The dichroic plate has a clear cut-off feature at 70 GHz, so that it can separate the operational frequency band for MIR (50-70 GHz) and ECE Imaging (ECEI) system (70-140 GHz) [1, 3].

The LHD plasma has an elliptical cross-section which is tilted at the port 4-O as shown in Fig.1(a). As the density

is higher, the right-hand cutoff layer is more tilted downward near the equatorial plane. The beam paths near the reflection surface is calculated by using a ray-tracing code. It shows that the illumination beam should be launched upward by a few degree in order to obtain considerable reflected power. In the new setup an ellipsoidal mirror with adjustable angle is installed into the vacuum chamber of LHD. It can be rotated poloidally and toroidally by remote-controlled actuators with ultrasonic motors to optimize the illumination angle for the wider range of the plasma parameters.

Figure 1(b) shows the example of the MIR signals in the case of the low density plasma ( $R_{ax} = 3.5$  m,  $B_{ax} = -2.829$  T,  $\gamma = 1.254$  and  $B_q = 100$  %). A slow oscillation with large amplitude appears in the MIR signal right after the ECRH is turned off at  $t = 0.46$  sec. The frequency varies from 20 to 40 Hz during  $t = 0.5 - 1.0$  sec. Since the oscillation signals are slightly different among the different channels, the oscillation is not a mechanical vibration. The amplitude of the oscillation is reduced and the oscillation disappears after the density is increased at  $t = 1.0$  sec. The corresponding oscillation is not observed in the ECE signals, therefore, the slow oscillation may be a density fluctuation in the plasma. This indicates that the MIR has a potential to observe phenomena that is not observed by ECE measurement.

### Reference

- 1) Nagayama, Y. et al. : J. Plasma Fusion Res. **81** (2005) 337
- 2) Mazzucato, E. et. al. : Nuclear Fusion **41** (2001) 203
- 3) Mase, A. et al. : Rev. Sci. Instrum. **74** (2003) 1445

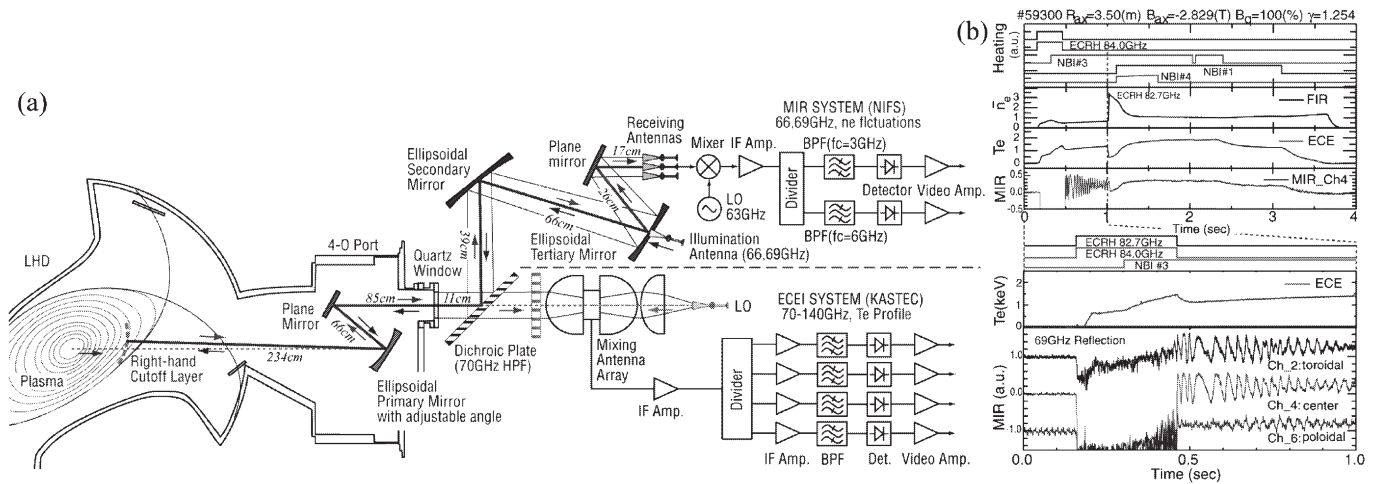


Fig.1. Schematic of the MIR system (a) and oscillations of the MIR signals in the case of the low density plasma (b).

## §25. High-Beta Experiments in LHD

Sakakibara, S., Watanabe, K.Y., Yamada, H.

In LHD, the production of high beta plasma has progressed successfully with increasing heating power of neutral beam. In recent experiments, a control of a plasma-aspect-ratio,  $A_p$ , was mainly performed from 6.3 to 8.3 to investigate the configuration dependence of MHD characteristics of high-beta plasmas. An increment of  $A_p$  causes an increase in central rotational transform and reduces the Shafranov shift. Large  $A_p$  is favorable for a heating efficiency and a transport because the outward shift of the magnetic axis leads to an increase in a helical ripple loss of particles. It is also suitable for raising an equilibrium beta-limit. However, a reduction of the plasma shift restricts spontaneous formation of magnetic well, and an increment of  $A_p$  reduces magnetic shear. Consequently, violation of MHD stability is concerned. The survey of the optimum operation provided the highest  $\langle\beta_{dia}\rangle$  value of 4.5 % at  $A_p = 6.6$ , and achieved  $\langle\beta_{dia}\rangle$  gradually decreases with an increment of  $A_p$ .

Figure 1 shows the typical discharge with  $\langle\beta_{dia}\rangle = 4.5$  % in the  $A_p = 6.6$  configuration. The plasma with  $\langle\beta_{dia}\rangle > 4$  % was maintained for  $10\tau_E$  or more. Shafranov shift  $\Delta/a_{eff}$  is around 0.2, which is much smaller than equilibrium beta-limit. Peripheral MHD activities, which are dominantly observed in the high-beta regime, are enhanced, whereas  $m/n = 1/1$ ,  $2/3$  and  $1/2$  modes were suppressed and/or intermittently behaved when the  $\langle\beta_{dia}\rangle$  exceeds

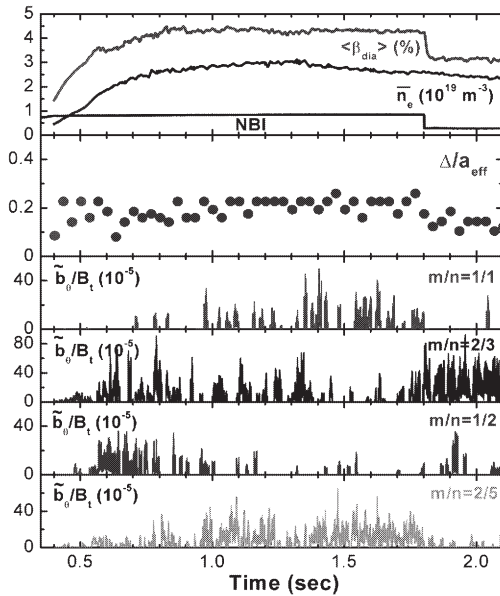


Fig.1 Typical MHD activities in high-beta discharges in  $A_p = 6.6$  configuration.

around 4 %. Although the  $m/n = 2/5$  mode where the resonance is located near plasma edge remained in the beta range over 4%, the amplitude on the resonance is relatively small compared with other modes. This tendency has been well observed in the high-beta regime and then profile flattening in the vicinity of the resonances occurs<sup>1)</sup>. Theoretical prediction suggests that these modes are resistive interchange ones because the resonances are located in periphery with magnetic hill. As an example, the dependence of the  $m/n = 1/1$  mode on magnetic Reynolds number  $S$  and  $\langle\beta_{dia}\rangle$  is shown in Fig.2. The mode is enhanced by increasing  $\langle\beta_{dia}\rangle$  and reducing  $S$ , and it is expected to be deeply related with the linear growth rate of the resistive mode<sup>2)</sup>.

The plasma confinement,  $H = \tau_E/\tau_{ISS95}$ , gradually degrades from 1.6 to 1.0-1.2. The transport analysis indicates that the thermal transport in the periphery significantly degrades with an increment of  $\langle\beta_{dia}\rangle$ , and the transport coefficient in high-beta regime is about ten times larger in a prediction by gyro-reduced Bohm model<sup>3)</sup>. As one of the reasons for the degradation, a turbulence caused by resistive-g mode has been considered. The predicted transport coefficient in periphery is quantitatively consistent with experimental results. The turbulence is caused by the decreases of  $S$  and magnetic shear, and an enhancement of magnetic hill as well as pressure gradient. It suggests that the large  $A_p$  leads to a degradation of the transport in addition to the finite-beta effects.

### Reference

- 1) A.Komori, S.Sakakibara et al., Phys. Plasmas **45**, 12 (2005) 056122
- 2) S. Sakakibara et al., to be published in Fusion Science and Technology (2006).
- 3) H. Funaba et al., to be published in Fusion Science and Technology (2006).

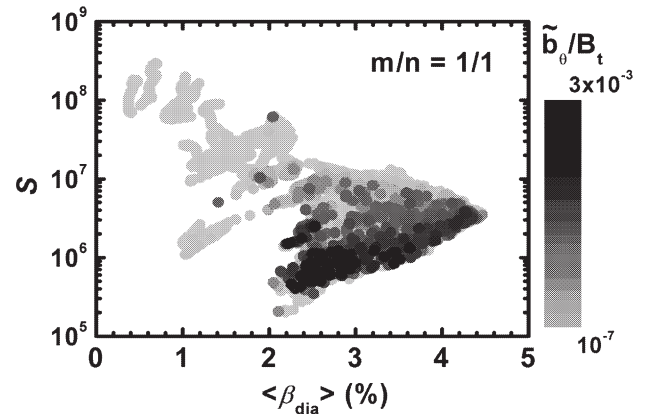


Fig.2 Amplitude of  $m/n = 1/1$  mode on the  $S$  and  $\langle\beta_{dia}\rangle$  diagram.



## §26. Effect of Resonant Magnetic Field on low- $m$ Mode in LHD

Sakakibara, S., Watanabe, K.Y., Yamada, H.

In standard configuration of LHD, the  $m/n = 1/1$  mode where the resonance is located in periphery with magnetic hill and strong magnetic shear has been enhanced with increasing beta and pressure gradient. The clear dependence of the mode on a magnetic Reynolds number has been found out, and it is close to that of growth rate predicted by linear theory of resistive interchange mode<sup>1)</sup>. On the other hand, when the magnetic shear is decreased by controlling magnetic configuration and/or by positive plasma currents increasing rotational transform, non-rotating  $m/n = 1/1$  mode appears and abruptly grows instead of the rotating resistive  $m/n = 1/1$  mode. The mode causes the minor collapse in the core region and the plasma energy loss reaches more than 50 % in case of the lowest magnetic shear configuration. It was found out that the mode clearly limits the operation regime of LHD, which is qualitatively consistent with predicted ideal stability boundary<sup>1)</sup>. Here, the control of non-rotating  $m/n = 1/1$  mode was attempted by means of an external magnetic field including the  $m/n = 1/1$  component mainly. Usually, the mode has no rotation frequency and grows at the place where a natural error field in LHD exists. The external coils are equipped in LHD in order to compensate the error field and/or to apply the local island divertor system. The effect of strength of external field on the activity of the mode was investigated through the experiments.

Typical NBI discharge in the configuration with  $R_{ax} = 3.6$  m,  $B_t = 0.9$  T and  $\gamma_c = 1.13$  is shown in Fig.1. The NBI in the co- direction was applied here and the port-through power was 2.9 MW. The strength of the radial component of the  $m/n = 1/1$  mode,  $b_{r11}/B_t$ , on the  $\iota/2\pi = 1$  surface, which was identified by magnetic measurements, non-linearly increase from 0.53 s despite no external field. Figure 2(d) shows the spatial location of the  $m/n = 1/1$  mode, and  $\phi_{011}$  is toroidal angle where the O-point of the  $m/n = 1/1$  island is located at poloidal angle  $\theta = 0$  and  $z = 0$ . The mode

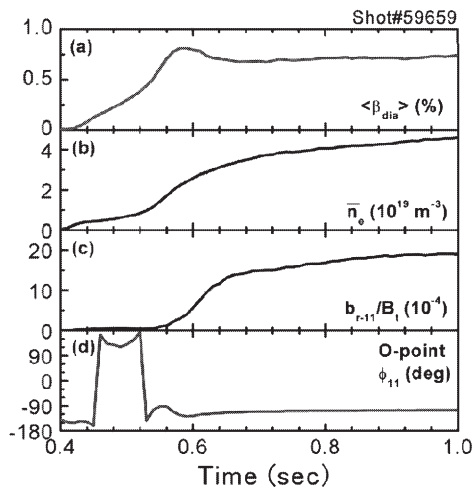


Fig.1 Typical discharge in the configuration with  $\gamma_c = 1.13$ .

grew and saturated at the specific location with  $\phi_{011} \sim -120^\circ$  where the natural error field exists. Here, the external magnetic field with the  $m/n = 1/1$  component was added to the same plasmas as fig.1 discharge, and the normalized coil current,  $I_{LID}/B_t$ , was changed from -833 to 833 kA/T. The positive coil current produces the  $1/1$  island at which the O-point is located at  $\phi_{011} \sim -126^\circ$ . The positive current extends the width of the natural island, whereas the negative current almost cancels it. The dependence of  $I_{LID}/B_t$  on plasma parameters and the activity of  $m/n = 1/1$  mode under the condition with constant  $n_e$  are shown in fig.2. The observed modes almost saturated. When the positive  $I_{LID}/B_t$  was increased,  $b_{r11}/B_t$  gradually increased and the location approached that of given  $m/n = 1/1$  island as shown in Fig.2(d). The  $\langle \beta_{dia} \rangle$  gradually decreases due to the extension of the island width.

On the other hand, when the negative  $I_{LID}/B_t$  was applied, the amplitude of the mode abruptly reduced with the increase in  $|I_{LID}/B_t|$  and had the minimum at -278 A/T. Then  $\langle \beta_{dia} \rangle$  recovered and had the maximum value. The amplitude of the mode increased again when  $I_{LID}/B_t < -278$  A/T. The location of the island gradually rotated in the opposite direction and approached the position of given  $1/1$  island when negative  $I_{LID}/B_t$  increased. Thus, the results suggests that it is possible to completely stabilize non-rotating  $m/n = 1/1$  mode by means of moderate external magnetic field. The saturation level of the mode strongly depends on given island width.

### Reference

1) S. Sakakibara et al., appear in Fusion Science and Technology (2006).

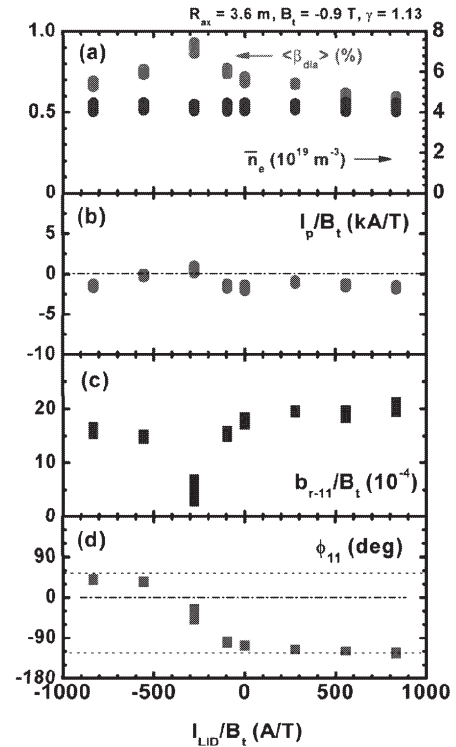


Fig.2 Changes of (a)  $\langle \beta_{dia} \rangle$ ,  $n_e$ , (b)  $I_p/B_t$ , (c)  $b_{r11}/B_t$  and (d)  $\phi_{011}$  as a function of  $I_{LID}/B_t$ .

## §27. On the Reconstruction in LHD High Beta Plasmas

Watanabe, K.Y., Yamaguchi, T. (Grad Univ.),  
Narihara, K., Tanaka, K., Suzuki, Y.

The establishment of the identification of MHD equilibrium is one of the very important subjects in the torus plasma study. In helical systems, strictly speaking, the nested magnetic surfaces do not exist, the practical magnetic surfaces exist, which is calculated by the numerical calculation. The above practical magnetic surfaces are predicted to be stochastic as the beta and PS currents increase by a theoretical calculation. In the above situation, we meet some difficulties when we identify the MHD equilibrium configuration in high beta and in peripheral region. Here we consider the more consistent method of the identification of the MHD equilibrium configuration.

Figure 1 shows a reconstructed MHD equilibrium for a LHD high beta operation with  $\langle\beta_{\text{dia}}\rangle\sim 2.9\%$  by HINT code. The observed pressure profile at the equatorial plane of the horizontally elongated cross section is shown in Fig.1 (circles). The solid line corresponds to the input data of pressure profile of HINT code. Here the applied boundary condition in HINT calculation is that the pressure set to zero where the field line connects to a wall before 1 toroidal turn and the pressure should be same with the field line averaged value over the 2 toroidal turns as a default so that the observed peripheral pressure profile is reproduced well. The center of the peripheral flux surface estimated by the constant pressure surface is predicted to be shifted torus outwardly by  $\sim 5\text{cm}$ , which corresponds to  $\sim 9\%$  of the averaged plasma minor radius. The torus outboard location of the OMFS in the high beta value of  $\langle\beta_{\text{dia}}\rangle\sim 2.9\%$  is predicted to be almost same with that of the OMFS of vacuum, the inboard location is shifted to torus-outwardly, and the volume of the OMFS is reduced by  $\sim 8\%$  comparing with that of vacuum.

Next we study the relationship between the connection length to a wall and the electron mean free path to consider the force balance of the MHD equilibrium in a open field line region. Figure 2 shows the observed electron temperature and density profiles, electron mean free ( $\lambda_e$ ) in a high beta LHD discharge with  $\langle\beta_{\text{dia}}\rangle\sim 2.9\%$ , which is for the same discharge and time slice with Fig.4. In a high beta operation with  $\langle\beta_{\text{dia}}\rangle\sim 2.9\%$ , the central electron temperature and the density are  $\sim 0.5\text{KeV}$  and  $\sim 2.7\times 10^{19}\text{m}^{-3}$ , respectively. They are fairly low temperature and density because of the low operational magnetic field strength ( $B_0=0.5\text{T}$ ). The connection length of the magnetic field line to a wall and the connection length between the torus-top and the bottom ( $L_{\text{C-TB}}$ ) predicted by HINT are shown by solid lines in Fig.2. It should be noted that when  $L_{\text{C}} < L_{\text{C-TB}}$ , an MHD equilibrium current cannot flow for the equilibrium force balance. In the LHD high beta operation with  $\langle\beta_{\text{dia}}\rangle\sim 2.9\%$ ,  $L_{\text{C}} > L_{\text{C-TB}}$  is always satisfied in the region with a finite electron pressure. And the region with the short electron mean free path,  $\lambda_e < 10\text{m}$ , is widely spread in the peripheral

region. Especially in an open magnetic field region shown by shadow in Fig.2, where the maximum of the field lines corresponds to less than 40 toroidal turns,  $\lambda_e/L_{\text{C-TB}}$  is less than 0.2, which is too small. In the above region, there is a possibility that a finite pressure gradient along the magnetic field line exists. The above fact suggests that in order to reproduce a more consistent MHD equilibrium with the experimental condition, we might take the inertial term ( $\mathbf{v}\cdot\nabla\mathbf{v}$ ) the viscosity and/or the anisotropic pressure, in the force balance equation into account. How large these effects influence the magnetic surfaces and the magnetic field line structure in the peripheral region is one of the big open issues.

[1] Harafuji K. et al., *J. Comput. Phys.* **81** 169 (1989).

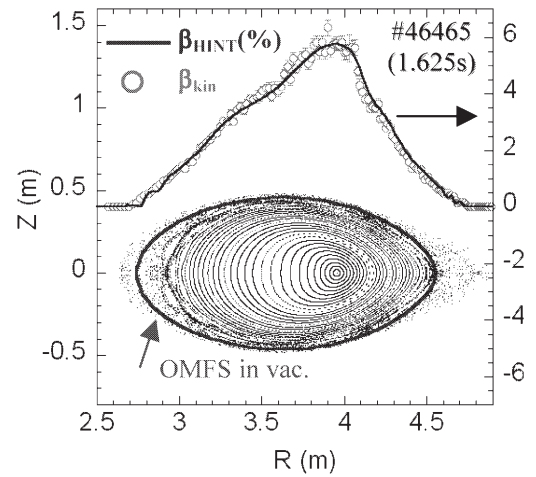


Fig.1 Predicted magnetic field structure by HINT and observed pressure profile in a high beta LHD discharge with  $R_{\text{ax}}^{\text{v}}=3.6\text{m}$ ,  $B_0=0.5\text{T}$  and  $\langle\beta_{\text{dia}}\rangle\sim 2.9\%$ .

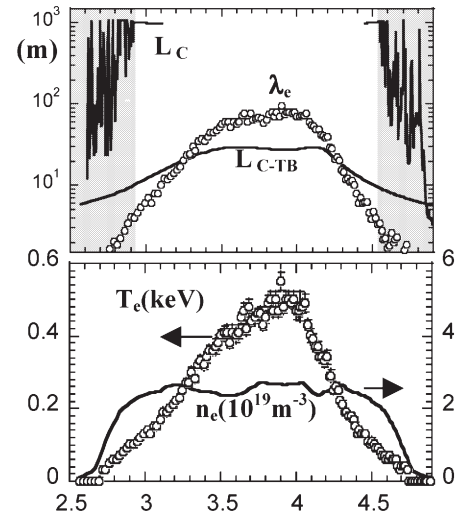


Fig.2 Observed electron temperature and density profiles, electron mean free in a high beta with  $\langle\beta_{\text{dia}}\rangle\sim 2.9\%$ . Predicted  $L_{\text{C}}$  and  $L_{\text{C-TB}}$  by HINT are shown. Shadow region denotes an open magnetic field region, where the min. of  $L_{\text{C}}$  is less than 40 toroidal turns.

## §28. Two-Dimensional Structure of the MHD Instabilities and Its Non-Linear Evolution in the Large Helical Device

Ohdachi, S., Toi, K.

It is important to further understand the role MHD instabilities play in plasma confinement in helical systems. Since mode amplitudes depend nonlinearly on the pressure gradient, it is not straightforward to make theoretical predictions of mode structures and amplitudes, and thus determine their effect on confinement. We experimentally study the evolution of pressure driven modes using images measured by a fast, tangentially-viewing soft X-ray camera [1]. Sawtooth-like MHD activity occurs in high density plasmas when the pressure gradient in the core region exceeds a limit. It is found that the magnetic surfaces are strongly deformed just before the sawtooth crash. The magnetic reconnection due to this deformation causes rapid energy flow from the core to the edge.

It is observed that the core pressure gradient after the sequential pellet injection is 2 ~ 3 times larger than found in normal operation with gas fueling. As the pressure gradient increases, sawtooth-like events begin. These events are often followed by large amplitude oscillations which persist for 0.1 - 0.3s. The electron density decreases and the electron temperature gradually increases during this time. Thus, we can investigate the influence of resistivity on the mode behavior by comparing cases with similar pressure gradients and different electron temperatures.

Fig.1 shows the fluctuating components of the image from the tangential soft x-ray camera at the time of the maximum fluctuation amplitude (1.515 s). First, an  $m=3$  mode evolves within 500ms and deforms the magnetic surface (Fig. 1(B2) white area). When the mode saturates, an enhanced heat flux from the core to the edge is observed, causing flattening of the pressure profile. The SX emission from the outer plasma increases after the event (see Fig.1 (B3)). The enhanced flux could be caused by reconnection where the magnetic surfaces are heavily compressed due to an interchange mode.

The pressure gradients at the rational surface are also studied. There is an onset of MHD events when the pressure gradient exceeds a limit ( $-d\beta/d\rho$

1 %). The onset value does not change significantly when the iota profile is modified by the plasma current. The magnetic Reynolds number  $S$  ( $= \tau_R / \tau_{alfven}$ ) is used as a measure of the resistivity. For similar pressure gradients, sawtooth activity occurs for lower values of  $S$  and saturated oscillations occur at higher values of  $S$ . This can be understood qualitatively from the following model. The amplitude of the MHD instabilities increases with the pressure gradient. It saturates when there is a balance between the fluctuation-driven flux and the pressure gradient. However, in higher resistive plasmas, reconnection occurs more easily at the same instability amplitude. Thus, sawtooth-like events are triggered in plasmas with lower  $S$ . This model is consistent with the observation that the repetition rate is higher when the electron temperature is low.

We have observed similar sawtooth-like activity near different rational surfaces, e.g.,  $\tau = 1/3$ ,  $1/2$ ,  $1/1$ , with  $m = 3, 2, 1$ . Though the pressure profile is modified by the sawtooth-like activity, the effect on the global confinement is small. The decrease in the stored energy is less than several % when the sawtooth-like activity is present.

[1] S. Ohdachi et al., Rev. Sci. Instrum **74**, 2136 (2003).

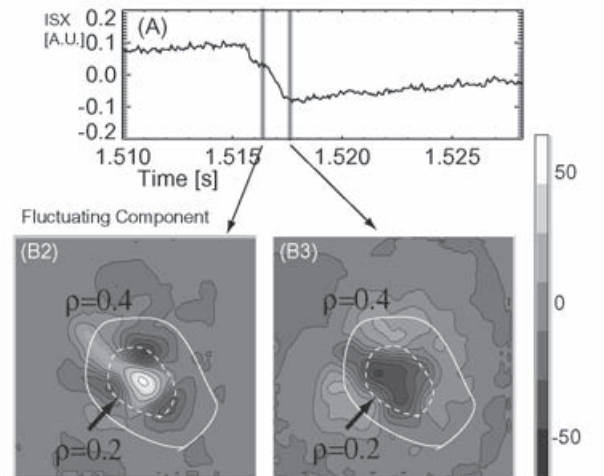


Fig.1: Two-dimensional structure of a sawtooth event is shown in (B2) and (B3).



## §29. Effect of Separatrix Geometry on Transport and MHD

Suzuki, Y., Yamada, H., Ida, K., Yoshimura, M., Kobuchi, T., Watanabe, K.Y., Tanaka, K.

Plasma shape control is a major knob to investigate confinement as well as MHD characteristics of magnetically confined plasmas. In particular, plasma elongation has been widely explored in many experiments and theoretical investigations. For example, optimization in the line of W7-AS and W7-X owes much to reduction of Pfirsch-Schluter currents due to elongation. It is also widely recognized that plasma elongation affects energy confinement in tokamaks, which can be seen in the ITER H-mode scaling. On the other hand, the role of separatrix has been attracting interest in both a fundamental issue of a dynamical system with cross of stable and unstable manifolds and applied issues for performance of magnetic confinement. Many reports can be referred to the latter issues, which are related to dynamics of magnetic islands and its effect on transport, equilibrium  $\beta$  limit and a function of divertor. Since the Shafranov shift is enhanced by horizontal elongation, equilibrium  $\beta$  limit is lowered in oblate configuration. In general, the equilibrium  $\beta$  limit is defined by the Shafranov shift as large as a half the minor radius, when the deformation of magnetic flux surface is thought not to be tolerable. However, this is not physically reasonable definition. In the tokamak case, the separatrix is generated inboard side due to enhanced Pfirsch-Schluter currents. Oblate configuration provides the experimental evidence what happens by a large Shafranov shift and can mitigate the approach to the question what the equilibrium  $\beta$  limit is.

Figure 1 shows the electron temperature profile in the experiment and the pressure profile calculated by HINT in the case of  $\kappa$  of 0.5 [1]. Both profiles are plotted along the major radius. As shown in Fig. 1 (a), the Shafranov shift beyond a half the minor radius is already observed in low  $\beta$  (0.3%). Along with the increase in  $\beta$ , inflection of temperature gradient appears inboard side of the peak. This evolution of profile is well reconstructed by the HINT calculation. The calculation of HINT indicates that large Shafranov shift occurs even in low  $\beta$  since the separatrix geometry already exists in the vacuum condition and the rotational transform is close to zero. With increase in  $\beta$ , the outer petal evolves while the inner petal degenerates. The outer region of the petal, namely the outside of the internal separatrix becomes stochastic and loses confinement capability. This trend is pronounced in the inboard side of the outer petal in the physical space. While large pressure gradient is maintained in the outer petal (outer separatrix domain), the pressure gradient declines in the outside of this region. This physical picture seems to be consistent with the experimental observation. The reason why the experimental observation in the inboard side is somewhat mitigated from the prediction by HINT may be healing of ergodization due to unresolved dynamics of the plasma or tolerable parallel heat transport. Although the direct measurement of the

change of magnetic geometry is not available, circumstantial evidence supports the validity of the calculation by HINT. Subsequently the picture of equilibrium  $\beta$  limit can be described based on results from the calculation by HINT [2].

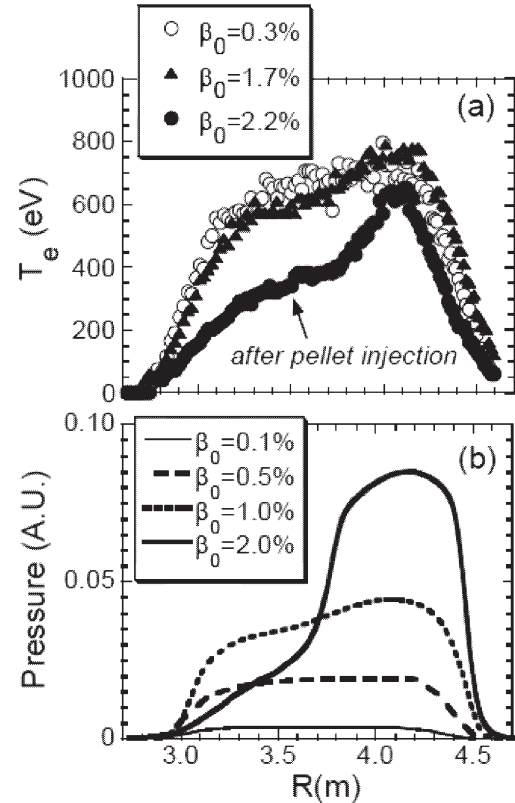


Fig.1 Profile evolution in the configuration with  $\kappa$  of 0.5. (a) Electron temperature in NBI heated plasmas measured by Thomson scattering, (b) Pressure profile calculated by HINT.

- [1] Y. Suzuki, *et al.* Nucl. Fusion **46** (2006) 123
- [2] H. Yamada, *et al.* Fusion Sci. Technol. (accepted)

### §30. Minor Collapse of Current-Carrying Plasma in LHD

Narushima, Y., Sakakibara, S., Watanabe, K.Y.

A minor collapse observed in current-carrying plasma has been investigated in Large Helical Device (LHD). Experiments were carried out in the configuration with a high central rotational transform of  $\iota_0/2\pi = 0.58$  in order to decrease the magnetic shear around the  $\iota/2\pi = 1$  surface. The target plasma is produced and maintained by the neutral beam injection (NBI), which drives the plasma current  $I_p$  in the co-direction. When the beam-driven current exceeds a certain value, the  $m/n = 1/1$  mode (here, the  $m$  and  $n$  are the poloidal and toroidal mode number, respectively) grows and causes a sudden drop of the plasma stored energy  $w_p$  (collapse) and the electron temperature  $T_e$ , and it also limits the plasma current itself. Before the collapse, the time evolution of the  $w_p$  and  $T_e$  are almost constant, while the  $I_p$  continues rising and the finite perturbed magnetic field with  $m/n = 1/1$  mode  $b_{r11}/B_t$ , which is the radial magnetic component of the  $m/n = 1/1$  mode estimated by the magnetic flux measurement, gradually increases. When the  $I_p/B_t$  (here,  $B_t$  is the toroidal magnetic field) reaches 39 kA/T, the electron temperature  $T_e$  measured with an electron cyclotron emission (ECE) diagnostic suddenly drops while the  $b_{r11}/B_t$  increases. At that time, the decay time of the  $w_p$  becomes  $\sim 40$  ms and the growth time of the  $b_{r11}/B_t$  is about 30 ms, which are slower than the growth time ( $\sim 100$   $\mu$ s) of the ideal MHD phenomenon. The magnetic fluctuation and the soft X-ray diagnostics do not show any precursors or post-cursors of the collapse. After the collapse, the  $b_{r11}/B_t$  increases faster than before the collapse

and the width of the flat region of the  $T_e$  profile expands toward the plasma center region. As a result, the central electron temperature decreases from  $T_{e(0)} = 1.2$  to 0.6 keV. The increase of the width of the flat region of the  $T_e$  profile indicates the growth of the magnetic island with  $m/n = 1/1$  structure by the development of the perturbed magnetic field. The toroidal angle of the X-point of the mode at the outboard side maintains a certain value during the discharge, which means that the mode almost does not rotate. The position of the flat region corresponds to the  $\iota/2\pi = 1$  resonant surface, which is measured with motional Stark effect spectroscopy (MSE) diagnostics in which the current density profile is parabolic. The plasma discharge is not terminated by this collapse. A collapse was observed in the current-carrying plasma in Heliotron-E [1], and the collapse was explained by the appearance of the  $m/n = 1/1$  internal kink mode at the  $\iota/2\pi = 1$  resonant surface in the negative shear ( $d\iota/d\rho < 0$ ) region of the rotational transform profile with the double resonant surfaces. In this experiment, the  $\iota/2\pi$  profile is not a double resonant one. Therefore, it seems that a physical mechanism different from that described in Ref.[1] exists in this experiment.

#### Reference

- 1) Wakatani M. et al., Nucl. Fusion **23**, (1983) 1669

### §31. Control of Magnetic Shear by Neutral Beam Injection in LHD

Ida, K., Yoshinuma, M., Kobuchi, T., Watanabe, K.Y., Nagaoka, K.

Control of magnetic shear has been recognized to be important issue in helical plasma as well as tokamak plasma, because it has significant impact to the transport and MHD stability at the rational surface. For example, the interchange mode appears, when the magnetic shear at the rational surface decreases. Further decrease of magnetic shear causes growing of 2/1 magnetic island at a rational surface of 0.5. Appearance of interchange mode and growing of 2/1 magnetic island have been observed in the plasma with counter-NBI, where the toroidal current in the counter direction is increasing[1,2].

Radial profile of rotational transform ( $\iota$ ) is measured with Motional Stark Effect (MSE) spectroscopy [3] during the transient phase where the direction of NBI is switched during the discharge in LHD. Figure 1 shows the time evolution of toroidal current driven by NBI and radial profile of rotational transform ( $\iota$ ) and shift of polarization angle due to toroidal current and Pfirsch-Schluter current. (The absolute value of polarization angle is a order of 10 degree at the plasma edge.) As seen in the time evolution of toroidal current, the toroidal current keep increasing or decreasing during the co- and ctr-NBI phase and does not reach to the steady state. This is because the diffusion time scale is much longer than the duration of discharge.

In order to study the effect of the current ramp rate on  $\iota$  profile and magnetic shear, the two  $\iota$  profiles are compared with similar magnitude of toroidal current ( $I_p = 56 - 59\text{kA}$  in counter direction) and different ramp rate: one is in the discharge where the counter current is decreasing with  $dI_p/dt = 42\text{kA/s}$  and the other is in the discharge where the counter current is increasing with  $dI_p/dt = -34\text{kA/s}$ . When the current is decreasing the polarization angles have negative values that indicate the decrease of  $\iota$ . This is contrast to the radial profile of polarization angle where the current is increasing, where the polarization angle changes its sign in radius. (positive values near the plasma center and negative values near the plasma edge). These polarization angle profiles clearly show the existence of  $d$  reversal of toroidal current near the plasma center. Please note the contribution of Pfirsch-Schluter current, which is typically causes the negative offset in polarization angle, is small in this experiment where the plasma density is low ( $0.67 \times 10^{19}\text{m}^{-3}$ ) and magnetic field is high (2.75T).

#### Reference

- [1] A.Isayama, et. al., Plasma Phys. Control. Fusion **48** L45 (2006)
- [2] M. Yakovlev, et al., Phys. Plasmas **12**, 092506 (2005)
- [3] K.Ida et al., Rev. Sci. Instrum. **76**, 053505 (2005)

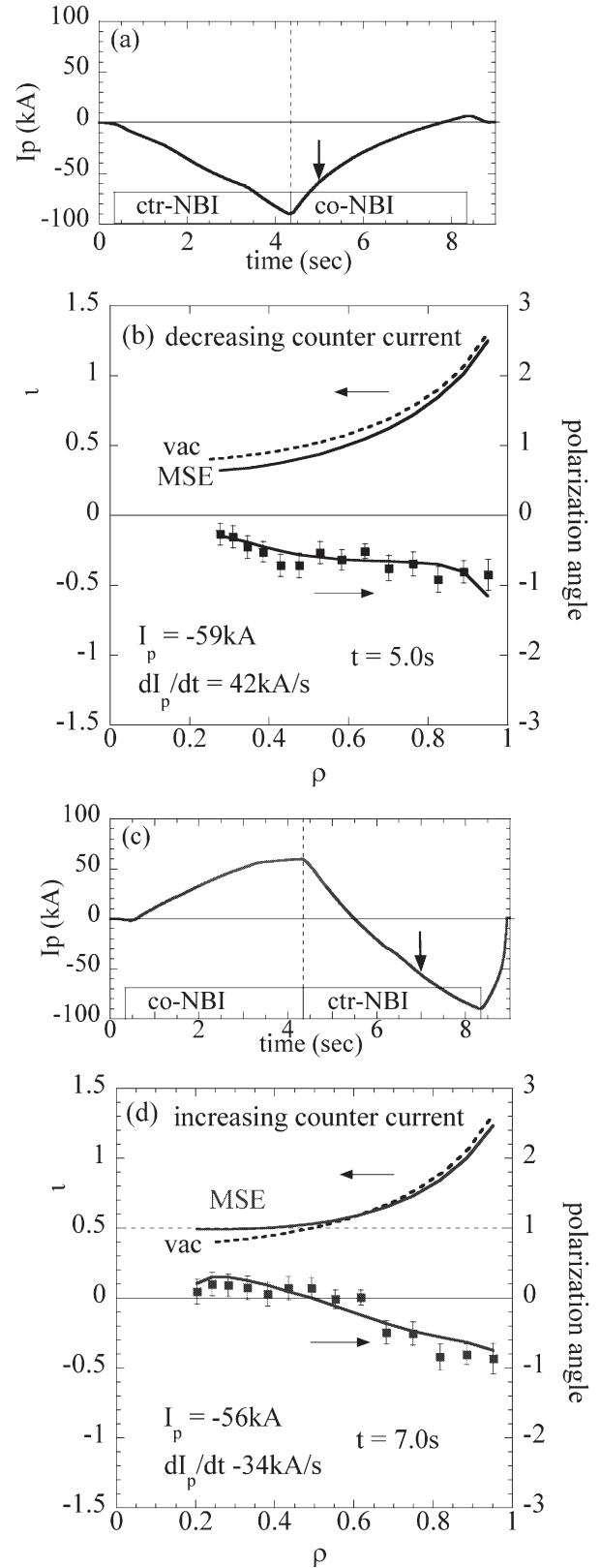


Fig.1. Time evolution of plasma current and radial profile of rotational transform and change in polarization angle for the discharge with (a),(b) decreasing counter plasma current and (c),(d) increasing counter plasma current.

### §32. Observation of Localized Oscillations at $m/n = 2/1$ Rational Surface during Counter Neutral Beam Injection

Isayama, A. (Japan Atomic Energy Agency), Inagaki, S., Watanabe, K.Y., Narushima, Y., Sakakibara, S., Funaba, H., Ida, K., Nagayama, Y., Yamada, H., Kawahata, K., Komori, A., Motojima, O., LHD Experimental Group

In LHD experiments, an instability localized at the  $\iota/2\pi=0.5$  surface during neutral beam injection (NB) in the counter direction is observed. In this study, characteristics of this instability have been investigated. Stability analysis using profiles and equilibrium in an LHD experiment has been also performed.

Spatial structure and its evolution of the localized instabilities in LHD experiments have been investigated using the signals of magnetic perturbation and electron temperature perturbation profile from electron cyclotron emission (ECE) diagnostic. It has been found that electron temperature perturbations exist at  $\iota/2\pi=0.5$  with the spatial extension of about 10% of the minor radius. The instability typically grows in several milliseconds and saturates. In a few discharges, the instability was triggered by a sawtooth crash. Under the condition of increasing plasma current in the counter direction and nearly constant pressure, the oscillations are observed at larger magnitudes of plasma current ( $\sim 20 \text{ kA T}^{-1}$ ). In the NB reversal experiments, where the direction of the NB is changed from the co- to the counter-direction and vice versa, the oscillations were observed only for the former case. These results suggest that the profile and magnitude of the plasma current play an important role in the mode onset. According to the motional Stark effect diagnostic, rotational transform at  $\iota/2\pi > 0.5$  decreases while it increases at  $\iota/2\pi < 0.5$  when the direction of NB is changed from co- to counter-direction, showing that magnetic shear at the  $\iota/2\pi=0.5$  surface decreases by the NB reversal. It is probable that the decrease in the magnetic shear at the  $\iota/2\pi=0.5$  surface is responsible for the onset of the localized oscillations.

In addition to the experimental study, stability analysis has been performed. Analysis based on the Mercier criteria using the VMEC code shows that at a fixed plasma current an interchange mode becomes more unstable when the current profile is hollow (Fig. 1). It has been also found that for a flat or a hollow current profile the interchange mode becomes more unstable at higher negative plasma current while the stability is improved by increasing the plasma current for a center-peaked current profile. The result suggests that the center-peaked profile is not likely to occur during the counter-NB or NB reversal from co- to counter-direction, which is a similar tendency to the above experimental observations. It is also found that radial displacement due to the localized oscillations evaluated from electron temperature perturbation profiles with the ECE diagnostic agrees well with that predicted by

a three-dimensional ideal magnetohydrodynamic stability code TERPSICHORE (Fig. 2).

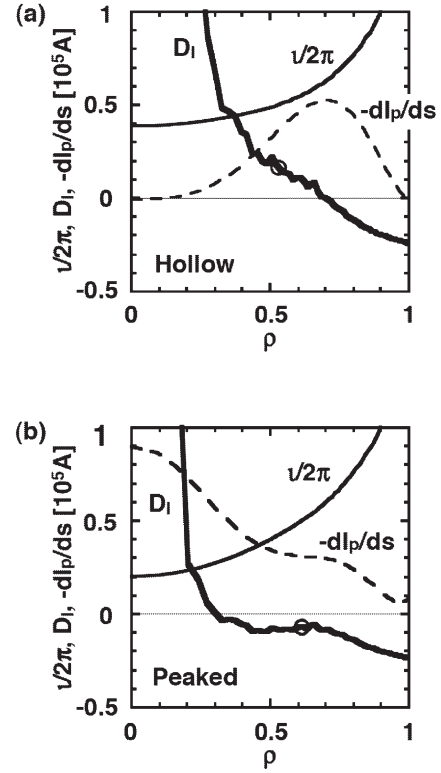


Fig. 1. Profiles of rotational transform ( $\iota/2\pi$ ), the Mercier parameter ( $D_1$ ) and current density ( $-dI_p/ds$ ) for different current profiles: (a) hollow current profile and (b) peaked current profile. In each figure, the location of  $\iota/2\pi=0.5$  is indicated on the  $D_1$  profile with an open circle.

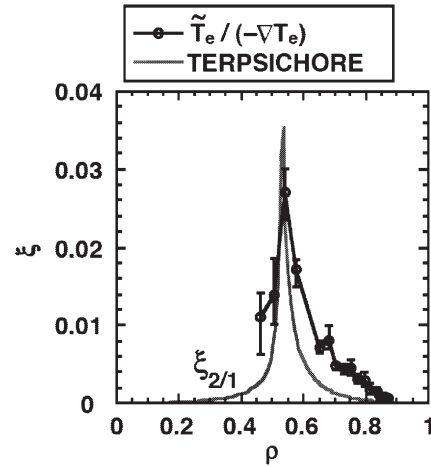


Fig. 2. Profiles of radial displacement evaluated from ECE measurements and TERPSICHORE calculations.

#### Reference

- 1) Isayama, A., Inagaki, S., Watanabe, K.Y., Narushima, Y., Sakakibara, S., Funaba, H., Ida, K., Nagayama, Y., Yamada, H., Kawahata, K., Komori, A., O. Motojima and LHD Experimental Group, Plasma Phys. Control. Fusion **48** (2006) L45-L55.



### §33. Particle Orbit Analysis in High Beta Plasma of LHD

Matsumoto, Y., Seki, R., Oikawa, S., Itagaki, M., Shimoda, H., Shimizu, N., Tanaka, H. (Hokkaido Univ.), Watanabe, K., Suzuki, Y., Sakakibara, S., Narushima, Y., Yamaguchi, T.

High beta plasmas more than 4 % have been obtained in the low magnetic field ( $\simeq 0.5$  T) discharges of LHD[1]. Although the particle orbit analyses in such finite beta plasmas of LHD have been done, they are restricted inside the last closed flux surface (LCFS)[2]. However, it is pointed out that the peripheral flux surfaces in the helical systems like LHD are destroyed with rising the plasma beta[3]. Since the particle drift in the low magnetic field, in which the high beta LHD experiments have been done, becomes large, it can be predicted that the particle started from the core go out of the LCFS. In such cases, the re-entering particles[4] would play an important role. Thus, the particle orbit analysis including the peripheral region is required.

In this study, the particles in LHD are traced with the use of the real coordinate system. The particle behavior in the high/low magnetic field and/or the high/low beta plasma is investigated.

Particles are traced in the four magnetic field configurations (case 1:  $B_{ax} = 3$  T,  $\beta = 0$  %, case 2:  $B_{ax} = 3$  T,  $\beta = 3.2$  %, case 3:  $B_{ax} = 0.5$  T,  $\beta = 0$  % and case 4:  $B_{ax} = 0.5$  T,  $\beta = 3.2$  %). In these magnetic field configurations, the vacuum magnetic axes are located at  $R_{ax} = 3.6$  m. The 100 keV protons are traced for a period of 30 ms by numerically solving the guiding-center equation. The particle loss boundary is set at the vacuum vessel wall. The starting points of particles are located at  $R$  axis on the horizontally elongated poloidal plane. Moreover, the initial pitch angles are varied from 0 to  $\pi$  with a step size of  $\pi/20$ .

We classify the particle orbit into four groups: passing particles, banana particles, chaotic orbit particles and prompt loss particles. By comparison in four cases, it is found that the particle orbit characteristics in the high beta plasma are almost the same as those in the vacuum magnetic field except the particles started from the inner side. In the low magnetic field cases, the number of prompt loss particles becomes large due to the large particle drift.

The summations of the pass length of the re-entering particles in the peripheral region are calculated. The pass length of the re-entering particles is up to 10 km. In addition, path length of the particles started from  $R \simeq 4$  m is  $\sim 1$  km. This indicates that even the particles started from the core also go out of and re-enter into the LCFS.

Moreover, the effect of the charge exchange on the re-entering particle orbit is studied. It is assumed that the neutrals exist only in the peripheral region of LHD on the constant density. The loss particle ratio is shown in Fig. 1. In all cases, the particle loss due to the charge exchange is small except for the particles started from the inner side of the torus. The numbers of loss particles due to the charge exchange in the high beta cases (2 and 4) are larger than those in the low beta cases. In cases 1 and 2, particles started from the LCFS neighborhood are lost due to the charge exchange. By contrast, in cases 3 and 4, the loss due to the charge exchange is incident for particles started from the core.

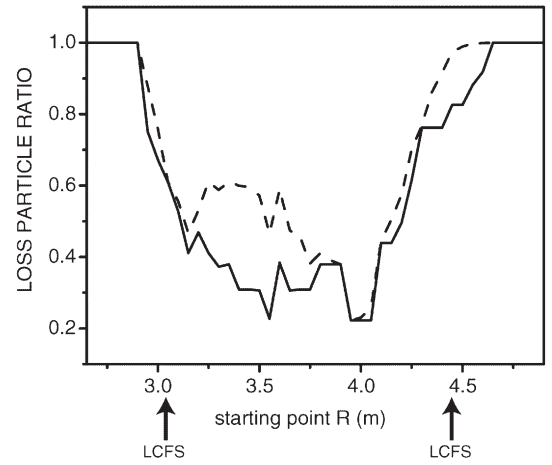


Figure 1: Loss particle ratio of particles in case 4. Values at each starting points are averaged over the pitch angle.

We analyze the particle orbit in the high/low beta plasma and/or the high/low magnetic field in LHD. Following information is obtained. The particle orbit characteristics in the high beta plasma are almost the same as those in the vacuum magnetic field. If the magnetic field strength is reduced, many particles with large  $v_{\perp}$  become the prompt loss particles. Even in the high beta cases, particles can repeatedly re-enter many times. The particle loss due to the charge exchange is small except for the particles started from the inner side of the torus.

#### Reference

- [1] Watanabe, K., *et al.*, 2004 EX3-3 20th Fusion Energy (Vilamoura, 2004).
- [2] Murakami, S., J. Plasma Fusion Res., **80**, 725 (2004).
- [3] Wakatani, M., *Stellarator and Heliotron Device*(Oxford University Press 1998), Chap. 5.
- [4] Hanatani, K. and Penningsfeld, F., Nucl. Fusion **32**, 1769 (1992).



### §34. Plasma Collapse Phenomenon in Ctr-NBI Heating Plasma with the Magnetic Configuration of Bq=200%

Nagaoka, K., Narushima, Y., Watanabe, K.Y.

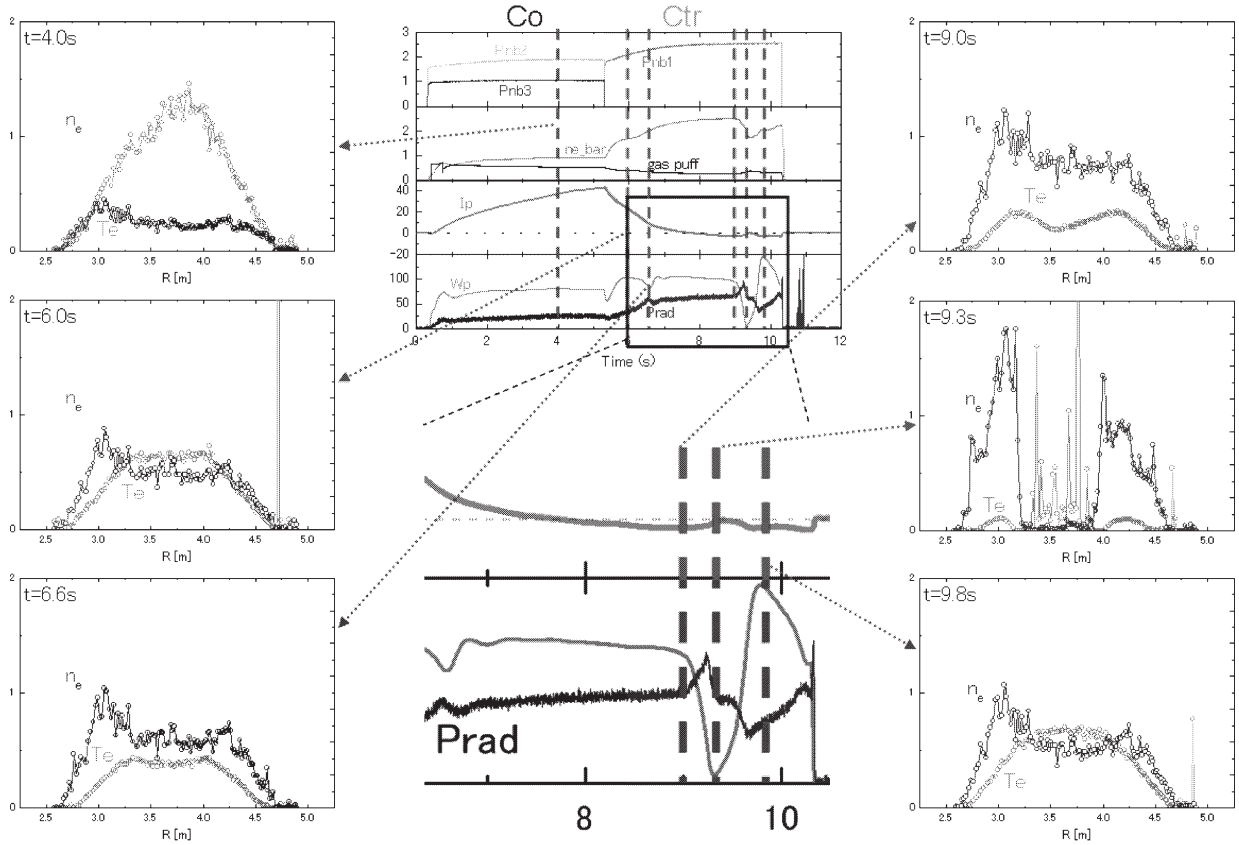
Recently, the magnetic axis sprit was observed in LHD with strongly elongated configuration in horizontal direction (Bq=300%) [1] and it was also investigated by analysis of MHD equilibrium [2]. A new type of plasma collapse phenomenon has been observed with the magnetic configuration of Rax=3.6m, Bt=1.5T, Gamma=1.254, Bq=200%, which is also horizontally elongated configuration.

The collapse was observed in the plasma heated by counter neutral beam injection (NBI), of which typical discharge is shown in below figure. The NBI is switched at  $t=5.3$  sec from dominated by co-beam with total port-through power of 3MW to ctr-beam with port-through power of 2.6MW. The electron density significantly increases from  $0.9 \times 10^{19} \text{m}^{-3}$  to  $2.5 \times 10^{19} \text{m}^{-3}$  after the switch of NBI direction, and plasma current can not be in the counter direction. The electron temperature profile becomes flat soon from peaky profile after the switch of NBI. In this discharge, two collapses occur, first one is minor

collapse at  $t=6.6$  sec and the stored energy of about 15% is lost. Second is complete collapse at  $t=9.3$  sec. The characteristics of the plasma going to the collapse are spontaneous density increase, increase of radiation, flattening of electron temperature profile. The collapse starts from center region of the plasma, and the electron temperature profile becomes hollow, which is most impressive feature of this phenomenon.

The necessity condition for the collapse is the magnetic configuration of Bq=200% and ctr-NBI heating. This collapse has a critical density, the low density plasma lower than  $\sim 0.7 \times 10^{19} \text{m}^{-3}$  can be sustained and plasma current can be driven in the counter direction. However the plasma density gradually increases and exceeds the critical density, and finally goes to collapse.

The electron temperature profile is clearly different from magnetic axis sprit for the point that two maximum electron temperatures appeared in hollow profile are always same. This indicates that magnetic equilibrium is completely different from magnetic axis sprit. This collapse is interesting phenomenon at the point of view of equilibrium limit.



### §35. Zeeman Spectroscopy with Tomographic Analysis

Goto, M., Morita, S.

Emission lines in the visible/UV wavelength ranges are observed with 80 lines of sight in total. Their field of view covers an entire poloidal cross section of the plasma as shown in Fig. 1. The emitted light is received with optical fibers having  $100\mu\text{m}$  diameter and is guided into a 1.33 m Czerny-Turner type spectrometer equipped with preoptics for the astigmatism correction. The entrance slit width is fixed to be  $30\mu\text{m}$ . A charge coupled device (CCD) having  $13.3\text{ mm} \times 13.3\text{ mm}$  area size is used as the detector and the spectra from all the lines of sight are recorded perpendicularly to the wavelength dispersion on the CCD.

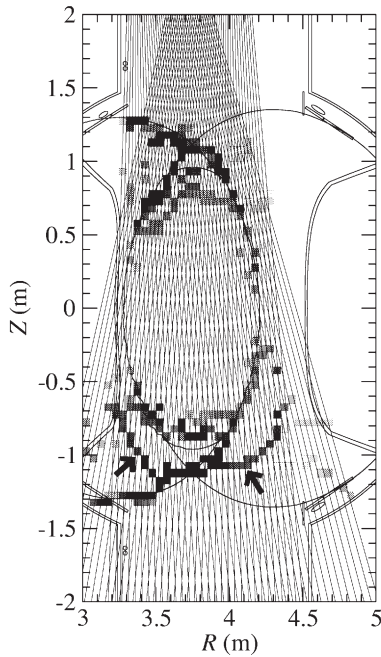


Fig. 1. Geometry for the observed plasma cross section and the obtained emission locations with all the lines of sight as a result of tomographic analysis. The darkness corresponds to the line intensity. The radiation regions indicated with arrows seem to be ghosts which have wrongly survived the tomographic analysis.

The Zeeman splitting of a neutral helium line,  $\lambda 667.8\text{ nm}$  ( $2^1\text{P}-3^1\text{D}$ ), which is caused by the magnetic field for plasma confinement, is measured. Though the obtained line profile is in general a superposition of several components on the same line of sight, they can be separated according to their different splitting widths. The measurement is made for a discharge with a magnetic configuration of  $R_{\text{ax}} = 3.75\text{ m}$ , where  $R_{\text{ax}}$  is the major radius of the magnetic axis. The magnetic field strength on the magnetic axis is 2.64 T. The plasma is sustained with hydrogen neutral beams and the electron density is controlled with helium gas puff. The spectra are taken every 250 ms (230 ms of exposure time and 20 ms of readout

time), and the data over five frames are summed up to reduce the statistical errors. During the time period for the observation the line-averaged electron density and the central electron temperature are almost kept constant to be  $2 \times 10^{19}\text{ m}^{-3}$  and 2.5 keV, respectively.

Figure 2 is an example of the observed spectra. The profile is understood as a superposition of two Zeeman components having different splitting widths. The magnetic field strengths of 2.56 T and 1.38 T are obtained from the least-squares fitting. The fitting result is shown with the dashed line in Fig. 2. The variation of the field strength along the line of sight

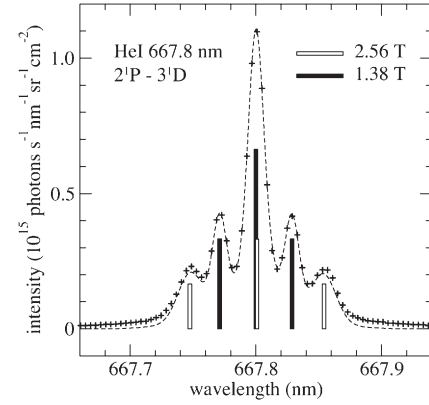


Fig. 2. Example of measured spectra for the HeI 667.8 nm line. The profile is well fitted with two Zeeman components and field strengths of 2.56 T and 1.38 T are derived.

is precisely known in LHD, and the emission locations are determined from the obtained field strength values. In many cases, however, a single field strength gives two locations on the line of sight and in such cases unique determination of the emission location is difficult. Here, let us remind that we observe the plasma with two different viewing angles as shown in Fig. 1 and a tomographic analysis might be possible. The observed area is divided into square cells having 50 mm side length and possible cells for the emission location are picked up in accordance with the Zeeman splitting analysis. Then the intensity distribution over the candidate cells is determined so that the following evaluation function,  $\varepsilon(f)$  where  $f$  represents the intensity distribution, has the minimum value,

$$\varepsilon(f) = \sum_i (I_i^{\text{cal}}(f) - I_i^{\text{obs}})^2. \quad (1)$$

Here,  $I_i^{\text{cal}}(f)$  and  $I_i^{\text{obs}}$  are the line-integrated intensities in the calculation and in the observation with the  $i$ th line of sight, respectively. The summation is made over all the lines of sight. The result is shown in Fig. 1. The line emissions along the inboard-side divertor legs and around the X-points are found to be rather strong while in the regions near the inboard- and outboard-side walls they are hardly detected. This suggests that the dominant particle recycling takes place on the divertor plate rather than the vacuum vessel wall. The radiation regions indicated with arrows in Fig. 1 are unrealistic and are considered to be ghosts which have wrongly survived the tomographic analysis. The present evaluation equation has yet to be optimized and further improvement is necessary.

### §36. High-Resolution Measurements of $H\alpha$ Spectral Line Profiles in LHD Steady State Plasmas

Kondo, K., Arimoto, H. (Kyoto Univ.),  
Oda, T. (Hiroshima Kokusai Gakuin Univ.),  
Takiyama, K. (Hiroshima Univ.),  
Masuzaki, S., Shoji, M., Goto, M., Morita, S., Noda, N., Ida, K., Sato, K., Ohyabu, N., Sudo, S.

The sustainable detachment has been obtained<sup>1)</sup>. The line-averaged electron density  $\bar{n}_e$  dependences of the parameters deduced from the  $H\alpha$  line profile have been investigated to discuss the differences in the neutral hydrogen behavior in the attachment and detachment plasmas.

Figure 1 shows the  $H\alpha$  spectral line profiles in the (a)attachment and (b)detachment discharges obtained at the sight line which view the inner divertor plate. These profiles can be decomposed into two Gaussian components of a narrow shape and a broad shape. The narrow component is considered to be the contribution of the dissociated atoms and the broad component represents the reflected and charge-exchanged atoms. The center of the broad component shows significant blue shift in attachment, while the shift is much smaller in detachment. The blue shift in attachment is due to the reflection by the divertor plates and corresponds to the inward flow velocity of up to  $1.5 \times 10^4$  m/s.

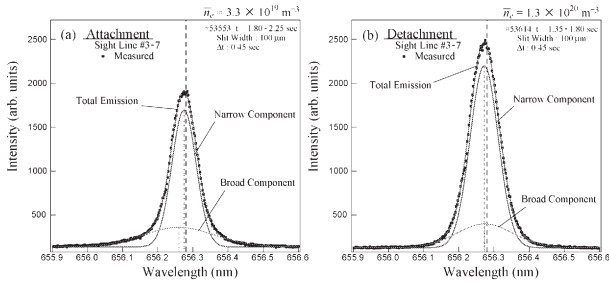


Fig. 1: The  $H\alpha$  spectral line profiles in the (a)attachment and (b)detachment discharges.

Figure 2 shows the  $\bar{n}_e$  dependences of the (a) $H\alpha$  line intensity, (b)flow velocity along the sight line, (c)temperature of the hydrogen atoms, (d)ion saturation current measured by the 6-I divertor probe and (e) $T_e$  at  $\rho = 0.9$  measured by the Thomson scattering system. The filled and open symbols indicate the narrow and the broad component, respectively, except for Fig. 2(d) and (e). As shown in Fig. 2(a), the line intensities of both components are almost proportional to  $\bar{n}_e$  in attachment. A similar dependence is found in the ion saturation current in Fig. 2(d). This means a clear correlation between the neutral hydrogen generation and the divertor flux in attachment. While in detachment, the line intensities are independent of the divertor flux and tend to increase in the higher  $\bar{n}_e$  conditions. As shown in Fig. 2(b) and (c), the flow velocity and the temperature of the narrow component do not depend on  $\bar{n}_e$ ,

and take almost constant value of  $\sim 3.0 \times 10^3$  m/s and  $\sim 3$  eV, respectively, regardless whether attachment or detachment. Those parameters of the broad component in attachment strongly depend on  $\bar{n}_e$ . The flow velocity drops from  $\sim 1.5 \times 10^4$  m/s to  $\sim 0$  m/s with the increase of  $\bar{n}_e$ . The broad component in this condition is considered to be mainly the reflected atoms by the divertor plates. The drop of the flow velocity with  $\bar{n}_e$  can be partly attributed to the decrease of the sheath potential and the energy of the incident ions due to the decrease of the edge electron temperature shown in Fig. 2(e). The temperature of the atoms is considered to be also affected by the edge electron temperature. In detachment, the contributions of the reflection are scarce because of the drastic decrease of the divertor flux. The flow velocity and the temperature are seemed not to depend on  $\bar{n}_e$ . The flow along the sight line can be regarded as almost isotropic with a little data scattering and the temperature ranges from about 7 eV to about 13 eV. The broad component in detachment could be qualitatively ascribed to the emissions from the charge-exchanged atoms around the shrunk core plasma. The difference in the broad component between attachment and detachment can be attributed to the significant differences in the divertor flux and the edge electron temperature<sup>2)</sup>.

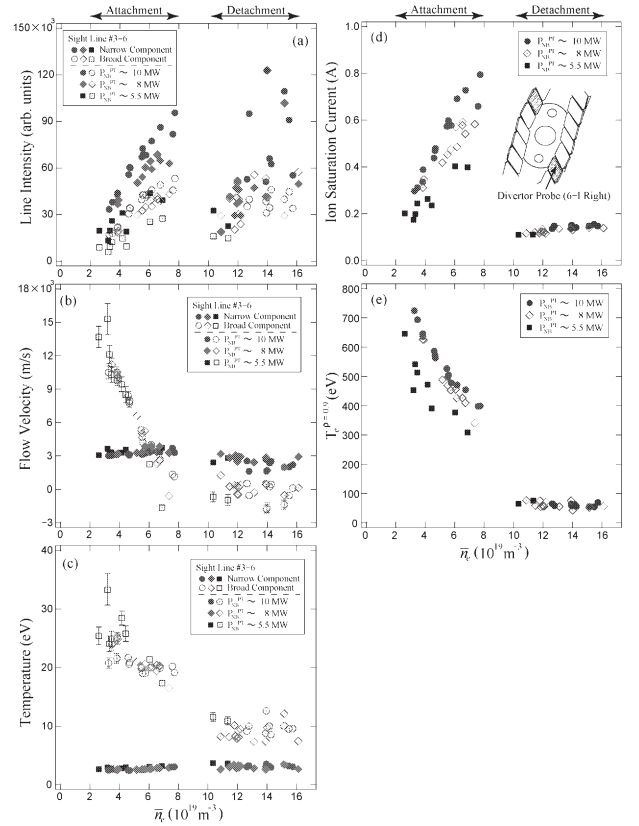


Fig. 2:  $\bar{n}_e$  dependence of (a) $H\alpha$  line intensity, (b)flow velocity, (c)temperature of the hydrogen atoms, (d)ion saturation current by divertor probe and (e) $T_e$  at  $\rho = 0.9$  by Thomson scattering.

#### References

- 1) Miyazawa, J. *et al.* : Nuc. Fusion **46** (2006) 532-540.
- 2) Arimoto, H. *et al.* : submitted to J. Nuc. Mater.

### §37. Application of Visible Bremsstrahlung to a Density Monitor in Steady State Fusion Reactor

Hisamichi, Y. (Grad. Univ. Adv. Stud.),  
Morita, S., Goto, M.

It is important to measure the electron density in the present toroidal devices in order to study the transport physics. In the fusion reactor, however, the density measurement becomes important in a viewpoint of feedback controls for the fusion output and maintenance of steady state discharges. At present, FIR interferometer and Thomson scattering are generally used for the density measurement. Both diagnostics need an external laser beam as a passive tool. It is very difficult to maintain them over a year in the future fusion reactor. Another reliable density monitor is needed in such a fusion reactor.

In the fusion reactor the electron density is high enough such as  $1 \times 10^{14} \text{ cm}^{-3}$  and the value of  $Z_{\text{eff}}$  is below 2 in order to gain the necessary fusion output. Intensity of visible bremsstrahlung is proportional to the square of the electron density if the  $Z_{\text{eff}}$  is close to unity. Then, the application of the visible bremsstrahlung [1-3] to the density monitor instead of such active diagnostic methods represents a necessary technique to the steady state fusion reactor. For the purpose of the density monitor in high-density plasmas, the visible bremsstrahlung has been measured in LHD and analyzed in comparison with signals from the FIR interferometer.

Visible bremsstrahlung profile has been measured with a combination of 80 optical fibers with a core diameter of  $300 \mu\text{m}$ , 80 photomultipliers and an interference filter. The optical fibers with a length of 100m transfer the visible emissions from LHD to a diagnostic room. The radial profiles of the visible bremsstrahlung consist of two sets of horizontal 40 chords, which measure the slightly different poloidal magnetic surfaces cross section. A time response of the photomultiplier tubes is  $10 \mu\text{s}$ . The data are normally taken by a 10kHz sampling A/D converter. Figure 1 (a) shows a comparison between temporal behaviors of  $n_e l$  and the square root of the visible bremsstrahlung signal. Both signals are taken from line-averaged data at the plasma center chord. The density is built up by continuous  $\text{H}_2$  gas puff. It is seen that both signals have the similar temporal behavior. Here, a ratio of the square root of the visible bremsstrahlung signal to the  $n_e l$  is analyzed. Increasing the density during the discharge, the electron temperature decreases as shown in Fig.1(b). As mentioned above, the

visible bremsstrahlung signal has weak temperature dependence. Two ratios are, then, considered. The ratios are

$$\text{expressed in eqs.(3) and (4) as follows; } R_1 = \frac{\sqrt{I_B}}{n_e l} \quad (3)$$

$$R_2 = \frac{\sqrt{I_B \times T_e^{0.35}}}{n_e l} \quad (4)$$

The eq.(4) corrects the weak temperature dependence included in the visible bremsstrahlung signal. The results are plotted in Fig.1(c).

A similar analysis is done in the repetitively injected  $\text{H}_2$  pellet discharge. The density rapidly goes up after the  $\text{H}_2$  pellet injection and decays with a core particle confinement time. The ratio with a correction of the temperature dependence denoted by the dashed line ( $R_2$ ) gives a smoother and constant value during the discharge, although the ratio without the correction gives a slight difference during the discharge.

The present experimental result strongly suggests the use of the bremsstrahlung signal to the density monitor instead of the present density diagnostic methods such as FIR interferometer and Thomson scattering in the future fusion reactor.

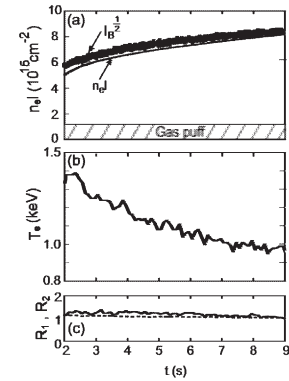


Fig.1

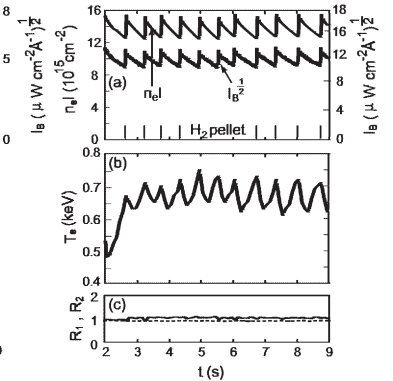


Fig.2

Fig.1  $\text{H}_2$  gas puff plasma. Fig.2  $\text{H}_2$  ice pellet injection plasma; (a) Time evolutions of  $n_e l$  and the square root of visible bremsstrahlung signal, (b) electron temperature measured by Thomson scattering and (c) ratios of  $R_1$  (solid line) and  $R_2$  (dashed line).

#### References

- 1) S.Morita, J.Baldzuhn, in: IPP-report (Garching, Germany), No.199 (1995).
- 2) S.Morita, R.K.Richards, L.D.Horton, R.C.Isler, E.C.Crume,Jr, M.Murakami in: OAK RIDGE NATIONAL LABORATORY/TM-11737 (1991).
- 3) K.Kadota, M.Otsuka and J.Fujita, Nuclear Fusion 20 (1980) 209-212.



### §38. Estimation of the Particle Confinement Time of the Helium Ash in LHD

Mitarai, O. (Kyushu Tokai University),  
Sakamoto, M. (Kyushu University),  
Tanaka, K., Goto, M., Morisaki, T., Masuzaki, T.,  
Ashikawa, N. (NIFS)

The ratio of the helium ash confinement time to the energy confinement time ( $\tau_{\alpha}^*/\tau_E$ ) should be lower than 7 in the FFHR helical reactor. However, for maintaining ignition  $\tau_{\alpha}^*/\tau_E=3$  is usually assumed. As such data are not yet available in any helical device, it is urgent to measure helium particle confinement time experimentally. While the charge exchange recombination spectroscopy with small S/N ratio has been used in many tokamak experiments, He lines and density decay are monitored by spectrometer and interferometer to estimate the helium particle confinement time roughly.

In 2004 campaign, Helium gas was injected in the helical divertor configuration without pumping. Therefore, the density decay was very slow. In 2005 campaign, LID configuration with active pumping has been used with  $B_0=2.64\text{T}$  and  $R_0=3.75$  to study the pumping effect on a helium confinement time. Two density regimes with  $3 \times 10^{19}$  and  $1.5 \times 10^{19} \text{ m}^{-3}$  are used for comparison. In a higher density regime, H-alpha signal is observed during He gas puffing. Hydrogen gas absorbed in the vacuum chamber or the LID head were released by He gas puffing. Therefore, the density waveform may not be made by He gas alone.

In the lower density regime, hydrogen line is not so strong during He gas puffing [ $t=2\text{--}2.1\text{s}$ ] (Fig. 1-(b)) as in the higher density regime. Then we estimated the He confinement time using the density decay waveform (Fig. 1-(c)) assuming the charge neutral condition:  $\Delta n_e = 2\Delta n_{\text{He4}}$ . The helium particle balance equation is

$$\frac{dn_{\text{He4}}}{dt} = S_{\text{He4}} - \frac{n_{\text{He4}}}{\tau_{\alpha}^*} \quad (1)$$

where  $\tau_{\alpha}^*$  is the effective helium particle confinement time. The helium source term  $S_{\text{He4}}$  is determined by the waveform of He-I line ( $4684 \text{ \AA}$ ) [Fig. 1-(c)]. The base line of the

density during He gas puffing is monitored in the separate shot without He gas puffing and is subtracted from the density waveform [Fig. 1-(c)]. Fitting the density and alpha particle confinement time using Eq. (1) were conducted. The resultant effective helium particle confinement time  $\tau_{\alpha}^*$  is  $0.16 \sim 0.29 \text{ sec}$  as plotted in Fig. 1-(d), which provides  $\tau_{\alpha}^*/\tau_E=3.2 \sim 5.8$  for the constant energy confinement time of  $50 \text{ ms}$  (#57594).

However, the effect of the small amount of Hydrogen injection observed by H-alpha line on the charge neutrality cannot be ruled out. More accurate experiments using the charge exchange recombination spectroscopy with NBI are required and is planned in 2006.

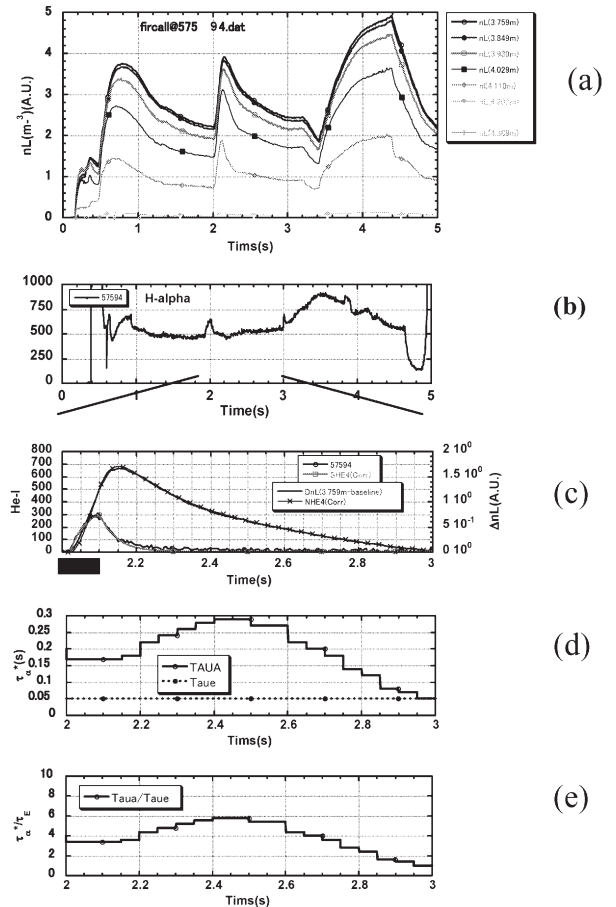


Fig. 1. (a) Density waveforms, observed at the various positions by the far infrared interferometer, by He gas puffing in the LID configuration (#57594). (b) H-alpha signal. (c) Density waveform corrected to the base line and H-I line ( $4684 \text{ \AA}$ ). Black square shows He gas puffing pulse. (d) Estimated effective helium particle confinement. (e) Estimated effective helium particle confinement to the energy confinement time ratio  $\tau_{\alpha}^*/\tau_E$ .



§39. Achievement of 1.6 GJ Input in Steady State Operation in LHD

Seki, T.

Investigation of steady state operation has been carried out in LHD using an ion cyclotron range of frequencies (ICRF) heating mainly. One of the main purposes of the research was to achieve the longer discharge length and the higher input energy, which were recorded in the 8th cycle experiment. As a result, discharge length of 54 minutes and 28 seconds and total input heating energy of 1.6 GJ were achieved.

The plasma was sustained by an ICRF heating mainly with an assist of electron cyclotron heating (ECH). The wave frequency of ICRF heating was 38.47 MHz and a magnetic field strength on magnetic axis was 2.75T. Helium majority plasma with hydrogen minority was used. Ion cyclotron resonance layers were located at saddle points of magnetic configuration. Plasma was heated by the minority heating regime. The heating efficiency was best in the ICRF heating modes. ECH power of 110 kW was injected as an assist. Averaged total heating power was 490 kW.

Figure 1 shows the time history of plasma parameters of the longest discharge. The total input energy of 1.6 GJ was achieved in this discharge. During long pulse operation, sparks were observed in the vacuum vessel by the CCD camera monitor. Some sparks were related with the plasma collapse. Frequency of sparks had a relationship to the ICRF power. Then, the ICRF power was controlled during the plasma discharge with monitoring the sparks in the vacuum vessel. A line-averaged electron density and ion and electron temperatures near plasma center were lower than the experiment in 8th cycle because the average heating power was lower. An average density was  $0.4 \times 10^{19} \text{ m}^{-3}$ . Central ion and electron temperatures were about 1 keV. Position of magnetic axis was swept so as to disperse heat load on the divertor plates. Temperatures at the vacuum vessel were saturated during the discharge. This operation method was established in the 8th cycle experiment. The range of sweep of the magnetic axis was inward shifted from the 8th cycle experiment and  $R_{ax} = 3.64 - 3.67\text{m}$ . Temperatures at the vacuum vessel and the divertor plate were saturated during the discharge. Temperatures at the feedthrough of the ICRF antenna were increasing gradually. Cooling of the feedthrough must be strengthened for further experiment. At the end of the discharge, plasma was collapsed by influx of iron impurities. This phenomenon occurred in the 8th cycle also. It is important for further experiment to avoid the plasma collapse caused by an impurity influx.

Figure 2 shows an injected heating energy as a function of a plasma discharge time. In the 8th cycle experiment, an injected heating energy of 1.3 GJ was achieved. This was the world record exceeding the achievement set by Tore Supra. The plasma duration time of 65 minutes was also attained using ECH. In the 9th cycle experiment, the

injected heating energy was renewed and 1.6 GJ was achieved. The next targets are an input energy of 2 GJ and plasma duration time more than one hour.

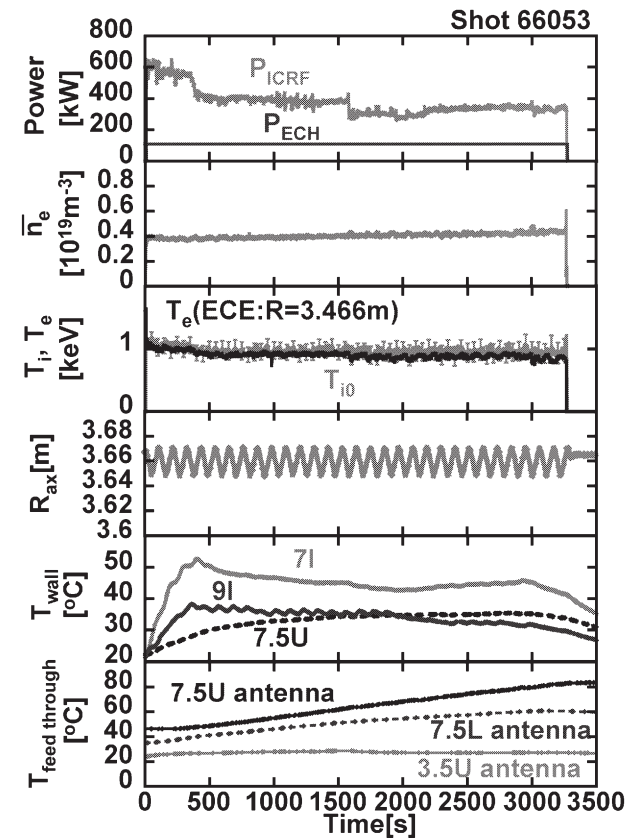


Fig. 1. Time evolution of plasma parameters of the longest discharge in the 9th cycle experiment. An input heating energy of 1.6 GJ was achieved.

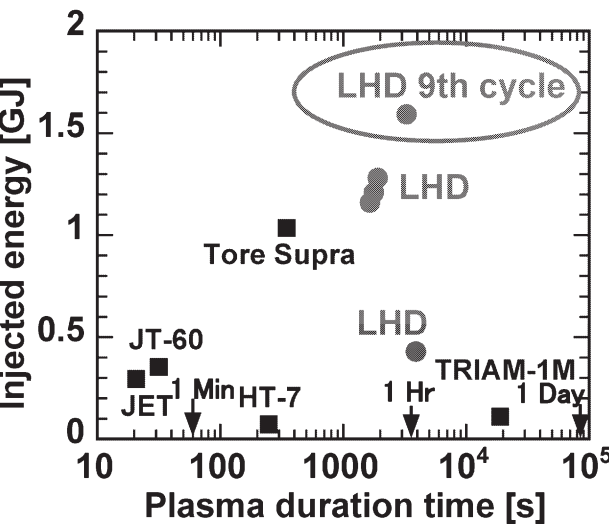


Fig. 2. Injected heating energy as a function of a plasma discharge time.

## §40. Long Pulse Discharge of MW-ICRF Heated Plasma

Kumazawa, R.

Achieving a long pulse plasma discharge is one of the main purposes of experiments on the Large Helical Device, (LHD) and attempts have been carried out in every experimental campaign. A long pulse plasma discharge of 1905 sec (with a total input energy of the plasma heating exceeding 1.3J) was achieved at less than 1MW in the 8<sup>th</sup> experimental campaign, i.e., in 2004, using mainly ion cyclotron range of frequency (ICRF) heating power [1~4]. In the 9<sup>th</sup> experimental campaign it was carried out with high power ICRF heating of more than 1MW. The plasma was terminated by the gradual density increase accompanying the increase in the radiated power or the sudden penetration of heavy impurity ions, e.g., of Fe; the former problem was overcome by aging graphite tiles with many long pulse plasma discharges up to 1.5MW of heating power, but the latter was an unsolved issue to be overcome in further trials of the long pulse operation with a higher heating power. This paper reports the experimental results for the long pulse plasma discharge using mainly ICRF heating in the 9<sup>th</sup> experimental campaign.

In the 9<sup>th</sup> experimental campaign trials were carried out of the long pulse discharge with more than 1MW of ICRF heating. The time evolutions of plasma parameters of a typical long pulse discharge are shown in Fig.1. A plasma of  $n_e=1 \times 10^{19} \text{ m}^{-3}$ ,  $T_e \sim T_{i0} = 1.2 \sim 1.3 \text{ keV}$  was sustained for 285 s. with an applied power of an ICRF heating power,  $P_{\text{ICH}}=1.33 \text{ MW}$  and an ECH (Electron cyclotron heating) power,  $P_{\text{ECH}}=0.11 \text{ MW}$ . At almost the middle of the plasma discharge the metal impurity penetrated the plasma accompanied by sparking on the vacuum vessel surface, which would have led to a decrease in the electron temperature with a sudden increase in the electron density and terminated the plasma. In this discharge, however more ECH power of 330kW was injected from another ECH power system for 0.6 s. at 178.4 s., being triggered by the sudden increase in the electron density.

The summarized result achieved in the 9<sup>th</sup> experimental campaign is shown in Fig.2, where the plasma duration time is plotted against the RF heating power (a summation of  $P_{\text{ICH}}$  and  $P_{\text{ECH}} \sim 0.1 \text{ MW}$  in every plasma discharge). Open circles were obtained in the 8<sup>th</sup> campaign, and solid circles and squares in the 9<sup>th</sup> campaign. It was found that the plasma duration time was extended to a higher RF heating power region in the 9<sup>th</sup> campaign. Solid squares denote a plasma discharge with an instantaneous ECH power injection and solid circles one without it. It is easily seen that the effectiveness of the ECH power injection is clear in the power range of 1.4 to 1.6MW. However the plasma duration time was decreased with the increase in the total RF heating power, though the plasma operation region was extended. The scaling law of the discharge duration time against  $P_{\text{RF}}$ ,  $\tau(\text{sec}) = 1,200 \exp\{-P_{\text{RF}}(\text{MW})\}$  is plotted using a dotted line. The other dotted line of a constant time of 300 s is found in Fig.2. It is a saturation time of thermal equilibrium in divertor plates. When the impurity penetration problem is

overcome, it suggests that a long pulse plasma discharge more than 1 hour will be achieved up to 1.4MW.

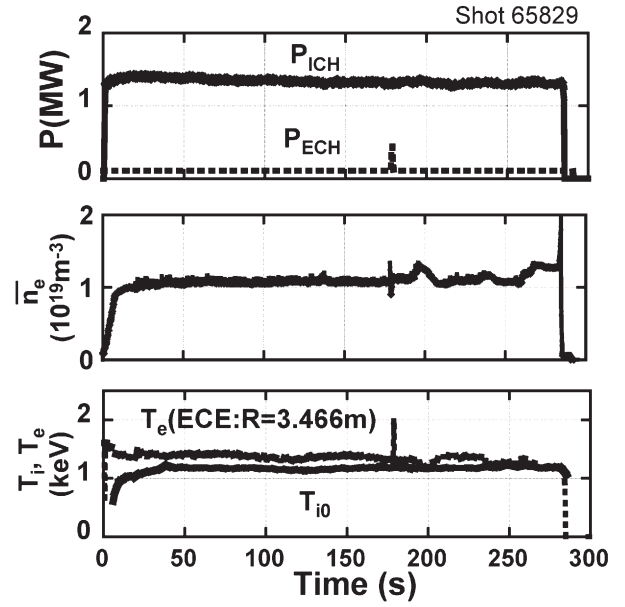


Fig.1 Time evolutions of plasma parameters,  $P_{\text{ICH}}$  and  $P_{\text{ECH}}$ ,  $n_e$ , and  $T_e$  and  $T_i$  in 1.3MW plasma discharge.

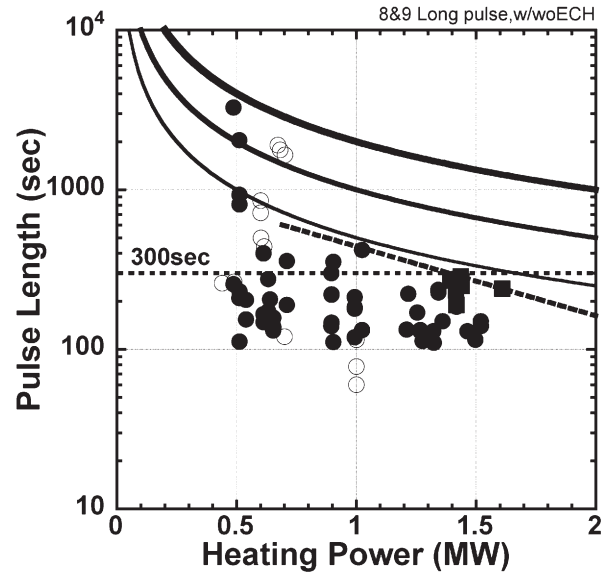


Fig.2 Plasma pulse length vs. heating power.

### References

- [1] T.Mutoh et al., J. of Plasma and Fusion Research, **81**(2005) 229
- [2] T.Seki et al., AIP Conference Proceedings **787**(2005) 98
- [3] R.Kumazawa et al., Nucl. Fusion **46**(2006) S13
- [4] Y.Nakamura et al., Nucl. Fusion **46**(2006) 714

#### §41. Density, ICRF Power and Pulse Length Operated in Steady State Experiment in the 9th Cycle Experiment

Seki, T.

Higher density operation is important for a steady state experiment. One reason is a slowing down of high-energy ions. The other is an engineering study of experimental devices for a steady state operation. During the long pulse operation, sparks are observed in the vacuum vessel. One of causes of plasma collapse is thought an iron impurity influx accompanied with the sparks. Frequency of the sparks is related with an electron density. When the line-averaged electron density is high, the sparks are rare. One possible speculation of source of the sparks is high-energy ions accelerated by ICRF waves. High-density operation is effective to decrease the high-energy ion tail and the sparks. Possibility of plasma collapse during a steady state operation will go down by a high-density operation. In case of a high power steady state operation, heat load on the divertor and the vacuum vessel is large. It will contribute to investigate an engineering evaluation of LHD for a steady state operation.

In the steady state experiments in the 9th cycle experimental campaign, higher density operation using a high power ICRF heating was carried out at the beginning. Figure 1 shows the maximum of a line-averaged electron density against the ICRF power. Symbols are classified by the experimental dates. Data of the 8th cycle experiment are also plotted. Figure 2 shows the pulse length of the ICRF pulse as a function of the ICRF power. The steady state experiment was started at an injection power of about 1 MW and a line-averaged electron density of  $1 \times 10^{19} \text{ m}^{-3}$  and a pulse length of 10 seconds. The ICRF power was increased and the pulse length was extended after that. The maximum density was about  $1.8 \times 10^{19} \text{ m}^{-3}$ . This is lower than that of the 8th cycle's value for the same ICRF power. The plasma with an electron density of  $1 \times 10^{19} \text{ m}^{-3}$  was sustained for 4 minutes and 45 seconds with an ICRF power of 1.35 MW. These power and density were almost same as target values for the 9th cycle steady state experiment. However, many sparks occurred and a long pulse discharge using a high power ICRF heating became difficult later. Higher power and longer pulse trial may have caused the problems in the ICRF antenna and the vacuum vessel. Traces of arcing were found at the ICRF antenna when inspection was conducted in the vacuum vessel after the experiment. The ICRF power was controlled with watching the sparks for the further long pulse experiment. A line-averaged electron density was reduced with the ICRF power.

Data from the 8th and the 9th cycle experiments in Fig.2, it seems that there is some threshold that the discharge extends to more than 1000 seconds. If the pulse length reached to around 400 seconds, possibility to get longer was high. This will help for an efficient steady state experiment as a criterion.

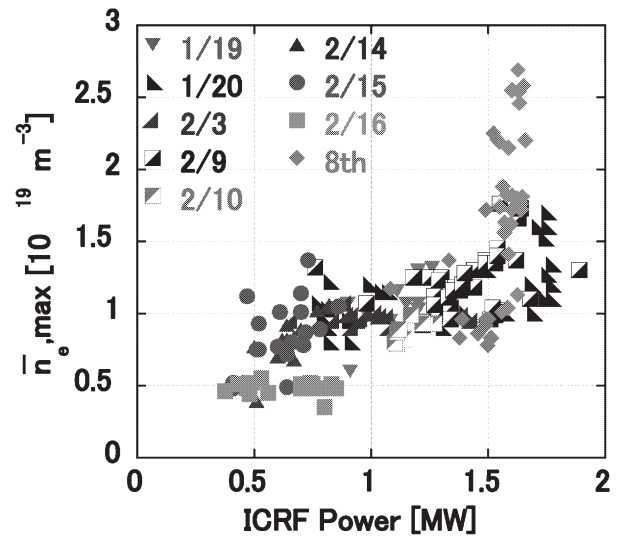


Fig. 1. Maximum of a line-averaged electron density against the ICRF power.

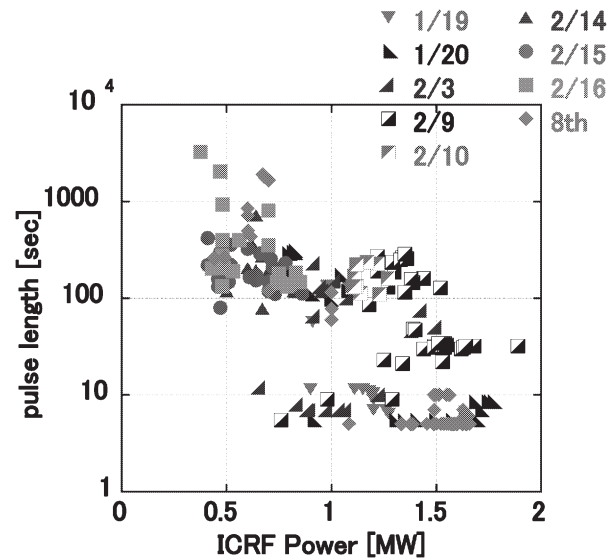


Fig. 2. Pulse length of the ICRF pulse as a function of the ICRF power.

## §42. Mechanism of Magnetic Axis Sweeping Divertor

Watanabe, T., Masuzaki, S., Nakamura, Y.

Steady state divertor operations with high performance plasmas have been demonstrated in the LHD. For achieving steady state operation, it is very important to control the deconcentration of divertor heat flux. Slow (period: about 100 seconds) and small periodic sweeping of magnetic axis position achieves the high performance long pulse discharge by overcoming the toroidal nonuniformity of heat load on divertor tiles. The magnetic axis position sweeping was carried out by preprogrammed current control of the poloidal coils. Physical mechanism of the magnetic-axis-sweeping-divertor is studied based on the chaotic nature of lines of force in the peripheral region of plasma column.

The LHD magnetic field is produced with the contin-

uous winding helical coils and without the toroidal coil. Then, a characteristic of the LHD magnetic field is the high magnetic shear configuration in the peripheral region of plasma column including the open field line region outside the last closed flux surface (LCFS) of the LHD. So, lines of force in open field line region show a fractal structure and create a chaotic field line layer. Whisker field lines constitute the divertor field lines in the LHD(Fig.1). It seems that numbers of whiskers and the thickness of each whisker field lines decides the heat flow to the divertor tiles. A slight change in a vertical magnetic field produces slight change in the rotational transform, which greatly changes the alignment of whiskers and the magnetic islands embedded in the chaotic field line region because of the high magnetic shear in the peripheral region. This should be the physical mechanism of the deconcentration of divertor heat flux by magnetic axis sweeping.

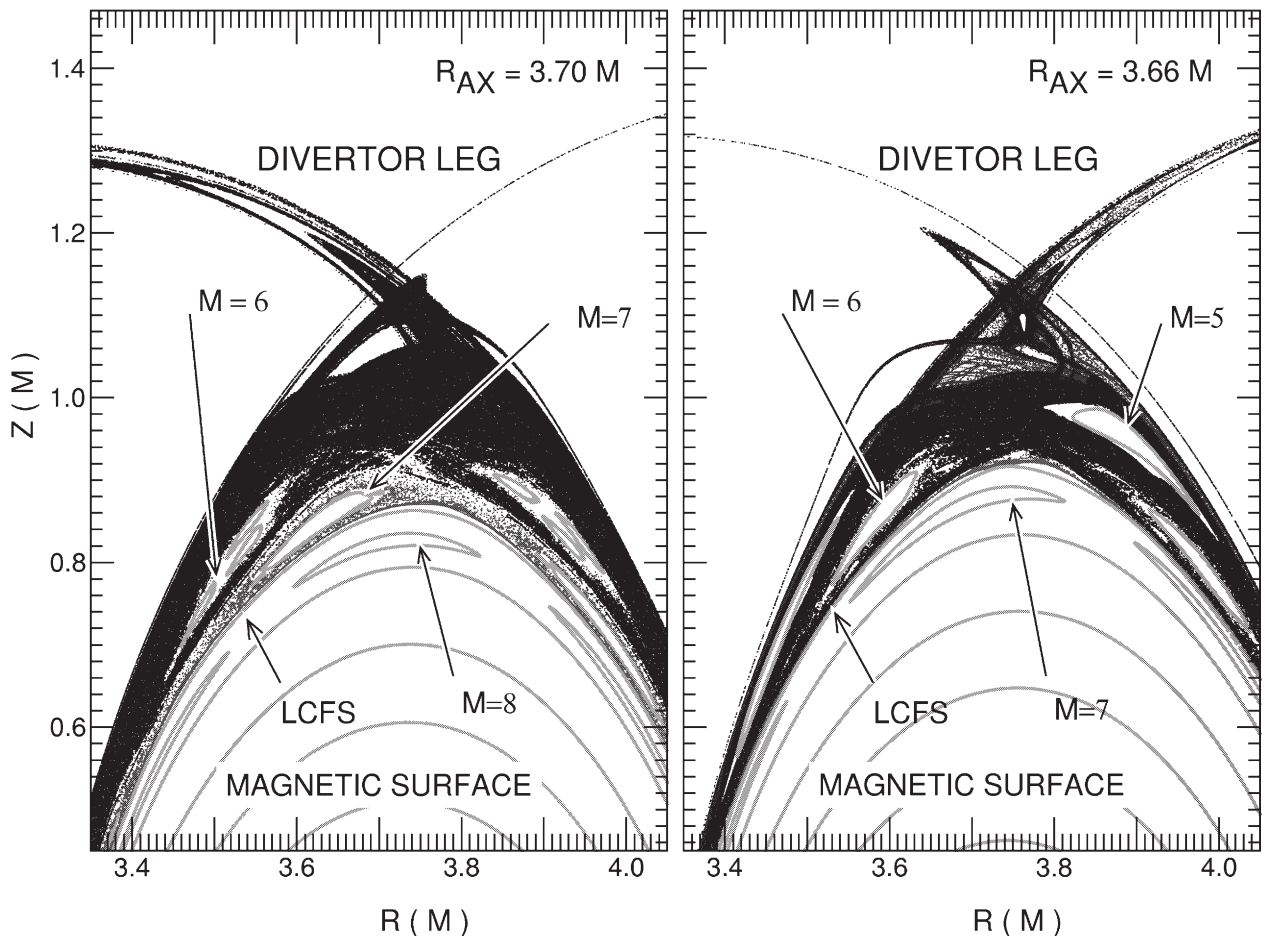


Fig.1. Poincaré plot of magnetic field lines in the  $\phi = \pi/10$  poloidal cross-section. Difference of divertor field lines (divertor leg) by small difference of magnetic axis position is shown. Magnetic surface region, the LCFS and mode number of relatively large magnetic islands are also specified. The  $M = 5$  island disappear and the  $M = 7$  island move to the chaotic field line region when  $R_{ax} = 3.70$  m.  $R$  is the major radius and  $z$  is the vertical position.



### §43. Characteristics of Impurity Content in Long-Duration Discharges with Magnetic Axis Sweeping

Nakamura, Y., Kumazawa, R., Mutoh, T., LHD Experimental Group

Significant progress in LHD has been made in terms of injected energy: an energy of 1.6 GJ has been injected into plasmas lasting more than 54 min in the 2005 experimental campaign. These long-duration discharges were terminated by radiation collapse due to penetration of metallic flakes into the plasma. Therefore, we investigate the dependence of impurity content on magnetic configuration and the direction of magnetic axis sweeping.

Steady state operation was carried out in various magnetic configurations by scanning the magnetic axis in time during the discharge. Figure 1 shows the discharge duration and the normalized radiation as a function of the magnetic axis. In the inward shifted configuration ( $R = 3.55 \sim 3.6$  m), the discharge duration was limited up to 160. The discharge duration was extended gradually by shifting the magnetic axis outward. Finally, the discharge was sustained for more than 30 min with real-time magnetic axis sweeping between  $R = 3.672 \sim 3.693$  m in the 2004 experimental campaign. In this experimental series, there exists another key point for extending the discharge duration. As seen in Fig. 1, the radiation normalized by the averaged electron density remarkably decreases by shifting the magnetic axis outward. An abrupt termination of the steady state plasmas was frequently observed without any trouble in the heating system. In that case, the abrupt increase of density and radiation was observed at the end of the discharge in spite of constant heating power input. Spectroscopic measurements show that light impurity line intensities do not increase but metallic impurity (mainly iron) line intensities increase suddenly at the same time as the increase of density and radiation. This suggests that a relatively large iron mass comes into the plasma. The events mentioned above can be seen in most of the long pulse discharges terminated unexpectedly. Most probably, the discharge durations are limited by the penetration of metallic flakes into the plasma, which may be caused by localized heat deposition or power concentration.

Figure 2 shows the time behavior of radiation and impurity line radiations in thirty minutes discharge. The averaged central chord radiation was maintained at a constant level during the discharge. The detailed time behavior is similar to that in the line radiation of the metallic impurity (FeXXIII). On the other hand, the light impurity line intensity (CIII) has no significant change in time. This suggests that the main impurity in the core plasma is iron and its content is significantly large. In addition, it is found that the normalized radiation is dependent upon the magnetic axis and the sweeping

direction as shown in Fig. 3. The radiation normalized by the line averaged electron density indicates the impurity content in the plasma. The data points indicate an averaged value in the magnetic axis sweeping of 18 times except for those during the injection of neutral beam. In the outward shifting phase, the normalized radiation increases in the vicinity of  $R = 3.678$  m and then decreases by shifting the magnetic axis outward. When the magnetic axis moves inward, the radiation increases monotonously. These results indicate a strong interaction between the plasma and SS wall in the inward shifted magnetic configuration.

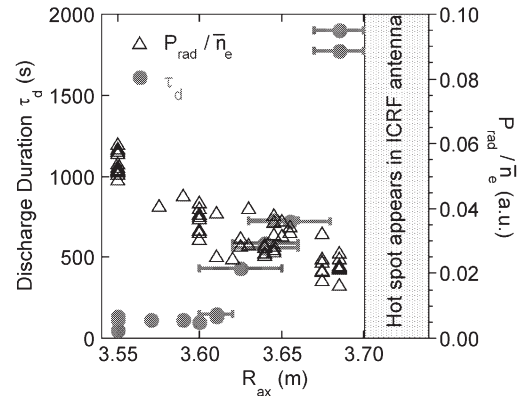


Fig. 1. Progress in discharge duration by scanning axis and dependence of normalized radiation on the magnetic axis.

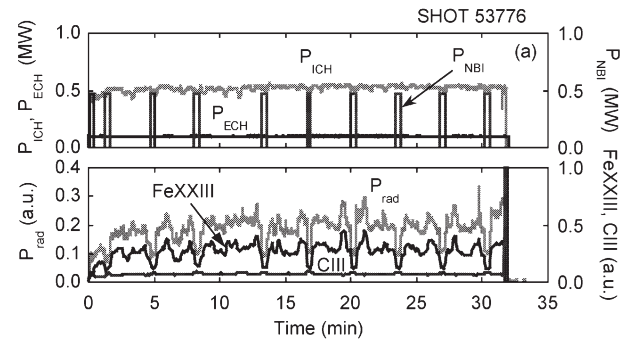


Fig. 2. Time behavior of radiation and impurity line radiation in thirty minutes discharge.

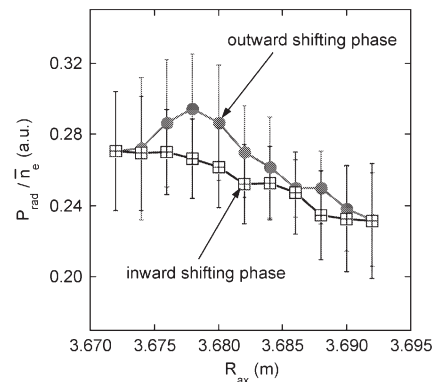


Fig. 3. Dependence of normalized radiation on the magnetic axis during thirty minutes discharge.

# §44. Distribution of Divertor Temperature after Long Pulse Operation Using ICRF Heating in 9th Cycle Experiment

Seki, T.

Heat load on divertor plates are important for a steady state operation. Outgas from divertor plates at high heat load is one of causes of a plasma collapse. To disperse the local heat load, an operation method of magnetic axis sweep was established in the 8th cycle experiment. Temperatures on the divertor plates were saturated during the long pulse discharge so far. However, the saturated temperatures were different from the position of the plates. Distribution of divertor temperature rise was compared.

Figure 1 shows the position and the number of the divertor plates. Eight positions of divertor plate temperature are measured at each toroidal section. There are 10 toroidal sections. Figure 2 shows a time history of the ICRF power and distribution of temperature increase of the divertor plate in the longest shot of the 9th cycle experiment. Figure 3 shows the same as the Fig.2 in the other shot of the 9th cycle experiment. Different ICRF antennas were used in Fig.2 and Fig.3.

Distribution of the divertor temperature is quite different. The ICRF antennas are located at 3.5U, 3.5L, 7.5U, and 7.5L ports. In Fig.2, 3.5U, 7.5U, and 7.5L antennas were used. Temperature rise near the 7.5-port was notable. Temperatures at 6.5L, 7.5L, 6I, 7I, and 8I were especially high. Temperatures near 3.5 antennas were also relatively increased. During the long pulse discharge, sparks were observed at around the 7I port and 7.5 section. Frequency of sparks at 7I port was related to the injection power of the 7.5L antenna. Temperatures of the vacuum vessel at 7I and 9I were also high. Temperature behavior of the vacuum vessel at 7I was closely related with the ICRF power at the 7.5L antenna.

In Fig.3, 3.5U, 3.5L, and 7.5U antennas were used. The ICRF power was higher and the pulse length was shorter than that of the Fig.2 case. Temperature increase near the 7.5 antennas was relatively small. Divertor temperature at 3.5L and 3I were increased particularly. Temperature at the 2O plate was also increased. Influence of the L antennas on temperature rise of the divertor plate was larger than that of the U antennas. Watching the high temperature plates and power control of each ICRF antenna may be important for the higher power and the longer pulse operation in the future.

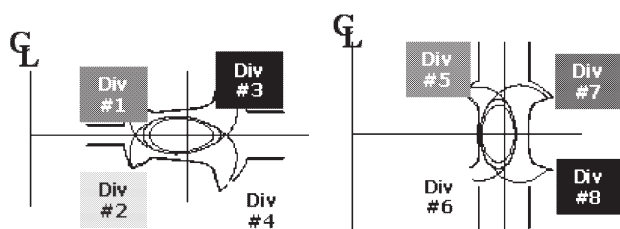


Fig. 1. Position and the number of the divertor plates.

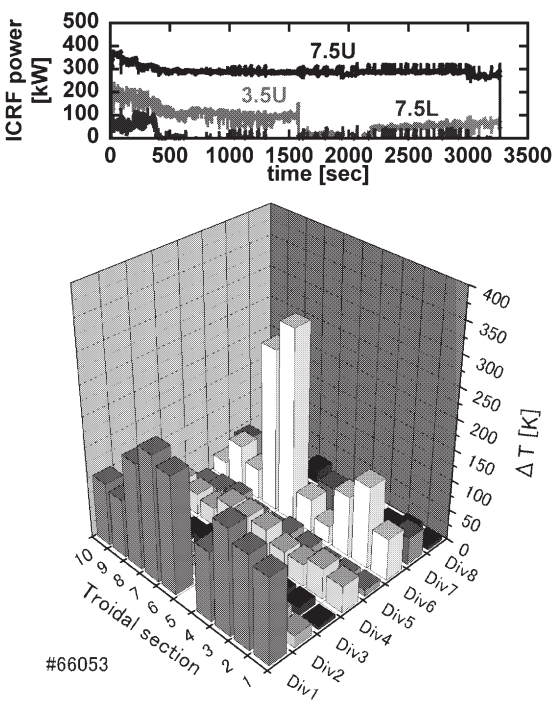


Fig. 2. Time history of the ICRF power and distribution of temperature increase of the divertor plates for the 1.6 GJ discharge.

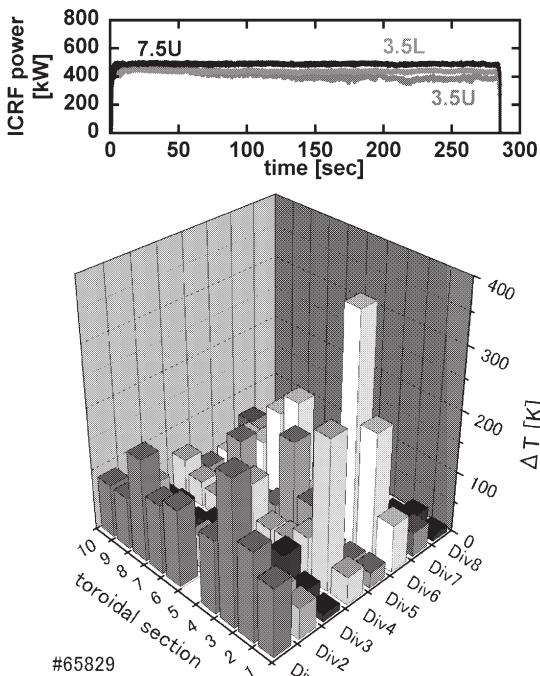


Fig. 3. Time history of the ICRF power and distribution of temperature increase of the divertor plates for the 1.35 MW injection.

#### §45. Wall Recycling Study Using Pulsed Gas Puffing during a Long Duration Discharge in LHD

Sakamoto, M. (Advanced Fusion Research Center, Research Institute for Applied Mechanics, Kyushu Univ.), Nakamura, Y., Takeiri, Y., Kumazawa, R., Tanaka, K., Noda, N., the LHD Experimental Group

The achievement of the stable steady state operation (SSO) is one of the requirements for the future fusion reactor. Understanding of the global wall recycling is critical in achieving the SSO. In this time, we investigated the wall recycling properties of long duration discharges of NBI heated hydrogen plasma using pulsed gas puffing (i.e. dynamic condition).

Figure 1 shows the time evolution of the decay time of the line averaged electron density  $\bar{n}_e$  just after gas puffing in CW-NBI discharges. The direction of NBI is clockwise (CW). The value of  $\bar{n}_e$  of the background plasma is about  $1 \times 10^{19} \text{ m}^{-3}$ . The gas puffing was carried out at the interval of 5 s. In the case of large gas puffing, the density decay time,  $\tau_d$ , increases with time and it becomes twice in the period from  $t = 5 \text{ s}$  to  $25 \text{ s}$ . The increment of  $\bar{n}_e$  due to gas puffing is about 25 %. On the other hand, in the case of small gas puffing,  $\tau_d$  only slightly increases. The increment of  $\bar{n}_e$  due to the gas puffing is about 7 %. It is found that there exists a big difference of  $\tau$  between large and small gas puffings.

Figure 2 shows a comparison of  $\tau_d$  between CW-NBI and CCW-NBI discharges. In both discharges, large gas puffing, i.e.  $\sim 25 \%$  increment of  $\bar{n}_e$ , was carried out. In the case of CCW-NBI discharge,  $\tau_d$  does not change so much and it seems to be almost constant during the discharge. In the case of CW-NBI, the result is the same as Fig.1. It is found that there also exists a big difference of  $\tau_d$  between CW-NBI and CCW-NBI discharges.

The decay time of  $\bar{n}_e$  just after the gas puffing means the effective particle confinement time  $\tau_p^*$  and it is a good scale for the evaluation of the wall recycling, since it is defined as the following equation:

$$\tau_p^* \equiv \tau_p / (1 - R),$$

where  $\tau_p$  is particle confinement time and  $R$  is a recycling coefficient. The density decay time depends on both particle confinement time and a recycling coefficient. It is expected that  $\tau_p^*$  increases with time, since  $R$  increases with time. Actually, increase in  $\tau_p^*$  with time was observed in TRIAM-1M [1]. On the other hand, it was also observed that the density decay time just after gas puffing did not change during a one-minute discharge which was sustained by lower hybrid current drive in TRIAM-1M [1]. This result is similar to the results of small gas puffing and CCW-NBI in LHD.

The difference of  $\tau_d$  in Fig.1 and Fig.2 seems to be an important key to understand the mechanism of the wall recycling in the case of the dynamic condition. Through a comparison of results between TRIAM-1M and LHD, the detailed investigation will be done.

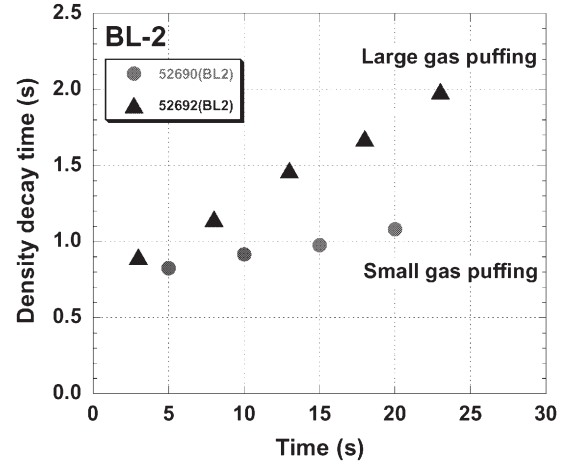


Fig.1 Time evolution of the density decay time just after gas puffing in CW-NBI discharges. Closed circles are data in the case of the density increment of about 7% and closed triangles 25%.

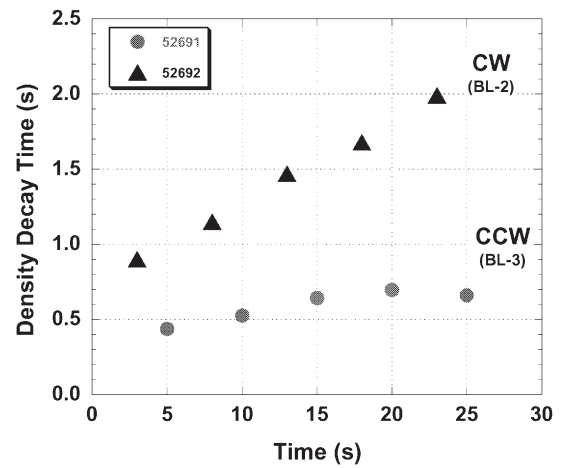


Fig. 2 Comparison of the time evolution of the density decay time between CW-NBI (closed triangles) and CCW-NBI (closed circles) discharges.

#### Reference

- 1) Sakamoto, M. et al., J. Nucl. Mater. 313, (2003) 519.



# §46. Instantaneous ECH Injection for ICRF Heated Long Pulse Plasma Discharge

Kumazawa, R., Shimpo, F., Kubo, S.

During the long pulse plasma discharge sparking was frequently observed especially just before the plasma collapse. It seemed that a heavy impurity such as Fe penetrate the plasma, which was often detected using VUV spectrum [1]. The sparking was found between the divertor tiles, whose position was sometimes different in different plasma discharges. A subsequent penetration of heavy impurities, eg., Fe resulted in the reduction of the electron temperature, the increase in the electron density and the collapse of the plasma.

A trial of the instantaneous ECH power injection (which we call ECH camphor injection) was carried out to restore the electron temperature using the sudden increase in the density as a trigger, as shown in Fig.1. A small amount of heavy metal penetrated at 178.2 sec, but the subsequent density increase was less than 25% (the level set to launch ECH power injection as the trigger threshold in this plasma discharge) and was not enough to trigger such ECH power injection. Heavier metal penetrated at 178.4 s. accompanied by a sudden increase in the electron density and a reduction of the electron temperature. Then the ECH power was simultaneously injected as shown in Fig.1; the electron temperature was increased to 2.1keV and the electron density was decreased by  $0.2\times10^{19}\text{m}^{-3}$ , as often observed in the high electron temperature plasma discharge [2, 3].

The effect of the ECH injection was confirmed in a series of 12 plasma discharges ( $n_e\sim1\times10^{19}\text{m}^{-3}$  with  $P_{\text{ICH}}+P_{\text{ECH}}=1.4\sim1.6\text{MW}$ ). Plasma duration times of five plasma discharges without ECH camphor injection and seven ones with it are described in Table. The average duration time of the plasma discharge was 136.6s ( $T_{\text{avwo}}$ ) without the ECH power injection and 235.6s ( $T_{\text{avw}}$ ) with it as seen in Table. The standard deviations from these samples are 26.1s ( $\sigma_{\text{wo}}$ ) and 32.6s ( $\sigma_{\text{w}}$ ), respectively. In accordance with t-test of statistics,

$$U^2 = \frac{N_{\text{wo}}\sigma_{\text{wo}}^2 + N_{\text{w}}\sigma_{\text{w}}^2}{N_{\text{wo}} + N_{\text{w}} - 2}$$

$$T = \frac{T_{\text{avw}} - T_{\text{avwo}}}{\{(\frac{1}{N_{\text{wo}}} + \frac{1}{N_{\text{w}}})U^2\}^{1/2}}$$

$|T|=5.128$  is calculated as shown above. Here  $N_{\text{wo}}$  and  $N_{\text{w}}$  are the number of plasma discharges without and with ECH camphor injection, respectively. The critical value  $a$  is deduced to be  $\alpha<0.001$  from  $t_{10}(\alpha)=5.128$ . The possibility that ECH injection was effective was deduced to be more than 99%. However, when the second impurity penetration occurred, further elongation has not been achieved so far even though more ECH power has been injected. It is thought that at the second penetration a larger heavy impurity might be penetrating, and the ECH power of 300kW for 0.6 s. is not enough to restore the plasma. An injection of ICRF heating power up to 1MW for 1~2 sec

using one antenna among 4 antennas is planned as a camphol injection in the next ( $10^{\text{th}}$ ) experimental campaign.

It is now an open question why sparking occurs between the divertor tiles, but there seems to be an intimate relation between frequent sparking and an excitation of RF electric field in the toroidal direction. A transverse electromagnetic wave (TEM) can travel in the presence of the plasma in the LHD vacuum. A phase control and employing a slightly different frequency between antenna sets will be tried in to reduce the the standing wave the next experimental campaign.

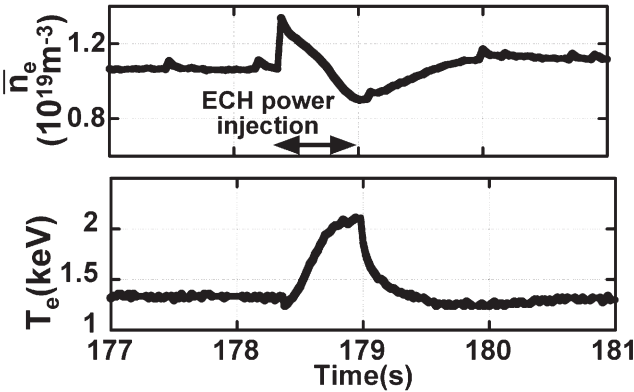


Fig.1 Time evolutions of  $n_e$  and  $T_e$  before and after ECH power injection at 178.4sec.

	without ECH (s)	with ECH (s)
1	103	190
2	175	185
3	135	230
4	155	270
5	115	263
6		261
7		250
average(s)	136.6	235.6
standard deviation from samples(s)	26.1	32.6

Table Experimental data from 12 discharges

References  
[1] R.Kumazawa et al., Nucl. Fusion **46**(2006) S13  
[2] H.Idei et al., Fusion Engineering and Design **26**(1995) 167  
[3] K.Tanaka et al., Nucl. Fusion **46**(2006) 110



## §47. Optimization of Magnetic Configuration and Polarization for Long Pulse Plasma Sustainment with ECH

Yoshimura, Y., Kubo, S., Shimozuma, T., Igami, H., Kobayashi, S., Ito, S., Mizuno, Y., Takita, Y., Notake, T., Mutoh, T., Inagaki, S., Sakakibara, S., Tanaka, K., Tokuzawa, T., Narihara, K.

In the 8th LHD experimental campaign in F. Y. 2004, a long pulse discharge with the plasma duration of 3900 seconds by 110 kW ECH, and a discharge of 1905 seconds by ICH, ECH and NBI were performed. In those long pulse discharges, ECH power injection was done with waveguide antenna, which was specially installed for long pulse ECH operation from a view point of unnecessary of water cooling inside the LHD vacuum vessel.

Before the 3900 seconds discharge, an optimization of magnetic axis setting was performed by scanning the magnetic axis with the second harmonic resonance condition, because the preciseness of the mechanical direction of the waveguide had some ambiguity. From the variation of plasma stored energy, the magnetic axis of 3.6 m and the magnetic field setting of 1.48 T were determined. With the magnetic field setting, the on-axis magnetic field on a poloidal cross section where the antenna is installed becomes 1.5 T, that is, the second harmonic field for the frequency 84 GHz of the CW gyrotron. The wave polarization setting was selected from only two values, + and - 45 degrees because those values have been used for O- and X-mode injections in other transmission lines. The polarization setting of -45 degrees was selected from a comparison of discharges. For the 1905 seconds discharge, the polarization was set at +45 degrees because the magnetic field of the discharge was 2.75 T, that is, nearly fundamental resonance field.

For the better performance in the future long pulse discharges, the optimized polarization setting was more precisely searched by scanning as -60, -45, -30, 0, 30, 45, 60 and 90 degrees.

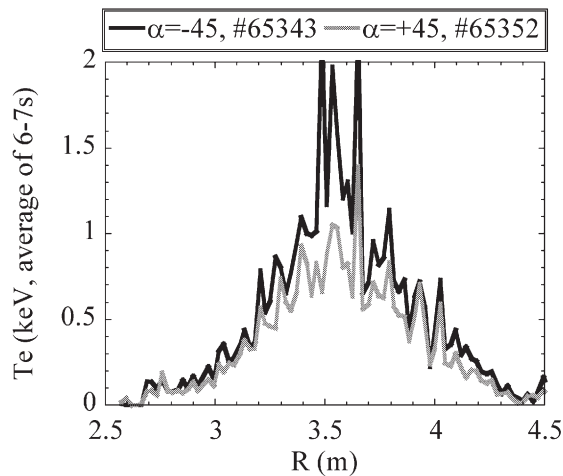


Fig. 1. Electron temperature distributions in the discharges with the polarization settings of + and - 45 degrees.

As seen from the  $T_e$  distributions in Fig. 1, it was confirmed that -45 degrees was the best and the +45 degrees was the worst. The  $T_e$  distributions with the other settings distributed between them.

The magnetic field setting was varied as 1.44, 1.48 and 1.52 T with the magnetic axis fixed at 3.6 m. The variation of 0.04 T corresponds to the shift of the resonant magnetic field layer of about 6 cm, while the beam waist size is 7 cm at the equatorial plane. It was also confirmed that the magnetic field setting of 1.48 T was the best.

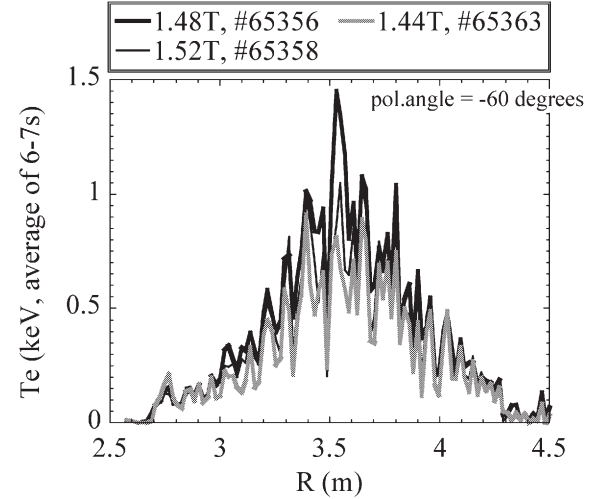


Fig. 2. Electron temperature distributions in the discharges with the magnetic axis settings of 1.44, 1.48 and 1.52 T.

The optimized polarization setting for the ICH discharges was also investigated. The discharges with 2.75 T, 3.75 m were sustained only with ECH power injected 9.5 seconds from the waveguide antenna, scanning the polarization setting in a shot by shot manner. As seen in Fig. 3, the plasmas were sustained till the end of the power injection only with the polarization setting around +45 degrees. With other values, the plasmas could not be fully sustained.

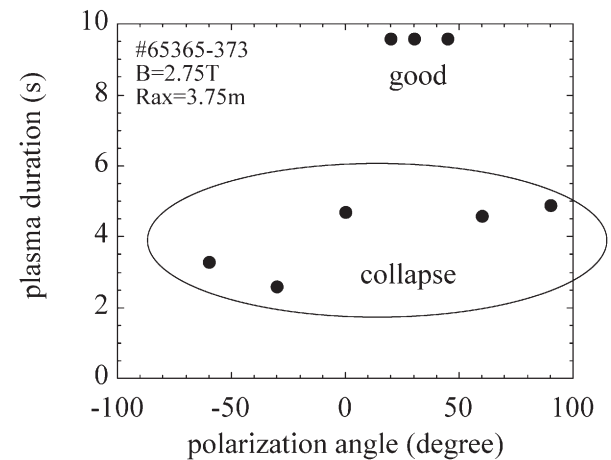


Fig. 3. Plasma duration time as a function of the polarization setting angle.

From those confirmations, the optimized parameters for the future long pulse discharges with ECH and with ICH supported by ECH were determined.

## §48. Density Limit Study in LHD

Miyazawa, J., Sakamoto, R., the High-Density Group

So-called Sudo density limit scaling has been often used to discuss the operational density limit of helical plasmas. The Sudo scaling is defined by;  $n_c^{\text{Sudo}} (10^{20} \text{ m}^{-3}) = 0.25 (PB/(a^2 R))^{0.5}$ , where  $P$  (MW),  $B$  (T),  $a$  (m) and  $R$  (m) are the total heating power ( $P_{\text{tot}}$ ), the magnetic field strength, the minor radius and the major radius, respectively [1]. It should be noted that strongly peaked density profiles are not in the scope of the Sudo scaling. This scaling is based on the power balance between the heating power and the radiation loss that is proportional to  $n_e^2$ . In LHD, radiative collapse is triggered even at a small radiation loss fraction of  $\sim 30\%$ . On the other hand, sustainable complete detachment, named *the Serpens mode*, has been found in LHD [2], and the radiation loss fraction ranges from 30 to 100 % at complete detachment. It is therefore difficult to determine a threshold radiation loss fraction that triggers radiative collapse.

Detachment in LHD proceeds as described below. When the density is increased by hydrogen gas puffing, the hot plasma boundary,  $\rho_{100\text{eV}}$ , given as the normalized minor radius where  $T_e = 100 \pm 50$  eV, gradually decreases. When  $\rho_{100\text{eV}}$  decreases to 1, *complete detachment* takes place and the ion saturation current begins to decrease at all the measured divertor tiles. In contrast to tokamaks, but similar to W7-AS, there are no clear indications of *high recycling* prior to detachment. As the edge  $T_e$  decreases, hydrogen volume recombination takes place and the ionization front moves from the ergodic region to the closed-flux-surface (CFS) region. The effective fueling efficiency for neutral particles is improved at complete detachment. This is due to the better particle confinement in the CFS region, where particle diffusion perpendicular to the flux surfaces is important, compared with that in the ergodic region, where parallel particle transport through the open field lines dominates. To avoid an excess of density increase that leads to radiative collapse, it is necessary to decrease the fueling rate. Therefore, the density that results in  $\rho_{100\text{eV}} = 1$  corresponds to the maximum density achievable under the attached condition. It is possible to increase the density further beyond this critical density, under the completely detached condition. The Serpens mode begins when  $\rho_{100\text{eV}}$  decreases to  $\sim 0.9$ .

Shaded regions in Fig. 1 denote the density regimes for complete detachment, where  $\langle n_e \rangle$  and the edge electron density,  $n_e^{100\text{eV}}$ , defined by the density at  $\rho_{100\text{eV}}$ , are plotted against  $P_{\text{tot}}$ . High-density reaching  $2.2 n_c^{\text{Sudo}}$  is sustainable in the Serpens mode plasmas. Higher densities as high as  $3.5 n_c^{\text{Sudo}}$  are achieved by applying pellet injection, although these are transient. Even in these pellet-fueled plasmas,  $n_e^{100\text{eV}}$  are similar to those obtained in the gas-fueled plasmas at the threshold for complete detachment ( $\rho_{100\text{eV}} \sim 1.0$ ). The high  $\langle n_e \rangle$  achieved in pellet-fueled plasmas are resultant of the strongly peaked density profiles (see Fig. 2). The ratio of  $\langle n_e \rangle / n_c^{\text{Sudo}}$

linearly increases with a peaking factor defined by  $\langle n_e \rangle / n_e^{100\text{eV}}$ , which reaches  $\sim 4$  in pellet-fueled plasmas. In detached plasmas,  $n_e^{100\text{eV}}$  are larger than in the attached plasmas, although the maximum peaking factor achieved so far is less than 2.

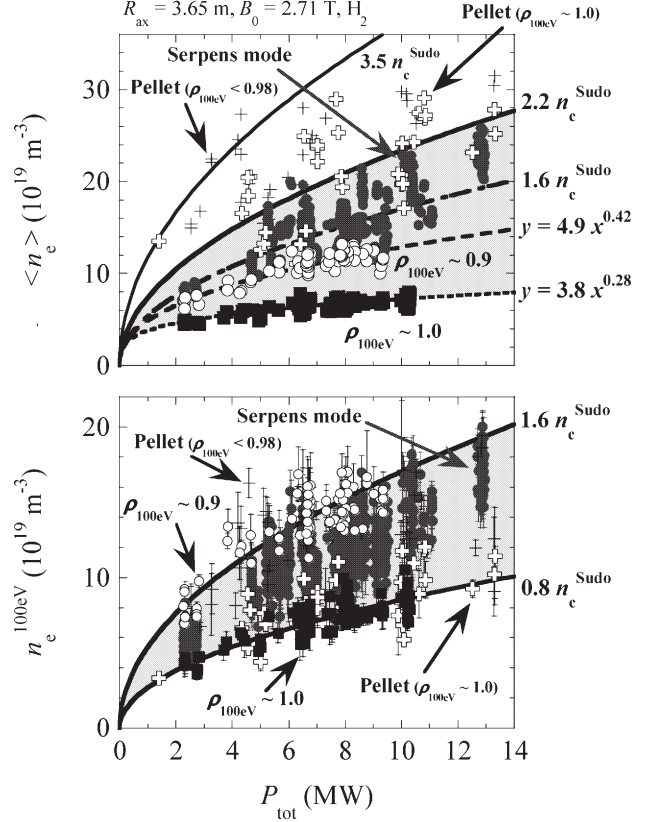


Fig. 1.  $P_{\text{tot}}$  v.s. (a)  $\langle n_e \rangle$  and (b)  $n_e^{100\text{eV}}$ .

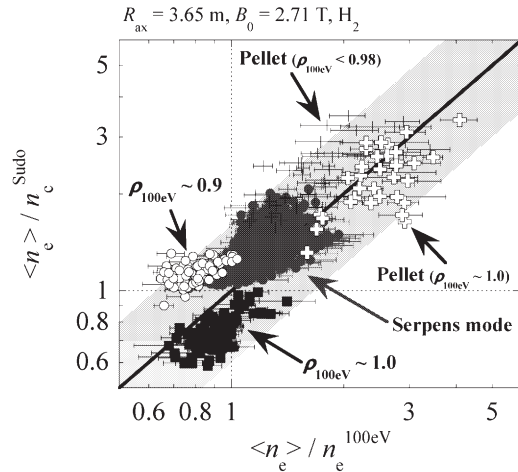


Fig. 2.  $\langle n_e \rangle / n_c^{\text{Sudo}}$  v.s.  $\langle n_e \rangle / n_e^{100\text{eV}}$ .

## References

- [1] S. Sudo *et al.*, Nucl. Fusion **30**, 11 (1990).
- [2] J. Miyazawa *et al.*, Nucl. Fusion **46**, 536 (2006).

## §49. The Highest Density Achieved in LHD

Miyazawa, J., Sakamoto, R., the High-Density Group

The highest central density in helical plasmas of  $5 \times 10^{20} \text{ m}^{-3}$  has been demonstrated on LHD. The volume-averaged electron density,  $\langle n_e \rangle$ , reaches  $3 \times 10^{20} \text{ m}^{-3}$ , in spite of the small absorbed power density in LHD ( $< 0.5 \text{ MW/m}^3$ ) compared to W7-AS ( $\leq 4 \text{ MW/m}^3$ ), where  $\langle n_e \rangle \sim 4 \times 10^{20} \text{ m}^{-3}$  was attained with divertor detachment.

Waveforms in the highest  $\langle n_e \rangle$  discharge are depicted in Fig. 1. This is obtained at an “inward-shifted” configuration, where the magnetic axis ( $R_{\text{ax}}$ ) of 3.65 m and the magnetic field strength on the magnetic axis ( $B_0$ ) of 2.71 T. Eight hydrogen ice pellets are injected from  $t = 0.7$  sec to 1 sec. Both the line-averaged electron density measured by  $\text{CO}_2$  laser interferometer and  $\langle n_e \rangle$  measured by Thomson scattering reach  $3 \times 10^{20} \text{ m}^{-3}$ . The density signals of Thomson scattering are calibrated to match the  $\langle n_e \rangle$  with that estimated from Abel inversion data of FIR interferometer signals at the density regime of less than  $1 \times 10^{20} \text{ m}^{-3}$ . Note that the absolute sensitivity of each channel is not yet calibrated.

The highest value of the central electron density ( $n_{e0}$ ) of  $5 \times 10^{20} \text{ m}^{-3}$  is obtained at an outward-shifted configuration of  $R_{\text{ax}} = 3.75 \text{ m}$  and  $B_0 = 2.64 \text{ T}$ , as is shown in Figs. 3 and 4 (a). Hydrogen ice pellet injection is also

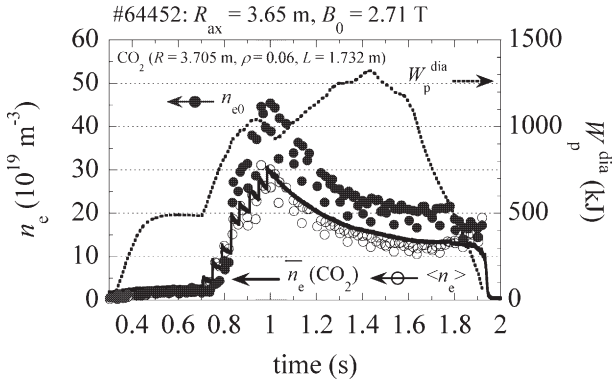


Fig. 1. Waveforms in the highest  $\langle n_e \rangle$  discharge.

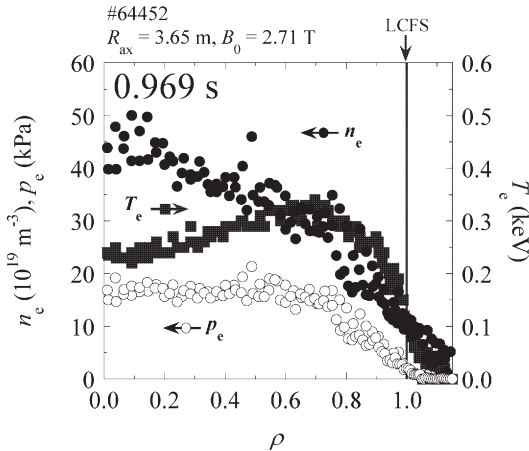


Fig. 2. Radial profiles in the highest  $\langle n_e \rangle$  discharge.

used in this case. After the pellet injection, the electron density decreases and the electron temperature increases vice versa (Fig. 4 (b)). The total stored energy increases in this phase, as is known as the “reheat” (Fig. 4 (c)). In this case, the Super-Dense-Core (SDC) is formed after  $t \sim 1.2$  sec. The central plasma pressure reaches 100 kPa ( $T_i = T_e$  and  $n_i = n_e$  are assumed). A large Shafranov shift from 3.75 m to 4 m is observed at the SDC phase. Although the SDC has been studied in the Local Island Divertor configuration, where  $n_{e0} \sim 5 \times 10^{20} \text{ m}^{-3}$  is also attained, it is possible to form the SDC in the usual helical divertor configuration.

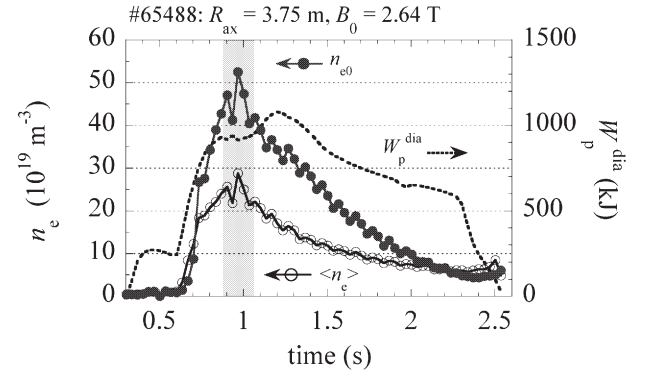


Fig. 3. Waveforms in the highest  $n_{e0}$  discharge.

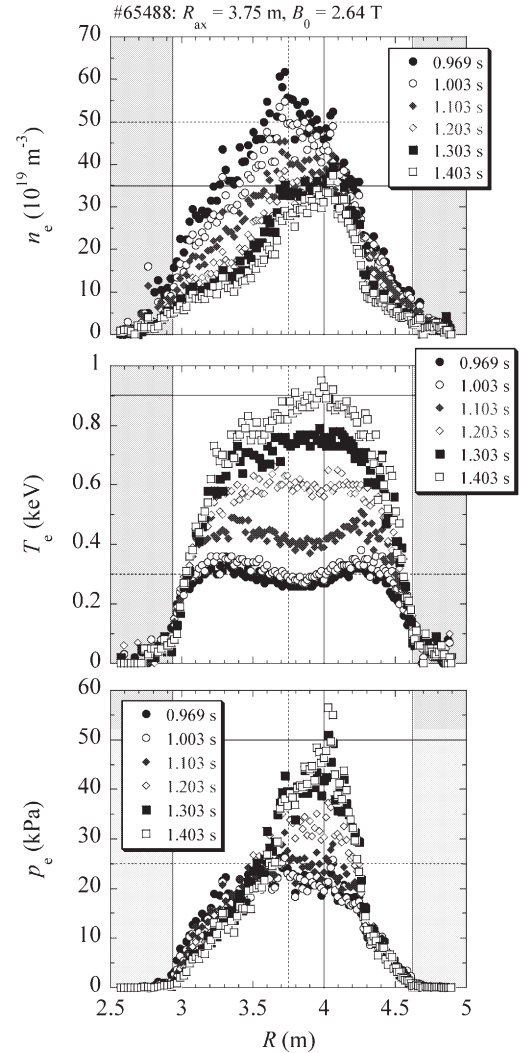


Fig. 4. Radial profiles in the highest  $n_{e0}$  discharge.

## §50. Divertor Transport Study of LHD

Kobayashi, M., Morisaki, T., Masuzaki, S., Shoji, M., Miyazawa, J., Ohya, N., Komori, A., Motojima, O., the LHD Experimental Group (NIFS), Feng, Y., Sardei, F., Igitkhanov, Y. (MPI, IPP), Reiter, D. (FZJ, IPP)

The divertor transport characteristics of LHD has been analyzed using the 3D edge transport codes, EMC3-EIRENE [1][2], and a 1D model. In LHD, the experiment shows that the plasma temperature drop from the LCFS to the divertor is more than an order of magnitude [3], and the SOL collisionality,

$$\nu_{SOL}^* = L_C / \lambda_{ee}, \quad (1)$$

is estimated at  $\sim 100$ , where  $L_C$  and  $\lambda_{ee}$  are the connection length of magnetic field lines and mean free path of electron self collision, respectively. Nevertheless, there is no evidence of high recycling regime, i.e.  $n_d \propto n_u^3, T_d \propto n_u^{-2}$ , here the subscript d and u denote downstream (divertor) and upstream values. But the dependence is rather modest, as shown in Fig.1 where electron temperature and density at the divertor and the LCFS are plotted as a function of line averaged density, together with the results of the 3D modelling. One sees that the code results are in a reasonable agreement with the experimental data.

In order to explain the modest change of  $T_d$  and  $n_d$  against the line averaged density, we introduce a cross field transport effect into the standard two point model [4]. The ratio of perpendicular and parallel transport scale is defined as,

$$\beta = \Delta x / L_C, \quad (2)$$

where  $\Delta x$  is a thickness of ergodic layer, several centimeters. In the helical divertor configuration,  $\beta \sim 10^{-4}$ . In the ergodic layer, the energy transport equation could be written as,

$$\beta \frac{d}{dx} \left( -\kappa_0 T^{5/2} \beta \frac{dT}{dx} \right) + \frac{d}{dx} \left( -\chi_{\perp} n \frac{dT}{dx} \right) = 0, \quad (3)$$

where  $x$  is a radial coordinate and it is assumed that  $T_e = T_i = T$ . The first term on the left hand side represents a projection of parallel transport onto  $x$ . The momentum equation is given by,

$$\beta \frac{d}{dx} \left( mn V_{||}^2 + p \right) = -D_{\perp} \frac{mn \Delta V_{||}}{\Delta^2}, \quad (4)$$

where the right hand side is accounting for a momentum loss in perpendicular direction. Especially, in the ergodic layer, this term becomes important because of friction between counter flows which are induced by the ergodic field lines.  $\Delta V_{||}$  and  $\Delta$  are thus the relative velocity of two neighboring flows and the characteristic distance between the flow channels. The boundary condition at the downstream is given by Bohm condition,

$$q_{||} = \gamma n_d T_d c_{sd}, \quad V_{||} = c_{sd} \quad (5)$$

with  $c_{sd}$  being a sound speed at the downstream. The equations (3)-(5) are solved to give the solutions,

$$T_u^{7/2} = T_d^{7/2} + \frac{7 q_{||} L_C}{2 \kappa_0} - \frac{7 \chi_{\perp} n_u}{2 \beta^2 \kappa_0} (T_u - T_d), \quad (6)$$

$$p_u = 2 p_d (1 + f_m), \quad (7)$$

where  $f_m$  is a momentum loss factor,

$$f_m = \frac{D_{\perp}}{\beta c_{sd}} \left( \frac{1}{c_{sd} n_d} \int \frac{n \Delta V_{||}}{\Delta^2} dx \right). \quad (8)$$

When  $\beta \rightarrow \infty$ , the third term on the right hand side of eq. (6) and  $f_m$  vanish, and the model becomes the standard two-point model for tokamaks. The results of eq.(6)-(8) are plotted in Fig.2 for different  $f_m$ 's, together with the 3D results. It is found that the solution becomes closer to those of EMC3-EIRENE, indicating that the cross-field momentum loss as well as low  $\beta$  affect the transport characteristics in the ergodic layer.

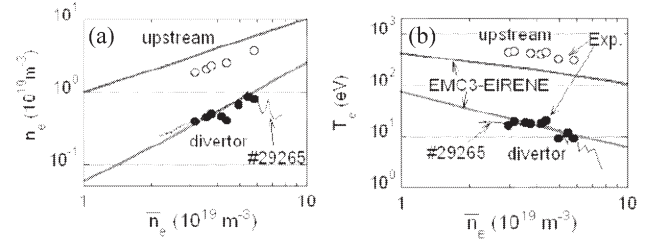


Fig.1 Plasma parameter dependence on the line averaged density, together with the 3D code results. (a) density, (b) electron temperature.

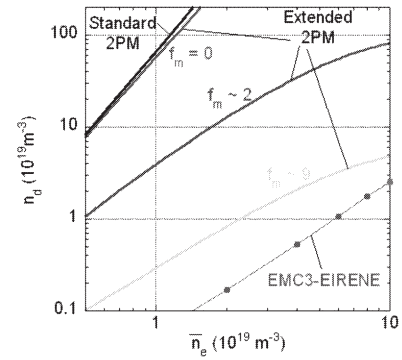


Fig. 2 Downstream density ( $n_d$ ) as a function of the line averaged density for a comparison of eq.(6)-(8) (extended two-point model) with the 3D modelling.

### References

- 1) Feng, Y. et al., Cont. Plasma Phys. **44** (2004) 57.
- 2) Reiter, D. et al., Fusion Science and Technology **47** (2005) 172.
- 3) Masuzaki, S. et al., Nucl. Fusion **42** (2002) 750.
- 4) Feng, Y. et al., 10th PET 2005, to be published in Nucl. Fusion.



## §51. Simulation of Sheet-Shaped Lithium Beam Probe Performance for Two-Dimensional Edge Plasma Measurement

Tsuchiya, H. (Graduate University for Advanced Studies), Morisaki, T., Komori, A.

The edge plasma has been considered to affect the overall energy and particle confinement in fusion test devices, since the formation of the transport barrier, excitation of turbulent fluctuation, edge localized modes, ELMs, blobs, etc. are taken place in this region. Recently it has been known that such phenomena do not always appear symmetrically in toroidal and/or poloidal directions. Thus the one-point or one-dimensional (1D) measurement is not sufficient to know the overall picture of the phenomena. The 2D diagnostics with sufficient time and spatial resolutions would be helpful. A sheet-shaped thermal lithium beam probe has been developed, and the 2D edge density profiles at the poloidal cross section were successfully obtained by one shot in LHD [1]. The density profile is reconstructed from the light emission profile due to the interaction between Li atoms and plasmas. In the reconstruction process, the conventional procedure so-called “the beam attenuation method” is often employed [2].

According to “the beam attenuation method”, the plasma density  $n_e(r)$  can be derived from the following equation.

$$n_e(r) = \frac{v_{th} I(r)}{\langle \sigma v \rangle_i \int_r^\infty I(r) dr} \quad (1)$$

where  $\langle \sigma v \rangle_i$ ,  $v_{th}$  and  $I(r)$  are the effective rate coefficient for ionization, the beam velocity and the rate of local photon emission, respectively. Since this method is based on the assumption that the density profile is in the steady state during the time concerned, there are uncertainties if it can simply be applied to fast and transient phenomena like blobs whose velocity is higher than that of the probe beam.

We simulated the 2D density profile reconstruction where a blob flies out from the confinement region to the SOL in the radial direction [3]. Referring to the reference [4], the diameter of a blob and its velocity in the radial direction were set to be  $\delta_{max} = 0.05$  m,  $V_{blob} = 5.0 \times 10^4$  m/s, respectively, using typical parameters of the LHD edge plasma. Fig.1(a) shows the assumed 2D density profile with

a blob flying radially in the SOL. Fig.1(b) are the reconstituted density profiles, assuming that the Li I light is observed by an ideal ultra fast camera with very short exposure time. The beam was injected to the plasma vertically from the bottom. The upper right corner colored red shows the confinement region whose electron density was set to be  $1 \times 10^{18} \text{ m}^{-3}$ . The wide blue region represents the SOL with uniform density of  $2 \times 10^{17} \text{ m}^{-3}$ .

Using the beam attenuation method, the blob density was reconstructed to be about  $0.6 \times 10^{18} \text{ m}^{-3}$  as shown in Fig.1(b), although it was assumed to be  $1 \times 10^{18} \text{ m}^{-3}$  as shown in Fig.1(a). This difference is caused by the fact that Eq.(1) which is originally for the steady state analysis was however applied to the transient phenomenon. In this situation no beam attenuation occurs on the down-stream side of the blob, because the beam which experienced the high density blob has not arrived there within such an extremely short period. Thus the integral term in Eq.(1) becomes large. Consequently, the reconstructed density of the blob becomes low. Because of the same mechanism, the density on the up-stream side of the blob is also reconstructed to be low.

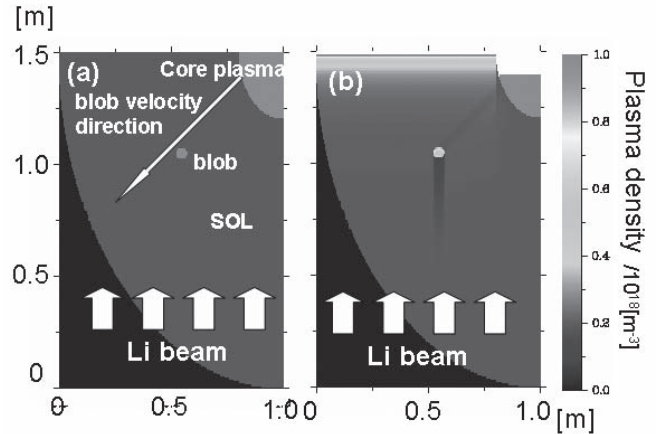


Fig.1 (a) assumed profile (b) reconstructed profile

- [1] Takahasi, Y. *et al.*, J. Plasma Fusion Res. **1**, (2006) 103.
- [2] Morisaki, T. *et al.*, Rev. Sci. Instrum **74**, (2003) 1865.
- [3] Tsuchiya, H. *et al.* (Submitted to Rev. Sci. Instrum).
- [4] S.I. Krashennnikov, Phys. Rev. Lett. **A 283**, (2001) 368.

## §52. Analyses of the Effect of a Closed Divertor Configuration on the Density Profile of the Neutral Hydrogen Molecules in the LHD Divertor

Shoji, M.

The isolation of neutral particles from the main plasma and the control of the neutral density in the plasma periphery are essential for achieving good plasma confinement and for sustaining the thermal transport barrier. The closed divertor configuration is one of promising measures to realize the above requirements.

For the detailed design of the closed divertor configuration, the behavior of neutral particles in the plasma periphery has to be investigated. For this purpose,  $H_\alpha$  intensity profiles have been monitored with a 10ch vertical detector array installed in an outer port (1-O). Recently, polarization resolved  $H_\alpha$  spectra are also measured with a spectrometer with polarization separation optics (PSO). The location and intensity of the emission along the line of sight of the detectors can be identified by the least-squares fitting [1].

Analyses of the behavior of neutral hydrogen were carried out by using the above two  $H_\alpha$  measurements and a fully three-dimensional neutral particle transport simulation code (EIRENE) [2] with including the effects of Doppler broadening, fine structure splitting of  $H_\alpha$  line by Zeeman effect, and polarization of the emission by the magnetic field. It proposed that the closed divertor configuration in the inboard side of the torus is efficient and realistic for particle control in the LHD plasma periphery.

For evaluating the effect of the closed divertor configuration, a detailed three-dimensional grid model for simulating the LHD vacuum vessel and the baffle plates installed in inboard side of the torus is assembled for the neutral particle transport simulation. The geometry of the model is limited to one toroidal pitch angle ( $\phi=36^\circ$ ) for the limitation of the computational resources. For performing full toroidal simulations, two toroidal ends of the grid surface ( $\phi=0^\circ$  and  $36^\circ$ ) are specially treated as toroidally periodic surfaces. The strike points are calculated by magnetic field line traces from the LCFS. The toroidal and poloidal distribution of hydrogen neutrals emitted from divertor plates is determined from that of the strike points. The component of the neutrals (reflected hydrogen atoms or released molecules) is derived from the database of the TRIM code. Non-reflected neutrals are treated to be the released hydrogen molecules which have a kinetic energy corresponding to the room temperature (300K).

Figure 1 shows the poloidal cross-sections of the calculated density profile of neutral hydrogen molecules in the plasma periphery in the case of the magnetic configuration ( $R_{ax}=3.60m$ ) at the four toroidal angles ( $\phi=0^\circ, 10^\circ, 18^\circ, 26^\circ$ ). The simulation clearly shows that the spontaneous formation of the high density neutral hydrogen molecules in inboard side of the torus. The reason of the

formation of the high density can be attributed to the three-dimensionally complicated shape of the vacuum vessel in which the inboard side locates between the two helical coils.

Figure 2 gives the poloidal cross-sections of the calculated density profile of neutral hydrogen molecules for the closed divertor (baffle plates) installed in inboard side of the torus at the four toroidal angles. The simulation predicts the formation of the higher density of neutral hydrogen molecules in the inboard side of the torus. The enhancement factor of the density of neutral hydrogen molecules in the closed divertor configuration is roughly estimated to be about factor 3. It quantitatively shows that the closed divertor configuration is effective for isolation of neutral particles from the main plasma and efficient particle control in the LHD plasma periphery.

### Reference

- 1) Iwamae, A. et al.: Phys. Plasmas 12 (2005) 042501.
- 2) Reiter, D. et al.: J. Nucl. Mater. 196-198 (1992) 1059.

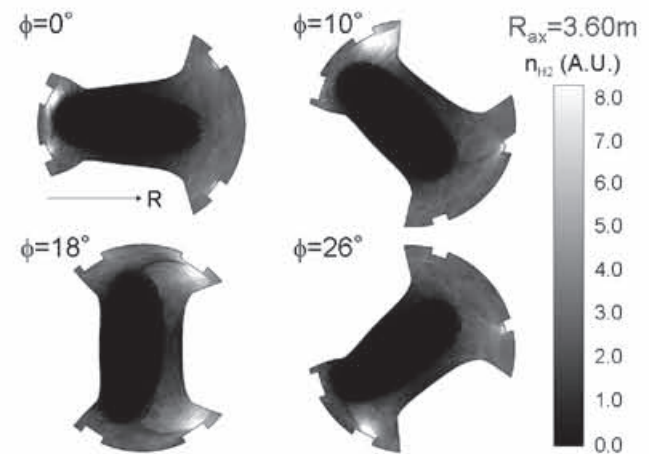


Fig. 1. Four poloidal cross-sections of the calculated density profile of neutral hydrogen molecules in the magnetic configuration ( $R_{ax}=3.60m$ ).

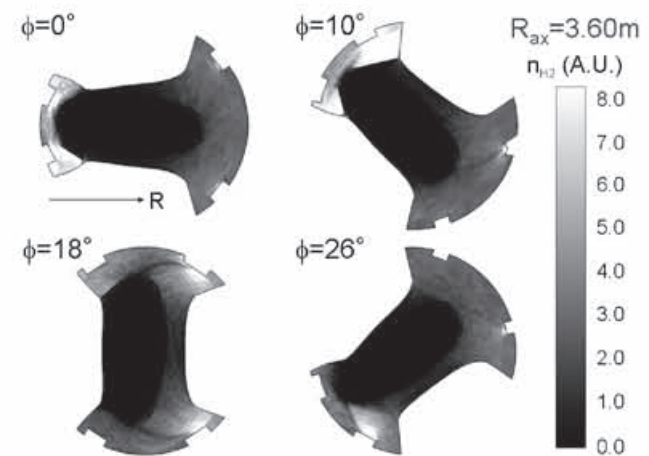


Fig. 2. Four poloidal cross-sections of the calculated density profile of neutral hydrogen molecules in the magnetic configuration ( $R_{ax}=3.60m$ ) for the closed divertor configuration in inboard side of the torus.

### §53. Analyses of the Polarization Resolved H-alpha Spectra in Various Magnetic Configurations in LHD

Shoji, M.,  
Iwamae, A., Sakaue, A., Atake, M. (Dept. Eng. Phy.  
Mech. Graduate School of Eng., Kyoto Univ.)

The analyses of the behavior of neutral particles in the divertor region and the plasma periphery are important issues for efficient particle control and divertor detachment. The control of the neutral density in the plasma periphery is essential for good plasma confinement and for sustaining the thermal transport barrier.

For measurement of the behavior of neutral particles,  $H_\alpha$  intensity profiles have been monitored with a 10ch vertical detector array installed in an outer port (1-O). Recently, polarization resolved  $H_\alpha$  spectra are also measured with a spectrometer with polarization separation optics (PSO). The location and intensity of the emission along the line of sight of the detectors can be identified by the least-squares fitting with abroad Gaussian profile [1].

The polarization resolved spectra are analyzed by a fully three-dimensional neutral particle transport simulation code (EIRENE) with newly including the following three effects:

1. Doppler broadening due to the velocity of neutral hydrogen atoms and molecules,
2. fine structure splitting of the  $H_\alpha$  line spectrum by Zeeman effect,
3. polarization of  $H_\alpha$  emission by the effect of the magnetic field.

Polarization resolved spectra (e-ray and o-ray) are calculated by integrating calculated  $H_\alpha$  spectra along the line of sights with considering the instrumental function of the detectors and the polarization angle of the PSOs.

The strike points are calculated by magnetic field line traces from the LCFS. The distribution of released neutral particles (hydrogen atoms and molecules) is determined

basing on that of the strike points. The simulation predicts that the density of neutral hydrogen molecules is relatively high in the inboard side of the torus in three magnetic configurations ( $R_{ax}=3.50, 3.65, 3.75\text{m}$ ). The reason for formation of the high density is attributed to the complicated shape of the vacuum vessel.

Figure 1 illustrates the measurements and calculations of the vertical profile of the  $H_\alpha$  intensity in the all magnetic configurations. The calculations are obtained by summing the  $H_\alpha$  emission along horizontal lines on the poloidal plane of the detectors. It shows quite agreement with the measurements, indicating that the calculated density profiles of neutral particles are reasonable.

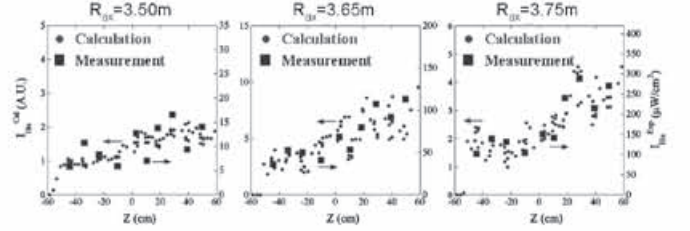


Fig. 1. The measurements and calculations of the vertical profile of the  $H_\alpha$  intensity in the three magnetic configurations ( $R_{ax}=3.50, 3.65, 3.75\text{m}$ ).

Figure 2 gives the calculations and measurements of the polarization resolved  $H_\alpha$  spectra in the three magnetic configurations, which shows no significant disagreement between them. The measured narrow peak of the o-ray ( $\lambda=656.24\text{nm}$ ) for  $R_{ax}=3.50\text{m}$  is likely to be reflected light from the vacuum vessel because of the unbalanced intensity of the two polarized spectra (e-ray and o-ray).

The simulation can reproduce the measurements of the vertical intensity profile and the polarization resolved spectra, which verify the high neutral density in the inboard side of the torus in all the magnetic configurations. It strongly suggests that the closed divertor configuration in the inboard side of the torus is efficient and realistic for particle control in LHD plasmas.

#### Reference

- 1) Iwamae, A. et al.: Phys. Plasmas 12 (2005) 042501.

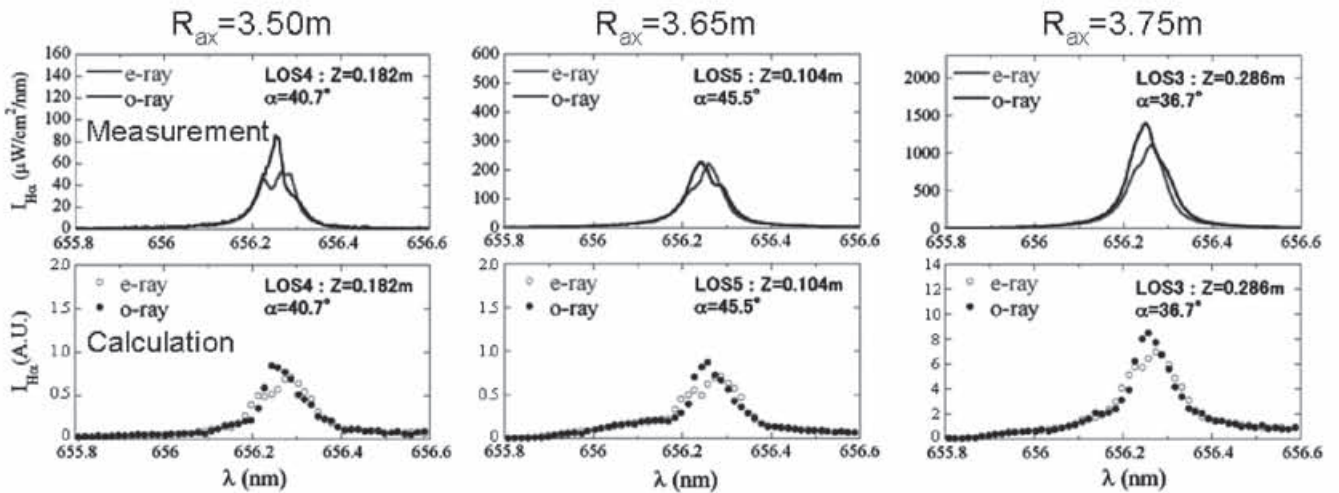


Fig. 2. The measurements and calculations of the polarization resolved  $H_\alpha$  spectra (e-ray and o-ray) in the magnetic configurations ( $R_{ax}=3.50, 3.65, 3.75\text{m}$ ), which are the results of a typical detector channel in each magnetic configurations.



## §54. Development of Pellet Ablation Model Considering the Effect of the Plasma Shielding

Hoshino, M. (Nagoya Univ.),  
Sakamoto, R., Yamada, H., Kumazawa, R., Watari, T.

For a future fusion reactor, an establishment of fueling scenario is prerequisite to attain and maintain an appropriate fusion gain. Gas puffing is not expected to fuel to the core region of hot plasmas because of a shallow neutral penetration due to a hot and thick scrape-off layer. Injection of cryogenic solid pellets has the advantage of deeper penetration and higher fueling efficiency than gas puffing since pellets ablate in a plasma and provide the particle directly. It is necessary for prediction of fueling performance to clarify physical mechanisms in two stages, i.e., the ablation process of pellets and the subsequent drift motion of the ablated plasmoid. The former has been generally interpreted by the neutral gas shielding (NGS) model [1,2] and the latter is often discussed by the  $E \times B$  drift model [3]. These theoretical models should be assessed and improved by comparing with experimental results and other models.

In LHD, the pellet-fueled experiments have been performed by two pellet injectors (an in-situ pipe-gun pellet injector and a repetitive pellet injector) to demonstrate high fueling efficiency and capability to control the electron density. Pellet penetration depth reflecting the ablation process in plasmas has been studied, which gives an initial condition of pellet fueling for a further study. The penetration depth predicted by the NGS model (ABLATE code [4]) considering not only thermal electrons but also fast ions produced by NBI heating accounts for the measured one in LHD, however there is a slight disagreement in the region of shallow penetration [5]. The neutral gas and plasma shielding (NGPS) model [6] is newly applied to solve this problem. This model takes into account **1**) the shielding effect due to the neutral cloud and plasmoid, **2**) the geometrical effect of incident particles (thermal electrons, ions and fast ions), **3**) the incident heat flux estimated by the cut-off energy and the energy distribution function and **4**) the ablation rate determined by the heat flux and the line integrated density of targets. A new code employing these items has been developed. In the initial calculation, the parameters of neutral cloud and plasmoid are assumed : the cut-off energy  $E_{C,e} = 1.4 \times T_{e\infty}$ , the neutral cloud radius  $r_{\text{cloud}} = 2 \times r_{\text{pel}}$ , the plasmoid radius, length and temperature  $T_0 = 1.0$  eV. Also, input parameters for hot plasmas in LHD are used as below; linear electron temperature profiles (6 types of  $T_e = T_i$  where  $T_{e0} = 1.0$ -3.5 keV), flat electron density profile ( $n_e = n_i = 2.0 \times 10^{19} \text{ m}^{-3}$ ) and linear fast-ion density profile ( $n_0 = 2.0 \times 10^{18} \text{ m}^{-3}$ ).

First of all, the penetration depth of the ABLATE code as the NGS model (Milora-Foster model [1] and Parks-Turnbull model [2]) is compared with that of the new

code as the NGPS model (only the effect of the neutral gas shielding is considered and the plasma shielding is ignored.) as shown in Fig. 1. The part of the NGS model on the new code agrees with the result of two models on the ABLATE code, therefore the neutral gas shielding model can be reproduced by this new code. Next, the effect of the plasma shielding is calculated by the NGPS model (see Fig. 2), the results from the model considering only the effect of thermal electrons on pellet ablation are similar for the NGS and NGPS models. However, the difference between these two models exists when the effect of fast ions on the ablation is included. The result shows that pellets deeply penetrate due to the effect of the plasma shielding for fast ions. The comparison of an observed plasmoid with the new NGPS model is underway.

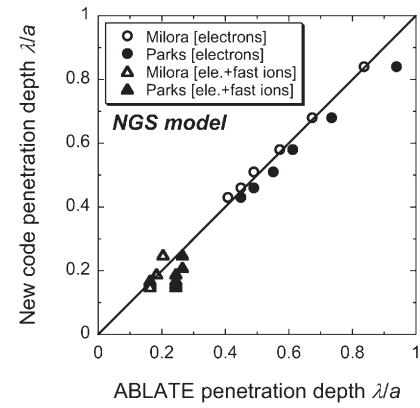


Fig. 1 Penetration depth of the ABLATE code is compared with the that of the new code for the part of the NGS model, (magnetic axis ;  $R_{ax} = 3.6$  m, minor radius ;  $a = 1.0$  m, plasma ellipticity ;  $\kappa = 0.47$ , magnetic field ;  $B_t = 3$  T, beam energy ;  $E_{\text{NBI}} = 180$  keV, pellet mass ;  $m_{\text{pel}} = 4.43 \times 10^{20}$  atoms and pellet velocity ;  $v_{\text{pel}} = 600$  m/s).

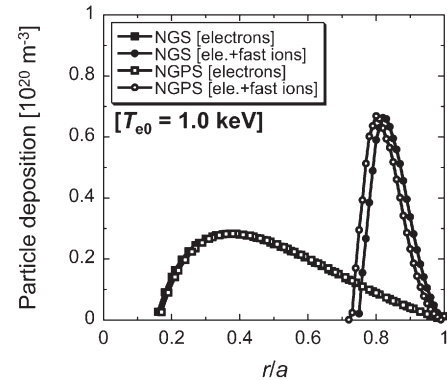


Fig. 2 Ablation rate profile of the NGS and NGPS model on the condition of Fig. 1 ( $T_{e0} = 1$  keV).

### Reference

- [1] Milora, S.L., et al., IEEE Trans. Plasma Sci. **PS-6**, (1978) 578.
- [2] Parks, P.B., et al., Phys. Fluids **21**, (1978) 1735.
- [3] Rozhansky, V., et al., Plasma Phys. Control. Fusion **37**, (1995) 399.
- [4] Nakamura, Y., et al., Nucl. Fusion **26**, (1986) 907.
- [5] Hoshino, M., et al., Plasma Fusion Res. **1**, (2006) 033.
- [6] Pégourié, B., et al., Plasma Phys. Control. Fusion **47**, (2005) 17.



## §55. Application of Tomographic Imaging to Photodiode Arrays in LHD

Liu, Y., Tamura, N., Peterson, B.J. (NIFS),  
Iwama, N. (Daido Institute of Technology)

To improve the understanding of radiative processes such as radiation collapse, transport of heavy trace impurities injected into the plasma, a fast AXUVD (Silicon absolute extreme ultraviolet diode) has been applied to supplement the standard foil bolometer diagnostic for radiated power measurements on the Large Helical Device (LHD).<sup>1</sup>

AXUVD allows measurements on time scales as short as  $10^{-4}$ s with continuous sensitivity from the near infrared into the soft x rays. Using multiple AXUVD emission viewing chords through the plasma, a spatial resolution of about 5cm can be obtained over a rectangular region of about 3 by 3m, providing a means for following the formation and subsequent evolution of a radiation structure in plasma in two dimensions. Several tomographic techniques have been used to reconstruct the radiation profile. A number of experimental situation have been explored in a detailed way from the AXUVD imaging system. Results are presented of the fast radiation process during impurity injection and of the highly localized radiation loss in the self-sustained detachment regime.

To take full advantage of the available information in our limited number of line integrated measurements, the local radiation emissivity is obtained by inverting the measured brightnesses with linear (Tikhonov-Phillips) or nonlinear (maximum entropy) regularisation methods which are more flexible than the hybrid method we used before.<sup>2</sup> The most important features of these improved methods are the capability of reconstructing radiation distributions without any symmetry assumptions, built-in smoothing, and useful reconstructions with relatively few detectors.

The plasma radiation distributions in a variety of discharge conditions have been visually characterized. Figure 2 shows a rotating radiation structure observed in a discharge of self-sustained detachment. The tomography method allows us to investigate in detail the temporal and spatial evolution of the rotating radiated belt, providing

quantitative information to the studies of the mechanism of the formation of a self-sustained detachment regime.

2-D tomography techniques applied to the semi-tangential cross-section data showed that the algorithms are powerful enough to reconstruct complicated asymmetric emissivity distributions. They are used in the examination of impurity emission images during TESPEL injection and used to study the radiation distribution during a self-sustained detachment regime on LHD.

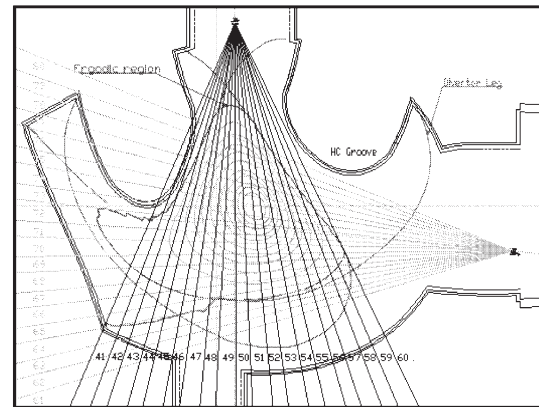


Fig. 1. Layout of the lines of sight of the AXUVD tomography system on LHD.

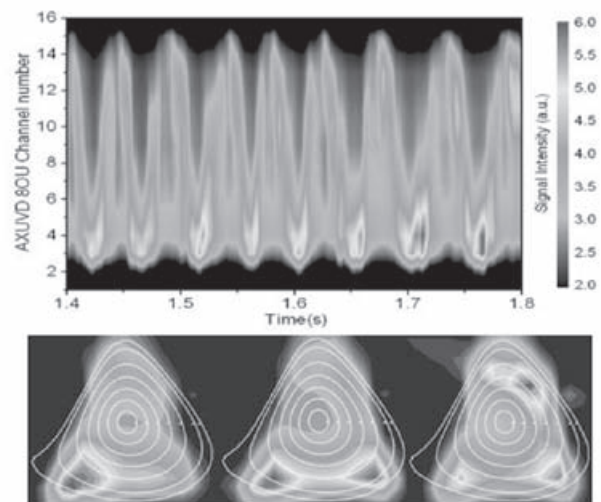


Fig.2 Reconstructed radiation distribution at three time slices ( $t_a=1.584s$ ,  $t_b=1.600s$ ,  $t_c=1.608s$ ), the upper contour shows the time evolution of AXUV signals during self-sustained detachment.

### References

- 1) B.J. Peterson et al., Plasma. Phys. Controlled. Fusion. 45(2003)1167.
- 2) Y. Liu et al., Rev. Sci. Instrum. 74 (2003) 2312.

## §56. Imaging of Radiation from TESPEL Injected into a Magnetic Island in LHD

Peterson, B.J., Tamura, N., Liu, Y. (NIFS)

Confinement and transport of impurities in plasma is an important topic for reducing radiative cooling and fuel dilution in a fusion reactor. Magnetic islands form and grow in magnetically confined plasmas through perturbations either external or internal to the plasma and can have a deleterious effect such as with neoclassical tearing modes in tokamaks or can be used to control the plasma such as with a Local Island Divertor in LHD. Advanced tomography techniques applied to the signals of arrays of highly sensitive photodetectors with fast time response can give information on the two-dimensional evolution of the radiation and hence of its source impurity [1]. Previous work has shown that an impurity tracer can be injected into and can be confined by a magnetic island (MI) [2]. In this article we show images of radiation from Titanium (Ti) locally deposited in an externally induced magnetic island, which provide new information on the confinement of impurities by a magnetic island.

The experiment is carried out by using TESPEL to inject a Ti tracer into an  $m/n=1/1$  MI produced by the LID coils on LHD. Care is taken to adjust the density to reduce the background radiation from the polystyrene shell of the TESPEL and to match the electron temperature profile to the MI location such that the radiation of Ti from the MI is optimized. The tracer deposition position is determined by the trajectory and speed of the TESPEL and the density and temperature profiles. The resulting radiation is measured by two 20-channel AXUVD arrays which view the same semi-tangential cross-section from upper and outer ports [3]. A method combining Tikhonov-Phillips and minimum Fisher regularization techniques is used to compute the tomographic inversion and produce two-dimensional images of the plasma radiation. The TESPEL injection was carried out with the positive and negative phases of the MI, which effectively exchanges the positions of the X-point (zero MI width) and the O-point (maximum MI width) of the MI and for the case of a small natural MI.

The results can be seen in Figures 1 to 3. In Figure 1 the Ti tracer is injected to the MI near its O-point. The peak in the radiation is localized to within the MI and disperses slowly. This indicates that the impurity is well confined for over 8 ms by the MI both radially and poloidally. In Figure 2 the case with the oppositely phased MI is shown which results in the Ti impurity being deposited near the X-point of the MI. In this case the radiation disperses radially and poloidally

within 4 ms, which indicates that the impurity is not well confined by the MI. In the case of Figure 3 the LID coils are not energized, leaving only a small natural MI. In this case the radiation is seen to disperse poloidally in one direction indicating that the impurity is rotating around the plasma. Therefore the impurity is either well confined or restricted from rotating poloidally depending on where in the MI it is deposited.

### References

- 1) Y.Liu et al., Rev. Sci. Instrum. **74** (2003) 2312.
- 2) N. Tamura, et al., J. Plasma Fusion Res. **78** (2002) 837.
- 3) B.J.Peterson et al., Plasma Phys. Contr. Fusion **45**(2003)1167.

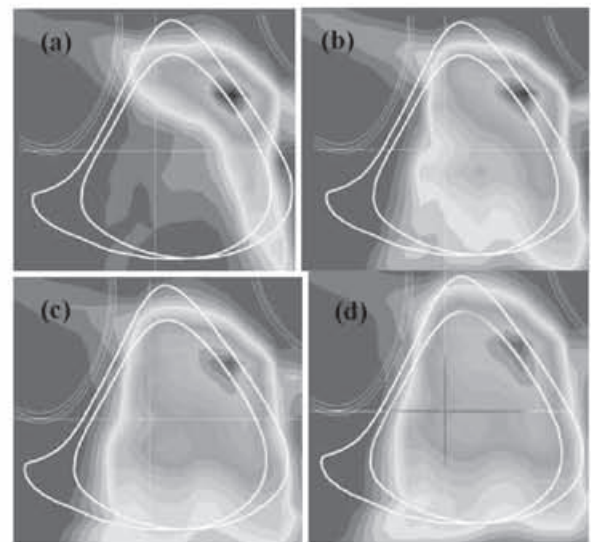


Fig. 1. Radiation intensity at (a) < 1 ms, (b) 2 ms, (c) 4 ms and (d) 8 ms after Ti TESPEL injection into the O-point of the MI (white).

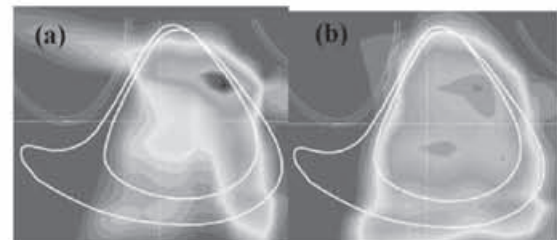


Fig. 2. Radiation intensity at (a) < 1 ms and (b) 4 ms after Ti TESPEL injection into the X-point of the MI (white).

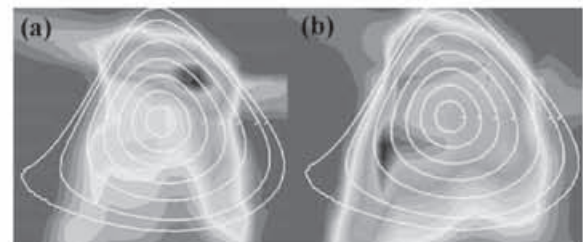


Fig. 3. Radiation intensity at (a) 1 ms and (b) 1.3 ms after Ti TESPEL injection into the natural (small) MI (flux surfaces shown in white).

## §57. Laser Calibration of the Infrared Imaging Video Bolometer

Parchamy, H., Peterson, B.J. (NIFS),  
Konoshima, S. (JAEA)

The energy loss from a magnetically confined plasma due to radiation (such as impurity line radiation) is an important measurement for describing a plasma. The infrared imaging video bolometer (IRVB) with a single large metal foil is a foil bolometer that absorbs the broad band radiation from nearly all spectral regions from the plasma.

The calibration technique of the IRVB gives confidence in the measured values of the plasma radiation that is necessary for tomographic analyses.<sup>1</sup> The foil calibration could be carried out in order to obtain local foil properties such as the thermal diffusivity,  $\kappa$ , and the product of the thermal conductivity,  $k$  and the foil thickness,  $t_f$ , of the foil.<sup>2</sup> These quantities are necessary for solving the two-dimensional heat diffusion equation of the foil which is used in the experiments. A schematic of the camera calibration and foil calibration setup is shown in Fig.1. For camera calibration (the IR camera calibration is made to determine the foil temperature from the IR camera signal) a heat lamp can be mounted behind a plate which is blackened with graphite in the same manner as the foil. Calibration of the foil was made in-situ using a HeNe laser ( $\sim 27$  mW) as a known radiation source to heat the foil from the IR camera side using a beam steerer and IR mirror. The calibration parameters are determined by comparing the measured temperature profiles and their decays from the experimental results (from laser profile on the foil) with the corresponding solution to the heat diffusion equation.

The IR thermal data from the foil during a steady state condition for the experiment can be taken by the IR camera to get the steady state data. The temperature profile is fitted to a 2-D Gaussian, to find the coefficient parameters. This is shown in Fig.2. The heat diffusion equations in two dimensions have been solved analytically by using the FEM. Then a 2nd order polynomial is fitted to the relationship between  $1/k \cdot t_f$  and the temperature rise ( $\Delta T$ ), so that the appropriate value of the  $k \cdot t_f$  could be determined from the experimental value of data.

The resulting temperature decay data is fit to the exponential equation to find  $\tau$  then a 2nd order polynomial is fitted to the relationship

between the inverse of the thermal diffusivity and the decay time and used to find the appropriate value of the thermal diffusivity ( $\kappa$ ) of the foil from the experimental value of the decay time. These results are shown in Fig. 3.

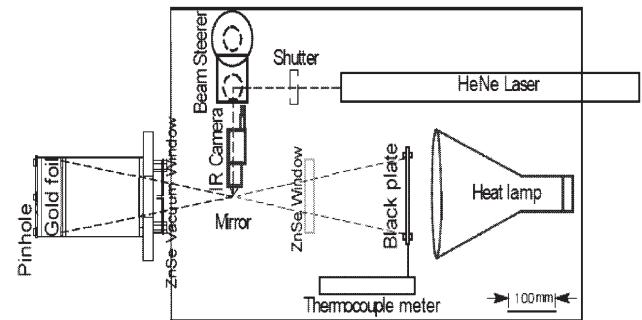


**FIG. 1.** Drawing of Calibration setup for the IRVB calibration.

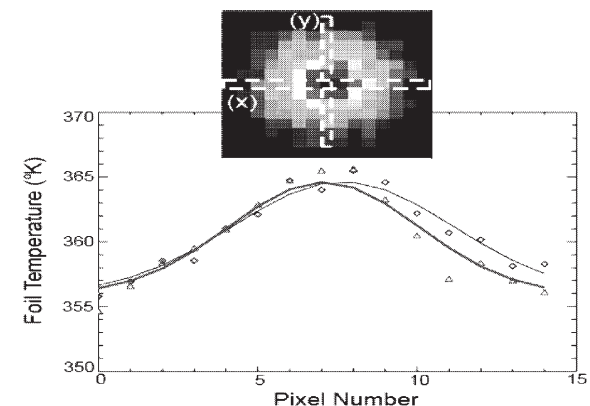


**FIG. 2.** The temperature profile is fitted to a 2-D Gaussian, thin line and diamonds symbol are from y direction of IR thermal data and Thick line and triangle horizontal symbol are from x direction.

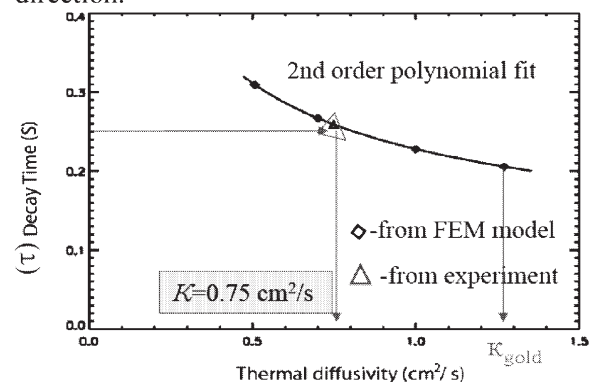


**FIG. 3.** A 2nd order polynomial is fitted (line to the  $\kappa$  and  $\tau$  data from the FEM to find the appropriate value of the thermal diffusivity of the foil (nominal value of  $\kappa_{Gold} = 1.27$  cm<sup>2</sup>/s) from the experimental value of the decay time.

### Reference

- [1]B. J. Peterson, *et al.*, Rev. Sci. Instrum. **74**, 2040 (2003).
- [2]H. Parchamy, *et al.*, Sub. to Rev. Sci. Instrum. (2006).



## §58. LHD Gauge by External Coil Currents

Watanabe, T., Akao, H.

The drastically improved plasma has been obtained through the LHD experiments started in 1998. In the recent experiments, the maximum averaged beta value  $\langle \beta_{\text{dia}} \rangle$  of 4.5% was obtained by high power NBI heating up to 12MW in the configuration with  $R_{\text{ax}} = 3.6\text{m}$  and  $B_{\text{ax}} = 0.45\text{T}$ , where  $R_{\text{ax}}$  and  $B_{\text{ax}}$  are magnetic axis position and toroidal magnetic field on the magnetic axis, respectively. Up to now, the beta collapse phenomenon has not been reported in the LHD experiment. Steady state divertor operation with high performance plasmas was demonstrated for more than 30 minutes in the LHD-ICRF heating experiments.

The LHD achieves these high-performance plasma confinement by the coordination of magnetic surface region and chaotic field line layer. Therefore, it is necessary to establish a numerical method to analyze the high beta equilibrium that doesn't assume the existence of the magnetic surface.

The magnetic field  $\mathbf{B}$  satisfies always the relation  $\nabla \cdot \mathbf{B} = 0$ . The essential freedom of  $\mathbf{B}$  is two and  $\mathbf{B}$  can be expressed by a vector potential of 2 component. In the rotating helical coordinate system  $(X, Y, \phi)$ , we can express  $\mathbf{B}$  as follows without loss of generality (LHD Gauge [1]).

$$\mathbf{B} = \nabla \times \mathbf{A}, \mathbf{A} = \begin{pmatrix} \Phi \\ 0 \\ p\{\Psi + Y\Phi\}/r \end{pmatrix}, \quad (1)$$

where  $p$  is the helical pitch ( $= 5$  for the LHD) and  $r = r_0 + X \cos p\phi - Y \sin p\phi$ . LHD equilibrium composed of magnetic surface region and chaotic field line region can be obtained numerically by the force balance equation

$$\nabla P = \mathbf{J} \times \mathbf{B}, \quad \mathbf{J} = \frac{1}{\mu_0} \nabla \times \mathbf{B}. \quad (2)$$

Profiles of  $[P(X, Y, \phi), \Phi(X, Y, \phi), \Psi(X, Y, \phi)]$  are obtained as the solution of eq.(2) under the appropriate boundary conditions. To solve the equation (2), we have developed an analytical expressions for the LHD gauge  $(\Phi, \Psi)$  created by external coil currents  $\mathbf{J}_{\text{ext}}(\mathbf{x})$ .

Under the Coulomb gauge, the vector potential of external coil currents  $\mathbf{J}_{\text{ext}}(\mathbf{x})$  is given by the Biot-Savart law. Therefore, vector potential under the LHD gauge is given by

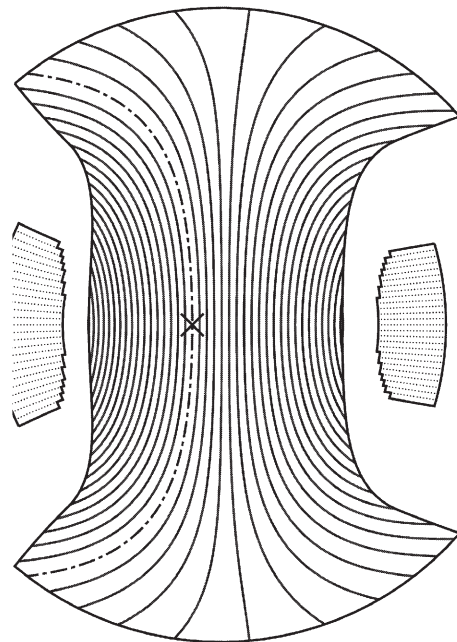
$$\mathbf{A}(\mathbf{x}) = \frac{\mu_0}{4\pi} \int d^3\mathbf{x}' \frac{\mathbf{J}_{\text{ext}}(\mathbf{x}')}{|\mathbf{x} - \mathbf{x}'|} + \nabla\chi, \quad (3)$$

where the scalar function  $\chi$  is determined by

$$0 = A_Y \quad (4)$$

$\Phi$  and  $\Psi$  are verified to be smooth and single-valued function in the vacuum vessel of the LHD (Fig.1).

(a)



(b)

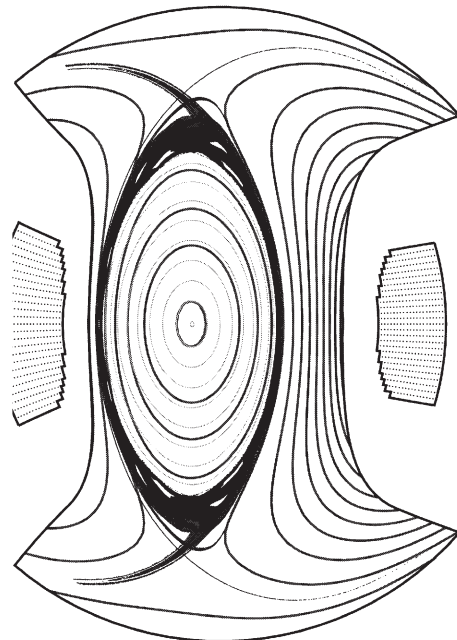


Fig.1. Numerical example of LHD gauge for the case of  $R_{\text{ax}} = 3.75\text{m}$ . (a)  $\Phi(X, Y, \pi/10)$ : The chain line shows the line of  $\Phi = 0$ , and  $\times$  represent the position of the magnetix axis. (b)  $\Psi(X, Y, \pi/10)$ : Poincare pltos of lines of force corresponding coil currents are also shown.  $\Psi$  can approximate automatically the magnetic surface.

Refference

- [1] T.Watanabe, et.al.: Nucl. Fusion **46** (2006) 291-305.



§59. Study on Generation Mechanism of Particles in LHD

Shiratani, M., Koga, K., Kiridoshi, S. (Dept. Electronics Kyushu Univ.),  
Ashikawa, N., Nishimura, K., Sagara, A.

Of late there has been growing concern over formation of dust particles due to plasma-surface interaction [1-4], because dust particles pose two potential problems: those remained in a fusion device are dangerous, as they can contain a large amount of tritium and can explode violently; they may lead to deterioration of plasma confinement. Therefore, it is important to reveal their formation mechanism, their transport as well as their accumulation area. Investigation of dust in fusion plasma research devices has been carried out using ex-situ dust sampling method [1-4]. Moreover, most such studies focused on dust particles around  $\mu\text{m}$  in size [1-4]. Recently, Kyushu University group of us reported formation of carbon dust nano-particles due to interaction between ECR hydrogen plasmas and carbon walls [5, 6]. This report motivates us to study small dust particles in LHD. Here, we will describe the results regarding characterization of dust particles collected from LHD using the filtered vacuum collection method.

The total mass of dust particles collected by each filter was obtained as the difference of filter mass before and after dust collection. Figure 1 shows the distribution of surface mass density after the 8th campaign. The mass densities depend little on the collected location, especially the values at the location No. 15 on the divertor made of carbon (IG-430) are similar to those at other locations where the first wall is made of stainless steel (SS316). The inner surface area of the LHD chamber without and with ports are  $400\text{ m}^2$  and  $700\text{ m}^2$ , respectively. Assuming the area of  $400\text{ m}^2$ , the total dust inventories after 7th, 8th, and 9th campaign are estimated to be 3.9, 1.4, and 1.1 g, respectively. The total inventory of dust particles collected from LHD after the 4th campaign in March 2001 is 16.2 g [3]. Therefore, LHD becomes cleaner during its operation history and the total dust inventory after the 9th campaign is the lowest among the reported values for several devices such as JT-60U and ASDEX-Upgrade [3, 4].

There exist dust particles ranging in size from 1 nm to  $10\text{ }\mu\text{m}$ . The smaller their size is, the higher their number density is. The size distribution of dust particles is expressed in terms of an inverse power law size distribution function, that is, the Junge distribution. This size distribution suggests that small dust particles grow into large ones in LHD. Dust particles are classified into small and large size groups: small dust particles below  $1\text{ }\mu\text{m}$  in size are spherical and their major composition is C, while large ones above  $1\text{ }\mu\text{m}$  in size are irregular in shape and their major compositions are Fe and Cr. Figure 2 shows cumulative percentage of volume and surface area of dust particles at location No. 13 after 8th campaign. Small dust particles of 1nm to  $1\text{ }\mu\text{m}$  in size have 70% of the total

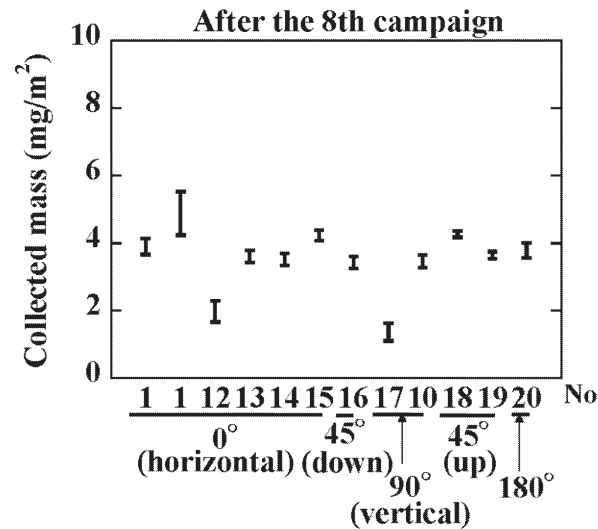


Fig. 1. Distribution of surface mass density of dust particles after 7th (a), 8th (b), and 9th campaign. No. 15 is on divertor target.

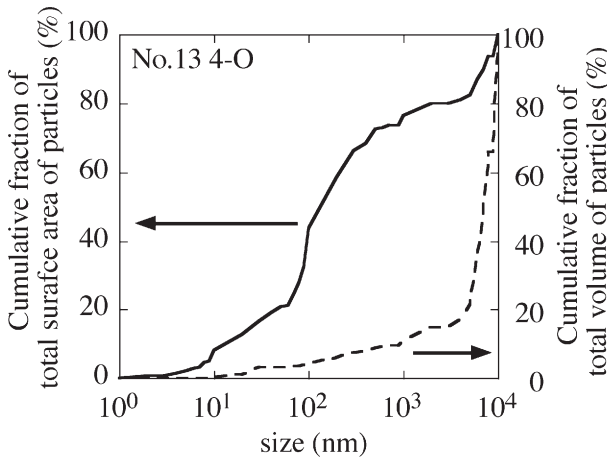


Fig. 2. Cumulative percentage of (a) volume and (b) surface area of dust particles at location No. 13 after 8th campaign.

surface area, while they have 10% of the total volume. These small dust particles cannot be bypassed, because they may contain a large amount of tritium due to their wide surface area in future fusion devices such as ITER.

References

- 1) Winter, J.: Plasma Phys. Control Fus. **40** (1998) 1201.
- 2) Sharpe, J. P., et al.: Fus. Eng. Design **63&64** (2002) 153.
- 3) Sharpe, J. P., et al.: J. Nucl. Matter., **313-316**, (2003) 455.
- 4) Sharpe, J. P., et al.: J. Nucl. Matter., **337-339** (2005) 1000.
- 5) Koga, K., et al.: Proc. ESCAMPIG16/ICRP5, (2002) I-173.
- 6) Koga, K., et al.: IEEE Trans. Plasma Science, **32**, (2004) 405.

§60. Erosion of Plasma Facing Materials by Charge Exchange Neutrals

Ono, K., Miyamoto, M. (Dept. Mater Sci. Shimane Univ.), Tokitani, M., Yoshida, N. (RIAM, Kyushu Univ.), Masuzaki, S., Ashikawa, N.

Charge exchange (CX) neutrals create radiation damages in the subsurface region of Plasma Facing Materials (PFMs) and contribute to the surface modification. Authors have reported that the surface modifications of PFMs caused by CX-neutrals in plasma confinement devices have large impacts on plasma density controlling through recycling and pumping in the wall <sup>1,2)</sup>. In the present work, microscopic damage in metals exposed to LHD hydrogen plasma was examined and the energy distribution and the flux of CX-neutrals were evaluated quantitatively.

To examine the surface modification caused by CX-neutrals, a materials probe experiment was carried out. Pre-thinned vacuum-annealed disks of 3 mmφ made of SUS316L, Cu, W and Mo were used as specimens. These specimens mounted on the material probe system were placed at the similar position of the first wall surface through the 4.5 L-port, and exposed to long discharges for about 150 sec. (Shot No. 58834-58984, hydrogen plasma). Typical plasma parameters were:  $T_i \sim 1$  keV,  $n_e \sim 3 \times 10^{19} \text{ m}^{-3}$ . After exposing the discharges, the microstructure of specimens was observed by means of transmission electron microscopy (TEM). In addition, irradiation experiments were carried out with hydrogen ions of 3 keV.

Fig. 1 shows dark field images of the microstructure in the specimens exposed to LHD hydrogen plasma. The radiation-induced dislocation loops with white contrasts were formed in these specimens. This figure also shows the threshold energies of hydrogen for knock-on damage in each specimen. In general, radiation induced secondary defects are formed as aggregates of point defects produced by knock-on processes. Accordingly, these defects indicate the existence of high energy incident particles. The existence of high energy CX-neutrals was suggested from the depth distribution of dislocation loops in SUS316L exposed to LHD hydrogen plasma as in Fig. 2. The damages are distributed to rather a deep range beyond 100 nm. This widespread depth distribution would be attributed to the high energy components of CX-neutrals with more than 8 keV with a little minor thermal effect.

The flux of CX-neutrals was evaluated from a result of the controlled irradiation experience. Fig. 3 shows fluence dependence of area density of dislocation loops formed in SUS316L under the irradiation with 3 keV hydrogen ions. Compare the defects density with the specimen exposed to the LHD plasma, the fluence of energetic CX-neutrals was roughly estimated to be  $2.8 \times 10^{20}$  atoms/m<sup>2</sup>. From this results, the mean flux of CX-neutrals with enough high energy to cause radiation damage (>370 eV) was estimated to be about  $2 \times 10^{18}$  atoms/m<sup>2</sup>s. On the

other hand, the slightly larger flux ( $\sim 10^{19}$  atoms/m<sup>2</sup>s) was evaluated in similar hydrogen discharges from the point of view of plasma density controlling in LHD <sup>3)</sup>. This discrepancy seems to be due to undetectable flux of the low energy CX-neutrals in this experiment.

In this experiment, the flux and energy of CX-neutrals were obtained as just averaged value for varied discharges. Therefore, the flux for individual cases and thermal effect are slate to be evaluated in next experiments with improved sample holder.

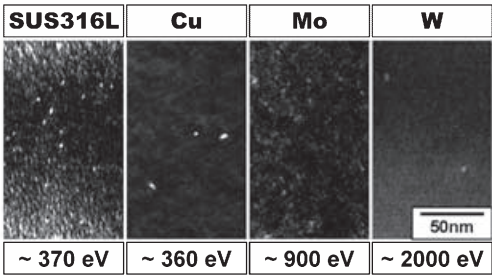


Fig. 1 Dark field images of the microstructures and the threshold energies of hydrogen for displacement damage in each probe specimen.

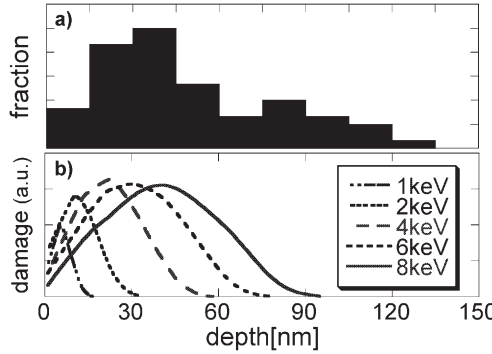


Fig. 2 a) Depth distribution of dislocation loops in SUS316L exposed to LHD hydrogen plasma and b) calculated depth distribution of damage in SUS316L with TRIM-code.

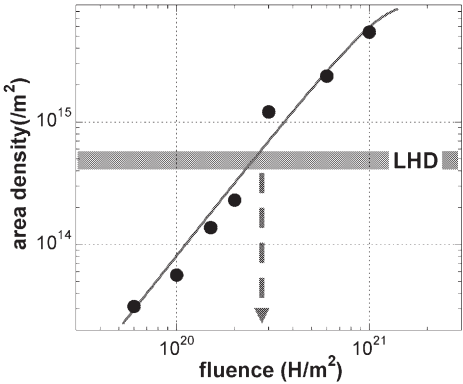


Fig. 3 Comparison of the area density of dislocation loops formed under the irradiation with 3 keV H or LHD plasma.

Reference  
1) M. Miyamoto et al., J. Nucl. Mater., 329-333 (2004) 742  
2) M. Miyamoto et al., J.Nucl.Mater., 337-339 (2005) 436  
3) M. Kobayashi, Annual Report of NIFS, to be published.

§61. The Effect of Argon and Helium Glow Discharge Cleaning on Boronized Surface in LHD

Kizu, K., Yagyu, J., Ishimoto, Y., Nakano, T., Tsuzuki, K., Miya, N. (JAEA),  
Ashikawa, N., Nishimura, K., Sagara, A.

The purpose of this study is acquiring basic data to design the effective surface conditioning system for next nuclear fusion experimental devices [1]. In late years, neon glow discharge cleaning (Ne-GDC) has been often performed in LHD because helium glow discharge cleaning (He-GDC) leads He accumulation in metal wall, and this helium slowly desorbs to hydrogen plasma as unwished impurity. However, the influence of glow discharge with higher atomic number than helium on boronized wall is not fully investigated, yet. Thus, in this work, boronized samples were introduced into He- and Ar-GDC in LHD and analyzed by Secondary ion mass spectrometry (SIMS).

Silicon (Si) and F82H samples were prepared for this study. These samples were boronized in Radiochemistry Research Laboratory in Shizuoka University. The boronization was conducted with glows discharge of decaborane and He gas mixture. Then, these samples were installed on the sample station at 4.5 L port in LHD, and were exposed to He-GDC (6 or 12 hours) or Ar glow discharge (Ar-GDC) (6.5 or 13 hours). Ne-GDC could not perform for schedule. The change of boron layer thickness and change of hydrogen retention in samples were investigated by SIMS. Impurity distribution like oxygen, carbon and iron will be measured by X-ray photoelectron spectroscopy (XPS) in future.

At first, SIMS measurements were performed to samples exposed to 6 and 12 hours He-GDC. The wear of boron layer was observed only for 12 hours He-GDC sample. The wear thickness was 24 nm. In previous work [2], clear change of thickness was not observed for the sample exposed to 6 hour He-GDC. These results mean that the wear of boron layer by He glow discharge is very small.

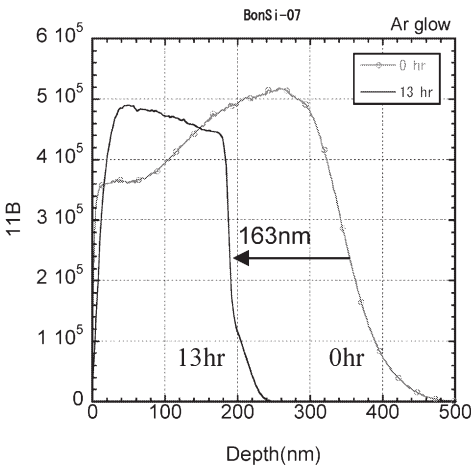


Fig. 1. Depth profile of boron on Si sample before and after 13 hr Ar glow discharge cleaning.

Then, SIMS measurements for samples exposed to Ar-GDC of 6.5 and 13 hours were performed. Figure 1 shows that the depth profile of boron on Si sample for unexposed and after 13 hours of Ar-GDC. The obvious decrease of boron layer thickness was observed. The average decrease of thickness was 150 nm for 6.5 hours of Ar-GDC and 190 nm of 13.5 hours of Ar-GDC, respectively.

The sputtering yield of boron with  $2.3 \text{ g/cm}^3$  in density by He normal injection with 150 eV is about 0.15. The He-GDC conditions of LHD are 130-180 V in glow discharge voltage and 20.5 A in current and  $700 \text{ m}^2$  in surface area of vacuum vessel. Therefore, calculated current density is  $29.3 \text{ mA/m}^2$ . This indicates that 4.6 and 9.2 nm of decrease of boron thickness are expected for 6 and 12 hours of He-GDC. On the other hand, the Ar-GDC conditions are 350 V, 30 A and the sputtering yield of 0.12. These mean that the sputtering thickness is expected to be same level as He-GDC. However, large sputtering thickness like Fig. 1 was observed. This probably means that the current density profile of glow discharge in LHD is different for Ar and He. This difference leads the localized sputtering as Ar-GDC case.

Finally, the hydrogen retention in boron layer before and after GDC were investigated. The tendency of hydrogen retention was same for all samples. After GDC, the hydrogen retention was increased at surface and not changed in boron layer. Figure 2 shows the depth profile of hydrogen in boron layer on Si sample after 12 hr He-GDC. Two processes are possible reason for the increment of hydrogen retention at surface

- (i) The impurity bonded to hydrogen like CH was sputtered by He- or Ar-GDC and retained on boron layer.
- (ii) Hydrogen atoms sputtered by He- or Ar-GDC were injected into boron layer.

The analysis of atomic ratio of B, C, O, Fe, etc. on surface by XPS is expected to clarify the process of hydrogen retention in boron surface.

Reference

- 1) Kizu, K. et al.; Ann. Rep. NIFS (2003-2004) 80.
- 2) Kizu, K. et al.; Ann. Rep. NIFS (2004-2005) 83.

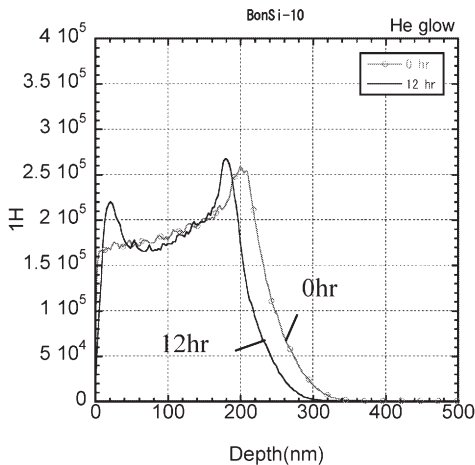


Fig. 2. Depth profile of hydrogen on Si sample before and after 12 hr He glow discharge cleaning.

§62. Toroidal Uniformity of Boronized Wall During 8<sup>th</sup> Experimental Campaign

Hino, T., Nobuta, Y. (Hokkaido Univ.), Ashikawa, N., Sagara, A., Nishimura, K., Masuzaki, S., Noda, N., Ohyabu, N., Komori, A., Motojima, O., LHD Experimental Group

Boronization experiments were conducted from the 5<sup>th</sup> experimental campaign. The oxygen impurity level in the LHD plasma was several orders of magnitude reduced after the boronization. In order to understand the reduction of oxygen impurity level, the boronized wall surface was analyzed using a material probe technique. Material probes were installed at 10 positions along the toroidal direction from the 6<sup>th</sup> experimental campaign, and the toroidal uniformity of the boron deposition was investigated. The boronization during the 8<sup>th</sup> experimental campaign was three times conducted using glow discharge. Two anodes between toroidal sectors 1 and 10 and between toroidal sectors 4 and 5 were employed for the glow discharge. The diborane plus helium gas was driven from three gas inlets between toroidal sectors 1 and 2, between toroidal sectors 3 and 4 and between toroidal sectors 7 and 8. After the campaign, the material probes were extracted and the depth profile of atomic composition was examined using Auger electron spectroscopy.

The thickness of boron film largely depended on the toroidal position. Figures 1 (a), (b) and (c) show the depth profiles of atomic composition in the probes placed at the toroidal sectors 1, 9 and 10. In the positions close to the anodes and gas inlets, the boron deposition was clearly observed. In opposition, the boron deposition was very small in the positions far from the anode. Thickness of the boron film was as high as approximately 500 nm. In the positions with a thick boron film, the discharge history is observed. After each boronization, the carbon deposition due to main and glow discharges in Figs. 1 (b) and (c).

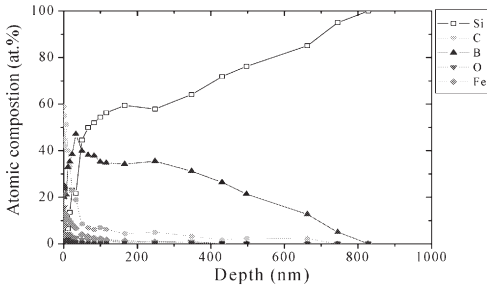
Figure 2 shows a plot of thickness of boron film against toroidal sector number. The ratio of the boronized wall to the entire wall was approximately 30 % and 40 % in the 6<sup>th</sup> and 7<sup>th</sup> experimental campaigns. The ratio in the 8<sup>th</sup> experimental campaign significantly increased (approximately 70 %). This increase is due to that the gas flow rate at every gas inlet was taken roughly the same. The amount of oxygen retained in the boron film was measured based upon the depth profile of atomic composition. The amount of retained oxygen was roughly proportional to the thickness of boron film. Thus, the oxygen impurity concentration might have been further reduced by the improvement of toroidal uniformity of boron film.

In summary, the boronization was very successfully conducted in the 8<sup>th</sup> experimental campaign, and the toroidal uniformity of the boron film was significantly improved. This result contributes to further increase of plasma stored energy in LHD.

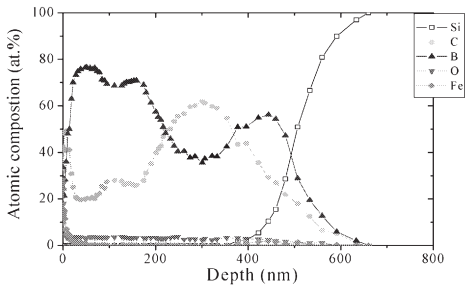
References

(1) Nobuta, Y., Ashikawa, N., Hino, T., et al, Fusion Eng. and Design, 81(2006)187-192  
(2) Hino, T., Nobuta, Y., Ashikawa, N., “New Development in Nuclear Fusion Research”, NOVA Scientific Publishers Inc., NY, (2006)

(a) Toroidal sector, 1



(b) Toroidal sector, 9



(c) Toroidal sector, 10

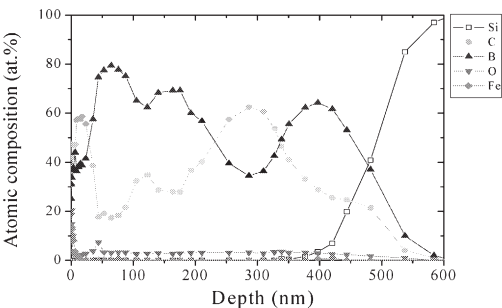


Fig. 1 Depth profiles of atomic composition at probes placed at toroidal sectors 1 (a), 2 (b) and 3 (c).

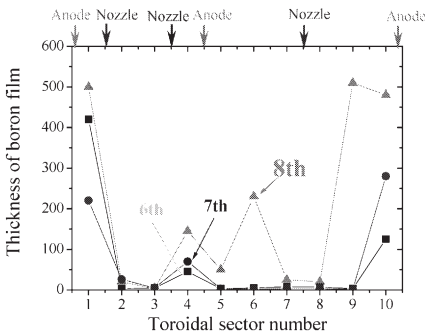


Fig.2 Boron thickness and amount of oxygen retained versus toroidal sector number.



§63. Study on Hydrogen Retention and Its Existing State in Boron Film Exposed to Hydrogen Glow Discharges

Okuno, K., Oya, Y., Yoshikawa, A., Oyaidzu, M. (Fac. of Sci., Shizuoka Univ.), Ashikawa, N., Nishimura, K., Sagara, A., Noda, N. (National Institute for Fusion Science)

1) Introduction

For the future D-D discharge experiments in LHD, it was important to estimate the desorption behaviors and retention of tritium trapped in boron films formed by boronization for first wall conditioning. In this study, the analyses of atomic composition and chemical states were performed for three kinds of boron films by XPS (X-ray photoelectron spectroscopy).

2) Experimental

The boron film deposited on the Si substrate in LHD (Sample A), and the oxygen-contained boron film (Sample B) and the pure boron film (Sample C) deposited on the Si substrate using P-CVD (Plasma-chemical vapor deposition) in Shizuoka University were prepared. After the heating treatment was performed at 993 K for 10 min and subsequent surface sputtering by 3 keV Ar<sup>+</sup>, atomic compositions and chemical states were evaluated by XPS (ULVAC-PHI ESCA 1600 System) at Shizuoka University

3) Results and discussion

The results of atomic composition analyses for Samples A, B and C are shown in Table. It was found that Sample A contained 12% of oxygen and 10% of carbon. In Sample B, the oxygen and carbon concentrations were 10% and less than 1% (impurity level), respectively, while, both of them in Sample C were not almost contained.

The analysis of chemical states of boron was performed for Samples A, B and C by means of XPS. Figure shows the B-1s XPS spectra. The B-1s binding energies of Samples A and B were shifted toward higher energy side compared to Sample C. The chemical shift of B-1s spectrum for Sample A was larger than that for Sample B. The shoulders of the spectra of Samples A and B were located at 191 eV. As these shoulders approximately corresponded to the binding energy contributed to boron oxide [1], it was suggested that boron oxide was formed in Samples A and B. The FWHM (Full Width of Half Maximum) of Sample A was larger than those of Samples B and C. It was suggested from these results that the B-C bond was formed as carbon concentration in film increased.

In future, the desorption behavior, retention and chemical states of hydrogen should be elucidated in the boron film exposed to discharge in LHD.

Table The atomic composition analyses for each sample (%)

	B	C	N	O
Sample A	73	10	5	12
Sample B	85	3	2	10
Sample C	96	2	1	1

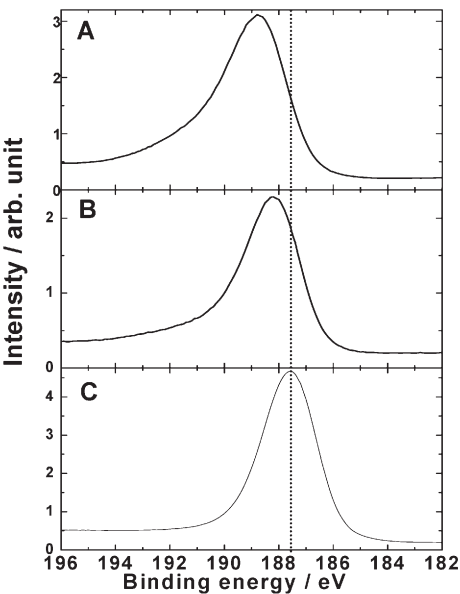


Figure The B-1s XPS spectra for each sample

4) Conclusion

To evaluate hydrogen isotope behaviors in the boron thin film, three kinds of samples, the ones prepared at NIFS and Shizuoka University, were prepared and the analyses of atomic composition and chemical states were studied by means of XPS. Concentrations of impurities, oxygen and carbon, for NIFS sample were higher than those for Shizuoka sample. These facts suggest that these impurities can be made large effects on the implanted hydrogen isotope retention and trapped states in the boron thin film.

[1] O. M. Moon, B.C. Kang, S.B. Lee, J.H. Boo, *Thin solid films*, **464-465** (2004) 164-169.

§64. Ion Cyclotron Conditioning with Strong Magnetic Field in LHD

Ashikawa, N., Masuzaki, S., Nishimura, K., Sagara, A., Saito, K., Seki, T.

The ion cyclotron conditioning (ICC) is one of the typical wall conditioning methods in current devices. The operation of experimental devices for fusion plasma with superconducting coils needs a long-time duration for increasing and decreasing the magnetic fields. As a typical wall conditioning method, DC-glow discharge cleaning is used in JT-60U and LHD with no magnetic field. In the future, the fusion reactors with superconducting coils will be operated over long discharge durations with deuterium/tritium mixtures. Therefore, for future devices, a wall conditioning method that can be used in a magnetic field will be required in general.

The impact of high-energy particles on the wall is considered to be one of the effective mechanisms for the high removal rate of hydrogen by ICC. In order to observe the confinement of a high-energy ion accelerated by ICRF heating, a silicon-diode-based fast neutral analyzer was installed in LHD. Figure 1 shows the distribution of high-energy particles every 5 shots. The energy range of the accelerated ions during these shots, #56155 and #56160, is over 60 keV.

A useful parameter for comparing the ICRF input power in different pressures is the power density,  $P_{in}/N$ , defined as the power normalized to the He particle number:  $P_{in}/N = P_{in}/(pV)$ , where  $P_{in}$  is the input power by an ICRF antenna,  $p$  is the pressure and  $V$  is the volume of a vacuum chamber. Consideration is given for the reason about the wide energy distribution of high-energy particles as shown in Fig.1. A comparison of input powers and the power density  $P_{in}/(pV)$ , in every 5 shots are plotted in Fig.2. Wide energy distributions of high-energy particles such as shot numbers #56155 and #56160 are also shown on the hatched period in Fig. 2. A comparison of input powers shows similar intensities in shots of #56155, #56165, #56170, #56175 and #56180. Therefore the wide energy distributions depend on the power density, rather than on the power. From this result, the controlling method of this high-energy distribution and an investigation into a producing mechanism of this distribution during ICC are considered as the important issues to optimize the operational method for ITER.

The ICC method was already tested in some fusion devices. The operation regions of the power density are quite different as shown in Fig. 3. The volume depends on each device and this number cannot be changed after construction. The operational range of the helium pressure is determined by the breakdown problem in tokamaks at present. The ICRF power designed for ITER is about 20 MW as a heating system. To get a high removal rate using the present devices, two kinds of optimizations are important. One is the relationship of the ICRF input power and the working gas pressure as the parameter of power density. The removal rate depends on the wide energy distributions, and controlling this distribution is important.

The second one is the phase of on or off of the RF input power with pumping efficiency. In Tore Supra, this experiment was carried out and published, but we did not get any answer regarding future operation in ITER. Because, a long-term operation with CW-ICC is difficult in many devices due to the property of each antenna. In the future, operations of CW-ICC are possible in LHD.

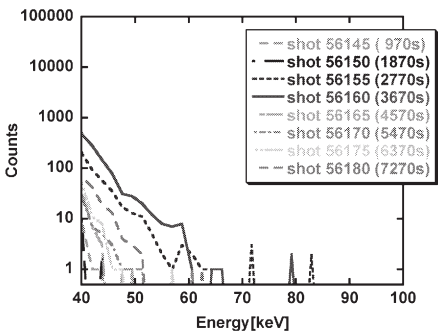


Fig.4 Energy distribution of high-energy particles for every 5 shots.

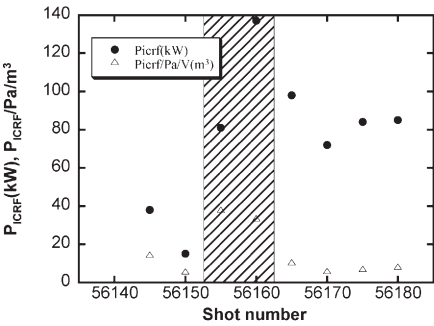


Fig.5 Comparison of power density and net power by ICRF heating.

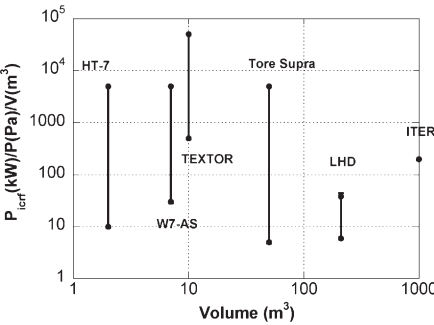


Fig.6 Operating region of each device in terms of power density and machine size.

Reference  
1) N.Ashikawa et al., to be published Fusion Eng. Design

## §65. Recent Progress on High Ion Temperature Experiment in the LHD

Ikeda, K., Morita, S., Takeiri, Y., Ida, K., Kaneko, O., Mutoh, T., Nakamura, Y., Tsumori, K., Oka, Y., Goto, M., Nagaoka, K., Kumazawa, R.

We had achieved the ion temperature of  $T_i=13.5\text{keV}$  on the argon discharge with the high-energy neutral beam heating (NNBI) of 10.5 MW in the 8th experimental campaign. Argon discharge is effective to improve the ion heating power even with the high-energy neutral beam. These experiments contributed to the research of the high temperature plasma above the 10keV

On the other hand, it is more important task to improve an ion temperature on a hydrogen discharge or a helium discharge that will be used for a fusion device. High-energy neutral beam is mainly deposit on electrons in the hydrogen plasma. Hydrogen beam stopping cross-section used the beam energy of 40keV is three times larger than the cross-section used the beam energy of 180keV. So we have adopted the low-energy NBI (PNBI) system to improve the hydrogen ion heating. Hydrogen neutral beams are injected perpendicularly with the beam power of 3MW at the beam energy of 40keV. Shine through ratio is designed to 50% at the electron density of  $n_e=1\times 10^{19}\text{m}^{-3}$ . The tasks of the high temperature group are the improvement of the hydrogen ion temperature and the measurement of a fine ion temperature profile used the charge-exchange recombination spectroscopy (CXRS) in the 9th experimental campaign.

We have achieved the ion temperature of  $T_i=2.6\text{keV}$  measured by the ArXVII X-ray spectroscopy on the hydrogen discharge with the heating of 11.5MW NNBI and 2.2MW PNBI at the shot number of 60502. The electron temperature and the averaged electron density is  $T_e=3.3\text{keV}$  from the Thomson scattering and the  $\langle n_e \rangle = 1.5\times 10^{19}\text{m}^{-3}$  from the far-infrared interferometer, respectively.

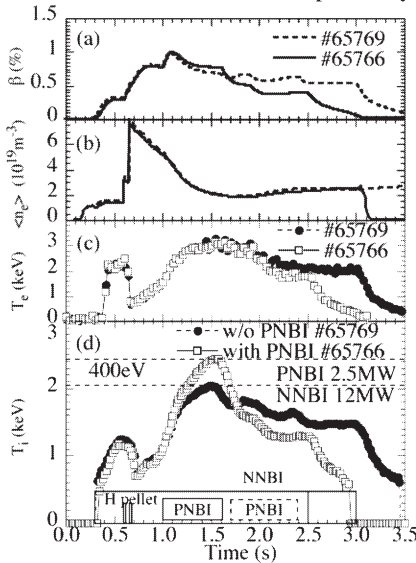


Fig. 1. Heating effect of hydrogen plasmas by PNBI

Figure 1 shows the effect of the PNBI with the power of 2.5MW at the energy of 40keV. Initial plasma is build up by ECRH and then it is sustained by NNBI heating. Electron density increases with the hydrogen ice pellet. The ion temperature increases to 2keV when the heating power of 12MW used three NNBI. The ion temperature is improved to 2.4keV when we use the additional PNBI heating at the peak ion temperature. Ion heating power evaluated by the absorption efficiency and the ion heating efficiency is 1MW. So the  $T_i$  increasing rate of  $T_i/(P_i/n_i)$  is estimated to be  $0.8\text{keV}/(\text{MW}10^{19}\text{m}^{-3})$  that is consistent of previous high-Z experiments.

We have installed two CXRS systems to measure the ion temperature profile. One views the plasma perpendicularly from the LHD 5-O port along the PNB used the convex mirror inside of the vacuum chamber, the other views the plasma tangentially from the LHD 7-T port along the NNBI. Visible carbon charge exchange spectrum is used for the measurement. We have clearly observed the ion temperature profile in two sight lines with the time resolution of 50ms. Figure 2(a) shows the fine profile of the ion temperature measured by the poloidal CXRS. The peak ion temperature is 2.2keV at  $t=2.1\text{s}$  with a PNB injection and a pellet fueling. In the gas-puff case, the electron density becomes hollow profile then we have not observed the increasing of the ion temperature around the plasmas center. The ice pellet is effective to increase the center ion temperature because the electron density peaks around the plasma center in the decay phase of the density at  $t=1.8\text{s}$ . We have also observed the increasing of the ion temperature around the center by the CXRS used NNBI as shown in Fig. 2(b). These results will expect the increasing of the ion temperature and formation of the ion internal transport barrier if we will improve the ion heating power at the plasma center using PNBI heating.

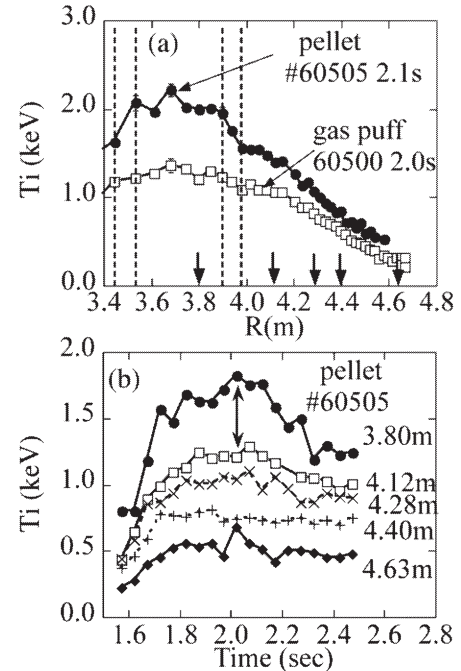


Fig. 2. Profile of the ion temperature from CXRS used PNBI (a). Time evolution of the ion temperature measured by the CXRS used NNBI (b)

## §66. Ion Temperature Rise in Electron-ITB Plasmas Formed with Combination of ECH and NBI

Takeiri, Y., Morita, S., Ikeda, K., Ida, K., Tsumori, K., Oka, Y., Osakabe, M., Nagaoka, K., Kaneko, O.

The increase in the ion temperature due to transport improvement has been observed in plasmas heated with high-energy negative-NBI, in which electrons are dominantly heated, in Large Helical Device (LHD). When the centrally focused ECH is superposed on the NBI plasma, the ion temperature rises, accompanied by formation of the electron ITB. This is ascribed to the ion transport improvement with the transition to the neoclassical electron root with a positive radial electric field.

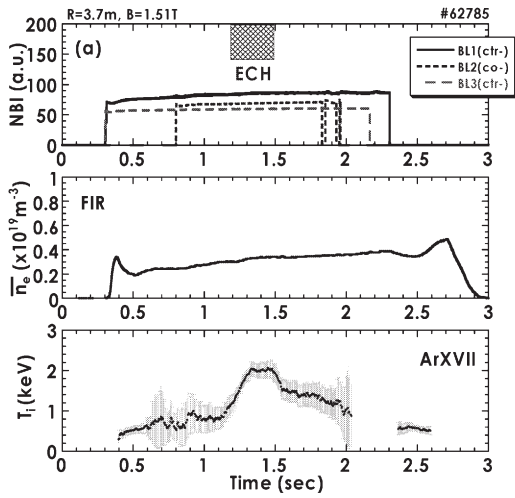


Fig. 1. Time evolution of the electron density and the ion temperature in an NBI+ECH plasma.

Figure 1 shows the time evolution of an NBI+ECH plasma. With superposition of the centrally focused second-harmonic ECH on a plasma heated with high-energy negative-NBI ( $>150\text{keV}$ , H), the central  $T_e$  is increased, and the electron ITB, which indicates a steep gradient in a core region, is formed in LHD [1]. Simultaneously, the central  $T_i$  is also raised with the superposition of the ECH, as shown in Fig. 1. The electron ITBs in helical systems are characterized by improvement of the core electron transport due to the neoclassical electron root, which is in contrast with the tokamak's ITBs. The neoclassical calculation shows the formation of positive radial electric field ( $E_r$ ) in the core region in the electron ITB plasma, in which the transport improvement of both ions and electrons is theoretically predicted. Figure 2 shows the radial profile of  $T_e$  measured with Thomson scattering, and those of  $T_i$  and  $E_r$  measured with CXRS, for an electron ITB plasma and a non-ITB plasma. A positive

increase in the  $E_r$  is observed in a core region with the superposition of the ECH, as shown in Fig. 2(c), and an increase in the  $T_i$  is also observed, as shown in Fig. 2(b).

Since the electron density profile is not changed with the superposition of the ECH, the NBI absorption power and profile are not so changed. Considering that the increase in the ion heating power ratio is as small as around 10% due to an increase in the  $T_e$  and that the heat exchange between the electrons and the ions is negligible, the ion temperature rise is ascribed to the improvement of the ion transport in the core electron root.

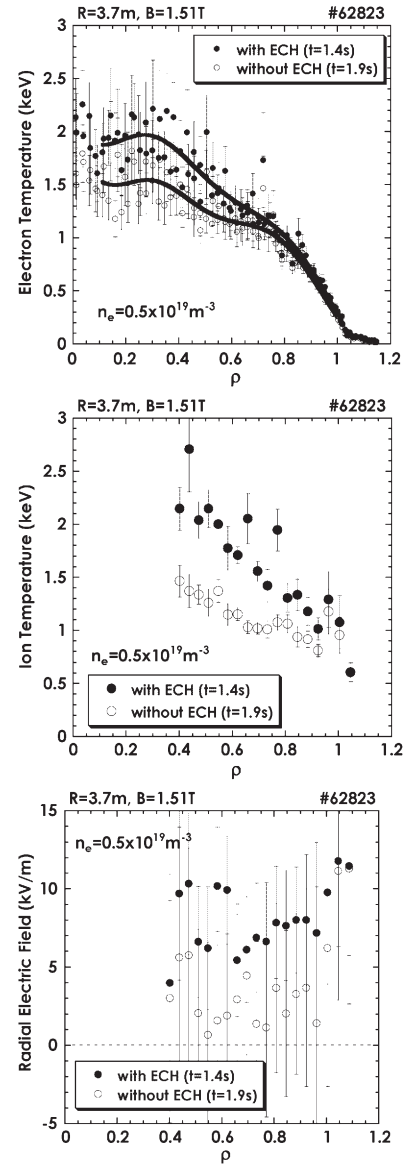


Fig. 2. Radial profiles of (a)  $T_e$ , (b)  $T_i$ , and (c)  $E_r$  for the electron ITB plasma and the non-ITB plasma at  $R_{ax}=3.7\text{m}$ .

### References

- [1] Y. Takeiri *et al*, Phys. Plasmas **10** (2003) 1788.



## §67. Effect of Ripple Trapped Electrons on Neutral Beam Driven Current in LHD

Nagaoka, K., Narushima, Y., Watanabe, K.Y.

Recently, the control of plasma current and/or iota profile is recognized to be important for confinement improvement not only in tokamaks but also in stellarators. The basic properties of neutral beam driven current have been experimentally investigated in LHD. In this report, the results of neutral beam current drive experiments in 9<sup>th</sup> campaign of LHD, in particular, the effect of ripple trapped electrons on the neutral beam driven current are experimentally investigated by changing plasma shape.

Three neutral beam injectors has been tangentially installed in LHD, and long pulse beams with the duration of about 5 second have been injected for the neutral beam current drive (NBCD) experiments. The hydrogen gas puffing has been used to keep the plasma density constant during the discharge, and the saturation of plasma current has been evaluated. The magnetic configurations of this NBCD experiment is  $R_{ax}=3.6\text{m}$ ,  $B_t=1.5\text{T}$  and  $B_q=72\text{--}200\%$ , where  $B_q$  is scanned in order to change plasma shape, that is, magnetic ripple. The plasma current includes two components; one is bootstrap current and the other neutral beam driven current. In order to evaluate the latter, discharges with co- and ctr-injection NBI have been compared.

In general, neutral beam driven current is given by

$$I_{NB} = \frac{I_b V_b \tau_s}{2\pi R} \left( 1 - \frac{1}{Z_{eff}} G \right) = I_{NB0} \left( 1 - \frac{1}{Z_{eff}} G \right) \quad (1)$$

where  $I_b$ ,  $V_b$ ,  $\tau_s$ ,  $Z_{eff}$  and  $G$  are neutral beam current injected by NBI, beam velocity, slowing down time of injected ions, effective charged number of bulk plasma ions and geometrical factor, respectively. In LHD case, slowing down time of beam ions is dominated by collisions with electrons, so it depends on electron temperature and density ( $T_e^{3/2}/n_e$ ). For simplicity, electron temperature on the magnetic axis and line averaged density experimentally obtained have been used to evaluate  $I_{NB0}$ . The current drive efficiency ( $I_{NB}/I_{NB0}$ ) is considered to depend on  $G$ , because it may be considered that  $Z_{eff}$  does not depend on the plasma shape, which is shown in Fig.1. The geometrical factor approximates ratio of toroidally circulating electron  $\langle \ell \rangle$  and depends on the magnetic configuration. The larger ratio of circulating electron, the smaller neutral beam driven current, because circulating electrons produce retarding current against the beam current. The

dependence of volume averaged ratio of circulating electron  $\langle \ell \rangle$  is also shown in Fig.2. The plasma destabilizes and can not be applied the ctr-current in the plasma with ctr-NBI heating in the case of  $B_q=200\%$ . The error bar becomes large because the plasma current can not be scanned in wide range. Thus, It is difficult to conclude whether the model given by eq.(1), which is also shown with dotted line in fig.2, can be applied for helical devices. The wider range scan of  $B_q$  in small  $B_q$  region is necessary for getting the clear experimental confirmation, which is planned in the LHD 10<sup>th</sup> campaign.

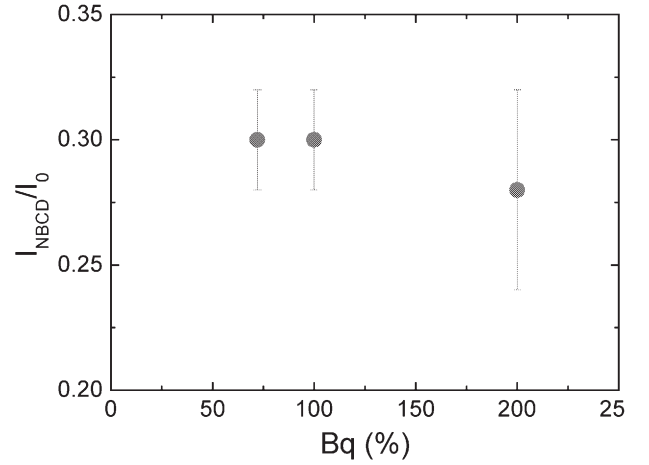


Fig.1 The NBCD coefficients v.s.  $B_q$ .

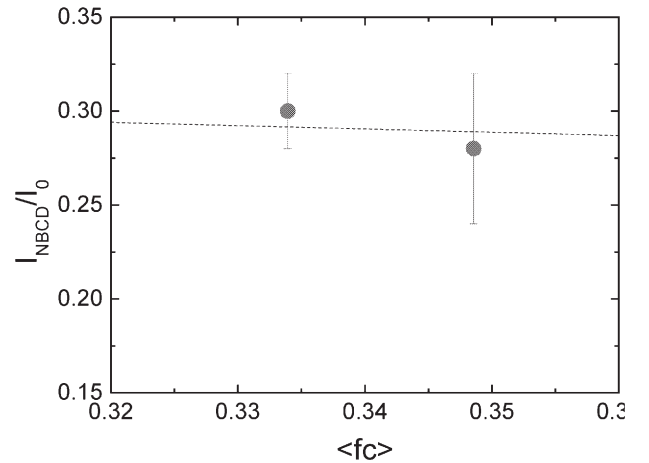


Fig.2 The NBCD coefficient v.s. the volume averaged fraction of toroidally circulating electrons. The dotted line shows the model given by eq.(1).

## §68. Fraction of Neutral Beam with Different Energies Measured by the Beam Emission Diagnostic

Ikeda, K., Nagaoka, K., Osakabe, M., NBI Group

Supply of fast ions is a key issue to produce high temperature plasmas for fusion development. Neutral beam injection (NBI) is one of the effective technique to heat fusion particles. We have installed the low-energy NBI system in order to improve the ion temperature in the LHD as shown in Fig. 1. The design of this system requires the 3MW of a hydrogen neutral beam power with two ion sources at the beam energy of 40keV. We have used a positive-ion source because high ion current density is necessary. It is well known that a hydrogen ion source produces  $H^+$ ,  $H_2^+$  and  $H_3^+$  ions<sup>1)</sup>. So the different energy particles such as the full energy of E, the half energy of E/2 and the one thirds energy of E/3 are produced in the neutralizer cell. Increasing of the full energy component of the neutral beam is necessary in order to improve a gross heating power. So the information of relative flux of the fractional-energy is important for improving the beam injection power. The optical system consists of quartz lenses and quartz optical fibers. The optical sight line is arranged along the beam injection axis with the angle of 14.3 degree on the LHD 5-O port. So the beam emission separates from a plasma emission spectrum by the Doppler effect. The intensified charge couple device (ICCD) detector is coupled on the focal plane of the spectrometer.

Figure 2 shows the measured spectrum from the hydrogen discharge with the magnetic field strength of 1.5 T. The spectrum of the Balmar- $\alpha$  from the neutral hydrogen atoms around the low temperature region is observed at 656.3nm. Beam emission spectra are shifted to the red shift side due to the Doppler effect. We have clearly observed the three beam emission components with the energy of 38keV, 19keV and 12.7keV. The Doppler shift values are the consistent of the expected shifts. We have also observed a few impurity spectra near the H $\alpha$  emission lines, but it dose not have an influence on the beam emission because it is sharp.

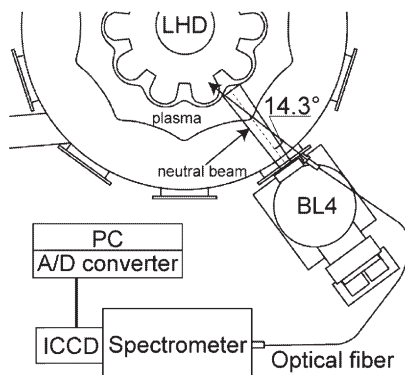


Fig. 1. Schematic diagram of the NBI and the measurement optics.

We estimate the strength of the beam emissions of the different beam energy by integrating of apart of the beam emission spectrum. Figure 3(a) shows the time evolution of  $I_{BE}E_{beam}/\sigma_{emi}$  that corresponds to the beam power. Here we use the cross-sections of  $\sigma_{emi}=8.39\times10^{16}cm^2$  for  $E=12.7keV$ ,  $\sigma_{emi}=7.88\times10^{16}cm^2$  for  $E=19keV$  and  $\sigma_{emi}=8.23\times10^{16}cm^2$  for  $E=38keV$ . The beam power of full energy beam at  $t=2.3s$  is improved from that power at  $t=0.5s$  by 3 times. The beam power of full energy beam is 2.7 times larger than that of the half energy beam at  $t=2.3s$ . Fraction of the injection beam power of the full energy has been improved to 63% at  $t=2.3s$  from 50% at  $t=0.5s$  as shown in Fig. 3(b). Intensities of the beam emission of E/2 and E/3 slightly increase, but these fractions decrease against of the total beam power. These results are the net fractions of the injected neutral beam after the neutralization. It is expected that the proton ratio inside of the arc chamber is larger than the fraction of the full energy beam component because of the neutralization efficiency decreases when the beam energy increases. Then the acceleration drain current increases to 126A at  $t=2.3s$  from the 92A at  $t=0.5s$  with the constant hydrogen feeding due to the increasing of the arc discharge current in the ion source. So injection beam power depends on the fraction of the full-energy beam influenced by an arc discharge condition.

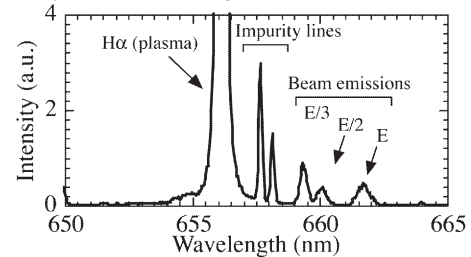


Fig. 2. Hydrogen Balmar- $\alpha$  spectrum of both plasma emission and the beam emission. Beam emission consists of three different energy spectra. Impurity spectra located near the hydrogen spectrum dose not have an influence on the beam emission measurement.

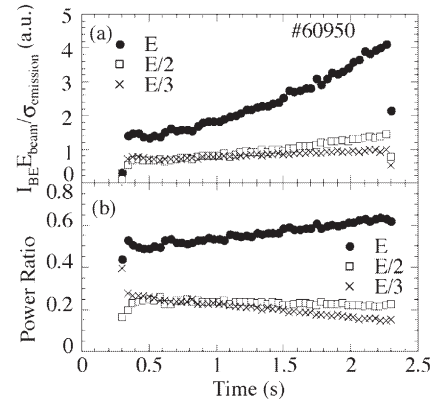


Fig. 3. Time evolutions of  $I_{BE}E_{beam}/\sigma^{eff}$  (a) and the ratio of the beam power for each energy beams (b). Beam power of the full energy component large increases. Fraction of the full-energy beam power has been improved at the last of the discharge.

Reference

- 1) Y. Oka et al., JJAP, **22**, (1983) 688.

## §69. Plasma Sustainment by the ICRF Mode Conversion Heating

Saito, K.

In the long pulse discharge by the ICRF minority ion heating in the large helical device (LHD), Plasmas collapse by the influx of iron impurity [1]. As an alternative heating method for long pulse discharge, ICRF mode conversion heating was investigated in 2005 with the frequency of 25.3MHz and the magnetic field strength on axis of 2.5T. Hydrogen and helium was used. The cyclotron resonance layer of hydrogen was located on the edge of plasma as shown in Fig.1. The ion-ion hybrid resonance layer where fast wave was mode converted to ion Bernstein wave was located upper and lower in front of ICRF antenna. By the analysis of power absorption by electron by use of ECE, it had been known that only electrons were heated directly by this heating method [2].

Plasma was sustained for 7 seconds by the ICRF mode conversion heating as shown in Fig.2. A couple of ICRF antennas were used. The plasma stored energy was 40kJ. Line averaged electron density and electron temperature on axis were  $0.6 \times 10^{19} \text{m}^{-3}$  and 0.5keV, respectively. The electron temperature profile was hollow as shown in Fig.3. Therefore, the mode conversion heating was the off-axis heating. In this discharge silicon-diode-based fast neutral analyzer (SiFNA) did not detect any high-energy ions. Therefore, it was clarified that only electrons were heated directly. This heating method has a disadvantage of a low loading resistance due to the low frequency, which results in the high voltage in the transmission line and limits the injection power. However, it was found that the loading resistance increases until approximately  $3.5\Omega$  by the increase of electron density in the case of the distance of 8cm between antenna and the last closed flux surface as shown in Fig.4. The loading resistance of  $3.5\Omega$  corresponds to 630kW with the limited voltage of 30kV to prevent arcing in the transmission line. Injection of 2.5MW will be possible with two couples of antennas.

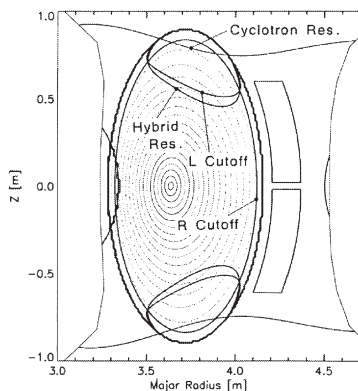


Fig.1 Plasma cross section in front of ICRF antenna calculated with the assumption of 50% of hydrogen concentration ratio.

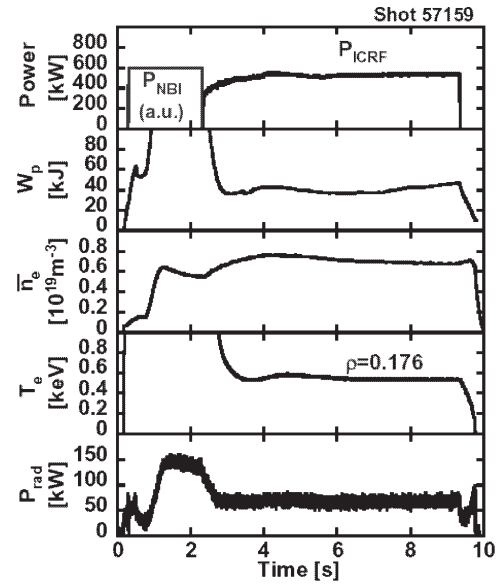


Fig.2 Plasma sustainment by the mode conversion heating.

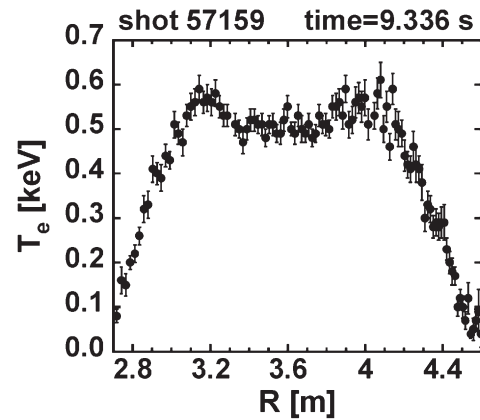


Fig.3 Electron temperature at the end of the discharge of Fig.2.

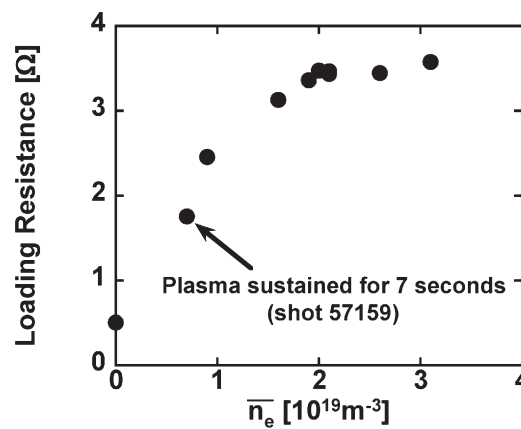


Fig.4 Relation between the loading resistance and the line averaged electron density.

### References

- 1) Kumazawa, R, et al.: Nuclear Fusion, **46** (2006) S13.
- 2) Saito, K, et al.: Nuclear Fusion, **41** (2001) 1021.

## §70. Experiment of Wave-Particle Interaction by Use of Second Harmonic ICRF Heating and NBI

Saito, K.

In the large helical device (LHD), the second harmonic ICRF heating had been conducted with the target plasma heated by tangential neutral beam injection (NBI) [1]. In this combination of heating, population of particles with the large Larmor radius was small. However, enhancement of high-energy ion tail formation was expected in the presence of these particles supplied by the perpendicular NBI.

In addition to the tangential NBIs, a perpendicular NBI was newly installed in the horizontally elongated plasma section in 2005. High-energy particles are detected by several detectors, such as silicon-diode-based fast neutral analyzer (SiFNA). Figure 1 shows 6I-SiFNA, which detects the particles with the perpendicular pitch angle at an inner port of LHD (6I port).

The second harmonic ICRF power was launched to the plasma sustained by the tangentially injected NBI as shown in Fig.2. The resonant particles were hydrogen ions. The applied ICRF frequency was 38.47MHz and the magnetic strength on axis was 1.375T. A pair of second harmonic ion cyclotron resonance layers were located at the off-axis. The innermost normalized minor radius of the resonance layer was 0.5. The particles of hydrogen were injected by the perpendicular NBI with the energy of 40keV. The ICRF heating power and the perpendicular NBI power were 2.7MW and 2.2MW, respectively. Electron and ion temperatures were not changed by the injection of perpendicular beam as well as electron density. Figure 3 shows the relation between the energy and the detected particle counts by 6I-SiFNA at the timings of (A) tangential beam only, (B) tangential NBI with ICRF heating and (C) tangential and perpendicular NBI with ICRF heating. The flux was enhanced by a factor of three in the presence of the perpendicular NBI. The population of low-energy neutral particles are deduced to be same since the intensities of  $H\alpha$  and  $HeI$  detected at the same toroidal section with the 6I-SiFNA did not change at the timing of perpendicular NBI injection. Therefore, charge exchange rate is same and the population of high-energy ion tail produced by second harmonic heating was thought to be enhanced in the presence of the perpendicular NBI.

The gradients of energy spectrum were same. The explanation is as follows. Fokker-Planck equation of steady-state condition at the higher energy than the source is written as follows with the assumption that particle loss is proportional to distribution function;

$$0 = \bar{C}(f_0) + \bar{Q}(f_0) - f_0 / \tau_{\text{loss}}.$$

Gradients are the same regardless of with and without source. Therefore the population of particles with much higher energy than the source energy could be enhanced.

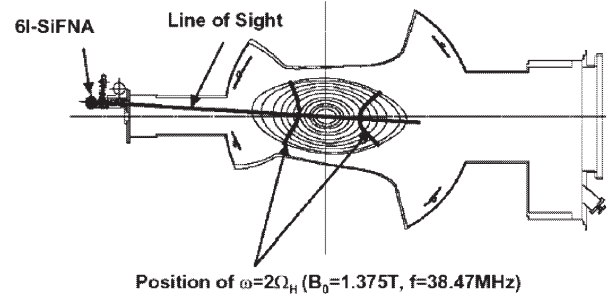


Fig.1 6I-SiFNA and line of sight.

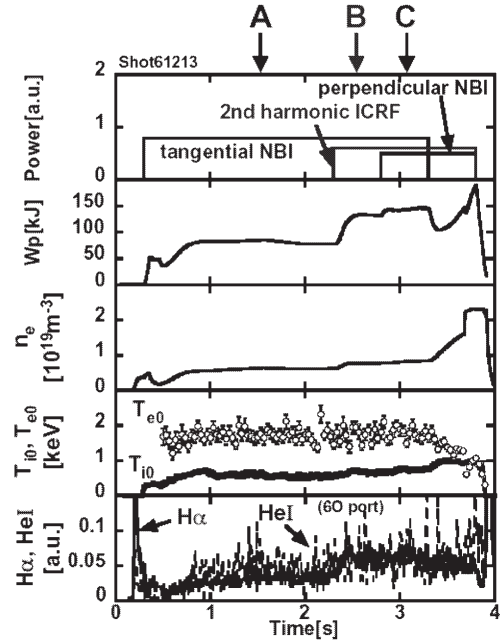


Fig.2 Time evolution of the plasma parameters with second harmonic ICRF heating and NBI.

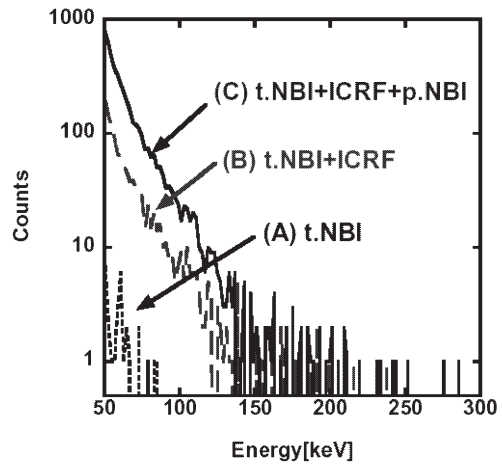


Fig.3 Increase in the high-energy ion population by the perpendicular NBI.

Reference

1) Saito, K, et al.: Plasma Physics and Controlled Fusion, **44** (2002) 103.



## §71. Excitation of High Frequency Fluctuations and Their Effects on High Energy Ions in LHD

Higaki, H., Kakimoto, S., Yamaguchi, Y., Ichimura, M. (Univ. Tsukuba), Kumazawa, R., Watari, T., Mutoh, T., Seki, T., Saito, K.

When a magnetized plasma has an anisotropy in its velocity distribution function, various fluctuations (or waves) can be excited spontaneously. For examples, Alfvén ion cyclotron waves are observed when high energy ions are confined in a mirror plasma<sup>1)</sup> and ion cyclotron emissions can be observed in Tokamaks associated with the fusion products<sup>2)</sup> and/or the high energy neutral beam injection (NBI)<sup>3)</sup>. The production of high energy ions with Ion Cyclotron Heating (ICH) can also excite these fluctuations<sup>4)</sup>. It is quite natural that these high frequency fluctuations to be observed in helical systems. Investigating these fluctuations is important because they are affected by the fusion reaction rate, high energy ions and edge localized modes.

To estimate if such a high frequency fluctuations around the ion cyclotron frequency can be excited in plasmas, the dispersion relation of an infinitely long uniform density plasma with a temperature anisotropy was considered as a first step. Shown in Fig.1 is the calculated contour plot of the growth rate for the slow and fast waves around the ion cyclotron higher harmonics. It is assumed in the calculation that a plasma has the density of  $2 \times 10^{13} \text{ cm}^{-3}$  and the bulk electron and ion temperature of 1keV at  $B=1\text{T}$ . Also included are 25% high energy ion components (80keV in perpendicular to B field).

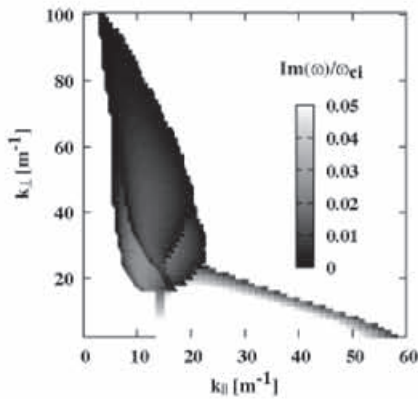


Fig. 1. A contour plot of the growth rate as a function of the parallel and perpendicular wave number.

For experiments in Large Helical Device (LHD), magnetic probes (MP) were employed to observe these high frequency fluctuations excited with NBI or high power ICH injection. Signals from MPs were recorded by an oscilloscope (250Ms/s) with the resolution  $\Delta f \sim 15\text{kHz}$ . Associated with the perpendicular injection of neutral beams (NBI#4), high frequency fluctuations were observed for the first time in LHD. An example is shown in Fig.2

when  $B = -2.71 \text{ T}$ . Shown in Fig.2 (a) is the plasma density and stored energy as a function of time. In this example, NBI#4 was injected from 1.1 to 1.5 sec. In Fig.2 (b), the FFT power spectrum obtained by a MP signal before the injection of NBI#4 ( $t = 1.06 \text{ sec}$ ) is plotted. And the power spectrum during the injection of NBI#4 is shown in fig.2(c). It is seen that fluctuations are excited around 71 MHz during the injection of NBI#4. The frequency of 71MHz is near the second harmonic of the ion cyclotron frequency of protons ( $2f_c \sim 82\text{MHz}$ ).

Although a high frequency fluctuation near the second harmonic of ion cyclotron frequency was observed, the systematic data accumulation is still necessary to reveal the features of the high frequency fluctuations in helical systems.

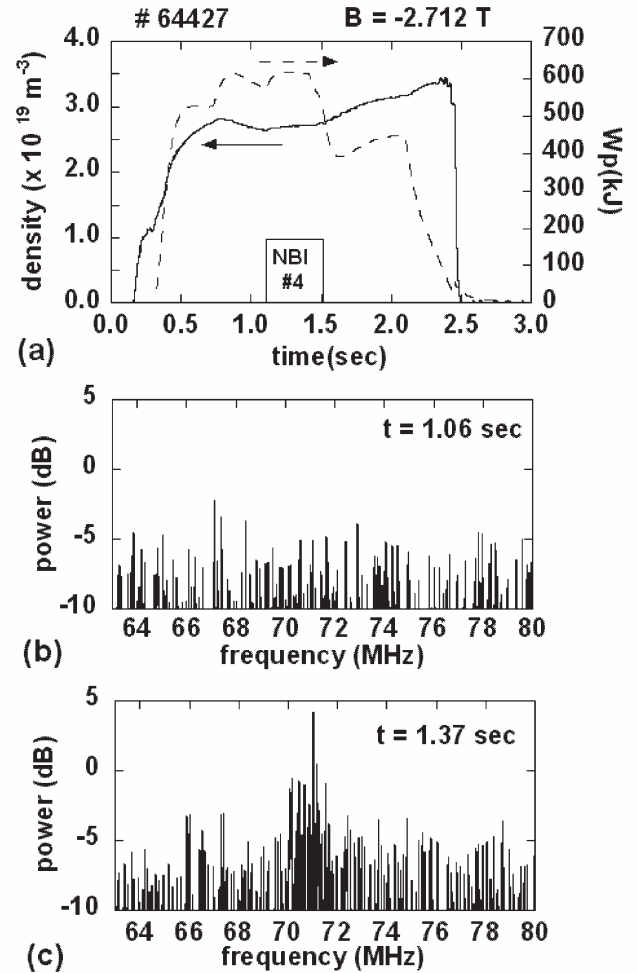


Fig. 2. (a) A plasma density and stored energy as a function of time. (b) A FFT power spectrum before the injection of NBI #4 ( $t = 1.06 \text{ sec}$ ). (c) A FFT power spectrum during the injection of NBI #4 ( $t = 1.37 \text{ sec}$ ).

### References

- 1) M.Ichimura, M.Inutake, R.Katsumata, et.al., Phys. Rev. Lett. **70** (1993) 435
- 2) G.A.Cottrell and R.O.Dendy, Phys. Rev. Lett. **60** (1988) 33
- 3) M.Seki, M.Saigusa, M.Nemoto, et.al., Phys. Rev. Lett. **62** (1989) 1989
- 4) G.A.Cottrell, Phys. Rev. Lett. **84** (2000) 2397

## §72. Study on Electron Bernstein Wave Heating in High Density Regime

Nagasaki, K., Mizuuchi, T., Kobayashi, S., Watanabe, S., Tsuji, T. (IAE, Kyoto Univ.), Igami, H. (NIFS), Murakami, M., Maekawa, T., Tanaka, H., Uchida, M. (Kyoto Univ.), Isayama, A. (JAERI), Kubo, S., Yanagi, N., Shimozuma, T., Yoshimura, Y., Notake, T., Inagaki, S. (NIFS), Idei, H. (Kyushu Univ.)

In toroidal devices, electron cyclotron heating and current drive is utilized for many purposes such as production of current free plasma, control of electron temperature profile, and suppression of MHD instabilities. Usually electromagnetic waves, the ordinary (O-) and extraordinary (X-) modes of fundamental and second harmonics are chosen because of high single pass absorption. However, these modes suffer from a cut-off density limit, preventing the ECH/ECCD scheme from accessing the high density regime. In order to overcome this problem, a mode conversion from electromagnetic waves to electrostatic waves is proposed in order to heat plasmas and drive the EC current at higher density.

Electron Bernstein waves (EBW), one of electrostatic waves, have advantage of no density limit and very high single pass absorption at electron cyclotron resonance. Theoretically an optimum launching condition for ordinary-extraordinary-Bernstein wave mode conversion process has been investigated for LHD and CHS configurations [1]. In the experiment, a crystal diode is set up to detect leak power from the vacuum chamber as a indicator of good conversion efficiency. Although this method can not measure the absolute leak power, a qualitative estimate is possible for the O-X mode conversion. Figure 1 shows the dependence of leak millimeter wave intensity on the injection angle. The detector signal intensity is dependent on both the toroidal and poloidal injection angles, indicating that the optimum injection angle exists for the leak power. This angle is a little smaller than the theoretical optimum angle under vacuum condition. This is possibly because the injected waves are subject to refraction.

We have observed a clear increase in stored energy in overdense plasma by applying 54.5GHz ECH [2]. The ECH power of 415 kW is superposed on the NBI plasma. The injection angle is set for minimum leak power and the magnetic field strength is adjusted to locate the Doppler shifted resonance around the plasma center. The time evolution of OXB heating of NBI plasma is shown in Fig. 2. The average electron density is  $4 \times 10^{19} \text{ m}^{-3}$ , which exceeds the cut-off density for the O-mode. The increase rate of stored energy depends on the magnetic field strength, suggesting the change in resonance position or change in power absorption.

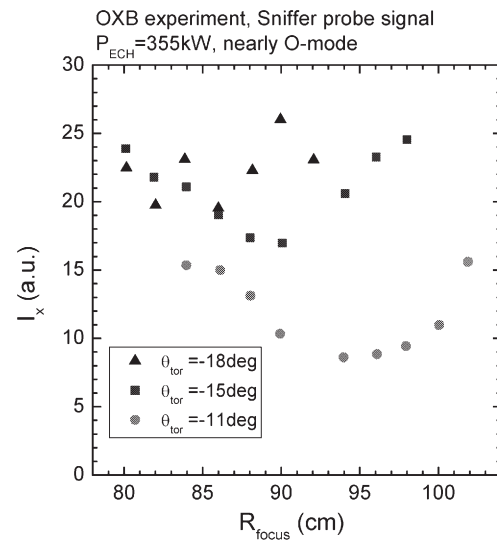


Fig 1 Leak millimeter wave signal intensity as a function of injection angle.

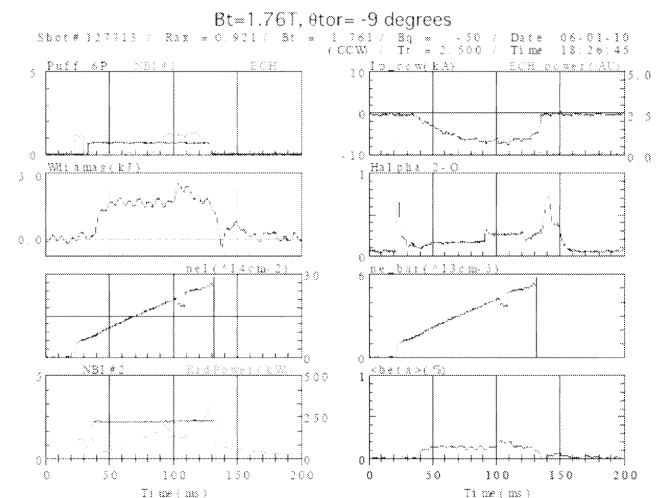


Fig 2 Time evolution of O-X-B heating in NBI plasma on CHS. The ECH power of 54GHz 415 kW is injected at high density over cut-off.

### Reference

- 1) Nagasaki, K., et al., Plasma. Phys. Cont. Fusion 44 (2001) 409
- 2) Yoshimura, Y., Nagasaki, K., et al., J. Plasma and Fus. Res. 1 (2006) 029

### §73. Excitation of Electron Bernstein Wave via O-X-B Mode Conversion Process in the Over-Dense Plasma on LHD

Igami, H., Kubo, S., Laqua, H.P. (IPP Griefswald), Nagasaki, K. (IAE, Kyoto Univ.), Inagaki, S., Shimozuma, T., Notake, T., Yoshimura, Y., Mutoh, T.

Electron cyclotron heating (ECH) by electron Bernstein waves (EBWs) excited via O-X-B mode-conversion process was demonstrated in the over-dense plasma on LHD for the first time. If the ordinary (O-) mode is injected obliquely to the external magnetic field so that the plasma cutoff point of O-mode coincides with, or is very close to the left-handed cyclotron cutoff point of extraordinary (X-) mode, it is mode converted to X-mode near the plasma cutoff then is mode converted to EBWs in the upper hybrid resonance layer. This O-X-B mode-conversion rate  $T$  is given as follows,

$$T = \exp\left\{-\pi k_0 L_n \sqrt{\frac{Y}{2}} [2(1+Y)(N_z - N_{zopt})^2 + N_y^2]\right\} \quad (1)$$

where,  $k_0 = \omega/c$ ,  $Y = \Omega/\omega$  and  $N_{zopt} = \sqrt{Y/(1+Y)}$ .  $c$  is the velocity of the light. Here we assume the slab geometry where the density increases along the  $x$  direction and the external magnetic field  $\vec{B}$  is parallel to the  $z$  direction.  $N_y$  and  $N_z$  are the  $y$  and  $z$  components of the refractive index. The injection angle is determined by the radial and toroidal focal point ( $R_{focal}$  and  $T_{focal}$ ) on the target plane on the midplane. We calculated the O-X-B mode conversion rate to investigate the mode-conversion window for the case of 84GHz wave injection for fundamental ECH. In Fig.1 (a), the calculated mode-conversion rate is shown as a contour plot versus  $R_{focal}$  and  $T_{focal}$ . In the calculation, we assumed that the edge of the electron density profile is located at  $\rho = 1.1$  and the plasma cutoff is located at  $\rho = 0.7$  in a magnetic configuration  $R_{axis} = 3.6$  m,  $B_{axis} = 2.75$  T.  $\rho$  is the normalized minor radius. In the experiment, 270 kW 84GHz microwaves were injected with 100% power modulation at 47 Hz into the target plasma sustained by 5.1 MW neutral beam injection (NBI). The magnetic configuration was  $R_{axis} = 3.6$  m,  $B_{axis} = 2.75$  T. Nearly O-mode (left handed circular polarized) and X-mode (right handed circular polarized) were injected. The line averaged electron density at the central code exceeded the cutoff density of 84 GHz,  $n_c = 8.98 \times 10^{19} m^{-3}$  during the injection. The reconstructed electron density profile from the line density profile indicates that the edge of the electron density profile is located at  $\rho \sim 1.1$  and the plasma cutoff is located at  $\rho \sim 0.7$ . We changed the focal point shot by shot as shown in Fig.1 (b). In Fig.2 (a)-(d), the modulation amplitude of the electron temperature during the modulated power injection at 47

Hz is plotted versus  $\rho$ . These results are obtained from FFT analysis of the ECE signals. The electron density was below the cut off for the frequencies used in the ECE measurement in this experiment. Focal points A, B and C correspond to the focal points A, B and C marked in Fig.1 (b). As shown in Fig.2 (a), power absorption takes place when O-mode is injected toward the focal point A, which is close to the calculated mode-conversion window. When O-mode is injected toward the focal point B, the modulated amplitude becomes smaller as shown in Fig.1 (b). As shown in Fig.2 (c), no applicable amplitude is seen in the case of injection toward the focal point C. In the case of X-mode injection toward the focal point A, as shown in Fig.2 (d), the profile of the amplitude is similar to those in the cases of O-mode injection although the peak is low. These experimental results suggest that EBWs were successfully excited and absorbed in the central part of the over-dense plasma in the case of O-mode injection toward the focal point A and B. We injected left handed and right handed circularly polarized waves instead of pure O-mode and X-mode. Therefore the injected "X-mode" waves had O-mode components to some extent and the electron temperature might rise a little as shown in Fig.2 (d) because of the absorption of the excited EBWs.

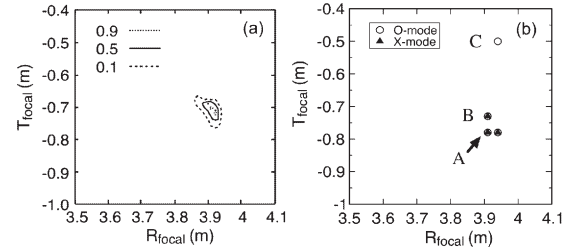


Fig. 1: (a) Calculated OXB mode-conversion rate and (b) experimental focal point setting plotted on the target plane on the midplane

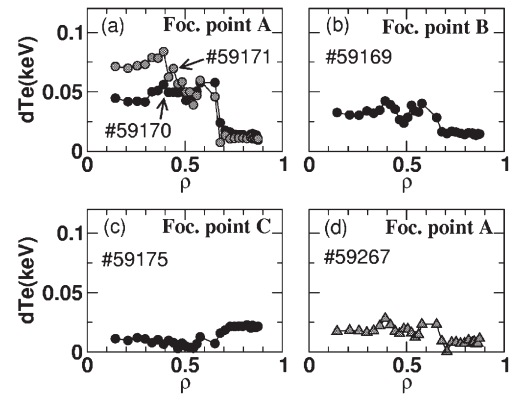


Fig. 2: Profiles of the modulation amplitude of the electron temperature. In the case of O-mode injection toward the focal point (a) A, (b) B, (c) C and X-mode injection toward the focal point (d) C.

## §74. Variation of EBW and X-Mode Absorption Profile with Changing the Electron Density

Igami, H., Shimozuma, T., Kubo, S., Nagasaki, K. (IAE, Kyoto Univ.), Inagaki, S., Notake, T., Yoshimura, Y., Mutoh, T.

In LHD, Electron cyclotron heating by electron Bernstein waves (EBWs) via X-B mode conversion process has been tried since 8th experimental campaign. When the extraordinary (X-) mode microwave beam is injected obliquely to the toroidal direction from the bottom port as shown in Fig. 1, the beam can directly access the UHR layer from the high field side and complete mode-conversion to EBWs can occur. Before the beam reaches the UHR layer, it passes the fundamental electron cyclotron resonance (ECR) layer. 350kW,

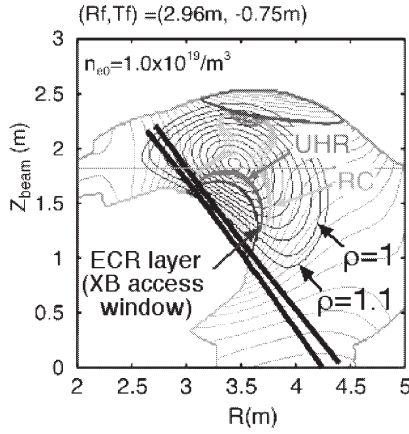


Fig. 1: Plasma and incident vacuum beam cross sections projected on the plane created by the beam vectors and the major radius R

84GHz microwave beam was injected toward the fixed focal point on the midplane as shown in Fig. 1 with 34Hz, 100% power modulation. If the electron density profile changes, the location of the UHR layer moves and the parallel refractive index of the mode-converted EBWs at the UHR layer changes. Therefore the ray trajectory and the power absorption region of EBWs can be expected to change. We changed the electron density of the target plasma to investigate the change of the power absorption profile. Thorough the experiment, the target plasmas were sustained by the neutral beam injection. The magnetic configuration was  $R_{axis}=3.6\text{m}$ ,  $B_{axis}=2.75\text{T}$ ,  $\beta=100\%$  and  $\gamma=1.254$ . The profiles of the modulation amplitude and phase of the electron temperature are plotted in Fig. 2 for each case of the line averaged central electron density  $n_{e0}$ . These profiles are obtained by FFT analysis of the ECE signals. In the case (a), (b), when X-mode was injected, double peaks were shown in the amplitude profiles. Each peak of amplitude

coincides the bottom of the phase. In the case (b), when O-mode was injected, only one peak was shown in the outer side compared to the case of X-mode injection. In the case (c) and (d) we can hardly see the double peaks and bottoms. The position of the inner peaks seems to move to the outer region as the electron density changes. These experimental results can be explained as follows. O-mode is absorbed near the ECR layer as electromagnetic waves. While, different two mechanisms of wave absorption may occur at the same time. One is the absorption as X-mode and the other might be the absorption as mode-converted EBWs. When X-mode has a finite parallel component of the refractive index, power absorption can take place even at the fundamental ECR layer. We had expected that the microwave beam of X-mode runs almost straight before it reaches the UHR layer and the power absorption in the ECR layer as X-mode is weak because the ECR layer is located in the peripheral low temperature region. However, if the plasma spreads over the region where the normalized minor radius  $\rho > 1$ , X-mode beam has possibility to be deflected and bend to the high density side. In that case, ECR layer is located at more inner side of the plasma and the absorption becomes stronger. A part of the X-mode beam is absorbed as X-mode and the rest pass through the ECR layer, then be mode converted to EBWs and absorbed at strongly doppler shifted ECR layer.

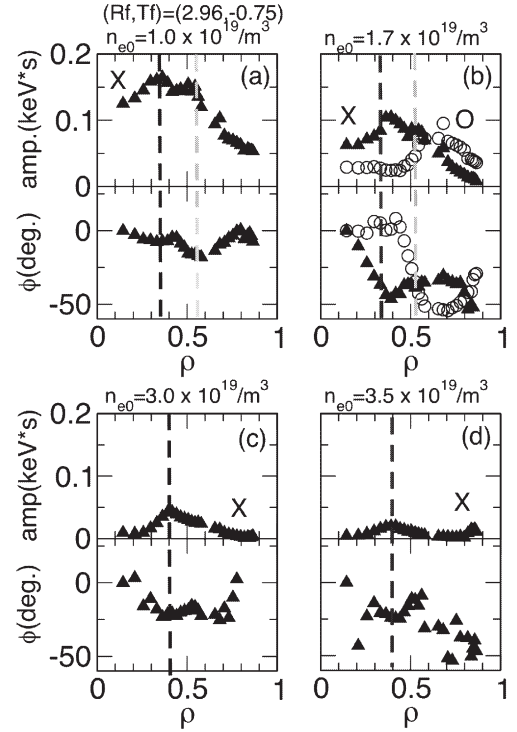


Fig. 2: Profiles of the modulation amplitude and the phase of the electron temperature for the cases of the different line averaged central electron density.



## §75. Analysis of Plasma Current Driven by Electron Cyclotron Waves

Idei, H. (Kyushu Univ.), Shimozuma, T., Fukuyama, A. (Kyoto Univ.), Notake, T., Kubo, S.

Electron Cyclotron Current Drive (ECCD) experiments have begun to investigate the effect of generated local current to MHD activities and plasma confinement in the LHD. The power deposition in the oblique injection (finite parallel refractive index  $N_{||}$ ) for the ECCD experiment was evaluated using a ray tracing code developed and modified at NIFS. Figure 1 shows the power deposition of a pencil beam in a second harmonic ECCD scenario at the magnetic field of 1.5T. The power was deposited in the central region ( $\rho \sim 0$ ). The finite Larmor radius effect in the thermal Maxwellian plasma was taken into account in the calculation. The central electron temperature was 2.5 keV. In plasmas with higher electron temperature, some relativistic effects should be included properly.

The ECCD experiments in the Lower Hybrid Current Drive (LHCD) plasma were conducted in the TRIAM-1M tokamak[1]. In the LHCD plasma, fast electrons were generated by the LH wave. The EC power deposition was evaluated using a TASK/WR code[2], including the relativistic effect. To evaluate the power deposited to the fast electrons, the velocity distribution function of the fast electrons was assumed here. The parallel and perpendicular electron temperatures for the forward fast electrons generated by the LH wave were 100 keV and 40 keV, respectively. The peak value of  $N_{||}$  at the LH launcher was 1.8, and thus, the maximum parallel energy by the LH wave was 103keV. For the backward fast electrons, both the parallel and perpendicular electron temperatures were 40 keV. The bulk electron temperature was 0.7keV. The fast electron component, which explained the observed plasma current, was 3.7%. The ratio of the density of the backward electron to that of the forward electron was 0.66. Figure 2 shows the ray trajectories and the deposition power density profile for the fundamental O-mode injection with  $N_{||} = 0.22$ . Multiple rays in the ray tracing were radiated as parallel rays from equal-area 64 segments in the radius of 1.5 times the beam size at the antenna output aperture. There was 99.5 % power of the beam in the radius. The total single absorption rate was 0.35, and the rest was absorbed by multiple wall-reflection effect. The uniform deposition power density due to the multiple reflections is also shown in the figure.

The TASK code is rebuilt to be applied to the power deposition analysis of the LHD experiment taking the relativistic effect into consideration. The helical geome-

try of the LHD will be included into the code. In order to evaluate the power deposition of the injected beam properly, the beam tracing analysis with the TASK code will be conducted in the LHD configuration as well as in the tokamak configuration. Finally, the deposition analysis will be linked to the velocity distribution analysis using Monte Carlo and/or Fokker-Plank codes to evaluate the generated current by ECCD. The TASK code can treat arbitrary velocity distribution functions in general.

This work was realized by the collaboration organized by NIFS (NIFS05KLRR005).

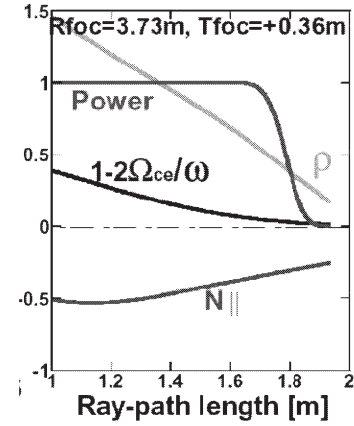


Fig. 1: Power deposition of a pencil beam at a second harmonic ECCD scenario in the LHD experiment.

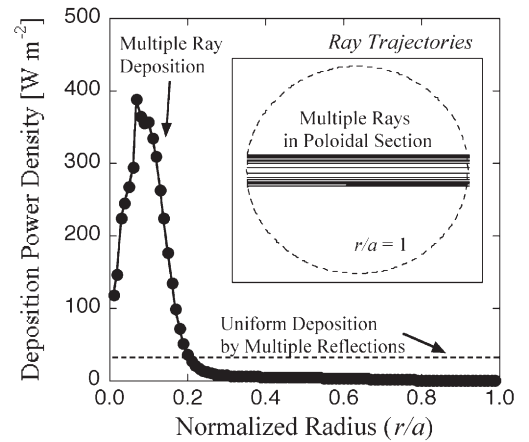


Fig. 2: Ray trajectories and the deposition power density profile for the fundamental O-mode injection with  $N_{||} = 0.22$  in the TRIAM-M experiment.

## References

- [1] Idei, H., *et al.*, Nuclear Fusion, **46**, 489 (2006).
- [2] Fukuyama A., *et al.*, Fusion Eng. and Design, **53**, 71 (2001).

## §76. Electron Cyclotron Current Drive Using 2O-port Antenna

Notake, T., Shimozuma, T., Kubo, S., Yoshimura, Y., Igami, H., Kobayashi, S., Ito, S., Mizuno, Y., Takita, Y.

A current drive can be one of strong tools to improve plasma performance even in helical devices through control of the iota-profile, magnetic shear, and suppression of some MHD activities. Non-inductive current drive using electron cyclotron waves (ECWs) propagating obliquely with respect to a magnetic field lines is possible and can localize driven current. ECWs are absorbed by electron that has velocity component satisfying the following condition considering the Doppler shift and fully relativistic effects in the mono-particle theory.

$$\frac{\omega^2 N_{\parallel}^2 + l^2 \Omega^2}{\omega^2 N_{\parallel}^2 + l^2 \Omega^2 - \omega^2} \left( \frac{v_{\perp}}{c} \right)^2 + \frac{\omega^4 N_{\parallel}^4 + 2\omega^2 N_{\parallel}^2 l^2 \Omega^2 + l^4 \Omega^4}{\omega^2 N_{\parallel}^2 + l^2 \Omega^2 - \omega^2} \left( \frac{v_{\parallel}}{c} - \frac{\omega^2 N_{\parallel}}{\omega^2 N_{\parallel}^2 + l^2 \Omega^2} \right)^2 = 1.$$

Where  $\omega$ ,  $N_{\parallel}$ ,  $l$ ,  $\Omega$ ,  $c$ ,  $v_{\perp}$ ,  $v_{\parallel}$  represent the frequency of waves, refractive index for parallel direction, harmonic number, cyclotron frequency, speed of light, perpendicular and parallel velocities of an electron, respectively. For  $N_{\parallel} < 1$  this is the equation for an ellipse and, for  $N_{\parallel} > 1$ , it designates a hyperbola in the velocity space. It is important to note that for  $N_{\parallel} < 1$  resonant interaction is impossible for

$$l\Omega/\omega > (1 - N_{\parallel}^2)^{0.5}$$

which excludes anomalous cyclotron resonance entirely. As shown in Fig.1, in the case of large  $N_{\parallel}$  injection, the resonant ellipse moves to a high parallel velocity region in momentum space due to strong up-shift of resonance. This indicates that ECWs tend to interact with an electron having high parallel velocity. So, large  $N_{\parallel}$  injection must be effective to achieve a high ECCD efficiency. Moreover, the effect of electron trapping will be significant, especially in LHD which has not only toroidal ripples but helical ones, since the diffusion in momentum space due to the electron cyclotron damping is mainly in the perpendicular direction. It reduces the ECCD efficiency or may reverse the direction of the driven current (Ohkawa effect). In order to avoid such problems, depositing the waves power in a location of ripple top is favored. Using an O-port antenna, which is installed at a horizontally elongated-cross section of LHD, is more suitable for this purpose than using an

L-port antenna, which is installed at a vertically elongated cross-section where a ripple top region exists.

In a F.Y.2005, ECCD experiments were carried out using the 2O-port antenna for the first time at a magnetic configuration of  $R_{ax} = 3.75\text{m}$ ,  $B_0 = 1.45\text{T}$ . Fig.2 shows the time evolution of hard X-ray emission measured by Ge-semiconductor and plasma current during a ctr-ECCD. A change of plasma current for reasonable direction, and intense hard X-ray emissions up to 200 keV during the ctr-ECCD were clearly observed. These results indicate that electron population having high parallel velocity were mainly accelerated selectively in weaker magnetic regions compared with the magnetic regions corresponding to the 2nd harmonic cyclotron resonance. As a result, driven current must be generated by this suprathermal electron population. Unfortunately in this experiment,  $N_{\parallel} \sim 0.4$  was fixed and linearly polarized waves were injected. To improve ECCD efficiency, these parameters must be optimized in the next experimental campaign and analyses based on the kinetic theory are prepared.

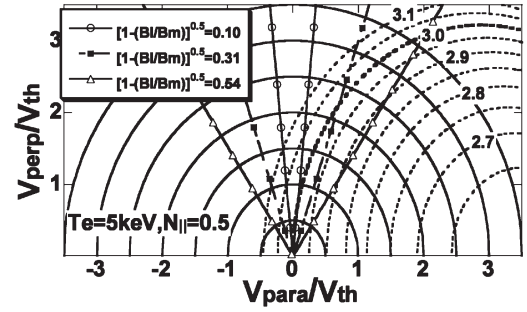


Fig.1. The ECWs resonant curve in a momentum space

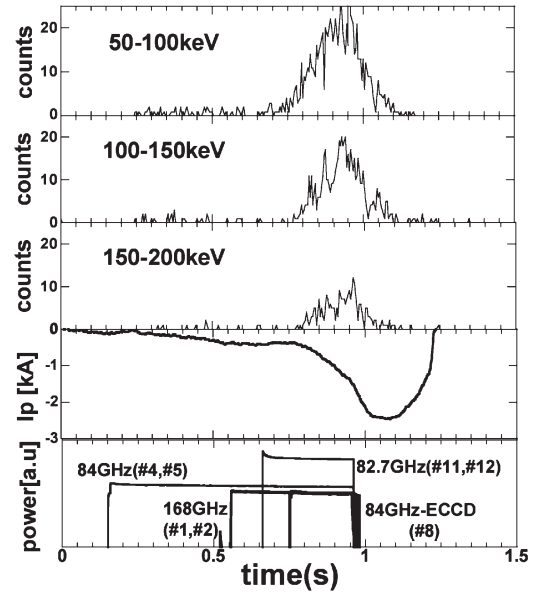


Fig.2 Temporal behaviors of HX-ray and plasma current during ctr-ECCD from 2O-port antenna.

## §77. Ray-Tracing for Electron Cyclotron Waves Propagating Obliquely with Respect to Magnetic Field Lines

Notake, T., Kubo, S., Shimozuma, T., Yoshimura, Y., Igami, H., Kobayashi, S., Ito, S., Mizuno, Y., Takita, Y.

A ray-tracing is a sophisticated tool, providing much insight on propagation and absorption of waves in plasmas. Its condition of validity is the following

$$|\nabla \vec{k}| \ll k^2$$

which states that the wavelength must not change much over a wavelength. Electron cyclotron waves in the ranges of mm-waves are sufficiently adequate for current fusion research machines. A ray-tracing code was developed for electron cyclotron heating (ECRH) in the 3-dimensional magnetic field structure of LHD [1], but in that code quasi-perpendicularly propagating waves with respect to magnetic field lines in weakly relativistic thermal plasma can only be treated.

On-axis ECRH using fundamental O-mode with 84GHz and 2nd harmonic X-mode with 168GHz from the 2O-port antenna is required for oblique injection in order to aim a electron cyclotron resonance layer at neighbor vertically elongated cross section. Because the cyclotron resonance layer doesn't across a magnetic-axis at a horizontally elongated cross section which is just positioned in front of the O-port antenna. Therefore, the existing ray-tracing code was extended so as to investigate the best condition for oblique on-axis ECRH using 2O-antenna in the LHD.

For propagation angles satisfying following condition  $N |\cos\theta| > |1 - l\Omega/\omega|, v_t/c$ , the relativistic down shift of the cyclotron frequency may be neglected because Doppler effect dominates. Where  $N, \theta, l, \Omega, \omega, v_t$  and  $c$  mean refractive index, propagation angle with respect to magnetic field lines, harmonic number, cyclotron frequency, wave frequency, electron thermal and light velocity, respectively. We can use absorption coefficients obtained from the non-relativistic dielectric tensor for a hot Maxwellian plasma [2]. In such frame, power absorption line is decided using the conventional plasma dispersion function [3] described by

$$Z(\zeta) = i\sqrt{2} \exp(-\zeta^2) \int_{-\infty}^{\sqrt{2}i\zeta} dt \exp(-t^2/2)$$

which can be calculated numerically. Here, an argument  $\zeta$  is defined as follows.

$$\zeta \equiv (c/v_t) (\omega - \omega_c) / (\sqrt{2} \omega N \cos\theta)$$

Absorption of obliquely propagating electron cyclotron

waves strongly depends on its angle, plasma density, electron temperature, wave polarization and its harmonic number. Especially, it must be cared that the propagating angle dependences for the absorption of O1 and X1 modes in the finite density region satisfying a condition

$$2N(v_t/c) |\cos\theta| < (\omega_p/\omega_c)^2$$

become inverse. Much detailed descriptions are given in the reference [2].

The oblique ECRH from 2O-port antenna was tried in the magnetic configuration of  $R_{ax}=3.75m$  and  $B_0=1.5T$  although in such configuration electron cyclotron resonance exists even in the magnetic-axis of horizontally elongated cross section. The experimentally deduced heating efficiencies from the time-derivatives of plasma-stored energy when ECRH was turned off are plotted as multiple marks in Fig.1. And, color mapping of absorption ratio obtained by the new ray-tracing code is also given. Here, horizontal and vertical axes are focal positions of toroidal and height directions of the torus respectively.  $T_{foc} = 0$  and  $\pm 0.6$  correspond to almost perpendicular injection to horizontally elongated cross section and obliquely injection to neighbor vertically elongated cross sections respectively.

It seems that a tendency of heating efficiency on injection angles is similar although the efficiencies deduced from the experiment is lower than expected those from the ray-tracing in whole region. One of causes would be inappropriate injection of linearly polarized waves in the experiment since in the case of oblique injection, polarization states should be elliptical to couple waves in free-space with them in plasma efficiently. This optimization will be performed in the 10th experimental campaign.

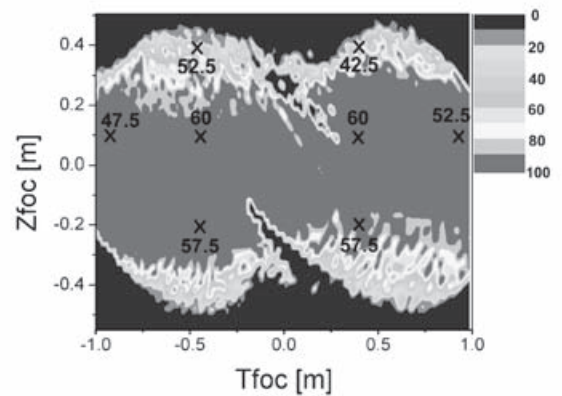


Fig.1 Comparison of absorption efficiencies between experiment and predictions from new ray-tracing code.

### References

- 1) S. Kubo, Journal of Fus. Res. Series, Vol.5 (2002)
- 2) M. Bornatciti, Nuclear Fusion, Vol.23 (1983)
- 3) B. Fried, Academic Press, New York (1961)

## §78. Study on Production of Energetic Ions in ECH/ECCD Plasmas in LHD

Kobayashi, S. (IAE, Kyoto Univ.), Osakabe, M., Isobe, M., Ozaki, T., Goncharov, P., Kubo, S., Shimoizuma, T., Yoshimura, Y., Igami, H., Muto, S., Nagasaki, K., Murakami, S. (Kyoto Univ.), Toi, K., Yamamoto, S. (Osaka Univ)

In some torus devices, tail ion has been observed only in the ECH/ECCD plasmas. These phenomena have been considered to be due to the anomalous electron-ion coupling or acceleration by LH-decay waves, however, the mechanism of the ion tail formation is still an open question.

In the 70 GHz 2nd harmonic ECH plasmas of Heliotron J, the energetic ions has been observed under the low density conditions below than  $1 \times 10^{19} \text{ m}^{-3}$ . The apparent tail temperature increases with decreasing the density. It is also found that the slope of the ion tail becomes large with the ECH injection power. In the 53 GHz ECCD plasmas of CHS, the energetic ions have been formed when the electron density was below than  $0.5 \times 10^{19} \text{ m}^{-3}$  and the toroidal plasma current was higher than 3.8 kA. Under the conditions, several modes of  $n=1$  and a mode of  $m/n=5/2$  having the frequency range from 50 kHz to 200 kHz has appeared. These modes have propagated in the ion diamagnetic drift direction and in the counter direction of the magnetic field. In these experiments, unfortunately, the plasma production and heating was done only by one ECH system.

In the LHD device, four ECH systems have been installed and various heating experiments, for example additional heating, modulation or current drive, can be performed. Figure 1 shows a typical time evolution of the averaged electron density and ion energy distribution in ECH plasmas (4 Units, 84GHz, 82.7GHz, 1MW). In the earlier phase of the discharge where the electron density was around  $0.1 \times 10^{19} \text{ m}^{-3}$ , the flux of the tail ion was observed in the energy more than 20 keV. The ion energy distribution was measured with compact NPA system. The apparent tail temperature, estimated from the slope of the energy spectrum as shown in Fig. 2, was found to be about 3 to 4 keV. The slope of the energy distribution did not depend on the electron density. Figure 3 shows the dependence of the apparent temperature and amount of the tail flux on the electron density. The obtained tail temperature was in the range from 2.5 to 5 keV and it was insensitive to the electron density, while the amount of the ion flux decreased rapidly as increasing the density. No coherent mode was observed like that obtained in CHS.

In the next experimental campaign, the ion energy distribution in the lower energy side ( $< 10 \text{ keV}$ ) will be

measured and compared with the bulk ion. The measurements of the high frequency wave will be tried in order to investigate the mechanism of the ion acceleration.

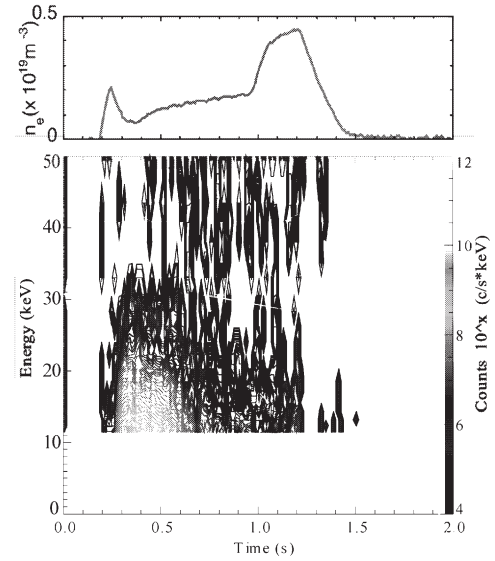


Fig. 1. Time evolution of electron density and ion flux measured with compact NPA in ECH plasmas of LHD.

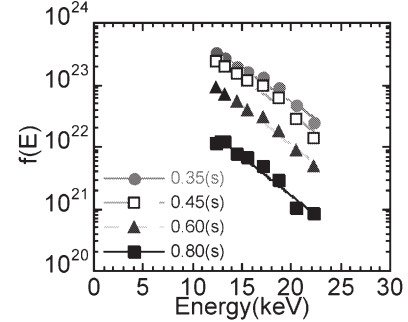


Fig. 2. Ion energy spectrum in ECH plasma.

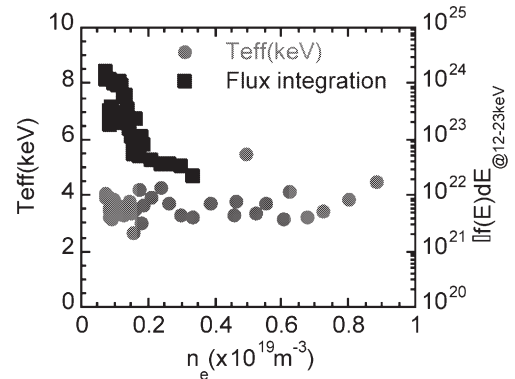


Fig. 3. Dependence of the apparent temperature of tail ion and amount of the tail flux on the electron density.



## §79. Stray Radiation Behavior Measured at Different Locations in the LHD Vacuum Vessel

Igami, H., Kubo, S., Laqua, H.P. (IPP Griefswald), Nagasaki, K. (IAE, Kyoto Univ.), Inagaki, S., Shimozuma, T., Notake, T., Yoshimura, Y., Mutoh, T.

Monitoring of the stray radiation with so-called sniffer probes 1) is helpful to confirm the effectiveness of electron cyclotron heating (ECH) absorption. If the level of the stray radiation with plasma is low as compared with that without plasma, we can guess that the injected microwave power is absorbed in the plasma. A sniffer probe consists of a stainless steel oversized wave guide antenna coupled to a spherical copper cavity. The diameter of the wave guide is several times of the vacuum wavelength, allowing many modes to propagate. All incoming waves into the integrating cavity are nearly equally coupled to the microwave detector after several reflections 1). Two sniffer probes are installed in different locations in the LHD vacuum vessel as shown in Fig.1 (a). One is installed in a horizontal port (2-O) and the other is installed in a bottom port (9.5-L). We changed 84GHz microwave beam focal point on the "target plane" on the midplane as shown in Fig.1(a) and (b), to search the good focal point to excite electron Bernstein waves (EBWs) in the over-dense plasma via O-X-B mode conversion process. In the over-dense plasma, the electron density exceeds the plasma cutoff density near the electron cyclotron resonance (ECR) layer. 270 kW microwaves were injected with 100% power modulation at 47 Hz into the target plasma sustained by 5.1 MW neutral beam injection (NBI). The magnetic configuration was  $R_{axis} = 3.6$  m,  $B_{axis} = 2.75$  T. Nearly O- and X-mode were injected. The line averaged electron density at the central code exceeded the cutoff density,  $n_c = 8.98 \cdot 10^{19} m^{-3}$  during the superimposed injection. In Fig.2 (a)-(f), the stray radiation levels at each probe are plotted for three different cases as a function of the toroidal focal point. Note that both cases of  $R_{focal} = 3.91$  m, and  $3.94$  m are included at  $T_{focal} = -0.78$  m. When the microwave beam was injected toward the focal point A, into the over-dense plasmas, the average of the stray radiation at the 2-O sniffer probe became minimal and the modulation profile of the electron temperature suggests that power absorption took place. While, the average at the 9.5-L sniffer probe did not vary significantly with changing the focal point. In the experiment, the over-dense plasma often collapsed during the discharge. As shown in Fig.2 (b), when microwaves were injected into the collapsing plasmas the stray radiation levels were high at the 2-O sniffer probe. While, the levels at the 9.5-L sniffer probe were as low as the case of the injection into the over-dense plasmas. When microwaves were injected into the vacuum, the stray radiation levels were not as high as in the

cases of the injection into the collapsing plasmas at 2-O sniffer probe, while at the 9.5-L sniffer probe, the stray radiation levels are higher than the cases of injections into over-dense plasmas and collapsing plasmas. These tendency can be explained as follows. The incident microwave beam passes close to the 2-O port. If an over-dense plasma exists in the vacuum chamber, the injected microwaves are reflected at the cutoff point in the plasma and large amount of the reflected power almost comes back around the 2-O port, except when the microwave beam successfully excite EBWs. The 9.5-L port is located in the opposite direction of the microwave beam direction. Therefore the stray radiation picked up at the 9.5-L sniffer probe may be the integration of the residual microwaves through multi reflection. When a plasma exists, the power of microwaves are gradually absorbed every time the waves are reflected on the wall and pass through the plasma. Even if the waves do not suffer the single path absorption, large portion of the injected power is absorbed in the plasma before the waves reach the sniffer probe at the 9.5-L port.

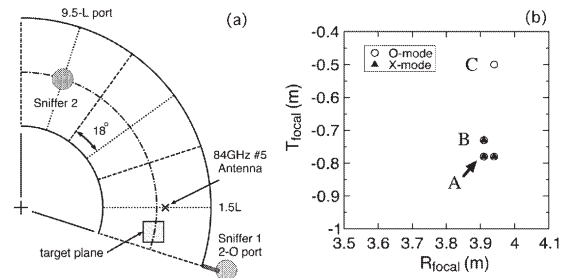


Fig. 1: (a) Positional relationship between the microwave beam injection antenna and the sniffer probes. (b) Experimental focal point setting plotted within the target plane drawn in Fig.1(a).

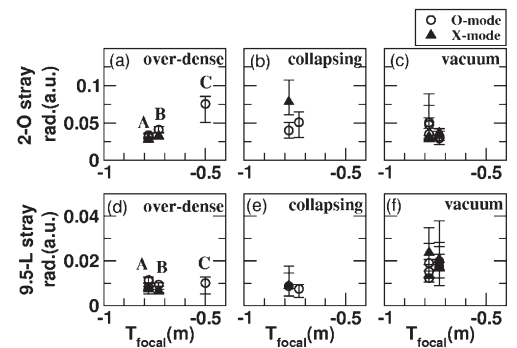


Fig. 2: Signal level of the stray radiation at the 2-O and 9.5-L sniffer probes for each case of injection into (a)(d) over-dense plasmas, (b)(e) collapsing plasmas and (c)(f) the vacuum space. Focal points A, B and C correspond to those plotted in Fig.1 (b)

### References

- 1) Gandini F et al., 2001, *Fusion Eng. Des.* **56-57** p.975-979

### (3) LHD Device Engineering Experiments

#### 1. Introduction

The LHD is the world's largest superconducting system that consists of a pair of pool-cooled helical coils (H1 and H2 coil), three pairs of forced-flow-cooled poloidal coils (IV, IS, and OV coils), nine superconducting bus-lines, a helium liquefier and refrigerator of 10 KW class, and six DC power supplies. The total weight of superconducting coils and their supporting structures is 822 ton, and the magnetic energy exceeds 700 MJ. Availability higher than 98% has been achieved in a long-term continuous operation both in the cryogenic system and in the power supply system since the first cool-down in February 1998. It will be owing not only to the robustness of the system but also to efforts of maintenance and operation. Results of device engineering experiments and the operations in the ninth cycle are summarized.

#### 2. Ninth Cycle Operation of LHD

The history of the ninth cycle operation of LHD is shown in Table 1. Main compressors of the cryogenic system started on August 19, 2005 and stopped on March 17, 2006. The total operating time was 5,035 hrs.

A major trouble in this cycle was a failure of a check valve in a water-cooling system. As supplying mass flow was suddenly reduced, a backup pump in the parallel line was started. However, the mass flow was not recovered. Since the reduction of the mass flow was caused by choking with the broken check valve, water driven by the backup pump was returned through the broken check valve. The water-cooling system finally recovered to a normal operation by closing the manual valve of the line with the broken check valve. The main compressors of the cryogenic system stopped for about two hours by this trouble, and not a small amount of helium was lost. It took three days to recover to the normal condition.

Table 1 The history of the ninth cycle operation.

Operation mode	Date
<Vacuum pumping system>	
Pumping of cryostat	8/8/2005-3/10/2006
Pumping of plasma vacuum vessel	8/9/2005-3/10/2006
<Cryogenic system>	
Purification	8/19/2005-8/30/2005
Cool-down	8/31/2005-9/26/2005
Steady state operation	9/27/2005-2/16/2006
Warm-up	2/17/2006-3/17/2006

#### 3. Device Engineering Experiments

The excitation tests of the superconducting coils before the plasma experiments were conducted from September 27 to 30. The following values were attained;

- (1) #1-o,  $B=2.70$  T @ 3.75 m (H-O/M/I = 11.25 kA)
- (2) #1-d,  $B=2.846$  T @ 3.60 m  
(H-O/M/I = 11.6/11.55/11.0 kA)

- (3) #1-d-R3.5m,  $B=2.927$  T @ 3.5 m  
(H-O/M/I = 11.6/11.55/11.0 kA)
- (4) #1-o,  $B=1.20$  T,  $\gamma=1.15$   
(H-O/M/I = 0.05/3.0/12.0 kA)
- (5) Mode transition at 11.0 kA of the helical coil.  
(radii of the plasma axis were 3.42 to 4.1 m, quadruple components were 72 to 200%)

The coil currents were almost same as the previous cycle. The definition of ramp rate was changed from T/min of the central toroidal field to A/s of the helical coil. Any normal zones were not observed in this cycle.

The device engineering experiments were conducted on the following schedule.

##### November 15, 2005

- (1) Performance examination of heaters that had been additionally installed on the outlet pipes of the helical coils for increasing the steady mass flow rate.

- (2) Measurement of loop currents decaying with a very long time constant in the poloidal coils by charging up to 2.5 T and discharging with a ramp speed of 0.2 T/min

##### November 16, 2005

- (1) Slow charge and discharge for strain measurements
- (2) Measurement of the loop currents by charging up to 2.5 T and discharging with a ramp speed of 0.1 T/min

##### November 17, 2005

- (1) Experiments of coil current control
- (2) Measurement of loop currents by charging up to 2.5 T by 0.1 T/min and discharging by 0.2 T/min

##### November 18, 2005

- (1) High power operation of the helium refrigerator

##### December 7, 2005

- (1) Excitation tests of the superconducting coils after recovering from the failure of the water-cooling system

#### 4. Summary

New achievement by device engineering experiments and operations are summarized as follows;

- (1) The soundness of the superconducting coils and the supporting structures was confirmed.
- (2) The measurement of mechanical disturbances with AE sensors was advanced. The investigation is progressing by being compared with the balance voltages of the coils.
- (3) Four Hall probes were installed near the OV coils in addition for further estimation of the magnetization of the superconducting coils. Loop currents decaying with a very long time constant were also observed near the OV coils.
- (4) It is needed to improve the thermal conductance of the new heaters at the outlet of the helical coil.
- (5) It was confirmed that the helium refrigerator had enough power to increase the mess flow of helical coil up to 50g/s and to install cold compressors to lower the inlet temperature down to 3.0 K.

(Imagawa, S.)

## §1. Influence of Magnetic Hysteresis on Quench-Voltage Detection in Large Superconducting Magnets

Takahata, K.

Here we present a technical problem caused by magnetic hysteresis in quench-voltage detection systems for large superconducting magnets. To detect a quench sensitively, it is necessary to use a balanced bridge circuit for canceling out inductive terminal voltages across a magnet. Fig. 1 illustrates a circuit diagram of the quench detection and protection systems for the LHD poloidal coils. Each pair of coils, which are symmetrically arranged with respect to the equatorial plane of the device, is connected to a dc power supply in series. Therefore, the upper and the lower coils generate the same inductive terminal voltage for all operating modes. The bridge circuit can eliminate the inductive voltage using a center tap at the joint between the upper and lower coils. Fig. 2 shows the observed output voltage from the bridge circuit when the IV coils are energized to a maximum current of 15.6 kA. Also shown is the energizing current. The graph indicates that two types of out-of-balance voltages appear. One is a mound-shaped change with a peak of approximately 10 mV (indicated by “A”). The second is a sharp spike with a peak of over 100 mV (indicated by “B”). These spikes occur only after the current has started or stopped changing. The observations suggest that the out-of-balance voltage is caused by a changing magnetization related to superconductivity.

The quench-voltage detection system can balance the voltage due to the magnetization as well as the inductive voltage if the two coils have the same magnetic properties. However, the observations of out-of-balance voltages suggest that there is a difference in magnetization between the two coils. We therefore tried to determine the conditions that reproduce the observed out-of-balance voltages using the analytical methods and assuming different magnetizations. As a result, we were able to confirm differences not only in the penetration field but also in the coupling time constant by our analysis. First, we assumed that the superconducting filaments in the upper coil have a 10% higher penetration field than those in the lower coil. Fig. 3 shows the experimental and the calculated waveforms. The comparison between these two waveforms confirms that the mound-shaped voltages, indicated by “A” in Fig. 2, are caused by the difference in penetration field between the coils. In addition, the sharp spikes, indicated by “B” in Fig. 2, can be explained by the difference in coupling time constant.

The observed out-of-balance voltages in the LHD poloidal coils can be explained by the difference in magnetization between the balanced coils. However, this phenomenon is not specific to these coils. For magnets as large as the LHD magnet system, the terminal voltage due to magnetization can influence the quench-voltage detection. To balance the terminal of two coils, it is

necessary to select coils that have the same magnetic properties.

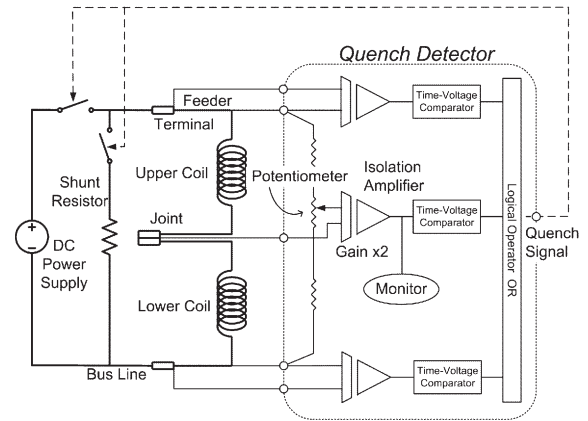


Fig. 1. Circuit diagram of the quench detection and protection systems for the LHD poloidal coils.

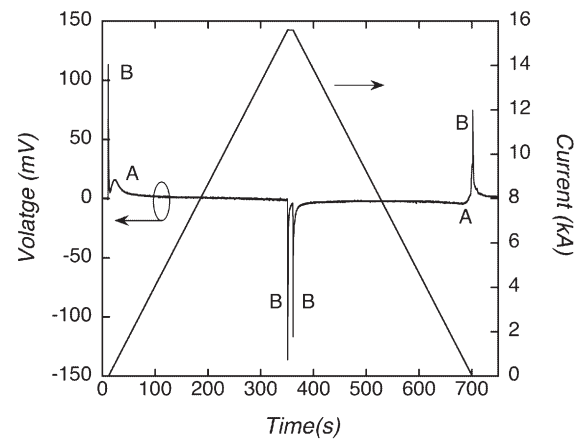


Fig. 2. Observed out-of-balance voltage in the quench detector for the IV coils. The energizing current is also shown.

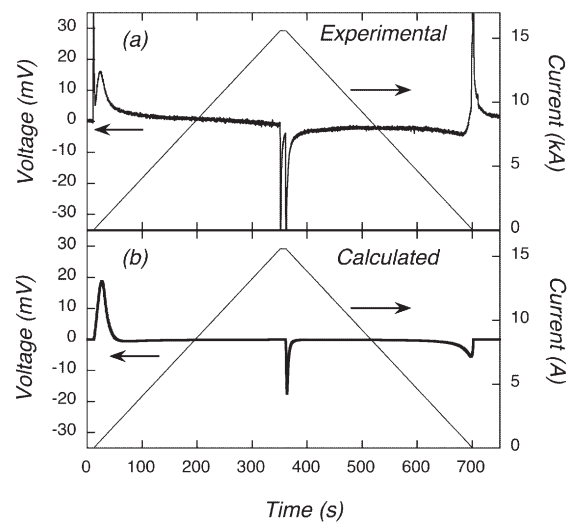


Fig. 3. Comparison of (a) experimental and (b) calculated out-of-balance voltages, assuming a difference in penetration field.

§2. Optimization of the Distribution of Mass Flow in the Helium Cooling System of the LHD

Okamura, T., Nagakura, Y. (Tokyo Tech.),  
Imagawa, S., Yanagi, N., Hamaguchi, S., Maekawa, R.

The LHD helical coil is planned to be cooled by subcooled helium to reduce the coil temperature and to improve its performance.1) The temperature of the subcooled helium rises when a heat is input.2) It is important to hold sufficient mass flow rate of subcooled helium as well as to reduce the helium temperature in this cooling system. The present helium refrigerator/liquefier for LHD is estimated to have an excess supply capacity of more than 2 kW. Helium mass flow rate of about 50 g/s can be expected to be supplied using this excess capacity.

The maximum flow rate that can be used for helical coil cooling is not clearly understood, since the cooling channels are connected in parallel for supporting structure cooling, superconducting bus line cooling, helical coil cooling, etc. The objective of the present study is to clarify the maximum flow rate for helical coil cooling or the minimum flow rate for the other components cooling by the present cooling system.

We need to evaporate liquid helium in the helical coil vessel by a heat deposition with heaters in order to obtain a flow rate more than 5 g/s of the amount of evaporation equivalent to the constant heat leakage (about 100 W), because the helical coil cooling system does not have a liquid helium return-line. At first, a performance test of these heaters has been carried out. Ten heaters were attached at the exit of the helical coil vessel before the 9<sup>th</sup> cycle test. We tried to input about 1 kW to the ten heaters to get about 50 g/s of mass flow rate of subcooled helium. But, described as follows, we could not increase the heater input power up to 1 kW because of a poor bonding of the heaters.

The temperature of Heater 4 reached 50 °C under the condition of the constant heater input power of 313 W, as shown in Figure 1. We can know from this figure that not only the Heater 4 temperature reached 50 °C but also the temperature of the all heaters continued to increase after 75 minutes' heat input. This fact suggests poor bonding between heaters and piping.

For the next step of this study, the excess capacity of the helium refrigerator/liquefier has been measured. We have gradually increased the liquefaction rate by increasing the mass flow rate through turbines T1-T3 and T4-T5. While the liquefaction rate has been increasing, the liquid helium level in the storage vessel has been kept constant at the present value (22%) by enhancing the heat input power to a heater in the storage vessel.

The helium mass flow rate in the cold box has been increased from 700 g/s to 760 g/s spending three hours. As a result, we could increase the excess capacity of the refrigerator/liquefier from 1.37 kW to 2.19 kW keeping the liquid helium level in the storage vessel constant. In this period, the mass flow rate from the compressor was kept constant, while the flow rate in the cold box was increased corresponding to the decrease in flow rate in the by-pass circuit. The flow rate in the by-pass circuit was 310 g/s when the flow rate in the cold box was 760 g/s. This means that the compressor has sufficient margin in its capacity for this refrigeration power enhancement.

Since the required refrigeration capacity for helical coil cooling is estimated to be 1.6 kW, more than 0.5 kW of refrigeration capacity can be used for supporting structure and superconducting bus line cooling. This result means that we can supply a sufficient amount of subcooled helium to the helical coil maintaining the present level of the refrigeration capacity for the cooling of the other parts.

We will clarify the optimal distribution of the helium mass flow rate in the cooling system when the flow rate of 50 g/s for the helical coil is kept after the repair of bonding the heaters.

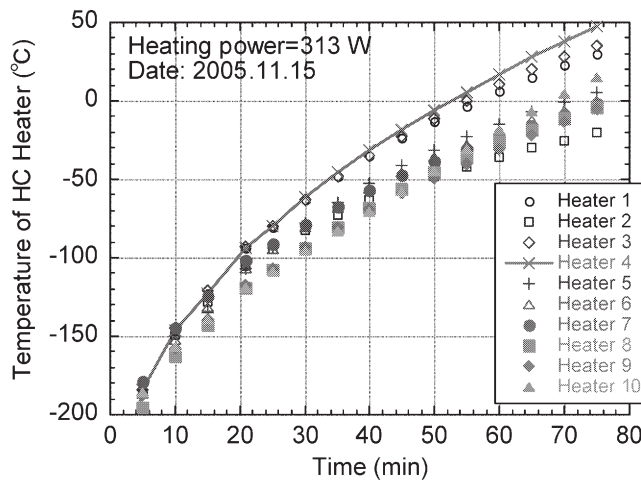


Fig. 1. Temperatures of HC heaters at heating power of 313 W.

- 1) Imagawa, S., et al., Fusion Engineering Design, to be published.
- 2) Hamaguchi, S., et al., IEEE Trans. on Applied Superconductivity 14 No. 2 (2004) 1439.



### §3. Monitoring and State Estimation of the LHD Coil

Ishigohka, T., Uriu, Y., Ninomiya, A. (Seikei Univ.), Mito, T., Imagawa, S., Yanagi, N., Sekiguchi, H., Yamada, S.

The normal zone expansion mode of the LHD coil is relatively complex. According to Yanagi et al., the behavior of the normal zone in the helical coil of the LHD includes, (1)expansion, (2)reduction, and (3)keeping constant level with one directional traveling<sup>2)</sup>. For such a complex phenomenon, a highly sophisticated quench protection system is necessary. So, the authors propose a quench protection scheme taking into consideration (1)the resistive voltage of the coil, (2)the velocity of the normal zone expansion, and (3)the effective stored heat in the coil.

The state of the coil can be estimated using; (1)the resistive voltage  $V_{res}$ , (2)velocity of normal zone expansion, or (3)effective stored heat. Among them, the resistive voltage  $V_{res}$  has a fundamental importance. It is almost proportional to the heat dissipation (Watt) in the coil. Through a careful observation of the resistive voltage (Fig. 1), we can conclude that the quench decision should be done as soon as possible if the resistive voltage exceeds the criterion voltage of 40 mV. This value corresponds to the normal zone length of 35 m for the coil current of 11.45 kA. Because the length of the conductor for 1 turn of H-I coil is 35 m, this value means the normal transition of 1turn length.

The velocity of normal zone expansion is also an important factor for the decision of quench. It is almost proportional to the derivative of the resistive voltage of the coil. In general, derivative of coil voltage includes large noises. However, in the case of H-I coil the noise can be suppressed by a smoothing process applying a moving averaging technique. In Fig. 2, we can recognize a clear large signal just after 2600 s. In this case, the appropriate quench decision threshold value for the velocity of normal zone expansion should be 3 m/s.

Effective stored heat in the coil is another important factor. This factor is obtained by an integration of the resistive voltage. So, fundamentally this factor is strong to noises. According to the experimental data shown in Fig. 3, the threshold value of quench for this factor would be 50 J.

As mentioned above, the criterions of the quench decision for each factor are summarized in Table 1<sup>2)</sup>. Applying these criterions to the experimental data shown in Fig. 1, 2, and 3, we can actuate the emergency shutdown process about at  $t = 2601$  s well before the full quench.

Thus, the authors proposed a quench protection scheme introducing some intelligent data processing techniques on the voltage signal of the helical coil of the LHD system. The conclusions are summarized as follows.

(1) A careful noise reduction effort to obtain a reliable resistive voltage is essential.

(2) Other than the resistive voltage, the velocity of normal zone expansion, and the effective stored heat would be effective as new criterion for the quench.

(3) Applying these new quench decision criterions for the LHD system, a full quench can be avoided.

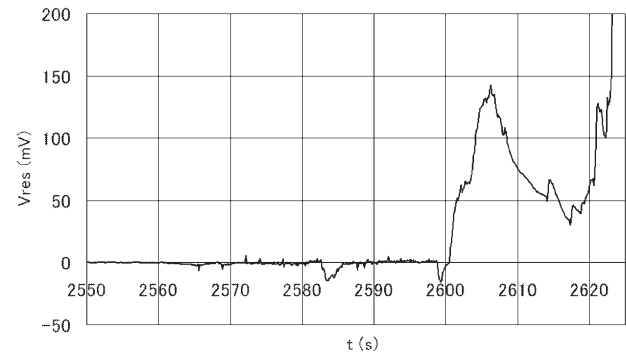


Fig. 1. Resistive voltage of H-I coil.

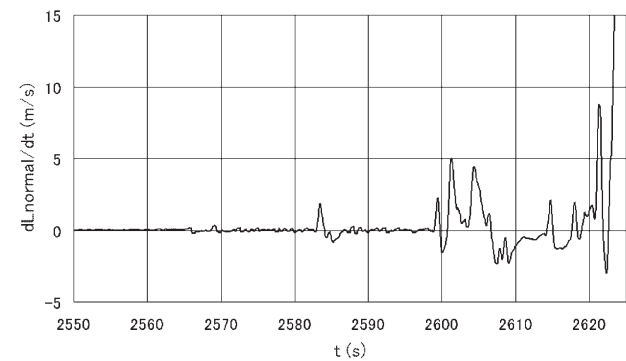


Fig. 2. Normal zone expansion velocity of H-I coil.

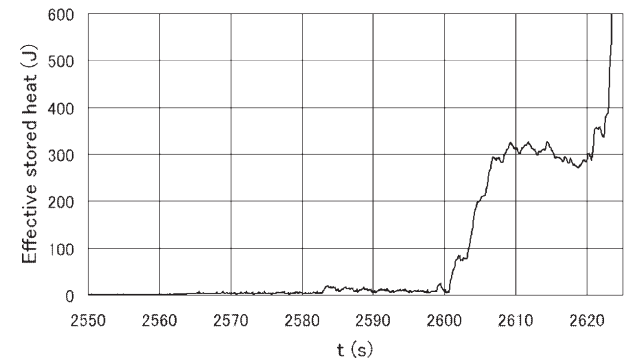


Fig. 3. Effective stored heat of H-I coil.

Table 1. Quench decision criterion of H-I coil.

Resistive voltage	40 mV
Normal zone expansion velocity	3 m/s
Effective stored heat	50 J

#### Reference

- 1) N. Yanagi, S. Imagawa, Y. Hishinuma, et al., IEEE Transactions on Applied Superconductivity, 14, (2004) 1507-1510.
- 2) T. Ishigohka, T. Mito, S. Imagawa, N. Yanagi, H. Sekiguchi, S. Yamada, "Protection of LHD coils by intelligent observation of voltage signals", Presented at ITC-15, Dec. 2005.

#### §4. Open-Loop Excitation and Electrical Parameter Estimation of LHD Superconducting Coils

Chikaraishi, H., Takami, S., Inoue, T., LHD Group, Ise, T. (Osaka Univ.)

In the LHD experiments regarding plasma current, the change of plasma current induced voltages to the coils and the coil current controller produced counter voltage to regulate the coil currents. These counter voltages induced a plasma one-turn voltage and affected the plasma current. This induced one-turn voltage depends on the current control scheme, and smaller one-turn voltage is expected in some plasma experiments. The use of an open loop-system, which involves no feedback of coil currents, is possible way to remove this effect. The design of such an open-loop system must take into account accurate electrical parameters of the inductance matrix and resistances of the coil system.

For this purpose, we estimated the circuit resistance from the steady state controll error of the coil current. Next, we estimated inductance matrix of the LHD coil with following way. Figure 1 shows waveforms when the HO coil current reference was changed. In the figure, the current drift was rejected. The coil current change  $\delta i$  and its reference  $\delta i^*$  have a relation of  $L\delta i = L^*\delta i^*$ . When we use six different references, the inductance matrix can be estimated as  $L = L^*\delta i^*\delta i^{-1}$ .

First, we measured the current drifts with open loop control to confirm the new estimated equivalent resistance. Figure 2 shows the current waveforms. For comparison, we set  $v^*$  to zero while  $40 < t < 100$ . All currents drifted in the same way when  $v^*$  was set to zero. In the open-loop controller with the new estimated resistances, the drift of the HM coil current was almost 0 A, and the HO and HI currents drifted the opposite way. The drift of the average coil current was well compensated using the new estimated resistance. Small estimation errors remained in the resistances and lead the coil current unbalance, which are sensitive to voltage error. Even though small current drifts about 20 A during 60 s operation occur, they are sufficiently smaller than the operation current of 866 A, and thus do not interfere with the power supplies.

Next, we tested the new inductance matrix. Figure 3 shows the test results using the previous inductance matrix and Figure 4 shows the results using the new matrix. With the new parameter, the turbulences of HM and HI coil currents were suppressed to 5A as shown in Figure 4. With these results, the new estimated inductance matrix has a closer fit to the actual inductance matrix than the previous one. In both figures, the waveform of the HO coil current shows offset of 5 A and a small over-shoot when the current ramps down. These offset and over shoot are caused by the induced voltages due to the change of the eddy current flowing in the structure. When more accurate control is required for

this control scheme, the effect of eddy current should be considered in the controller's design.

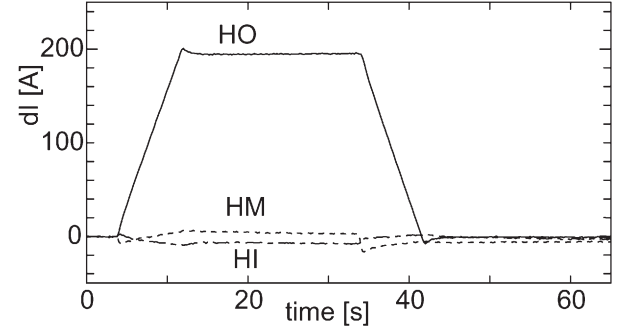


Figure 1. Current response using open loop controller

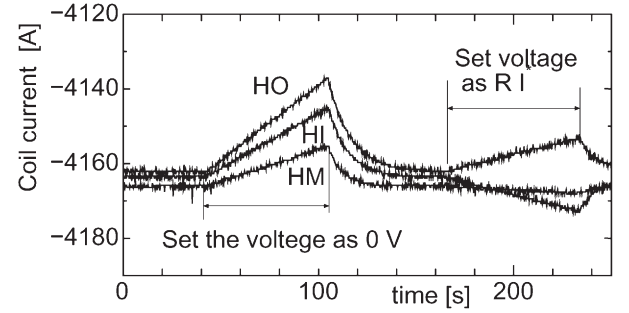


Figure 2. Current drift when open loop controller with new estimated parameters is used

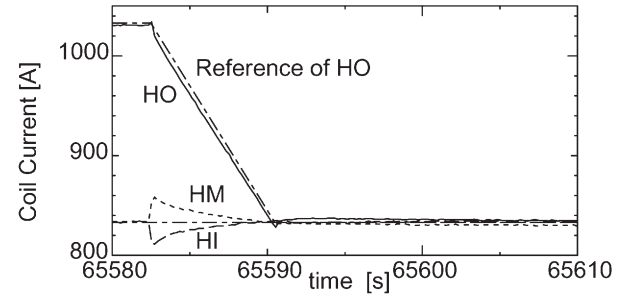


Figure 3. Current waveforms when the previous inductance matrix is used in the controller

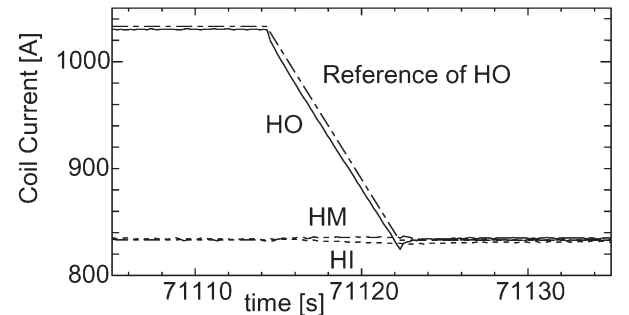


Figure 4. Current waveforms when the new estimated inductance matrix is used in the controller

## §5. Strain Measurement of Cryogenic Support Structure of LHD

Nishimura, A.

The strain measurement of the Large Helical Device (LHD) has been conducted from the first cool down in 1998. In the plasma experiment period, slower ramp-up and ramp-down tests to/from 2.85 T were performed to evaluate the strain on the equator of the cryogenic support structure of LHD keeping AC losses small.

The strain measurement system was already reported and some results were published before [1-4]. The location of the strain gages and the structure of data acquisition system are able to be referred to these papers.

In the 9<sup>th</sup> cycle of plasma experiments in 2005, the strain measurement with slower ramp rate was carried out twice on September 30 and November 16. The strains in toroidal and poloidal directions on inner and outer equators are summarized in Fig. 1 and 2, respectively. In these figures, the horizontal axis shows the sector number (The LHD cryogenic structure consists of ten sectors), and the vertical axis is the strain. The minimum measurable strain is  $2.5 \times 10^{-6}$  strain ( $\mu\epsilon$ ) because it corresponding to one digit. Since  $\pm 3$  digits are considered to be the scatter,  $\pm 7.5 \mu\epsilon$  is the scatter in strain. In Figure 1, the new data on the sector 10 (HSNE3012) shows the lower results over the scatter. The data obtained on September 30 and November 16 were the same of  $27.5 \mu\epsilon$  and the older data was about  $42.5 \mu\epsilon$ .

To investigate the reason for the different strain behavior, the outputs of HSNE3013 and 3014 were studied, for the tri-axial gage, 3012, 3013 and 3014, was used. If the active mechanical strain should change actually, some changes will occur on other two gages. As shown in Fig. 3 and 4, when the outputs are compared with the old data on October 4, 2000, it is clear that only the HSNE3012 shows the different output behavior from before. Therefore, it is considered that dummy gages for HSNE3012 or gage- leads must be damaged and such output was generated.

The measurement will be performed in the next cycle.

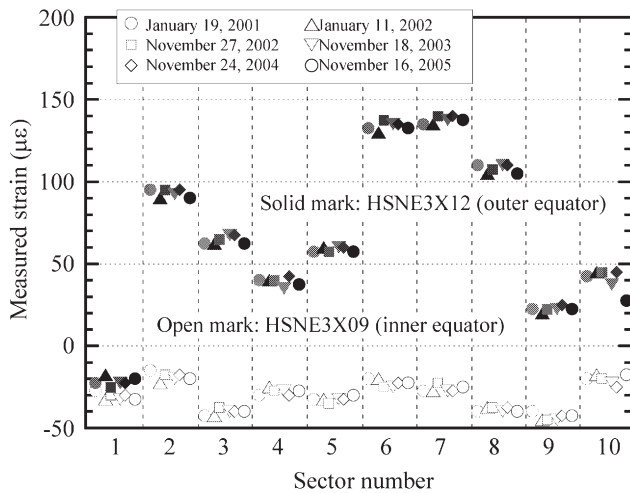


Fig. 1 Change in toroidal direction strain measured.

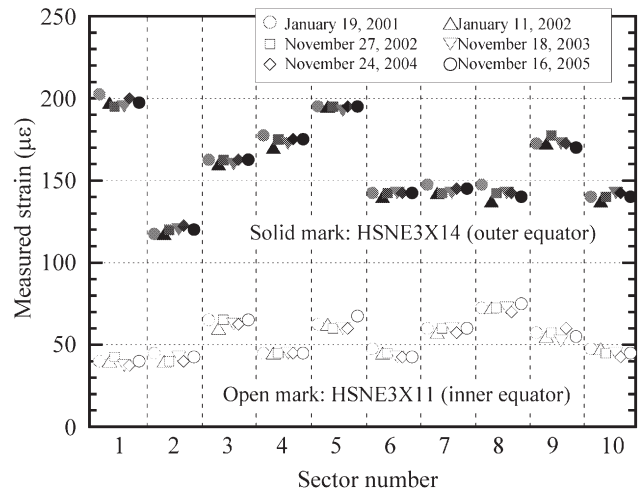


Fig. 2 Change in poloidal direction strain measured.

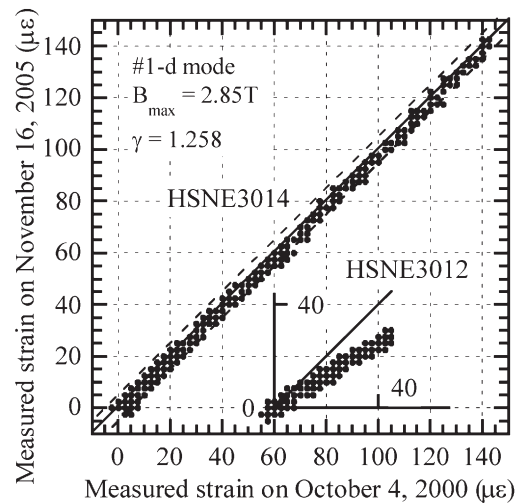


Fig. 3 Comparison of strains of HSNE3014 and 3012.

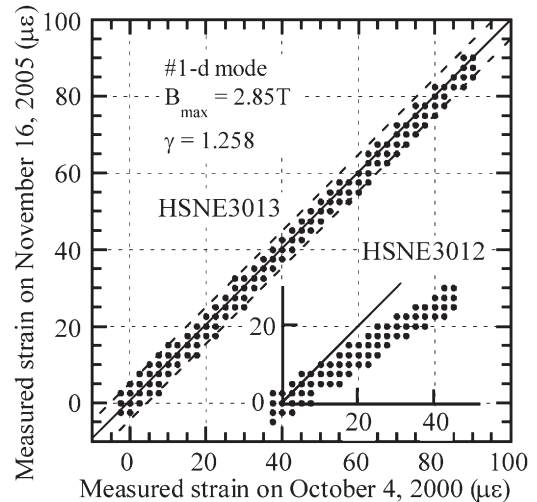


Fig. 4 Comparison of strains of HSNE3013 and 3012.

### Reference

- 1) A. Nishimura et al., Adv. in Cryo. Eng., 45 (2000) 745.
- 2) A. Nishimura et al., Fusion Eng. & Design, 58-59 (2001) 253.
- 3) A. Nishimura et al., J. Plasma Fusion Res. SERIES, 5 (2002) 250.
- 4) A. Nishimura et al., Fusion Eng. & Design, 66-68 (2003) 1087.

## §6. Upgrading Program of LHD Helical Coils by Subcooling

Imagawa, S., Yanagi, N., Hamaguchi, S., Mito, T.

Helical coils of the Large Helical Device are pool-cooled superconducting magnets. Methods for improving their cryogenic stability have been examined. Considering the withstanding voltage of the coil and the possibility of air mixing, the method of being subcooled was selected. In order to mitigate the modification, cold compressors were selected as shown in Fig. 1, and the design values of the mass flow and the inlet temperature are 50 g/s and 3.1 K, respectively, by utilizing the surplus power of an existing helium refrigerator. The average temperature of the helical coil is expected to be lowered to 3.5 K. Remodeling is progressing, and it will be completed by August in 2006.

In order to estimate the effect and to demonstrate the subcooling system, a test facility with cold compressors was assembled, and cryogenic stability tests have been carried out with a model coil. In subcooled helium, the minimum current for dynamic propagation of a normal-zone  $I_{(mp)}$  increases in proportion to the degree of sub-cooling from 11.2 kA at the saturated temperature of 4.4 K to 11.7 kA at 3.5 K. This improvement is considered to be caused by the slightly higher heat flux in the convection and nucleate boiling region at the lower temperature of helium. In saturated helium, the  $I_{(mp)}$  varies from 10.7 to 11.2 kA, and the cryogenic stability is divided into two groups[1]. The well-cooled condition was attained by being subcooled once, and it continued even after the coil quench. The reason is not understood well, but the wetting area at the narrow space between the conductors and the spacers could be improved. From analyses of propagation velocities with the quasi-static heat balance equation, the equivalent heat transfer coefficient  $h$  in saturated helium before being subcooled is estimated to be 0.50 kW/m<sup>2</sup>/K, and it is improved by 20% after being subcooled. Furthermore, it is improved by 30% by being subcooled to 3.5 K.

The propagation velocities in the LHD helical coils can be estimated from the time difference of peak voltage induced in pick-up coils along the helical coils. Figure 2 shows the distribution of the propagation velocities for the 14th to 16th propagation of a normal-zone. The velocity is faster at the higher magnetic field. All the initiated positions for 10th to 17th propagation are near the bottom of the coil, where the field is not the highest. Therefore, the cooling condition around the innermost high field layers is considered to be deteriorated at the bottom by accumulated bubbles. The average  $h$  of the helical coil for the 14th to 16th propagation is estimated to be 0.39 to 0.43 kW/m<sup>2</sup>/K by the same equation with the absolute magnetic field. Therefore, the present cryogenic stability of the LHD helical coil is considered to be worse than the model coil before being subcooled. It will be caused by worse quality, which is the higher ratio of gas to liquid, of inlet helium due to a long connection line.

Figure 3 shows the load lines and the minimum currents for propagation of the model coil and the helical coil. If the helical coils are cooled down to 3.5 K, the operating current is expected to be increased to 12.0 kA that corresponds to 3.0 T at the major radius of 3.6 m.

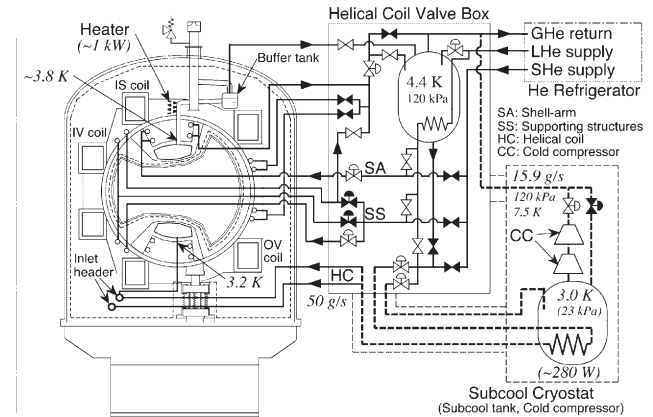


Fig. 1. Flow diagram of the helical coil and supports. The additional flow lines are drawn with dashed lines.

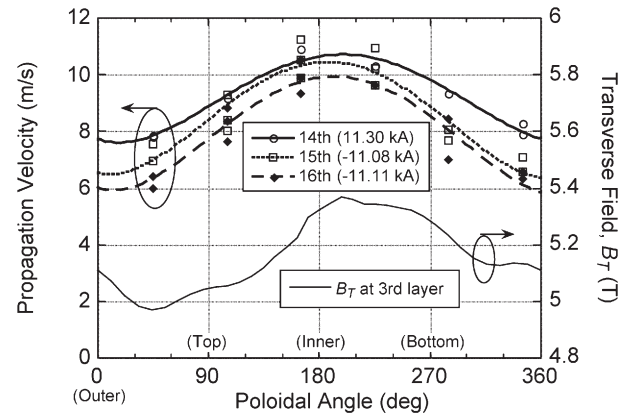


Fig. 2. Temperature dependence of minimum currents for dynamic propagation of a normal-zone in the R&D coil.

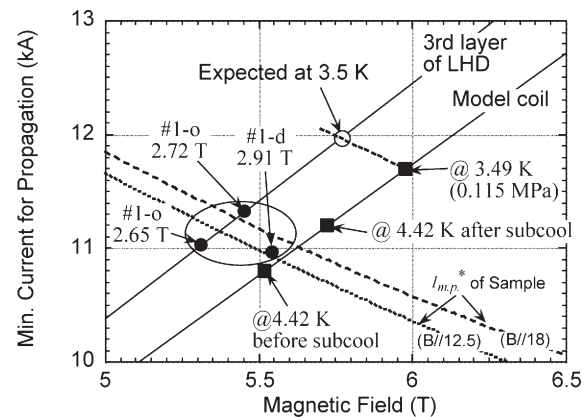


Fig. 3. Minimum current for a normal-zone propagating in the LHD helical coil and the model coil. The maximum field of the LHD helical coil is in the last turn of the third layer where normal-zones were considered to be initiated.

### Reference

- 1) Imagawa, S. et al.: IEEE Trans. Appl. Supercond., 16 (2006) 755.



## 1-2. Device Engineering and Cooperative Development Research

### (1) Physics and Engineering of LHD Torus System

The Compact Toroid (CT) injector of SPICA (SPeromak Injector using Conical Accelerator) has been developed for an advanced refueling in LHD. Through experimental results, the SPICA device has achieved CT parameters to penetrate into LHD plasmas at  $B = 0.8$  T. However, after considering CT transport in long distance to plasma central region and CT injection into LHD plasmas at higher  $B$ , the injector performance needs to be enhanced much more.

In this fiscal year, we have conducted the experiments with a focus on surveying the basic CT parameters to clear the requirements for the improvement of the SPICA device. As the first step, the electrodes for CT acceleration were shortened to half, and then a flux conserver (FC) and a compressor, which were provided from the other CT injector, were connected to the exit of the SPICA. The preliminary tests indicated that CT plasmas could not move into the FC owing to worse-than-expected CT deceleration through the compressor. Thus we designed and made a new FC to be directly connected to the SPICA device without the compression part. The ratio of inner diameter to length was determined at 720/400 based on an obtained equilibrium solution for sphromak. The experimental setup with the new FC is shown in Fig. 1. PIN diodes were mounted at port P1-P4 for the observation of CT transit to calculate CT speed. In the FC, the He-Ne laser interferometer measured the line-averaged electron density of a CT plasma. The magnetic probe arrays also provide magnetic field profile measurements of the CT.

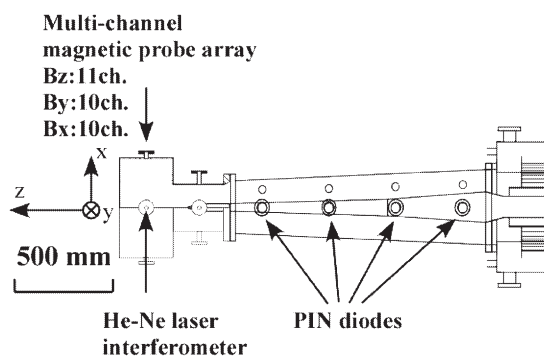


Fig. 1. Measurement system for SPICA device and flux conserver.

Vanadium alloys are potential candidates of low-activation structural material for fusion blanket. In order to understand the plasma-surface interactions of vanadium alloys, the surfaces of V-4Cr-4Ti alloy specimens exposed to LHD plasma were analyzed by means of Auger electron spectroscopy, Raman spectroscopy and X-ray diffraction. No harmful modification of the alloy took place by the exposure to LHD plasma at around room temperature. It was difficult to understand the interaction between hydrogen plasma and the alloy under the present conditions because of the masking effects by deposited layer. In addition, vanadium alloys would be exposed to plasma at elevated temperatures (e. g. 600 °C) in future fusion reactors. The reaction between constituent elements of the alloy and deposited materials may take place at such temperatures. These effects could be investigated through the optimization of experimental condition by, for example, using material probe system of LHD.

Boronization and titanium flash have been employed to reduce fuel hydrogen recycling and oxygen impurity concentration in plasma. If both boronization and titanium flash are conducted, the boron-titanium is produced on the first wall surface. The fuel hydrogen retention of this material has not been investigated so far. In the present experiment, the boron-titanium was prepared using electron beam evaporation, and irradiated by deuterium ions. After the deuterium ion irradiation, the deuterium retention and desorption behavior was investigated. The present results suggest that both fuel hydrogen retention and a baking temperature required for reduction of hydrogen retention can be reduced by an use of boron-titanium. A further study will be conducted to clarify the reason why the boron-titanium has a low desorption temperature by using surface analysis techniques.

(Ohyabu, N.)

## §1. Improvement of Compact Torus Injector for Fuelling LHD

Fukumoto, N., Nagata, M. (Univ. Hyogo),  
Masamune, S., Sanpei, A. (Kyoto Inst. Tech.),  
Takahashi, T., Asai, T. (Nihon Univ.),  
Irie, M. (Waseda Univ.),  
Miyazawa, J., Yamada, H.

The Compact Toroid (CT) injector of SPICA (SPeromak Injector using Conical Accelerator) has been developed for an advanced refueling in LHD. Through experimental results, the SPICA device has achieved CT parameters to penetrate into LHD plasmas at  $B = 0.8$  T. However, after considering CT transport in long distance to plasma central region and CT injection into LHD plasmas at higher  $B$ , the injector performance needs to be enhanced much more.

In this fiscal year, we have conducted the experiments with a focus on surveying the basic CT parameters to clear the requirements for the improvement of the SPICA device. As the first step, the electrodes for CT acceleration were shortened to half, and then a flux conserver (FC) and a compressor, which were provided from the other CT injector, were connected to the exit of the SPICA. The preliminary tests indicated that CT plasmas could not move into the FC owing to worse-than-expected CT deceleration through the compressor. Thus we designed and made a new FC to be directly connected to the SPICA device without the compression part. The ratio of inner diameter to length was determined at 720/400 based on an obtained equilibrium solution for sphromak. The experimental setup with the new FC is shown in Fig. 1. PIN diodes were mounted at port P1-P4 for the observation of CT transit to calculate CT speed. In the FC, the He-Ne laser interferometer measured the line-averaged electron density of a CT plasma. The magnetic probe arrays also provide magnetic field profile measurements of the CT.

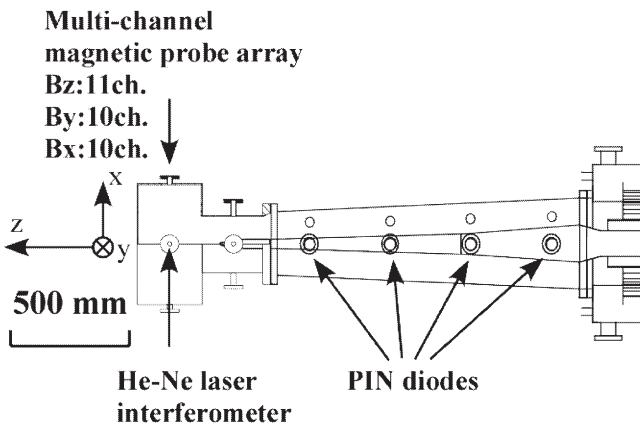


Fig. 1. Measurement system for SPICA device and flux conserver.

Figure 2 shows the typical time evolution of PIN diode signals and the CT density for the current fed through the bias poloidal coil  $I_{\text{bias}} = 210$  A, the charging voltage on the formation bank  $V_{\text{form.}} = 8$  kV, the voltage on the acceleration bank  $V_{\text{acc.}} = 12$  kV. Here, CT speeds are estimated at 126 km/s between VL2 and VL3 (P2 and P3) and 56 km/s between VL3 and VL4 (P3 and P4). The peaked CT density is  $9.6 \times 10^{20} \text{ m}^{-3}$  in the FC. In addition, the magnetic field profile in the FC indicated a typical sphromak configuration. In these experiments the noise in observed signals, which occur when CT plasmas eject from the SPICA device, are extremely lower than those in previous experiments. This is considered to be due to change of acceleration current pathway at the time of separation of the current and the CT plasma ejecting from the muzzle of the SPICA. Therefore we have investigated the adverse effects of long electrodes in the experiments with different length accelerators. Decrease of noise level allows us to operate the SPICA device at higher voltage on the CT accelerator bank, leading to enhancement of CT parameters.

On the measurement system, we have modified the He-Ne interferometer to add one more channel in order to investigate the density decay in a CT plasma moving through the accelerator into the FC. As future works, we will measure CT parameters and magnetic field profiles to investigate the dependence on the operation parameters (the trigger timings of gas-puffing, formation and acceleration, the duration of the gas-puffing, the bias poloidal (BP) magnetic field, and the charging voltages of the formation and acceleration capacitor banks) on the any stages of CT formation, acceleration, ejection and transportation. Moreover, a BP coil will be added on the SPICA injector. Various systematic scan of the CT operation parameters will be conducted to find suitable positions of the BP coil and the gas puff valves for CT formation and acceleration. The SPICA injector will be effectively improved through the series of experiments.

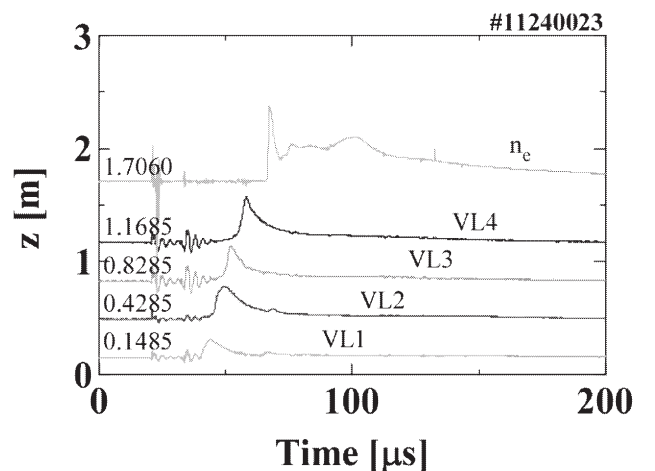


Fig. 2. Typical evolution of PIN diode signals in the acceleration region and line-averaged electron density in the FC.

§2. Hydrogen Retention in Vanadium Alloy Exposed to Hydrogen Plasma

Hatano, Y., Hara, M. (Univ. Toyama), Ashikawa, N., Nagasaka, T., Sagara, A., Muroga, T.

Vanadium alloys are potential candidates of low-activation structural material for fusion blanket. In order to understand the plasma-surface interactions of vanadium alloys, the surfaces of V-4Cr-4Ti alloy specimens exposed to LHD plasma were analyzed by means of Auger electron spectroscopy, Raman spectroscopy and X-ray diffraction.

Sheet type specimens of a V-4Cr-4Ti alloy (NIFS-HEAT-2) were placed on the first wall of LHD during 6th cycle experimental campaign and exposed to plasma at around room temperature. After the experimental campaign, the specimens were analyzed with a scanning Auger microscope in Institute of Nuclear Safety System and Raman Spectrometer in Kyushu University. X-ray diffraction analyses were carried out in Toyama University.

Fig. 1 shows a typical example of secondary electron images of specimen surface. Particles giving dark contrast were observed as indicated by an arrow in this figure. The size of such particles was about 10  $\mu\text{m}$  or smaller. Carbon was sole element detected by point analysis of such particles by Auger electron spectroscopy (Fig. 2). A typical Raman spectrum obtained by point analysis of the particle is shown in Fig. 3. All peaks observed were assigned to C-H vibrations and not to C-C vibrations. These results indicate that the particles giving dark contrast are co-deposits of carbon and hydrogen formed as a result of erosion of divertor plates.

A typical example of Auger spectra of matrix is shown in Fig. 4. No constituent element of specimen (i. e. V, Cr and Ti) was detected, whereas large peaks of carbon, oxygen and iron were observed. Such depositions of carbon and iron were ascribed to the erosion of divertor plates and first wall, respectively. Analysis of matrix by means of Raman spectroscopy was impossible because the deposited layer was too thin.

No peak of reaction product between constituent elements of the alloy (V, Cr and Ti) and deposited materials (C and Fe) was observed in X-ray diffraction pattern. Namely, no harmful modification of the alloy took place by the exposure to LHD plasma at around room temperature.

It was, however, difficult to understand the interaction between hydrogen plasma and the alloy under the present conditions because of the masking effects by deposited layer. In addition, vanadium alloys would be exposed to plasma at elevated temperatures (e. g. 600  $^{\circ}\text{C}$ ) in future fusion reactors. The reaction between constituent elements of the alloy and deposited materials may take place at such temperatures. These effects could be investigated through the optimization of experimental condition by, for example, using material probe system of LHD.

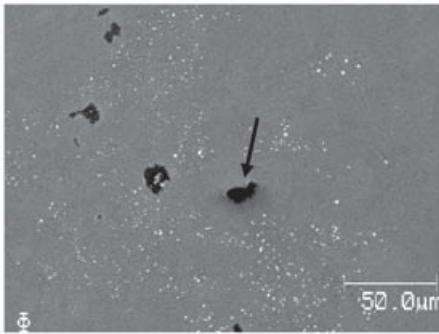


Fig. 1 Secondary electron image of V-4Cr-4Ti alloy exposed to LHD plasma.

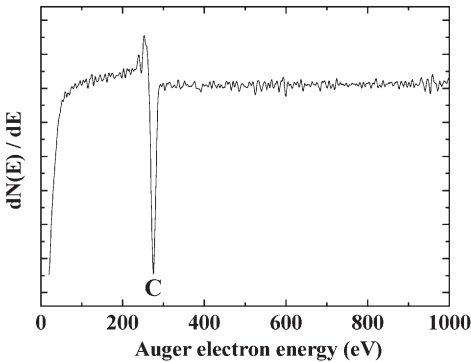


Fig. 2 Auger spectrum of dark part.

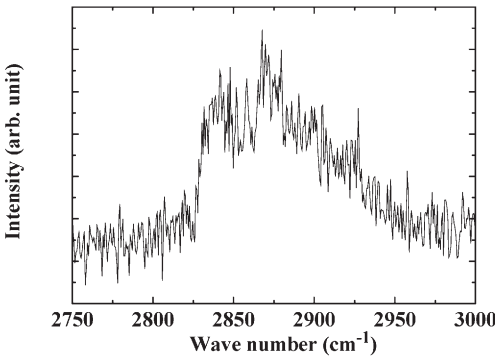


Fig. 3 Raman spectrum of dark part.

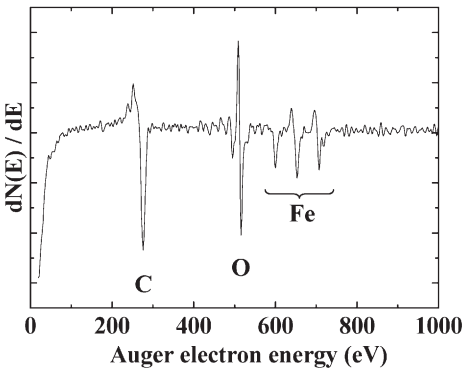


Fig. 4 Auger spectrum of matrix.

## (2) Applied Superconductivity and Cryogenics

### 1. Introduction

The superconducting technology becomes indispensable to construct a large-scale fusion experimental device for the magnetic confinement of plasma because of the requirements for efficient operation and steady state plasma experiment. Furthermore, considering the energy balance, adoption of superconducting systems is essential for the future fusion reactors. Research activities concerning with applied superconductivity and cryogenics are summarized in this section. The research subjects concerning on the superconducting system for LHD are summarized in 1-1-(3) LHD (Device) Engineering Experiments. The research subjects concerning design studies of advanced superconducting systems for a helical reactor are also summarized in 2-2-(2) Helical Reactor Design.

The ninth cycle operation of LHD superconducting system began with the purification operation of the cryogenic system on August 19, 2005, and completed the warm up of the whole system on March 17, 2006. The steady-state operation time to have kept the system under superconducting state reached to 3,470 hours and the total operation time of the cryogenic system was 5,035 hours from the start up of compressors to the end of warm-up operation. Total operating time of the LHD superconducting system until the end of ninth cycle was 41,788 hours, and the steady-state operation time to have kept the coil in the superconducting state reached to 28,501 hours. The total coil excitation number became 985. The serious failure of the superconducting system that causes the obstacle to stable continuous operation has not occurred. The LHD superconducting system, in which the cryogenic system and the coil power supplies are included, has realized a high availability factor of 97 % or more on average during the eight year operations. To achieve such a high availability factor, the extensive maintenance works of each component have been done during the operation dormant period of LHD. To improve the cryogenic stability of the helical coils, the quality improvement of the pool-boiling helium by the sub-cooling modification has been planned. A quantitative evaluation of the stability improvement by the sub-cooling modification has been done by the experiments with the sub-cooling R&D coil<sup>17)</sup>. Based on the successful R&D results, the sub-cooling upgrading of the helical coil cooling system is scheduled in 2006 as one of the performance improvement plans of LHD. We expect that a steady high magnetic field operation, such as the plasma center magnetic fields of 3 T with a magnetic axis at 3.6 m becomes possible by the upgrade.

The Fifteenth International Toki Conference (ITC-15) was held during December 6-9, 2005, with the theme "Fusion and Advanced Technology". The topics of ITC-15 specified on superconducting fusion devices, superconducting magnets and conductors, cryogenics, fusion reactor designs, and advanced technologies related to fusion reactors. The outline of the conference has been summarized in the following report<sup>29)</sup>.

### 2. Research activities of collaboration

We have promoted research collaboration on superconducting technology and cryogenic engineering. The collaborations include basic and applied studies. The purpose of these research activities is early realization of a fusion reactor and application of developed technologies to different areas. A variety of research collaborations with universities and/or national institutes concerning applied superconductivity and cryogenics have been carried out, such as fundamental researches about thermo-mechanical properties of a High T<sub>c</sub> bulk superconductor, current lead applications of High Temperature Superconductor (HTS), characteristics of super-fluid helium, superconducting magnet for SMES application, electromagnetic phenomena of Cable-in-Conduit superconductors, development of an advanced superconductor, etc. The titles of researches are list in the following. The collaboration research items of the LHD Project Research Collaboration are summarized in the section 1-4.

- (1) Studies on the Thermo-Mechanical Strength Characteristics of Single Crystal RE High T<sub>c</sub> Bulk Superconductors. (Katagiri, K., Iwate Univ.)
- (2) Design and Optimization of High T<sub>c</sub> Superconductors for Current Lead Application. (Yamada, Y., Tokai University)
- (3) Effect of the Superheating on Heat Transfer in Two-dimensional Channels in He II. (Kobayashi, H., Nihon Univ.)
- (4) Feasibility Study on SMES Systems Using Stress-Minimized Helical Coils. (Shimada, R., Tokyo Institute of Technology)
- (5) Basic Studies of Electric Properties of Polymeric Silver (I) Complexes at Low Temperature. (Chikaraishi, N., Kanagawa University)
- (6) Study on Long Loops with Long Time Constants in Cable-in-Conduit Superconductors. (Hamajima, T., Tohoku University)
- (7) Reliability of Cryogenic Composite Electrical Insulation for LHD. (Nagao, M., Toyohashi University of Technology)
- (8) Evaluation of Electrical Insulation Properties of Superconducting Coils. (Hara, M., Kyushu Univ.)
- (9) Study on Cryogenic Characteristics of Advanced Uni-Polar Power Electronics Devices and Their Application to High Efficiency AC/DC Converter. (Matsukawa, T., Mie Univ.)
- (10) Fundamental Study on Application of Magnetic Levitation Using YBCO Bulk Superconductor to Fusion Research. (Tsuda, M., Tohoku Univ.)
- (11) Standardization of the Fabrication and the Operation Technologies for Large Scale Superconducting and Cryogenic Systems. (Haruyama, T., KEK)
- (12) Development of a New Conductor Controlled the Twist Angle to Improve the Performance of LTS Coils. (Sumiyoshi, F., Kagoshima Univ.)



(13) Basic Study on Oxide Superconductors for Nuclear Fusion Reactor. (Iwakuma, M., Kyushu University)

(29) Summary of Fifteenth International Toki Conference: ITC-15. (Mito, T., NIFS)

### **3. Research activities of the Applied Superconductivity Group of NIFS**

(Mito, T.)

The Applied Superconductivity Group is belonging to the Fusion & Advanced Technology Systems Division of the Department of Large Helical Device Project. The group is pursuing not only the establishment of operation of LHD superconducting system but also rigorous researches to improve the performance of LHD. Furthermore, our focus is on the design study of a helical-type fusion reactor and the development of its superconducting and cryogenic technologies. In 2005, we requested the Cryogenic Association of Japan for an external evaluation of the group. According to valuable proposals, comments and suggestions, we will promote a wide joint research with a related field of overall nuclear fusion system. Research activities of applied superconductivity and cryogenics including the applications to the other fields by downsizing of Fusion Technology are listed below.

- (14) A Co-axial Pulse Tube Current Lead Development. (Matsubara, Y., NIFS)
- (15) Cryodielectrics - Electrical Insulation of Superconducting Power Equipment Based on Partial Discharge Measurements. (Hayakawa, N., Nagoya University, NIFS)
- (16) Validation of the High Performance Conduction-Cooled Prototype LTS Pulse Coil for UPS-SME. (Mito, T., NIFS)
- (17) Improvement in Cryogenic Stability of the Model Coil of the LHD Helical Coil with Lower Temperatures. (Imagawa, S., NIFS)
- (18) Power Saving Trial of Helium Compressors for the LHD Cryogenic System. (Yamada, S., NIFS)
- (19) Cryogenic Stability of LTS/HTS Hybrid Superconductors. (Yanagi, N., NIFS)
- (20) Operating Test of 100 kW Class DEMO SMES. (Chikaraishi, H., NIFS)
- (21) Dynamic Simulation of a Large Cryogenic Plant. (Maekawa, R., NIFS)
- (22) Design Optimization of Bi2212 HTS Tubular Bulk with Conical Shape for Current Lead. (Tamura, H., NIFS)
- (23) Preliminary Cool-Down Tests of the Cryogenic Target for the FIRE-X Project. (Iwamoto, A., NIFS)
- (24) Experimental and Numerical Studies on Heat and Mass Flow of He II through Porous Media. (Hamaguchi, S., NIFS)
- (25) Effect of Shielding Currents on Current Decay Behaviors in HTS Coils. (Hemmi, T., NIFS)
- (26) Development of HTS Loops for Long-Time Plasma Diamagnetic Measurements. (Hemmi, T., NIFS)
- (27) Stability of NbTi/Cu CICC with Artificial Non-Uniform Current Distribution. (Bansal, G., Sokendai)
- (28) Cryogenic Stability of LTS/HTS Hybrid Superconductors. (Bansal, G., Sokendai)

# §1. Studies on the Thermo-Mechanical Strength Characteristics of Single Crystal RE High $T_c$ Bulk Superconductors

Katagiri, K., Kasaba, K., Shoji, Y. (Fac. Eng., Iwate Univ.), Iwamoto, A., Mito, T.

In order to develop the large superconducting devices such as magnetically confined fusion reactor, development of the current lead which allows large current and suppresses heat is required. Although rare earth high  $T_c$  bulk superconductors have these characteristics, and have already commercialized as a current lead of 1 kA, not only the superconductivity but also the thermo-mechanical characteristics which bears to the cycles of large thermal shocks and thermal stresses are important for larger machines applications. In this experiment, evaluation of thermo-mechanical characteristics of the bulk and clarification of its fracture mechanisms were conducted and the direction of the bulk fabrication process and current lead design were obtained.

14x11x15(c-axis) mm specimens were cut from commercial  $DyBa_2Cu_3O_x$  ( $Dy_2BaCuO_5$  being 25 % mol fraction) bulk samples with 46 mm diameter and 25 or 15 mm thickness. Tensile tests were conducted on the two kinds of 3x3x4 mm specimens, loading in the bulk c axis and perpendicular to it, after 110 rising and cooling thermal cycles between 393K and 77K using a 2 kN Shimadzu servo-pulsating universal testing machine at the cross head speed of 0.15 mm/min. Further, Finite Element Mode analysis ANSYS were used to analyze non-stabilized thermal stress analysis on cooling.

Tensile strength: As shown in Fig. 1, the average tensile strength for the specimens thermal cycled 110 were not changed for loading perpendicular to c-axis and 2/3 for loading parallel to c-axis compared with those without thermal cycles. On the surface of specimens experienced thermal cycles, cracks perpendicular to the c-axis, which have not been seen were observed by an optical microscope. By these cracks, the strength in the specimens loaded in the c-axis direction was thought to be degraded.

Thermal stress analysis: The changes in the maximum value of non-stable tensile thermal stress on cooling of the bulk sample analyzed by ANSYS were shown in Fig. 2. The maximum stress in the direction perpendicular to the c-axis was 40 MPa and was 1.5 times of the tensile strength in this direction, 4.5 MPa (Fig. 1). Because the large thermal stresses were induced, cracks in the direction

perpendicular to c-axis were induced and the strength of the thermal stressed samples were thought to be decreased. In the calculation, thermal conductivity, the coefficient of thermal dilatation, specific heat and Young's modulus in the Ref.1, 2) and the heat transfer coefficient in Ref. 3) were used.

References:  
 1) H. Fujishiro et al., Physica C **426-431**, (2005) 699-704  
 2) K. Katagiri et al., Supercond. Sci. Technol. **19**, (2006) in press  
 3) J. Mosqueira et al., Supercond. Sci. Technol. **6**, (1993) 584-588

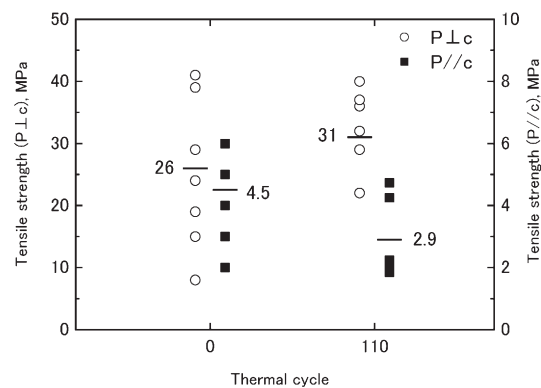


Fig. 1. Tensile strength prior to- or post-heat cycles.

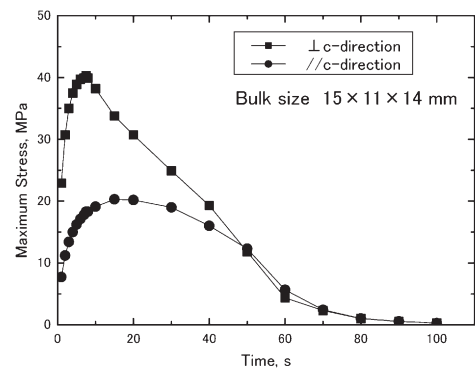


Fig. 2. Changes in the maximum stresses (non-stable thermal stress analysis).

## §2. Design and Optimization of High T<sub>c</sub> Superconductors for Current Lead Application

Yamada, Y., Ohkubo, J., Shimohiro, T., Tachikawa, K. (Tokai University),  
Tamura, H., Mito, T.

High temperature superconductors (HTS) can be synthesized by the diffusion process between the two components in an appreciably shorter reaction time than that of the HTS prepared by the conventional sintering process. In the Bi-Sr-Ca-Cu-O system, a homogeneous HTS layer of Bi<sub>2</sub>Sr<sub>2</sub>CaCu<sub>2</sub>O<sub>8+x</sub> (Bi2212) is easily synthesized by the diffusion reaction between Bi-free Sr-Ca-Cu oxide substrate and Bi-Cu oxide coating<sup>1)</sup>. In the present study, the transport current performance and heat loads of Bi2212 HTS conical tubular bulk will be reported. The conical shaped tube may be expected to yield larger transport current due to the larger cross-sectional area at warm joint and smaller heat leakage due to the smaller cross-sectional area at cold joint in comparison with the cylindrical tubes. The Bi2212 HTS conical tubes by the diffusion process are attractive for current lead applications in superconducting magnet systems<sup>2)-4)</sup>.

Fig. 1 shows the Bi2212 HTS conical tube specimen 47/39 mm in outside/inside diameter at the larger end, 27/19 mm in outside/inside diameter at the smaller end and 200 mm in length. The Ag contact joints of 100 μm in thickness are formed around both ends of the specimens. One of the advantages in diffusion process enables to form HTS diffusion layer on substrates of any shape.

Fig. 2 shows the test set-up of the Bi2212 conical tube specimen connected to the Cu bus bar and NbTi superconducting wires. The conical specimen is soldered to both Cu end caps using commercial Sn-Pb solder. Seven voltage taps were attached on the upper and lower Cu cap (V1 and V5), outer HTS surface (V2, V3 and V4) and inner HTS surface (V6 and V7), respectively. Five Platinum-Cobalt resistance thermometers were attached to the upper and lower Cu cap (T1 and T5), and to the HTS (T2, T3 and T4). A pair of SUS304 stainless steel boards serves as a shunt, and relieves thermal stress in the specimen. Resistive heaters were installed on the upper Cu cap to adjust the temperature of the larger end of the conical specimen. Then, the specimen was cooled using liquid helium in a cryostat.

The transport current for the conical tube decreases with increasing temperature at the warm joint, and is about 5,000 A at 40 K and 4,000 A at 50 K, which corresponds to the current density of 12,500 A/cm<sup>2</sup> and 10,000 A/cm<sup>2</sup>, respectively. Fig. 3 shows the transport current performance for the conical tube specimen at the warm joint of 50 K and 55 K, respectively. The transport current of 2,000 A was stably run with no voltage on the HTS part (between V2 and V4). The voltage of the warm joint increased with increasing transport current, and were 800 μV at 50 K and 1,100 μV at 55 K after reaching 2,000 A.

On the other hand, both voltages of cold joint at 4.2 K remained approximately constant at 45 μV after reaching 2,000 A. Therefore, the Joule heat generated by transport current of 2,000 A are as small as 90 mW at the cold joint.

The heat leakage conducted through the specimen increases with increasing temperature at the warm joint, that is, the temperature difference between the warm and the cold joint. The heat leakage for the conical tube is calculated to decrease by 30% compared to that of the cylindrical tube with the same cross-sectional area at the warm joint. Present Pb-free Bi2212 conical tubes seem to be promising as large transport current leads with small heat loads for superconducting magnets.



Fig. 1. Bi2212 HTS conical tubular conductor with Ag contact joint on both ends.

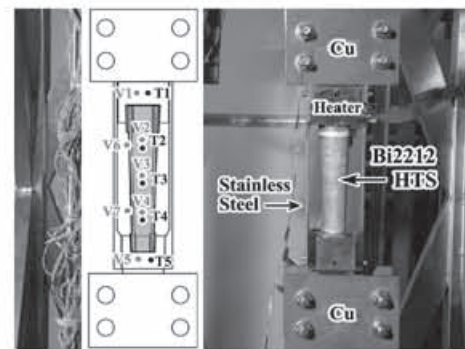


Fig. 2. Test set-up of the Bi2212 conical tube connected to Cu end caps, bus bar and NbTi superconducting wires.

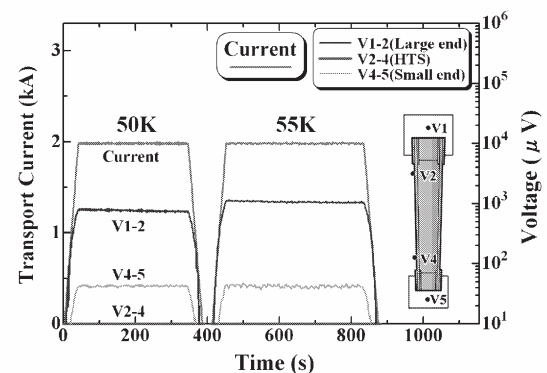


Fig. 3. Transport current performance and voltages of the Bi2212 HTS conical tube at 50 K and 55 K in self-field.

### References

- 1) Yamada, Y. et al. : Adv. Cryo. Engr., 44 (1998) 547.
- 2) Yamada, Y. et al. :IEEE Trans. Appl. Supercond., 14 (2004) 638.
- 3) Tamura, H. et al. :IEEE Trans. Appl. Supercond., 14 (2004) 686.
- 4) Ohkubo, J. et al. : ITC15-PS1-01.

### §3. Effect of the Superheating on Heat Transfer in Two-Dimensional Channels in He II

Kobayashi, H. (Inst. Quantum Sci., Nihon Univ.)

Researches on the heat transfer from a good conductor to He II in a narrow two-dimensional channel are required to compact a He II-cooled apparatus such as heat exchanger and superconducting magnet. One of the necessary conditions for the compactness is that the temperature rise of the conductor is not sudden but gradual and reversible at a critical heat flux  $Q_\lambda$  at which a part of He in the channel reaches the  $\lambda$ -temperature. The condition is achievable if He II cools a good conductor in a two-dimensional channel with the gap distance of sub-millimeter even below the  $\lambda$ -point pressure  $P_\lambda$ . It has been observed in the present work that the superheated phase begins to spread on the heated surface at  $Q_\lambda$  almost the same as that in the pressurized He II (He II<sub>p</sub>).

To study the specific heat transfer characteristics, disk-shaped channels with radial heat flow were fabricated. The channel shown in Fig. 1 is made of copper disk with the radius of 10 mm and the thickness  $t$  of 13 mm. The radius of the insulator disk is 11 mm. The disks face parallel each other leaving a space  $g$ , 0.15 mm ~ 0.3 mm. Figure 2 shows the heat transfer characteristics accompanied with the superheating. The good conductor stabilizes not only the superheated He II ( $^s\text{He II}$ ) but also the superheated He I ( $^s\text{He I}$ ) in a wide range of bath pressures even in a vibrating cryostat. On the phase diagram, there is neither He II-phase nor He I-phase above the saturation temperature in a state of equilibrium though [1~3]. From experimental results, the metastable  $^s\text{He I}$  layer is estimated to cover the hottest spot as well as in He II<sub>p</sub> [4]. In other words, the  $^s\text{He I}$  phase coexists steadily with the  $^s\text{He II}$  phase on the same heated surface between  $Q_\lambda$  and the critical boiling heat flux  $Q_N$ . Although the appearance of  $^s\text{He I}$ -phase is not directly seen from Fig. 2a, the temperature very near the heated surface keeps rising above  $Q_\lambda$  up to  $Q_N$  due to the growth of  $^s\text{He I}$ . In narrower channel, temperatures increase in  $T_{1-3}$  beyond the  $T_\lambda$  have been observed (not shown). The heat transfer state is switched from the non-boiling state to a state of boiling at  $Q_N$ . The in-situ pressure gauge detects the sudden pressure change due to the boiling. At the moment of the boiling the temperature of the conductor changes a little although the superheated phase collapses entirely as shown with line-a in Fig. 2a and b. Therefore, heat transfer curves below  $P_\lambda$  traverse on a relatively low temperature side. However, the curves trace higher side along line-b above  $P_\lambda$ . The non-boiling state through  $Q_\lambda$  and  $Q_N$  successively until the film boiling occurs entirely at heat flux  $Q_M$  much above  $Q_\lambda$ . On the other hand, in He II<sub>p</sub>, the temperature of the conductor increases rapidly with increasing heat between  $Q_\lambda$  and  $Q_N$ , since a localized dried area starts to spread above  $Q_N$ , since the stable subcooled He I prevents the conductor from cooling in such narrow channels.

Although either the stable subcooled He I or the metastable superheated He I reduces the heat transfer rate, the nucleation of He I-phase on the spot of the heated surface

makes heat transfer characteristics reversible without the sudden temperature rise in the conductor.

#### References

- 1) Rybaryk, L.J. et al.: J. Low Temp. Phys. 43 ('81) 197
- 2) Helvensteijn, B.P.M. et al.: Adv. in Cryo. Eng. ('81)
- 3) Kobayashi, H. et al.: Cryogenics 37 ('97) 851
- 4) Nishigaki, K. et al., :Phys. Rev. B33 ('86) 1657 27, 485
- 5) Gentile, D. et al.,: Cryogenics 21, ('81) 234

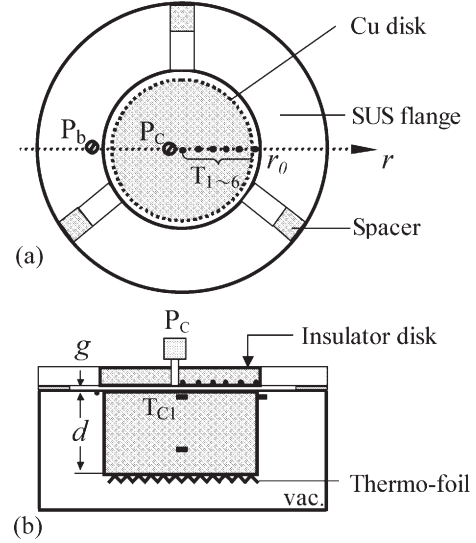


Fig. 1 Schematics of the two-dimensional channel (a) Top view, (b) the view cut across the diameter. The many solid marks indicate the positions of thermometers. In-situ pressure gauges are attached at positions  $P_b$  and  $P_c$ .

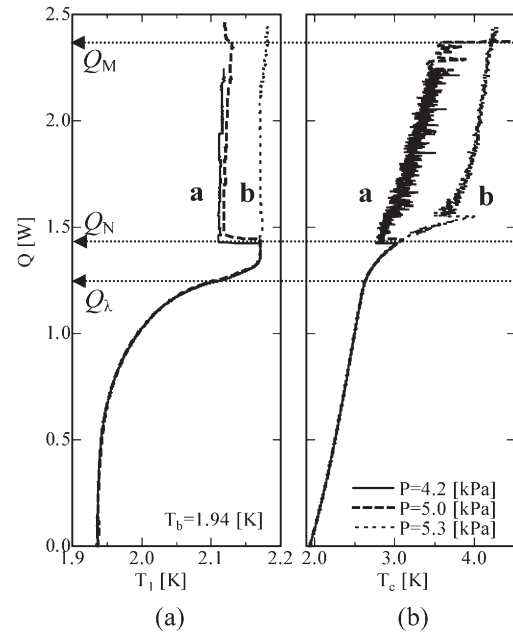


Fig. 2 Heat transfer characteristics (a)  $T_1$  vs.  $Q$ , (b)  $T_c$  vs.  $Q$  for  $d$ : 13 mm,  $g$ : 0.168 mm. The parameters indicate the bath pressure.



§4. Feasibility Study on SMES Systems Using Stress-Minimized Helical Coils

Nomura, S., Tsutsui, H., Tsuji-Iio, S., Shimada, R. (Tokyo Tech.), Chikaraishi, H.

Design considerations for large-scale SMES that has same stored capacity of pumped hydro storage have been discussed [1, 2]. Fig. 1 indicates a schematic diagram of the back-to-back (BTB) interconnection with SMES based on the force-balanced coil (FBC) design. The FBC is a helically wound hybrid coil of toroidal field coils and a solenoid. The FBC is an optimal SMES coil that can minimize the required mass of the structure for induced electromagnetic forces. Since the BTB interconnection already has AC/DC converters, by using superconducting coils instead of DC reactors, the SMES can be easily incorporated into the BTB interconnection. The suggested system enables flexible power interchange between interconnected power networks.

Fig. 2 shows a schematic illustration of the BTB interconnection with 600-MWh SMES based on the FBC design. In the case of large-scale SMES, the superconducting coils require special structural considerations for induced electromagnetic forces, such as bedrock support. In order to reduce the risk in the coil manufacturing process, the 600-MWh is composed of 4000 superconducting coils. Each coil has the stored energy of 150 kWh (540 MJ). When the several SMES coils have been constructed, these coils will be put into operation immediately. Then the stored energy can be continuously enlarged.

In order to demonstrate the feasibility of the FBC concept for large-scale SMES, a one tenth sized model coil of the 150-kWh SMES coil has been designed [3]. The model coil with an outer diameter of 0.53 m will have

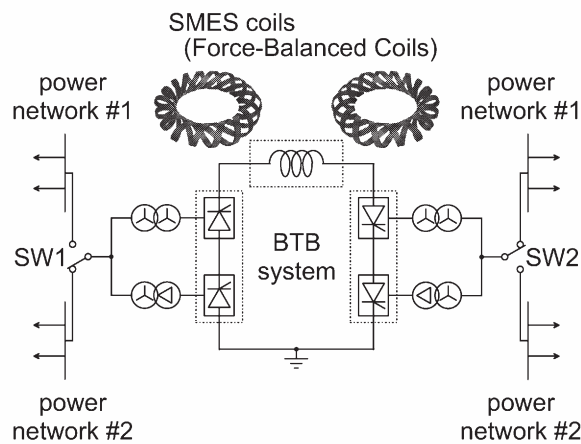


Figure 1: Schematic diagram of the BTB interconnection with the SMES.

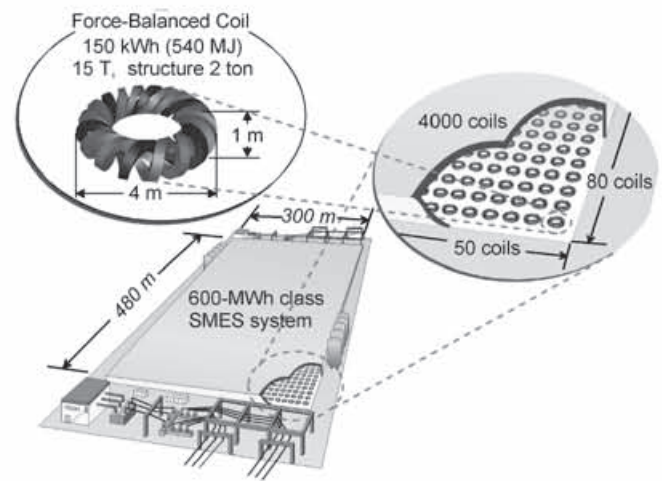


Figure 2: Schematic illustration of the 600-MWh SMES based on the FBC design.



Figure 3: Winding form for the model coil.

270-kJ stored energy at the maximum magnetic field of 7.0 T using NbTi superconductors. Fig. 3 shows a photograph of the winding form made of aluminum alloy. In this demonstration, the winding of the model coil will be carried out without reinforcing materials for the NbTi superconductors, and the mechanical properties of the model coil will be investigated.

References

[1] S. Nomura, T. Hagita, H. Tsutsui, Y. Sato, R. Shimada, "Interconnected Power Systems with Superconducting Magnetic Energy Storage," *IEEJ Trans. Power and Energy* **126** (2) (2006) pp. 251–256 (in Japanese).

[2] S. Nomura, H. Tsutsui, S. Tsuji-Iio, R. Shimada, "Flexible Power Interconnection With SMES," *IEEE Trans. Applied Superconductivity* **16** (2) (2006) pp. 616–619.

[3] S. Nomura, H. Tsutsui, S. Tsuji-Iio, H. Chikaraishi, R. Shimada, "Feasibility Study on High Field Magnets Using Stress-Minimized Helical Coils," to be published in *Fusion Engineering and Design*.

## §5. Basic Studies of Electric Properties of Polymeric Silver(I) Complexes at Low Temperature

Chikaraishi, N. (Kanagawa University)

The chemistry of coordination polymers has attracted much attention as they have potential as functional materials. Recently, a new simplified synthetic procedure for commercial manufacture of ternary single-source precursors (SSPs) to form polycrystalline  $\text{AgIn}_x\text{S}_y$  and  $\text{CuInSe}_2$  type semiconductors was reported [1]. We reported the preparation of six water-soluble, relatively light-stable, chiral and achiral silver(I) complexes ( $\infty\{\text{[Ag}_2(\text{ca})_2]\}$  and  $\infty\{\text{[Ag}_2(\text{ca})_2(\text{Hca})_2]\}$ ). Slow evaporation of saturated aqueous solutions of the complexes gave needle single crystals. As shown in Fig. 1, the silver(I) complexes formed linear polymers in the crystal and their Ag-Ag separation indicated the existence of a van der Waals contact between silver(I) atoms.

In attempting to explore electrical properties of these

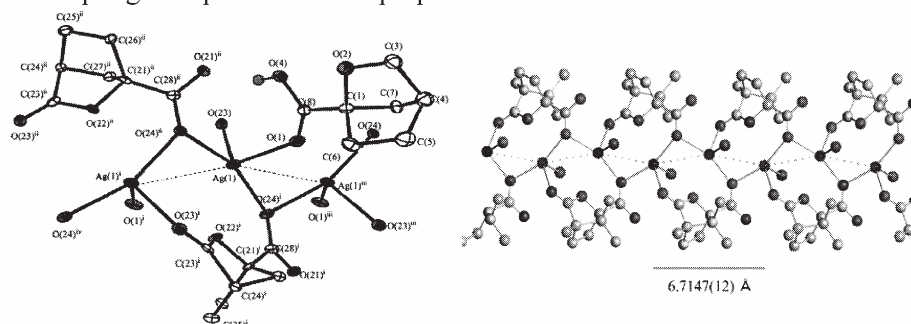


Fig. 1 Molecular structures of the local coordination around the silver(I) centers in the complexes.

crystalline silver(I) complexes at low temperature, we made test samples for preliminary measurements of electric resistance.

Sample A: Needle crystals of each silver(I) complexes were grown on slide glasses followed by silver paste painting (Fig 2). Electric resistances was estimated as  $2.3\text{M}\Omega$  at room temperature and  $10\text{M}\Omega$  at  $77\text{K}$  using  $0.1\mu\text{A}$  current source. The esd's of electric resistance were within 10% for three-times repeating, but voltage became larger in the fourth cycle of cooling.

Sample B: Electrodes were prepared by silver paste painting on the slide glasses followed by crystal growth of silver(I) complexes (Fig. 3). The distance of the electrodes was shorted but needle crystals came up from the slide glass.

Future plans: To increase stability of the sample electrodes, test samples using water-insoluble linear silver(I) complexes polymers with shorter distances of electrodes would be made for measurements.

[1] Kulbinder K. Banger, et al, *Inorg. Chem.*, 2003, 42, 7713-7715

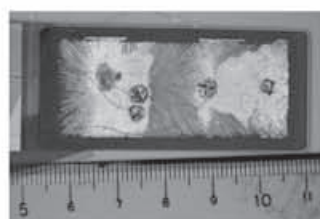


Fig. 2. Sample A

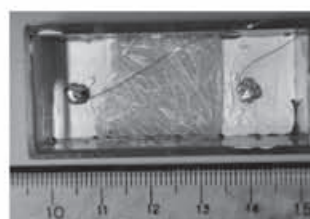


Fig.3. Sample B

## §6. Study on Long Loops with Long Time Constants in Cable-in-Conduit Superconductors

Hamajima, T., Yagai, T., Tsuda, M., Sato, H. (Tohoku University),  
Takahata, K.

The superconducting coils wound with Cable-In-Conduit Conductors (CICCs) which are composed of several stages of sub-cable has been applied to large devices such as experimental fusion apparatuses and Superconducting Magnetic Energy Storage (SMES) devices because of its high mechanical and dielectric strength. In recent years there has been a growing interest in coupling loss with long time constants ( $> 1\text{sec}$ ) which are not observed in test result using short sample conductor [1]. In addition, the extra increment of the loss with 15% is observed when the large electromagnetic force is applied to the conductor[2]. Our previous works revealed that the production of the coupling loss with long time constants is due to the line contact condition between strands. The loss is expected to be large as a result of the longer contact length, in other words, the lower contact resistance.

In this work, we investigate the change of the contact condition between strands induced by the electromagnetic forces by applying the transverse compression to the conductor.

Figure. 1 shows the experimental setup for the measurement of the change of the transverse resistance of the conductor. The sample conductor is the OV coil conductor of 210mm in length which consists of 486 ( $3^4 \times 6$ ) NbTi strands. In order to apply the compression, the conduit of the conductor is removed of 70mm in length at both up and down side. Two Cu electrodes put pressure and feed the constant current to measure the transverse resistance. The resistance, deformation of the conductor and the applied pressure are measured through a data acquisition system.

The compression procedure is that the pressure is held during 120sec at interval of 4kN/m from 0kN/m to 100kN/m, and repeated three times. Fig. 2 shows the deformation of the conductor versus applied load in each compression cycle. In the 1<sup>st</sup> cycle, the deformation range is large compare to other cycle. In the 2<sup>nd</sup> and 3<sup>rd</sup> cycle, the deformation does not start from 0mm. This indicates that the conductor deformed plastically at the first cycle. On the other hand, the deformation at all cycle converges to a fixed value.

Figure. 3 shows the transverse resistance versus applied load in each cycle. In the 1<sup>st</sup> cycle, the resistance decreased significantly. But in the 2<sup>nd</sup> and 3<sup>rd</sup> cycle, the decrement was smaller than that in the 1<sup>st</sup> cycle. The initial resistance in 2<sup>nd</sup> and 3<sup>rd</sup> cycles were smaller than that in the 1<sup>st</sup> cycle.

It is predicted that the reduction of the resistance is

caused by increment of inter-strand contact cross section. According to the Elastic theory, the contact width is expressed as the equation:

$$b = 1.6 \sqrt{p \frac{d_f}{2} \left( \frac{1 - \nu^2}{E} \right)} \quad (1)$$

Where  $b$  is the contact width,  $p$  is applied load,  $d_f$  is strand diameter,  $\nu$  is Poisson's Ratio of Cu and  $E$  is Young's Modulus. Assuming that the contact resistance is inversely proportional to the contact width, the resistance is proportional to  $p^{(-1/2)}$ . The  $p^{(-1/2)}$  line is also shown in Fig. 3. The resistances with high pressure side in all cycle agree with the  $p^{(-1/2)}$  line, it is indicated that the inter-strand contact conditions are subjected to the elastic deformation of strands. It is thought that the curves which are different from  $p^{(-1/2)}$  line are caused by increment of the current paths or contact length due to deformation of the strand positions.

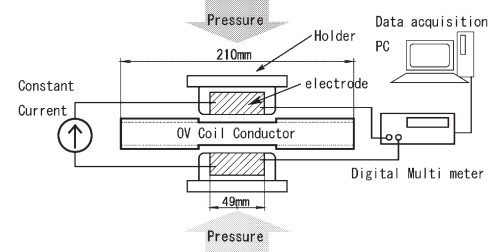


Fig. 1: Experimental setup for compression test

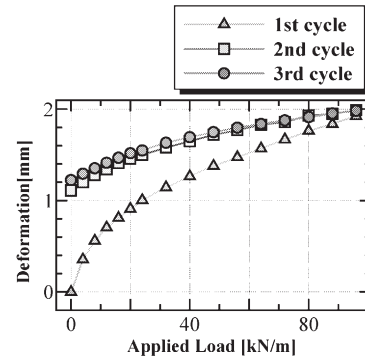


Fig. 2: Deformation of the conductor vs. applied load

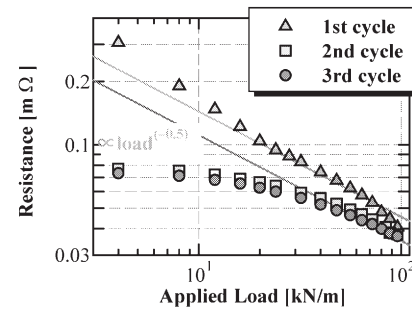


Fig. 3: Transverse resistance of CICC vs. applied load.

### Reference

- 1) Hamajima, T., et al.: Cryogenics, **39** (1999) 947.
- 2) Hamajima, T., et al.: IEEE Trans. Appl. Supercond. **10**, (2000)812

## §7. Reliability of Cryogenic Composite Electrical Insulation for LHD

Nagao, M., Hozumi, N., Murakami, Y. (Toyohashi University of Technology),  
Hara, M., Suehiro, J. (Kyushu University),  
Kosaki, M. (Gifu College of Technology),  
Shimizu, Y., Muramoto, Y. (Meijo University),  
Mizuno, Y. (Nagoya Inst. of Technology),  
Minoda, A. (Mastue College of Technology),  
Yamada, S. (National Institute of Fusion Science)

The world's largest class superconducting coil is used for the "Large-scale Helical Device". Its electrical insulation system might be exposed to considerably severe multiple stresses including cryogenic temperature, large mechanical stresses and strong magnetic fields. It is therefore very important to study its electrical insulation performance under these severe conditions in order to establish the reliability of the coil. If a superconductor quenches from superconducting state to normal state, the liquid coolant vaporizes very easily and turns into high-density gas at cryogenic temperature. The partial discharge (PD) or electrification would become the cause of this quench. So it is required to clarify the influence of the PD and electrification on the insulation performances.

### 1. Measurement of PD characteristics and PD current waveform in composite insulation system of LN<sub>2</sub> and solid insulator

This research was conducted using electrode system that simulated the insulation system included triple junction, which is consisting of the electrode, solid insulator and LN<sub>2</sub>, to investigate the PD phenomena.

Figure 1 shows typical current waveform of PD under the condition of the super cooling. Under the super cooling, the half band width is about 12 ns because micro bubble was not generated by the PD. The current waveform of PD under atmosphere pressure is shown in Fig.2. The half band width is about 20 ns and is longer than that compared with Fig.1. Under the atmosphere pressure, both of Fig.1 and Fig.2 were observed as the current waveform. It is considered that longer half band width is observed due to the generation of the micro bubble.

Figure 3 shows classification of the PD by the half band width under the atmosphere pressure. The PD pattern was clearly separated into two clusters. It is thought that the open circles and solid circles in Fig.3 indicate the PD in LN<sub>2</sub> and in micro bubble, respectively. Therefore, it is suggested that the current waveform

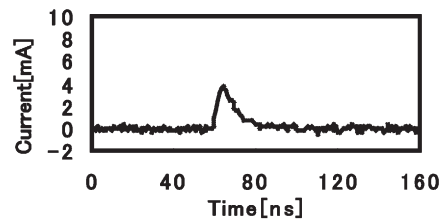


Fig.1 Current waveform of partial discharge in LN<sub>2</sub> (12[ns])

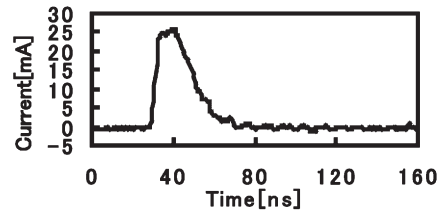


Fig.2 Current waveform of partial discharge in bubble (20[ns])

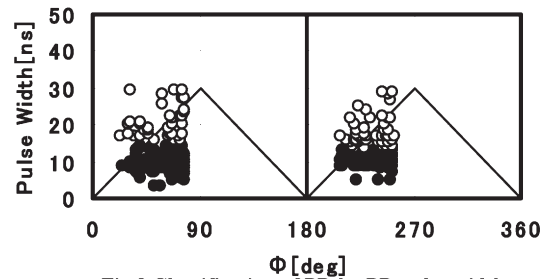


Fig.3 Classification of PD by PD pulse width

measurement with the measurement of the PD pattern brings the possibility to ascertain presence of the micro bubble in LN<sub>2</sub>.

### 2. Electrification of liquid nitrogen flowing electrical insulating pipe

The measurement system of electrification of nitrogen was improved by using an instrument with higher internal resistance. Amount of charge of liquid nitrogen was measured with a so-called Faraday cage, which passed inside a PVC pipe of 1 m in length and 13 mm in inner diameter. The measured charge lay in the range of 100-300 pC for 1000 cm<sup>3</sup> liquid nitrogen, which was much bigger compared with charge measured in a former system.

When a joint was introduced in a straight PVC pipe at its center length, the amount of charge increased. When a cylinder of acrylic resin was placed in the space of liquid nitrogen flowing in the PVC pipe, the amount of charge was also increased. Uneven inner surface at the joint or increase in surface area by the cylinder may result in increase in charge.

### Reference

- 1) Nakamura E., Murakami.Y., Hozumi.N., Nagao.M., Minoda.A., Kosaki.M. & Yamada.S., 2006 Annual Meeting Record I.E.E. Japan, Vol.2, p.54 (2006)
- 2) Noda T., Yasui S., Mizuno Y. and Minoda A., 2006 Annual Meeting Record I.E.E. Japan., Vol.2, p.52(2006)



§8. Evaluation of Electrical Insulation Properties of Superconducting Coils

Hara, M., Suehiro, J. (Kyushu Univ.), Yamada, S.

A superconducting coil of LHD is exposed to various stresses, such as a thermal, electrical or mechanical one. Electrical insulation systems of LHD are placed in liquid helium, and when transition from superconducting state into normal conducting state called quench occurs on superconductors, it is possible that its electrical insulation strength is significantly reduced by the vaporization of the liquid helium due to the Joule heat at the quenched part of the superconductors. These cryogenic environments and the quench phenomena must be taken into account in the electrical insulation design as well as in high voltage tests of LHD. As the first approach to this issue, this project focused on power frequency withstand voltage tests of HTS (High Temperature Superconductor) power apparatus with pancake coil structure cooled by liquid nitrogen (Fig. 1.). Medium factors of insulation weak parts and insulation elements were theoretically and experimentally obtained and a significant unique medium factor of the apparatus were discussed with them. The studied insulation elements were coil-to-coil and current lead insulation elements. The insulation weak parts chosen mainly from the coil-to-coil insulation element were (i) uniform field gap, (ii) non-uniform field gap, (iii) triple junction defined as a contact point between a metal, a solid insulator and liquid or gaseous dielectrics and (iv) solid insulator surface. Main results are summarized as follows.

- 1) Uniform and non-uniform field gaps, triple junction and solid insulator surface were chosen as the insulation weak parts, and their medium factors were theoretically and experimentally clarified as a function of the gap length between electrodes and the nitrogen gas temperature.
- 2) The measured values medium factors were compared with the medium factor of a coil-to-coil insulation element experimentally obtained with its modeled electrode system under a given condition. It was pointed out that the medium factor of the coil-to-coil insulation element should be determined from that of its insulation weakest part, which was triple junction or solid insulator surface in our case.
- 3) Based on these findings, It was recommended for the safest side of the insulation design that the equivalent insulation test voltage at room temperature for the finished HTS apparatus should be determined by the maximum value of the medium factor selected from those of the insulation elements (Fig. 2.).
- 4) It was suggested that additional insulation distance is needed in at least one of the insulation elements for preventing discharge activities at room temperature if the ratio of the maximum medium factor to the

minimum one is larger than the safety factor in the standard test voltage.

Reference

1) Hara, M., Maeda, Y., Nakagawa, N., Suehiro, J., Yamada S.: "DC breakdown voltage characteristics of saturated liquid helium in the presence of metallic particles", IEEE Trans. on DEI (in press)  
2) Hara M., Kurihara T., Nakano R., Suehiro, J.: "Medium factors of electrical insulation systems in high temperature superconducting power apparatus with coil structure for equivalent ac withstand voltage test at room temperature", Cryogenics, Vol.45, pp.705-717 (2005)

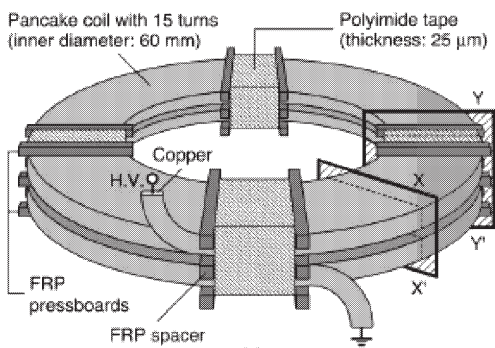


Fig. 1. Schematic diagram of modeled electrode system of coil-to-coil insulation element.

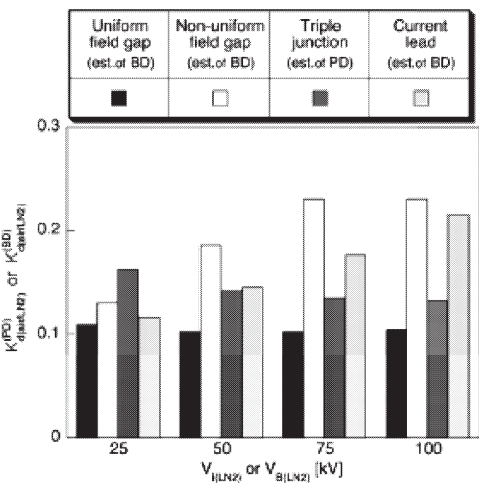


Fig. 2. Comparison between values of medium factors for various insulation systems.

§9. Study on Cryogenic Characteristics of Advanced Uni-Polar Power Electronics Devices and Their Application to High Efficiency AC/DC Converter

Matsukawa, T., Ishida, M. (Dept. of Electrical and Electronic Eng., Mie Univ.),  
Sato, Y. (Dept. of Electrical and Electronic Eng., Daido Inst. of Tech.),  
Chikaraishi, H.

The super junction type power-MOSFET is one of advanced power electronics devices to achieve lower on-state resistance value in higher voltage region, which has excellent electrical characteristics to be applied to high current AC/DC converter. A super junction type power-MOSFET is investigated on its static voltage-current characteristics and the on-resistance value. The super junction type power-MOSFET SPA20N60C3 has the voltage and current ratings of 650V and 20.7A respectively, and also, the temperature dependence of its voltage-current characteristics is clarified. Considering to cool down the power electronics device for high current operation, the static voltage-current characteristics are measured in room and liquid nitrogen temperature.

Fig. 1 shows the schematic diagram of single phase full-bridge synchronous rectifier for testing operation with small voltage and current. The symbol of power-MOSFET means one super junction type power-MOSFET SPA20N60C3 investigated in the previous section. Two switching units of super junction type power-MOSFET devices are used for converting AC to DC in full cycle period. According to the AC voltage polarity, each device is supplied with synchronized gate signal voltage to flow the current through main part of power-MOSFET element, not through the body diode. Each power-MOSFET device is triggered in every half cycle synchronizing to the AC voltage. In the positive half cycle, the upper side power-MOSFET (FET1) turns on to flow the current as mentioned in the previous section. To output the current in the negative half cycle period, the inverse side power-MOSFET (FET2) is to flow the current as same process as in the positive half cycle.

In Fig. 2, The AC voltage ( $V_1$ ) is the voltage appearing in secondary side of transformer and the drain-source voltage ( $V_{DS1}$ ) is the voltage appearing in the upper side power-MOSFET (FET1). It is observed that the power-MOSFET (FET1) is turning on and turning off in every 180 electrical degrees with synchronizing to the applied AC voltage ( $V_1$ ). The final waveform of output voltage ( $V_0$ ) is similar to that of a normal single phase full-bridge circuit with diode rectifier, and it is also shown that the inverse side power-MOSFET (FET2) is switched on/off according to the corresponding gate signal voltage. The converter system including power-MOSFET devices will be cooled down in liquid nitrogen to make its operational loss extremely low. And, as another type advanced uni-polar power device, SiC-based

power-MOSFET will be developed for lower on-state resistance and higher operational temperature than that of conventional Si-based power-MOSFET. The advantage of synchronous rectifier using power-MOSFET is to minimize total on-state resistance of parallel connected devices. The principle of basic operation of synchronous rectifier is described, and is tested experimentally with single phase full-bridge circuit. The operational results of single phase synchronous rectifier are successful, and super junction type power-MOSFET device, which is an advanced uni-polar power electronics device, is demonstrated to be applied to synchronous rectifier.

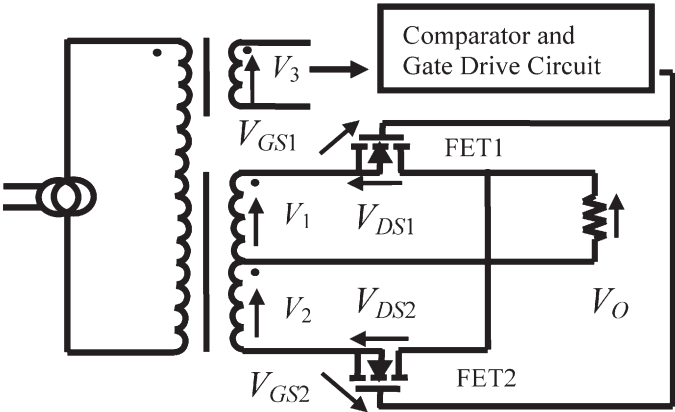


Fig. 1. Diagram of single phase full-bridge synchronous rectifier

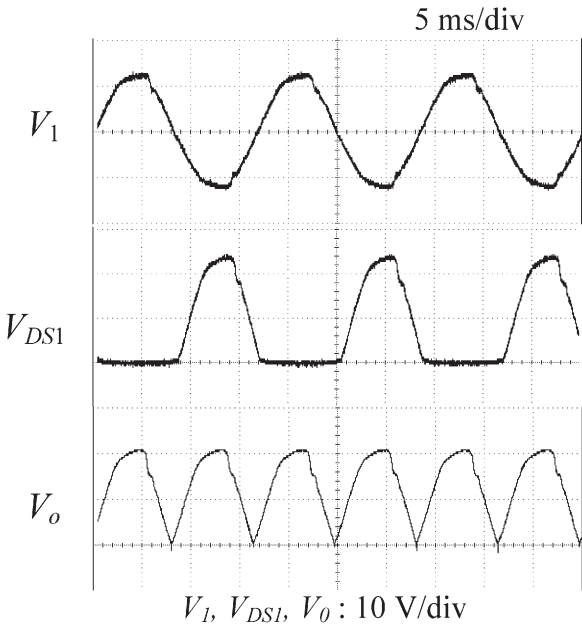


Fig. 2. Voltage waveforms of single phase full-bridge synchronous rectifier

§10. Fundamental Study on Application of  
Magnetic Levitation Using YBCO Bulk  
Superconductor to Fusion Research

Tsuda, M., Hamajima, T. (Tohoku Univ.),  
Ishiyama, A. (Waseda Univ.),  
Noguchi, S. (Hokkaido Univ.),  
Mito, T., Yanagi, N., Iwamoto, A.

Stable levitation and precise levitation height control of a spherical cryogenic target are required in a magnetic levitation system for laser fusion system. The spherical target is surrounded by HTS thin layer of less than 100  $\mu\text{m}$ . Large levitation force enough to levitate the target has to be generated in such the HTS thin layer. The characteristics of magnetic levitation, such as stability, levitation force and levitation height, have been already investigated both experimentally and theoretically. The most of investigations, however, are about disk- and ring-shaped HTS bulks and the characteristics of magnetic levitation in a spherical target with a concentric spherical HTS thin layer have not been investigated yet. The characteristics of magnetic levitation are closely related to supercurrent distribution. The supercurrent distribution strongly depends on the size and shape of HTS region. It is very difficult to produce the spherical target with a concentric spherical HTS thin layer. Furthermore, it is expected that the supercurrent distribution in the HTS layer of a spherical target would be similar to that of a spherical HTS bulk. Therefore, we investigated supercurrent distribution and the characteristics of magnetic levitation of a spherical YBCO bulk.

Since supercurrent distribution and levitation force strongly depend on equivalent critical current density of HTS bulk, it is very important to estimate the equivalent critical current density as accurate as possible. The equivalent critical current density can be estimated by both measurement and numerical analysis of levitation force using an active magnetic levitation system composed of HTS bulk and electromagnet. Therefore, we prepared a spherical YBCO bulk sample and three sets of copper coils. Then we measured levitation force of the spherical YBCO sample using the active magnetic levitation system shown in Fig.1. The diameter and weight of the YBCO sample are 15mm and 11g, respectively. The inner and outer diameters and height of copper coil are 20mm, 72mm and 12mm, respectively. In numerical analysis, we adopted the FEM-BEM coupling method to evaluate levitation force of the YBCO sample. We calculated the levitation force as a function of the equivalent critical current density and compared them with that of experiment. From the experimental and numerical results, the equivalent critical current density of  $4 \times 10^7 \text{ A/m}^2$  was obtained. To validate the obtained equivalent critical current density, we measured levitation height of the YBCO sample using laser displacement meter. Good agreement between experiment and analysis was obtained. This means that the estimated equivalent critical current density is reliable.

Using the estimated equivalent critical current density, we simulated supercurrent distribution within the spherical YBCO sample. The computed supercurrent distribution at the coil current  $I_{\text{coil}}$  of 0 A (just after field-cooling process), 5 A (levitation height = 0 mm), 15 A (levitation height = 3.75 mm), and 45 A (levitation height = 44.2 mm) are shown in Fig.2. As shown in Fig.2, supercurrent flows only outermost layer of the spherical YBCO sample; the layer thickness of supercurrent region of about 0.8mm is independent of coil current and levitation height. This means that the thickness of the concentric spherical YBCO layer of 0.8mm is enough to levitate the sample of weight of 11g.

Accurate evaluation of supercurrent distribution within a concentric spherical HTS thin layer of a very small cryogenic target is necessary for the precise estimation of levitation force and the investigation of relationship between HTS layer thickness and levitation force. A strong nonlinearity of the  $E$ - $J$  power law in the HTS layer, however, results in bad convergence of the nonlinear equation solvers, i.e., the Newton-Raphson method. Consequently, the unsuitable and/or undulating supercurrent distribution is sometimes observed. Therefore, we developed a new method combined a line search with the Newton-Raphson method. It was observed in the analysis by the developed method that the convergence was considerably improved and the supercurrent distribution was suitably smooth.

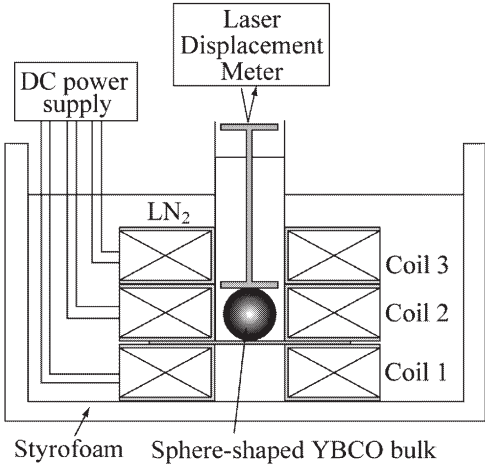


Fig. 1. Schematic drawing of an active magnetic levitation system.

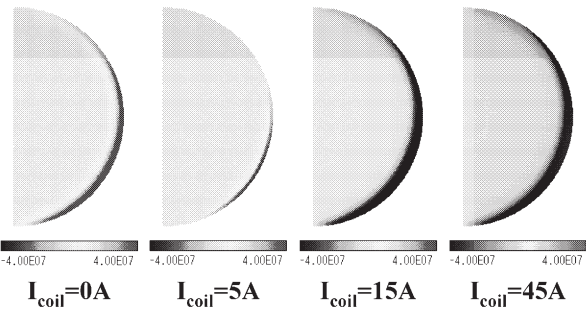


Fig. 2. Supercurrent distributions of a spherical YBCO sample in an active magnetic levitation system.



# §11. Standardization of the Fabrication and the Operation Technologies for Large Scale Superconducting and Cryogenic Systems

Haruyama, T., Kimura, N., Nakai, H., Aoki, K. (KEK), Shintomi, T. (Nihon, Univ.), Sato, A., Yuyama, M., Maeda, M., Dantsuka, T. (NIMS), Shiotsu, M., Shirai, Y., Hata, K. (Kyoto Univ.), Mito, T., Yanagi, N., Maekawa, R., Iwamoto, A., Hamaguchi, S.

## i) Introduction

Large superconducting magnets and accompanying large cryogenic systems have been fabricated in a lot of institutes; the Large Helical Device (LHD) is an example. The magnet systems were specially designed for each purpose so that its technology cannot directly transfer to other systems. This is a trouble to large scale superconducting magnet system.

The superfluid helium (He II) database have been arranged for design of superconducting magnet system by arrangement of a large number of data and by investigation of complementary data of He II. Researchers can apply its data for design. Using this database, we suppose that magnet systems can be divided into classes of cooling technology. This concept would be expanded into whole existing large scale magnet systems. Then, we hope to establish the standardization of the fabrication and the operation technologies for large scale superconducting and cryogenic systems.

This group consists of five institutions of various fields: high-energy physics, applications of high magnetic field, power application, fusion science, and so on. Therefore, ideas from various fields can be integrated for the establishment of the standardization.

## ii) He II database

The He II database is categorized as shown in Table 1. It has enough information to apply by researchers who design He II cooled magnet system. So far, more than 850 data have been completed in the database.

In FY 2005, we integrated the He II database by searching and collecting data from literatures published from 2000 to 2003. Some new data have been found and have checked on the effectiveness and reliability. Their graphs, figures and required information is still selecting for the database. The utility of the database was also upgraded. Users can search and access required

data though the internet web site. For the convenience of its access, the computer for the database was renewed, and the program for its homepage was improved. For easy integration of the database, the method of information input is modified, and data can be directly sent and is stored in the computer though the internet.

Table 1. Technical items for He II database.

Head items	Items	Sub items
Heat transfer	He II pressurized	plate
		channel
	He II saturated	plate
		channel
System	Cryostat	
	Heat exchanger	JT
		Helip-Hells
	Pumping	vacuum pump
		cold compressor
Cooling technology	Measurement	temperature
		pressure
		flow rate
		level
		miscellaneous
	Special technique	seal
		miscellaneous
Operated cases	Refrigeration	
	Magnet	
	Magnet stability	
	Conductor	

## iii) Discussion on the standardization of the fabrication and the operation technologies for the large scale superconducting magnet and cryogenic systems

We discussed how to standardize large scale superconducting magnet and cryogenic systems once in FY 2005. First, we had to have a common idea what is the standardization. Some existing large scale systems: LHD, the Large Hadron Collider (LHC) at CERN, the 920MHz NMR Magnet at NIMS, and 45T hybrid magnet at National High Magnetic Field Laboratory (NHMFL), were chosen as examples for a discussion. Their magnets applied various cooling methods and conductors. We could recognize the difficulty of the standardization because the systems were specially designed with different concepts so that it is difficult to divide the systems into common units. However, only a liquefier, especially a compressor, was thought to be able to become one of example for the standardization. In FY 2006, we will start to consider solutions for the standardization.

## Reference:

1) Yuyama, M., et al., Abstracts of CSJ Conference, Vol. 74 (2006), p.101 (in Japanese).



## §12. Development of a New Conductor Controlled the Twist Angle to Improve the Performance of LTS Coils

Sumiyoshi, F., Kawabata, S., Kawagoe, A.  
(Kagoshima Univ.),  
Mito, T.

The development of SMES to protect from momentary voltage drops is conducted. In this SMES, conduction-cooled low temperature superconducting (LTS) pulse coils are used. The conduction-cooled prototype coil was fabricated and tested.[1,2] The coil was wound by new design method for coils, in which the twist angles around the axis of the conductor are controlled according to the coil shape. The results of the tests on the coil showed that the coil has high performances. In this coil, however, there are some problems, for example, the winding conductor is not optimized, and the special winding machine is needed for winding this coil. As a result, the cost of the coil is increased.

The purpose of this study is to develop the new conductors which are used as windings of conduction-cooled LTS pulse coils with both low ac loss and high stability. For the purpose, several kinds of NbTi/Cu multifilamentary tapes with high aspect ratio were fabricated. For these tapes, critical currents, magnetizations, coupling losses were measured.

The aspect ratio of the fabricated test tapes were increased by rolling the round wires composed of single matrix of cooper. Therefore, the conductors are expected to have high performances as follows: (1) Ac loss in the tape under changing transverse magnetic fields oriented to parallel to its flat face is reduced. (2) The stability increases because matrix of the tape is cooper and surface cooling is possible. (3) The cost is reduced, because the tape can be fabricated by simple fabrication process which is rolling the round wire.

The parameters of four samples are shown in Table 1. 'HA00' is before rolling. The other three samples are new tapes which are increased their aspect ratio by rolling the sample HA00. The sample HA11 with the highest aspect ratio of 7.4 are most interest samples

When the transverse magnetic fields were applied parallel to the flat face of the new tapes with high aspect ratio, the measured critical currents of these samples were increased with increase in aspect ratio. Especially, the critical currents of the sample HA11 increased to 1.19 times that of the sample HA00 at 8 T.

The magnetization curves of each sample were measured by VSM. The transverse magnetic fields applied perpendicular and parallel to the flat face of tapes. In the measured magnetization curves, the proximity effect was not observed. In addition, the effective diameter of filaments,  $d_{\text{eff}}$ , which were

normalized  $J_M$  by critical current densities,  $J_c$ , were obtained. When transverse magnetic fields applied parallel to the flat face of samples, the  $d_{\text{eff}}$  of HA00 was 4  $\mu\text{m}$ , and one of HA11 was 2.8  $\mu\text{m}$ . The  $d_{\text{eff}}$  of HA11 is smaller than that of HA00. Therefore, it is found that the hysteresis losses in the tape decrease in spite of increase in critical current by rolling process.

Coupling losses were measured. Measuring conditions are as follows: The measurements were carried out in liquid helium, at 4.2 K. The dc bias magnetic fields were 0.5 T and 1.0 T. Amplitudes and frequencies of the ac ripple magnetic fields are from 0.1 to 1.6 mT and from 0.7 to 335.5 Hz. Transverse magnetic fields applied to the samples in directions parallel to the flat face of the tape.

The coupling time-constants of each sample, which are obtained from measured their coupling loss properties, are listed in Table 2. The coupling time-constants are given by dividing measured coupling losses by  $\mu_0 H_m^2 \pi \omega$ , where  $H_m$ ,  $\mu_0$  and  $\omega$  are amplitude of applied magnetic fields, permeability of vacuum and angular frequency, respectively. The experimental values almost agree theoretical values. The coupling losses in the samples with high aspect ratio, HA09, HA10, HA11 are decreased by rolling process. Especially, coupling loss in the sample HA11 are 1/17 times that of the sample HA00.

Consequently, we found as follows: (1) The hysteresis losses were decreased in spite of increase in critical currents. (2) The coupling losses in the sample with high aspect ratio decreased greatly than the coupling loss in the round wire.

### References

- [1] T. Mito, et al., IEEE Trans. Appl. Supercond., Vol.15, No.2, pp. 1935-1938
- [2] A. Kawagoe, et al., IEEE Trans. Appl. Supercond., Vol.15, No.2, pp. 1891-1894

Table 1 Parameters of samples

Sample	HA00	HA09	HA10	HA11
Dimension	1.24mm <sup>φ</sup>	0.502mm <sup>t</sup> ×2.483mm <sup>w</sup>	0.461mm <sup>t</sup> ×2.736mm <sup>w</sup>	0.403mm <sup>t</sup> ×2.984mm <sup>w</sup>
Diameter of filament	16 $\mu\text{m}$	—	—	—
Aspect ratio	1	4.9	5.9	7.4
Cu ratio	2.4	←	←	←
Twist pitch	27mm	←	←	←
RRR	50	39	37	37

Table 2 Coupling loss time-constants

Sample	HA00	HA09	HA10	HA11
Experiment [msec]	8.61	0.76	0.47	0.14
Theory [msec]	14.3	1.06	0.76	0.46
Experiment/Theory	1/1.66	1/1.41	1/1.61	1/3.24

### §13. Basic Study on Oxide Superconductors for Nuclear Fusion Reactor

Iwakuma, M. (Kyushu University),  
Mito, T.

#### 1. Introduction

This year we measured the temperature dependences of the magnetization curves of YBCO superconducting tapes and estimated the temperature dependences of the  $I_c$ - $B$  characteristics to understand the basic electromagnetic properties of YBCO tapes.

#### 2. Magnetization measurement and $I_c$ estimation

A sample straight YBCO tape with a length of 60mm was inserted into a saddle-shaped pickup coil shown in Fig.1. Magnetic field was applied in perpendicular to the wide surface. Temperature ranged from 31K to 77K. The observed magnetization curves are shown in Fig.2.

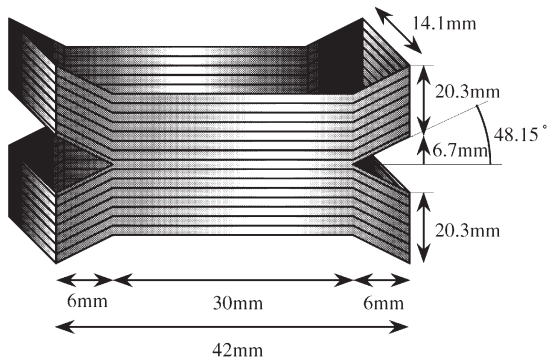


Fig.1 Saddle-shaped pickup coil

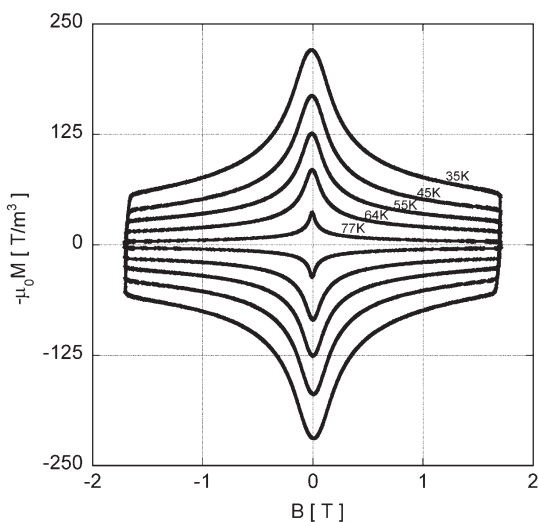


Fig.2 Observed magnetization curves

Next we estimated  $I_c$ - $B$  characteristics by using the magnetization curves and the following expression,

$$\begin{aligned} I_c(B) &= 4h \times \{((I_c(B)/2) \times (w/2)) / wh\} \\ &= 4h \times (m(B)/wh) \\ &= 4h \times M(B) \end{aligned}$$

where  $m(B)$  is the magnetic moment due to the induced shielding current at the applied field,  $B$ ,  $w$  and  $h$  is the width and the height of superconducting layer. The estimated  $I_c$ - $B$  characteristics are shown in Fig.3 in log scale.

Here we found out that the specific field at the breaking point of  $I_c$ - $B$  curves,  $B_b$ , and the constant  $I_c$  around zero field,  $I_{c0}$ , have the same temperature dependence and that the  $B$  dependences of  $I_c$  are the same for  $B > B_b$  regardless of temperature. So we normalized the  $I_c$ - $B$  curves by  $I_{c0}$ . The obtained result is shown in Fig.4. We can see that the normalized  $I_c$ - $B$  curves coincide with each other and the  $I_c$ - $B$  characteristics are scaled with temperature.

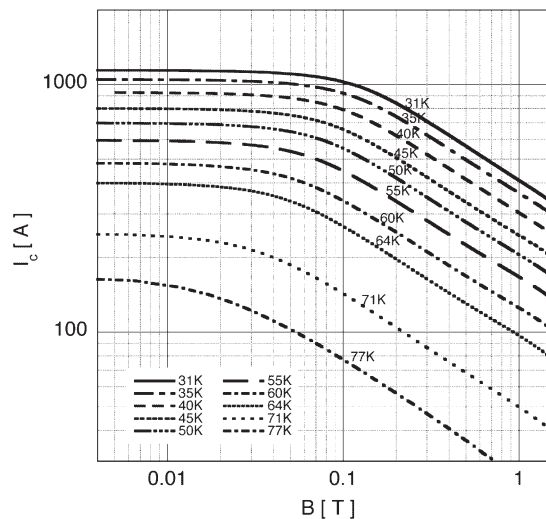


Fig.3 Estimated  $I_c$ - $B$  curves by using the observed magnetization curves

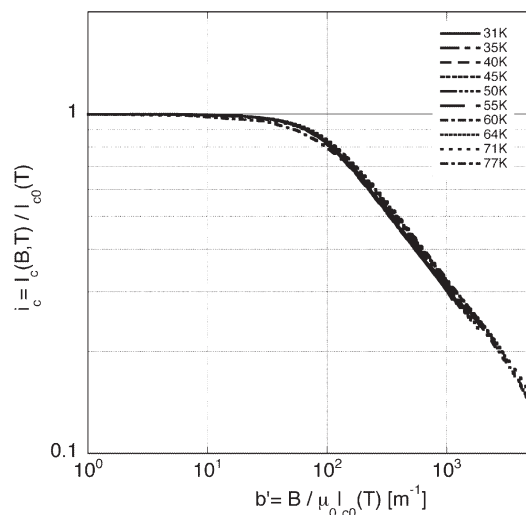


Fig.4 Normalized  $I_c$ - $B$  curves by using zero field  $I_c$  at the respective temperatures

§14. A Co-axial Pulse Tube Current Lead Development

Matsubara, Y., Maekawa, R., Takami, S., Kato, A.

Development of pulse tube cryocooler has been conducted extensively to realize the next generation of cryocooler applications. Since the pulse tube does not possess any moving parts at the low temperature region, which intrinsically has a high potential to be used as a part of applications combined with other apparatus such as current leads for superconducting coils. To demonstrate its potential, we have investigated the possibility to utilize it as a current lead system to improve the reliability of superconducting coil systems. A pair of prototype pulse tube current leads had been fabricated. The integrated current lead (ICL) consists of a co-axial pulse tube cryocooler with a current lead, a copper rod, penetrating its axis. The design work had been performed using a numerical program. The program had been written based upon an Equivalent Pressure-Volume method. The target for the current carrying capacity was 1 kA and the first prototype successfully achieved its goal. Consequently, the integration of a pulse tube refrigerator with a current lead showed the high potential to utilize as a conductively cooled superconducting coil application.

FIGURE 1 shows the schematic of pulse tube cryocooler for the numerical calculation model. In this case, the 4-valve operation scheme is described. A fundamental concept of the model is the existence of a highly elastic gas piston in the pulse tube. The gas piston is assumed to be present in the pulse tube with its ends

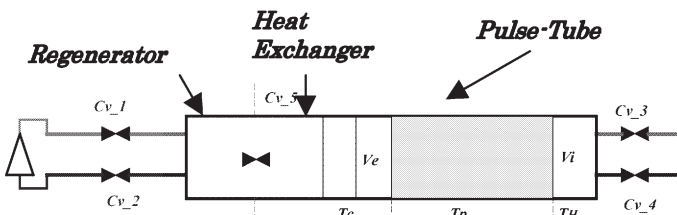


Fig. 1 Schematic of numerical model

displaced as a function of time. Therefore, the “ideal” pulse tube cryocooler cycle can be determined by analyzing gas processes in terms of equation of state. To do so, the system was divided in subsections. Working gases are either flowing in or out to the system via control valves from Cv\_1 to Cv\_4. Ve indicates the expansion volume, which provides a cooling power. Tc, Tp and TH represent temperature of a cold-end, a pulse tube and the warm end. Pressure of each section was determined by the ideal gas law. The program was designed to determine the position of a gas piston with iterations, using mass and pressure balance within the system. The calculated results reflect the pressure-volume change within the pulse tube which in turn reveals the expansion work at the cold end. Another interesting feature was dividing the regenerator in two-section by a Cv\_5 valve, reducing the computational speed. The computational result does not provide the information of pulse tube dimension. The interaction between the diameter and length of pulse tube to the refrigeration capacity has to be estimated empirically.

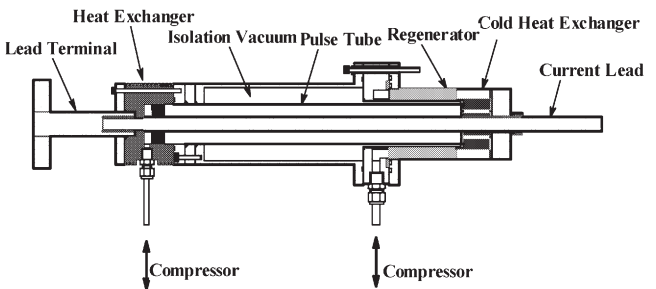


Fig. 2 A prototype pulse tube current lead.

According to the numerical design, a pair of pulse tube current leads was fabricated as shown in Fig. 2. Validation of the prototype was confirmed by the series of performance test: measuring the refrigeration capacities and study current carrying properties. The prototype achieved a steady operation up to 2.17 kA. After that the cold end temperature could not sustain the steady-state condition. This was not the optimum operating condition, however. According to the measured voltage drop across the current-lead, the temperature peak was located close to the warm-end of pulse tube. Optimization of the current-lead length and diameter will improve the current carrying capacity.

## §15. “Cryodielectrics” – Electrical Insulation of Superconducting Power Equipment Based on Partial Discharge Measurements

Hayakawa, N. (Nagoya University)

### 1. Introduction

Superconducting power equipment such as HTS power cables and magnets are expected to have higher power density and lower losses than conventional ones. However, electrical insulation technology of the superconducting power equipment, i.e. *Cryodielectrics*, has not yet been established. Partial discharge (PD) inception characteristics and mechanisms should be understood in order to prevent the degradation of insulation performance leading to breakdown (BD).

### 2. Partial Discharge Measurement of HTS Power Cables

Electrical insulation of HTS power cables consists of liquid nitrogen (LN<sub>2</sub>) / polypropylene (PP) laminated paper composite insulation system as shown in Fig. 1. We have been investigating the PD inception and BD characteristics of HTS cable models. We have already evaluated the volume effect of PD inception strength (PDIE), as shown in Fig. 2, as a function of statistical stressed liquid volume (SSLV) defined by the following equation [1, 2]:

$$SSLV = \iiint \left( \frac{E_i}{E_m} \right)^m dv$$

where  $E_i$  is the electric field strength at a volume unit  $i$ ,  $E_m$  is the maximum electric field strength, and  $m$  is the Weibull shape parameter for PDIE.  $(E_i/E_m)^m$  corresponds to the relative PD probability at the volume unit  $i$ .

Electrical and optical PD measurements with statistical analyses revealed that, at the lower stress levels, PD was generated not only in butt gaps but also in micro gaps between PP laminated paper layers caused by its own surface roughness. After the PD inception, PD activity could be propagated in the butt gaps at the higher stress levels, finally leading to BD. A detailed observation of the test samples decomposed after the experiments confirmed discolored PD traces on the PP laminated paper layers as well as BD traces in the butt gap area [3]. The PD traces were distributed along the whole butt gap area on the paper layers. These results suggest that PD would be originated between the PP laminated paper layers and developed in the butt gaps before BD. Figure 2 also shows the volume effect on BD strength (BDE) as a function of SSLV [3]. The difference between PDIE and BDE can be recognized as the margin from PD inception to BD.

A novel PD measurement under ac and lightning impulse voltage applications has also been carried out by electrical, optical and acoustic methods [3, 4]. Such PD inception, propagation and BD characteristics together with their physical mechanisms are crucial for the reliable, efficient and practical electrical insulation design of HTS power cables.

### 3. Electrical Insulation Technologies for Superconducting Power Equipment

In order to review the state-of-the-art technologies on electrical insulation of superconducting power equipment, a seminar was organized and held in NIFS on November 17, 2005. The seminar consisted of 7 lectures focusing on fusion magnets, fault current limiters and power cables, and present status and future perspectives on *Cryodielectrics* were discussed. The details of the seminar can be found at [http://www.istec.or.jp/Web21/PDF/06\\_5/J8.pdf](http://www.istec.or.jp/Web21/PDF/06_5/J8.pdf).

### References

- 1) N.Hayakawa, T.Kobayashi, M.Hazeyama, T.Takahashi, K.Yasuda, H.Okubo: IEEE Trans. on Dielectrics and Electrical Insulation, Vol.12, No.1 (2005) 166
- 2) N.Hayakawa, M.Nagino, H.Kojima, M.Goto, T.Takahashi, K.Yasuda, H.Okubo: IEEE Trans. on Applied Superconductivity, Vol.15, No.2 (2005) 1802
- 3) N.Hayakawa, K.Sahara, H.Kojima, F.Endo, H.Okubo: IEEE Conference on Electrical Insulation and Dielectric Phenomena (CEIDP) (2005) 345
- 4) N.Hayakawa, M.Nagino, H.Kojima, M.Goto, T.Takahashi, K.Yasuda, H.Okubo: International Conference on Dielectric Liquids (ICDL) (2005) 429

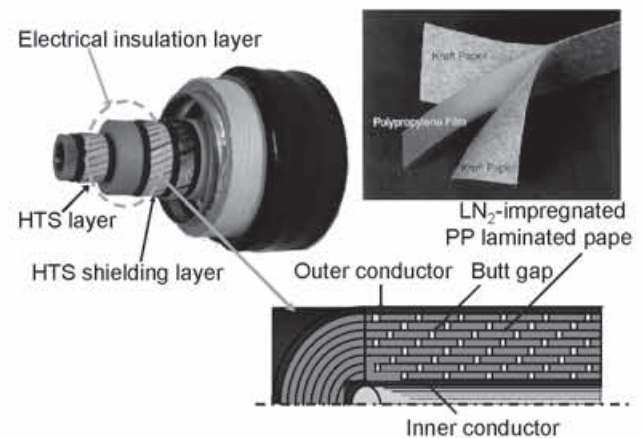


Fig.1. Electrical insulation structure of HTS power cables

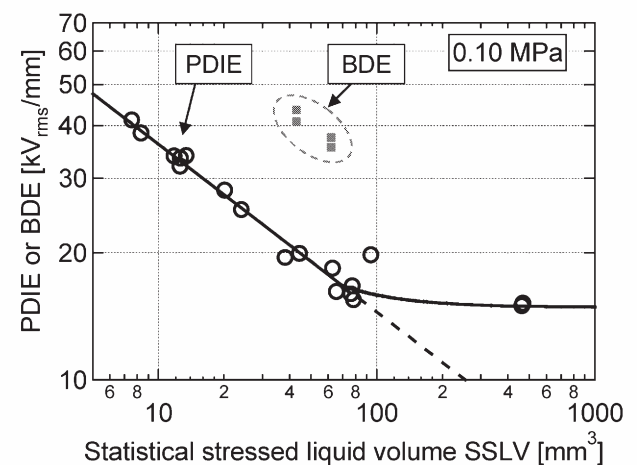


Fig.2. Volume effect on partial discharge inception strength (PDIE) and breakdown strength (BDE) as a function of SSLV for LN<sub>2</sub>/PP laminated paper composite insulation system



# §16. Validation of the High Performance Conduction-Cooled Prototype LTS Pulse Coil for UPS-SME

Mito, T., Chikaraishi, H., Maekawa, R., Baba, T., Yokota, M., Morita, Y., Ogawa, H., Yamauchi, K., Kawagoe, A., Sumiyoshi, F. (Kagoshima Univ.), Iwakuma, M. (Kyusyu Univ.), Hemmi, T. (Graduate Univ. for Advanced Study), Okumura, K., Kuge, A. (Technova), Abe, R., Nakamura, A. (Shibuya Kogyo Co.)

A conduction-cooled low temperature superconducting (LTS) pulse coil has been developed as a key technology for UPS-SMES. We have been developing a 1 MW, 1 s UPS-SMES for a protection from a momentary voltage drop and an instant power failure. A conduction-cooled LTS pulse coil has excellent characteristics, which are adequate for a short-time uninterruptible power supply (UPS). The LTS coil has better cost performance over the HTS coil at present and the conduction cooling has higher reliability and easier operation than the conventional cooling schemes such as pool boiling with liquid helium or forced flow of supercritical helium. To demonstrate the high performances of the LTS pulse coil, we have fabricated a prototype coil with stored energy of 100 kJ and have conducted cooling and excitation tests. The successful performance test results including current shut-off test with a time constant of 1.3 s and repeated excitation of a triangular waveform with high ramp rate are reported in the paper (1).

UPS-SMES as a protection from momentary voltage drop and power failure are required for industrial fabrication facilities such as semiconductor chip production equipment or large-sized experimental facilities for big science such as a nuclear fusion experimental device. A five-year project to develop UPS-SMES is being started from 2002 fiscal year as one of the research promotion programs of the New Energy and industrial technology Development Organization (NEDO). We have developed a 100 kJ class UPS-SMES in order to do a principle actual proof. According to the successful results of the cooling and excitation tests, we have proceeded to construct 1 MJ LTS pulse coils used for 1 MW, 1 s UPS-SMES.

The design of conduction-cooled pulse coil is determined by the temperature margin during pulse operation. The temperature increase of the prototype coil after 1 s discharge is estimated as 6.7 K assuming an adiabatic condition in which the heat transfer from the SC conductor to the DFRP spacers and other winding components was neglected. According to the performance test, the prototype demonstrated its high potentiality for the SMES applications. In fact, the performance values well exceeded the prototype design. Thus, the compact design of an actual system can be achieved and the running cost will be substantially reduced. Effective thermal design, arrangement of bundled Litz wires, leads to these high performances of the prototype.

Further, the supporting structure with Dyneema FRP (DFRP) spacers in the coil winding enhances the thermal performance. Since the coil consists of copper, aluminum, epoxy resin and DFRP, these materials have relatively high thermal diffusivities below 10 K. The time constants of thermal diffusivities for each component with the total amount of thickness used in the coil are estimated approximately 1 s around 4 K. Therefore, the heat generated within the coil was dissipated within the winding with a very short period. So, the spatial temperature distribution within the coil becomes negligibly small against heat generations. The detailed analysis including the heat transfer during the pulse operation and the comparison with the experimental data have been carried out in the paper (2).

We have successfully developed the conduction-cooled prototype LTS pulse-coil for UPS-SMES. The performance tests validate the design and fabrication technique of the coil. As a matter of fact, the data exceeded the design performance such as; the stored energy was 200 kJ instead of design value of 100 kJ. Since the coil was designated for a pulse operation, the effective thermal diffusivity results in the rapid temperature stabilization. Consequently, the design philosophy has been established and the much compact system with a high efficiency can be developed.

TABLE I  
SPECIFICATIONS OF THE SC CONDUCTOR

Conductor type	Aluminum coated NbTi/Cu compacted strand cable
Conductor diameter	5.8 mm
Critical current	3740 A @ 5 T, 4.2 K
Coupling time constant of AC loss: $A \tau^{-1}$	82 msec for face-on (FO) orientation 10 msec for edge-on (EO) orientation
Compacted strand cable	1.55 × 3.36 mm
Aluminum coating	Al- 1197
RRR of Al coating	9.85

TABLE II  
SPECIFICATIONS OF THE LTS PULSE COIL

Specification	100 kJ Prototype coil	1MJ Full size coil
Dimension of the coil windings		
Inner diameter: 2a1	0.305 m	0.600 m
Outer diameter: 2a2	0.509 m	0.804 m
Length: 2L	0.402 m	1.098 m
Total turn number	67 x 14 layers = 938 turns	183x 14 layers = 2562 turns
Coil inductance	0.20 H	2.00 H
Maximum magnetic field	2.2 T	2.48 T
Magnetic stored energy	100 kJ	1 MJ
Operating current	1000 A	1000 A
Coil weight	400 kg	1,100 kg

## References

- 1) Mito, T. et al., “Validation of the High Performance Conduction-Cooled Prototype LTS Pulse Coil for UPS-SMES”, IEEE Trans. Appl. Supercond, Vol. 16, No. 2, (2006), pp.608-611.
- 2) Kawagoe, A. et al., “Heat Transfer Properties of a Conduction Cooled Prototype LTS Pulse Coil for UPS-SMES”, IEEE Trans. Appl. Supercond, Vol. 16, No. 2, (2006), pp.624-627.

## §17. Improvement in Cryogenic Stability of the Model Coil of the LHD Helical Coil with Lower Temperatures

Imagawa, S., Yanagi, N., Hamaguchi, S., Mito, T.

The cryogenic stability of a model coil of the LHD helical coil was examined in saturated and subcooled helium. The cool-down and series of stability tests were carried out three times. In subcooled helium, the increment of the minimum current for dynamic propagation of a normal-zone  $I_{(mp)}$  of the model coil is almost proportional to the degree of subcooling, and it increases from 11.2 kA at the saturated temperature of 4.4 K to 11.7 kA at 3.5 K, as shown in Fig. 1. This improvement is considered to be caused by the slightly higher heat flux in the convection and nucleate boiling region at the lower temperature of helium. In saturated helium, the  $I_{(mp)}$  varies from 10.7 to 11.2 kA, and the cryogenic stability is divided into two groups[1]. The well-cooled condition was attained by being subcooled once, and it continued even after the coil quench. The reason is not clear, but the wetting area at the narrow space around the conductors could be improved.

Average propagation velocities in tested turns are shown in Fig. 2. Their reproducibility is fairly good, and the propagation velocities at the same current are slower at the lower temperature in subcooled helium. The stability test before subcool was carried out 20 hours after being immersed in liquid helium. It must be sufficient time to cool-down the coil. The tests after subcool were carried out after all thermo-sensors in the coil had indicated 4.4 K. The propagation velocity after subcool was obviously slower than that before subcool. The latter in the third cool-down is almost same as that in the first cool-down, even though the steady heat load is decreased to one third. It means that the deterioration of heat transfer before subcool is caused not only by the heat load. Although the cause is not understood well, the wetted condition of the conductor surface could be improved by being subcooled once.

From the quasi-static heat balance equation, the propagation velocity  $v_g$  is expressed as

$$v_g = \sqrt{\frac{phk}{A} \frac{\Gamma - 2}{F \cdot c \sqrt{\Gamma - 1}}} \quad (1)$$

$$\Gamma = \frac{\rho l^2}{Aph \left( \frac{T_c + T_s}{2} - T_b \right)}$$

where  $p$ ,  $A$ ,  $h$ ,  $k$ ,  $\rho$ ,  $c$ ,  $l$ ,  $T_c$ ,  $T_s$ ,  $T_b$ ,  $F$  are the perimeter, the cross-sectional area, the equivalent heat transfer coefficient, the thermal conductivity, the resistivity, the specific heat, the current, the critical temperature, the current sharing temperature, the bath temperature, and the factor of effective heat capacity, respectively. The  $\rho$ ,  $T_c$ , and  $T_s$  are dependant on the magnetic field, and the  $\rho$  is derived by multiplying the average resistivity by 2.0 as the effect of the slow current diffusion. The  $k$  and  $c$  are averages of the composite conductor, and they are dependant on the  $T_s$ .

The values of  $F$  and  $h$  were surveyed to fit the experimental results. Figure 3 shows the calculated result for  $F$  of 0.63. The  $h$  in saturated helium before being subcooled is estimated to be 0.50 kW/m<sup>2</sup>/K, and it is improved by 20% after being subcooled. Furthermore, it is improved by 30% by being subcooled to 3.5 K.

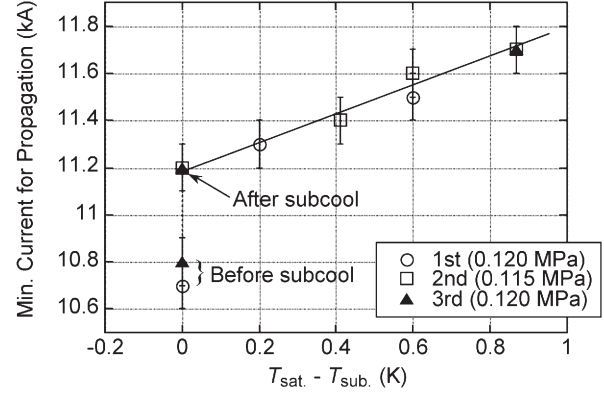


Fig. 1. Increase of the minimum currents for propagation of the model coil with the degree of subcooling.

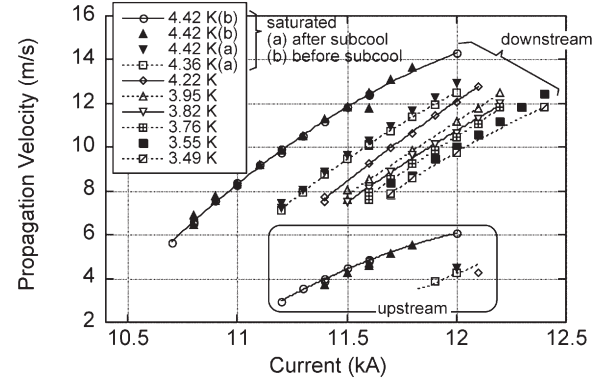


Fig. 2. Propagation velocity of the model coil in the first (solid lines), the second (dashed lines), and the third (close symbols) cool-down.

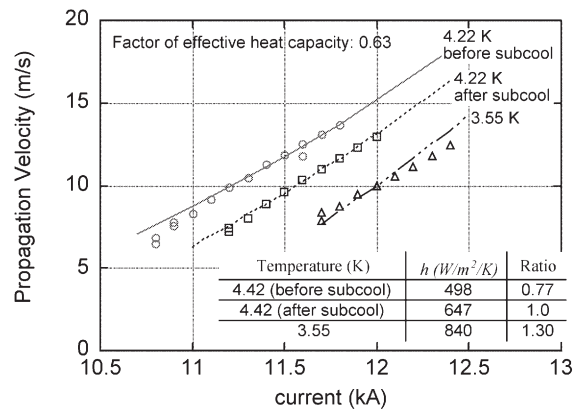


Fig. 3. Estimated heat transfer of the model coil. The symbols are measured propagation velocities, and the lines are calculated ones to fit the measured data around 10 m/s.

### Reference

1) Imagawa, S. et al.: IEEE Trans. Appl. Supercond., **16** (2006) 755.

§18. Power Saving Trial of Helium  
Compressors for the LHD Cryogenic System

Yamada, S., Moriuchi, S.

Figure 1 gives an arrangement of compressors for the LHD cryogenic system. Eight single-stage compressors of oil injection type were applied. They have a discharge capacity of 1100 g/s for the electric power of 3.45 MW. Massflow rate of the main circulation is controlled to 700 g/s, and the other of 400 g/s was bypassed for the typical operation w/o pulse operation mode, because the heat load and heat input into the cryogenic parts is not so large than that of the designed values.

In long-term operation, reduction of power consumption will be one of the most important issues. To minimize the bypass flow and to reduce the electric power consumption, unload operating characteristics of the compressor system were investigated. In this test, the compressors of AL1 and AL4 of low pressure stage were used. Following method was applied for the unload test: (1) set the stroke of the valve of AL1 gradually from 100% to 5%, and come back to 100% again, then (2) set the stroke of the valve of AL4 gradually from 100% to 0%, and come back to 100% again. To avoid the perturbation for cooling the SC coil system of the LHD, we watched carefully whether the cooling conditions of the turbines in a cold box would change. The stroke of the valve and the massflow rate change are shown in Fig. 2, and the relation of the electric power consumption and massflow rate change are shown in Fig. 3.

It was clearly seen that the massflow rate of a compressor responded with sufficient accuracy to a gradual change of a stroke. The maximum flow rate of the compressors, AL1, AL2, and AL3 were 240 g/s. The maximum flow rate of AL4 was 120 g/s. All compressor units have the capacity margin of more than 10 %.

Figure 4 shows the relation between the electric power consumption and massflow rate. The experimental result of the power consumption to a massflow rate was

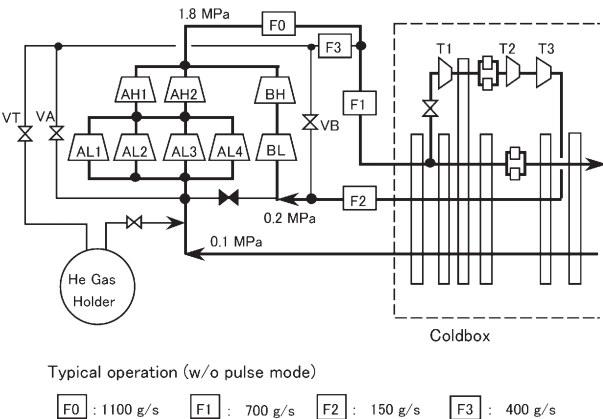


Fig. 1. Arrangement of compressors and measuring points of mass flow rates.

almost the same for the compressors AL1 and AL4. The slight difference of inclination in a Figure may originate in the difference of the load efficiency of the induction motors. It was confirmed that power consumption of 500 kW can be decreased by reducing the massflow rate of 200 g/s in the bypass circuit.

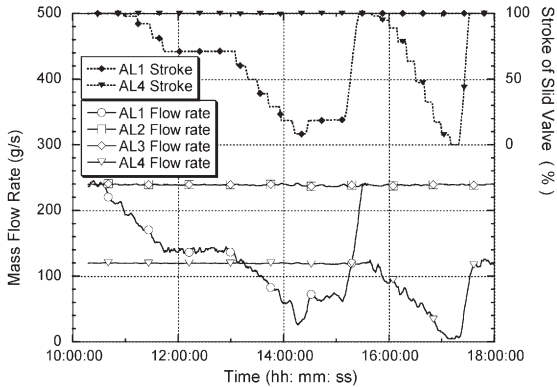


Fig. 2. Typical waveforms of slide valve stroke and massflow rate change.

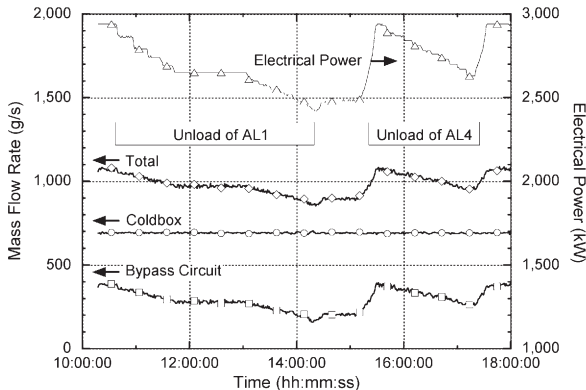


Fig. 3. Typical waveforms of slide valve stroke and massflow rate change.

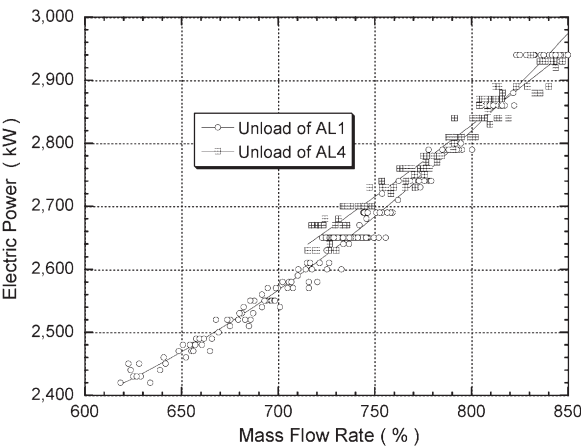


Fig. 4. Typical waveforms of slide valve stroke and massflow rate change.

## §19. Cryogenic Stability of LTS/HTS Hybrid Superconductors

Yanagi, N., Hemmi, T.,  
Bansal, G. (Sokendai)

Large current capacity with high current density is supposed to be achieved by solid composite-type superconductors when they are extra stabilized with low resistive metals. Such an example is seen in the aluminum-stabilized superconductor used for the helical coils of the Large Helical Device (LHD). However, it was found in this conductor that the cold-end recovery current was lower than the expected value due to the enhancement of the magnetoresistivity of aluminum-copper composites by the generation of the so-called Hall currents under high magnetic field. Moreover, in the transient process, the minimum propagation current becomes even less due to the long magnetic diffusion time constant in the pure aluminum, and traveling normal-zones are observed to propagate only in one direction along the conductor [1].

If these problems with composite-type superconductors are solved, the cryogenic stability can be highly improved, and this type of conductors will still be used in the near future middle-scale or large-scale superconducting coils. In this connection, we consider that high-temperature superconducting (HTS) wires can be used as a stabilizer in place of pure aluminum. An HTS wire has effectively zero resistivity as long as the transport current is lower than the critical current, and thus they can be regarded as an ideal stabilizer. In such a “hybrid” conductor, we can assume that the transport current flows initially in the low-temperature superconducting (LTS) wires. When there is a normal-transition in the LTS wires due to some external disturbances, the transport current may immediately transfer to HTS and thus the heat generation can be suppressed and a quench will be avoided. Here it should be noted that HTS wires need not to be supplied in long length but in short pieces, and therefore, the problems related with mechanical robustness and AC losses can be solved. We believe that hybrid conductors will explore a new research field in terms of the cryogenic stability of LTS conductors. At the same time, they will also contribute in the development of full HTS conductors in the future.

In order to develop LTS/HTS hybrid conductors, we started by the combination of NbTi/Cu and Bi-2223/Ag wires. Figure 1 shows the cross-sectional view of the hybrid conductor, which is the modified version of the original aluminum-stabilized superconductor for the LHD helical coils by replacing the aluminum-stabilizer by a bundle of Bi-2223/Ag tapes. This conductor is now being fabricated

and it will be tested soon. Before actually examining the properties of this conductor, we have prepared a series of small-scale samples in order to carry out proof-of-principle experiments. Here, a NbTi/Cu cable with the cross-sectional area and current capacity roughly ten times smaller than those of the LHD conductor was used and two and/or three tapes of Bi-2223/Ag wires were soldered together and thus hybrid conductors were formed. The stability tests were performed by initiating a quench in the NbTi/Cu cable using a resistive heater and the propagation of the generated normal-zone was investigated. The results are shown in Fig. 2 both for the two-tape and three-tape samples. As is expected, hybrid conductors show good stability and the minimum propagation current can be improved by using HTS tapes as a stabilizer.

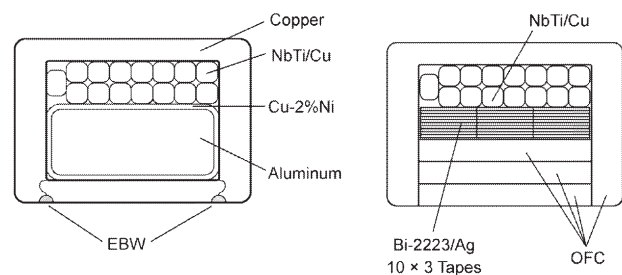


Fig. 1 Cross-sectional views of the aluminum-stabilized superconductor used for the LHD helical coils (left) and its modified version as a hybrid conductor (right).

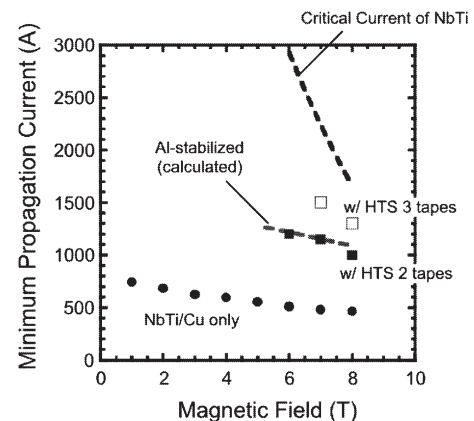


Fig. 2 Experimentally observed minimum propagation currents of small hybrid conductor samples (with two and three HTS tapes) as well as a NbTi/Cu cable.

### References

- 1) Yanagi, N., Imagawa, S., et al., IEEE Trans. Appl. Supercond. Vol.14, No.2 pp.1507-1510.
- 2) Bansal, G., Yanagi, N., et al., to be published in Fusion Engineering and Design.



§20. Operation Test of 100kW Class DEMO SMES

Chikaraishi, H., Hemmi, T., Mito, T.,  
Abe, R. (Shibuya Co., Ltd.)

The operation test using 100kJ SMES and the power converters are performed. The test circuit is shown in Figure 1. To show the large power operation of this test system, the regenerating power is circulated to the electrical utility network. In the experimental room, there is no 400V line for test, we made a test line using step up transformer.

In the preliminary operation design, the exciter will be turned off while the system supply the power to the facility. This exciter is based on the switching regulator and the dc side circuit is simple diode rectifier and the circuit to circulate dc current can be kept. Therefore, we changed the control sequence that the exciter is not turned off even if the SMES supplies power.

The electrical line used in this test supplies many utilities in the Superconducting Magnet Lab. and a hard power change in short time may makes problem to other utilities. Therefore, we limit ramp up rate of the power to 1.5 MW per second. Previous experiments show that the superconducting coil has enough operation margin and the power converters made with rating of 140kW for short time operation. Therefore we discharge at the maximum rate of 140kW to show the temperature rising in the coil clear.

Figure 2 and Figure 3 show the test results. Dc line voltage, the coil voltage and current are shown in Figure 2. The discharge started at  $t=1000\text{ms}$  and stopped at  $t=1720\text{ ms}$ . To check the operation of the chopper, the discharge operation was continued until coil current became zero. The available power is limited be coil current and dc voltage. In this system, dc voltage is 300V and 150kw output is possible while coil current is lager than 500A. At the beginning of the operation, disturbance was observed in dc current and coil voltage. The coupling between inverter control and chopper control caused this disturbance. In the next 1MW class system, a computer controller is used and decoupled control will be installed. Figure 3 shows the stored energy in the coil, power flowing dc link. The dc power is kept constant as 150kW while  $1000\text{ms} < t < 1440\text{ms}$ . After this operation, the temperature of coil increased 1K and it is smaller than the designed value. In this test operation, the capacity of the utility line used in this test was about 20kVA and is smaller than SMES output of 150kW then the line voltage raised about 30%. In the actual system line capacity and SMES capacity are balanced and the voltage change will not be occurred.

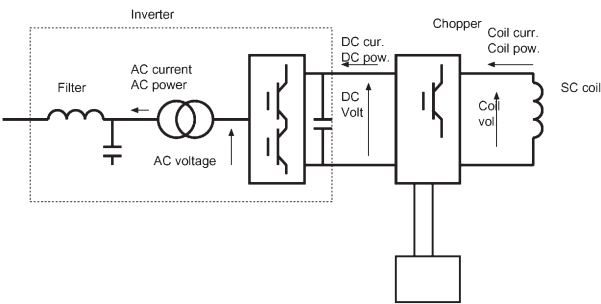


Figure 1. Test circuit diagram

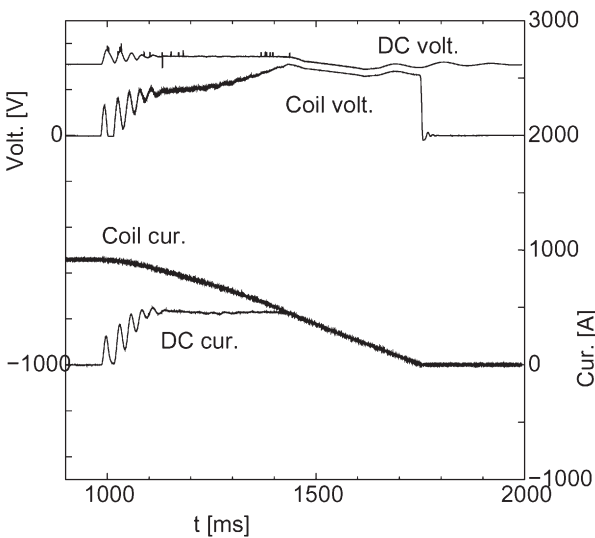


Figure 2. Coil voltage and current for 150kW discharge operation

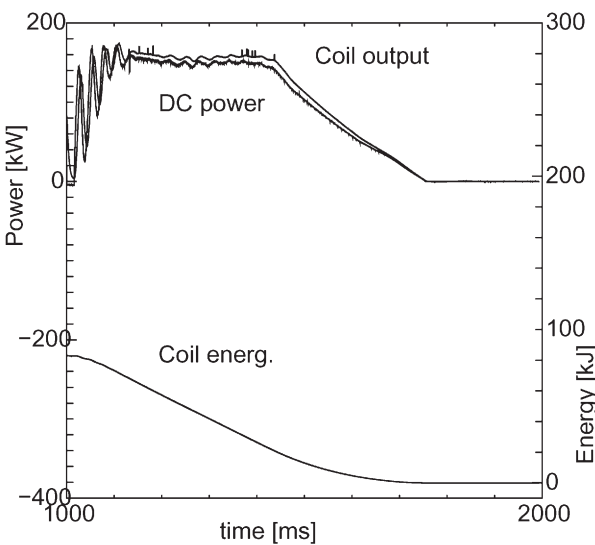


Figure 3. Stored energy and power flow

## §21. Dynamic Simulation of a Large Cryogenic Plant

Maekawa, R., Ooba, K., Mito, T.,  
Ando, K. (Taiyo Nissan Co.)

The real-time simulator for the large-scale cryogenic system has been developed since 1993. In 2004, as a result of extensive collaboration with Taiyo Nippon Sanso Co., National Institute for Fusion Science (NIFS) successfully demonstrated the capability of C-PREST, simulating the LHD helium refrigerator/liquefier. As for the next step of the development program, LHD cryogenic system was selected to be the target plant. LHD has been operated since 1998, conducting eight-year of operating campaign. Since then, the cryogenic plant has been demonstrating its reliability. Still, it is mandatory to pursue its safety and reliability, and efficient operation procedures as well. As increasing the operating period, the hardware and/or software required to be updated and/or replaced. This is primarily caused by the termination of products, especially for the control system hardware. Since the processing speed of the hardware unit has been greatly improved, it is inevitable to replace the old one. The driver or the system software has to be modified as replacing the hardware unit; otherwise this would induce the software crash and/or malfunction of other hardware. To secure the reliability of a new system, it is required to test the system before installing to the plant. To do so, the most reliable way should be the testing a new system, utilizing the identical control system and the plant. In addition to these, it is essential to study the plant process to increase its efficiency which will lead to a reduction of running cost,

A simulation model has been implemented to demonstrate the cooldown process of LHD. In this study, the modeling of LHD components was limited to the following; a pair of helical coils, three sets of poloidal coils and supporting structures. To save the CPU time, a

simulation of thermal radiation shields was substituted by the heat input to the refrigerator. A cooldown process of LHD has been designed to maintain the temperature difference within the system for less than 50 K, it is obvious to assign the massflow rate to each component with its cold mass. Since some components were eliminated for this simulation study, the total massflow ratio is less than one. The Process and Instrument Diagram (P&ID) for the simulation model has been developed. The priority for the simulation was set to achieve a real-time computation and to understand a dynamic behavior of the total cryogenic system, even though the model accuracy is considered to be more important. So, the model was executed to sustain the fast computational speed and was simplified to eliminate any additional CPU load to the process calculation. The lumped-capacitance model, neglecting any spatial temperature variations, was employed to implement the components as:

$$M_i C_i \frac{dT_i}{dt} = m C_p (T_{in} - T_{out}) \quad (1)$$

where  $M_i$  is a mass and  $C_i$  is a specific heat of component  $i$ ;  $m$  is a massflow rate of helium gas and  $C_p$  is its specific heat.  $T_{in}$  and  $T_{out}$  are the inlet and the outlet of helium gas temperature, respectively.

Equation 1 has been solved with imposing the efficiency of temperature,  $\eta$ , between the helium gas and the component  $i$ :

$$\eta = \frac{T_{out} - T_{in}}{T_i - T_{in}} \quad (2)$$

Cooldown operation was conducted and compared with the cooldown process during the 7<sup>th</sup> experimental campaign in August, 2003. There are numbers of temperature sensors in LHD system, while the simulation, as mentioned before, was done based on one temperature for each component. The simulated data were considered as an averaged temperature of the component, which agrees well with the actual operation.

§22. Design Optimization of Bi2212 HTS Tubular Bulk with Conical Shape for Current Lead

Tamura, H., Mito, T., Yamada, Y., Tachikawa, K. (Tokai Univ.), Heller, R. (FZK)

The performance of high-Tc superconductors (HTS) has been improving and many practical applications have been introduced. The major advantage of using a HTS system is a low heat load to the lower temperature region since it has a low thermal conductivity compare with a metallic conductor. They are expected as a current lead between a low-Tc superconductor and a conventional current lead which is used between room temperature and intermediate temperature. Yamada et al. has developed Bi2212 bulk material by using diffusion reaction. To obtain high transport current, increasing of the cross-sectional area can be efficient since the diffusion layer is synthesized on the surface of the substrate. A tubular bulk seemed to be appropriate to maximize the surface area. We have made some tubular bulk to investigate an electrical performance of the HTS bulk and the maximum transport current of 8 kA was achieved at 4.2K.

A current lead usually has a temperature distribution along its warm end to the cold end. From the result of the transfer current against temperature rise, the maximum transfer current was 2 kA under the condition of warm end temperature was 50 K<sup>1)</sup>. Under this condition, the cross section of the cold end can be smaller since the temperature of cold end is almost 4.2K<sup>2)</sup>. Based on the consideration, we made a new type of tubular bulk which had a conical shape. The conical bulk had 47 mm/39 mm in diameter at the warm end and that of 27 mm/19 mm at the cold end. The bulk was connected to end caps made of copper with solder. Fig. 1 shows the current profile and the temperature change at the warm end, HTS part, and cold end. No temperature rise due to the current flow was observed for any region of the specimen. The voltage generation in the HTS region was less than 25 μV. These data show that the current transport behavior is quite stable in the HTS region even when the current exceeded to 4 kA.

To show the effect of the conical HTS and for a practical use of the Bi2212 bulk, we considered a conceptual design of a current lead. The nominal current was set to 2 kA. The calculation model of the current lead consists of 3 parts; conventional heat exchanger part, HTS part, and low Tc superconductor part. The heat exchanger part was assumed that consisting of 114 bundle copper wires being 1.5 mm in diameter. The warm end of the HTS part was assumed to be cooled by 60 K helium gas with 0.9

g/s of mass flow rate. The cold end was connected to NbTi/Cu low Tc superconductor which was in the liquid helium. Thermal conductivity of the HTS part was obtained from the measurement of the Bi2212 plate. CURLEAD analysis code was used for the calculation. Fig. 2 shows the results of the calculations. We fixed the outer/inner diameter at the warm end to 47 mm/39 mm. The outer/inner diameters at the cold end of the cylindrical and conical model were set to 47 mm/39 mm and 27 mm/19 mm, respectively. Then the length of the HTS part was changed to obtain an effect for the heat leakage to the cold end. As the result, the heat leakage of the conical shaped HTS was almost 2/3 of that of the cylindrical one. The heat leakage would be less than 1 W if the length of the HTS part was longer than 150 mm.

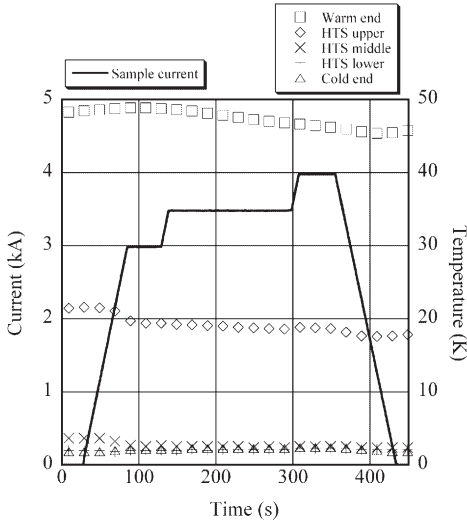


Fig. 1. Current profile and temperature of each part.

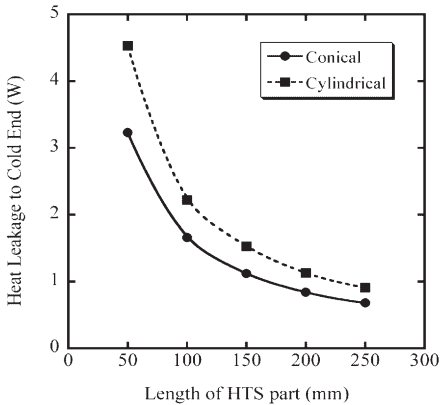


Fig. 2. Heat leakage to the cold end of the current lead as a function of length of the HTS part.

References

- 1) Yamada, Y. et al.: IEEE Trans. Appl. Superconduct. 13 (2004) 638.
- 2) Tamura, H. et al.: IEEE Trans. Appl. Superconduct. 13 (2004) 686.

## §23. Preliminary Cool-Down Tests of the Cryogenic Target for the FIREX Project

Iwamoto, A., Maekawa, R., Mito, T., Motojima, O., Nakai, M., Norimatsu, T., Nagai, K. (ILE, Osaka Univ.)

### i) Introduction

To accomplish the Fast Ignition Realization EXperiment (FIREX) project, key technologies are higher power lasers and a cryogenic target. In regard to lasers, the existing compression lasers, GEKKO XII will be utilized, and the heating laser called LFEX with 10kJ/10ps are under construction. On the other hand, the fabrication technology of the cryogenic target has been developed at the Institute of Laser Engineering (ILE), Osaka University. Furthermore, the collaborative research between ILE and the National Institute for Fusion Science (NIFS) has been started to demonstrate the fuel layering process. This paper focuses on the cryogenic target development at NIFS.

The target for the project has a unique design which have been proposed by ILE. It consists of three parts: a foam shell, a conical laser guide and a liquid or gas feeder. Epoxy resin was used as the adhesive to assemble them into a target. The difference of thermal contraction among the materials is one of the possibilities to damage the target. Therefore, to check the validity of the target at cryogenic environment, preliminary cool-down tests using the dummy target with a polystyrene shell were conducted at NIFS. In this paper, a confirmation of helium (He) leak tightness and a demonstration of  $H_2$  liquefaction on the dummy target are described.

### ii) Specification of the target

Fig. 1 shows the schematic illustration of the target applied for FIREX. The target consists of three parts: a foam shell, a conical laser guide made of a gold thin plate and a gas or liquid feeder made of a glass tube. The shell is a sphere shape with uniform and thin foam layer and has a diameter of 500  $\mu m$  with the thin layer of  $\sim 20 \mu m$ . The foam is low density porous plastic and a supporting material of fuel. The foam material is expected to be impregnated uniformly with solid fuel, so that an ideal target is formed.

### iii) Dummy target and experimental procedure

The dummy target was prepared for the preliminary study as shown in Fig. 2. A polystyrene shell with  $\sim 2$  mm in diameter and  $\sim 30 \mu m$  in layer thickness was substituted for the foam shell because of easy observation by a digital camera. The feeder with an inner tip diameter of 30  $\mu m$  was arranged. The dummy target was set in a target can. Target temperature can be controlled by the heat exchange gas-He (GHe) filled in the can. Gaseous  $H_2$  ( $GH_2$ ) was used as the substitute for  $D_2$  or DT fuel under self-imposed control of NIFS.

The validity of the target at cryogenic environment was

checked in the following two steps: the confirmation of helium (He) leak tightness and the demonstration of  $H_2$  liquefaction. At first, GHe was filled at 2.5 kPa in the target can. A leak rate through the target was measured at room temperature and at cryogenic environment by a helium leak detector. At the second step, the exchange GHe was added up to 4 kPa.  $GH_2$  was fed into the target and its pressure was kept at the saturated vapour pressure, where  $H_2$  liquefaction was started and was checked by a visual observation. During the demonstration, the temperature of the exchange GHe was controlled at 18.5 K.

### iv) Results

He leak rates through the dummy target were measured at 300 K and at 18 K. The measured leakage was  $2.5 \times 10^{-10} \text{ Pa} \cdot \text{m}^3/\text{s}$  at room temperature, whereas was  $8.2 \times 10^{-10} \text{ Pa} \cdot \text{m}^3/\text{s}$  at 18 K. A serious leak was not observed on the target. Judging from this result, it was sure that the epoxy resin was useful as the adhesive to assemble the practical target.

Figures 3(a) and (b) show successfully liquefied  $H_2$  in the dummy target. The photographs were taken by a digital camera. The liquefaction started at  $\sim 85 \text{ kPa}$  of the partial pressure of  $GH_2$ . According to saturated vapour pressure of  $H_2$ , the inside temperature of the shell at this point must be  $\sim 20 \text{ K}$ . The temperature difference between the exchange GHe and the inside of the shell results in  $\sim 1.5 \text{ K}$ .

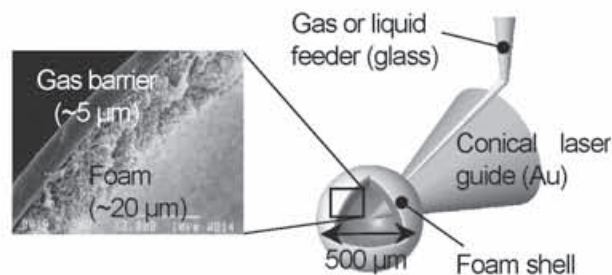
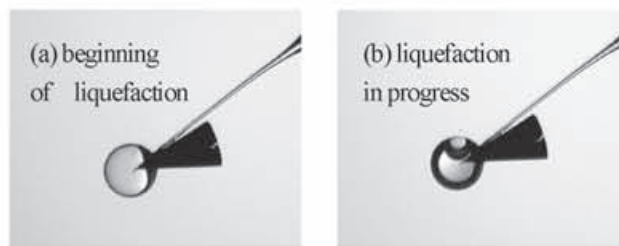


Fig.1. Cryogenic target for FIREX project.



Fig. 2. Dummy target with a polystyrene shell.



Figs. 3(a) and (b). Liquefied  $H_2$  in the dummy target.



## §24. Experimental and Numerical Studies on Heat and Mass Flow of He II through Porous Media

Hamaguchi, S., Maekawa, R.,  
Okamura, T. (Tokyo Tech.),  
Baudouy, B. (CEA Saclay)

For superconducting magnets cooled with He II, the conventional electrical insulation of the superconducting cables also works as the thermal insulation. So, it is considered that porous media are applied as electrical insulation on superconducting cables, because the flow of the superfluid component through the porous media would make a good thermal connection between the He II and the superconducting cables. To use the porous media as the electrical insulation of superconducting magnets, it is important that the heat and mass flow of the He II through the porous media is investigated. In the present study, a numerical code, which can calculate the heat and mass flow of He II both in micro channels of porous media and in He II bath and He II chamber simultaneously, have been developed.1) The present numerical model was based on the two-fluid model with the Gorter-Mellink mutual friction and dealt with the classical friction loss and the tortuosity in the porous media.2) In the present calculations, the steady state problems of the heat and mass flow of the He II through the porous media were analyzed for various porous media and the numerical results are compared with the experimental results.

Fig. 1 shows a schematic view of an experimental apparatus. The apparatus consists of 3 parts, which are an outer cylindrical vessel, an inner cylindrical vessel and a disk with a porous medium, made of SUS304. The disk is 15 mm thick with the diameter of 120 mm and has a hole in the center of the disk. A porous medium, 10 mm thick with the diameter of 40 mm, is attached into the hole. The porous medium is made of  $\text{Al}_2\text{O}_3$ , the porosity is 32 % and the average pore diameter is 1  $\mu\text{m}$ . These parts are sealed with indium wire, the diameter of 1 mm. The space between the outer vessel and the inner vessel is evacuated to interrupt the heat flux from the He II bath to the He II chamber. The He II chamber is 40 mm high with the diameter of 60 mm. A heater and a germanium thermo sensor are fixed in the He II chamber. A pressure sensor, which is connected to the He II chamber by a narrow tube, is located out of the He II chamber. The He II chamber is only open to the He II bath through the porous medium at the bottom. The apparatus is immersed in the pressurized He II bath. In the present experiment, steady heat and mass flow of He II through the porous medium was measured.

Some calculations were carried out as to the experimental apparatus before the experiments were conducted. The tortuosity of 4.6, which was estimated from previous experiments by Maekawa et al.3), was used. The numerical results are shown with the results of the

following experiment in Fig. 2. The calculations were consistent with the experimental results. The validity of the present numerical model was confirmed as to this porous media immersed in the pressurized He II. However, a little discrepancy between the numerical outputs and the experimental data occurred in the regime of the high heat flux. Subsequently, it was found that the accurate tortuosity of the porous media, obtained from the results of the following experiments, was 4.8. It is guessed that the difference of the tortuosity depends on the influence of the variation of the average pore diameter. It is expected that the numerical results will be closer to the experimental results if the corrected tortuosity is applied to the calculations.

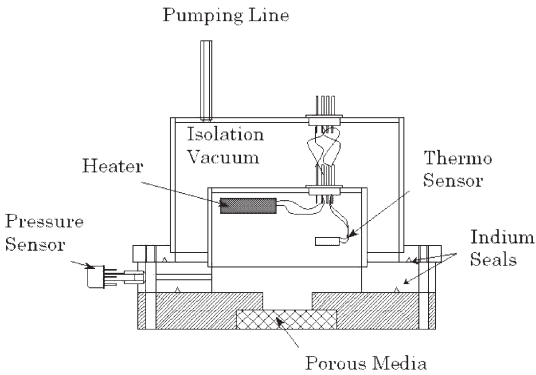


Fig. 1. A schematic view of the experimental apparatus.

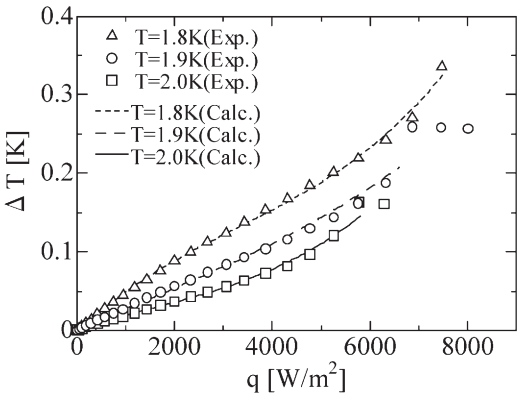


Fig. 2. Temperature difference as a function of the bath temperature for the  $\text{Al}_2\text{O}_3$  porous media with 10 mm thick in the pressurized He II. Open marks show the experimental results, while solid and dashed lines express the numerical results.

### Reference

- 1) Hamaguchi, S., et al., Journal of Plasma and Fusion Research 5 (2003) 570.
- 2) Hamaguchi, S., et al., Advances in Cryogenic Engineering 51A (2006) 105.
- 3) Maekawa, R., et al. Advances in Cryogenic Engineering 49B (2004) 983.

§25. Effect of Shielding Currents on Current Decay Behaviors in HTS Coils

Hemmi, T., Yanagi, N., Seo, K., Takahata, K., Mito, T., Bansal, G. (Grad Univ.)

HTS coils with persistent current operation are employed for high beta plasma confinement by dipole field with an internal ring. The current decay behaviors have been evaluated using the joint resistance and E-J characteristics of the HTS tape. In the past studies of LTS coils, the effect of the decay of coupling currents was discussed<sup>1)</sup>. It was suggested that the transport current could be changed by the decay of coupling currents. In the case of HTS coils, the flux creep of the shielding currents is supposed to play the key role to affect the transport current in place of the coupling currents in the LTS wires. In order to achieve magnetic stability of 0.1 ppm/h like NMR magnets, the effect of shielding currents on magnetic stability of HTS coils in persistent current operation has to be studied, and a series of experiments have been carried out and a numerical analysis using finite element method (FEM) was conducted<sup>2)</sup>.

A Bi-2223/Ag tape having the critical current of 104 A and n-value of 24.4 (at temperature 77 K under self-field) was used to wind HTS coils with a number of turns of 160 and the inductance of 4.0 mH. The joint resistance is 8 nΩ as a whole. From the experimental results at temperature of 60 K, it was found that the decay rate of the persistent current could not be fitted by an exponential function of time up to about 1000 s. In the long-time range after 1000 s, it is well fitted by an exponential function which can be determined by the joint resistance. The effective resistance can be evaluated from the decay rate of the current and the result is shown in Fig. 1. It was also found that the current decay behaviors could be changed by excitation process, as is shown in Fig. 2. In the case of an overshooting excitation, the effective resistance becomes close to the value given by the joint resistance.

The current decay behavior has been numerically analyzed using FEM by taking account of the non-linear E-J characteristics of the HTS wires. The HTS coil is assumed to be a double-pancake coil of 8 turns with the same inner radius and tape configuration. The joint resistance is assumed to be zero in the present calculation. The calculated current decay behaviors by changing the excitation process are shown in Fig. 3. The current decay behaviors are improved by having an overshooting excitation process in which the current distribution is gradually changed to the reverse direction. In the overshoot case which is first charging to 120 A, ramping down to 60 A and then

switching to a persistent current mode, the magnetic field direction, which is made by the shielding currents, becomes the same as that of the major field of the coil. Therefore, the transport current increases due to the decrease of the shielding current.

In summary, current decay behaviors of HTS coils in persistent current operations are discussed by carrying out experiments and numerical analysis. The current decay behaviors are found to be affected by shielding currents. It has been shown that the improvement in decay behaviors is possible using appropriate excitation process. We can conclude that the current decay behaviors of HTS coils should be determined by the joint resistance, the E-J characteristics of HTS wires and shielding currents.

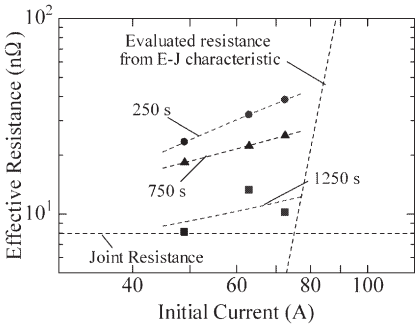


Fig. 1. Effective Resistances evaluated from current decay.

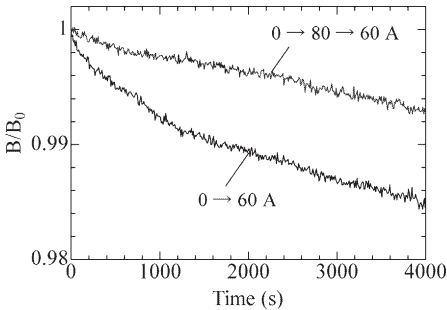


Fig. 2. Effect of excitation process on current decay.

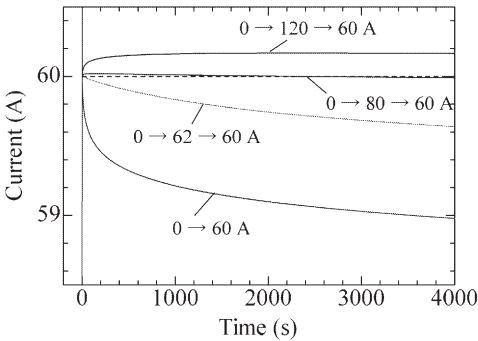


Fig. 3. Calculation results of current decay properties.

Reference

1) Cesnak, L. et al., Cryogenics 17 (1977) 107  
2) Hemmi, T. et al, to be published in Fusion Engineering and Design

§26. Development of HTS Loops for Long-Time Plasma Diamagnetic Measurements

Hemmi, T., Yanagi, N., Mito, T., Bansal, G. (Grad Univ.), Yamazaki, K. (Nagoya Univ.)

In the conventional diamagnetic measurement, the time variations of plasma energy and beta-value are evaluated using diamagnetic loops made of normal conductor, such as copper. In order to obtain the diamagnetic flux, the induced voltage is integrated. However, the integrator has drift characteristics. Therefore, the diamagnetic measurement using integrators are considered to be difficult in long pulse operations, such as longer than 1 hour. In order to improve this problem, another diamagnetic measurement system, which converts the magnetic flux into a current of a superconducting loop, is being studied. In order to arrange a loop in locations with high temperature near plasma, high-temperature superconducting (HTS) loop can be used. Here, an HTS loop is operated in a persistent current mode. In this study, a long-time plasma diamagnetic measurement system has been designed, fabricated and tested.

The schematic of a superconducting diamagnetic loop and the photograph are shown in Figs. 1 and 2. The HTS loop consisting of two double-pancakes were wound using a Bi-2223/Ag tape. The tape has a dimension of 4.1 mm width and 0.23 mm thickness, and it has the critical current of 104 A and the n-value of 24.4 (at temperature 77 K under self-field). The HTS coils have a number of turns of 80, the inner and outer radius of 50 and 65 mm, respectively. A persistent current switch (PCS) and another superconducting coil were wound by NbTi/Cu superconducting wires. The current of the HTS coils was measured by a Hall probe. The PCS is turned off during the excitation. The superconducting coil has limited the current of the HTS loop.

The HTS loop was excited using a copper coil as the primary loop, which imitated plasma diamagnetic flux. The test results are shown in Fig. 3. From Fig. 3(a), the decay time constant of the superconducting loop is evaluated to be 814 hours. The joint resistance determines this decay behavior in this system. Fig. 3(b) is the measured magnetic field when the current of the copper coil is changed.

In summary, a plasma diamagnetic measurement system using an HTS loop has been examined for long-time measurement. From the test results, the principal of this system has been demonstrated. In the future, reduction of joint resistance and high-resolution current sensor will be developed for a high-performance system. Installation of an HTS diamagnetic loop to the Large Helical Device will be considered.

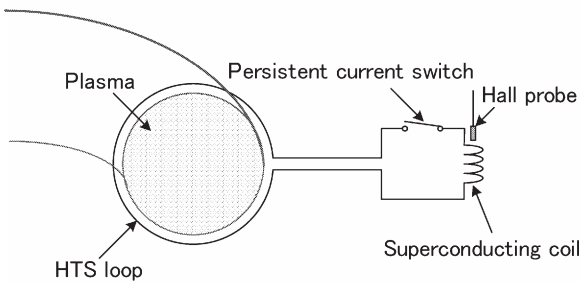


Fig. 1. Schematic of a superconducting diamagnetic loop.

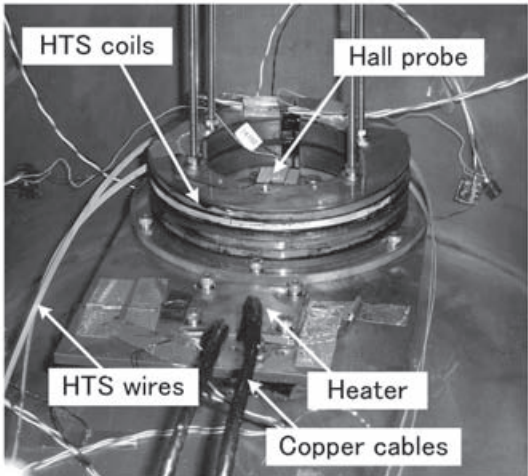
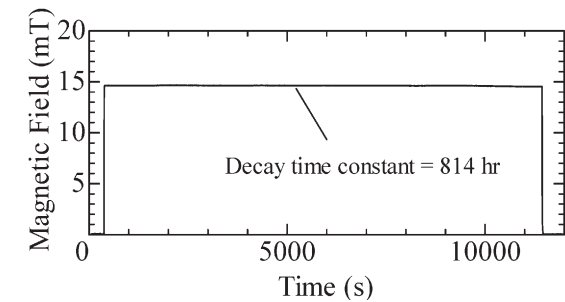
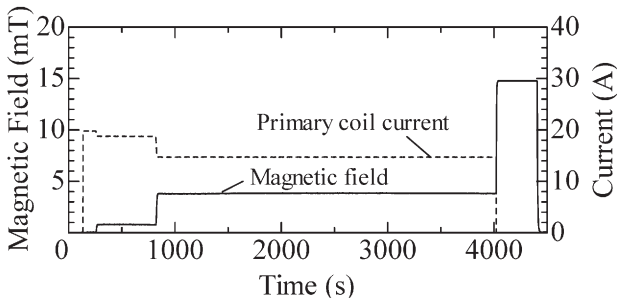


Fig. 2. Photograph of the fabricated HTS loop.



(a) Measurement of the decay time constant.



(b) Operational test.

Fig. 3. Test results of the HTS loop.

## §27. Stability of NbTi/Cu CICC with Artificial Non-Uniform Current Distribution

Bansal, G. (Sokendai), Seo, K., Yanagi, N., Hemmi, T., Takahata, K., Mito, T. (NIFS), Sarkar, B., Saxena, Y.C. (IPR, INDIA)

**Abstract:** The effect of non-uniform current distribution (NUCD) on stability of NbTi/Cu cable-in-conduit conductor (CICC) for the Steady State Tokamak (SST-1) [1] has been investigated by artificially introducing NUCD in the cable. The stability was found to decrease in case of NUCD. A transition from high stability to low stability is observed at around 13 kA current in bias field of 6 T in case of uniform current, whereas it is around 11 kA with NUCD. The dependence of stability on helium pressure is also investigated. The stability increases in liquid helium as compared to that in supercritical helium.

**Introduction:** A short sample of NbTi/Cu CICC was prepared and the stability was examined at different operating currents with uniform and non-uniform current distributions in the bias field of 6 T. The CICC has 135 strands of diameter 0.86mm without insulation in a twisting pattern of  $3 \times 3 \times 5$ . The copper to superconductor ratio is 4.9. The experiments were performed in stagnant supercritical helium at 0.4 MPa and 4.4 K. The experimental set-up details are found in reference [2].

**Experimental Method:** The last two twisting stages of the CICC were opened up into 15 sub-cables at the current inlet and outlet of the sample. Thin film resistive heaters were mounted on individual sub-cable line to introduce non-uniform current distribution in the cable. A number of combinations of the heated sub-cables of different twisting stages may be chosen using this technique. Fig.1 shows some of the combinations. The white portion in the figure shows the heated sub-cables to introduce the non-uniform current distribution in the cable. Step-0, Step-1, Step-3, and Step-6 correspond to 0%, 20%, 47%, and 66.67% heated sub-cables in the whole cable. During the experiments, initially, the sample was charged up to the desired current and then the selective heaters were turned on to obtain the non-uniform current distribution in the cable. After reaching the steady state in about 30 sec, the inductive heater was turned on to initiate a normal zone in the cable.

**Experimental Results:** Fig.2 shows the results of the measured stability margin of the NbTi/Cu CICC with uniform current and different NUCD patterns. Sharp transitions in the stability were observed with and without NUCD. A decrease in the stability was observed in case of NUCD in the cable.

The stability of the conductor was examined by varying the helium pressure as well. Fig.3 shows the results of this experiment with and without NUCD. The conductor showed high stability in liquid helium. The quench was not observed in case of liquid helium due to the restrictions of the induction heater voltage. The increased stability of CICC in liquid helium might be due to the large latent heat of vaporization ( $\sim 20$  J/g) of liquid helium.

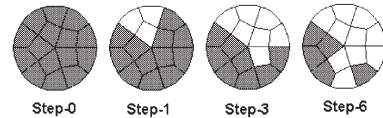


Fig.1: NUCD Patterns. The white portion is heated bundles.

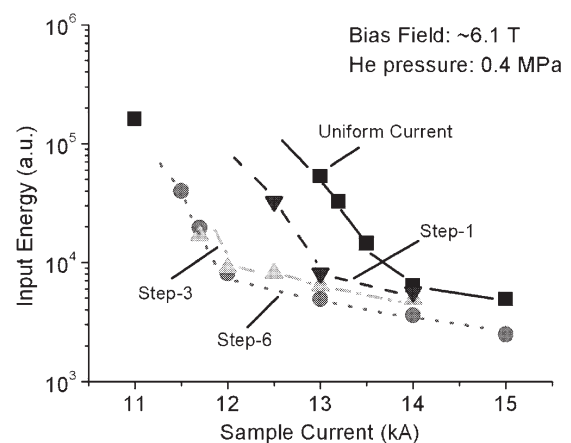


Fig.2: Stability of the conductor with and without NUCD.

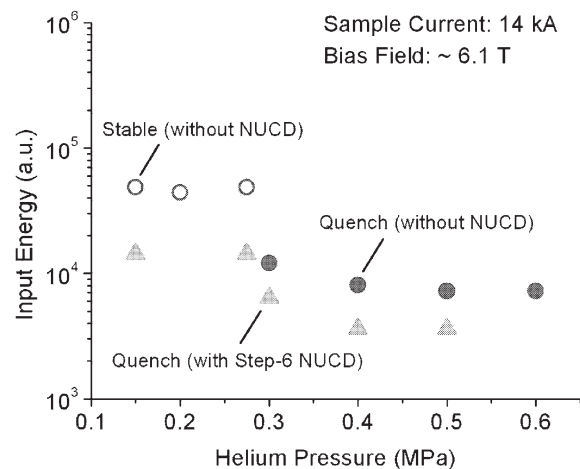


Fig.3: Dependence of stability on helium pressure.

### References:

- [1] Saxena, Y.C. et al.: Nucl. Fusion, 40, (2000) 1069.
- [2] Seo, K. et al.: 74<sup>th</sup> Cryogenic Society of Japan meeting, 2006, 2P-P34.



## §28. Cryogenic Stability of LTS/HTS Hybrid Superconductors

Bansal, G. (Sokendai), Yanagi, N., Hemmi, T., Takahata, K., Mito, T. (NIFS)

**Introduction:** Pure aluminum stabilized superconducting cables have been used in many applications such as accelerator magnets, fusion devices, SMES etc. It has been found in some cases that these conductors show rather lower recovery currents than expected due to the enhanced longitudinal resistivity by the so called Hall current generation in the pure aluminum used together with copper [1]. In transient conditions, rather lower minimum propagation currents,  $I_{mp}$ , have also been observed due to the long magnetic diffusion time constant in the pure aluminum compared to the steady-state recovery currents [2]. In the present experiment the high temperature superconducting (HTS) tapes, in place of aluminum, have been used as a stabilizer to the low temperature superconducting (LTS) NbTi/Cu cable to increase the minimum propagation currents.

**Experimental set-up:** The NbTi/Cu cable with a cross-section of  $3.36 \times 1.55 \text{ mm}^2$  was first tested and then the same cable with two layers of HTS tapes soldered on to it was tested. The sample was prepared by winding one layer of the NbTi/Cu cable into the grooves of a Bakelite bobbin. The end terminals of the sample coil winding were shorted by making a soldered lap joint so that the sample coil could be charged inductively by the background 9 T magnet. The experimental set-up schematic, and sample coil winding are shown in Fig. 1.

**Experimental Procedure:** The sample coil was charged inductively by the bias coil itself. For  $I_{mp}$  measurements, a thin film resistive heater was used to initiate a normal zone in the conductor. Voltage taps attached to the sample coil at the heater location (V2) and 4 cm away from V2 in both directions (V2R and V2L) provide information of normal zone growth in the cable. The sample coil current was measured by a calibrated Hall sensor at the center of the sample coil.

**Experimental Results:** Fig. 2 shows the typical measured voltage signals of V2, V2R, and V2L in the case of 6 T bias field. The measured  $I_{mp}$  of LTS/HTS hybrid conductor are plotted in Fig. 3. As expected, the graph shows that the minimum propagation currents increase in hybrid conductor as compared to the NbTi/Cu cable. The critical currents of HTS tapes (the sum of critical currents of two HTS tapes) and NbTi/Cu cable are also plotted for comparison. Using the observed voltage signals, the normal zone propagation velocity is estimated at different sample currents. The linear fitting of the propagation velocity on the y-axis and sample current on the x-axis gives the minimum propagation

current of the conductor. The measured minimum propagation currents of NbTi/Cu cable have also been plotted in Fig. 3.

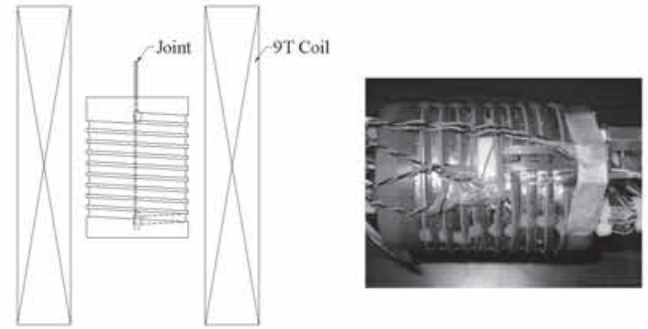


Fig.1: Experimental set-up schematic, and sample winding photograph.

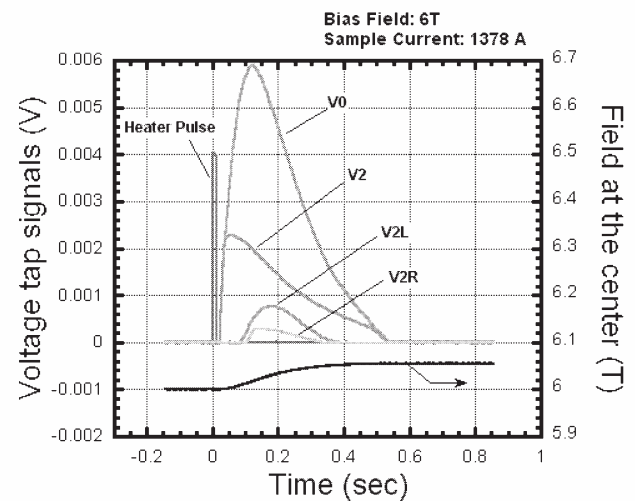


Fig.2: Typical voltage tap signals observed during the LTS/HTS hybrid conductor testing.

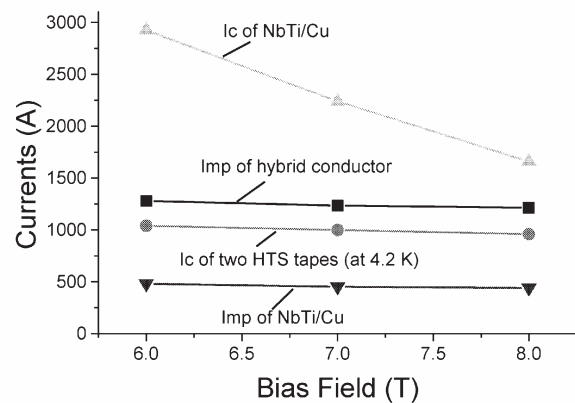


Fig.3: Minimum propagation currents of NbTi/Cu cable and LTS/HTS hybrid conductors.

### References:

- [1] Kaneko, H., and Yanagi, N.: Cryogenics 32 (1992) 1114.
- [2] Yanagi, N. et al.: IEEE Trans. on Applied Superconductivity 14 (2004) 1507.

## §29. Summary of Fifteenth International Toki Conference (ITC-15)

Mito, T.

The Fifteenth International Toki Conference (ITC-15) was held at “Ceratopia-Toki” in Toki-city, Gifu, Japan during December 6-9, 2005, with the theme “Fusion and Advanced Technology”. In the conference, 137 researchers from 12 countries throughout the world participated, and valuable presentations and fruitful discussions were held throughout the week. The number of participants from each country was found as follows: the United States (10), China (10), Germany (5), India (4), Russian Federation (3), Korea (2), France (2), Austria (1), Slovakia (1), Italy (1), Ukraine (1), and Japan (97).

The International Toki Conference (ITC), which is series of conferences dedicated to the discussions and presentations of research activities related to fusion science, was initiated in 1989 and has been held annually since then for commemorating the foundation of the National Institute for Fusion Science (NIFS). Toki-city, which is located in the central area of Japan and famous for pottery industry with 1300-year traditions, has been serving as the hosting city of the conference.

The ITC-15 focused on the science and engineering issues related to fusion experimental devices, fusion reactor designs and related advanced technologies. The topics specified on superconducting fusion devices, superconducting magnets and conductors, cryogenics, fusion reactor designs, and advanced technologies related to fusion reactors.

The conference consisted of three plenary presentations, 23 invited talks, 12 contributed oral presentations, and 76 poster presentations. Prof. Koichi Kitazawa, Executive Director of the Japan Science and Technology Agency gave the first plenary presentation with the title “Twenty Years since the Discovery of High Temperature Superconductivity”. Twenty years have passed and it was emphasized that the HTS application is proceeding into the practical stage to fulfill the dream in the future. The second keynote speech was presented by Prof. Osamu Motojima, Director General of NIFS with the title “Progress of Plasma Experiments and Superconducting Technology in LHD”. Outstanding results of the plasma experiments in the Large Helical Device (LHD) were clarified along with the engineering features of the large-scale superconducting magnet system. The third keynote speech was given by Prof. Peter Komarek, Director of the Institute for Technical Physics (ITP) of the Forschungszentrum Karlsruhe (FZK) with the title “Potential and Desire for HTS Application in Thermonuclear Fusion”. The tasks of applying HTS to fusion reactors were addressed after the present studies were reviewed regarding the development of the

superconducting technologies for nuclear fusion devices. It was also proposed that now is the time to start the application of HTS to fusion reactors because it requires a long-term research.

In the invited talks, the latest results of engineering research of the world projects were discussed by the representative researchers in each laboratory regarding the superconducting fusion experimental devices, such as Tore Supra, TRIAM-1M, Wendelstein 7-X, EAST, KSTAR, SST-1 and LHD. Moreover, 23 invited talks were presented on the latest technological developments on ITER, reactor design studies of such as FFHR, HELIAS, ARIES, VECTOR and KOYO, high magnetic field superconducting magnets, advanced metallic superconductors, HTS wire developments, and the applied superconductivity and cryogenic research activities in the world projects. Furthermore, regarding the theme of the conference, 12 contributed oral presentations and 76 poster presentations were given, accompanied by extensive discussions. The Proceedings of ITC-15 are going to be published as the special issue of Fusion Engineering and Design.

ITC-15 was organized by NIFS partly as an internal collaboration program of the National Institutes of Natural Sciences (NINS) with the support of Toki-city, Gifu-prefecture, the Japan Society of Plasma Science and Nuclear Fusion Research, the Cryogenic Association of Japan, the Fusion Engineering Division of the Atomic Energy Society of Japan. The conference was also supported by the Ministry of Education, Culture, Sports, Science and Technology, as well as by the Fusion Science Association.

The chair of the international organizing committee of ITC-15 was Prof. Osamu Motojima, and the chair of the scientific program committee was Prof. Akio Sagara. Prof. Toshiyuki Mito served the chair of the local organizing committee, Prof. Shinsaku Imagawa, the chair of the conference secretariat.

We wish to express our gratitude to all participants of ITC-15 for wonderful presentations and fruitful discussions. We would like to say many thanks to a lot of people who cooperated for holding the conference.

### (3) RF Heating Technologies

In the experimental campaign of 2005FY, EC and ICRF heating have made steady progress for high power and long pulse operations. The most noteworthy result was almost one hour plasma sustainment using both ICRF and ECH, and the 1.6 GJ was achieved as the new world record of input energy to plasma. The average input power was 490 kW (ICRF: 380kW, ECH: 110kW) and the plasma was sustained for 54 minutes. In 2004FY we achieved the record of 1.3 GJ for input energy which was the monumental success of long pulse operation of helical devices, and at the same time, it was the highest value in the world magnetic fusion devices. The input energy was not limited by heating system problems and mainly limited by sudden impurity influx inside the plasma chamber.

At the long pulse operation, impurity influx of metal dusts or flakes from the wall or divertor tiles was important factor of plasma termination in both 2004 and 2005FYs. Especially in the higher power operation of more than one mega watt, the impurity influx frequently caused bright sparks. After the bright sparks, a plasma was usually terminated by radiation collapse. In the last year campaign, the long pulse discharge by mega watt power injection was an important task in LHD. Because the high power can sustain high density plasmas and it improves the plasma parameters such as temperature and confinement time. For this purpose, a new technique, booster ECH, was developed. A plasma sustainment in 1.4 MW and 4 minutes operation was successfully achieved at the higher plasma density by using the instantaneous booster ECH pulse injection just after the sudden impurity influx. The additional ECH injection was effective to recover the plasma from the radiation collapse due to sudden impurity influx.

Besides the long pulse operation, the high power RF heating was also the main topic of this year. The ECH system was improved to inject higher power by changing one of the large diameter (88.9 mm) waveguide lines to an evacuated type to improve the stand-off voltage and also by introducing the high power 84 GHz gyrotron. After that, ECH system achieved efficient electron heating power of over 2 MW.

The impedance matching system of ICRF was also improved for efficient operation to increase the injection power. At the second harmonic heating mode, the maximum ICRF input power of 3 MW was achieved at the 38.5 MHz operation.

**ECH** In 2005FY, one of 6 waveguide transmission lines having large inner diameter of 88.9 mm, which has been used in the atmospheric pressure, was modified to be evacuated to improve the

stand-off voltage at the high power transmission. After the reconstruction of the transmission line, the conditioning process was shortened and the allowable injection power was much improved. To increase the injection power into the LHD, a new high power gyrotron (800 kW / 3s / 84 GHz) was installed and connected with this evacuated line. As a result, the maximum injection power of 530kW / 1s and a stable injection of 340 kW / 3 sec from one gyrotron became possible.

The technology of transmitting the microwave power with high efficiency through the long-distance transmission line is one of the key technologies of future fusion devices. The alignment method of a wave beam based on the moment and the phase information retrieved from infra-red images are developed under US-Japan collaboration with MIT group, and it was demonstrated the beam could be aligned within the tolerance of the required precision. The mode analysis in the waveguide will be performed as the next step.

To evaluate and measure the ECH power in any positions along the transmission line and even in LHD chamber, the new handy dummy load was developed. The octanol filled Teflon tank dummy load played an important role to evaluate the accurate power along the transmission line from the gyrotrons to the LHD plasma positions in the vacuum vessel.

**ICRF** Long pulse operation was an important item for ICRF team. To achieve successful results, many improvements were enforced. As for the impedance matching system, the feedback control system to realize the real time matched condition during the long pulse operation was developed and installed. The signals of directional coupler which include reflected power ratio and phase information were used to calculate the impedance matched conditions to control the liquid levels of stub tuners. This system was checked by using the artificial time varying dummy load, and after that, it was applied to the real long pulse experiment.

In 2005, the installed antenna number was reduced from 3 pairs of former experimental campaign to 2 pairs to check the interference with the perpendicular NBI injector which was firstly installed in LHD. As mentioned above, long pulse operation was sometimes terminated by sudden impurity influx from the LHD chamber wall or divertor plates during normal operation. Plasma was collapsed just after the some sparks around the plasma column (sometimes they came from the divertor section). These sparks seemed to be suppressed by reducing the RF field around the antenna and also by reducing the plasma density outside the scrape off layer.

(Mutoh, T.)



## §1. Development of an Evacuated Transmission Line with $\phi 88.9$ Diameter Waveguides for ECH

Ito, S., Kubo, S., Shimosuma, T., Yoshimura, Y., Igami, H., Kobayashi, S., Mizuno, Y., Takita, Y., Notake, T.

For the plasma ignition or heating, Electron Cyclotron Heating (ECH) is widely used for its stability. For the plasma experiments that depend on magnetic field, the frequency of an injected microwave has to be selected as the fundamental or 2nd harmonic cyclotron resonances. In LHD, the microwave that is generated by a gyrotron is transmitted to LHD through the corrugated waveguide with  $\phi 88.9\text{mm}$  or  $\phi 31.75\text{mm}$  diameter. The latter waveguide is used to transmit the microwave of 84GHz frequency under the vacuum condition. The former waveguide is used for the transmission of 84 and 168GHz power under both atmosphere and vacuum condition. In the transmission line in air, the transmission is limited the power level and pulse length because the arcing often occurs by the concentrated electric field in the line. Although flowing dry air through the line reduces the possibility of arcings, it is difficult to transmit the high-energy microwaves. Once a gas such as  $\text{CO}_2$  was filled in the waveguide previously, it was very difficult to eliminate the produced carbon perfectly when the arcing occurred. Therefore, we decided that the transmission line should be evacuated to avoid the arcings effectively.

As the  $\phi 88.9\text{mm}$  diameter waveguides was usually used in the atmosphere, it seemed to be easy to evacuate this line. At first, the direction of beam in the waveguide was aligned from gyrotron to LHD and the constitution supporting of the line was enforced to avoid the movement by a force of the atmospheric pressure. After that, we checked the vacuum leak in the system. There, however, were many leak points because of the original architecture of waveguide (pressure-tight structure). As the beam line and the architecture could not be changed after that, the all of leaks were sealed by a sealant. The two turbo-molecular pumps with 200L/sec pumping speed, four vacuum indicators, and two pumping ports from waveguides were prepared to evacuate the line. They were installed in adequate points for effective evacuation and the vacuum condition was monitored. Especially it is important to monitor the pressure around the barrier window between the transmission line and LHD. The detector was installed near the window and finally the achieved pressure of  $1\text{-}1 \times 10^{-2}\text{Pa}$  was accomplished in the line.

After the procedure, the system was conditioned quickly and we could inject the higher power than in the pervious

experiments. This effect is shown in Fig. 1. The arcings in the transmission line were drastically suppressed. The higher power injection obviously increases in the plasma stored energy and the electron temperature. The increment of the stored energy reaches 1.3 times by additional power injection from the new system. The electron temperature increment is also about 2keV at the  $3 \times 10^{18}\text{ m}^{-3}$  plasma density and the electron temperature of 7keV was achieved by using all of gyrotrons with three 168GHz for 2nd harmonic X-mode and five 84GHz for fundamental O-mode injection.

During the 9th experimental campaign in 2005, we could stably transmit the high power and long pulse microwave to the LHD. Some arcings, however, occurred even though the transmission line was evacuated. It originated from the insufficient evacuation. When the high-energy microwave was transmitted, the vacuum level was degraded instantaneously. On that time, the arcing was detected in the location where the vacuum level was low. There seems to be little margin of the vacuum level required for the stable operation without arcings. Therefore, we need further improvement of the transmission line, especially in the waveguide joints where many leaks were found. The structure is inadequate for highly evacuation because it is difficult to suppress the leak by tightening flanges more. Improvement of the joints of waveguides will be required. By next experiments, we will prepare another vacuum transmission line that has the improved joint-system. It is expected that the higher energy microwave can be injected steadily and repeatedly.

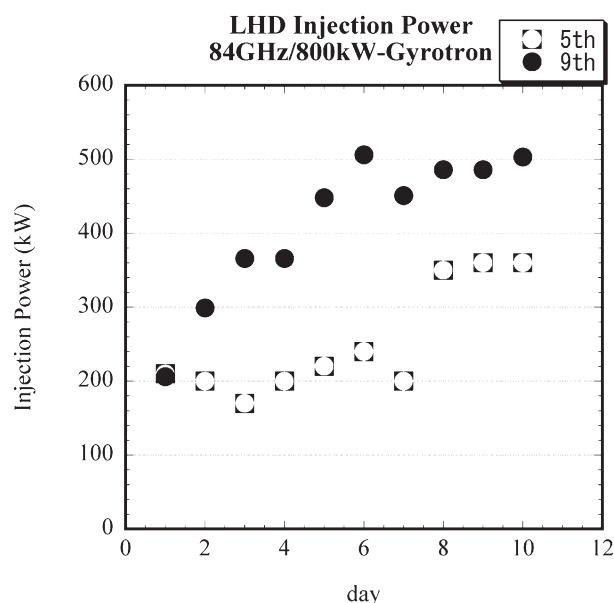


Fig. 1 Comparison of the possible injection power between in 5th (2002) and 9th (2005) experimental campaign. Progress of the conditioning during start-up period ( $\sim 11$  days) is shown in special.



## §2. Evaluation of Transmission Efficiency by Power Measurement Using a Compact Portable Dummy-Load

Shimozuma, T., Kubo, S., Kobayashi, S., Ito, S., Igami, H., Notake, T., Yoshimura, Y., Mizuno, Y., Takita, Y., Mutoh, T.

We have developed a compact portable dummy-load to measure millimeter wave power at any places along the transmission lines even in LHD vacuum vessel. Requirements for the purposes are (1) portable and compact, (2) closed system without cooling water and electricity, (3) high precision of temperature measurement, (4) thermal insulation from ambient temperature, (5) rapid thermal equilibration and so on.

The dummy-load consists of 250mm × 250mm × 80mm Teflon<sup>®</sup> tank (thickness is 10mm), a precise RTD(Resistance Temperature Detector) and a stirrer to uniformize the temperature of absorbing liquid shown in Fig. 1. The Teflon tank can be filled with about 2-liter octanol and is thermally insulated from an aluminum frame surrounding the tank. The RTD has the measurable accuracy of 0.01 degree and the temperature data can be transferred through RS232C and recorded every 0.2 sec. The stirrer is driven by a rechargeable battery. The dummy-load can be set in the measuring positions both vertically and horizontally.

Teflon is adequate for high power millimeter transmission because of its low permittivity and low loss-tangent. It also has low thermal conductivity. We initially used water as a absorbing liquid. Since water has very high permittivity (88 at 0 deg.C) , the reflection from teflon-water layers is about 80% for the right angle injection. Octanol has low permittivity and low absorption coefficient and has linear absorption of 13 dB per cm traversed<sup>1)</sup>. And it has the same level of the boiling point as water. So we chose it as a working liquid.

By using the octanol dummy-load, transmitted power was measured at several positions along the transmission line. Figure 2 shows the result of temperature evolutions of octanol. Injected power into the dummy-load was a single shot of 200kW with 10ms pulse width, which was measured by a normal Teflon tubing-load installed at the MOU out. The temperature reached the maximum about 20 seconds after the pulse, then it gradually decreased. We used the maximum temperature rise to estimate a millimeter wave energy absorbed in the octanol and calculated the power. Such values are also indicated in the Fig. 2. The positions of measuring point are as follows. The position of "MOU out" is the output from the matching optics unit near the gyrotron. The position of "Miterbend in LHD room" locates about 100m apart from "MOU out", in which

there are 7 miterbends and a polarizer system that consists of 3 mirrors and 2 polarizers. The position of "LHD window" is about 15m apart from "Miterbend in LHD room" and is just above the LHD injection port. Finally the position of "in LHD" corresponds to the focal point of the mirror antenna on the equatorial plane of LHD. The evaluated transmission efficiency between "MOU out" and "LHD window" is agreed with the value obtained another measuring method within the error of 6%. Big difference was observed between the measured and expected values for the efficiency of "in LHD". After the LHD window, there are only four mirrors and spill-over loss was estimated as 2-4%. The reason is unknown for the present. Possible reasons are an error in measurement method, low mode purity in the waveguide, unexpected absorption on the mirror and so on. The load still needs some improvements, such as stirring working liquid, rapid time response of RTD, reducing reflection from the Teflon surface, thermal insulation from ambient temperature. Those issues are under consideration.

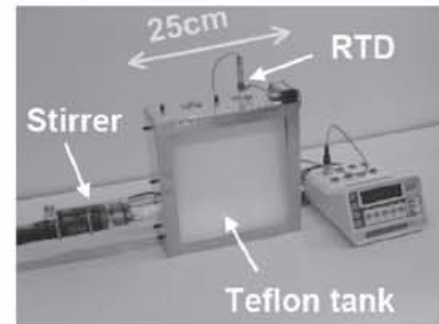


Fig. 1: Teflon<sup>®</sup> dummy load with RTD and stirrer

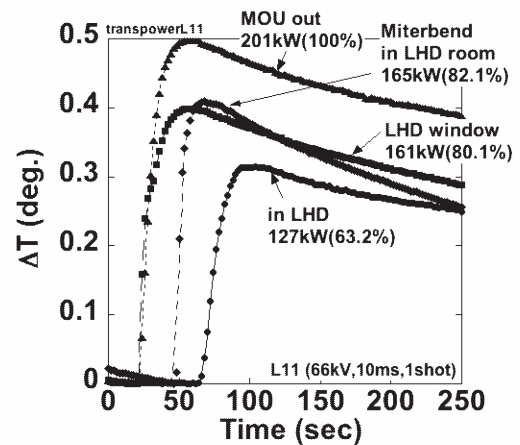


Fig. 2: Time evolution of the temperature of octanol in the dummy-load, which is measured at several positions

### References

- 1) H. Stickle, Int J. Electronics 64, 63 (1988).

### §3. Moment Analysis of Power Profiles Radiated from Corrugated Waveguides of ECH Transmission Lines

Shimozuma, T., Ito, S., Kobayashi, S., Mizuno, Y.,  
Kubo, S., Yoshimura, Y., Igami, H., Takita, Y.,  
Notake, T., Idei, H. (Kyushu Univ.)

In an ECH system, the improvement of the transmission efficiency is getting more important, because long-distance transmission is required for large fusion devices such as ITER. It is very easy to deteriorate the transmission efficiency, because the used millimeter wave(mmW) has short wave length compared with the size of some transmission components. We proposed a mmW alignment method based on moment and phase information retrieved from IR (Infrared) images<sup>1)</sup> under the US-Japan collaboration with MIT group, and demonstrated the beam could be aligned within the tolerance of the required precision<sup>2)</sup>. The next step is the mode analysis in the waveguide which is deduced from retrieved phase and amplitude information.

Prior to the mode analysis, we measured radiation patterns from the corrugated waveguide of the several transmission lines at some positions, which were used in LHD ECH system. The method of the measurement was the same as before described in ref.2). Measurements were performed for four lines (two 82.7GHz and two 168GHz lines). The measured position was mainly at the ECH transmission stage in the LHD room, which located about 100m far from the beam entering position into the corrugated waveguide. Figure 1 shows radiation patterns at the several distances  $L$  from the corrugated waveguide mouth of the 82.7GHz line with 88.9mm in diameter. The power profile at the waveguide mouth has two peaks around the axis. The profile, however, becomes one peak through the propagation. The propagation characteristics agree with the evolution of the Gaussian beam which is deduced from the calculated second moments. The spatial profile of temperature increment of the target is plotted in Fig. 2 at  $L = 810\text{mm}$  in logarithmic scale. The dashed line is a Gaussian profile that is normalized at  $x = 0$ . The radiation pattern can be well described by a Gaussian profile. The first moments,  $x_0$  and  $y_0$ , which correspond to the center of the mmW power, show obvious inclination of the mmW beam axis shown in Fig.3. This fact suggests that the mmW beams axis is probably changed in the waveguide by some imperfection of transmission line alignment, for example, miterbend mirrors and tilt, offset at the waveguide coupling points.

#### References

- 1) M. Shapiro et al., Fusion Eng. Design 53(2001)537-544.
- 2) T. Shimozuma et al., J. Plasma Fusion. Res. 81(2005)191.

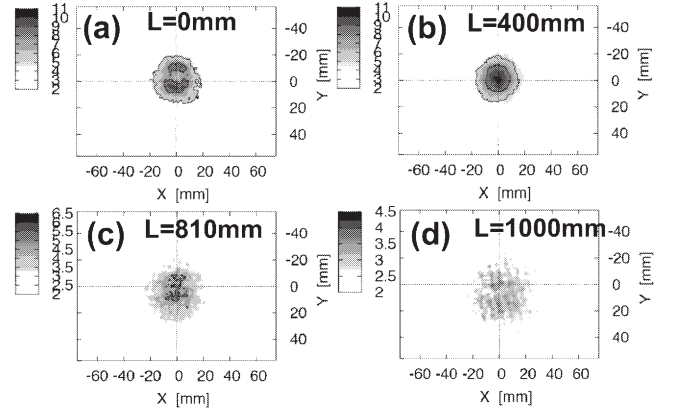


Fig. 1: Radiation patterns measured at several distances  $L$  from the corrugated waveguide mouth. (a) at the mouth, (b)  $L = 400\text{mm}$ , (c)  $L = 810\text{mm}$  and (d)  $L = 1000\text{mm}$

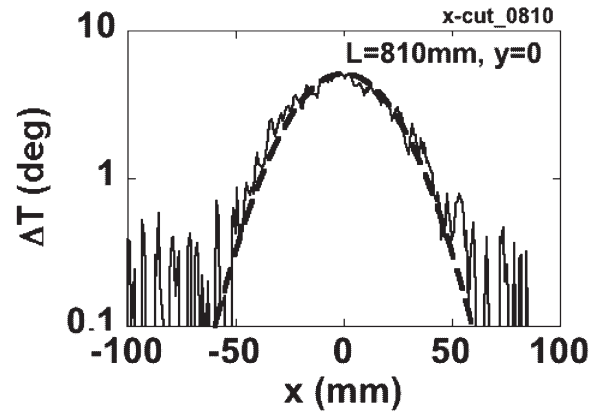


Fig. 2: Radiation pattern (temperature increase of the target measured at  $L = 810\text{mm}$ . The dashed line shows a fitted Gaussian profile

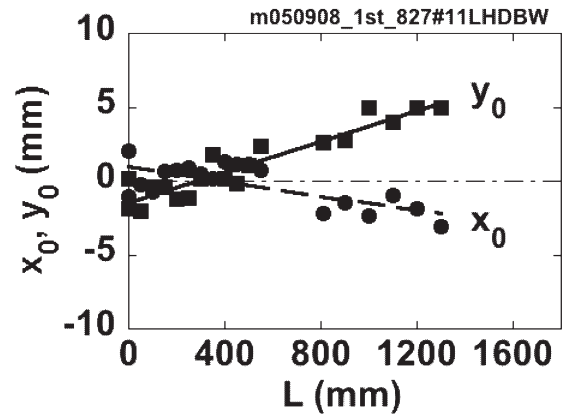


Fig. 3: The evolution of the power center, which is the first moment of the radiation profile.

§4. Installation and Operation of New 84GHz Gyrotron System

Kobayashi, S., Kubo, S., Shimozuma, T., Yoshimura, Y., Igami, H., Takita, Y., Ito, S., Mizuno, Y., Notake, T.

We have installed an 84 GHz gyrotron of 800 kW output power for the 9th experimental campaign to perform high power heating experiments at fundamental electron cyclotron resonance condition. In order to operate this gyrotron, we have newly added a body power supply (30kV, 0.2A), a heater power supply and a crowbar switch to the existing collector power supply No. 3, with which another gyrotrons can be operated in parallel. Figure 1 shows a block diagram of these power supplies used for this gyrotron.

We have also installed a new gyrotron tank, since all existing ones are occupied. Due to the limitation of the allowed space and furthermore in order to reduce the total volume of insulation oil, we made a compact gyrotron tank structure of 1 x 2 m<sup>2</sup> in occupying area. Gyrotron, SCM (super conducting magnet), and MOU (matching optics unit) can be firmly supported by this structure and attached oil jacket surrounding the gyrotron body and cathode works as an interface of the high voltage. This MOU has vacuum tight structure so as to connect to the evacuated waveguide system. Water pipes of ceramic or Teflon are placed inside the MOU to absorb stray microwave power. Figure 2 is a whole view of this gyrotron system. The other important new components are a vacuum tight multi-hole power monitor and a dummy load, which are modified from those originally designed for use in the air. Using these new components, transmission power and gyrotron oscillation states are monitored in real time. Figure 3 shows a correspondence of the monitored signal level and injected power into LHD. As the result, the power of 340kW/3sec is stably transmitted and injected into the LHD from this gyrotron system.

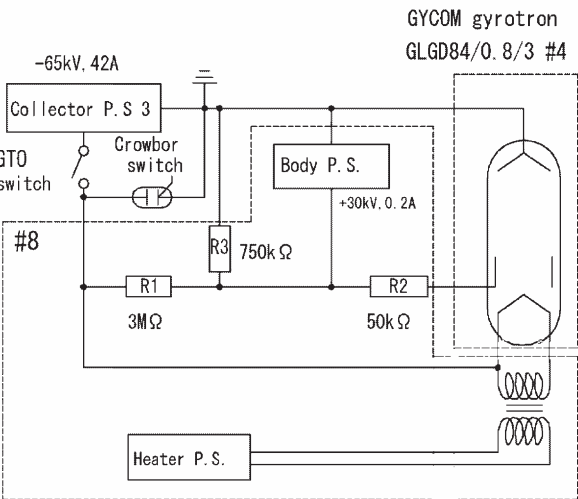


Fig. 1. A connection diagram of gyrotron power supply No, 3

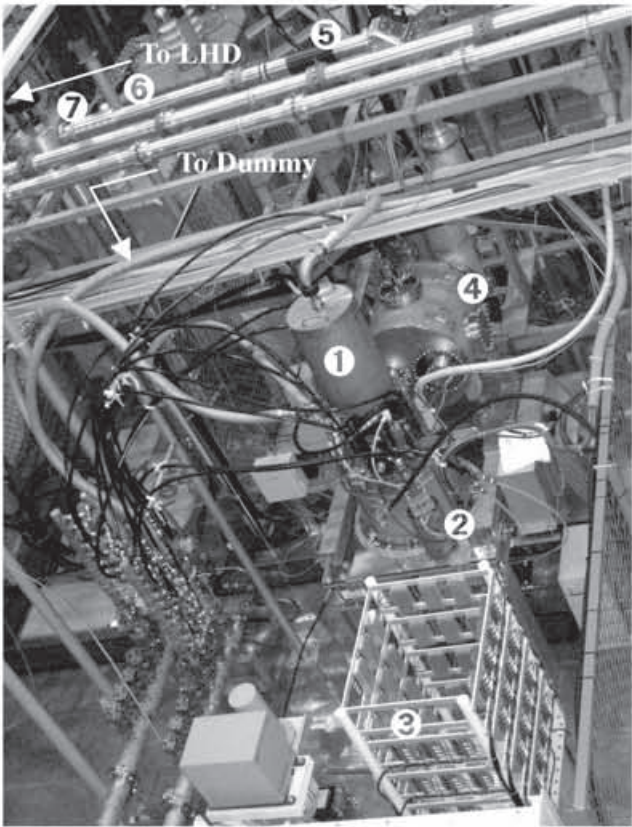


Fig. 2. 84GHz Gyrotron and power supply assembly.  
①: Gyrotron, ②: SCM, ③: Body power supply, ④: MOU, ⑤: Power monitor, ⑥: 88.9mm waveguide, ⑦: waveguide switch,

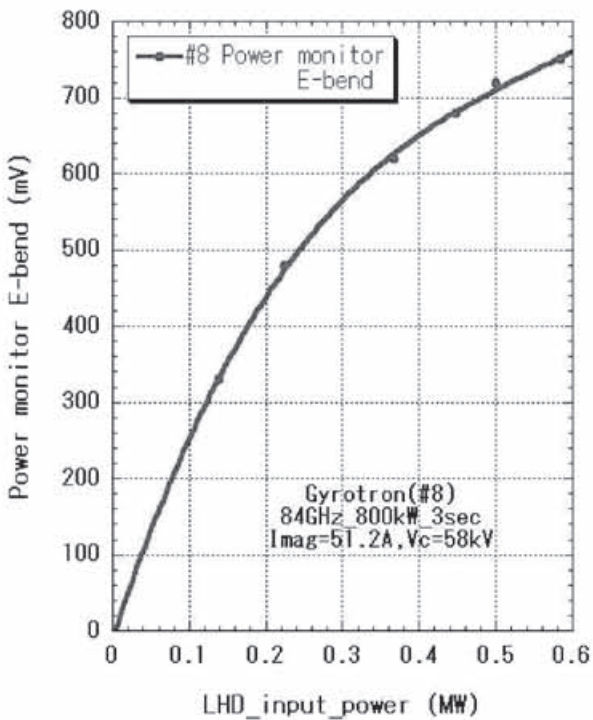


Fig. 3. A correlation between output level of power monitor and the power injected to LHD.



## §5. Study on High Energy Particles Escaped from LHD Using Lost Ion Probe

Nishiura, M., Isobe, M., Mutoh, T., Osakabe, M., Kubo, N., Sasao, M. (Tohoku Univ.), Murakami, S. (Kyoto Univ.), Darrow, D.S. (PPPL)

For understanding fast ion behaviors, a scintillator type lost ion probe is newly developed and installed into 2.5U port of LHD. 1, 2) The lost ion probe has measured the loss signals of fast ions near the edge region throughout the 9th campaign.

The location of the lost ion probe was determined using the collision less orbit code of single particle and Delta5d code taking into account the particle collisions inside plasmas. Both results are crosschecked. The Delta5d code calculates the fast ion behaviors using NB deposition profile. In the case of the magnetic axis  $R_{ax}=3.75\text{m}$  and  $B_t=3\text{T}$ , the ion loss points across the last closed flux surface of  $\rho=1$  are mapped on the  $\theta$ - $\Phi$  space, where  $\theta$  and  $\Phi$  are the poloidal and the toroidal angles, respectively.

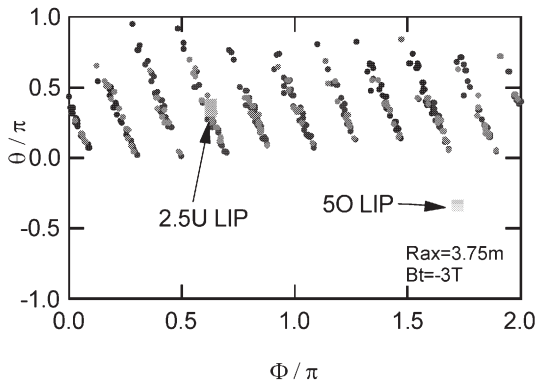


Fig. 1. Maps of ion loss points and detector positions (2.5U: new location, 50: location before 8th campaign)

The lost ion probe measures the pitch angles and the gyro radii of fast ions directly and simultaneously by observing the ion strike points on the scintillator plate passing through the entrance slit and the collimator slit. The emitted light from the scintillator plate is detected by a CCD camera for relatively slow signals of 33 msec/frame and by a 3x3 photomultiplier array for fast signals from dc to 20 kHz. Figure 2 shows that the gyro radius estimated from the peaks of striking points on the scintillator plate becomes small as the toroidal magnetic field increases.

The confinement time of fast ions can be obtained from the ICRF power modulation experiments. The phase delay between the ICRF sine wave and the detected signal is used to estimate the confinement time of fast ions.

3) From this result, the phase delay is found to be 20.7 degrees. In the previous experiments, the neutral particle analyzer is used as a detector. However since a direct detection of fast ions is possible without the effect on a sight line integration, the confinement time would be obtained more precisely.

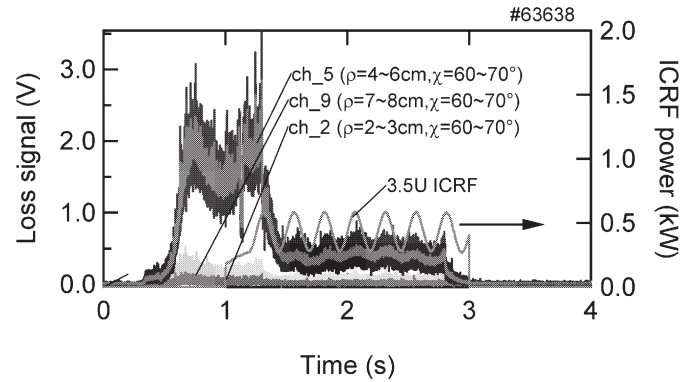


Fig. 2. Fast ion losses for gyro radii. The signal of Ch5 corresponds to the ion energy with more than 30 keV. The ICRF power is modulated with a sine wave of 4 Hz.

The spatial distribution of lost fast ions is measured in the vicinity of the LHD plasmas, shown in Fig. 3. At  $Z=1000\text{ mm}$ , the intensity of lost fast ions has almost disappeared. These data are important, and can use the estimations of deposition profile of NB with the combination of HFREYA code.

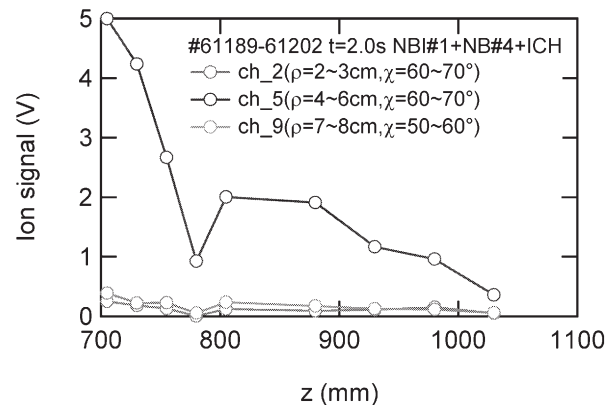


Fig. 3. Spatial distribution of lost fast ions is measured in the edge region at  $R=3.45\text{m}$ . Plasma parameters are  $n_e(\text{FIR})=0.75 \times 10^{19} \text{ m}^{-3}$ ,  $R_{ax}=3.6\text{m}$ , and  $B_t=-1.375\text{T}$ .

### References

- 1) Nishiura, M., Isobe, M., Saida, T., Sasao, M., and Darrow, D. S., Rev. Sci. Instrum. **75**(2004)3646.
- 2) Nishiura, M., Isobe, M., et al. NIFS-PROC-63, (2006)194-198.
- 3) Mutoh, T., et al. Nucl. Fusion **43**(2003)738-743.



§6. Sparks from Inner Side of Torus during ICRF Long Pulse Heating

Saito, K.

In the large helical device (LHD), plasma collapses due to the abrupt electron density increase and the radiation power increase were often observed at the end of the long pulse discharge by the ICRF minority ion heating [1]. At the same timing of the abrupt plasma collapses, an increase in the FeX intensity was observed. Therefore, plasma collapses was attributed to the influx of iron impurity. One of causes of influx of iron impurity was due to sparks, because in several discharges sparks were seen in the inner side of the vacuum vessel near the 7.5U and L antennas. Fig.1-(a) shows the sparks from the inner side of 7th toroidal section (7I) viewed by the CCD camera installed in the 6T port (tangential). In 2006, another CCD camera was installed at the 7O port to observe the sparks from 7I. Fig.1-(b) shows the same sparks with Fig.1-(a) by the CCD camera in the 7O port. In this discharge sparks occurred on the divertor plates or the wall of vacuum vessel and at the same timing the plasma collapsed, but the precise position of the sparks was not clear because no damage was found inside of LHD. Sparks were usually not seen initial few minutes but gradually small sparks occurred and finally plasma collapsed. This phenomenon of sparks is therefore thought to be closely related to the temperature increment of the chamber wall including the divertor plates.

In the case of the minority ion heating, temperature distribution is localized in the toroidal direction [2]. The temperature of divertor plates around ICRF antenna is higher than that of the other area. According to the calculation of particle orbit, accelerated protons at the cyclotron resonance layer out of the last closed flux surface (LCFS) in front of the antennas can result in the localized intense heat load in the toroidal direction. Squares in Fig.2 indicate the temperature increment of the divertor plate located at the inner side of 7.5L port near 7.5U and L antennas in two minutes normalized by the injected power from these antennas (300-500kW) depending on the distance between these antennas and LCFS. Circles indicate the normalized temperature increment of the wall of the vacuum vessel located 7I in two minutes. It was found that the temperatures increased with the distance between antennas and LCFS. Temperatures were thought to be increased due to the increase of resonant hydrogen ions accelerated in the peripheral region by widening the distance.

Sparks may be suppressed by narrowing the distance between antenna and LCFS by the reduction of temperatures around ICRF antenna, but temperature of antenna itself increases. In the case of the distance of 6cm, the temperature surpassed 1000°C in two minutes. Therefore we cannot use this method for the long pulse discharge. Suppression of particle acceleration in the peripheral region is necessary.

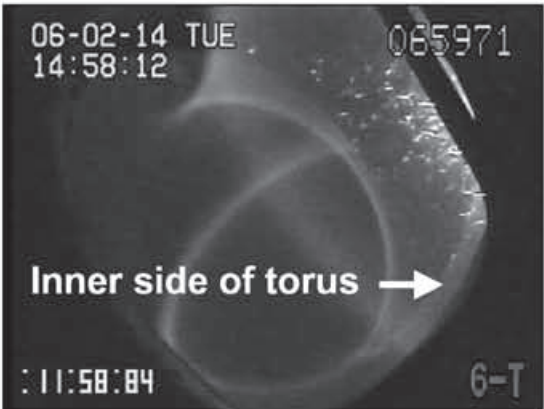


Fig.1-(a) Sparks viewed from 6T port.

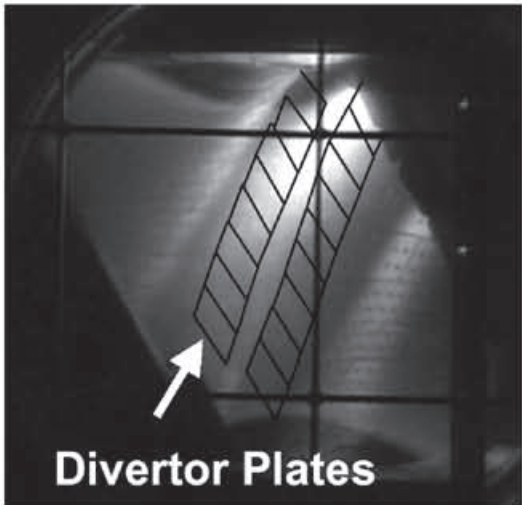


Fig.1-(b) Sparks viewed from 7O port.

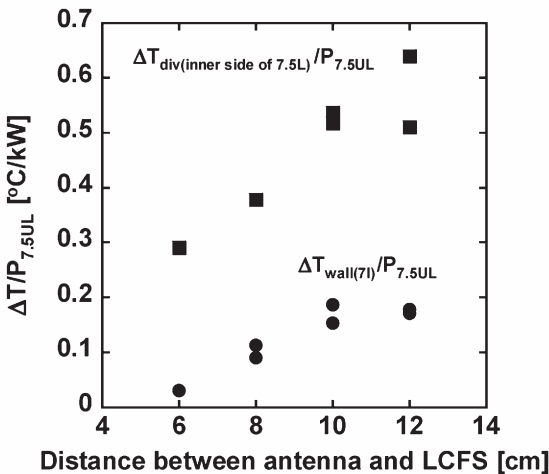


Fig.2 Wall and divertor plate temperatures depending on the distance between antenna and LCFS.

References

- 1) Kumazawa, R, et al.: Nuclear Fusion, **46** (2006) S13.
- 2) Saito, K, et al.: J. Nucl. Mater. 337-339 (2005) 995.

## §7. Improvement of Real-Time Impedance Matching System for the ICRF Long Pulse Heating

Saito, K., Takahashi, C., Yokota, M.

For a long pulse discharge we had conducted two methods of impedance matching in ICRF heating in LHD to reduce the reflected power caused by the change of antenna impedance [1]. One was manual frequency control. By this method, the reflected power fraction initially decreased. However, the frequency was limited to within the allowable bandwidth of the amplifiers without tuning; therefore, the reflected power eventually increased. Therefore this method was insufficient. Another method was automatic feedback control utilizing a trial-and-error method by using liquid stub tuners. Since this method has the risk of increasing the reflected power fraction by incorrectly shifting the liquid height, it is useful only for very slow variations in antenna impedance. Moreover, it took some time to reduce the reflected power fraction because the liquid stub tuners have to be controlled one by one.

Since the above-mentioned methods have limitations, a new real-time impedance matching method was required. Since fine impedance matching through the use of a prediction method has been established for short pulse discharges in the LHD [2], the reflected power fraction was expected to be kept low during a long pulse discharge by the application of this method to real-time feedback control.

Figure 1 shows the real-time impedance matching system using the prediction method. It consists of the liquid stub tuners, a directional coupler, 3dB couplers, a phase detector, diodes, an analog-digital converter (ADC), a computer, motor drivers, and pulse motors. The signals of the forward and reflected waves are measured by the directional coupler. The waves' signals are divided by 3dB couplers. One signal is rectified by a diode and the other signal is input to the phase detector. The outputs of the phase detector, the rectified forward and reflected wave amplitudes, and the liquid height voltages are converted to a digital signal by the ADC. Then a computer calculates the antenna impedance and the liquid heights are predicted so as to achieve an impedance matching. Pulses are sent to the motors via motor drivers as determined by the calculation.

The feedback experiments were conducted by attaching a variable resistor to the outlet of stub tuners at a power of less than 1W. The frequency was set to 38.47MHz, which is the standard frequency of the LHD plasma experiment. Figure 2 shows the result of the experiment. Resistance changed between  $3\Omega$  and  $6\Omega$ . Without feedback control reflected power fraction  $P_r/P_f$  reached 13.5%, but by adjusting liquid lengths  $L_2$  and  $L_3$ , it was kept low under 1%.

Since this system was verified to be useful, we utilized it for long pulse plasma discharges. In 2006 we achieved the world record of input energy of 1.6GJ by using this system.

Figure 3 shows the liquid lengths and the reflected power fraction of 7.5U ICRF antenna which contributed most to the 1.6GJ input energy. Liquid lengths were adjusted and reflected power fraction was kept low under approximately 1%. A calculation showed that the ratio would have reached up to 70% as shown by dashed line without feedback control.

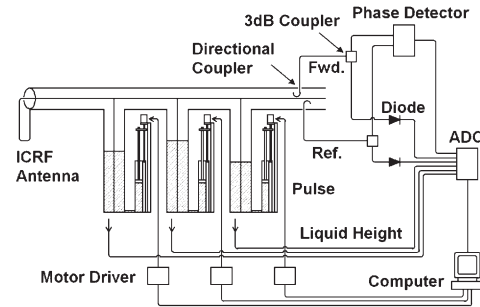


Fig.1 Real-time impedance matching system.

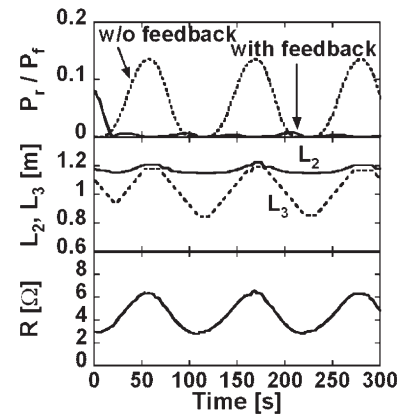


Fig.2 Result of impedance matching with variable resistance.

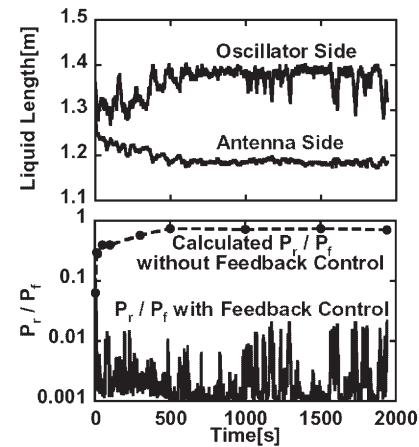


Fig.3 Impedance matching during the long pulse discharge of the 1.6GJ input energy.

### References

- 1)Saito, K, et al.: Long Pulse Discharge with ICRF Heating in LHD, in: Proc. of 32nd EPS Plasma Physics.
- 2)Saito, K. et al.: Fine Impedance Matching by Use of Liquid Stub Tuners in ICRF Experiment on LHD, J. Korean Phys. Soc., submitted for publication.

## §8. Workshop on Generation, Application and Measurement of High Power Millimeter Waves

Maekawa, T. (Graduate School of Energy Science, Kyoto Univ.), Shimozuma, T.

### 1. Objectives

Many devices and components over 100GHz frequency range have been developed day by day. The related information of the cutting-edge technologies in these fields should be consolidated constantly. In National Institute for Fusion Science, there are lots of millimeter wave devices such as gyrotrons, transmission lines and millimeter wave detectors for plasma experiments. The millimeter wave power is utilized not only plasma heating, but also electron temperature measurement through the electron cyclotron emission from the LHD plasmas. Since the millimeter wave technology, which includes power sources, detectors and components, is still developing, it is important to catch up with the leading edge of such technology for the improvement of ECH and ECE system. The objectives of this workshop are the information exchange between the researcher of millimeter wave and microwave technologies, the improvement of each millimeter wave systems through the workshop and development of combined research fields.

### 2. Activities in FY2005

The activities of this fiscal year were to research methods and computer codes to design and analyze millimeter wave devices and components, to establish the database, and to make CD-ROM archives. Front-line researchers made presentations of their latest research activities and computer codes. Through this process, the technologies of high power millimeter wave generation, application and measurement have been organized.

On the workshop, all participants from nine research institutes and universities presented their researches. The following researchers made detailed presentation of research results with the related computer codes.

Program and contents of the lectures are as follows.

(1) "Analysis of slow-wave electron cyclotron instabilities due to anomalous Doppler effect" by Dr. Kazuo Ogura (Niigata University)

It is shown that the slow-wave electron cyclotron instability due to the anomalous doppler effect occurs in addition to the Cherenkov instability in the interaction between axially injected electron beams and slow

electromagnetic waves. Although this instability is excited through an electron cyclotron resonance, the electron energy perpendicular to the magnetic field is not necessary because it is a slow cyclotron mode. The analysis includes the model in which the three-dimensional perturbation of the electrons is taken into account. the slow-wave cyclotron instability is analyzed on the actual boundary condition which is used in the real slow-wave microwave devices. Application to microwave sources is also discussed.

(2) "Recent topics of ECH analysis computer codes in Tsukuba University" by Dr. Yoshimori Tatematsu (Plasma Research Center, Tsukuba University).

In the plasma research center of Tsukuba University, a high power 28GHz gyrotron system was developed and installed for the production of electric fields in the plug region of GAMMA 10. It was necessary to design and manufacture a new transmission line for the gyrotron. A launcher of the antenna was designed by the electromagnetic code to produce a axially-symmetric field profile at the resonance. Using the launcher leads to the highest electric field production. Another application of the code is the design of the transmission system in the central-cell ECH system. The modification of the system resulted in the achievement of the highest temperature of the bulk electron,

(3) "Optimization of ECH system in LHD: Computer codes related ECH" by Dr. Shin Kubo (NIFS).

In LHD, the ECH system consists of many kinds of gyrotrons, transmission lines and antennas. A lot of computer codes, such as propagation analysis of electromagnetic waves in the waveguide and in free space, mirror design code, polarization analysis, ray tracing code of ECW, etc., have been developed and used for the system design, optimization and operation. He explained the principle, configuration, problems and calculation examples.

The attendances distributed over wide area related to the millimeter wave technology. About 20 members joined the workshop. (1) High power millimeter wave application to plasma heating: NIFS, Tsukuba Univ. Kyushu Univ. Kyoto Univ. (2) Generators of high power micro and millimeter waves: Fukui Univ. Niigata Univ. Kanazawa Univ. Tohoku Univ. (3) Millimeter wave technology: JAEA

This workshop was continued for two years. In future the main theme will be concentrated on the higher frequency range such as submillimeter wave (Tera Hertz) range. This expands RF technologies to the wider area; communication, remote sensing, biology applications and so on.



#### (4) High Energy Beam Technology

High energy beams are used in various fields of magnetic field confining nuclear fusion research. Neutral hydrogen/deuterium beam is commonly used for plasma heating, current drive, and diagnostics such as charge exchange recombination spectroscopy (CXRS) and beam emission spectroscopy (BES). Heavy Ion Beam Probe (HIBP) is another diagnostic tool using high energy beam. These tools are also used in LHD, and the successive development on the beam formation system or improvement of the diagnostic system is undertaken through the collaborations. Among them, the activities on the development of NBI system are reported here. Those of diagnostics (BES and HIBP) are reported in other category of this annual report.

In LHD, neutral beam injection (NBI) is a main plasma heating source as in other helical devices and tokamaks. NBI is also utilized as plasma production, which is a unique feature of LHD assisted by the fact that the confining magnetic field exists in steady state. The neutral beam is also used for measurement of ion temperature and velocity profiles via CXRS, and the induced current can be used to change magnetic field configuration for MHD studies under the weak magnetic field strength.

The very specific feature of LHD NBI systems is that most of them are negative-ion based injection systems, which includes an advanced technology for making a high energy neutral beam that can be applicable for future reactors ( $>1\text{MeV}$ ). In LHD, the maximum injection energy of hydrogen beam is 180 keV, which is even too high to construct an injection system by using a conventional positive ion because the neutralization efficiency is so small. The negative ion technology is still in the course of development. Therefore, the R&D activity continues in NIFS as well as other institutes such as JAERI and CADARACHE.

A new NBI has been constructed this year which is a low energy (40keV), positive-ion based hydrogen beam injector for CXRS. The specific feature of this beamline is that the injection angle is normal to the LHD plasma. The choice of beam angle was done considering that the ICRF heating works in the case of inner-shifted discharge of LHD. By this beamline, spatial profiles of Ti has become available by CXRS without doping impurities such as Ar or Ne.

*The report-1 by Takeiri et al.* is a summary of the injected beam power of three negative-ion based NBI's in LHD through the 9<sup>th</sup> experimental campaign in FY 2005. Although total input power could not exceed the maximum achieved power of 13MW in FY2003, it should be noted that high power level was available throughout the experimental campaign. The reproducibility of three beamlines were improved. The reason that the maximum

total input power was small is due to the low performance of BL-3. The voltage withstanding of BL-3 did not recovered through long conditioning, the reason of which is not found yet.

*The report-2 by Oka et al.* is on the behavior of cesium in the negative ion source of BL-2. The lines of cesium atom and cesium ion are observed. The remarkable feature is that both lines increase during beam extraction. This may show the fact that the cesium that covers the cold wall is released by bombardment of back stream ions. It should be noted that the extracted negative ion current does not change even though the cesium lines increase.

Five reports (3 to 8) are on a new low energy beamline;

*The report-3 by Nagaoka et al.* is on the performance of new injector called BL-4. The input power (current) achieved its specification very quickly, but unfortunately the pulse length was limited due to unexpected local heat load on the beam dump. The design and the obtained performance of the arc chamber and accelerator of new ion source for BL-4 are reported separately in *the report-4 and the report-5 by Osakabe et al.* Two magnetic cusp configurations were compared to determine the design of arc chamber. The arc efficiency was higher than expected. On the other hand, the obtained optimum perveance was smaller than expected, although this was able to be shifted by changing the accelerating gap of grids. The other performance of the beam; proton ratio was evaluated by measuring Doppler shifts of  $\text{H}_\alpha$  in the beamline (*the report-6 by Nagaoka et al.*) and in the plasma (*the report-7 by Ikeda et al.*). More than 80% of full energy beam power is expected at the optimum condition.

There are several R&D's of ion sources;

*The report-8 by Shinohara et al.* is on the study of dense plasma source produced by helicon wave, which can also be used as a unit source for constructing a large ion source. Using Xe gas, high density plasma of  $10^{19} \text{ m}^{-3}$  can be obtained with input RF power of 0.5kW in the quartz tube of 10 cm in diameter, 90 cm in length, and magnetic field strength of 1360 Gauss. *The report-9 by Shoji et al.* is on the development of multi-antenna RF plasma source. By adjusting the current profile of four antennae, spatially uniform plasma can be generated in the large area of 30cm x 30cm. *The report-10 by Shinto et al.* is on the development of high convergence helium ion source for  $\alpha$  particle diagnostics. Because very short focal length is required, concave grid system are adopted. The design and fabrication of ion source was done in this year.

(Kaneko, O.)



## §1. Performance of Neutral Beam Injection Systems in the 9th Campaign

Takeiri, Y., Kaneko, O., Oka, Y., Tsumori, K., Osakabe, M., Ikeda, K., Nagaoka, K., Asano, E., Kondo, T., Sato, M., Shibuya, M., Komada, S.

The LHD is equipped with three negative-ion-based neutral beam injectors (NBI) --- BL1, BL2, and BL3. In the 9th campaign, a positive-ion-based NB injector, named BL4, has been newly constructed and installed for a diagnostic of the charge-exchange spectroscopy and a plasma control. The positive-NBI was designed to inject 40keV-3MW hydrogen beam with two positive ion sources. Arrangement of the NB injectors is shown in Fig. 1. BL4 injects low-energy beams perpendicularly to the magnetic axis, while the negative-NBI systems of BL1, BL2 and BL3 inject high-energy beams tangentially.

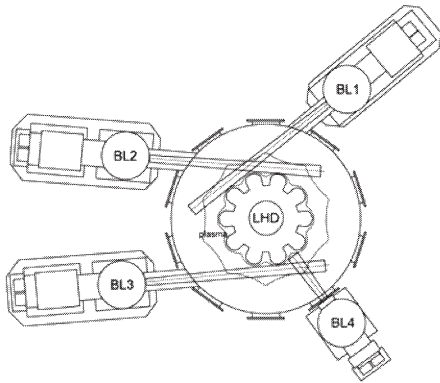


Fig. 1. Arrangement of the neutral beam injectors.

The construction of BL4 was completed in September, 2005, and the injection started successfully at the first experimental day of the 9th campaign (October 4). After the first injection, the injection power of BL4 was rapidly increased, and the specified injection energy and power of 40keV-3MW was achieved in three weeks.

As for the negative-NBI systems, the injection histories in the 9th campaign are shown in Figs. 2 and 3, for the total port-through injection power and the individual injection powers of three injectors, respectively. The maximum total injection power was 11.9MW, and high-power beams of more than 10MW were injected reliably for many LHD plasma shots.

BL1, which has already achieved a high-power injection of 184keV-5.7MW using the ion sources with multi-slotted grounded grid, had a trouble of water leak from the grounded grid. The arc and filament power supplies had also a trouble with thyristors by the high-voltage surge. Although the BL1 operation was restricted to an extent due to the above troubles, stable injection of 4-5 MW was carried out.

The grounded grid of the ion sources in BL2 has multi-round apertures, and the aperture diameter was enlarged in the 9th campaign for reduction of the grid heat load. As a result, the injection energy was increased above

170keV and the maximum injection power was increased to 4.2MW. Although the operation was not enabled for two weeks due to a trouble with a motor of the water pump, reliable injection of 3-4MW was carried out.

In BL3, there is no trouble in the operation during the campaign. However, the injection energy was not raised and remained at less than 160keV. No definite cause was found on inspection inside the accelerator after the campaign. Although stable injection was carried out, the injection power was around 3MW.

In the next campaign, a new grid system is planned to increase the injection power in BL1, and by improving the accelerator the injection power will be recovered in BL3. Therefore, the total injection power is expected to be much increased in the next campaign.

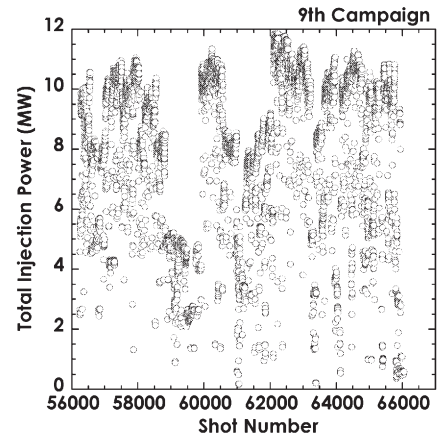


Fig. 2. History of the total injection power in the 9th campaign.

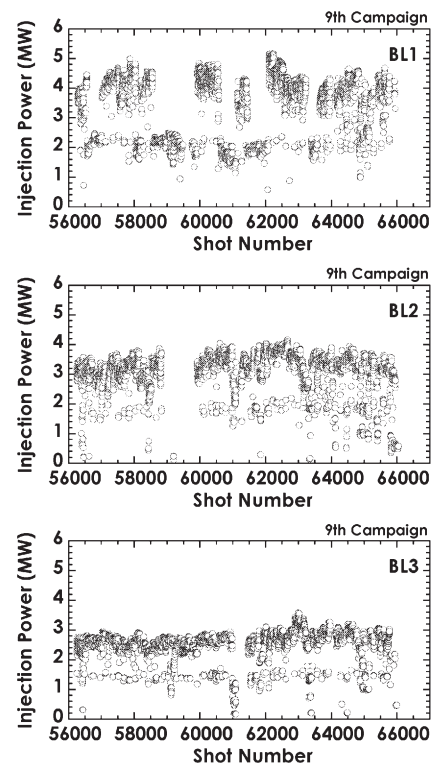


Fig. 3. History of the injection power of the individual injectors of BL1, BL2, and BL3.

## §2. Spectra of H $\alpha$ Lines and Cs Lines from the Negative Ion Sources during NB Injection

Oka, Y., Ikeda, K., Takeiri, Y., Tsumori, K., Kaneko, O., Nagaoka, K., Osakabe, M., Asano, E., Komada, S., Kondo, T., Sato, M., Shibuya, M., Grisham, L. (PPPL), Umeda, N. (JAEA), Honda, A. (JAEA), Ikeda, Y. (JAEA), Yamamoto, T. (JAEA)

High-performance negative-ion source requires further improvement to achieve reliable long-pulse high-power capability. The velocity spectra of the negative ion based neutral beams with doppler-shifted H $\alpha$  spectroscopy, as well as the effectiveness of the spectroscopy have been studied / collaborated<sup>1)</sup>. In the 9<sup>th</sup> experimental cycle, the spectra from a beam-line light as well as plasma source light have been accomplished newly by a switching unit controlled remotely to six optical-fibre channels.

The velocity distribution profiles during long-pulse LHD-NBI injection over the course of 74 s ~ 128s long-pulsed beams with reduced power were demonstrated. In Fig.1, intensity of the Doppler-shifted H $\alpha$  profile with the full energy peak reduces gradually along with beam pulse duration. When a plasma grid actively cooled is applied, this permits efficient H<sup>-</sup> production at a constant level for pulses up to ~70s in 128s NB(sn56208), while the standard PG with a little conduction cooling at the PG periphery keeps constant for 10~30s in 74s NB(sn48818). Scaled-up profiles of the latter spectra suggested that by about 30s cesium has migrated from the high-temperature PG portions to the lower-ones<sup>1)</sup>.

The Doppler-shift spectroscopy system was used to measure cesium lines from the source plasma in standard LHD-NNBI injection. Interestingly, we found in Fig.2 that both the amount of CsI(Cs<sup>0</sup>) line and CsII(Cs<sup>+</sup>) line in the source plasma rose sharply when beam acceleration began, and continued high. It was considered in Fig.3 that this was because the cesium was sputtered off by the back-streaming ions, as was reported in the 6<sup>th</sup> Joint Conference for Fusion Energy<sup>2)</sup>.

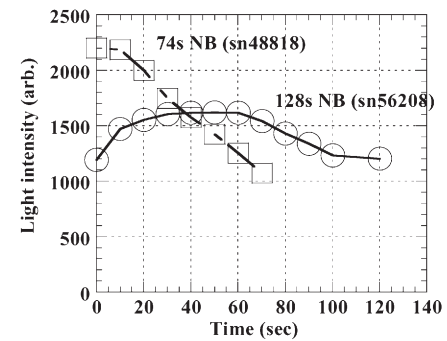


Fig. 1 Temporal dependence of H<sup>-</sup> production during long-pulse injection. With an actively cooled PG in 128s injection. With a little conduction cooling PG in 74s one.

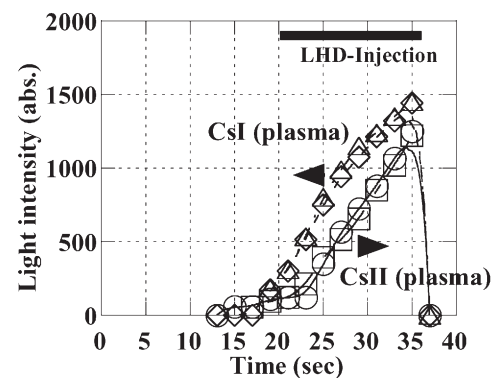


Fig.2 Temporal dependence of CsI(Cs<sup>0</sup>) and CsII(Cs<sup>+</sup>) line intensity from plasma source during the NB injection.

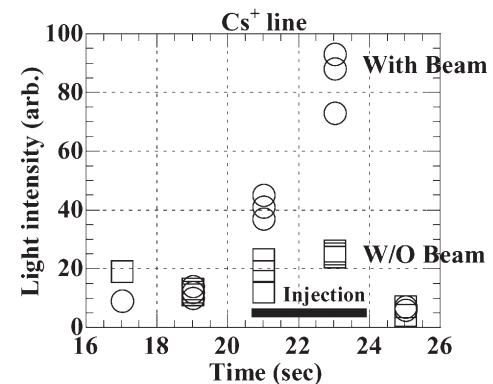


Fig.3 Temporal dependence of CsII(Cs<sup>+</sup>) line intensity with- or without beam acceleration voltage.

### Reference

- 1) Y. Oka et al., Rev. Sci. Instrum. **77**, (2006)03A538.
- 2) Y. Oka et al, in Proc. 6<sup>th</sup> Joint Conference for Fusion Energy, Toyama, JPN, Jun.13 2006

### §3. Operation Start of Diagnostic Neutral Beam Injection in LHD

Nagaoka, K., Osakabe, M., Takeiri, Y., Sato, M., NBI Group

Diagnostic neutral beam injector (NBI-BL4) was installed in LHD and beam injection into the LHD plasma was performed in the 9<sup>th</sup> LHD experimental campaign. The main purpose of this injector is diagnostic for charge-exchange spectroscopy, which gives profile information of ion temperature and plasma rotation. Moreover, this beam is useful for many experiments, for example, ion heating using low energy and high current beam, particle fueling in center region, helically trapped fast-ion confinement with almost perpendicular pitch angle, and so on. The beam energy and total port-through power were 40keV and 6MW, respectively, and the beam energy was optimized for the diagnostic beam. Four positive ion sources (ISs) can be mount in NBI-BL4, however in the 9<sup>th</sup> campaign, only two ISs were mounted, so total port-through power is 3MW in this campaign. The BL4 is installed on 5-O port in LHD and the schematic of BL4 is shown in Fig.1. The focal point and pivot point of each IS are same position at 8.3m far from ISs, and geometrical port-through rate is almost 90%.

The construction and tune-up of the beam line and power supply system were completed at end of September. The beam injection into the LHD plasma was successfully started from first day of the 9<sup>th</sup> LHD experimental campaign, and design specifications of beam energy of 40keV and port-through power of 3MW were achieved after three week later (shown in Fig.2). Almost steady operation was kept during the campaign and this injector was used for many experiments; measurement ion temperature profile, high ion temperature discharges with low  $Z_{eff}$ , high stored energy mission, and so on.

On the other hand, a few problems were revealed in the beam operation. The pulse duration with maximum beam power was limited to 0.5 sec, because of beam concentration on the residual ion beam dump. This is considered to be caused by fringe field produced by bending magnet coil and capability of heat removal. In the next campaign, new beam dump which consists of swirl tubes will be introduced. And much neutral gas leak into LHD vacuum vessel also made some troubles. The base pressure in vacuum vessel of LHD increased about one order from  $5.7 \times 10^{-4}$  Pa to  $6.1 \times 10^{-3}$  Pa, when BL4 was operated, which make it difficult to produce low density discharge and start up using only NBI. In order to improve gas leak into LHD, the reduction of gas conductance at drift tube and neutralization duct will be done, and reduction of base pressure in the beam line also done by the expansion of the beam line vessel and insertion of additional cryo-sorption pump. These modifications are considered to reduce gas leak into LHD about half level and reasonably solve this problem.

In 9<sup>th</sup> campaign, the operation of diagnostic NBI was started and it was confirmed that perpendicular NBI can be useful for not only diagnostics but plasma heating in helical devices, so in 10<sup>th</sup> campaign, four ISs will be mounted in BL4 and 6MW beam injection will be started.

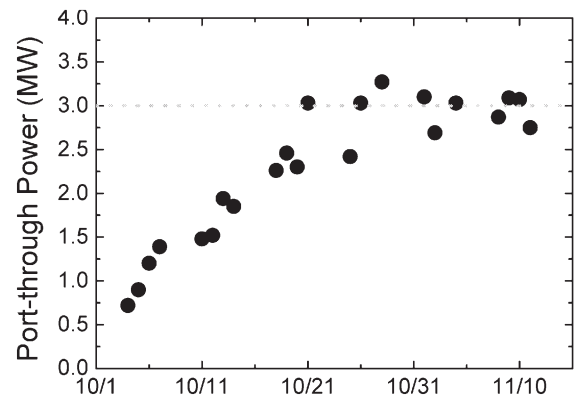


Fig.2 Historical trend of port-through power of NBI-BL4.

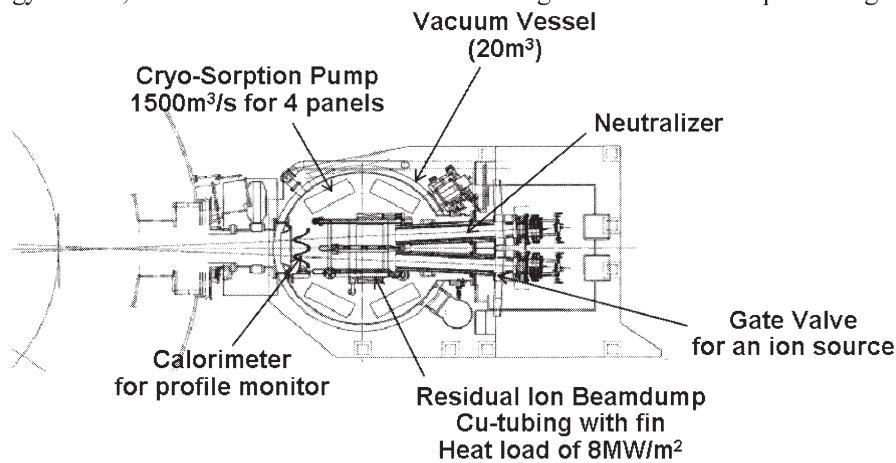


Fig.1 Top view of NBI-BL4.

#### §4. Development of Positive Ion Sources for a Perpendicular Neutral Beam Injector (I) –Development of Plasma Generator–

Osakabe, M., Nagaoka, K., Tsumori, K., Takeiri, Y., Sato, M., Shibuya, M., NBI Group

A Neutral Beam(NB) injector based on positive ion-sources of hydrogen was newly installed on the Large Helical Device(LHD). The primary purpose of the beam is the use as a diagnostic NB for charge exchange resonant emission spectroscopic measurement. Thus, the beam energy was chosen to be 40keV in hydrogen. To have enough penetration of NB into the core of the LHD plasmas, the beam was injected perpendicularly to the magnetic-field lines, so that the NB is injected radially. The specification of the beam current and the power are 150A and 3MW, respectively, with two ion sources. The required pulse duration of the beam is 10sec.

To achieve the above requirement, new positive ion-sources have been developed. The one of the most important issues on the ion-source development is the heat-load handling onto the plasma-grid from the arc-discharge and the beam. To reduce the heat-load onto the plasma-grid from arc-discharges, it is important that ion-sources have high arc-efficiency, which is defined by normalizing the extracted beam current with the applied arc-power, since the required beam current is fixed.

In designing the ion-sources for the perp.-NB, the cusp-magnetic field configuration is numerically determined by using a orbit following code for primary electrons from the filaments of ion-sources. The distributions of these electrons without collisions were calculated for various cusp-configurations. In the design study of the configurations, we have obtained two candidates for the source. One has better confinement of primary electrons, which is called as “type-2f”. Figure1(a) shows the distribution of primary electrons in this configuration. About 63% of the primary electrons are confined in this configuration, and these electrons are staying away from the Plasma Grid(PG). The other configuration, which is called “type-2fa8”, has less probability for primary electron survival(15%), but it has more electrons and better uniformity near the PG than type-2f(Fig.1(b)). These two cusp-configurations are almost similar, but the type-2fa8 has an additional cusp-lines at  $z=40$ [mm], which locates between the PG and the cusp-line at  $z=50$ [mm].

To clarify which feature of primary electrons are more important, i.e., “the confinement of primary electrons” or “the existence of primary electrons near the PG”, we have compared

the arc-efficiency of these two configurations using a same arc-chamber. To keep the same experimental condition of the source, the experiment was performed within a day by adding the cusp-line at  $z=40$ [mm] without breaking the vacuum. As shown in Fig.2, the type-2f has better arc-efficiency than the type-2fa8, which experimentally confirms the importance of the primary electron confinement in the arc-efficiency. Thus, we have adopted the type-2f as the cusp-configuration of our positive ion-sources.

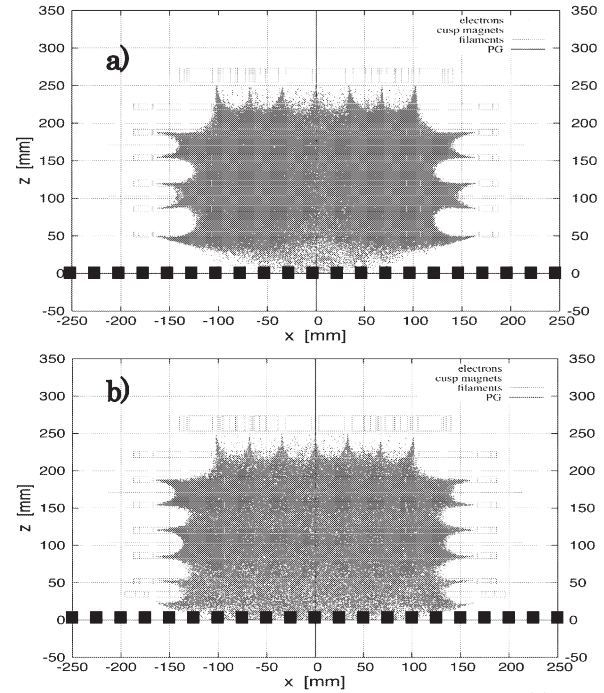


**Fig.1 Primary electron distributions for type-2f(a) and type-2fa8(b) cusp-configurations. A plasma-grid locates at  $z=0$ [mm] and is indicated by dashed-lines in the figures. The locations of primary electrons are expressed by the dots in the figures.**

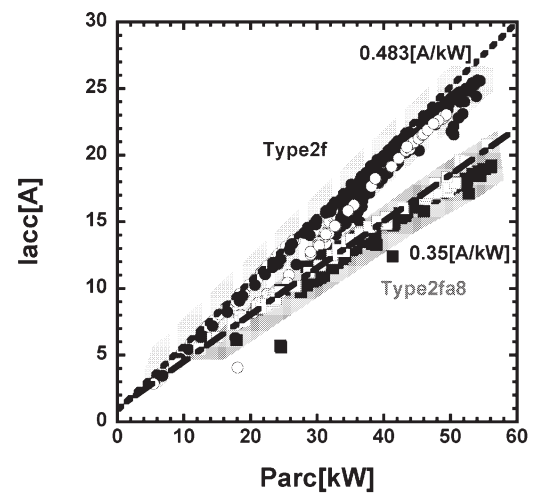


**Fig.2 Arc-efficiency of type-2f(dashed-lines with circles) and that of type-2fa8 (center-dashed lines with squares).**



## §5. Development of Positive Ion Sources for a Perpendicular Neutral Beam Injector (II)

### –Development of Accelration Grid System–

Osakabe, M., Nagaoka, K., Takeiri, Y., Tsumori, K., Sato, M., Shibuya, M., NBI Group

The heat-load handling onto the plasma-grid from the arc-discharge was one of the most important issues on the development of the positive-ion source for the perpendicularly injected Neutral Beam(NB) on the Large Helical Device(LHD)[1]. Thus, the selections of the grid material and its structure are one of the most interest.

Copper is adopted as a grid material of the ion source due to its high thermal conductivity and the easiness of its handling. On the other hand, it does not have enough mechanical strength to form a thin large grid. Considering the electric field penetration to the beam extraction hole, the thickness of the Plasma Grid(PG) is preferred to be thin. On the contrary, the thickness is preferred to be thick if we consider the mechanical and thermal strength of the grid. Therefore, the choice of its thickness is a key issue of the ion source design.

Two candidates have arisen as the thickness of the PG. One is 4[mm], which is emphasized on the mechanical strength and the heat capacitance. The other is 3.3[mm], which is designed to have better optics for beam extraction. Since two of ion-sources are necessary for the perp.-NB, we had prepared plasma grids of both thickness and evaluated their performances, experimentally.

Figure 1 shows the comparison of these two grids. accel.-decel grid systems are applied for the ion-sources. In Fig.1, the perveance dependence ( $\text{Perv.} = I_{\text{beam}}/V_{\text{acc}}^{1.5}$ ) of the beam width are shown for plasma grids of both thickness. In both cases, the optimum perveance where the beam width becomes its minimum locates at around  $0.12[\text{A}/\text{kV}^{1.5}]$ . The gaps between the plasma-grid and the decel-grid are 4.5mm for the PG of 4mm thickness and 6.5mm for that of 3.3mm thickness. This fact indicates the advantage of the thinner PG in the beam optics since the electric field applied for the beam extraction is weaker in the case of Fig.1(b).

In Fig.2, the beam width dependence on the PG-heat load is shown for both cases. The PG-heat loads are obtained by the integration of the PG cooling-water temperature rise during the shots. In both cases, the perveance of the beam is set to be its optimum value and fixed. The beam width stays constant during the PG heat-load scan in both cases, which indicates that there are no significant distortion of PG due to the heat load

onto the grid. Combining the result shown in Fig.1, it is experimentally confirmed that we can adopt the thickness of 3.3mm as a plasma grid being made of copper.

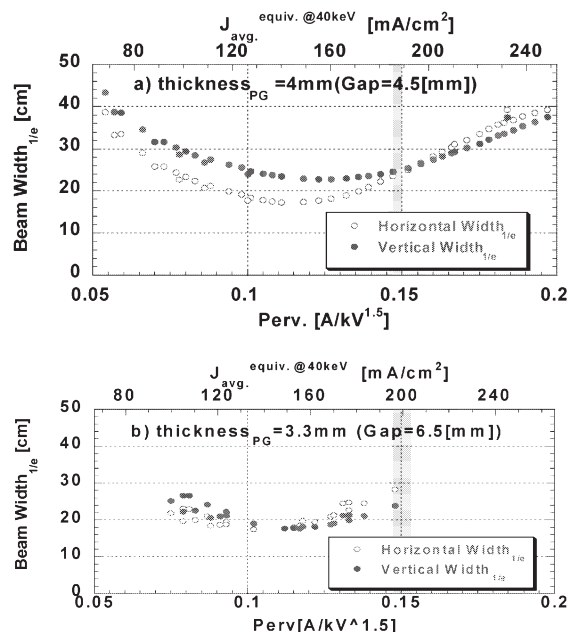


**Fig.1** Perveance dependence of the beam width for (a) PG-thickness of 4mm and (b) PG-thickness of 3.3mm. The open circles indicate the horizontal e-holding half width, while the closed circles do the vertical width. Applied acceleration voltages are 30kV in both cases. The gray areas show the target of the ion-source design.

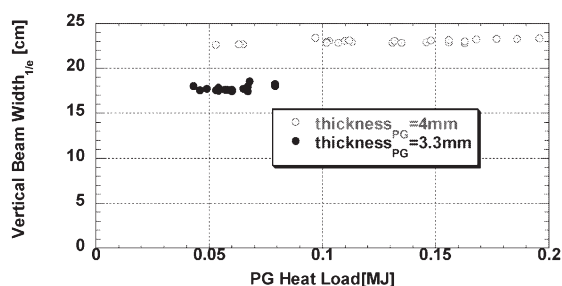


**Fig.2** PG heat-load dependence of beam width. The open circles are for PG of 4mm thickness, while closed circles are for that of 3.3mm thickness.

## Reference

- [1] M.Osakabe, *et.al.*, Annual Repot of NIFS for 2005

## §6. Proton Ratio and Beam Divergence Measurement of Diagnostic Neutral Beam

Nagaoka, K.

Diagnostic neutral beam injector (NBI-BL4) started the beam injection into LHD plasma in the 9<sup>th</sup> LHD experimental campaign. The NBI-BL4 mounts two positive ion sources (ISs) and produces the beam with the energy of 40keV and the port-through power of 3MW, which was achieved after three weeks later the star of 9<sup>th</sup> campaign. In general, positive IS produces not only full energy beam but also half and one-third energy beam, and the existence of half and one-third energy component affects on the beam deposition into the plasma and heating coefficient. Thus, the measurement and control of proton ratio of injected beam is important. On the other hand, beam divergence is also important parameter in order to avoid serious damage of beam line components and high voltage break down in the acceleration region.

In order to measure proton ratio and beam divergence, the beam emission spectroscopy in the NBI-BL4 was designed and performed in 9<sup>th</sup> campaign. The line of sight was arranged to obtain both parallel and perpendicular components, of which schematic is shown in Fig. 1. This line of sight sees both beam emission from UA-IS and LA-IS, so NBI calibration shots and conditioning shots using one IS were used for this measurement. In Fig. 2, the full, half and one-third power ratio are shown as a function of perveance (arc power), and proton ratio decreases and one-third component increases in low perveance operation. The usual operation was performed with perveance of about 30, so in the high proton ratio region. The width of full energy spectrum in wave length space was compared with beam width measured on the calorimeter, which is shown in Fig. 3. The linear relation between them was clearly seen, which indicates that width of line spectrum gives direct information of beam divergence.

These demonstrations confirm that this system is useful for monitor of proton ratio and beam divergence. The development of the routinely analyzing system is under construction. The comparison of analysis of geometrical port-through coefficient using beam orbit calculation and shine-through measurement on armor tile is necessary for the calibration of absolute value of beam divergence, which is left for future work.

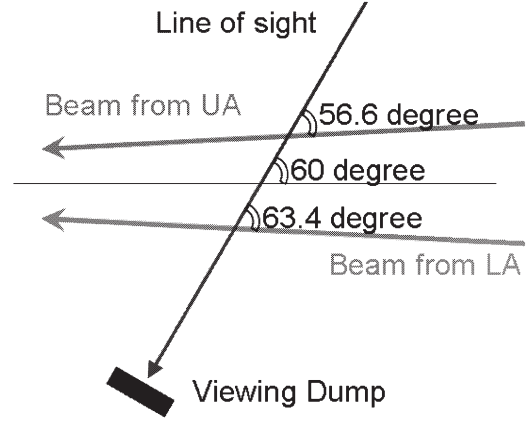


Fig. 1 The geometrical relation between the beams and line of sight.

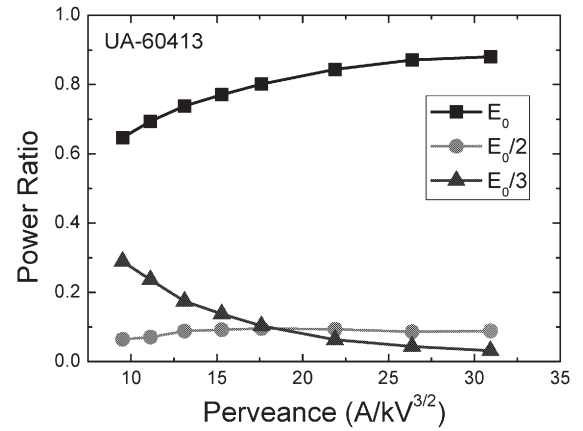


Fig. 2 Power ration of full, half and one-third energy components as a function of perveance.

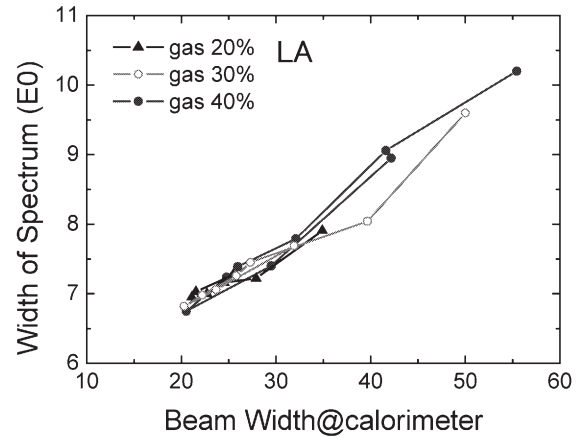


Fig. 3 The width of full energy component, which indicates beam divergence, as a function of the beam width measured on the calorimeter.

## §7. Development of RF Plasma Source for Negative Ion NBI

Shinohara, S., Kamataki, K., Nishijima, T. (Interdis. Grad. Sch. Eng. Sci., Kyushu Univ.),  
Kaneko, O., Tsumori, K.

Intensive studies of the high power neutral beam injection (NBI) heating utilizing negative ions have been actively executing in NIFS. As to the future plasma source in NBI, key issues are easier plasma production with a good stability, higher plasma density and higher ionization, and developments of large or compact plasma sources. In addition, developing a neutral beam source with the high particle flux is important in the charge-exchange recombination spectroscopy. The present objective is, first, characterizing a high-density, compact plasma source, using a helicon wave scheme [1] in the range of radio frequency. Then, developing a negative ion source with, e.g., hydrogen gas, will be carried out to apply to the advanced NBI in NIFS.

The main device parameters of the compact helicon plasma source with the strong magnetic field [2,3] are as follows: the discharge chamber uses a quartz tube, which has an outer (inner) diameter of 10 (9.5) cm and 90 cm axial length. The magnetic field  $B$  can be applied up to 10 kG, whose main strong field region extends to  $\sim 30$  cm in the axial direction. Here, iron yokes were added to increase the field.

Two parallel copper plates with 3 cm in the axial direction each used as the rf antenna, were wound around the quartz tube at the midplane. Here, the spacing between plates was 6 cm. By changing the electrical connection (parallel and anti-parallel current directions), the excitation of the axial wavenumber spectrum can be changed [4,5]. The rf frequencies in this experiment were 7 and 14 MHz with a fill pressure of 1-33 mTorr (with pulsed as well as continuous operation modes). In order to estimate the antenna loading, a directional coupler monitoring the incident and reflected powers was used in addition to measure the antenna voltage and current. A Langmuir probe was scanned radially at the midplane.

Here, we present the results on the plasma performance using various gas species [2,3]. In Ar discharges, we could obtain the electron density  $n_e$  more than  $10^{13} \text{ cm}^{-3}$  with the input rf power  $P_{rf}$  of less than 1 kW. Here, with the increase of  $B$ ,  $n_e$  was higher in the high field region before the so-called density jump due to the better radial confinement. However, this jump became weaker with the increase of  $B$ .

Figure 1 and 2 show examples of the plasma density  $n_e$  vs.  $P_{rf}$  (rf frequency is 7 MHz) with Xe (He) pressure of 10 mTorr and  $B$  of 1.36 kG (0.48 kG). The density jump to the range of  $10^{13} \text{ cm}^{-3}$  was observed in

Xe discharges with less than 0.5 kW of  $P_{rf}$  (Fig. 1). To the contrary, in the He discharges (Fig. 2), a monotonic increase of  $n_e$  was found with  $P_{rf}$ , and  $n_e$  itself was much lower, e.g.,  $\sim 10^{11} \text{ cm}^{-3}$  with  $P_{rf}$  of 1 kW, than Ar and Xe discharges. We have also found that the maximum density was obtained when the excitation frequency was near the lower hybrid frequency from the dependence of  $n_e$  on the magnetic field, by changing the gas species and the rf frequency.

In conclusion, the experiments on the plasma production with  $n_e$  up to the range of  $10^{13} \text{ cm}^{-3}$  were successfully carried out using a compact, high magnetic field device, changing gas species. The more detailed characterization in a wide range of operating parameters will be done, which is expected to contribute to the advanced NBI system in NIFS.

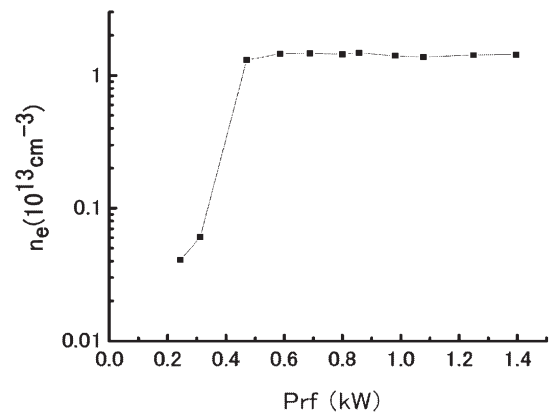


Fig. 1. Electron density as a function of rf power (Xe).

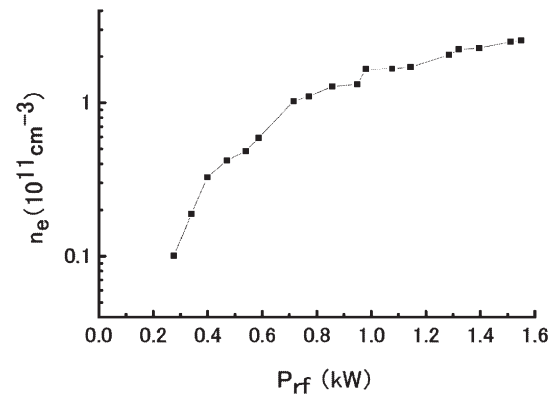


Fig. 2. Electron density as a function of rf power (He).

### Reference

- 1) S. Shinohara, J. Plasma Fusion Res. **78** (2002) 5.
- 2) H. Mizokoshi and S. Shinohara, 21<sup>st</sup> JSPF Annual Meeting (2004) 25pA30P.
- 3) S. Shinohara and H. Mizokoshi, Rev. Sci. Instrum. **77** (2006) 036108.
- 4) S. Shinohara *et al.*, Plasma Phys. Control. Fusion **42** (2000) 41 and **42** (2000) 865.
- 5) S. Shinohara *et al.*, Phys. Plasma **8** (2001) 3018.

## §8. Development of High Power Multi-Antenna rf Ion Source

Shoji, T. (Dept. Energy Eng. and Sci., Nagoya Univ.),  
Oka, Y.

### 1, Multi-antenna ion source

We have been developing the multi-antenna rf system for large size and high power sources. The multi-antenna ion source consists of four antenna elements of 20cm long and the 35 cm x 35 cm x 21 cm rectangular source chamber. An extractor installed on the bottom of the chamber has a single hole with 5 mm in diameter. The rf power of 50kW at 9MHz and the pulse width of 10msec is connected to the antenna through the matching circuit.

### 2, Rf power dependence on plasma density

The dependences of plasma characteristics on rf power,  $P_{rf}$  are shown in Fig.1, which are measured by Langmuir probe placed at the center of the chamber in the driver region. For the 2 antenna system there is a density jump around  $P_{rf} \sim 25$  kW and no such a jump seems to be observed on the 4 antenna system in this power range. The result from the prototype rf ion source<sup>3)</sup> showed such a tendency

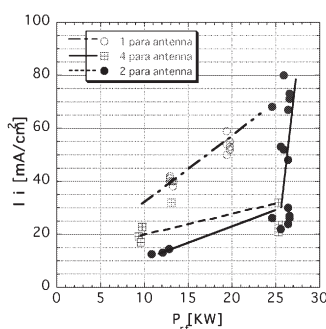


Fig.1 (a)  $I_i$  as a function of  $P_{rf}$  for  $P_{H_2} = 6-9$  mtorr for 1,2,4-antenna systems. There is no rf breakdown up to 30kW while the break down happened in the prototype antenna.

### 3, Density profile for multi-antenna system

In order to evaluate the density profile for different antenna configurations, we solve the steady state particle balance equation with the antenna and the wall boundary conditions. We assume that the plasma is produced near the antenna by the accelerated electrons and then the plasma diffuses into the chamber through mainly collision process with neutrals. We demonstrate examples in Fig.2. If the rf current ratio of 4-antennas are set as (1.3, 0.9, 0.9, 1.3) (Fig.2 (a)), the uniformity of density within 10cm long (half antenna length) in y direction become 0.03% while it is almost 5% for the equal current ratio. If the each antennas are split into three identical segments and set the rf current ratio as (1, 0.67, 1) in x direction and (1.3, 0.9, 0.9, 1.3) in y direction (Fig.2 (b)), 2 dimensionally more uniform density profile is obtained compare to the 4-antenna case. Practically, the each antenna current can be controlled by inserting the

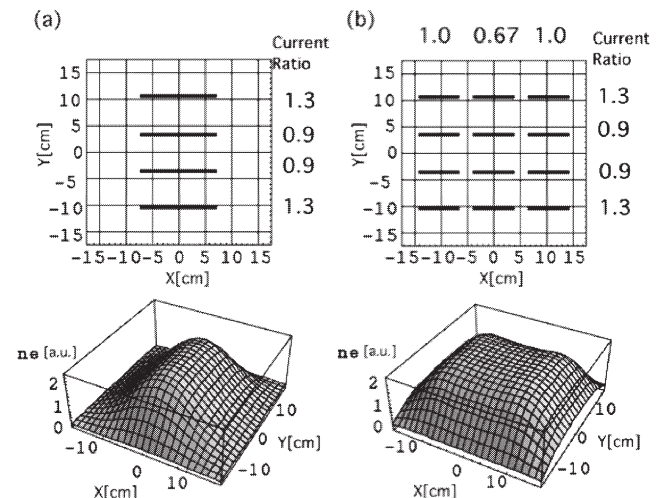


Fig.2 Density profile at  $z=0$  for (a) the 4-antenna system with different current ratio, ( 1.3, 0.9, 0.9, 1.3) and (b) the 12-antenna system with the current ratio (1, 0.67, 1) in x direction and (1.3, 0.9, 0.9, 1.3) in y direction

variable short inductance strip at the end of antenna outside.

### References

- 1) Shoji, T, Sakawa, Y, Hamabe, M and Oka, Y., Ann. Rev, NIFS, (2001) 141
- 2) Oka, Y, Shoji, T, Rev. Sci. Instruments, 75(2004)1841
- 3) Shoji, T, Oka (NBI Group), Rev. Sci. Instruments, 77(2006)03B513
- 4) Oka, Y, Shoji, T, et. al., Rev. Sci. Instruments, 77(2006), 03B506



## §9. Development of a High Intensity He<sup>-</sup> Beam Source for Fusion-Produced Alpha Particle Measurement

Shinto, K., Sasao, M., Kitajima, S., Okamoto, A., Sugawara, H., Takenaga, M., Takeuchi, S., Tanaka, N. (Tohoku Univ.), Kiyama, S., Sakakita, H., Hirano, Y., Yagi, Y. (AIST), Wada, M. (Doshisha Univ.), Kaneko, O., Nishiura, M.

To measure the spatial profile and velocity distribution of fusion-produced alpha particles, an active beam probe system based on double-charge-exchange neutralization of the alphas confined in a reactor core plasma has been being investigated. An energetic He<sup>0</sup> beam produced by the spontaneous electron detachment from He<sup>-</sup> ions is considered as the probe beam. The He<sup>-</sup> beam is produced by the double-charge-exchange reaction of He<sup>+</sup> ions in the alkali metal vapor cell with the charge-exchange efficiency less than a few per cent. A high-intensity He<sup>+</sup> beam with a good beam quality is required to compensate the low charge-exchange efficiency. Highly convergent beam directed to the double-charge-exchange cell can create an intense He<sup>-</sup> beam of enough brightness to diagnose the alphas in the core plasma.

A design of an energetic He<sup>0</sup> beam system for feasibility study of charge-exchange alpha-particle diagnostics in a thermonuclear reactor was studied and reported.<sup>1),2)</sup> Two programs have started to progress the active beam probe system. One is the proof-of-principle (POP) He<sup>0</sup> beam system being constructed at Tohoku University. The system consists of a compact multicusp He<sup>+</sup> beam source<sup>3)</sup>, an alkali metal vapor cell, an ion separator with stigmatic focusing, a post-accelerator, a free flight tube and a He<sup>0</sup>/He<sup>+</sup> fraction diagnostic chamber. The other is the strongly-focused high-intensity He<sup>+</sup> beam source system, being assembled at NIFS. This source can be utilized as the first part of the actual diagnostic system for ITER. A photograph of the He<sup>+</sup> beam source is shown in Fig. 1. The source consists of an arc chamber of 300 mm in diameter and 280 mm in length. Three concave extraction electrodes are made of molybdenum having 100 mm diameter beam forming area. The detailed specifications of the source are listed in Table 1.

The He<sup>+</sup> beam diagnostics have been started at NBI test stand in NIFS in JFY 2006. R&D items of the He<sup>+</sup> beam source for the alpha particle measurement system are;

- He<sup>+</sup> beam energy and beam current density
- He<sup>+</sup> beam emittance and energy distribution, and
- Beam size and profile at the focal point.

The first ion source plasma has been ignited successfully, and the beam extraction experiment will be attempted in this summer. Because of the high power density of the extracted He<sup>+</sup> beam, particularly at the focal point ( $\sim 300 \text{ MW/m}^2$ ), some of the beam diagnostic apparatuses should possess unique characteristics and designs.

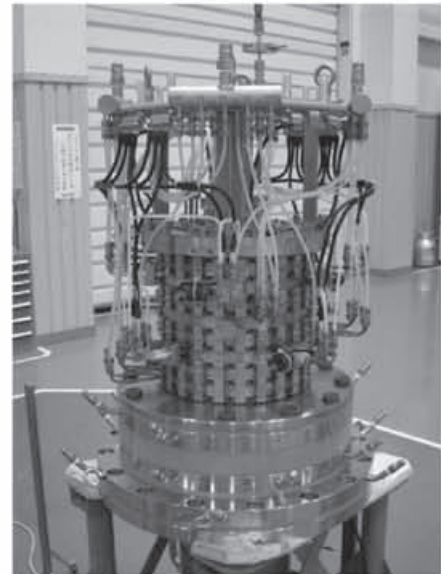


Figure 1: Photograph of a strongly focused He<sup>+</sup> beam source.

Table 1: Specifications of the strongly focused He<sup>+</sup> beam source. (Design parameters)

Arc Power	$\sim 40 \text{ kW}$
Pulse Duration	$< 10 \text{ s}$
Pulse Reputation	$< 0.01 \text{ Hz} (> 120 \text{ s})$
Beam Energy	$< 30 \text{ keV}$
Beam Current	$\sim 3 \text{ A}$
Extraction Region	$\phi 100 \text{ mm}$ , Concaved
Extraction Apertures	$\phi 4 \text{ mm} \times 300 \text{ apertures}$
Beam Divergence	$< 0.7 \text{ deg.}$
Focal Length	$750 \text{ mm}$

### References

- 1) Shinto, K. *et al.*, Proc. PAC05 (2005), 2630.
- 2) Shinto, K. *et al.*, :NIFS-PROC-63 (2006), 184.
- 3) Shinto, K. *et al.*, Rev. Sci. Instrum., **77** (2006), 03B512.

## (5) Diagnostic Systems

For the precise measurement of plasma parameters in the three dimensional helical plasma, an extensive set of diagnostics have been routinely operated. The present status is that the total number of diagnostics is over 60 owing to the continuous efforts for the development of new diagnostic instruments by researchers.

The YAG laser Thomson scattering system and the ECE system have proven as reliable diagnostics for the temporal evolution of the electron temperature profile. The YAG laser TS system works routinely to provide the electron temperature profile with a flexible repetition rate (from  $\mu\text{s}$  to hundreds of ms). One of the key issues of the LHD Thomson system is absolute calibration of polychromators for electron density profile measurements. So far, we have tried absolute calibration using hydrogen Raman scattering and nitrogen Raman scattering several times, but the results were not reproducible. In this fiscal year we have tried Rayleigh calibrations as well as Raman calibration, and found that both of the calibration factors show a good agreement.

A 13-channel far infrared laser and a CO<sub>2</sub> laser imaging interferometers have been routinely operated for the precise measurement of the electron density profile in the Large Helical Device. The imaging system is employed by using three slab-like beams and multi-channel detector arrays to measure the fine structure of the density profile with a spatial resolution of 15 mm. In order to get a fine structure of a density profile, a new type of reflectometer using an ultra-short sub-cycle pulse has been developed. The reflectometer system operates with the ordinary mode polarization and has 24 channels of *Ka* band and 4 channels of *X* and *Ku* bands. This convenient multi-channel system was utilized by introducing a new switching technique. A new two color far infrared laser interferometer system using short wavelength laser sources around 50  $\mu\text{m}$  is under development for future high-performance LHD plasmas. This two color interferometer system is unique one compared with the conventional two color interferometer system. By introducing Ge:Ga detectors operating at liq. He temperature, two color beat signals were successfully detected with excellent signal to noise ratio ( $\sim 40$  dB).

The plasma potential profile is an important quantity in a helical system since the radial electric field plays an important role in particle orbits and their losses. A heavy ion beam probe (HIBP) is being developed to measure potential and density fluctuation in high temperature plasmas. The HIBP system is composed of a negative ion source, a tandem accelerator of 6 MeV, beam lines, and an energy analyzer. In the 9th campaign, the plasma potential has been

measured during NBI heating at the magnetic field of 2.75 T. According to the trajectory calculation, the potential profile can be measured within the normalized radius of  $\sim 0.2$ . The potential tends to become positive by about 2 kV during NBI. The result suggests that the radial electric field ( $E_r$ ) of the electron-root is formed predominantly in the plasma. The positive potential measured by the HIBP is qualitatively consistent with the positive  $E_r$  measured by the CXS.

A tracer-encapsulated solid pellet (TESPEL) has been developed for impurity particle and heat transport studies. A TESPEL ball consists of polystyrene polymer as an outer shell in diameter of 300 – 900  $\mu\text{m}$  and tracer particles as an inner core. This fiscal year, in addition to the TESPEL a tracer-encapsulated cryogenic pellet (TECPEL) has been developed. The shell of the TECPEL is made of ice of hydrogen the same as a fuel gas so that extra impurities due to capsule evaporation of the TESPEL can be reduced. When the TECPEL enters the plasma, the outer solid hydrogen layer is ablated first, keeping the impurity core from ablation up to the plasma axis. This results in an intensive ablation of the core providing the small localization of the deposited tracer ions.

For multi-dimensional measurements of the non-axisymmetric LHD plasma 2-D or 3-D imaging diagnostics are under intensive development with national and international collaborators. A 3-D ECE imaging system has been developed in collaboration with Kyushu University for the measurement of an electron temperature profile and its fluctuations. The ECEI system is composed of a detector array, quasi-optical system, and IF system. The optical system is composed of optical mirrors and dielectric lens. Poloidal and toroidal temperature distribution is measured by a 2D detector array.

A data acquisition system with parallel processing technology has been developed for diagnostics with a 3 minute cycle during LHD operation. Data of most diagnostics are taken by the CAMAC system. The total number of CAMAC modules and channels are about 300 and 2000, respectively. The raw data size is up to 3GB/shot with 150 shots/day. In the 9<sup>th</sup> campaign the longest discharge duration of LHD was over than one hour. The LHD data acquisition system had established a new world record for the acquisition data amount  $\sim 90$  GB in a single plasma discharge. For effective remote participation with domestic universities, LHD has a powerful network realizing 1 Gbps streaming by introducing the super science information network.

(Kawahata, K.)

## §1. Raman and Rayleigh Calibrations of the LHD YAG Thomson Scattering

Yamada, I., Narihara, K., Hayashi, H., Funaba, H.,  
LHD Experimental Group

The LHD YAG Thomson scattering [1][2] has been applied successfully to the measurements of electron temperature profiles of LHD plasmas. For electron density measurements, absolute calibration is required, and some techniques have been proposed, Rayleigh and Raman calibrations. In previous experiments, we have applied Raman calibration to obtain reliable absolute calibration factors [3]. In this experiment, we tried Rayleigh calibration as well as Raman calibration.

Experimental settings in Raman calibration are the same as in Thomson scattering measurements. Since wavelength of Raman scattered photons are shifted as Thomson scattering, no changes are needed. This is a great advantage when carrying out calibration experiments. However, Raman calibration has a disadvantage too. In the previous experiments, we pointed out that the calibration factor is very sensitive to the spectral responsibility of polychrometers, and huge error might be caused due to the uncertainties in determination of the spectral responsibility. Therefore extremely precise measurements of the responsibility are required to obtain accurate calibration coefficients.

In the experiments, we tried Rayleigh calibration as a substitution for Raman calibration. As is well known, Rayleigh scattering doesn't shift the wavelength. Therefore special wavelength channel for detecting unshifted Rayleigh scattered light must be equipped in polychrometers, and very careful measures to suppress strong stray light are required. These are disadvantages in Rayleigh calibration. Especially the later will be a serious problem in many cases. We eliminated the difficulty as follows. Generally, Rayleigh scattering signal intensity,  $S$ , is proportional to scattering cross section,  $\sigma$ , times gas density,  $n_g$ , times laser intensity,  $I_{Laser}$ , whereas stray signal is proportional to laser intensity only,

$$S \propto \sigma n_g I_{Laser}$$

$$N \propto I_{Laser}.$$

The stray light intensity can be reduced by decreasing laser intensity. In the Rayleigh calibration, we decreased laser intensity by about  $10^{-4}$ - $10^{-5}$  (1-10 mJ/pulse). In this case, stray light became negligibly small in the LHD YAG Thomson scattering. Since Rayleigh cross section is about  $10^3$ - $10^4$  times larger than effective Raman cross sections, necessary signal intensity can be obtained easily. It is noted that 20 polychrometers with a Rayleigh wavelength channel have been calibrated by both Rayleigh and Raman calibrations whereas the other 124 polychrometers without the special channel have been calibrated by only Raman calibration.

Typical examples of target gas density dependence of Raman and Rayleigh scattering signals in Fig.1. Both the calibrations, pure nitrogen gas was introduced into the LHD

vacuum chamber up to 50 kPa. As expected, both of them show a clear linear dependence. Absolute calibration factors for electron density measurements are directly determined from the gradients of the lines [3].

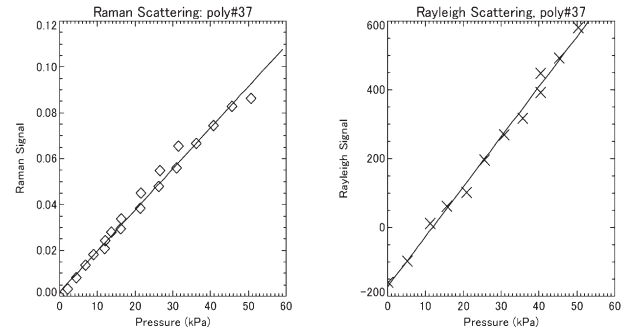


Fig.1, Gas density dependence of Raman scattering signal intensity (a) and Rayleigh scattering (b).

Figure 2 shows the comparison of the calibration factors obtained from Raman and Rayleigh calibrations. The horizontal axis is the observation point along with the LHD major radius. Both of the calibration factors show a good agreement, and a gradual spatial dependence.

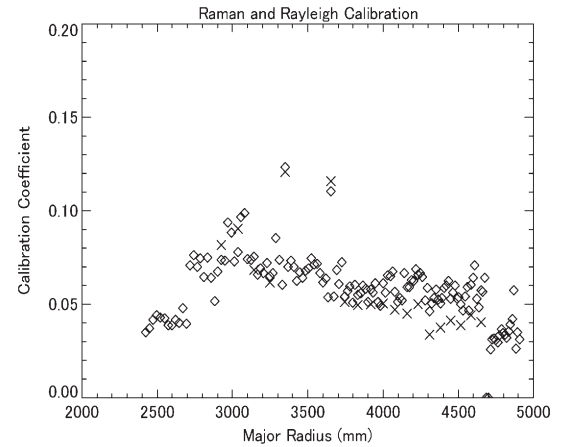


Fig.2, Comparison of the calibration coefficient determined from gas calibrations using Raman ( $\diamond$ ) and Rayleigh ( $\times$ ) scatterings.

We have found that reliable calibration factors can be determined from both Raman and Rayleigh calibrations in the LHD YAG Thomson scattering. Detailed analysis of the Raman and Rayleigh calibrations is now in progress for accurate and reliable density measurements.

### References

- [1] Narihara, K., *et al.*, Fusion Eng. Design, Vol.34-35, 67-72 (1997).
- [2] I. Yamada *et al.*, J. Plasma Fusion Res., Vol.76, 863-867 (2000).
- [3] I. Yamada *et al.*, Rev. Sci. Instrum., Vol.74, No.3, 1675-1678 (2003).



## §2. Development of Multichannel Ultrashort Pulsed Radar Reflectometer for Electron Density Profile Measurement

Tokuzawa, T., Kawahata, K.

Recently we have been developing a new type of reflectometer which uses an ultrashort sub cycle pulse. It is called as an ultrashort pulsed radar reflectometer. An ultrashort pulse has broad band frequency components in Fourier space. It means one ultrashort pulse can take the place of a broad band microwave source.

Currently an impulse of -2.2 V, 23 ps FWHM is used as a source. To extract the desired probing range of the frequency (8 - 40 GHz), we utilize a 500 mm *Ka*-band rectangular waveguide for 26–40 GHz microwaves and a 500 mm *X*-band waveguide for 8–18 GHz. When the impulse is launched into the waveguide, it is transformed to a chirped wave including broad frequency components. The lowest frequency component is determined by the waveguide size. Also higher frequency components than the maximum frequency in the standard frequency band are filtered out by a low pass filter. Therefore we can obtain the microwave of each desired frequency band.

Each obtained chirped microwave is amplified by a power amplifier and launched into the plasma. The incident wave reflects back from the cut-off layers corresponding to each frequency component. The reflected wave is divided and led to the detection stage of each frequency band. *X*-band frequency components are detected directly through each bandpass filter (BPF). *Ka*-band components are detected by a superheterodyne detection system. In a mixer the reflected wave is downconverted by the local microwave frequency of around 42 GHz. The output from the mixer is amplified by the intermediate frequency (IF) amplifier 2–18 GHz and then led to a single-pole double-throw (SPDT) switch. Each IF signal is filtered by 12 BPFs of which the center frequencies are from 3 to 14 GHz. The 12 signals are detected by Schottky barrier diode detectors to obtain the reflected signal pulses. Then TOF measurement is carried out using these pulses.

For the convenient multichannel system we utilize the switching technique. The frequency of the local oscillator is changed from 41.5 to 42.0 GHz with the repetition rate of  $f_0$ . A SPDT switch is operated at a  $2f_0$  repetition rate. Then the frequency components of the detector output are changed four times in one operation. For example, when the 9 and 10 GHz BPFs are paired, the measurable frequencies are 31.5, 32.0, 32.5, and 33.0 GHz in the incident microwave components. The important advantage is that there is no need for additional TOF measurement electronics. Figure 1 shows an example of the frequency switching operation.

divider and the 8 GHz BPF, which has an incident frequency component of 34 GHz, is located after another divider. When the level of the switching signal is high, only the 34 GHz signal is passed. Then the same discriminator collects both the 37 GHz signal and the 34 GHz signal.

Currently this reflectometer system operates with the ordinary mode polarization and has 28 channels of which 24 channels are *Ka* band and 4 channels are *X* and *Ku* bands. An example of the temporal behaviors of the TOF of each reflected pulse is shown in Fig. 2. The delay time is defined by the traveling time from the plasma edge, the position of which is calculated using the result of *in situ* calibration and a MHD equilibrium calculation, to each cut-off layer. When the corresponding cut-off layer is generated in the plasma, each reflected wave appears in order.

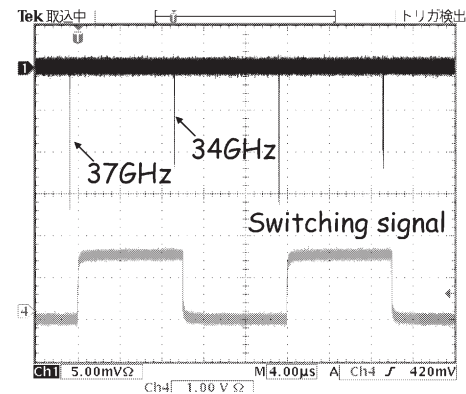


Fig. 1. Example of the frequency switching operation.

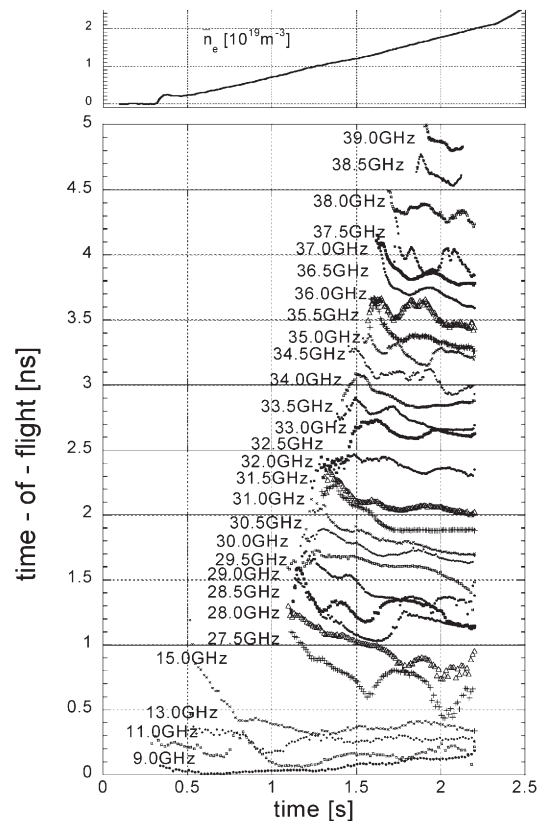


Fig. 2. Time evolution of the averaged density (top) and the delay time of the reflectometer each channel.



### §3. Application of Ultrashort-Pulse Reflectometer to LHD

Mase, A., Yokota, Y., Uchida, K., Kogi, Y. (KASTEC, Kyushu Univ.),  
Hojo, H. (University of Tsukuba),  
Kawahata, K., Tokuzawa, T.

Ultra short pulse reflectometry (USPR) is one of the methods to measure density profiles of plasmas. The frequency source of the reflectometer is replaced by an ultrashort pulse which pulse width is less than 100ps. The density profiles can be reconstructed by collecting time-of-flight (TOF) signal of each frequency component of an impulse reflected from each cutoff layer.

The detail of the USPR system was shown in elsewhere.<sup>1)</sup> Remote control system using super science information network (super-SINET) has been introduced to the USPR system since 2003. Bandwidth of the main backbone and branch line is 10 Gbps and 1 Gbps, respectively. The control client can operate the control server by using this network. The general-purpose interface bus (GPIB) card is installed in the control server. The remote console, which has a graphical user interface (GUI) is prepared to control the instruments of the USRM via GPIB. The operations such as adjustment of supply voltage fed to amplifiers and the doubler, timing control of the impulse, data acquisition and monitoring can be performed from the remote site. In FY2004, the position of the transmitter and receiver antennas can be controlled remotely. The two antennas can be rotated in order to observe the cut-off layer depending on the various plasma conditions even between the plasma shots.

The remote site monitor can display the current view of a sampling scope for various times. The directly recorded signal by the sampling scope is analyzed and reconstructed by means of the signal record analysis (SRA) method. We have assumed the initial position where the electron density equals to 0 corresponds to the one of the separatrix.<sup>2)</sup>

In Fig. 1 are shown the reflected signals from the wall and from the plasma and their frequency spectrum. In the LHD experiment, a multi-channel far-infrared (FIR) laser interferometer is utilized for measurement of density profiles. We have also utilized the density profiles obtained by the interferometer for the initial condition of density reconstruction. Figure 2 shows the comparison of the density profiles obtained by the USPR and the FIR laser interferometer. In the edge plasma region, the FIR laser interferometer can measure only a few chords. The behavior of the edge plasma and the plasma position is quite important for the control of the plasma. The USPR system seems to be useful for this purpose. However, in the edge plasma region ( $n_e < 2.0 \times 10^{19} \text{ m}^{-3}$ ), the FIR laser interferometer can measure only two chords or less. The behavior of the edge plasma and the plasma position is quite important for the control of the plasma. This USPR system seems to be useful for this purpose

In summary, an ultra short pulse reflectometer has been

applied to LHD for the measurement of edge region of plasmas. The whole system (both hardware and software) is controlled via the super-SINET from Kyushu University. The reflected waves are directly recorded by a high-speed digitizing scope, and analyzed by the signal record analysis for density reconstruction. The density profiles in the edge region are successfully determined during the shot and compared with those obtained by an FIR laser interferometer.

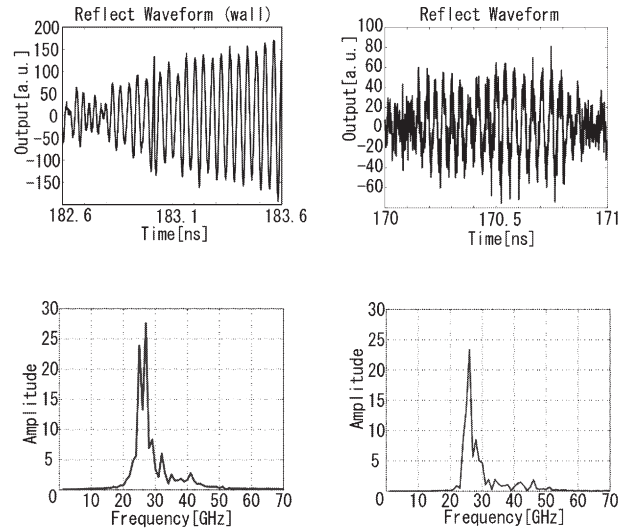


Fig. 1 Reflected waves from the wall (top left) and from the plasma (top right) and their spectrum (bottom).

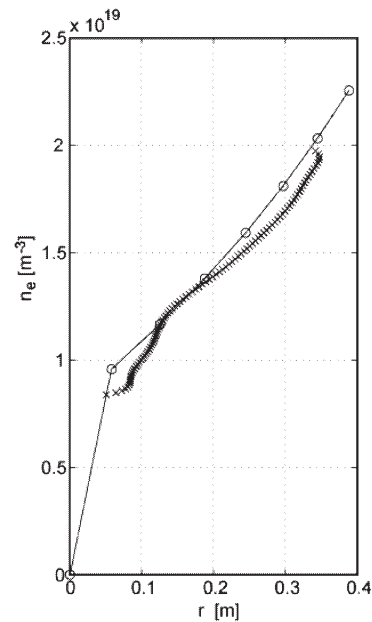


Fig. 2. Comparison of reconstructed density profiles obtained by the USPR and the FIR laser interferometer.

#### References

- 1) Kogi, Y., et al., Rev. Sci. Instrum. **75**, 3837 (2004).
- 2) Mase, A., Yokota, Y., Uchida, K., Kogi, Y., Ito, N., Tokuzawa, T., Kawahata, K., Tanaka, K., Nagayama, Y., and Hojo, H., to be published in Rev. Sci. Instrum.

## §4. Developments of Millimeter-Wave Diagnostic Simulator

Hojo, H. (Univ. Tsukuba, NIFS),  
Mase, A. (Kyushu Univ.), Kawahata, K.

Millimeter-wave diagnostics such as reflectometry are receiving growing attention in magnetic confinement fusion research. The detailed measurements on density profile and its fluctuations might be required in order to obtain the better understanding of plasma confinement physics. Recently, the new methods of microwave reflectometry such as ultrashort-pulse reflectometry and imaging reflectometry have been developed. We here think that it is very important to demonstrate computationally the usefulness of the new diagnostic methods before the experiments. Therefore, we state that the development of millimeter-wave diagnostic simulator is also of importance.

The basic equations for the millimeter-wave diagnostic simulator are the Maxwell equation for the electromagnetic wave fields,  $\mathbf{E}$  and  $\mathbf{B}$ , and the equation of motion for the induced current density  $\mathbf{J}$  as follows[1,2]:

$$\frac{\partial}{\partial t} \mathbf{B} = -\nabla \times \mathbf{E}, \quad (1)$$

$$\frac{\partial}{\partial t} \mathbf{E} = c^2 \nabla \times \mathbf{B} - \frac{1}{\varepsilon_0} \mathbf{J}, \quad (2)$$

$$\frac{\partial}{\partial t} \mathbf{J} = \varepsilon_0 \omega_{pe}^2 \mathbf{E} - \frac{e}{m_e} \mathbf{J} \times \mathbf{B}_0, \quad (3)$$

where  $\omega_{pe} (= (e^2 n / m_e \varepsilon_0)^{1/2})$  the electron plasma frequency, and  $\mathbf{B}_0$  is the external magnetic field. In the derivation of eq.(3), we assumed that the induced current density  $\mathbf{J}$  is approximated as  $\mathbf{J} = -en_0 \mathbf{v}_e$ ,  $\mathbf{v}_e$  being the electron flow velocity, as we consider electromagnetic waves in GHz range. The above coupled equations can describe both of the ordinary (O) and extraordinary (X) modes for the perpendicular propagation to an external magnetic field  $\mathbf{B}_0$ . When  $\mathbf{B}_0 = B_0 \mathbf{e}_z$ , the wave component  $E_z$  denotes the O mode with the dispersion relation:

$$\omega^2 = \omega_{pe}^2 + c^2 k^2, \quad (4)$$

on the other hand,  $E_x$  and  $E_y$  correspond to the X mode with the dispersion relation:

$$\left(\frac{kc}{\omega}\right)^2 = 1 - \frac{\omega_{pe}^2}{\omega^2} \frac{\omega^2 - \omega_{pe}^2}{\omega^2 - \omega_{pe}^2 - \omega_{ce}^2}, \quad (5)$$

where  $\omega_{ce}$  is the electron cyclotron frequency. The cross

polarization scattering between the O and X modes is generated from the  $\mathbf{J} \times \mathbf{B}_0$  term in eq.(3). The numerical scheme for solving eqs.(1)-(3) is based on the FDTD method.

Hereafter, we discuss the relativistic effects of wave propagation in plasma. The most important effect is the change of cutoff layer due to the relativistic electron mass modification[3]. The electron mass  $m_e$  is modified to  $m_e(1+5/\mu)^{1/2}$ , where  $\mu = m_e c^2 / T_e$ ,  $T_e$  being the electron temperature. In this case, the change of the cutoff density is given as follows:

$$\frac{\Delta n}{n_c} = \frac{n_{c,rel} - n_c}{n_c} = \begin{cases} \sqrt{1+5/\mu} - 1, & \text{(O-mode cutoff)} \\ \frac{\sqrt{1+5/\mu} - 1}{1 - \omega_{ce}/\omega}, & \text{(upper X-mode cutoff)} \end{cases}$$

The shift of the cutoff density due to relativistic effects is more significant for X modes. Figures 1 and 2 show the result of 2-d simulation on X-mode beam propagation. Theoretical cutoff positions are  $x_c = 98.2$  for  $T_e = 0.1\text{keV}$  and  $x_c = 112.5$  for  $T_e = 20\text{keV}$ , and we see that the numerical result coincides with the theoretical estimation.

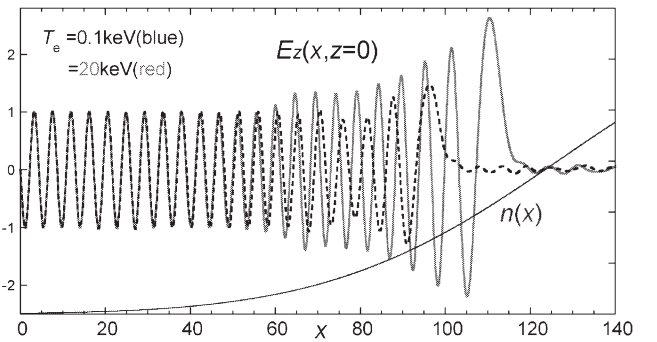


Fig.1. Snapshots of  $E_z(x, z, t)$  with  $T_e = 20\text{keV}$  (solid line) and  $0.1\text{keV}$  (dashed line) at the beam center  $z = 0$ .

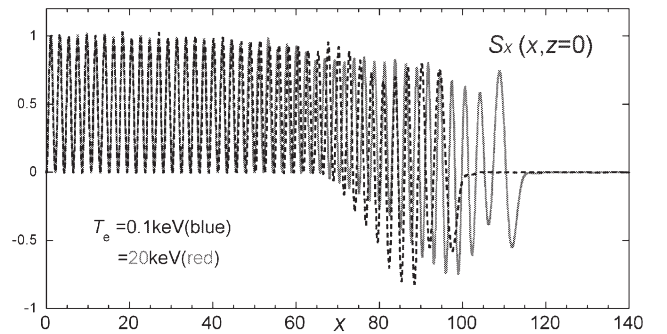


Fig.2. Snapshots of  $S_x(x, z, t)$  with  $T_e = 20\text{keV}$  (solid line) and  $0.1\text{keV}$  (dashed line) at the beam center  $z = 0$ .

### References

- 1) H. Hojo et al., Rev. Sci. Instrum. **70**, (1999) 983.
- 2) H. Hojo et al., Rev. Sci. Instrum. **75**, (2004) 3813.
- 3) E. Mazzucato, Phys. Fluids B **4**, (1992) 3460.

## §5. Potential Measurement by 6 MeV Heavy Ion Beam Probe on LHD

Ido, T., Shimizu, A., Nishiura, M., Kato, S.,  
Nishizawa, A., Tsukada, K., Yokota, M., Ogawa, H.,  
Inoue, T., Hamada, Y.

A heavy ion beam probe (HIBP) is a unique diagnostic technique to measure the electrostatic potential, its fluctuation and density fluctuation directly and simultaneously in high temperature plasmas. Hitherto, HIBPs have been applied for various magnetically confined plasmas and they have obtained significant results related to transport physics in plasmas. The radial electric field is recognized to be one of key parameters for the transport in Large Helical Device (LHD). Thus, we have developed an HIBP for LHD. The installation of the whole system has been recently completed, and the probing beam was detected and its energy was analyzed successfully<sup>1) 2)</sup>. In this report, results of the potential measurement are described.

The plasma potential has been measured during neutral beam injection (NBI) heating. The magnetic field strength is 2.75 T, and the major radius of the magnetic axis is 3.6 m. The beam energy of the HIBP is set to 5.042 MeV. According to the trajectory calculation, which is provisional, the potential profile can be measured within the normalized radius ( $\rho$ ) of about 0.2 during the sweep of the probing beam (Fig. 1 (a)).

The waveforms are shown in Fig. 1 (b). The plasma is produced by electron cyclotron heating (ECH) and sustained by co- and counter-NBI with the total power of 7.0 MW.

The measured profile of the plasma potential is shown in Fig. 1 (c). The potential tends to become positive by about 2 kV during NBI. The result suggests that the radial electric field ( $E_r$ ) of the electron-root is formed predominantly in the plasma. The  $E_r$  at the plasma edge is measured by charge exchange spectroscopy (CXS), and the positive  $E_r$  is observed. The positive potential measured by the HIBP is qualitatively consistent with the positive  $E_r$  measured by the CXS. The HIBP measurement is limited around the plasma center because the probing beam is blocked by the vacuum vessel, and the CXS can not measure at the plasma center in this magnetic configuration because of the low emission. Thus, the data measured by the HIBP and CXS are not crosschecked, yet. But, they can probably measure at same magnetic surface when the major radius of the magnetic axis is 3.9 m, so they will be crosschecked quantitatively in the magnetic configuration in future.

A serious problem related to the potential measurement remains. During ECH, the secondary beam profile changes drastically, even though the density and temperature profiles do not change. Judging from the behavior of the secondary beam profile, the probing beam seems to shift, though the sweep voltages are constant. One of possible causes is that the acceleration voltage and the

applied voltage in the beam line components change because of the voltage-drop of the power supply during the ECH. The cause must be clarified and be solved in order to measure the behavior of the potential in the plasma accurately.

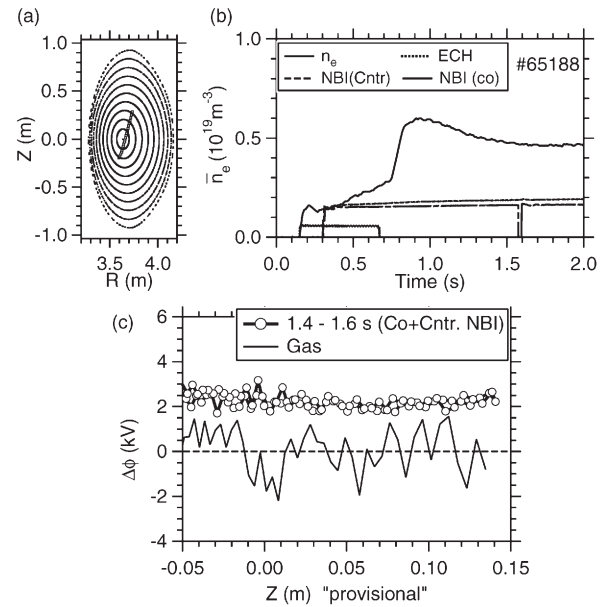


Fig. 1 (a) The magnetic surface and the calculated position of the sample volumes. Note that the calculation is provisional. (b) Line averaged electron density and timing of NBI and ECH. (c) Measured potential profile in balance-NBI plasma. The horizontal axis is the position of the measurement and it is provisional. The solid curve indicated as "Gas" is the potential of the vacuum vessel.

### Reference

- 1) Ido, T., et al.: submitted to Rev. Sci. Instrum (2006)
- 2) Shimizu, A., et al.: in this Annual report

## §6. Calibration of Tandem Energy Analyzer of Heavy Ion Beam Probe on LHD

Shimizu, A., Ido, T., Nishiura, M., Nakano, H., Kato, S., Nishizawa, A., Tsukada, K., Yokota, M., Ogawa, H., Inoue, T., Hamada, Y.

By using a high gain current detector, a micro channel plate (MCP), the secondary beam was successively detected on the Heavy Ion Beam Probe of LHD. By analyzing obtained signals, we checked the beam orbit and calibrated the tandem-energy analyzer. We report the experimental result for the calibration of the tandem-energy analyzer.

Usually for a heavy ion beam probe, a Proca-Green type parallel energy analyzer is used. However, if we apply this type of analyzer to HIBP on LHD, the required voltage to analyze the energy of 6MeV  $\text{Au}^+$  beam reaches to 500 keV~1 MeV. The power supply to generate this range of voltage is very expensive. Therefore, in order to reduce the required voltage, the tandem type of energy analyzer 1) has been developed.

In Fig.1, a schematic view of the tandem energy analyzer is shown. The beam injection angle to the first electrodes of the analyzer is 6 degrees, and to the second is 10 degrees, these are smaller than that of conventional type of energy analyzer, 30 degrees. Due to this small injection angle, the required voltage can be reduced to 56.5 kV for the first parallel electrodes and 113.6 kV for the second parallel electrodes to analyze 6 MeV beam.

For the calibration of the tandem analyzer, the secondary beam originating in the neutral gas scattering is used because the potential in the neutral gas is zero. The total secondary ion beam current obtained by using the high gain detector, MCP, is about a few tenths of pA. This current level is very small to achieve a good signal-to-noise ratio. In order to reduce noise level, the signal of the secondary beam current is filtered by averaging in the each duration of 100 ms. In the calibration experiment, we change the voltage of beam accelerator, and the change in the beam energy is measured by the tandem analyzer. In Fig.2, the temporal evolution of measured beam energy with the tandem analyzer is shown. In this figure, the 3 cases of the accelerator voltages that we set are shown: 5.042 MeV, 5.045 MeV and 5.046 MeV. The vertical axis is the change in the beam energy measured by the tandem

analyzer, and the offset level is determined by averaging the case of 5.042 MeV. The horizontal lines show the averaged values of each case in the temporal duration from -2 to -1 sec. In the case of 5.042 MeV, the variation level of the signal is larger than other two cases, because the secondary ion beam current is smaller than others: ~0.05 pA in the case of 5.042 MeV, ~0.15 pA in 5.045 and 5.046 MeV.

In Fig.3, the beam energy measured with the tandem-analyzer as a function of the accelerator voltage is shown. Here, for error bars, the standard deviations calculated from signals in Fig.2 are used. The magnitude of error is a few keV. The secondary beam current originating in the plasma is larger than in the neutral gas-scattering, therefore, the less error level is expected in measuring the plasma potential. However, for realizing more high temporal resolution (<10ms), larger current is required for the probing beam.

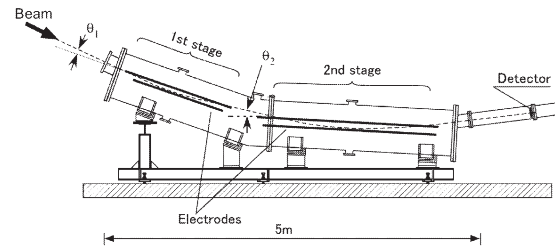


Fig.1. A schematic view of the tandem energy analyzer.

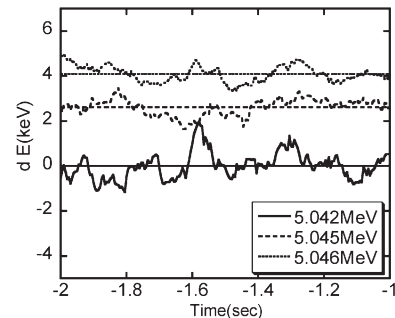


Fig.2. Temporal evolution of beam energy measured by the tandem analyzer. The 3 cases of acceleration voltages are shown.

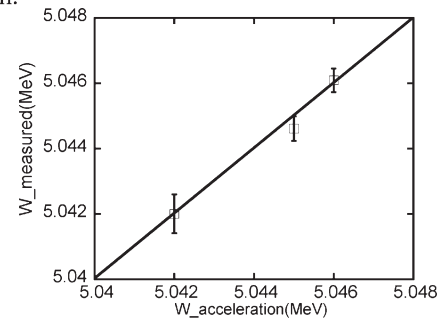


Fig.3. The beam energy measured with the tandem-analyzer as a function of the accelerator voltage

Reference

- 1) Y. Hamada, et al., Rev. Sci. Instrum. **68**, (1997) 2020



# §7. Development and Optimization of New Negative Ion Source for a Heavy Ion Beam Probe

Nishiura, M., Ido, T., Shimizu, A., Kato, S., Tsukada, K., Nishizawa, A., Hamada, Y., Matsumoto, Y., Mendenilla, A., Wada, M. (Doshisha Univ.)

A HIBP system has been installed in the LHD to measure the local plasma potential and the fluctuations [1]. It consists of a sputter type Au<sup>-</sup> ion source [2], a tandem accelerator, beam steering electrodes and an energy analyzer. The accelerated Au<sup>-</sup> beam undergoes double charge exchange and the resulting Au<sup>+</sup> beam (primary beam), which normally reaches up to 6 MeV, is injected into the LHD plasma. The secondary beam of Au<sup>2+</sup> produced from the primary beam by electron stripping in the LHD plasma is detected by the energy analyzer. The energy difference between the primary and the secondary beam corresponds to the value of the local plasma potential.

The plasma-sputter negative ion source installed in the present HIBP system produces the mass separated dc Au<sup>-</sup> beam with 10 micro ampere current and 10 keV mean energy. In the experimental campaign of the LHD in 2004, the secondary beam was successfully detected with an adequate S/N ratio for an operational regime with the plasma density lower than 10<sup>19</sup> cm<sup>-3</sup>. However, it is predicted that a more intense beam of Au<sup>+</sup> should be injected to realize enough S/N ratio, when the LHD is operated in a regime with the density higher than 10<sup>19</sup> cm<sup>-3</sup>. To produce Au<sup>+</sup> primary beam of enough intensity for diagnostics of high density and temperature plasmas, Au<sup>-</sup> beam current of the order of a hundred micro ampere is required.

To enhance the Au<sup>+</sup> primary beam current, a negative ion source having larger sputtering target and plasma volume has been designed. For the scale up of the negative ion source, the characteristics of the plasma sputter negative ion source are investigated at a separate test bench. The computer code, PBGUNS [3], is used to study the properties of Au<sup>-</sup> beam extracted from the ion source in Fig. 1.

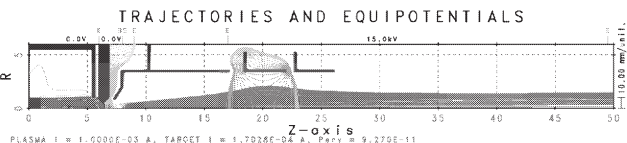


Fig. 1. Au<sup>-</sup> beam trajectories for new sputter type negative ion source and extraction system.

The new ion source has 16 Samarium Cobalt magnets to produce the multicusp magnetic fields for plasma confinement, and its volume is 3 times larger than

that of the present ion source. To tolerate high input power operation, the ion source body and the target rod are cooled by water. The characteristics of two ion sources are summarized in Table 1.

Table 1. Comparison between present and new ion sources at the similar discharge conditions.

	Present source	New source
Plasma volume (cm <sup>3</sup> )	346	1057
Target size (cm)	φ1.4	φ2.0
Extraction hole (cm)	φ0.5	φ0.8
Au <sup>-</sup> current (μA)	6.75 at 9.8 keV	65 at 14 keV
Target voltage and current	300V, 15mA	600V, 10mA

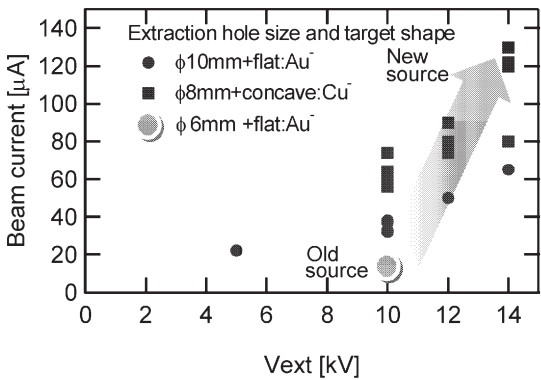


Fig. 2. Au<sup>-</sup> and Cu<sup>-</sup> beam currents for present and new sputter type negative ion sources as a function of extraction voltage. The data point of φ6mm+flat Au<sup>-</sup> is measured by the old source for the comparison

At the discharge current of approximately 4 A, the Au<sup>-</sup> beam current of 65 μA could be extracted with the energy of 14 kV from the ion source [4]. The Au<sup>-</sup> beam current enhances by a factor of 4 ~ 10, compared with the present ion source. We consider the possibility for a stable discharge and a high beam output of the new ion source. Owing to the scale up of the ion source, the plasma volume of the new ion source becomes larger than that of the present ion source. It would lead to the enhancement of the uniformity and the stability of plasmas in front of the gold target for sputtering. The optimizations of target temperature and electrode shapes will be continued for higher beam currents.

## References

- 1) Fujisawa, A., Iguchi, H., Taniike, A., Sasao, M., Hamada, Y., IEEE trans. on Plasma Sci. 22(1994)395.
- 2) Taniike, A., NIFS report, NIFS-352, (1995).
- 3) PBGUNS, Thunderbird Simulations, <http://www.thunderbirdsimulations.com>.
- 4) Nishiura, M. *et al.* Rev. Sci. Instrum 77(2006)03A537.

§8. Development of a Compact Au<sup>-</sup> Source for Local Electric Potential Measurement of a LHD Plasma

Wada, M., Mendenilla, A. (Doshisha Univ.),  
Sasao, M., Shinto, K. (Tohoku Univ.),  
Nishiura, M.

The plasma potential measurement system based on a negative ion beam probe has become operational at Large Helical Device in the fiscal year 2005. The system successfully yielded signals corresponding to local plasma fluctuations. However, the present signal is not adequate to give precise information of plasma fluctuation, but more probe beam current improves the signal-to-noise ratio of the overall system. Thus, a study to enhance Au<sup>-</sup> beam current extracted from a small plasma-sputter-type negative ion source has been started.

Two approaches have been taken to accelerate the source performance development. In one design, the size of the ion source discharge chamber has been enlarged so as to contain a larger sputtering target. The sputtering target is located at the center of the plasma confined in a multi-line-cusp magnetic field. A larger sputtering target is installed at the end wall of a smaller multi-cusp plasma source in the other design. These sources have been installed on test stands of proper extraction systems, and heavy negative ion beam currents are measured on each setup.

Total amount of beam current has increased in accordance with the size of the sputtering target.<sup>1)</sup> However, the beam quality did not improve much, indicating a growth of beam emittance with the target size. An attempt to enhance the beam brightness is being conducted with the smaller ion source by changing the size of the sputtering target. As shown in Fig. 1, the size of the sputtering target can be made as large as entire back end plate, while the diameter can be reduced down to 2.5 cm through changing the design of a floating potential plasma shield. The results have shown

that more stable operation of the ion source with smaller diameter sputtering target.

Optimization of Cs coverage on the sputtering target is another important subject to study with the test ion source. Consumption of Cs by the ion source is reduced by modulating the discharge current. Deposited Cs during the discharge-off period is removed from the target when heavy negative ion beam is extracted. Pulse waveforms of negative ion beam current with the flat top period of 200 ms have been successfully obtained as shown in Fig. 2, and more negative ion current is extracted stably with smaller Cs consumption.

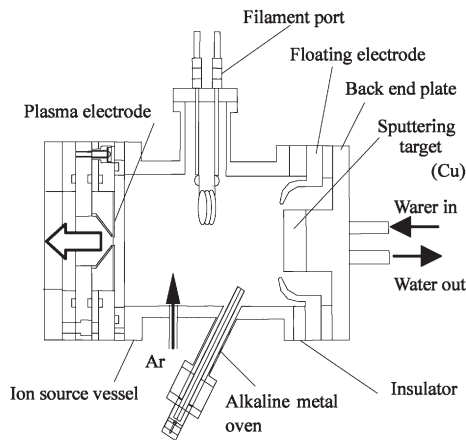


Fig. 1. Schematic illustration of an ion source used to study the dependence of beam brightness upon sputtering target size.

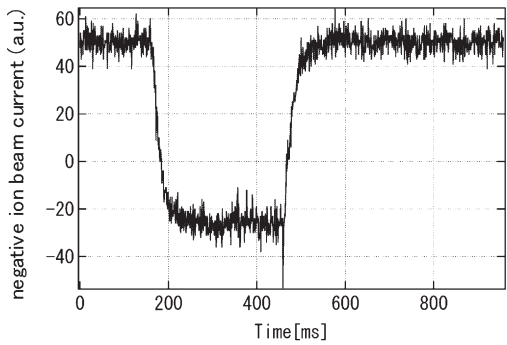


Fig. 2. An oscillograph trace showing the temporal change of heavy negative ion beam current as discharge power is modulated.

References

1) M. Nishiura, T. Ido, A. Shimizu, S. Kato, K. Tsukada, A. Nishizawa, Y. Hamada, Y. Matsumoto, A. Mendenilla, M. Wada, Rev. Sci. Instrum. **77**, 03A537 (2006).

## §9. Estimation Method of Impurity Transport by Means of Pulse-Height Analyzer in LHD

Muto, S., Morita, S.

An argon transport depending on magnetic island has been successfully estimated from the experimental results obtained with an assembly of Pulse-Height Analyzers (PHA) in Large Helical Device (LHD). In the present article it is preliminarily reported how diffusion coefficient and convective velocity have been estimated.

The assembly has been constructed to investigate the profiles of the x-ray spectra in the range from 1 to 13 keV.[1] In the present experiment several identical discharges have been performed, while the sight line of the PHA can change to measure the profile of argon  $K_{\alpha}$  line shot by shot.[2]

In the present research the transport of argon particles in LHD plasma has been derived from a continuity equation which is described by

$$-\frac{\partial}{\partial t}n(\vec{r},t) = \nabla \cdot \vec{\Gamma}(\vec{r}), \quad (1)$$

where  $n(r,t)$  and  $\Gamma(r)$  are an impurity density and an impurity flux, respectively.[3] It is assumed that the impurity flux is expressed by the summation of a diffusion term and a convective term as follows,

$$\vec{\Gamma}(\vec{r}) \equiv -D(\vec{r})\nabla n(\vec{r}) + \vec{V}(\vec{r})n(\vec{r}), \quad (2)$$

where  $D(r)$  and  $V(r)$  are the diffusion coefficient and the convective velocity, respectively. By making the assumption in the following equation

$$n(\rho,t) = A(\rho)f(t - \phi(\rho)), \quad (3)$$

it is possible to solve Eq.(1) as follows,

$$D(\rho) = -a^2 \left( \rho A(\rho) \frac{\partial \phi(\rho)}{\partial \rho} \right)^{-1} \times e^{-\frac{\phi(\rho)}{\tau}} \left[ \frac{Y_0}{\tau} + \left( 1 - \frac{1}{\tau} \phi(\rho) \right) X_0 \right], \quad (4)$$

where  $a$ ,  $\rho$ ,  $A(\rho)$ ,  $f(t)$ ,  $\tau$ , and  $\phi(\rho)$  denote an averaged plasma radius, a normalized radial coordinate, the density profile of the impurity, the time evolution of the impurity, the decay time of  $f(t)$ , and a phase-shift profile which is time necessary for the impurity particles to penetrate to a position of  $\rho$  in the plasma. The sign  $X_0$  and  $Y_0$  are defined by

$$X_0 \equiv \int_0^1 d\zeta \zeta A(\zeta) e^{-\frac{\phi(\zeta)}{\tau}}, \quad \text{and} \quad (5)$$

$$Y_0 \equiv \int_0^1 d\zeta \zeta \phi(\zeta) A(\zeta) e^{-\frac{\phi(\zeta)}{\tau}}, \quad (6)$$

respectively. In addition the convective velocity is also

solved as,

$$V(\rho) = \frac{1}{a} e^{-\frac{\phi(\rho)}{\tau}} D(\rho) \frac{\partial}{\partial \rho} \ln A(\rho) + \frac{a}{\rho} A(\rho)^{-1} e^{-\frac{\phi(\rho)}{\tau}} \frac{1}{\tau^2} [\phi(\rho) X_0 - Y_0]. \quad (7)$$

Fig.1 shows the measured phase-shift profiles of the argon particles in LHD. The penetration time of the argon particles into the plasma center is approximately 0.15 sec as is shown in the figure. However, the spatial derivative of the phase shift is different between in the island case and no island case.

The estimated diffusion coefficient and the convective velocity are shown in Fig.2. In the region where the normalized radial coordinate is less than 0.6, the diffusion coefficient of the island case seems to be better than that of no island case.

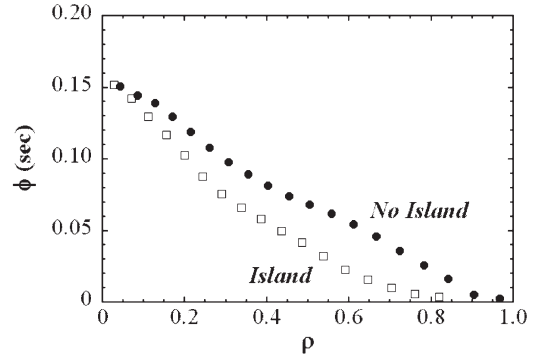


Fig.1. The phase-shift profiles of argon particles measured with the assembly of PHA. The filled circles and the open squares denote the cases of no island and island, respectively. The horizontal axis represents the normalized radial coordinate in the case of no island. The region higher than 0.7 is corresponding to the island. The timing of argon injection is corresponding to  $\phi = 0$  in the vertical axis.

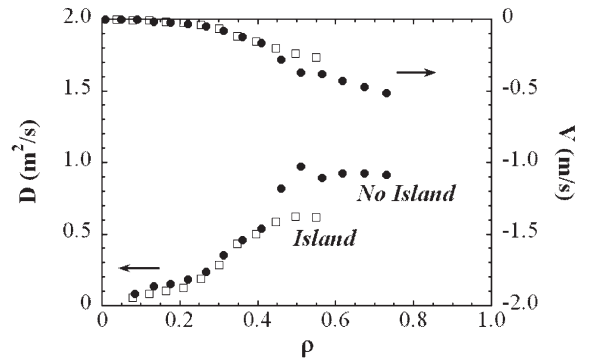


Fig.2. The diffusion coefficients and the convective velocities derived from the measured phase-shift profiles.

## References

- [1] Muto S., and Morita S., Rev.Sci.Instrum. **72**(2001)1206.
- [2] Muto S., and Morita S., J.Plasma Fus.Res.SERIES **7**(2006)27.
- [3] Takenaga H., et.al., J.Plasma Fus.Res. **75**(1999)952.

## §10. Initial Experiment on the Tracer-Encapsulated Cryogenic Pellet (TECPEL) Injection into LHD Plasmas

Tamura, N., Vinyar, I. (St. Petersburg State Polytechnical Univ.), Kalinina, D.V., Sudo, S., Sakamoto, R., Kato, S., LHD Experimental Groups

In order to develop understanding of impurity particle transport in magnetically confined toroidal plasmas, a double-layered impurity pellet, a tracer-encapsulated pellet has been proposed 1). This idea has been realized first as a tracer-encapsulated solid pellet (TESPEL). TESPEL consists of polystyrene polymer ( $-\text{CH}(\text{C}_6\text{H}_5)\text{CH}_2-$ ) as an outer shell and tracer particles as an inner core. Thus a very easy operation of loading and injecting the pellet has been achieved at room temperature, whereas the carbon from the shell of the TESPEL is an inevitable side impurity. In order to eliminate the side impurity from the tracer-encapsulated pellet, a tracer-encapsulated cryogenic pellet (TECPEL) has been developed 2). The shell of the TECPEL is made of ice of hydrogen the same as a fuel gas.

In the 9th LHD experimental campaign, the TECPEL injector, which is a pneumatic pipe-gun type injector, has been installed at Port 3-O of LHD. The installation of the TECPEL injector has been completed in a short time, since the TECPEL injector shares a part of guide tubes, a differential pumping system and a pellet monitor with a 10 barrel normal hydrogen ice pellet injector, and a part of the controlling system of the injector with the TESPEL injector. The size of the TECPEL, which is fabricated in the injector based on the in situ condensation technique, is 3 mm in diameter and  $\sim 3$  mm long almost the same as the normal hydrogen ice pellet for plasma fueling (see 2) for more details). Figure 1 shows the typical signals from the pellet monitor with the TECPEL injection. The TECPEL velocity is obtained by measuring the time of flight between signals from a microwave mass analyzer and a light gate and is typically around 1 km/s. A large dip observed in the  $\text{H}\alpha$  emission from the TECPEL ablation cloud could be related to the major rational surface of unit, as reported in many experiments regarding the hydrogen ice pellet injection. The signals from the pellet monitor show that the integrity of the TECPEL is kept until the TECPEL enters the plasma. Figure 2 shows the temporal evolution of the LHD discharge with the TECPEL injection. In the figure, the TECPEL injection time ( $\sim 2.73$  s) is indicated as the vertical dashed line. In this shot, the tracer of the TECPEL is the carbon ball with a diameter of 0.2 mm. Just after the TECPEL injection, the line-averaged electron density, measured with the far-infrared interferometer, is increased by 63 %. The rapid increase of the

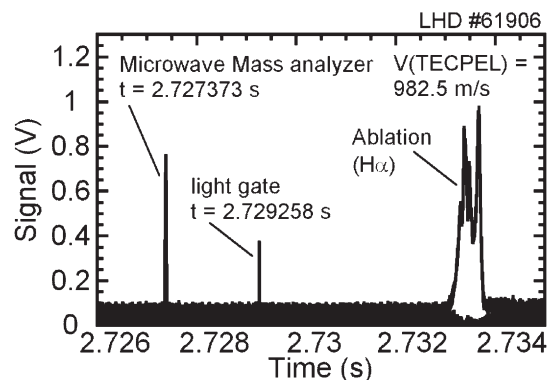


Fig. 1. Temporal evolution of the pellet monitor signals of the discharge with the TECPEL injection.

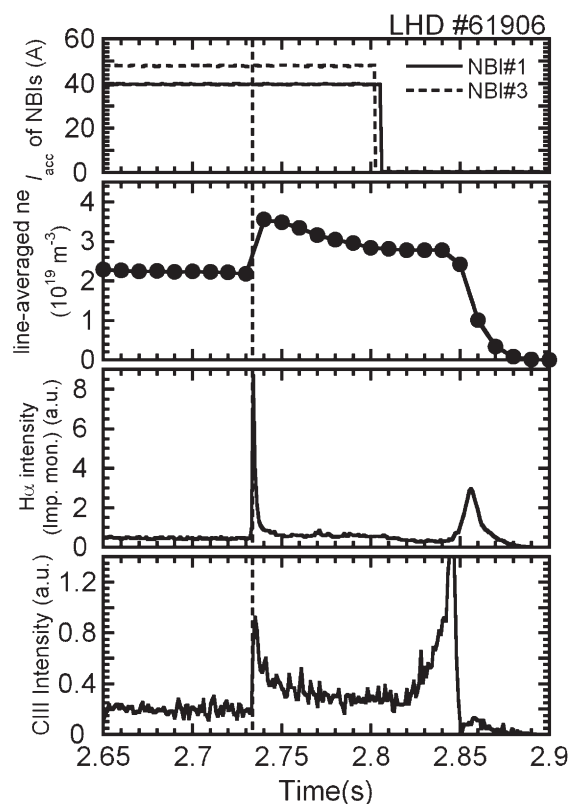


Fig. 2. Plasma waveforms of the LHD discharge with the TECPEL injection. The vertical dashed line indicates the TECPEL injection time ( $\sim 2.73$  s)

intensity of C III (97.7 nm), which is measured using a 20 cm normal incidence VUV monochromator equipped with a secondary electron multiplier, could be attributed to the carbon tracer in the TECPEL. However, since the increase of the intensity of C III (97.7 nm) has been also observed, in some cases, even after the normal hydrogen ice pellet injection, the spectroscopic observation of the carbon from the TECPEL should be optimized. Nevertheless, the initial experiment of the TECPEL injection into the LHD plasma has been implemented successfully.

### References

- 1) Sudo, S.: J. Plasma Fusion Res. **69**, (1993) 1349.
- 2) Sudo, S. et al.: Rev. Sci. Instrum. **76**, (2005) 053507.



## §11. Identification of Micro-Turbulence in LHD from 2d Phase Contrast Imaging

Michael, C.A. (JSPS fellow), Tanaka, K., Vyacheslavov, L.N. (Budker institute of nuclear physics), Sanin, A. (Budker institute of nuclear physics), Yamagishi, O., Yoshinuma, M., Ida, K., Kawahata, K.

It is well known that particle and energy transport are strongly influenced by fluctuation-driven processes. Here we focus the relationship between parameter profiles and fluctuation profiles. The purpose of such an investigation is twofold, since fluctuation profiles have ramifications for the transport and may regulate the profiles, and also to provide evidence for particular theoretical descriptions of the turbulence behaviour. Drift-wave like fluctuations are driven by gradients in density and ion/electron temperature profiles, and are affected by magnetic properties. Linear growth rates for ITG have been performed in LHD [1].

Fluctuation measurements presented here were made using a novel 2-d CO<sub>2</sub> laser phase contrast imaging (PCI) system, which was recently upgraded in the 9<sup>th</sup> cycle [2]. This diagnostic has the capability to simultaneously resolve line-integrated fluctuations both along the line of sight, which we label by flux coordinate  $\rho$  (with  $\pm$  denoting above/below the midplane), and in  $k$ . The system uses a (6x8) 2d detector array to measure to determine the position of fluctuations. The phase velocity of the fluctuations conveys information about the underlying nature of the instability, depending on whether it is in the ion or electron diamagnetic direction. It is necessary to compare fluctuation velocities with the ion/electron drift velocities in the plasma frame of reference:  $v_{ph} = v_{ExB} \pm v_{dr}$ . The ExB rotation is measured directly from the Doppler shift of C VI CX radiation driven by perpendicularly injected positive NBI, recently installed in the last experimental campaign, providing detailed information near the edge of the plasma. A comparison of PCI phase velocity and diamagnetic velocities is shown in Fig. 1. The measurements are consistent in that the shape of the ExB profile closely corresponds with the fluctuation velocity. In the edge, there is a significant ExB shear. This may play a role in regulating the transport in certain scenarios. The fluctuation velocities are approximately offset from the ExB velocity by the electron drift velocity, which would be expected of primary TEM-driven modes.

We consider the change of the profile from peaked to hollow, after pellet injection, to elucidate the role of density gradient. The fluctuation profiles are shown in Fig. 2. In the peaked density profile, fluctuations are strongest in the edge, while when the profile hollows, a new branch is excited towards the core, in the hollow part of the profile. The temporal dynamics at  $\rho=0.7$  are shown explicitly in Fig.

3. After pellet ablation, the density profile is transiently hollow. When the profile switches to peaked, fluctuations are reduced. At around  $t=1.8s$ , the heating power is increased and the profile returns to hollow. Again, when the sign of  $\eta$  changes, fluctuations increase again. Because the temperature gradient is non-zero, and density gradient is a regulating parameter, this is evidence of a slab-like ITG mode. However, ITG dominated modes propagate in the ion-diamagnetic direction, contrary to the observed phase velocity described in the previous section. This feature is also inconsistent with the theoretical expectations [1], which show that fluctuations should be reduced in the hollow part of the density profile, for a peaked temperature profile. The presence of a fluctuation peak in the hollow region of the density profile is universal in that it occurs in a variety of discharges, though exceptions can be found with no peak in the hollow region. The direction and magnitude of the fluctuation-induced flux may have ramifications for the causality of the hollow density profile.

[1] O. Yamagishi et al., *submitted to PoP*

[2] C. Michael et al., *RSI. (proc. HTPD), accepted (2006)*

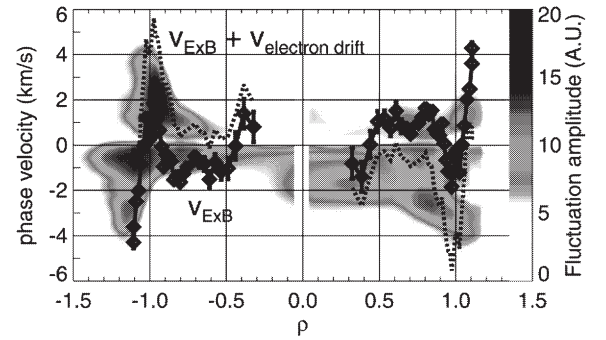


Fig 1: Fluctuation phase velocity compared with ExB and drift velocities

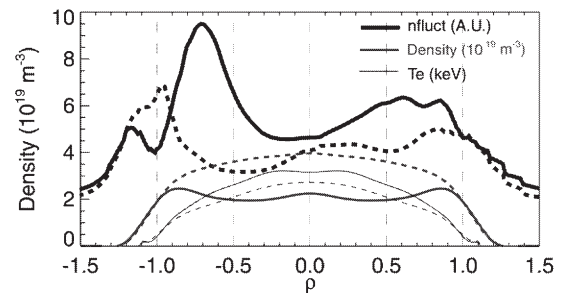


Fig 2: Comparison of profiles of fluctuation amplitude, density and temperature at  $t=1.9s$  (dashed lines) and  $t=2.2s$  (solid lines)

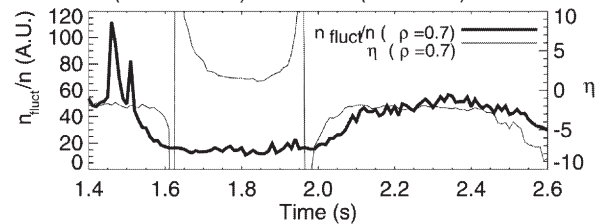


Fig 3: Time evolution of relative fluctuation level and  $\eta = (\nabla T/T) / (\nabla n/n)$  at  $\rho=0.7$

## §12. Application of Precise Phase Detector for Density Profile and Fluctuation Measurements Using CO<sub>2</sub> Imaging Heterodyne Interferometer on LHD

Vyacheslavov, L.N. (Budker Institute of Nuclear Physics), Khilchenko, A.D. (Budker Institute of Nuclear Physics), Zubarev, P.V. (Budker Institute of Nuclear Physics), Tanaka, K., Michael, C. (JSPS fellow), Sanin, A.L. (Budker Institute of Nuclear Physics)

A two-color CO<sub>2</sub>/YAG laser imaging heterodyne interferometer (HI) was recently equipped with a precise digital phase detector (PD), which was developed at Budker Institute of Nuclear Physics in Novosibirsk and is described in detail elsewhere [1, 2]. The PD has phase resolution  $1 \cdot 10^{-4}$  fringes and temporal resolution 1  $\mu$ s. Both are one order of magnitude finer than that of previously employed analog phase detectors. This modification enables detailed measurements of plasma density dynamics during pellet ablation and, in addition, observations of density fluctuations [3]. Better temporal resolution is important in pellet discharges with fast rising density gradients. With new PD, it is possible to combine HI with a phase contrast imaging (PCI), particularly in discharges with relatively large edge fluctuations. Though HI has a lower sensitivity to density fluctuations compared to the phase contrast method, it is free from the inherent shortcoming of PCI - the insensitivity to low-k fluctuations. The additional advantage of HI for measurement of density fluctuations is that absolute calibration is not required.

The temporal resolution of the new PD is illustrated by Fig. 1 where a small fraction of 3-second time trace of the line-integrated density of the discharge with multiple pellet injection is presented. The spatial resolution of the heterodyne interferometer and sensitivity of the PD to density fluctuations is demonstrated in Fig. 2. The line-average density fluctuation amplitude profile,  $\langle \delta \text{NeL} \rangle$ , has a maximum at chord position  $R=4.15$  m, which penetrates to a minimum normalized radius of  $\rho=0.9$ . The total frequency spectrum for this discharge is shown in Fig. 3. The plasma signal exceeds the noise more than order of magnitude. At low frequencies, the noise level is mostly determined by vibrations. The spatial spectrum is shown in Fig. 4

### References

1. P.V.Zubarev, A.D. Khil'chenko, Instruments and experimental techniques, 46, 171, (2003)
2. V.F.Gurko, et al, Instruments and experimental techniques, 46, 619, (2003)
3. L.N. Vyacheslavov et al., to be published Rev. Sci. Instrum.

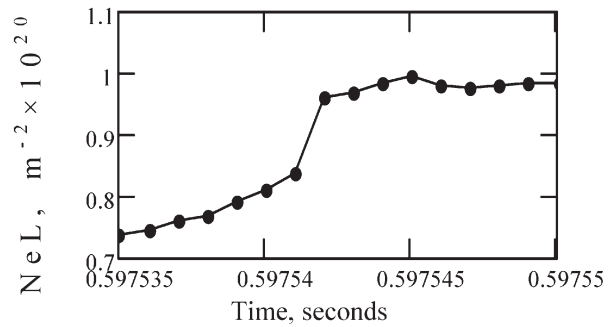


Fig.1. Line-integrated density recorded in a pellet discharge with magnetic configuration having  $R_{ax}=3.75$  m

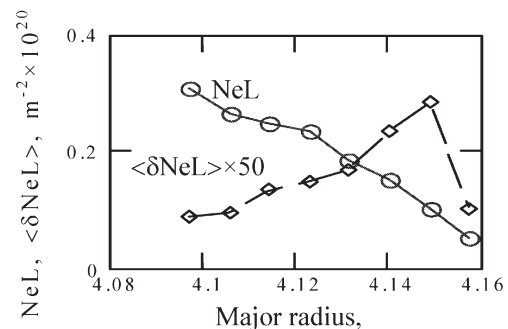


Fig.2 Line-integrated density recorded in a pellet discharge with magnetic configuration having  $R_{ax}=3.75$

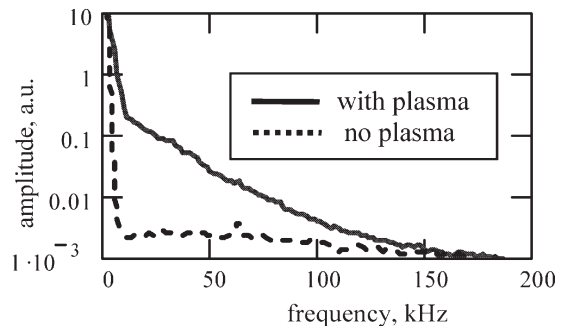


Fig.3. Frequency spectra of density fluctuations. No vibration compensation is applied in these experiments.

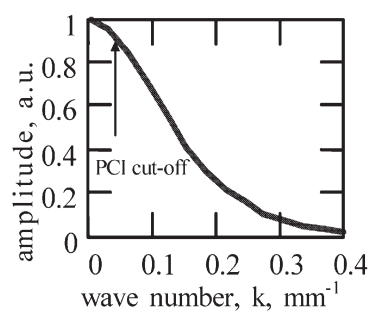


Fig.4. Spatial spectrum of density fluctuations for frequencies greater than 5 kHz. The arrow indicates the low k limit that the phase contrast technique would have, for this system.

### §13. New Calibration Method of Magnetic Measurements Based on the MHD Equilibrium with the Ergodic Region

Yamaguchi, T. (Grad Univ.), Watanabe, K.Y., Sakakibara, S., Suzuki, Y.

A relationship between a signal of magnetic measurement and equilibrium parameters such as the beta value and its radial profile, can be investigated using the equilibrium analyzing code and the magnetic measurement's signal analyzing code, which calculates signals of magnetic measurements from a result of the equilibrium code. The calibration using the relationship is necessary to evaluate equilibrium parameters from magnetic measurements. The conventional calibration method is based on the three-dimensional (3-D) free-boundary MHD equilibrium solver (free-boundary VMEC[1]) which assumes nested flux surfaces and the magnetic measurement's signal analysis code (DIAGNO[2]). On the other hand, the invasion of the ergodic region to the plasma core region is shown by the theoretical study based on real coordinate MHD equilibrium solver (HINT[3]). This phenomena may affect the accuracy of equilibrium parameter's identification for high beta plasma through the identification of the size and the shape of peripheral flux surfaces. The new method to evaluate equilibrium parameters based on HINT code, is proposed to improve an accuracy [4].

We applied the new method to the calibration of the diamagnetic loop and the saddle loop in LHD. Figure 2 shows the dependence of the diamagnetic loop flux and the saddle loop flux on volume averaged beta  $\langle\beta_{dia}\rangle$  proportional to the volume plasma energy. The calculated conditions are 1)LHD standard magnetic configuration at magnetic axis is 3.6m, 2)the pressure profile is  $\beta=\beta_0(1-\rho^8)(1-\rho^2)$  where  $\beta_0$  shows a central beta, and 3)zero toroidal current on each flux surface. The difference in the diamagnetic loop is small ( $\sim 5\%$ ). But the large difference in the saddle loop ( $\sim 40\%$ ) can be seen. The comparison with experimental data is shown in Fig.3. In Fig.3, the experimental data set whose electron pressure profiles measured by Thomson scattering and FIR laser interferometer are nearly  $\beta=\beta_0(1-\rho^8)(1-\rho^2)$  and the effect of toroidal current to the saddle loop is  $<15\%$ , is selected. The large pressure anisotropy is observed in case of neutral beam heating and the low-density plasmas. The experimental data shown in Fig. 2 is selected to be (beam pressure/thermal pressure)  $< 20\%$  to compare them in an isotropic pressure condition. The new method based on HINT is closer to the experimental data than the conventional method based on VMEC. It is confirmed that the method based on HINT is useful as the calibration method to evaluate  $\langle\beta\rangle$  and the pressure profile. In the previous report[6], it is shown that the experimentally observed Shafranov shift is closer to one calculated by HINT than one by free-boundary VMEC. The difference is considered to be due to the difference of the identification of outer most flux surface in free-boundary VMEC and HINT because the magnetic axis, which evaluated by

fix-boundary VMEC using the boundary of HINT, is almost same as one by HINT (within 1 cm). The result shown in Fig.2 is consistent with the report because Shafranov shift depends on P.S. current.

- [1] S.P. Hirshman et. al., Comput. Phys. Commun. **43** 143 (1986).
- [2] H.J. Gardner, Nucl. Fusion **30** 1417 (1990)
- [3] K. Hara Fuji et. al., J. Comput. Phys. **81** 169 (1989)
- [4] T.Yamaguchi et al., Plasma Fusion Res. **1** 011 (2006).

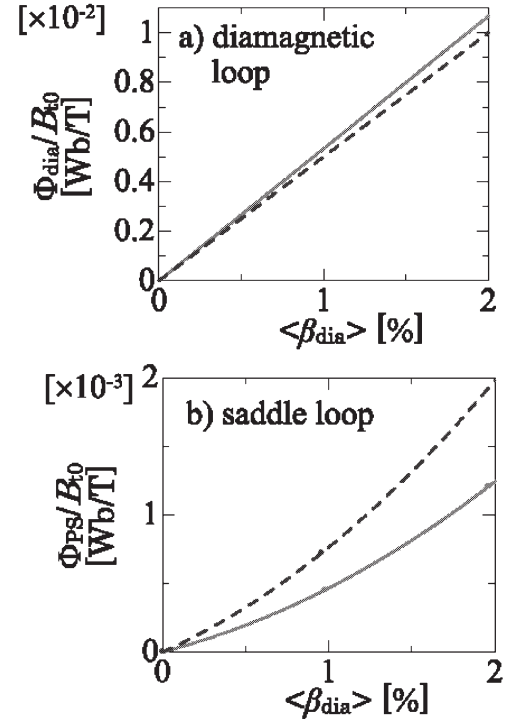


Fig.1 The comparison between the new method based on HINT (solid line) and the conventional method based on VMEC (broken line) for a) the diamagnetic loop and b) the saddle loop. Here those fluxes are normalized by toroidal magnetic field.

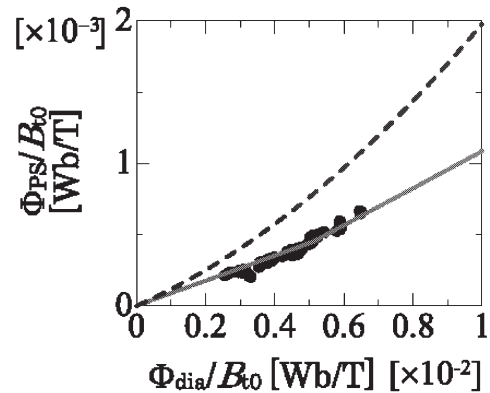


Fig.2 The comparison of the new method based on HINT (solid line) and the conventional method based on VMEC (broken line) and experimental data (dot).

## §14. Effect of Net Toroidal Current on Measurement of Diamagnetic Beta Value in Heliotron Plasma

Yamaguchi, T. (Grad Univ.), Watanabe, K.Y., Sakakibara, S., Ida, K.

We study the effect of the net toroidal plasma current on the diamagnetic measurement for large toroidal current experiments in the Large Helical Device (LHD). As a conventional method to compensate the effect of the net toroidal plasma current, the method based on the cylindrical and large aspect ratio plasma model is well known [1]. There the plasma current pass is assumed on the above model geometry. In order to treat precisely the effect, we apply a new method, which evaluates magnetic fluxes of magnetic measurements directly from plasma currents of a MHD equilibrium state with net toroidal current [2]. There is a large difference between the value calibrated by the new method and by a conventional method under the cylindrical and large aspect ratio plasma model because the current pass is quite different in the above two methods.

We apply the new calibration method of the diamagnetic flux based on the calculation of 3-D MHD equilibria with the net toroidal current to the experimental data analysis in order to confirm the validity of the method. Figure 1 shows the time evolution of the acceleration voltage of the neutral beam injectors (NBI), the net toroidal current, the beta value and the line averaged electron density. Here  $\langle\beta_{kin}\rangle$  is the volume averaged thermal beta value.  $\langle\beta_{\perp}\rangle$  is the perpendicular component of the volume averaged beta value, which is evaluated from the diamagnetic loop flux. One NB is injected in the co-direction during the first half of this discharge ( $\sim 4.8$ sec) and two NB are injected in the ctr-directions during the latter half. Because the main direction of the NB is changed from the co- to the ctr-direction, the toroidal current changes from the co- to the ctr-direction. Reasons for the difference between  $\langle\beta_{kin}\rangle$  and  $(3/2)\langle\beta_{\perp}\rangle$  are considered to be the effect of  $\Phi_p$  (the flux due to toroidal flux), the flux due to the net toroidal current. Here it is considered that the change of the beam pressure is small during that time because the density and the NBI power are almost constant. The new method is applied to the experimental data during 5.0-6.5 sec.  $\Phi_p$  is evaluated as:

$$2 \frac{\Phi_p}{\Phi_{vac}} = 2 \frac{\Phi^{cal}(\beta = \beta_{kin}, J_{\phi} = J_{\phi}^{MSE})}{\Phi_{vac}} - 2 \frac{\Phi^{cal}(\beta = \beta_{kin}, J_{\phi} = 0)}{\Phi_{vac}}.$$

The first term of right hand side is the calculation result of VMEC [3] for the pressure profile evaluated by Thomson scattering and far-infrared interferometers and the toroidal current profile by MSE. The second term of the right hand side shows a calculation result for the measured pressure profile and zero toroidal current on all flux surfaces. Figure 2 shows  $\langle\beta\rangle$  after the calibration of  $\Phi_p$  using the new method. The calibrated  $\langle\beta\rangle$  hardly changes during the period 5.0-6.5 sec unlike before the calibration, and it is 1.5

times larger than that evaluated from the profile measurement,  $\langle\beta_{kin}\rangle$ . It is thought that the main reason is considered to be the beam pressure.

[1] S. Besshou, C.E. Thomas, T. Ohbata, A. Iiyoshi and K. Uo, Nucl. Fusion **26** 1339 (1986).

[2] T. Yamaguchi T, Plasma Phys. Contr. Fusion to be published in 2006.

[3] S.P. Hirshman et. al., Comput. Phys. Commun. **43** 143 (1986).

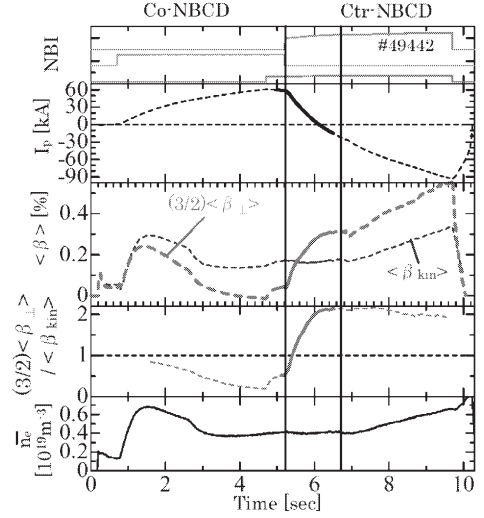


Fig.1 Time evolutions of beta values and some key parameters.

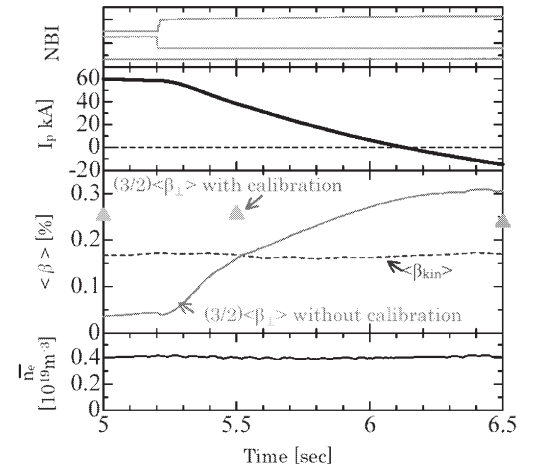


Fig.2 The time evolution of the calibrated beta value after a correction of the net toroidal current effect.



## §15. Progress on Temporally and Radially Resolved Charge Exchange Diagnostics of Fast Ions on LHD

Goncharov, P.R., Ozaki, T.

Experiments on suprathermal ion physics are carried out on LHD with a 40 channel Compact Neutral Particle Analyzer (CNPA) [1]. The analyzer is used both in passive non-perturbing chord-integral neutral particle flux measurements and for local probing with an impurity pellet. The analyzer observes trapped particles with  $|v_{\parallel}/v| \lesssim 0.25$  and the pitch angle cosine value  $v_{\parallel}/v$  changes sign along the diagnostic sightline. The measurable energy range for  $H^0$  is 1 - 170 keV.

The analysis of escaping neutral particles formed from plasma ions in charge exchange (CX) collisions serves as one of the principal tools to study the core ion temperature,  $T_i(\rho)$  radial profiles, fast ion confinement, ion kinetics and heating mechanisms by  $f_i(v, \vartheta, t)$  measurements. A significant progress on the CNPA diagnostic has been made recently on LHD [2, 3].

The illustrative experimental results presented here show the time and energy resolved non-perturbing measurements of the natural neutral flux from tangential and perpendicular hydrogen NBI and hydrogen minority ICRF heated Ar/He background plasma (Fig. 1) and the active probing with a polystyrene pellet during the steady state with combined heatings (Fig. 2).

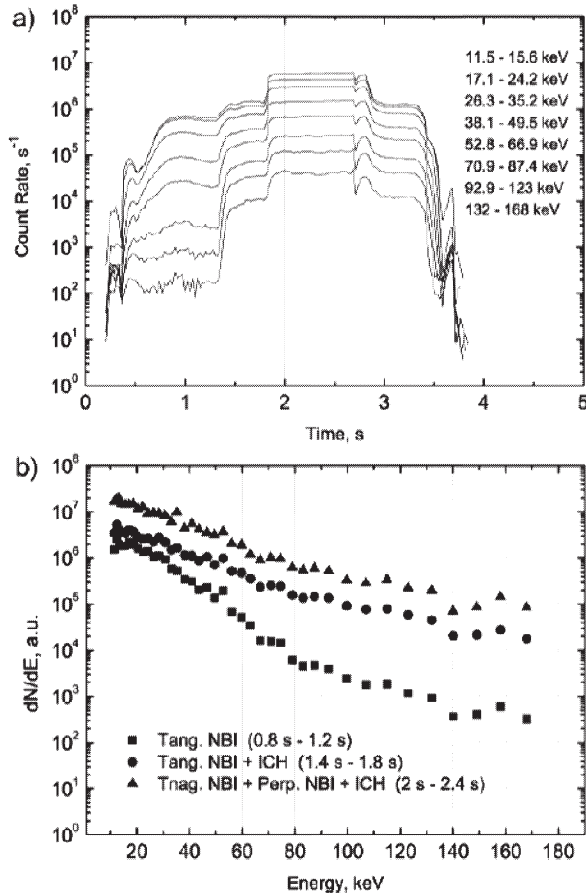


FIG. 1. Passive non-perturbing measurements: a) time behavior of the neutral particle flux in eight energy subintervals; b) neutral spectra obtained in different heating conditions.

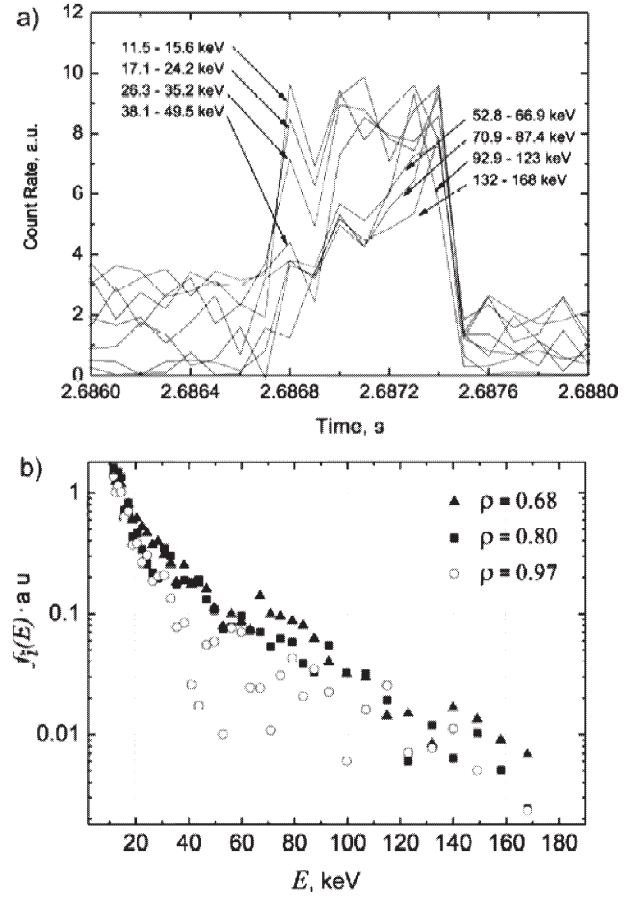


FIG. 2. Active PCX measurements: a) time behavior of the neutral particle flux in eight energy subintervals; b) neutral spectra obtained from different radial positions.

The tangential NBI #1  $E_{inj} = 153$  keV and the perpendicular NBI #4  $E_{inj} = 40$  keV. Fig. 1 (a) shows the time behavior of the neutral flux in eight subintervals of the total range. The uppermost curve corresponds to the lowest energies. A pronounced response to ICRF can be seen as a substantial increase of the high energy CX particle flux. The perpendicular NBI pulse causes a clear further increase. This is consistent with the measurement geometry and the observable particle pitch angles. The CX neutral spectra corrected for detection efficiencies, shown in Fig. 1 (b) reflect the fast ion population growth and the distribution tail slope change due to ICH accelerating particles orthogonally and the perpendicular NBI.

The response of the CEM currents to the injection of  $D_{pel} = 880 \mu\text{m}$ ,  $v_{pel} = 477$  m/s ( $-C_8H_8-$ )<sub>n</sub> pellet can be seen in Fig. 2 (a). Summary curves are shown for the same eight energy subintervals as above. The ablation signal time abscissa corresponds to the pellet penetration into the plasma column. The energy spectra from the outer (ablation start), intermediate, and inner (ablation end) radial locations are presented in Fig. 2 (b). The time resolution of  $100 \mu\text{s}$  allows one to obtain several radially resolved spectra depending on the pellet ablation time interval. These  $f_i(E)$  histograms were reconstructed from PCX neutral spectra by using the detection efficiency data and the energy dependent equilibrium neutral fraction  $F_0(E)$ .

### References

- 1) Chernyshev, F.V., et al., Instr. and Exp. Tech., **47** (2004) 214
- 2) Goncharov, P.R., et al., Fusion Sci. Technol., **49** (2006)
- 3) Goncharov, P.R., et al., Rev. Sci. Instrum. **77** (2006)

## §16. Progress of a New Two Color FIR Laser Interferometer

Kawahata, K., Akiyama, R., Pavlichenko, T., Tanaka, K., Okajima, S., Nakayama, K. (Chubu Univ.)

For high-density operation of the Large Helical Device, we have been developing short wavelength far infrared laser oscillation lines [1,2] by using CO<sub>2</sub>-laser-pumped FIR laser. So far, we have achieved high power laser lines oscillating simultaneously at 57.2  $\mu\text{m}$  ( $\sim 1.6$  W) and 47.6  $\mu\text{m}$  ( $\sim 0.8$  W) in a twin optically-pumped far-infrared CH<sub>3</sub>OD laser. These two color laser oscillation lines enable us to construct a new two color laser interferometer [3]. This two color interferometer system is unique one compared with the conventional two color interferometer system, where two independent lasers are used to be combined. By introducing Ge:Ga detectors operating at liq.He temperature, we have successfully detected two color beat signals with excellent signal to noise ratio.

Figure 1 shows a view of the detector/cone assemblies mounted on the cold-plate of the cryostat. The cooled detector system contains three unstressed gallium-doped germanium photoconductors. The detectors view incoming radiation via a focusing Winston cone and through a set of low-pass filters via vacuum windows located in the bottom plate of the cryostat. The detecting elements are small compared to the beam-size so they are mounted in integrating cavities immediately behind a Winston cone which has an entrance aperture of 15mm in diameter and has an f/3.5 field of view. This arrangement permits multi-pass absorption by the detector, thereby significantly improving optical coupling efficiency. Two filters are located in the detector system. The first one is mounted on the 77K radiation shield, where it serves to block and reflect unwanted higher frequencies from the 300K background radiation. This greatly reduces the thermal load on the cryogenic stages of the cryostat and generates a conveniently long run-time from a single fill of liquid helium. The second identical filter sits on the entrance aperture of the Winston cone where it ensures that no unwanted higher frequencies are incident on the detector from leakage within the cryostat.

Figure 2 shows the frequency spectrum of two color beat signals at 1.2 MHz for 57.2  $\mu\text{m}$  and 0.55 MHz for 47.6  $\mu\text{m}$ . It can be seen in this figure that the signal-to-noise ratio is excellent to be about 40 dB. This high signal-to-noise ratio was achieved when the input power to the detector was reduced by 30 dB. The beat frequency of each laser oscillation line can be set at the optimum value

by changing the pressure of the FIR laser cavity and by tuning the cavity length. The optimum value of the beat frequency is determined from the following factors; detector band width (3dB bandwidth is 2 kHz to 3 MHz), fringe counting electronics to separate each laser beat frequency and laser tunability. So far single mode beat frequency is achieved up to  $\sim 2$  MHz without large reduction of laser oscillation power. The interference signals detected are separated electronically at different frequencies, and then introduced into phase comparators for phase measurement.

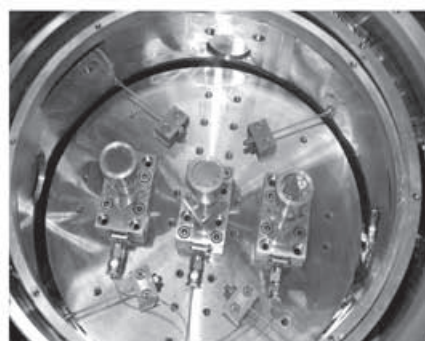


Fig.1. A bottom looking photograph of the cooled detector system which contains three unstressed gallium-doped germanium photoconductors with a focusing Winston cone.

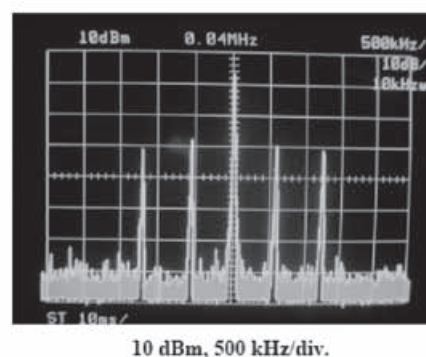


Fig.2. Two color beat signals detected by the gallium-doped germanium photoconductor. The spectrum analyzer trace shows two color beat signals corresponding to a 57.2  $\mu\text{m}$  beat of 0.55 MHz and a 47.6  $\mu\text{m}$  beat of 1.2 MHz.

### 3. References

- [1] S. Okajima, K. Nakayama, H. Tazawa, K. Kawahata, et al., Rev. Sci. Instrum. **72**, 1 (2001) 1094.
- [2] K. Nakayama, H. Tazawa, S. Okajima, K. Kawahata, K. Tanaka, et al., Rev. Sci. Instrum. **75**, 2 (2004) 329.
- [3] K. Kawahata, K. Tanaka, T. Tokuzawa et al., Rev. Sci. Instrum. **75**, 10 (2004) 3508.

## §17. Design of the Diverter Interferometer Combined with ECA Measurement on LHD

Akiyama, T., Kawahata, K., Tokuzawa, T. (NIFS)

Transmitted transport, which increases wall recycling and make density control difficult is commonly observed in tokamaks and linear machines [1]. “Blobs” are thought to induce such the transport. In the case of LHD, the  $H\alpha$  intensity is strong around X-points in regions that are far from the vacuum chamber wall. This observation suggests that blobs go to the diverter due to short magnetic field lines. In addition, L-H transitions, which change the particle and heat flux, and Serpens modes, in which radiation belts rotate in the edge region, are observed in LHD and the dynamic change in particle flux to the diverter is expected. Accordingly measurement of the electron density and the temperature in diverter legs will be useful information on the transport.

Since the maximum electron temperature in diverter legs is about 50 eV, usual Langmuir probes cannot be used. Although the reciprocating probe has provided data of ion saturation currents around the diverter leg, the temporal resolution is not enough for the measurement of the transmitted transports (a time constant of 10  $\mu$ m in DIII-D). Large heating power limits the use of even the reciprocating probe because of large heat load. Accordingly, a millimeter wave interferometer for electron density measures in a diverter plasma is designed. The electron density is planned to be measured with the use of electron cyclotron absorption (ECA) combined with the interferometer. The absorption of the second harmonic X-mode depends on the plasma pressure as follows.

$$P_{out}/P_{in} = 1 - \exp(-t/\tau)$$

$$\tau \propto n_e T_e$$

$P_{in}$  and  $P_{out}$  are power of an incident and returned waves, respectively, and  $\tau$  is the optical depth. Hence the plasma pressure and then the electron temperature can be estimated from ratio of the power.

The measured position is at the middle point between the X-point and diverter plates as shown in Fig.1. Since the magnetic field strength at the measurement point is 1.3 T ( $B_{ax}=2.75$  T), the frequency of the probe wave is decided to be 75 GHz for ECA measurement. Supposing an electron density of  $1 \times 10^{19} \text{ m}^{-3}$  and a width of the diverter leg of 2 cm, the expected phase shifts as a function of the frequency is shown in Fig.2. The phase shifts of 75 GHz are 400 and 500 deg. for O- and X-mode, respectively, while phase resolution of a phase counter made in NIFS is 3.6 deg. [2]. From the viewpoint of signal to noise ratio of the interferometer, the probe wave with a frequency of 75

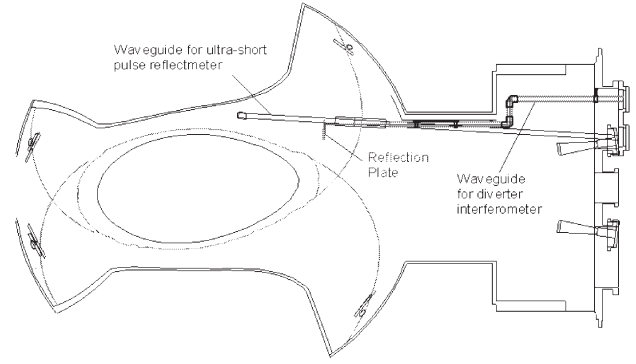


Fig.1: Design of the waveguide for the diverter interferometer installed in LHD (3-O port).

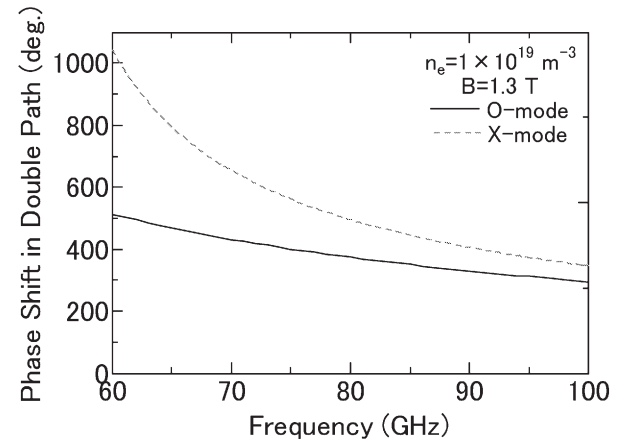


Fig.2: Phase shift of O- and X-mode probe beam passing through the diverter leg (in the double path).

GHz is also preferable. Circular waveguides are planned to be installed in 3-O port. The magnetic field line is tilted at the measurement position; the polarization of the probe wave has to be adjusted the direction. Since the circular waveguide is insensitive to the polarization, it makes the design more flexible. The waveguide is made of aluminum and the inner diameter is 25 mm. That is an oversized waveguide for low attenuation. The reflection plate is fixed at the waveguide for the ultra-short pulse reflectometer. The particle flux to the outboard diverter legs in horizontally elongated cross sections is smaller than that to inboard legs [3]. However, it is easier to access than inboard side and preferable as the first trial of the measurement of the diverter leg.

As shown in Fig.1, the waveguide has to bend eight times and transmission loss at bends is expected. The transmission test will start in the Diagnostic lab.

### Reference

- 1) T. Ohno, J. Plasma Fusion Res. **80** (2004) 212.
- 2) Y. Itoh *et. al.*, Fusion Engineering and Design **56-57** (2001) 965.
- 3) S. Masuzaki *et. al.*, Nucl. Fusion **42** (2002) 750.



## §18. Bench Testing of New Polarimeter with Use of Si Photo Elastic Modulator for 57 & 48 $\mu\text{m}$ Laser

Akiyama, T., Kawahata, K. (NIFS),  
Okajima, S., Nakayama, K. (Chubu Univ.),  
Oakberg, T. (HINDS Ltd.)

As the electron density in LHD is getting higher, a reliable electron density measurement is indispensable. A  $\text{CH}_3\text{OD}$  laser (57 and 48  $\mu\text{m}$ ) has been developed [1, 2] because a beam bending effect ( $\propto \lambda^2$ ) in a plasma, which causes fringe jump errors, is small due to the short wavelength and is suitable for the laser source of an interferometer in LHD. On the other hand, a  $t$  profile can be evaluated by polarimetry. The importance of measurement of the  $t$  profile is increasing since a position of a rational surface seems to be correlated with confinement improvement mode. Therefore we are designing an interferometer combined with a polarimeter with the use of the  $\text{CH}_3\text{OD}$  laser conceptually now. This system can also be adapted to the poloidal polarimeter in ITER.

From the viewpoint of maintenance and compatibility with the present interferometer system, a measurement method with the use of two photo elastic modulators (PEMs) is appropriate for polarimetry. PEM modulates the polarization of an incident beam periodically by stressing the photoelastic material and then arising time-varying birefringence.

Since there was no PEM for the FIR range so far, the new PEM shown in Fig.1 was developed. It adopts a Si plate with the high resistivity (several  $\text{k}\Omega/\text{m}$ ), which has high transmissivity in the FIR region, as the photoelastic material. The measured maximum transmissivity is 60% for both 57 and 48  $\mu\text{m}$ . However, multi-reflection inside the Si plate is found to be significant due to high refractivity of Si ( $N=4.2$ ).

Because this is the first PEM for the FIR region, a calibration of the optical retardation had not been done. Figure 2 shows the optical arrangement for the calibration and the initial trial of the polarimeter with one PEM. The detector output  $I$  is as follows.

$$I = \frac{I_0}{2} \{1 + J_0(\rho_0) + 2J_2(\rho_0)\cos(2\omega_m t) + 2J_4(\rho_0)\cos(4\omega_m t) + \dots\}$$

$J_k$  : Bessel function,  $\rho_0$  : Maximum of retardation,

$\omega_m$  : Drive frequency

From the ratio of DC and the second harmonics of the drive frequency  $I(2\omega_m)/I(\text{DC}) = 2J_2(\rho_0)/\{1 + J_0(\rho_0)\}$ , the maximum retardation can be evaluated. The measured optical retardation is confirmed to be more than  $\lambda/4$  for both wavelengths, which is enough for polarimetry.

Putting a rotatable polarizer in front of the PEM, a test of the polarimeter is performed. Figure 3 shows the

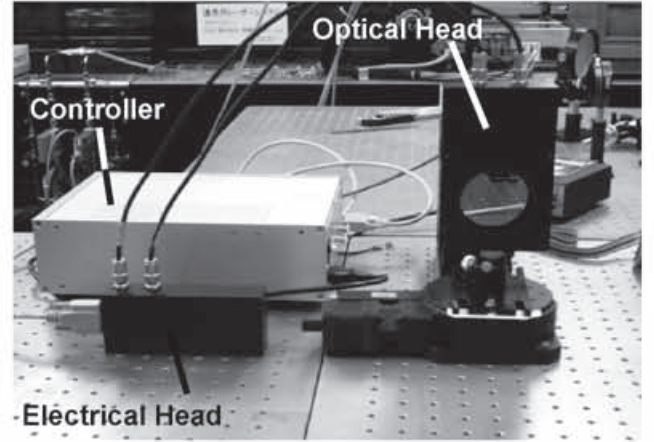


Fig. 1: Photograph of the Si PEM. It consists of the controller, the electrical and the optical head.

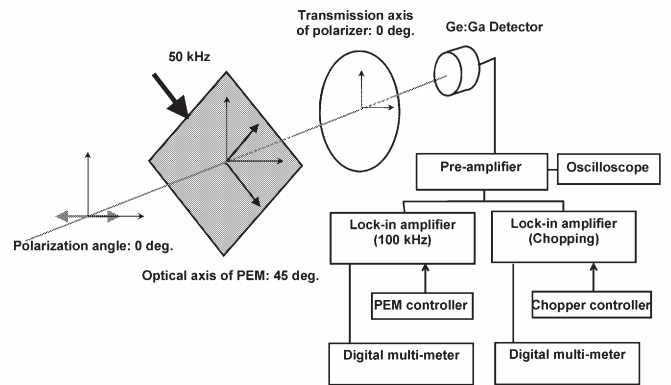


Fig.2: Optical arrangement for the retardation calibration and polarimeter.

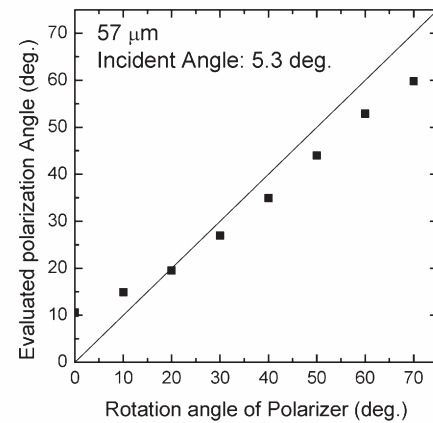


Fig.3: Measured polarization angle with Si PEM polarimeter

measurement result. Although the deviation in a small rotation angle is large, the trend seems right. The reason of the deviation is speculated to be caused by additional modulation components due to the multi-reflection. This will be improved by an AR-coating of the Si plate.

### Reference

- 1) K. Kawahata et. al., Rev. Sci. Instrum **70** (1999) 707.
- 2) S. Okajima et. al., Rev. Sci. Instrum **72** (2001) 1094.



# §19. Development of the Interface to the Magnetic Force Line and Magnetic Surface Visualization Program

Emoto, M., Watanabe, T., Yoshida, M., Nagayama, Y. (National Institute for Fusion Science)

The Magnetic Surface Visualization Program has been developed by Watanabe. This program enables users to investigate the interference between devices installed in the LHD vacuum vessel and magnetic surfaces. This program was written by Fortran 90 and it runs in the calculation servers hosted by Kaiseki Group. The specifications of the calculation servers are listed in table.1. In these calculation servers, necessary applications to handle LHD experimental data and Data Visualization tools are installed in advance, and the visitors can begin to view and analyze the experimental data soon after their arrival at NIFS.

The execution time of this program is shown in Table.1. Calculation time increases as the number of grids increases, and it takes about 1.5 hours on the condition that the number of grids is 500. Therefore, the user has to wait more than one hour if he wants to obtain enough accuracy. Until the calculation ends, the user has to wait without closing their network session to the calculation servers. Furthermore, during the calculation, the program consumes CPU power, and it affects other users in the computers.

To improve the situation, the authors have developed a new interface to run this program. The new system is a batch based system. The system accepts requests from the users. If the server cannot allocate enough CPU resource, the request is in queue until the resource is available. When the calculation is done, the system notifies the user that the job is finished. Therefore, it can minimize the influences to the other users and it can use CPU resource more efficiently. Furthermore, the user doesn't need to watch his program running during the calculation. In addition, this system is scalable; even if the number of users increases in the future, it is easy to meet the demand by adding calculation servers.

The Figure 2 shows the overview of this system. The jobs are managed by PBS (Portable Batch System)<sup>1)</sup>. The PBS is a flexible batch system developed for NASA. It can use various computers in the same way. PBS consists of three main components; PBS server, scheduler, and pbs mom or, a execution server. The PBS server accepts user requests, and the scheduler manages the job and asks pbs mom to do the job. These components are loosely linked, and they can be replaced with other components. For example, the scheduler can be replaced with another to fit their computer environments. The author adopted TORQUE<sup>2)</sup> as the main PBS system and MAUI<sup>3)</sup> as the scheduler. Input parameters are given by the web server, and the user submits the job request to the PBS server by Web browsers (Fig.2). The PBS servers ask one of the two execution servers to do this job. When the calculation finishes, the execution server stores the data into the file sever, and notifies the user that the program finished by e-mail. The results are saved as PostScript file or PNG file into the file server.

CPU	Opteron 280 x 2 (4way)
OS	Fedora Core 4 (x86_64)
Memory	8GB
HDD	1.5TB

Table 1. Specification of Calculation Server

Number of Grids in the radius direction	Total Execution Time (sec)
50	1329
100	1802
250	3264
500	5684

Table 2. Calculation Time

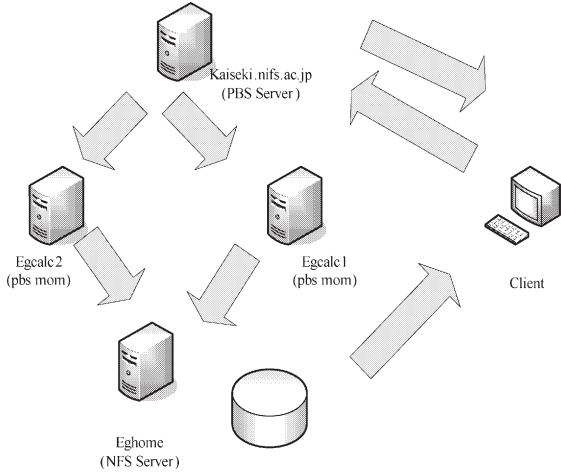


Fig1. System Overview

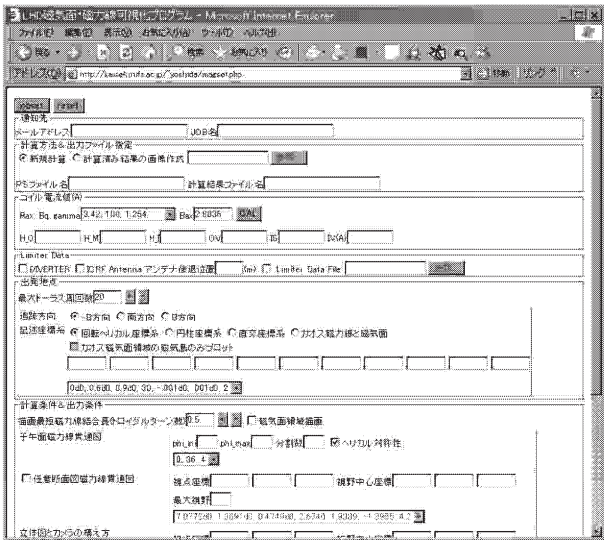


Fig 2. Parameter Setting Window

Reference

- 1) <http://pbs.mrj.com>
- 2) <http://www.clusterresources.com/pages/products/torque-resource-manager.php>
- 3) <http://www.clusterresources.com/pages/products/maui-cluster-scheduler.php>

## §20. The Next-Generation Technology of Data Acquisition and Analysis Environment for Fusion Experiments

Okumura, H. (Mie Univ.),  
Nakanishi, H.

LHD diagnostic information system is always expected to take the head of research and development in fusion experiments of the world, and even in such the ITER-BA remote experiment center and All-Japan ST research project. In 2006 LHD renewed the world record of acquired data amount with 90 GB/shot again <sup>1)</sup>, however, the tendency of substantial data increase is quite common in these several years. As this problem becomes quite remarkable in large scale experiments, innovative data processing technology is urgently needed to be fit for practical use. It would be indispensable to attain above-mentioned concrete goals.

Here, research subjects which are considered to be quite urgent;

1. Handling of huge data and massive-sized database <sup>2)</sup>
2. Application technology of long fat network (LFN)
3. Remote experimental environment (framework)

were intensively examined in this study. Their output will be applied and verified in LHD experiment. We aim to establish the next-generation technology to advance the remote collaboration experiments.

### DAQ Workshop for Fusion Experiments

From February 28<sup>th</sup> to March 1<sup>st</sup> 2006, the DAQ (data acquisition) workshop was held in NIFS (Table I). It had four sessions within two days, and thirteen oral speakers gave presentations about new technology for DAQ and remote participation (RP), in addition to the upcoming related conference, i.e. IAEA-TM.

In this workshop, positive arguments were done about more intensive use of CPU and storage resources and the introduction of Grid computing technology for the sake of reducing the management burden of the drastically growing experimental data. Problems in long-distance Internet data transfer and its solution have been also discussed. Thus we could effectively explore some possible directions for our future research and development.

Especially, the joint development between the fusion experimental data system and ITBL (IT-based laboratory), which is a Japanese Grid technology, was deeply discussed. To link the LHD and JT-60 DAQs with the new ITBL network middleware has been chosen as the first task there. We could also obtain the opportunity to start cooperation relationship to contribute to All-Japan ST research project.

To support collaborators' communication and document sharing, the necessity of having a "collaboration groupware" tool has been pointed out. Therefore, a new Wiki page, named as "DAQ Wiki", has been opened at

<http://oku.edu.mie-u.ac.jp/daq/>

to make the collaboration-related information sharable.

Another big fruit of this study is that we examined the most effective algorithm for loss-less image archives to finally find the JPEG-LS method is the best in both the processing speed and the compression ratio. Compared with "zlib" single-block compression, it can deflate/inflate image data frame by frame to archive/retrieve one by one. It is more convenient for normal client PCs to retrieve image data by frame, because they do not have enough memory to process a full-length movie.

The output of these collaborating works would become applicable to LHD experiment and newer fusion projects.

### References

- 1)Nakanishi, H. et al.: J. Plasma Fusion Res. **82** (2006) 171.
- 2)Nakanishi, H. and Okumura, H.: J. Plasma Fusion Res. **81** (2005) 112.

**Table I** Presentation Program of DAQ Workshop in NIFS

Session I. New Challenges and Recent Topics (Feb. 28 <sup>th</sup> 13:30~15:15)	
Okumura H. (Mie Univ.)	Introduction
Sueoka M. (JAEA)	Database Construction of JT-60 Plasma Image Database and its Web Distribution
Wang F. (Kyushu Univ.)	Plasma Shape Reproduction of Spherical Tokamak by Using CCS Method
Nishihara K. (Osaka Univ.)	DAQ System in ILE Osaka Univ., and Collaborating Simulation Grid Portal for Developing the EUV Light Source
Session II. 6 <sup>th</sup> IAEA TM for Control, Data Acquisition, and Remote Participation for Fusion Research (15:30~16:00)	
Nagayama Y. (NIFS)	Report of 1 <sup>st</sup> Executive Committee Meeting and Request for Further Cooperation
Session III. RP Technology and Broadband Application (16:00~17:30)	
Hasegawa M. (Kyushu Univ.)	DAQ and RP Environment for All-Japan ST Research Project
Emoto M. (NIFS)	File Transfer through SuperSINET
Yamamoto T. (NIFS)	Data Transfer Technology through the Long Fat Network (LFN)
Session IV. Framework for DAQ System (Mar.1 <sup>st</sup> 9:00~12:00)	
Ohsuna M. (NIFS)	Total Package of LHD DAQ System
Okada H. (Kyoto Univ.)	Heliotron-J DAQ and its S-SINET Utilization
Ueshima Y. (JAEA)	Data Management Technique Based on XML
Nakanishi H. (NIFS)	Attempt for Constructing a New DAQ Framework
Suzuki Y. (JAEA)	ITBL Application for Fusion Research Grid

## §21. On the Construction of Databases of Experiment Data

Hochin, T. (Kyoto Institute of Technology),  
Nakanishi, H., Kojima, M.

Experiments of fusion plasma phenomena produce a lot of sequences of time-varying values which form waveforms. If the waveforms similar to a desired one can be obtained by using computer system, the burden of researchers in searching for similar waveforms will be extremely decreased. We have addressed to the issue on this kind of retrieval<sup>1)</sup>. We have recently addressed the subsequence matching, where a query sequence is shorter than the sequences stored in a database. We have proposed a method of searching for subsequences. The proposed method uses a multi-dimensional index and an additional file for quick search<sup>2)</sup>. This paper describes the refinement of this method for increasing retrieval accuracy.

The index is constructed as follows. A waveform is divided into  $m$  segments. Each segment has  $n$  points, where  $n$  is a power of two because Fast Fourier Transformation (FFT) is applied to a segment for obtaining the frequency components. For every segment, the following procedure is applied to. FFT components are obtained for a segment. FFT components are divided into  $k$  segments, which are called *frequency segments*. An average value is calculated for each frequency segment. As FFT components are divided into  $k$  frequency segments,  $k$  average values are obtained. These average values are inserted into a multi-dimensional index as a point in the  $k$  dimensional space. A point has the shot number and the segment number as its attribute values. The shot number is the number distinguishing a waveform from the other ones. The segment number is the serial number put to a segment in a waveform. Moreover, an additional file, which is called the *seek file*, which was previously called the binary file<sup>2)</sup>, is used for the quick retrieval. This file contains the segment information.

Next, the retrieving procedure is described. When a key waveform is given, it is divided into  $m$  segments. FFT is applied to each segment to obtain FFT components, and  $k$  average values of its frequency segments. By using  $k$  average values of the  $i$ th segment of a waveform, where  $i = 1 \cdots m$ , the multi-dimensional index is looked up to obtain the candidate segments in the specified region of multi-dimensional space. Next, the seek file is consulted. The remaining  $m-1$  segments of a waveform are obtained by using the segment found in the above step as the  $i$ th segment. The  $k$  average values are obtained for each segment. The Euclid distance of  $m$  segments is calculated. This Euclid distance is called the *index distance*. After the index distances are calculated for all of the waveforms obtained, those having large index distance are discarded. FFT is applied to the segments of the remaining waveforms, and the spectrum distances are calculated. Finally, the waveforms are sorted according to the order of the spectrum distance.

The proposed retrieval method is evaluated. The 10,000 waveforms obtained through the fusion plasma experiments are used. The waveform originally consists of about 130,000 points of data. A waveform is divided into 256 segments. Each segment has 512 points. There are  $256 * 10,000$  segments in a database. FFT components are divided into 4 frequency segments. The SR-tree is used as the multi-dimensional index structure. As the number of the frequency segments is four, a segment is stored as a point in a four-dimensional space. The key waveform and the waveforms obtained are shown in Fig. 1. This key waveform has 8192 points. It is divided into 16 segments ( $k = 16$ ). In Fig. 1, the second, the fourth, the fifth, and so on are not shown because these are very similar to the third one. The waveforms obtained are similar to the key one.

The retrieval time is measured by varying the number of the candidates. The number of the candidates is changed by using different key waveforms. Every waveform has 16 segments. In this case, it takes 16 hours to create the index, and creating the seek file takes 20 minutes. The result is shown in Fig. 2. The index look-up time, the seek file access time, and the calculating spectrum time as well as the total time are shown. When the number of candidates is large, the time of calculating spectrum distance is dominant. On the other hand, the index look-up time and the seek file access time are even. Decreasing the number of candidates seems to be effective for the performance of retrieval.

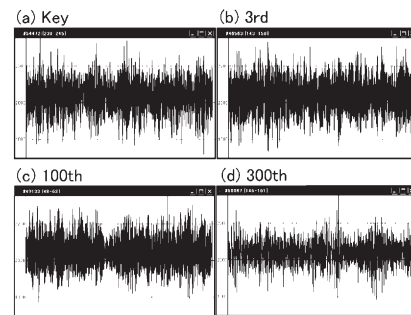


Fig. 1. Key and retrieved waveforms.

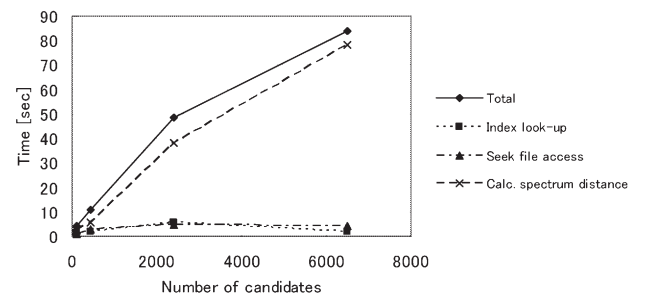


Fig. 2. Result of performance evaluation.

### Reference

- 1) Nakanishi, H., Hochin, T., Kojima, M., LABCOM group : Search and retrieval method of similar plasma waveforms, Fusion Engineering and Design, Vol. 71, pp. 189-193 (2004).
- 2) Hochin, T., Nakanishi H. and Kojima M.: On the Construction of Databases of Experiment Data, Ann. Rep. NIFS (2005).



§22. Framework Remodeling of LABCOM Data Acquisition System for the Next-Generation “LABCOM/X” Project

Nakanishi, H., Ohsuna, M., Kojima, M., Nonomura, M., Kuroda, N., Imazu, S. (Pretech Corp.), LABCOM Group

The LABCOM data acquisition system (DAQ) has been operated for the LHD plasma diagnostics for nine years. It has set up a new world record of acquired data amount of 90 GB/shot in 2005-2006 campaign (Fig. 1). Its ultrawide-band DAQ based on the CompactPCI digitizers has enabled about 80 MB/s real-time data acquisition for each plasma measurement<sup>1)</sup>. Actually proved 80 MB/s bandwidth could easily satisfy the requirement for the advanced, large-scale fusion experiments, such as LHD and ITER. The basic performance of our DAQ unit has enough capability, but the subsidiary tools are not fully developed<sup>2)</sup>.

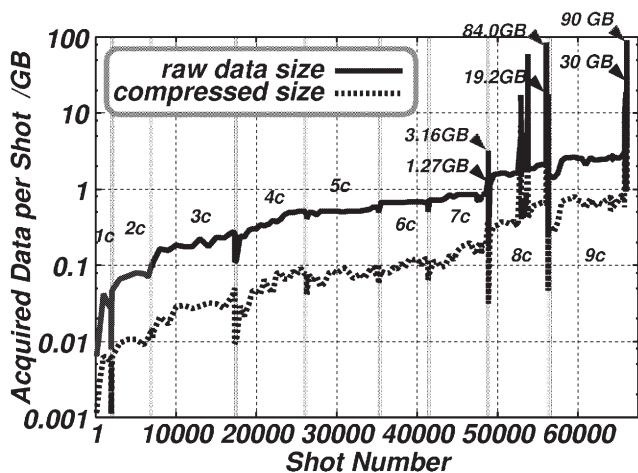


Fig. 1. Growth of shot-by-shot acquisition data amount in LABCOM system: At the end of 9<sup>th</sup> campaign, we had 170 shot/day, and produced about 3.0 GB/shot.

“DAQ Box” Development

LHD already had over sixty DAQs in the 9<sup>th</sup> campaign, and its increase has made the operational and maintaining burden quite heavy. The data migration procedures between multi-tier distributed storages also need much closer attention. Therefore, “more distributed acquisition and centralized operations” would be indispensable to cope with both high-efficiency I/O throughputs and much enlarged data volume. In this study, DAQ front-end that consists of some digitizer chassis and an acquisition computer has been entirely re-designed to realize a low-cost and maintenance-free “DAQ Box” for fusion plasma measurements.

To satisfy those necessary conditions, Linux OS and its free drivers for digitizers, such as CAMAC and CompactPCI, have been adopted. Network-bootable diskless computers are desirable for reducing the possibility of hardware troubles in the bad noise environment. To wire it

adjacently to the digitizer controller could get rid of the cost for electrically isolating uplinks. Our inspection revealed that SCSI-USB2.0 conversion cables are the most promising in both transferring speed and the cost to replace the former SCSI optical extenders (Fig. 2).

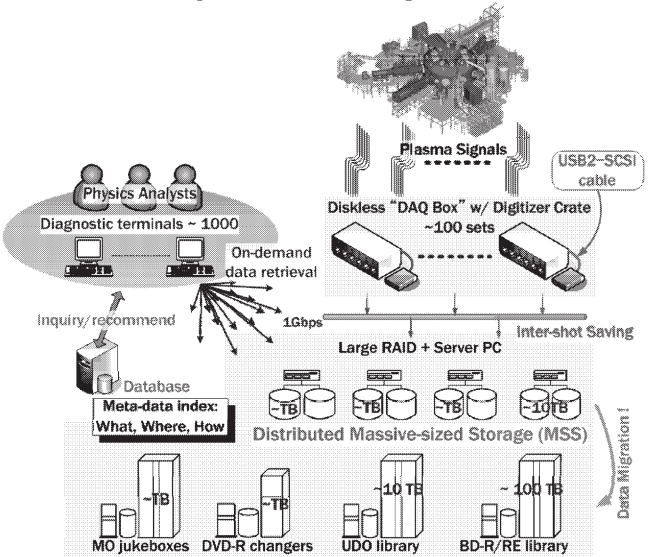


Fig. 2. Revised diagram of LABCOM DAQ and multi-tier storage system: As the 1<sup>st</sup> layer “DAQ Box” keeps raw data only on its volatile memory, they must be saved to RAID just after the acquisition is finished.

It also means that the first-tier data storage becomes extinct, and thus could reduce the migration cost and time.

Development of New FPGA-based Timing Demodulator

For replacing the costly VME-based timing demodulator, we have newly developed its FPGA version. It adopts the embedded device “Suzaku” that combines the Spartan-3E FPGA and MicroBraz Linux software processor. Original logics have been newly rewritten by VHDL and C (ONC RPC on Linux). Its cost is almost one-tenth of the previous VME one.

Multi-site Abstraction and DAQ Logical Extension

Another functional extension is to cope with multiple sites and experiments, in which remote participation mechanisms and utilities would be essential. The introduction of so-called “DataGrid” technology, which will be provided by the specific middleware such as Globus toolkit or ITBL (IT-based laboratory), seems to be a shorter way for revising the LABCOM data system.

This conceptual re-design for the DAQ framework would provide universal data accessing environments logically. Simultaneously, users could obtain the proper access controlling functionality for data and system security. For advancing necessary R&D, we have some discussion with JAEA (JT-60) and All-Japan ST research groups.

References

- 1)Nakanishi, H. et al.: J. Plasma Fusion Res. **82** (2006) 171.
- 2)Nakanishi, H. and Okumura, H.: J. Plasma Fusion Res. **81** (2005) 112.



## §23. Higher Harmonic Electron Cyclotron Emission Diagnostics

Idei, H. (Kyushu Univ.), Inagaki, S., Wataya, Y. (Kyushu Univ.), Shimozuma, T., Nagayama, Y., Kawahata, K.

Electron cyclotron emission (ECE) measurement has been a main diagnostic to measure the temporal behavior of electron temperature profiles in plasmas. The second harmonic ECE is widely used for the electron temperature diagnostics. The higher harmonic components are important to diagnose the non-thermal energetic-electron distributions in plasmas. In the LHD experiment, the second harmonic component is measured using heterodyne radiometers with high time and spatial resolutions, while the higher harmonic components are measured using a Michelson spectrometer. A double-side-band high frequency ( $\sim 300$ GHz) radiometer system has been developed to measure the higher harmonic components. In order to measure the ECE signal with high time resolution, a local oscillator with a fast frequency-switching synthesizer was prepared. The frequency-switching time was 5  $\mu$ s for the 288 MHz step in the high frequency range. The radiometer has much higher time and frequency resolutions than those of the Michelson spectrometer.

In the setup of the high frequency radiometer to the LHD, a quasi-optical system to couple the emission transmitted by the corrugated waveguide into a receiver horn antenna was designed. Figure 1 shows beam intensity profiles from the horn antenna along the beam. The  $x$  axis is in perpendicular to the propagating  $z$  axis. The operation frequency was 318GHz. The waist size and position were derived from the beam-size evolution along the propagation direction using Gaussian optics, and thus, a quasi-optical mirror was designed for the coupling between the waveguide and the antenna using the obtained Gaussian parameters. In the LHD, a vacuum quartz-window with a thickness of 12 mm was used at the viewing port. The transmission at the window was tested in the high frequency range of 291-320GHz. Figure 2 shows frequency dependencies of the measured and calculated transmission rates. The measured rate has a sinusoidal dependence with a period of about 6GHz as calculated, but is deformed with some aberrations. The detector was set across the window from the millimeter launcher. The measured transmission rate was affected by the reflection and scattering at the window as resulted in the interference. The transmission rate will be measured in the quasi-optical transmission to reduce the reflection and scattering effects

in the measurement, again.

The sensitivity of the radiometer system, including the waveguide and quasi-optical transmissions, and the window, will be calibrated using a high temperature ( $\sim 800$ K) calibration source. The frequency dependence of the sensitivity can be checked from the signals modulated by the frequency switching. This fast frequency-switching radiometer system will be applied to the higher harmonic ECE diagnostics for the LHD experiments.

This work was realized by the collaboration organized by NIFS (NIFS05KCHP006). This work was supported by a Grant-in-Aid for Scientific Research from Ministry of Education, Science and Culture of Japan.

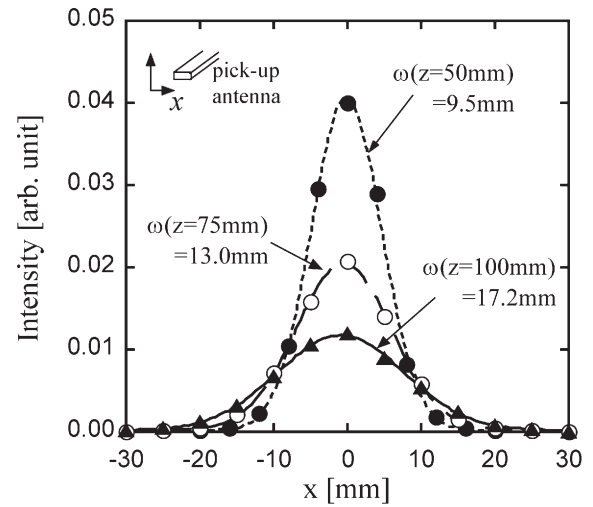


Fig. 1. Beam intensity profiles from the horn antenna along the propagation.

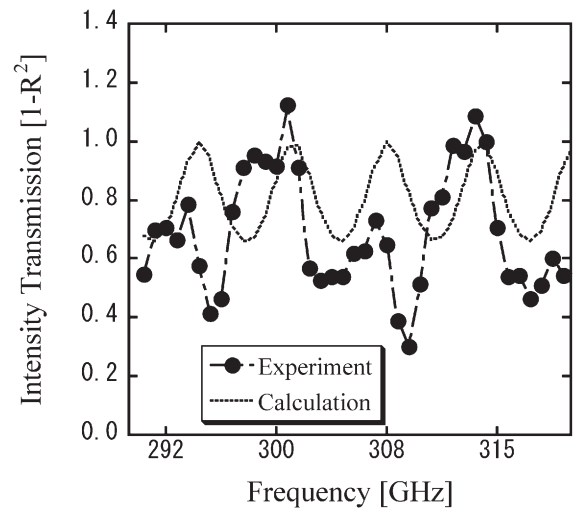


Fig.2. Frequency dependencies of measured and calculated transmission rates at a vacuum quartz-window with a thickness of 12 mm.

## §24. Measurement of Soft X-Ray Emission from LHD Plasma

Ishiguro, E., Kawamitsu, S. (University of the Ryukyus), Sato, K.

A grazing incidence monochromator equipped with a laminar grating with the radius of 10 m was completed in 2004 under the joint research project for LHD. The monochromator is designed to cover the wavelength region below 2 nm. We expect that emission lines caused from 2s-3p transitions of H-like(Fe XXVI) and He-like(Fe XXV) ions of Fe could be observed at 0.963 nm and 1.018nm, respectively, from LHD plasma by using the monochromator. Furthermore, it is important to observe a spatial distribution of 1.502 nm line of Ne-like(Fe XVIII) ion which has a closed shell structure with a high ionization potential. This observation makes the determination of the transportation coefficient possible with a high precision, independent of such atomic processes such as ionization and recombination.

In addition, there are many lines due to the 2l-3l transitions from Li-like ion of Fe to F-like ion in the 0.7-2 nm region, the intensities of which are strongly depend on the electron temperature. The observation of these lines is expected to provide basic data on energy transportation from the core plasma to the surrounding.

In 2005, the monochromator was attached to the LHD chamber through a differential pumping system. Measurements on LHD plasma were carried out in 2006. The monochromator has a large f-number of 143, which seems to suggest that the observed spectra may have a poor S/N ratio. However, we succeeded in observing spectra with a good S/N ratio, as seen in Fig.1. We consider that this is probably due to a reduction of the scattered component of the zero-order light, which is diffracted by using a SiO<sub>2</sub> holographic ion-beam etched laminar grating with a small surface roughness in the nanometer order. (The grating has the groove density of 1600 gr/mm, effective area of 76 × 76 mm<sup>2</sup> and groove depth of 6 nm, and is coated with Au of the

thickness 20 nm.)

In Fig.1, the 2p-3d transitions of Ne-like ion of Fe at 1.501 nm and 1.526 nm, and Fe-like ion at 1.563 nm are a tentatively assigned to the observed spectrum. The spectral lines in Fig.1 have a inclination with respect to the perpendicular, and those in the short wavelength side have a broad width. The distortions may be due to insufficient adjustment of the position of the MCP and CCD camera. We will complete the optical adjustment of the monochromator this year by using LHD in the operation mode of long duration discharge.

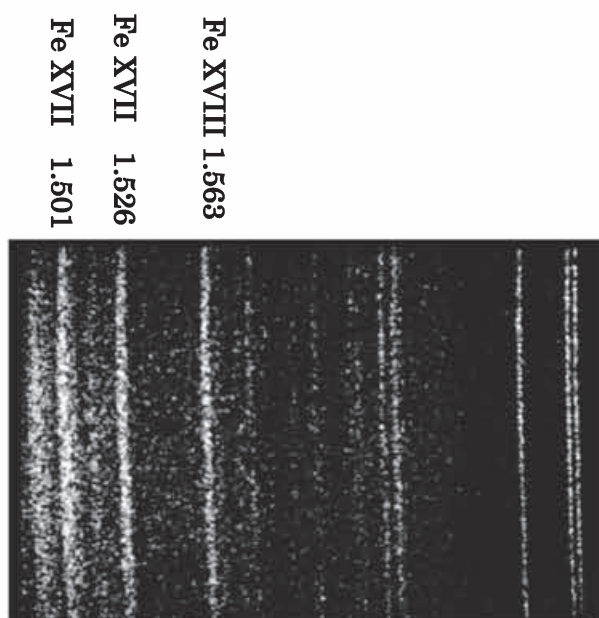


Fig.1. Example of a Soft X-ray spectrum of the LHD plasma. The exposure time was 4 sec.

§25. Study of High-Performance Array  
Antennas for Millimeter-Wave Imaging  
Array

Kogi, Y., Mase, A., Ignatenko, M., Kudo, K. (ASTEC  
Kyushu Univ.),  
Nagayama, Y., Kawahata, K.

It is considered to be one of the major issues to clarify the behavior of various instabilities and relations between instabilities and plasma confinement. ECE imaging (ECEI) is a promising method to measure electron-temperature profile and its fluctuations precisely. An ECEI system is composed of a detector array, quasi-optical system, and IF system. Each subsystem plays following roles. The optical system is composed of optical mirrors and dielectric lens. These optics are utilized to focus ECE from plasma on the detector array within the specific bandwidth. In the present plan of the beginning experiment, we will collect the fundamental component of ECE with frequency range from 70 to 76 GHz. The ECE is then received by the detector array, and is frequency-converted to IF signal by means of LO wave. In the IF system, signal is then fed to power dividers and bandpass filters to resolve radial temperature distribution, since the frequency of ECE is proportional to magnetic field strength. While poloidal and toroidal temperature distribution is obtained by 2D array of the detector. We have studied and improved design of the detector to be suitable for ECEI measurement. In this report, we will describe prototype design of ECEI system and application to LHD plasma.

Figure 1 shows the prototype 3ch ECE detector array. The LO wave and the ECE wave are received in the antenna region indicated in fig. 1. The antenna corresponding to 1 detector channel is composed of 4 patch antennas for conditioning radiation pattern of the antenna. The detected LO and ECE waves are mixed in a Schottoky barrier diode denoted by "mixer" in fig. 1. The IF signal is then fed to a HBT amplifier, which has bandwidth of DC - 6 GHz and gain of 12 - 18 dB. The amplified signal is then fed to IF system as shown in figure 2.

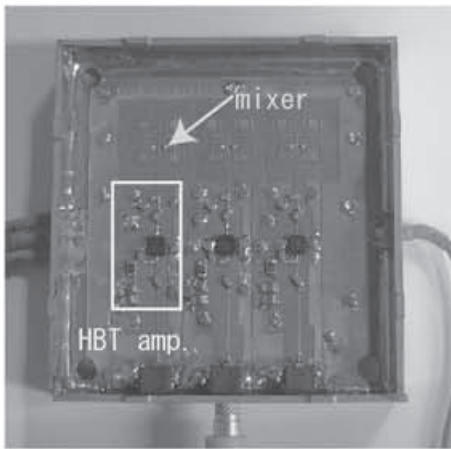


Fig. 1 Prototype 3ch detector array

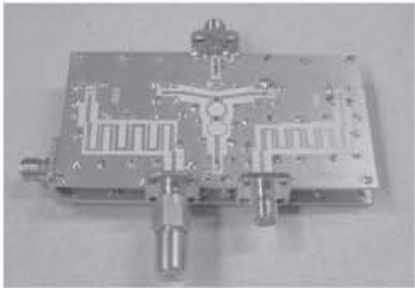


Fig. 2 IF system corresponding to 1 detector channel

The IF signal is amplified again by the same type 2-stage HBT amplifiers and divided by Wilkinson power divider into 4 channels. Each divided signal is fed to band-pass filter whose band centers are 2.5, 3.5, 4.5, and 5.5GHz. The bandwidth of each filter is 1GHz. The filtered signals are detected by video detectors of commercial components. Finally these signals are digitized by ADCs.

We have installed the ECE system at 4-O port, and performed preliminary experiment in order to confirm applicability of our system. Figure 3 shows observed detector signal. Red, blue, yellow, and black curve indicate bandpass frequencies of 2.5, 3.5, 4.5, and 5.5GHz, respectively. We have confirmed that these signals are proportional to the electron temperature. We consider that signal amplitude difference in each channel is due to the gain and NF property of the HBT amplifiers, and antenna performance.

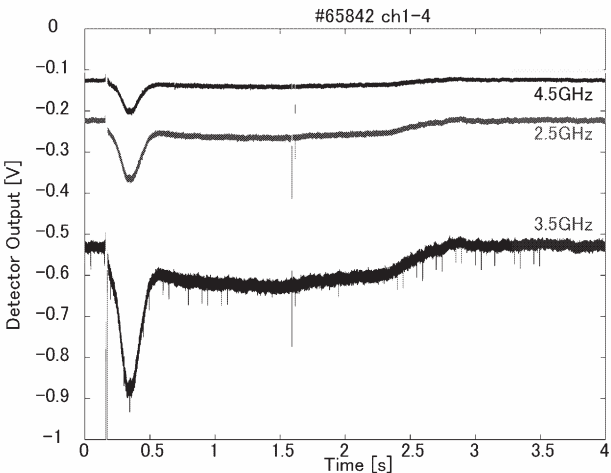


Fig. 3 Detector output

This deterioration of S/N ratio will be fixed by increment of the transmission at the diagnostic window by cleaning of adhesive object onto the window surface in the next experimental campaign.

## §26. Poloidal Polarimetry for ITER

Pavlichenko, R., Kawahata, K.

Control of the current density profile becomes a paramount issue for the modern tokamak experiments. The polarimeter under study is based on the system that was originally proposed for ITER-98, ITER-FEAT designs<sup>1-3)</sup>. The modified system featured a fan of chords viewing the plasma through an equatorial port. The updated system will be operating at a wavelength of 48 or 57  $\mu\text{m}$  (instead of originally proposed 118  $\mu\text{m}$ ). This allow to increase the maximum number of chords via the equatorial port up to 12, which was limited to 9 (see Fig. 1), viewing the plasma via penetration through the blanket modules. For the best optimization of the plasma coverage up to six chords in vertical direction via an upper plug are proposed. The beams are reflected back along the same path through the plasma by means of 38 mm wide circular shaped retroreflectors indented about 25 cm deep at the bottom of remote handling grips in the blanket modules opposing the ports. The base issue for the optical system design is the retroreflectors fault tolerance in respect to vignetting. This brings of the optical system starting point to comply the diameter limit of the retroreflectors with the well known formula:  $D_{\min.} > 2.2d$ , where  $d$  the  $1/e$  width of the laser Gaussian beam intensity distribution. This corresponds to a ~99% transmission (reflection) by (through) the optical system. The basis of the method is the change of the polarization of electromagnetic wave passing magnetized plasma. The state of polarization can be described by the Stokes vector  $s(z)$ <sup>1)</sup>. The evolution along the line of sight ( $z$  direction) is given by  $d\vec{s}(z)/dz = \vec{\Omega}(z) \times \vec{s}(z)$ , where

$\vec{\Omega}(z)$  is the vector describes the plasma wave interaction

$$\begin{pmatrix} \Omega_1 \\ \Omega_2 \\ \Omega_3 \end{pmatrix} = \frac{\omega_p^2}{2c\omega} \begin{pmatrix} e^2/m^2(B_x^2 - B_y^2) \\ e^2/m^2(2B_x B_y) \\ e/m(2\omega B_z) \end{pmatrix}$$

The calculations of the *rotation angle* (related to the Faraday effect  $\Omega_3$ ) and the *ellipticity* (related to the Cotton-Mouton effect  $\Omega_1, \Omega_2$ ) were done for ‘thin plasma layer’ approximation. The plasma was divided into 1cm slabs. For each layer the transformation matrices were derived. Then obtained matrices were applied these the electric field vector of the beams. Refraction in the plasma due to density gradients was excluded at the present time. Here we will only present as example the calculations for a fan of beams through the equatorial port and for the flat density profile. The calculated values of the Faraday rotation angle are in the range of  $\pm 30^\circ$  (see Fig. 2) and can be easily measured with high accuracy. Similar conclusions can be made for the upper chord and for the other plasma scenarios.

The data from the horizontal polarimeter fan give a substantial improvement of the  $q$ -profile determination in the plasma center. Including the chords via the upper port gives a further, but smaller, improvement.

### References

- 1) DeMarco F., Segre S. E. : Plasma Phys. 14 (1972) 245.
- 2) A. J. H. Donné, A. J. H. et al. : Rev. Sci. Instrum. 70 (1999) 726.
- 3) A. J. H. Donné, A. J. H. et al. : Rev. Sci. Instrum. 75 (2004) 4694.

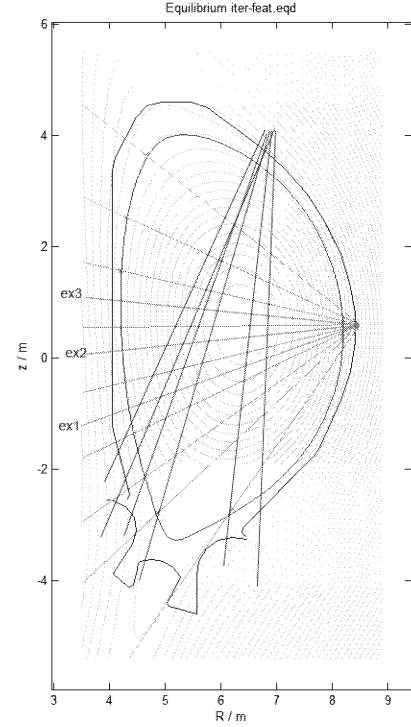


Fig.1. Schematic layout of the polarimeter chords in the poloidal cross-section of ITER; ex1, ex2, ex3 – are three additional chords.

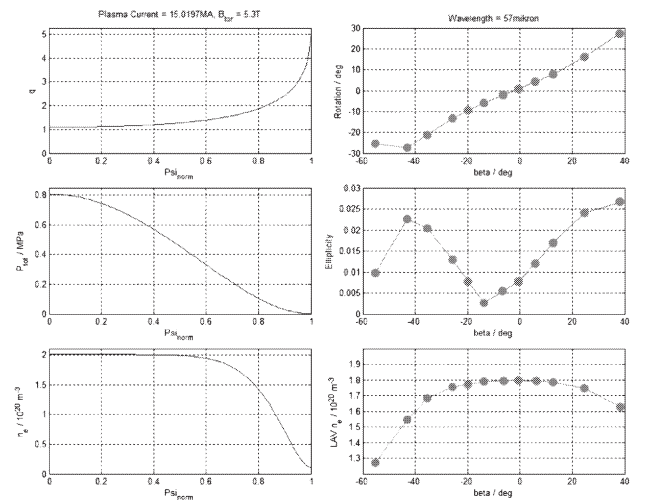


Fig.2. Calculated Faraday rotation angles for a horizontal fan of chords (right top) and the corresponding ellipticity values (right center).



§27. Research and Development of an  
Extremely Compact Fusion Neutron  
Source by Spherically Converging Ion  
Beams

Yoshikawa, K., Masuda, K., Yamamoto, Y., Toku, H.,  
Takamatsu, T. (Inst. Advanced Energy, Kyoto Univ.),  
(Graduate School of Energy Science, Kyoto Univ.),  
Sudo, S., Tomita, Y.

An inertial electrostatic confinement (IEC) fusion neutron source is a device injecting ions towards the spherical center through a transparent hollow cathode (see Fig. 1), trapping them in the electrostatic self-field and making fusion reactions in the dense core. The present IEC devices utilize the dc glow discharge to produce ions in an extremely simple configuration, and steady-state D-D neutron production rates (NPR) of  $10^7 - 10^8 \text{ sec}^{-1}$  have been obtained at several institutions. This makes the glow-driven IEC suitable for some applications though enhanced neutron yields is desired to extend their application.

However, low fusion efficiencies of the glow discharge based IEC, typically in the range of  $Q \sim 10^{-8}$ , greatly limits the use of IEC. The main causes for this low fusion efficiency are the rapid loss of ion beam energy by charge exchange collisions with background neutrals and fractional ion energies inherent in glow discharge. In order to sustain the glow discharge, the operating gas pressure of  $\sim 1 \text{ Pa}$  is typically needed. Thus a reduced operating gas pressure could enhance the efficiency on one hand, while on the other hand a higher pressure could result in higher neutron yield since the beam-gas colliding fusion is regarded predominant in the present glow-driven IEC.

Firstly we carried out experiments with different cathode diameters of 50, 58, 65 and 95 mm $\phi$  in an anode of 200 mm $\phi$ . As shown in Fig. 2, pressure multiplied by distance between the electrodes is kept constant as predicted well by numerical simulations, and therefore the ion loss probability through the acceleration is expected independent from the cathode diameter. Thus the neutron yield is found to be enhanced by the larger cathode as seen in Fig. 3, because of the higher target gas pressure.

For further enhancement in the neutron yield, we have developed a magnetron-discharge-based built-in ion source to improve the fusion efficiency of IEC device by reducing the operating pressure [1]. Figure 4 shows comparison

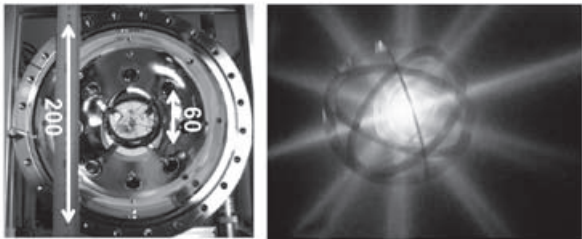


Fig. 1. The hollow cathode at the center of the spherical vacuum chamber as the anode, and an IECF plasma within the hollow cathode.

between the conventional glow-discharge-based IEC (at 1.3 Pa) and the ion source aided IEC, where the operating gas pressure can be controlled independent from the cathode bias voltage. The normalized neutron yield shown in Fig. 4 is the neutron yield divided by the gas pressure and cathode current, which can be used as a figure of merit to compare the IEC operation in different modes since it depends on ion energy and life. In the figure, the normalized neutron yield is seen improved greatly with decreasing pressure. It shows that the ion energy distribution with a lower pressure maintains beam-like characteristics to some extent desired for the efficient fusion generation.

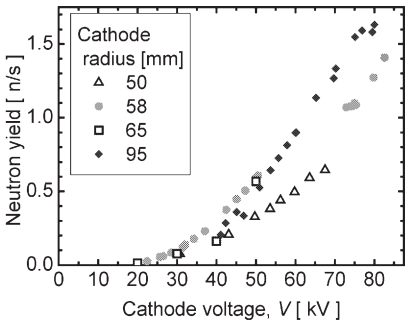


Fig. 2. Neutron yield dependences on cathode bias voltage comparing uses of different cathode diameters

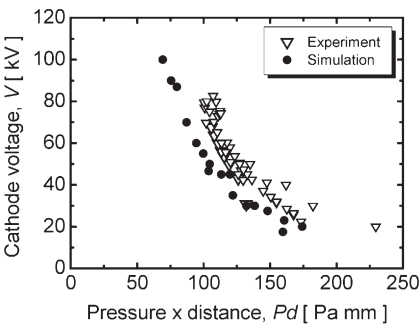


Fig. 3. Pressure – voltage characteristics by experiments and simulations for various cathode diameters ranging from 50 to 95 mm  $\phi$

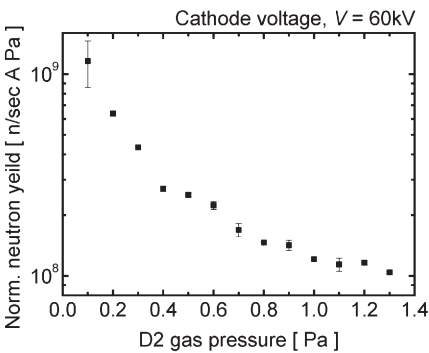


Fig. 4. Normalized neutron yield by magnetron ion source aided IEC as a function of operation gas pressure

References  
1) Yoshikawa, K. et al.: Ann. Rep. NIFS (2004-2005).

## §28. Two Dimensional Ion Temperature and Velocity Measurements by Use of Visible Light Tomography Technique

Ono, Y., Balandin, A.L., Imazawa, R., Kawamori, E., Murata, Y., Itagaki, T., Yamanoue, T., Sato, K., Arimoto, K., Timura, T., Tawara, T. (Univ.Tokyo, High Temperature Plasma Cent. / Dept. Electr. Eng.), Narushima, Y., Nagayama, Y., Yamazaki, K.

For the past five years, we have been developing a new visible-light tomography system for two dimensional (2-D) measurements of ion temperature and velocity. In 2005, we developed, 1) a new reconstruction software for 2-D plasma velocity measurement and 2) a part of optical fiber system and optical lens system for this system. As for (1), we reconstructed the local 2-D plasma velocity profile from the measured line-integrated line spectrum with Doppler shift. The 2-D plasma velocity profile is composed of two components as shown in

$$\mathbf{v} = \nabla \times \psi + \nabla \phi \text{-----}(1),$$

so that we obtain the following Radon transformation form:

$$R\{\xi\}(u, \eta) = - \int_{-\infty}^u \mathbf{v}\{\theta\}(u', \eta) du' \text{-----}(2),$$

based on an assumption that our plasma is incompressible as  $\nabla \cdot \mathbf{v} = 0$ . We solved the equation (2) using the maximum entropy method. Figure 2 shows the 2-D velocity profiles (vectors plot) (a) and the 2-D vorticity  $\psi$  contours (b) for an assumed toroidal velocity profile of low aspect ratio toroid which was peaked at the magnetic axis. Artificially, 10% white noises (n=1 component) were added to the line-integrated signals of line spectrum. Figures 2 indicate that the assumed 2-D velocity profile was reconstructed successfully within the error of 20%. As for (2), we installed the initial set of optical fibers: 9 channels to complete the 1-D velocity measurement system in order to test one section of the 2-D measurement system. Figure 3 shows the measured radial velocity profile of two merging spheromaks with counter helicity. It indicates that the bipolar toroidal velocity by the counter helicity reconnection was reconstructed successfully using our 1-D velocity

measurement system.

### References

- [1] A.Balandin, Y.Ono, J Comp. Phys. 202, (2005), 52.

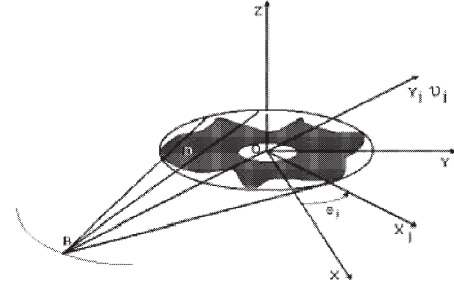


Fig. 1 Ion flow measurement by the vector tomography technology for visible light Doppler spectroscopy.

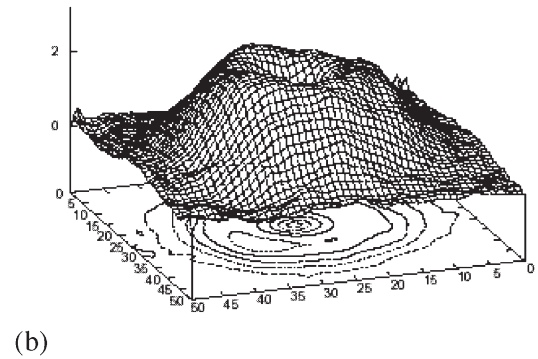
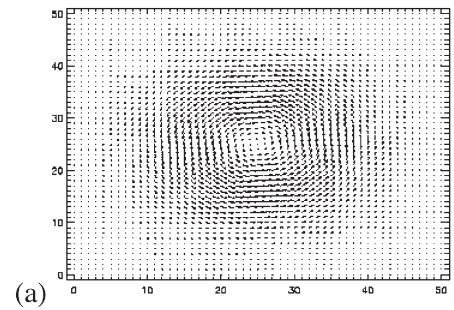


Fig. 2 2-D contours of plasma velocity (a) and vorticity (b) for a low aspect ratio toroid.

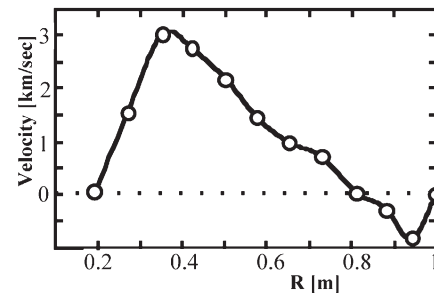


Fig. 3 Radial velocity profile of the two merging spheromaks with counter-helicity, which was measured by Doppler shift of ArII line.

## §29. Development of Diode Laser Absorption Spectroscopy for Diagnostics of Hydrogen Atoms at the $n=2$ State

Sasaki, K. (Nagoya Univ.),  
Goto, S., Morita, S.

Measuring the density ratio between deuterium (D) and tritium (T) is an issue in the control of nuclear fusion plasmas. Considering nuclear fusion reactors working at power plants, the measurement method should be simple and robust as much as possible. We propose a simple diagnostic method for monitoring the D/T density ratio based on diode laser absorption spectroscopy. Recently, diode laser absorption spectroscopy becomes popular in diagnostics of low-temperature plasmas for material processing. The use of diode lasers in diagnostics of fusion plasmas is rare, but we believe that they are useful for fusion plasma diagnostics.

We carried out a simulation experiment for the measurement of the D/T density ratio in  $H_2/D_2$  mixture plasmas. We measured H and D densities at the  $n=2$  state in a high-density, helicon-wave excited plasma source by diode laser absorption spectroscopy. This plasma source has been developed with the intension of using it as a divertor simulator. The electron density obtained in this source was close to  $10^{13} \text{ cm}^{-3}$  in a pure hydrogen discharge at a relatively low rf power of 3 kW. The  $H(n=2)$  and  $D(n=2)$  densities were evaluated from absorptions at  $H\alpha$  and  $D\alpha$  lines. The light source was a diode laser which yielded tunable laser radiation around the  $H\alpha$  and  $D\alpha$  lines. The intensity of the diode laser transmitted through the plasma was detected using a photomultiplier tube via a monochromator.

Figure 1 shows the absorption line profiles at the  $H\alpha$  and  $D\alpha$  lines observed experimentally. The rf power was 3 kW, and both the pressures of  $H_2$  and  $D_2$  were 25 mTorr. The Balmer- $\alpha$  line is composed of seven transitions among three and five sublevels belonging to the  $n=2$  and  $n=3$  states, respectively. The absorption line profiles were fitted well by the superposition of the seven transitions as shown in Fig. 1. The seven components had Gaussian profiles of the same width, and the amplitude ratio was assumed by considering the transition probabilities and the statistical weights of the relevant sublevels. The temperatures of H (0.14 eV) and D (0.16 eV) were evaluated from the width of the Gaussian profiles, and the densities of  $H(n=2)$  and  $D(n=2)$  were deduced from the magnitudes of absorptions.

We repeated the measurements of the  $H(n=2)$  and  $D(n=2)$  densities at various mixing ratios of  $H_2$  and  $D_2$ . The total gas pressure and the rf power were 50 mTorr and 3 kW, respectively. Figure 2 shows the relationship between the

$D(n=2)/H(n=2)$  density ratio and the mixing ratio of the feedstock gas ( $D_2/H_2$ ). As shown in the figure, the  $D(n=2)/H(n=2)$  density ratio nicely represented the gas mixing ratio. In other words, the mixing ratio of the feedstock gas is known by measuring the  $D(n=2)/H(n=2)$  density ratio.

In principle, the  $D(n=3)/T(n=3)$  density ratio is evaluated from the emission intensities of the  $D\alpha$  and  $T\alpha$  lines. However, since the wavelength difference between the  $D\alpha$  and  $T\alpha$  lines is very small, we need a large spectrograph with a very fine resolution. The wavelength resolution of diode laser absorption spectroscopy is very high, and is sufficient to separate the  $D\alpha$  and  $T\alpha$  lines. Considering the result shown in Fig. 2, we believe that this method is useful for monitoring the D/T density ratio in a nuclear fusion reactor.

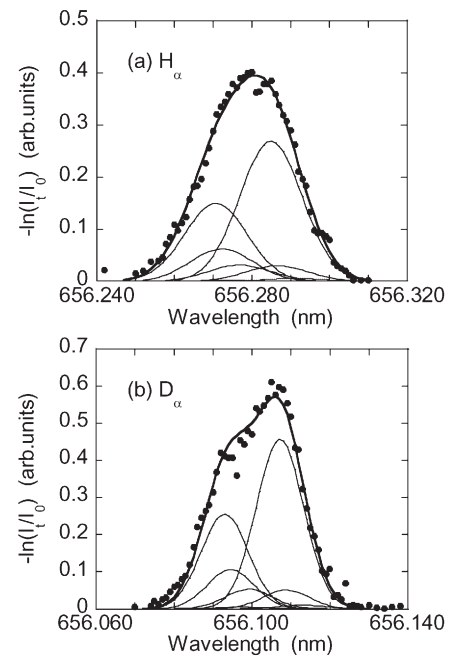


Fig. 1 Absorption line profiles at (a)  $H\alpha$  and (b)  $D\alpha$  obtained by diode laser absorption spectroscopy.

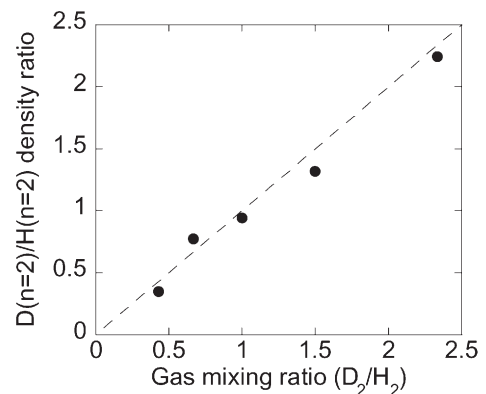


Fig. 2 Relationship between the  $D(n=2)/H(n=2)$  density ratio and the mixing ratio of feedstock  $D_2$  and  $H_2$ .

### 1-3. Theoretical Study

A wide range of theoretical studies on helical devices like LHD and other magnetically confined devices has been carried out in this fiscal year. In order to comprehensively understand the physics mechanism of plasma confinement in toroidal devices, theoretical researches on distinct experimental devices and pioneering theories of confinement plasmas are promoted.

An MHD equilibrium solver; HINT, developed by the late Professor Hayashi, has been improved as HINT2 by using modern coding techniques, in order that the users can easily use it and modify it according to their purposes. The HINT2 will be open to researchers. By using the properties that the HINT or HINT2 can calculate MHD equilibria with magnetic islands and stochastic magnetic field, the doublet-like configuration has been considered in LHD. The fast change in the MHD equilibrium by the nonlinear saturation of interchange modes has been coupled with the evolution of MHD equilibrium by external heating. The second stability of ideal ballooning modes in the standard LHD configuration is considered with being related to the recently obtained Super Dense Core (SDC) or Internal Density Barrier (IDB). The evolution of the magnetic island induced by the resonant deformation due to external current is analyzed in helical systems such as LHD. The modeling of the Edge Localized Mode (ELM) crash in the spherical tori such as MAST and NSTX has been proposed as spontaneous growth of the ideal ballooning modes.

The structure of the radial electric field and the transport dynamics are investigated, in order to obtain the scaling relation between the reduced thermal diffusivity and the normalized temperature gradient, where the comparison of the theoretical results with the experimental results in LHD has been done. Accessibility to a two-dimensionally steep structure of the radial electric field in tokamak H-modes is demonstrated by calculating the time evolution of the potential structure on L-H transition, and the existence of the two-dimensionally steep structure in the H-mode transport barrier has been confirmed. The simulation study of Neoclassical transport and Geodesic Acoustic Mode (GAM) oscillation has been done in LHD by using  $\delta f$  code, where it is shown that the behavior of GAM can be controlled by the vacuum magnetic axis shift and

that the Finite Orbit Effects (FOE) are not significant compared with those in tokamaks. A new  $\delta f$  code based on the geometrical coordinates has been developed in order to study the neoclassical transport in the magnetic islands and stochastic magnetic field. The test guiding particle simulation is carried out for neoclassical effects on the strike point patterns on the Local Island Divertor (LID) head of LHD.

In order to investigate the resistive drift wave turbulence in cylindrical plasmas, a set of model equation including collisions with neutrals has been derived, and the linear eigenmode analyses are performed to examine the condition for drift wave excitation. With being related to the turbulence by the micro instabilities, analytical methods on linear eigenmodes are revisited, and the multiple eigenmodes of GAM in collisionless plasmas and the critical gradients for Short Wavelength Ion Temperature Gradient modes (SWITG) in a simple model tokamak are investigated. The simple  $s - \alpha$  analyses of the high- $n$  ballooning modes in tokamaks are extended into the high- $n$  kinetic ballooning modes, where effects of the scale length of the density, of the electron temperature, and of the ion temperature are treated separately. Effects of trapped particles and of the Finite Orbit Width (FOW) on residual zonal flows are analytically examined in a simple model helical configuration, and the comparison with numerical simulations shows good agreement. The study is now under developing in a more realistic model helical configurations. The effects of the geodesic curvature on zonal flow are examined in H-1 heliac. In order to understand the tendency of the density profiles experimentally observed in two LHD configurations, the particle flux balance is considered by using neoclassical flux and anomalous quasi-linear flux, leading to a qualitative agreement.

The statistical theory of strong turbulence in inhomogeneous plasmas has been extensively developed continuously, where an analytical model for the turbulent damping coefficient is derived by using the Green's function. The turbulent transport and the relation to zonal flow are also studied. The bicoherence of fluctuations in a system of drift wave and zonal flows is discussed by using a Langevin equation formalism. The energy partition between fluctuations and zonal flows is investigated, where high-order corrections by zonal



flow on the zonal flow drive are renormalized, and the driving term at an arbitrary magnitude of zonal flow vorticity is derived. Based on the nonlinear form of the zonal flow growth rate, the steady state solution is obtained. The influence of the turbulence spreading on the self-sustained turbulence of subcritical instabilities is studied, leading to the existence of the minimum radial plasma extent in order for a self-sustained turbulence to exist in linearly stable plasmas. Explicit forms of the transport coefficient and the Dimits shift are obtained for practical usage. Such studies on the zonal flows in plasmas are reviewed, where a comprehensive review of zonal flow phenomena in plasmas is presented. On the other hand, the probability density functions and structure of singularities in non-dissipative fields are discussed by numerically comparing MHD and NS turbulences.

The plasma-sheath having charged-dust grains is considered, in order to understand the sheath structures near the wall and/or divertor and the trapped position of dust grains. The ion temperature effects on the equilibrium of the electrostatic torus plasmas with electrostatic field in addition to simple torus magnetic field are examined based on the non-resistive two-fluid model under the thin plasma ring approximation. As a future reactor core for D-D and D-<sup>3</sup>He fusion reaction, a Field-Reversed Configuration (FRC) is under investigation, because of its extremely high- $\beta$  nature. The steady state operation of FRC by Neutral Beam Injection (NBI) is discussed. As a new type of aid system for fusion reactor design, a system with the virtual reality (VR) visualization and sonification techniques is developed, which might lead to various technical applications.

The late professor Hayashi directed the researches in the field of simulation, theory and data analysis. His leadership and prospects led wide range of theoretical researches to success. We would like to express thanks to him sincerely.

(Nakajima, N.)

## §1. Development and Application of HINT2 to Helical System Plasmas

Suzuki, Y., Nakajima, N., Hayashi, T., Nakamura, Y. (Kyoto University)

The MHD equilibrium is the basis of both most theoretical considerations and physics interpretation of the experimental results. As a standard technique to calculate the 3D MHD equilibrium, inverse equilibrium solver VMEC [1], assuming the existence of perfect nested flux surfaces, is widely used. In such a technique, a magnetic coordinate system is directly constructed so as to satisfy the force balance, or, MHD equilibrium equation  $\vec{J} \times \vec{B} = \nabla p$ . For low  $\beta$  equilibria, since the magnetic field sustains clear flux surfaces, the standard technique is acceptable. However, by nature, 3D MHD equilibria have magnetic islands and stochastic regions in the plasma because of the absence of toroidal symmetry. For high  $\beta$  equilibria, the degradation of flux surfaces by the finite  $\beta$  effect is not avoidable, so that the standard technique based on the nested flux surfaces could not be directly applicable to them. On the other hand, in recent experiments, various types of 3D MHD equilibrium are obtained, namely, low-shear 3D MHD equilibria with magnetic islands, 3D MHD equilibria with multiple magnetic axes, 3D MHD equilibria with zero rotational transform, two dimensional MHD equilibria with current hole near the magnetic axis. The standard technique based on the nested flux surfaces is not suitable in such situations. In order to analyze such MHD equilibria with magnetic islands and stochastic magnetic field, other techniques are required such as the HINT [2] and PIES [3] codes.

The HINT code is one of such solvers, where a relaxation method based on the dynamic equations of the magnetic field and pressure is used. Details of the numerical scheme of the relaxation process are seen in references. The HINT code has been applied to the study of MHD equilibrium in many helical configurations, in order to clarify the properties inherent to 3D MHD equilibrium in various types of helical systems. However, it is fairly difficult to use it because of its code structure coming from the conventional coding style of Fortran77 and older ones. The HINT code also consumes large computational memory and a lot of computational time by the same reason. To use the HINT code more easily for analyzing MHD equilibria in many devices, those features become obstacles.

In order to remove those obstacles, the HINT2; a new version of HINT, has been created [4]. Some features and improvements are the followings.

1. HINT2 succeeds basic functions of older version HINT.
2. The coordinate system used in HINT2 is improved.
3. HINT2 is written in the modern coding style of Fortran90/95.
4. HINT2 is an efficient code by optimizing to vector supercomputer and parallel computer.
5. HINT2 is developed and administered on CVS (Concurrent Versions System), so that the users can easily access current source codes.

As mentioned above, the HINT2 code is a powerful and user-friendly code. By using HINT2, 3D MHD equilibria of the Large Helical Device (LHD) are studied as a first demonstration of HINT2. Figure 1 shows (a) Poincaré plots of a finite- $\beta$  equilibrium ( $\langle\beta\rangle\sim 3.5\%$ ) in LHD and (b) radial profiles of the rotational transform and the connection length for a inward shifted configuration ( $R_{\text{axis}}=3.6\text{m}$ ,  $\gamma=1.254$ ). All figures are plotted on the horizontally elongated cross section. Two vertical lines and arrows in figures indicate a well-defined last closed flux surface (LCFS) in the vacuum configuration. For the finite- $\beta$  equilibrium, field lines in the edge region are strongly ergodized by the finite- $\beta$  effect and the region with clear flux surfaces decreases. The ergodic region spreads over the vacuum LCFS. On the other hand, the connection length of the field line in the ergodic region is still long ( $> 10\sim 10^2\text{m}$ ). From the viewpoint of the parallel transport along the field line, since the connection length of the field line is longer than the mean-free path of the electron, the sustaining of the pressure is expected. In order to confirm the role of ergodic region on 3D MHD equilibrium, it is under the investigation.

### References

- [1] Hirshman S. P., et al. Phys. Fluids 26 (1983) 3553
- [2] Harañji K., et al., J. Comput. Phys. 81 (1989) 169
- [3] Reiman A., et al., Comput. Phys. Comm. 43 (1986) 169
- [4] Suzuki Y. "Development and Application of HINT2 to Helical System Plasmas" in Joint meeting of 2<sup>nd</sup> 21COE Plasma Theory Workshop and US-Japan JIFT Workshop (2004, Kyoto) submitted to Nucl. Fusion.

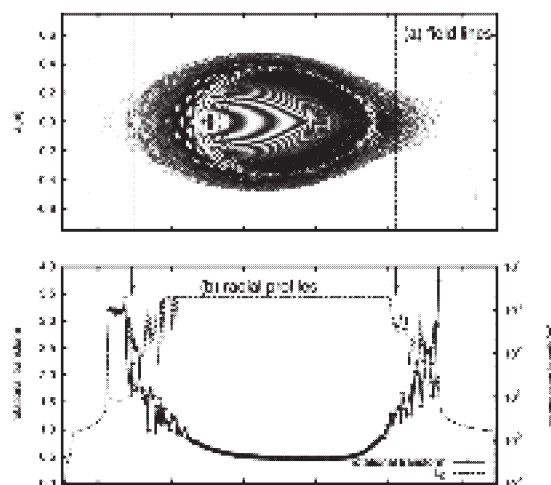


Fig. 1 (a) Poincaré plots of a finite- $\beta$  equilibrium ( $\langle\beta\rangle\sim 3.5\%$ ) in LHD and (b) radial profiles of the rotational transform and the connection length for a inward shifted configuration ( $R_{\text{axis}}=3.6\text{m}$ ,  $\gamma=1.254$ ).

## §2. Theoretical Considerations of Doublet-Like Configuration in LHD

Suzuki, Y., Yamada, H., Nakajima, N., Watanabe, K.Y., Hayashi, T., Nakamura, Y. (Kyoto University)

In recent experiments of JT-60U and LHD, MHD equilibrium, which has the separatrix and stochastic field line regions inside the plasma, has been observed as the tokamak current-hole equilibrium[1] and doublet-like equilibrium of LHD[2]. Since in those MHD equilibria not only there are cases in which high performance is obtained but also the concept of MHD equilibrium is beyond the conventional MHD theory, the theoretical consideration of those MHD equilibria is urgent and critical issue. In tokamaks without vacuum flux surfaces, equilibrium flows may play an essential role to create and sustain the separatrix structure. On the other hand, in helical systems, MHD equilibrium with the separatrix structure may be created and sustained not by plasma flows but by the external coil. Recently, doublet-like configurations were produced by the control of the external quadrupole field. The doublet-like equilibrium has two split axes and an eight-figured separatrix. Thus, in order to understand the basic physics of MHD equilibrium with the separatrix structure, as a first step, the doublet-like equilibrium of LHD is considered theoretically using the HINT code[3].

Figure 1 shows MHD equilibria of a vertically elongated doublet-like configuration ( $BQ=-100\%$ ) obtained from HINT. Vacuum flux surfaces are shown for a comparison. For finite- $\beta$  equilibrium, though the horizontal shift of two axes toward the outside of the torus is very small, the vertical shift from the equatorial plane is very large and the X-point of the separatrix moves slightly outward. The volume inside the eight-figured separatrix is increased with  $\beta$ , but closed flux surfaces still exist on the outside of the separatrix up to  $\beta_0 \sim 6\%$ . Poincaré plots of the magnetic field lines are ergodized by finite- $\beta$  effects.

The particle orbit on the separatrix is studied by solving the guiding-centre drift equation on the rectangular grid. Figure 2 shows Poincaré plots of drift orbits and magnetic field lines of a vertically elongated configuration for the vacuum and a finite- $\beta$  equilibrium ( $\beta_0 \sim 2\%$ ). The particle indicated by red symbols is the passing particle and the deviation of the drift from the flux surface is small. Green symbols indicate the passing particle but it moves with the figure-eight structure. Though the particle is started from the upper region in the inside of the figure-eight separatrix, the particle moves along the figure-eight separatrix. Since there is a singular region on the separatrix, the orbit behaves stochastically and the particle alternately encloses both O-points. The particle indicated by purple symbols is initially trapped in the region above the X-point. Since the poloidal field is very small near the separatrix, the curvature drift moves in the Z direction. Thus, the particle comes and goes in both regions.

## References

- [1] Fujita T., *et al.*, Phys. Rev. Lett. **87** (2001) 245001-1
- [2] Yamada H., *et al.*, 13<sup>th</sup> Int. Toki Conference, (Toki,2003) I-10
- [3] Suzuki Y., *et al.*, Nucl. Fusion **46** (2006) 123

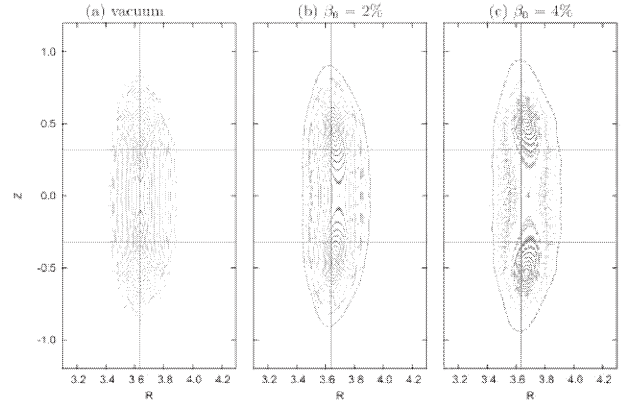


Fig. 1 Poincaré plots of magnetic field lines of a vertical elongated configuration in LHD for (a) the vacuum field, (b)  $\beta_0 \sim 2\%$  and (c)  $\beta_0 \sim 4\%$ .

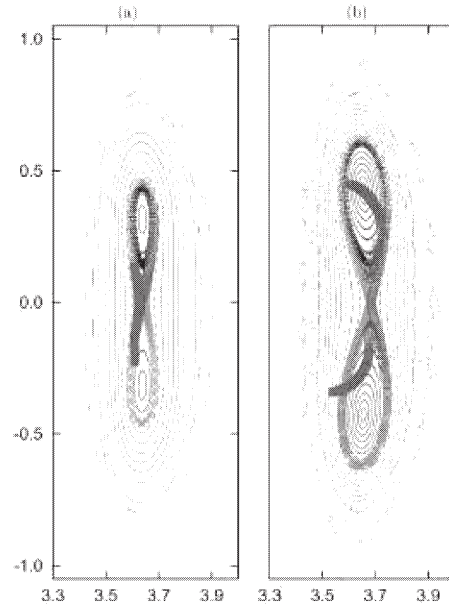


Fig. 2 Poincaré plots of drift orbits and magnetic field lines of a vertically elongated configuration in LHD are shown for (a) the vacuum and (b) finite- $\beta$  fields ( $\beta_0 = 2\%$ ).

### §3. Development of Multi-Scale MHD Simulation Scheme

Ichiguchi, K., Carreras, B.A. (ORNL)

In order to investigate the potential mechanism for the plasma stabilization, we have developed a nonlinear MHD code, NORM, based on the reduced MHD equations<sup>1)</sup>. To consistently understand the plasma dynamics, we need to examine a continuous evolution of the plasma as the beta increases. Therefore, we have to evolve not only the perturbation but also the equilibrium to include the beta increase effect. However, equilibrium evolution takes place over times of the order of 10msec and the basic time scale linked to the instabilities is  $0.5\mu\text{sec}$ . Therefore, the evolutions involve a change of time scales of the order of  $10^5 - 10^6$ . Thus, we develop a numerical scheme to treat this multi-scale problem. We consider an iterative scheme with the VMEC<sup>2)</sup> and the NORM codes.

We consider the numerical scheme for the multi-scale problem in the beta range of  $\beta_{min} \leq \beta \leq \beta_{max}$ . Figure 1 shows the flow chart of the scheme.

At first, we divide the whole range of  $\beta$  into  $N$  intervals. We focus on the interval of  $\beta^i \leq \beta \leq \beta^{i+1}$  and consider the equilibrium evolution from  $\beta^i$  to  $\beta^{i+1}$  ( $0 \leq i \leq N$ ,  $\beta^0 = \beta_{min}$ ,  $\beta^N = \beta_{max}$ ). In the end of the nonlinear calculation for  $\beta^{i-1} \leq \beta \leq \beta^i$ , both the equilibrium and the perturbed parts of the pressure at  $\beta^i$  are already obtained as shown later, which are denoted by  $P_{eq}^i$  and  $\tilde{P}^i$ , respectively. Then, the average pressure profile at  $\beta^i$  can be calculated, which is defined by  $\langle P \rangle^i = P_{eq}^i + \tilde{P}_{0,0}^i$ . Here  $\tilde{P}_{0,0}^i$  is the  $(m, n) = (0, 0)$  component of  $\tilde{P}^i$ , where  $m$  and  $n$  are the poloidal and the toroidal mode numbers, respectively. We assume that the equilibrium pressure at  $\beta^{i+1}$  is given by  $P_{eq}^{i+1} = (\beta^{i+1}/\beta^i)\langle P \rangle^i$ . By employing this pressure, we calculate the equilibrium at  $\beta^{i+1}$  with the VMEC code. Then we obtain the equilibrium quantity for  $\beta^{i+1}$ , which is denoted by  $Q_{eq}^{i+1}$  generically. This part of the scheme gives the evolution in the time scale of  $\sim 10\text{msec}$ .

Next, we consider the calculation of the nonlinear dynamics with the NORM code for the interval of  $\beta^i \leq \beta \leq \beta^{i+1}$ . We can calculate the nonlinear dynamics only separately for different beta values. Thus, in order to keep a smooth continuity of the perturbation,

we divide the nonlinear calculation of this interval into  $L + 1$  steps. The beta value and the equilibrium quantity are updated every step by utilizing a linear interpolation. The beta value of the  $j$ -th step  $\beta^{i,j}$  is given by  $\beta^{i,j} = \beta^i + j\delta\beta^i$  for  $0 \leq j \leq L$ , where  $\delta\beta^i = (\beta^{i+1} - \beta^i)/L$ . The equilibrium quantity of the  $j$ -th step  $Q_{eq}^{i,j}$  is given by  $Q_{eq}^{i,j} = Q_{eq}^i + j\delta Q_{eq}^i$ , where  $\delta Q_{eq}^i = (Q_{eq}^{i+1} - Q_{eq}^i)/L$ . Note that  $\beta^{i,L} = \beta^{i+1,0} = \beta^{i+1}$  and  $Q_{eq}^{i,L} = Q_{eq}^{i+1,0} = Q_{eq}^{i+1}$ . Then, the nonlinear dynamics of the perturbation  $\tilde{Q}^{i,j}$  is calculated for  $\beta^{i,j}$  and  $Q_{eq}^{i,j}$  at the  $j$ -th step. The time range of  $\delta t_j(\tau_A)$  is assigned to each step. Here  $\tau_A$  denotes the poloidal Alfvén time, which corresponds to  $0.5\mu\text{sec}$  in the LHD plasma. Therefore, we can examine the nonlinear evolution in the time scale of  $\mu\text{sec}$  in this part.

In the end of the interval of  $\beta^i \leq \beta \leq \beta^{i+1}$ , we set  $\tilde{P}_{0,0}^{i+1} = \tilde{P}_{0,0}^{i,L}$ . This quantity is used in the VMEC calculation for the next interval. By employing appropriate initial value of  $\langle P \rangle^0$  at  $\beta = \beta^0$  and  $t = T_{min}$  and continuing this iteration scheme until  $\beta$  reaches  $\beta_{max}$ , we can obtain the solution for the whole beta region. The solution is given by the sequence of the total quantity  $Q_T^{i,j} = Q_{eq}^{i,j} + \tilde{Q}^{i,j}$ .

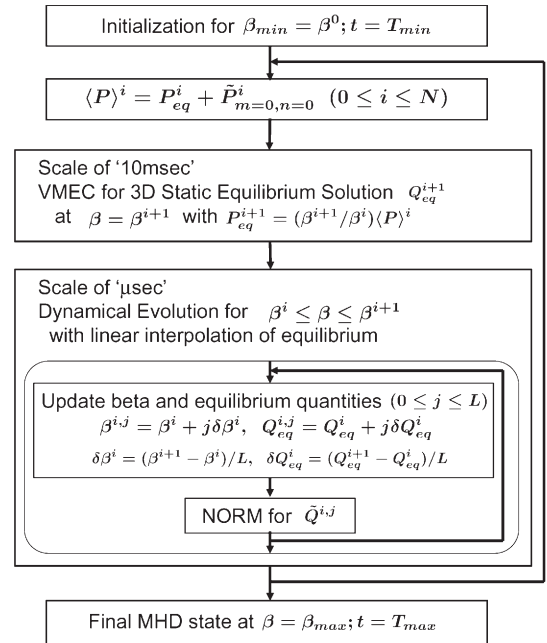


Fig.1 Flow chart of numerical scheme.

#### References

- 1) Ichiguchi, K., et al.: Nucl. Fusion 43 (2003)1101.
- 2) Hirshman H.P. et al. : Comput.Phys.Commun. 43(1986)143.



## §4. Multi-Scale MHD Simulation of LHD Plasma

Ichiguchi, K., Carreras, B.A. (ORNL)

In the LHD experiments, good confinement of the plasma has been observed even in region of parameters predicted to be linearly unstable to ideal interchange modes. In order to investigate the potential mechanism for the plasma stabilization in the beta increase consistently, we have developed a multi-scale MHD simulation scheme<sup>1)</sup>. We apply the multi-scale scheme to the LHD plasma with the vacuum magnetic axis located at  $R_{ax} = 3.6m$ .

Figure 1 shows the time evolution of the kinetic energy. The average beta values at  $t = 10000\tau_A$  and  $60000\tau_A$  are  $\beta = 0.221\%$  and  $0.498\%$ , respectively. The total energy varies smoothly in the evolution, which indicates the present multi-scale approach works well. Figure 2 shows the time evolution of the total pressure profile. The profile is deformed continuously as the beta value increases. The deformed structure depends on the interchange mode excited at each beta value. In the present case, the free energy of the mode is not accumulated so much as the disruptive phenomenon is caused. Therefore, the driving force of the mode is weak and the saturated mode width is narrow. Hence, the pressure deformation due to each mode is localized around the corresponding resonant surface through the whole time sequence. Figure 3 shows the Mercier stability for the resultant equilibrium at  $t = 60000\tau_A$ . The linear stability is improved at dominant resonant surfaces with  $\iota = 2/5, 3/7$  and  $1/2$  through the local pressure flattening.

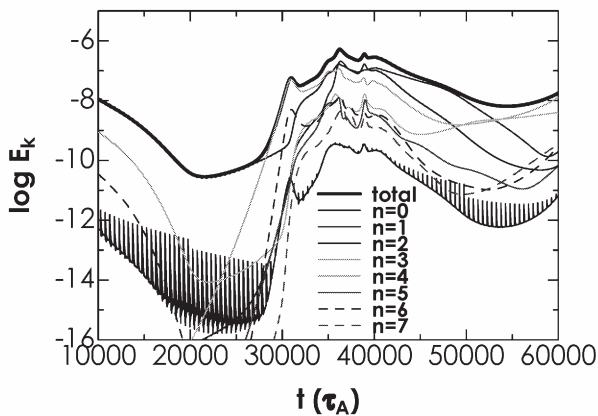


Fig.1 Time evolution of kinetic energy.

This result indicates that the pressure in the LHD can increase with releasing the free energy gradually so as to suppress disruptive phenomena. It can be considered as a self-organization of the pressure.

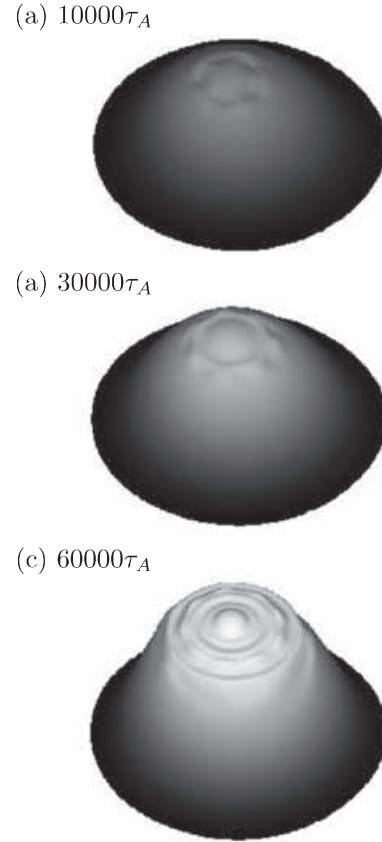


Fig.2 Bird's eye view of the total pressure profile in the region of  $\rho \leq 0.8$ .

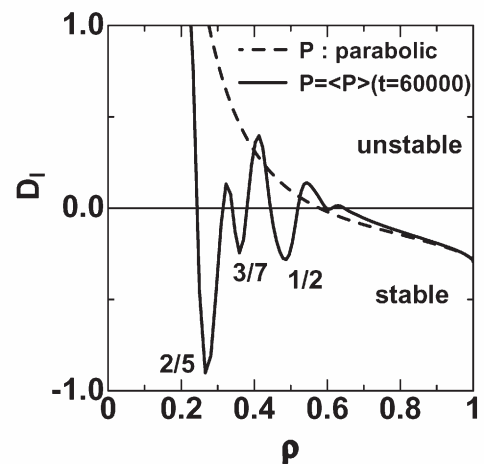


Fig.3 Mercier stability at  $\beta = 0.498\%$ .

### References

- 1) Ichiguchi, K., Carreras, B.A.: J. Plasma Phys. (accepted).

## §5. On the 2nd Stability of Ballooning Modes in the Standard LHD Configuration

Nakajima, N.

Recently Super Dense Core plasmas with  $n_{eo} \sim 4.5 \times 10^{20}(\text{m}^{-3})$  have been obtained in the standard LHD configuration with the vacuum magnetic axis  $R_{av} = 3.75(\text{m})$ . Such dense plasmas are established by both continuous pellet injection and/or strong gas pumping and  $(m/n) = (1/1)$  magnetic island due to the Local Island Diverter (LID) system [1].

In the standard operations on obtaining the high- $\beta$  plasmas, strong gas puffing is used for target plasmas strongly heated by the NBI. In such a case, the inward-shifted LHD configuration with  $R_{av} = 3.6(\text{m})$  is used in order to ensure the good energy deposition by the NBI. As results, the density profile is very flat or hollow, and the temperature profile is approximated as  $T = T_0(1 - s)$ , where  $s$  is the normalized toroidal flux. The resultant pressure profile is given as

$$P(s) \sim P(0)(1 - s)(1 - s^\alpha) \quad (1)$$

where  $\alpha \sim 4 \sim 9$ . Although, in the inward-shifted LHD configuration with  $R_{av} = 3.6(\text{m})$ , currentless MHD equilibria with the pressure profile given by Eq.(1) are strongly Mercier unstable under the fixed boundary condition, MHD equilibria have self-stabilizing effect due to the Shafranov shift of the whole plasma under the free boundary condition [2].

The SDC plasmas are relatively easily obtained in the standard LHD configuration with the vacuum magnetic axis  $R_{av} = 3.75(\text{m})$ . From those conditions, the resultant pressure profile is approximately given as

$$P(s) \sim P(0)(1 - s)^2, \quad (2)$$

or profiles with steeper gradient. Note that the pressure profile of SDC given by Eq.(2) is fairly peaky compared with that in the high- $\beta$  plasmas, and that the pressure profile given by Eq.(2) is the profile used in the previous MHD stability analyses including both global and local ballooning analyses in the standard LHD configuration with the vacuum magnetic axis  $R_{av} = 3.75(\text{m})$ [3 – 5]. The currentless MHD equilibria with the pressure profile given by

Eq.(2) are Mercier stable. It has been found out in the high-mode-number local ballooning analyses and global mode analyses that

1. the high-mode-number ballooning modes (quasi-modes) in the covering space become unstable only in the peripheral region with the stellarator-like magnetic shear ( $d\epsilon/ds > 0$ ), where  $\epsilon$  is the rotational transform, and the magnetic hill for  $\beta \sim 3\%$ ,
2. such the high-mode-number ballooning modes are three-dimensional ballooning modes, namely level surfaces of eigenvalues  $\omega^2$  in the  $(\psi, \theta_k, \alpha)$  are spheroidal, where  $\psi$ ,  $\theta_k$ , and  $\alpha$  are the label of the flux surfaces, the radial wave number, and the label of the magnetic field lines on a flux surface, respectively.
3. the corresponding global modes consist of the quite high mode numbers, and are highly localized in some flux tubes due to the strong poloidal and toroidal mode coupling.
4. in the plasma core region with tokamak-like magnetic shear ( $d\epsilon/ds < 0$ ) and the magnetic well, the high-mode-number ballooning modes and global modes are always stable. Tokamak-like magnetic shear is created under the currentless condition or sufficiently small net toroidal current.

From those analyses, it is expected from the equilibrium variation method [6, 7] that the plasma core region with tokamak-like magnetic shear stays in the 2nd stability region against ballooning modes, even if the stability properties of ballooning modes depend on the pressure profile in the plasma periphery and the boundary condition of MHD equilibrium.

- [1] N. OHYABU, *et al.*, Phys.Rev.Lett. (accepted).
- [2] N. NAKAJIMA, S. R. HUDSON, C. C. HEGNA, and Y. NAKAMURA, Nucl. Fusion **46** 177 (2006).
- [3] N. NAKAJIMA, Physc. Plasmas **3** 4545 (1996).
- [4] N. NAKAJIMA, Physc. Plasmas **3** 4556 (1996).
- [5] J. CHEN, N. NAKAJIMA, and M. OKAMOTO, Physc. Plasmas **6** 1562 (1999).
- [6] C. C. HEGNA and N. NAKAJIMA, Physc. Plasmas **5** 1336 (1998).
- [7] S. R. HUDSON and C. C. Hegna, Physc. Plasmas **10** 4716 (2003).

## §6. Self-Sustained Annihilation of Magnetic Islands in Helical Plasmas

Itoh, K.,  
Itoh, S.-I., Yagi, M. (RIAM, Kyushu Univ.)

The evolution of the magnetic island which is induced by the resonant deformation by external currents in helical systems (such as LHD) is analyzed [1]. The defect of the bootstrap current, caused by the magnetic island, has a parity which reduces the size of the magnetic island, if the bootstrap current enhances the vacuum rotational transform. The width of magnetic island can be suppressed to the level of ion banana width if the pressure gradient exceeds a threshold value. This island annihilation is self-sustained. That is, the annihilation continues, for fixed beta-value, until the external drive for island generation exceeds a threshold. Effects of the reversal of the direction of the bootstrap current and of the sign of radial electric field are also investigated. The possibility of the neoclassical tearing mode in the LHD-like plasma is discussed.

The equation that describes the evolution of the resonant magnetic island is given as  $\frac{\partial}{\partial t} A + \eta \Delta A = 0$ , where  $A \equiv \tilde{A}_* q^2 R / B r_s^3 q'$  is the normalized amplitude of the  $(m, n)$ -Fourier component of helical vector potential perturbation  $\tilde{A}_*$  at the mode rational surface,  $r = r_s$ ,  $\eta = \eta_{||} \mu_0^{-1} r_s^{-2} \tau_{Ap} = R_M^{-1}$ . An explicit form of the growth rate is given, within the neoclassical transport theory, by

$$-\Delta A = 2 \Delta' A^{1/2} - \beta_{bs} \left( a_{bs} \frac{A}{W_1 + A} + \frac{\rho_b^2}{r_s^2} \frac{L_q}{L_p} a_{pc} \frac{A}{W_2^2 + A^2} \right)$$

and  $\beta_{bs} = 2\epsilon^{1/2} L_q L_p^{-1} \beta_p$  [2]. An induction of the magnetic island by the external coil is parameterized by the magnetic island width at the stationary state,  $\delta$ :

$$\Delta' = \left( \frac{\delta^2}{r_s^2} \frac{1}{A} - 1 \right) |\Delta'_0|,$$

where the coefficients  $\Delta'_0$  represents the stabilizing influence in the absence of the external current.

This model explains the annihilation of magnetic island by plasma pressure (Fig.1). This annihilation is self-sustaining. That is, under the variation of control parameters (such as beta or external perturbation), the suppression persists up to a critical boundary. Response to the externally-driven island is shown in Fig.2. Possibility of spontaneous island generation is illustrated in Fig.3.

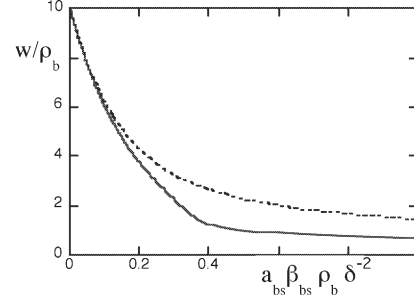


**Fig.1** Width of magnetic island as a function of the plasma beta. Parameter  $\delta$  is fixed,  $\delta/\rho_b = 10$ . The dashed line indicates the suppression by bootstrap current, and the solid line includes the ion polarization drift.  $2|\Delta'_0| = 1$ ,  $L_q/L_p = 3$  and  $a_{pc} = a_{bs}$ .

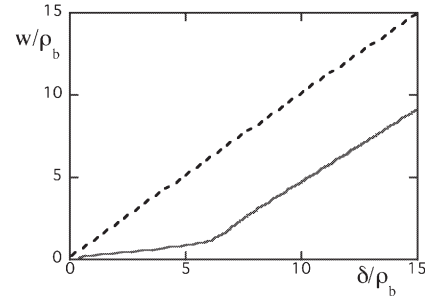


**Fig.2** The width of the island as a function of the intrinsic island width  $\delta$  for a fixed value of the plasma pressure,  $a_{bs}\beta_{bs} = 0.3$  and  $r_s/\rho_b = 50$ . (Other parameters are the same as in Fig.1)

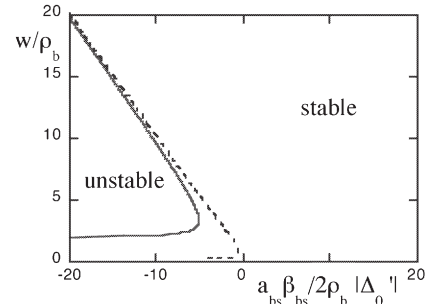


**Fig.3** Magnetic island width as a function of the plasma pressure gradient when the bootstrap current is in the counter direction. Solid and dashed lines show cases where the ion-polarization current is stabilizing,  $a_{pc} = |a_{bs}|$ , and destabilizing for  $a_{bs} < 0$ . ( $\delta = 0$  and other parameters are the same as in Fig.1)

### Reference

- [1] K. Itoh, S.-I. Itoh, M. Yagi, Phys. Plasmas Vol.12 (2005) 072512
- [2] S.-I. Itoh, Itoh K and M. Yagi: Phys. Rev. Lett. 91 045003 (2003)

## §7. Nonlinear Dynamics of an ELM Crash in Spherical Tokamak

Khan, R. (Grad. Univ. Advanced Studies),  
Mizuguchi, N., Nakajima, N., Hayashi, T.

ELMs are often observed in the H-mode operations of ST experiments, as well as the conventional large tokamaks. To control the ELMs is one of the most important issues for the sustainment of a good confinement state. Experimentally, several characteristic structures of ELMs are observed in the middle-sized ST devices such as MAST and NSTX. In this paper, we propose a modeling of an ELM crash with a consecutive scenario which is initiated by the spontaneous growth of the ballooning mode instability, comparing with the experimental observations. Furthermore, more realistic situations are examined by using the drift model.

Firstly, a nonlinear MHD simulation is executed in a three-dimensional full toroidal geometry[1]. The initial condition is given by a reconstructed equilibrium from the NSTX, where  $\beta_0=28\%$ ,  $q_0=0.89$ , and  $A=1.4$ . The system is linearly stable for the ideal modes, but weakly unstable for the resistive ballooning modes. the simulation result shows a two-step relaxation process induced by the intermediate- $n$  ballooning instability followed by the  $m/n=1/1$  sawtooth crash, where  $m$  and  $n$  are the poloidal and toroidal mode number, respectively. Especially, thin and elongated balloons are formed along the field lines on the plasma surface on the nonlinear phase. They eventually turn into bubbles, and are isolated from the core plasma, as shown in Fig.1. This behavior well agrees with the experimental observation by using fast camera images in MAST. After the eruption of the balloons, the poloidal pressure profile becomes a peaked one from a broader one in the central region due to the convection motions of the ballooning modes. The  $q$  profile also goes below 1 at the center. These profile changes can induce another instability, i. e., the  $m/n=1/1$  kink mode. The system crashes once again due to the  $1/1$  mode, and recovers a broader profile, just like the well-known sawtooth crashes. During this process, one can see a characteristic non-axisymmetric structure with a large  $n=1$  component, which is also clearly observed in the experiments.

Thus, our simulation result explains several characteristic features of the so-called type-I ELM:(1)relation to the ballooning instability (2)intermediate- $n$  precursors (3)low- $n$  structure on the crash (4)formation and separation of the filament (5)considerable amount of convective loss. As for the time scale, the simulation result is consistent with the experimental ELM rise times of the order of  $\sim 100 \mu\text{sec}$ .

Furthermore, we have examined the drift model simulation to follow the dynamics under more realistic situations[2]. Including the lowest order modification of the ion diamagnetic drift effect, we introduce the flow velocity variable as the sum of the conventional MHD velocity and the ion diamagnetic drift velocity. The result shows that the

mode structures rotate both toroidally and poloidally. Under this situation, the higher- $n$  modes are linearly stabilized, whereas the lower- $n$  modes remain unstable. This changes the linear toroidal mode structures drastically. On the other hand, it is found that the nonlinear dynamics is not so affected by those modifications, i. e., the filament separation from the core can take place universally for the drift model case as well as the MHD case (see Fig.2), despite a remarkable changes in the nonlinear flow patterns on the filaments due to the diamagnetic rotation.

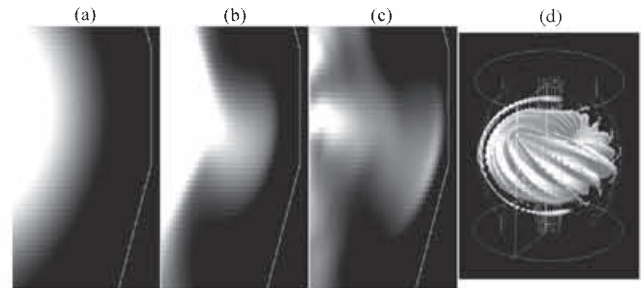


Fig.1 (a)-(c) Formation of the plasma balloons and separation from the core. (d) Formation of the filamentary structure.

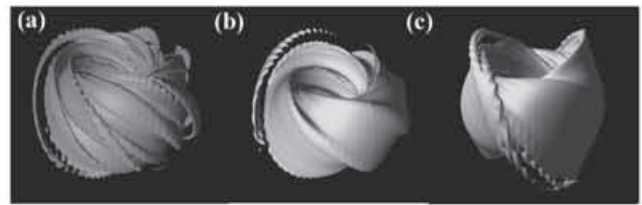


Fig.2 Universally formed plasma filaments for the drift model cases. Different control parameters for the diamagnetic drift term are used for each cases ((a)-(c)).

### Reference

- 1) N. Mizuguchi, et al., IEEJ Trans. FM **125**, (2005) 934
- 2) R. Khan, et al., to appear in J. Plasma Phys. (2006)



## §8. Theoretical Study of Structure of Electric Field and Transport Dynamics

Toda, S., Itoh, K.,

Itoh, S.-I., Yagi, M. (RIAM, Kyushu Univ.)

The steep gradient in the radial profile of the electric field was shown in the core plasma region and the transport barrier was confirmed in the Electron Cyclotron Resonance Heating (ECRH) plasma in helical plasmas. Examples include the experimental results in the Compact Helical System (CHS), the Large Helical Device (LHD) and the Wendelstein7-AS (W7-AS). Theories of the improvement confinement have been composed of the two main issues, i.e., the bifurcation mechanism of the radial electric field and the suppression of the turbulent transport associated with the profile of the radial electric field. The radial electric field in helical plasmas is assumed to be determined by the ambipolar condition for the neoclassical particle flux. The generation of the electric field in helical systems could be investigated more quantitatively because the neoclassical transport is found to play the dominant role in generating the radial electric field. We have examined the one-dimensional transport equations which describe the temporal evolutions of the density, the electron and ion temperatures, and the radial electric field in a cylindrical configuration. The radial transition with the multiple ambipolar solutions of  $E_r$  has been obtained related with the transport barrier and the improved confinement state is reproduced. Because the anomalous transport plays the dominant role in the present-day helical plasmas, a quantitative test for a theoretical model of the turbulent transport in the improved confinement state is an urgent issue. We derive a scaling relation between the reduced thermal diffusivity and the normalized temperature gradient. The comparison of the theoretical results with the experimental results in LHD is made.

We adopt a theoretical model for the anomalous transport diffusivities driven by the current diffusivity as a candidate. We discuss the validity of this model comparing the calculation results with the experimental results in LHD. At first, we obtain profiles of  $n$ ,  $T_e$ ,  $T_i$  and  $E_r$  as the steady state for the given particle source. The line-averaged value of the obtained density is chosen at the value such as  $\bar{n} \approx 1 \times 10^{19} \text{ m}^{-3}$ . The radial electric field is negative (the ion root) in the entire radial region. Next, we use these obtained profiles as the initial condition, i.e., we begin the new calculation from the negative  $E_r$  in the entire region. The steep gradient of  $T_e$  can be found in the radial profile of  $T_e$ . We obtain the positive  $E_r$  (the electron root) and the transport barrier especially in the core region in the final steady state. The obtained line-averaged value of the steady profile for the density is found to be  $\bar{n} \approx 7 \times 10^{18} \text{ m}^{-3}$  as the result of this calculation. To examine the reduction of the heat transport associated with the improved confinement state, the total electron diffusivity  $\chi_{\text{etotal}} (= \chi_a + \chi_e^{\text{NEO}})$  is normalized by the gyro-Bohm factor  $T_e^{3/2}$ , where  $\chi_e^{\text{NEO}}$  and  $\chi_a$  are the neoclassical and anomalous parts of electrons, respectively. This normalized coefficient is

plotted with the closed circles in Fig. 1 at  $\rho = 0.26$  as the function of  $R/L_{T_e}$ , where  $L_{T_e} = -T_e / T_e'$ . The relation between the normalized transport coefficient and the temperature gradient parameter  $R/L_{T_e}$  is summarized in Fig. 1. After the jump to the electron root in the  $E_r$  profile, the value of  $\hat{\chi}$  at  $\rho = 0.26$  decreases to  $0.4 \text{ m}^2 \text{ s}^{-1} \text{ keV}^{-3/2}$  in Fig. 1 in the steady state, where  $\hat{\chi} \equiv \chi_{\text{etotal}} / T_e^{3/2}$ . At this time, the transport barrier in the  $T_e$  profile can be obtained at  $\rho = 0.26$  in the core region. The value of the gradient parameter  $R/L_{T_e}$  at which the radial transition of  $E_r$  occurs is found as  $R/L_{T_e} > 20$  and a scaling relation  $\hat{\chi} \propto (R/L_{T_e})^{-1.5}$  is derived from the calculation shown with the dotted line in Fig. 1.

The analysis is compared with the experimental observations. From the observation in LHD, the threshold value of the onset of the improvement was reported as  $R/L_{T_e} \approx 20$  and the dependence of  $\hat{\chi}$  on  $R/L_{T_e}$  is shown as  $\hat{\chi} \propto (R/L_{T_e})^{-5.0}$ . These relations in the LHD experiment were also obtained in the temporal transient response. The observation for the threshold of the onset of the improvement is in good agreement with the calculation results. The dependence of  $\hat{\chi}$  on  $R/L_{T_e}$  in the improvement confinement is qualitatively similar so that the calculation by use of this theoretical model can reproduce the dependence of the normalized heat diffusivity of electrons on the temperature gradient. However, the dependence of  $\hat{\chi}$  on  $R/L_{T_e}$  in the improved mode is stronger in experimental results. This difference may come from the different situations of the calculation and the experiment. Within the theoretical models, the present model is one of those which have the strongest dependence on the gradient of the radial electric field. This discrepancy may not be resolved by other turbulent transport models.

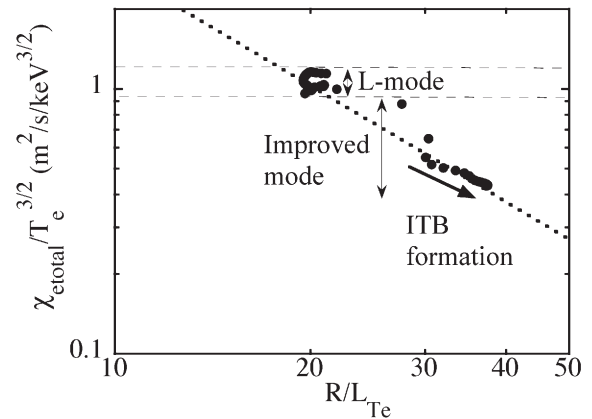


Fig. 1 Normalized heat diffusivity calculated as a function of  $R/L_{T_e}$  at  $\rho = 0.26$  with closed circles.

1) Toda S. and Itoh K.: Journal of Physical Society of Japan, Vol. 74 No. 11 (2005) 2987

## §9. Accessibility to a Two-Dimensionally Steep Structure of the Electric Field in Tokamak H-mode

Kasuya, N., Itoh, K.

The electric field plays an important role in H-mode transition. The poloidal structure, in addition to the radial structure, has been pointed out to become steep in the H-mode transport barrier<sup>1)</sup>. The formation of the poloidal electric field induces a radial convective flow by the radial  $E \times B$  flow, which is candidate to give a new explanation of the rapid H-mode pedestal formation<sup>2)</sup>. We have demonstrated the accessibility to the two-dimensionally steep structure by calculating the time evolution of the potential structure on L-H transition<sup>3)</sup>.

Two-dimensional structures of the electrostatic potential, density and flow velocity near the edge of H-mode tokamak plasma are investigated. We have studied the two-dimensional structure in the transport barrier with the model including the nonlinearity in bulk-ion viscosity and turbulence-driven shear viscosity<sup>3)</sup>. The model equation, which describes the poloidal variation as deviation from the flux-surface-averaged quantities, is solved with that describing the radial structure by using the shock ordering<sup>1)</sup>. The following analysis is carried out with the parameter set of the electrode biasing experiment. Electrode biasing is one of the methods for controlling the radial electric field externally, and can induce a transition to an improved confinement state in a controlled manner<sup>4)</sup>.

The time evolution of the two-dimensional structure is calculated in accordance with variation of the applied voltage. The case is shown in Fig. 1 when the applied voltage is ramped up from 200 [V] to 600 [V] in duration of 1 [ms] with the following parameter set:  $R = 1.75$  [m],  $a = 0.46$  [m],  $B_0 = 2.35$  [T],  $T_i = 40$  [eV],  $I_p = 200$  [kA] and the boundaries  $r = a$ ,  $a - 5$  [cm]. The electrode current increases and then decreases as the applied voltage increases. The profile of the radial electric field also changes, accordingly. The poloidal flow is given by a  $E \times B$  flow, so the poloidal Mach number  $M_p$  corresponds to the normalized radial electric field. The structural transition of the radial electric field from flat one to solitary one occurs in this case, and the poloidal structure is formed, accordingly. The  $\Delta\Phi$  is rather constant at  $t = 0$  [ms], and the perturbation becomes large as the applied voltage increases. At  $t = 1.6$  [ms], the potential perturbation is developed and has  $\Delta\Phi_{\max} = 50$  [V], because  $M_p$  becomes large ( $M_p = 1.4$ ), though  $M_p$  has a flat profile. For the duration  $t = 1.6 - 5.0$  [ms], the radial structure evolves from a flat profile to a solitary profile. The poloidal shock becomes steep in accordance with the radial electric field profile, and the absolute value of the poloidal electric field increases up to 270 [V/m]. The final state ( $t = 5$  [ms]) has steep gradients both in the radial and poloidal directions, so the accessibility to the two-dimensionally steep structure as obtained in Ref. [2] is confirmed. The typical time scale of the poloidal structural change is given

by the poloidal rotation time, which is 100 [ $\mu$ s] with the parameter set used here, and becomes small with larger ion temperature and smaller device radius  $a$ . This time scale is shorter than the typical time scale of the radial structural change  $\sim 1$  [ms]. Therefore, a two-dimensional structure evolves in accordance with the radial structural change, which has a longer time scale.

In this way, the existence of the two-dimensionally steep structure in the H-mode transport barrier is confirmed, which shows that the poloidal shock evolves in accordance with the transition of the radial electric field structure, being associated with the radial convective flow. The convective flow velocity is inhomogeneous in radius, and the gradient of the convective flux can be positive in some region. Therefore, sudden increase of derivative of the convective transport at the onset of the transition is candidate to give a new explanation of the rapid H-mode pedestal formation.

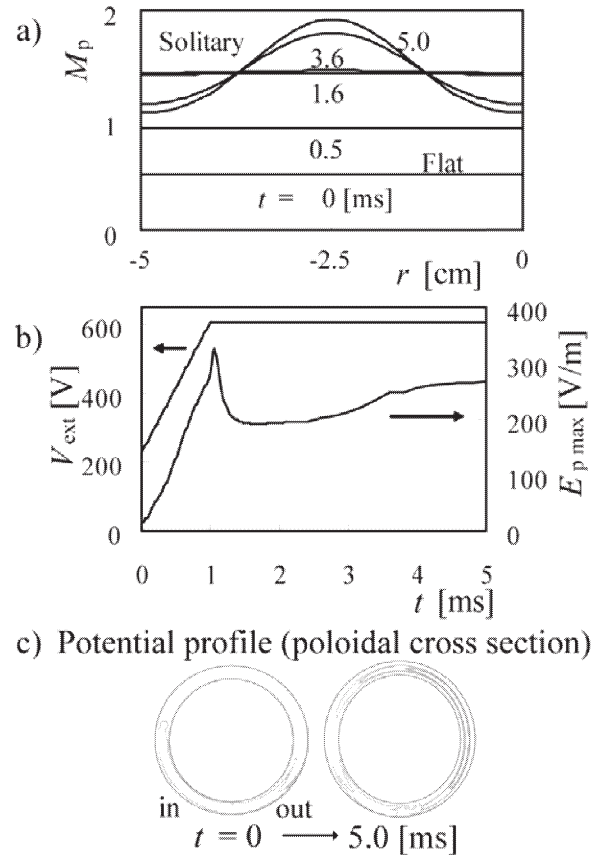


Fig.1: Time evolution of the two-dimensional potential structure in accordance with the applied voltage ramp-up. Time evolutions of (a) the  $M_p$  profile, (b) the maximum of  $|E_p|$  and (c) the potential contours on the poloidal cross section are shown.

### References

- 1) Shaing, K. C. et al.: Phys. Fluids B **4** (1992) 404.
- 2) Kasuya, N. and Itoh, K.: Phys. Rev. Lett. **94** (2005) 195002.
- 3) Kasuya, N. and Itoh, K.: Plasma Phys. Control. Fusion **48** (2006) A319.
- 4) Weynants, R. R. et al.: Nucl. Fusion **32** (1992) 837.

## §10. Simulation Study of Neoclassical Transport and GAM Oscillation

Satake, S., Okamoto, M., Nakajima, N., Sugama, H., Yokoyama, M.

To study the Neoclassical transport and time evolution of radial electric field, especially in Large Helical Device (LHD), we have developed a Monte-Carlo transport simulation code “FORTEC-3D”[1,2], using the  $\delta f$  method. In this method, the distribution function of plasma is separated into  $f = f_M + \delta f$ , where  $f_M$  is a local Maxwellian and  $\delta f$  is considered as a small perturbation from  $f_M$ . We solve the linearized drift-kinetic equation for  $\delta f$  as follows

$$\left( \frac{\partial}{\partial t} + (\mathbf{v}_{\parallel} + \mathbf{v}_d) \cdot \nabla + e\mathbf{v}_d \cdot \mathbf{E}_r \frac{\partial}{\partial \mathcal{K}} - C(\cdot, f_M) \right) \delta f = -\mathbf{v}_d \cdot \left( \nabla - \frac{e\mathbf{E}_r}{T} \right) f_M + C(f_M, \delta f), \quad (1)$$

where  $\mathcal{K} = mv^2/2$ .  $C(\delta f, f_M)$  is the test-particle collision term implemented by random kicks in the velocity space, and  $C(f_M, \delta f)$  is the field-particle collision term defined so that the collision operator satisfies the conservation properties. In eq. (1), the term  $\mathbf{v}_d \cdot \nabla \delta f$  brings the finite-orbit-width (FOW) effect and non-local nature of neoclassical transport, which is neglected in standard formulation. The radial electric field develops according to

$$\epsilon_0 \left( 1 + \frac{c^2}{v_A^2} \right) \frac{\partial E_r(r, t)}{\partial t} = -Z_i e \langle \Gamma_i(r, E_r, t) - \Gamma_e(r, E_r, t) \rangle. \quad (2)$$

In FORTEC-3D, only the ion particle flux  $\Gamma_i$  is calculated, and  $\Gamma_e$  is obtained from GSRAKE code[3], which solves a bounce-averaged kinetic equation. The adoption of GSRAKE is to reduce the calculation time.

In the time evolution of  $E_r$ , a rapid oscillation called geodesic acoustic mode (GAM) occurs. It is known that GAM shows a collisionless damping. Recently, analytic estimation of the GAM damping rate has been shown[4]. It is expected that the collisionless damping rate in helical system depends on the relative magnitude of Fourier spectrum of magnetic field evaluated in Boozer coordinates. To investigate the dependence of the GAM damping rate on magnetic configuration in LHD, we compare the simulation results of LHD changing the magnetic axis position  $R_{ax} = 3.7\text{m}$  and  $3.6\text{m}$ . We also compare the simulation result which used only the major 3 modes of magnetic field spectrum ( $B_{0,0}$ ,  $B_{1,0}$ , and  $B_{2,10}$  where  $B_{m,n}$  is the Fourier component of the magnetic field expressed as  $B(\rho, \theta, \zeta) = \sum_{m,n} B_{m,n}(\rho) \cos(m\theta - n\zeta)$ ) and the one in which as much as 12 modes are used. Figure 1 shows the time evolution of radial electric field in those simulations. As it can be seen from Fig.1, the damping of GAM oscillation is slightly rapid in the  $R_{ax} = 3.7$  case, and 12-modes calculation shows rapid damping

compared with the simulation using only 3 modes. We confirmed that these tendencies agree with the expectation from the analysis in [4]. This suggests that the behavior of GAM in LHD can be controlled by shifting the magnetic axis.

We have also investigated the FOW effect on the damping rate. Using a simple tokamak geometry and changing the magnetic field strength, we compared the GAM damping rate  $\gamma$  as shown in Figure 2. It is shown that the damping rate is higher as typical banana width  $\propto 1/B$  becomes larger (magnetic field weaker). In helical systems, however, we find that the FOW effect is not significant.

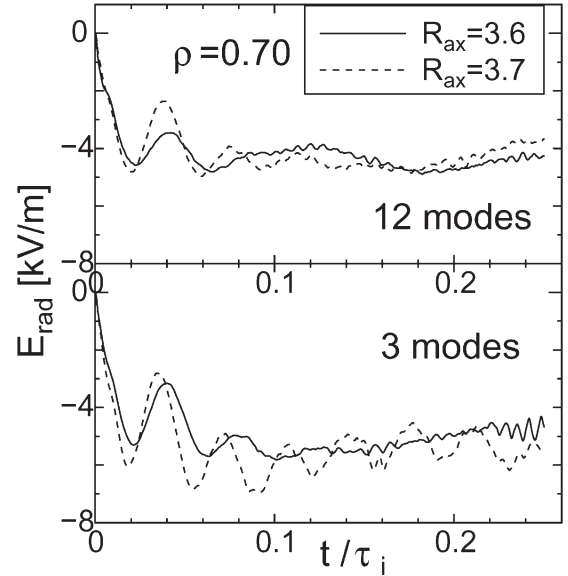


Fig. 1 : Simulation of GAM oscillation in LHD with finite number of magnetic field spectrum

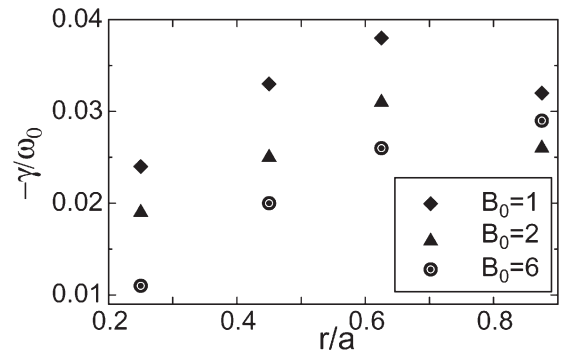


Fig. 2 : Comparison of the GAM damping rate  $\gamma$  (normalized by the real frequency  $\omega_0$ ).

- 1) Satake, S. et al.: Nucl. Fusion **45** (2005) 1362.
- 2) Satake, S. et al.: Plasma and Fusion Res. **1** (2006) 002.
- 3) Beidler, C. D. et al.: Plasma Phys. Control. Fusion **37** (1995) 463.
- 4) Sugama, H. and Watanabe, T.-H.: Phys. Plasmas **13** (2006) 012501.

## §11. Development of Neoclassical Transport Code Using the $\delta f$ Method

Nunami, M., Kanno, R., Satake, S.,  
Takamaru, H. (Chubu Univ.), Hayashi, T.,  
Sugama, H.

Recently, the Large Helical Device (LHD) experiments found that if the field which is made by external perturbation magnetic field is sufficiently large, and if the vacuum magnetic island width exceeds the critical value (15%–20% of minor radius), the flow along the magnetic flux surface inside the magnetic island in the direction to reduce the flow shear at the boundary of the magnetic island is observed. And radial profiles of temperature of ion and the plasma flow are measured in  $m/n = 1/1$  island<sup>1),2)</sup>. These results suggest that the potential is not flat in magnetic island. This is very interesting for us.

We attacked for the experimental results using neoclassical transport analysis. At first, to analyze the transport phenomena in such complicated magnetic field structure, we developed the neoclassical transport code without any magnetic coordinate systems. Then we used the helical coordinate system. And this code is based on the  $\delta f$  method. In this method, the distribution function of plasma is separated into  $f = f_M + \delta f$ , where  $f_M$  is a local Maxwellian and  $\delta f$  is considered as a small perturbation from  $f_M$ . And then, using 2-weight scheme, we solve the linearized kinetic equation for  $\delta f$ ,

$$\frac{D}{Dt}\delta f \equiv \frac{\partial}{\partial t}\delta f - C_T(\delta f) = \mathbf{v}_d \cdot \nabla f_M + C_F f_M \quad (1)$$

where  $C_T$  is the test particle collision operator implemented by random kicks in the velocity space, and  $C_F$  is the field particle collision term. We named the developed code “KEATS” (Kinetic EquATion Solver in the helical coordinate system).

In order to check validity of KEATS, we compared our results with the “FORTEC-3D” in tokamak configuration, where the FORTEC-3D is a neoclassical transport simulation code which is coded in Boozer coordinate system<sup>3)</sup>. Now, we compared radial profile of the neoclassical heat flux. We show the radial profiles of neoclassical heat flux in the simple tokamak magnetic field in Fig.2. From this, we can see that our results agree with the results of FORTEC-3D.

When the plasma transport is numerically analyzed, an average over a magnetic flux-surface is a very useful

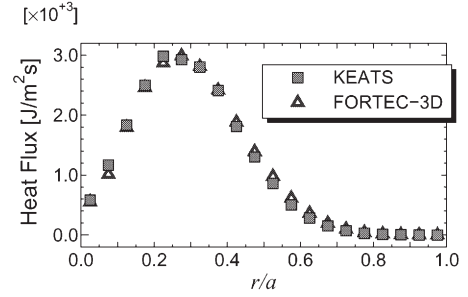


Figure 1: Comparison of radial profile of heat flux.

concept to understand the transport. When averaging, a proper labeling of the flux-surfaces is necessary. In general, it is not easy to label the flux-surfaces in a magnetic field containing the island, compared with the case of a magnetic field configuration having nested flux-surfaces. Then we have developed a new computational technique to label the magnetic flux-surfaces<sup>4)</sup>. This technique uses an optimization algorithm, called the *simulated annealing method*. The flux-surfaces are discerned by using two labels: one is classification of the magnetic field structure, i.e., core, island, ergodic, and outside regions, and the other depends on the value of the toroidal magnetic flux. We have applied this technique to an LHD configuration with the  $m/n = 1/1$  island, and successfully discriminated of the magnetic field structure.

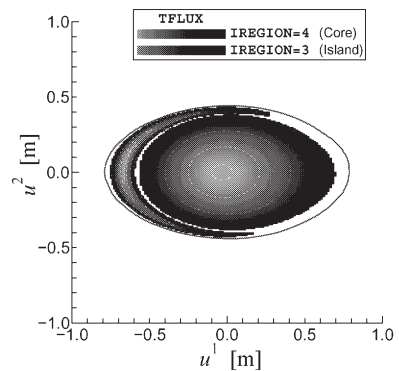


Figure 2: Label of the magnetic flux-surfaces in the LHD configuration with the  $m/n = 1/1$  island on a poloidal cross section ( $u^3 = \pi/10$ ). The labels, IREGION and TFLUX, are indicated by colors and their hues, respectively.

### References

- 1) K. Ida, *et al.*, Phys. Rev. Lett. **88**, 015002 (2002).
- 2) K. Ida, *et al.*, Nucl. Fusion **44**, 290 (2004).
- 3) S. Satake, *et al.*, Plasma Fusion Res. **1**, 002 (2006).
- 4) M. Nunami, *et al.*, Plasma Fusion Res. (accepted)



## §12. Strike Points of High Energy Particles on the LID Head in LHD

Kanno, R., Takamaru, H. (Chubu Univ.),  
Nunami, M., Satake, S., Okamoto, M.

Test particle simulation is carried out in order to understand the neoclassical effect on strike point patterns of ions on the Local Island Divertor (LID) head in a Large Helical Device (LHD) configuration. The LID is one of the divertor concepts in the LHD configuration, and it utilizes an  $m/n = 1/1$  magnetic island formed at the edge region of the LHD. In the LID experiments, it is important to examine whether or not the particle flux, in particular the ion flux crossing the island separatrix, is successfully guided to the rear side of the island where the target plates are placed to receive the particle load.

The orbits of the guiding centers of the test particles starting from a magnetic flux surface in the edge of the core region are traced in the fixed magnetic field under the effects of the Coulomb collision and anomalous diffusion. By tracing the orbits, the strike point pattern which is caused by ions supplied from the core region can be numerically observed. If the effects of anomalous diffusion and collisions with charged particles, neutrals, solid surfaces, etc. are neglected, the guiding center motion is expressed as

$$\frac{d\mathbf{X}}{dt} = \mathbf{v} = \frac{1}{B_{\parallel}^*} \left[ v_{\parallel} \left( \mathbf{B} + \frac{m_i}{e_i B} v_{\parallel} \nabla \times \mathbf{B} \right) + \left( \frac{\mu}{e_i} + \frac{m_i}{e_i B} v_{\parallel}^2 \right) \mathbf{b} \times \nabla B \right], \quad (1)$$

$$\frac{dv_{\parallel}}{dt} = -\frac{\mu}{m_i B_{\parallel}^*} \left( \mathbf{B} + \frac{m_i}{e_i B} v_{\parallel} \nabla \times \mathbf{B} \right) \cdot \nabla B, \quad (2)$$

$$\frac{d\mu}{dt} = 0, \quad (3)$$

where  $B_{\parallel}^*$  is given as  $B_{\parallel}^* = B + (m_i/e_i B) v_{\parallel} \mathbf{b} \cdot \nabla \times \mathbf{B}$ ,  $v_{\parallel} = \mathbf{v} \cdot \mathbf{b}$  is the parallel velocity,  $\mathbf{b} = \mathbf{B}/|\mathbf{B}| = \mathbf{B}/B$  is a unit vector of a magnetic field  $\mathbf{B}$ , and  $\mu$  is the magnetic moment. We assume that the pitch angle scattering is dominant compared with the other effects of the collisions. The Lorentz collision operator is considered as

$$d\xi = -\nu_d \xi dt + \sqrt{(1 - \xi^2) \nu_d} dW_t, \quad (4)$$

where  $\xi = v_{\parallel}/|\mathbf{v}| = v_{\parallel}/v$  is the cosine of the pitch angle,  $\nu_d$  is the deflection frequency, and  $W_t$  denotes a Wiener process. When an anomalous diffusion process in configuration space is considered so as to generate a perpendicular particle flux  $\mathbf{\Gamma}_{a\perp} = -\vec{D}_a \cdot \nabla n_i$ , which models electrostatic turbulence  $(1/B_{\parallel}^*) \mathbf{b} \times \nabla_{\perp} \tilde{\Phi} = \nabla \cdot \vec{D}_a dt + \vec{\sigma}_a \cdot d\mathbf{W}_t$ , the motion in configuration space (1)

can be modified to the following stochastic differential equation

$$d\mathbf{X} = \left\{ \mathbf{v}(\mathbf{X}) + \nabla \cdot \vec{D}_a(\mathbf{X}) \right\} dt + \vec{\sigma}_a \cdot d\mathbf{W}_t, \quad (5)$$

where  $\vec{D}_a = D_a(\vec{I} - \mathbf{b}\mathbf{b})$  denotes the tensor of the anomalous diffusion coefficient,  $\vec{\sigma}_a = \sqrt{D_a}(\vec{I} - \mathbf{b}\mathbf{b})$  satisfies the condition  $D_a^{\alpha\beta} = \sigma_a^{\alpha k} \sigma_a^{\beta l} g_{kl}$ ,  $\vec{I}$  is the identity tensor, and  $g_{kl}$  is the metric coefficient. The differential equations (1)-(5) are solved by using Monte Carlo techniques [1, 2].

We find in the test particle simulations that the strike point patterns on the LID head are varied according to collisionality, field line structures and energy of a test particle. The pattern for the case of test particles having  $E = 300$  eV sensitively depends on the collisionality and is not symmetric. For the case of high energy particles with  $E = 5$  keV, the strike point pattern on the LID head is calculated in Fig.1. Effect of the particle energy is important to the strike point pattern. We have seen that the strike point pattern is also unsymmetrical, and the neoclassical effect plays the important role in determining the strike point patterns for the case of high energy particles.

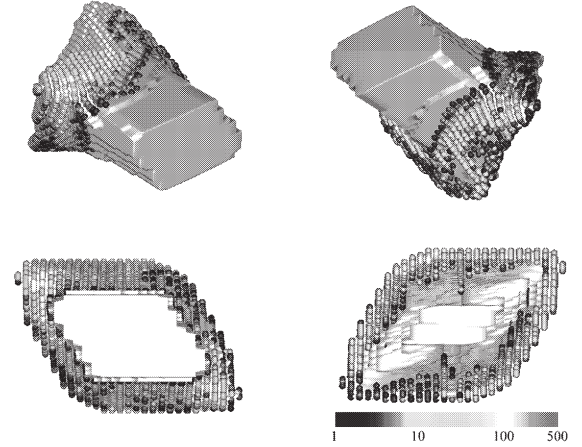


Figure 1: The strike point patterns, indicated by colored dots, on the LID head for the case of  $E = 5$  keV, where  $R_0 = 3.6$  m.

## References

- [1] Kanno, R. et al. : J. Plasma Fusion Res. Ser. **6** (2004) 527.
- [2] Jimbo, S. et al. : Nucl. Fusion **45** (2005) 1534.

### §13. Set of Model Equations for the Analysis of the Resistive Drift Wave Turbulence in Cylindrical Plasmas

Kasuya, N., Yagi, M. (RIAM, Kyushu Univ.), Azumi, M. (JAEA), Itoh, K., Itoh, S.-I. (RIAM, Kyushu Univ.)

Turbulent plasmas form a variety of structures, and researches have been carried out to clarify their role in plasma transport. Recently, plasma experiments in a simple linear configuration have been revisited for quantitative understandings of the structural formation mechanism by turbulence<sup>1)</sup>. These results motivate the detailed simulation study of plasma turbulence in a linear device. We have been developing a three-dimensional numerical simulation code called ‘Numerical Linear Device’ (NLD), which simulates the drift wave turbulence in a linear device<sup>2)</sup>. Turbulence characteristics obtained from the numerical simulation are compared with experiments to give comprehensive understanding of plasma transport. The model used in NLD for the analysis of the resistive drift wave turbulence is described here.

Turbulence measurements in linear devices, such as LMD in Kyushu University<sup>3)</sup> and CSDX in University of California San Diego<sup>1)</sup> are compared with our simulation. The plasma has a simple cylindrical shape. The plasma boundary is given at  $r = a$ . In this model, we do not solve the vacuum region, simply assuming that a background density profile has a fixed nonzero value at  $r = a$ . The magnetic field has only the component in the axial direction  $z$  with the uniform intensity  $B$ . According to experiments, high density ( $n_e > 1 \times 10^{19} [\text{m}^{-3}]$ ) and low temperature ( $T_e < 5 [\text{eV}]$ ) plasmas in an argon or neon discharge are analyzed. Only monovalent ions are considered, and the density of neutral particles is high even in the plasma core region, so the effect of neutral particles should be taken into consideration.

For describing the resistive drift wave turbulence in a linear device, the fluid model including the continuity equation, the momentum conservation equation of electrons and the charge conservation equation are used<sup>2)</sup>:

$$\frac{\partial n}{\partial t} + \vec{\nabla} \cdot (n \vec{v}_e) = 0, \quad (1)$$

$$nm_e \frac{d\vec{v}_e}{dt} = -\nabla p - ne(\vec{E} + \vec{v}_e \times \vec{B}) + n v_{ei} m_e (\vec{v}_i - \vec{v}_e) - n v_{en} m_e \vec{v}_e, \quad (2)$$

$$\vec{\nabla} \cdot \vec{J} = 0, \quad (3)$$

where  $d/dt = \partial/\partial t + [\varphi, \ ]$  is the convective derivative,  $\varphi$  is the electrostatic potential,  $n = n_e = n_i$  is the density,  $m_e$  is the mass of electron,  $p = nT$  is the pressure,  $\vec{J}$  is the current,  $\vec{v}_e$  and  $\vec{v}_i$  are the velocity of electron and ion,  $v_{ei}$  and  $v_{en}$  are the electron-ion and electron-neutral collision frequency, respectively. Quasineutrality holds for the dynamics of our interests, so that the charge conservation gives the form of Eq. (3). This set of equations gives an extension of the Hasegawa-Wakatani equations<sup>4)</sup> by (i) inclusion of an inertial term of electron and a resistive term caused by neutrals in Eq. (2), and (ii) consideration of

three-dimensional dynamics. The current in Eq. (3) is divided into components perpendicular and parallel to the magnetic field, and the perpendicular current is given to be

$$\vec{J}_\perp = en(\vec{v}_{i\perp} - \vec{v}_{e\perp}) = \frac{Mn}{B^2} \left( -\frac{d}{dt} \nabla_\perp \phi - v_{in} \nabla_\perp \phi \right), \quad (4)$$

where  $M$  is the mass of ions, and  $v_{in}$  is the ion-neutral collision frequency. The first and second terms of Eq. (4) come from the polarization current and the Pederson current, respectively. Equations (1) - (3) are written to be

$$\frac{dN}{dt} = -\nabla_\parallel V - V \nabla_\parallel N + \mu_N \nabla_\perp^2 N, \quad (5)$$

$$\frac{dV}{dt} = \frac{M}{m_e} (\nabla_\parallel \phi - \nabla_\parallel N) - v_e V + \mu_v \nabla_\perp^2 V, \quad (6)$$

$$\frac{d\nabla_\perp^2 \phi}{dt} = \nabla N \cdot \left( -v_{in} \nabla_\perp \phi - \frac{d\nabla_\perp \phi}{dt} \right) - v_{in} \nabla_\perp^2 \phi - \nabla_\parallel V - V \nabla_\parallel N + \mu_w \nabla_\perp^4 \phi, \quad (7)$$

by assuming  $v_{i\parallel} \ll v_{e\parallel}$ , substituting Eq. (4) into Eq. (3), and using normalization  $N = \ln(n/n_0)$ ,  $V = v_{i\parallel}/c_s$ ,  $\phi = e\varphi/T_e$ , where  $n_0$  indicates the value of density at  $r = 0$ ,  $v_{i\parallel}$  is the electron velocity parallel to the magnetic field,  $c_s = \sqrt{T_e/M}$  is the ion sound velocity and  $T_e$  is the electron temperature. Note that the time and distance are normalized by the ion cyclotron frequency  $\Omega_{ci} = eB/M$  and Larmor radius (at the electron temperature)  $\rho_s = c_s/\Omega_{ci}$ , respectively. The collision frequencies are normalized by  $\Omega_{ci}$  and  $v_e \equiv v_{ei} + v_{en}$ . The effects of neutrals are taken into account by  $v_{in}$  and  $v_{en}$  in Eq. (6) and (7). Artificial viscosities  $\mu_w$ ,  $\mu_N$  and  $\mu_v$  are added in Eqs. (5) - (7) for the purpose of numerical stability in nonlinear simulation.

Equations (5) - (7) compose the set of model equations for analyzing the resistive drift wave turbulence in NLD. The boundary condition in the radial direction  $r$  is set to  $\tilde{f} = 0$  at  $r = 0$ ,  $a$  when  $m \neq 0$ , and  $\partial \tilde{f} / \partial r = 0$  at  $r = 0$ ,  $\tilde{f} = 0$  at  $r = a$  when  $m = 0$ , where  $r = a$  gives an outer boundary of the plasma column and  $f$  implies  $\{N, \phi, V\}$ . The periodic boundary conditions in the azimuthal  $\theta$  and axial  $z$  directions are assumed, and the Fourier spectral expansion in  $\theta$  and  $z$  directions is adopted. To obtain  $\tilde{N}$ ,  $\tilde{\phi}$  and  $\tilde{V}$ , the terms in equations (5) - (7) are divided into linear and nonlinear parts. The linear parts are solved implicitly, and the nonlinear terms are advanced in time by using predictor-corrector method. The background density  $N_{bg}$ , potential  $\phi_{bg}$  and parallel velocity  $V_{bg}$  also affect the stability of the drift wave. Giving these quantities as the initial conditions, numerical simulations are carried out.

#### References

- 1) Tynan, G. R. et al.: Plasma Phys. Control. Fusion **48** (2006) S51.; Schröder, C. et al.: Phys. Plasmas **12** (2005) 042103.
- 2) Kasuya, N. et al.: J. Plasma Phys., in press.
- 3) Shinohara, S. et al.: Meeting Abstract Phys. Soc. Japan **61**, Vol. 2 (2006) 210.
- 4) Hasegawa, A. et al.: Phys. Rev. Lett. **59** (1987) 1581.

## §14. Linear Analysis of the Resistive Drift Wave Instability in Cylindrical Plasmas

Kasuya, N., Yagi, M. (RIAM, Kyushu Univ.), Azumi, M. (JAEA), Itoh, K., Itoh, S.-I. (RIAM, Kyushu Univ.)

Structural formation mechanisms in magnetically confined plasmas are crucial issues in plasma physics. We have been developing a three-dimensional numerical simulation code called Numerical Linear Device (NLD), which models a cylindrical plasma configuration<sup>1)</sup>. The three-field (density, potential and parallel velocity of electrons) reduced fluid model is adopted. Using this code, linear eigenmode analyses are performed to examine the condition for drift wave excitation in LMD in Kyushu University<sup>2)</sup>. The result of the parameter scan is reported here.

Simulation parameters are chosen, referring to the typical parameters in LMD with plasma turbulence: an argon discharge with  $B < 0.12$  [T],  $T_e < 5$  [eV],  $a = 50$  [mm],  $\lambda = 1.7$  [m],  $n_0 = n_e(r=0) \sim 1 \times 10^{19}$  [m<sup>-3</sup>], and neutral pressure  $p_0 \sim 3$  [mTorr]. Collision frequency  $\nu_{ei}$  is given by coulomb collisions. With these parameters,  $\nu_{ei}$  is larger than  $\nu_{en}$  given by elastic collisions<sup>3)</sup>. One has  $\nu_e \sim \nu_{ei} = 400$ , which is normalized by  $\Omega_{ci}$ , and  $v_{in}$  around 0.05 is used as a test parameter. The background density profile  $n_{bg}$  is fitted to the form

$$N_{bg} = \ln(n_{bg}/n_0) = N_0 \left( \exp\left[-(r/L_N)^2\right] - 1 \right),$$

where  $N_0 = 4$ , and gradient length  $L_N = 60$  are chosen based on the measurement in experiments.

Using these parameters, a linearly unstable eigenmode is obtained. The contour of the mode shows a weakly twisted shape in the  $\theta$  direction. This corresponds to the existence of the imaginary part in  $\tilde{N}$ . Similarly, the contour of  $\tilde{\phi}$  shows a twisted shape. The dependency of the eigen frequency and growth rate on the azimuthal mode number  $m$  shows that modes with low  $m$  are unstable.

There are adjustable parameters, which contribute to excite the drift wave turbulence. Dependencies of the mode growth rate and eigen frequency on the strength of the magnetic field, the device length, and the collision frequency are investigated for the  $(m, n) = (1, 1)$  mode to obtain an operation window. Figure 1 shows the dependency of the growth rate and frequency of the  $(m, n) = (1, 1)$  mode on the magnetic field in the case with  $T_e = 2$  [eV],  $a = 5$  [cm],  $v_{in} = 0.03$ ,  $\nu_e = 400$ ,  $N_0 = 2.0$ ,  $L_N = 50$ ,  $\phi_{bg} = 0$  and  $V_{bg} = 0$ . The strength of the magnetic field should be sufficiently high to obtain plasma turbulence. On the other hand, if the magnetic field is too strong, then the drift velocity becomes small, which gives a smaller growth rate of an unstable mode. There exists a maximum value of the growth rate as a function of the strength of the magnetic field. A wave with the wave length larger than the device length cannot be excited, so that the device length restricts the value of  $k_{||}$ . This is also the important factor to excite resistive drift wave. The dependency of the growth rate on the device

length shows that the necessary device length exists for resistive drift wave excitation. In this case,  $\lambda > 2$  [m] and  $B > 0.07$  [T] is necessary for the  $(m, n) = (1, 1)$  mode to be unstable.

The collision frequencies play an important role in the excitation of the resistive drift wave. The electron collision destabilizes the drift wave, so that it should be large. Since the ion-neutral collision strongly stabilizes the drift wave, it should be small. The stability boundaries for various strengths of the magnetic field on the  $v_{in} - \nu_e$  phase space are summarized in Fig. 2. The suitable parameters are  $B = 0.1$  [T] and  $\lambda = 4$  [m] for which wider unstable regime exists. It is found that on the experimental condition,  $\nu_e$  has a weak dependence and the threshold of  $v_{in}$  exists for the stability boundary. The smaller values of  $v_{in}$  by reduction of the neutral density or increase of the ionization ratio, or both, are necessary for excitation of the resistive drift waves<sup>4)</sup>. It is also desirable to produce a steep density profile.

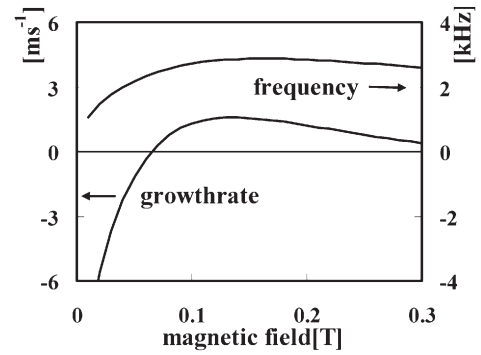


Fig. 1: Growth rate and frequency of linear eigenmodes  $(m, n) = (1, 1)$ . The dependencies on the strength of the magnetic field  $B$  with  $\lambda = 4$  [m] are shown.

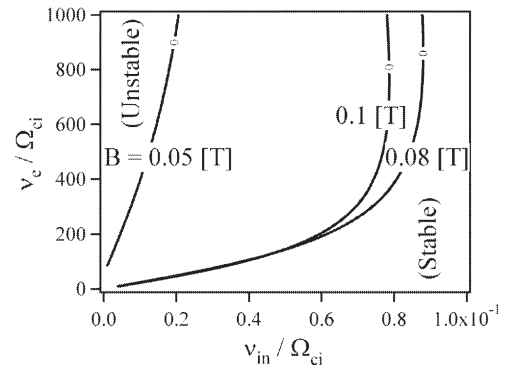


Fig. 2: Stability boundaries of the  $(m, n) = (1, 1)$  mode on the  $v_{in} - \nu_e$  phase space. The boundaries for various strengths of the magnetic field with  $\lambda = 4$  [m] are shown.

### References

- 1) Shinohara, S. et al.: Meeting Abstract Phys. Soc. Japan **61**, Vol. 2 (2006) 210.
- 2) Kasuya, N. et al.: J. Plasma Phys, in press.
- 3) Hayashi, M.: Institute of Plasma Phys., Nagoya Univ., Report IPPJ-AM-19 (1981).
- 4) Saitou, Y. et al.: in Proceedings of 33<sup>rd</sup> EPS Conference on Plasma Physics, Roma, 2006, in press

## §15. Nonlocal Stability Analysis of Microinstabilities in Inhomogeneous Plasmas

Sanuki, H.,  
Gao Zhe (Tsinghua Univ., China),  
Dong, J.Q. (SWIP, China)

In the present work, **analytical** methods such as WKB method associated with both differential equation and integral equation in wave number space (k-space) and numerical analysis with gyrokinetic integral equation are reviewed. Drift waves such as ion temperature gradient modes (SWITG) and electron temperature gradient modes (SWETG) in short wavelength region are studied with a gyrokinetic integration code in both slab and toroidal plasmas.

We here discuss the WKB analysis in different two approaches on the basis of the differential equation and the integral equation in k-space.

(1) WKB Solution of second order differential equation

For simplicity, we first consider an electrostatic modes in an inhomogeneous plasmas, which is described by the following equation,

$$\frac{d^2\phi}{dz^2} - Q(z)\phi = 0, \quad (1)$$

where  $\phi(z)$  is the electrostatic potential and  $Q(z)$  is complex in general.

We finally obtain the WKB solution as

$$\phi(z_c) = \sum_{+,-} A_{\pm} Q^{-1/2}(z_c) \exp[\pm \int_{z_1, z_2}^{z_c} Q^{1/2}(z) dz]$$

and the eigenvalue relation can be derived from the connection formulae between the solutions of inside and outside of turning points as

$$\int_{z_1}^{z_2} [-Q(z_c)]^{1/2} dz_c = \pi(n + 1/2), \quad (n = 0, 1, 2, \dots)$$

(2) WKB Solution of Integral Equation in K-Space

We also discuss the highly localized electrostatic modes in an inhomogeneous (x-direction) plasma in case of  $k\rho \geq 1$ . The Vlasov – Poisson equations give the following integral equation in k-space instead of (1)

$$(k^2 + k_y^2 + k_z^2)\phi(k) = \int K(k', k; \omega)\phi(k') dk'$$

and we introduce an eikonal function in k-space in a form,

$$\phi(k) = \exp(-i \int g(k') dk'),$$

then, we finally have the following so called quantization condition,

$$\oint g_0(k) dk = 2(n + 1/2)\pi$$

These results have been presented in 5<sup>th</sup> APFA conference in Jeju island, Korea, August, 2005.



## §16. Multiple Eigenmodes of Geodesic Acoustic Mode in Collisionless Plasmas

Gao Zhe (Tsinghua Univ., China),  
Itoh, K., Sanuki, H.,  
Dong, J.Q. (SWIP, China)

Zonal flow (ZFs), which are poloidal  $E \times B$  plasma flows due to toroidally and poloidally symmetric ( $m=n=0$ ) potential perturbations, have attracted increasing attention. It is widely accepted that there are two types of ZFs, namely, one is the low/zero frequency branch, the other is higher frequency oscillation, so called the geodesic acoustic mode (GAM). ZFs are believed to be driven by turbulence, and moderate turbulence and turbulent transport. However, both the low frequency ZF and GAM are plasma eigenmodes. Recent progress of the experimental research on GAM has shown that multiple eigenmodes of GAM coexist simultaneously. This encourages the research on various types of branches in the family of ZFS.

In the present work, for simplicity, we consider a simple axisymmetric toroidal system with standard model magnetic

field. An electrostatic potential, which is rigid constant on a magnetic surface, is assumed. This simplification is valid in the case of  $T_e \ll T_i$  since the potential variation is related to finite  $T_e/T_i$ . Using this model under some assumptions, a series of GAM eigenmodes is studied, which includes the standard GAM, a branch of low frequency mode and a series of Ion Sound Wave (ISW)-like modes. Eigenfrequencies of these modes are obtained analytically from a linear gyrokinetic model in collisionless toroidal plasmas with a constant electrostatic potential around a magnetic surface. The ISW-like mode has a discrete frequency spectrum roughly with a progression of  $\sqrt{n\pi}$  times the transit frequency and strongly damped, where  $n$  is the natural number. The low frequency eigenmode has a rigid zero frequency for low  $q$  but oscillates with a finite frequency of  $0.2(v_{ti}/qR)\sqrt{1-1.4/q^2}$  for  $q>1.2$ , and relaxes on the scaling with the order of transit frequency,  $v_{ti}/qR$ . Considering different damping rates of these modes, only a few (the least damped and/or the most excited) modes may play an important role in the turbulence dynamics.

These results will appear in PoP.

## §17. Critical Gradients for Short Wavelength Ion Temperature Gradient Instability in Toroidal Plasmas

Gao Zhe (Tsinghua Univ., China),  
Sanuki, H., Itoh, K.,  
Dong, J.Q. (SWIP, China)

Recently, the short wavelength ion temperature gradient (SWITG) instability has attracted increasing attention, partly because it can produce a significant level of anomalous transport with mixing length estimate theory and partly because the excitation of the SWITG mode seems to require both ion and electron temperature gradient ( $\eta_i$  and  $\eta_e$ ) exceed thresholds. We studied the physical mechanism of toroidal SWITG instability and confirmed that the double-humped behavior in the growth rate, that is, conventional ITG and SWITG modes, is attributable to the toroidal drift/Landau resonance mechanism and the nonmonotonic behavior of the effective frequency as the wavelength varies. In this paper, a systematic parameter study of the toroidal SWITG modes is performed with a gyrokinetic integral code. Marginal stability curve in  $\eta_e - \eta_i$  space is numerically obtained, as well as the scaling of the critical gradient with respect to temperature ratio, toroidicity, and magnetic shear and safety factor. Algebraic formulae for the critical gradient are presented. Possibility of

the SWITG instability as a possible candidate to explain anomalous transport is discussed.

We employ a gyrokinetic integral equation code, where the ballooning representation for an axisymmetric toroidal geometry with circular flux is applied. The magnetic curvature and gradient drift, transit effect and finite Larmor radius effect are all retained for both ions and electrons, but the finite  $\beta$  and trapped particle effect are neglected. The eigenmode equation is as follows

$$(1 + Z_i \tau_i) \phi(k) = \int_{-\infty}^{\infty} dk' / \sqrt{\pi} [H_j(k, k') \phi(k')]$$

where  $\phi(k)$  is the extended Fourier component in ballooning space of  $\phi(r)$ .

The stabilization diagram of the  $l=0$  and  $l=1$  modes in  $\eta_e - \eta_i$  space is shown in Fig. 1.

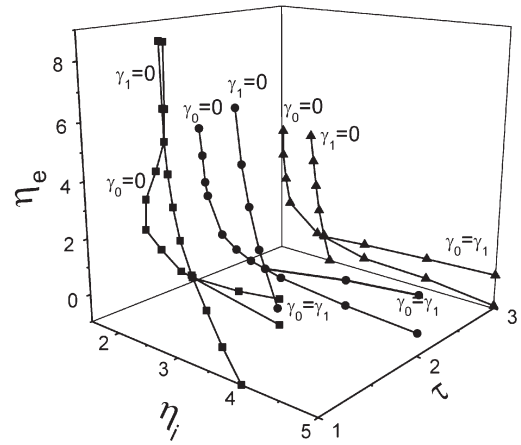


Fig.1 The stabilization diagram in the  $\eta_e - \eta_i$  space

Zhe Gao, H.Sanuki, K. Itoh and J.Q.Dong, presented in ICNSP in Nara and also submitted to J. Plasma Physics.

## §18. Kinetic Ballooning Mode in s- $\alpha$ Tokamak

Yamagishi, O., Sugama, H., Watanabe, T.-H.

A simple concentric tokamak are described by the model MHD equilibrium with two parameters; shear  $s$  and pressure-gradient  $\alpha$ , which is known to s- $\alpha$  model. Thus the linear ideal ballooning modes are characterized by these two parameters. When we consider more exact formulation than the ideal MHD, such as gyrokinetics or two-fluid model, the only one parameter  $\alpha$  in the s- $\alpha$  model is decomposed into  $\alpha = -q^2 R d\beta / dr = q^2 [(\beta_e + \beta_i) R / L_n + \beta_e R / L_{Te} + \beta_i R / L_{Ti}]$ , which includes betas, density gradient and temperature gradient for each species. Here  $1/L_X = -d \ln X / dr$ .

In this report, the linear stability in a s- $\alpha$  tokamak is investigated based on the gyrokinetics. The modes are electromagnetic shear Alfvén modes, so called KBM. We concentrate on  $\alpha$  parameter dependence, and the results are compared with ideal ballooning case.  $\beta_i = \beta_e = \beta / 2$  is assumed, and  $\beta$ ,  $R/L_n$ ,  $R/L_{Ti}$ , and  $R/L_{Te}$  are scanned for  $\alpha$ . Other parameters are fixed:  $s=0.78$ ,  $q=1.4$ ,  $r/R=0.18$ ,  $k_\theta / \rho_{thi}=0.4$ .

The results are shown in Fig.1. From top to bottom, the gradient  $1/L_n$ ,  $1/L_{Te}$ , and  $1/L_{Ti}$  respectively are changed separately for  $\alpha$ , and other gradients are set to zero. Followings are expected as main kinetic effects: (i) ion FLR effects, (ii) trapped particle effects, and (iii)  $k_\parallel v_{||}$  resonance.

For  $1/L_n$ - and  $1/L_{Te}$ -KBM, the 1<sup>st</sup> stability boundary almost coincides with that of ideal MHD. On the other hand,  $1/L_{Ti}$ -KBM is unstable lower than the MHD 1<sup>st</sup> stability boundary. This may be a result of coupling of ITG branch and KBM branch, with  $k_\parallel v_{||}$  resonance. There is a possibility that the  $1/L_n$ -KBM can also be coupled with the TEM driven by  $1/L_n$  to make the 1<sup>st</sup> stability boundary lowered; however it is not found. This may be because the sign of real frequency of TEM is positive and opposite to that of KBM (coupling needs the jump). As the gradient increases, the FLR effects become strong for  $1/L_n$  and  $1/L_{Ti}$  cases. Simple FLR model suggests that the stabilization of FLR by  $1/L_{Ti}$  is as twice strong as that for  $1/L_n$ . Thus,  $1/L_{Ti}$ -KBM is stabilized at sufficiently lower critical  $\alpha$  than that of MHD. For  $1/L_n$ - and  $1/L_{Te}$ -KBM, the trapped particle (TP) effects can also be effective. Unlike the conventional analytic arguments, the TP effects are found to be destabilizing. In the  $1/L_n$  case, the stabilizing FLR and destabilizing TP effects co-exist, and the 2<sup>nd</sup> stability boundary is almost the same as that

of MHD. On the other hand, since FLR never work for  $1/L_{Te}$ -KBM, it is unstable well beyond the MHD boundary, by the TP effects. In usual experiments, these different gradients co-exist, and both the 1<sup>st</sup> and 2<sup>nd</sup> stability boundary will not coincide with that of ideal MHD.

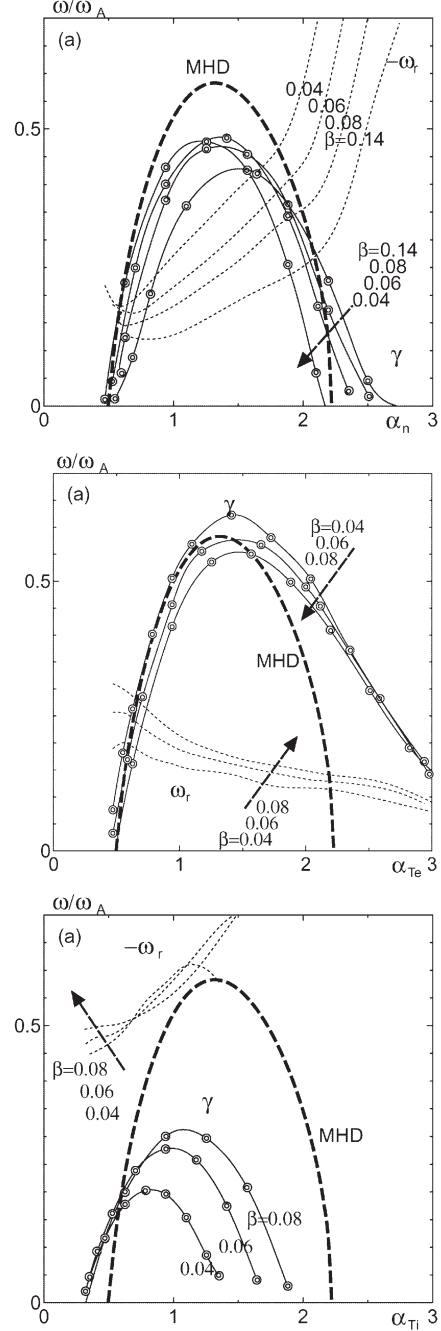


Figure 1: KBM growth rate(lines with marks) and real frequencies(dotted lines), and ideal MHD growth rate (thick dashed lines), which are driven by the density gradient(top), electron temperature gradient(mid), and ion temperature gradient(bottom).

## §19. Effects of Trapped Particles on Residual Zonal Flows in Helical Systems

Sugama, H., Watanabe, T.-H.

An initially-supplied  $\mathbf{E} \times \mathbf{B}$  rotation is not fully damped by collisionless processes but it approaches a stationary flow called the residual zonal flow. In helical systems, the long-time limit of the zonal-flow potential [1,2] is written as

$$\lim_{t \rightarrow \infty} \phi_{\mathbf{k}_\perp}(t) = \mathcal{K}_> \phi_{\mathbf{k}_\perp}(0), \quad (1)$$

where

$$\begin{aligned} \mathcal{K}_> &\equiv \lim_{t/\tau_c \rightarrow +\infty} \mathcal{K}_L(t) \\ &= \langle k_\perp^2 a_i^2 \rangle \left[ 1 - (2/\pi) \langle (2\epsilon_H)^{1/2} \rangle \right] \\ &\quad \times \left\{ \langle k_\perp^2 a_i^2 \rangle [1 - (3/\pi) \langle (2\epsilon_H)^{1/2} \rangle + G] \right. \\ &\quad \left. + (2/\pi)(1 + T_i/T_e) \langle (2\epsilon_H)^{1/2} \rangle \right\}^{-1}. \end{aligned} \quad (2)$$

Here, effects of the helical configuration are included in  $\epsilon_H$  as well as  $G$  that represents the geometrical factor defined by the ratio of the neoclassical polarization due to toroidally trapped ions to the classical polarization. In order to examine the analytical results shown above, a linearized ion gyrokinetic equation combined with the quasineutrality condition is numerically solved by a toroidal flux-tube gyrokinetic Vlasov code [3]. Here, we consider the  $L = 2/M = 10$  single-helicity case, in which  $\epsilon_H \equiv \epsilon_h$  is independent of  $\theta$ . A good agreement between our theory and simulation results is confirmed as shown in Fig.1.

Figure 2 shows the real part of the perturbed ion gyrocenter distribution function  $\delta f_{i\mathbf{k}_\perp}^{(g)}$  on the  $(v_\parallel, v_\perp)$ -space obtained by the gyrokinetic Vlasov simulation at  $t = 12.5(R_0/v_{ti})$  for the case of the helical system. Here,  $r/R_0 = 0.1$ ,  $\epsilon_h = 0.1$ ,  $q = 1.5$ ,  $k_r a_i = 0.131$ , and  $(\theta, \zeta) = (8\pi/13, 12\pi/13)$  are used and  $\delta f_{i\mathbf{k}_\perp}^{(g)}$  is normalized by  $e\phi_{\mathbf{k}_\perp}(0)/T_i$ . For the poloidal and toroidal angles  $(\theta, \zeta) = (8\pi/13, 12\pi/13)$ , helical-ripple-trapped particles have relatively large radial drift velocities  $\bar{v}_{dr}$ . Due to the parallel streaming of passing ions, stripes (or ballistic-mode structures) appear along the  $v_\perp$ -direction in Fig.2, where significantly deformed ion-distribution structures due to the resonances between the GAM and passing ions are observed. These resonances contribute to collisionless damping of the GAM oscillations. We see that the ion gyrocenter distribution in the helical-ripple-trapped region localized around  $v_\parallel \sim 0$  has a distinctive hollow that is produced by a modulation along the  $v_\perp$ -direction due to the finite radial drift and influences the magnitude of the residual zonal flow.

It is expected that, in optimized helical configurations where the neoclassical ripple transport is significantly reduced by suppressing both  $|\bar{v}_{dr}|$  and  $G$ , large

zonal flows can be maintained for a long-time period and contribute to a reduction of anomalous transport as well.

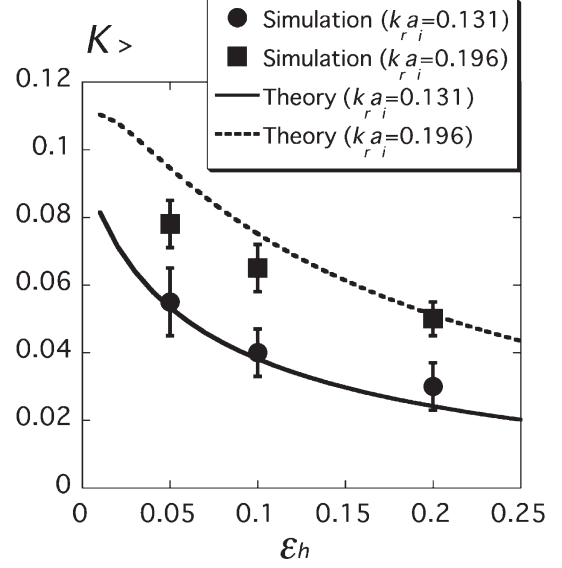


Fig.1. The long-time limit of the response kernel  $\mathcal{K}_>$  as a function of  $\epsilon_h$  for  $k_r a_i = 0.131, 0.196$ , and  $\epsilon_t = 0.1$ . The simulation results and the theoretical formula in Eq. (2) are represented by symbols with error bars and curves, respectively.

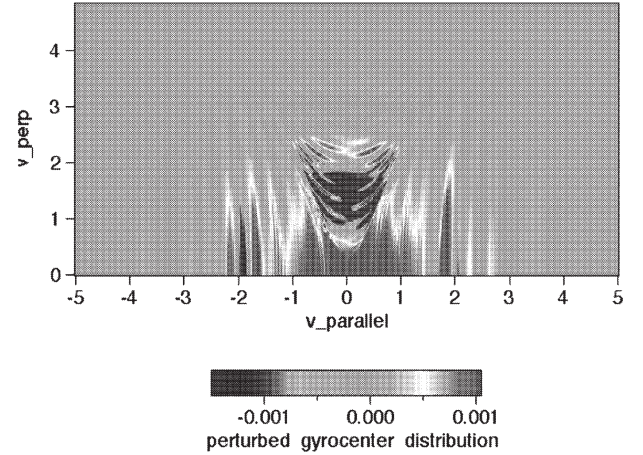


Fig.2. The real part of the perturbed ion gyrocenter distribution function  $\delta f_{i\mathbf{k}_\perp}^{(g)}$  on the  $(v_\parallel, v_\perp)$ -space obtained by the simulation at  $t = 12.5(R_0/v_{ti})$  for the case of the helical system. Here,  $r/R_0 = 0.1$ ,  $\epsilon_h = 0.1$ ,  $q = 1.5$ ,  $k_r a_i = 0.131$ , and  $(\theta, \zeta) = (8\pi/13, 12\pi/13)$  that corresponds to the bottom of the local helical ripple with helical-ripple-trapped particles having relatively large radial drift velocities.

### References

- 1) H. Sugama and T.-H. Watanabe, Phys. Plasmas **13**, 012501 (2006).
- 2) H. Sugama and T.-H. Watanabe, Phys. Rev. Lett. **94**, 115001 (2005).
- 3) T.-H. Watanabe and H. Sugama, Nucl. Fusion **46**, 24 (2006).



## §20. Collisionless Damping of Zonal Flows in Helical Systems

Sugama, H., Watanabe, T.-H.

We here consider helical systems with the magnetic field strength written by a function of poloidal and toroidal angles as  $B = B_0[1 - \epsilon_{10} \cos \theta - \epsilon_{L0} \cos(L\theta) - \sum_{|n| \leq n_{max}} \epsilon_h^{(n)} \cos\{(L+n)\theta - M\zeta\}] = B_0[1 - \epsilon_T(\theta) - \epsilon_H(\theta) \cos\{L\theta - M\zeta + \chi_H(\theta)\}]$ . Using the gyrokinetic equations combined with the quasineutrality condition, an analytical expression describing the collisionless response of the zonal-flow potential to the initial potential is derived [1,2] as

$$\phi_{k\perp}(t) = \mathcal{K}(t) \phi_{k\perp}(0) \quad (1)$$

where the response function (or kernel)  $\mathcal{K}(t)$  is written as

$$\mathcal{K}(t) = \mathcal{K}_{GAM}(t)[1 - \mathcal{K}_L(t)] + \mathcal{K}_L(t). \quad (2)$$

The long-time response is denoted by  $\mathcal{K}_L(t)$  that gives the residual zonal-flow level in the limit  $t \rightarrow \infty$ . The short-time response  $\mathcal{K}_{GAM}(t)$  represents the GAM oscillations given by

$$\mathcal{K}_{GAM}(t) = \cos(\omega_G t) \exp(\gamma t). \quad (3)$$

with  $\omega = \omega_G + i\gamma$  determined by  $1/\mathcal{K}_{GAM}(\omega) = 0$ . Here,  $\mathcal{K}_{GAM}(\omega)$  is defined by

$$\begin{aligned} \frac{1}{\mathcal{K}_{GAM}(\omega)} \equiv & -i\hat{\omega} - i\frac{q^2}{2} \left[ \left( \frac{R_0 \epsilon_{10}}{r} \right)^2 \{J(\hat{\omega}) + J_{FOW}(\hat{\omega})\} \right. \\ & + L \left( \frac{R_0 \epsilon_{L0}}{r} \right)^2 J \left( \frac{\hat{\omega}}{L} \right) \\ & + \sum_{|n| \leq n_{max}} \frac{(L+n)^2}{|L+n-qM|} \left( \frac{R_0 \epsilon_h^{(n)}}{r} \right)^2 \\ & \left. \times J \left( \frac{\hat{\omega}}{|L+n-qM|} \right) \right], \end{aligned} \quad (4)$$

with  $\hat{\omega} \equiv R_0 q \omega / v_{Ti}$  ( $v_{Ti} \equiv \sqrt{2T_i/m_i}$ ),

$$\begin{aligned} J(\hat{\omega}) \equiv & 2\hat{\omega}^3 + 3\hat{\omega} + (2\hat{\omega}^4 + 2\hat{\omega}^2 + 1)Z(\hat{\omega}) \\ & - \frac{\hat{\omega}}{2} \left\{ 2\hat{\omega} + (2\hat{\omega}^2 + 1)Z(\hat{\omega}) \right\}^2 \\ & \times \left\{ \frac{T_i}{T_e} + 1 + \hat{\omega}Z(\hat{\omega}) \right\}^{-1}, \end{aligned} \quad (5)$$

and

$$\begin{aligned} J_{FOW}(\hat{\omega}) \equiv & i\frac{\sqrt{\pi}}{2} \left( \frac{k_r v_{Ti} q}{\Omega_i} \right)^2 e^{-\hat{\omega}^2/4} \\ & \times \left\{ \frac{\hat{\omega}_r^6}{64} + \left( \frac{\hat{\omega}_r^4}{8} + \frac{3\hat{\omega}_r^2}{4} + 3 + \frac{6}{\hat{\omega}_r^2} \right) \right. \\ & \times \left( 1 - \frac{3\hat{\omega}_r}{16} \left\{ 2\hat{\omega}_r + (2\hat{\omega}_r^2 + 1)Z_r(\hat{\omega}_r) \right\} \right. \\ & \left. \left. \times \left\{ \frac{T_i}{T_e} + 1 + \hat{\omega}_r Z_r(\hat{\omega}_r) \right\}^{-1} \right\} \right\}. \end{aligned} \quad (6)$$

On the right-hand side of Eq. (5), the plasma dispersion function  $Z(\hat{\omega}) \equiv \pi^{-1/2} \int_{-\infty}^{\infty} d\alpha e^{-\alpha^2}/(\alpha - \hat{\omega})$  is used.  $J_{FOW}$  given in Eq. (6) is derived from retaining the finite-orbit-width (FOW) effect on the gyrocenter distribution function. The validity of our analytical results is verified by gyrokinetic Vlasov simulation as shown in Fig.1. It is found that helical ripples in the magnetic field strength as well as finite orbit widths of passing ions enhance the GAM damping.

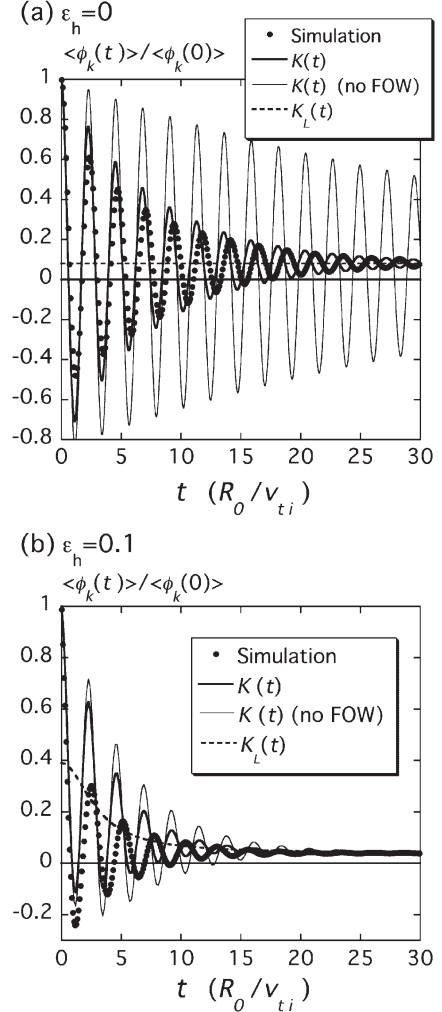


Fig.1. Time evolution of the zonal-flow potential obtained by the simulations for the tokamak case ( $\epsilon_h = 0$ ) (a) and for the helical system ( $\epsilon_h = 0.1$ ) (b). In both case,  $r/R_0 = 0.1$ ,  $q = 1.5$  and  $k_r a_i = 0.131$  are used. The simulation results are plotted by solid circular symbols. Thick solid curves represent the response kernel  $\mathcal{K}(t)$  obtained by Eq. (2) with the use of the complex-valued GAM frequency  $\omega = \omega_G + i\gamma$  calculated by numerically solving  $1/\mathcal{K}_{GAM}(\omega) = 0$  where  $\mathcal{K}_{GAM}(\omega)$  is defined by Eq. (4). Thin solid curves represent the response kernel  $\mathcal{K}(t)$  obtained by neglecting the FOW effect when calculating  $(\omega_G, \gamma)$ . The long-time response kernel  $\mathcal{K}_L(t)$  is also plotted by dashed lines.

### References

- 1) H. Sugama and T.-H. Watanabe, Phys. Plasmas **13**, 012501 (2006).
- 2) H. Sugama and T.-H. Watanabe, Phys. Rev. Lett. **94**, 115001 (2005).

## §21. Simulations of Electron Bernstein Waves and Zonal Flow Damping in Helical Systems

Ferrando i Margalet, S., Yoshimura, Y., Suzuki, Ch., Sugama, H., Watanabe, T.-H.

### 1) Simulation of EBW and EBCD in CHS

Recent work at the CHS experiment in NIFS has revealed an enhancement of the stored energy that is thought to be due to the absorption of Electron Bernstein Waves (EBW). The O-mode wave utilised in the shot studied (#129213) has its resonant region beyond the O-mode cutoff. Thus, in this case, the power deposition can only exist after mode-conversion into a EBW which is unaffected by cutoffs due to its electrostatic nature. In the present work, simulations of OXB mode-conversion and EBW absorption are performed for this experimental scenario with the ART code [1](see Fig.1). In addition, self-consistent MHD equilibria with Bootstrap Current (BC) (calculated with the VMEC [2] and the TERPSICHORE [3] codes, respectively) are carried out in order to establish which fraction of the measured total current is due to the BC. A discrepancy between BC and total current may suggest the presence of EBW induced current (EBCD). EBCD is estimated with the JALON module [4] implemented within the ART ray-tracing code [5]. The final aim is the reproduction of the experimental results when both EBCD and BC are calculated self-consistently with the equilibrium.

This studies are to be bench-marked with calculations carried out with the TRUBA code [6] in CIEMAT (Madrid, Spain).

### 2) Gyrokinetic simulation of zonal-flow evolution in multiple-helicity helical fields

Experimental results in LHD have shown an improvement of the confinement when the magnetic axis of the configuration is shifted inwards and a deterioration when it is shifted outwards. Zonal Flows (ZF) are widely accepted to be a source of reduction of anomalous transport and, hence, of enhancement of the confinement when they are not fully damped in the long term. This fact has been theoretically studied in the past for tokamaks [7] and later extended to helical systems [8]. In addition, gyrokinetic simulations in helical systems with single-helicity magnetic fields have also been performed [8,9]. However, the modelling of the LHD shifted-axis configurations re-

quires the inclusion of multiple-helicity terms in the magnetic field expansion. At present, linear gyrokinetic Vlasov simulations of ZF and Geodesic Acoustic Mode (GAM) damping in multiple-helicity configurations are in progress together with their comparison with the unstable modes behaviour. The results of these simulations will provide a starting point to non-linear calculations required to describe accurately the turbulent transport in these multiple-helicity scenarios. Finding a correspondence between certain multiple-helicity terms and the ZF damping will help to elucidate the optimal magnetic geometry for greater improvement of confinement.

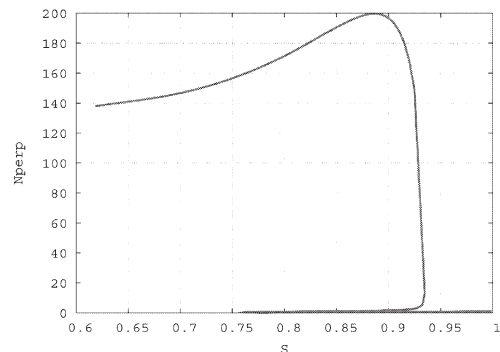


Fig.1.  $N_{\perp}$  profile for CHS shot #129213. The characteristic OXB mode conversion behaviour can be seen, i.e.,  $N_{\perp}$  goes to 0 at the O-X conversion region (O-mode cutoff,  $\omega = \omega_{pl}$ ) and becomes a vertical line in the Upper Hybrid Resonance Layer where the X-B mode conversion takes place. The power deposition occurs beyond the O-mode cutoff region.

### References

- 1) S.P. Hirshman and Hogan, Jour. Comp. Phys. **63**, 329 (1986).
- 2) W.A. Cooper *et al*, Plas. Phys. Cont. Fusion **44**, B357 (2002).
- 3) F. Volpe, PhD Thesis Max-Planck Institute (2003).
- 4) F. Castejon and S. Eguilior, Plas. Phys. Cont. Fusion **45**, 159 (2003).
- 5) S.Ferrando i Margalet, PhD Thesis CRPP Lausanne (2005).
- 6) F. Castejon *et al*, Fus. Scie. Techn. **46**, 327 (2004).
- 7) M. N. Rosenbluth and F. L. Hinton, Phys. Rev. Lett. **80**, 724 (1998).
- 8) H. Sugama and T.-H. Watanabe, Phys. Rev. Lett. **94**, 115001 (2005).
- 9) H. Sugama and T.-H. Watanabe, Phys. Plasmas **13**, 012501 (2006).

## §22. Zonal Flows, Geodesic Acoustic Modes and Geodesic Transfer in the H-1 Helic

Yokoyama, M.,  
Shats, M.G., Xia, H. (Australian National Univ.)

Evidence in support of strong geodesic transfer of energy from mean zonal flow to sideband modes in the H-1 heliac has been revealed. Analysis of the heliac magnetic structure shows that geodesic curvature is considerably stronger in H-1 than in tokamaks and should have stronger impact on geodesic transfer.

Poloidal variation of  $B$  in toroidal devices is associated with the geodesic curvature, that is, the surface component of the magnetic field line curvature [1]. A parameter which we use here to characterize the geodesic curvature is also a measure of the poloidal viscosity. We evaluate the poloidal viscous damping rate coefficient,  $C_p$ , derived in Ref [2], which can be calculated from the variation of the magnetic field strength,  $B$ , in the poloidal direction in the Hamada coordinates. Larger  $C_p$  corresponds to larger geodesic curvature effect. We will focus on the magnetic configuration, characterized by very low magnetic shear and relatively high rotational transform, which we will refer to as the  $\kappa_H=1$  configuration. Here,  $\kappa_H$  denotes the ratio of the helical winding current to the current in the poloidal field coil.

Figure 1 shows radial profile of  $C_p$  for two cases, the H-1  $\kappa_H=1$  configuration, and the tokamak-like configuration. In the latter case of an equivalent tokamak, only contributions from axisymmetric components of magnetic field spectrum in the Hamada coordinates are taken into account. The horizontal axis represents geometrical inverse aspect ratio,  $r/R$ . It is obvious that  $C_p$  for the H-1 heliac is significantly larger than that in the equivalent tokamak. This difference arises from the variation of  $B$  due to higher poloidal mode numbers. Since poloidal mode numbers contribute to  $C_p$  in a square manner, the magnetic field components with higher poloidal mode numbers substantially increase  $C_p$  even if their amplitudes are relatively small.

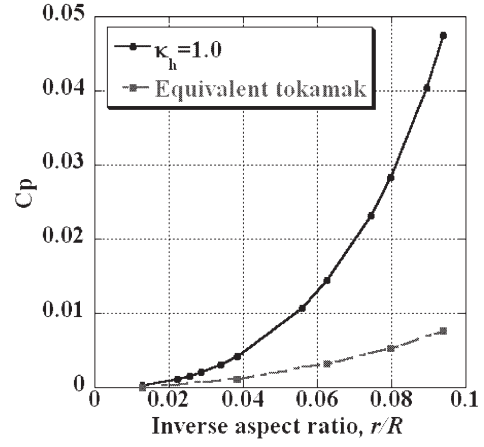


Fig. 1. The radial profile of  $C_p$  for a  $\kappa_H=1$  configuration in H-1 and its equivalent tokamak.

This strong geodesic curvature in H-1 should lead to the generation of geodesic acoustic oscillations and GAM for even modest mean zonal flows. A clear correlation between the increase in the nonlinear energy transfer from the unstable range, the increase in the mean zonal flow and the increase in the level of the sideband modes is observed, which supports this expectation. At low  $\langle E_r \rangle$  a geodesic acoustic oscillation seen as a  $m=1, n=0$  mode in both the density and electrostatic potential is observed as expected from theory [1]. As the drive for the geodesic transfer is increased, spectrum of the sideband modes becomes richer showing more modes including the  $m=0, n=0$  finite frequency zonal flow, or GAM. This is similar to the results of numerical simulation of turbulence [3] which show several sideband oscillations at frequencies up to  $f_{\text{GAM}}$  (GAM-frequency) in the presence of strong geodesic transfer, while in the absence of the geodesic curvature all these frequencies are greatly reduced leaving only one prominent feature at  $f \approx 0$ , mean zonal flow.

### References

- 1) N.Winsor, J.L.Johnson and J.M.Dawson, Phys. Fluids **11** (1968) 2448.
- 2) H.Wobig et al., Plasma Phys. Controll. Fusion, **37**(1995)893.
- 3) B.D.Scott, New J. Phys. **7** (2005) 92.

## §23. Hollow Density Profile in LHD

Yamagishi, O., Nakajima, N., Yokoyama, M., Tanaka, K., Michael, C.

In the LHD, observed density profiles are often hollow in various configurations, for example R=3.75m configuration, which seems to be different from tokamaks whose the density profile is flat or peaked. On the other hand, it is discussed recently that the density profile tends to be flat near the R=3.53m configuration, which is neoclassically optimized configuration<sup>1)</sup>.

In this report, we will investigate the neoclassical(NC) and anomalous quasi-linear(QL) particle fluxes across a magnetic surface, in order to discuss the tendency of the density profiles observed in two LHD configurations whose magnetic axis in vacuum are R=3.75m and R=3.53m. For the QL anomalous flux, GOBLIN code<sup>2)</sup> based on the linear gyrokinetics is used. For the NC ambipolar flux, GSRAKE code<sup>3)</sup> based on the bounce-averaged drift kinetics is used.

Three density profiles are assumed as in Fig.1; peaked (circles), intermediate (triangles) and squares (hollow). The temperature is assumed as  $T=T_0(1-\rho^2)$  with  $T_0=1$ [keV]. Also  $B_0=1$ [T] is assumed.

The neoclassical particle fluxes for these density profiles are shown in Fig.2, in R=3.75m and R=3.53m configurations. It can be seen that the NC particle flux is almost independent of density profiles, and shows strong configuration dependence. The latter is explained by the strong change of  $\varepsilon_{\text{eff}}$ <sup>1)</sup>. The weak dependence on the density profiles, or  $1/L_n$  on the NC particle flux in the  $1/\nu$  regime can be also explained<sup>2)</sup>; it is dominated by  $1/L_T$ .

Next the QL particle flux are plotted as a function of  $1/L_n$  in Fig.3. Here a surface  $\rho=0.8$  and  $k_\perp \rho_{\text{thi}}=0.5$  are chosen. Since the parameters above give  $\beta_{\text{ax}} \sim 0.8\%$  so that the mode can be considered electrostatic. The ITG and TEM are candidates in this case, and we can confirm that the modes here are basically ITG modes with weaker TEM-drive. We can also confirm that the results are insensitive to the magnetic configurations. On the other hand, as is contrast with the neoclassical case, it strongly depends on  $1/L_n$ ; the sign is changed as  $1/L_n$  becomes negative.

Here we consider the particle balance equation,  $\partial n / \partial t + \nabla \cdot \Gamma = S$ , where  $S$  is particle source. In the gas puff plasmas, the NBI is not main particle source, so the source is deposited only near the edge. Thus in the steady state, in the core,  $(1/r) \partial / \partial r [r(\Gamma^{\text{NC}} + \Gamma^{\text{QL}})] = 0$  should

be satisfied, yielding (by integrating with  $rdr$ )  $\Gamma^{\text{NC}} + \Gamma^{\text{QL}} = 0$ . When  $\Gamma^{\text{NC}}$  is large, since the positive tendency of  $\Gamma^{\text{NC}}$  is robust, the negative  $\Gamma^{\text{QL}}$  is needed. This will impose the density profile to be hollow, from Fig.3. This discussion will be applicable to other devices if  $1/\nu$  NC flux can become large.

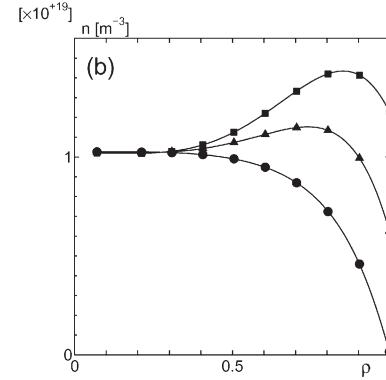


Figure 1: Assumed density profiles.

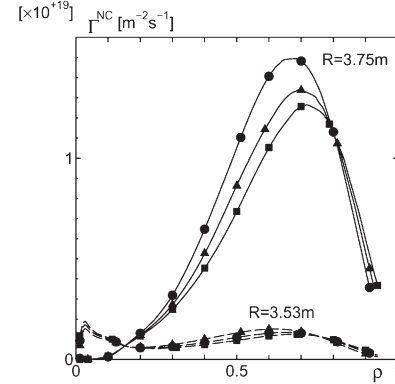


Figure 2: Neoclassical particle flux in R=3.75m(solid) and R=3.53m(dashed) LHD configurations.

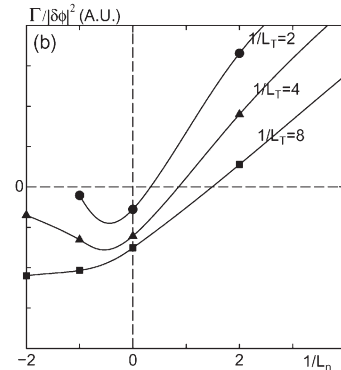


Figure 3: Quasi-linear particle flux in R=3.75m configuration at  $\rho=0.8$ , which is mainly by the ITG .

- 1) S.Murakami et al., Nucl. Fusion **42** L19 (2002)
- 2) O.Yamagishi et. al., to be submitted to Phys. Plasmas
- 3) C.D.Beidler et. al., Plasma Phys. Control. Fusion **37**, 463 (1995)



## §24. On the Basis of Statistical Theory of Strong Turbulence in Inhomogeneous Plasmas

Itoh, S.-I., Mori, H. (RIAM, Kyushu Univ.),  
Itoh, K.

A statistical model for plasma turbulence is examined [1] by employing a basis from the Mori method [2]. The Mori method provides a base for the existence of the separation of the memory function from fluctuating force in the nonlinear dynamical equations. An analytic model for the turbulent damping coefficient is derived by use of the Green's function. The model formula takes a non-Markovian form, representing the property of the time-reversibility of the basic equation. A recurrence formula is derived. The continued fraction form is also derived. A formula of the eddy-damping rate is derived. A rigorous relation which is derived by the Mori method is discussed, and is compared to the modelling. This comparison explains a nature of approximation in the modelling.

The dynamical nonlinear equations of fluctuations are given in terms of Fourier components, Eq.(2) is rewritten as

$$\partial f_k / \partial t + \mathcal{L}_k^{(0)} f_k = \mathcal{N}_k \equiv \sum_{k=p+q} M_{kpq} f_p f_q \dots$$

where  $\mathcal{L}^{(0)}$  denotes the linear operator,  $J$  denotes the fluctuating fields,  $f^T = (\phi, J, \beta)$ , and  $\mathcal{N}(f)$  stands for the nonlinear terms. According to the Mori's method, the nonlinear term is deduced to the memory function  $\Gamma_k(s)$ , and the fluctuating force  $\mathcal{R}_k(t)$  as

$$\partial f_k / \partial t + \mathcal{L}_k^{(0)} f_k = i\Omega_k f_k + \mathcal{R}_k(t) - \int_0^t ds \Gamma_k(s) f_k(t-s),$$

where  $\Omega_k$  is the nonlinear frequency shift and.

The projection operators  $\mathcal{P}$  and  $\mathcal{Q}$  are introduced ( $\mathcal{P} + \mathcal{Q} = 1$ ).  $\mathcal{P}$  represent the projection

$$\mathcal{P} Y = \langle Y(t) f^*(0) \rangle \langle f(0) f^*(0) \rangle^{-1} f(0),$$

where

$$\langle A_l(t) A_m^\dagger(0) \rangle \equiv \lim_{T \rightarrow \infty} \frac{1}{T} \int_0^T ds A_l(t+s) A_m^\dagger(s).$$

By use of this projection operator, the memory function  $\Gamma_k(t)$ , the fluctuating force term  $\mathcal{R}_k(t)$  and nonlinear frequency shift  $\Omega_k$  are given as

$$\begin{aligned} \Gamma_k(t) &= \langle \mathcal{R}_k(t) \mathcal{R}_k^\dagger(0) \rangle \langle f_k(0) f_k^\dagger(0) \rangle^{-1}, \\ \mathcal{R}_k(t) &= \exp(tQ\Lambda) Q \mathcal{N}_k, \\ i\Omega_k &= \langle \dot{f}_k f_k^\dagger \rangle \langle f_k f_k^\dagger \rangle^{-1}, \end{aligned}$$

respectively. The fluctuating force is orthogonal, i.e.,  $\langle \mathcal{R}_k(t) f^\dagger(0) \rangle = 0$ .

By use of the dressed test mode method, we have the continued fraction expression for the Laplace transform of the memory function as

$$\bar{\Gamma}_k(\beta) = \sum' \frac{V_{k,1,2}}{\beta + \sum' \frac{V_{2,3,4}}{\beta + \left( \sum' \frac{V_{4,5,6}}{\beta + \sum' \frac{V_{6,7,8}}{\beta + \left( \sum' \frac{V_{8,9,10}}{\beta + \dots} \right)} \right)}}}$$

where  $V_{k,k_1,k_2} \equiv -2 M_{k,k_1,k_2} M_{k_2,k,-k_1} C_{k_1}(s=0)$ ,  $p_n = p + \mathcal{L}_{k_n}^{(0)}$  and  $\langle f_{k_1}(t) f_{-k_1}(t') \rangle = C_{k_1}(t-t')$  is the autocorrelation function of fluctuations. The eddy damping rate  $\bar{\Gamma}_{0,k_j}$ , at which the dressed test mode of  $k_j$  decays due to turbulent damping, has a relation with the Laplace transform  $\bar{\Gamma}_k(\beta)$  as  $\bar{\Gamma}_{0,k_j} = \bar{\Gamma}_k(p=0)$ , ( $k_j = k, k_1, k_2, \dots$ ). The expression for  $\bar{\Gamma}_{0,k_j}$  by use of the continued fraction is deduced from Eq.(44). In the case of the matrix operator  $\mathcal{L}_k^{(0)}$ , the least-stable eigenvalue  $\lambda_k$  is used, in the continued fraction as

$$\bar{\Gamma}_{0,k} = \sum' \frac{V_{k,1,2}}{\lambda_{k_2}^{(0)} + \sum' \frac{V_{2,3,4}}{\lambda_{k_4}^{(0)} + \left( \sum' \frac{V_{4,5,6}}{\lambda_{k_6}^{(0)} + \sum' \frac{V_{6,7,8}}{\lambda_{k_8}^{(0)} + \left( \sum' \frac{V_{8,9,10}}{\lambda_{k_{10}}^{(0)} + \dots} \right)} \right)}}}$$

The approach in pervious work [3] is re-examined, and an analytic model for the turbulent damping coefficient is derived by use of the Green's function.

## References

- [1] S.-I. Itoh, K. Itoh, H. Mori: J. Phys. Soc. Jpn. Vol.75, No.3 (2006) 034501
- [2] H. Mori: Prog. Theor. Phys. Vol. 33 (1965) 423
- [3] S.-I. Itoh and K. Itoh: J. Phys. Soc. Jpn. **68** (1999) 1891, 2611; *ibid.* **69** (2000) 408, 427, 3253.

## §25. On the Bicoherence Analysis of Plasma Turbulence

Itoh, K., Fujisawa, A.,  
Nagashima, Y., Itoh, S.-I., Yagi, M. (RIAM, Kyushu Univ.),  
Diamond, P.H. (UCSD), Fukuyama, A. (Kyoto Univ.)

The bicoherence of fluctuations [1] in a system of drift waves and zonal flows is discussed. In strong drift-wave turbulence, where broad-band fluctuations are excited, the bicoherence is examined [2]. A Langevin equation formalism of turbulent interactions allows us to relate the bicoherence coefficient to the projection of nonlinear force onto the test mode. The dependence of the summed bicoherence on the amplitude of zonal flows is clarified. The importance of observing biphasic is also stressed. The results provide a basis for measurement of nonlinear interaction in a system of drift waves and zonal flow.

The nonlinear dynamical equation may be written in a form

$$\frac{\partial}{\partial t} g + (-\gamma + i\mathcal{L}_0)g = \sum N gg$$

where  $\gamma$  is a linear growth rate,  $\mathcal{L}_0$  represents the linear frequency, and  $N$  denotes the coefficient of nonlinear interaction. Considering these experimental situations, we introduce Fourier components as  $g(t) = \sum_p g_p \exp(-ipt)$ .

A response of  $g_p$  to the imposition of the nonlinear term  $g_\omega$  is evaluated as follows. We separate one term  $N_{p\omega} g_{p-\omega} g_\omega$  from the total nonlinear terms  $\sum N gg$ , and express the rest in terms of the nonlinear damping term and fluctuating force as

$$\sum N gg - N_{p\omega} g_{p-\omega} g_\omega e^{-ipt} = -\nu_T' g + \tilde{S}'.$$

We have a solution

$$g_p = \exp(-\hat{\nu}_p t) \int_{-\infty}^t dt' \exp(\hat{\nu}_p t') N_{p\omega} g_{p-\omega} g_\omega + \tilde{g}_p$$

$$\text{and } \tilde{g}_p = \exp(-\hat{\nu}_p t) \int_{-\infty}^t dt' \exp(\hat{\nu}_p t') \tilde{S}_p.$$

The bispectrum estimator  $\hat{B}(\omega, p)$ , the squared bicoherence  $\hat{b}^2(\omega, p)$ , and the summed-bicoherence  $\sum \hat{b}^2$  are defined as

$$\hat{B}(\omega, p) = \langle g_p^* g_{p-\omega} g_\omega \rangle, \quad \hat{b}^2(\omega, p) = \frac{|\hat{B}(\omega, p)|^2}{\langle |g_p g_{p-\omega}|^2 \rangle \langle |g_\omega|^2 \rangle},$$

$$\text{and } \sum \hat{b}^2(\omega) = \sum_p \hat{b}^2(\omega, p).$$

**A. Case of broad band turbulence** For broad band fluctuations, one has simplified evaluation as

$$\sum \hat{b}^2(\omega) \sim 3 |\tau_p N_{p,\omega}^*|^2 |g|^2,$$

with  $|g|^2 = \sum_p \langle |g_p|^2 \rangle$ . The term  $|N_{p,\omega}| |g|$  represents a nonlinear force (in a normalized unit in a dimension of the 'frequency'), and  $\tau_p |N_{p,\omega}| |g|$  indicates the competition

between this nonlinear force and the effective correlation time  $\tau_p$ . The nonlinear interaction can be evaluated from experimental data as

$$|N_{p,\omega}| \approx \frac{1}{\sqrt{3} \tau_p |g|} \sqrt{\sum \hat{b}^2(\omega)}.$$

### B. Case of a sharp peak within a broad band fluctuations

Here, the suffix  $\omega$  indicates the mode which belongs to the sharp peak of the spectrum, and  $(p, p-\omega)$  denotes the broad band background turbulence. The bicoherence is estimated as

$$\hat{B}(\omega, p) \approx 2\tau_{p-\omega} N_{p-\omega}^* |g_{p-\omega}|^2 |g_{\omega,0}|^2 + \tau_{c,p-\omega} N_{\omega,p}^* |g_{p-\omega}|^2 |g_p|^2$$

The leading term in the summed bicoherence is

$$\sum \hat{b}^2(\omega) = 4 M \tau_{p-\omega}^2 |N_{p-\omega,p}|^2 |g_\omega|^2.$$

**C. Application to Hasegawa-Mima Model** The response of drift wave-zonal flows system is given by

$$\frac{\partial}{\partial t} \phi_d + \frac{i\omega_*}{1 + k_\perp^2 \rho_s^2} \phi_d - \frac{c_s \rho_s^4}{L_n} [\phi_d, \Delta_\perp \phi_d] = \frac{c_s}{L_n} \frac{q k_y k_\perp \rho_s^4}{1 + k_\perp^2 \rho_s^2} \phi_Z \phi_d$$

The interaction of drift waves has the coupling coefficient

$$N \approx \frac{c_s}{L_n} \frac{q k_y k_\perp \rho_s^4}{1 + k_\perp^2 \rho_s^2},$$

while the interaction between the zonal flow and drift waves has the coefficient

$$N = \frac{c_s}{L_n} \frac{q k_y k_\perp \rho_s^4}{1 + k_\perp^2 \rho_s^2}$$

The decorrelation time of drift waves through self-nonlinear interaction has been evaluated as  $\tau_p^{-1} \sim h(k_\perp \rho_s) \omega_* \phi$ , in the strong turbulence limit. One has the total bicoherence for the mutual nonlinear interaction of drift waves as

$$\sum \hat{b}^2(\omega) \sim 3 \left( \frac{1}{h(k_\perp \rho_s)} \frac{k k_\perp \rho_s^3}{1 + k_\perp^2 \rho_s^2} \right)^2.$$

The total bicoherence at the frequency of zonal flows and that at the drift wave range of frequencies are compared as

$$\frac{\sum \hat{b}^2(\text{GAMs})}{\sum \hat{b}^2(\text{drift})} \sim \frac{4M}{3} \left( \frac{q_x}{k_x} \right)^2 \frac{\phi_Z^2}{\phi_d^2} + \frac{4}{3}.$$

The importance of observing the biphasic was also demonstrated. When  $\omega$  is chosen at the frequency of zonal flows, the phase of the bispectrum estimator  $\hat{B}(\omega, p)$  has a weak dependence on  $p$ . In contrast, the biphasic of  $\hat{B}$  spreads over the range of 0 and  $2\pi$  for the interaction of drift waves. These properties will be used in the experimental study of turbulence.

### References

- [1] Y. Nagashima, et al., Phys. Rev. Lett. **95** (2005) 095002
- [2] K. Itoh, Y. Nagashima, S-I Itoh, P. H. Diamond, A. Fujisawa, M. Yagi, A. Fukuyama  
Phys. Plasmas **12** No.10 (2005) 102301

## §26. Energy Partition between Fluctuations and Zonal Flows

Itoh, K.,  
Hallatschek, K. (IPP), Itoh, S.-I. (Kyusyu Univ.),  
Diamond, P.H. (UCSD), Toda, S.

In this study, the higher-order corrections by zonal flow on the zonal flow drive are renormalized, and the driving term at an arbitrary magnitude of zonal flow vorticity is derived [1]. Based on the nonlinear form of the zonal flow growth rate, the steady state solution is obtained. In the collisionless limit, the turbulence level is shown to vanish while the zonal flow remains at finite amplitude, when instability is weak. The critical condition for the onset of drift wave turbulence in the presence of zonal flow is derived. The turbulent transport, including the zonal flow effects, is obtained. The partition ratio of fluctuating field energy among the drift wave turbulence and zonal flow is also obtained. A comparison with DNS [2] is also made.

The model dynamical system for the drift wave action  $N_k$ ,  $N_k = (1 + k_\perp^2 \rho_s^2)^2 |\tilde{\phi}_k|^2$ , and the zonal flow velocity  $V_Z$  are introduced as

$$\frac{\partial}{\partial t} U = \frac{\partial^2}{\partial r^2} \frac{c^2}{B^2} \int d^2k \frac{k_\theta k_r}{(1 + k_\perp^2 \rho_s^2)^2} \hat{N}_k - \gamma_{damp} U,$$

$$\frac{\partial}{\partial t} N_k + \frac{\partial \omega_k}{\partial k} \cdot \frac{\partial N_k}{\partial x} - \frac{\partial \omega_k}{\partial x} \cdot \frac{\partial N_k}{\partial k} = 0,$$

where  $U$  is the vorticity of the zonal flow  $U = \partial V_Z / \partial r$ . By expansion with respect to the vorticity of the zonal flow as,  $\hat{N}_k = \hat{N}_k^{(1)} + \hat{N}_k^{(2)} + \hat{N}_k^{(3)} \dots$ , where  $\hat{N}_k^{(n)}$  is the  $n$ -th order term of  $U$ , the evolution equation for the zonal flow is rewritten as

$$\frac{\partial}{\partial t} U = \sum_m G^{(m)} - \gamma_{damp} U.$$

By use of the higher order kinetics for the drift wave packets in the zonal flow field, we have

$$\frac{\partial}{\partial t} U = \frac{q_r^2 D_{rr}}{1 + \frac{H k_\theta^2 \rho_s^2 U^2}{\Delta \omega_k^2 + \Gamma^2}} U - \left( \mu_\parallel (1 + 2q^2) q_r^2 + \nu_{damp} \right) U$$

where  $D_{rr} = -\frac{c^2}{B^2} \int d^2k \frac{R(q_r, \Omega) k_\theta^2 k_r}{(1 + k_\perp^2 \rho_s^2)^2} \frac{\partial N_k}{\partial k_r}$  is the

result of the quasilinear theory,  $q_r$  is the wavenumber of zonal flow,  $\Delta \omega_k$  is the decorrelation rate of drift waves,  $\Gamma = \max(\omega_b, q_r v_{gr})$ ,  $\omega_b$  is the bouncing frequency of drift wave packet,  $\nu_{damp} \approx \nu_{ii}/\epsilon$  is the collisional damping rate,  $H$  is a numerical coefficient, and  $\mu_\parallel$  is the turbulent shear viscosity for the flow along the field line and  $q$  is the safety factor.

This result gives the partition of energy between the microscopic fluctuations and zonal flows. The other limit of interest is the collisionless limit,  $\nu_{damp}/q_r^2 D_{rr} \rightarrow 0$ . In this case, the fluctuation amplitude  $\tilde{\phi}$  vanishes at a critical vorticity of zonal flow,

$$U = U_c,$$

where

$$U_c = \max \left( \frac{2(1 - \mu)}{\mu H}, \sqrt{\frac{2(1 - \mu)}{\mu H}} k_r \rho_s \right) q_r V_d,$$

and  $V_d$  is the diamagnetic velocity. (See [1] for details.) The analytic theory in this work and the result of direct numerical simulation is compared in Fig.1. Satisfactory agreement is obtained.

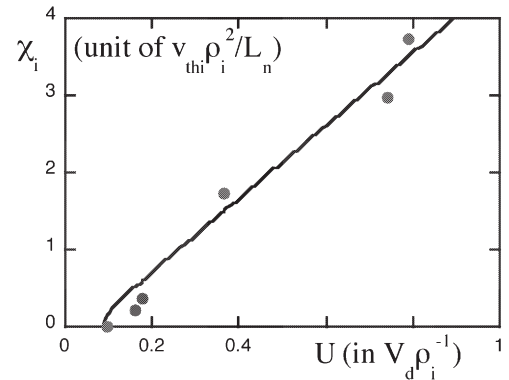


**Fig.1** Comparison of the relations  $\chi_i(U)$  for the steady state of ITG mode. Zonal flow vorticity is measured in a unit of  $V_d \rho_i^{-1}$  and thermal conductivity is in  $v_{thi} \rho_i^2 L_n^{-1}$ . Theory (solid line) and DNS data (dots) quoted from [2].

### References

- [1] Itoh, K., K. Hallatschek, S.-I. Itoh, P.H. Diamond and S. Toda, Phys. Plasmas Vol. **12** (2005) 062303
- [2] K. Hallatschek: Phys. Rev. Lett. **93** (2004) 065001.

## §27. Impact of Turbulence Spreading on Subcritical Turbulence in Inhomogeneous Plasmas

Itoh, K.,  
Itoh, S.-I. (RIAM, Kyushu Univ.), Hahm, T.S. (PPPL),  
Diamond, P.H. (UCSD)

Recent progress of the plasma turbulence has shown that the fluctuations are possibly excited by nonlinear instabilities, i.e., through subcritical excitations, and that the spreading of turbulence has considerable impact on the turbulent transport. We study the influence of the turbulence spreading on the self-sustained turbulence of subcritical instabilities. It is shown that there is a minimum radial plasma extent, in order for a self-sustained turbulence to exist in linearly stable plasmas [1]. The new phase boundary in parameter space is derived, in which the effect of turbulence spreading is included.

We study a one-dimensional model to study the turbulence spreading into stable regions. The turbulence quantities are averaged over the magnetic surface, and a profile in the  $x$ -direction is studied. We take the case that the plasma has a subcritical instability in the region of  $0 \leq |x| \leq L$ , and it is strongly stable in the regions  $|x| > L$ .

A dynamical equation is formulated in a form as

$$\frac{\partial}{\partial t} I = \Lambda I + \chi_0 \frac{\partial}{\partial x} I^\alpha \frac{\partial}{\partial x} I, \quad (1)$$

where  $I = |\tilde{\phi}^2|/|\tilde{\phi}_{\text{local}}^2|$  is the normalized electrostatic potential fluctuation amplitude,  $|\tilde{\phi}_{\text{local}}^2|$  is the level which is given by the local balance of drive and damping  $\Lambda = 0$ ,  $\Lambda$  is the decorrelation rate (including the growth rate and local nonlinear damping rate), and  $\chi_0 I^\alpha$  is the diffusion coefficient due to a turbulence spreading, in which the dependence on the fluctuation level is represented by use of the index  $\alpha$ . (In a weak turbulence limit,  $\alpha = 1$  holds, and  $\alpha = 1/2$  for strong turbulence limit.) This model has several limitations. First, the fluctuations, the wavelengths of which are comparable to  $L$ , are not included. Second, the incoherent and fluctuating kicks are not taken into account. Noticing that these additional processes may have a substantial influence, we choose the model (1) as a starting point of the analysis.

We introduce a characteristic length  $\ell = \sqrt{\frac{\chi_0}{(1+\alpha)\Lambda_0}}$ , and the lengths and  $\Lambda$  are normalized with respect to  $\ell$  and  $\Lambda_0$ , respectively,  $\zeta = x/\ell$ ,  $\hat{L} = L/\ell$ ,  $\hat{\Lambda} = \Lambda/\Lambda_0$ . By use of this normalization, Eq.(1) is rewritten as

$$\frac{d^2}{d\zeta^2} F + \hat{\Lambda} F^{1/(1+\alpha)} = 0, \quad (2)$$

where a new variable for the fluctuation amplitude is introduced as  $F = I^{1+\alpha}$ .

We have the solution

$$\int_0^F \frac{dF}{\sqrt{H(F(0)) - H(F)}} = \hat{L}, \quad (3)$$

where the Sagdeev potential is given as

$$H(F) \equiv 2 \int_0^F dF \hat{\Lambda} F^{1/(1+\alpha)} \quad (4)$$

The asymptotic relation for the turbulent transport coefficient, which has the dependence  $\chi = \chi_0 I^\alpha$ , is given as

$$\chi = \chi_0 \left\{ 1 - \frac{\alpha}{1+\alpha} \sqrt{\frac{1}{2|\Lambda'(1)|}} \exp\left(-\sqrt{|\Lambda'(1)|} \hat{L}\right) \right\} \quad (5)$$

This analysis provides a generalized Maxwell's construction rule as

$$H(1) \geq \exp \left\{ -2\sqrt{|\Lambda'(1)|} \left( 2\hat{L} - \int_0^{F_*} \frac{dF}{\sqrt{-H(F)}} \right) \right\} \quad (6)$$

In the absence of turbulence spreading (i.e.,  $\hat{L} \rightarrow \infty$ ), this recovers standard result of Maxwell's construction rule,  $H(1) \geq 0$ .

### Reference:

[1] K. Itoh, S.-I. Itoh, T.S. Hahm, P.H. Diamond  
J. Phys. Soc. Jpn., Vol.74, No.7 (2005) 2001



## §28. Transport Coefficient Induced by Drift Wave Turbulence Screened by Zonal Flows

Itoh, K.,  
Hallatschek, K. (IPP), Itoh, S.-I. (Kyusyu Univ.),  
Diamond, P.H. (UCSD), Toda, S.

In this work, an explicit forms of the transport coefficient and the Dimits shift is discussed for a practical use [1].

An analytic estimate for the quasi-linear driving coefficient of zonal flows by drift waves,  $D_{rr}$ , has been given

$$D_{rr} \approx \frac{1}{B^2} \frac{k_\theta^2}{\gamma_L} |\tilde{\phi}|^2,$$

in the vicinity of the marginal condition of the linear stability  $\Delta\omega_k \approx \gamma_L$ . It is given, in terms of the normalized fluctuation amplitude, as  $D_{rr} \approx (k_\theta^2 k_\perp^{-4}) \omega_*^2 \gamma_L^{-1} \hat{\phi}^2$ . The growth rate of the zonal flow energy has been introduced by the definition  $2D_{rr} q_r^2 = \alpha \hat{\phi}^2$ . That is, the time rate  $\alpha$  is given as

$$\alpha \approx \frac{\omega_*}{\gamma_L} \frac{2 k_\theta^2 q_r^2}{k_\perp^4} \omega_*.$$

The Dimits shift is given by the critical condition, which is explained in terms of the linear growth rate,

$$\gamma_{L,c} = \frac{4(1-\mu)^2}{\mu^2 H^2} \frac{q_r^2}{k_\theta^2} \alpha.$$

(See [1] for the expression of the parameters  $H$  and  $\mu$ .) Elimination  $\alpha$ , at  $\gamma_L = \gamma_{L,c}$ , provides an equation of the critical growth rate  $\gamma_{L,c}$  at the boundary of Dimits shift as

$$\gamma_{L,c} = \frac{2\sqrt{2}(1-\mu)}{\mu H} \frac{q_r^2}{k_\perp^2} \omega_*.$$

For the least stable mode,  $q_r$  is estimated as,

$$q_r \approx \frac{\sqrt{1-\mu}}{2} K_0, \text{ which gives an estimate of } \gamma_{L,c}$$

$$\gamma_{L,c} = \frac{(1-\mu)^2}{\sqrt{2} \mu H} \frac{K_0^2}{k_\perp^2} \omega_*.$$

One estimate for  $K_0 = k_r$ :

$$\gamma_{L,c} = \frac{(1-\mu)^2}{\sqrt{2} \mu H} \frac{k_r^2}{k_\perp^2} \omega_*$$

For parameters  $\mu \approx 1/2$ ,  $\gamma_{L,c}$  is of the order of one-tenth of  $\omega_*$ .

The fluctuation amplitude is given as follows.

(a) Small growth rate limit: In the case of weak instability, i.e.,

$$\gamma_L < \frac{1}{(1-\mu)} \frac{k_\perp^4}{k_\theta^2 q_r^2} \nu_{\text{damp}} \quad [\text{region I}]$$

the fluctuation level is given by

$$\hat{\phi} = \frac{\gamma_L}{\omega_*} \equiv \hat{\phi}_I$$

(b) Intermediate growth rate limit: For the case of

$$\frac{1}{(1-\mu)} \frac{k_\perp^4}{k_\theta^2 q_r^2} \nu_{\text{damp}} < \gamma_L < \gamma_{L,c}, \quad [\text{region II}]$$

the fluctuation level is given by

$$\hat{\phi} = \frac{1}{\sqrt{1-\mu}} \frac{k_\perp^2}{k_\theta q_r} \sqrt{\frac{\nu_{\text{damp}}}{\omega_*} \frac{\gamma_L}{\omega_*}} \equiv \hat{\phi}_{II}.$$

(c) Large growth rate limit: The transition from the collisional-damping-dominated region [region II] to the nonlinearity-dominated region is expected to occur at

$$\frac{1}{\mu H \rho_s^2 k_\theta^2} \nu_{\text{damp}} + \gamma_{L,c} < \gamma_L. \quad [\text{region III}]$$

One has,

$$\frac{\Delta\omega_k}{\omega_*} \approx \frac{\mu H \rho_s^2 k_\perp^4}{4(1-\mu) q_r^2} \left( -1 + \sqrt{1 + \frac{8(1-\mu) q_r^2}{\mu H \rho_s^2 k_\perp^4} \left( \frac{\gamma_L - \gamma_{L,c}}{\gamma_L} \right)} \right) \frac{\gamma_L}{\omega_*} \equiv \hat{\phi}_{III}$$

The asymptotically-linear dependence on  $\gamma_L$  in this model is recovered, and a suppression factor appears. The suppression factor, which is induced by the co-existence of the zonal flow, is approximately evaluated as  $\sqrt{\mu H/2(1-\mu)} \rho_s k_\perp^2 q_r^{-1} \sim k_\perp \rho_s$ .

A similar argument is possible for the thermal conductivity. In the regions I and II, a fitting formula is given as

$$\chi_{I+II} = \frac{\gamma_L \sqrt{v}}{\sqrt{\gamma_L + \sqrt{v}}} \frac{1}{k_r^2}.$$

Where  $v = (1-\mu)^{-1} k_\perp^4 k_\theta^{-2} q_r^{-2} \nu_{\text{damp}}$  denotes the impact of collisional damping of the zonal flow. In the region III, one has

$$\chi_{III} = \frac{\mu H \rho_s^2 k_\perp^4}{4(1-\mu) q_r^2} \left( -1 + \sqrt{1 + \frac{8(1-\mu) q_r^2}{\mu H \rho_s^2 k_\perp^4} \left( \frac{\gamma_L - \gamma_{L,c}}{\gamma_L} \right)} \right) \frac{\gamma_L}{k_r^2}.$$

A fitting in the regions I, II and III provides a formula of turbulent transport coefficient which is screened by zonal flows as

$$\chi_i = \chi_{\text{fit}} \equiv \sqrt{\chi_{I+II}^2 + \chi_{III}^2 \Theta(\gamma_L - \gamma_{L,c})}$$

where  $\Theta(\gamma_L - \gamma_{L,c})$  is a Heaviside function.

## References

[1] Itoh, K., K. Hallatschek, S.-I. Itoh, P.H. Diamond and S. Toda, Phys. Plasmas Vol. **12** (2005) 062303

## §29. Zonal Flows in Plasma – A Review

Diamond, P.H. (UCSD), Itoh, S.-I. (Kyushu Univ),  
Itoh, K.,  
Hahm, T.S. (PPPL)

Zonal flows, by which we mean azimuthally symmetric band-like shear flows, are a ubiquitous phenomena in nature and the laboratory. The well-known examples of the Jovian belts and zones, and the terrestrial atmospheric jet stream are familiar to nearly everyone - the latter especially to travelers enduring long, bumpy airplane rides against strong head winds. Zonal flows are also present in the Venusian atmosphere (which rotates faster than the planet does!) and occur in the solar tachocline, where they play a role in the solar dynamo mechanism. In the laboratory, the importance of sheared  $\mathbf{E} \times \mathbf{B}$  flows to the development of L-mode confinement, the L-to-H transition and internal transport barriers (ITBs) is now well and widely appreciated. It is now widely recognized and accepted that zonal flows are a key constituent in nearly all cases and regimes of drift wave turbulence - indeed, so much so that this classic problem is now frequently referred to as "drift wave-zonal flow turbulence". This paradigm shift occurred on account of the realization that zonal flows are ubiquitous in dynamical models used for describing fusion plasmas (i.e. ITG, TEM, ETG, resistive ballooning, and interchange, etc.) in all geometries and regimes (i.e. core, edge, etc.), and because of the realization that zonal flows are a critical agent of self-regulation for drift wave transport and turbulence.

A comprehensive review of zonal flow phenomena in plasmas is presented [1]. While the emphasis is on zonal flows in laboratory plasmas, planetary zonal flows are discussed as well. The review presents the status of theory, numerical simulation and experiments relevant to zonal flows. The emphasis is on developing an integrated understanding of the dynamics of drift wave - zonal flow turbulence by combining detailed studies of the generation of zonal flows by drift waves, the back-interaction of zonal flows on the drift waves, and the various feedback loops by which the system regulates and organizes itself. The implications of zonal flow phenomena for confinement in, and the phenomena of fusion devices are discussed. Special attention is given to the comparison of experiment with theory and to identifying directions for progress in future research.

The review explains the following issues:

1. Introduction
  2. Basic Physics of Zonal Flows: A Heuristic Overview
    - 2.1 Introduction
    - 2.2 Basic dynamics of zonal flows
    - 2.3 Self-consistent solution and multiple states
    - 2.4 General comments
    - 2.5 Implications for experiments
  3. Theory of zonal flows
    - 3.1 Linear Dynamics of Zonal Flow Modes
    - 3.2 Generation mechanism
    - 3.3 Shearing and back reaction of flows on turbulence
    - 3.4 Nonlinear Damping and Saturation: Low Collisionality Regimes
    - 3.5 The Drift Wave - Zonal Flow System: Self-consistent State
    - 3.6 Suppression of Turbulent Transport
  4. Numerical Simulations of Zonal Flow Dynamics
    - 4.1 Introduction
    - 4.2 Ion Temperature Gradient Driven Turbulence
    - 4.3. Electron Temperature Gradient Driven Turbulence
    - 4.4. Fluid Simulations with Zonal Flows
    - 4.5 Edge turbulence
    - 4.6 Short summary of the correspondence between theoretical issues and numerical results
  5. Zonal Flows in Planetary Atmospheres
    - 5.1 Waves on a rotating sphere.
    - 5.2 Zonal Belts of Jupiter
    - 5.3 Superrotation of the Venusian Atmosphere
  6. Extensions of Theoretical Models
    - 6.1 Streamers
    - 6.2 Noise Effects and Probabilistic Formulations
    - 6.3 Statistical properties
    - 6.4 Non-Markovian Theory
    - 6.5 Envelope Formalism
  7. Laboratory Experiments on Zonal Flow Physics
    - 7.1 Characteristics of Zonal Flows
    - 7.2. Zonal Flow Dynamics and Interaction with Ambient Turbulence
    - 7.3. Suggestions on future experiments and information needed from simulations and theory
  8. Summary and Discussion
- Acknowledgements
- Appendix A Ray of Drift Wave Packet and Trapping
- Appendix B Hierarchy of Nonlinear Governing Equations
- Appendix C Near isomorphism between ETG and ITG

[1] P. H. Diamond., S.-I. Itoh, K. Itoh and T.S. Hahm, Plasma Phys. Control. Fusion, **47** No.3 (2005) R35; See also NIFS Report 805 (2004)

### §30. Probability Density Functions and Structure of Singularities in Non-Dissipative Fields in MHD and NS Turbulences

Gotoh, T. (Nagoya Inst. of Tech.)

Recent studies on a passive scalar convected by an artificial random solenoidal velocity field (Kraichnan model) have found that the scaling of the high order structure functions of the scalar increments tends to the normal scaling in the large spatial dimensions [1]. Also in the equilibrium statistical mechanics, fluctuations near phase transition point obey the Gaussian in large dimensions too, and the mean field theory works well. Then it is quite natural to ask whether the intermittency of turbulence changes when the spatial dimensions becomes larger than 3. In 2-dimensions there is no vortex stretching so that the fair comparison with 3-dimensional turbulence is difficult. On the other hand, in 4-dimensions there exists the stretching of the velocity 2-form and thus the energy cascade towards large wavenumbers can be expected [2].

NS equation in 4-dimensions is written in terms of the velocity 2-form  $\Omega_{ij} = \partial u_j / \partial x_i - \partial u_i / \partial x_j$  as

$$\partial u_i / \partial t + u_k \Omega_{ki} = -\partial_i P + \nu \nabla^2 u_i, \quad \partial_i u_i = 0$$

Under the periodic boundary conditions, we have numerically integrated the above equation by using the spectral method and 4th order Runge-Kutta-Gill method. With the same energy per each direction, the comparison of the 4-dimensional turbulence with that in 3-dimensions was done at similar Reynolds numbers.

Figure 1 shows the evolution of the average rate of the energy dissipation  $dE^{(d)}/dt = -\epsilon^{(d)}$  normalized by their initial values. It follows that the energy transfer in 4d is more efficient than in 3d, so that the decay of the total energy in 4d is faster than in 3d. The time needed for formation of the singular structure is shorter in 4d and its strength is bigger than in 3d. Correspondingly to this, the skewness and flatness factors of the longitudinal velocity gradient in 4d are bigger than in 3d. Figures 2 and 3 show the distribution of the enstrophy  $\sum_{ij} \Omega_{ij}^2$  visualized by the same threshold value. The high intensity domains of the enstrophy in 4 dimensions are less space filling when compared to those in 3 dimensions. This is a dimension effect that the number of terms becomes larger in high space dimension so that the fluctuations become milder with increase of dimensions.

References 1) G. Falkovich, K. Gawedzki and M. Vergasola, Rev. Mod. Phys. **73**, 913 (2001).

2) E. Suzuki, T. Nakano, N. Takahashi, and T. Gotoh, Phys.

Fluids **17**, 081702 (2005).

3) Y. Watanabe, *Statistics of the large scale velocity field in turbulence*, NIT Master Thesis (in Japanese) (2006).

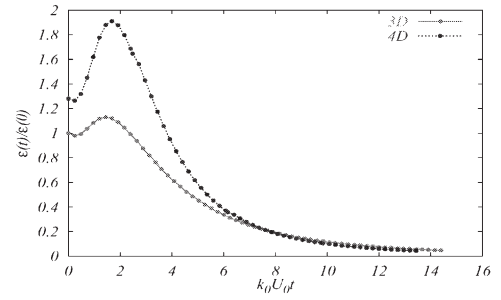


**Fig.1**  $\epsilon^{(d)}(t)/\epsilon^{(d)}(0)$

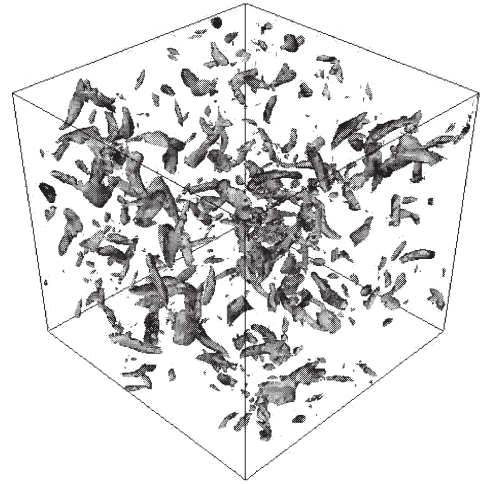


**Fig.2**  $\sum_{ij} [\Omega_{ij}^{(3)}(x)]^2 > 6\sigma(\sum_{ij} [\Omega_{ij}^{(3)}]^2)$  where  $\sigma$  is the standard deviation.

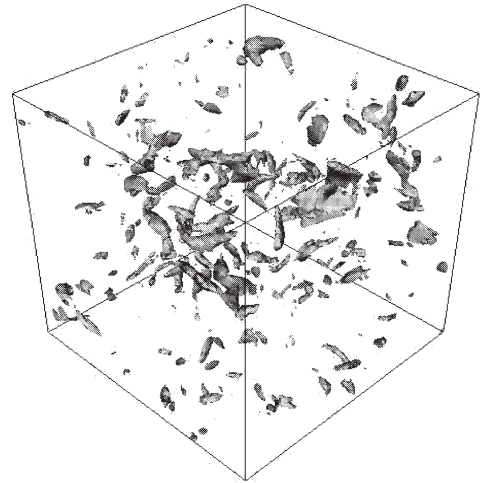


**Fig.3**  $\sum_{ij} [\Omega_{ij}^{(4)}(x_1, x_2, x_3, 0)]^2 > 6\sigma(\sum_{ij} [\Omega_{ij}^{(4)}]^2)$ .

### §31. Investigation on the Application of the Plasma-Sheath Having Charged-Dust Grains

Nejoh, Y.N. (Graduate School of Engineering, Hachinohe Institute of Technology), Sanuki, H.

Plasma properties of dust grains suspending near the wall of fusion devices attract attention in a development of stable operation. There is still no model describing adequately plasma dynamics of fusion devices, in particular, the sheath having dust grains<sup>1)</sup> and secondary electrons. In many reports, collisional sheath structures have not been well-established in the vicinity of the diverter plate. It is important to develop a reliable model that improves our understanding of the factors which control plasma structure when we attempt to improve upon the existing fusion device designs.

Sheath is formed in the region where the wall of the devices are in contact with plasmas, and is the source of the most fundamental information in order to settle the problems of dust grains and secondary electrons and surface charging. The wall environment is a complex plasma including electrons, ions, secondary electrons and neutrals, and positive ions are accelerated gradually due to the negatively-charged surface wall<sup>1-5)</sup>. In addition, the inter-particle collision occurs frequently because of the existence of neutral particles, which do not depend on the outer fields whereas observational data have not been reported sufficiently. In order to study the acceleration of ions and the distribution of particulates, we propose a model of trapped dusts except for Boltzmann type dusts. The constituents of particles we consider are electrons, ions, secondary electrons, neutrals and dust grains. The equation of motion for ions with the ion-neutral collision and Poisson's equation are considered. Our aims of the investigation are to study sheath structures near the wall and/or diverter and to show the trapped position of dust grains. It is assumed that the ions flow to the wall, the dust grains run slowly and secondary electrons emit from the wall due to the collision of high speed ions. From the results of numerical calculation, we observe that the sheath potential, the densities of electron, ions, secondary electrons and the space charge density. It is obvious that most of the space charge lies in the vicinity of the wall and at the edge. In order to derive the dust grain density, we assume the velocity distribution function of dust grains including trapped dusts, which is not Boltzmann type. Integrating the velocity distribution function, we obtain the dust grain density as

$$n_d = (\delta_i - \delta_s - 1) \left[ \exp\left(-\frac{Z\phi}{\tau_f}\right) \left(1 - \operatorname{erf}\sqrt{\frac{Z\phi}{\tau_f}}\right) + \frac{2}{\sqrt{\pi\tau_i/\tau_f}} \left( \sqrt{-\frac{Z\phi}{\tau_f}} - \sqrt{\frac{Z(-\phi+\phi_0)}{\tau_i}} \right) + \frac{1}{1 + \sqrt{\tau_i/\tau_f}} \exp\left(\frac{Z(-\phi+\phi_0)}{\tau_i}\right) \right]$$

$$\times \operatorname{erf}\left( \left(1 + \frac{1}{\sqrt{\tau_i/\tau_f}}\right) \sqrt{\frac{Z(-\phi+\phi_0)}{\tau_i}} \right)$$

The parameters used for numerical calculation as follows;  
 $\phi = e\Phi/T_e$ ,  $\delta_i = n_{i0}/n_{e0} = 5$ ,  $Z = 30$ ,  $\delta_s = n_{s0}/n_{e0} = 0.2$ ,  
 $\tau_i = T_i/T_e = 0.5$ ,  $\tau_f = T_f/T_e$ ,  $\tau_t = T_t/T_e$  and  
 $\phi_w = \Phi/\Phi_w = -10$ . We compare our result with the experimental one (Iowa state university), and the result is shown in Fig.1. Following facts are found: When the temperature of trapped dusts increases, the trapped region becomes wider. When the ion density changes, the trapping of dusts varies more complicatedly. The sheath structure changes from triple to quadrupole according to the ion density, as the charge number increases.

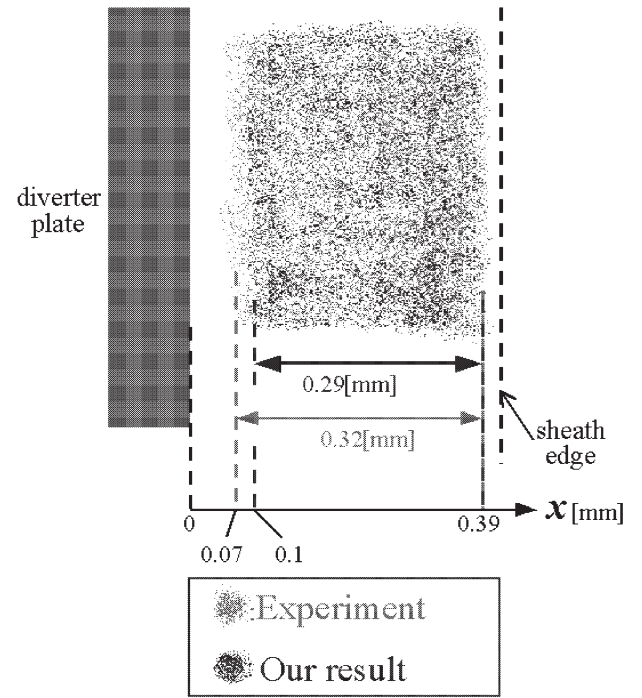


Fig.1 Comparison between experiments and our result on the trapped position of dust grains in the sheath region

Features presented here have not been shown in laboratory experiments. In this respect, the results may be useful in understanding the properties of the sheath structure including trapped dust grains near the diverter plate.

#### References

- 1) Winter, J., Physics of Plasmas, **7**, (2000) 3862.
- 2) Hiwatashi, T. and Nejoh, Y.N., Papers of Tech. Mtg on Plasma Sci. Tech., IEE Japan, PST-03-19 (2003).
- 3) Nejoh, Y.N. and Yamamura, Y. Physics of Plasmas **13**, (2005) 033506.
- 4) Nejoh, Y.N. Physics of Plasmas **19**, (2002) 03811.
- 5) Nejoh, Y.N. and Yamamura, Y. Proc. Int Conf. Electrical Engineering, Vol. **1**, (2004) 736.



### §32. Equilibrium of Electrostatic Torus Plasma – Ion Temperature Effect

Aizu, K., Unno, H., Saeki, K. (Fac. of Sci., Shizuoka Univ.),  
Tsushima, A. (Grad. School of Eng., Yokohama Univ.),  
Sanuki, H.

Taking account of the finite temperature effect extends equilibrium of the electrostatic torus plasmas with electrostatic electric field in addition to simple torus magnetic field. In particular, equilibrium in simple torus configuration with radial electric field is obtained on the basis of non-resistive two-fluid model under the thin plasma ring approximation. Considering both  $E \times B$  drift and diamagnetic drift correctly, we finally obtained an equilibrium equation describing the potential and an equation, which describes the deviation of equi-potential contour and equi-density contour and/or equi-current surface. The equilibrium solution for potential is plotted in Fig.1. In this figure, we used

$$\nu = (\omega_{pi} / \omega_{ci})^2 / 2 = 1.8$$

$$\gamma = m C_s^2 n_0 / 2 \epsilon_0 (\phi_0 / a)^2 = 18$$

$$\lambda_i = k T_i / (e \phi_0) = -0.1.$$

Here,  $\nu$  corresponds to the strength of convective derivatives and the equation reduces to a nonlinear differential equation.

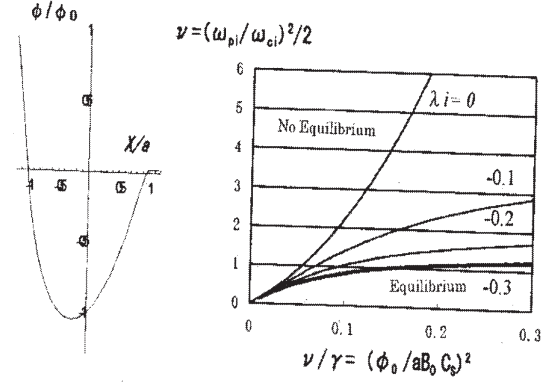


Fig.1 potential distribution at the threshold value (left) and rotation velocity dependence on confinement density (right).

In this case,  $\nu/\gamma = (\phi_0/aB_0C_s)^2 = 0.1$  and plasma density  $n_0$  is the maximum  $n_{0cr}$ . When  $n_0 > n_{0cr}$ , plasma tends to escape from the region (1,0). It turns out from the left figure of Fig.1 that density threshold value  $n_{0cr}$  increases in proportion to the value,  $\nu/\gamma = (\phi_0/aB_0C_s)^2$  but it tends to saturate toward some levels due to finite temperature effect as  $\lambda_i$  increases.

Some of the present results have been presented at the Japan Physical society Meeting in Ehime Univ., 17aUC-4.

### §33. Steady State Operation of a Field-Reversed Configuration Plasma by NBI

Asai, T., Takahashi, T., Matsuzawa, Y., Fujino, T. (Nihon Univ),  
Takahashi, T. (Gunma Univ.),  
Hirano, Y. (AIST),  
Mizuguchi, N., Tomita, Y.

A field-reversed configuration (FRC) has an attractive attention as a future reactor core for D-D and D-<sup>3</sup>He fusion reaction because of its extremely high beta nature. The magnetic configuration of FRC has a center closed region and open field region. Because of this geometrical property, a FRC can be translated from formation theta-pinch region into confinement region while it keeps the closed magnetic field. Field-reversed theta-pinch (FRTP) is most appropriate formation technique for high-beta FRC and its possibility is verified by numerical methods. Because of high beta nature of FRC (*i.e.* very low magnetic field), NBI is the only candidate for sustainment of steady-state operation. However, the plasma parameter formed by FRTP method, *i.e.* very high density of  $\sim 10^{21}\text{m}^{-3}$ , is not suitable for application of additional heating method of the NBI heating.

For the effective application of NBI, the plasma parameters have to be changed into lower density  $\sim 10^{20}\text{m}^{-3}$ , higher trapped flux and larger plasma volume. In this work, the “equivalent” NBI in the translation process has been proposed as a heating and particle injection method for FRC. Translating a FRC plasma through a neutral gas background is equivalent an end-on NBI into the FRC. The estimation has been performed for the FRC plasma produced on NUCTE (Nihon University Compact Torus Experiment) device 1. The typical plasma parameters in a formation region are electron density  $n_e \sim 3 \times 10^{21}\text{m}^{-3}$ , total temperature  $T_i \sim 300\text{eV}$  and poloidal magnetic field at separatrix  $B_z(r_s) \sim 0.4\text{T}$ . For these parameters of plasma and translation velocity of  $\sim 100\text{km/s}$  (equivalent kinetic energy  $\sim 100\text{eV}$ ), most likely atomic and molecular process are an electron impact ionization on deuterium molecule and atom, an electron impact dissociation on  $\text{D}_2^+$  and charge exchange with  $\text{D}^+$ . To estimate the characteristic length between FRC plasma and neutral particle ( $\text{D}_2$ ), the following rate equations of the above atomic processes are solved,

$$\frac{\partial n_j}{\partial t} + \vec{\nabla} \cdot (n_j \vec{V}_j) = \sum_{k=1}^M \sum_{m=1}^M \sum_{q=1}^N i_{kmq} n_m n_k \langle \sigma V_j \rangle_{kmq} \quad (1)$$

where,  $n_j$ ,  $V_j$  are density and velocity of  $j$  species, and  $\langle \sigma V_j \rangle$ ,  $i_{kmq}$ , are Maxwellian averaged reaction rate coefficient and the number of particles lost or gained from a single reaction. The steady state solution ( $\partial n_j / \partial t = 0$ ) is calculated. A characteristic length of the ionization of the injected  $\text{D}_2$  molecule is about  $\sim 10\text{mm}$  under the assumption of uniform distribution of density and electron temperature. The gyro-radius of the ionized ion is  $\sim 3\text{mm}$  and it is much less than plasma radius of  $\sim 50\text{mm}$ . Therefore, at least particle injection effect can be expected by this “equivalent” NBI. Other effects depend on the conditions of background neutral particle density and translation velocity of FRC. For the neutral particle density of  $1 \times 10^{20}\text{m}^{-3}$ , translation velocity of  $100\text{km/s}$  and translation length of  $1\text{m}$ , the particle number of  $\sim 3 \times 10^{18}$  and the kinetic energy of  $\sim 40\text{J}$  are supplied due to the equivalent NBI.

A slowing down time of the injected neutral particle is also estimated as,

$$\tau_{\text{slow}} = \int_0^{W_b} \frac{dW_b}{W_b \left( 1/\tau_{bi}^E + 1/\tau_{be}^E \right)} \approx \int_0^{W_b} \frac{\tau_{bi}^E}{W_b} dW_b, \quad (2)$$

where  $W_b$  is a neutral beam energy and  $\tau_{bi}^E$  and  $\tau_{be}^E$  are energy loss times by collisions with ion and electron, respectively. When the beam energy is about  $100\text{eV}$ , the beam energy loss rate of ion is much larger than that of electron. The estimated slowing down time of this experimental parameter is about a few tens  $\mu\text{s}$ .

On basis of the above calculation, we assume that the all particles in the column, which the translated FRC passes through, are injected and trapped by the FRC. Then, injected particle number  $N_{\text{injected}}$  can be written as

$$N_{\text{injected}} = \pi r_s^2 L n_D. \quad (3)$$

Here,  $L$  is translated distance. Then  $N_{\text{injected}}$  is estimated into  $1 - 4 \times 10^{18}$  and injected energy  $E_{\text{injected}} = 13 - 43\text{J}$  for  $n_D \sim 2 - 6 \times 10^{20}\text{m}^{-3}$  and  $v = 100\text{km/s}$ . These values are consistent with the experimental results of NUCTE experiments.

To study the orbital effect of injected particles, two-dimensional particle simulation has also been performed<sup>2</sup>. When the condition of translation velocity is  $100\text{km/s}$  and neutral particle density:  $2 \times 10^{20}\text{m}^{-3}$ , the beam energy is deposited on the ion at the vicinity of the separatrix and the energy deposition rate is about 45%. Dependence of the energy deposition effect on translation speed and back-ground neutral density has also been performed to make a suggestion for experiments.

#### References

- 1) Fujino, T. *et al*, Phys. Plasmas **13**, (2006) 012511.
- 2) Takahashi, T. *et al*, J. Plasma Fus. Res. **81** (2005) 421

## §34. Development of Reactor Design Aid Tool Using Virtual Reality Technology

Mizuguchi, N., Tamura, Y., Sagara, A.

A new type of aid system for fusion reactor design, to which the virtual reality (VR) visualization and sonification techniques are applied, is developed. This system provides us with an intuitive interaction environment in the VR space between the observer and the designed objects constructed by the conventional 3-D computer-aided design (CAD) system. We have applied the design aid tool to the heliotron-type fusion reactor design activity FFHR2m[1] on the virtual reality system, *CompleXcope*[2], of NIFS, and have evaluated its performance[3].

In recent years, there have been remarkable progresses in the methodology of engineering design, including the CAD techniques with the help of rapid advances in the computer environment. A nuclear fusion reactor is one of the most complicated, massive, and expensive products in present engineering subject. The design aid system described in this report provides us with an intuitive interaction environment between the observer and the designed objects, which are constructed by the conventional 3-D CAD system. If we apply VR to the engineering design, it will be possible to obtain a near-complete model at much lower cost, both economically and temporally, than making a conventional mockup like a clay model.

The *CompleXcope* system has 4 screens, on which stereoscopic images are projected, and 8 loudspeakers to enable a sonification approach. The observer can walk in a room surrounded by the screens, wearing the glasses with a head-tracking device to inform the system of the position and the direction of the observer's head. Thus, the observer can actually feel immersed in the VR world. If he wants to see the hidden side of the object, the only thing he has to do is to move his own head behind it and look back at it. In the VR room the observer makes a communication with VR world by a simple input device called Wanda, which have 3 buttons and the tracking sensor.

The design aid tool provides us with a convenient means to check subtle points, such as the motions of the movable parts and the interference among the structures, which have been examined conventionally with the help of a mockup or a scale model. It would help the designers refine the productions much more easily.

The output of CAD is converted into raw polygon data in an appropriate format beforehand. The given numeral polygon data is modeled into 3-D graphical objects by using the OpenGL library. Simultaneously, the information which is needed for numerical analyses like interference check is extracted from the raw data. The main program manages the objects and various kinds of functions, referring the signals from the sensors and buttons, and compiles the final 3-D models together with some supporting images for interface. The example of the execution of the aid tool is

shown in Fig.1.

All the commands for handling the VR are arranged in a menu panel, which appears on the right wall while a button of the Wanda is keeping pressed. In addition to the standard functions like a translation of the observer's position and a scale measurement, this system has several unique functions by making use of the VR's capability. As a tool for manipulating the movable components, we have developed an intuitive method called a *fork* tool, which is shown in Fig.2. The observer can handle the object just like a forked hunk of meat, i.e., the object follows the motion of the Wanda held in his hand, including the translation and the twisting motion of the Wanda. The system can also record such motions into an external file, and can play automatically anytime. Moreover, to examine the interference among the movable and the fixed components, a new real-time interference check tool using the sonification technique has been developed. The latest version of the aid tool has a simplified one, where an alarm rings with a stereo sound from the position of the movable components approaching to the fixed objects.

This aid tool is applied and benchmarked to the heliotron-type fusion reactor design, FFHR2m. The total number of the polygons is around 710000 triangles and 350000 vertices at the maximum. It has been proved that the data are correctly and smoothly projected into a VR image, and that the functions run correctly. However, it is still to be hard to calculate the realtime interference check with the original data size. To seek for more accurate and faster examinations is our ongoing research.



Fig.1 Example of the execution of the aid tool.



Fig.2 The "fork" tool.

### Reference

- 1) A. Sagara, et al., Nucl. Fusion **45**, (2005) 258
- 2) Y. Tamura, et al., Comp. Phys. Comm. **142**, (2001) 227
- 3) N. Mizuguchi, et al. to appear in Fusion Eng. Design.

## 1-4. LHD Project Research Collaboration

The LHD project has two purposes: to perform plasma confinement research in a steady-state machine and to elucidate physical and engineering issues for a helical fusion reactor. In order to realize such purposes, both fusion technology and the plasma physics must be developed in a long-term program. Success with this program will require collaboration with scientists and researchers from universities and institutes in Japan and also from all over the world.

The aim of the LHD Project Research Collaboration, being reported here, is to research and develop both technology and the scientific foundations that are useful for both the LHD group and the universities, and then, to apply these results to LHD experiments for the improvement of LHD. The characteristic of this collaboration program is that some R&D's are performed in each domestic university or institute, instead of in NIFS as conventional research collaborations. The advantage of this type collaboration over conventional one is that co-workers can devote themselves to R&D's more efficiently and enthusiastically by spending much more time.

From two years before, the LHD Project Research Collaboration started to invited public participation from universities and institutes in Japan. Three committees and one advisory council participate in selection process of collaboration subjects. At the beginning, the committees of the Fusion Network in Japan select and recommend some proposed plans to the committee of the LHD Project Research Collaboration in NIFS. NIFS has partnerships with Fusion Network linking three major research fields in Japan: fusion engineering, fusion science and plasma science. Although these fields have been developed independently, intimate collaboration between them is essential for further progress of fusion research. NIFS, as a Center of Excellence (COE) should develop a network of fusion research activities of universities and government institutions, including information exchange, planning, collaboration with foreign institutions and education of graduate course students. The Fusion Network has two committees related to this collaboration: one deals with the fields of fusion and plasma science and another with fusion engineering. Then, the committee of the LHD Project Research Collaboration in NIFS determines the collaboration subjects, together with their budgets. They finally require the approval of the Advisory Council for Research and Management of NIFS. An important point to choose a subject of collaboration is to know whether it was already carried out or will be done firstly in NIFS. A new attempt, which is useful for the LHD project and is not planned in NIFS, is, of course, always welcome to the collaboration program for LHD project. Another important point is whether that program can contribute to stimulate university researches and LHD programs.

As the fusion-plasma science program, following subjects were approved last year and reported in this book.

1. Direct energy conversion for advanced fueling fusion.
2. Development of high beta plasma formation using ICRF high harmonic fast wave.
3. Experimental study of compatibility of a transport barrier and energetic ion confinement.
4. Study of the fueling pellet transportation in the guiding tube.
5. ECH and ECCD using new remote steering antenna.
6. Production mechanism of  $D^+$  ions and evaluation of  $D^+$  ion current extraction.

7. Development of fine size variable pellet injector and study of transportation in curved drift tube.
8. Chaos control of fluctuations caused by flute instability in ECR Plasma.
9. Development of 2 color multi channel interferometer using 48- and 57-mm FIR lasers.
10. Dynamics of hydrogen atoms and molecule in the periphery plasma studied by mean of polarization separated spectra.
11. Spectroscopy and atomic modeling of EUV light from LHD plasma.
12. Development of wide band and compact X-ray spectrometer.
13. Optical diagnostics of non-contact divertor plasma.
14. Improvement of plasma performance by strong ECH with high power gyrotron.
15. Formation mechanism and transport of dust particles in the divertor plasmas.
16. Development of integrated simulation code for helical plasma experiments

As the fusion-engineering program, following subjects were also approved last year and reported here.

1. Study on effects of bending strain to critical current characteristics of  $Nb_3Al$  CIC conductors.
2. 14MeV-neutron beam induced change in characteristics of materials for superconducting magnets under 4.5 K.
3. Development of New High Field and High Current Density Superconductors for Fusion Devices.
4. Suitability of Boron-titanium as First Wall.
5. Measurement of the negative ion and control of recombination plasma in the LHD Divertor.
6. Kinetics of Hydrogen Isotopes at Surfaces and Bulks of Plasma Facing Materials Based on Group 5 Metals.
7. Heat Removal Enhancement of Plasma-Facing Components by Using Nano-Particle Porous Layer Method.
8. Investigation of tritium behavior and trachability in in-vessel systems of LHD during D-D burning.
9. Assessment study on biological effects of radiation in LHD.
10. Study on environmental behavior of tritium.
11. Experimental study on liquid lithium flow for IFMIF target.
12. Integrated Experimental Process Study for Removal of Tritium and Impurities from Liquid Lithium.
13. Optimized thermo-mechanical design of high intensity neutron source test cell for material irradiation.
14. Application of Advanced High Temperature Superconductors for Fusion Plasma Experimental Devices.
15. Effects of Simultaneous Helium Irradiation on Hydrogen Behavior in Plasma Facing Materials.

These subjects are planned basically as the three years program. Therefore, the reports presented here represent one portion of the total subjects.

(Mutoh, T., Sagara, A.)



## §1. Experiment on Charge Separation and Direct Energy Conversion Using a Slanted CUSP Field

Yasaka, Y., Takeno, H. (Kobe Univ.),  
Ishikawa, M., Nakashima, Y.,  
Cho, T. (Univ. Tsukuba), Ohnishi, M. (Kansai Univ.),  
Sato, K. (Hyogo Univ.), Tomita, Y.

In an advanced fusion, direct energy conversion is applicable, and sufficient separation of charged particles is a key issue to obtain high efficiency. The authors are continuing basic experiments to realize charge separation and direct energy conversion in a small-scale CUSPDEC device<sup>1)</sup>.

Charged particles flowing into a cusp field are separated according to the difference of their Larmor radii. In general, movable region of a charged particle in an axisymmetric field is evaluated by Störmer potential. When the field is described by vector potential  $A_\theta(r, z)$ , the condition of the movable region of the particle which has charge of  $q$ , mass of  $m$ , and an incident velocity of  $v_0$  at the point  $(r_0, z_0)$  where  $A_\theta = A_0$  is expressed by  $P(r_0/r)|1 - rA_\theta/r_0A_0| \leq 1$ , where  $P = |qA_0/mv_0|$ . For electrons,  $P$  is large and  $r_0/r$  is around unity, thus its motion is restricted to be  $rA_\theta \sim r_0A_0$ , that means its orbit is on the field line. For ions, however,  $P$  is small, thus it can move in a wide region.

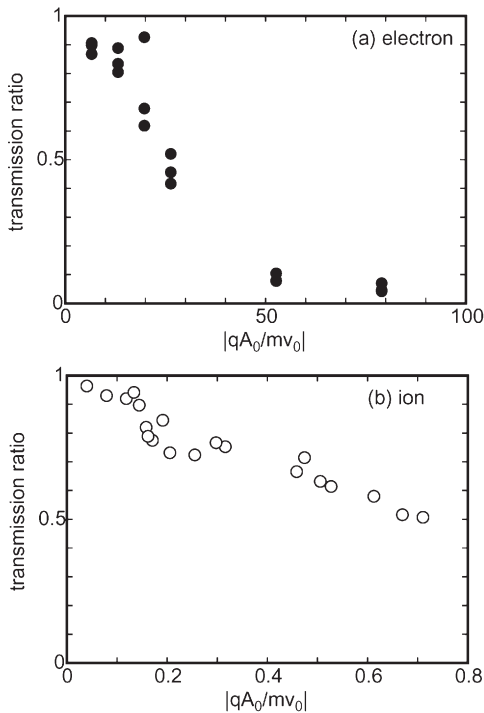


Fig. 1 Transmission ratio through the cusp region as a function of  $|qA_0/mv_0|$ , (a) and (b) are for electron and ion, respectively.

We measured transmission ratio of charged particle in the experiment on the CUSPDEC device, which is the ratio of the amount of particles passing through the cusp field to the amount of incident particles. In Fig. 1, its dependence on the value of  $P$  is shown. For electrons of Fig. 1(a), transmission ratio rapidly decreases as  $P$  increases, and it shows slight decrease for ions of Fig. 1(b). These results are consistent with above theoretical consideration.

The experiment of the direct energy conversion by the separated ions was also performed using a plane-electrode-type ion collector placed in the downstream of the cusp field. The optimum bias of the collector was examined, and the maximum energy conversion efficiency  $\eta$  was estimated.

Fig. 2 shows the dependence of  $\eta$  on averaged ion energy  $E_0$ , and  $\eta$  is constant within the measured range of energy. The dependence on spread of energy  $\Delta E$  was also measured and is shown in Fig. 3. In the figure, open circles are obtained from low power plasma sources, and closed circles are for endloss plasma of GAMMA 10. All data points are on a curve, and  $\eta$  is interpolated to be 0.65 for a fusion oriented device in which  $\Delta E/E_0 \sim 0.5$ .

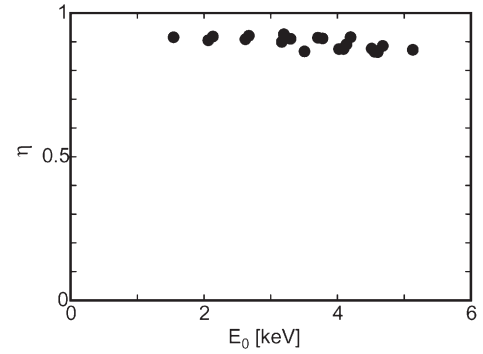


Fig. 2 Energy conversion efficiency as a function of averaged ion energy.

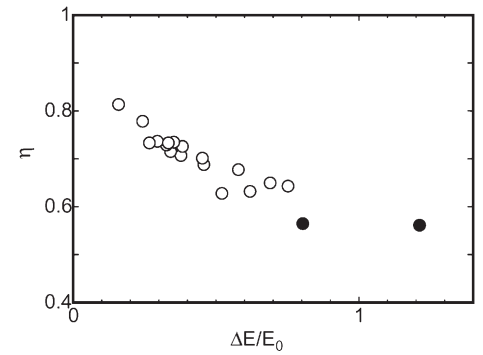


Fig. 3 Energy conversion efficiency as a function of normalized spread of energy. Open circles are for low power plasma sources, and closed circles are for endloss plasma of GAMMA 10.

### Reference

- 1) Yasaka, Y., *et al.*, Ann. Rep. NIFS April2004-March2005 (2005) 194, 195.

## §2. Optimization of Phase Velocity of Traveling Wave in a TWDEC Simulator

Takeno, H., Yasaka, Y. (Kobe Univ.),  
Ishikawa, M. (Univ. Tsukuba), Tomita, Y.

Traveling wave direct energy converter (TWDEC) is expected to recover energy of fast proton in D-<sup>3</sup>He fusion. The authors are continuing fundamental experiments of TWDEC using a small size simulator<sup>1)</sup>. In the research on beam deceleration, the simulator works in the active decelerator mode<sup>2)</sup>, in which traveling wave in the decelerator is excited externally.

As the beam deceleration is enhanced, mismatch between the beam velocity and the phase velocity of traveling wave becomes significant. In order to achieve the complete matching between them, an optimized structure of the decelerator was designed. For single particle deceleration, the phase velocity of traveling wave ( $v_\phi(z)$ ) is expressed by

$$\frac{v_\phi(z)}{v_{\phi 0}} = \left\{ 1 + \frac{3}{2} \frac{E_{M0}}{V_{\text{ex}}} z \right\}^{1/3}, \quad (1)$$

where  $z$  is an axial coordinate in which the origin is at the entrance of the decelerator.  $V_{\text{ex}}$  is an initial beam energy in the unit of eV, and  $E_{\text{M0}}$  and  $v_{\phi 0}$  are the wave field strength and the phase velocity of the wave at  $z = 0$ , respectively.

We realized the axial variation of the phase velocity expressed by Eq. (1) in two ways. One was using an electrode array aligned with the same distance<sup>1)</sup>. We varied relative phase difference between electrode voltages by adjusting the length of delay lines between electrodes, which was schematically shown in Fig. 1. By designing the length of delay lines according to Eq. (1), we can optimize the decelerator structure. The other way was to adjust the distance between electrodes with keeping the relative phase difference between electrode voltages constant. The amount of adjustment can be also derived from Eq. (1).

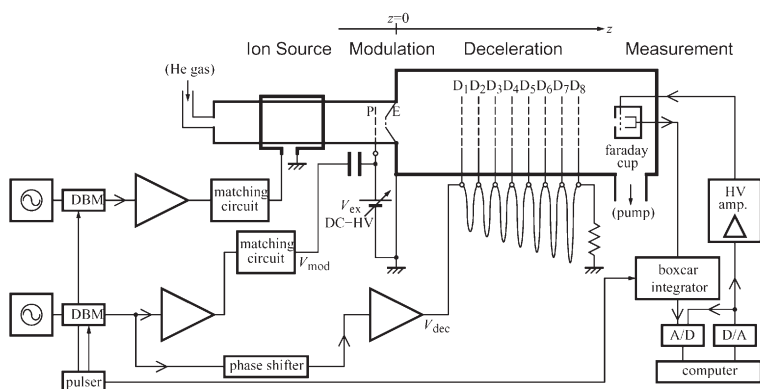


Fig. 1 Experimental setup of the TWDEC simulator.

The experiments were performed with the setup shown in Fig.1. The results are summarized in Fig.2 with the results of 1-D numerical calculation<sup>1)</sup>. The abscissa of Fig.2 is a normalized length of the decelerator. An actual length of the decelerator  $L_D$  is normalized by the maximum length of the decelerator  $L_{DM}$ , which is determined by the condition that the argument of cubic root of Eq.(1) is positive. The ordinate of Fig.2 is deceleration efficiency for unit wavelength  $\eta_1$ . Open and closed circles indicate experimental results for axially varied  $v_\phi$  and fixed  $v_\phi$ , respectively. The previous results of fixed  $v_\phi$  in the low beam energy are also presented by closed triangles. The results of 1-D numerical calculation for varied  $v_\phi$  and fixed  $v_\phi$  are indicated by thick curves and thin curves, respectively. The solid curves are for the ratio of thermal spread of energy to the averaged energy  $\langle K_T \rangle = 9.6\%$ , which is near the condition of the present experiment. The dotted curves are for  $\langle K_T \rangle = 4.8\%$ , which is the fusion oriented condition. The open diamonds are for 2-D numerical calculations<sup>3)</sup> under the fusion oriented condition.

According to 1-D numerical calculations, using varied  $v_\phi$  design,  $\eta_{\text{I}}$  is relatively kept constant, although it declines for fixed  $v_\phi$  condition. On  $L_{\text{D}} \sim L_{\text{DM}}$  of the fusion oriented condition, 1-D calculation roughly agree with 2-D calculation.

Comparing experimental results with 1-D calculation, the dependence on  $L_D$  roughly agrees with each other. The slight gap of the absolute values might be caused by insufficient modulation<sup>4)</sup> of the experiments. The optimization technique of phase velocity of traveling wave was confirmed to be effective.

## Reference

- 1) H. Takeno, *et al.*, Jpn. J. Appl. Phys. **39**(9A) (2000) 5287.
- 2) H. Takeno, *et al.*, Ann. Rep. NIFS April2004-March2005 (2005) 199.
- 3) Ishikawa, M., *et al.*, Ann. Rep. NIFS April2002-March2003 (2003) 358.
- 4) K. Sugihara, *et al.*, Proc. 5th APFA (2005) TP22.

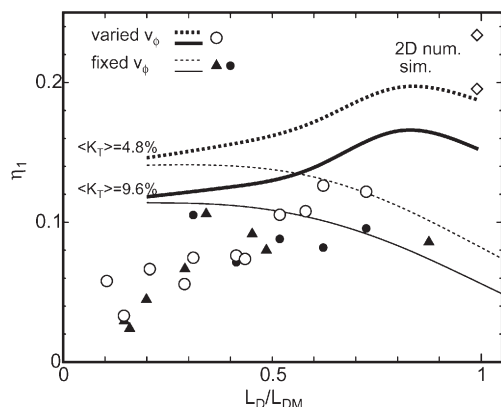


Fig. 2 Scaling of energy recovery.

### §3. Fast Power Control Capability of Large-Scale Travelling Wave Direct Energy Conversion

Ishikawa, M., Nemoto, T., Kawana, R., Okayama, S. (Univ. of Tsukuba), Yasaka, Y., Takeno, H. (Kobe Univ.), Tomita, Y.

#### 1) Objectives of Study

The major energy produced in D-<sup>3</sup>He fusion plasma is released as a kinetic energy of charged particles, especially that of the high energy protons. Objectives of the present study is to reveal behavior of self-excitation of a commercial scale travelling wave type direct energy converter (TWDEC) and to explore a capability of fast power control of TWDEC by numerical simulation.

#### 2) Basic Equations and Numerical Schemes

The basic equations used in the one (z-direction) dimensional analysis are the momentum conservation equation for fusion protons, Poisson's equation for the electric field, and external electric circuit equations. In the present analysis, the cylindrical coordinates are used because the basic configuration of the TWDEC is a cylinder.

#### 3) Self-excitation of Commercial Scale TWDEC

It has been found that the self-excitation is difficult with the designed load resistance but becomes possible with switching the load resistance from a smaller value to the designed value, resulting in the electrode voltage of about 1 MV with about 7 milliseconds and about 65 % of energy conversion efficiency.

#### 4) Fast Control of Electric Output Power

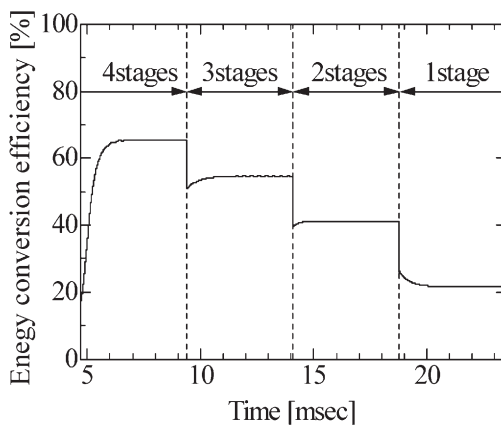


Fig.1 Time variation of the energy conversion efficiency when the number of stages is changed.

Figure 1 shows the time variation of conversion efficiency by changing the operation stages of TWDEC. Figures 2 and 3 depict the electric potential distributions along TWDEC with 3 and 2 stages operation, respectively.

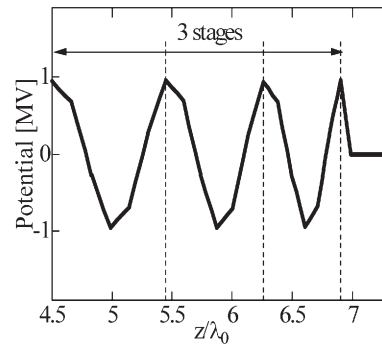


Fig.2 Electric potential distribution along TWDEC with 3 stages operation.

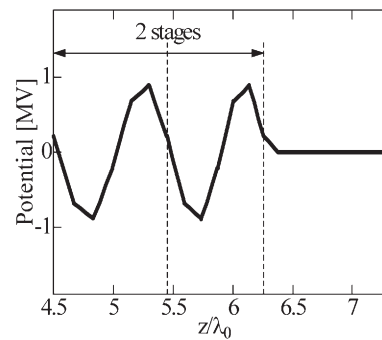


Fig.3 Electric potential distribution along TWDEC with 2 stages operation.

#### 2) Conclusions

The commercial scale travelling wave type direct energy converter (TWDEC) has been studied, and the following results have been obtained:

- (1) The TWDEC can be self-excited with the electrode voltage of about 1 MV with about 7 milliseconds by switching the load resistances. About 65 % of energy conversion efficiency is obtained.
- (2) The electric power becomes 100 %, 84 %, 63 %, and 33 % by decreasing the number of operation electrodes, and the time required for changing the load is about 5 milliseconds, suggesting that TWDEC can rapidly control the electric power.

#### References

- 1) Kawana, R. and Ishikawa, M.; 15th Int. Conf. on MHD Energy Conversion, Moscow (2005) Vol.1, p.302.
- 2) Ishikawa, M., Horita, K., Yasaka, Y., Takeno, T., and Tomita, Y.; Fusion Engineering and Design 181 (2006) 1689.

#### §4. Effects of Non-Axisymmetric Magnetic Field on Characteristics of Non-Neutral Plasma

Tomita, Y.,  
Yasaka, Y., Takeno, H. (Kobe Univ.),  
Ishikawa, M., Nakashima, Y., Katanuma, I., Cho, T.  
(Univ. Tsukuba)

In order to investigate the effect of electric field, we considered the axisymmetric hollow equilibrium of the non-neutral plasma, where the densities are uniform. The ions are located at a center region,  $0 \leq r \leq R_i$  and the electrons are cylindrically distributed,  $R_i < R_{e,in} \leq r \leq R_{e,out}$ .

The momentum equation of the non-diamagnetic equilibrium of the  $j$ -th species, where the self magnetic fields are neglected, is expressed as

$$-\frac{m_j V_{j\theta}^2}{r} = q_j (E_r + V_{j\theta} B_z^0). \quad (1)$$

The radial electric field is obtained from the Poisson equation,

$$E_r = \frac{1}{\epsilon_0 r} \sum_k q_k \int_0^r dr' r' n_k(r'). \quad (2)$$

The momentum equation, Eq.(1), has the quadratic form with respect to the angular frequency  $\omega_j = V_{j\theta} / r$ ,

$$\omega_j^2 + \sigma_j \Omega_j \omega_j + \frac{q_j E_r}{m_j r} = 0. \quad (3)$$

In the case of ions, the equilibrium are obtained by the rigid rotor configuration,

$$\omega_i / \omega_{ci0} = \frac{1}{2} [-1 \pm \sqrt{1 - 2n_{i0} / (\epsilon_0 B_{z0}^2 / m_i)}], \quad (4)$$

where  $\omega_{ci0}$  is the ion cyclotron frequency to the unperturbed axial magnetic field  $B_{z0}$ . The condition of the real rotation frequency gives the upper limit of the uniform ion density,

$$n_{i0} \leq \frac{\epsilon_0 B_{z0}^2}{2m_i} = 2.65 \times 10^{15} B_{z0,T}^2 (m^{-3}), \quad (5)$$

where  $B_{z0,T}$  is the unperturbed axial magnetic field in the unit of Tesla.

For electrons, the rotation frequency is not uniform,

$$\omega_e / \omega_{ce0} =$$

$$\frac{1}{2} [1 \pm \sqrt{1 - \frac{2n_{e0}}{r^2} \frac{\epsilon_0 B_{z0}^2}{m_e} (R_i^2 - r^2 + R_{e,in}^2)}], \quad (6)$$

which is shown in Fig.1, where  $R_{e,in} / R_i = 2.0$ ,

$R_{e,out} / R_i = 3.0$ , and  $n_{e0} / (\epsilon_0 B_{z0}^2 / m_e) = 1.0$ , where

$\omega_e^\pm$  corresponds to the sign  $\pm$  of the solution in Eq.(6).

This condition satisfies the real condition of the electron angular frequency.

The non-axisymmetric uniform magnetic field  $B_1$  to the vertical direction to the axisymmetric equilibrium configuration changes the radial component of the momentum equation,

$$\omega_j^2 + \sigma_j \Omega_j \omega_j + \frac{q_j}{m_j r} (E_r + V_{jz} B_1 \sin \theta) = 0. \quad (7)$$

One can see that the perturbation changes the effective electric field and deform the axisymmetry. The magnitude of the effect can be estimated by

$$\frac{|V_{jz} B_1|}{E_r} \sim \frac{V_{jz}}{R_i \omega_{cj0}} \frac{B_1}{B_{z0}} \sim \frac{c_s}{R_i \omega_{cj0}} \frac{B_1}{B_{z0}} \sim \frac{B_1}{B_{z0}}, \quad (8)$$

where  $B_{z0} = 100 \text{ G}$ ,  $R_i = 1 \text{ m}$  and  $T_e = 10 \text{ eV}$ . This estimation means the change of the radial electric field is the same order of the perturbed magnetic field to the unperturbed magnetic field.

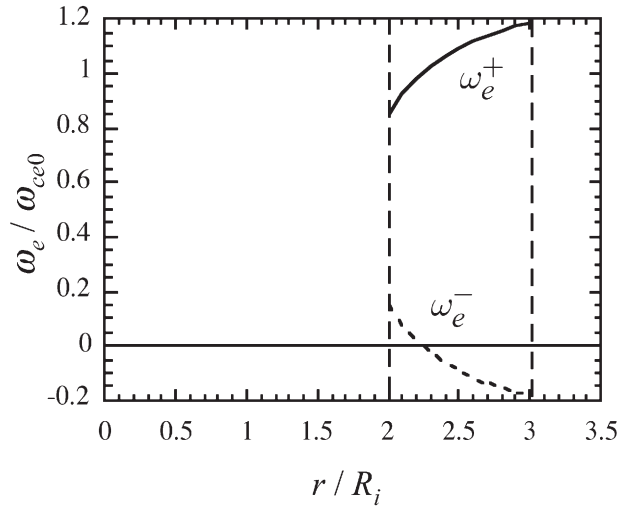


Fig. 1. Angular equilibrium frequency of electrons, which is hollow distribution with the inner and outer radius are 2.0 and 3.0, respectively.



## §5. Development of High Beta Plasma Formation Using ICRF High Harmonic Fast Wave

Takase, Y., Kasahara, H., Adachi, Y., Sasaki, M., Oosako, T., Tojo, H., Sumitomo, N., Shimada, Y., Nuga, H., Tsujimura, J. (Frontier Sci. and Sci., U. Tokyo),  
Fukuyama, A. (Eng., Kyoto U.),  
Watari, T., Mutoh, T., Kumazawa, R., Seki, T., Saito, K.

The purpose of this collaborative research is to develop a radiofrequency (RF) heating method to produce high beta plasmas, which is a common issue in spherical tokamaks (ST) and helical systems. In particular, electron heating and current drive by Landau damping and transit time damping of the fast wave at relatively high harmonics of the ion cyclotron frequency are explored. The fast wave in this frequency range is called the high-harmonic fast wave (HHFW).

The development of heating scenarios is carried out on both LHD at NIFS and the TST-2 spherical tokamak at the University of Tokyo. On LHD, existing ICRF transmitters and ICRF loop antennas can be used. The transmitters can provide RF power in the frequency range 30 to 80 MHz. TST-2 is presently the largest ST device in Japan, with  $R = 0.38$  m and  $a = 0.25$  m (aspect ratio  $R/a = 1.5$ ). It has already achieved toroidal magnetic fields of up to 0.3 T and plasma currents of up to 0.14 MA. RF power of up to 400 kW in the frequency range 10–30 MHz is available for this experiment. In addition, transmitters at 200 MHz, previously used on the JFT-2M tokamak, have been transferred from JAEA. TST-2 has the advantages of ample experimental time and flexibility with short turn-around time for hardware modifications. For example, different wave excitation schemes using different antennas can be studied.

During Fiscal Year 2005, HHFW heating experiments on TST-2 have resumed after completing power supply and RF system upgrades, following the relocation of TST-2 to the Kashiwa Campus of the University of Tokyo. The two RF transmitters were brought up at a frequency of 21 MHz, and it was confirmed that each transmitter can produce output powers of up to 200 kW for about 10 ms, which is longer than the energy confinement time in TST-2. The antenna for exciting the HHFW in the plasma was upgraded to allow variation of the  $k_{\parallel}$  spectrum, where  $k_{\parallel}$  is the component of wavenumber parallel to the magnetic field. This antenna consists of two vertically oriented induction loops (called current straps) which can be positioned at three different locations toroidally. Up to 200 kW of power can be delivered to each strap. When the RF currents flowing in the straps are out of phase, the spacing between the two current straps defines half a wavelength in the toroidal direction. The range of toroidal wavenumbers that can be excited by this antenna corresponds to toroidal mode numbers of 4 to 10. In addition, to avoid impurity generation by the RF sheath, the Faraday shield is tilted by

$30^{\circ}$  to align with typical magnetic field lines in front of the antenna.

Electron heating experiments using the HHFW have restarted on TST-2. The antenna input impedance changes in the presence of the plasma. Therefore, it is necessary to realize appropriate impedance matching in order to transfer the RF power delivered from the transmitters to wave power in the plasma. This is accomplished by use of matching circuits consisting of parallel and series variable capacitors. The development of a matching algorithm has enabled easy achievement of impedance matching.

Time evolutions of the soft X-ray emission intensity are shown in Fig. 1 for different RF powers: 0 kW, 180 kW and 360 kW. A doubling of the injected RF power causes a doubling of the soft X-ray emission increase. Since no appreciable changes are observed in the electron density or the radiated power, the sudden changes of the time derivative of soft X-ray emission at RF turn-on and turn-off are interpreted to be due to the electron temperature increase. Furthermore, the larger increase and the faster response observed on channels viewing the plasma core indicate that the wave absorption and electron heating are occurring in the plasma core.

The wavenumber spectrum differs greatly when only one strap is used to excite the wave instead of two straps. When only one strap is used, the fraction of power at low toroidal mode numbers (5 or less) is larger, and wave absorption is expected to be less effective. Both the wide-band (visible to soft X-ray) radiation increase and the stored energy increase were greater for two strap excitation, indicating that better absorption is achieved when the wavenumber spectrum is peaked at finite  $k_{\parallel}$ , as expected.

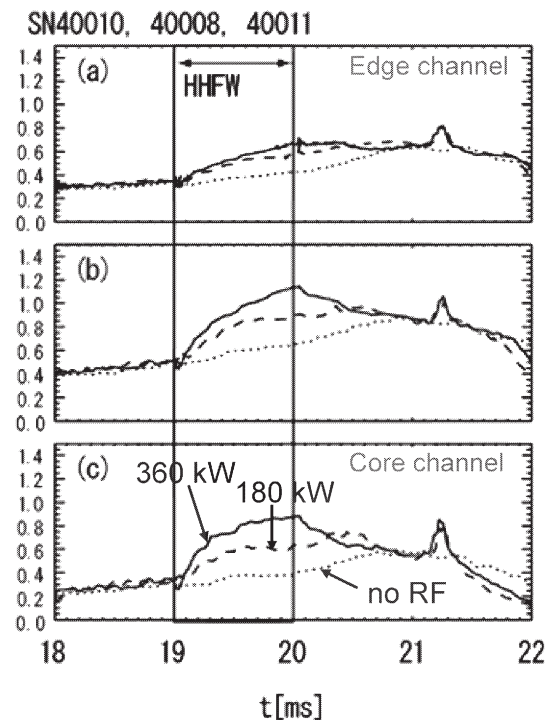


Fig. 1. Time evolutions of soft X-ray emission intensity for different HHFW powers, 0 kW, 180 kW, and 360 kW.

## §6. Experimental Study of Compatibility of a Transport Barrier and Energetic Ion Confinement

Sasao, M., Utoh, H., Nishimura, H., Kitajima, S., Shinto, K., Okamoto, M., Takahashi, H., Tanaka, Y. (Tohoku Univ.),  
Ogawa, H. (JAERI),  
Takayama, M. (Akita Pref. Univ.),  
Nishimura, K., Osakabe, M., Nagayama, Y., Isobe, M., Nishiura, M., Inagaki, S., Yokoyama, M.

The confinement of energetic ions is one of key issues for the prospect to a steady state reactor plasma using a helical system[1]. Complex motions of trapped particles in helical systems tend to enhance the radial transport. It has been known that a radial electric field might effect on the confinement of energetic particles, while it play an important role to form transport barriers and to realize improved modes. In this Joint Research, we study the compatibility of a transport barrier and energetic ion confinement in helical systems.

In order to study the effect of a radial electric field,  $E_r$ , on the energetic particle confinement in LHD, four types of  $E_r$  profile (shown in fig. 1) were assumed and the orbit calculation were performed. In fig. 2 are shown some examples of the results, for 50 keV passing protons in the  $R_x = 3.6$  [m] and  $B = 2.829$  [T]. Although the effect is small, there is obvious change in the orbit after several toroidal rotation.

In the Tohoku University Heliac (TU-Heliac), the influence of a radial electric field on the improved modes has been investigated in both positive and negative biasing experiments by using various types of electrode, such as a stainless steel (SUS) electrode, an electron emission hot cathode[2], or a Titanium electrode[3].

In this academic year, a Vanadium electrode was developed. When it was biased negatively after treatment, the high-density plasma was produced, similarly to the Titanium electrode experiment. High-density plasma production was observed up to 24 times with the V electrode after one treatment, and it was observed in not only Ar plasmas but also He plasmas. The electrode current,  $I_E$ , increased up to about 100 A and the line electron density,  $n_e l$ , and the electron density,  $n_e$ , increased by about 5-fold as compared with those before biasing. Figure 3 shows the radial profiles of the electron density and radial electric field in the V electrode biasing experiments both before (solid circles) and during biasing (open triangles) in the He plasma. With V electrode biasing, the radial distribution of the electron density sloped steeply at the electrode position and a strong negative radial electric field was formed outside the electrode. It is expected that high-density plasma will be observed in the hydrogen plasma. The  $E \times B$  drift velocity was calculated from the local electric field, which was about 30 km/s, and the Mach number,  $M_p$ , was estimated to be  $M_p \sim 20$ . This  $M_p$  was 5-fold larger than that obtained in low-density H mode.

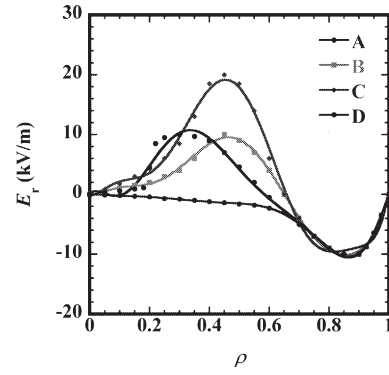


Fig. 1. The  $E_r$  profiles assumed for the orbit calculation in LHD.

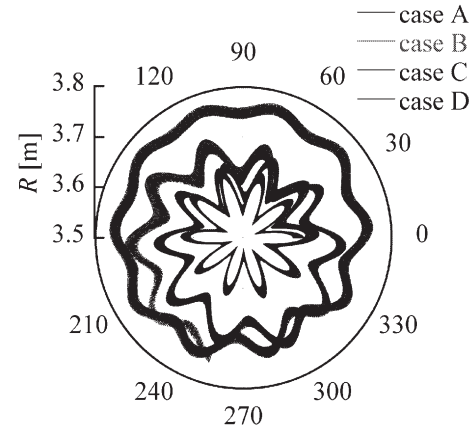


Fig. 2. Examples of the effect of  $E_r$  profiles (Fig. 1), on 50 keV passing proton orbits in the LHD configuration of  $R_x = 3.6$  [m] and  $B = 2.829$  [T].

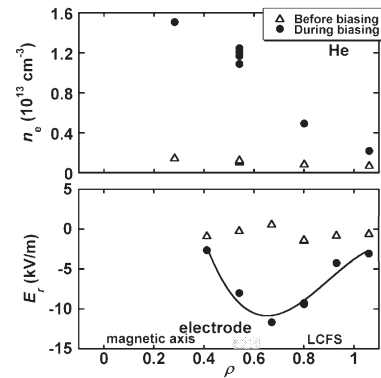


Fig. 3. The radial profiles of the electron density,  $n_e$  and radial electric field,  $E_r$  in the V electrode biasing experiments.

### References

- [1] Sasao, M. et al., Proceedings of 18 IAEA Fusion Energy Conference, IAEA-CN-77/EX9/1(Sorento, October 2000).
- [2] Kitajima, S. et al. Proceedings of 20 IAEA Fusion Energy Conference, IAEA-CN-116/EX/9-3(October 2004).
- [3] Utoh, H. et al. Proceedings of EPS2005 (P2.006).

§7. Study of the Fueling Pellet Transportation in the Guiding Tube

Yoshikawa, M., Kubota, Y., Kobayashi, T., Matama, K., Nakashima, Y. (Univ. Tsukuba, PRC), Yamada, H., Sakamoto, R.

In recent fusion researches, a hydrogen ice pellet injection is an indispensable method for fueling to plasmas. A measurement of pellet parameters (velocity, mass and shape) just before injection to the plasma is important for evaluation of the fueling efficiency and the transport efficiency (the loss of the pellet velocity and mass) through the guiding tube. However the mechanisms of the pellet transformation in the guiding tube have been not yet clear. We developed a new diagnostic system for a pellet size, speed and shape, simultaneously.<sup>1-2)</sup> We have developed a new diagnostic system in order to study a pellet transformation in a guiding tube. Figure 1 shows a schematic diagram of a pellet reflection

measuring system for studying the pellet transformation in the guiding tube. The system consists of three parts. They are: light gate systems, a pellet reflected section on the steal plate, and a position detecting shadowgraph systems. This system provides the pellet reflection angle, velocity and shape change by the reflection on the stainless plate, simultaneously.

Moreover, we tried to produce the sub-millimeter sized pellet for studying the pellet transformation in the guiding tube in the GAMMA 10 pellet injection system. We succeeded to make pellet of 0.4 mm in diameter for detailed density control of the GAMMA 10 plasma.

Reference

1) Yoshikawa, M., et al. ; Annual Report of NIFS, April 2003-March 2004 (2004) 98.  
2) Yoshikawa, M., et al. ; Annual Report of NIFS, April 2004-March 2005 (2005) 202.

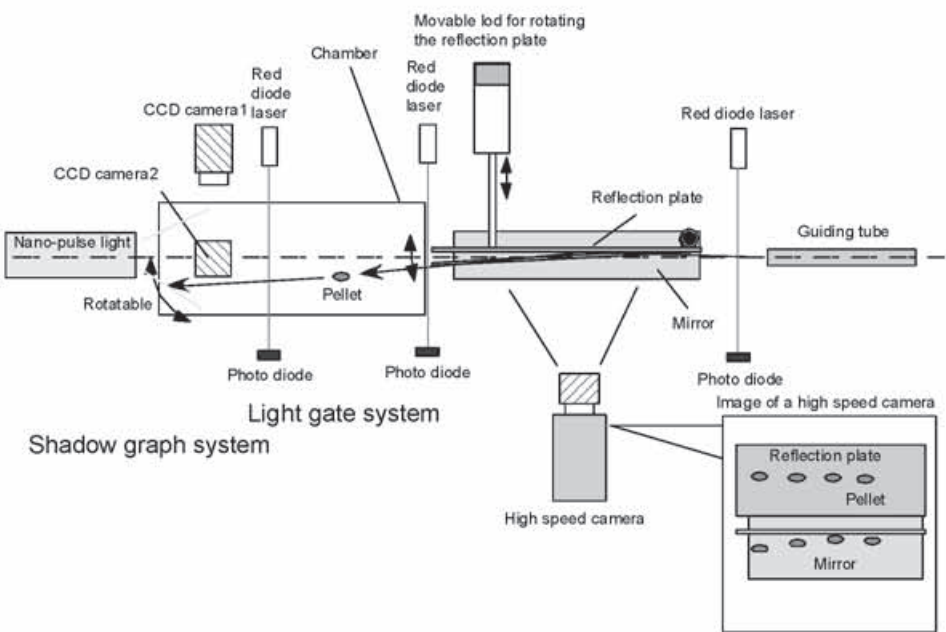


Figure 1: Schematic diagram of the pellet reflection measuring system for studying the pellet transformation in the guiding tube.

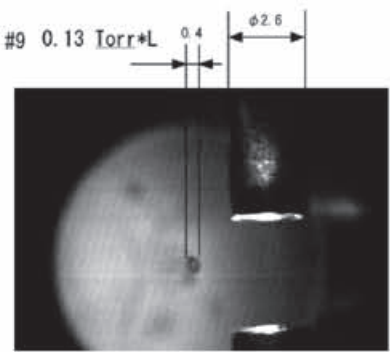


Figure 2: A sub-millimeter sized pellet produced for GAMMA 10 plasma fueling.

## §8. Performance of Remote Steering Antenna in Anti-Symmetric and Symmetric Directions

Idei, H. (Kyushu Univ.), Shimozuma, T., Ohkubo, K., Kubo, S., Notake, T., Hanada, K. (Kyushu Univ.)

A remote steering antenna concept has been proposed and developed for Electron Cyclotron Heating and Current Drive (ECH/ECCD) experiments at the International Thermonuclear Experimental Reactor (ITER). There are two operation modes in a remote steering antenna, anti-symmetric and symmetric modes. The anti-symmetric antenna has been considered as the ITER-antenna, and the symmetric antenna with an extended steering-angle capability was developed and used for the ECH/ECCD experiment in the TRIAM-1M tokamak[1]. The antenna length and the side of squared cross-section determine an operation range in anti-symmetric and symmetric directions. The output beams were calculated with a basis of the imaging property of a square corrugated waveguide[2]. Figure 1 shows the transmission efficiencies as a fundamental mode in the imaging property calculation for various antenna lengths  $L$ , when the electric field is perpendicular to the steering  $x-z$  plane. The remote steering configuration with the coordinate system ( $x-y-z$ ) is illustrated in Fig.2. A side of the square was fixed at 40mm, and the frequency was 170GHz. The input beam had a waist size  $w_0$  of 14mm at the input aperture. The antenna with  $L=3.60$  m was the normal ITER-type anti-symmetric direction antenna, while the antennae with  $L= 3.15$  m and 3.30 m were two operation region with the high transmission efficiencies in the anti-symmetric and symmetric directions, respectively.

In order to test the antenna performance experimentally at various antenna lengths, low power test facilities have been built. Figure 3 shows photographs of the low power test facilities. The facilities had a large moving measurement-stage, and the wide area of  $1.6 \text{ m} \times 0.6 \text{ m}$  was able to be scanned in the ( $x-y-z$ ) coordinates. The spatial setting resolution was 0.01 mm in the area of  $1.6 \text{ m} \times 0.6 \text{ m} \times 0.5 \text{ m}$ , which was the order of  $1/100$  for the wavelength at the frequency. The He-Ne laser was set at the detector stage to align the test components. The intensity measurements have been begun at the low power test facilities. An  $\text{HE}_{11}$  mode generator, which was composed of a scalar horn antenna and a circular corrugated waveguide, was used to generate a Gaussian beam. The mirror array composed of four quasi-optical mirrors was prepared to modify the beam profiles, and to inject the beam into the antenna with

proper input angles. The input angles were able to be set from 0 to 25 degrees. The obtained input beam respectively had the beam sizes of  $w_x = 13.5 \text{ mm}$  and  $w_y = 14.2 \text{ mm}$  in the  $x$  and  $y$  directions at the input aperture of the antenna, being similar sizes in the imaging property calculation. In order to test the antenna performance, the phase profile measurement was important as well as the intensity measurement[1]. The phase measurement system will be prepared, and the output beam from the antenna will be analyzed from the measured intensity and phase profiles.

This work was realized in the LHD-project collaboration (NIFS04KOAR005) organized by NIFS.

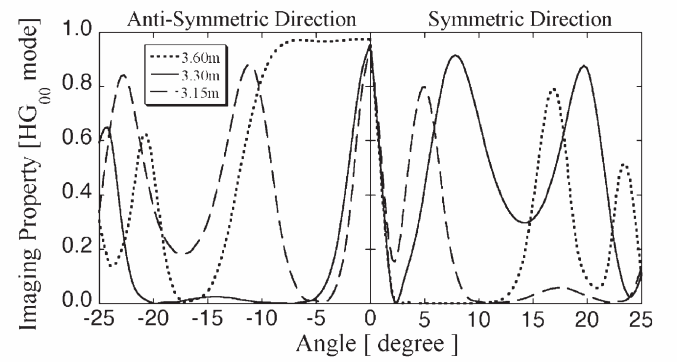


Fig. 1: Imaging property calculation of a fundamental mode as a function of the input angle.

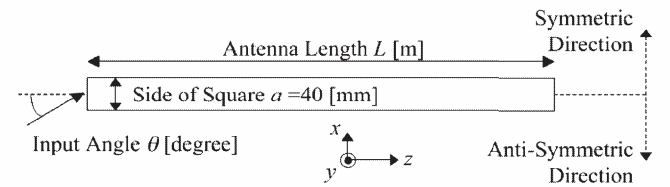


Fig. 2: Illustration of the remote steering configuration.

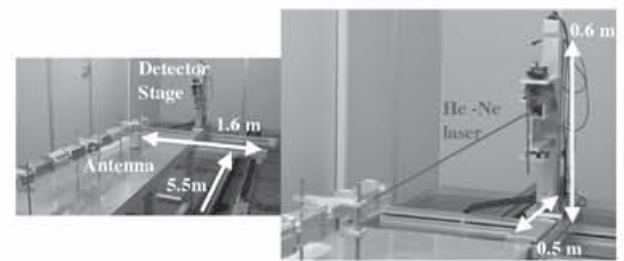


Fig. 3: Photographs of low power test facilities

## References

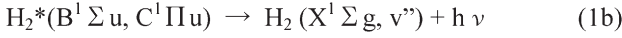
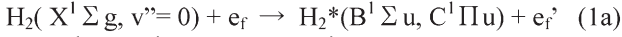
- [1] Idei, H., *et al* , Nuclear Fusion, **46**, 489 (2006).
- [2] Ohkubo, K., *et al* , Fusion Eng. and Design, **65**, 657 (2003).



## §9. Production Mechanism of D<sup>-</sup> Ions and Evaluation of D<sup>-</sup> Ion Current Extraction

Fukumasa, O., Naitou, H., Tauchi, Y., Mori, S. (Dept. Elect. Electronic Eng. Yamaguchi Univ.),  
Sawada, K. (Shinsyu Univ.), Hamabe, M. (Chubu Univ.),  
Takeiri, Y., Tsumori, K.

In a tandem volume source, H<sup>-</sup> ions are generated by the dissociative attachment of slow plasma electrons  $e_s$  ( $T_e \sim 1$  eV) to highly vibrationally excited hydrogen molecules  $H_2(v'')$  (effective vibrational level  $v'' \geq 5-6$ ). These  $H_2(v'')$  are mainly produced by collisional excitation of fast electrons  $e_f$  with optimum energy of about 40 eV. Namely, H<sup>-</sup> ions are produced by the following two step process, i.e.  $H_2(v'')$  production and H<sup>-</sup> formation:



Production process of D<sup>-</sup> ions is believed to be the same as that of H<sup>-</sup> ions described above. We have studied relationship between negative ion production (i.e. H<sup>-</sup> and D<sup>-</sup> ions)<sup>1-3)</sup> and plasma parameters across the magnetic filter (MF). By varying the intensity of the MF, axial distributions of  $T_e$  and  $n_e$  in both H<sub>2</sub> and D<sub>2</sub> plasmas are changed strongly in the downstream, i.e. extraction region<sup>3, 4)</sup>.

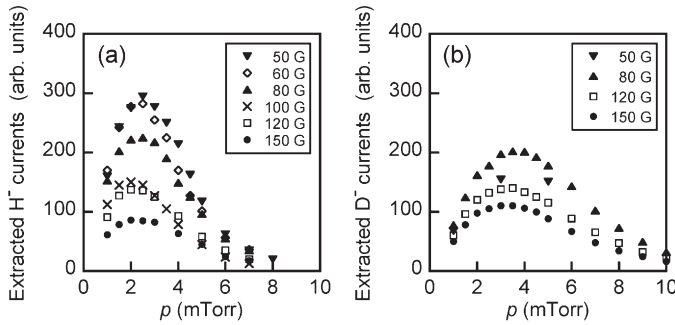


**Fig. 1.** Pressure dependences of extracted (a) H<sup>-</sup> and (b) D<sup>-</sup> currents. Experimental conditions are as follows:  $V_d = 70$  V,  $I_d = 5$  A, and extraction voltage  $V_{ex} = 1.5$  kV. Parameter is the magnetic field intensity of the MF.

Figure 1 shows the pressure dependence of extracted negative ion currents from (a) H<sub>2</sub> and (b) D<sub>2</sub> plasmas. In both cases, as described above, the negative ion currents are varied due to the change in plasma conditions with decreasing the MF intensity. In both cases, there are also some optimum pressures. With increasing gas pressure, negative ion currents (i.e. the H<sup>-</sup> current,  $I_{H^-}$  and the D<sup>-</sup> current,  $I_{D^-}$ ) increase in their magnitude, reach the maximum value, and then, decrease. Decreasing MF intensity, the optimum pressure  $p_{opt}$  shifts to higher pressure. For D<sup>-</sup> production,  $p_{opt}$  is from 0.27 to 0.47 Pa. On the other hand, for H<sup>-</sup> production,  $p_{opt}$  is from 0.2 to 0.27 Pa. Optimum

pressure in D<sub>2</sub> plasmas is slightly higher than one in H<sub>2</sub> plasmas.

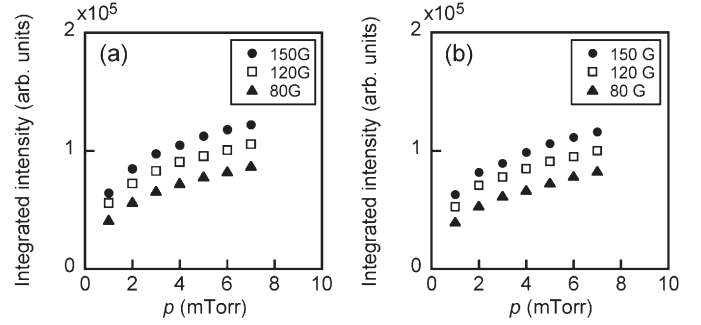


**Fig. 2.** Pressure dependence of integrated intensities of VUV spectra from (a) H<sub>2</sub> and (b) D<sub>2</sub> plasmas, where  $V_d = 70$  V and  $I_d = 5$  A. Parameter is the magnetic field intensity of the MF.

Figure 2 shows pressure dependence of integrated intensities of VUV spectra from H<sub>2</sub> plasmas, where the intensity of the MF is a parameter. The VUV emissions increased gradually with gas pressure. The values of integrated intensities with 150 G are highest in the entire region of gas pressure, and intensities are decreased with the intensity of the MF. As shown in Fig. 1, the extracted H<sup>-</sup> and D<sup>-</sup> currents vary with the intensity of the MF. It is noted that the integrated intensity of the VUV emissions and the extracted H<sup>-</sup> and D<sup>-</sup> currents vary in opposite directions, respectively, when the MF is varied<sup>4)</sup>. Numerical calculations show that the VUV emissions associated with the process (1b) are a function of the fast electron density. Therefore, as the VUV measurements were made in the source region, these should be higher with  $B_{MF} = 150$  G than with  $B_{MF} = 80$  G. We have also confirmed the same tendencies on the discharge power dependences between VUV emissions and H<sup>-</sup> and D<sup>-</sup> currents as those on pressure dependences above-mentioned MF intensities.

According to the results shown in Figs. 1 and 2 and related discussions, our present picture on negative ion production is as follows: In the present experimental conditions with low-pressure, electron-neutral collision mean free paths for destruction of the vibrationally excited molecules (i.e. ionization and dissociation collisions) are a few tens of centimeters. Therefore, sufficient amount of H<sub>2</sub>( $v''$ ) and D<sub>2</sub>( $v''$ ) are transported to the extraction region, although H<sub>2</sub>( $v''$ ) and D<sub>2</sub>( $v''$ ) are produced by the collisions between the ground state molecules and fast primary electrons in the source region. The negative ions are produced by the process (2) of slow plasma electrons to H<sub>2</sub>( $v''$ ) and D<sub>2</sub>( $v''$ ) in the extraction region. Namely, negative ion production is rate-determined by the plasma parameters in the extraction region.

## References

- 1) Mori, S. et al.: 30th IEEE Conf. Plasma Science (2003).
- 2) Fukumasa, O. et al.: Contrib. Plasma Phys. **44** (2004) 516.
- 3) Mori, S. and Fukumasa, O.: Thin Solid Films **506-507** (2006) 531.
- 4) Fukumasa, O. and Mori, S.: Nucl. Fusion **46** (2006) S287

## §10. Development of Continuously Size-Controllable Pellet Injector

Sato, K.N., Thang, D., Sakamoto, M., Kawasaki, S., TRIAM Exp. G. (RIAM, Kyushu Univ.), Goto, K., Rego, I. (IGSES, Kyushu Univ.), Sakakita, H. (AIST), Kogoshi, S. (Fac. Sci. Tech., Tokyo Univ. of Sci.), Yamada, H., Sakamoto, R.

In order to have a common measure of pellet ablation, the regression study has been performed as an international cooperation activity, obtaining "IPAD" (International Pellet Ablation Database) [1]. However, these are an empirical scaling, and the mechanism of pellet ablation still remains to be studied.

According to the code calculations based on a typical pellet ablation model (e. g., so-called the neutral gas shielding model), it is understood that the penetration depth into plasma is always quite sensitive to the pellet size. If the pellet size is too large, the pellet passes through the plasma, and if it is too small, it is trapped at the plasma surface. Also, an

effective range of the pellet size for a certain plasma is generally very narrow, and this range largely varies depending on each plasma parameters and plasma size. Thus, the precise controllability of the pellet size, especially the size controllability with continuously variable system will be quite effective in order to carry out the detailed studies on pellet ablation and associated phenomena.

A pellet injector of new type with precisely and continuously controllable system of pellet size has been developed. This has a unique mechanics and structure of producing a frozen pellet in extremely low temperature region. In the device the length of the cylindrical pellet ( $\Phi$  1.0mm) will be precisely controlled from 0.5 to 3 mm by using the special "length restriction rod". Preliminary results show that the pellet sizes are not well controlled (Fig.1) because of the attachment of frozen pellet and the rod. The improvements of core structure of the injector and procedure in the pellet production (Fig.2) are now underway.

[1] L.R.Baylor et al.; Nucl. Fusion 37 (1997) 445.

[2] K.N.Sato et al.; APFA (2005) IO5.

[3] K.N.Sato et al.; 32nd EPS (2005) P5.128.

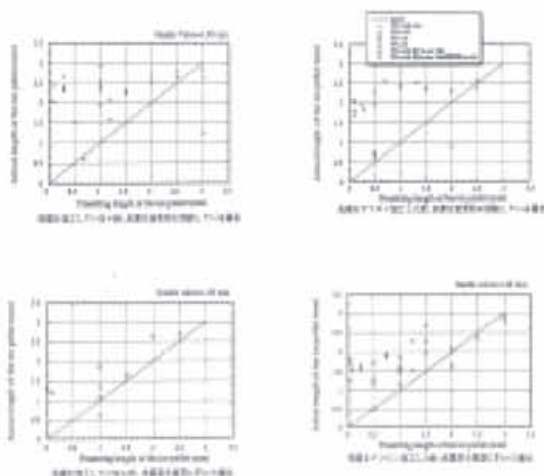


Fig.1 Preliminary results of the pellet size controlling experiment.

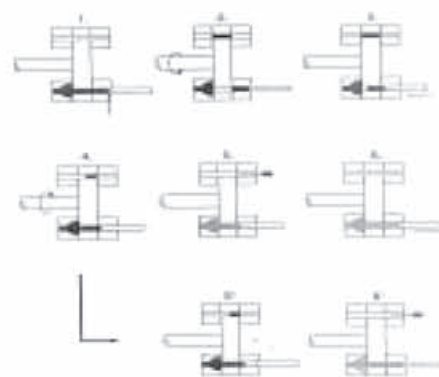


Fig.2 New procedure of pellet production in the continuously size-controllable system.

## §11. Chaos Control of Fluctuations Caused by Flute Instability in ECR Plasma

Kawai, Y. (Research Institute for Applied Mechanics, Kyushu University)

There is an increasing interest in chaos and turbulence observed in plasmas. It is well known that turbulence causes many troublesome features in fusion oriented plasmas, that is, the instability evolves into fully developed turbulence and leads to the anomalous transport. Therefore, suppression and control of turbulence is necessary for improving the confinement. Thus, to control turbulence in plasma is one of the most important subjects in plasma physics. Although the control of turbulence is generally hard, the control of chaos will be possible. The experiments on controlling chaos have been realized in various fields, such as electronic chaos oscillator, mechanical pendulums, lasers, chemical systems and even a cardiac system. Controlling chaos in plasma has attracted much attention since controlling chaos has the advantage that it does not need high power to control. Pyragas has proposed a time-delayed feedback technique by modifying the OGY (Ott, Grebogi, and Yorke) method, which is appropriate for experimental systems working in real time. This method is based on the feedback perturbation constructed in the form of the difference between the delayed output signal and the output signal itself.

When the stabilization of unstable period is attained, this perturbation vanishes identically. Therefore, this is also a controlling method by a tiny perturbation and is a rather effective method to control a system with big power.

Here a new feedback method by modulating microwaves for ECR discharge is proposed to perform controlling chaos of fluctuations caused by the flute instability with the time-delayed auto synchronization (TDAS) method.

The experiments were performed using a large diameter ECR plasma device with an inner diameter is 400 mm and a length 1200 mm. The pressure of Ar gas is around 0.5 mTorr.

The frequency of microwaves is 2.45 GHz. Microwaves are launched into a chamber as a circular TE<sub>11</sub> mode thorough the waveguide uptaper and the quartz window. The plasma parameters were measured with a cylindrical single Langmuir probe. The ECR plasma parameters generated by the microwaves of 500 W are :the electron density  $n_e \sim 10^{11} \text{ cm}^{-3}$ , the electron temperature  $T_e \sim 4 \text{ eV}$  and the ion temperature  $T_i \sim 0.1 \text{ eV}$ . The experiments on controlling chaos were performed by applying a feedback signal to the microwave power source.

We examined the behavior of the ion saturation current fluctuation when the microwave was injected with CW mode. Observed fluctuation had the characteristics of the flute instability, i.e., the phase difference between density fluctuation and potential fluctuation is out of phase at the same point, the fluctuation grows at the point where the density profile has steep gradient, and the phase of the fluctuation is constant along the direction parallel to the magnetic field. The frequency of the flute instability ranged from 3 kHz to 5 kHz, depending on the gas pressure.

We calculated the correlation dimension from time series data by using the method of Grassberger and Procaccia in order to estimate the state; periodic, chaotic or turbulent. The correlation dimension saturated to non-integer at 450 W while it did not saturate at 700 W. Therefore it is concluded that the system is chaotic and turbulent for the low microwave power and the high microwave power, respectively. We attempted controlling chaos to the present chaotic system using the TDAS, where the gas pressure and the microwave power is 0.4 mTorr and 500 W, respectively. Without feedback control, large amplitude bursts were observed. On the other hand, when TDAS feedback control was performed, such bursts disappeared, that is, the intermittency decreased considerably. The calculated correlation dimension of the data with TDAS became 4.0 which means that the system is periodic. Thus, we succeeded in the control of the chaos caused by the flute instability.

§12. Water Vapor Absorption for 48-, 57-, and 119- $\mu\text{m}$  Far-Infrared Laser Wavelength

Nakayama, K., Okajima, S. (Chubu Univ.),  
Kawahata, K., Tanaka, K., Tokuzawa, T., Akiyama, T.,  
Ito, Y.

A new two-color interferometer system using 48- and 57- $\mu\text{m}$   $\text{CH}_3\text{OD}$  lasers pumped by a continuous wave 9R(8)  $\text{CO}_2$  laser is under development to measure the electron density profile of the LHD [1]. In the short wavelength far-infrared region, water vapor absorption in the atmosphere is one of severe problem for laser beam transmission [2]. Although the absorption for some FIR laser lines has been reported, those for 48- and 57- $\mu\text{m}$  laser lines have not been measured. Accordingly, we have measured the water vapor absorption in the atmosphere by using 48-, 57-, 119- $\mu\text{m}$  lasers as the sources.

Figure 1 shows the schematic diagram of the measurement system. The cell is a 1.25-m-long glass tube with an inner diameter 90 mm, and the both ends are sealed by the 1mm-thick polyethylene sheets which transmit FIR laser light. The humidity in the cell is adjusted by a moist air and a dry air. The humidity and the temperature are measured by two thermometer / hygrometer at both ends. A transmitted laser beam after passing through the cell which filled water vapor is detected by a pyroelectric detector, and the attenuation is calculated by using monitor signal. The measurement is carried out at 22  $^{\circ}\text{C}$  and standard atmospheric pressure (1 atm) except for 0% humidity in a vacuum.

Figure 2 shows the relative humidity dependence of the ratio of the transmitted signal. The water vapor absorption of 48- and 57- $\mu\text{m}$  laser lights is larger than that of 119- $\mu\text{m}$  laser light. The transmissivity has nearly linear dependence on relative humidity. The absorption coefficient of each laser light is calculated, and the result is shown in Fig. 3. If humidity is 5% at 22 $^{\circ}\text{C}$  (actual vapor density  $\rho = 0.97 \text{ g/m}^3$ ), the absorption coefficients for 48- and 57- $\mu\text{m}$  laser lights are about 0.060  $\text{m}^{-1}$  and 0.031  $\text{m}^{-1}$ , respectively. In this condition, transmission losses of both lasers at a distance of 80 m are 99% at 48- $\mu\text{m}$  laser and 92 % at 57- $\mu\text{m}$  laser. It is therefore very important to maintain transmission area at sufficiently lower humidity, when 48- and 57- $\mu\text{m}$  lasers are used as light sources of the interferometer.

Reference

- 1) K. Kawahata, et al., Rev. Sci. Instrum. **75**, (2004) 3508
- 2) J. J. Gallagher, et al., Infrared Physics **17**, (1977) 43

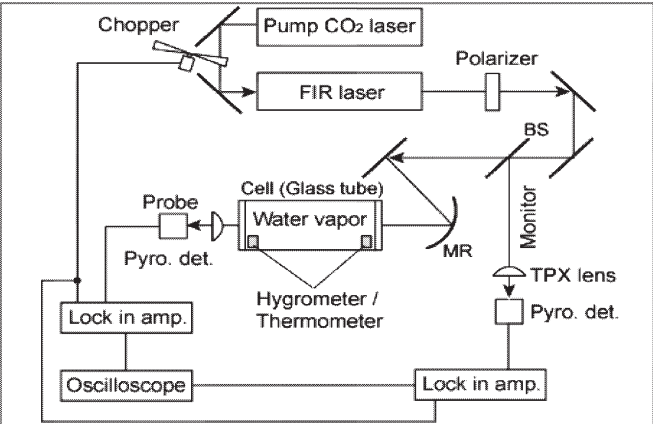


Fig. 1: Schematic diagram of the measurement system of water vapor absorption.

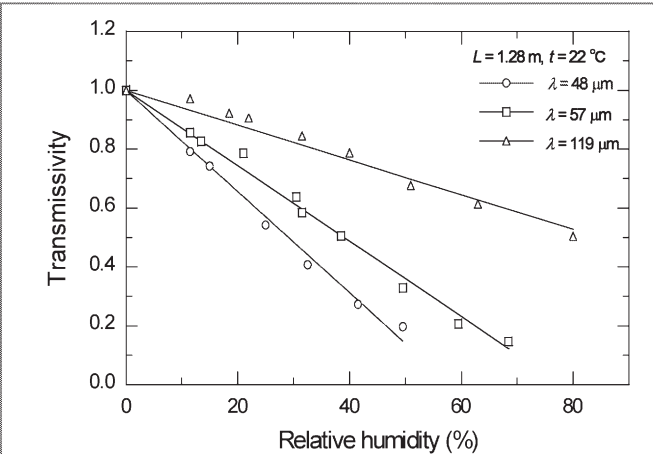


Fig. 2: Transmissivity of water vapor as a function of relative humidity for 48-, 57-, and 119- $\mu\text{m}$  laser lights.

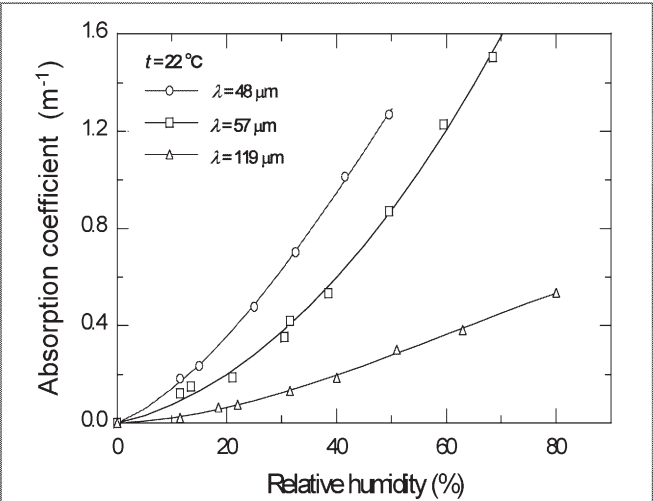


Fig. 3: Absorption coefficient of water vapor as a function of relative humidity for 48-, 57-, and 119- $\mu\text{m}$  laser lights.



### §13. Dynamics of Hydrogen Atoms and Molecule in the Periphery Plasma Studied by Means of Polarization Separated Spectra

Iwamae, A., Sakaue, A., Sakaue, M. (Dept. Mech. Eng. Sci. Kyoto Univ.),  
Sawada, K. (Faculty of Eng., Shinshu Univ.),  
Goto, M., Morita, S.

Plasma transport studies in the open field line regions are of great importance for understanding how to transfer heat fluxes to the diverter, and how to secure the core plasma from being contaminated.

Emission from a plasma in the Large Helical Device (LHD) was observed from 1-O port with ten lines-of-sights equipped with polarization separation optics<sup>1)</sup> as shown in Fig. 1. The emission from a cylindrical region of 70 mm in diameter in the plasma collimated by lenses was transmitted through optical fibers to a spectrometer ( $f = 1.33$  m, 1800 grooves/mm).

Figure 2 show an example of the polarization separated line profiles of the  $H\alpha$  emission observed at  $z = -0.026$  m, slightly below the equatorial plane. The peak of the  $-37^\circ$  polarized component is located at the longer wavelength direction from the stationary  $H\alpha$  line position, and the peak of the  $53^\circ$  polarized component is slightly shifted to the shorter wavelength direction. The  $\pi$  polarized light ( $\Delta m_j = 0$  transitions) of the line is parallel to the magnetic filed direction. We interpret above spectral structures as that the  $H\alpha$  line is emitted at two locations, the inner and the outer points, on the line-of-sight and there are two atom temperature components at each point, which move with a certain velocity component along the line-of-sight. Least-squares fitting is performed on the observed both polarized components simultaneously, with four set of Zeeman profiles, cold and warm components in inner and outer regions, pulse a broad Gaussian profile with a magnetic field structure of the magnetic field axis  $R_{ax} = 3.70$  m and the strength at the axis  $B_{ax} = -2.676$  T. Hyper-fine structures are considered to synthesis line profiles. The result of the fitting is shown in Fig. 2. Table I summarizes the parameters deduced from the fitting. From the parameter values of the magnetic field vectors, the emission

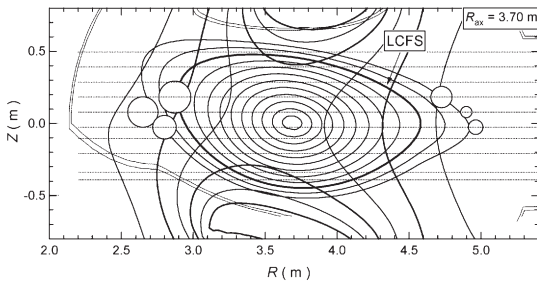


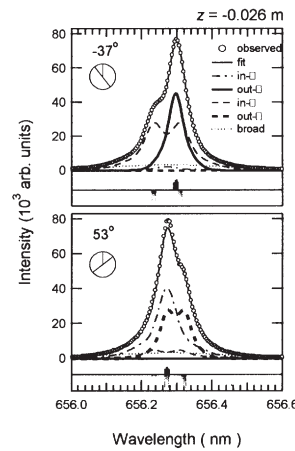
**Fig. 1.** Locations of the  $H\alpha$  emission obtained by means of the fitting to the polarization separated spectra.

locations are identified to be  $R_{in} = 2.89$  m and  $R_{out} = 4.83$  m. These locations are shown in Fig. 1 with the consistent results of the fitting for other line-of-sights. It is difficult to reach reasonable convergence of the fitting with two emission locations for the upper and lower line-of-sights. This is likely to be reflected light from the divertor plates or the vacuum vessel because of the unbalanced intensity of the two polarized components.

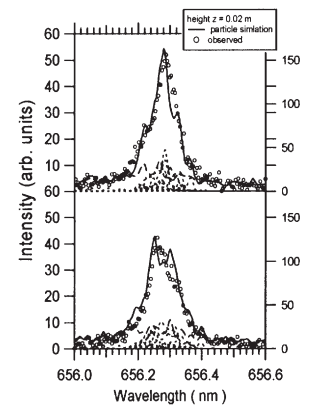
The polarization separated spectra are synthesized with a fully three-dimensional neutral transport code including molecular dissociation processes. Figure 3 shows the observed and synthesized  $H\alpha$  spectra. The synthesized spectra are obtained by summing the  $H\alpha$  emission along horizontal lines on the line-of-sight. The polarization of  $H\alpha$  emission by Zeeman effect is considered. The synthesized spectra show the reasonable agreement with the observed. The profile is explained as composed of cold and warm components: dissociative excitation and electron collisional excitation of the atoms produced by dissociation, and hot component: electron collisional excitation of atoms produced by charge exchange.

Table I. The determined parameters by the fitting.

	Inner		Outer	
	cold	warm	cold	warm
$R$ (m)	2.89		4.83	
$B$ (T)	2.06		1.35	
$T_a$ (eV)	0.4	1.0	2.8	11.8
$v$ (km/s)	4.1		-7.2	



**Fig. 2.** The observed  $H\alpha$  spectra and the fitting results.



**Fig. 3.** The observed and synthesized polarization separated spectra.

1) A. Iwamae, *et. al.*, Phys. Plasmas **12**, 042501 (2005).

## §14. Spectroscopy and Atomic Modeling of EUV Light from LHD Plasmas

Nishimura, H. (Institute of Laser Engineering, Osaka U.)

### i) Introduction

EUV (extreme ultraviolet) line radiations from medium-Z impurity elements plays an important role in taking into account the core energy balance in fusion plasmas. Such EUV emissions also attract attention as a highly bright light source including 13.5 nm EUV for use in next-generation lithography of semi-conductor devices. A lot of issues associated with atomic modeling must be addressed to realize a clean and efficient EUV source. Magnetically confined plasmas such as LHD are one of the best standard plasma sources because plasma profiles are steady, and temperature and density profiles are well diagnosed.

A time-resolving CCD detector has been implemented to the EUV spectrometer prepared in last year and temporal evolution of EUV spectra from Sn plasma confined in the LHD were observed.

### ii) CCD detector

The CCD system adopts a back-illuminated CCD of 26x26  $\mu\text{m}$  pixel size in a 1024x256 format. A drive frequency of 1 MHz and a rapid-charge-transfer mode enable us a temporal resolution of 10 ms for 30 minutes seamless-data acquisition. After careful alignment at ILE, Osaka University, the spectrometer was implemented to the LHD at NIFS to carry out over-all operation test and spectroscopic observation. A newly developed jig for the alignment procedure was fabricated to correct an angular misalignment of 0.2 deg.

### iii) Inclusion of high order diffraction components

The spectrometer adopts a grazing-incidence HITACHI grating of 1200 lines/mm. This grating is made as a replica of mother-form with grooves fabricated mechanically with a ruling-engine. This grating has been widely used for EUV spectroscopy but the dispersed spectra inherently involve high order components. When the emission lines from high-Z material such as Sn are observed in dense plasmas, the elimination of such components becomes really important. Then, Influence of the high order components was experimentally investigated. Figure 1 shows an EUV spectrum after C pellet injection. The 2nd, 3rd, and 4th order components of C VI (33.7 Å) are clearly seen. And their intensities are nearly the same as those of the 1st order.

### iv) Spectroscopic observation

Sn-coated graphite pellets were injected into the LHD using a pressurized gas gun. The size of the pellets was typically 0.9 mm in diameter and 0.9 mm in length. By adjusting the Sn overcoat thickness to an adequate range,

LHD discharges could be maintained without radiation collapse. Typical spectra are shown in Fig. 2. The time of the pellet injection was 1.02 sec. The emission intensity from Sn ions drops rapidly after the injection, based on the particle diffusion process of the LHD plasma. A steady emission was maintained during 1.07 and 1.14 sec. The EUV spectra during this interval are useful as benchmark data for the present atomic modeling. The plasma temperature and density at the moment are 1-2 keV and  $3 \times 10^{13} \text{ cm}^{-3}$ , respectively. In the wavelength region around 13-14 nm, intense emissions arising from  $\text{Sn}^{8+ \sim 12+} 4d-4f$  transitions are visible. Spectroscopic analyses are now under way by using FAC code and a rate-equation solver.

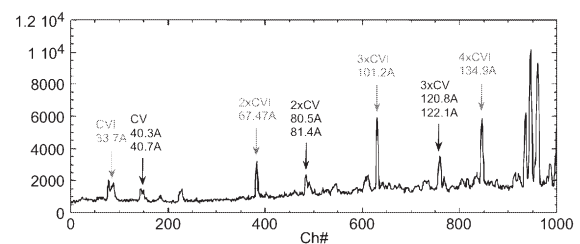


Fig. 1 High order diffraction components from C VI (33.7 Å) in LHD plasma.

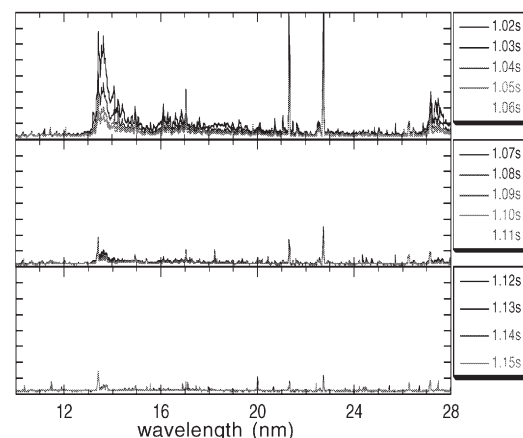


Fig. 2 Time resolved Sn spectra from LHD plasma.

### v) Report

- S. Morita, et al., J. of Plasma Science and Technology, Vol.8, No.1 pp.55-60 (2006).

### vi) Collaborators

The author would like to express his sincere appreciation to all contributors for their invaluable collaborations listed below: Morita, S., Goto, M., and Katai, R., Suzuki C. (NIFS), Nozato, H. (AIST), Amano, T. (Prof. Emeritus of NIFS), Nishihara, K., Norimatsu, T., Fujioka, S., Nagai, K., and Kai T. (ILE, Osaka U.).

## §15. Development of Wide Band and Compact X-Ray Spectrometer

Tawara, Y., Sakurai, I., Matsumoto, C., Furuzawa, A. (EcoTopia Sci. Inst. Nagoya Univ.), Morita, S., Goto, M. (NIFS)

A wide band and compact X-ray spectrometer has been constructed to measure simultaneously the  $K\alpha$  X-ray transition array from all Fe ionization stages and to evaluate the charge state distribution in the plasma center. We started to develop the wide band and compact X-ray spectrometer from 2004 and installed the spectrometer at #1-O port on the LHD in 2005 Nov (Fig.1a). As the first step, we checked vacuum leakage of the spectrometer. Then, we regulated the alignments between a CCD detector and a crystal position using CCD 2D-image data of LHD plasmas. At present, the data are taken with a time interval of 10ms under a full vertical charge shift mode. Thus we have obtained the X-ray spectra in the wide energy range of 6.4-7.0keV from 2005 Nov to 2006 Feb., routinely.

The spectrometer consists of a Johan-type LiF(220) (Lithium Fluoride:  $2d=2.848\text{\AA}$ , Fig.1b) crystal and a back-illuminated CCD detector (Andor model DO420-BN)<sup>1</sup>. The energy resolution of the spectrometer has been evaluated using the He-like Fe  $K\alpha$  resonance line from LHD plasmas and estimated to be 10eV at 6.7keV as a value of FWHM.

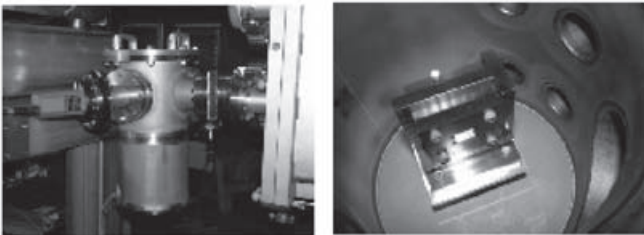


Fig.1 Photographs of (a: left) wide band and compact X-ray spectrometer and (b: right) Johann-type LiF(220) curved crystal set in crystal holder on rotary stage.

Figure 2 shows typical examples of Fe  $K\alpha$  spectra emitted from LHD plasmas with electron temperatures of 1.0keV (top) and 1.7keV (bottom). The electron temperature is measured with Thomson scattering diagnostic. It is seen that the dominant charge state of Fe ions at the plasma center moves from FeXXIII (Be-like) to FeXXV (He-like) according to the temperature. The impurity charge distribution is mainly a function of the electron temperature, but significantly affected by the radial transport coefficient. The relationship of the intensities of He-like and C-like  $K\alpha$  lines to the electron temperature is plotted in Fig.3. It should be noticed that the vertical axis is logarithmic. The temperature dependence of the Fe  $K\alpha$  lines is very strong and the experimentally obtained curves fundamentally express excitation rate coefficients to the Fe ions.

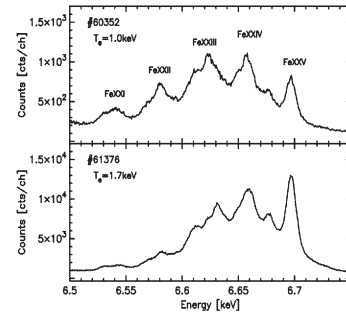


Fig.2 Typical examples of Fe  $K\alpha$  spectra observed with compact crystal spectrometer. (Top: shot number #60352,  $T_e=1.0\text{keV}$ ,  $B=-2.789\text{T}$ ,  $R_{ax}=3.55\text{m}$ ; bottom: #61376,  $T_e=1.7\text{keV}$ ,  $B=-2.750\text{T}$ ,  $R_{ax}=3.60\text{m}$ ).

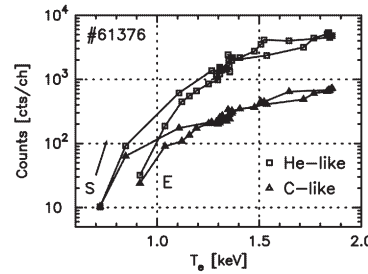


Fig.3 Relationship of Fe  $K\alpha$  line intensities to central electron temperature for He-like and C-like Fe ions. (S: start, E: End)

However, a small difference appears at temperatures lower than 1.3keV and the counts at last phase of the discharge become larger than at initial phase of the discharge. In LHD the density profile becomes peaked at the plasma decay phase suggesting an appearance of large inward flux. The difference originates in different central densities of electrons and Fe ions. Effective excitation coefficients of such  $K\alpha$  lines will be experimentally determined after detailed analysis.

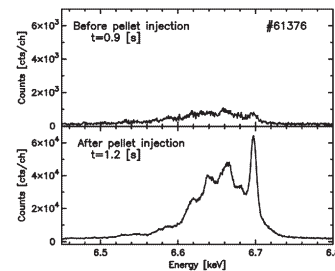


Fig.4 Fe  $K\alpha$  spectra before (top:  $t=0.9\text{s}$ ) and after (bottom:  $t=1.2\text{s}$ ) pellet injection ( $t=1.0\text{s}$ ).

A carbon pellet ( $0.9\text{mm}^{\phi} \times 0.9\text{mm}^L$ ) coated by iron with a thickness of  $13\mu\text{m}$  was injected using an impurity pellet injector<sup>2</sup> to confirm the brightness of Fe  $K\alpha$  lines and to test the signal response. The pellet with a speed of 200m/s is ablated at the plasma center, at least within a half radius of the LHD plasma. The pellet was injected at 1.0s from the initiation of plasma. Figure 4 shows  $K\alpha$  spectra before (top:  $t=0.9\text{s}$ ) and after (bottom:  $t=1.2\text{s}$ ) pellet injection. It is understood from the figures that the Fe  $K\alpha$  intensities required in this measurement can be sufficiently obtained using the Fe-coated carbon pellet. This was a very important step in the present work. Any metallic impurities can be used for the observation by selecting a material for the coating.

### Reference

- 1) I.Sakurai, Y.Tawara, C.Matsumoto et al., submitted to Rev. Sci. Instrum. (2006)
- 2) H.No zato, S.Morita, M.Goto et al., Rev. Sci. Instrum. 74, 2032 (2003).



## §16. Measurement of the Non-Parallel Flow Velocity Using a Mach Probe in Divertor-Simulating Weakly Magnetized Plasmas (NIFS04KOAB009)

Kado, S., Shikama, T. (The Univ. of Tokyo)

Plasma flow patterns are linked to the various kinds of phenomena both in fusion-relevant magnetic confinement devices and laboratory plasmas. The flow usually has components parallel and perpendicular to the magnetic field direction and the both are needed to be known. Although diagnosing techniques of parallel flow have been widely investigated so far, there is still an interest to identify the perpendicular flow which determines various kinds of plasma phenomena.

As a technique to obtain the magnitude and direction of the local flow velocity, Mach probe has been investigated. In a previous paper [1], we have revealed that similar size of ion gyro-radius and probe tip causes the strong dependence of ion collection on probe geometry. In order to compensate for the effect of probe geometry, we derived a practical formula based on the unmagnetized models with eliminating the effect of magnetic field. Theoretically this formula can be applied to the perpendicular flow as well as the parallel flow. However, the experimental confirmation of its applicability is an important task.

In the Mach probe experiment, the ion current angular distribution in unmagnetized plasmas can be expressed as  $j(M, \theta) = j_0 \exp(-KM \cos \theta / 2)$ , where  $j_0$  is the unperturbed ion current density,  $K$  is a model dependent constant,  $M$  is the Mach number defined as  $M = v_f / c_s = v_f / [(T_e + T_i) / m_i]^{1/2}$  with  $v_f$  being the flow velocity,  $c_s$  is the ion sound velocity,  $m_i$  is the ion mass,  $T_e$  and  $T_i$  are the electron and ion temperatures, and  $\theta$  is the polar angle relative to the direction of flow. In our previous work, the above equation was modified from a practical point of view. The difference of probe geometry can be compensated for by integrating the equation over  $\theta \pm \Delta\theta$ , where  $\Delta\theta$  is the collection angle of the Mach probe. In addition, the equation, which is originally derived without taking the effect of magnetic field into consideration, can be applied to weakly magnetized plasmas by taking the ratio of ion currents  $j(M, \theta + \pi) / j(M, \theta)$ . This procedure can eliminate the magnetic field effect assuming that the effect is independent of the flow field [2]. A practical formula to determine Mach numbers in weakly magnetized plasmas, then, can be written as

$$\frac{\int_{\theta-\Delta\theta}^{\theta+\Delta\theta} j(M, \theta + \pi) d\theta}{\int_{\theta-\Delta\theta}^{\theta+\Delta\theta} j(M, \theta) d\theta} = \exp \left[ K (M_{\parallel} \cos \theta + M_{\perp} \sin \theta) \cdot \frac{\sin \Delta\theta}{\Delta\theta} \right]$$

where  $M_{\parallel}$  and  $M_{\perp}$  are the parallel and perpendicular Mach numbers which can be determined as the sine and cosine components of the ion current angular distribution, if  $K$  is predicted for a specific condition.

The experiment was performed in a linear divertor-simulator MAP-II [3]. A plasma was generated by a low pressure dc-arc discharge and radially confined by axial magnetic field of about 300 Gauss. A typical plasma

parameters measured by a single probe were the electron density of  $10^{17} \text{ m}^{-3}$  and electron temperature of 10 eV for hydrogen plasmas. The plasma potential was measured using an emissive probe with a thoriated tungsten wire 0.2 mm in diameter operated at the emission current of 5.3 A. For the Mach probe measurement, a slit-shaped Mach probe (SP) [1] with the collection angle of  $\Delta\theta \sim 50$  degrees ( $\sin \Delta\theta / \Delta\theta \sim 0.88$ ) was installed and rotated by a stepping motor. The SP consists of an  $\text{Al}_2\text{O}_3$  insulator 4 mm in diameter and a tungsten electrode 5 mm in diameter.

In cylindrical plasmas the azimuthal rotation is induced by the  $\mathbf{E} \times \mathbf{B}$  and ion-diamagnetic drifts. The radial profiles of plasma parameters were measured to calculate the drift velocities using the single and emissive probes in the different magnetic field conditions (121 and 205 Gauss). In the MAP-II device, a negative plasma potential is formed as a result of the ambipolar diffusion so that the  $\mathbf{E} \times \mathbf{B}$  and ion-diamagnetic drifts have the opposite rotational directions. A comparison of the Mach numbers between the calculation of drift velocities and measurement using the SP is given in figure. In the figure, filled circles show the Mach numbers measured by the Mach probe and open diamonds show that of calculation. Here, a constant ion temperature of  $T_i \sim 1 \text{ eV}$  was assumed over the whole plasma column and spatial variation of  $K$  was neglected. Note that the velocity of ion-diamagnetic drift is small compared to that of  $\mathbf{E} \times \mathbf{B}$  so that this assumption does not change the conclusion. In the figure, the Mach numbers obtained by Mach probe with  $K = 1.4$  (no magnetic field,  $T_i = 0.1 T_e$ ) [4] shows good agreement with that of calculation even in the case of changing the magnetic field condition.

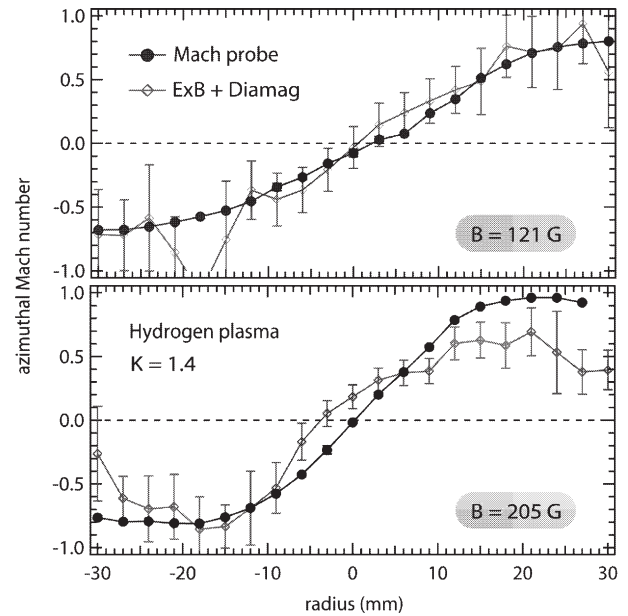


Figure. Radial profile of Mach numbers.

- [1] T. Shikama, S. Kado, A. Okamoto, S. Kajita, and S. Tanaka, *Phys. Plasmas* **12** (2005) 044504.
- [2] K. Nagaoka, A. Okamoto, S. Yoshimura, and M. Y. Tanaka, *J. Phys. Soc. Jpn.* **70** (2001) 131.
- [3] S. Kado, et al. *J. Plasma Fusion Res.* **79** (2003) 841.
- [4] I. H. Hutchinson, *Plasma Phys. Control. Fusion* **44** (2002) 1953.



## §17. Improvement of Plasma Performance by Strong ECH with High Power Gyrotron

Imai, T., Cho, T., Saito, T., Tatematsu, Y., Ichimura, M., Hirata, M., Kohagura, J., Hojo, H., Numakura, T. (Univ. of Tsukuba), Sakamoto, K. (JAEA), Saigusa, M. (Ibaraki Univ.), Kubo, S., Shimozuma, T.

An Electron Cyclotron Heating (ECH) is a key tool for electron heating and plasma control on magnetic confinement systems. It is, especially, important to get high ion confining potential and high electron temperature in tandem-mirror devices. For the purpose of the research of plasma potential physics and high power gyrotron development for LHD, power upgrade of 28GHz gyrotron to 0.4-0.5MW have been explored on GAMMA 10 ECRH system, from 200kW to push high confining potential formation and high power central electron heating, based on the unified scaling of potential formation[1] and high power gyrotron technology developed for ITER[2]. Main subject of the first year of this program is to increase power of the central cell ECH. Despite of the restrictions of present system, the gyrotron of central cell ECH delivered 400-500 kW as expected from design. The ion confining potential of 3kV was obtained with high power plug ECH. The electron heating of the central cell plasma using high power gyrotron has started.

The GAMMA 10 is a tandem-mirror device and axisymmetric mirror cells in both ends play important role to improve axial confinement of both ions and electrons through the formation of thermal barrier for electrons and plug potential for ions. The ECH power is a main tool to produce these confining potential in these plug/barrier in mirror cells. In last 20 years, ECH power source of the GAMMA 10 was 200 kW gyrotrons at 28 GHz and the ECH power produced 0.7 kV ion confining potential and electron temperature of the central cell was less than 100 eV. Much higher potential formation and electron heating would be expected corresponding to the ECH power upgrade.

New high power gyrotron of 500kW level at 28GHz has been developed for this ECH system upgrade. TE<sub>4,2</sub> mode is selected to reduce wall ohmic loss and beam current density for the new gyrotron. The major specification is listed in the table 1, comparing with previous one. The output mode is Gaussian like mode using quasi-optical mode converter, which couples efficiently to HE<sub>1,1</sub> mode transmission line.

Parabolic mirror was designed to make transmission efficiency high and power profile at resonance surface axisymmetric in both plug and central antennas using newly developed code[3]. Using these new high power gyrotron and efficient antenna, high power ECH experiment is going on.

As the base plasma experiments, the maximum ion confining potential of 3kV was obtained, which is four times higher than the previous value before the gyrotron upgrade. As for the central ECRH, the new antenna was tested before installing the new gyrotron and remarkable electron heating from tens eV to hundreds eV was obtained. An upgrade of the central ECH system is being made, with the DC power supply of JFT-2M ECH system. The output power test of this upgrade central system with the upgrade gyrotron was conducted and ~ 400 kW power at MOU (Matching Optics Unit) was successfully obtained as shown in Fig. 1, where the performance of the upgrade gyrotron is compared with previous 200kW one. It is seen that the output power is 2 times higher than previous one. The combination of this gyrotron, new antenna, and transmission line system will be experimented in the next campaign aiming to high central electron temperature which reduces electron cooling of high energy ions and hence improves the ion confinement of the tandem mirror.

Table 1 Comparison of specifications of 28GHz gyrotrons

	Upgrade tube	Previous
Frequency	28 GHz	28GHz
Output power	500kW	200kW
Cavity mode	TE <sub>42</sub>	TE <sub>02</sub>
Output mode	Gaussian	TE <sub>02</sub>
Pulse length	0.1	0.075
Efficiency	40%	34%

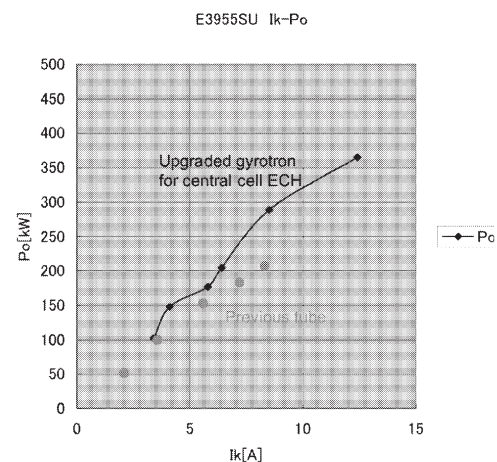


Fig. 1 Test results of output power vs beam current (Ik). Upgrade gyrotron (diamond) and previous (closed circle) are compared.

### References

- [1] T. Cho *et al.*, *Phy. Rev. Letters*, 94(2005)085002, *20th IAEA Fusion Energy Conf.* (Villamoura, 2004) EX/9-6Rd.
- [2] T. Imai, *et. al.*, *Fusion Eng. and Des.* **55**, 281 (2001).
- [3] Y. Tatematsu *et. al.*, *Japanese J. of Applied Physics*, 44(2005)6791.

§18. Formation Mechanism and Transport of Dust Particles in the Divertor Plasmas

Uesugi, Y., Ohta, K., Nakasaki, Y., Tanaka, Y.  
(Kanazawa Univ.),  
Ohno, N. (Nagoya Univ.),  
Masuzaki, S.

Dust particles collected in magnetically confined fusion devices have many significant effects on a fusion reactor, such as tritium retention, impurity release, degradation of vacuum sealing and electrical isolation, etc. Since the dust particles collected on the first walls of fusion devices are formed by series of different plasma shots, it is not easy to clarify the fundamental processes of the dust formation mechanism in the fusion plasmas. So far, laboratory scale experiments using a high density divertor simulator with DC discharges[1], DC glow plasmas and so on, mainly contribute to experimental studies on the basic mechanism of dust formation.

In the present experimental study high power inductively coupled plasmas(ICPs) with a power level of 10~20 kW are used to study plasma-material surface interactions and dust formation mechanism. High pressure ICPs have characteristic features, such as high density( $10^{19}\sim10^{21}\text{ m}^{-3}$ ), high heat flux( $\sim1\text{ MW/m}^2$ ), flexible working gas mixtures and so on. These plasma features are very helpful to study the material erosion, redeposition and dust formation, comparing with other laboratory experiments with different plasma parameter ranges. Here initial results from the experiments of argon or argon-hydrogen mixture plasma irradiation onto graphite targets are reported. The electron temperature and density of the plasmas near the target are  $\sim1\text{ eV}$  and  $\sim10^{19}\text{ m}^{-3}$ , respectively. Since the surface temperature of the graphite targets are 1300~1600 K and the incident energy of ion and neutral particles is below 10 eV, dominant processes of graphite target erosion should be radiation enhanced sublimation(RES) and chemical sputtering in our experiment. Figure 1 shows a picture of Ar plasma irradiation experiment. The target is placed at downstream region

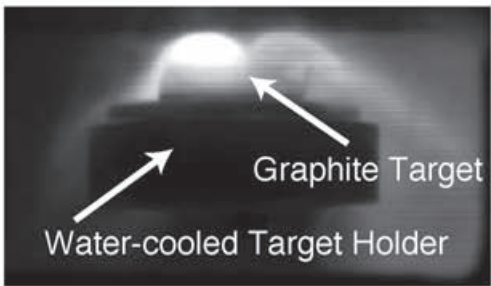


Fig. 1 Picture of Ar plasma irradiation onto graphite Target

$\sim250\text{ mm}$  away from the core plasmas and is inclined to measure the surface temperature by radiation thermometer. In Figs 2(a)~(d) surface modification of graphite target in different irradiation condition are shown. Just a 30 minutes plasma irradiation changes the surface morphology strongly as shown in Fig. 2. In the present preliminary experiments graphite targets are mainly eroded not deposited by plasma irradiation of Ar and Ar+H<sub>2</sub>, but small dusts of  $\sim1\text{ mm}$  size are observed in Ar+H<sub>2</sub> plasma(Figs. 2(c), (d)). Now we are constructing a new ICP device for plasma irradiation experiments and new results will be shown soon.

In parallel to experimental study on dust properties we are carrying out computer simulations on dust transport in the divertor plasmas[2] using DUSTT code. In Fig. 3 typical results of dust particle transport in DIII-D are shown. Detailed analysis will be shown elsewhere.

References

[1]Ohno, N., Kobayashi, Y., et al., J. Nucl. Mater., **337-339**, (2005)35.  
[2]Krashenninnikov, S. I., Soboleva, T. K., et al., J. Nucl. Mater., **337-339**, (2005)65

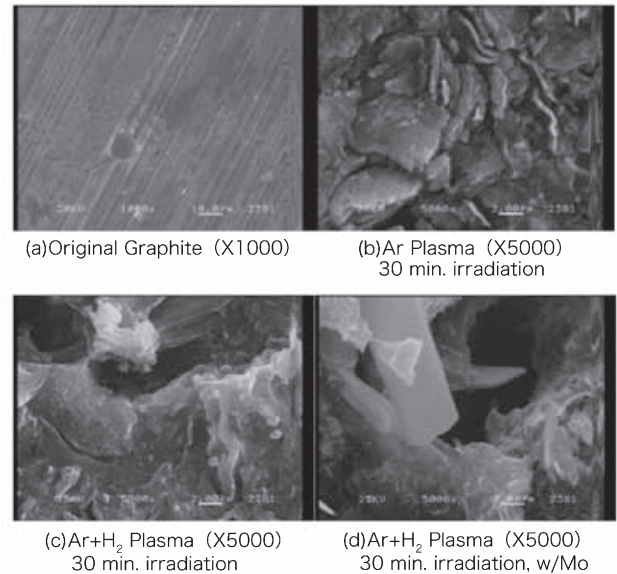


Fig. 2 SEM pictures of graphite target of different plasma irradiation condition.

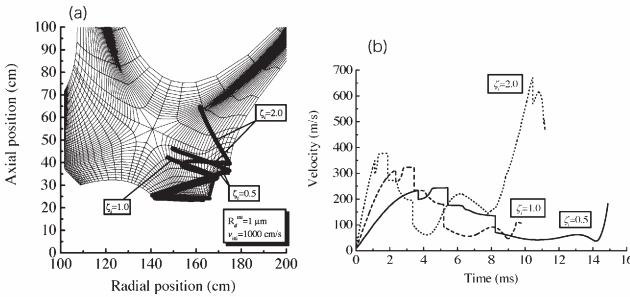


Fig. 3 DUSTT simulation results, trajectories of carbon dust(a) and dust velocity changes(b).

## §19. Development of Integrated Simulation Code for Helical Plasma Experiments

Nakamura, Y. (Kyoto Univ.), Yokoyama, M., Nakajima, N., Fukuyama, A. (Kyoto Univ.), Watanabe, K.Y., Funaba, H., Suzuki, Y., Murakami, S. (Kyoto Univ.), Ida, K., Sakakibara, S., Yamada, H.

Recent development of plasma diagnostics technique combined with the progress of computers and numerical code for non-axisymmetric plasmas such as helical plasmas enable us to do detailed theoretical analyses of individual experimental observation. We can obtain detailed and fine scale experimental data, and theoretical analysis for realistic configuration becomes possible. This background motivates us to develop an integrated simulation code for non-axisymmetric plasmas to draw up new experimental plans including those in a new device and to do experimental data analysis from the view point of integrated physics.

The integrated simulation system to be developed has a modular structure which consists of modules for calculating MHD equilibrium/stability, transport and heating. Each module can be selected in accordance with a user's request and can be combined with other modules. In order to maintain the independence of each module, which is an independent and complete program, sequences of the integrated simulation are controlled by a shell or script (perl or ruby, for example). Since some modules are suitable for running on the vector machine and others are on the PC cluster, we are going to develop a module-by-module distributed computing system through the network.

If we need to perform an integrated simulation during the entire plasma duration, a transport module is to be a core module. In our project, an integrated tokamak transport code, TASK<sup>1)</sup>, which is a core code for BPSI (Burning Plasma Simulation Initiative; research collaboration among universities, NIFS and JAERI in Japan) activity, will be extended for non-axisymmetric configurations and used as a transport module.

Though the most transport simulations done for helical plasmas have neglected the net toroidal current, finite net plasma current has been observed in actual experiments. It is considered that non-inductive currents such as bootstrap currents or beam driven currents are included in it. However, it is difficult to estimate fraction of these components accurately because plasmas are not stationary in many cases. So, as a first step of the extension of the TASK, time evolution of the plasma net current, which is consistent with the three-dimensional MHD equilibrium, is solved for LHD plasmas by using time evolution of density and temperature profiles obtained by the experiment and by taking into account of the bootstrap current and the beam-driven current.

In order to calculate the bootstrap current, we have developed the BSC code, which is suitable for the usage as a module, by improving SPBSC code<sup>2)</sup>. This code

uses a connection formula of asymptotic solutions for bootstrap currents of non-axisymmetric plasmas in Pfirsch-Schlüter, plateau, and low collisionality regimes. Ohkawa current driven by the NBI is calculated by the FIT code<sup>3)</sup>.

In order to estimate the inductive currents, evolution of the rotational transform by the plasma resistivity in a non-axisymmetric plasma is derived as<sup>4)</sup>

$$\frac{\partial \iota}{\partial t} = \frac{1}{4\rho\Phi_{Ta}^2} \left\{ \frac{\partial}{\partial \rho} \left[ \eta_{\parallel} \frac{dV}{d\rho} \frac{\langle B^2 \rangle}{\mu_0 \rho^2} \frac{\partial}{\partial \rho} [\rho(S_{11}\iota + S_{12})] \right] + \frac{\partial}{\partial \rho} \left[ \eta_{\parallel} \frac{dV}{d\rho} \frac{1}{\rho} \frac{dp}{d\rho} (S_{11}\iota + S_{12}) - \eta_{\parallel} \frac{dV}{d\rho} \frac{1}{\rho} \langle \mathbf{j}_s \cdot \mathbf{B} \rangle \right] \right\}$$

where  $S_{11}$  and  $S_{12}$  are susceptance matrix elements<sup>5)</sup> calculated by the metric tensors of three dimensional equilibrium, and  $\langle \mathbf{j}_s \cdot \mathbf{B} \rangle$  represents the non-inductive current. A numerical simulation is done for an LHD neutral beam heated plasma (Fig.1). In this simulation, non-inductive current  $\langle \mathbf{j}_s \cdot \mathbf{B} \rangle$  (Ohkawa current and bootstrap current in this case) is calculated by BSC/FIT code. It is shown that the abrupt increase of plasma current by Ohkawa current is suppressed by the inductive component of the plasma current. Because of the finite resistivity, total net current gets close to the non-inductive current with time.

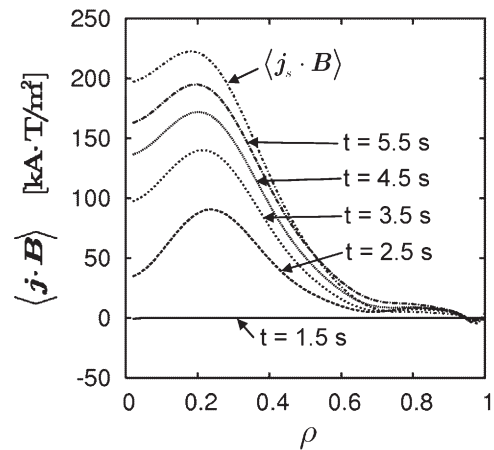


Fig. 1. Time evolution of net plasma current profile in an LHD NB heated plasma.

### References

- 1) A. Fukuyama, et al., Proc. of 20th IAEA Fusion Energy Conf., IAEA-CSP-25/TH/P2-3 (Vilamoura, Portugal, Nov. 1-6, 2004).
- 2) K. Y. Watanabe, et al., Nuclear Fusion **35** (1995) 335.
- 3) S. Murakami et al., Trans. Fusion Technol., **27** (1995) 259.
- 4) Yuji Nakamura, et al., Fusion Sci. and Technol., to be published in October (2006).
- 5) P. I. Strand and W. A. Houlberg, Phys. Plasma, **8** (2001) 2782.



§20. Study on Effects of Bending Strain to Critical Current Characteristics of Nb<sub>3</sub>Al CIC Conductors

Tamai, H., Kizu, K., Tsuchiya, K., Shimada, K., Matsukawa, M., Koizumi, N., Okuno, K. (JAEA), Ando, T. (NAT), Miura, Y.M. (Osaka Univ.), Nishimura, A., Hishinuma, Y., Yamada, S., Takahata, K., Seo, K.

The Nb<sub>3</sub>Al is one of the attractive superconducting materials for future fusion devices like DEMO because of its higher critical current density ( $J_c$ ) than Nb<sub>3</sub>Sn at around 16 T. In cable-in-conduit (CIC) conductor like the ITER conductor, strands suffer thermal and bending strain. The  $J_c$  of Nb<sub>3</sub>Al strand is generally decreased by longitudinal strain. However, in previous work, no degradation of  $J_c$  by bending strain of 0.4% was observed for a Nb<sub>3</sub>Al D-shaped coil made by react-and-wind (R&W) method in the R&D campaign for the JT-60 superconducting modification. The same tendency was also observed in the Nb<sub>3</sub>Al-insert coil manufactured through ITER R&D. These observations suggest that some cabling effect causes the relaxation of the bending strain in the strands. In this work, bending strain dependence of critical current ( $I_c$ ) of a CIC conductor wound like a torsion coil spring was measured. The new experimental apparatus which can bend samples in the cryostat was developed.

The CIC conductor for sample consisted of 54 Nb<sub>3</sub>Al strands and 27 copper (Cu) wires. The diameter of Nb<sub>3</sub>Al strands and Cu wires was 0.74 mm. The strand manufactured by the jelly roll process had Cu/non-Cu ratio of 4.0 and twist pitch of 50 mm. The non-copper critical current density was 1945 A/mm<sup>2</sup> at 4.2 K, 7.4 T. The thickness of chromium coating on Nb<sub>3</sub>Al strands and Cu wires were 2.3  $\mu$ m. The final twist pitch and the void fraction of the CIC conductor were 270 mm and about 36%, respectively. The inner and outer diameter of the conduit made of JIS SUS304 were 8.4 mm and 12.4 mm, respectively. The CIC conductor of 2.3 m in length was wound into 4.5 turns of torsion coil spring as shown in Fig. 1. The diameter and winding pitch were 150 mm and 18.4 mm, respectively. This sample was heat-treated for 50 hours at 750°C and was soldered in the groove of upper and lower flanges to install the apparatus.

The test apparatus [1] for the measurement of the  $I_c$  in

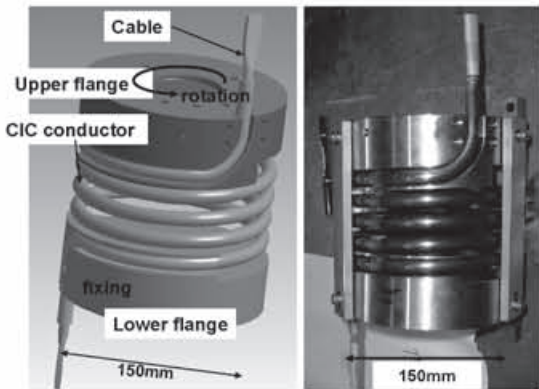


Fig. 1. The schematic drawing and the photograph of CIC conductor sample wound like a torsion coil spring.

various range of bending strain at 4.2 K in the presence of the external magnetic field consists of double shafts referred as the inner shaft and outer shaft. The external gear rotation generates bending strain in the CIC conductor sample from outside of the cryostat. The external magnetic field was generated by a 240 mm bore-13 T superconducting coil. The backfield magnet and the sample were cooled by pool boiling liquid helium.

The  $I_c$  of the CIC conductor sample versus bending strain was measured at 4.2 K in the range of perpendicular external magnetic field of 9.2, 10.2 and 11.3 T as shown in Fig. 2. Measured  $I_c$  was normalized by  $I_c$  without bending. The  $I_c$  was not decreased up to 0.4% and be slightly decreased when bending strain exceeds 0.4%. The  $I_c$  at maximum bending strain of 0.55% was 96% of  $I_c$  without bending. The only 5% of  $I_c$  decrease by 0.6% of bending strain is expected.

The compressive strain dependence of the Nb<sub>3</sub>Al strand at 11T measured in the previous work [1] is also shown in Fig. 2. In order to compare the strand data with the CIC conductor data, the  $I_c$  of compressive strain of 0.7% converted to the  $I_c$  of 0%, since all strands in the CIC conductor sample suffer -0.7% in thermal strain. The degradation tendency of the CIC conductor is clearly different from that of strand. The difference suggests the cabling effect. Because strands in the cable are twisted, the strand placing at the inside of the cable moves to the outside of the cable with the twisting pitch of 135 mm. Thus, one strand in the cable suffers both compressive force and tensile force longitudinally. If strands slip each other by bending, compressive and tensile strain in one strand can cancel out each other. Another sample which has smaller void fraction is planned to be fabricated in future. Strands in new sample are hard to slip compared to the sample of this work. Thus, it will be clarified whether the reason of smaller degradation of  $I_c$  of CIC conductor relates to the strand movement.

Reference

- 1) Kizu, K., IEEE Transactions on Applied Superconductivity, Vol. 16, No. 2, JUNE 2006, pp. 872-875.

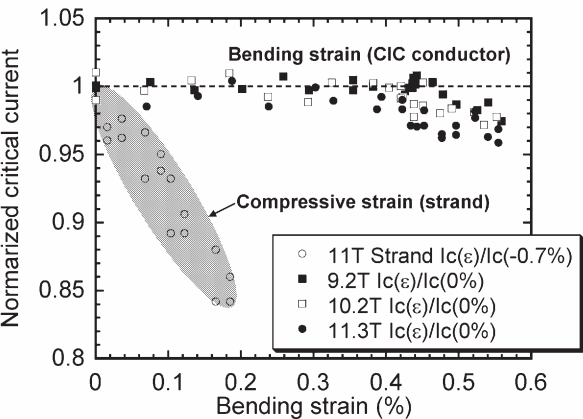


Fig. 2. The strain dependence of normalized critical current.



## §21. 14MeV-Neutron Beam Induced Change in Characteristics of Materials for Superconducting Magnets under 4.5 K

Nishijima, S., Izumi, Y., Takeda, S. (Osaka Univ.), Ochiai, K., Nishitani, T. (JAEA), Takeuchi, T. (NIMS), Nishimura, A., Seo, K., Hishinuma, Y., Muroga, T., Tanaka, T.

Accumulation of a quantitative database of performance deterioration and recovery of superconducting coil system elements adopted in a nuclear fusion device in the next generation by irradiation of 14MeV neutron under cryogenic temperature are important. In this study, we aimed at clarifying a characteristic of 14MeV neutron irradiation effects from mechanism and enabling feedback for a design of superconducting coil system materials for fusion reactors in the next generation.

The 14MeV neutron irradiation experiments were performed by using a 14MeV neutron generator (FNS) installed in JAEA. The 5 kinds of samples, (i) the tough pace copper wire, (ii) the oxygen-free copper wire, (iii) the Nb<sub>3</sub>Al wire rod flash-heated and rapid cooled (RHQ), (iv) the Nb<sub>3</sub>Al wire rod annealed after RHQ, and (v) the Nb<sub>3</sub>Sn wire rod, were consecutively maintained at 4.5 K using compact-type refrigerating machine during irradiation. In the region at an ambient temperature, different types of polystyrene with different molecular weight, glass-fiber reinforced plastic (GFRP), and a MgB<sub>2</sub> trial manufacture wire rod were arranged. From consideration to a security aspect of treating work after irradiation, the structural material of vacuum chamber was changed from SUS-304, which has been used in the last year, to aluminum alloy in order to reduce the influence of  $\gamma$ -rays.

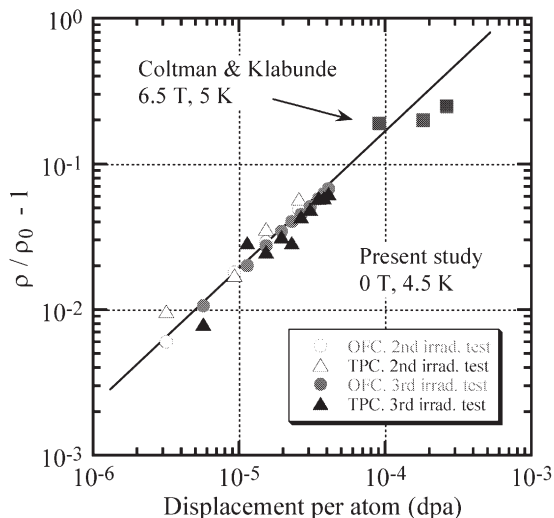


**Figure 1** The resistance of copper irradiated with neutron at a cryogenic temperature. OFC: oxygen-free copper, TPC: the tough pace copper.

Some important results were obtained this year. The resistance of copper was increased with increase of a neutron irradiation dose by cryogenic temperature irradiation. **Figure 1** shows this results in which the

irradiation dose was converted to dpa in order to compare with data by nuclear reactor irradiation in the literatures. In cases of fission neutron and 14MeV neutron irradiations,  $3.06 \times 10^{-7}$  dpa /  $1.00 \times 10^{19}$  n/m<sup>2</sup> and  $3.67 \times 10^{-6}$  dpa /  $1.00 \times 10^{19}$  n/m<sup>2</sup> were used, respectively. It was suggested that increase in resistance of copper irradiated with neutron was caused by growth of a defect cluster.

The interlaminar shear strength of GFRP was measured after 14 MeV neutron irradiation at a room temperature. For comparison, the interlaminar shear strength of  $\gamma$ -irradiated sample was also measured. The decomposition or chain scission effect by neutron irradiation was lower than that by  $\gamma$ -irradiation. However, a boron compound is included in glass fiber, and influence of deterioration in a glass / resin interface due to n,  $\alpha$  reaction by <sup>10</sup>B is large. Because LET of the formed  $\alpha$  particle is high,  $\alpha$  particle gives energy highly in glass fiber / resin interface, and extremely reduces adhesive property between fiber and resin. This is supported from an observation of FRP sample section after shear strength testing.

In order to clarify the degree of side-effects of induced  $\gamma$ -rays affecting the observed characteristics, the contribution rate of  $\gamma$ -rays for an absorbed dose was calculated by Monte Carlo simulation. As a result, the influence of  $\gamma$ -rays from SUS304 steel was less than 1/20 among total absorbed doses. Therefore, almost whole of observed change was suggested to be due to 14 MeV neutron. For example, crosslinking and main chain scission simultaneously undergoes in the case of 14 MeV neutron irradiation of single dispersion polystyrene at room temperature, which was concluded by the experiments in the last year. Such an observed change is also due to not  $\gamma$ -rays but 14 MeV neutron. Furthermore, a similar result was obtained in the experiments in this year; aluminum alloy with a little influence of  $\gamma$ -rays was used in the supporting material. In addition, molecular weight distribution was broadened, that was different from the formation of new peak by a neutron irradiation, in the case of <sup>60</sup>Co  $\gamma$ -irradiation experiments. The reason why only 14 MeV neutron irradiation generates the new peak in molecular weight distribution is under consideration. Some of possible mechanisms are as following. Recoiled proton, recoiled carbon atom and  $\alpha$  particle formed *via* n,  $3\alpha$  nuclear reaction have high LET. Such particles with high LET induce the track-structured energy transfer distribution like a heavy ion beam irradiation. Thus heterogeneous crosslinking and/or chain scission reaction undergoes. Crosslinking and main chain scission are not caused outside track structure.

The experimental studies have been performed about a performance change by 14MeV neutron irradiation of a superconducting coil system element adopted in a fusion device in the next generation. It was found that new indexes not only fluence but also dpa was necessary in the dosimetry of 14 MeV neutron. In addition, in GFRP, the consideration of effect of  $\alpha$  particle from boron included in glass fiber. The heterogeneousness of an energy transfer, such as track structure in the heavy ion beam irradiation, can be important in the 14 MeV neutron irradiation effect on the polymeric materials.

§22. Development of New High Field and High Current Density Superconductors for Fusion Devices

Tachikawa, K. (Faculty of Engr., Tokai University), Mito, T. (NIFS)

High field superconductors, e. g.  $\text{Nb}_3\text{Sn}$  and  $\text{Nb}_3\text{Al}$ , are indispensable for generating fields over 15T, and are expected to improve the efficiency and compactness of future fusion devices. Present author recently fabricated  $(\text{Nb,Ta})_3\text{Sn}$  wires with attractive high field performance through a Jelly Roll(JR) process from Sn-Ta-Cu/Nb sheet composites<sup>1)</sup>. Ta in the Sn-Ta sheet is incorporated into the  $\text{Nb}_3\text{Sn}$  layer improving the high-field performance, while a small amount of Cu addition to the sheet reduces the reaction temperature. In this study, the effect of a small amount of Ti addition to the Sn-Ta-Cu sheet on the structure and high-field performance of JR processed  $(\text{Nb,Ta})_3\text{Sn}$  wires has been studied.

Sn-Ta-Cu-Ti ingots were prepared by a melt reaction of Sn at 775°C for 10 h in vacuum. Sn,Ta and Cu-Ti powders containing 20 and 25at%Ta as well as a few at%Ti were mixed. Subsequently a few wt% Cu powder was added to the mixed powder. In the melt reaction, the mixed powder shrinks naturally in a silica crucible to form a solidified button. A few at% Ti addition to the mixed powder produces a more tightly shrunk ingot. Moreover, the Ti addition facilitates the reduction of optimum Ta concentration in the powder from 25-30at% to 20at%, which is favorable for reducing the material cost. The resulting Sn-Ta-Ti-Cu ingot was pressed to a plate and then rolled to a sheet 90  $\mu\text{m}$  in thickness. The Sn-Ta-Ti-Cu sheet was laminated with a Nb sheet, 100  $\mu\text{m}$  in thickness, and wound around a central Nb-3.3at%Ta rod to form a JR composite. The number of turns of the sheet in the JR composites was six. More tightly wound nine turn composites were also prepared. The resulting JR composite was encased in a Nb-3.3at%Ta tube with outer/inner diameters of 10.0/7.2 mm. These composites were fabricated into 2.7 mm square rods by grooved rolling and then drawn into wires 1.4 mm in diameter. Finally the JR wires were heat treated at 700°-775°C in vacuum.

Fig. 1 illustrates  $I_c$  and non-Cu  $J_c$  versus magnetic field curves for JR wires prepared in the present study. The performance of bronze processed  $(\text{Nb, Ti})_3\text{Sn}$  wire in practical use is also illustrated by dashed line. The non-Cu  $J_c$  of the wires is increased by increasing the number of turns of the sheet in the JR composites. This may be due to the increase of the volume of Sn-Ta-Cu and Nb components in the JR composites. A small amount of Ti addition to the sheet appreciably improves the non-Cu  $J_c$  of the wires over entire field range. A non-Cu  $J_c$  of  $\sim 150 \text{ A/mm}^2$  has been obtained at 22 T and 4.2 K, which is the highest value so far reported in  $\text{Nb}_3\text{Sn}$ -based superconductors. The optimum sheet

composition to yield a high performance in the wire is  $3/1(\text{Sn/Ta})+3\text{Cu}+4\text{Ti}$  or  $4/1+3\text{Cu}+3\text{Ti}$ . The upper critical field of the new  $(\text{Nb, Ta})_3\text{Sn}$  wire seemed to be higher than that of  $(\text{Nb, Ti})_3\text{Sn}$  wire by  $\sim 1\text{T}$ . The non-Cu  $J_c$  versus magnetic field curve of  $(\text{Nb, Ta})_3\text{Sn}$  wire shifts to higher field by 2-3T by reducing the measuring temperature from 4.2K to 2.1K. The Ti addition to the sheet enhances the formation of  $(\text{Nb, Ta})_3\text{Sn}$  layers increasing the areal fraction of  $(\text{Nb, Ta})_3\text{Sn}$  layers, which may be the main origin of the enhancement of the non-Cu of the wire.

Meanwhile, three monocoil wires, each  $\sim 100\text{m}$  in length, have been successfully fabricated, and wound into small test coils shown in Fig. 2. The composition of the Sn-Ta sheet was  $3/1+4\text{Cu}$  containing no Ti. The three wires were fabricated through a different technical procedure each other. The  $J_c$  of the JR part in the wires showed slightly higher value compared to the laboratory wires described before. The optimum reaction temperature was found to be decreased by increasing the reduction in area of the wires. Moreover, a multifilamentary JR wire, several hundred meters in length, was fabricated through the double stack procedure.

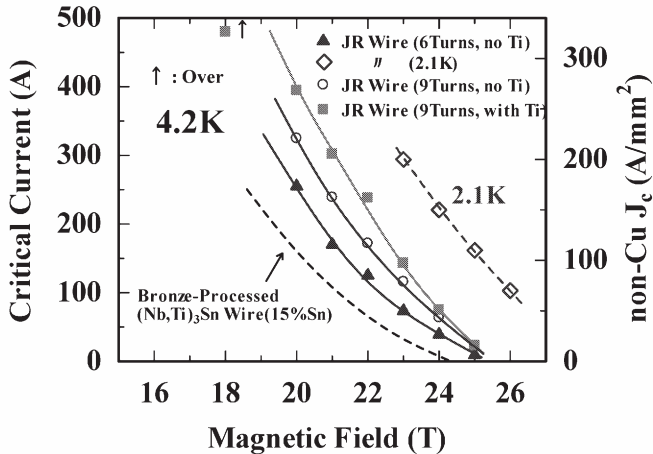


Fig.1  $I_c$  and non-Cu  $J_c$  versus magnetic field curves of different JR processed  $(\text{Nb, Ta})_3\text{Sn}$  wires

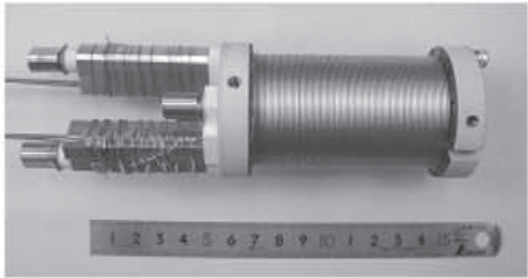


Fig.2 Test coil wound by the JR  $(\text{Nb, Ta})_3\text{Sn}$  wire 1.0mm in diameter. Inner/outer winding diameter : 26/38.5mm, Winding length : 70mm, Generated field :  $\sim 0.6\text{T}$  @ 100A @ 17T.

Reference

1) K. Tachikawa, et. al., IEEE Trans. Appl. Supercond., 15(2005) pp3490-3489.

### §23. Suitability of Boron-Titanium as First Wall Material

Hino, T., Hashiba, Y. (Hokkaido Univ.),  
Nishimura, K., Ashikawa, N., Masuzaki, S., Sagara,  
A., Noda, N., Ohyabu, N., Komori, A.

Boronization and titanium flash have been employed to reduce fuel hydrogen recycling and oxygen impurity concentration in plasma. If both boronization and titanium flash are conducted, the boron-titanium is produced on the first wall surface. The fuel hydrogen retention of this material has not been investigated so far. In the present experiment, the boron-titanium was prepared using electron beam evaporation, and irradiated by deuterium ions. After the deuterium ion irradiation, the deuterium retention and desorption behavior was investigated.

The boron-titanium was prepared by the titanium deposition followed by the boron deposition on stainless steel substrate. The annealing at 1000 K was conducted to mix the boron and the titanium. The boron-titanium was irradiated by deuterium ions with energy of 1.7 keV and fluence of  $1 \times 10^{18}$  D/cm<sup>2</sup> at RT. After the irradiation, the thermal desorption spectrum of deuterium was obtained using a technique of thermal desorption spectroscopy. Similar experiments were carried out for the boron film and the titanium film prepared by electron beam evaporation, and for titanium boride, TiB<sub>2</sub>.

Figures 1 (a) and (b) show the depth profiles of atomic composition for the boron-titanium and the titanium boride, respectively. The ratio of atomic composition, B/Ti, is approximately 2 in the titanium boride. The boron concentration was approximately twice of the titanium concentration at the surface in the boron-titanium.

Figure 2 shows the desorption spectra of deuterium for boron, titanium, boron-titanium and TiB<sub>2</sub>. The scale for titanium in this figure is 1/20 of the actual value. The desorption peaks of the boron-titanium were 500 K and 600 K. The former peak corresponds to the de-trapping of deuterium from B-D-B bond, and the later one from Ti-D bond. The amount of retained deuterium in the boron-titanium was twice or triple times smaller than that of boron or titanium, and comparable with that of TiB<sub>2</sub>. The desorption temperature in the boron-titanium was lower than that of boron, titanium or TiB<sub>2</sub>. In the present experiments, it is clearly shown that the amount of retained deuterium in the boron-titanium is small and that the desorption temperature is low.

The present results suggest that both fuel hydrogen retention and a baking temperature required for reduction of hydrogen retention can be reduced by an use of boron-titanium.

A further study will be conducted to clarify the reason why the boron-titanium has a low desorption temperature, using surface analysis techniques.

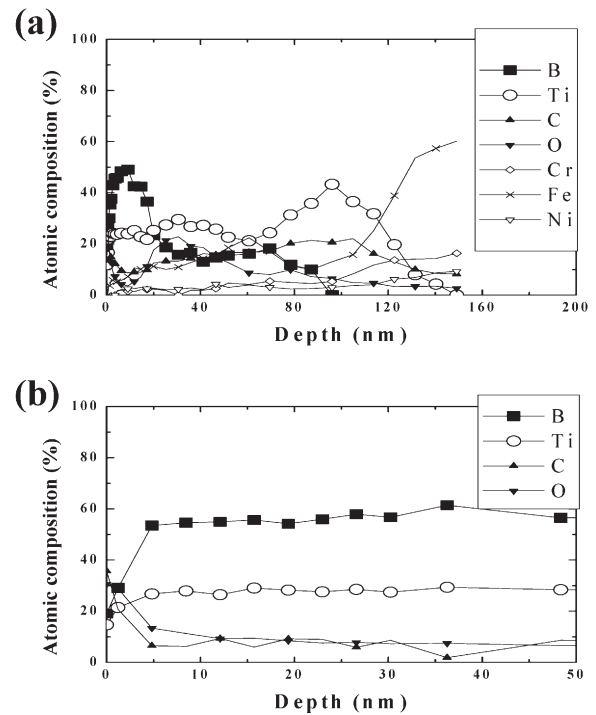


**Fig. 1** Depth profiles of atomic composition for boron-titanium (a) and titanium boride (b).

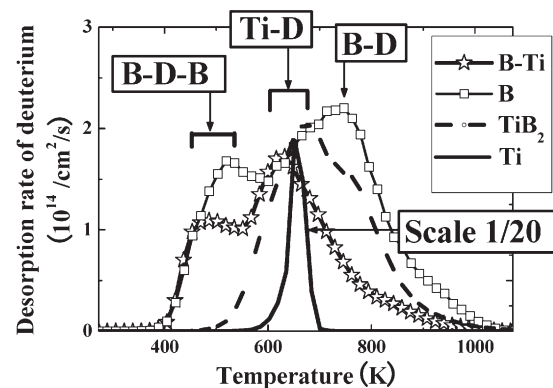


**Fig. 2** Thermal desorption spectra of deuterium after deuterium ion irradiation for boron-titanium (B-Ti), boron (B), titanium (Ti) and titanium boride (TiB<sub>2</sub>).

#### References

- (1) Hino, T., Hashiba, Y., et al, Fusion Eng. and Design, **81**(2005)127-131.
- (2) Hino, T., Hashiba, Y., Ashikawa, N., et al, Presented in 17<sup>th</sup> PSI Conference, Hefei, China, (2006)

## §24. Measurement of the Negative Ion and Control of Recombination Plasma in the LHD Divertor

Tonegawa, A., Shibuya, T., Kawamura, K. (Dept. Phys. Tokai Univ.),  
Masuzaki, T., Sagara, A., Ohya, N.

We have presented the experimental observation of the spatial structure of MAR in the detached hydrogen plasma at the periphery of the plasma in the linear divertor plasma simulator, TPD-SheetIV [1]. It is observed that the mutual neutralization in MAR via hydrogen negative ion formation, which is produced by dissociative electron attachment to  $H_2(v)$ , occurs in the periphery of the plasma where cold electrons ( $\sim 1$  eV) are found [2]. In fusion experiments, the negative ions, that is deuterium negative ion ( $D^-$ ), play an important role in the mutual neutralization of MAR, providing a new method of controlling detached plasmas.

In this paper, we have developed a new method to control a detached plasma based on utilizing  $D^-$  ions which are formed as part of the MAR mutual neutralization process occurring in the periphery of the deuterium plasma on the linear divertor plasma simulator, TPD-SheetIV.

The experiment was performed in the linear divertor plasma simulator TPD-SheetIV. Ten rectangular magnetic coils formed a uniform magnetic field of 0.08 T in the experimental region. The neutral pressure  $P_{Div}$  in the divertor test region was controlled between 0.1 and 20 mtorr with a secondary gas feed. The heat load on the target plate  $Q$  was measured by a calorimeter. At a discharge current of 100 A, the value of  $Q$  reaches about  $0.6 \text{ MW/m}^2$ . A cylindrical probe made of tungsten was used to measure the spatial profiles of the deuterium negative ion density  $n_{D^-}$  by a probe-assisted laser photodetachment method. At a repetition rate of 50 Hz, the Nd-YAG laser had an energy per pulse of 100 mJ.

The concept of control of a detached plasma using negative ions can be illustrated through the following steps; (1) measure the experimental data related to the minimum and maximum basic parameters (gas pressure  $P_{Div}$ , heat load  $Q$ ) in order to determine for controlled region, (2) control the secondary gas-flow rate  $G_{Div}$  rapidly so as to maximize the value of  $n_{D^-}$ , (3) carry out a real time feedback control in order to maintain a steadily detached plasma in the neighborhood of the target plate.

By defining  $Q_{att}$  as the heat load in attached plasma

and  $Q_{pm}$  as the heat load at the maximum negative ion density for a particular pressure  $n_{D^- \max}$ , we can express the reduction of the heat load as the ratio of  $Q_{att}$  to  $Q_{pm}$ , that is,  $\Delta Q = Q_{pm}/Q_{att}$ . The variations of  $n_{D^- \max}$ , heat load  $Q_{att}$ ,  $Q_{pm}$ , and heat load ratio  $\Delta Q$  with the discharge current  $I_d$  is shown in fig. 1. In the deuterium plasma,  $Q_{att}$  increases from 0.1 to  $0.58 \text{ MW/m}^2$  and  $n_{D^- \max}$  is nearly constant value with increasing  $I_d$ . In spite of these characteristics of the deuterium negative ions,  $\Delta Q$  gradually decreases from 60 to 40 % with increasing heat load to the target.

Similarly to the characteristics of  $\Delta Q$  on the detached hydrogen plasma[3], these results indicate that this new way of controlling a detached deuterium plasma, based on the feedback control of the relative negative ion density in the high density part of the plasma. The new system has achieved the goal of reducing the target heat flux while simultaneously minimizing the amount of gas puffed in a detached hydrogen or deuterium plasma without radiative and three-body recombination processes.

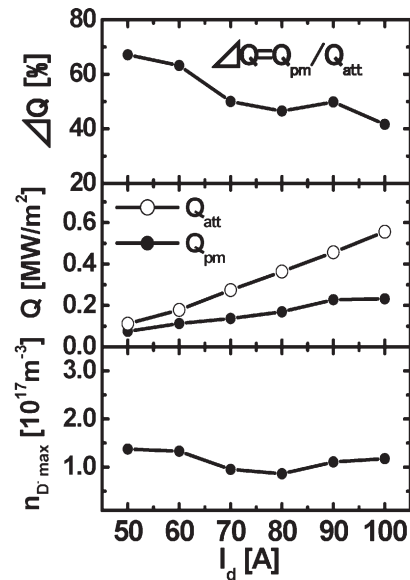


Fig.1 The variations of  $n_{D^- \max}$ , heat load  $Q_{att}$ ,  $Q_{pm}$ , and the heat load ratio  $\Delta Q$  with the discharge current  $I_d$ .

### Reference

- 1) Tonegawa, A., Ono, M., Morihira, Y., Ogawa, H., Shibuya, T., Kawamura, K. and Takayama, K., J. Nucl. Mater. **313-316**, (2003) 1046.
- 2) Tonegawa, A., Ono, M., Kumita, K., Shibuya, T. and Kawamura, K., J.JAP to be accepted (2006).
- 3) Ono, M., Tonegawa, A., Kumita, K., Shibuya, T. and Kawamura, K., J. Nucl. Mater. **337-339**, (2005) 264.



## §25. Kinetics of Hydrogen Isotopes at Surfaces and Bulks of Plasma Facing Materials Based on Group 5 Metals

Hatano, Y., Hara, M., Homma, H. (U. Toyama), Hashizume, K. (Kyushu Univ.), Saitoh, H. (Muroran Inst. Tech.), Suzuki, A. (U. Tokyo), Hirohata, Y. (Hokkaido Univ.), Ashikawa, N., Nagasaka, T., Sagara, A., Muroga, T., Nakamura, Y.

Group 5 metals including V are candidate materials of superpermeable membranes for pumping fuel particles in divertor region. In addition, V alloys have attractive mechanical and nuclear properties as structural materials of fusion blankets. From these viewpoints, the interactions of hydrogen isotopes including tritium with V and V alloy were investigated by different experimental techniques.

Nakamura et al. [1] have examined the absorption of hydrogen atoms by Nb panel and observed sufficient pumping speed at specimen temperatures,  $T$ , above 200 °C. In the lower  $T$  region, however, the pumping speed dropped sharply with decreasing  $T$ . Such reduction in pumping speed at low  $T$  poses a serious problem in performance tests in existing fusion devices including LHD. The reduction in pumping speed can be caused by (1) saturation of surface by hydrogen adsorbed from gas phase or segregated from the bulk, (2) contamination by adsorbed impurities such as water vapor, and/or (3) surface oxidation. In the present study, absorption of atomic hydrogen by V panel near room temperature was examined as functions of incident flux, bulk hydrogen concentration and chemical surface state to understand the mechanism underlying the reduction in pumping speed observed at low  $T$ .

The atom-driven hydrogen absorption by V panel was examined near room temperature in an UHV chamber equipped with Ta filament serving as an atomizer ( $T$  increased from 30 to 70 °C during experiment due to radiation from atomizer). A Nb ribbon which was kept at 400 °C was used as a reference sample providing constant pumping speed. The chemical surface state was analyzed by means of X-ray photoelectron spectroscopy (XPS).

Fig. 1 shows the flux dependence of the absorption coefficient of atomic hydrogen by V panel. No significant change in absorption rate was observed in a wide range of incident flux ( $10^{17} - 10^{21} \text{ H} \cdot \text{m}^{-2} \cdot \text{s}^{-1}$ ). In addition, the absorption rate was almost independent of the bulk hydrogen concentration in a range from  $10^{23}$  to  $10^{26} \text{ H} \cdot \text{m}^{-3}$ . Hence, it was concluded that the reduction in pumping speed was not due to the surface saturation by hydrogen.

The influence of impurity gases on absorption coefficient of atomic hydrogen is shown in Fig. 2. No noticeable change was induced by exposure to CO. On the other hand, the absorption coefficient sharply dropped by exposure to  $\text{O}_2$ . Exposure to  $\text{H}_2\text{O}$ , however, led to reduction in the absorption rate only at very large extent of exposure corresponding to  $10^4$  monolayers. Namely, the reduction in pumping speed could not be ascribed to the surface contamination by water vapor adsorption.

The surface analyses by XPS showed that oxide films (mainly  $\text{V}_2\text{O}_3$ ) were formed by the exposure to  $\text{O}_2$  and the extended exposure to  $\text{H}_2\text{O}$ . These observations indicate that the formation of oxide layer is the dominant mechanism underlying the reduction in pumping speed observed at low  $T$ . In other words, performance tests of membrane/panel at low  $T$  are possible if the growth of oxide layer could be avoided by reduction of oxygen partial pressure and/or periodical surface conditioning.

Diffusion of tritium is also important issue for the application to structural materials of blankets. Hence, the diffusion coefficient  $D$  of tritium in recrystallized specimen of V-4Cr-4Ti alloy (NIFS-HEAT-2) was measured by glow discharge implantation method [2] in a temperature range from 100 to 300 °C. The temperature dependence of  $D$  thus obtained was described as

$$D (\text{m}^2 \cdot \text{s}^{-1}) = 7.5 \times 10^{-8} \exp(-0.13 (\text{eV}) / kT).$$

This value was noticeably smaller than that for pure V and comparable with the value for binary V-4Ti alloy, indicating the trapping effect by Ti. The observations of tritium distributions in several specimens having different microstructures indicated that the spatial distribution of trapping sites depended on the conditions of rolling and heat treatments.

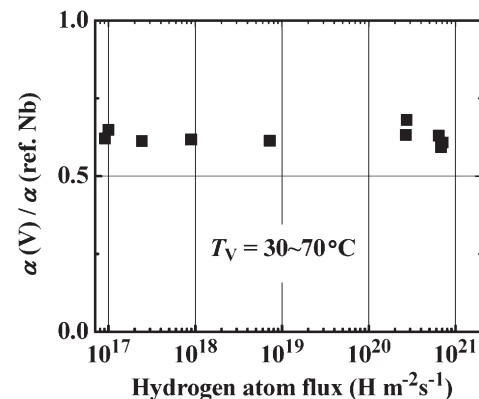


Fig. 1 Correlation between absorption coefficient of hydrogen atoms on V surface and incident flux.

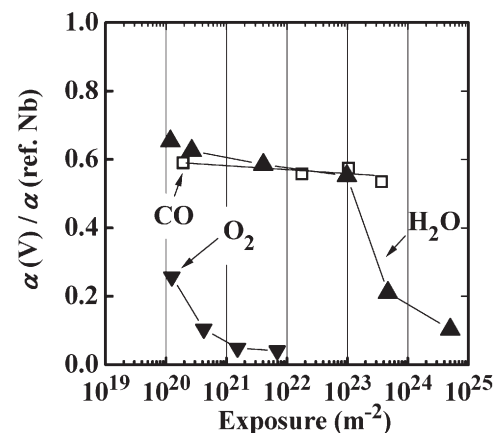


Fig. 2 Change in H atom absorption coefficient by exposure to impurity gases.

### References

- 1) Nakamura Y., et al.: J. Nucl. Mater. **337-339** (2005) 461.
- 2) Hashizume K., et al.: Fusion Technol. **28** (1995) 1175.

## §26. Heat Removal Enhancement of Plasma-Facing Components by Using Nano-Particle Porous Layer Method

Kunugi, T., Okamoto, Y., Kawara, Z. (Kyoto Univ.), Hashizume, H., Yuki, K. (Tohoku Univ.), Shibahara, M. (Osaka Univ.), Satake, S. (Tokyo Univ. Of Science), Sagara, A.

Heat transfer enhancement is one of key issues of saving energies and compact designs for mechanical and chemical devices and plants. Until today people have made effort to enhance convective heat transfer by means of the surface enlargement using obstacles such as ribs and fins and the increase of flow turbulence. However, additional pressure losses increase with increases of introducing obstacles and turbulence. A very high convective heat transfer performance compared to the well-known conventional heat transfer correlations caused by a nano-particle porous layer formed on the heat transfer surface was discovered by the authors (Kunugi, 2004a, 2004b). Two fabrication methods have been developed such as a “Nano-Particle Layered Surface (NPLS)” method and a “Fine Precipitate (FP)” method. Heat transfer surfaces treated by the NPLS or FP method showed very high heat transfer performance compare to the conventional surfaces: the maximum increase of heat transfer performance was up to 120% (Kunugi, 2003, 2004a). However, the lifetime of the high heat transfer surface was rather different between them: the surface made by the FP method covered with Silicon oil as a stain material and the surface made by the NPLS method is contradictory to maintain the high heat transfer performance. Third fabrication method with combining two methods has been developed: a “Nano- and Micro Particle Layered Surface (NMPLS)” method. This method is that the FP method applied to the heat transfer surface at first, and then the NPL method applied to the surface treated by the FP method. This NMPLS method also shows high heat transfer performance and would have a long lifetime because of the nature of NPL surface.

In this year, in order to understand these high heat transfer mechanism, the temperature profile in the parallel flow channel has been measured by using a K-type sheath thermocouple of 250 $\mu$ m in diameter. The experimental apparatus is shown in Fig. 1. The flow channel consists of 500mm long with 5mm in height and 50mm in width. The upper wall is made of stainless plate of 5mm thickness and a rubber heater attaches on the top to provide the uniform heating condition. A test plate attaches on the backside of the upper wall and the bottom and side walls are made of polyvinyl chloride to be insulated walls. The thermocouple can be vertically moved by a linear electromagnetic drive with 100 $\mu$ m intervals. The heater is set to around 200W (200Vx1A). The Reynolds number ( $=2UH/\nu$ , U is mean velocity, H channel height,  $\nu$  viscosity) is set to around 1200. The calorimetric balance of the experimental apparatus is satisfied within less than 10% accuracy. Figure 2 shows a scanning electron microscope (SEM) image of nano- and

micro-scale porous layered surface (NPLS) on the test plate. Figure 3 shows the temperature profile in the parallel channel flow. The solid circle shows the bare plate case and the open one for the NPLS plate. The wall temperature in case of NPLS is rather lower than the bare plate case. This discrepancy leads to the heat transfer increase at the NPLS surface. The temperature profile in case of NPLS plate case is also lower than that of the bare plate case. Moreover, the temperature fluctuation very close to the wall has been measuring and shows a bit difference from that of center in the channel. In the report written in Japanese, the reasons of heat transfer enhancement mechanism are discussed.

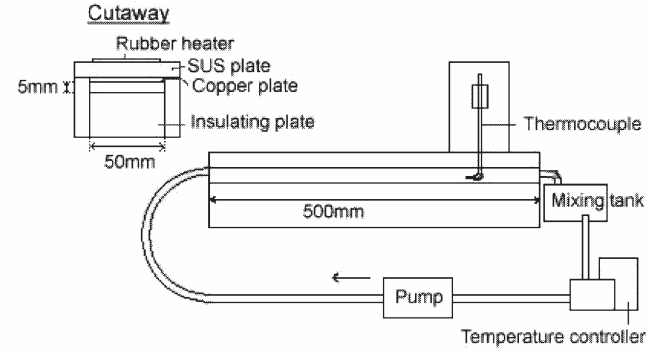


Fig. 1 Experimental apparatus

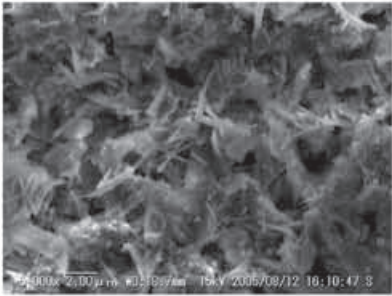


Fig. 2 SEM image of nano- and micro-scale porous layered surface: NPLS (many board- and needle-shaped crystals can be seen)

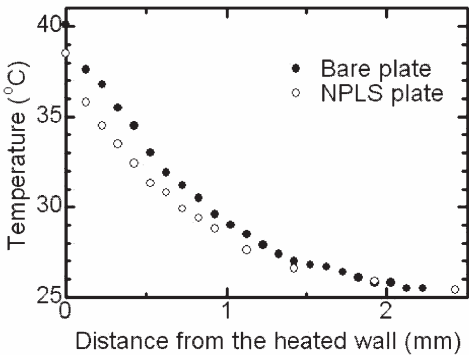


Fig. 3 Temperature profiles for bare copper plate and NPLS plate

### REFERENCES

- Kunugi, T. et al., Proc. Int. Sympo. Micro-Mechanical Engi., Tsuchiura, Japan, pp. 129-134 (2003).
- Kunugi, T. et al., Proc. 1<sup>st</sup> ISMNT, 14-17 March, 2004, Honolulu, Hawaii, USA, CDROM XXVII-3-01 (2004a).
- Kunugi, T. et al., Superlattices and Microstructures, vol. 35, Issues 3-6, pp. 531-542 (2004b).

## §27. Investigation of Tritium Behavior and Tracability in In-Vessel Systems of LHD during D-D Burning

Tanabe, T. (Kyushu University), representative of a cooperation program with 24 participants

Tritium (T) produced by D-D reactions is a safety concern in deuterium discharges planned in LHD. Estimation of tritium remained in and released from the vacuum vessel of LHD, chemical forms of released tritium by pumping, recovery of tritium, and how to reduced tritium release to the environment. As for tritium in the vessel, locations of high tritium retention and development of methods to remove tritium are

We have studied that tritium produced by DD-reaction behaves quite different way from hydrogen isotopes (hydrogen (H), and deuterium (D)) and even tritium (T) fueled into the tokamaks [1]. The results are summarized as,

(1) More than half of tritium produced by DD reaction would be implanted into plasma facing wall in the depth of more than 1  $\mu\text{m}$ , which can not be easily removed. Although high temperature thermal release of tritium implanted into the wall is promising, it can not be applied for tritium release from the whole vacuum vessel.

(2) Remaining tritium is thermalized to the plasma temperature and impinges the surface of the plasma facing wall. Most of them, however, would be replaced by subsequently coming fuel particles (H and D) and released with chemical forms of mostly DT or HT with little hydrocarbon and pumped out from the vacuum vessel.

(3) Tritium remaining in the vessel is very hard to quantize because various radiations from radio active nuclei produced by DD neutrons superpose tritium  $\beta$  electron, and should be discriminated for T analysis.

(4) In addition, the amounts of the retained tritium in the vessel must be strongly modified by temperature and materials of plasma facing tiles. The high energy tritium is implanted deeply with quite low concentration compared to the highly concentrated hydrogen co-depositions; the former is likely trapped strongly and hard to remove. If we could keep the temperature of the deposited area above 800 K, tritium inventory may be reduced significantly.

All above results are for tokamaks using carbon as a plasma facing material. In LHD, large part of PFM is composed of stainless steel, in which hydrogen solubility is less and hydrogen diffusivity is larger than those in carbon. Nevertheless, most of tritium having its initial energy of 1MeV is not thermalized in LHD plasma but implanted into plasma facing surfaces. Hence behavior of hydrogen implanted in stainless steels with rather high energy, up to 1MeV becomes important and should be investigated.

In addition, carbon materials eroded at divertor area could be transported and deposited on the first wall. Hence hydrogen behavior in not only bare stainless steels but also carbon deposition on them is our research targets.

Thus we have put particular emphases on,

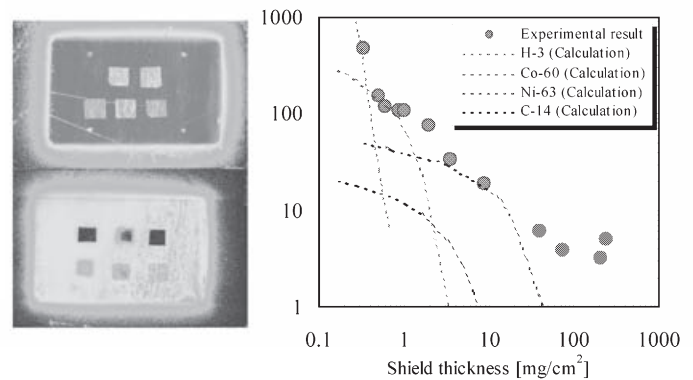


Fig.1 Discrimination of T from  $^{60}\text{Co}$ ,  $^{63}\text{Ni}$ , and  $^{14}\text{C}$  which were deposited on the bumper limiter of TFTR, using a film insertion method for radiation detection by an imaging plate technique [2]

- 1) To estimate tritium retention in the first wall and divertor area
- 2) To recover or remove diluted T in exhausted D gas during discharge.
- 3) To remove tritium implanted rather deep (more than  $1\mu\text{m}$ ) in the plasma facing wall.

In the preliminary study shows that above 400K, hydrogen retention in a stainless steel is very small and even long term release is possible. However, carbon deposition on the surface could enhance the tritium retention. This is very important for the ventilation of the LHD torus to keep people going into the vacuum vessel safe.

Concerning discrimination of tritium  $\beta$ -ray from other radio-activities made by DD neutrons we have tried a film insertion technique for tritium measurements by an imaging plate technique. Fig.1 is an example for discrimination of T from  $^{60}\text{Co}$ ,  $^{63}\text{Ni}$ , and  $^{14}\text{C}$ , which were deposited on the bumper limiter of TFTR [2].

For the purpose of tritium removal from carbon co-deposits on plasma-facing material of fusion device, pulsed-laser induced desorption of hydrogen from co-deposits on JT-60 open-divertor tile has been investigated. The fundamental (1064 nm) and fourth harmonic (266 nm) emission of a 20 ps-Nd: YAG laser were used, and dependences of hydrogen desorption on laser intensity  $I_L$  and wavelength  $\lambda$  were studied. Hydrogen-desorption efficiency, defined as the ratio between the number of desorbed hydrogen by laser irradiation and that of hydrogen retained in the ablated volume, was largest in the region, where strong ionization of  $\text{C}^+$  occurred, and was larger for  $\lambda = 266\text{ nm}$ , in which a laser photon can cut C-H bond, compared with that for  $\lambda = 1064\text{ nm}$ . For the ablative removal of hydrogen, a short-wave length and high-power laser is desirable [3].

### References

- [1] T. Tanabe, K. Sugiyama, C. H. Skinner, et al. J. Nucl. Mater. **345** (2005) pp.89-95.
- [2] Y. Sakawa, K. Satoh, T. Shibahara et al., Fusion Eng. & Design, **81**(2006)pp.381-386
- [3] K. Sugiyama, T. Tanabe, T. Saze et al. Fusion Eng. & Design, **81**(2006)pp1111-1116.



## §28. Assessment Study on Biological Effects of Radiation in LHD

Ichimasa, Y. (Fac. Sci., Ibaraki Univ.), Komatsu, K. (Fac. Sci. Rad. Biol. Center, Kyoto Univ.), Kamiya, K. (Res. Inst. for Radiat. Biol. and Med., Hiroshima Univ.), Norimura, T. (Univ. Occupational and Environ. Health, Japan), Tauchi, H. (Fac. Sci., Ibaraki Univ.), Takeda, H. (NIRS), Ono, T. (Tohoku Univ., Graduate School Med. & School Med.), Uda, T.

The main results of this program were as follows.

### (1) Analysis of mutation induction by low dose rate tritium radiation using a hyper-sensitive system.

Hiroshi Tauchi, Maki Ohara, Takeshi Suzuki, Eigo Mastumoto, Kenta Iijima, Daisuke Yokozawa, Hisako Daikai, Kenshi Komatsu, Yusuke Ichimasa

An exposure condition of tritium radiation from nuclear fusion reactor could be a long-term exposure at low dose rate. The biological effects of low dose (rate) radiation are not clear because none of suitable detection system has been established. Regarding to mutation induction by high LET radiation such as neutrons, the reversed dose rate effect has been reported when the dose rate is lower than a certain value. On the other hand, it is not clear whether this phenomenon could be seen in the case of tritium radiation. To examine the low dose rate effect of tritium radiation, we established a hypersensitive mutation detection system using hamster cells carrying a human X-chromosome. In this system, any mutation or deletion in the human X chromosome will not affect cell viability when cells are cultured in normal medium. This system appears to be able to detect a wide spectrum of mutations, even mutations affecting the expression of important genes in the neighborhood of the Hprt gene. We have tested mutation induction by tritiated water at dose rate between 0.13 and 4.4 cGy/h. Although mutation frequency seems to be slightly increased at lower dose rate tritium radiation, it was not statistically significant. Our results suggest that the reversed dose rate effect may not be seen for mutation induction by tritium radiation.

### (2) Tritiated Water Behavior in Vinclozolin Administered Pregnant Mouse

Yusuke Ichimasa, Sho Takizawa, Yu Nagaoka, Hiroshi Tauchi, Michiko Ichimasa

The fetus is known to be radiosensitive. The increased radiosensitivity of the gonocytes with fetal age was reported when pregnant mice were exposed to single doses of X rays. Fetuses are also very sensitive to environmental endocrine disruptors. In the present study, we examined the effects of multiple contamination of tritiated water and vinclozolin, an endocrine disruptors with antiandrogen activity, orally administered to pregnant mouse on the fetus. Pregnant mice were orally administered HTO and vinclozolin at the middle gestation, and tritium concentrations of urine of pregnant mouse, blood and tissues of fetus and placenta and fetal membrane were determined with time until 20 days after the administration. The accumulation doses and biological half lives of HTO in mother mouse and fetus

were calculated. Antiandrogenic effects of vinclozolin were also examined.

### 1) Transfer of tritium from the pregnant mice administered HTO to their fetus and offspring.

Pregnant mice were administered HTO(20MBq) by oral ingestion at gestational day 14, and tritium contents in urine, tissues fetus and offspring were determined at various time points after ingestion. Offspring were born at gestational day 19. The accumulation dose for 15 days after ingestion of HTO was 108mGy for the parent mice and 122mGy for their offspring, respectively. No significant difference in the dose was observed ( $p < 0.05$ ).

### 2) Combined effects of HTO, gamma ray and Vinclozolin one of environmental hormone disruptors). Five groups of pregnant mice were exposed to Vinclozolin, HTO, Vinclozolin + HTO, gamma ray, gamma ray + Vinclozolin, respectively gestational day 14. Vinclozolin and HTO were administered orally. Fetus survival rate and testis weight of male fetus were determined at gestational day 19. No significant combined effects were observed.

### (3)Function analysis of human Rad62 in SMC5-6 complex member.

Kenshi Komatsu, Saori Itoh, Hiroko Fujimoto, Junya Kobayashi, Kiyoshi Minagawa

The structural maintenance of chromosome (SMC), family proteins that plays a central role in chromosome dynamics and stability, is categorized to three groups in eukaryotes: SMC1-3 as a core protein of the cohesions which regulates the chromosome synapsis, SMC2-4 as a core protein of condensins which plays a role in chromosome condensation during meiosis and SMC5-6 complex possibly involved in DNA repair and chromosome segregation. Yeast SMC5 or SMC6 mutants showed increased sensitivity to DNA damage-inducing agents such as methyl methanesulfonate (MMS) and hydroxyurea (HU), suggesting the potential involvement in homologous recombination repair and stabilization of replication fork. Moreover, high sensitivity to MMS and ionizing radiation is reported in the mutants of yeast Rad62, non-SMC proteins formed complex with SMC5-6.

To clarify the function of SMC5-6/non-SMC protein complex in higher eukaryotes, we identify human Rad62 gene and analysis the role in a response to radiation damage. Two orthologs of Rad62, Rad62A and Rad62B, were identified when human cDNA was screened. The modification of Rad62A protein was observed after exposure to radiation (IR). We are presently preparing Rad62A knock-down cells to examine the sensitivity to DNA damage agents, such as UV and radiation.

### (4) Radioadaptation response for protection against radiation-induced apoptosis in mouse spleen.

Toshiyuki Norimura, Ryuji Okazaki, Akira Ootsuyama

The effects of priming dose on the frequency of apoptosis and the expression of p53 in C57BL/6N mouse spleen were investigated. Mice received a whole body irradiation with 0.02Gy and 2Gy (an omission of a middle part.)

It was suggested that p53 stimulates repair system and then protects from apoptosis in the adaptive response.



## §29. Study on Environmental Behavior of Tritium

Momoshima, N. (Fac. Sci. Kumamoto Univ.),  
Okai, T. (Fac. Eng. Kyushu Univ.),  
Amano, H., Atarashi, M. (JAERI),  
Miyamoto, K. (NIRS),  
Takahashi, T. (Kyoto Univ.),  
Sugihara, S. (Isotope center, Kyushu Univ.),  
Uda, T., Sakuma, Y., Yamanishi, H., Sugiyama, T.

### i) Comparison of atmospheric tritium concentrations at Kumamoto and NIFS

Atmospheric tritium concentrations of three different chemical forms have been measured at Kumamoto (Kumamoto Univ.) and Toki (NIFS) to elucidate background levels and their variations in the general environment. Three chemical forms, water vapor (HTO), hydrogen gas (HT) and hydrocarbon mostly methane ( $\text{CH}_3\text{T}$ ) are the major chemical species of tritium in the atmosphere and would be key species for environmental tritium monitoring around a nuclear fusion facility. The sampling systems collect three tritium species successively and concentrations were determined by liquid scintillation counting (LSC). As far as very low tritium concentrations of these species in the general environment, sampling and measurement techniques should be applicable to be low level. The sampling systems used at Kumamoto Univ. and NIFS are quite similar collecting tritium in molecular sieves (MS) after converting their chemical forms to water. The recovery of water from MS is carried out by flowing  $\text{N}_2$  under heating MS. No alteration in tritium concentration during sampling and recovery from MS was confirmed by simultaneous sampling at NIFS using the each sampling system following recovery from MS and LSC at Kumamoto Univ. Simultaneous sampling was carried out three times in 2005 and the tritium concentrations were consistent as shown in Fig. 1 within counting error for three chemical species suggesting no bias or contamination of tritium during the sampling and recovery process adopted at Kumamoto Univ. and NIFS.

### ii) Model calculation

Basic concept of tritium transfer model should be expanded to a site specific model. Tritium transfer model applicable to HTO release from NIFS site was considered. The model consists in underground reservoirs and rivers which defined as water catchments for rain. The river network at Toki area which includes NIFS was constructed: representative rivers in Toki area; Tsumaki River, Ikuta River and Toki River and their branches are considered, and sizes of underground reservoirs were determined in proportion to the size of each catchment. The residence times of the underground reservoir and river water, and precipitation are variable parameters in the model, which influence transfer of HTO released from NIFS to the branch of IKUTA River. The response of the model was examined to idealized releases of HTO from NIFS at different parameter conditions to validate the constructed

model. The tritium concentrations in river and underground reservoir with time after HTO release showed quick response in river water and slow change in tritium concentrations in underground reservoir coupling with the short and longer residence times for river and underground water. The model would realize by fitting actual tritium level in river waters using rain data, which gives us a way to evaluate realistic parameter value for residence times of the underground reservoirs.

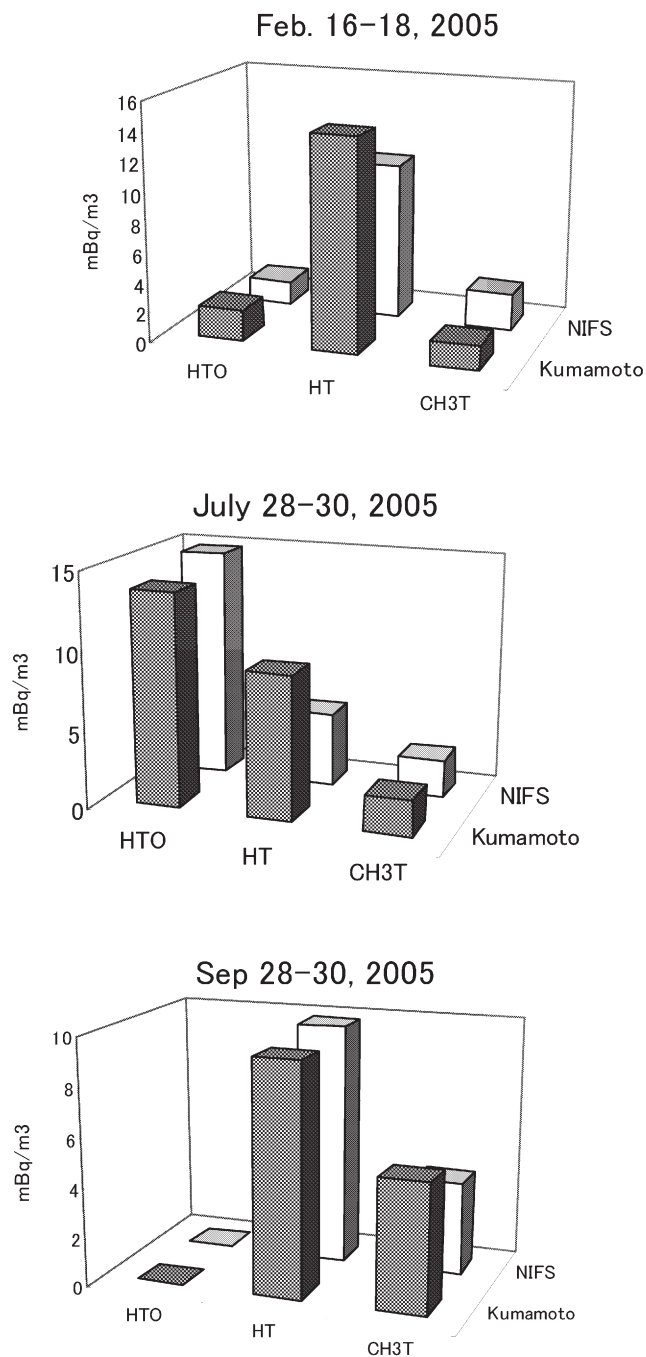


Fig. 1. Tritium concentrations at NIFS in 2005. Sampling was carried out by Kumamoto Univ. and NIFS using each sampling and recovery system. Tritium concentrations were measured at Kumamoto Univ. by LSC.

§30. Experimental Study on Liquid Lithium Flow for IFMIF Target

Horiike, H., Kondo, H. (Osaka U.), Ida, M. (JAEA), Iida, T., Inoue, S. (Osaka U.), Kukita, Y. (Nagoya U.), Matsui, H. (Tohoku U.), Miyamoto, S. (Osaka U.), Nakamura, Hideo, Nakamura, Hiroo (JAEA), Suzuki, A. (Tokyo U.), Yamanaka, S., Yamaoka, N. (Osaka U.), Tanaka, T., Muroga, T.

In the current design of IFMIF (International Fusion Materials Irradiation Facility), liquid Li plane jet of 25 mm in depth and 260 mm in width with a flow velocity of 10 to 20 m/s is designed as the deuteron beam target. The target flows along a concave wall with curvature radius of 0.250m, in the vacuum of  $10^{-3}$  Pa. In the present study, Li jet stability is experimentally examined. Free surface waves and wakes generated on the Li jet surface were measured by an electro-contact probe and a pattern projection method.

Test section of the Li loop at Osaka University has a two-stage contraction nozzle that is 1/2.5 scaled model of IFMIF nozzle. The nozzle creates the Li jet of 10mm deep and 70mm wide. The test channel is placed horizontally. Figure 1 shows picture of the free surface waves on Li jet taken by a CCD camera and strobe. The picture was taken from a viewing port set vertically to the test channel. The port is set at 175 mm downstream from the nozzle on which D beam axis are placed in design. As shown in the figure, waves were generated on the surface, and amplitude of the waves was measured by an electro-contact probe for the velocities of 1 to 15 m/s.

Figure 2 shows experimental results of wave amplitude. The amplitude increases with the velocity and lead to 2.5 mm at the velocity of 15 m/s (center of the flow).

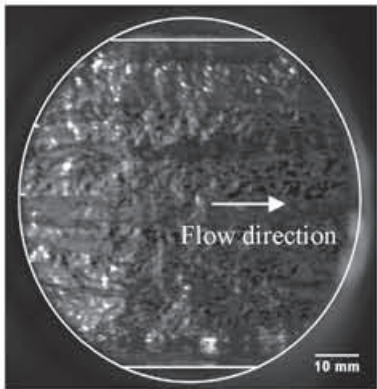


Fig.1. Free surface waves on Li target at the flow velocity of 15m/s

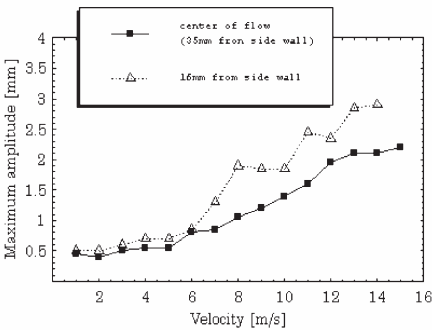


Fig.2. Wave amplitude vs flow velocity at 175 mm from the nozzle. Circles indicate those at the center, and triangles those at 16 mm from the side wall of the channel.

Figure 3 shows surface wakes that are stationary wave pattern caused by a deficit on the nozzle edge. Visual observation showed a small dent in the center of the nozzle edge, which may be produced by erosion or corrosion by Li. The surface wakes were measured by a image measurement method called as the pattern projection<sup>[1]</sup>. One result is shown in Fig.4, clearly shows a dent at 1.5mm in Y. The two diagnostics were found to be effective to measure the surface waves on Li flow and would be instrumented in IFMIF.

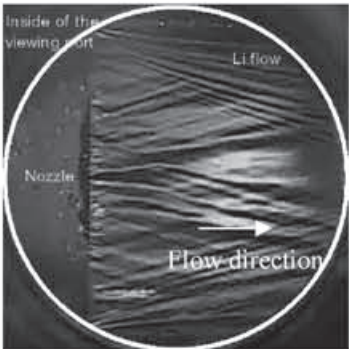


Fig.3 surface wakes on the lithium surface

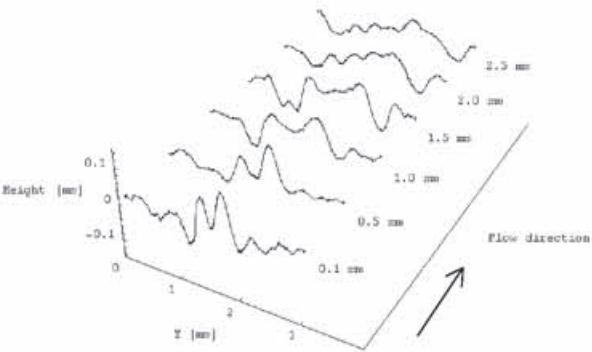


Fig.4 surface wake measured by pattern projection method

Reference  
[1] M.Takeda and K.Mutoh, “Fourier transform profilometry for the automatic measurement of 3-D object shapes”, Appl. Opt. 22, 24 pp.3977~3982 (1982)

### §31. Integrated Experimental Process Study for Removal of Tritium and Impurities from Liquid Lithium

Tanaka, S., Suzuki, A. (University of Tokyo),  
Fukada, S. (Kyushu University),  
Muroga, T.

Liquid Li is proposed as a flowing target for a high-energy neutron generator of IFMIF. Since radioactive T is generated by the nuclear reaction and its solubility in the Li is quite high, T removal is one of the most important issues for IFMIF target. In addition, N impurity in the Li not only enhances corrosion or erosion to tubing materials, but also promotes nitride contamination on a surface of Y, which is considered to be a T gettering candidate. The Li flow of the target system will be divided into a main flow and a sub loop, where impurity will be controlled. Through the sub loop, Li after the reduction of N impurity will be sent to the T hot trap system. To realize this composite impurity recovery system, it is necessary to investigate on integrated recovery process of N and T, which consists of cold trap, N hot trap, and T hot trap. N recovery by hot trap method with Fe-5at.%Ti alloy as a gettering material showed a high N reduction capacity. To enhance efficiency of the integrated recovery system, it is mandatory to shorten the N recovery time. As for T recovery, a Y particle bed is proposed as a method that can recover T down to 1 ppm. However, there was no study to prove 1 ppm T recovery by using Y. In this report, we describe recent progress on the integrated removal system, focusing on increase of N recovery coefficient by Fe-Ti alloys, and efficient T recovery by Y treated by HF.

Three plates of Fe-4at.%Ti alloy were immersed into 25 g of liquid Li in Mo crucible under Ar atmosphere. The crucible was put in a SUS316 stainless steel pot heated at 600, 700, or 800°C for more than 100 hours. A small portion of the Li in the crucible was sampled out with adequate time interval, and the N concentrations in the sampled Li were observed by changing N to ammonia. Fig. 1 shows the change of N concentration in Li. The maximum recovery rates, pointed by arrows in Fig.1, became faster with increasing temperature. In case of 800°C, the N concentration was reduced below 20wt.ppm. However, a thick TiN layer, which is considered to decrease N absorption into bulk was observed. On the other hand, no Ti-rich layer nor TiN were observed on the surface of the alloy immersed in Li at 600°C and 700°C. Optimization of temperature and Ti concentration in the alloy will be conducted to realize high efficiency consisted with long-life by avoiding TiN formation.

Y is a unique metal that can recover T dissolved in Li. However, since its surfaces are usually covered with oxides, hydrogenating rate is very low. As-received Y plate was treated by a 46% HF solution for 30 min. The HF treatment removed oxides on its surface and changed to YF<sub>3</sub>. When a Y plate covered with YF<sub>3</sub> was immersed into Li, YF<sub>3</sub> was dissolved into Li and, therefore, metallic Y surface was disposed to Li. Thus the HF treatment is effective to remove oxide layer on Y loaded in the trap at primary stage.

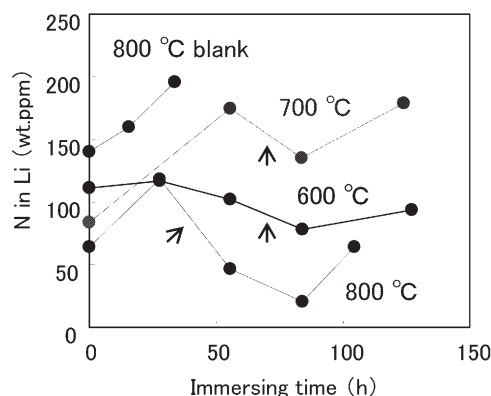


Fig.1 Temperature dependence of nitrogen recovery.

Several Li samples of 50 mg enclosed in a polyethylene capsule under He atmosphere were irradiated under a neutron flux of  $2.75 \times 10^{13}$  n/cm<sup>2</sup>s for several minutes in KUR. After the irradiation, Li was put in a Mo crucible along with a Y plate with 0.25mm in thickness and 1.3cm<sup>2</sup> in area. The concentration of T generated in Li was maximally 0.03 ppm in T/Li molar ratio. A set of Li and Y in a Mo crucible was heated at 300 – 500°C for 6 to 50 hours under Ar atmosphere. After heating, the T activity left in Li without absorption and that transferred to Y after heating were analyzed. The analysis revealed the following results on T recovery by Y plates: (i) Six hours heating at 400 or 500°C achieved the recovery of 1-6% of T generated in Li. The T chemical form in Li was atomic T. Its molecular form released to Ar is HT. (ii) 120 hours heating at 400 or 500°C made it possible to recover more T generated in Li (around 50%). (iii) T was transferred to Y more effectively by heating operation, and its chemical form was atomic T in Y. (iv) The HF treatment affected less the T recovery rate. This may be because oxygen that is inevitably present in Li delayed the T recovery rate regardless of the HT treatment. The last result revealed that the Y trap should be set after the oxygen and nitrogen traps in the IFMIF loop.

This work is performed with the support of the NIFS LHD Collaborative Research Program NIFS05KOB010.

#### References

- [1] S. Hirakane et al., Fus. Eng. Des., (2005)
- [2] S. Fukada et al., J. Nucl. Mater., 346 (2005) 293-297.
- [3] S. Fukada et al., Proc. IEA tritium management and corrosion activities for LB materials, (2005) 79-82.
- [4] M. Kinoshita et al., Fus. Eng. Des., 81 (2006) 567-571.

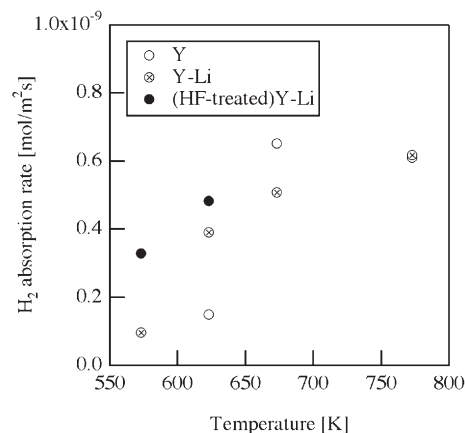


Fig. 2 Enhancement of H absorption rate by HF treatment



§32. Optimized Thermo-Mechanical Design of High Intensity Neutron Source Test Cell for Material Irradiation

Shimizu, A., Yokomine, T., Ebara, S., Yoshida, N., Matsuo, K. (Kyushu Univ.), Nakamura, H., Yutani, S. (JAEA), Matsui, H., Hasegawa, A. (Tohoku Univ.), Noda, N., Muroga, T., Sagara, A.

For material irradiation tests in IFMIF, temperature control of high accuracy is indispensable since neutron irradiation characteristics of material depend on irradiation temperature strongly. Especially in the high flux test module (HFTM), the space allowed for the temperature control is a little because the irradiation volume is remarkably restricted, and it makes the irradiation test very severe from the viewpoint of heat transfer. We have proposed a test module design that an accurate temperature control and monitor of temperature of irradiated specimens are possible. In our design, by making a cast-like capsule that is irradiation unit and accommodates specimens elongated in the spanwise direction, uniform temperature distribution in the capsule is promoted. A series of heat transfer experiment and numerical analysis and the upgrade of the design have so far been done in Kyushu University.

Since the temperature control of the HFTM is done with the electric heater installed in the capsule and He gas cooling, control of a flow rate and velocity profile of the flowing coolant is necessary to achieve the accurate temperature control. The coolant is supplied from the lower side of the HFTM and it passes through the irradiated region. Its velocity distribution is required to become uniform until it reaches the irradiated region. In addition, the coolant must be distributed equally into four channels in the irradiated region and this must be achieved without applying an independent gas supply system. In this case, because the mechanical device is inapposite under the irradiation environment, it is necessary to hold an accurate distribution of flow rate only by geometrical configurations of the channels. For this purpose, we have been proposing a porous-type manifold which is used as a flow distributor of coolant entering an irradiation region of the module. The manifold is comprised of a straightener part with porous plates located upstream of the irradiated region and a bifurcation part into four cooling channels just before entering the region. Porous plates are considered suitable for mixing the flowing coolant and making its velocity profile spatially uniform even in a short flow path. In this study, we manufacture a mock-up of the manifold and performe fluid flow experiment by varying the porous plates inserted in the straightener part.

Fig. 1 shows a schematic of the test section. The test section is the one as big as the original dimension based on the JAEA test module design, and N<sub>2</sub> is used for the gas. The most controversial part of development of the manifold is whether velocity profiles in the four channels after passing

the manifold become the same. Fig. 2 shows velocity profiles in the measurement part in Fig. 1 in case without porous plates while Fig. 3 shows those which are obtained by using three porous plates. From these figures, it is found that the velocity profiles which are not uniform at all in case without porous plates are well modified by inserting the porous plates and almost uniform over the channel just before branching into four channels. In the experiment, pressure drop by the porous plates is up to about 3 % of the total. Distribution of the flow rate into the four channels is sufficiently achieved, but this is considered due to not the porous plates but a geometrical configuration of the bifurcation part. The porous plates contribute to the velocity profile. The velocity profile can be remarkably changed by the porous plates and made spatially uniform.

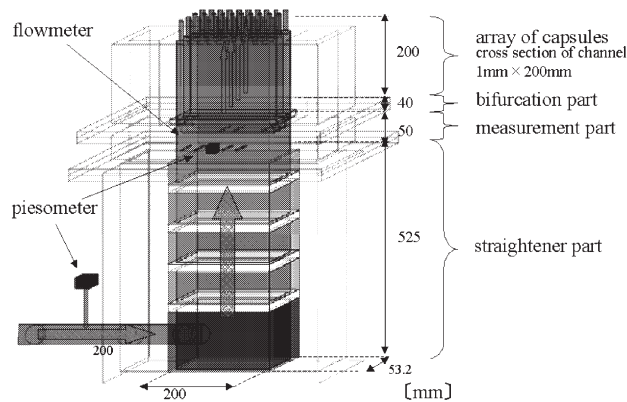


Fig. 1 Schematic view of test section

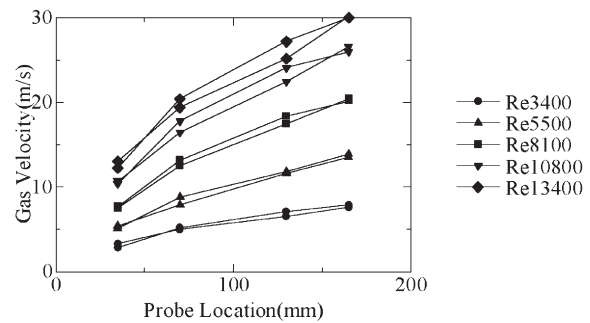


Fig. 2 Velocity profiles in case without porous plates

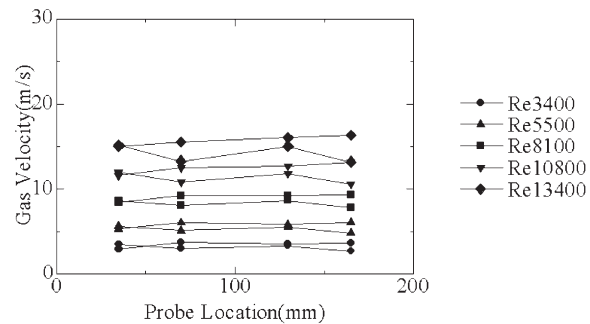


Fig. 3 Velocity profiles in case with porous plates



§33. Application of Advanced High Temperature Superconductors for Fusion Plasma Experimental Devices

Ogawa, Y., Morikawa, J., Kato, H. (The University of Tokyo),  
Iwakuma, M. (Kyushu University),  
Yanagi, N., Mito, T.

Recent progress on a YBCO tape is quite promising, and a tape with a 212.6 m x 245 A has been developed in ISTEC. In comparison with the BSCCO tape, a YBCO has great advantages; e.g., the current density is much higher than BSCCO, and higher magnetic field larger than 20 T might be feasible. Taking these advantages into account, a tokamak fusion reactor design with a YBCO coil has been carried out.

We are considering to apply this YBCO tape for the internal coil device. Since fabrication and operation of the YBCO coil seems to be premature, we have started from the feasibility study with the miniature floating coil device FB-RT, where a small-sized coil is levitated with a feedback control. Here we have prepared two different YBCO tapes, and characteristics of these tapes are listed in Table 1.

Table 1. Specifications of YBCO tapes.

ISTEC/SRL Nagoya	Critical current	~ 210 A and ~ 88 A
	Width	10 mm
	Thickness	0.12 mm
	Length	10 m
AMSC	Critical current	70 A
	Width	4.35 mm
	Thickness	0.20 mm
	Length	10 m

We tried to wind these tapes for FB-RT coil, a diameter of which is around 90 mm. Winding fabrication was easy for an AMSC tape, while an ISTEC/SRL tape was not so easy due to the stiffness of the tape. Here we have fabricated a coil for the FB-RT with the AMSC tape. A photo of this coil is shown in Fig. 1.



Fig. 1. A photo of FB-RT coil made of a YBCO tape.

Coil parameters are listed in Table 2. The coil is cooled with a field cooling method by using liquid nitrogen, and the coil current is inductively excited. Figure 2 shows the temporal evolution of the coil current for the persistent current mode. The decay constant is estimated to be 2.3 hours.

Table 2. Specification of a YBCO coil for the FB-RT

Inner and Outer diameters	90.8mm/98.4mm
Total turns	30turns
Winding method	Double pancake
Total length	10m
Total weight	123.5g

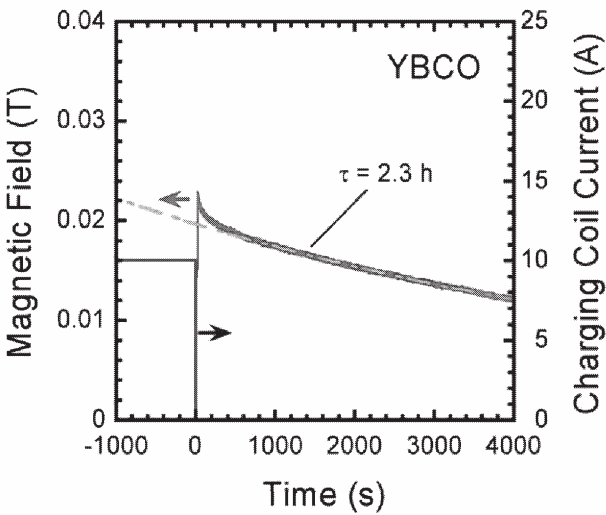


Fig. 2. A current decay of the YBCO coil at the persistent current mode.

Next we have considered the application of a HTS coil for LHD device. In LHD correction coil system called LID is equipped, where a magnetic field of LHD plasma is controlled; e.g., a large m/n=1/1 magnetic island is produced for the plasma experiment. These LID coils are made of water-cooled copper conductors, and located outside the cryostat. We have examined that these copper coils could be replaced with HTS coils installed inside the cryostat. Table 3 shows the comparison between two coil systems.

Table 3 Comparison between copper and HTS coil systems for the LID coil.

	Copper coil	HTS coil
Coil size	2.3 m x 1.9 m	~φ0.8 m
Coil turns	48	2000
Coil current	1920 A	200 A
Magnetomotive force	92 kA	400 kA
Power supply	~ 2 MW	< 10 kW

Since the correction coils are located near by the plasma surface in the case of the HTS coil system, the flexibility for the magnetic field configuration is quite superior. In addition, if the PCS switch is employed for the HTS coil, the passive control of the plasma could be available.

§34. Effects of Simultaneous Helium  
Irradiation on Hydrogen Behavior in  
Plasma Facing Materials

Ueda, Y., Nishikawa, M., Ohtsuka, Y. (Osaka Univ.),  
Yoshida, N., Tokunaga, K. (Kyusyu Univ.),  
Ohno, N. (Nagoya Univ.),  
Sagara, A., Masuzaki, S. (NIFS)

In fusion reactors, tungsten is a leading candidate for plasma facing materials (PFMs) due to high melting point, low sputtering yield by light ions, and high thermal conductivity. Its brittleness by hydrogen isotope and helium ions, however, is one of the serious concerns. To study this subject in detail, it is important to study hydrogen and helium behavior in tungsten. In fact, quite a few studies have been done on hydrogen or helium behavior in tungsten by mono-species ion irradiation to tungsten. In actual fusion devices, however, hydrogen isotopes (D and T) and helium ions (~5%) simultaneously impinge on plasma facing materials. Therefore, it is important to study synergistic effects of hydrogen and helium to correctly evaluate tungsten materials response in fusion reactors.

In our laboratory in Osaka University, from 1996 to 2001, new steady state high flux ion beam irradiation test devices, called HiFIT, was constructed by LHD collaboration study with NIFS. One of the result of mixed ion irradiation with hydrogen and helium by using HiFIT is shown in Fig.1. Without helium ions in the beam (hydrogen with slight carbon addition (~0.8%)), dome-shape blisters clearly appeared on the tungsten sample. Addition of only 0.12% He to hydrogen and carbon mixed ion beam, however, completely suppressed blistering. It is known that He atoms in tungsten form He bubbles, which do not disappear even over 1500 K. These He bubbles could affect hydrogen retention and diffusion in tungsten, leading to suppression of blistering.

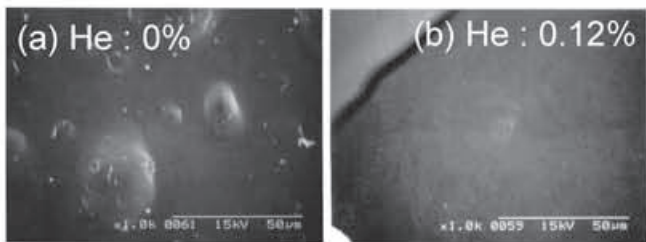


Fig. 1 Blistering due to hydrogen and carbon mixed ion beam irradiation (1 keV  $H_3^+$  as main component, C concentration ~0.8%). Sample temperature is 653 K. Sample is sintered tungsten plate with hot rolled process with stress relieved annealing process.

From this result, it is clear that He effects must be taken into consideration to understand hydrogen isotope behavior in tungsten. In previous study with

HiFIT, hydrogen ions and helium ions were extracted from one ion source, which means relative energies of hydrogen and helium cannot be changed. In actual fusion devices, helium ions exist in edge plasmas as doubly charged ions and impinging energy of helium is approximately twice as large as hydrogen isotopes. If helium energy becomes higher than hydrogen isotope ions, the helium ion range is larger and the location of helium bubble formation becomes deeper. This fact could affect helium effects on hydrogen behavior in tungsten. In our present HiFIT system cannot cope with this situation.

In present framework in LHD collaboration study, in order to study this complicated hydrogen and helium irradiation condition to plasma facing materials new mixed ion beam irradiation device has been constructed based on HiFIT. The schematics of the new device is shown in Fig. 2. New helium ion source with helium energy from 0.2 keV to 2 keV will be installed to HiFIT to make independently controlled hydrogen and helium mixed ion irradiation experiments to plasma facing materials. Helium ion species ratio in hydrogen dominant ion beam can reach as high as about 10%, which can cover actual fusion edge plasma conditions.

In the first year of this collaboration study (2005), new helium ion beam source was purchased and we confirmed that this ion source worked properly with helium working gas. In the next year, we will install this helium ion source to HiFIT to complete the preparation for mixed ion beam irradiation study.

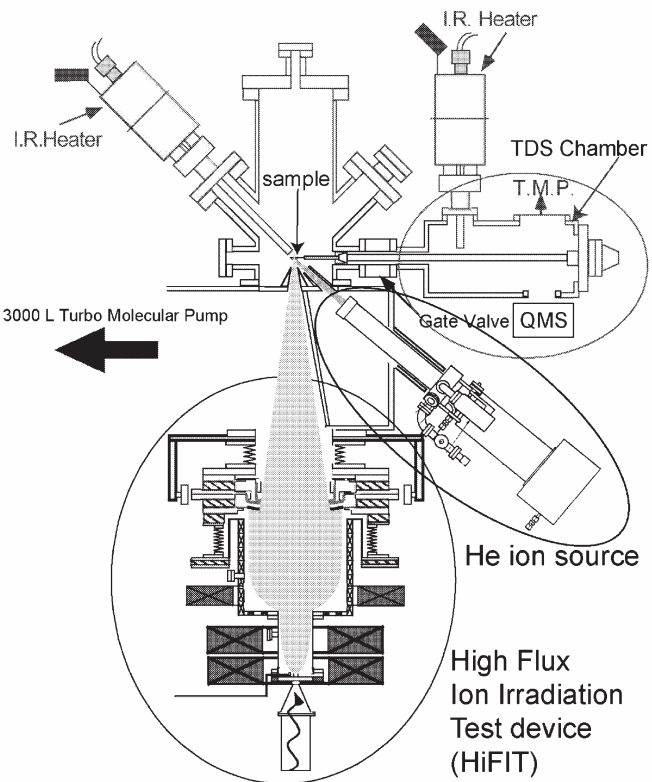


Fig. 2 New H and He ion beam irradiation device

§35. Development of Current Leads  
Combined with the Pulse-Tube  
Cryocooler

Maehata, K., Ishibashi, K., Takeo, M. (Kyushu Univ. Eng.), Maekawa, R., Iwamoto, A., Tamura, H., Hamasaki, S., Mito, T.

In operating usual large superconducting magnets such as LHD coils, the high current of 10 kA class is supplied through current leads into the cryogenic region from a power supply located at room temperature. The heat leak from the current leads causes a large load of the refrigeration system. Therefore it is necessary to reduce the heat leak from the current leads with a minimum refrigeration load for a low cost and stable operation of the superconducting magnet system. Optimization methods have been studied for designing gas cooled current leads with copper conductor, and the heat leak into the liquid helium region is evaluated to be 1 W/kA for the optimum gas cooled current leads. Several types of high temperature superconducting (HTS) current leads were developed for further reduction of the heat leak. The HTS conductor is

employed in the HTS current leads in the temperature region below  $\sim 50$  K, while the copper conductor feeds the current from a room temperature to the HTS conductor. Although a large reduction in the heat leak has been demonstrated in the operation of the HTS current leads, large heat load to the refrigeration system is still generated in the conventional copper conductor part.

In this work, we apply advantageous characteristics of a pulse-tube cryocooler to the copper conductor region of the 3kA HTS lead system for a reduction of the refrigeration load caused by with a compact structure.

Since the thermoacoustic effect is utilized for operation, the pulse-tube cryocooler consists of a pulse tube, a regenerator and warm-and cold heat exchangers without moving element in the cryogenic region. Fig. 1 shows a schematic drawing of a pulse-tube current lead. The copper-rod conductor is concentrically inserted into the pulse tube. In Fig. 1, geometrical dimension of the copper conductor was optimized for supplying current of 3 kA to a temperature of 80 K in the adiabatic condition. The heat leak through the copper rod is estimated to be 200 W at the cold end of 80 K. In this work, the inner volume of the pulse tube is optimized to be 650 cm<sup>3</sup> by employing numerical analysis of the dynamics of a virtual gas piston in the pulse tube. The cooling power is estimated to be 196 W at 80 K.

A group of Maekawa developed a prototype of 2 kA pulse-tube current lead system. In this work, we carried out measurements of the temperature at the cold end of the conductor rod in the operating test of the prototype of the 2 kA pulse-tube current lead. For constructing a reliable numerical design code of the pulse tube current lead, temperature profiles along the conductor rod were estimated for several operation currents by solving a general heat conduction equation with using experimental data of the cold end temperatures.

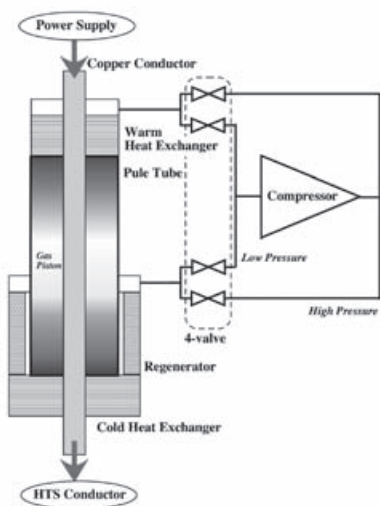


Fig. 1 Concept of the pulse tube current lead.

## 2. Collaboration on Fusion Engineering

### (1) Fusion Engineering Studies

In the fusion engineering research field, 25 collaboration programs in total have been carried out. Subjects are relating to low activation structure materials, insulating materials, plasma-facing materials, blanket technology and neutronics, superconducting materials and technology *etc.*

The number of reports on low activation structure materials, insulating materials is 9. Materials such as ferritic steel, vanadium alloy, or SiC/SiC are investigated and titles are listed as follows:

- Development of fracture toughness evaluation method by round bar with circumferential notch (Kasaba),
- Retention and Desorption of Deuterium in Model Alloys of Ferritic Steel (Iwakiri),
- Development of reduced activation ferritic steels with improved heat resistance and elemental property characterization for high efficiency water-cooled blankets (Kohyama),
- Small specimen test techniques for IFMIF (Kimura),
- Study on radiation induced precipitates in vanadium alloys (Nita),
- Thermal Creep Mechanism of NIFS-Heat2 alloys by Using Pressurized Creep Tubes (Fukumoto),
- The microstructure of laser welded V-4Cr-4Ti alloy after neutron irradiation (Watanabe),
- Radiation resistance and mechanical properties of solution and dispersion hardened vanadium alloys with fine grains of high purity matrix (Kurisita),
- Development of joint technique of SiC/SiC composites (Hinoki),

General information exchange and discussions on IFMIF have been organized as a collaboration program in this framework. A report titled as “Summary of key element technology verification and preparation for engineering validation of intense neutron source” is given here by H. Matsui.

Three reports are given for activities on plasma facing components. They are

- Joining heat load test of tungsten divertor (Tomota),

- Synthetic evaluation of ultra-fine grained nanoparticle dispersed tungsten alloys as plasma facing materials (Kurisita),
- Influence of heating rate on subcooled flow boiling critical heat flux in a short vertical tube (Hata),

Five reports are given for collaborations on key technology in blanket systems. They are

- Basic study on self-healing of  $\text{Er}_2\text{O}_3$  coating for vanadium lithium blanket system (Terai),
- Investigation of issues in neutronics evaluations for advanced liquid blanket systems (Iida),
- Examination of irradiation damage in electrical insulating coating using ion beam irradiation (Shikama),
- Development of multi layer wall channel to reduce MHD pressure drop (Hashizume),
- Overall characterization of high purity reference vanadium alloys NIFS-HEATs (Satou),

The number of reports on superconducting magnet is 6. Titles are listed as follows:

- Cryogenic fatigue delamination growth in material systems for superconducting fusion magnets (Shindo),
- Thermal and mechanical properties of composite materials for superconducting coils (Takao),
- Development of V-Ti and V-Ti-Ta superconducting wires (Inoue),
- Development of low activation compound superconducting wires for fusion reactor (Kikuchi)
- Large-sized cylindrical superconductor composed with Ni meshes for a current lead (Yoshizawa),
- Effect of Test Equipment Configuration on Interlaminar Shear Fracture and Strength of Glass Fiber Reinforced Plastics (Nishimura),

A report titled as “Transmutation of high-level wastes in a FLiBe-cooled spherical-tokamak reactor” is given by Y. Tanaka, in which a new concept of utilizing ST is presented.

(Noda, N.)



§1. Development of the Fracture Toughness Test Method by Round Bar with Circumferential Notch

Kasaba, K., Katagiri, K., Shoji, Y. (Iwate Univ.), Nishimura, A.

1. Introduction

Fracture toughness is one of the most important mechanical properties among various properties of structural materials for machinery. Test methods of plane strain fracture toughness  $K_{IC}$  and elastic-plastic fracture toughness  $J_{IC}$  are standardized in ASTM<sup>1)</sup>. However the methods are time-consuming and expensive. On the other hand, a convenient new test method, named J evaluation on tensile test (JETT), has been proposed to evaluate the fracture toughness of the tough materials<sup>2-3)</sup>. The procedure of JETT developed in this two year joint research was shown.

2. The procedure of JETT

Searching for the size of JETT specimen with the same strain constraint around tip area as that of CT specimen by FEM calculations

In this research, for example, JETT625-6 indicates the ratio of notch and radius  $a/R=0.625$  and radius  $R=6$ . Fig.1 shows the representative value concerning with maximum stress around tip area of each specimen with increasing J. To obtain Fig.1, the relationship between stress and strain of the material needs to be measured beforehand. The ordinate on the right shows maximum stress normalized by 0.2 % proof stress and that on the left shows such the normalized stress minus 3.5. In general, the normalized stress of plane strain CT specimen is independent of J and calculated on almost constant 3.5 of this material (Manganese steel quenched from 840 °C in a oil). Therefore the value zero of the ordinate on the left shows the same strain constant as the crack tip of CT specimen. The value of the ordinate on the left is called Q-factor. Since Q-factor of JETT625-8 and 625-6 within 40~190KJ/m<sup>2</sup> of J are almost zero, these specimens are candidates as an alternative specimen of CT. However the strain constrains around tip area of JETT625 series specimens below  $J=40\text{kJ/m}^2$  are lower than that of CT. Therefore if an obtained experimental critical J of JETT625 series specimen is below  $40\text{kJ/m}^2$ , the value is invalid. On the other hand, the strain constraint at tip area of JETT750 series found to be too high.

Experiments of candidate specimens

In a procedure to evaluate a fracture toughness, the specimens other than candidate ones (in this

material: JETT625-6, 625-8) don't need to be prepared for the experiments. However the other specimens were also tested for comparison in this research and the results are shown in Fig.2. Since obtained critical J values depend much on the R and a/R, the guideline to select equivalent one to the CT specimen is indispensable. The specimens with  $R=2\text{mm}$  or  $a/R<0.5$  are excluded in Fig.2 because of too high or too low constraint around tip area, respectively. These tendencies of strain constraint were obtained by the experiments of last year.

Verify the predict critical J

252 ~ 302kJ/m<sup>2</sup> of JETT625-6 and 625-8 is predicted critical J values equivalent to the CT specimen. The values have to be verified by fracture mode observed by SEM fractography. Acoustic emission for detecting threshold load or displacement of the initial crack propagation is also useful to verify the estimation of critical J value. Both JETT625-6 and 625-8 are verified in these points. On the other hand, actual critical J value obtained by CT specimen was 275 kJ/m<sup>2</sup>. It was within the predict value by JETT.

References

- 1) ASTM E1820-99a.: Annual book of ASTM standards (1999) 1000
- 2) Nishimura A. et al. : Adv. Cry. Eng. 44 (1998) 145
- 3) Nishimura A. et al. : Adv. Cry. Eng. 46 (2000) 33

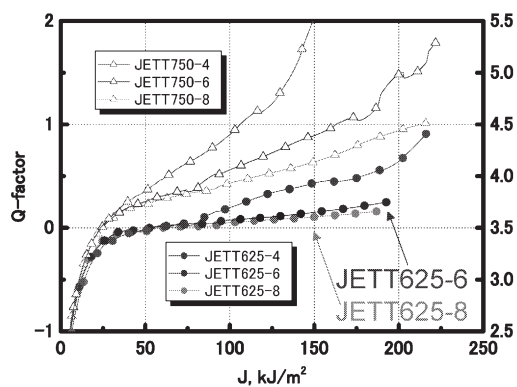


Fig.1 Q-factor of JETT

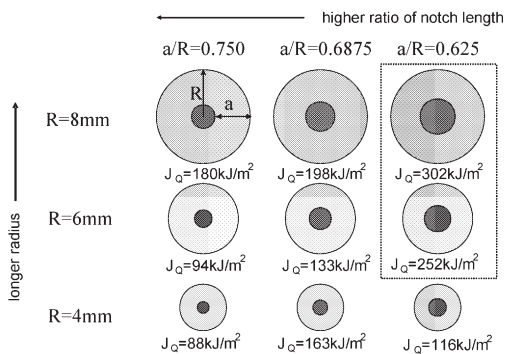


Fig.2 Experimental results

§2. Retention and Desorption of Deuterium in Model Alloys of Ferritic Steel

Iwakiri, H., Baba, T., Tani, M., Tokitani, M., Kawakami, M., Miyamoto, M., Yoshida, N. (Kyushu Univ.), Morishita, K. (Kyoto Univ.), Miyamoto, M. (Shimane Univ.), Muroga, T., Kato, D.

Retention and desorption of injected deuterium into model alloys of ferritic steel were investigated by using TDS, XPS, and TEM complementary. Three model alloys (Fe-9Cr) and Pure-Fe were prepared as test materials. After rolled to 0.2 mm thickness, some of them were annealed at 1023 K for 2 hours to reduce dislocations. As-rolled and annealed specimens were irradiated at room temperature with 8keV-deuterium ions up to the fluence of  $6 \times 10^{21} \text{ D}^+/\text{m}^2$ , and successively thermal desorption of  $\text{D}_2$  and HD under the constant heating rate (1K/s) was measured using quadruple mass spectroscopy.

In general, retention of deuterium in the rolled Fe-Cr alloys was quite low and most of them desorbed up to 700 K. Remarkable desorption was observed even at room temperature, which indicates the existence of rather weak traps.

Figure 1 shows thermal desorption spectra of D released from As-rolled and annealed Fe-9Cr specimens irradiated with 8 keV- $\text{D}_2^+$  ions to  $2 \times 10^{21} \text{ D}^+/\text{m}^2$  at room temperature respectively. The retention decreased drastically in the annealed specimens. This fact indicates that the dense dislocations formed by cold work provide good trapping sites for deuterium diffusing deeply into the specimen.

Figure 2 shows thermal desorption spectra of D from annealed Fe-9Cr irradiated with 8 keV- $\text{D}_2^+$  ions up to  $6 \times 10^{21} \text{ D}^+/\text{m}^2$  at room temperature. A special feature of the Fe-Cr alloys was the remarkable decrease of the retention above the fluence of  $3 \times 10^{21} \text{ D}_2^+/\text{m}^2$ .

The composing elements and their chemical states at the surface were examined by means of XPS technique. Figure 3 Shows Depth profile of Atomic concentration. It was found that the surface of the alloys was covered with oxide layer of about 7 nm thickness, which is just the thickness of sputtering erosion by the irradiation of 8 keV- $\text{D}_2^+$  for  $6 \times 10^{21} \text{ D}_2^+/\text{m}^2$ . Taking into account that 8 keV- $\text{D}_2^+$  is injected in the much deeper region (projected range is about 30 nm), it is likely that the surface oxide layer acts as desorption barrier and once the layer is removed by the sputtering desorption during and after irradiation occurs actively. As a result, retention of deuterium decreases above  $3 \times 10^{21} \text{ D}_2^+/\text{m}^2$  as observed. Interstitial type dislocation loops are formed in the narrow subsurface region. But their density and size are too low to explain the retention of the deuterium, namely, these defects don't work as main deuterium trapping site.

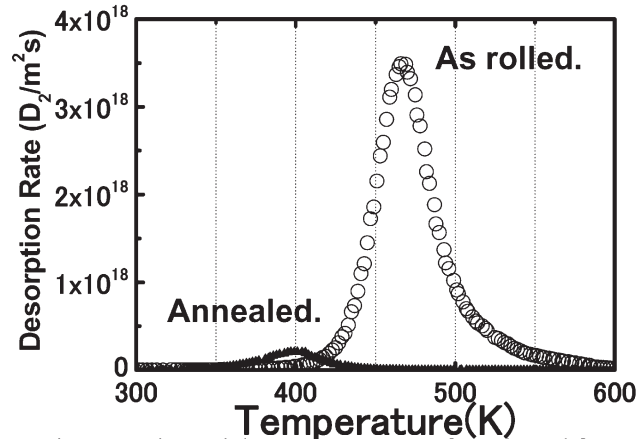


Figure 1 Thermal desorption spectra of D released from As-rolled and annealed Fe-9Cr specimens irradiated with 8 keV- $\text{D}_2^+$  ions to  $2 \times 10^{21} \text{ D}^+/\text{m}^2$  at room temperature.

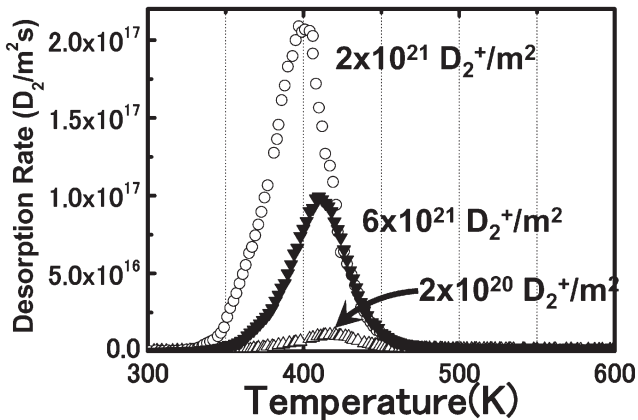


Figure 2 Thermal desorption spectra of D from annealed Fe-9Cr irradiated with 8 keV- $\text{D}_2^+$  ions up to  $6 \times 10^{21} \text{ D}^+/\text{m}^2$  at room temperature.

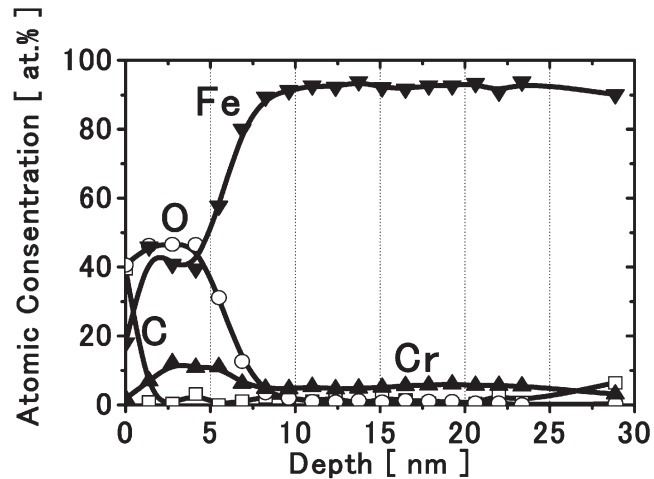


Figure 3 Depth profile of Atomic concentration in annealed Fe-9Cr.

§3. Development of Reduced Activation Ferritic Steels with Improved Heat Resistance and Elemental Property Characterization for High Efficiency Water-Cooled Blankets

Kohyama, A., Kim, S.W., Ogiwara, H. (Institute of Advanced Energy, Kyoto University), Muroga, T.

For a life-time design of a blanket for fusion power reactors, thermal fatigue property of structural materials is particularly important. The cyclic stress loading in blankets mainly comes from pulsed generation of fusion neutrons under the current operation scenarios of fusion reactors. Although materials-wall interaction and radiation damage by fusion neutrons have a strong influence on the stress loading and strain responses, the cyclic loading depends on operation conditions, including cycle length, material properties, including thermal properties and blanket design, including cooling system design. Thus fatigue resistant Reduced Activation Ferrite steels (RAFs) development and establishment of fatigue evaluation methodology and design code including fatigue resistance design are of urgent needs for ITER and ITER-BA activities.

This study focused on influence of surface morphology to fatigue properties in order to establish design and fabrication of test blanket module for ITER.

The material used was F82H IEA heat which was normalized at 1313 K for 40 min air-cooled and tempered at 1023 K for 60 min air-cooled. The mini-sized hourglass type specimens (SF-1) were used for low cycle fatigue (LCF) tests. It is well known that the hourglass type specimen has good resistance to buckling, which is a very important issue to miniaturize specimens for push-pull tests. Test specimens with three kinds of surface roughness were used in order to investigate the effect of surface roughness on fatigue properties. For the test, an electromotive testing machine with a 200 kg load cell was used. Diametral strain controlled fatigue tests were carried out with a triangular stress waveform and a total diametral strain range,  $\Delta\epsilon_d$  of 0.4-0.6 %.  $\Delta\epsilon_d$  was converted to total axial strain range,  $\Delta\epsilon_a$ , by the following formula;

$$\Delta\epsilon_a = (\sigma / E) (1 - \nu_e) - 2\Delta\epsilon_d,$$

where  $\sigma$  is applied stress, E the elastic modulus,  $\nu_e$  is the elastic Poisson's ratio.

In this work, the surface roughness profiles in seamless tube and rectangular channel for ITER-TBM were measured with a laser microscope, as shown in Fig.1.

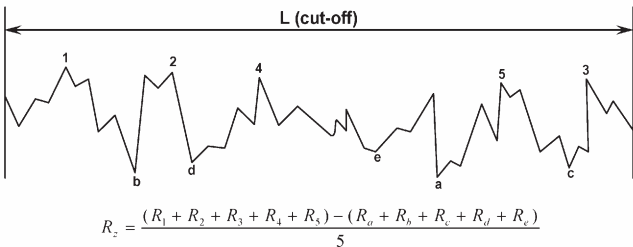


Fig. 1 Surface roughness calibration (JIS B 0601)

The surface roughness was defined by “ten point median height roughness ( $R_z$ )”. The seamless tube used showed surface roughness ( $R_z$ ) of 2.695  $\mu\text{m}$ , and the rectangular channel before and after pickling shows a surface roughness ( $R_z$ ) of 3.163  $\mu\text{m}$  and 7.625  $\mu\text{m}$ , respectively. The surface roughness traces of the seamless tube showed a large difference before and after pickling (Fig.2).

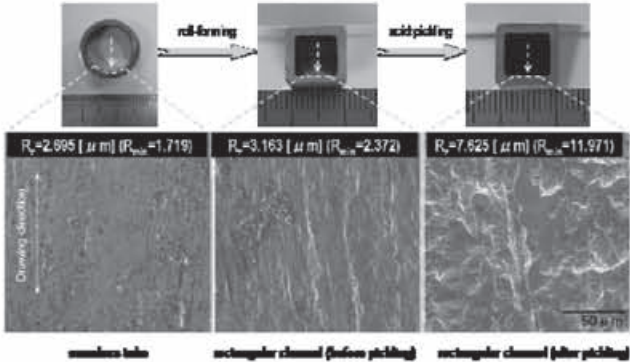


Fig. 2 Surface configuration of cooling channels

The fatigue lifetime of fine finishing specimens ( $R_z = 0.53 \mu\text{m}$ ) was slightly longer than those of rough finishing specimens. In the mean time, the fatigue lifetime of very fine finished specimen ( $R_z = 0.89 \mu\text{m}$ ) significantly increased about 61.3%. As the fatigue lifetimes are strongly dependent on the surface conditions, surface roughness of the various LCF specimens tested from the rough finishing, fine finishing and very fine finishing specimen were characterized.

Fig. 3 shows the surface roughness as a function of the number of cycles. Linear regressions of the data shown in this figure demonstrate the trends of the fatigue lifetime decrease with increasing surface roughness. From these results, it can be assumed that the fatigue lifetime of cooling channels for ITER-TBM might be decreased significantly compared with the fatigue life of standard test specimen. Thus the surface roughness control in blanket to meet fatigue property requirement is very important.

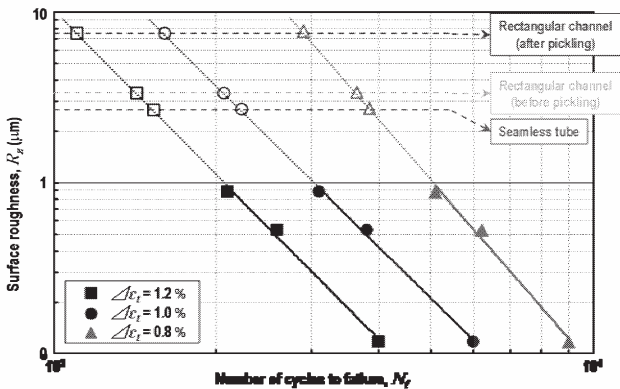


Fig. 3 Relationship between surface roughness and fatigue life in F82H steel

References  
1) Hirose, T. et al. : J. Nucl. Mater. 283-287 (2000) 1018.  
2) Kim, S.W., et al. : Presented at ICFRM-12 (Dec. 2005 Santa Barbara).



§4. Small Specimen Test Techniques for IFMIF

Kimura, A., Kasada, R., Ono, H. (IAE, Kyoto University)

International Fusion Materials Irradiation Facility (IFMIF) is essential to evaluate the material performance under fusion relevant environment.

The required irradiation volume for fracture toughness measurement is estimated to be 560cc that exceeds the irradiation volume of the speck of IFMIF where the available displacement damage is 20dpa/year. In order to effectively produce IFMIF irradiation database, reduction of the specimen volume is strongly demanded without losing data reliability by the specimen miniaturization.

Material used in this study was the JLF-1LN steel (JLF-1 JOYO-heats). The steel plate of 30 mm thickness was heat-treated at 1323K for 1h and air-cooled (normalizing), and then tempered at 1053K for 1h, followed by air-cooling (tempering). Four different sizes of compact tension (CT) specimens were fabricated. Prior to the fracture toughness test, a fatigue pre-crack with a ratio of the crack length to specimen width ( $a/W$ ) of 0.5, was introduced to the specimen until the final  $K$  value to be 21.7, 21.4 and 20.1 MPa $\sqrt{m}$  for 1t-1CT, 1/2t-1CT and 1/4t-1CT specimen, respectively. And then the specimens were side-grooved by 25% (25% SG) of their thickness with the root radius of 0.1 mm. The fracture toughness tests were carried out at room temperature referring to the ASTM E1820-99a by means of the unloading compliance method.

The  $J_Q$  values obtained for the 1t-1CT and 1/2t-1CT specimens were 425 and 560 kJ/m<sup>2</sup>, respectively. The fracture toughness increased as decreasing in the specimen thickness. On the other hand, the fracture toughness decreased when the specimens were miniaturized while keeping the similar figure, resulting that the  $J_Q$  values for the 1/2CT and 1/4CT specimens were 382 and 300 kJ/m<sup>2</sup>, respectively.

The weibull distribution analysis (Fig.1) of the measured fracture toughness is necessary for dealing with a variability in the obtained data such as  $J_Q$ . The parameter  $m$  (shape parameter) is determined from the slope of the line. For each line, the values were ranging from 10 to 14, suggesting that fracture toughness data with high reliability is obtained even for the miniaturized 1/4CT specimens.

The fracture toughness increased as decreasing in the specimen thickness. Two of the possible explanations of the above results are as follows.

1) It is considered that the plane stress state becomes predominant as specimen thickness decreases, and the plastic zone size at the crack tip increases near specimen side surfaces. Since the energy spent on the plastic deformation increases, the fracture toughness increased.

2) The crack growth occurs at the weakness part of crack front (weakest-link theory), it is considered that the fracture probability increases as the specimen thickness increases, and the 1t-1CT specimen presented a low fracture toughness. However, since the weibull distribution form of the 1t-1CT were similar to 1/2t-1CT, it is considered that the first factor is more predominant in the specimen thickness effect on the fracture toughness obtained for the above two type of specimens.

Among the obtained  $J_Q$  values for the different size of specimens, only the value of 1CT specimen was valid and those of other size of specimens were invalid, according to the valid criteria of equation. However, the reduction of fracture toughness coupled with hardening, which will be induced by high dose of neutron irradiation, may decrease the specimen thickness that satisfies the criteria equation. An assumption that the irradiation-induced reduction of fracture toughness and irradiation hardening is 40% and 300MPa, respectively, the minimum thickness required to keep a valid value was estimated to be 9 mm, indicating that even after neutron irradiation, the fracture toughness obtained with using 1/4CT specimen will still be in valid.

Since the first wall thickness is estimated to be less than 5 mm for ferritic steel-water blanket system, the obtained fracture toughness values of the first wall were always invalid before and probably even after irradiation. It is demanded that new valid/invalid criterion can be established for thin specimens to provide a valid database, if necessary, of fracture toughness of fusion blanket structural materials.

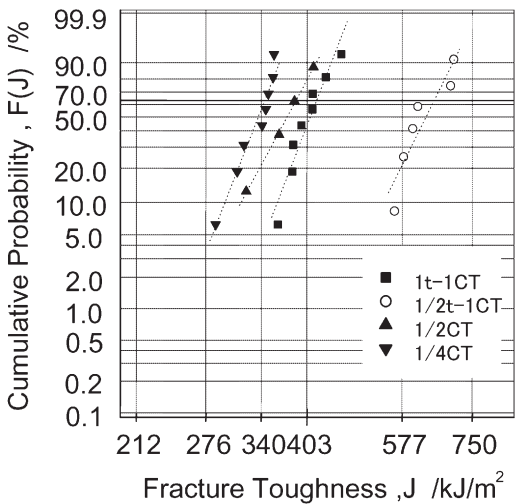


Fig. 1 Weibull plots of fracture toughness  $J_Q$  obtained from the CT specimens of JLF-1 at various specimen sizes.



## §5. Study on Radiation Induced Precipitates in Vanadium Alloys

Nita, N., Anma, Y., Matsui, H. (IMR, Tohoku Univ.), Nagasaka, T.

### Introduction

Vanadium alloy is one of the excellent candidate materials for fusion reactors. Because of its good resistance to neutron irradiation, V-4Cr-4Ti, in particular, has been studied extensively in the past decades [1]. However, it has been reported that significant radiation hardening and embrittlement occurred in V-4Cr-4Ti irradiated at relatively low temperatures by neutrons. According to the previously reported TEM studies [2], radiation-induced titanium precipitates are the major cause of irradiation hardening, while the microstructural information is still far from comprehensive. Especially, the nature of black-dot clusters which were observed under irradiation at low temperatures is still not clear while the large size of Ti-precipitates with platelet shapes are relatively well characterized. The objective of this study is to investigate both the nature of black dotted cluster formed under low temperature irradiation and the chemical composition of titanium rich precipitates in vanadium alloy. For the analysis of fine precipitates, 3-dimensional atom probe microanalysis (3DAP) is a very powerful tool with its atomic scaled spatial resolution. In the present paper, experimental results using 3DAP combined with TEM observation on fine Ti-precipitates in vanadium alloys are presented.

### Experimental procedures

V-4Cr-(0.1,1,3wt.%)Ti were prepared. Neutron irradiation was conducted in Japan Material Testing Reactor (JMTR) up to 0.2 dpa at 350°C. The damage rate was  $9.4 \times 10^{-8}$  dpa/sec. After electro polishing, TEM observation was performed using JOEL-2010 equipped with an energy dispersive X-ray spectrometry (EDX) detector. To prepare needle-like specimens for the 3 dimensional atom probe (3DAP) analysis, the irradiated tensile specimens were cut into small square rods of approximately  $0.25 \times 0.25 \times 7$  mm, which were subsequently electropolished to blunt needles. Finally a sharp needle tip were fabricated by the focused ion beam (FIB) processing with an annular gallium ion beam of 30 keV. 3DAP measurements were carried out using energy compensated position-sensitive atom probe facilities which consists of a reflectron energy compensator, a position sensitive detector and a high-resolution flight time detector. Measurements were conducted at a sample temperature of 60 K with the pulse fraction of 0.2 under an ultra-high vacuum condition.

### Results and discussions

In TEM observations, platelet precipitates on {100} planes were observed in V-4Cr-4Ti-0.1Si, while a high density of small defect clusters was observed as black

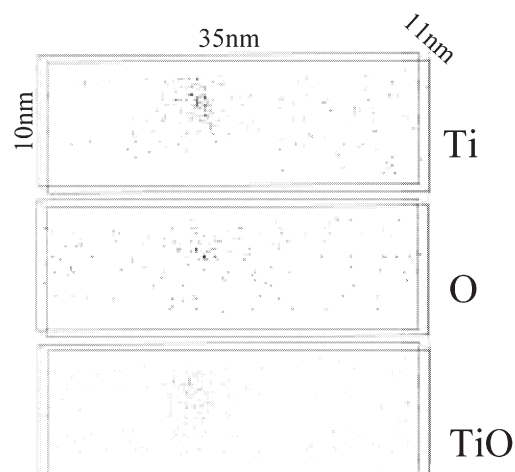


Fig.1 Atom maps of V-4Cr-0.1Ti

dotted contrast in V-4Cr-1Ti. Enrichment of titanium as well as oxygen and titanium oxide in the matrix were observed by 3DAP microanalysis in V-4Cr-3Ti, V-4Cr-1Ti, V-4Cr-0.1Ti (Fig.1), which may corresponds to the precipitates and black dotted defect clusters observed by TEM. The size of precipitates increased with the titanium concentration. Small cluster with a sphere shape were observed in V-4Cr-0.1Ti, while the platelet shape in other alloys. It could be deduced that the spherical cluster was on the nucleation stage of precipitates. In other words, the nucleation of titanium-rich precipitates might be started with the segregation of titanium and oxygen to dislocation loop. Nitrogen and carbon were also contained in the large precipitates of platelet shape in V-4Cr-3Ti, which will be explained by the difference in the extent of strain field depending on the coherency of precipitates.

### Conclusions

Neutron irradiated vanadium alloys were examined by TEM and 3DAP. A high density of small defect clusters was observed as black dotted contrast in V-4Cr-1Ti. Although it was difficult to determine the nature of these fine defect clusters by a conventional TEM with an EDX technique, enrichment of titanium as well as oxygen and titanium oxide in the matrix were observed by 3DAP microanalysis. It could be deduced that the spherical cluster was on the nucleation stage of precipitates. In other words, the nucleation of titanium-rich precipitates might be started with the segregation of titanium and oxygen to dislocation loop. It could be said that the precipitates grow with changing their morphology from sphere to platelet and the ratio of titanium to oxygen. The spherical cluster during the nucleation stage is  $\text{Ti}_3\text{O}_2$  and the planar cluster during the growth stage is  $\text{Ti}_3\text{O}_2$ .

### References

- [1] H. Matsui, K. Fukumoto, D. L. Smith, H. M. Chung, W. V. Witzenburg and S. N. Votinov, J. Nucl. Mater, 233-237 (1996) 92-99
- [2] N. Nita, T. Iwai, K. Fukumoto and H. Matsui, J. Nucl. Mater, 283-287 (2000) 291-296

§6. Thermal Creep Mechanism of NIFS-Heat2 Alloys by Using Pressurized Creep Tubes

Fukumoto, K. (Univ. Fukui.),  
Matsui, H., Narui, M. (IMR/Tohoku Univ.),  
Nagasaka, T., Muroga, T.

Vanadium alloys are candidate materials for fusion reactor blanket structural materials because of their potentially high operation temperatures. However the knowledge about mechanical properties of vanadium alloys at high temperatures is limited and there are uncertainties that may have influenced the results such as the interstitial impurity content of specimens. The National Institute for Fusion Science (NIFS), in collaboration with Japanese industry has initiated a program to fabricate a large ingot of highly purified V-4Cr-4Ti alloys [1]. A medium size (~160kg) ingot of V-4Cr-4Ti was fabricated by EB and VAR methods, which was designated as NIFS-Heat2. The impurity level for fabricating large V-Cr-Ti ingots was achieved as ~80wppm C, ~100ppm O, ~120wppm N and 1wppm or less of metallic elements. The objective of this study is to investigate the creep properties and microstructural changes of the high-purified V-4Cr-4Ti alloys, NIFS-HEAT2 by using pressurized creep tubes (PCTs), in order to prepare for in-pile creep tests.

The V-4Cr-4Ti alloy used in this study was produced by NIFS and Taiyo Koko Co. and designated as the NIFS-HEAT2 [1]. Tube processing of NIFS-Heat2 alloys was successfully done by NIFS and Daido Co. and the tube fabrication was done by JAEA and IMR/Tohoku Univ. The final heat treatment of PCTs was done at 1000°C for 2 hrs in vacuum of <1x10<sup>-4</sup> Pa. The detailed tubing process and fabrication process of pressurized creep tubes have been reported in the ref [2]. The PCTs wrapped with Ta and Zr foils were enclosed in a quartz tube in vacuum. Thermal creep tests were done in Univ. of Fukui using the sealed quartz tubes in Muffle furnace at 600, 700, 750, 800 and 850°C. Dimensional changes of PCTs were measured with a precision laser profilometer at five axial and 18 azimuthal locations to an accuracy of 1µm for the outer diameter measurement.

The incursion of impurities in PCTs was not accepted by a result of analysis of chemical composition before and after creep tests. The result of chemical analysis is shown in table 1.

Table1. Chemical analysis before and after creep test.

Condition	Oxygen conc. (wppm)	Nitrogen conc. (wppm)
Pre-creep test	370	80
850°C, 150MPa 50hrs	330	110
750°C, 150MPa 660hrs (Ex.3times)	270	110

From the results of dimensional changes, the activation energy of creep deformation in the NIFS-Heat2 alloys was about 210kJ/mol. This amount of creep activation energy of PCTs is very similar to that of uniaxial creep specimens of NIFS-Heat1 alloys in the previous study [3]. The absolute value of creep strain rate of PCTs is several times larger than that of uniaxial specimens. On the powerlaw dependence of secondary creep rate on stress,  $d\varepsilon/dt = A\sigma^n$ , where  $\varepsilon$  is creep strain,  $A$  is constant and  $\sigma$  is creep effective stress,  $n=4.9$  in this study is good agreement with the value of creep stress exponent of  $n=4$  in a review of thermal creep for V-4Cr-4Ti by Kurtz [3]. This result also suggests that creep mechanism appears to be climb-assisted dislocation motion and the idea is supported by the result of microstructural analysis. From the results of this study, the database of thermal creep behavior is established as the reference for irradiation creep behavior that will be obtained in the future plan.

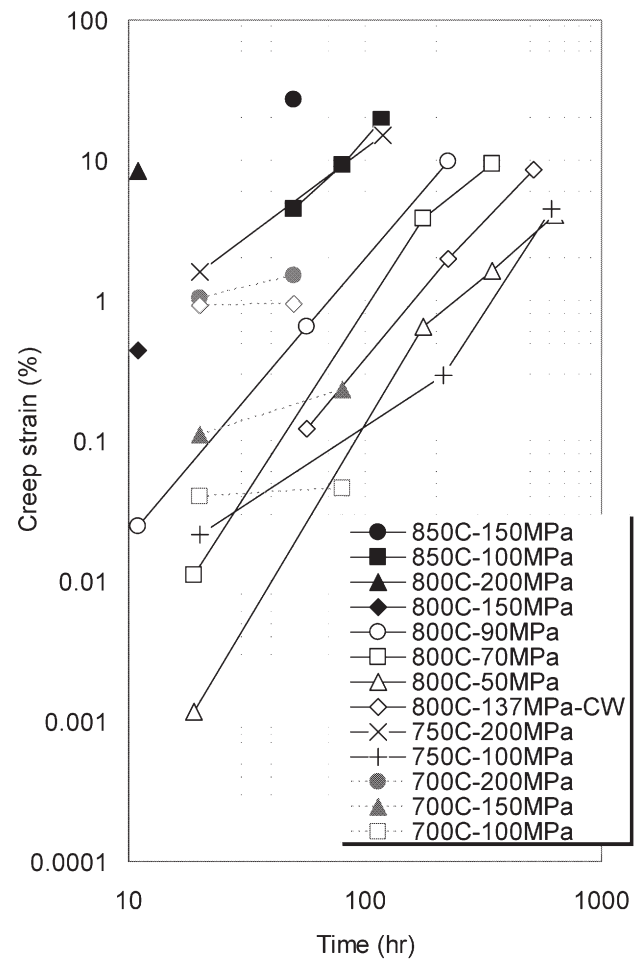


Fig. 1. Time dependence of creep strain rate in temperature from 700°C to 800°C examined by using PCTs

Reference

- 1) Muroga, T., et al., J. Nucl. Mater. 283-287 (2000) 711
- 2) Fukumoto, K., et al., J. Nucl. Mater. 335 (2004) 103
- 3) Kurtz, R. J., et al., J. Nucl. Mater. 283-287 (2000) 628

## §7. The Microstructure of Laser Welded V-4Cr-4Ti Alloy after Neutron Irradiation

Watanabe, H., Yamasaki, K., Yoshida, N. (RIAM Kyushu Univ.), Nagasaka, T., Muroga, T.

### 1. Introduction

It is recognized that welding procedure is one of the key technologies for use of V-4Cr-4Ti alloys as a large component [1]. Recently, laser welding technology for the alloys was developed by NIFS (National Institute for Fusion Science) by controlling the flow rate of high purity argon gas [2]. However, quite little is known to the neutron irradiation effect on the weldment. Nagasaka et al. [3] revealed that weld metal showed larger irradiation hardening than that of the base metal after neutron irradiation at 563K. The Irradiation hardening at 563K was mainly controlled by very high density of dislocation loops. But higher irradiation temperature regions, formation of radiation induced Ti(CON) precipitates becomes prominent. Therefore, the present paper summarized the recent progress on microstructural evolution of laser welded V-4Cr-4Ti alloy during neutron irradiation at higher irradiation temperature regions.

### 2. Experimental Procedure

Welded joints used in this study were prepared from high purity V-4Cr-4Ti alloy, which was designated as NIFS-HEAT-2 [1]. Before the YAG laser welding (bead-on-plate welding) in a high purity argon atmosphere, the samples were annealed in a vacuum at 1273K for 2hr. Oxygen concentrations of the sample before welding, and weld metal are 139 and 158 wt ppm, respectively. The PWHT was carried out in a vacuum of about  $1 \times 10^{-5}$  Pa at 1023K for 1 or 100hr. Fission neutron irradiation was carried out in JMTR under improved temperature control condition at 673, 723 and 873K in the same irradiation cycle (namely, JMTR 03M-69U). The total neutron dose of irradiation was  $5.18 \times 10^{24}/\text{m}^2$  ( $>1.0$  MeV), which corresponds to 0.45 dpa.

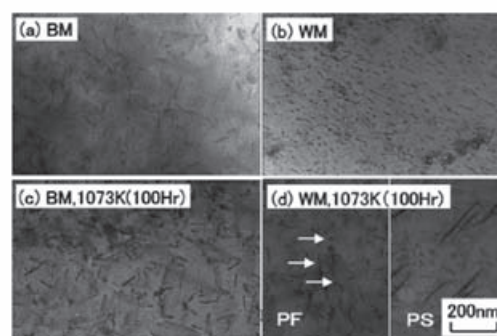
### 3. Results

Microstructure of laser welded NIFS-HEAT-2 was strongly depended on irradiation temperature. Upper part of fig. 1 shows the TEM images of base metal (a) and weld metal (b) after irradiation at 673K, respectively. In the figure, corresponding images of base metal (c) and weld metal (c) with annealed at 1073K for 100 hour are also shown. The figure shows that the radiation enhanced formation of Ti(CON) precipitates with {100} habit planes and dislocations. Ti(CON) precipitates were homogeneously formed in weld metal. In weld metal, number density of Ti(CON) precipitates was higher than that in base metal. Measured number density of precipitates in base metal and weld metal were  $1.4 \times 10^{21}$  and  $4.3 \times 10^{21}/\text{m}^3$ , respectively. And average precipitates size of base metal and weld metal were 43.5 and 17.7 (nm), respectively. From our previous results, tiny Ti(CON) precipitates were heterogeneously

formed in weld metal and segregated during the PWHT at 1073K. Namely, after the annealing, the microstructure of weld metal was divided into two regions, precipitate-segregation (PS) and precipitate-free (PF) areas. As shown in fig.1 (d), after the irradiation at 673K, relatively larger Ti(CON) precipitates were observed in PS area and small precipitates of about 40 (nm) (shown by arrows in the figure) were also observed in PF area of the weld metal. At 873K PS and PF areas were also observed in weld metal without the PWHT at 1073K. With increasing irradiation temperature, growth of Ti(CON) precipitates became prominent and the precipitate can be easily identified by their habit planes.

### 3. Discussion

And as shown in fig.1, at 673K irradiation, Ti(CON) precipitates were homogeneously formed in weld metal and number density of Ti(CON) precipitates was about three times higher than that of base metal. At temperature above 723K, formation of Ti(CON) precipitates were not formed uniformly. Namely, precipitate – segregation (PS) and precipitate-free (PF) area, which were commonly observed after the PWHT at 1073K, were appeared in weld metal. At 873K, large Ti(CON) precipitates were commonly observed in PF area in weld metal. It is important to note that the absorbed energy of welded sample increased significantly, when microstructure is divided into PS and PF areas. But once, plate like precipitates with typical orientation are formed, the absorbed energy of welded sample drops drastically. Therefore, the effects of PWHT on weld metal, which are useful for unirradiated and lower temperature irradiations, are not effective or very limited at higher irradiation temperatures where plate like Ti(CON) precipitates were formed.



### References

- [1] T. Muroga, T. Nagasaka, K. Abe, V. M. Chernov, H. Matsui D. L. Smith, Z. -Y. Xu and S. J. Zinkle, J. Nucl. Mater. 307-311(2002)547.
- [2] Nam-Jin Heo, T. Nagasaka, T. Muroga, A. Nishimura, K. Sinozaki and H. Watanabe, Fusion Science and Technology, 44(2003)470.
- [3] T. Nagasaka, Nam-Jin Heo, T. Muroga, A. Nishimura, H. Watanabe and K. Sinozaki, J. Nucl. Mater. 329-333 (2004)1539.



## §8. Radiation Resistance and Mechanical Properties of Solution and Dispersion Hardened Vanadium Alloys with Fine Grains of High Purity Matrix

Kurishita, H. (IMR, Tohoku Univ.),  
Sakamoto, T., Kobayashi, S., Nakai, K. (Ehime Univ.),  
Nagasaka, T., Muroga, T., Noda, N.

In order to improve the resistances to both radiation embrittlement and strength decrease at high temperatures in vanadium (V) and its alloys, one of the authors has processed V alloys with very fine grains and dispersed particles of  $Y_2O_3$  and YN by powder metallurgical methods utilizing mechanical alloying (MA) and hot isostatic pressing (HIP). The fabricated alloys were confirmed to exhibit good resistance against neutron irradiation to 0.25 and 0.6 displacement per atom (dpa) at 563 and 873K. In addition, the alloys showed a stable microstructure for annealing up to 1573K and good ductility in the HIPed and annealed state (no plastic working). These features of the alloys are due to a solute oxygen and nitrogen free V matrix phase.

Regarding the high temperature strength, V-(1.7-2.4)Y (in mass%) alloys exhibited higher strengths up to around 1023K than solution hardened V-4Cr-4Ti (Nifs heat-1), however above 1173K the alloys showed lower strengths. The deformation mode of the V-Y alloys changed from a recovery controlling process of a long-range internal stress field to grain boundary sliding. It is thus likely that the lower strength above 1173K was attributed to grain boundary sliding caused by a very fine grain size and much less solution hardening. Our recent studies showed that the high temperature yield strength of V-1.7Y-2.1Ti was appreciably higher than that expected from the grain size dependence of the yield stress of V-1.7Y without Ti addition, especially at 1273K. This strength increase of V-1.7Y-2.1Ti is likely due to solution hardening by Ti. Solution hardening significantly contributes to high temperature strength and is an important mechanism for improvement of the strength. The elucidation of the high temperature deformation behavior of solution hardened V alloys with fine grains and fine dispersoids can be hence considered to provide valuable findings useful for improvement of the high temperature strength.

In this study a 4%Ti added V-2.4%Y alloy with fine grains and dispersoids of (Y, Ti) $_2O_3$ , YN, Ti $_2O_3$  and TiO

was fabricated by MA and HIP processes. For the MA process three mutually perpendicular directions agitation ball milling with vessels and balls made of TZM (Mo-0.5%Ti-0.1%Zr) was performed for 144 ks in a H $_2$  atmosphere. The consolidated body of V-2.3Y-4Ti-3Mo was subjected to XRD, TEM observations and tensile tests at temperatures from 285 to 1273 K at initial strain rates from  $2.5 \times 10^{-5}$  to  $1.0 \times 10^{-1} s^{-1}$  in a vacuum better than  $3 \times 10^{-4}$  Pa. The results were compared with those for V-2.4Y-3.4Mo without Ti addition, which were reported previously. The main results obtained are as follows.

1. V-2.3Y-4Ti-3Mo contains solutes of 3%Ti and 3%Mo and dispersoids of a large amount of (Y, Ti) $_2O_3$  and small amounts of YN, Ti $_2O_3$  and TiO. The average grain size is 620 nm, and the average diameter and number density of the dispersoids are 42 nm and  $1.2 \times 10^{20} m^{-3}$ , respectively. The grain and particle sizes are considerably larger and the number density is much lower than those for V-2.4Y-3Mo. This indicates that Ti has a negative influence on size refinement of the dispersoids probably due to higher diffusivity of Ti than Y and consequently causes a rather sparse distribution of the dispersoids.

2. The yield stress,  $\sigma_y$ , of V-2.3Y-4Ti-3Mo is slightly lower than that of V-2.4Y-3Mo over the test temperature range. The lower yield stress is attributable to a much less number density of the dispersoids. The test temperature dependence of  $\sigma_y$  normalized by the Young's modulus is divided into three regions, I, II and III, where regions II and III can be treated as thermally activated processes.

3. The plastic strain rate dependence of the normalized yield stress in regions II and III is classified in three stages with different stress exponents, suggesting three different deformation controlling mechanisms: the recovery processes of a long range internal stress field associated with dispersed particles (the high-strain-rate region), grain boundary sliding (the medium-strain-rate region) and presumably solute atmosphere dragging (the low-strain-rate region). The transition temperatures between the regions depend strongly on test temperature and tend to shift to higher strain rates with increasing temperature.

4. The occurrence of the low-strain-rate region exhibits a beneficial effect of 4%Ti addition because it favors the suppression of strength decrease due to grain boundary sliding by enhancing the effect of solute atmosphere dragging for V-2.3Y-4Ti-3Mo.

5. The apparent activation energies for deformation in regions II and III are 410 and 420 kJ/mol, respectively. These values are larger than those of interdiffusion of Ti in V (280 kJ/mol) and self-diffusion of V (300 kJ/mol).



## §9. Development of Joint Technique of SiC/SiC Composites

Hinoki, T., Eiza, N. (Institute of Advanced Energy, Kyoto University),  
Muroga, T.

Silicon carbide composites (SiC/SiC) are considered for use in extremely harsh environments at high temperature primarily due to their excellent thermal, mechanical and chemical stability, and the exceptionally low radioactivity following neutron irradiation. In particular, recent improvement in the crystallinity and purity of SiC fibers and improved composite processing have improved physical and mechanical performance under harsh environments<sup>1)</sup>. The novel processing called Nano-powder Infiltration and Transient Eutectic-phase (NITE) Processing has been developed based on the liquid phase sintering (LPS) process modification<sup>2)</sup>. The NITE processing can achieve both the excellent material quality and the low processing cost. The important issues to use the NITE SiC/SiC composites for industry are development of joining technique. Several kinds of joining techniques have been developed for SiC and SiC/SiC using polymer, glass-ceramics and reaction bonding. One of the key for the development is the stability of the joining at application temperature. Using a SiC for joint of SiC or SiC/SiC composites has the advantage at the high temperature due to the no coefficient of thermal expansion (CTE) mismatch. The objective of this work is to develop joint technique for SiC and SiC/SiC composites using the SiC formed by modification of NITE processing.

The substrate material for joining was Hexoloy® SA SiC (sintered  $\alpha$ -SiC) and SiC/SiC composites fabricated by NITE processing. The substrates with dimension 23 mm (long)  $\times$  were machined from plate. The faces with 38 mm (wide)  $\times$  3 mm (thick) of the substrate SiC were joined with the slurry including SiC nano-powder ( $<20\text{nm}$ ) and the sintering additive of  $\text{Al}_2\text{O}_3$ ,  $\text{Y}_2\text{O}_3$ ,  $\text{SiO}_2$ . They were hot-pressed at 1800 °C with the pressure of 15-30 MPa in Ar environment. Butt joint was applied to the SiC bars and 46 mm (long)  $\times$  2.7 mm (wide)  $\times$  3 mm (thick) bars were obtained for mechanical tests. Mechanical properties of the joint were evaluated using the bars by tensile test according to ASTM C1275 and asymmetric four points bend test according to ASTM C1469. For the tensile test, the gauge section was 20 mm-long in the middle of the specimen. The specimens were gripped using a pair of wedge-type grips. The grips were connected to the load train using universal joints to promote self-alignment of the load train during the movement of crosshead and to reduce unwanted bending strains in the specimen. All tests were conducted at a cross-head speed of 0.3 mm/min at ambient temperature. Asymmetric four point flexural test was conducted using the same specimen for the tensile test. Inner span and outer span of the asymmetric four points test were 8 mm and 44 mm, respectively. The microstructure of joining interface and fracture surfaces following mechanical test were

observed by optical microscopy (OM) and field emission scanning electro microscopy (FE-SEM), and analyzed by energy dispersive X-ray spectroscopy (EDS).

Silicon carbide substrates were successfully joined. No concentration of sintering additive and no pores were observed. Both in tensile test and asymmetric four point bend test, the joint processed at optimized condition didn't fail at the joint but at substrates. Although the real strength of the joint was not obtained, the tensile strength and the shear strength were over 250 MPa and over 115 MPa, respectively. The other test method or the notched specimen at the joint is required to evaluate real strength. The joint obtained in this method is sufficiently strong compared with the other joint for SiC or SiC/SiC composites<sup>3)</sup> and further improvement to increase joint strength is not required. The issue for this joint is to evaluate flexibility of process for realization.

SiC/SiC were also joined using the same technique. Figure 1 shows a SEM image of the joined interfaces for NITE-SiC/SiC. No pores were observed like the joint for monolithic SiC. The tensile strength and the shear strength were 166 MPa and 103 MPa, respectively, and sufficiently strong compared with the other joint for SiC or SiC/SiC composites<sup>3)</sup>. However concentration of sintering additive was observed at interface between joint and substrates. The effect of the concentration on the mechanical strength was not obtained. Further improvement to reduce the concentration might be required.

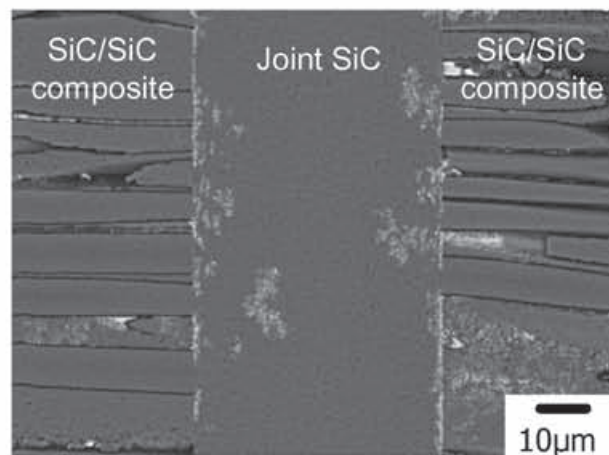


Figure 1: SEM Image of interface of joint for SiC/SiC composites

### References

- 1) Hinoki, T. et al.: J. Nucl. Mater., 307-311 (2002) 1157-1162.
- 2) Kohyama, A. et al.: Ceramic Transactions, 144 (2002) 3-18.
- 3) Katoh, Y. et al.: J. Nucl. Mater., 283-287 (2000) 1262-1266.

§10. Summary of Key Element Technology  
Verification and Preparation for  
Engineering Validation of Intense  
Neutron Source

Matsui, H. (Tohoku U), Sugimoto, M. (JAEA),  
Muroga, T.

The world fusion program is now entering a new phase to construct, operate and exploit the ITER with a programmatic objective to demonstrate the scientific and technological feasibility of fusion energy for peaceful purposes. In anticipation that the ITER will be made operational in a decade and the programmatic objective can be met in the succeeding seven or eight years, the roadmap toward the DEMO can be revisited and R&D elements indispensable for fusion energy utilization can be aligned in the horizon of the ITER schedule. A minimum set of R&D elements essential for fusion energy utilization can be categorized in the following:

- 1) demonstration of technologies essential to a reactor in an integrated system under fusion environments through ITER construction and operation;
- 2) integrated testing of the high-heat-flux and nuclear components required to utilize fusion energy through ITER exploitation; and
- 3) development of structural materials with high irradiation resistance and low neutron-induced activations.

Development of radiation-resistant and low-activation materials is a central R&D issue to realize fusion energy utilization. The world fusion community can now identify candidate materials for the DEMO and extensive R&D efforts have been devoted worldwide to data accumulation and evaluation of the candidates by means of irradiation testing as well as modeling and simulation. In addition, the world fusion community stresses the necessity of an appropriate irradiation test facility, which can adequately simulate the fusion environment and provide qualified data under fusion-relevant neutron irradiation.

To this end, the IFMIF Project has been implemented under the framework of IEA Implementing Agreement of Fusion Materials, and conceptual design and key elements R&Ds have been successfully completed during the period of so-called ‘Key Element Technology Phase (KEP)’. Discussions are in progress on a possible framework and content of technical activities for the succeeding phase, Engineering Validation and Engineering Design Phase (EVEDA), on the basis of the Joint Paper attached to the Joint Declaration by the Negotiators of the six ITER Parties, 28 June 2005. The EVEDA is planned to focus on the detailed engineering design and the associated prototypical component tests with an objective to providing engineering database necessary for making a decision of IFMIF construction.

EVEDA is then nominated as one of the major activities in the framework of Broader Approach agreed by

Japan and EU, with potential participation by other ITER parties.

In the present collaboration, preliminary discussion on the participation of Japanese Universities to EVEDA activities was made, taking into account the infrastructure established during the KEP phase. Efforts were focused on planning the subjects in which Japanese Universities are expected to play leading roles, such as Li Target technology, Test Cell design and optimization and Small Specimen Test Technology.

Also discussed was the consistency of the EVEDA activity with overall road-map for materials/blanket development as shown in Fig. 1.

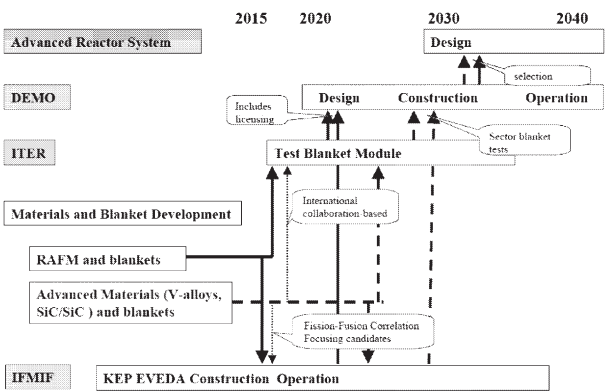


Fig. 1 Roadmap for materials and blanket development discussed in the collaboration

§11. Joining and Heat Load Test of Tungsten Divertor

Tomota, Y., Kurumada, A., Imamura, Y. (Ibaraki Univ.),  
Kurishita, H. (Tohoku Univ.), Noda, N.

Since tungsten materials have high heat resistance, high thermal shock resistance and excellent erosion resistance, they have used for heat resisting structural materials in various fields. From viewpoints of thermal characteristics and plasma particle control, the tungsten materials are particularly expected to be used as an armor tile material of the next divertor plate for the LHD during the steady state and the long pulse operations. In this study, the divertor plate models made of tungsten materials are manufactured to contribute to the development of the plasma facing components having high performances. And the integrity of the divertor model is tested by a deflection-type electron beam heating apparatus.

Tested materials are the stress removal and the re-crystalline processing specimens of the pure tungsten material made by Allied Materials Corp. The re-crystalline processing tungsten material is treated further to the stress removal one for obtaining the grain size from 10 to 20 micron.

Fig.1 shows the joining method of tungsten divertor model. Tungsten specimens of 4 pieces (20x5x5 mm) are joined with an oxygen-free copper block (20x20x20 mm) having a cooling pipe (7 mm in inner diameter, 10 mm in outer diameter and 70 mm in length) after polishing and acetone washing. Titanium and copper foils (0.05 mm in thickness) are inserted for the joining. And an interlayer (20x20x1 mm) of Mo or Ni or Pt is also inserted for the prevention of crack propagation and the relaxation of thermal stresses. The joining specimens are held for 40 minutes at 1000 degrees C in a vacuum of  $1 \times 10^{-4}$  Torr. [1]

In heat load tests, heat fluxes from 0.5 to 15 MW/m<sup>2</sup> are irradiated to the tungsten divertor models by a deflection-type electron beam heating apparatus. The one cycle is 10 seconds irradiation and 15 seconds interval. The speed and the temperature of the water coolant are 15 l/min and 15 degrees C, respectively. And the temperatures of the surface and the joining part are measured by a radiation thermometer and CA thermocouples, respectively. The microstructures are observed by SEM before and after the heat load tests.

Fig.2 shows a photograph near the joining part inserted a interlayer of Pt. Good joining without cracks is observed.

The good joining technique between tungsten and copper materials has been established by inserting the interlayer in this study.

Fig.3 shows the relationship between temperatures of the tungsten divertor model and the heat flux. In this figure, the data of the tungsten divertor model inserted a interlayer of Pt are a little higher than another model without the interlayer, and are lower than the model made of the re-crystalline pure tungsten. One of the reasons is considered that the interlayer has lower thermal conductivity and affects heat resistance. On the other hand, the temperatures of the joining parts are nearly the same because of the good heat transfer.

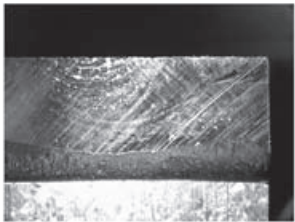
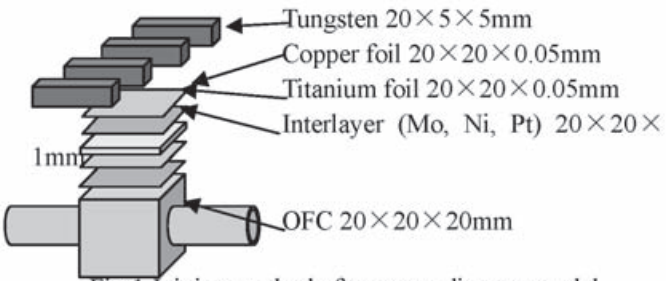


Fig.2 Observation near the joining part with Pt interlayer.

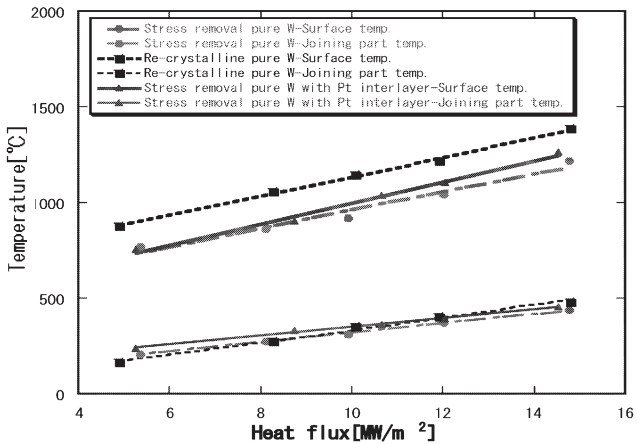


Fig.3 Relationship between temperatures of the tungsten divertor model and the heat flux.

Ref. [1] Suzuki,A., Imamura,Y., Kurumada,A., et al.,  
Extended Abst. of Ibaraki District Conf. (2003.9.19) 55-56.

## §12. Synthetic Evaluation of Ultra-Fine Grained, Nano-Particle Dispersed Tungsten Alloys as Plasma Facing Materials

Kurishita, H. (IMR, Tohoku Univ.),  
Yoshida, N. (RIAM, Kyushu Univ.),  
Tanabe, T. (Kyushu Univ.),  
Noda, N.

A LHD research project entitled "Development and synthetic evaluation of high-Z plasma facing materials" was performed for three years from 2001, by a collaborative group consisting of PSI and materials researchers from universities, NIFS, JAERI and private corporations. After that, research activities related to the project are still being continued by each member of the group, with emphasis on the synthetic evaluation of ultra-fine grained, nano-particle dispersed W-TiC alloys as plasma facing materials. The W-TiC alloys with 0.06~0.2 $\mu$ m in grain size and 99% of relative density were successfully developed in 2004-2005 using modified powder metallurgical fabrication processes and are expected to be very promising as PFM and PFC.

The following meeting was held on March 13, 2006 at NIFS in order to report the main results obtained for the ultra-fine grained W-TiC alloys and discuss the future task. Approximately 15 members got together. After the meeting, a LHD tour was also offered. The program of the meeting was as follows:

13:30-13:35 Opening H. Kurishita (Tohoku Univ.)

### **1. Material Development**

13:35-14:05 Current status of development of ultra-fine grained, nano-particle dispersed W alloy

H. Kurishita, H. Arakawa (Tohoku Univ.), T. Takida,  
M. Kato (A. L. M. T. Corp.)

### **2. Neutron Irradiation Effects**

14:05-14:40 Neutron irradiation effects on microstructural

evolution in ultra-fine grained W-TiC alloy

K. Nakai, S. Kobayashi, Y. Amano (Ehime Univ.),  
H. Kurishita (Tohoku Univ.)

### **3. He Irradiation Effects**

14:40-15:10 Effects of He irradiation on pulsed heat-load damage in W materials

K. Tokunaga, N. Yoshida (Kyushu Univ.)

15:10-15:45 Blister formation in ultra-fine grained W-TiC alloys irradiated with low-energy He ions

H. Iwakiri, T. Baba, N. Yoshida (Kyushu Univ.)

15:45-16:15 Effects of high-energy He ion irradiation on surface damage in various W alloys including ultra-fine grained W-TiC

T. Ogawa, A. Hasegawa, K. Abe (Tohoku Univ.)

### **4. W Coating**

16:15-16:45 Tungsten coating on low activation vanadium alloy by plasma splay process

T. Nagasaka, T. Muroga, N. Noda (NIFS), M. Kawamura,  
H. Ise (Kawasaki Heavy Ind.), H. Kurishita (Tohoku Univ.)

### **5. Proposal of Next LHD Research Project (2006-2009)**

16:45-17:15 Assessment of applicability of advanced W alloys for plasma facing materials

N. Yoshida, K. Tokunaga (Kyushu Univ.)

17:15-17:25 Summary and closing N. Noda (NIFS)

These presentations showed that the ultra-fine grained W-TiC alloys exhibit superior resistance to neutron and He irradiations, demonstrating that significant progress has been achieved towards the use of W-TiC alloys as plasma facing materials. The research outcomes will be succeeded to the next LHD research project entitled "Assessment of applicability of advanced W alloys for plasma facing materials"; the project will be conducted from 2006 to 2009 (Prof. N. Yoshida organizes the project).



### §13. Influence of Heating Rate on Subcooled Flow Boiling Critical Heat Flux in a Short Vertical Tube

Hata, K. (Inst. of Advanced Energy, Kyoto Univ.),  
Shiotsu, M. (Dept. of Eng. Sci. and Tech., Kyoto Univ.), Noda, N.

The influence of heating rate on subcooled flow boiling critical heat flux (CHF) is necessary to investigate the reliability of a divertor in a nuclear fusion facility for short pulse high heat flux test mode. The transient critical heat flux of subcooled water flow boiling for the inner-diameter ( $d=6$  mm), the heated length ( $L=60$  mm) and  $L/d=10$  with the inner surface of rough finished are systematically measured for the dissolved oxygen concentration ( $O_2=5.88$  and  $7.34$  ppm) with the flow velocities ( $u=4.0$  to  $13.3$  m/s), the inlet subcoolings ( $\Delta T_{sub,in}=130$  to  $161$  K), the outlet subcoolings ( $\Delta T_{sub,out}=99.3$  to  $151$  K), the inlet pressure ( $P_{in}=812$  to  $1315$  kPa), the outlet pressure ( $P_{out}=801$  to  $1293$  kPa) and the exponentially increasing heat input ( $Q_0 \exp(t/\tau)$ ,  $\tau=38.1$  ms to  $8.3$  s) [1-3].

#### Transient Critical Heat Flux

The CHF,  $q_{cr,sub}$ , on rough finished inner surface was measured at the outlet pressure of around  $800$  and  $1100$  kPa for the dissolved oxygen concentration,  $O$ , of  $7.34$  and  $5.88$  ppm with the flow velocities of  $4.0$  to  $13.3$  m/s respectively. Figure 1 shows the transient CHF,  $q_{cr,sub}$ , obtained for the exponential periods,  $\tau$ , ranging from  $38.1$  ms to  $8.3$  s for the inlet subcoolings,  $\Delta T_{sub,in}$ , of around  $145$  at  $P_{out}=800$  kPa. The exponential period represents the  $e$ -fold ( $2.71828$ -fold) time of heat input. As shown in figure, the  $q_{cr,sub}$  at a fixed flow velocity is almost constant for the periods from  $800$  ms to  $8.3$  s and it becomes higher with the decrease in period from around  $800$  ms. The CHF become higher with an increase in flow velocity at a fixed exponential period.

#### Influence of Heating Rate

The experimental results for the ratios of the difference between the transient CHF,  $q_{cr,sub}$ , and the steady state ones,  $q_{cr,sub,st}$  to the  $q_{cr,sub,st}$  are shown versus non-dimensional period,  $\tau u / \{\sigma/g(\rho_l - \rho_g)\}^{0.5}$ , at the outlet pressure of around  $800$  with the flow velocity ranging from  $4.0$  to  $13.3$  m/s in Fig. 2. The ratios become linearly higher

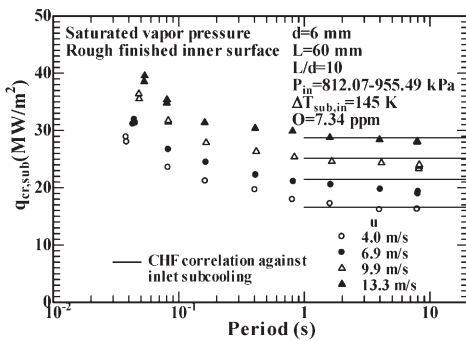


Fig. 1 The  $q_{cr,sub}$  on  $d=6$  mm with RF at  $P_{out}=800$  kPa for  $\tau=38.1$  ms to  $8.3$  s.

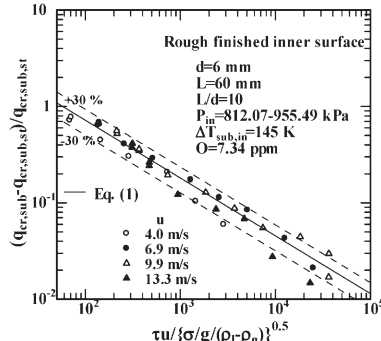


Fig. 2  $(q_{cr,sub} - q_{cr,sub,st}) / q_{cr,sub,st}$  vs  $\tau u / \{\sigma/g(\rho_l - \rho_g)\}^{0.5}$  at  $P_{out}=800$  kPa.

with the decrease in the  $\tau u / \{\sigma/g(\rho_l - \rho_g)\}^{0.5}$ . The slope on the log-log graph kept almost constant about  $-0.6$  with the flow velocity ranging from  $4.0$  to  $13.3$  m/s. These data can be expressed by the following empirical correlation [1-3].

$$\frac{q_{cr,sub} - q_{cr,sub,st}}{q_{cr,sub,st}} = 11.4 \left\{ \frac{\tau u}{\sqrt{\sigma/g(\rho_l - \rho_g)}} \right\}^{-0.6} \quad (1)$$

The correlation can almost describe the CHF data (108 points) for the inner diameter of  $6$  mm at the outlet pressure of around  $800$  and  $1100$  kPa obtained in this work within  $30\%$  difference for  $130 \text{ K} \leq \Delta T_{sub,in} \leq 161 \text{ K}$  as shown in Fig. 2.

#### Transient CHF Correlation

The ratios of transient CHF data for wide exponential period (108 points) to the corresponding values calculated by the steady state CHF correlation against inlet subcooling are almost constant for the  $\tau u / \{\sigma/g(\rho_l - \rho_g)\}^{0.5}$  greater than around  $1500$  and equivalent to unity, and it becomes higher with the decrease in non-dimensional period from around  $1500$ . And the values of the transient CHF almost become two times as large as the steady state ones at the non-dimensional period of  $57.8$ . The transient CHF correlation against inlet subcooling for wide exponentially increasing heat input ( $Q_0 \exp(t/\tau)$ ,  $\tau=38.1$  ms to  $8.3$  s) is derived as follows based on the effect of the non-dimensional period clarified in this work [1-3].

$$Bo = C_1 \left\{ \frac{d}{\sqrt{\sigma/g(\rho_l - \rho_g)}} \right\}^{-0.1} We^{-0.3} \left( \frac{L}{d} \right)^{-0.1} e^{-\frac{(L/d)}{C_2 Re^{0.4}}} Sc^{*C_3} \times \left[ 1 + 11.4 \left\{ \frac{\tau u}{\sqrt{\sigma/g(\rho_l - \rho_g)}} \right\}^{-0.6} \right] \quad \text{for inlet subcooling } (\Delta T_{sub,in} \geq 40 \text{ K}) \quad (2)$$

where,  $C_1=0.082$ ,  $C_2=0.53$  and  $C_3=0.7$  for  $L/d \leq$  around  $40$  and  $C_1=0.092$ ,  $C_2=0.85$  and  $C_3=0.9$  for  $L/d >$  around  $40$ . The ratios of transient CHF data for wide exponential period (108 points) to the corresponding values calculated by the transient CHF correlation against inlet subcooling, Eq. (2), are shown versus the non-dimensional period,  $\tau u / \{\sigma/g(\rho_l - \rho_g)\}^{0.5}$ , in Fig. 3. Most of the data for increasing heat input ( $Q_0 \exp(t/\tau)$ ,  $\tau=38.1$  ms to  $8.3$  s) are within  $15\%$  difference of Eq. (2).

#### Reference

- 1) Hata, K., et al., Paper No. ICONE13-50307, (2005) 1
- 2) Hata, K., et al., Paper No. NURETH11-281, (2005) 1
- 3) Hata, K., et al., *JSME Int. J. Series B* **49**, (2006) 309

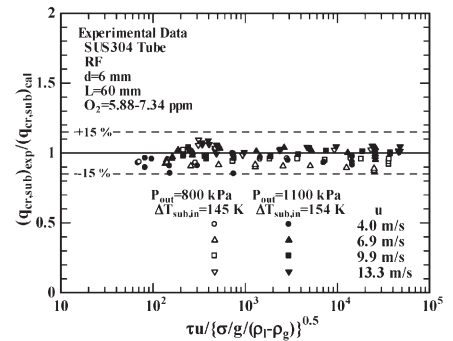


Fig. 3 Ratios of CHF data to Eq. (2) vs  $\tau u / \{\sigma/g(\rho_l - \rho_g)\}^{0.5}$  at  $P_{out}=800$ - $1100$  kPa.

## §14. Basic Study on Self-Healing of $\text{Er}_2\text{O}_3$ Coating for Vanadium-Lithium Blanket System

Terai, T., Suzuki, A., Chikada, T. (The University of Tokyo), Yao, Z., Muroga, T.

A self-cooled liquid lithium/vanadium-alloy blanket system is attractive from the viewpoint of energetic conversion efficiency and tritium breeding ratio. One of the critical issues involved in this system is magneto-hydrodynamics (MHD) pressure drop, which is induced by liquid metal flowing across strong magnetic fields. In order to reduce MHD pressure drop to acceptable levels, fabrication of thin insulating coatings at inner wall of duct tubing has been proposed. In the previous studies, erbium oxide ( $\text{Er}_2\text{O}_3$ ) was selected as one of the best candidate oxide materials for the MHD coating from the point of view of compatibility with lithium [1]. And recently  $\text{Er}_2\text{O}_3$  coatings fabricated by PVD method showed high electrical resistance and high compatibility with liquid lithium [2]. In-situ formation of  $\text{Er}_2\text{O}_3$  coatings was also explored to show that oxygen in the V-alloy substrate and Er dissolved in lithium could react to form thin  $\text{Er}_2\text{O}_3$  layer at the interface [3]. In this report, feasibility of self-healing of  $\text{Er}_2\text{O}_3$  coating is explored by observing its in-situ formation at cracks on the coatings fabricated by PVD method as indicated in Fig. 1.

V-4Cr-4Ti substrates were oxidized at 973 K for 6-12 h in flowing argon (99.9999% purity;  $\text{O}_2 < 1\text{ppm}$ ) and mass of each sample increased at 4000-6000 ppm-O. Subsequently, oxidized substrates were annealed in vacuum (about  $10^{-5}$  Pa) at 973 K for 16 h to homogenize oxygen into bulk and mass change was not occurred. Then  $\text{Er}_2\text{O}_3$  coatings were deposited on these substrates at room temperature (R.T.) and 873 K. The coatings deposited at 873 K had peeled off at most area. On the contrary, the coatings deposited at R.T. were uniformly flat. After introducing cracks on  $\text{Er}_2\text{O}_3$  coatings by heating at 773 K for 50-100 h in argon, the samples were exposed in liquid lithium doped with Er at 873-973 K for 100-200 h to heal the cracks. At the large peeled-off area, no in-situ formation was observed, while small cracks were healed. If oxygen had remained in the substrates,  $\text{Er}_2\text{O}_3$  would have generated under coating deposited by PVD method and peeled off. Therefore, there is a high possibility that the substrates have lost oxygen when coating had been peeled off.

To ascertain mechanism of peel-off and healing, depth profiles of elements in  $\text{Er}_2\text{O}_3$  coatings were analyzed by X-ray photoelectron spectroscopy (XPS) with Ar sputtering. As shown in Fig. 2, Er and O drastically and V increased near the surface in case of the sample deposited at R.T.. In contrast, those of samples deposited at 873 K and heated after deposition at R.T. showed gradual decrease of Er and O and gradual increase of V. These indicated heating during or after deposition contributed to form Er-V-O intermediate layer between the coating and the substrate. It was suggested Er-V-O layer were formed by taking oxygen from substrate in case of oxidized substrates as well. It is considered

Er-V-O layer itself has been peeled off and substrate without oxygen was remained on the surface, and therefore in-situ formation had not been observed at peeled-off area. At the small cracks which have healed, it is considered the oxygen was supplied from Er-V-O layer from the remained coatings at surroundings as indicated in Fig. 3. Thus, oxygen supply in the system, especially Er-V-O layer, is a key investigation point to control the healing of cracks on  $\text{Er}_2\text{O}_3$  coating at Li/V-alloy blanket.

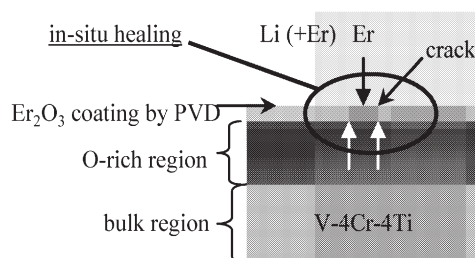


Fig. 1 The scheme of self-healing coating.

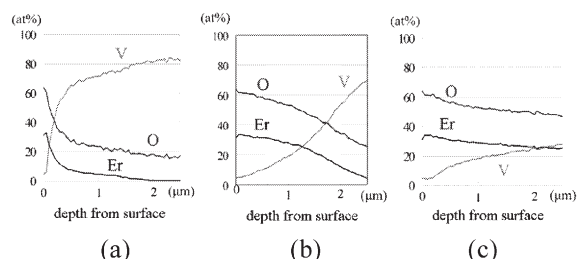


Fig. 2 Depth profiles of elements by XPS deposited by arc source plasma assisted deposition. (a) deposited at R.T. (b) deposited at 973K (c) annealed for 3h at 873K after deposition

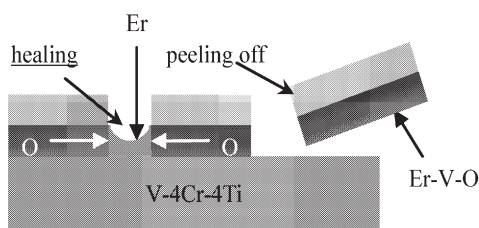


Fig. 3 Process of healing cracks and peeling V-Er-O layer.

### References

- [1] B. A. Pint, *et al.*, *J. Nucl. Mater.*, 329-333 (2004) 119-124.
- [2] A. Sawada, *et al.*, *Fusion Eng. Design*, 75-79 (2005) 737-740.
- [3] Z. Yao, *et al.*, *J. Nucl. Mater.*, 329-333 (2004) 1414-1418.

## §15. Investigation of Issues in Neutronics Evaluations for Advanced Liquid Blanket Systems

Iida, T., Murata, I., Kondo, K. (Osaka Univ.),  
Tanaka, T., Muroga, T., Sagara, A.,  
Sato, S., Ochiai, K., Nishitani, T. (JAEA)

The purpose of the present study is to investigate issues in neutronics evaluations for the Flibe-cooled and Li-cooled blanket systems. Benchmark experiments at the FNS (Fusion Neutronics Source) facility of JAEA have been also considered to verify the accuracy of the evaluations performed with neutron transport calculation system. Most of the benchmark experiments with the DT neutron source have been focused on a single material or features of solid breeder blanket systems. A proposal of the benchmark featuring the advanced liquid blanket systems has been discussed especially on the basis of the blanket design for the helical-type reactor FFHR2.

The neutronics performances of the advanced blanket systems in the FFHR2 have been evaluated with 3-D neutron transport calculations on the helical configuration. The results of the evaluations indicated that both of the Flibe-cooled and Li-cooled blanket systems would achieve sufficient tritium breeding and shielding performance. As to the benchmark for the Flibe breeder/coolant, it is difficult to obtain the sufficient amount of Flibe for the experiment at present. In contrast, Li breeder/coolant consists of the single element and the FNS facility stores a large number of small solid Li blocks for benchmark experiments. The blocks are canned in thin stainless steel cases. Therefore, investigation of the benchmark experiment has been started for verification of the neutronics performance in the Li-cooled blanket system.

Figures 1 (a) and (b) show the structure of the Li/Vanadium-alloy blanket system and the distribution of tritium production rate (TPR) in the Li breeding layer calculated with the neutron transport code MCNP-4C and the nuclear data library JENDL-3.2, respectively. Results for the geometries without the vanadium-alloy structures and the shielding layer are also plotted to examine their impact on the tritium production. Comparison of the TPRs indicates that the vanadium-alloy structures significantly enhance the tritium production around the first wall through the  $(n, 2n)$  reaction. The shielding layer also enhances the tritium production at backside through the reflection of neutrons. In the benchmark experiment on the tritium breeding of the Li-cooled blanket system, the neutron transport in the vanadium-alloy structures including the  $(n, 2n)$  reaction and its impact on the tritium production are important factors to be verified in addition to those in the Li breeding layer and the shielding layer.

Based on the investigation described above, benchmark experiments at the FNS facility have been planned for the verification of the neutron transport and tritium production in the Li-cooled blanket system, a mock-up constructed with solid Li and vanadium blocks as shown in Fig. 2. Measurement methods and procedures for

the verification have been discussed. The experiment is planned to start with activation detectors and to expand to tritium production measurement with  $\text{Li}_2\text{TiO}_3$  pellets, neutron spectrum measurement with scintillation detectors etc. The neutron shielding performance of the Li-cooled blanket system is also an important factor to be verified with the mock-up.

As to activation properties of the materials for the advanced liquid blanket systems, which are important from the safety aspect, DT neutron irradiations have been performed on foils of teflon (for fluorine in Flibe), vanadium-alloy NIFS-HEAT2 (Structural material) and metal erbium ( $\text{Er}_2\text{O}_3$  electrical insulator) in this year. The accuracy of activation calculation system has been evaluated for eight radioactive nuclides by comparison with the radioactivities obtained from gamma-ray measurements after the irradiations. The activation experiment is also planned using the Li mock-up.

Data analysis after the experiments and feedback to the blanket design activity will be discussed in this collaborative study. Investigation of neutronics issues in the Flibe-cooled blanket system also has been continued in parallel for improvement of the blanket design and the future benchmark experiment.

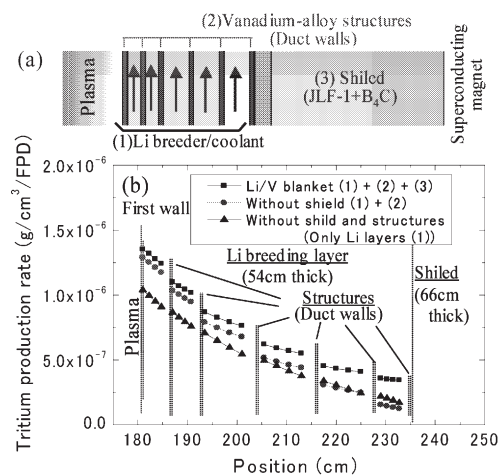


Fig. 1. (a) Structure of Li/V-alloy blanket system. (b) Contribution of structures and shielding layer on tritium production rate.

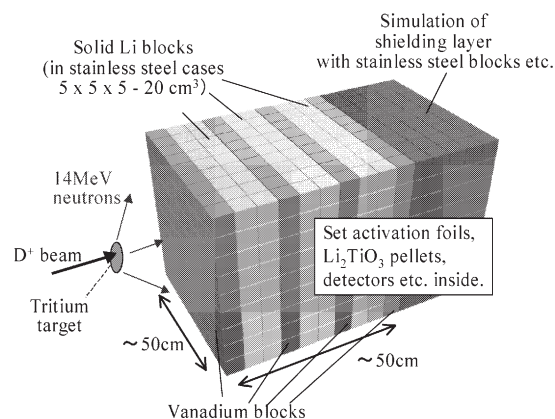


Fig. 2. Tentative drawing of Li mock-up for benchmark experiment for Li-cooled blanket system.



## §16. Examination of Irradiation Damage in Electrical Insulating Coating Using Ion Beam Irradiation

Shikama, T., Tsuchiya, B., Nagata, S., Toh, K. (IMR, Tohoku Univ.),  
Tanaka, T., Muroga, T.,  
Sawada, A., Suzuki, A. (Univ. of Tokyo),  
Sato, F. (Osaka Univ.)

Permanent electrical degradation of ceramic materials due to irradiation damage is called RIED (Radiation Induced Electrical Degradation) and one of concerned issues for the long-term usage in a fusion blanket environment. The candidate ceramic materials of the electrical insulating coating developed for reduction of the MHD pressure drop in the Li/V-alloy blanket system ( $\text{Er}_2\text{O}_3$ ,  $\text{Y}_2\text{O}_3$ ,  $\text{AlN}$  etc.) will be used in the condition of high fluence, high temperature and high electric field where the RIED has been reported in the studies on  $\text{Al}_2\text{O}_3$ . However, almost no data can be found for the irradiation damages on the candidate materials. The purpose of the present study is to examine the irradiation damage in the candidate ceramic coating materials using ion beam irradiation.

While the thickness of the insulating coating in the Li/V-alloy blanket system would be several tens  $\mu\text{m}$ , that of a sample for the in-situ measurement of electrical conductivities under irradiations should be less than several  $\mu\text{m}$  considering the ranges of ion beams injected into the ceramic materials. Although some  $\text{Er}_2\text{O}_3$  samples of  $\sim 1 \mu\text{m}$  in thickness were fabricated on polished stainless steel plates with the RF sputtering method in this year, high insulating performance required for the conductivity measurement could not be obtained due to small pores observed on the coating surfaces. Therefore, in parallel with the effort for improving the coating quality, spectrum measurement of ion beam induced luminescence, which is considered to include the information on the irradiation damages, has been performed for an  $\text{Er}_2\text{O}_3$  coating layer.

A sample of  $\text{Er}_2\text{O}_3$  coating was fabricated on a  $\text{SiO}_2$  plate with the RF sputtering method with the thickness of  $1.5 \mu\text{m}$ . The schematic arrangement of the irradiation is shown in Fig. 1. Visible light spectrum of ion beam induced luminescence in the  $\text{Er}_2\text{O}_3$  layer was measured under irradiation of 100 keV  $\text{H}^+$  beam at room temperature with a spectrometer. The beam flux was  $\sim 5.5 \times 10^{13} \text{ H}^+/\text{cm}^2/\text{s}$ . After the first measurement, 100 keV  $\text{Ar}^+$  beam of  $5.6 \times 10^{16} \text{ ions/cm}^2$  was irradiated. From the second measurement, 100 keV  $\text{H}^+$  beam was irradiated continuously up to the fluence of  $2.2 \times 10^{17} \text{ H}^+/\text{cm}^2$ .

Figure 2 shows the results of the spectrum measurements of ion beam induced luminescence in  $\text{Er}_2\text{O}_3$ . Since the erbium is rare earth and has the suitable properties for light emission, data on luminescence spectra from Er doped in Si substrates and  $\text{Er}_2\text{O}_3$  on Si substrate have been reported in the studies on optoelectronic devices. In the present ion beam irradiation, two peaks were observed in the visible light region as same as the reported cathode

luminescence spectrum [1]. The peaks at  $\sim 560 \text{ nm}$  are corresponding to emissions between the levels of  $^2\text{H}_{11/2} \rightarrow ^4\text{I}_{15/2}$  and/or  $^4\text{S}_{3/2} \rightarrow ^4\text{I}_{15/2}$  and the peaks at  $\sim 650 \text{ nm}$  are corresponding to those between  $^4\text{F}_{9/2} \rightarrow ^4\text{I}_{15/2}$  and/or  $^4\text{F}_{7/2} \rightarrow ^4\text{I}_{13/2}$  as described in literature [1]. During the irradiations, the heights of the peaks around  $\sim 650 \text{ nm}$  has been decreased with the ion fluence, while significant change has not been observed in the peaks around  $\sim 560 \text{ nm}$ .

It is estimated by ion transport calculation using the SRIM code that the irradiation of  $\text{H}^+$  beam of  $2.2 \times 10^{17} \text{ ions/cm}^2$  introduced damage of  $\sim 2 \text{ dpa}$  in the  $\text{Er}_2\text{O}_3$  coating layer, which is depending on the depth from the surface. The information on the mechanism corresponding to the decreasing in the peak heights could be found also in literatures on luminescence studies for optoelectronics devices. It is considered that the measurement of the infrared ( $\sim 1.5 \mu\text{m}$ ) peak emitted from  $\text{Er}^{3+}$  and the temperature dependence of the spectra would be important in the future luminescence experiments to examine the relations with the electrical insulating performance under irradiations.

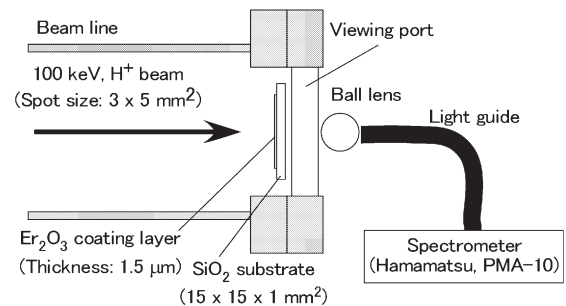


Fig. 1. Schematic arrangement of spectrum measurement of ion beam induced luminescence.

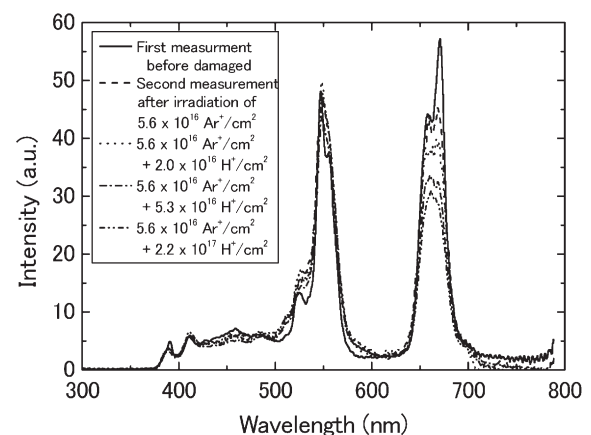


Fig. 2. Visible light spectra of luminescence in  $\text{Er}_2\text{O}_3$  coating layer under 100 keV  $\text{H}^+$  beam irradiation. Peak heights around 650 nm have been decreased with ion fluence.

- [1] E. Nogales *et al.* J. Phys. D: Appl. Phys. 35(2002) 295-298.
- [2] A. Kasuya *et al.*, Appl. Phys. Lett. 71(1997)2728-2730.



# §17. Development of Multi Layer Wall Channel to Reduce MHD Pressure Drop

Hashizume, H., Yuki, K., Satake, M., Kobayashi, T. (Tohoku Univ.),  
Muroga, T., Sagara, A. (NIFS)

When liquid lithium is employed as coolant material in blanket system, it becomes critical to reduce MHD pressure drop. For this purpose, some concepts are proposed where insulating material is coated on the inside wall of metal channel. In these concepts, however, cracking in the insulator layer might become fatal to increase the MHD pressure drop drastically[1]. In order to avoid this fatal failure, three layer wall is proposed where inner thin metal layer protect permeation of lithium into the crack of coated layer. In this concept, structural integrity of the inner thin layer becomes important because shear stress from the liquid metal flow is relatively large. In this study, therefore, a method to coat the insulating ceramic to the thin metal is examined to make the thin metal layer become rigid. Especially, thermal characteristics are examined since the metal layer is very thin like 100μm and then there is some possibility that melting of the metal can occur when the cooling performance is not enough. In order to evaluate the thermal characteristics in terms of gap conductance between the thin metal and heat sink, experimental system as shown in fig.2 is set up to find the suitable experimental condition to keep the good heat conductance. From the experimental results, the heat conductance is improved so much by using Ag or Cu paste. Using these date, numerical analysis is performed to evaluate the metal temperature during the coating. The results indicate that the metal temperature is less than its melting point when the melted Al<sub>2</sub>O<sub>3</sub> of 20μm thickness is coated on the stainless steel of 1mm thickness. Finally, we performed coating experiment using HVOF system, which does not require blasting the meal surface as is used for plasma spray coating. Stainless steel of 100 μm and 1mm is chosen as the base metal and cermet is selected as coating material due to its relatively low melting point. In both cases, penetration or melting of the stainless steel did not occur, while the 0.1 μm stainless steel deformed so much as shown in fig.4 due to plastic deformation introduced by pining effect of the cermet anchored into the steel. This result indicates that we must control this deformation by introducing initial deformation to cancel the pining effect or by heat treatment during the coating process. From the present results, we can say that there is large possibility to develop thin metal layer with ceramic insulator possessing structural integrity. As future works, we must improve the coating method for thicker coating layer of ceramics under controlling the deformation and then examine the structural integrity against the shear stress.

Reference [1] H. Hashizume, Fusion Eng. and Design, 81, 1421-1438(2006)

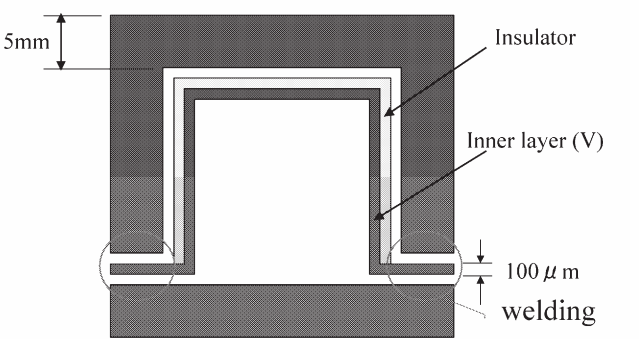


Fig.1 Three layer channel for Lithium

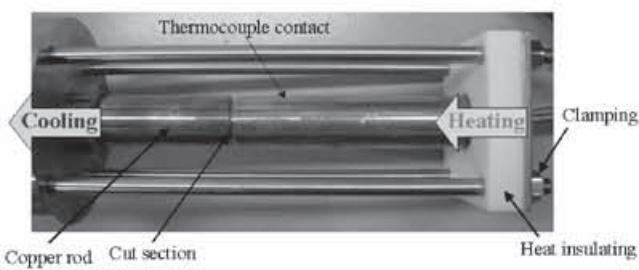


Fig.2 Experimental system to measure heat conductance

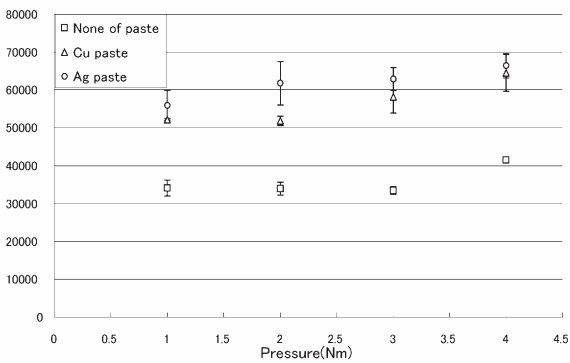


Fig.3 Gap conductance between two metals

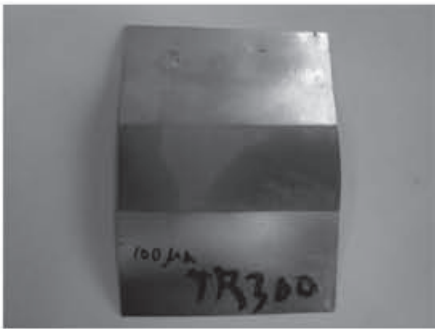


Fig.4 Deformation after coating

## §18. Overall Characterization of High Purity Reference Vanadium Alloys NIFS-HEATs

Satou, M., Hino, T., Abe, K. (Tohoku Univ.),  
Nagasaka, T., Muroga, T.

Vanadium alloy is metallic and nonmagnetic material among the prime candidates for fusion reactor first wall application, yet lack of industrial background that include large-heat productivity and fabricability was weakness from viewpoints of material developments. Successful production of high purity reference vanadium alloys known as NIFS-HEATs alloy demonstrates its capability for large production and provides an opportunity to carry out round-robin tests and full size industrial standard tests. Research activities in each organization were also utilized for overall characterization of the vanadium alloy for fusion applications. Basic physical properties, workability, weldability, interaction with gaseous elements, defects production after irradiation, mechanical properties, compatibility, joining or coating with ceramics materials, etc. were studied. Guideline for the alloy development was discussed in this collaboration study based on individual research results.

Since mechanical properties, that include irradiation properties, of the V-Cr-Ti type alloy depend on interstitial impurity levels, controlling the interstitial elements is a key for the alloy development. Initial impurity levels can be reduced by modification of melting process as NIFS-HEATs. Further modification of the high purity vanadium alloy is possible by means of a small addition of chemically reactive elements such as yttrium. In this report, tensile properties after neutron irradiation of a series of V-4Cr-4Ti-Si-Al-Y alloys are briefly described.

The alloys used in this work were V-4Cr-4Ti-0.1Si-0.1Al-0.1Y alloy and V-4Cr-4Ti-0.1Si-0.1Al-0.3Y alloy (nominal weight percentage) fabricated by a levitation melting method and V-4Cr-4Ti alloy (NIFS-HEAT). Miniaturized tensile specimens annealed at 900 °C for 3.6ks were used. Tensile tests at ambient temperature were carried out using an Instron-type machine with strain rate of  $6.7 \times 10^{-4} \text{ s}^{-1}$  at the Oarai Branch, Institute for Materials Research, Tohoku University. The specimens were irradiated in MNTR capsules with purified sodium bond at JOYO. Irradiation temperature was 450 °C. Neutron fluences were  $2.5 \times 10^{21} \text{ n/cm}^2$  and  $1.1 \times 10^{22} \text{ n/cm}^2$  corresponding to 1.7 and 7.4 dpa (displacements per atom) for vanadium, respectively.

Figure 1 shows typical stress-strain curves of the specimens after irradiation. All of the specimen show fairly good ductility. In case of V-4Cr-4Ti-Si-Al-Y type alloys, the uniform elongation of the specimens irradiated to 1.7 and 7.4 dpa were 15 and 13.8 %, respectively.

The yield stress of the V-4Cr-4Ti-Si-Al-Y type alloys was about 530MPa, while that of the V-4Cr-4Ti alloy was 625MPa at the lower fluence irradiation condition. Work hardening rate of the V-4Cr-4Ti-Si-Al-Y type alloys was larger than that of the V-4Cr-4Ti alloy. The differences probably represent the scavenging effects of the interstitial impurities by small amounts of the additives.

The difference of the yield stress became negligible at the higher fluence condition. The ultimate tensile strength of the V-4Cr-4Ti-0.1Si-0.1Al-0.1Y alloy was the largest 730MPa, while the others were about 700MPa. It is possible that the differences correspond to microstructure evolution during irradiation, such as irradiation enhanced precipitates.

The amount of yttrium contents had the optimum between 0.1 and 0.2 weight percents so far from the Charpy impact properties before neutron irradiation. The present results of the irradiation behavior of the V-Cr-Ti type alloy may lead slightly different optimum composition from previously reported. More detailed examination including the Charpy impact test after neutron irradiation and microstructure observation will soon be carried out.

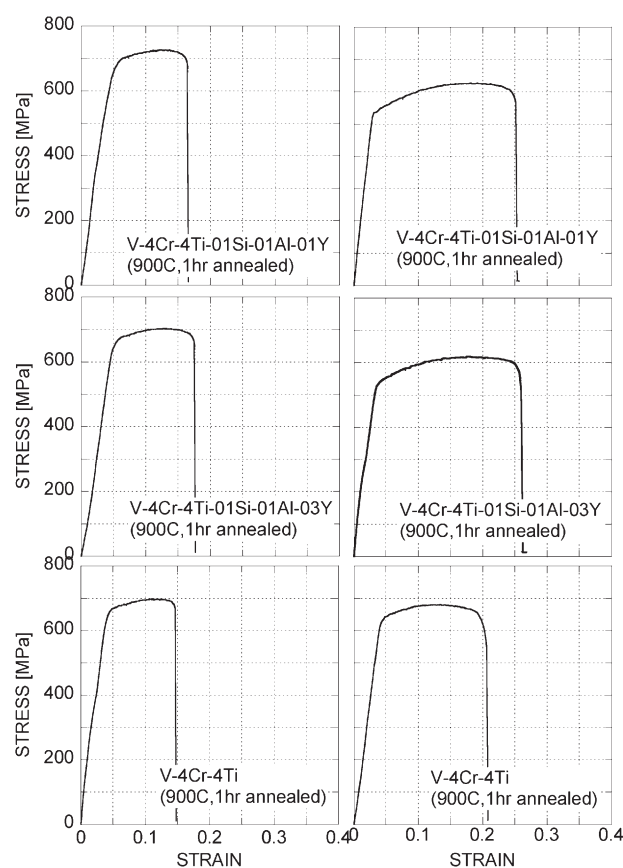


Fig. 1 Typical stress-strain curves for the V-4Cr-4Ti-type alloys after neutron irradiation at 450°C to the fluences of  $1.1 \times 10^{22}$  (left column) and  $2.5 \times 10^{21}$  (right column) ( $\text{n/cm}^2$ ,  $E_n > 0.1 \text{ MeV}$ ).

## §19. Cryogenic Fatigue Delamination Growth in Material Systems for Superconducting Fusion Magnets

Shindo, Y., Horiguchi, K., Narita, F. (Dept. of Mater. Processing, Graduate School of Engineering, Tohoku Univ.), Sanada, K. (Dept. of Mechanical Systems Engineering, Faculty of Engineering, Toyama Prefectural Univ.),  
Nishimura, A., Tamura, H.

### 1. Purpose

Glass fiber reinforced polymer (GFRP) woven laminates are widely used for the insulation of superconducting magnet coils in future fusion reactors. The study of composite laminates actually involves many topics, such as, for example, manufacturing processes, anisotropic elasticity, micromechanics, and fracture and damage mechanics. Delamination is a primary mode for failure of composite laminates. Therefore, the susceptibility of composite laminates to initiation and growth of delaminations must be considered already at the design phase. The resistance to delamination is normally characterized by fracture toughness, and test standards have been developed to measure delamination fracture toughness under various modes of loading at room temperature (RT). However, prediction of initiation and growth of delaminations is complicated and the success of the predictions relies on accurate interlaminar toughness data for the material under both static and fatigue loading and at different environmental conditions. Furthermore, few data are available on composite laminates at low temperatures. This study presents experimental and numerical results on the fatigue delamination growth behavior of GFRP woven laminates at low temperatures<sup>1)</sup>. A previous study<sup>2)</sup> deals with the translaminar crack growth behavior in woven laminates, whereas the present work focuses on research to understand the interlaminar crack growth.

### 2. Procedure

The composite laminate sample was cut into rectangular specimens for double cantilever beam (DCB) testing. All the tests were conducted using a 30 kN axial loading capacity servo-hydraulic testing machine at RT, liquid nitrogen temperature (77 K), and liquid helium temperature (4 K). The constant force amplitude tests were performed in sinusoidal load control at a frequency of 2 Hz and a constant load ratio,  $R = 0.1$ . A scanning electron microscopy was also used in observations of fatigue delamination growth mechanisms for each environment.

A three-dimensional finite element analysis was made, and the  $J$ -integral range was calculated. The failure criteria (Hoffman criterion and maximum strain criterion) were incorporated into the model to study the damage distributions within the DCB specimen.

### 3. Results

(1) Fatigue delamination growth rates of the GFRP woven laminates at low temperatures were much lower than that at RT. The Mode I cyclic fatigue delamination growth rate  $da/dN$  in SL-EC woven laminates is shown in Fig. 1 as a function of the  $J$ -integral range  $\Delta J$  at RT, 77 K and 4 K. (2) The dominant fatigue delamination growth mechanisms were different at RT and low temperatures. At RT, fiber/matrix debonding was the main fracture mechanisms. However, at low temperatures, both fiber/matrix debonding and brittle fracture of matrix were the dominant fatigue delamination growth mechanisms. (3) The finite element method coupled with damage can be used to predict the damage zone within the woven laminates DCB specimen. The cryogenic fatigue delamination behavior is not significantly affected by the damage.

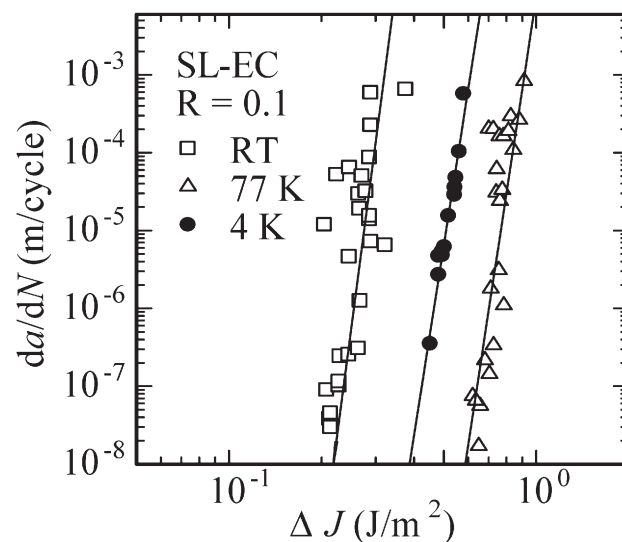


Fig. 1 Cyclic fatigue delamination growth rate in SL-EC woven laminates at RT, 77 K and 4 K (load ratio  $R=0.1$ , frequency 2 Hz).

### References

- 1) Shindo, Y., Inamoto, A., Narita, F. and Horiguchi, K.: Eng. Fract. Mech., in press.
- 2) Shindo, Y., Inamoto, A. and Narita, F., Acta Mater., 53 (2005) 1389.

§20. Thermal and Mechanical Properties of Composite Materials for Superconducting Coils

Takao, T., Nakamura, K., Watanabe, A. (Sophia University)

Decreasing of weight of a large-scale superconducting coil such as the coils for nuclear fusion reactor is one of important issues. For one solution we use high strength and high-thermal-conduction non-metallic composites in the coils. In the study, we proposed those materials and experimentally studied to apply the composites to a structural material in the coil.

The proposed material is the Dyneema fiber reinforced plastic (DFRP). To compare the data a glass fiber reinforced plastic (GFRP), and aluminum nitride (AlN) are also used. An experimental setup is that a short Bi-2223 tape is clamped from both sides of the tape faces by the material. That experimental arrangement is cooled down using a GM refrigerator. In the experiments, liquid nitrogen as a coolant has not been used. At a cryogenic temperature, a constant DC current was applied to the Bi tape, and the voltage and temperature rise of the tape were measured.

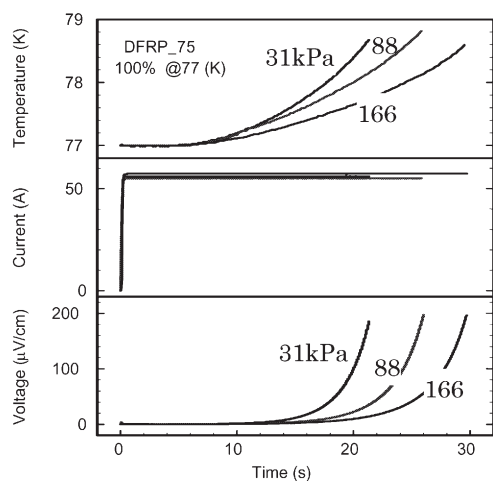


Fig. 1. Dependence of contact stress.

Fig. 1 shows the measured data whose sample material is DFRP. The tape current is approximately 56 A, and the contact stress between the tape and the

composite are 31, 88, and 166 kPa. From the figure, increasing of the stress effectively decreased the temperature rise of the tape.

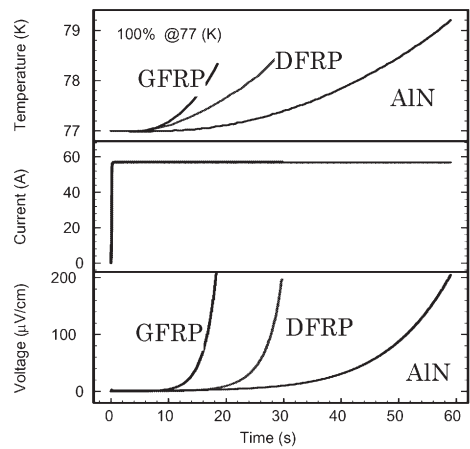


Fig. 2. Comparison of sample materials.

The comparison of the sample materials is shown in Fig. 2. The DFRP was not best in the samples; however the cooling performance increased when a high-thermal-conduction grease was coated on the face of the DFRP (whose data are not shown in the figure). The performance became approximately 10 or 20 percent better than that of the bare DFRP.

From those results, the DFRP's performance does not reach the AlN's performance. But, we think it is possible to apply the DFRP to the coils if the techniques to increase the cooling performance such as increasing of the contact force and coating of the grease and so on are applied.

List of publications and presentations:

- (1) K. Nakamura, T. Takao, A. Nishimura, "Electrical and mechanical properties of strands in superconducting bundle conductors," IEEE Trans. on Applied Super., vol.16, No.2, pp.108-110 (2006).
- (2) T. Takao, A. Watanabe, Y. Iso, K. Nakamura, A. Nishimura, A. Yamanaka, "Heat drain effects from HTS tapes to high thermal conduction plastics for conduction-cooled magnets," presented at EUCAS, Austria, 2005.
- (3) A. Watanabe, K. Nakamura, T. Takao, A. Nishimura, A. Yamanaka, presented at Fall Meeting of Cryogenic Eng., No. 1D-p03, Niigata, 2005.
- (4) T. Takiyama, A. Watanabe, K. Nakamura, T. Takao, A. Yamanaka, A. Nishimura, National convention of IEE-J, No. 5-030, Yokohama, 2006.



§21. Development of V-Ti and V-Ti-Ta Superconducting Wires

Inoue, K. (the University of Tokushima, Department of Energy System, Institute of Technology and Science)

In the practical fusion reactor, superconducting materials will be exposed to heavy neutron irradiation during a long term. Therefore the use of Nb- or Ag-based superconductors for the practical fusion reactor may force us to keep the Nb and Ag in custody for a long term of more than 1000 years in order to reduce their radioactivity below a safety level after the reactor shutdown. For avoiding the radioactivity problem we must avoid the use of Nb and Ag-based superconductors. Then we may not use Nb<sub>3</sub>Sn, Nb<sub>3</sub>Al, Nb-Ti, Bi-2223, and Bi-2212 conductors for the practical fusion reactor, which are the present practical superconductors or the next-generation practical superconductors .

We planned to investigate V-Ti and V-Ti-Ta alloys as the substitution of the Nb-Ti alloy. We can expect the alloys to have the excellent mechanical properties as well as the Nb-Ti alloy. In a practical fusion reactor a huge electromagnetic force will be induced in the superconductors. In addition, after the heavy neutron irradiation, the required enclosing term is about ten years for the alloys.

At first we made arc-melted V-40, 45, 50, 55, 60, 65, and 70at%Ti alloy ingots, from which many rods were cut and cold-rolled into long V-Ti wires with the outer diameter of 3.1 mm by using a grooved-roll. Then these V-Ti alloy wires were cold drawn into the fine wires with the diameter of 0.8 mm by using cassette roller-dies. Finally, the V-Ti alloy wires were flat-rolled into the thin V-Ti tapes with 0.15 mm in thickness and 1.8 mm in width in order to reduce the flux jumps during I<sub>c</sub> measurements.

The effects of α-Ti depositions, with annealing at 573-773 K, were studied for various V-Ti alloys through T<sub>c</sub> measurements, I<sub>c</sub> measurements, and X-ray diffraction patterns. The α-Ti deposition were confirmed through the X-ray diffraction patterns. Moreover, the α-Ti deposition caused J<sub>c</sub> increasing as well as Nb-Ti alloys. The α-Ti particles are very effective pinning centers for the V-Ti alloys. T<sub>c</sub> and I<sub>c</sub> increased with the α-Ti depositions whenever the Ti contents of V-Ti alloy were near 40at%. The maximum T<sub>c</sub> of 7.9 K were obtained for the V-40 to 45at%Ti alloys annealed at 673 K for 5 h, while the maximum B<sub>c2</sub> (4.2 K) of 8.5 T were obtained for the V-50 to 55at%Ti alloys. J<sub>c</sub> (4.2 K, and 6.5 T) of 168 A/mm<sup>2</sup> was obtained for the V-45at%Ti alloy annealed at 723 K for 4 h. The J<sub>c</sub> value is relatively high, considering that we have not yet optimize the V-Ti fabrication process. We are now optimizing the cold-reduction ratio before deposition, the deposition temperature, and heat-treatment duration in order to increase J<sub>c</sub> of V-Ti alloys.

In order to stabilize the V-Ti alloy wire, we also try to

fabricate the V-Ti multifilamentary wire.

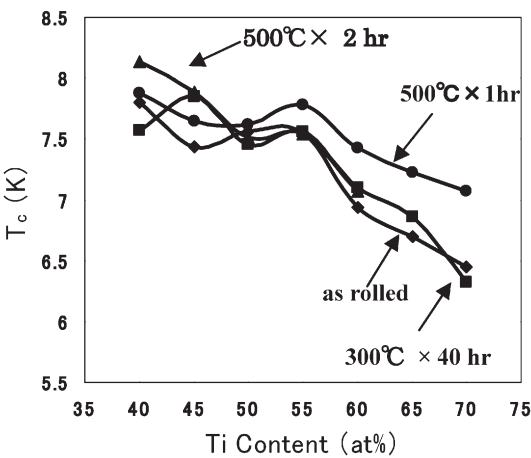


Fig. 1. T<sub>c</sub> dependence on Ti content for V-Ti alloys, heat treated at various conditions.

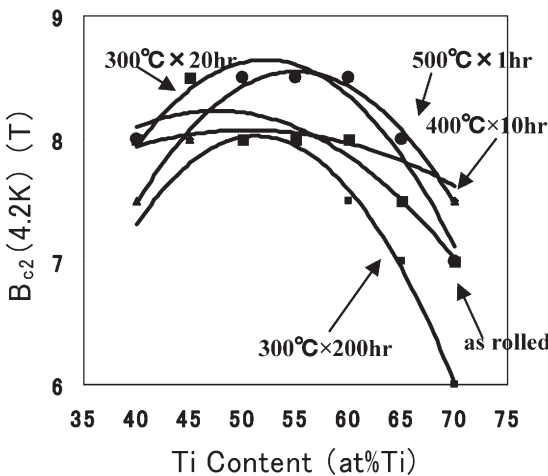


Fig. 2. B<sub>c2</sub> (4.2 K) dependence on Ti content for V-Ti alloys, heat treated at various conditions.

T<sub>c</sub> vs. Ti content curves are shown in Fig. 1 for the V-Ti alloys heat treated at various conditions. These heat treatments were performed after the cold-reduction with 1/15. Excepting the heat treatment at 300°C for 200 hr, T<sub>c</sub> of V-Ti wire increased a little.

B<sub>c2</sub>(4.2 K) vs. Ti content curves are shown in Fig.2. for the V-Ti alloys heat treated at various conditions. Although the heat treatment at 300°C for 200 hr caused much B<sub>c2</sub> degradation, the effect on B<sub>c2</sub> of other heat treatment conditions is not so clear, depending on Ti content.

References:

[1] M. Tai, and S. Okada, “Superconducting properties of V-Ti and Ta-Ti alloys”, Graduation theses of the University of Tokushima, 2005 and 2006.

§22. Development of Low Activation Compound Superconducting Wires for Fusion Reactor

Kikuchi, A., Iijima, Y., Takeuchi, T. (NIMS), Hishinuma, Y., Nishimura, A.

V-based compound superconductors are suitable for applying as a high field conductor for advanced fusion reactors, because they show lower activation compared with those of Nb-based A15 wires. We investigated to develop the V<sub>3</sub>Ga compound which was one of the V-based superconducting materials. The rapidly heating and quenching (RHQ) processing has been applied to various A15 compounds such as Nb<sub>3</sub>Sn, Nb<sub>3</sub>Ga, Nb<sub>3</sub>Ge and Nb<sub>3</sub>(Al,Ge) wires, bcc phase supersaturated solid solution filament like the Nb<sub>3</sub>Al wire can not have been formed in each case. In this study, the RHQ process was applied at the V<sub>3</sub>Ga compound which existed by stabilizing the V-25at%Ga solid solution in the high-temperature region above 1300°C. We focused and observed that the stacking fault was formed in the V<sub>3</sub>Ga phase transformed from supersaturated solid solution as well as Nb<sub>3</sub>Al compound.

V<sub>3</sub>Ga compound was produced to grinding by hands using Arc-melted V<sub>3</sub>Ga compound button. Prepared V<sub>3</sub>Ga compound powder was packed into Nb tube having 20 mm outer diameter and 10 mm inner diameter, and then this composite was cold rolled with a grooved and the wire drawn a diameter of about 2.00 mm through Powder-In-Tube method. This mono-cored wire was cut into short piece, and they were stacked into Nb tube. The number of stacked mono-cored wire was 55 pieces. The stacked composite was cold-rolled with a grooved roller and drawing machine to wire of about 0.74 mm diameter. This composite has good workability without breaking of wire during wire deformation, and average diameter of V<sub>3</sub>Ga filament is about 20μm. This multifilamentary wire was set into RHQ apparatus, and it was applied to the RHQ treatment in a dynamic vacuum chamber with moving at 0.4 m/sec of velocity. Then some of as-RHQ wires were additionally post-annealed at 800 °C for 12 hours in vacuum.

Fig.1 shows that typical  $J_c$  dependence of magnetic field on V<sub>3</sub>Ga/Nb multifilamentary wires.  $J_c$  was defined as the value which divided critical current ( $I_c$ ) by cross sectional area of V<sub>3</sub>Ga filaments.  $J_c$  property of V<sub>3</sub>Ga wire which post-annealed at 800°C for 12 hours was remarkably improved compared with as-RHQ wires under the magnetic field above 10 T. And then,  $H_{c2}$  value was also improved by post-annealing. Figs.2 and 3 show that the typical TEM image of the cross-section on samples before and after post-annealing. We found that the stacking fault was formed in the V<sub>3</sub>Ga bcc phase supersaturated solid solution by RHQ as well as Nb<sub>3</sub>Al compound shown in Fig.2. The grain size of V<sub>3</sub>Ga phase which was transformed from bcc supersaturated solid solution by post-annealing was very small. We thought that the drastic

$J_c$  and  $H_{c2}$  improvement by post-annealing was caused by the small grain size of V<sub>3</sub>Ga phase. We concluded that the applying of RHQ and post-annealing process was effective to form minute V<sub>3</sub>Ga grains.

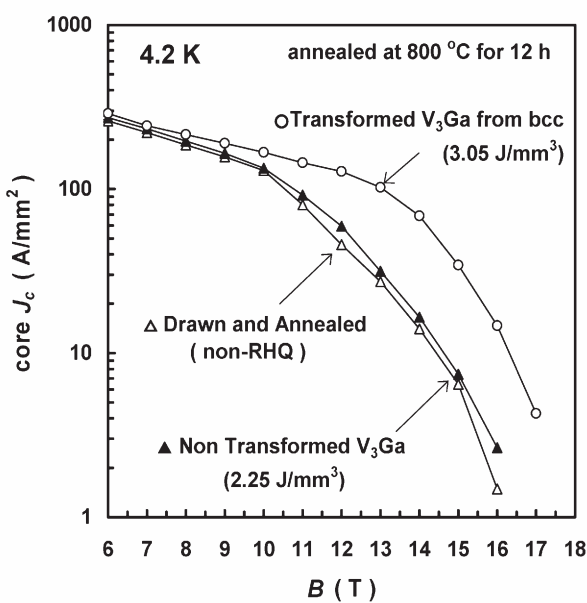


Fig.1  $J_c$  dependence of magnetic field on V<sub>3</sub>Ga PIT multifilamentary wire using rapid-heating/quenching treatment

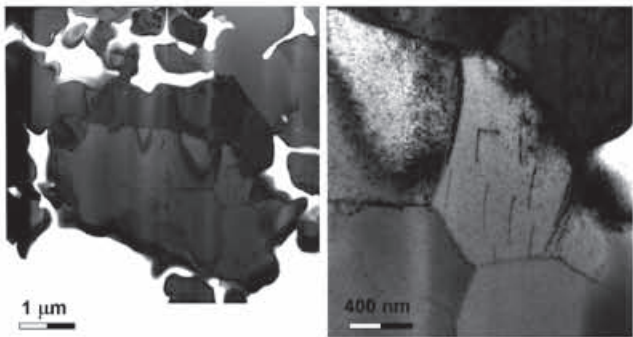


Fig. 2 Typical TEM image on the cross-section of the V<sub>3</sub>Ga/Nb multifilamentary PIT wire after RHQ treatment.

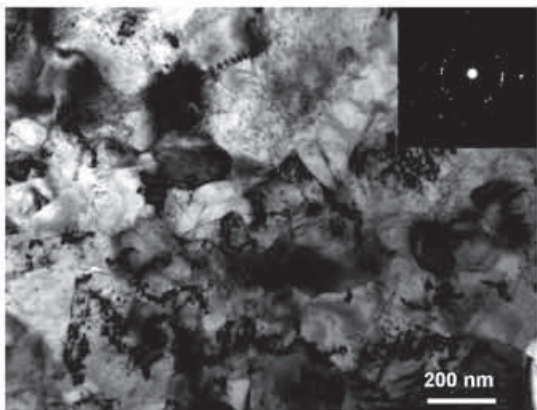


Fig. 3 Typical TEM image on the cross-section of the V<sub>3</sub>Ga/Nb multifilamentary PIT wire after ordering treatment.

### §23. Large-Sized Cylindrical Superconductor Composed with Ni Meshes for a Current Lead

Yoshizawa, S. (Dept. Environmental Sys., Meisei Uni.)

Bi-2223 sintered bulk has a critical temperature ( $T_c$ ) over boiling point of liquid nitrogen 77 K and low thermal conductivity. It has been used as a current lead for the liquid He-free cryocooler-cooled magnet and a current limiter. However, Bi-2223 sintered bulk is fragile because a ceramic material. Ag-plated Ni wire meshes were added into Bi-2223 bulk [1]. By adding metal meshes into the sintered bulk, it can be expected that the mechanical property of the composite is strengthened for the bending stress from various directions. Small-sized cylindrical bulk of Bi-2223/Ni meshes composite, 27 mm in outer diameter, 2 mm in thickness and 50 mm in length, was experimentally prepared last year [2]. It is mentioned that, in preparing a cylindrical composite, the sample with meshes is easy to produce compared with a lot of wires.

This year we prepared large-sized cylindrical Bi-2223 sintered bulk composed with Ag-plated Ni meshes for a prototype of a current lead, 32 mm in outer diameter, 2 mm in thickness and 110 mm in length.

Cylindrical Bi-2223 bulk composed with Ni wire meshes was prepared. The mesh concentration was  $18 \times 18$  meshes/cm<sup>2</sup> using Ni wires of 0.25 mm in diameter. The Ni meshes were plated with Ag by 0.03 mm in thickness. The Ni meshes were centered between vinyl tube and brass rod molds, and calcined powder the constant mass of 100 g was molded using an isostatic cold pressing (CIP) method with two tons. The prepared samples were sintered at 845 °C for 50 hours in air. After treatment again with CIP as an intermediate pressing, the samples were re-sintered. Fig. 1 shows prepared cylindrical sample.

$T_c$  (on-set) values of the both samples without and with the intermediate pressing and resintering process are 108 K. The  $T_c$  (off-set) value of the sample without the intermediate pressing process is at ca. 98 K. By adding the intermediate pressing and resintering process, the  $T_c$  (off-set) values shifts to ca. 101 K. It is observed that there remain two transitions in the magnetization curves. These results suggest that the sample consists of mixture of high and low temperature transition phases, which are supported with the result of XRD patterns of the surface of the sample. It was observed in both samples without and with intermediate pressing and resintering process that (00 $l$ ) peaks of Bi-2223 phase is mainly obtained indicating the  $c$ -axis oriented structure, and there are found some peaks originated from Bi-2212 phase.

$J_c$  values of the cylindrical Bi-2223/Ni meshes composite bulks were studied. The small specimens, 5 mm in width, 22 mm in length and 2 mm in thickness, were cut out from the

cylinder. The  $J_c$  values at 77 K under self-field were measured for the cylinder without and with Ni meshes and for the composite without and with intermediate pressing and resintered. The  $J_c$  values are scattered indicating the cylinder is inhomogeneous. By addition of Ni meshes to the bulk, there are two kinds of state in the samples; one is increase of  $J_c$  and another is low  $J_c$  samples. Then, with the intermediate pressing and resintering process, the tendency is emphasized. It is mentioned that the  $J_c$  values are relatively low because the superconducting phase is mixture of main phase of Bi-2223 and sub phase of Bi-2212.

Cross sectional SEM photographs in the vicinity of interface between the Bi-2223 oxide and Ag-plated Ni meshes in the cylindrical sample were taken. SEM photographs of the higher  $J_c$  samples without and with intermediate pressing and resintering process. There is found dark grey thin layer of ca. 10  $\mu$ m in thickness between Ag layer and Ni metal, which was assigned to NiO by

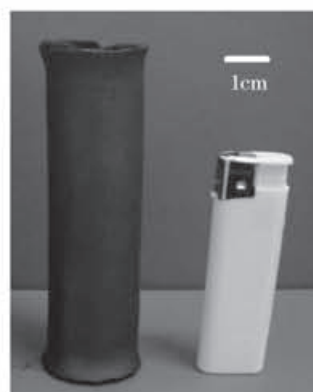


Fig. 1 Prepared large size Bi-2223 bulk composed with meshes

SEM-EDX. The NiO layer should be formed by oxidation of the Ni surface during the heat treatment process. The NiO layer seems not affect the superconductivity of the composite. In the high  $J_c$  samples with the intermediate pressing process, Bi-2223 plate-like grains grow and highly  $c$ -axis oriented and densely structured plate-like grains are formed around the Ag-plated Ni wires. It is mentioned that the  $J_c$  increase of the Bi-2223 bulk by composing with Ni meshes and treating with intermediate pressing process is attributed from formation of the Bi-2223 plate-like grains. In the low  $J_c$  level sample, fine crack lies across Ni wires and small voids leave around Ni wires. It is also suggested that these dislocations cause the inferior superconducting property.

#### References

- 1) S. Hirano, et al.: *Physica C*, 412, (2004) 734.
- 2) S. Yoshizawa, et al.: *J. of Phys.: Conference Series (JPCS)*, 7th EUCAS, 2006. in press
- 3) M. Sakamoto, et al.: *Physica C*, (2006). in press



§24. Effect of Test Equipment Configuration on Interlaminar Shear Fracture and Strength of Glass Fiber Reinforced Plastics

Nishimura, A.

Glass fiber reinforced plastics (GFRP) is an electric insulation material for a superconducting magnet. An epoxy resin type GFRP with glass clothes is commonly used for many magnets and it is well known that the radiation resistance is not strong because of an organic material. The interlaminar shear strength (ILSS) has been investigated to clarify the fracture behaviors of GFRPs and the test procedures have been discussed empirically.

When the radiation effect of GFRPs is investigated, the smaller samples are welcomed because of limited space for irradiation. In addition, it is better to determine ILSS using small number of specimens. Since there is not enough data on the effect of test equipment configuration, the effect of radius of loading and supporting jigs is investigated systematically.

To simplify the research purpose, the test conditions except for the radius were not changed. The ILSS test was performed by a short beam test process (three-point-bending). The specimen configuration was 2.5 mm thick, 10 mm wide and 15 mm long, and the span was 12.5 mm. Stroke rate was 0.75 mm/min and the short beam test was carried out in liquid nitrogen (77 K). The ILSS was obtained by the following equation:  $\sigma_{ILSS} = (3 \times P_B) / (4 \times b \times h)$ , where  $P_B$  is the maximum bending load,  $b$  is specimen width (10 mm) and  $h$  is specimen thickness (2.5 mm).

The radii of the loading and supporting jigs are designated as  $R_l$  and  $R_s$  for the radius of loading jig and that of supporting jig. They were changed from 1 mm to 7 mm by 1 mm. Figure 1 shows the loading and supporting jigs used. The combination of loading and supporting jigs was as follows: (1) Cases that  $R_l$  and  $R_s$  are the same. (2) Cases for supporting jig radius of from 2 mm to 5 mm under constant loading jig radius of 6 mm. (3) Cases for loading jig radius of from 1 mm to 5 mm under constant supporting jig radius of 7 mm.

The results are shown in Fig. 2 and 3. In the case that  $R_l$  and  $R_s$  are the same, round symbols show the bending fracture and square symbols show the interlaminar shear fracture. When the radius is smaller than 5 mm, all specimens showed bending fracture. However, when the radius became larger than 4 mm, the interlaminar shear fracture occurred.

When the radius of loading jig was 6 mm, the interlaminar shear fracture occurred even at the supporting jig radius of 3 mm. When the radius of supporting jig was 7 mm, translaminar fracture was observed smaller loading jig radius which showed that the shear fracture happened on the plane between the loading point and the supporting points. The interlaminar fracture occurred even at the supporting jig

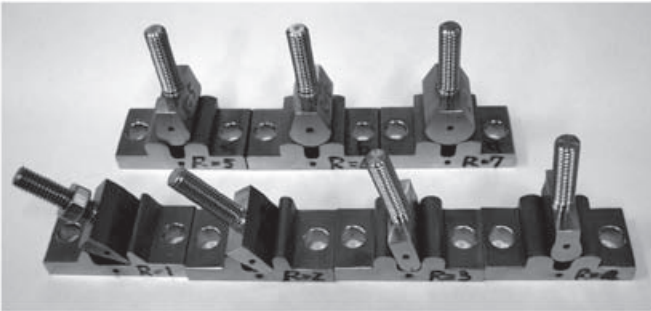


Fig. 1 Loading and supporting jigs for short beam test.

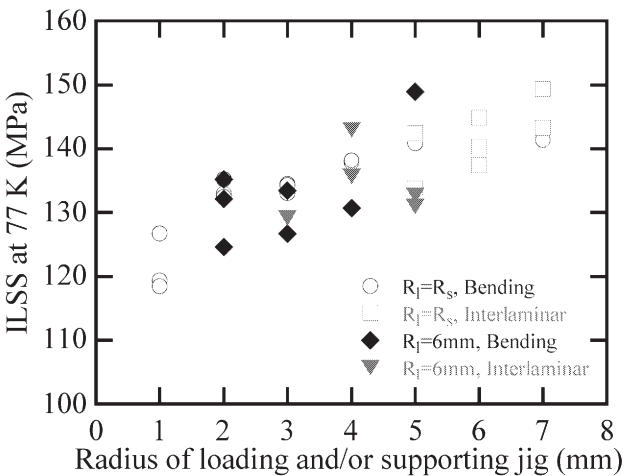


Fig.2 ILSS test results of cases that  $R_l$  and  $R_s$  are the same, and cases for supporting jig radius of from 2 mm to 5 mm under constant loading jig radius of 6 mm.

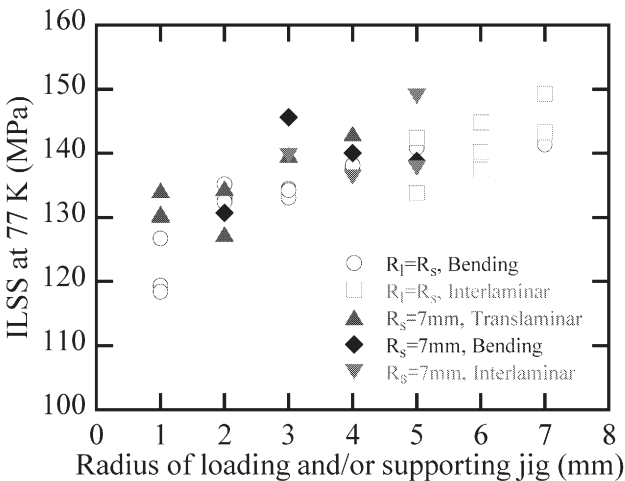


Fig. ILSS test results of cases that  $R_l$  and  $R_s$  are the same, and cases for loading jig radius of from 1 mm to 5 mm under constant supporting jig radius of 7 mm.

radius of 3 mm.

From these results, it would be concluded that larger radius of the loading supporting jigs is better for generating the interlaminar fracture and ILSS will scatter  $\pm 10$  MPa around the average of about 140 MPa. In the case of larger radius supporting jig, the contact points shift to inside resulting in decreasing the span. And the curvature radius becomes larger and local deformation is hard to occur.



## \$25. Transmutation of High-Level Wastes in a FLiBe-Cooled Spherical-Tokamak Reactor

Tanaka, Y. (Nagoya Inst. of Tech.), Nagayama, Y.

In the previous publication [1], transmutation of high-level wastes (HLW) in a water-cooled spherical-tokamak (ST) reactor was discussed. In the following, transmutation of HLW in a FLiBe-cooled ST reactor will be discussed.

We have performed a neutron transport calculation [2] on a model of ST shown in Fig. 1. The model has a cylindrical symmetry with respect to the left side as its symmetry axis. The sizes are given in cm. They are referred to the Aries-ST [3]. The area for transmutation is 414 m<sup>2</sup>, which occupies 63% of the first wall.

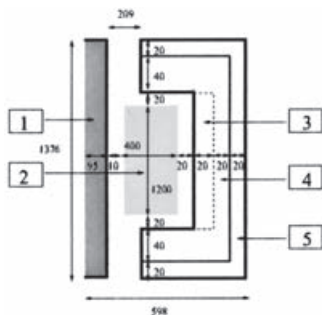


FIG. 1: Model for a ST reactor.

The plasma region is denoted by [2]. The fuel zone [3] is composed of HLW (30vol%), Zr-cladding (10vol%) and  $F_2Li_4Be$  (60vol%). The tritium-breeding zone [4] is composed of  $F_2Li_4Be$  (100vol%). The neutron reflector [5] is composed of natural carbon. The walls and shield are made of Ferritic steel ( $Fe_9Cr_2W$ ).

The loaded spent fuel has the composition taken from Ref. [4]. The reprocessed waste is composed 0.1% of uranium and plutonium isotopes, 100% of the minor actinides and 100% of the fission products of the spent fuel. The resulting waste is concentrated by 50 times in order to restore its normal density.

In a fusion-driven transmuter, a fusion neutron must be bred via the (n,f) and/or (n,2n) reactions because the fusion neutron is spent for both tritium-breeding and nuclear transmutation. In addition, the power of a fusion reactor is inevitably high. The fusion power should not be amplified much by the fission energy. Therefore a fusion-driven transmuter must meet the following criteria; The tritium breeding ratio (TBR) must be greater

than one. A reasonable amount of nuclear transmutation must occur. The (n,f) reaction must be suppressed well.

We found that the reprocessed waste with FLiBe coolant meets these criteria. The FLiBe coolant provides fast neutrons for nuclear transmutation. Fast neutrons are suited to suppress the (n,f) reaction and enhance the (n,2n) reaction. Reprocessed waste also helps to suppress the (n,f) reaction because the major actinides, which are dominant fission energy generators, are involved only a little in the reprocessed waste. However, highly enriched  $^6\text{Li}$  must be used for the FLiBe coolant in order to make the TBR greater than one.

Table I shows reaction rates per fusion neutron and the estimated mass of nuclide in kg transmuted annually by the FLiBe-cooled 1 GW<sub>(th)</sub> ST reactor.

TABLE I: Transmutation of the reprocessed waste in the FLiBe-cooled 1 GW<sub>(th)</sub> ST reactor. The column RWeF denotes the FLiBe coolant composed of 100% enriched <sup>6</sup>Li, while the column RWnF denotes the FLiBe coolant composed of natural Li. The column PWR shows the mass of nuclide in kg produced annually in the 1 GW<sub>(e)</sub> pressurized water reactor [4].

	RWeF		RWnF		PWR
$k_{\text{eff}}$	0.068		0.076		
fission energy (MeV)	6.19		6.84		
number of fissions	0.033		0.037		
number of fission neutrons	0.130		0.141		
number of $^9\text{Be}(n,2n)$	0.084		0.088		
tritium-breeding ratio	1.11		0.67		
	(n,f)	(n, $\gamma$ )	(n,f)	(n, $\gamma$ )	
$^{234}\text{U}$	0.0	0.0	0.0	0.1	6.4
$^{235}\text{U}$	1.4	0.3	4.2	1.5	...
$^{236}\text{U}$	0.2	0.2	0.2	1.0	130.2
$^{238}\text{U}$	23.4	19.2	24.3	102.6	...
$^{237}\text{Np}$	55.8	66.3	60.9	352.3	19.6
$^{238}\text{Pu}$	0.1	0.0	0.1	0.1	6.0
$^{239}\text{Pu}$	1.1	0.2	2.7	1.5	174.6
$^{240}\text{Pu}$	0.2	0.1	0.3	0.4	71.6
$^{241}\text{Pu}$	0.1	0.0	0.2	0.1	11.6
$^{242}\text{Pu}$	0.1	0.0	0.1	0.1	15.1
$^{241}\text{Am}$	95.6	10.3	104.5	59.0	29.8
$^{242\text{m}}\text{Am}$	0.6	0.1	1.8	0.2	0.1
$^{243}\text{Am}$	9.7	3.2	10.9	26.1	3.9
$^{244}\text{Cm}$	1.7	0.5	2.0	3.9	0.5
$^{245}\text{Cm}$	0.5	0.1	1.6	0.3	0.1
$^{93}\text{Zr}$	...	20.0	...	223.2	28.7
$^{99}\text{Tc}$	...	27.0	...	127.7	25.0
$^{129}\text{I}$	...	3.9	...	26.1	6.1
$^{135}\text{Cs}$	...	1.5	...	17.8	13.1
$^{137}\text{Cs}$	...	0.6	...	4.5	21.5

- [1] Y. Tanaka, K. Arita, Y. Nagayama and S. Kiyota, IEEJ Trans. FM, Vol. 125 (2005) 953.
- [2] MCNP4C2, Rsicc Computer Code Collection, Oak Ridge National Laboratory (2000).
- [3] F. Najmabadi and The ARIES Team, Fusion Eng. Design, Vol. 65 (2003) 143.
- [4] DOE/EIS-0250D, U. S. Dept. of Energy, Vol. II (1999) A17.

## (2) Helical Reactor Design

On the basis of physics and engineering results established in the LHD project, the LHD-type D-T demonstration reactors have been studied with collaboration works in wide research areas on fusion science and engineering in the Fusion Research Network in Japan, because there are a lot of common issues to be developed for magnetic fusion energy MFE systems and inertia fusion energy IFE systems. The main purpose is to make clear the key issues required for the core plasma physics and the power plant engineering, by introducing innovative concepts expected to be available in this coming decades.

Activities on international collaborations with US, EU, and China are also increasing in many aspects and wide areas of physics and engineering in order to advance the reactor design studies. Results are presented in many international workshops and conferences.

Due to inherent current-less plasma and intrinsic diverter configuration, helical reactors have attractive advantages, such as steady operation and no dangerous current disruption. In particular, in the LHD-type reactor design, the coil pitch parameter  $\gamma$  of continuous helical winding can be adjusted beneficially to reduce the magnetic hoop force (Force Free Helical Reactor: FFHR) while expanding the blanket space.

Since 1993, collaboration works have made great progress in design studies, which was started as the Phase-I for the concept definition prior to the present-day Phase-II for the concept optimization and the cost estimation. There are two types of reference designs: the large size reactor FFHR-1 ( $l=3$ ,  $m=18$ ) with the major radius  $R$  of 20m and a reduced size reactor of FFHR-2 ( $l=2$ ,  $m=10$ ). The design studies on the compact reactor FFHR2 was reported in the 17<sup>th</sup> IAEA Conference on Fusion Energy in 1998. Design studies on modified FFHR2m1 and 2m2 in the Phase 2 has been reported in the 20<sup>th</sup> IAEA Conference on Fusion Energy in 2004.

These FFHR designs have been studied from both aspects of physics and engineering: MHD equilibrium and stability analysis, alpha-particle confinement analysis, ignition access analysis using the simplest control algorithm, 3-D SC supporting structure analysis, SC magnet system design, advanced blanket and energy transfer system design, and system safety analysis. As for the blanket system, molten-salt Flibe has been selected as

a self-cooling tritium breeder from the main reason of inherent safety.

In this fiscal year, design studies in wide areas of collaboration have been carried out on key issues and important subjects for the system integration of reactor design. (1) Reactor size optimization of FFHR2m1 at a neutron wall loading of about  $1.5\text{MW/m}^2$  for the replacement free long-life STB (Spectral-shifter and Tritium breeder Blanket) blanket concept. (2) Design studies on optimum layout of magnets and supporting structures to reduce the magnetic stored energy under constraints on blanket space and their maintainability for FFHR2m1. (3) Effects of the confinement time scaling during the transient phase on ignition access analyses for FFHR2m designs. (4) Development of a simple system code consisted of engineering design and plasma performance evaluation for sensitivity analysis and designing helical fusion reactor. (5) Design studies of an indirect cooling superconducting magnet for the FFHR large-scale continuous helical winding. (6) Design and evaluation of tritium recovery system for the Flibe blanket concept, using dynamic material balance equations on redox control of TF by Be. (7) Analyses of feasibility and key issues on the gas-turbine energy conversion system in high Pr number fluid blanket, which is very crucial for high thermal efficiency with low tritium permeation. (8) Development of heat transfer enhancement technique in high Pr number fluid blanket, using sphere packed pipes (SPPs) in the molten salt forced-circulation TNT loop (Tohoku-NIFS Thermofluid loop). (9) Studies on heat transfer between pebbles in solid blanket designs (10) 3D DNS (direct numerical simulations) code studies on turbulent MHD flows of molten salt to evaluate the effect of high electrical-conducting wall on heat transfer. (11) Design of electrical power system for FFHR. (12) Studies on vapor shielding effect under ablation of the first wall in laser fusion reactors. (13) Investigation of burning criteria for D-<sup>3</sup>He reactor with zero dimensional analyses under conditions of the ITB mode on temperature and density.

(Sagara, A.)

## §1. Reactor Size Optimization of LHD-Type Reactor FFHR2m

Sagara, A., Imagawa, S.,  
Mitarai, O. (Kyushu Tokai University)

The design parameters of the LHD-type helical reactor FFHR2 are modified to those of FFHR2m, as shown in Table 1 [1]. Figure 1 shows the 3D view of the FFHR2m1. The coil pitch parameter  $\gamma$ , which is defined by  $(m/l)(a_c/R_c)$ , is 1.15 in FFHR2m1 to expand the blanket space and to reduce electromagnetic force, while  $\gamma$  is 1.25 in FFHR2m2 with the inner shift of the plasma center as same as the standard condition in the present LHD. In both cases the major radius  $R$  is increased and the toroidal field  $B_0$  is decreased within  $B_{\max}$  of 13T. Then the blanket space is as wide as 1.2m, resulting in sufficient TBR and nuclear shielding for SC magnets. At the same time the wide maintenance ports are possible due to simplification of coil-supporting structures as shown in Fig.1 under the averaged stress level below 200MPa.

Figure 2 shows the major radius  $R$  dependences of capital cost on reactor construction, helical-coil (HC) supporting mass weight, COE (cost of electricity) and the magnetic field  $B_0$  at the plasma center, which are normalized at the FFHR2 design ( $R = 10\text{m}$ ) under the constraints of an ISS95 enhancement near 1.6 achieved in LHD, the maximum magnetic field  $B_{\max}$  (13-15T) with the current density  $J$  (25-33 A/mm<sup>2</sup>) and the neutron wall loading  $\Gamma$  (1.3-1.5MW/m<sup>2</sup>) limited by the long-life STB blanket concept [1]. With increasing  $R$  (namely FFHR2, FFHR2m1 and FFHR2m2),  $B_0$  can be reduced and COE decreases because of the increase of fusion output as listed in Table 1. On the other hand, the capital cost increases more slowly, because the mass of HC supporting structure increases only in proportion to  $R^{0.4}$  due to the decrease of  $B_0$  [2]. Therefore, a reactor size

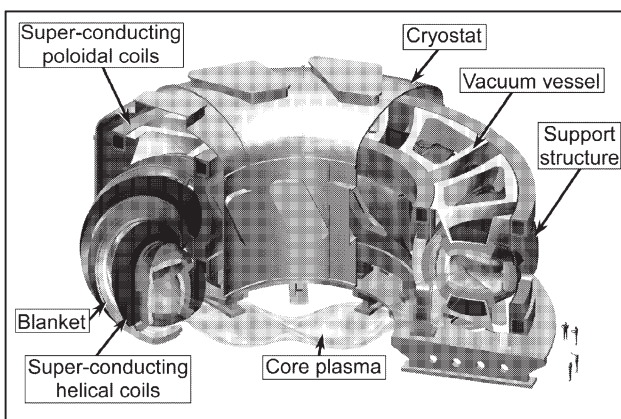


Fig.1. The 3D illustration of the FFHR2m1.

Table 1. Design parameters of helical reactor

Design parameters			LHD	FFHR2	FFHR2m1	FFHR2m2
Polarity	l		2	2	2	2
Field periods	m		10	10	10	10
Coil pitch parameter	$\gamma$		1.25	1.15	1.15	1.25
Coil major Radius	$R_c$	m	3.9	10	14.0	17.3
Coil minor radius	$a_c$	m	0.98	2.3	3.22	4.33
Plasma major radius	$R_p$	m	3.75	10	14.0	16.0
Plasma radius	$a_p$	m	0.61	1.2	1.73	2.80
Blanket space	$\Delta$	m	0.12	0.7	1.2	1.1
Magnetic field	$B_0$	T	4	10	6.18	4.43
Max. field on coils	$B_{\max}$	T	9.2	15	13.3	13.0
Coil current density	j	MA/m <sup>2</sup>	53	25	26.6	32.8
Weight of HC support		ton	400	2880	3020	3210
Magnetic energy		GJ	1.64	147	154	142
Fusion power	$P_F$	GW		1	1.9	3
Neutron wall load	$\Gamma_n$	MW/m <sup>2</sup>		1.5	1.5	1.3
External heating power	$P_{\text{ext}}$	MW		70	80	100
$\alpha$ heating efficiency	$\eta_\alpha$			0.7	0.9	0.9
Density lim.improvement				1	1.5	1.5
H factor of ISS95				2.40	1.92	1.76
Effective ion charge	$Z_{\text{eff}}$			1.40	1.34	1.35
Electron density	$n_e(0)$	10 <sup>19</sup> m <sup>-3</sup>		27.4	26.7	19.0
Temperature	$T_i(0)$	keV		21	15.8	16.1
Plasma beta	$\langle\beta\rangle$	%		1.6	3.0	4.1
Plasma conduction loss	$P_L$	MW			290	463
Diverter heat load	$\Gamma_{\text{div}}$	MW/m <sup>2</sup>			1.6	2.3
Total capital cost		G\$		5.1	5.8	6.6
COE		Yen/kWh		21	13	9.5

around 15m of  $R$  is the present candidate for FFHR designs within those conditions. R&D on SC magnet systems of large scale, high field and high current-density are new challenging targets based on the LHD.

Reference:

- 1) A.Sagara et al., Nuclear Fusion 45 (2005) 258-263.
- 2) S.Imagawa et al., Plasma Science and Technology, 7 (2005) 2626-2628.

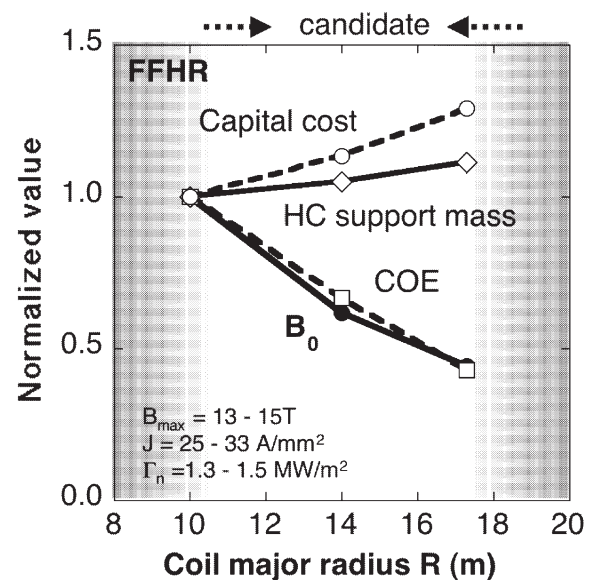


Fig.2 R dependences of the reactor capital cost, helical-coil supporting mass, cost of electricity and magnetic field  $B_0$  at the plasma center, which are normalized at the FFHR2 design ( $R = 10\text{m}$ ).



## §2. Study on Position of Magnets and Supports for Heliotron-type Reactors

Imagawa, S., Sagara, A.

Heliotron-type reactors have attractive advantages for power plants, such as no current-drive, no current-disruptions, and wide ports between helical coils. They are useful to maintain in-vessel components. In comparison with tokamak reactors, a major radius is necessarily large due to a high aspect ratio. According to recent design studies, the major radius of plasma is set to 14 to 18 m in order to install shielding and breeding blankets with total thickness of about 1.2 m [1]. The central toroidal field is 5 to 6 T. Although the major radius is two to three times larger than the design of an advanced tokamak reactor, the magnetic stored energy is comparable. It means that the amount of superconducting wires and necessary supporting structures can be comparable with those of a tokamak reactor. It is important to optimize the layout of magnets and their supporting structures to reduce the total amount. Maintainability of the blankets must be regarded in this optimization.

The magnet system of heliotron-type reactor consists of a pair of continuous helical coils and more than one pair of poloidal coils. The position of the poloidal coils is determined by the dipole magnetic field, the quadruple magnetic field, the stray field, and necessary ports. In the case of one pair of the poloidal coils, the magnetic field around the center is fairly high, and the magnetic stored energy is large. Two pairs of poloidal coils, as shown in Fig.1, are needed to minimize the stored energy and to control the position of plasma against the plasma current. At first, the position of the two pairs of poloidal coils was investigated. In order to produce the required dipole and quadruple field under the condition of low stray field, the position of the outer poloidal coils is restricted by that of the inner poloidal coils. A typical position was selected to diminish the field at the torus center, and supporting structures for the coils were designed, as shown in Fig.2. Wide ports are secured at upper, lower, and outer sides for maintenance of blankets. The supports for hoop forces are contained inside the coils themselves. The upper and lower poloidal coils are linked by thick shell structures with apertures for the ports. The helical coils are fixed to the shell structures at the horizontal position. Preliminary structural analyses were carried out, and the maximum stress intensity was successfully reduced below 1,000 MPa that will be allowable for strengthened stainless steel[1].

In the analysis, the highest stress was induced in the outer shell structure near the cross point of the helical coil and the OV coil. The highest stress will be reduced by shifting the OV coils outwards. Since the stored energy must be reduced to lessen the amount of supports, the effect of the position of poloidal coils on the stored energy was investigated. The larger radius of the IV coil is effective to enlarge the radius of the OV coil with smaller increase of the stored energy. In order to gain the space for blankets of divertor area, larger minor radii of both the IV and OV coils against the plasma center is preferable.

Appropriate radii of IV and OV coils for FFHR2m1 of major radius of 14 m will be about 10 m and 18 m.

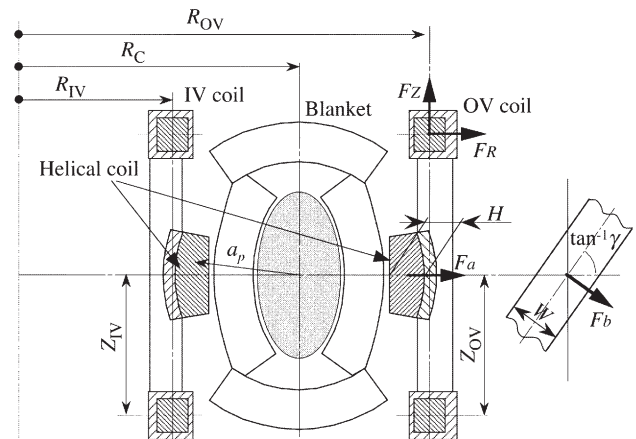


Fig. 1. Magnets and supporting structures of heliotron-type fusion reactor.

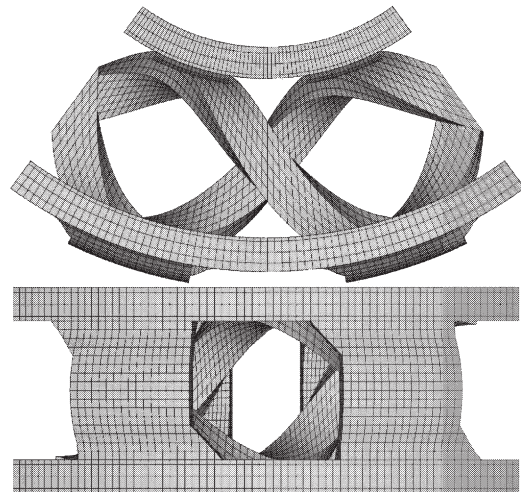


Fig. 2. Concept of supporting structures for magnets of FFHR2m1, where  $R_0 = 14.0$  m,  $B_0 = 6.18$  T, and  $\gamma = 1.15$ ,  $R_{IV} = 9.5$  m,  $R_{OV} = 17.28$  m,  $Z_{IV} = Z_{OV} = 3.6$  m.

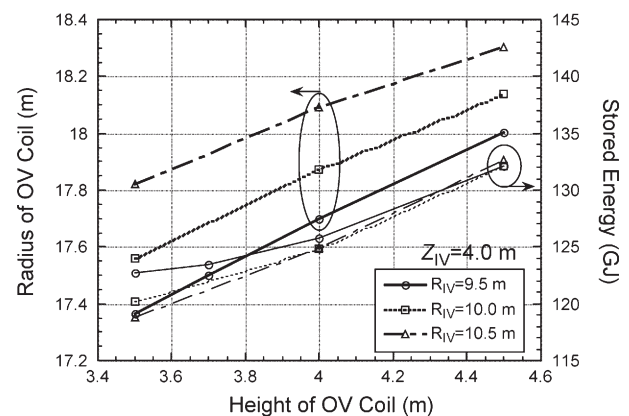


Fig. 3. Position of poloidal coils and the stored energy of FFHR2m1, where  $R_0 = 14.0$  m,  $B_0 = 6.18$  T, and  $\gamma = 1.15$ .

### Reference

1) A. Sagara, S. Imagawa, O. Mitarai, et al., Nuclear Fusion, 45 (2005) pp.258-263.



### §3. Study of the Fusion Power Rise-Up, Steady State, and Shutdown Scenarios in Helical Reactors

Mitarai, O. (Kyushu Tokai University),  
Oda, A. (Yatsushiro National College of Technology),  
Matsumoto, Y. (Hokkaido University),  
Sagara, A., Imagawa, S., Watanabe, T., Watanabe, K.,  
Yamazaki, K., Shimizu, A., Tomita, Y.

When the major radius of the present LHD is scaled up to 14 m with the pitch parameter of  $\gamma=1.15$ , it is possible to meet the minimum requirement for the blanket and shield thickness with 1.2 m. In this report, the fusion power rise-up phase, steady state phase, and shutdown phase are studied in this FFHR2m-1 reactor with the major radius 14 m, the minor radius 1.73m, the magnetic field strength 6.0 T, and the fusion power 1.9 GW.

In the temporal evolution of the plasma parameters where the plasma energy is changed, it is important to take the  $dW/dt$  effect into account in the heating power term in the confinement time scaling. The following question arises; In an actual experiment, the scaling is made in the steady state or at the small  $dW/dt$  value. Can such scaling be used during the transient phase? Recent examination of LHD data has confirmed that such scaling can be used in the transient phase, which is justified by comparing the experimentally determined confinement time and formulated scalings with  $P_{\text{net}}-dW/dt$  [1]. In this report, we study this effect in the fusion power rise-up phase and shutdown phases by comparing the scalings with  $P_{\text{net}}$  and  $P_{\text{net}}-dW/dt$ . We have confirmed that it is better to use the confinement scaling with the plasma conduction loss  $P_L=P_{\text{net}}-dW/dt$ , and the density limit scaling with the net heating power  $P_{\text{net}}$  for the 0-dimensional modeling.

In Fig. 1 is shown the temporal evolution of the plasma parameters in the case of the density limit factor  $\gamma_{\text{SUDO}}=1.5$ , the confinement factor  $\gamma_{\text{ISS}}=1.92(\gamma_{\text{LHD}}=1.2)$ , and 10 % alpha prompt loss. Upon consideration of the discharge initiation by NBI alone, the preprogrammed and step like heating power is applied up to 80 MW, and then the heating power is feedback controlled after 30 sec. The heating power is increased to 100 MW due to the artificial large margin of the density limit (MDNL), and then decreased due to ignition at 100 sec. During the fusion power rise-up phase, the  $dW/dt$  effect is not so large, then the difference with/without it is not so large. The temperature is slightly larger in the case of  $P_L=P_{\text{net}}-dW/dt$ .

The peak density at the steady state is  $2.67 \times 10^{20} \text{ m}^{-3}$ , the density limit is 10% over the operation density, temperature is 15.8 keV, averaged neutron wall loading is

$1.5 \text{ MW/m}^2$ . Beta is 3 % which is already achieved in LHD.

The heating power should be applied during the shutdown phase to keep the density limit higher than the operating density. After shutdown ( $> 250 \text{ s}$ ), discharge behaviors for the confinement scaling for  $P_{\text{net}}$  and  $P_{\text{net}}-dW/dt$  are quite different. For the case of  $P_{\text{net}}$ , the temperature is kept high around 8 keV after shutdown. However, for the experimentally verified case of  $P_{\text{net}}-dW/dt$  in the confinement scaling, the temperature is decreased to a reasonable value as shown in Fig.1-(a) after 250 sec. This is because that  $dW/dt < 0$  provides the larger plasma conduction loss  $P_L$  and hence the smaller confinement time after shutdown.

The bootstrap current of  $\sim 2 \text{ MA}$  is expected in the FFHR2m-1, which should be considered separately for the safe fusion power shutdown.

This work is performed with the support and under the auspices of the NIFS Collaborative Research Program NIFS05KFDH001.

#### References:

- [1] J. Miyazawa FFHR meeting 2005, July.

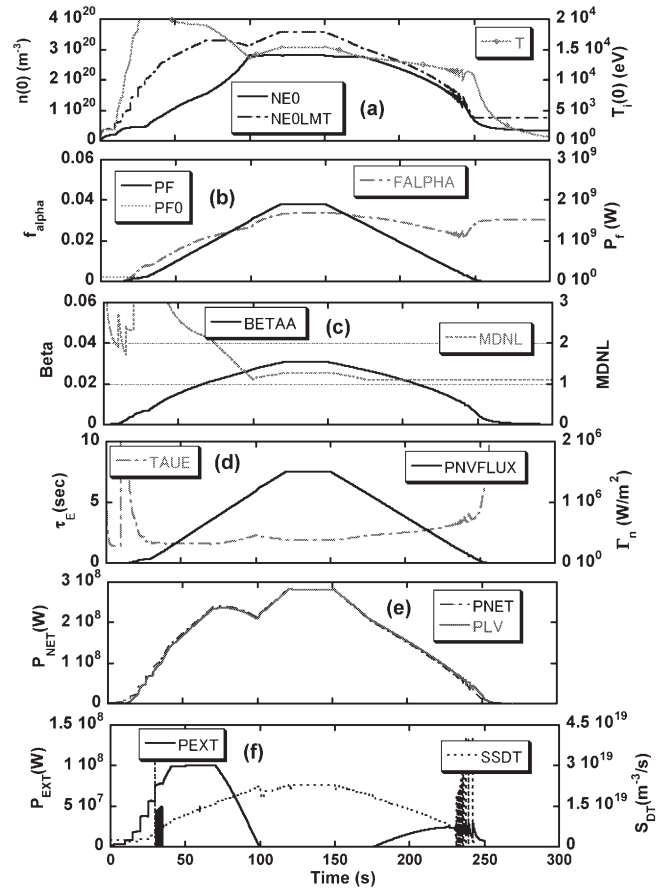


Fig. 1 The temporal evolution of the plasma parameters for the confinement scaling with  $P_{\text{net}}-dW/dt$  in FFHR2m-1.

## §4. Development of a System Code for a Helical Fusion Reactor

Goto, T. (Grad. Sch. Frontier Sci., Univ. of Tokyo),  
Ogawa, Y. (High Temp. Plasma Cntr., Univ. of Tokyo),  
Sagara, A., Imagawa, S., Yamazaki, K.

In order to realize a commercial fusion reactor, optimization of plasma performance from a broad viewpoint is indispensable. Many conceptual designs of a DEMO and a commercial reactor in tokamak system have been carried out through optimization studies through a sensitivity analysis by using simple but comprehensive system codes to take the opportunity of its symmetric nature. In the helical system, such optimization study is difficult due to the flexibility in the coil and plasma design. Helical reactors, however, have the specific feature to be inherently free from several problems by a plasma current, which may lead to the realization of the operation regime that is fundamentally different from that of tokamak. Thus the sensitivity analysis based on the inherent characteristics of helical system is quite important. We therefore have developed a simple system code for designing helical fusion reactor.

The developed system code has two main parts: the engineering design and the plasma performance evaluation. In the engineering design part, the shape of the coil is determined by a radial build scheme (see Fig.1). The consistent design is realized by using the detailed analysis results of heliotron-type reactor<sup>1)</sup> and the stress constraint (here 300 MPa is used). The plasma performance evaluation part, the performance of the designed reactor (i.e., fusion power  $P_{fus}$ , energy confinement time  $\tau_E$ , etc.) is evaluated. Here Sudo density limit<sup>2)</sup> and ISS95 confinement scaling<sup>3)</sup> are used. More detailed description of the system code is found in Ref.4.

In this study, we have tried to design a commercial plant. Thus we carried out a sensitivity analysis and selected design points which have minimum major radius  $R_0$  for a given parameter set with the constraint of  $P_{fus}=3\text{GW}$ . To design a smaller reactor, the increase in fusion power density, which may cause the degradation of confinement, is needed. The calculation shows this problem can be solved by increasing the magnetic field strength  $B_{max}$ . If  $B_{max}>15\text{T}$  is achieved, confinement enhancement factor  $H_{ISS}$  falls within the range of 1.5-2.0 for most design points with aspect ratio  $A_p\sim 5.0$ . The increase of magnetic field strength has a further favorable effect. Figure 2 shows that a high density and low temperature operation (i.e.,  $n_e>4\times 10^{20}\text{m}^{-3}$ ,  $T_e=8\text{keV}$ ) is feasible if the magnetic field strength is increased to greater than 20T. While the operation density of tokamak systems are laying around  $2\times 10^{20}\text{m}^{-3}$  irrespective of magnetic field strength because that the density is limited due to current drive power. If density limit of  $1.4\times n_{sudo}$  is allowed, this operation is possible with further lower magnetic field strength. Such increase in the magnetic field can lead the increase in the reactor weight. However, this effect can be canceled out with the weight decrease by the decrease of reactor size under relatively conservative conditions,  $A_p>5$ ,

$\beta<5\%$ ,  $n_e<n_{sudo}$  and  $P_w<7\text{MW/m}^2$  (see Fig.3).

Consequently, we can conclude that the design of a relatively small size helical commercial reactor which has high density and low temperature operation regime is feasible with the increase in the magnetic field strength. This new operation regime is quite meaningful because it leads the reduction of heat load on the divertor. The experimental research in such new regime is also worthwhile in the viewpoint of the plasma physics study.

This work was performed with the support and under the auspices of the NIFS Collaborative Research Program NIFS (NIFS04KFDF001).

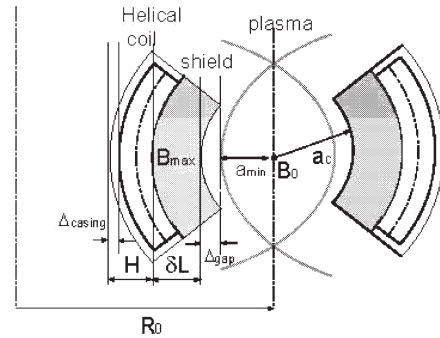


Fig. 1 Cross-section of the designed reactor

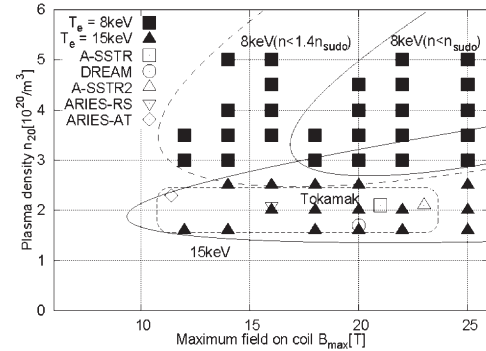


Fig. 2 Operation density  $n_{20}$  vs. magnetic field strength  $B_{max}$  for two temperature regime.

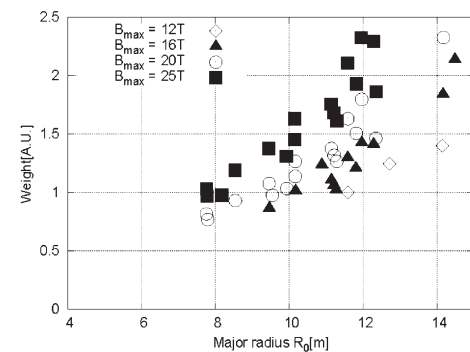


Fig. 3 Reactor weight vs. major radius  $R_0$ .

## REFERENCE

- (1)K., Yamazaki, et al., Fusion Technology, vol.21, 1992, pp.147-160.
- (2)S., Sudo, et al., Nuclear Fusion, vol.30, 1990, pp.11-21.
- (3)U., Stroth, et al., Nuclear Fusion, vol.36, 1996, pp.1063-1077.
- (4)T., Goto, Y., Ogawa, Fusion Engineering and Design, vol. 81, 2006, pp.1251-1255.

## §5. Design Study of Indirect Cooling Superconducting Magnet for the Helical Reactor

Mito, T., Takahata, K., Tamura, H., Imagawa, S., Sagara, A.

The design study of the superconducting magnet for the helical reactor has been started considering the condition of continuous helical winding, steady state operation without pulse magnetic field change and plasma disruption in a Tokamak reactor. The design of the superconducting magnet for a helical reactor has been facilitated because there is no magnetic field change to induce the plasma current, and there is no rapid change such as plasma disruption. However, the conventional forced-flow cooled magnet with CICC may not be applicable for a helical reactor because the conductor length of the continuous helical winding becomes too long and the pressure drop becomes too much. Then, we are examining the introduction of the indirect cooling method as one example of a new superconducting coil structure to make the best use of the feature of a helical reactor.

The concept design of the conductor for the indirect cooling method is shown in Fig. 1 and the coil structure is shown in Fig. 2. The transposed conductor composed of several compacted strand cables, where the increase of AC losses caused by the non-uniform cabling, etc. doesn't occur, is assumed as a basic structure of the conductor. The A15 inter-metallic compound superconductor such as  $\text{Nb}_3\text{Sn}$  or  $\text{Nb}_3\text{Al}$  is used so that a maximum magnetic field of 13 T – 15 T is applied to the conductor in the windings. The conductor achieves coexisting of a mechanical strength and the heat conduction characteristic for the indirect cooling by covering the superconducting conductor with the aluminum alloy. After the heat treatment, the superconducting conductor is covered with the aluminum alloy because the melting point of the aluminum alloy is close to the temperature of the heat treatment of superconductor. Therefore, it becomes React & Wind as a fabrication sequence of the superconducting magnet. The winding work is done by burying the above-mentioned conductor insulated with the ceramic coating etc. on the electromagnetic force supporting plate where the ditch was processed to the shape of the conductor. In the windings, the cooling panels are inserted in every winding block of a few layers and it is cooled indirectly. The cooling panel has the internal cooling passes and is cooled by circulating the supercritical helium etc.

The magnet design with high degree of freedom is enabled by separating the cooling passing and the current passing with the indirect cooling concept. Becoming the problem by the indirect cooling method is whether nuclear heat generation in the superconducting magnet is removed enough, and the temperature rise in the windings can be suppressed. The nuclear heating in the magnet is lower than about  $100 \text{ W/m}^3$ , and assuming the thickness of a winding

block to be  $0.1 \text{ m}$  and if  $10 \text{ W/m}^2$  can be achieved as heat removal ability of the cooling panel, the magnet can be cooled enough. The temperature rise in the windings by nuclear heat generation becomes  $0.25 \text{ K}$  or less if it is assumed  $4 \text{ W/mK}$  (corresponding to the heat conduction of aluminum alloy) as thermal conductivity of the winding. It is possible to suppress the maximum temperature in the winding to  $1 \text{ K}$  or less even if it is considered that the thermal conductivity in the electric insulation layer is low. From the above-mentioned outline examination, the application possibility of the indirect cooling method to a helical reactor was shown. The development of the large current capacity conductor, the insulation structure that can be used in the neutron irradiation environment, and the development of the winding structure to satisfy the mechanical characteristic are important tasks to realize an indirect cooling superconducting coil for a helical reactor.

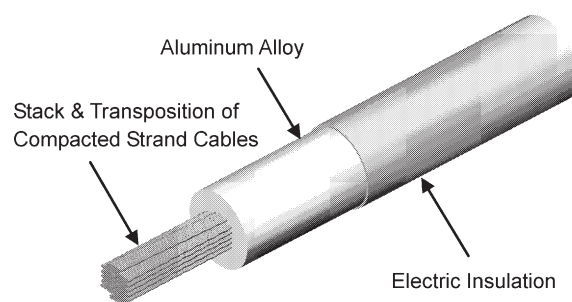


Fig. 1. Conceptual design of the indirect cooling conductor.

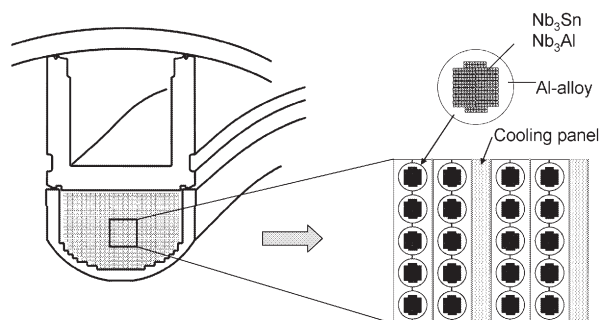


Fig. 2. Conceptual design of the indirect cooling coil.

## References

- 1) Mito, T. et al., "Applied Superconductivity and Cryogenic Research Activities in NIFS", presented at ITC-15, Dec 6 – 9, 2006 and to be published on Fusion Engineering and Design.

## §6. Analysis of Tritium Fluoride Behavior and Recovery of Tritium in a Molten Salt Flibe Blanket

Fukada, S. (Dept. App. Qua. Phys. Nucl. Eng. Kyushu University), Sagara, A., Uda, T.

### 1. Purpose of Study

Flibe is one of the most advanced self-cooled liquid blanket materials for a fusion reactor, *e.g.*, FFHR-2. It is expected that Be can work as a redox-control agent as well as a neutron multiplier. Advantages of Flibe blanket are stable at higher temperatures, low reactivity with oxygen and water vapor, low electric conductivity and so on. Tritium will be generated in Flibe as a form of TF. Since TF is corrosive to structural materials, conversion of TF to T<sub>2</sub> is necessary in a Flibe blanket. Otherwise, we need to recover TF down to an allowable concentration immediately after the blanket outlet. In the present study, we investigate the possibility of a redox control by contact with a Be rod in the Flibe loop of FFHR-2, and the behavior of TF and HT released from neutron-irradiated Flibe.

### 2. Results and Discussion

#### (1) Conversion of TF to T<sub>2</sub> in a blanket

The Be dissolution rate and its saturated concentration were determined  $j_{Be}=1.8 \times 10^{-4}$  mol-Be/m<sup>2</sup>s and  $x_{Be,sat}=4 \times 10^{-3}$  from the JUPITER-II experimental study in 2005. Dissolved zero-charge Be works as a reduction agent for the conversion of HF (TF) to H<sub>2</sub> (T<sub>2</sub>). The reduction rate is correlated to a first-order reaction-rate equation as follows:

$$m_{BeF_2} = k_{BeF_2} \left( x_{Be} x_{TF} - \frac{x_{BeF_2} x_{T_2}}{K_{BeF_2} x_{TF}} \right)$$

**Fig. 1** shows a comparison of the effluent HF concentration between analysis and experiment using 0.5L Flibe enclosed in a Ni pot. Close agreement was obtained between them.

1 GW fusion power needs to produce 1.6 MCi/day tritium under steady-state operation of a commercial fusion reactor with TBR=1. Flibe flow rate is maintained at 200 m<sup>3</sup>/s to keep the temperature difference of  $T_{in}=500^\circ\text{C}$  and  $T_{out}=600^\circ\text{C}$  from a viewpoint of Flibe-material consistency. **Fig. 2** shows calculation results of the expected TF concentration in the blanket outlet as a function of the dissolved Be concentration. The predicted TF partial pressure is around 1 Pa.

#### (2) Recovery of TF and T<sub>2</sub> from Flibe

**Fig. 3** shows tritium effluent curves from neutron-irradiated Flibe under a 5% H<sub>2</sub>-Ar flow condition. At first isotopic-exchanged HT and then resolved TF were in turn released from Flibe even at 300°C. The result reveals the possibility of direct TF recovery by a He-Flibe extraction tower installed immediately after the reactor outlet.

This work is performed with the support and under the auspices of the NIFS Collaborative Research Program NIFS04KFDS001.

### 3. Studies published or presented in 2005

[1] S. Fukada, R. A. Anderl, T. Terai, A. Sagara, Fus. Sci. Technol., 48 (2005) 666-669.

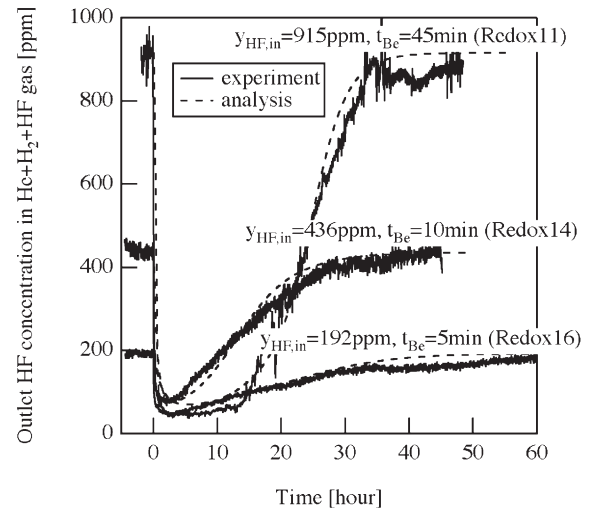


Fig. 1 Experimental results of redox control by Be

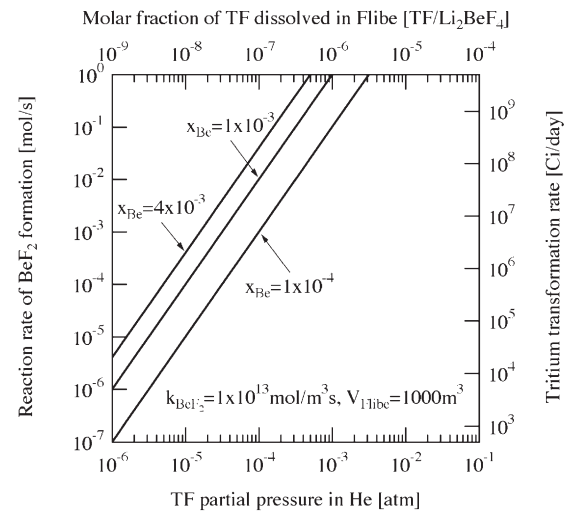


Fig. 2 Tritium concentration in Flibe blanket

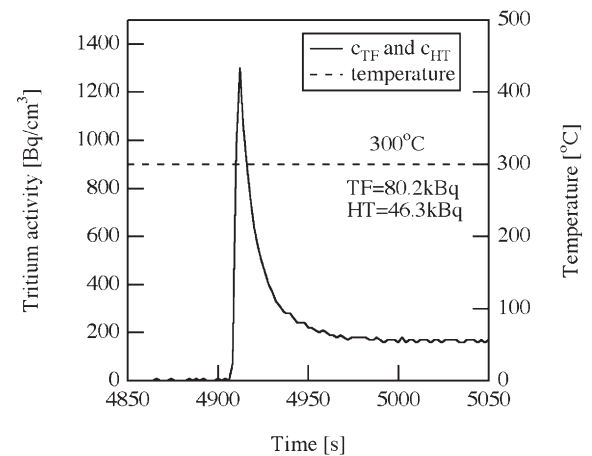


Fig. 3 Tritium released from neutron-irradiated Flibe

[2] S. Fukada, A. Morisaki, A. Sagara, Proc. ISFNT-7, (2005).

[3] S. Fukada, M. F. Simpson, R. A. Anderl, et al., Proc. ICFRM-12, (2005).



## §7. Feasibility of Helium Gas Turbine System for Molten Salt Blanket

Shimizu, A., Yokomine, T., Ebara, S. (Interdisciplinary Grad. Sch. Eng. Sci., Kyushu Univ.),  
Imagawa, S., Sagara, A.

### 1. Introduction

In the FFHR design activity, gas turbine is considered to be the candidate for energy conversion system. However, output temperature from nuclear reactors is very restricted for both fission and fusion compared to conventional fossil fuel combustion so that an improvement of thermal efficiency cannot be realized by any extended version of conventional Brayton cycle. Therefore, adoption of multi-stage compression/expansion process is the quite natural alternative choice for total cycle improvement.

### 2. Previous estimation of thermal efficiency

Based on these considerations, numerical estimation had been performed in last several years on the thermal efficiency of multi-stage closed gas turbine cycle and it was concluded that when five stage compression/expansion is adopted, the gas turbine cycle efficiency up to 42 % is possible even for the narrow temperature design window of FFHR, namely between 450°C and 550°C. However, that estimation has been based on very optimistic evaluation of pressure loss within the cycle path so that more realistic estimation has been expected.

Following this, the research effort of this year was turned to the direct evaluation of Ericsson cycle in which heat addition and rejection in respective expansion and compression phases are performed isothermally. Its TS diagram is illustrated in Fig.1 along with that of the ideal Carnot cycle. As the diagram indicates, the ideal Ericsson cycle is equivalent the Carnot one.

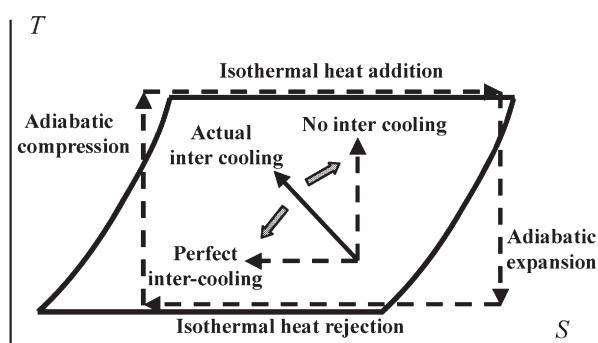


Fig.1 Carnot and Ericsson: cycles

### 3. Validation of Ericsson Cycle: Heat transfer through casing wall

The keys for realizing Ericsson cycle are as follows

(1) As high gas temperature as possible is favorable even for the Ericsson cycle.

(2) Heat transfer coefficient between operating gas and casing wall or turbine blade must be raised typically several orders higher compared to the conventional equipment. Of possible heat transfer enhancement techniques available at present, the heat transfer enhancement by use of nano-particle coating is most promising. However, reported heat transfer improvement is barely twice of the conventional value so that more innovation is strongly expected. Moreover, there remains some uncertainty in the enhancement effect for gaseous heat transfer. Another possibility is to ultra-fine heat transfer structure between turbine blades.

(3) Extension of heat transfer surface

The possible heat transfer surface for additional heat input in expansion stage is restricted to the casing wall and turbine blade surfaces. Of these, the former requires less change in the whole turbine geometry while the latter must accompany with a drastic change in the blade design.

Accordingly, a simple estimation was made for the required heat transfer performance in the expansion phase. (assumption)

(1) When inner diameter and length of casing are  $2\text{m} \times 2\text{m}$ , the heat transfer area is  $6.3\text{m}^2$ .

(2) The order of heat transfer coefficient is at most  $3000\text{kcal/m}^2\text{hr}^\circ\text{C}$ . The conventional value for He is of  $1000\text{kcal/m}^2\text{hr}^\circ\text{C}$  order

(3) Temperature difference is about  $200^\circ\text{C}$  (gas- $650^\circ\text{C}$ , casing wall- $850^\circ\text{C}$ )

The rough estimation gives the heat transfer value of  $6.3 \times 3000 \times 200 \times 4.19/3600 = 4400\text{ kw}$  ( $=4.4\text{MW}$ )

In fact, the value required for actual gas turbine is about 100 times of the above. Namely, simple heat input only through the casing wall will be unrealistic.

The similar estimation was performed for the expansion stage and conclusion was that the maximum attainable heat transfer rate was estimated to be barely  $3.3\text{MW}$  for the casing size of  $2\text{m}$  inner diameter  $\times$   $3\text{m}$  length. This value was compared with the actual required level and the conclusion was that the heat transfer enhancement of two order higher is required.

It is concluded therefore that the Ericsson type expansion/compression gas turbine cannot be realized at least through heat addition/rejection by way of casing walls.

Remaining possibility is the heat addition/rejection by making the flow path between expander and compressor blades the heat transfer structure.

This subject is left to the task in FY2006.

[1] "An Ericsson cycle GT design by LNG cryogenic heat utilization", 45th ASME/IGTI Congress ASME TURBO EXPO 2000, May 2000, Munich Germany, ASME 2000-GT-0166.

[2] "The design of high-efficiency turbomachinery and gas turbines", D.G Wilson & T. Korakianitis, Prentice Hall, 1998.

§8. Research on the First Wall Cooling Technique in a Flibe Liquid Blanket System

Yuki, K., Hashizume, H. (Tohoku Univ.), Sagara, A.

In the LHD-type heliotron power reactor FFHR promoted by NIFS, the greatest benefit of the Flibe-blanket system adopting Spectral-shifter [1] which Sagara et al. proposed is that it is basically maintenance-free for 30 years, with emphasis on blanket maintainability. However, against that, heat load on the first wall shoots up higher than ever before. Heat removal of approximately  $1\text{MW/m}^2$  high heat flux, in the single-phase flow condition, is therefore a significant R&D issue which holds the key to the blanket development.

In order to develop a heat transfer promoter for a high Pr number fluid Flibe in accordance with the strict conditions in the reactors, the authors noted Sphere-Packed Pipes (SPP) as a basic heat transfer promoter and have been examining the fundamental heat transfer performance of an SPP in the TNT (Tohoku-NIFS Thermofluid) loop facility which can be regarded as a forced circulation apparatus for high temperature molten salt [2, 3]. The purpose of this research is, first of all, to evaluate the flow structure in a sphere-packed pipe using comparatively large spheres by visualization experiments. After that, this research highlights the correlation between the local heat transfer performance and the flow structure obtained by the PIV, by conducting heat transfer experiments.

To clarify the inside flow structure in a sphere-packed pipe with the sphere of  $D/2$  in diameter ( $D$ : pipe diameter), PIV visualization is conducted first by utilizing a matched refractive-index method with NaI solution as the working fluid. As the basic flow structure in the pipe, the following three flows are confirmed: the bypass flow with high flow velocity due to wall effect (see Fig. 1(a)), the complicated wake formed behind the sphere that also works as an impinging jet to the wall (see Fig. 1(b)) and the spouting flow from the central part of pipe. Furthermore, through heat transfer experiment, wall-temperature distribution is measured with thermocouples and an infrared thermography, which clarifies the relation between the flow structure and local heat-transfer performance as shown in Figure 2. The area with high wall-temperature is formed in the stagnation area located around at a contact point between the sphere and the heating wall. However, the heat transfer performance is quite high in the area with a large gap between the upstream and downstream spheres by means of the influence of a separation vortex and the impinging-flow effect, which are both a part of complicated wake. In addition, the high-velocity bypass flow significantly affects the heat transport in the stagnation area. Figure 3 shows the influence of the pumping power on the heat transfer performance. It shows that, under the lower power conditions, the heat transfer coefficient of the SPP flow shows a higher value than that of a swirl flow as well as a circular pipe flow. This indicates that it is effective especially under lower

pump-power conditions. However, the heat transfer performance of the SPP flow at high pumping power is much lower than that of the other typical promoters, which suggests that it needs to dramatically enhance the heat transfer performance at the contact point by using fin-effect from the heating wall to the sphere and changing the packing structure etc. in a case of using the sphere of  $D/2$  in diameter. For reference, heat transfer performances for the different sizes of sphere,  $D/d=3.0$  and  $1.4$ , are also shown in the same figure by use of Fand's correlation. The utilization of smaller size of sphere is much more effective than that of  $D/2$  size of sphere in the case without the fin-effect. This indicates high potential for the heat transfer performance of the SPP flow, so that it is evident that the SPP's heat transfer performance dominates other heat transfer promoters, especially when considering all pressure drops of coolant circulating system

This work was performed with the support and under the auspices of the NIFS Collaborative Research Program NIFS (NIFS05KFDA005)

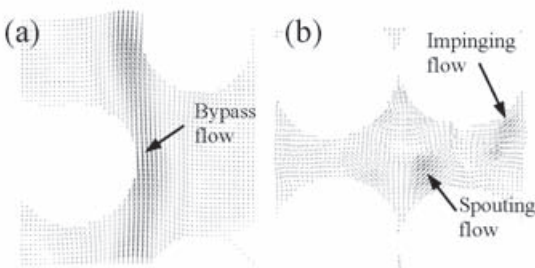


Fig. 1 Flow structures in Sphere-Packed Pipe

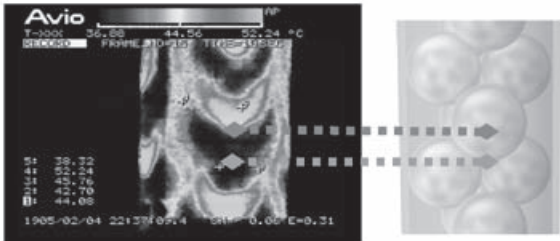


Fig. 2 Temperature distribution of wall

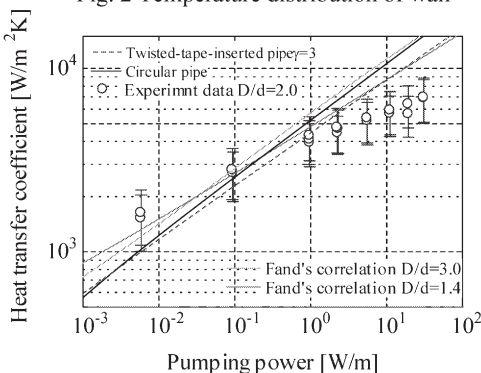


Fig. 3 Heat transfer performance of SPP

REFERENCE

- (1) A., Sagara, S. Imagawa, et al., Fusion Engineering and Design, vol. 81, 2006, pp.1299-1304.
- (2) S. Toda, S. Chiba, K. Yuki, et al., , Fusion engineering and design, vol. 63-64, 2002, pp. 405-409.
- (3) S. Chiba, M. Omae, K. Yuki, et al., Fusion science and technology, vol. 47, no.3, 2005, pp. 569-573.

# §9. Heat Transfer Between Pebbles Considering Large Temperature Gradient Inside Pebble

Yokomine, T. (Kyushu Univ.),  
Seo, K., Sagara, A.

Conventional experimental study for heat transfer in a pebble bed has been conducted by means of oven-type experimental apparatus, that is, all pebbles is equally heated by external heaters. After all, it is found that the effective heat conductivity of bed is affected by the external load. That means the heat transfer between pebbles near their contact region is dominated for the effective heat conductivity. When the volumetric heating is occurred in the each pebble, the large temperature gradient will be generated and/or inhomogeneous temperature profile will be occurred near the interface. The effects of above phenomena cannot be taken into consideration by oven-type experiment. In present study, focusing attention on two contacting pebbles, the effect of the amount of heat flow through the interface and the each temperature gradients near the interface on the thermal conductance is investigated and estimated quantitatively by using two contacting rods in which heaters is amounted to simulate the volumetric heating.

Fig.1 shows the schematic view of experimental apparatus. Two test specimens are contacted vertically. Each test specimen is copper block (W30mm×H100mm×D 85mm) and the boundary of contact area has 15mm of curvature radius. Plate heater is mounted on the upper test specimen. Two cartridge heaters (φ6×100mm) are inserted into each test specimen: each location is 15mm apart from the contacting interface. A cooling block cooled by flowing water thorough a channel in it is mounted under the lower test specimen. The temperature is measured by inserted thermocouple into specimen: φ0.25mm thermocouple is located at 3mm, 6mm and 9mm away from the contact interface and φ1.0mm thermocouple is used at distance of 55mm, 65mm and 75mm from the contact interface.

Fig.2 show the dependence of the input power ratio of heater #1 and #2 ( $Q_2/Q_1$ ) on the heat flow ratio of overall heat flow ( $Q_{2S}$ ) and heat flow through the contact interface ( $Q_{1-2}$ ) and thermal contact conductance  $h$ . The heat flow through the contact interface is at the most 10% of the overall heat flow. When the  $Q_2/Q_1$  is constant, heat flow ratio and contact thermal conductance are both increased 20 to 30% with increasing the input power of heater #3. It is considered that the heat flow is contracted and the turbulence is suppressed near the interface by the existence of heat generation in the low temperature side of test specimen. That is, it should be considered for the design of solid blanket that the inhomogeneity of volumetric heating between the contacting pebbles.

The dependence of the theoretical contact pressure on the heat flow rate is showed in Fig.3. The theoretical value of contact pressure is derived from Hertz's contact theory by using measured contact area. From the measured contact area, the corresponding theoretical pressure becomes 3GPa on the assumption that the contact body is

complete circle. Using the value of 10MPa as a maximum pressure referred to the conventional solid blanket design, the heat flow rate is only 2% regardless of presence of volumetric heating at a low temperature side. Therefore, it should be emphasized that the effective introduction of convective heat transfer with fluid is dispensable for actual design of a solid blanket.

This work is performed with the support and under the auspices of the NIFS Collaborative Research Program NIFS05KFDF002.

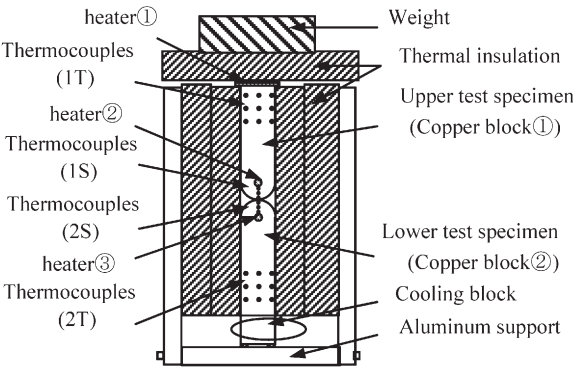


Fig. 1. Schematic view of experimental apparatus

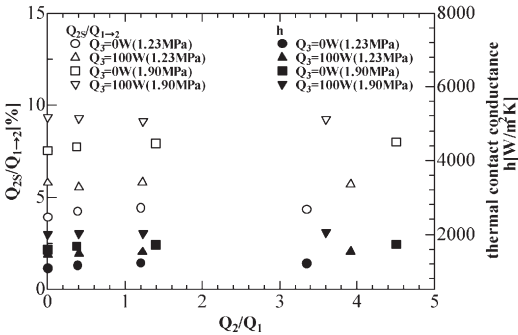


Fig. 2. Heat flow rate and thermal contact conductance

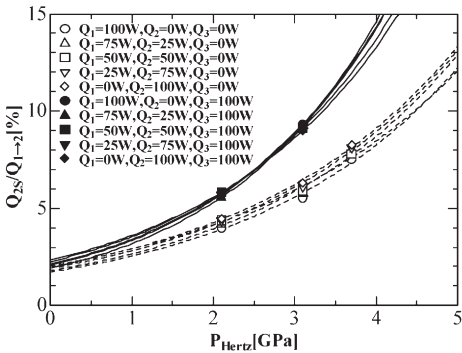


Fig. 3. Heat flow rate vs. load pressure



# §10. Study on Heat Transfer Region for Fluid System in a Liquid Blanket

Satake, S. (Tokyo University of Science), Kunugi, T. (Kyoto University), Yokomine, T. (Kyusyu University), Kawahara, Z. (Kyoto University), Yuki, K. (Tohoku University), Sagara, A.

## 1. Objectives

In the region of transition Reynolds numbers, the increase or decrease of friction coefficients of the coolant like a Molten Salt having a low magnetic conductivity is obtained: a transition Hartmann number behavior. This behavior also leads the deterioration of heat transfer. Therefore, the thermo-fluid design of blanket under the magnetic filed fluctuation is very important. Since the magnetic field is strongly influenced by mean velocity when the magnetic field applies perpendicular to the flow direction, it is necessary to investigate the turbulent MHD flow behaviors for each direction of the applied magnetic field normal to the main flow one. Furthermore, in case of considering the wall with various electrical conductivities, the flow characteristics of the coolant could be different from the usual turbulent non-MHD flows. In this sense, the numerical simulation is very convenient to evaluate the flow changes due to the change of physical properties of the wall materials or the direction of applied magnetic field.

In the present study, to evaluate the effect of interaction of wall and fluid in 3D field, fully developed turbulent channel flow is carried out with high conducting wall. The difference for Reynolds shear stress budget near wall region is clearly observed compared with that of insulated wall.

## 2. Numerical method and boundary condition for turbulent channel flow with conducting walls

Our DNS code is hybrid spectral finite difference method. The periodic boundary conditions are applied to the streamwise ( $x$ ) and the spanwise ( $z$ ) directions. As for the wall normal direction ( $y$ ), non-uniform mesh spacing specified by a hyperbolic tangent function is employed. The mesh number of  $128 \times (64) + 128 + (64) \times 128$  are used for the computational domain of  $5\pi\delta x (\delta) + 2\delta + (\delta) \times 2\pi\delta$ .in the sreamwise, the wall-normal, and spanwise directions. The all velocity components imposed the non-slip condition at the wall. The non-slip condition is used at the wall. A uniform magnetic field  $\mathbf{B}_0$  defines that the magnetic orientation is parallel to the axis of the streamwise direction in Fig.6. The Neumann condition for the electrical potential is adopted at outside the wall: Conducting wall assumption. The Hartmann numbers ( $Ha = \mathbf{B}_0\delta (\sigma/\rho\nu)^{1/2}$ ) based on the magnetic field  $\mathbf{B}_0$ , the kinematic viscosity  $\nu$ , the electrical conductivity  $\sigma$ and the channel width  $\delta$  are set to 15.0. The  $\sigma$  at fluid is 1.0. The  $\sigma$  at solid wall is 62.27. If these parameters are assumed as actual material, fluid and solid wall are mercury and copper, respectively. The Reynolds number is 4590 based on the bulk velocity. The fluid flows with constant mass flux condition.

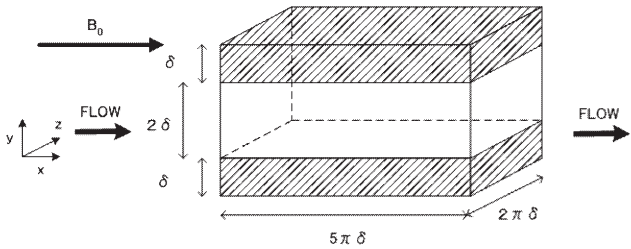


Figure 1 Computational domain.  
Table 1

	Cf	Cf/Cf,0
Non MHD	$8.5523 \times 10^{-3}$	1
Insulated wall, Ha=15	$8.2894 \times 10^{-3}$	0.969
Conducting wall, Ha=15	$8.1848 \times 10^{-3}$	0.957

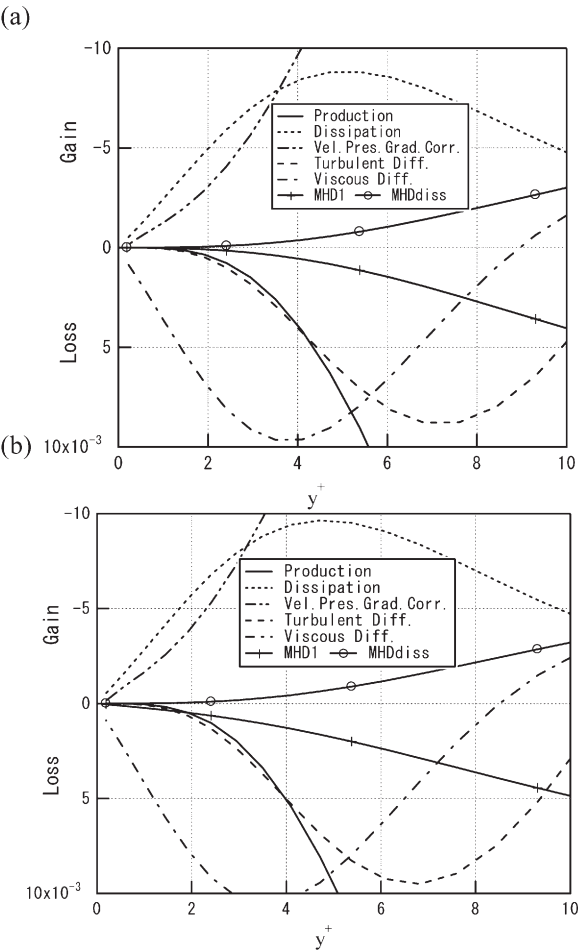


Figure 2 Reynolds shear stress budget: (a) Conducting wall, (b) Insulated wall.

The terms in Reynolds shear stress budget equation for the conducting wall and the insulated wall are shown in Figures 2 (a) and (b). The production terms of the conducting wall decrease at  $y^+ < 4$  compared with those of the insulated wall. The production terms consist of the normal stress and the mean velocity gradient. Although the mean velocity gradient is increased, the normal stress is further decreased. It is evident that the normal stress (not shown here) of the conducting wall is decreased compared with that of the insulated wall.

NIFS Collaborative Research Program NIFS06KFDA008.



§11. Design Study of the Electrical Power System for FFHR

Chikaraishi, H., Sagara, A., FFHR Design Group

In this report, the design study of the electrical power system for the FFHR is described.

In addition to the reactor and generator, some components are necessary to operate the FFHR as an energy plant. The diagram of the outline of the plant is shown in Figure 1.

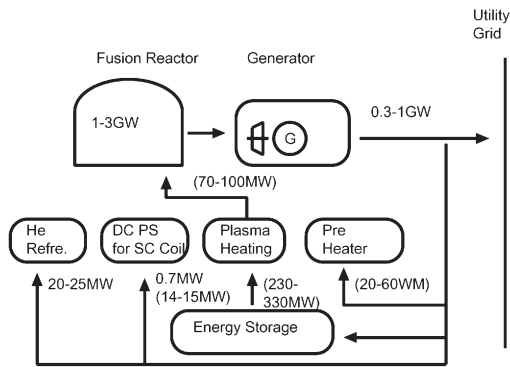


Figure 1: Diagram of the FFHR plant

In the figure, thermal power and electrical power is described. The number shown in the blanket is the necessary power to start up the reactor.

In this figure, we assumed that the efficiency of NBI is 30%, conduction loss of the power supply is 5% respectively. The circulation power in the plant, that is necessary to maintain the plant operation, is used in the He refrigerator and power supplies for coils. These powers are 7-3 % of electrical output of the FFHR plant and it is kept small compared with the plant output. In this point, the merit of FFHR operation that does not require the external plasma heating in the steady state becomes clear.

The outline of the electrical power used in the FFHR2 plant is shown in Figure. 2.

When the FFHR is in the steady stat operation, only the He refrigerator and power supplies for superconducting coils consume the electric power. When start up the FFHR, a pre-heater and dc power supplies for coils require the 8-10% of the plant electrical output. This power is required for several hours and an energy storage device is not suitable for this purpose. Therefore some local generator or power supplies from utility network is necessary.

Plasma heating using the NBI requires 230-330MW in short time. This power is about 30% of the plant output, and the energy storage device such as a flywheel motor-generator should support this energy.

When we consider the maximum voltage while quench protection, the turn numbers of coils are limited.

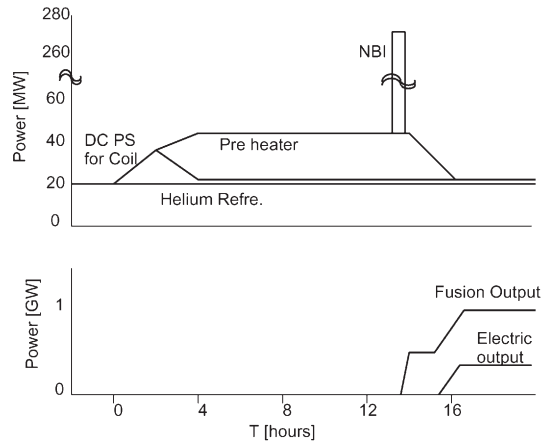


Figure 2: Electrical power used at the start up of the FFHR

Table 1: superconducting coils				
	coil cur. [kA]	turn num.	vol. [V]	number of Coils
H	100.1	54	16	8
OV1	100.1	110	18	1
OV2	100.1	115	18	1
IV	100.1	116	0.1	1

In the current design, we assume that the superconducting coil currents of FFHR are ramped up within 5 hours. With this scenario, the required excitation voltages become about 18 V as shown in Table 1. In this coil system, the operating currents of coils are same and they can be connected in series to be excited by a single power supply. With this architecture, the power loss generated by dc power supply in the steady state can be suppresses.

The effect to the plasma operation caused by the series connection of superconducting coils should be studied to realize this architecture.

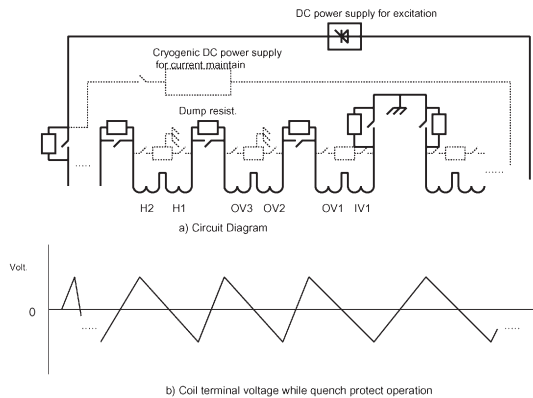


Figure 3: An example of circuit diagram for the excitation of superconducting coils using single dc power supply.

## §12. Study on Vapor Shielding Effects under High Temperature and Particles for Nuclear Fusion Reactor

Furukawa, H., Norimatsu, T., Mima, K. (ILE, Osaka University),  
Sagara, A.

Critical issue in designing an advanced fusion reactor with high output energy density is the ablation of the hot first wall exposed by energetic particles from plasma. In a case of a dry wall reactor for laser fusion operated with a 150 MJ yield target, the total thermal load on the surface is estimated to be  $4.5 \times 10^{18} \text{ W/cm}^2$ , which heats the initially 500°C tungsten surface to 3000°C at the chamber radius of 6 m [1]

To experimentally simulate the ablation process, laser irradiation is often used. We, however, found that ablation process by ions is quite different from that by lasers. The range of  $\alpha$  particles in solid Tungsten is roughly 10  $\mu\text{m}$ . As the result, tungsten evaporates as a high density, low temperature plasma with low ionization rate or neutral gas. One of aims of our study is to clarify vapor shielding against incident energetic charged particles.

In this study we have developed an integrated ablation simulation code DECORE[2,3] ( Design Code for Reactor ). We estimate temperatures, densities, and velocities of ablated lead ( liquid wall material ) using DECORE for the case of first ignition with 200 MJ power output[2,3].

Figure 1 shows the schematic diagram of DECORE. As shown in Fig. 1, DECORE consists of atomic process code, stopping power code, EOS code, emissivity and opacity code, and ablation code.

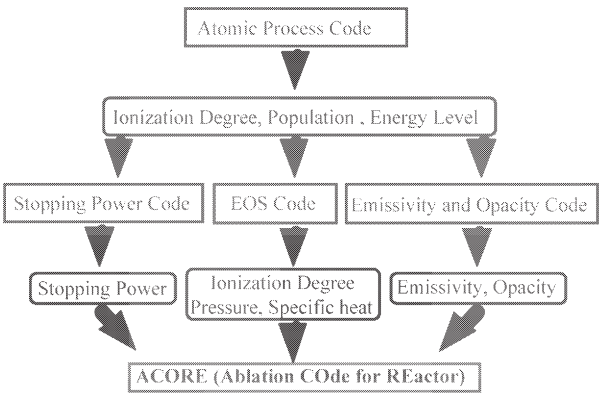


Fig. 1 Schematic diagram of DECORE.

Figure 2 shows number density and velocity profiles of lead. As shown in Fig. 2, ablated lead moves as a clump with velocities of a few hundred m/s.

Figure 3 shows temperature profiles of lead. For these temperature, ablated lead may condensates and a lot of nano clusters may exist in lead plume.

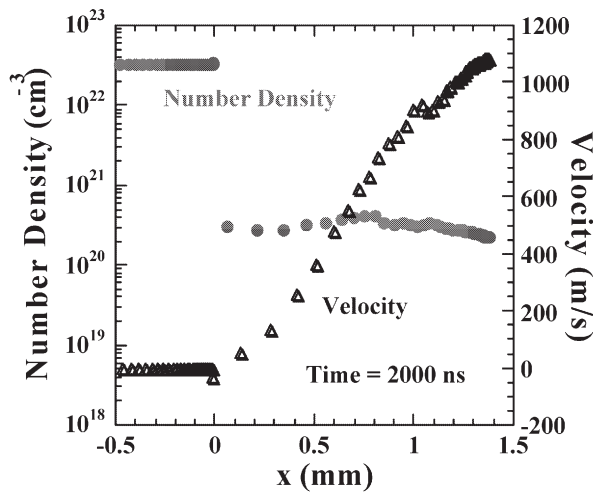


Fig. 2 Number density and velocity profiles of lead. Locations  $-0.5 < x < 0$  and  $0 < x$  mean liquid and vapor phases, respectively.

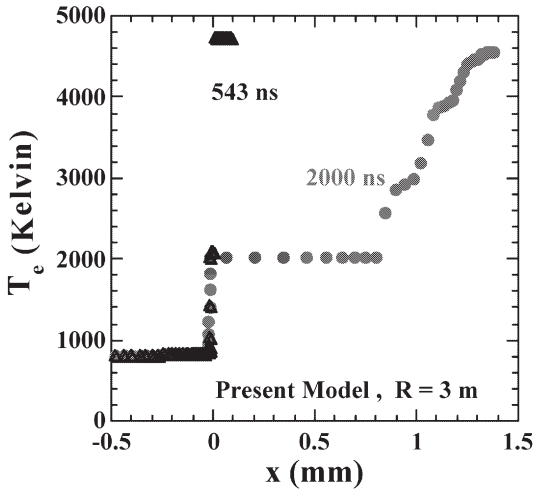


Fig. 3 Temperature profiles of lead.

### References

- [1] A. R. Raffray et al., Presented at ISFNT-7, May 22-27 (2005) Yokohama, Japan.
- [2] H. Furukawa, Y. Kozaki, K. Yamamoto, T. Johzaki, and K. Mima ; Fusion Engineering and Design **73** (2005) 95-103.
- [3] Simulation on Ablation for Design of Liquid Wall Chamber of Laser Fusion Reactor : H. Furukawa, T. Johzaki, et. al.; J. Plasma Fusion Research in press (2006).

### §13. Burning Criteria for D-<sup>3</sup>He Reactor

Nagayama, Y., Tomita, Y.

Burning criteria for a D-<sup>3</sup>He fusion reactor have been investigated by using the 0-D power and particle balance equations and the IPB98(y,2) scaling law [1]. In order to simplify the problem, ST configuration with ITB and the bootstrap current fraction of 100 % are assumed.

The model is as follows: Equations to be solved in this paper are the energy balance equation, as

$$\frac{dW}{dt} = P_{heat} - \frac{W}{\tau_E}$$

and the particle balance equations, as

$$\frac{dN_k}{dt} = v_k - \frac{N_k}{\tau_p} - \frac{1}{V} \sum_i S_{jk} + \frac{1}{V} \sum_{i+j \rightarrow k} S_{ij}$$

where  $W(t)$  is the internal plasma energy,  $N_k$  and  $v_k$  is the total particle number and the external particle supply of nucleus  $k$ , respectively. The summation indicated by  $i+j \rightarrow k$  is the whole fusion reaction creating a nucleus  $k$ , ( $i, j, k=H, T, D, {}^3\text{He}, C$ ). The electron density  $n_e$  and the ion density  $n_i$  satisfy the charge neutrality. The energy confinement time  $\tau_E$  is assumed to be  $\gamma_{HH}$  times of the IPB98(y,2) scaling. Spatial profiles of the temperature and density are assumed to be an ITB model as  $T_j(r) = T_{j0} g(x; b_T, m_T)$  and  $n_j(r) = n_{j0} g(x; b_n, m_n)$ . Here  $x=r/a$ , and

$$g(x; b, m) = \begin{cases} 1 - \frac{x^{2m}}{b^{2(m-1)}} & (0 \leq x \leq b) \\ \frac{(1-x^2)^m}{(1-b^2)^{m-1}} & (b \leq x \leq 1) \end{cases}$$

Figure 1 shows the  $T_i/T_e$  and the fraction of neutron power in the total fusion power versus the <sup>3</sup>He in the case of  $R=6$  m. When  $T_i=T_e$ ,  $n_D: n_{{}^3\text{He}}=2:1$  and the neutron fraction is 10 %, which is 1/8 of the D-T reactor. When  $n_{{}^3\text{He}}=60$  %, the neutron fraction is 1.9 % of the total fusion power, which is less than 1/40 of the D-T fusion. The  $T_i/T_e$  should be greater than 2 in order to operate the reactor with  $n_{{}^3\text{He}}=60$  % even if no impurity other than fusion ashes (H and <sup>4</sup>He)

exists in plasma. D-D reactor or a low-neutron D-<sup>3</sup>He reactor require the condition  $T_i/T_e > 2$  even if no impurity other than the <sup>4</sup>He ash remains.

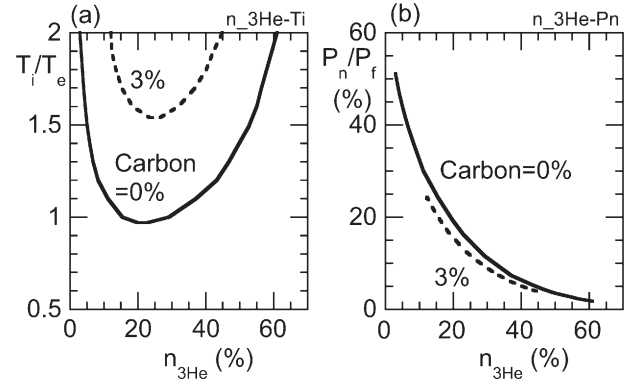


Fig. 1 (a) Temperature ratio ( $T_i/T_e$ ) and (b) fraction of neutron power in total fusion power versus <sup>3</sup>He contamination in the steady burning state.

Figure 2(a) shows the minimum toroidal field ( $B_t$ ) to obtain a particular central beta ( $\beta_0$ ). Fig.2 (b) shows the averaged beta ( $\langle\beta\rangle$ ) versus normalized radius of ITB foot point ( $b_{ITB}$ ) in the case of,  $B_{coil}=20$  T ( $B_t=3.63$  T) and  $\beta_0=1$ . Other conditions ( $R=6$  m,  $T_i/T_e=1.6$ ,  $n_D: n_{{}^3\text{He}}=2:1$  and  $n_C=3$  %) are common in both figures.

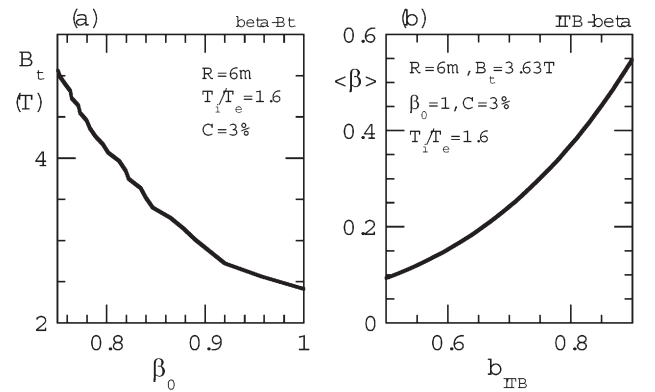


Fig. 2 (a) Required  $B_t$  to obtain  $\beta_0$  in the case of  $b_{ITB}=0.85$ . (b) Averaged beta ( $\langle\beta\rangle$ ) versus  $b_{ITB}$ .

The result shows that when  $\langle\beta\rangle=10$  %, D-<sup>3</sup>He reactor is possible if  $\beta_0$  is about unity and  $T_i/T_e>2$ . This is applicable to helical reactors.

- [1] Y. Nagayama, Y. Tomita, IEEJ Trans. FM, Vol.125, 947 (2005)

### (3) Fusion Reactor System and Safety

Safety and environmental research and development are important to design and construction of a future nuclear fusion reactor and to secure sufficient safety. Major issues are as follows.

- (1) Fundamental concept to secure safety in fusion reactor.  
It includes studies of radiation protection considering radiation generating devices and radioactive materials in a nuclear fusion reactor.  
Safety analysis presuming a helical type power reactor had been made considering engineering safety systems, functions, and sequential schemes presuming abnormal events.
- (2) Safety consideration of tritium fuel cycle.  
The fusion reactor system includes large amount of tritium in the vacuum vessel and fuel cycle. So safety handling technology and robust confinement system are required. Major safety issues are to prevent tritium release accident and to recovery of the tritium released to a radiation control room. Also research of tritium behavior in the environment and its biological effect is important considering radiation protection for occupational health hazard.
- (3) Biological shields and radiation monitoring.  
Much induced radioactive materials are produced in a nuclear fusion reactor. Shielding analysis of neutron and radiation from the radioactive materials are required. Also radiation measurements and monitoring are important for radiation protection.
- (4) Radioactive waste management.  
Waste management of tritium containing gas, liquid and contaminated solid are important problems. Major issues are recovery of tritium, decontamination or volume reduction of the wastes.
- (5) Safety and public consent.  
Comprehensive safety analysis and risk analysis should be made and the accountability is required.

Major safety issue specific for a future fusion reactor is to avoid the release accident of large amount of tritium. Fundamental safety of tritium processing would be secured by low tritium inventory, tritium dispersion to various partitioned components, and multiple protection systems.

Results of some collaborating studies are shown as follows. They will be useful not only for the DD experiment of LHD, but also for a future fusion reactor.

- (a) Tritium behavior in cooling pipe of stainless steel  
This basic study has been carried out as collaborations with University of Tokyo and Shizuoka University. D<sub>2</sub> or D<sub>2</sub>O was sorbed on/in the stainless steel samples by water adsorption, ion injection or electrolysis. The chemical forms of hydrogen isotopes on/in SS-316 were studied by XPS (X-ray photoelectron spectroscopy) and their desorption behavior was evaluated by TDS (thermal desorption spectroscopy). It has been

suggested that the reduction of oxide layer formation and/or removal of oxyhydroxide layer after tritium exposure will be important to reduce tritium retention in SS.

- (b) Hydrogen isotope separation system in liquid phase  
Two collaborating developments have been carried out. One is the study with Nagoya University on higher performance tritiated water volume reduction system by chemical exchange reactions between hydrogen gas and liquid water. The other is the study with Kyushu University on advanced catalysts for the chemical exchange reactions between hydrogen gas and liquid water. It has been demonstrated that the homogeneous bed where Kogel catalysts and Dixon gauze ring are mixed in the optimum ratio and filled in the chemical exchange column homogeneously is more efficient than the conventional layered type bed. Benchmark tests using tritiated water is planning to be carried out at FZK(Forschungszentrum Karlsruhe, Germany) in September 2006.
- (c) Hydrogen isotope separation system in gas phase  
The basic study about the gaseous hydrogen isotope separation and purification system by pressure swing adsorption(PSA)has been carried out as collaborations with Kyushu University. Progresses in this basic studies will be expected to realize advanced high-power adsorbents for tritium recovery systems in a future D-T burning reactor.
- (d) Atmospheric tritium recovery system  
Recovery of released tritium gas in working area is a major safety system. The conventional tritium recovery process is to oxidize the tritium to water with catalyst and to dehumidify with dry absorber. To develop more compact and cost-effective system, the collaborating development on the polymer membrane type dehumidifier has been carried out with Shizuoka University. Promising experimental results will be expected to realize advanced tritium recovery systems in the DD experiment of LHD. The detailed performance analyses have been carried out for the optimum design of the actual dehumidifier.

As for a candidate blanket system, molten salt Flibe liquid blanket, that is using compound of LiF and BeF<sub>2</sub> is selected. It has inherent safety features like low tritium inventory, self cooling effect and low chemical activity. But the Flibe contains Beryllium, which is known as poisonous material and it causes occupational health hazard. To prevent the acute and chronic health hazard, safety handling technology must be accomplished. The Flibe safety handling study has been performed and reported as the collaboration project with US-Japan.

(Asakura, Y.)



## §1. Studies of Interaction between Cooling Pipe Materials and Tritium, and Their Chemical Behaviors

Oya, Y. (Radioisotope Center, Univ. of Tokyo),  
Oyaidzu, M., Yoshikawa, A., Miyauchi, H.,  
Nakahata, T.,  
Okuno, K. (Shizuoka Univ.),  
Tanaka, S. (Univ. of Tokyo),  
Kawano, T., Asakura, Y., Uda, T.

### i) Introduction

Stainless Steel (SS-304 [1], 316 etc) is expected to be used in fusion reactors as various component materials like cooling pipe because of its good mechanical properties and corrosion resistance. The elucidation of tritium behavior in SS and its interaction are important issues for the safety evaluation of DD experiment in LHD. In especially, the tritium retention and desorption behaviors are largely influenced on the chemical states of tritium on the SS surface. However, the chemical behaviors of hydrogen isotopes with various adsorption/absorption have not been well studied. In the present study, the typical material for components, SS-316, was chosen as specimen and tritium retention behavior in SS was evaluated.

### ii) Experimental

The SS-316 sample with size of  $10 \times 10 \times 1 \text{ mm}^3$  was used. Two kinds of sample with different surface finish, namely the non-pretreated sample and pretreated sample by mechanical polish and annealing at 1273 K in vacuum for 30 minutes to remove surface oxide layers, have prepared. For these samples,  $\text{D}_2$  or  $\text{D}_2\text{O}$  was sorbed on/in the sample by various methods, such as water adsorption, ion irradiation and electrolysis. In the water adsorption, the sample was immersed in heavy water for 30 min. In the electrolysis experiment, the sample was used as a cathode for 60 min with the current of 0.1A. For deuterium ion irradiation, the 4.0 keV  $\text{D}_2^+$  ion was implanted into the sample with the flux of  $5.1 \times 10^{18} \text{ D}^+ \text{ m}^{-2} \text{ s}^{-1}$  up to the fluence of  $2.04 \times 10^{22} \text{ D}^+ \text{ m}^{-2}$ . The chemical states of iron, chromium, nickel, molybdenum, carbon and oxygen on the SS-316 specimen were evaluated by X-ray photoelectron spectroscopy (XPS). The thermal desorption spectroscopy (TDS) was also applied to the evaluation of the desorption behavior of hydrogen isotopes from the stainless steel. The heating rate was set to 30 K/min from room temperature to 1273K.

### iii) Results and discussion

According to the previous study<sup>1)</sup>, it was found that the oxyhydroxides, namely  $\text{FeOOD}$  or  $\text{CrOOD}$ , were formed on the

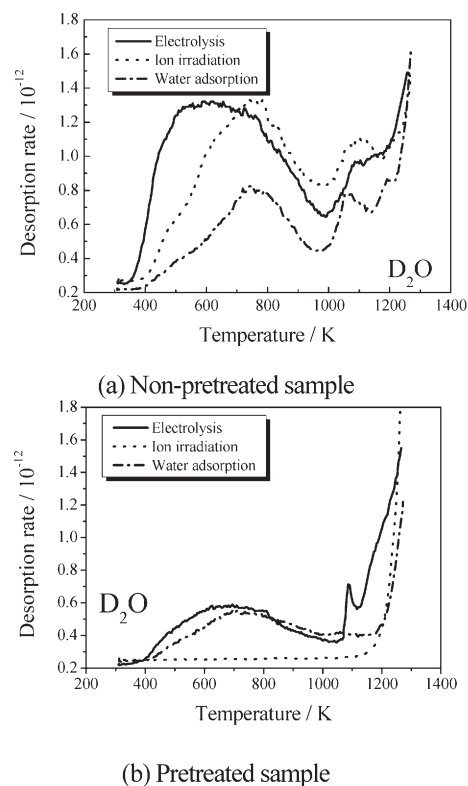


Fig.1 The  $\text{D}_2\text{O}$  TDS spectra for SS-316 sample after various treatments

surface of the sample after electrolysis according to the XPS results. The thickness of the oxide layer for the sample after electrolysis was thicker than that after water adsorption. Fig.1 shows the  $\text{D}_2\text{O}$  TDS spectra after various treatments. The reduction of  $\text{D}_2\text{O}$  was observed for the pretreated samples, which indicate that the surface oxide layer retains large amount of deuterium. The oxyhydroxide layer was almost removed by pretreatment. These facts show that the reduction of oxide layer formation and/or removal of oxyhydroxide layer after tritium exposure will be important to reduce tritium retention in SS. In future, the effective tritium removal technique will be developed.

### iv) Conclusion

The chemical forms of hydrogen isotopes on/in SS-316 were studied by XPS and their desorption behavior was evaluated by TDS. It was found that the deuterium desorption stages consisted of three stages. Most of deuterium would be retained in the oxide layer on the surface and it concluded that the reduction of oxide layer formation and/or removal of oxyhydroxide layer after tritium exposure will be important to reduce tritium retention in SS.

### References

- 1) Oya, Y. et al., Fusion Sci. & Tech., **44** (2003) 359.

## §2. Advancement of Water-Hydrogen Chemical Exchange Apparatus by Introducing Trickle Bed Reactor

Yamamoto, I., Enokida, Y., Sawada, K. (Nagoya Univ.),  
Uda, T., Asakura, Y., Sugiyama, T.

Experimental studies on hydrogen isotope separation by a Combined Electrolysis Catalytic Exchange (CECE) have been carried out in order to apply it to the system of water detritiation for fusion reactors.

In order to improve the separative performance of the CECE process we compared the separative performances of two types of packed bed. One was the layered bed where layers of Kogel catalysts and that of Dixon gauze rings were filled in the column alternately. The other was the homogeneous bed where Kogel catalysts and Dixon gauze rings were mixed and filled in the column homogeneously. The conclusion was that the homogeneous bed was more efficient than the layered bed.

The purpose of the present study is to investigate the optimal quantity of the catalyst in the homogeneous bed.

### i) Experiments

The reactor column is a Pyrex glass tube with 25 mm internal diameter and 60 cm length. The column is filled with Kogel catalysts (1.0 wt% Pt deposited) and Dixon gauze rings. These packings are shown in Fig. 1. The catalyst packed-ratio is defined as follows.

$$\text{Catalyst packed - ratio} = \frac{\text{Grain volume of the catalyst}}{\text{Grain volume of all the packings}}$$

Grain volumes mean the volume of sphere with average diameter of the Kogel catalyst and the volume of cylinder which has the outer shape same as a Dixon gauze ring.

Hydrogen-deuterium isotope separation with the CECE equipment was performed at 101 kPa, 343 K for various values of the catalyst packed-ratio. Flow rates of fluids in the column were 8 L/min for hydrogen gas, 2.5 g/min for water vapor and 6.5 g/min for liquid water. The concentrations of HD or HDO in gas and liquid samples were measured using a stable isotope ratio mass spectrometer (MAT252, Thermo Finnigan) with a relative accuracy to 1 %.

### ii) Separation factors of the packed beds

Separation factor of the water phase  $\alpha$  and that of the hydrogen gas phase  $\beta$  are defined as follows with the molar concentration of deuterated molecule  $C$  and the molar flow

ratio  $F$ :

$$\alpha = C_{(\text{Feed})} / C_{(\text{Extracted water})}, \quad \beta = C_{(\text{Extracted hydrogen gas})} / C_{(\text{Feed})},$$

$$C_{(\text{Feed})} = \frac{F_{(\text{Feed water})} C_{(\text{Feed water})} + F_{(\text{Feed hydrogen gas})} C_{(\text{Feed hydrogen gas})}}{F_{(\text{Feed water})} + F_{(\text{Feed hydrogen gas})}}$$

Calculated separation factors are plotted against catalyst packed-ratio in Fig. 2. It is very clear from the figure that both separation factors have peaks in their values around 30 % of catalyst packed-ratio. We set the catalyst packed-ratio at 13 % in the previous experiments. Separative performance is then remarkably improved by increasing the catalyst packed-ratio to 30 %.

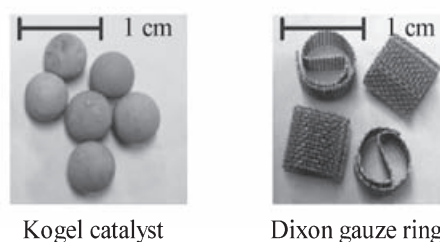


Fig. 1: Packings filled in the reactor column

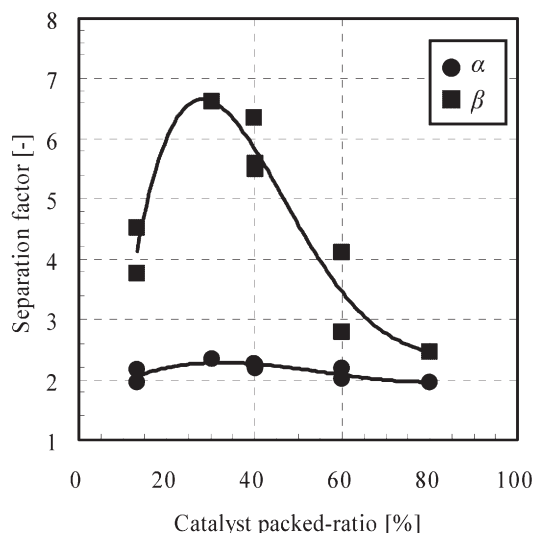


Fig. 2: Separation factors of the homogeneous bed for various catalyst packed-ratios

### Reference

- 1) Sugiyama, T., Asakura, Y., Uda, T. *et al.*: *Fusion Sci. Technol.*, 48 [1], pp. 132-135 (2005).
- 2) Sugiyama, T., Asakura, Y., Uda, T. *et al.*: *ISFNT-7*, P1-33, Tokyo, May (2005).
- 3) Sugiyama, T. *et al.*: *Proc. AESJ Fall Meeting 2005* (in Japanese), K20, Aomori, September (2005).
- 4) Sugiyama, T., Asakura, Y., Uda, T. *et al.*: *Fusion Eng. Design*, 81, pp. 833-838 (2006).
- 5) Ushida, A. *et al.*: *Proc. AESJ Spring Meeting 2006* (in Japanese), D37, Ibaraki, March (2006).

### §3. Development of Advanced Catalyst for Isotope Exchange Reaction Quantification of Reaction Rate

Munakata, K., Shinozaki, T. (Interdisciplinary Graduate School of Engineering Sciences Kyushu University),  
Asakura, Y., Uda, T. (National Institute for Fusion Science),  
Sugiyama, K. (Nagoya University)

The isotope separation by chemical exchange is an indispensable process, which is used for the treatment of tritiated water generated in heavy water reactors. In fusion power plants, which are now under development, the treatment of tritiated water is required as well, and thus the establishment of the chemical exchange process is necessary. In the chemical exchange process, the catalyst, which promotes the isotope exchange reaction, plays a key role. Therefore, catalysts with advanced performance need to be developed. Diversified processes would be placed in the limited space of fusion power plants. The development of the catalysts with advanced performance could lead to higher operation efficiency and decreased volume of the chemical exchange process. In this work, an experimental apparatus used for measurement of the isotope exchange reaction rate was prepared, and the performance of the Pt/Kogel catalyst, which is generally used in the chemical exchange process, was examined.

In the experiments, a reactor made of quartz was used. The temperature of the reactor was changed in the range of 20 K to 373 K. The argon gas containing hydrogen and heavy water vapor was introduced to the reactor. The concentrations of hydrogen and heavy water vapor at inlet and outlet stream of the reactor were measured with a mass spectrometer. The flow rates were controlled with conventional mass flow controllers.

Figure 1 shows the conversion ratio of deuterium atom from heavy water to  $D_2$  when the argon gas containing hydrogen of 4900 ppm and heavy water vapor of 5300 ppm was introduced to the reactor charged with the 0.46 g of Pt/Kogel catalyst. Detailed experimental conditions are summarized in the figure. As seen in the figure, the temperature dependence of conversion ratio is small, which is almost 35 % in the whole temperature range. Since isotope ratio of  $D_2O$  and  $H_2$  in the argon gas introduced to the reactor, the conversion ratio is expected to be 50 % if the exchange reaction rate is very fast and it reaches equilibrium. However, the conversion ratio obtained in the experiment is lower than the value. Therefore, the experimental condition used in the experiment is thought to be appropriate for the quantification of the exchange reaction rate. Experiments with different conditions in terms of concentration of hydrogen isotopes, gas flow rate and amount of catalyst are planned to be carried out to quantify the exchange reaction rate.

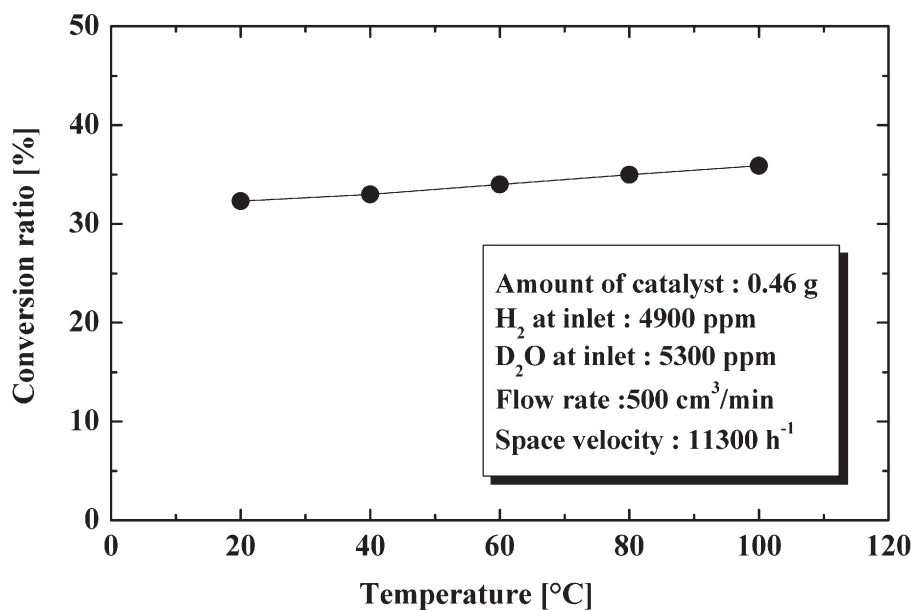


Fig. 1 Conversion ratio of deuterium over Pt/Kogel catalyst

#### §4. Development of High-Power Adsorbents for Hydrogen Isotope Separation by Pressure Swing Adsorption Method

Kotoh, K., Kudo, K. (Kyushu Univ. Eng.),  
Nishida, T. (Kinki Univ. Ind. Eng.),  
Sugiyama, T., Asakura, Y., Uda, T., Kawano, T.

A process of hydrogen isotope separation is necessary in the environmental safety treatment of exhaust gases from LHD deuterium experiments. We have attempted to develop a pressure swing adsorption (PSA) process, using a general adsorbent such as synthetic zeolite 5A, for hydrogen isotope separation. In the last fiscal year, we began to research and develop adsorbents suitable to the PSA process for hydrogen isotope separation, aiming at improving its performance. In this work program, a volumetric adsorption apparatus was made to investigate the characteristics of adsorptive function of candidate materials. On the other hand, we proposed theoretical model equations for describing multi-component adsorption behavior of hydrogen isotopes on zeolites, based on chemical thermo-dynamics. The theoretical expression was verified with experimental results.

In this fiscal year a work was to calibrate the volumetric adsorption test device for determining correct values from observed pressures affected by a system effect. In this test device, thermal transpiration occurs. Pressures measured by the gage attached to one gas container at high temperature are not equivalent to those in the other gas container at low temperature. The effect of thermal transpiration depends on the ratio of the mean-free-path of gas molecules  $\lambda$  resulting in gas density to the inner diameter of a pipe connecting two containers  $d_p$ . This device has a connection pipe with an inner diameter of  $\phi$  15.6 mm. From the experiment with He, H<sub>2</sub> and D<sub>2</sub>, we derived an equation to calibrate the system effect of thermal transpiration, as follows:

$$\Phi = \frac{1 - (P_{cold}/P_{hot})}{1 - \sqrt{T_{cold}/T_{hot}}} \quad (1)$$

$$\Phi = c \left[ 1 - \int_{-\infty}^{\mu_x} \exp \left\{ -\frac{(\mu - \bar{\mu})^2}{2\sigma^2} \right\} d\mu \right] \quad (2)$$

where  $\mu = \log(P_{hot} d_p)$ .

The thermal transpiration factor  $\Phi$  can be shown by an error-functional expression. In Eq.(2),  $c$  is a coefficient indicating the non-ideality of molecular reflection on a pipe wall surface, and  $\bar{\mu}$  and  $\sigma$  are respectively the mean and the deviation of the Gaussian distribution.

Experimental results and characteristic curves are shown in Fig. 1. Coefficient values and deviation values among He, H<sub>2</sub> and D<sub>2</sub> are respectively agreeable, those are  $c = 0.9005$ ,  $\sigma = 0.5583$ . Values of the mean are also agreeable between hydrogen isotopes H<sub>2</sub> and D<sub>2</sub>:  $\bar{\mu}_{H_2}, \bar{\mu}_{D_2} = -1.533$ . The mean for He  $\bar{\mu}_{He}$  is -1.336. The difference  $\Delta\bar{\mu}_{He/H_2} = \bar{\mu}_{He} - \bar{\mu}_{H_2}$

can be related to the logarithm of the molecular mean-free-path ratio,  $\log(\lambda_{He}/\lambda_{H_2})$ . A value of 1.574 was obtained for  $\lambda_{He}/\lambda_{H_2}$  and  $\lambda_{He}/\lambda_{D_2}$ . This value may be adoptable for the other hydrogen isotopes. Hence, the system effect on tritium became predictable. The characteristic curves of  $\Phi$  shown here are also available for another system using a different size pipe.

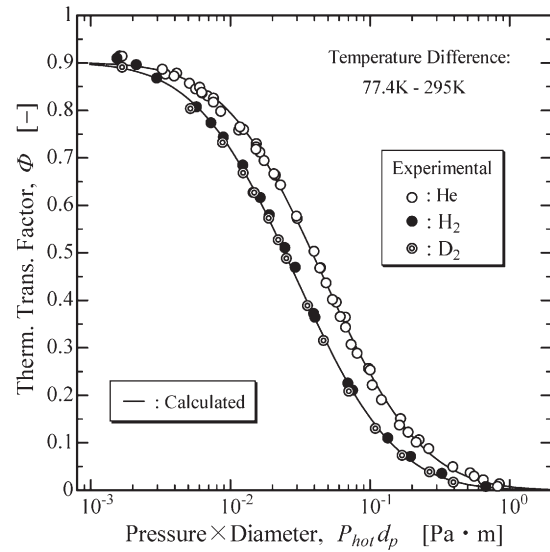


Fig. 1 Thermal Transpiration Factor with respect to Hot Pressure times Pipe inner Diameter.

The other work in this fiscal year was to develop materials having the adsorptive functions advantageous to the PSA operation, such as to exhibit a stepwise profiling isotherm for hydrogen. We have taken note of the crystal lattice structure of cobalt tris-ethylenediamine [Co(en)<sub>3</sub>]Cl<sub>3</sub> having homogeneous pore channels of  $\phi$  0.6 nm, because this type pores may show stepwise-shaped adsorption isotherms. In this work program, a fine crystal sample of [Co(en)<sub>3</sub>]Cl<sub>3</sub> was prepared, and then, the amount of hydrogen isotopes able to be adsorbed on this sample was measured by the method using the volumetric adsorption apparatus. A result so far is that the amounts adsorbed at 77.4 K around a pressure of 17 kPa are indicated as 1/3 times of those on synthetic zeolites. Treatment of the candidate sample is not easy because this complex compound is decayed by heating at a temperature higher than around 400 K. The investigation of functional materials is to be continued.

#### References

- 1) Kotoh, K., Kudo, K., *Fusion Sci. Technol.*, 48 [1], pp. 148-151 (2005)
- 2) Sugiyama, T., *et al.*, *Fusion Sci. Technol.*, 48 [1], pp. 163-166 (2005)
- 3) Kotoh, K., Kudo, K., *J. of Soc. of Isotope Sci.*, 1, pp.28-32 (2005)
- 4) Kotoh, K., Kudo, K., *19<sup>th</sup> Annual Meeting of Jpn Soc. on Adsorption*, 2-17, Kyoto, September, (2005)
- 5) Kotoh, K., Kudo, K., *Meeting on Isotope Sci.*, Nagoya Univ. COE, Nagoya, March, (2006)



## §5. Study on Polymer Membrane Type Dehumidifier for Tritium Removal

Okuno, K., Oya, Y., Oyaidzu, M., Yoshikawa, A. (Fac. of Sci., Shizuoka Univ.),  
Asakura, Y.

### 1) Introduction

In future DD experiments for LHD, it is important to establish the removal technique of tritium produced in vacuum vessel by DD reaction. In this collaborative study, the acquirement of dehumidify characteristics for a membrane type dehumidifier and theoretical study was done for achievement of high performance dehumidify compared to molecular sieve method. Simulation study using perfect mixture model performed in the last fiscal year was performed. However, the simulative and experimental estimations of the water recovery ratio from the membrane could not be agreed with each other. Therefore, in this fiscal year, critical factor of this disagreement was considered and analyses using alternative simulation were attempted and discussed.

### 2) Model

There are many simulation models proposed for analyzing gas separation behavior using a membrane type dehumidifier. It is well known that the combination of counter-flow and cross-flow model is the most ideal model. However, some specific parameters related to membrane are required and some of them are hard to determine. To avoid these problems, we adopted the model of two component mixture gases. Fig. 1 shows schematic drawing of gas stream inside of a membrane module. In this figure,  $F_f$  [mol/s] is supply mixture gas flow rate, and  $x_f$ ,  $x_0$  and  $x_p$

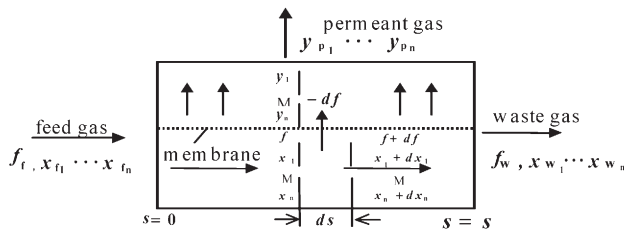


Fig.1 Schematic drawing of membrane module for the model.

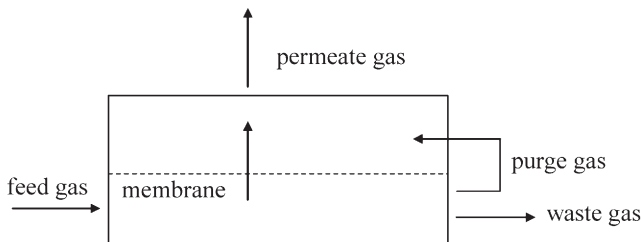


Fig.2 Schematic drawing of membrane module in NIFS.

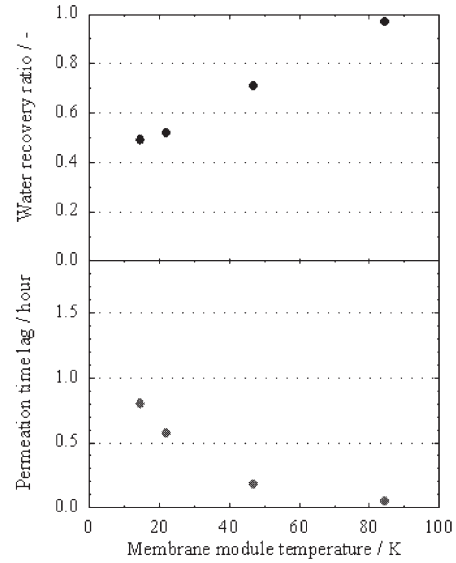


Fig.3 Dependence of water permeation on membrane module temperature.

are, respectively, mole fraction of inlet, high pressure outlet and low pressure outlet gas stream of each component. The gas component for outlet side was expressed by the

$$y_p = \frac{(\alpha - 1)(\phi + x_f) + 1 - \sqrt{\{(\alpha - 1)(\phi + x_f) + 1\}^2 - 4\phi(\alpha - 1)\alpha x_f}}{2\phi(\alpha - 1)}$$

following equation,

In this equation,  $\phi$  is an operation factor, and explained in the following equation;

$$\phi = \gamma + \theta - \gamma\theta,$$

where,  $\theta$  is a cut rate and  $\gamma$  is a pressure ratio. And  $\alpha$  is ideal separation factor of gas described by the ratio of permeation factors. On the other hand, the membrane module studied in NIFS could not be described as Fig. 1 but Fig.2: a part of feed-through gas was introduced into permeant gas as purge gas.

### 3) Results and discussion

The effects of the temperature of membrane module and cut rate on the membrane dehumidifier in NIFS were estimated and discussed using this model. Fig.3 shows the experimental results of recovery ratio and time lag from feed to permeate as a function of temperature obtained from the same membrane type as that in NIFS. However, the cut rate in this model was quite different from that in NIFS, since the flow rate of purge gas was taken account to the latter. More than 99% of water recovery ratio was achieved by the membrane module in NIFS, while approximately 50% was done by that in Shizuoka University. This would be mainly reasoned by the increase of permeation rate on the membrane surface of the lower pressure side due to the introduction of purge gas into the lower pressure side. Therefore, taking the effects of purge gas into consideration, alternative analyses with considering the module temperature dependence will be studied in the future works.

### 3. CHS Experiments

CHS experiment program has been completed at the end of Japanese fiscal year 2005. In the first phase of the program in the Nagoya university site starting at 1988, CHS had been leading Japanese stellarator program owing to its modern diagnostics and the flexible magnetic configuration control. In the second phase in Toki site, the program focused on more fundamental research of toroidal confinement physics in cooperation with LHD experiment which has started at 1998. This annual report describes the experimental results from the last year of CHS program.

A big advantage of stellarator confinement to tokamak is a potentiality of stable high density operation. It is a common understanding that a good program of fueling or the neutral particle control is important to obtain a good confinement of a high density plasma. In CHS, the reheat mode with a gas puffing control is a basic operation technique to obtain the maximum energy and the density limit because the pellet injection was not successful for the high density operation in CHS due to the small plasma volume. The largest energy record in CHS was obtained in 2005 in the reheat mode using two NBIs with both co-injection and a full magnetic field operation.

Because the conventional ECH does not work on high density plasmas above the cut-off density, a new ECH scenario with the mode conversion to the static electron Bernstein wave was investigated in CHS. A clear evidence of the O-X-B heating was confirmed for high density NBI plasmas with full launching controls of microwave direction and polarization.

H-mode (in other word, Edge Transport Barrier formation) in CHS had been studied mostly for 0.95 T operation and the effect of the plasma position control (Rax control) was investigated. Last year, the operation range of H-mode was extended to the high magnetic field and high plasma density. A combination of ETB and the reheat mode gave the simultaneous increase of the edge electron density and temperature for high density plasma together with an improvement of the global confinement.

Evolutions of various physical quantities have been measured for the ETB transition such as the charge exchange (CX) ion flow measurements for the electric field (using carbons), edge temperature, density and potential measurements by probes, VUV emissions from various impurities, local density and fluctuation measurement by the beam emission spectroscopy (BES) and the fluctuation measurements by HCN laser scattering methods. CX measurements show the increase of ExB flow at the transition with an improved spatial resolution. Possibility of non-uniform structure of plasma parameters and the electric field has been suggested by the probe measurements at two different toroidal positions. BES shows the edge harmonic

oscillations (EHO) during H-phase and the relation between the EHO and the density gradient evolution at the plasma edge. The mode structure and the phase relations were also measured.

The ITB (Internal Transport Barrier) in CHS has an advanced characteristic of confinement improvement for both electrons and ions, which has not been observed in any other stellarators. Profile measurements of both species had indicated that the locations of transport barriers are different. A new diagnostics of ion temperature gradient measurement using the modulation charge exchange spectroscopy clearly located the enhanced ion temperature gradient region (transport barrier) that is different from the electron transport barrier position.

The fluctuation measurements using two heavy ion beam probe systems (duo HIBP) in CHS has made a progress in the zonal flow physics study and the continuous improvements of more reliable analysis of profile measurements. Through the precise FFT analysis of large amount of data, power spectra of density, potential and electric field fluctuations were obtained which have characteristics of the geodesic acoustic mode (GAM). Coherence analyses between two HIBP signals at different toroidal positions showed correlation length of these modes.

Since the HIBP uses particle beams passing through plasmas, the attenuation effect (continuous level and fluctuation part) of a beam is added to the local density and fluctuation information. Mathematical techniques of reconstruction of profiles separating these path integral parts have been developed for the static density profile and the density fluctuation profile measurements. A new operation of HIBP with rubidium ion beam (instead of cesium) was successful for higher density plasmas. Internal profile structures of MHD modes were measured with this technique for the study of fast ion loss mechanism with energetic ion driven MHD modes.

The interactions of fast ions and MHD modes have been studied in CHS especially for Alfvén eigenmodes and energetic particle modes. New diagnostics were developed to obtain quantitative measurements of fast ion loss. First one is a lost ion probe using thin Faraday films, which detects direct electric current of lost ions. Another one is calorimetric probe to measure the heat deposition (on the probe) of fast ions, giving the radial distribution of fast ions.

Plasmas produced with 2.45 GHz microwave ( $P_{ECH} < 20$  kW) in low magnetic field (613 G) were investigated from the aspect of the dimensional similarity. Plasmas with the density higher than the cut-off density of microwave were obtained and the mode conversion to the electron Bernstein wave was considered as the candidate mechanism. Density fluctuation spectra were analyzed.

(Okamura, S.)

## §1. Reheat Mode Discharges in Search of Attainable High Stored Energy of CHS

Isobe, M., Yoshimura, Y., Nagaoka, K., Akiyama, T., Minami, T., Suzuki, C., Okamura, S. (NIFS)

The significant increment of plasma stored energy has been observed in the NB-heated high density plasmas of CHS after intense gas puffing is terminated. This is called the 'reheat mode'. In CHS, a high-beta plasma having a volume-averaged beta value of 2.1 % so far has been obtained in a low toroidal magnetic field strength with the help of the reheat mode[1]. In order to bring out the maximum performance of CHS while exploring the improved confinement regime in high density operation, a reheat mode experiment is being conducted under the maximum NB heating power and the highest toroidal magnetic field strength. This article reports the recent results on reheat mode discharges to attain high stored energy and density limit of CHS.

Figure 1 shows the typical time evolution of a reheat mode discharge of CHS. This discharge was obtained in an inward shifted configuration having  $R_{ax}$  of 0.921 m and  $B_t$  of 1.76 T. Two NBs were tangentially co-injected in this shot to heat target plasmas as efficient as possible. The total port-through power  $P_{nb-port}$  was 1.64 MW. It is seen that the evolution of  $W_p$  tends to saturate as the line-averaged  $n_e$  increases in the gas puffing phase and begins to drop when  $n_e$  exceeds about  $8.0 \times 10^{19} \text{ m}^{-3}$ . This indicates degradation of confinement with increase of  $n_e$ . After the gas puffing is turned off at  $t=105 \text{ ms}$ ,  $P_{rad}$  is significantly suppressed and  $W_p$  begins to increase, going up to 6.4 kJ in this shot although  $n_e$  gradually decreases in time. One of the remarkable differences between the gas puffing and the reheat phases is in the  $n_e$  profile. The Thomson scattering diagnostic shows excessively hollowed  $n_e$  profile in the gas puffing phase because of intense gas fueling from the outside of the plasma while  $n_e$  profile is relatively peaked in the reheat phase. Stored energies of kinetic electron  $W_e$  evaluated from the radial profiles of  $T_e$  and  $n_e$  are plotted in Figure 1(b). The evaluated  $W_e$  is roughly half of  $W_p$  measured with a diamagnetic loop. The trend of  $W_e$  as a function of  $n_e$  agrees well with that of  $W_p$ .

Figure 2 shows  $W_p$  as a function of  $n_e$  in the high  $B_t$  operation for two different configurations, i.e.  $R_{ax}=0.921 \text{ m}$  and  $0.949 \text{ m}$ . The data points represented by the crosses are taken from discharges with gas-puff fueling.  $W_p$  linearly increases in the low  $n_e$  region ( $n_e < 3.0 \times 10^{19} \text{ m}^{-3}$ ) and saturates gradually as  $n_e$  increases. Finally, it begins to drop once  $n_e$  reaches a critical value. Critical  $n_e$  in drop of  $W_p$  during the gas puffing phase is about  $(8\sim 9) \times 10^{19} \text{ m}^{-3}$  for both configurations. The increase of  $W_p$  resulting from the reheat phenomena takes place at  $n_e \sim 9 \times 10^{19} \text{ m}^{-3}$ . In the configuration having  $R_{ax}$  of 0.949 m, with a help of the reheat mode,  $W_p$  goes up to 9.4 kJ, which is the highest value of CHS as of March, 2006. In the configuration with  $R_{ax}=0.921 \text{ m}$ , the maximum  $W_p$  of 6.6 kJ has been obtained. The experimental stored energies were

compared with stored energies predicted from the international stellarator scaling law (ISS04), represented by solid line in Figure 2. The dotted lines correspond to dispersion of data sets of CHS treated in the ISS04 scaling law[2]. It should be noted that the predicted stored energies are calculated by use of  $\tau_E^{ISS04, CHS} (= \tau_E^{ISS04} \cdot f_{ren})$  where  $f_{ren}$  is a renormalization factor, i.e.  $0.43 \pm 0.08$  for CHS. The values of experimental  $W_p$  and its trend with the increase of  $n_e$  basically agree with those predicted from the ISS04 law in the density region less than  $8 \times 10^{19} \text{ m}^{-3}$ . However, the experimental  $W_p$  goes down apart from the ISS04 prediction in the high  $n_e$  region more than  $8 \times 10^{19} \text{ m}^{-3}$  during gas puffing phase. The stored energies are recovered by the reheat mode and the mode pushes up them over the ISS04 prediction in the high  $n_e$  region.

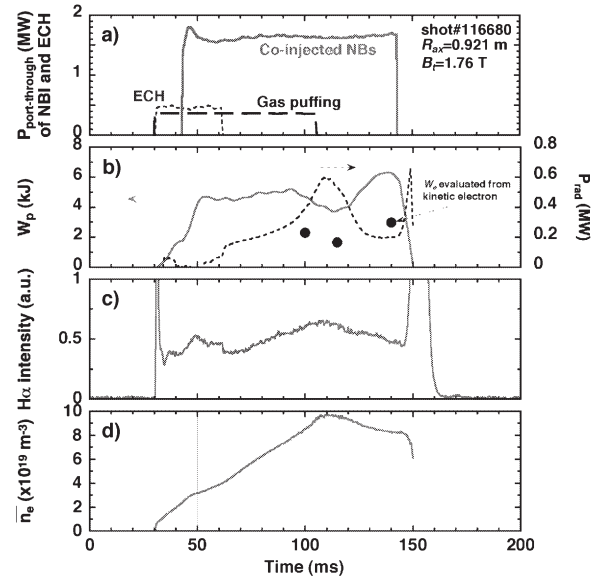


Figure 1 Typical waveforms of the reheat discharge in CHS ( $B_t/R_{ax}=1.76 \text{ T}/92.1 \text{ cm}$ ).  $P_{nb-port}$  was 1.64 MW.

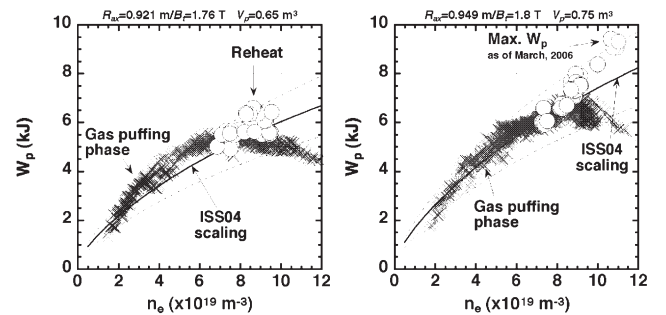


Figure 2 Stored energies as a function of  $n_e$  in the high field operation for two different configurations.  $P_{nb-port}$  was  $\sim 1.6 \text{ MW}$ . Solid lines represent stored energies predicted by the ISS04 renormalized by a factor for CHS. The dotted lines correspond to dispersion of data sets of CHS treated in the ISS04 scaling law.

### References

- [1] Okamura, S. *et al.*, Nuclear Fusion **35**, (1995)283.
- [2] Yamada, H. *et al.*, Nuclear Fusion **45**, (2005)1684.



## §2. Observation of Overdense Plasma Heating by ECH Due to O-X-B Mode Conversion in CHS

Yoshimura, Y., Nagasaki, K. (Kyoto Univ.), Akiyama, T., Isobe, M., Shimizu, A., Suzuki, C., Takahashi, C., Nagaoka, K., Nishimura, S., Minami, T., Matsuoka, K., Okamura, S., CHS Group, Kubo, S., Shimozuma, T., Igami, H., Notake, T., Mutoh, T.

Electron Bernstein wave heating via an Ordinary – extraordinary – Bernstein (O-X-B) mode conversion process has been tried in CHS using a 54.5 GHz ECH system which is equipped with a 2-D steerable beam injection mirror antenna. The EC-wave power of 415 kW was obliquely injected in the toroidal direction twice during a discharge. The first one was for plasma generation, and the second one was applied to high-density plasmas sustained with 860 kW neutral beam injection (NBI). The magnetic field on the magnetic axis was set at 1.9 T, slightly below the resonant magnetic field 1.95 T. Figure 1 shows a typical time evolution of O-X-B heating. Here, the O-mode cut-off density for the 54.5 GHz waves is  $3.8 \times 10^{19} / \text{m}^3$ . A clear increase in the plasma stored energy of more than 30 % was observed by the second EC-wave power, and the stored energy was kept high until the end of the EC-wave application. On these discharges, intensive gas-puffing was continuously applied, resulting in the monotonous increases of the density. At the end of the second EC-wave application, the density reached over  $8 \times 10^{19} / \text{m}^3$ . Without the EC-wave application after 112 ms, the NBI power could not sustain this high-density plasma, and the radiation collapse occurred. During the second EC-wave application, the radiation power from the plasma was reduced probably due to the suppression of radiation losses at the peripheral region by slightly increasing or keeping the electron temperature all over the plasmas, and/or a reduction of accumulation of impurities.

By scanning the EC-wave beam direction, the leakage EC-wave power from the CHS vacuum vessel varied systematically as seen in Fig. 2. The leakage power level is considered as a measure of mode conversion and/or power absorption efficiency. The toroidal angle  $\theta_{\text{tor}}$  scan was performed by keeping the radial beam position at the equatorial plane fixed at  $R = 92.1$  cm where the magnetic axis was set. Here both the beam steering mirror and the detector for leakage power measurement were set at the poloidal cross section of  $\theta_{\text{tor}} = 0$  deg. Beam direction scanning in the radial direction also resulted in the variation of leakage power having a minimum. Around the beam direction where the leakage power reached the minimum, the stored energy showed evident increases. The increments of the stored energy are also plotted in Fig. 2. Among the 4 variations (left-hand and right-hand circular, two orthogonal directions of linear) in polarization with the beam direction optimized, the left-hand circular polarization which is supposed to contain a high fraction of O-mode showed the best performance. The discharge

shown in Fig. 1 was performed with the optimized beam direction ( $\theta_{\text{tor}} = -9$  deg. and  $R = 92.1$  cm) and the left-hand circular polarization.

No heating effect was observed for normal beam injections ( $k_{\parallel} = 0$  with  $\theta_{\text{tor}} = 0$ ) with O-mode aiming at the fundamental resonance heating layer at the plasma peripheral region where the density was less than the cut-off. Therefore, the significant increase in the stored energy observed with oblique incidences should be attributed to the O-X-B heating at the core plasma region and the resultant decrease in the radiation losses, not to the cyclotron resonance heating at the peripheral region. Theoretical investigations on power deposition of the O-X-B heating under the experimental conditions are now underway.

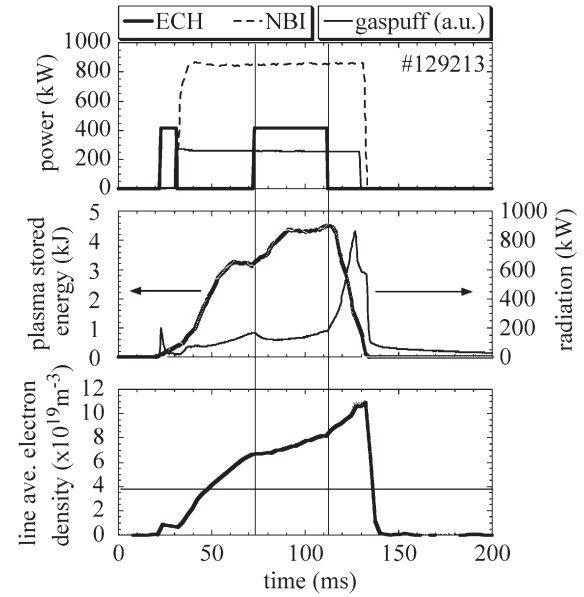


Fig. 1. Time traces of a discharge of O-X-B heating. A horizontal thin line on the bottom column denotes the cut-off electron density for the waves of frequency 54.5 GHz.

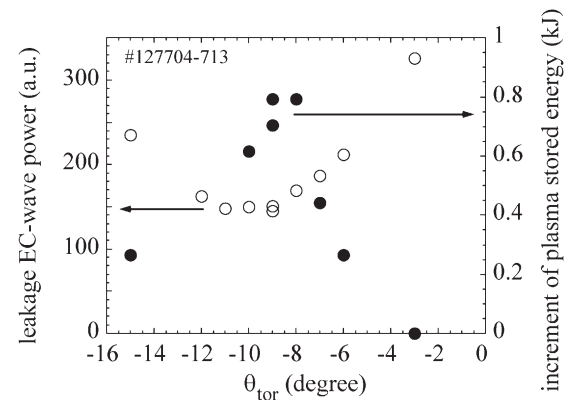


Fig. 2. Variations of leakage power of EC-waves from the CHS vacuum vessel and the maximum increment of plasma stored energy during the second EC-wave application as functions of the EC-wave beam injection direction. The leakage power was averaged over the period of the second EC-wave application.



### §3. First Observation of High Density Edge Transport Barrier Formation during Reheat Mode of Helical Plasma on CHS

Minami, T., Akiyama, T., Okamura, S., Isobe, M.

A reheat mode and an edge transport barrier (ETB) are improved confinement modes that have been observed on CHS. The reheat mode is initiated by shutting off fueling with stopping gas-puff[1, 2]. The electron temperature in the peripheral region is raised up resulting from suppression of neutral particle density causing the charge exchange loss. However, the reheat mode has a problem: the peripheral density continues to decrease after the gas-puff stopping. Meanwhile, the ETB mode on CHS has a problem that the edge temperature decrease by large density increase in the peripheral region, then the confinement improvement is degraded. This paper is the first report for the observation of the confinement improvement in high density range by the simultaneous achievements of both the reheat mode and the ETB. This mode provides the good confinement improvement, because the temperature and density in the peripheral region increase simultaneously.

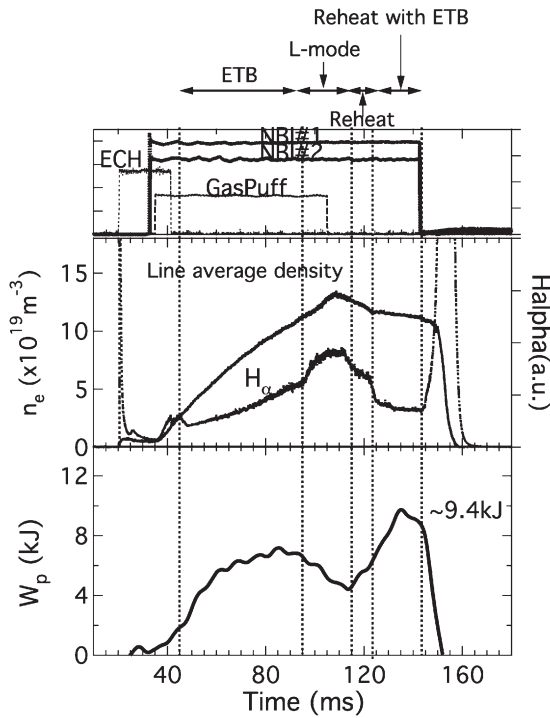


Fig. 1: Global behavior of ETB plasma during reheat mode: line average density,  $H_\alpha$  signal, and the stored energy  $W_p$  are plotted with the injection timings of NBI and ECH heatings.

Figure 1 shows a global behavior of the reheat mode discharge with the ETB. Although the high field strength ( $B_T = 1.86T$ ) is favorable for the reheat mode, the formation of the ETB under high magnetic field condition is difficult, because

NBI power threshold of the ETB formation depends on the magnetic field strength[3]. When the field strength increases, the NBI power threshold becomes larger. When the vacuum magnetic axis location ( $R_{ax}$ ) shifts outwards, the threshold NBI power decreases. Accordingly, the experiment is carried out for the magnetic configuration of  $R_{ax}=94.9$  cm, which is larger than that of the standard configuration ( $R_{ax}=92.1$  cm).

As shown in Fig. 1, the two co-NBIs (total power is 1.6 MW) are injected to the target plasma that is produced by the 54.5 GHz gyrotron. The ETB is formed below an upper density limit that is related to the NBI power threshold: the power threshold is determined by the heating power normalized with the electron density ( $P/n_e$ ) [3]. On the other hand, because the higher plasma density is required for a good reheat mode, the plasma density is increased by a gas-puffing until the ETB formation disappears once.

As shown in Fig. 1, the initial ETB mode is formed at 45 ms, then the ETB disappeared and the plasma returns to the L-mode again at 95 ms resulting from the electron density exceeding the upper limit. The plasma density, as shown in the middle of the Fig. 1, decreased after the gas-puff stopping at 105ms. The onset of the reheat mode is denoted by the plasma stored energy increase from 115 ms due to the temperature increase in the peripheral region. When the density decreased below the upper limit, the density reduction was suppressed due to the reformation of the ETB (123 ms) during the reheat mode. As a result, the stored energy increased up to  $\sim 9.4$ kJ.

In conclusion, improved confinement mode with reheat and edge transport barrier is observed on CHS. This mode provides good improved confinement in high density region ( $\bar{n}_e \sim 1.2 \times 10^{20} m^{-3}$ ) due to the temperature rising with keeping high density in peripheral region.

## References

- [1] S. Morita, et al., Proc. 14th Int. Conf. Plasma Physics and Controlled Nuclear Fusion Research, Würzburg, Germany, 1992,
- [2] M.Isobe, et al., Fusion Science and Technology Vol.50 (2006)
- [3] T.minami, et.al., Plasma and Fusion Research Vol.1, 032 (2006)

#### §4. Confinement of High Density Edge Transport Barrier during Reheat Mode on CHS

Minami, T., Akiyama, T., Okamura, S., Isobe, M.

This paper describes a characteristic of a plasma profile during the reheat mode with the ETB and a confinement characteristic of this mode. Figure 1 shows time behaviors of the electron temperature, the density and the pressure of the reheat plasma with the high density edge transport barrier at the peripheral region ( $\rho=0.7$ ) and the plasma center ( $\rho=0$ ). These results are obtained with a YAG Thomson scattering measurements. During the initial ETB phase, the temperature from the plasma center to the edge decreased due to the density rising. In the subsequent L-mode phase, the peripheral pressure decreases due to the temperature decrease in the peripheral region resulting from the disappearance of ETB. On the contrary, in the ETB during the reheat mode, the density reduction is suppressed and slightly increases by the ETB formation in the peripheral region, and the temperature continues to increase due to the improvement by the reheat mode. Consequently, the peripheral plasma pressure and the pressure gradient becomes larger than that of the ETB alone. These results show that the anomalous transport in the peripheral region might be suppressed by the simultaneous achievement of the reheat mode and the ETB.

In typical L-mode plasma or ETB plasma, the improved confinement is degraded with the density increase. However, in the reheat mode with the ETB, good confinement is achieved in high density range. Figure 2 shows H-factor plot derived from ISS04 CHS/Heliotron/ATF[1] scaling as a function of the plasma density. The H-factor decreases with the density increases during the L-mode or the initial ETB

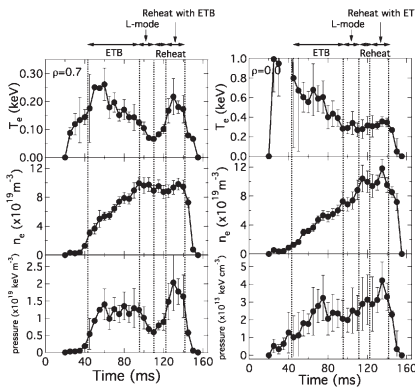


Fig. 1: Time evolutions of electron temperature, density and pressure in the peripheral region ( $\rho=0.7$ ) and the plasma center ( $\rho=0$ ) measured with YAG thomson scattering.

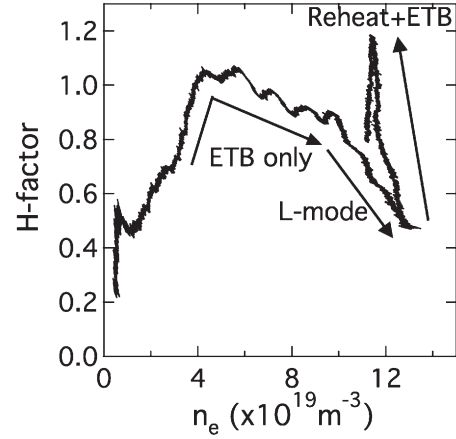


Fig. 2: H-factor plot for the same discharge as a function of the plasma density.

phases. However, the ETB phase during the reheat mode, the good improved confinement is realized on the high density range ( $\bar{n}_e \sim 1 \times 10^{20} m^{-3}$ ), because the H-factor increases up to two times just before L-mode value. Although the H-factor ( $\sim 1.2$ ) of the ETB plasma during the reheat mode is same as the value of the typical ETB plasma in the  $R_{ax}=92.1$  cm configuration, this value at  $R_{ax}=94.9$  cm might be underestimated, because the scaling is derived from the data of the  $R_{ax}=92.1$  cm configuration. The CHS L-mode confinement is degraded by the outward shift[2]. For the realization of the helical fusion reactor, it is a key issue that the product of the density and energy confinement time ( $n\tau_E$ ) should increase as the ion temperature increases. In the reheat mode with the ETB, the triple product of  $n\tau_E$  and the temperature increases by two times compared to the value of the ETB alone and five times compared to the L-mode value. Although the improvement of the reheat mode with the ETB is transient at this time, it is one of the candidates for the confinement improvement method of the helical plasma.

In conclusion, this mode provides good improved confinement in high density region ( $\bar{n}_e \sim 1.2 \times 10^{20} m^{-3}$ ) due to the temperature rising with keeping high density in peripheral region.

#### References

- [1] H.Yamada, et.al., Proc. of 31th EPS Conf. on Contr. on Fusion and Plasma Phys. ECA Vol. **28G**, P-5 099 (2004)
- [2] S. Okamura, et.al., Nucl. Fusion **39** (1999), 1337

## §5. Comparison between Magnetic Configuration and Rotational Transform Profile during ETB formation on CHS

Minami, T., Akiyama, T., Okamura, S.

As is previously reported[1], formation condition for edge transport barrier depends on the magnetic configuration, which is changed by the shift of the magnetic axis. There is a hypothesis to explain the reason for the dependence: the ETB formation relates to the existence of  $\iota=1$  surface in the plasma. To investigate this hypothesis, the VMEC calculation[2] is performed for the ETB plasma on the different locations of the magnetic axes. The pressure profile is derived from the YAG Thomson scattering measurement. We assumed that the current profile shape is

$$I_p(\rho) \propto T_e(\rho)^{1.5}. \quad (1)$$

The results of the VMEC code calculations are shown in Fig.1. The calculation is performed for the typical ETB plasma on the magnetic axes of 94.9 cm, 92.1 cm, and 89.9 cm. The typical plasma on 88.8 cm without the ETB is also calculated for comparison.

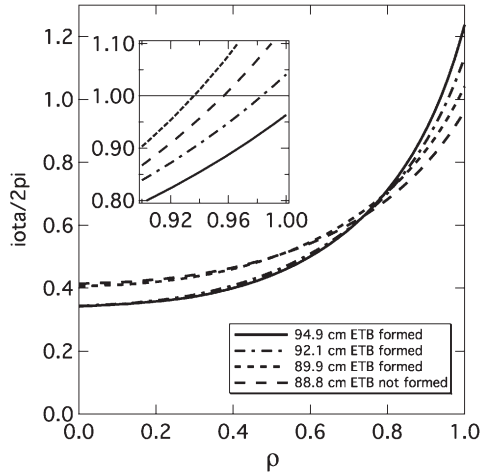


Fig. 1: Rotational transform profiles derived from VMEC calculation on different magnetic axis location.

The calculations show that the  $\iota=1$  rational surface always exists near the plasma edge when the ETB is formed, while no  $\iota=1$  surface exists in the plasma of 88.8 cm cases, in which no ETB was observed during the whole discharge. Because the  $\iota=1$  surface moves to the outward plasma by the inward shift of the magnetic axis, the limit of ETB formation have an accordance with the limit of the existence of the  $\iota=1$  rational surface in the plasma. Since the ETB appears to be located

around  $\rho \sim 0.95 \pm 0.05$  on  $R_{ax} = 92.1$  cm cases[1], this location might correspond to the location of the  $\iota=1$  surface.

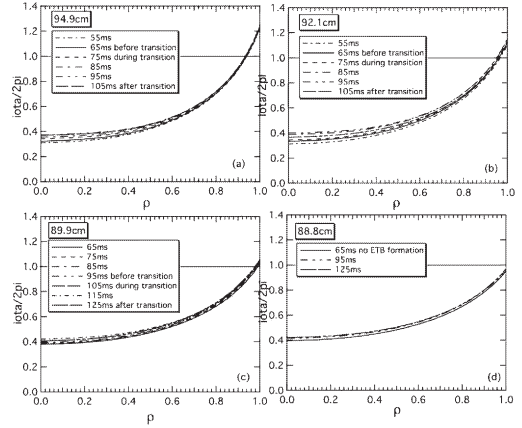


Fig. 2: Time evolutions of rotational transform profiles derived from VMEC calculation on different location of magnetic axes. (a)94.9cm, (b)92.1cm, (c)89.9cm, (d)88.8cm

Figure 2 shows time evolutions of the  $\iota$  profiles for the plasma of 94.9cm, 92.1cm, 89.9cm and 88.8cm. The calculation show that the changes of the  $\iota$  profiles in edge region are small during the NBI injection for all cases. It is difficult to explain the ETB formation only by the current profile scenario: the ETB is triggered by the  $\iota=1$  rational surface production due to the increase of the plasma current, because the  $\iota=1$  surface exists in the plasma from the start to the end of the NB injection. However, the present calculation has an ambiguity of the  $\iota=1$  surface location due to the ambiguity of the several parameters: the plasma pressure and current profiles have the ambiguity, because an accurate measurement is difficult for these parameter in the peripheral region. The langmuir probe measurement shows the possibility that the plasma pressure does not equal zero at the LCFS. Accordingly, the large delay of the ETB formation in the  $R_{ax} = 89.9$  cm case might be explained by this scenario. Because the  $\iota$  exists very close to the LCFS in  $R_{ax} = 89.9$  cm case on the present calculation, there is possibility that  $\iota=1$  surface moved from the outside to the inside of the plasma. The peripheral measurements are required for the further investigation.

## References

- [1] T.minami, et.al., Plasma and Fusion Research Vol.1, **032** (2006)
- [2] S.P.Hirshman, J.C.Whitson, Phys, Fluids **26** (1983), p 3553

## §6. Edge Pedestal Structure Measured with CXS at a Horizontally Elongated Cross Section

Nishimura, S., Nagaoka, K., Yoshimura, Y., Nakamura, K., Ohishi, T., Minami, T., Akiyama, T., Ida, K., Toi, K., Isobe, M., Suzuki, C., Okamura, S., Matsuoka, K.

A main improvement of the ETB plasmas can be seen in the particle confinement [1], and the increase of electron and ion temperatures was not always clear [2]. This is a contrastive characteristic of ETB compared with the N-ITB plasmas [2]. Another important question still remained on plasma rotations and/or radial electric fields in ETB plasmas. In contrast to tokamak H-mode plasmas, the plasma rotation in the core region in ETB plasmas is slower [2]. However, the radial electric field and/or the rotations of ions are connected to the ion pressure gradient by the radial force balance, and therefore the steep density gradient at the edge region in the H phase will make some changes of the electric fields and/or the ion rotations. For collisional plasmas, the neoclassical theory for non-symmetric toroidal systems predicts the negative radial electric fields determined by the ion pressure gradients [3], and therefore a role of the ion pressure gradients [4] is a theme to be studied in helical systems. From various edge plasma measurements in ETB plasmas, it is suggested that the edge pedestal region, where the ion pressure gradients and corresponding ion rotation are expected, is very narrow (for e.g.,  $\Delta\rho\approx 0.05$ ) if it exists. Detections of the rotations and the ion temperature profile in the narrow region are impossible with previous charge exchange spectroscopy (CXS) at a vertically elongated section [2] with the chord spacing  $\Delta R=7.5\text{mm}$  corresponding to a spatial resolution of  $\Delta\rho\approx 0.06$ . To improve this spatial resolution, we carried out the CXS at a horizontally elongated cross section. The chord spacing  $\Delta R=6.3\text{mm}$  at the equatorial plane  $Z=0$  corresponds to a spatial resolution of  $\Delta\rho\approx 0.02$ . Figure 1 shows results in an ETB plasma in a configuration with a magnetic axis position of  $R_{ax}=92.1\text{cm}$ , a quadrupole magnetic field of  $B_q=0$ , and a magnetic field strength of  $B_t=0.9\text{T}$ . The line averaged electron density is controlled to keep a slow raise up to  $5\times 10^{13}\text{cm}^{-3}$ . The ion temperature has a pedestal structure of  $\Delta T_i\approx 100\text{eV}$  at the edge and does not show clear changes at the L/H transition timing  $t=80\text{ms}$ . It is consistent with previous measurements at the vertically elongated section indicating that the edge temperature is about  $T_i\approx 100\text{eV}$  and do not change at the transition [2]. However, the plasma density in this region is being increased in this transition phase, and thus the ion pressure gradient also grows. The Doppler shift indicating the edge poloidal rotation of fully ionized carbon ions ( $\text{C}^{6+}$ ) in a direction of the electron diamagnetic drift shows a change corresponding to this growth. Here, it should be noted that this velocity of impurity ions is dominated by the  $\mathbf{E}\times\mathbf{B}$  drift [5], and that the observed values are large in spite of a fact that the potential gradient  $\partial\phi/\partial R$  at the horizontally elongated sections is

smaller than that in the vertically elongated sections. The electric field strength seems to be saturated at  $E_r\approx -10\text{kV/m}$  in the H phase. This electric field strength at the region of  $T_i\leq 100\text{eV}$  may be enough in viewpoint of the poloidal Mach number and will be an important key in considering the transition mechanisms. In contrast to the N-ITB plasmas with the ion temperature pedestal of  $\Delta T_i\approx 100\text{eV}$  and  $\Delta\rho=0.3$  at the  $E_r$  shear region with  $E_r\approx +20\text{kV/m}$  [2], the edge ion temperature pedestal region with the relatively large poloidal rotation seems to be narrow ( $\Delta\rho\leq 0.1$ ) in the ETB plasmas. This width may be one key to understand the difference between N-ITB and ETB plasmas. As mentioned above, the time evolution of the edge electron density is important to understand these results, more detailed analyses of results of the edge density measurements using LiBP[6] are planned in FY2006.

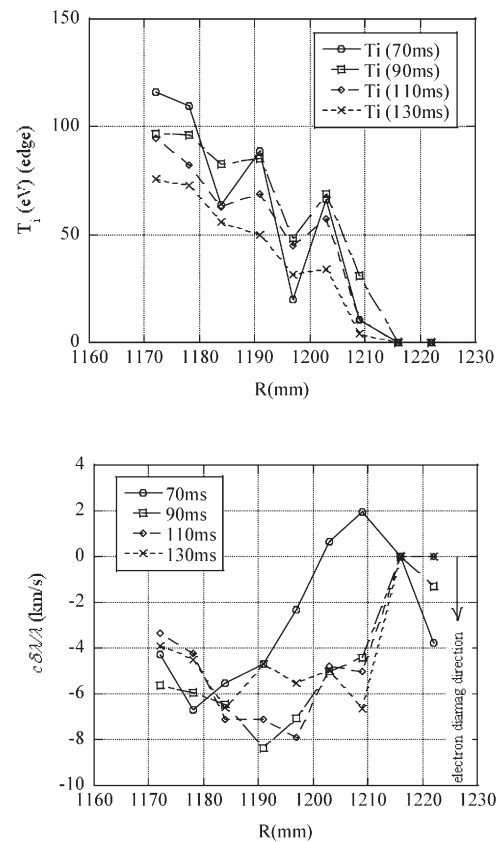


Figure 1 The ion temperature  $T_i$  and the Doppler shift  $\delta\lambda$  of the charge exchange excited CVI line( $\lambda=529\text{nm}$ ) observed near the LCFS at  $R\approx 1.2\text{m}$ . The L/H transition occurred at  $t=80\text{ms}$ .

## References

- [1] Okamura, S., et al., Nucl.Fusion **45**, 863 (2005)
- [2] Nishimura, S., et al., Ann.Pep of NIFS 2005 p.271, p.272
- [3] Shaing, K.C., et al., Phys.Fluids **29**, 521 (1986)
- [4] ITER Physics Expert Group, Nucl.Fusion **39**, 2175 (1999)
- [5] Nishimura, S., Phys.Plasmas **7**, 437 (2000)
- [6] Nakamura, K., et al., Rev.Sci.Instrum. **76**, 013504 (2005)



## §7. Study of an Edge Transport Barrier by Langmuir Probes in the Compact Helical System

Takeuchi, M. (Dep. of Energy Eng. and Sci., Nagoya Univ.), Toi, K., Nagaoka, K., Suzuki, C., Minami, T., Akiyama, T., Yoshimura, Y., Nishimura, S., Isobe, M., Shimizu, A., Takahashi, C., Matsuoka, K., Okamura, S., CHS Group

Measurements of detailed structure of ETB plasmas are crucial for better understanding of the L-H transition and ETB formation. A triple Langmuir Probe (LP) is well suited for this purpose, because it can measure electron temperature ( $T_e$ ), density ( $n_e$ ), space potential ( $V_s$ ) and their fluctuations in the plasma edge having high time (1  $\mu$ s) and spatial resolutions. Moreover, measurements of the toroidal uniformity of the ETB structure are particularly important for an ETB plasma in three-dimensional configuration such as CHS. We attempted to measure the ETB structures by using two sets of LPs at two toroidal locations of CHS (the “6U port” and the “3U port”) as shown in Fig.1. The LP installed at each port section was moved vertically shot by shot from the normalized minor radius ( $\rho = r / \langle a \rangle$ )  $\rho \sim 0.93$  to  $\rho \sim 1.1$  for about 40 ETB shots with high reproducibility.

Figure 2 shows the radial profiles of  $T_e$ ,  $n_e$ , floating potential ( $V_f$ ),  $V_s$  and radial electric field ( $E_r$ ) measured at the 6U port section (left) and at the 3U port section (right), for four time slices averaged over a 1 ms time window, where “0 ms” stands for the transition defined by the start time of the drop in the  $H_\alpha$  emission. At the 6U port, the radial profile of  $T_e$  has a hollow structure at  $0.95 < \rho < 0.98$  before the transition, and evolves to the profile with a modest gradient inside  $\rho \sim 1.0$  after the transition. Just after the transition ( $t = +4 \sim +5$  ms), the radial profile of  $n_e$  has a steep gradient inside  $\rho \sim 0.96$ , having a hollow structure at  $0.95 < \rho < 0.98$ . After that ( $t = +8 \sim +9$  ms), the hollow region of  $n_e$  is filled from the inner side toward  $\rho \sim 0.97$ , and at  $t = +16 \sim +17$  ms the hollow structure of  $n_e$  disappears and is filled up to  $\rho \sim 1.0$ . This peculiar edge structure may be linked to the presence of a magnetic island at the rotational transform  $\iota / 2\pi = 1$ , of which the position of the rational surface is calculated to be  $\rho \sim 0.95$ - $0.96$ . On the other hand, at the 3U port,  $n_e$  has a steep gradient inside  $\rho \sim 1$  just after the transition. The radial profile of  $T_e$  is almost fixed across the transition. These observations suggest that the ETB will be formed inside  $\rho \sim 1$ . However, the initial growth of the ETB in  $n_e$  and  $T_e$  profiles at the 6U port section may be locally blocked by the presence of a non-rotating magnetic island, which is predicted to be in the region of  $0.95 < \rho < 0.98$  from the shape of the  $n_e$ -profile and to be  $\sim 6$  mm width. It is seen from time evolutions of  $n_e$  and  $T_e$  profiles that the island seems to shrink in the deep H-phase after  $\sim 15$  ms from the transition.

It is generally thought that  $E_r$  and its shear ( $E_r'$ ) play an important role in the formation of an ETB. The  $E_r$  was evaluated from the radial derivative of fitted profiles of  $V_s$ . In the 6U port,  $E_r$  behaves peculiarly having a positive hump for about 10 ms after the transition in the region of

$0.96 < \rho < 0.99$ . Before ( $t = -4 \sim -3$  ms) and just after ( $t = +4 \sim +5$  ms) the transition, the  $E_r$  shear in the region of  $0.94 < \rho < 0.96$  changed largely from  $\sim -600$  kV/m<sup>2</sup> to  $\sim 2700$  kV/m<sup>2</sup> and that in the region of  $0.98 < \rho < 1.0$  also changed from  $\sim 200$  kV/m<sup>2</sup> to  $\sim -1800$  kV/m<sup>2</sup>. On the other hand, at the 3U port, the  $V_s$  and  $E_r$  profiles have a rather monotonic shape without any hollowness or hump. And the  $E_r$  shear changed from  $\sim -200$  kV/m<sup>2</sup> to  $\sim 400$  kV/m<sup>2</sup> in the region of  $0.94 < \rho < 0.96$ .

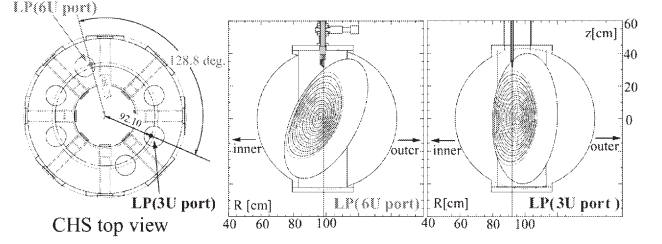


Fig.1 Arrangement of two LPs at two toroidally different sections in CHS (6U and 3U port sections).

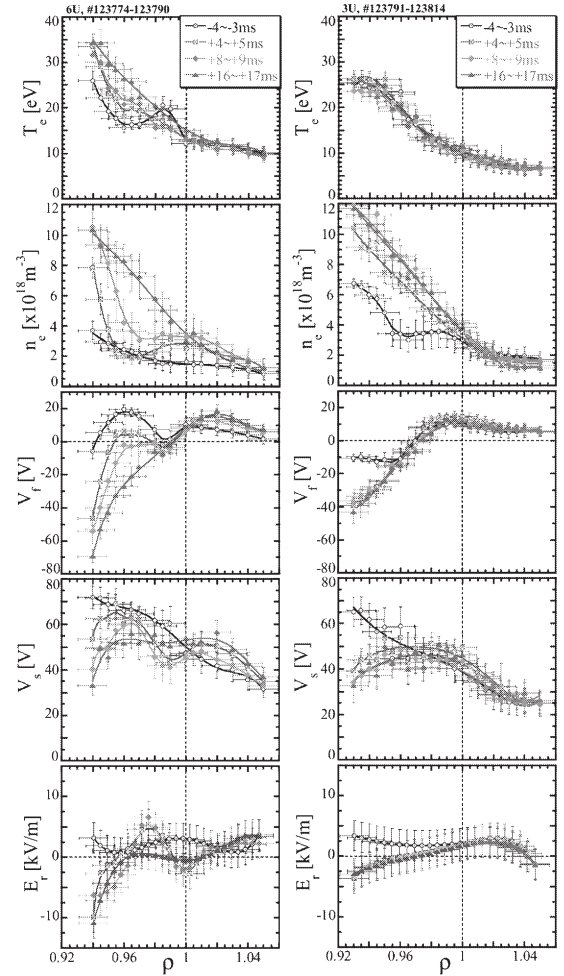


Fig.2 Radial profiles of  $T_e$ ,  $n_e$ ,  $V_f$ ,  $V_s$  and  $E_r$  at four time slices averaged for a 1 ms time window at the 6U port section (left) and at the 3U port section (right).

## §8. Impurity Measurements for Edge Transport Barrier Discharges in the Compact Helical System

Suzuki, C., Okamura, S., Minami, T., Akiyama, T., Fujisawa, A., Ida, K., Isobe, M., Matsuoka, K., Nagaoka, K., Nishimura, S., Peterson, B.J., Shimizu, A., Takahashi, C., Toi, K., Yoshimura, Y.

The formation of an edge transport barrier (ETB) has recently been found in the Compact Helical System (CHS) plasmas heated by neutral beam injection (NBI) with strong gas puffing.<sup>1)</sup> In order to study impurity behaviors in the ETB discharges, we have measured the radiation profiles and the vacuum ultraviolet (VUV) spectra by using an absolute extreme ultraviolet (AXUV) photodiode array and a grazing incidence spectrometer. The experimental setup of the photodiode array and the spectrometer have already been reported elsewhere.<sup>2),3)</sup> The lines of sights of these diagnostics are arranged within a horizontally elongated cross section. The total radiation power from the plasma is routinely monitored by a single channel pyroelectric detector. The temporal and spectral resolution of the spectrometer is about 10 ms and 0.3 nm, respectively.<sup>3)</sup>

The time traces of the various signals in a typical ETB discharge are shown in Fig. 1. The magnetic axis position and the toroidally averaged ellipticity in this case are  $R_{ax}=92.1$  cm (in major radius) and  $\kappa=1.22$ , respectively. A spontaneous transition to the ETB phase occurred at 70 ms with an abrupt drop of  $H_\alpha$  intensity. The Thomson scattering diagnostics shows that the electron density steeply in-

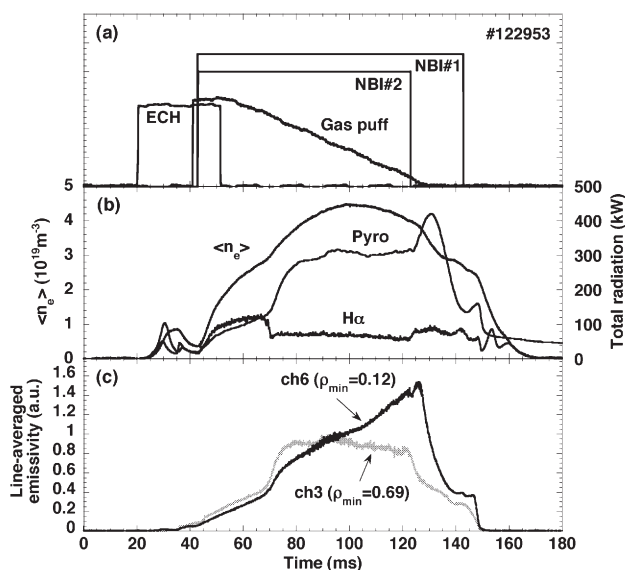


Fig. 1. Time traces of the parameters for a typical ETB discharge. Line averaged emissivity measured by the AXUV photodiode array is shown in (c) for the two lines of sights.

creases only near the edge, while the the electron temperature is almost unchanged at the transition. The signals of all the channels of the AXUV photodiode array also increase more steeply at the transition as shown in Fig. 1 (c) for the center (ch6) and edge (ch3) viewing chords. The radiation profile rapidly changes into more hollow one immediately after the spontaneous transition to the ETB phase. This observation indicates that the radiation power tends to increase especially near the edge just after the transition.

Several resonance lines of metallic (iron, chrome, titanium) and oxygen impurities are identified from the VUV spectra in the ETB discharges. The temporal evolutions of the intensities of several representative lines in an ETB discharge are plotted in Fig. 2 at 10 ms intervals. The transition occurred at 73 ms in this discharge, and the signals are normalized to those just before the transition (at 65 ms). The line intensities of all impurities increase more steeply just after the transition in the same way as the radiation emissivity. Judging from the ionization potentials for these ions, three metallic impurity lines appear to represent mainly the radiation from the core region. Since the electron density and temperature in the core does not change at the transition, the metallic impurity ion densities actually seem to increase inside the transport barrier. Though changes in metallic impurity transport coefficients inside the ETB are inferred from the VUV spectra, numerical simulations of impurity transport are required for the quantitative analyses.

### References

- 1) Okamura, S. et al.: Plasma Phys. Control. Fusion **46** (2004) A113.
- 2) Suzuki, C., Peterson, B. J., Ida, K.: Rev. Sci. Instrum. **75** (2004) 4142.
- 3) Suzuki, C. et al.: J. Plasma Fusion Res. SERIES **7**, 74 (2006)

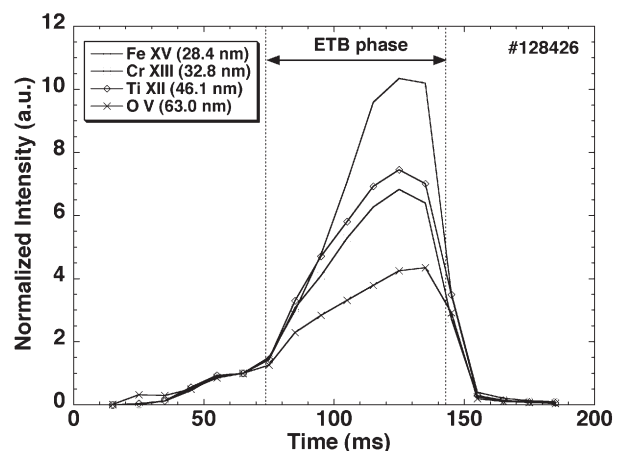


Fig. 2. Temporal evolutions of several representative impurity line intensities in an ETB discharge.

## §9. Radial Phase Shift of the EHO Measured Using Beam Emission Spectroscopy in ETB Discharge in CHS (NIFS02KZPD003)

Kado, S. (Univ. of Tokyo), Oishi, T., Yoshinuma, M., Ida, K., Okamura, S.

Accompanied by the formation of the edge transport barrier (ETB) in the compact helical system (CHS)1), a coherent MHD mode which has the frequency around 4.5 kHz and its second harmonic appears. Beam emission spectroscopy (BES)2) has been developed in CHS to measure the local density fluctuations and gradients simultaneously.3,4) The BES measurement has shown that this coherent mode has similar characteristics to the edge harmonic oscillations (EHO)5) in tokamaks.6,7)

Figure 1 shows the power spectra of (a) the magnetic fluctuation and (b) the density fluctuation measured using BES for observation region  $\rho = 0.95$ . They are averaged over 8 msec. Thin and bold trace is for the period just after the ETB formation (64 – 72 msec) and of the later half of the discharge (80 – 88 msec), respectively. The noise level of the density fluctuation is evaluated from the signal of BES before the beam is injected. In the latter half of the discharge, an oscillation with a fundamental frequency around 4.5 kHz and its 2nd harmonic frequency appear clearly in both the magnetic fluctuation and the density fluctuation, which we call “EHO”.

The radial structure of the fundamental mode of EHO with the frequency of 4.5 kHz was investigated by mean of BES.8) Figure 2(a) shows the density profile at the ETB transition and at the onset of EHO. The density gradient around the last closed flux surface (LCFS) is steepened at the transition. The steep gradient is maintained at almost constant value during the period in which the EHO appears. The solid line of Fig. 2(b) shows the radial profile of the root mean square (RMS) value of the density fluctuation at the frequency of the mode 4.5 kHz. This value represents summation of the intensity of the mode and that of the background turbulence at this frequency. Dotted line in Fig. 2(b) shows the level of turbulence. The fundamental mode of the EHO was observed in four channels covering  $\rho = 0.85 - 1.10$ . The peak value of the amplitude of the mode locates  $\rho = 0.95$ , where the rational surface, rotational transform  $\iota = 1$ , locates. We have found that the position of this mode follows that of the  $\iota = 1$  surface in the case that the  $\iota = 1$  surface locates inside LCFS.7) Figure 2(c) shows the spatial coherence of the mode. Spatial coherence of more than 0.8 is observed for  $\rho = 0.85 - 1.10$ . Figure 2(d) shows the phases of the fluctuation for the region where coherence is high. The convention for the phases is that their trend decreasing in the radial direction corresponds to the outward propagation. If we could interpret this phase shift shown in Fig. 2(d) as the radial propagation, the mode propagates in the outer radial direction with the apparent

phase velocity of several hundreds of m/s. That is a similar characteristic to the radial phase shift of EHO in tokamaks.9,10) However, there is also a possibility that the phase shift is caused simply by the rigid rotation of the mode. A preliminary phase analysis of the magnetic fluctuation measurement showed that EHO has a mode number of 2/1 in the poloidal/toroidal direction.11) More detailed measurements for the mode structure and the rotation will be needed to investigate the relationship between the plasma rotation and the radial phase shift.

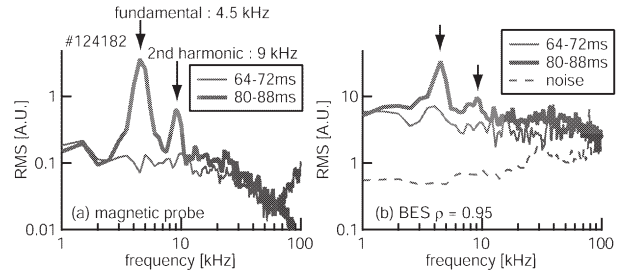


Fig. 1. The power spectra of (a) the magnetic fluctuation and (b) the density fluctuation measured using BES for observation region  $\rho = 0.95$ .

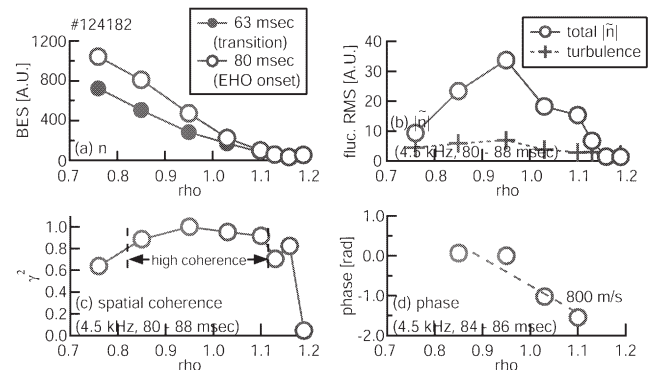


Fig. 2. (a) Density profiles at the ETB transition and at the onset of EHO. (b) RMS value of the density fluctuation at 4.5 kHz which is the frequency of the fundamental mode of EHO. (c) Spatial coherence and (d) phase of EHO. In (c) and (d), the channel for  $\rho = 0.95$  is reference of the coherence and the phase.

### Reference

- 1) Okamura, S. et al., J. Plas. Fus. Res. **79**, (2003) 977
- 2) Fonck, R. et al., Rev. Sci. Instrum. **61**, (1990) 3487
- 3) Oishi, T. et al., Rev. Sci. Instrum. **75**, (2004) 4118
- 4) Oishi, T. et al., J. Plas. Fus. Res. SERIES **6**, (2004) 449
- 5) Greenfield, C. M. et al., Phys. Rev. Lett. **86**, (2001) 4544
- 6) Oishi, T. et al., *proc. 32nd EPS conference on plasma physics* (Tarragona, Spain) (2005)P4.094.
- 7) Oishi, T. et al., Nucl. Fusion **46**, (2006) 317
- 8) Oishi, T. et al., *submitted to Phys. Plasmas*
- 9) Burrell, K. H. et al., Plasma Phys. Control. Fusion **44**, (2002) A253
- 10) Oyama, N. et al., Nucl. Fusion **45**, (2005) 871
- 11) Kado, S. et al., *17th International Conference of PSI in Controlled Fusion Devices* (Hefei, China) (2006)O-31



## §10. HCN Laser Scattering Measurement of ETB-Formed Plasmas in CHS

Tsuji-Iio, S., Shimada, R., Tsutsui, H., Tomita, N. (Tokyo Tech.),  
Akiyama, T., Okamura, S., Kawahata, K., Tanaka, K. (NIFS),  
Okajima, S. (Chubu Univ.)

Anomalous transport plays a dominant role in plasma confinement in magnetic confinement fusion devices. Hence it is indispensable to understand fluctuations to improve confinement since they are supposed to cause the anomalous transport. An edge transport barrier (ETB), which can improve particle transport in the edge region, has been observed in CHS [1, 2]. The relationship between transport and fluctuations can be made clear in these plasmas with transitions to H-mode. In this research we develop an HCN laser scattering measurement system [3] to examine correlations between electron density fluctuations and confinement. In order to reveal the relation between the transport barrier and fluctuations we have investigated changes in features of turbulences before and after transitions to the improved mode.

The position of the scattering volume is shown in Fig. 1 (a). The position of the magnetic axis is 0.921 m and the magnetic field strength at the magnetic axis is 0.88 T. In this configuration, the dominant wavenumber component of measured fluctuations is the radial one. Figure 1 (b) shows temporal evolutions of operation and plasma parameters and the frequency spectra of fluctuations of an ETB-formed plasma. The positive and negative frequencies correspond to the inward and outward directions of the propagation of fluctuations, respectively. After injections of two NBs, the  $H\alpha$  emission signal decreases spontaneously at  $t = 0.053$  s. Then the density gradient in the plasma edge region becomes steeper and the edge transport barrier is thought to be formed [1, 2]. Frequencies of fluctuations with a wavenumber of  $5.4 \text{ cm}^{-1}$  increase up to  $\pm 200$  kHz after NB injections. However, they are suppressed after the transition. When the heating power approaches the threshold for the transition, the delay time of the transition from the start of NB injection becomes longer. The timing of the suppression of fluctuations is confirmed to be late accordingly. These measurement results suggest the improvement of particle confinement with the edge transport barrier. While the beam emission spectroscopy also shows the reduction of density fluctuations, langmuir probes do not. It may suggest the toroidal asymmetry of the confinement improvement. It is under study to determine the causality between the transition and the suppression of fluctuations.

We are designing a modified optical system to install additional two channels (radial wavenumbers of 10 and  $20 \text{ cm}^{-1}$ ).

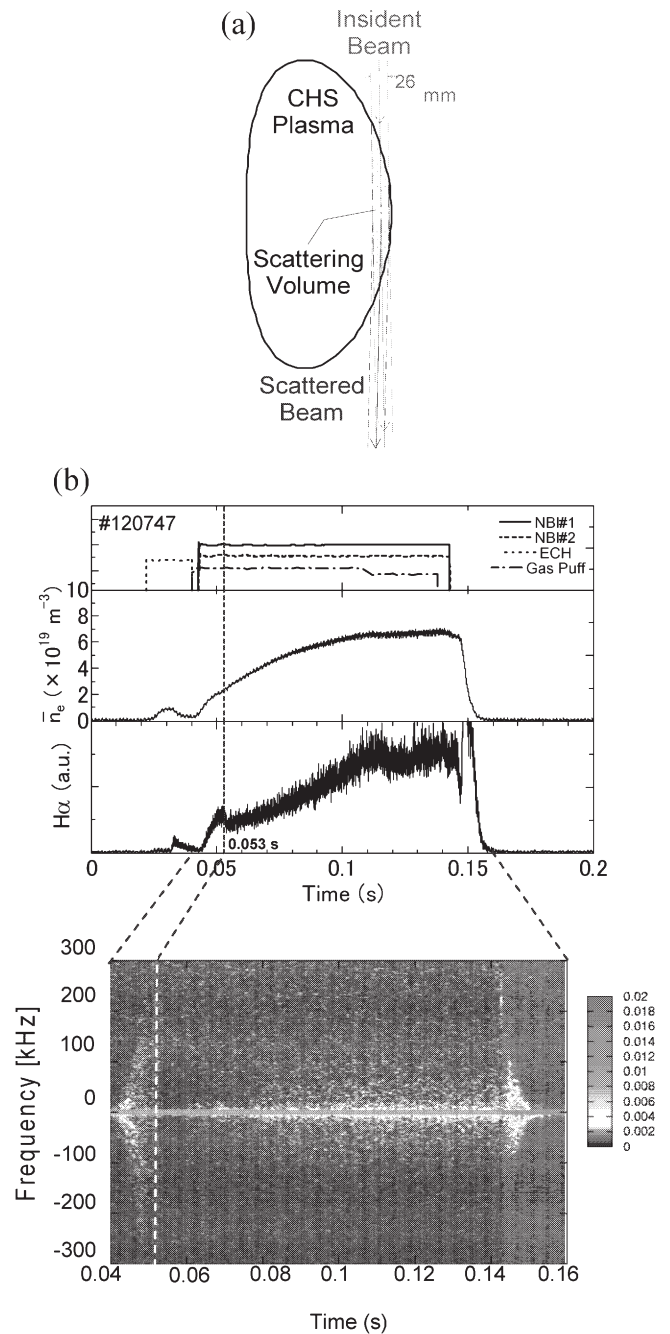


Fig. 1: (a) The location of the scattering volume in a CHS plasma. Here  $k_r$  is  $5.4 \text{ cm}^{-1}$ . (b) Temporal evolutions of operation and plasma parameters and frequency spectra of fluctuations with a wavenumber of  $5.4 \text{ cm}^{-1}$ . The transition occurs at  $t = 0.053$  s.

### References

- 1) Okamura, S. *et al.*, J. Plasma Fusion Res. Vol.79, No.10 (2003) 977.
- 2) Okamura, S. *et al.*, Plasma Phys. Control. Fusion **46** (2004) A113.
- 3) Akiyama, T. *et al.*, to be published in Journal of the Japan Society of Infrared Science and Technology.



## §11. Neutral Particle Transport in CHS Edge Region

Matsuura, H. (Osaka Pref. Univ.),  
Suzuki, C., Okamura, S.

Improvement of plasma confinement such as H-mode is one of urgent issues in the fusion research. Edge transport barrier ( ETB ) discovered recently in the compact helical system ( CHS ) is characterized by clear drop of  $H\alpha$  emissions. So it is expected that the profile of atomic/molecular hydrogen is one of key parameters to trigger and sustain this ETB. In order to understand the mechanism of ETB, measurement and control of neutral particle behavior are necessary. But, until now, we have only very limited experimental knowledge on them in helical systems, especially in CHS. So, we have used Monte Carlo simulation code DEGAS. We start simulation study with two-dimensional axial-symmetric model,<sup>1)</sup> then expand the simulation model into the three-dimension to include the toroidal behavior of neutral particles.<sup>2, 3)</sup>

In Fig. 1, a example of 3D calculation geometry is shown, where the CHS plasma is in the standard magnetic configuration (  $R_{ax} = 92.1$  [cm] ) and has contact with the inside wall like as the material limiter. The neutral recycling becomes dominant at torus inside. Core plasma and “vacuum” region is divided into 45 zones poloidally and into 13 zones radially. Toroidally 48 cross sections are selected to construct the 3 dimensional mesh. Hydrogen molecules are produced at the recycling area on the wall. Hydrogen atoms are also produce near the recycling area by interactions between molecules and plasma particles. As the mean free path of these neutral particles is a few cm or less under plasma parameters around Last Closed Flux Surface ( LCFS ), radial and poloidal transport is almost prohibited. So, neutral density is localized to torus inside. As for toroidal transport, there exists a gap between LCFS and chamber wall. So neutral particle can easily move several cm in toroidal direction.

Though  $H\alpha$  emission intensity is often used as the measure of recycling particle flux, this must be checked carefully, since  $H\alpha$  emission has deep relationship with the profile of atomic/molecular hydrogen, which is very complicated in helical systems like CHS. According to Collisional Radiation ( CR ) model the population density of an excited level with principal quantum number  $p$  is given by

$$n(p) = R_0(p)n_i n_e + R_1(p)n_H n_e + R_2(p)n_{H_2} n_e \quad (1)$$

where population coefficients (  $R_0, R_1, R_2$  ) can be calculated by Sawada code. They are less dependant on plasma density (  $n_e = n_i$  ) and the weak increasing function of  $T_e$ . The first term of the right hand side of Eq.( 1 ) is the contribution from recombining ions. In the CHS edge parameter region,  $R_0$  is too smaller than  $R_1$  or  $R_2$  and this term can be negligible. Though  $R_2$  is

smaller than  $R_2$ , we must estimate balmer series emission not only from excited atoms ( ie. the second term of Eq.( 1 ) ) but also from dissociating molecules( ie. the third term ), since the molecular hydrogen density may be much larger in the recycling region than atomic density.

In Fig. 2,  $H\alpha$  emission profiles from excited atoms( left side ) and from dissociated molecules( right side ) are shown. The cross section of these figures are selected to be those where a  $H\alpha$  detector called as 2O is equipped and no recycling source exists. Plasma parameters are given from NBI-heated plasma data with ETB. In this cross section,  $H\alpha$  emission from atomic hydrogens is larger by a factor of 10 than that from molecular hydrogens. Due to large penetration length of atoms, Fig. 2(a) show broader profile.

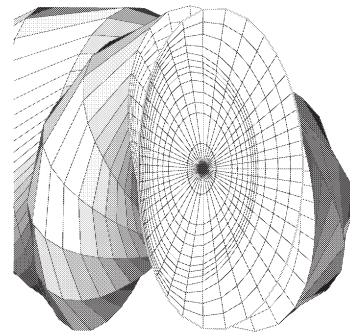


Fig. 1: Calculation geometry for the DEGAS simulation.

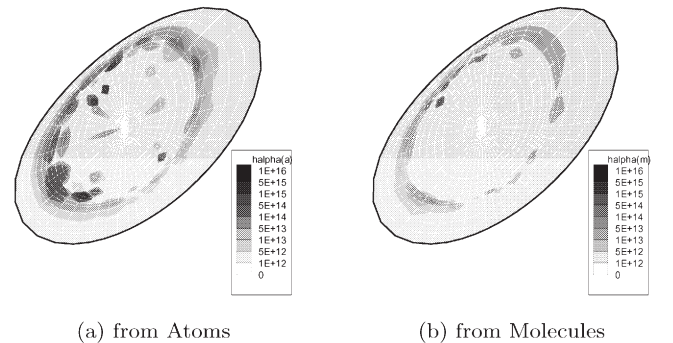


Fig. 2:  $H\alpha$  emission profile at poloidal cross section where 2O detector is equipped.

## References

- 1) H.Matsuura et al.: J.Plasma Fusion Res. SERIES, **7**, (2006)106.
- 2) H.Matsuura et al.: to be publish in J. Plasma Phys..
- 3) H.Matsuura et al.: Proc. 17th PSI17, (Hefei, 2006)P1-82.

## §12. Ion Internal Transport Barrier in CHS

Ida, K., Yoshinuma, M., Minami, T.

It is interesting phenomena that the location of electron internal transport barrier (ITB) is different from that of ion ITB. In CHS ( $R = 0.9 - 1.0\text{m}$  and  $a = 0.2\text{m}$ ) the electron ITB typically located near the plasma center at  $\rho = 0.3$ , while the ion ITB locates outside of electron ITB, where the ratio of electron temperature to ion temperature is low enough not to degrade ion transport.

In order to investigate the mechanism of ion internal transport barrier, the modulation charge exchange spectroscopy (MCXS), where the observation pointed is scanned with 20mm with a frequency up to 100Hz, has been developed to study the location of maximum ion temperature gradient. The modulation charge exchange spectroscopy consists of object lens mounted on the stage with piezo elements, optical fiber, Fabry-Perot spectrometer, fast 256 channel photo diode detector (PDA) with image intensifier (I.I.). Ion temperature gradient can be derived every 5 ms (half of the modulation period) by taking the slope of ion temperature to the displacement of observation points. The error bar of the ion temperature gradient is estimated by the scatter of ion temperature.

Figure 1 shows the radial profile of ion temperature gradient in the discharge with NBI ( $t = 40 - 140\text{ms}$ ) and ECH ( $60 - 100\text{ms}$ ) at low density ( $0.2-0.3 \times 10^{19}\text{m}^{-3}$ ). Just after the ECH is turned on the ion ITB appears at  $t = 66\text{ms}$ . When there is no ion ITB the ion temperature gradient is order of 1-2 keV/m (central ion temperature is  $0.2 - 0.3\text{keV}$ ). The ion temperature gradient increases 10 - 15keV/m at the ion ITB region. The region with a large ion temperature gradient is localized at  $\rho = 0.66$  within  $\Delta\rho = 0.1$ . Associated with the gradual increase of electron density, the ion ITB region becomes expands and becomes weaker at  $t = 70\text{ms}$  and finally disappears at  $t = 100\text{ms}$ .

Figure 2(a) shows the time evolution of ion temperature gradient for the discharge with the magnetic axis of 94.9cm. The ion temperature gradient at  $\rho = 0.66$  increases up to 10 keV/m after the ECH pulse is tuned, while the ion temperature gradient outside ITB ( $\rho = 0.48$  and  $\rho = 0.78$ ) stays low values ( $<3\text{keV/m}$ ). How long the ITB can be sustained depends on the period in which the electron density can be sustained below the critical value. The ITB is sustained longer in the discharge with the magnetic axis of 97.4cm, where the increase of density after the ECH pulse is slower as shown in Fig.2(b). It should be noted that there are two ITBs observed at  $\rho = 0.52$  and  $\rho = 0.74$ , while the ion temperature gradient between two ITBs stays low value ( $<2\text{keV/m}$ ). It is open to question why the outside ITB ( $\rho = 0.74$ ) appears first and the inner ITB ( $\rho = 0.52$ ) appears later.

This observation clearly shows that the location of ion ITBs ( $\rho=0.66$  for  $R_{\text{ax}}=94.9\text{cm}$  and  $\rho = 0.52$  and  $\rho = 0.74$  for  $R_{\text{ax}} = 97.4\text{cm}$ ) is always outside the electron ITB

( $\rho=0.3$ ), where the electron temperature is low ( $<0.5\text{keV}$ ) and the ratio of electron temperature to ion temperature is relatively small ( $<2$ ).

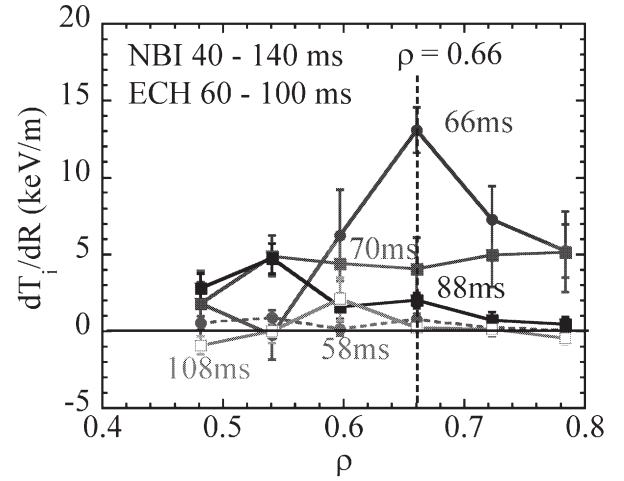


Fig.1 Radial profile of ion temperature gradient measured with MCXS for the plasma with the magnetic axis of 94.9cm

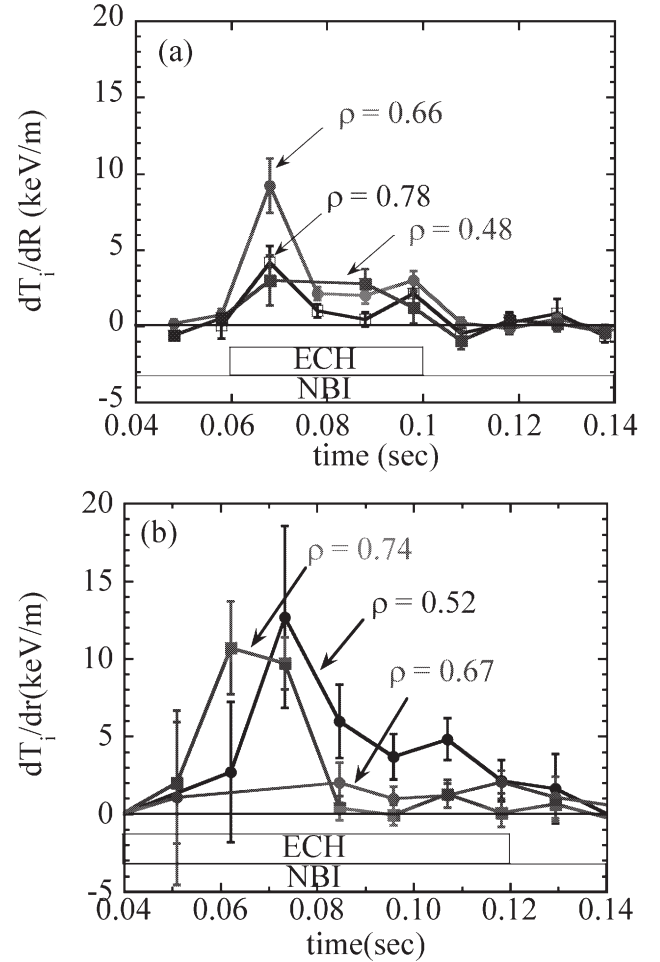


Fig.2. Time evolution of ion temperature gradient measured with MCXS for the plasma with the magnetic axis of (a) 94.9cm and (b) 97.4cm.

### §13. Effect of Magnetic Configuration on Confinement Improvement of CHS Plasmas

Matsuoka, K., Isobe, M., Minami, T., Yoshimura, Y., Fujisawa, A., Okamura, S., Itoh, K., CHS Group

New type of the discharge with improved confinement was found in CHS; both of an edge transport barrier (ETB) of the electron density and an elevated electron temperature ( $T_e$ ) in the core region are realized simultaneously. The high  $T_e$  in the core region that is typical of ITB has been obtained so far in CHS when the electron density was on the order of  $10^{18} \text{ m}^{-3}$  in the plasma heated with 53 GHz ECH with the maximum power of about 400 kW. The mechanism for the ITB is thought to be due to the increased shearing rate ExB.

The elevated  $T_e$  in the new discharge was found when the ETB was obtained under two co-injected NBI heatings with the maximum total power of about 1.4 MW and under rather strong gas puffing. The plasma has the line-averaged electron density of  $3\text{--}4 \times 10^{19} \text{ m}^{-3}$  that is much higher than that of ITB induced with ECH. The mechanism that brings about the increase in  $T_e$  should be different from that in the ITB because the density range is much different. The discharge is shown in Fig. 1. The transition of ETB is at about 67 ms that is shown by the drop in the  $H\alpha$  signal. The electron temperature profiles are shown at four timings in Fig. 2: 2 ms before the transition, and 3 ms, 8 ms, and 13 ms after the transition. It is seen that the electron temperature is substantially increased at 3 ms after the transition (at 70ms). The

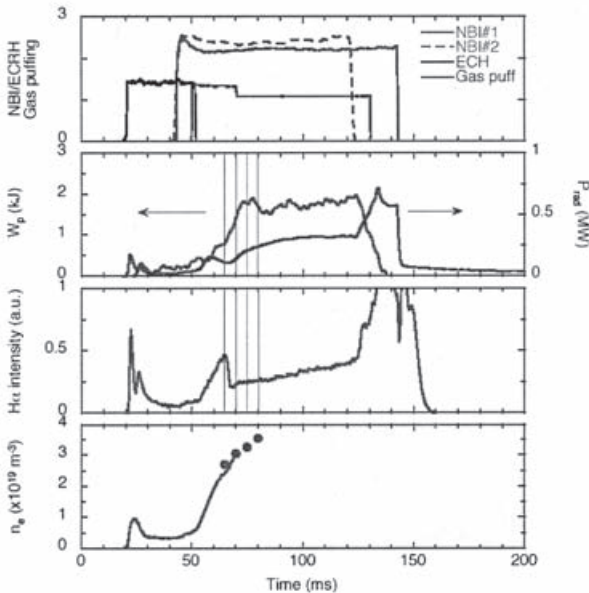


Fig.1. Waveforms of the discharge with new type of improved modes.

electron density profiles are hollow as is shown in Fig.3. The following consideration on the magnetic configuration that is different from the ExB shearing rate is given to this discharge for the mechanism of the elevated  $T_e$ . From studies on new helical magnetic field configurations the simultaneous realization of the magnetic well and the stellarator shear is predicted to be favorable to stabilize micro-instabilities induced by trapped particles because of the drift reversal. The magnetic well is formed in the core region only at 70 ms, however, not formed at 65 ms (before the ETB transition) and at 75 and 80ms (after the transition). On the other hand, the stellarator shear is

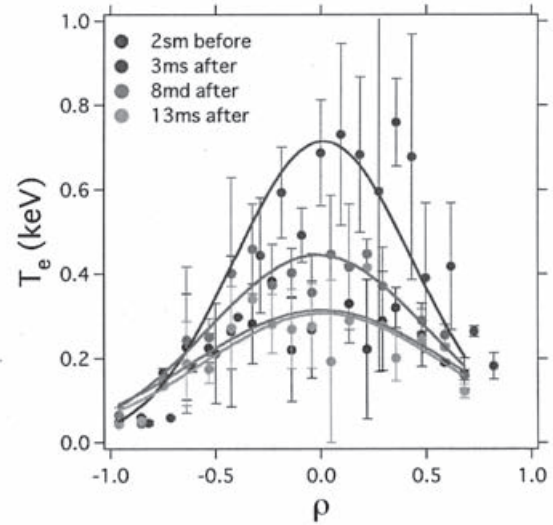


Fig.2.  $T_e$  profiles before and after the ETB transition.

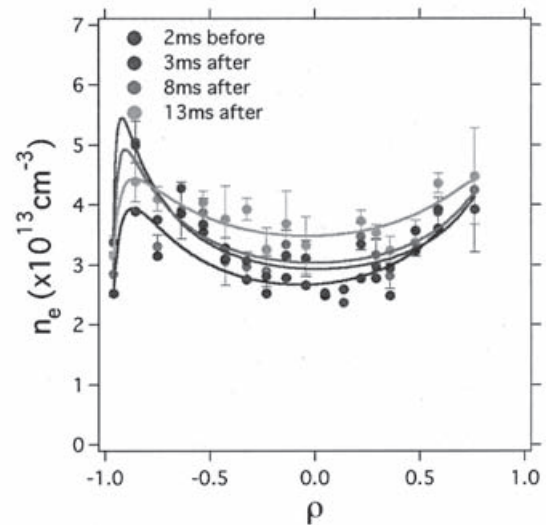


Fig.3. The  $n_e$  profiles at four timings.

formed at these timings over the whole plasma region. However, it is difficult to explain why the improved confinement with the elevated  $T_e$  has faded out so quickly in a few ms. In summary, the new improved confinement regime was found, however, its mechanism has not been explained.



## §14. Spectrograph of Electric Field Fluctuation in Toroidal Helical Plasma

Fujisawa, A., Shimizu, A., Nakano, H., Ohshima, S., Okamura, S., Matsuoka, K., Itoh, K., CHS Group

A heavy ion beam probe (HIBP) can measure potential and density fluctuation simultaneously. CHS has two heavy ion beam probes in order to investigate fluctuation structure of a core of toroidal plasma. Recently, we have found existence of multiple coherent modes indicating a long-distance correlation[1]. Here, we report the basic features of the coherent modes that are conjectured as Geodesic Acoustic Modes, that belong to an oscillatory branch of zonal flows.

Figure 1 shows power spectra of density, potential and electric field fluctuations at the position of  $r=12$  cm in the frequency range from 5 to 100 kHz. The normalized density fluctuation defined as  $\delta n/n$  is displayed. The plotted spectra are the ensemble averages of more than forty shots, and the spectra are evaluated as the averages of  $\sim 2$  ms windows in a stationary period of  $\sim 40$  ms in a discharge duration of  $\sim 100$  ms. A spectrum of a window including  $2^{10}$  digital data is calculated using the Fast Fourier Transform (FFT) technique to give a frequency resolution of  $\sim 0.48$  kHz. The Nyquist frequency is 250 kHz for 2  $\mu$ s sampling.

Several peaks are found to be superposed on broad-band spectra in both density and potential fluctuation spectra; for density fluctuation the peaks are at the frequencies of 8, 16, 23, 35, 44, 50 and 125 kHz, while 8, 16, 18, 23, 29, 35, 44, 50 and 125 kHz for potential fluctuation. The spectrum of electric field fluctuation also shows peaks, however, the number of the countable peaks is reduced compared to that in the density and potential fluctuations. Since the density and potential fluctuations suffer from the path-integral fluctuations, the absence of the peaks in electric field fluctuation indicates that the modes should be localized somewhere along the beam orbit. On the other hand, the modes of the peak frequencies at 8, 16, 18, 35 and 50 kHz are localized around  $r=12$  cm.

The coherence between fluctuations at two toroidal locations are calculated in three manners; (1) coherence between potential fluctuations, (2) that between electric field and potential fluctuations, and (3) that between electric field fluctuations.

Figure 2 shows the shot-averaged coherences for the above three cases.

In the first case, the local maxima corresponding to the peaks of the potential spectrum are found to have the highest values among the three cases of coherence. In the second case, the coherence values at the peaks decrease and some of the peaks are lost in the background level. This reduction of the coherence can be ascribed to the loss of the path integral term. In particular, the two peaks are clearly distinguished around the frequency of 17 kHz, demonstrating the presence of two different modes in the narrow frequency range. Finally, in the third case the four peaks at 8, 16, 18 and 35 kHz can be still recognized although the absolute values of coherence are extremely reduced, since the electric field measurement reflects quite local characteristics.

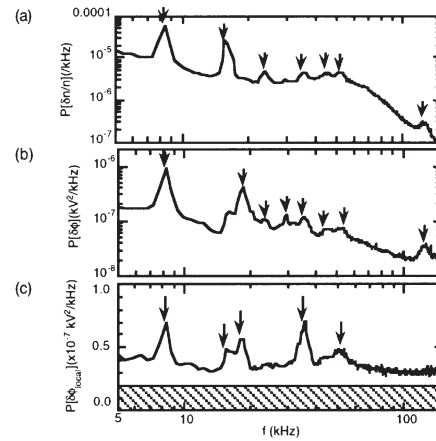


FIGURE1. Spectra of (a) density, (b) potential and (c) electric field fluctuations in an ECR-heated plasma. The observation point is  $r=12$  cm.

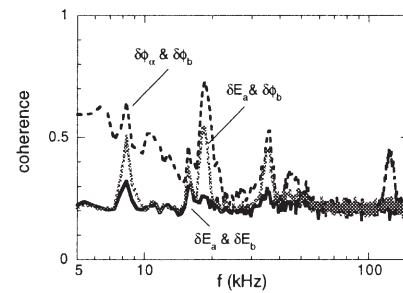


FIGURE2. Coherence between fluctuations at two toroidal locations. The solid, grey-dashed and the black-dashed lines represent the curves of coherence between electric field fluctuations, electric field-potential fluctuations, and potential-potential fluctuations at two toroidal locations.

### REFERENCE

- 1) A. Fujisawa et al., Plasma Phys. Control. Fusion **48** (2006) S31–S39



## §15. The Density Profile Measurement with Heavy Ion Beam Probe System on CHS

Shimizu, A., Fujisawa, A., Nakano, H., Oshima, S. (Nagoya Univ.), Iguchi, H., Minami, T., Suzuki, C., Akiyama, T., Yoshimura, Y., Nagaoka, K., Isobe, M., Takahashi, C., Okamura, S., Matsuoka, K., CHS Group

Diagnostics to measure the density profile is indispensable to study the particle transport. In CHS, phenomena such as MHD instability and bifurcation are often accompanied by the change in the density profile. Therefore it is important to measure the density profile with high temporal resolution to make clear the physical mechanism of these phenomena. Conventionally, Thomson-scattering and FIR are used to measure the density profile. Heavy Ion Beam Probe (HIBP) also has the possibility to be a powerful tool to measure it. In CHS, by sweeping the probing beam fast, density profile is obtained with relatively fast temporal resolution ( $\sim 4$  ms).

In HIBP diagnostics, the intensity of secondary beam detected at the detector is roughly proportional to electron density of plasma at the ionization position. However, the beam current decays on the beam path by collisions, so we must take this effect (so called "the path integral effect") into account to obtain the accurate density profile from HIBP diagnostics. The intensity of secondary beam current is expressed as,  $I_s = I_0 n_e \langle \sigma_{12} v_e \rangle \exp(-\beta_1 - \beta_2) \delta \ell_s / v_B$ . Here,  $I_s$ : secondary beam current,  $I_0$ : injected beam current,  $\langle \sigma_{12} v_e \rangle$ : the ionization rate averaged by the Maxwell velocity distribution,  $n_e$ : electron density at the ionization point,  $\delta \ell_s$ : sample volume size,  $v_B$ : the velocity of beam. The coefficient  $\beta_1$  ( $\beta_2$ ) is the attenuation factor of beam on primary (secondary) beam path, and is expressed as  $\int n_e \langle \sigma_{12} v_e \rangle / v_B d\ell_1$  ( $\int n_e \langle \sigma_{23} v_e \rangle / v_B d\ell_2$ ). Here,  $\langle \sigma_{23} v_e \rangle$  is the ionization rate of double charged ions to triple or higher charged state. The injected beam current  $I_0$  is not easy to measure accurately, so we develop a method to obtain  $n_e$  profile without the information of  $I_0$  itself [1]. In this method, the following equation should be solved:

$$-\frac{1}{n_e(\rho)} \frac{\partial n_e}{\partial \rho}(\rho) = -N^-(\rho) + \frac{1}{\langle \sigma_{12} v_e \rangle(\rho)} \frac{\partial \langle \sigma_{12} v_e \rangle}{\partial \rho}(\rho)$$

$$-\frac{1}{2} \left[ \frac{\partial \beta_1}{\partial \rho}(\rho) - \frac{\partial \beta_1}{\partial \rho}(-\rho) + \frac{\partial \beta_2}{\partial \rho}(\rho) - \frac{\partial \beta_2}{\partial \rho}(-\rho) \right] \quad (1).$$

Here,  $N^-(\rho) = \left[ \frac{1}{I_s(\rho)} \frac{\partial I_s}{\partial \rho}(\rho) - \frac{1}{I_s(-\rho)} \frac{\partial I_s}{\partial \rho}(-\rho) \right]$  and  $\rho$  is the normalized minor radius at the ionization points.

Because  $\beta_1$  and  $\beta_2$  include path integral of  $n_e$ , Eq. (1) is an integral equation of  $n_e$ . According to the paper [1], the Eq.(1) can be solved numerically by the iterative calculation. In this method, the path integral effect can be reduced because in the Eq.(1)  $\partial \beta_1 / \partial \rho(\rho) \sim \partial \beta_1 / \partial \rho(-\rho)$  and  $\partial \beta_2 / \partial \rho(\rho) \sim \partial \beta_2 / \partial \rho(-\rho)$  so the sum of terms in the rectangular bracket of Eq.(1) becomes small. In Fig.1, the first, the second and the third terms in R.H.S of Eq.(1) at the last iteration are shown as a function of  $\rho$ . The third term (sum of  $\beta'$  terms) is small and has only small effect on  $n_e$  profile.

In the Fig.2, the temporal evolution of density profile measured with HIBP is shown. Up to 100 ms, plasma is sustained by ECRH, and after 100ms, it is sustained by NBI. We can see the hollow profile for ECR heated plasma and the parabolic profile for NB heated plasma. We will use this method to study the particle transport in phenomena such as bifurcation, radiation collapse etc.

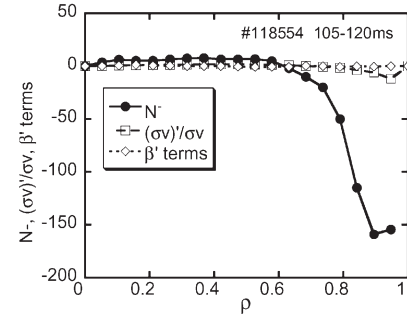


Fig.1. Terms in Eq.1 as a function of  $\rho$

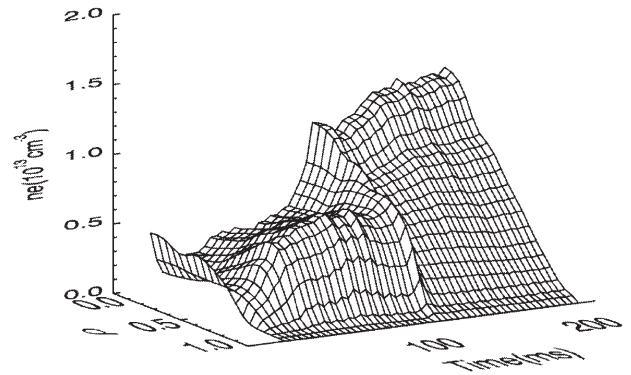


Fig.2. Temporal evolution of density profile measured with HIBP. Up to 100 ms, plasma is sustained by ECRH, after 100 ms it is sustained by NBI.

### Reference

- 1) A. Fujisawa, et al., Rev. Sci. Instrum. **74**, (2003) 3335

## §16. Reconstruction Method of Local Density Fluctuation Spectrum with a Heavy Ion Beam Probe

Nakano, H., Fujisawa, A., Shimizu, A., Ohshima, S.

A heavy ion beam probe (HIBP) can measure density fluctuation from the detected beam fluctuation, although the measured fluctuation contains so-called path integral effects. This report describes a method to reconstruct the normalized local density fluctuation,  $\xi = d n_e / n_e$ , from the normalized detected beam fluctuation,  $\eta = d I_d / I_d$ , and presents the obtained spectrum of local density fluctuation in CHS. The relation between these two quantities  $\xi$  and  $\eta$  are written in the following integral equation for each frequency,

$$\begin{aligned} \langle \eta^2(\rho_*) \rangle &= \langle \xi^2(\rho_*) \rangle \\ &- 2 \int \langle \xi(\rho_*) \xi(\rho_1) \rangle S_1(\rho_1) d l_1 \\ &- 2 \int \langle \xi(\rho_*) \xi(\rho_2) \rangle S_2(\rho_2) d l_2 \\ &+ \iint \langle \xi(\rho_1) \xi(\rho_1') \rangle S_1(\rho_1) S_1(\rho_1') d l_1 d l_1' \\ &+ \iint \langle \xi(\rho_2) \xi(\rho_2') \rangle S_2(\rho_2) S_2(\rho_2') d l_2 d l_2' \\ &+ 2 \iint \langle \xi(\rho_1) \xi(\rho_2') \rangle S_1(\rho_1) S_2(\rho_2') d l_1 d l_2' \end{aligned} \quad (1)$$

where  $S_i$  and  $d l_i$  represent ionization ratio which describe electron density,  $n_e$ , and temperature,  $T_e$ , and line element of beam orbit, respectively. Subscripts \*, 1 and 2 indicate ionize point, primary and secondary beam orbits, respectively. A bracket,  $\langle \rangle$ , means ensemble average. If  $\langle \xi(\rho_i) \xi(\rho_j) \rangle$  can replace  $|\xi(\rho_i)| |\xi(\rho_j)| \exp(-\Delta_{ij}^2 / l_c^2)$ , a correlation length,  $l_c$ , can be defined, where  $\Delta_{ij}$  is a distance between  $\rho_i$  and  $\rho_j$ .

In Eq. (1), the ionization position and the distance are known from trajectory calculation,  $\eta$  is measured with HIBP, and  $n_e$  and  $T_e$  are also measured with other diagnostics. Hence, the normalized density fluctuation  $\xi$  can be obtained by solving Eq. (1) with an iteration method if the correlation length  $l_c$  is given.

The CHS-HIBP measures simultaneously neighboring three positions, where distance is a few centimeter, and  $l_c$  can evaluate approximately from coherence of detected beam fluctuations. Using this approximation, the iteration process to solve Eq. (1) succeeds in finding solutions in a higher frequency range above 50 kHz, while it fails in lower frequency.

This is caused by the fact that the correlation length appears to become longer than the actual value because of path integral effect on the correlation length. The fluctuations of local three channels are strongly affected by the fluctuations in the outer plasma regions, where the density fluctuation is large. The correlation between detected beam fluctuations at two neighboring points is related to that between the corresponding local density fluctuations, as

$$\langle \eta^*(\rho_a) \eta(\rho_b) \rangle = \langle \xi^*(\rho_a) \xi(\rho_b) \rangle + \beta^2(\xi^*(\rho_a), \xi(\rho_b)), \quad (2)$$

where superscript \* indicates complex conjugate, and

$\beta^2$  is path integral term which has eight integral terms. The term  $\beta^2$  should be necessary to be estimated to obtain the local power density in the low frequency regime, where the iteration process fails. As the first order approximation, we evaluate the correlation length by substituting  $\eta$  instead of  $\xi$  into the term,  $\beta^2(\xi^*(\rho_a), \xi(\rho_b))$ , of Eq. (2).

Figure 1 show correlation length as a function of radius before and after this correction at 10 kHz for the plasma maintained by ECRH with parameters,  $n_e \sim 0.5 \times 10^{19} \text{ m}^{-3}$  and  $T_e(0) \sim 1.5 \text{ keV}$  in CHS. Before correction, gray line in Fig. 1, correlation length has a maximum around  $r/a = 0.85$  and gradually decreases toward the center. After correction, black line in Fig. 1, the correlation length takes a maximum at the same radius, but the length become much shorter inside  $r/a < 0.7$ . Hence, the path integral effect on the correlation length is quite large in this region.

We succeed in estimating the power spectra of local density fluctuation by using corrected correlation length. Figure 2 shows an example of the reconstructed power spectrum of local density fluctuation, whose position is  $r/a = 0.26$  in  $n_e = 1.0 \times 10^{19} \text{ m}^{-3}$  and  $T_e(0) \sim 1.0 \text{ keV}$  maintained by ECRH. The result shows that the path integral effect is larger in low frequency than in high frequency. The proposed method expands the applicability of HIBP to higher density regime where the path integral effect largely deviates the detected beam fluctuation from the local density fluctuation. It helps understanding physics of high-density plasma, for example, NBI plasma, density collapse, etc.

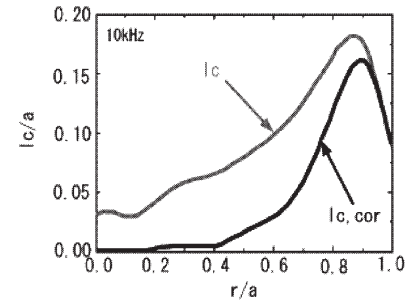


Fig.1. Correlation lengths before (gray line) and after (black line) the correction at 10 kHz.

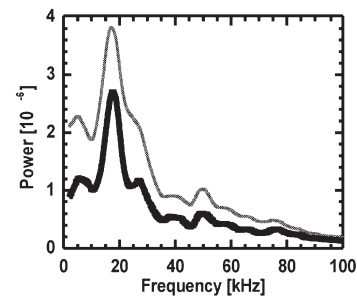


Fig. 2. Detected beam (gray line) and local density fluctuation (black line) spectrum.

## §17. Fluctuation Measurement of High Density Plasma using HIBP with Rb Ion Beam

Ohshima, S. (Dep. Energy Eng. Sci., Nagoya Univ.),  
Fujisawa, A., Shimizu, A., Nakano, H., CHS Group

In operation of heavy ion beam probe (HIBP), higher beam energy is required to sense higher density plasmas. In HIBPs on the CHS, Cs beam with about 70keV is usually used as a probing beam and the maximum of measurable plasma density is about  $1.0 \times 10^{19} \text{ m}^{-3}$ , because of attenuation of the Cs beam. Recently, we have developed the rubidium (Rb) ion source and have succeeded in operating the HIBP measurement using Rb beam. Sufficient beam current to measure the fluctuation can be obtained at the detector of the HIBP using the Rb beam, up to or above  $3.0 \times 10^{19} \text{ m}^{-3}$ .

Here, an example of HIBP measurement using Rb beam is demonstrated. The experiments were operated in NBI plasmas on CHS and in the following condition; The toroidal magnetic field strength and the magnetic axis are  $B_t = 0.88 \text{ T}$  and  $R_{\text{Axis}} = 0.92 \text{ m}$  and the line-averaged plasma density is  $n_e \sim 1.5 \times 10^{19} \text{ m}^{-3}$ .

On this condition, sufficient beam current of the HIBP to measure fluctuations was obtained, successfully. In the plasma, fishbone-like oscillation (called “CHS-burst” here) and high frequency mode (HFM) conjectured as Alfvén eigenmode were observed, in magnetic probe signal and potential signal obtained by HIBP. The typical signals are shown in figure.1. The observation point of the HIBP is  $r/a = 0.5$ . Obviously, the potential signal is highly correlated with magnetic probe signals located at the plasma outside. In addition, band-pass filtered signals of potential are also shown in the figure. One is the filtered signal from 5 to 75 kHz, corresponding to frequency of the CHS-Burst oscillation. The other is the filtered signal from 75 to 125kHz, containing the frequency component of HFM oscillation. In the figures, it is shown that the two modes appeared alternately.

Time development of frequency spectrum for the potential signal at  $r/a = 0.6$  is exhibited in Figure. 2. The spectrum is obtained by wavelet transform to attain high time resolution. Clearly, the frequency of the burst oscillation is found to be swept from 50 to 10 kHz. On the other hand, the frequency of the HFM is constant around 100kHz.

From potential fluctuation amplitude, we can infer the internal structure of the modes. If we assume that potential on a magnetic surface is constant, the potential fluctuation reflects oscillation of the flux surface. Radial profiles of the fluctuation amplitude are presented in Fig. 3. For the burst oscillation, two profiles of frequency components from 30 to 50kHz and from 5 to 15kHz are shown in the figure. The profiles of the amplitudes have maximum at  $r/a = 0.6$ . The amplitude of CHS-burst decreases as frequency decreases, but the relative shape of the profile has no significant change. For the HFM, the profile is very similar to that of burst oscillation. The profile also has maximum at  $r/a = 0.6$ . In the radial region, the magnetic configuration has  $q=2$  surface and their modes have poloidal mode number  $m=2$ .

In summary, we succeeded in detecting fluctuation in high density plasma using HIBP. Thereby, internal structure of potential fluctuation for MHD modes are obtained.

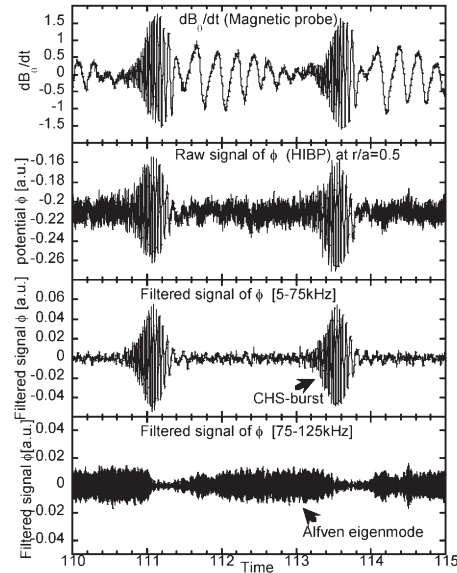


Fig. 1. Typical potential signal obtained by HIBP at  $r/a = 0.5$  and band-pass filtered signals of 5-75kHz and 75-125kHz.

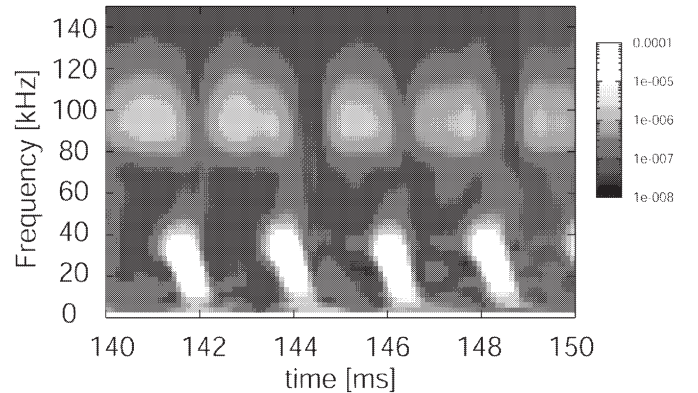


Fig.2 Time development of frequency spectrum for potential signal (obtained by wavelet transform)

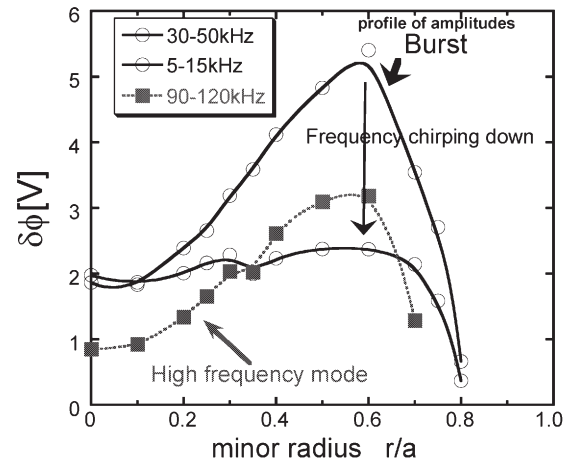


Fig.3 Radial profile of fluctuation amplitudes. Solid and dotted lines indicate fluctuation amplitudes of burst and high frequency mode, respectively.



## §18. Observation of Nonlinear Interaction between Coherent and Turbulent Magnetic Fluctuations on CHS

Nagashima, Y., Itoh, S.-I., Yagi, M. (RIAM, Kyushu Univ.),  
Nagaoka, K., Fujisawa, A., Ida, K., Okamura, S.,  
Matsuoka, K., Itoh, K.

A study of nonlinear self-regulation processes in plasma turbulence has crucial importance for clarifying the mechanism of anomalous transport in magnetically confined plasmas. Recent theoretical progress has highlighted the importance of nonlinear couplings between meso-scale structures and micro-scale turbulent fluctuations. In this report, we show an observation of nonlinear interaction between a low frequency coherent magnetic fluctuation and a few hundred kHz turbulent fluctuations in the H-mode edge plasmas of the CHS device. The coherent magnetic fluctuation has been intensively studied by a beam emission spectroscopy [1]. We have performed edge fluctuation measurements by the hybrid probe (HP) [2] for investigating edge nonlinear processes and contribution of the coherent fluctuations to transport. The HP has 4 electrodes. One electrode measured the ion saturation current fluctuation  $I_{i,\text{sat}}$  and other three electrodes were used for floating potential fluctuation  $\phi_{\text{float}}$  measurements.

Cross correlation is measured transport process. For instance, particle flux is estimated from a summation of quadratic spectra,  $\Gamma_r = \text{Re}\{\sum \langle (-ik_\theta n_e(f)\phi_p(f))/B_0 \rangle\}$ , where  $n_e(f)$  is the density fluctuation at frequency  $f$ , and  $-ik_\theta\phi_p(f)$  is the poloidal electric field, respectively.

Cross-biphase is useful in measuring nonlinear processes in convection. In the case that a (coherent) fluctuation has a density fluctuation and modulates other higher frequency density and poloidal electric field fluctuations (forward interaction), radial particle fluxes driven by the modulation,  $n_e(f_1)E_\phi(f_2)$  is synchronized with the modulating fluctuation at  $f=f_1+f_2$ . This flux is not DC flux, but has a nonlinear effect on the modulating density fluctuation ( $f_1+f_2$ ). The cross-bicoherence,  $\langle n_e(f_1)\phi_p(f_2) \rangle^2 / \{ \langle n_e(f_1)\phi_p(f_2) \rangle^2 + \langle n_e(f_1+f_2) \rangle^2 \}$  indicates the process that the modulating density fluctuation  $n_e(f_1+f_2)$  is affected by the radial particle transport (backward interaction).

Figures 1 show quadratic spectra of  $\phi_{\text{float}}$ . Three types of fluctuations were observed. First one is a low frequency coherent fluctuation around 4 kHz with a long-range poloidal correlation (Type A). This is the same fluctuation studied in Ref. [1]. The second one is broadband fluctuations in several tens kHz. From correlation analysis, the second one has short poloidal correlation length (Type B). The third one is broadband fluctuations around a few hundreds kHz, which has also long-range correlation (Type C). Type A and C in  $I_{i,\text{sat}}$  have significant correlation with magnetic fluctuations.

Figures 2 show results of bispectral analysis applied to the hybrid probe data. Auto-power spectra of  $I_{i,\text{sat}}$ , auto-bicoherence of  $I_{i,\text{sat}}$ , and total squared cross-bicoherence

$\Sigma[\langle I_{i,\text{sat}}(f_1)\phi_{\text{float}}(f_2)I_{i,\text{sat}}(f_1+f_2) \rangle^2 / \{ \langle I_{i,\text{sat}}(f_1)\phi_{\text{float}}(f_2) \rangle^2 + \langle I_{i,\text{sat}}(f_1+f_2) \rangle^2 \}]$  are shown in Figs. 2(a), (b), and (c), respectively. The significant nonlinear couplings between type A and C are observed, indicating that the coherent fluctuation modulates type C. In the total squared cross-bicoherence, we can observe a spectral peak around the same frequency as type A, and this identifies existence of modulated radial particle flux and its effects on the modulating MHD fluctuation. In this report, we have presented first observation that coherent magnetic fluctuations are interacted with the broadband fluctuations.

For quantitative identification of radial fluxes by the modulation process, conclusive cross-bispectra well above the significance level should be obtained, and this is a future task.

This work was partially supported by Grant-in-Aid for Specially-Promoted Research (16002005) of MEXT Japan, by the 4-2-4 program of Kyushu University, and Grant-in-Aid for Scientific Research (15206106). Supports of all members of the CHS group in carrying out the experiments are appreciated.

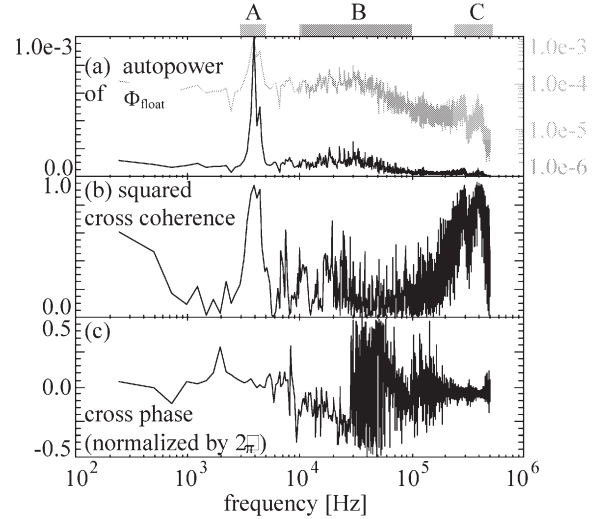


Fig. 1. Quadratic  $\phi_{\text{float}}$  spectra. (a) Auto-power, (b) poloidal coherence, and (c) cross-phase. Gray line in Fig. (a) indicates same plots as black line in log scale.

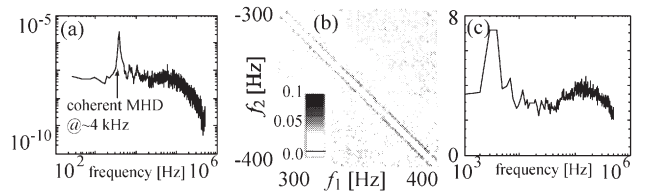


Fig. 2. Results of bispectral analyses. (a) Auto-power of  $I_{i,\text{sat}}$ , (b) auto-bicoherence of  $I_{i,\text{sat}}$  in the 300-400 kHz range, and (c) the total squared cross-bicoherence,  $\Sigma[\langle I_{i,\text{sat}}(f_1)\phi_{\text{float}}(f_2)I_{i,\text{sat}}(f_1+f_2) \rangle^2 / \{ \langle I_{i,\text{sat}}(f_1)\phi_{\text{float}}(f_2) \rangle^2 + \langle I_{i,\text{sat}}(f_1+f_2) \rangle^2 \}]$ .

### Reference

- 1) Oishi, T., et al., Nucl. Fusion **46**, (2006) 317.
- 2) Nagaoka, K., et al., Plasma Fusion Res. **1**, (2006) 005.



## §19. Measurements of Electron Density Fluctuations in CHS Plasmas by Using YAG Laser Imaging Method

Matsuo, K. (Fukuoka Institute of Technology), Iguchi, H., Okamura, S., Matsuoka, K.

We have applied a novel technique of a YAG laser imaging method for obtaining information on electron density fluctuations, including the spatial distribution in CHS plasmas.<sup>1)</sup> In this fiscal year, i) a dual beam optical system developed for increasing further the signal intensity was applied to CHS, and ii) by the system the density fluctuations were measured during discharge with transport barrier.

Figure 1 shows the optical system for CHS. The YAG laser ( $\lambda_i = 1.064 \mu\text{m}$ , 1.2 W) beam is transported by a PM optical fiber near the CHS plasma. A radiation beam from the fiber is expanded and collimated by a beam-expander, and injected into the plasma. Transmitted beam is reflected by a mirror with  $\lambda/4$  waveplate and passes through the plasma again. This beam is reflected by polarizer toward imaging optics. The beam is then transmitted through focusing and imaging lenses along with a phase mirror, and then received by a one-dimensional 16-fiber array connected to low noise detectors. In addition to the one-dimensional spatial measurements, two-dimensional spatial measurements at the detecting plane were performed by making the detector array to rotate shot by shot under the condition of fixed operation to observe 2D image equivalently. The measurable frequency range determined by the frequency response of the detector is 20 kHz to 1 MHz. The measurable wavelength determined by the beam width and number of detector channels ranges 2 mm to 47 mm.

Plasma is initially produced and heated by ECH and further heated by NBI. Figure 2 shows an example of a distribution of propagational direction of the fluctuations at  $t=40\text{--}48.4\text{ms}$  (before the transition) as a function of the frequency by the contour lines. The spectrum of the density fluctuation distributes broadly between 20 kHz – 80 kHz, and decreases as the frequency increases. 0 and 90 degrees show the components which propagate in major radius and toroidal directions respectively. In this method spatial positions of the density fluctuations are required by the correspondence of observed propagational direction with direction of magnetic line of force, because the observed micro-turbulence generally propagates toward perpendicular direction to a magnetic filed. In Fig. 2, “+ $\theta$ ” means upper half region and “- $\theta$ ” means lower half region along the probe beam path in the plasma cross section. The fluctuations are strong near +23 and -17 degrees. These angles are corresponding to normalized radius  $\rho \sim 0.8$  when they are correspondent to

the direction of magnetic lines of force of CHS.

Obtaining and analyzing the fluctuation data in the discharges with the transition of confinement condition are in progress.

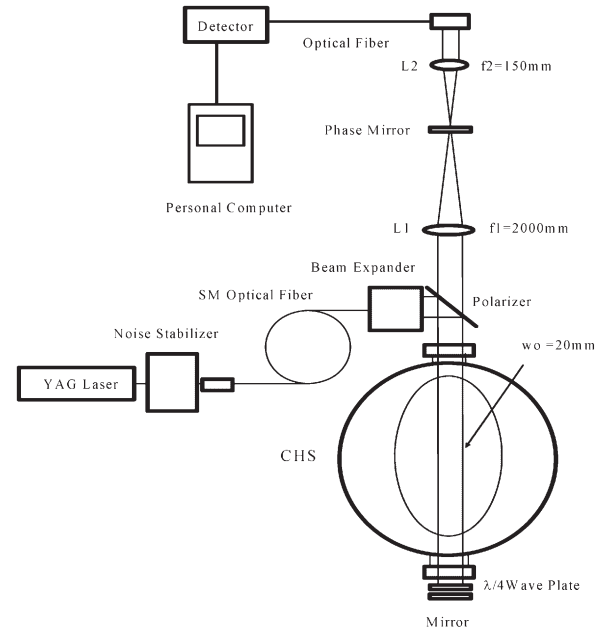


Fig. 1 Laser Imaging System for CHS.

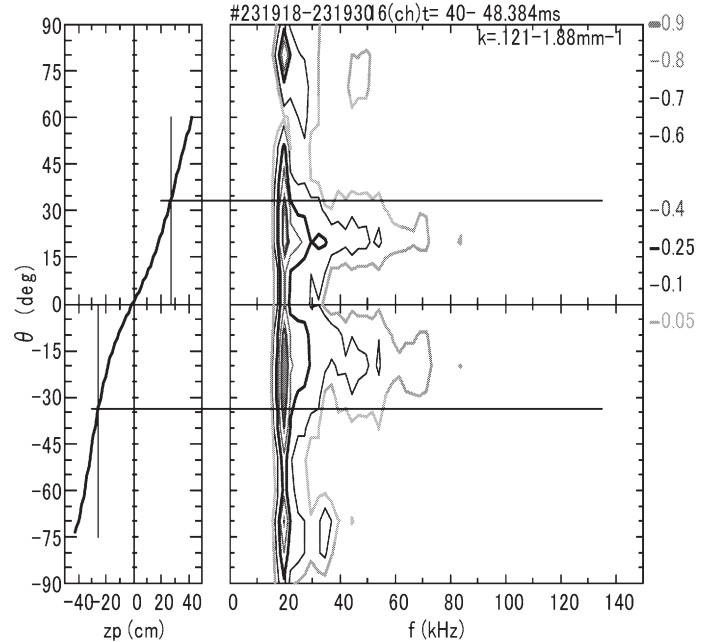


Fig. 2 An example of the distribution of the propagational direction as a function of the frequency. (The transition happened at  $t=54\text{ms}$  in observed discharge.) Upper and lower solid lines indicate coordinates of each plasma edge.

## §20. Up-Down Asymmetry of the Plasma in the Ergodic Layer of CHS

Nakamura, K., Iguchi, H., CHS Group

Plasma structures near and out side of the last closed flux surfaces (LCFS) have been measured by use of the lithium beam probe (LiBP) in CHS. There are two typical magnetic configurations for edge plasmas, namely, the inboard limiter configuration and the magnetic limiter configuration.

When the magnetic axis is shifted outward, a chaotic magnetic field layer appears surrounding the core plasma. The layer is formed because the magnetic field line wanders in and out and no closed flux surfaces are formed.

A lithium neutral beam with the energy up to 15 keV and with the equivalent beam current of a hundred microamperes is injected from the M-port (located upside of the torus). Light emission from the beam due to plasma particles impact excitation (670.8 nm) is collected through a window mounted on the O-port (located outside of the torus).

Experiments have been carried out for the magnetic axis of  $R_{ax} = 1.016$  m and the magnetic field strength of 0.93 T on the axis. A hydrogen plasmas are produced by electron cyclotron resonance (ECR) heating with a gyrotron of 53 GHz. Neutral beam injection (NBI) heating with the beam energy of 40 keV is added. Plasma density is controlled by preprogrammed gas puff system. The average electron density is about  $0.8 \times 10^{19} \text{ m}^{-3}$  in the ECH plasma and is  $2 \times 10^{19} \text{ m}^{-3}$  in the NBI plasma. Two-dimensional profile of the electron density for the ECH plasma is shown in Fig.1, which shows that the electron density distribution of the ECH plasma shifts up-ward in the chaotic field region ( $x > 1275$  mm) near the separatrix. The NBI plasma also shows up-ward shift similar to the ECH plasma. Figure 2 shows the density distributions along vertical lines (a) ~ (e) in Fig.1. Up-down asymmetry is clearly shown. The density peak shifts further upward as horizontal location goes outward.

In order to see the effect of magnetic field direction on the plasma shifts, experiments for the reversed magnetic field direction have been carried out. The average electron densities are about  $0.6 \times 10^{19} \text{ m}^{-3}$  and  $0.8 \times 10^{19} \text{ m}^{-3}$  for ECH and NBI plasmas, respectively. Figure 3 shows the electron density profile in the ECH plasma along the same line (a) ~ (e) in Fig.1. The electron density distribution now shifts downward. It is found that the up-down asymmetry of electron density distribution reverses with the reversed magnetic field direction. Plasma shift is apparently in the direction of ion  $\mathbf{B} \times \nabla B$  drift.

It is noted that the up-down asymmetry is sustained in steady state. The experimental result suggests that plasma equilibrium in the ergodic layer is not determined simply by the magnetic field structure. Since the  $\mathbf{B} \times \nabla B$  drift is directed opposite for ions and electrons, electric field will be induced. Then the  $\mathbf{E} \times \mathbf{B}$  drift will also affect the final

flow patterns. Information on electric field is necessary to confirm this model, which is unknown at the moment. The observed asymmetry will be a source of loss flux asymmetry on divertor plates, which is observed various helical devices.

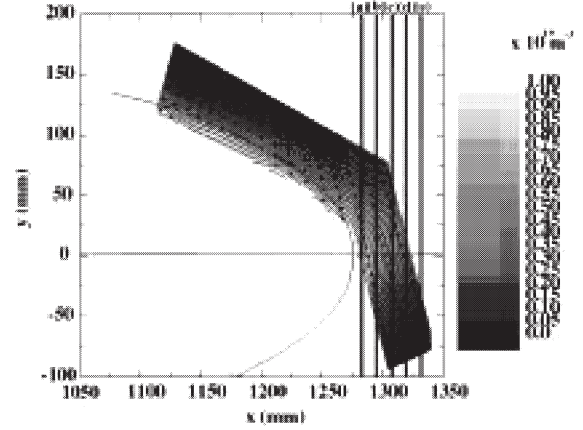


Fig. 1 Two-dimensional profiles of the electron density for the ECH plasma for magnetic limiter configuration.

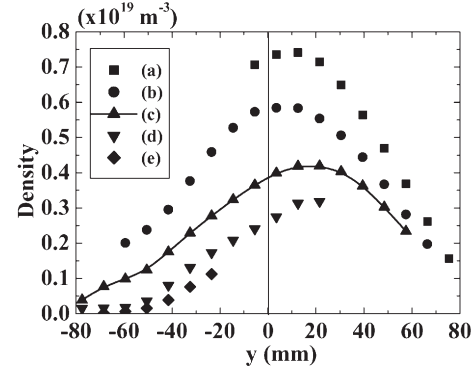


Fig. 2 Density distributions along vertical lines (a) ~ (e) in Fig 1.

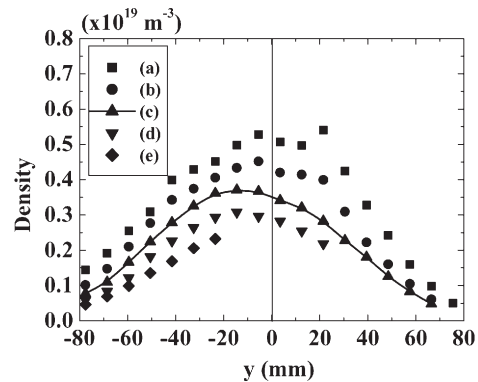


Fig. 3 Density distributions along vertical lines (a) ~ (e) in Fig 1 at the reversed magnetic field directions.

## §21. Design and Initial Operation of Lost Fast-Ion Probe Based on Thin Faraday Films in CHS

Isobe, M., Toi, K., Nagaoka, K., Okamura, S. (NIFS), Goto, K. (Nagoya Univ.)

A scintillator-based lost fast-ion probe (SLIP) has been employed in CHS to study anomalous transport and/or resulting losses of fast ions caused by fast-ion-driven MHD instabilities in NB-heated plasmas. Although the SLIP can provide relative intensity of lost fast-ion flux at the probe position and information of their gyroradius centroid and pitch-angle  $\chi$ , an issue on their absolute flux still remains because of difficulty of absolute calibration of the SLIP. In order to enhance further fast ion physics experiment in CHS, we have designed and constructed a new lost fast-ion probe based on thin Faraday films (FLIP), providing the electric current generated by lost fast ions. Compared with the SLIP, primary advantages of the FLIP are lower system cost and capability for quantitative evaluate of absolute flux of lost fast ions. Also, the FLIP is supposed to be promising for lost alpha diagnostic in a future reactor plasma because it can be operated in hostile thermal and radiation environments, whereas the SLIP may not be because the luminosity of scintillator depends on temperature and largely falls when temperature goes over about  $150^{\circ}\sim 200^{\circ}$ . A possible major drawback of the FLIP is that it may easily suffer from electromagnetic noise because a weak current have to be measured. In this article, the design concept of the FLIP and initial results of lost fast ion diagnostic in NB-heated plasmas of CHS are reported.

The FLIP is installed on an upper diagnostic port at the outboard sides of CHS ( $R=1.2$  m) where the cross section of plasmas is horizontally elongated and can be moved vertically. The essential part of the FLIP is a molybdenum steal box with thin films of aluminum (Al) vapor-deposited onto one face of the quartz substrate ( $34\text{ mm} \times 34\text{ mm}$ ) on the bottom of the box. The thickness of thin Al films is about  $0.2\text{ }\mu\text{m}$ . Two apertures, one behind the other, are on one side, and restrict the orbits of fast ion that can enter the probe. The aperture structure is basically the same as those of the existing SLIP. The Al film ( $10\text{ mm} \times 15.5\text{ mm}$  for each) is divided into six zones to provide gyroradius centroid and pitch-angle of lost fast ions simultaneously. Fast ions with larger gyroradii strike the Al films farther from the apertures than those with smaller gyroradii and their strike points are dispersed along a line passing through the center of two apertures according to their pitch angles. Currently, the Al films, i.e., ion collectors are operated without biasing voltage.

The electric circuit employed here is shown in Figure 1. The frequency response and gain of the current preamplifiers are chosen to be from DC to 20 kHz and  $10^6$  V/A, respectively. The ion current signals are digitized with the sampling frequency of 500 kHz. The electric currents generated by escaping fast ions have been

successfully observed in NB-heated plasmas. Figure 2 shows waveforms of line-averaged  $n_e$ , magnetic spectrogram,  $H\alpha$  light emissivity and the FLIP currents originating in lost fast ions obtained from the ion collector of Ch. 3 and Ch. 5 in  $R_{ax}/B_t=0.974\text{ m}/0.91\text{ T}$ . In this shot, two NBs ( $E_b=40\text{ keV}$  and  $32\text{ keV}$ ) are tangentially co-injected into a low density target plasma ( $n_e=(0.3\sim 0.6)\times 10^{19}\text{ m}^{-3}$ ). The current measured in Ch. 3 is expected to be the largest among all ion collectors. Here, the films of Ch. 3 and Ch. 5 collect lost beam ions having energy close to  $E_b$ . The orbit calculation shows that the corrector of Ch. 3 can detect co-going transit beam ions having relatively low pitch-angle ( $\chi(=\arccos(v_{||}/v)) > 133^{\circ}$ ). Their orbits deviate substantially from the magnetic flux surfaces toward the large major radius side. On the other hand, the collector of Ch.5 can detect trapped beam ions having relatively high pitch-angle  $\chi < 132^{\circ}$ . The FLIP current appears just after NB injection and evolves gradually in time. In this discharge, the energetic particle mode (EPM) ( $m/n=3/2$ ) and the toroidicity-induced Alfvén eigenmode (TAE) ( $m/n=2,3/1$ ) are excited due to tangentially co-injected beam ions. Correlated with these modes, the FLIP current is periodically enhanced, indicating beam ion losses due to the EPM activities.  $H\alpha$  light emissivity from the edge chord at the outboard side of horizontally elongated cross section also increases periodically. This is due to enhanced transport of beam ions toward the outboard side of the torus.

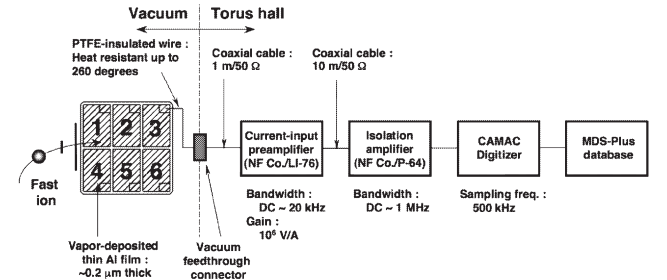


Fig. 1. Electric circuit used for the FLIP of CHS.

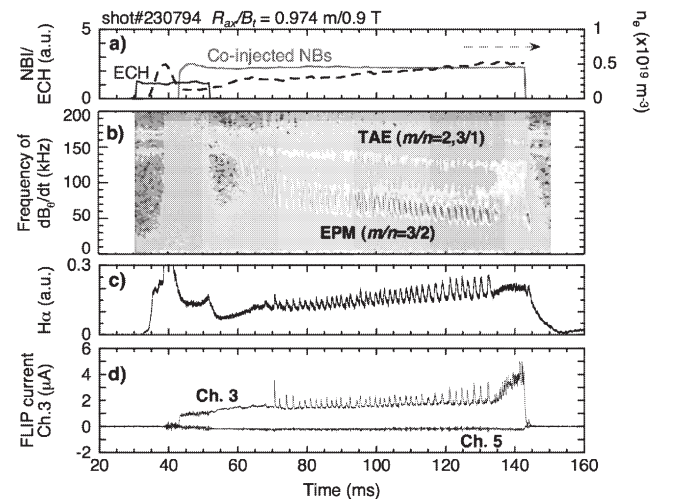


Fig. 2. Typical waveforms for fast-ion-driven MHD instabilities.

## §22. Measurement of Energetic Ion Profile by Calorimetric Method

Nagaoka, K., Isobe, M., Toi, K., Goto, K. (Nagoya Univ.), Osakabe, M.

MHD instabilities induced by energetic ions are crucial issues in burning plasmas. In many experimental devices, some kinds of Alfvén eigenmodes (AEs) and energetic particle modes (EPM) were observed, and loss mechanism of energetic ions has been studied both experimentally and theoretically. The mode excitation mechanism is also important topics in this field. The energetic particle profile, however, can be scarcely experimentally measured, though it is very sensitive to EPM excitations. In this research, a calorimetric method was applied to measurement of energetic ion profile.

Ten-thermocouple array is installed in a large probe (40mm in diameter) and local heat flux measurements have been performed in CHS. In order to distinguish energetic ion heat flux from bulk plasma one, co-going heat flux and ctr-going heat flux are measured each other, which is shown in Fig.1. The heat flux from the bulk plasma (ctr heat flux) is very small and 10% of that from energetic ions (co heat flux). The heat fluxes decrease in small  $z$  region, when the probe is deeply inserted in the core plasmas. In the low  $z$  region, it is considered that the probe intercept energetic ion orbits, because the diameter of the probe is comparable with that Larmor radius of energetic ions ( $\sim 30\text{mm}$ ).

In order to avoid the intercept effect, a small probe (4mm in diameter) was used for this measurement. In the plasma with excitation of MHD bursts, the energetic ion profile was measured along a probe insertion angle, which is shown in Fig.2, and the result is also shown in Fig.3. The lump is observed in the energetic ion profile in the region of  $0.8 < r/a < 0.9$ . This structure is considered to be important for excitation of EPM. In this measurement, the heat load gives terrible damage to the probe, although short pulse injections of neutral beam were used. This method has limitations of time resolution and heat removal, so further improvement is necessary for systematic experimental researches.

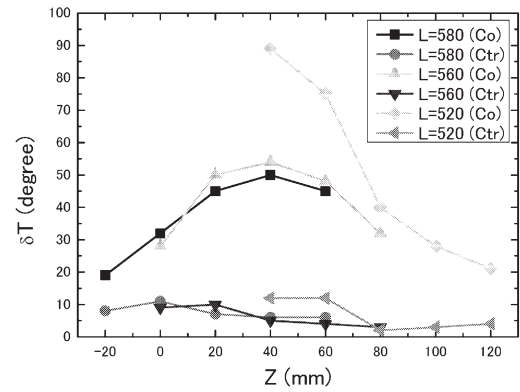


Fig.1 Heat flux profiles measured by the large probe.

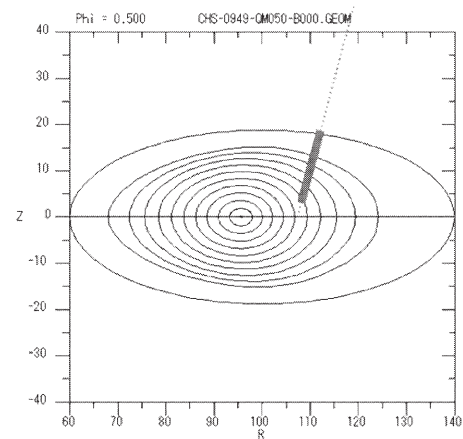


Fig.2 The schematic of probe insertion angle and measuring positions..

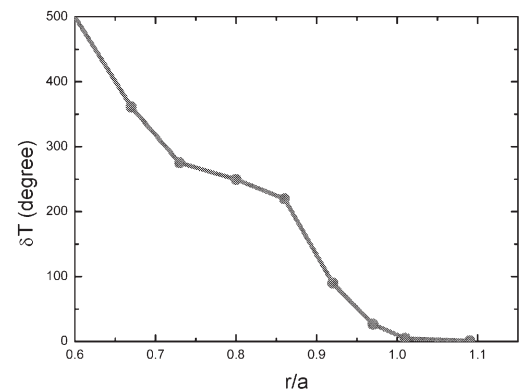


Fig.3 The energetic ion profile as a function of minor radius.



### §23. Formation of Peaked Density Profile in Dimensionally Similar Low Temperature Plasmas at Very Low Toroidal Magnetic Field on CHS

Toi, K., Ikeda, R.,<sup>1)</sup> Takeuchi, M.,<sup>1)</sup> Suzuki, C.,  
Jinguji, Y.,<sup>1)</sup> CHS Experimental Group  
<sup>1)</sup> Dep. Energy Sci. Eng., Nagoya Univ.

We are attempting experimental simulation of particle and energy transport in high temperature plasma produced at high toroidal field ( $B_t \geq 1\text{ T}$ ) using dimensionally similar low temperature and density plasma produced at very low  $B_t$  ( $\leq 0.1\text{ T}$ ) in CHS [1, 2]. The latter plasma is produced by two sets of 2.45 GHz micro-wave source of which launching power  $P_{\text{ECH}}$  is up to 20 kW, respectively. Over-dense plasma is routinely obtained. It is interpreted that heating by electron Bernstein waves converted from launched electron cyclotron waves near the plasma edge having steep density gradient is dominant [3].

When the second heating pulse is superimposed from  $t=120\text{ ms}$  on an over-dense plasma produced by the first pulse, strong peaking of electron density profile occurs during the second pulse. In this plasma, electron temperature is in  $T_e=10\text{--}30\text{ eV}$  and electron density in  $1\text{--}3 \times 10^{17}\text{ m}^{-3}$ . Typical waveforms are shown in Fig.1. This phenomenon is more pronounced in the case that a target plasma produced by the first pulse is in lower collisionality. The information of neutral density was obtained with a fast ionization gauge and a multi-channel visible spectrometer. In Fig.2, local emission profiles of  $\text{H}\alpha$  light are shown for the times before and during the second pulse, where a crude assumption is introduced that local  $\text{H}\alpha$  emissivity is constant on the magnetic surface. These profiles have almost the same shape as those of electron density as shown in Fig.3. This indicates hydrogen atoms fully penetrates into this low density plasma. Figure 3 also shows time evolution of electron temperature and space potential profiles. As seen from Fig.3, electron density profile becomes strongly peaked around  $\rho \sim 0.3$  and has steep gradient in the region of  $\rho=0.3\text{--}0.6$  during the second heating pulse, while electron density is reduced by a factor of  $\sim 2$  in the outer portion of the plasma ( $\rho > 0.6$ ). During the second heating pulse, the effective particle diffusivity is reduced by a factor of  $\sim 2$  in  $\rho=0.3\text{--}0.6$  and enhanced by a factor of  $\sim 2$  in the outer part of  $\rho > 0.6$ . During the second heating pulse, the turbulence induced particle flux increases. The radial electric field in  $\rho < 0.7$  is relatively weak and electron temperature profile is almost flat there. Therefore,

neoclassical flux will not be changed by the second pulse. Electron Bernstein waves (EBW) converted near the edge from electron cyclotron waves will play an important role in the change in particle transport phenomena shown here. The EBW power is absorbed in the core region, which has been clarified by heating power modulation technique [4].

#### References

- [1] K. Toi et al. in Proc. 29th EPS on Plasma Phys. Control. Fusion (Motreux, 2002) P-4.061.
- [2] K. Toi et al., J. Plasma Fusion Res. SERIES 6, 516 (2004).
- [3] R. Ikeda et al., J. Plasma Fusion Res. **81**, 478 (2005).
- [4] R. Ikeda et al., this annual report.

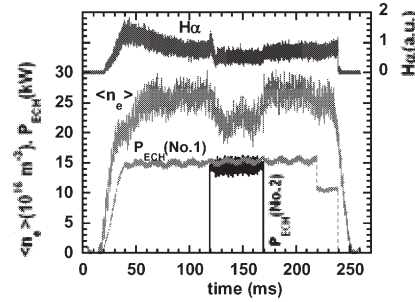


Fig.1 Typical waveforms of microwave heating power, line averaged electron density and  $\text{H}\alpha$  light.

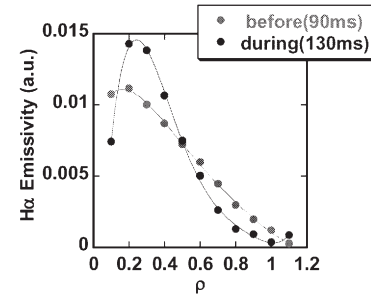


Fig.2 Radial profiles of  $\text{H}\alpha$  emissivity before and during the 2<sup>nd</sup> heating power.

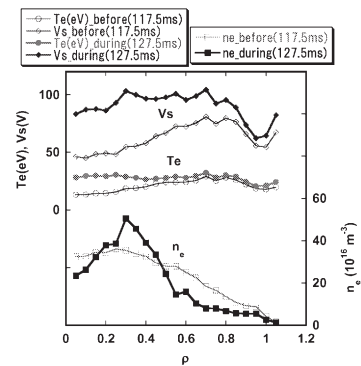


Fig.3 Radial profiles of electron density, electron temperature and plasma potential before and during the 2<sup>nd</sup> heating power.

## §24. Measurement of Power Deposition Profile by Heating Power Modulation of 2.45 GHz Microwaves in CHS

Ikeda, R. (Dep. Energy Eng. Sci., Nagoya Univ.), Toi, K.,  
Takeuchi, M. (Dep. Energy Eng. Sci., Nagoya Univ.),  
Suzuki, C., CHS Experimental Group

A new transport simulation based on the concept of “dimensional similarity” using a low temperature and density helical plasma is currently underway in the CHS [1]. Previous experiment showed that an over-dense plasma was produced by 2.45 GHz microwaves of which power was absorbed in the inaccessible region for electron cyclotron waves [2]. This result suggests a possibility of the mode conversion to electron Bernstein wave (EBW).

Recently, power modulation method was used in order to derive more detailed absorption profiles and clarify the possibility of absorption of mode-converted EBW. This method is often used to measure power absorption or study of heat transport in high temperature plasmas. This method is also applicable to low temperature and over-dense plasmas. In these plasmas, responses in electron temperature ( $T_e$ ), electron density ( $n_e$ ), and space potential to modulated heating power are measured simultaneously by a triple-Langmuir probe. In this experiment, microwave power is injected from two microwave sources (#1, #2). In order to investigate effective excitation of EBW, microwaves are launched by two different ways: one is perpendicularly injected to the toroidal field for #1 source, and the other obliquely injected for #2 source. Polarization of launched wave is typically selected to be X-mode for the perpendicular injection and O-mode for oblique one, respectively. Figure 1 shows time evolutions of modulated microwave power from #1 source ( $P_1$ ), steady microwave power from #2 source ( $P_2$ ), line averaged density ( $\langle n_e \rangle$ ), and  $T_e$ ,  $n_e$  and electron pressure ( $P_e$ ) measured at  $\rho = 0.3$  at the toroidal field  $B_{t0} = 613$  G in the magnetic configuration of  $R_{ax} = 97.4$  cm. In this experiment, the modulation frequency and amplitude are selected to be 1 kHz and about 5 kW, respectively. Power spectral densities (PSD) of  $T_e$ ,  $n_e$  and  $P_e$  at  $\rho = 0.3$  and 0.7 are shown in Fig. 2(a). The time window for FFT analysis is 55ms from 110 ms. PSDs of  $T_e$  at  $\rho = 0.3$  and 0.7 are comparable level, while PSDs of  $n_e$  and  $P_e$  at  $\rho = 0.3$  is much larger than ones at  $\rho = 0.7$ . Figure 2(b) shows radial profiles of  $T_e$ ,  $n_e$  and  $P_e$  and these of modulated amplitudes ( $\delta T_e$ ,  $\delta n_e$  and  $\delta P_e$ ).  $\delta T_e$  profile has the maximum around  $\rho \sim 0.4$  and spreads widely from core to edge region. On the other hand,  $\delta n_e$  and  $\delta P_e$  increase rapidly from  $\rho \sim 0.5$  and have the peak around  $\rho \sim 0.3$ . Figure 3 illustrates the radial profiles of characteristic frequencies in the equatorial plane of the horizontally elongated section where microwave is injected perpendicularly for the toroidal field from #1 source. As seen from the  $\delta P_e$  profile shown in Fig. 2, most of heating power is expected to be deposited in the region beyond the inaccessible region of O-mode and X-mode powers. This

result indicates that EBW converted at upper hybrid resonance layer is absorbed in over-dense region of the plasma core. We are studying whether the modulation frequency is high enough for the characteristic frequency of electron heat transport to derive the power deposition profile straightforwardly.

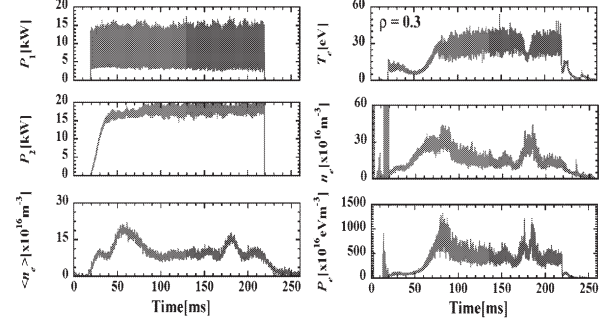


Fig. 1 Time evolutions of microwave powers ( $P_1$ ,  $P_2$ ), line averaged density ( $\langle n_e \rangle$ ),  $T_e$ ,  $n_e$  and  $P_e$  at  $\rho = 0.3$ , where the modulation frequency of  $P_1$  is 1 kHz and  $B_{t0} = 613$  G.

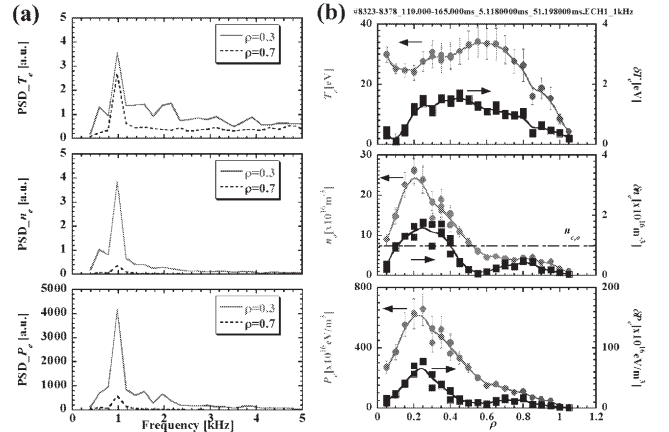


Fig. 2 (a) Power spectral densities of  $T_e$ ,  $n_e$  and  $P_e$  at  $\rho = 0.3$  and 0.7. (b) Radial profiles of  $T_e$ ,  $n_e$ ,  $P_e$  and those modulated amplitudes.

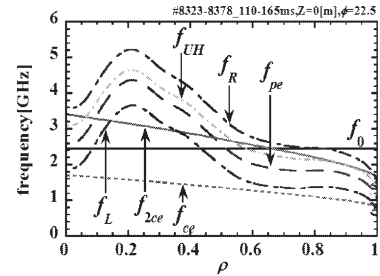


Fig. 3 Radial profiles of characteristic frequencies in the equatorial plane of the horizontally elongated section. The frequency  $f_0$  is 2.45 GHz,  $f_{pe}$  is plasma frequency,  $f_{R,L}$  are right and left hand cutoff frequency,  $f_{UH}$  is upper hybrid frequency,  $f_{ce,2ce}$  are fundamental and 2<sup>nd</sup> harmonic electron cyclotron frequency.

- [1] K. Toi *et al.*, 29<sup>th</sup> EPS on Plasma Physics and Controlled Fusion, Montreux, 2002, paper No.P4-06.
- [2] R. Ikeda *et al.*, J. Plasma Fusion Res. **81**, 478 (2005).

## §25. Intermittent Transport of Particle and Heat in Scrape-Off Layer of Limiter and Divertor Configurations of CHS

Ohno, N., Takamura, S. (Nagoya Univ.), Toi, K.

Recently, there are many observation of intermittent transport of particle and heat fluxes in the scrape-off layer (SOL) even in L-mode plasmas and advanced H-mode plasmas with few ELMs in tokamaks. 2D measurement of SOL in DIII-D and MAST by using fast camera clearly showed intermittent convective plasma transport, so-called "density blobs", which is thought to play a key role for cross-field plasma transport in SOL. However, there are few studies on intermittent convective plasma transport in helical devices.

In this article, we will report a statistical analysis of the intermittent edge plasma fluctuation of plasma density  $n(t)$  measured with a multi-pin probe in the CHS device.

Plasma with low density and temperature was generated by electron cyclotron resonance heating (ECR). Fig. 1 shows the typical power spectrum  $S(f) = |n(f)|^2$  of the density fluctuation measured at normalized minor radius  $r$  of unity. There are no apparent peaks observed in the signal. The shapes of  $S(f)$  allow one to conclude whether the scaling behavior of the fluctuation can be described by power-law dependences of the type  $S(f) \sim f^\gamma$  with the single exponent  $\gamma$ . Kolmogorov theory (K41) predicts the inertial sub-range with self-similar properties leading to a power law dependence  $S(f) \sim f^\gamma$ ,  $\gamma = -1$ . The typical value of the scaling exponent of the power spectra in the high frequency range of Fig. 1 is  $\gamma = -3.0$ , which is nontrivial one. Fig. 2 shows that dependence of the  $\gamma$  on the normalized minor radius. In the whole radial positions, the scaling exponent  $\gamma$  is found to be close to -3.0. This results means there would be intermittent coherent events in the density signal.

The density fluctuation property was analyzed with probability distribution function (p.d.f.). The p.d.f. gives important statistical quantities for turbulence research. The skewness is defined as  $S = \langle x^3 \rangle / \langle x^2 \rangle^{3/2}$  to describe the asymmetry of the p.d.f., and the flatness  $F = \langle x^4 \rangle / \langle x^2 \rangle^2$  measures the tail's weight with respect to the core of the distribution, where  $x$  is the deviation from averaged value. In the Gaussian distribution function, the skewness and flatness are 0 and 3, respectively.

Fig. 3 shows radial distribution of the skewness and the flatness. The skewness increases toward the edge to be  $S = 1$  at  $r = 1$ , which means the positive density bursts is dominating at the edge plasma region, which could be related to the density blobs observed in tokamak devices.

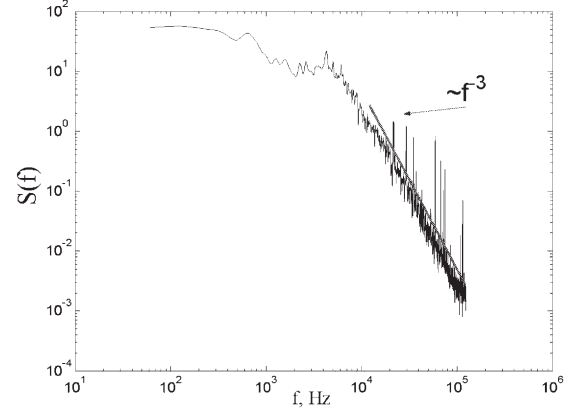


**Fig 1.** Power spectrum of plasma density fluctuation measured at the normalized minor radius  $r$  of unity.

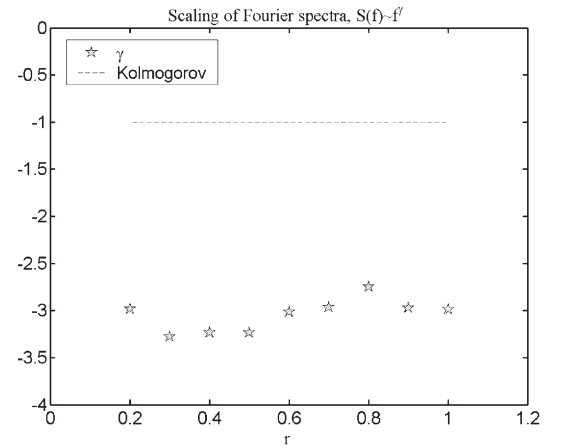


**Fig 2.** Dependence of the scaling exponent  $\gamma$  of the power spectra of density fluctuation on the normalized minor radius  $r$ .

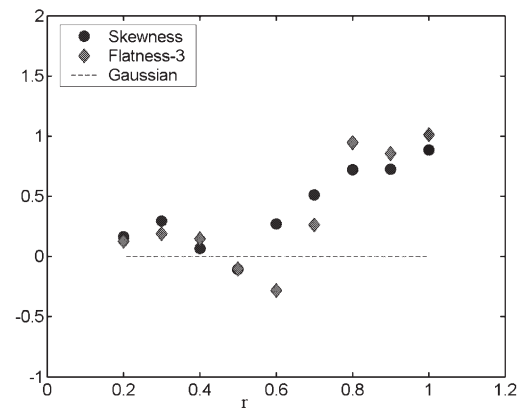


**Fig 3.** Skewness and flatness as a function of the normalized minor radius  $r$ .

## §26. Electron Heating and Plasma Production by Whistler Wave and Microwave Discharges in Low Toroidal Field

Shoji, T. (Dept. Energy Eng. and Sci. Nagoya Univ.), Suzuki, C., Takeuchi, M., Ikeda, R., Toi, K.

### Introduction

Whistler wave discharges in MHz range of frequency studied in CHS have the notable feature of producing plasmas in a low magnetic field strengths of kG range, which is important in the high beta and some Alfvén wave related studies of helical systems. We compare the density and electron temperature profiles of the plasma production by the Whistler wave discharge and 2.45GHz microwave discharges<sup>1-3)</sup>.

### Electron temperature and density profiles

Rf (9MHz, 10ms) and microwave (2.45GHz, 200ms) powers of 500kW and 30kW are used, respectively. The Whistler wave of parallel refractive index  $N_{||} \sim 38$  which is excited by Type III antenna in CHS can propagate deep in the plasma when  $B_t < 400\text{G}$  and  $n_e \sim 10^{18-19} \text{ m}^{-3}$ . Electron density  $n_e$  and temperature  $T_e$  are measured by the scanning Langmuir probe. Examples of  $n_e$  and  $T_e$  behaviors in time and radial profiles of helium plasmas are shown in Fig. 1, where pressure, toroidal field, rf and microwave powers of  $3.3 \times 10^{-5} \text{ torr}$ ,  $B_t = 175\text{G}$ , 117kW and 30kW, respectively. Figure 1(a) shows that the time evolutions of  $n_e$  and  $T_e$  at radius  $\rho = 0.2$  which is normalized by the radius of outmost closed flux surface. While the rf power creates the low  $n_e$  plasma at start-up phase, the density increases up to  $10^{18} \text{ m}^{-3}$  with the additional microwave power. This density exceeds more than 10 times larger than the density cut-off for the microwave and such a high density is kept even after the rf power is shut off. The microwave power without the rf can not ignite the plasma in this power level at low  $B_t$ . The  $n_e$  profile is hollow at the initial rf phase and then peaked at the center in the following combined microwave. The  $n_e$  is decreased and the profile becomes a little flatter in the central region after the rf is shut off (Fig. 1(b)). It is observed from the  $T_e$  profiles (Fig. 1(c)) that the electrons are heated mostly at surface in the rf start-up phase and the center  $T_e$  increases with the additional microwave power. The edge  $T_e$  is reached to  $\sim 23 \text{ eV}$  while the central one is  $\sim 10 \text{ eV}$  in this phase. After the rf is shut off the edge  $T_e$  decreases more than the central one but the hollow  $T_e$  profile is kept. The rf frequency closes to lower hybrid one at  $B_t = 275\text{G}$  at plasma center and the increase in central  $T_e$  is observed in the experiment. The comparison of these results with the Ray trace calculations of the rf waves is now under way.

### References

- 1) Shoji, T, Sakawa, Y, Suzuki, C., Matsunaga, G., Toi, K. Ann. Rev. NIFS, (2003) 283
- 2) Toi, K., Matsunaga, G., Ikeda, R, Takeuchi, M., Suzuki, C., Shoji, T. Ann. Rev. NIFS, (2003) 281

- 3) Shoji, T, Sakawa, Y, Suzuki, C., Takeuchi, M., Ikeda, R., Toi, K. Ann. Rev. NIFS, (2005) 296

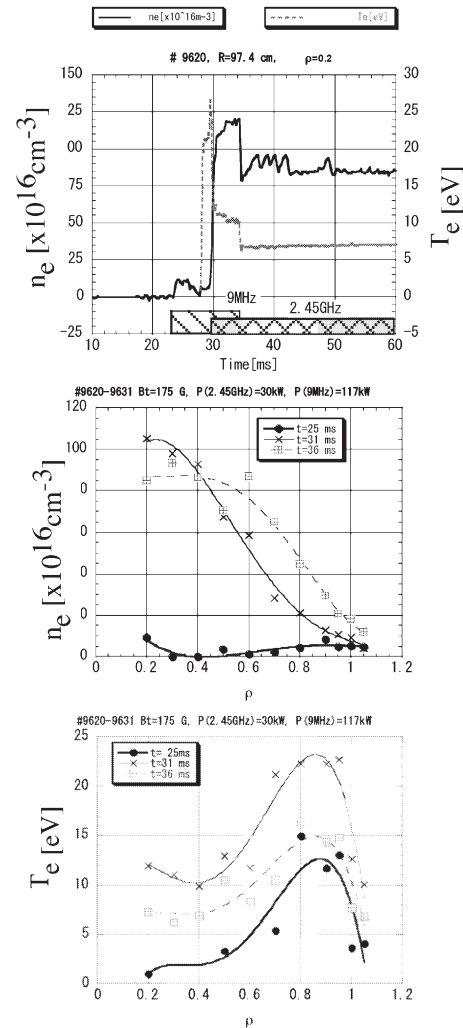


Fig. 1 (a) time evolution of electron density  $n_e$  and temperature  $T_e$  at  $\rho = 0.2$  for micro wave + whistler discharges. Radial profiles of (b)  $n_e$  and (c)  $T_e$  at  $t = 25, 31, 36 \text{ ms}$ .  $B_t = 175\text{G}$ ,  $P_{\mu} = 20\text{kW}$ ,  $P_{rf} = 117\text{kW}$



## §27. Radial Electric Field Control by Electron Injection in CHS

Kitajima, S., Sasao, M., Shinto, K., Okamoto, A., Takahashi, H., Tanaka, Y., Utoh, H., Takenaga, M., Ogawa, M., Shinde, J., Aoyama, H., Iwazaki, K. (Dept. Eng. Tohoku Univ.), Takayama, M. (Akita Prefectural Univ.), Takeuchi, M., Ikeda, R. (Dept. of Energy Engineering and Science, Nagoya Univ.), Okamura, S., Toi, K., Iguchi, H., Fujisawa, A., Isobe, M., Suzuki, C., Yokoyama, M.

The radial electric field control experiments were carried out by an electrode biasing in the Compact Helical System (CHS). In L-H transition theories, the local maximum in ion viscosity versus poloidal Mach number  $M_p$  around  $-M_p \sim 1-3$  is considered to play a key role. This maximum is considered to be related to the toroidicity. In stellarators each machine has its own Fourier components of the magnetic field configuration, causing complexity in radial particle fluxes and in the ion viscous force. In the Tohoku University Heliac (TU-Heliac), the effects of the viscosity maxima on the L-H transition have been experimentally investigated. The poloidal viscosity was estimated from the  $\mathbf{J} \times \mathbf{B}$  driving force for a plasma poloidal rotation, where  $\mathbf{J}$  was a radial current controlled externally by the LaB<sub>6</sub> hot cathode biasing. It was experimentally confirmed that the local maxima in the viscosity play the important role in the L-H transition<sup>1-4)</sup>. However, in the operation condition on TU-Heliac the collisionality is comparatively high (plateau regime) and the friction of neutral particles affects the poloidal damping force. Therefore it is important to perform this biasing experiments mentioned above in the confinement system that has sophisticated diagnostic systems, abilities to produce low collisional plasmas and changeability of the Fourier components of the magnetic configurations. The purposes of our electrode biasing experiments in CHS were, (1) to estimate the ion viscous damping force from the driving force for the poloidal rotation, and (2) to study the dependence of the ion viscosity on helical ripples.

In the biasing experiments in CHS, the target plasma was produced by the ECH of 2.45 GHz. We observed some experimental results implying the improvement in the plasma confinement, i.e. the increase in line-averaged electron density by three times, the formation of the steep gradient of the electron pressure and the formation of the negative radial electric field<sup>5)</sup>. We evaluated the poloidal ion viscosity and the poloidal Mach number from the result of the electrode biasing experiment in CHS and compared with the theoretical calculations based on the Shaing model<sup>6)</sup>,

which includes the effect of the helical ripple. The dependence of the experimental ion viscosity on the poloidal Mach number shows qualitative agreement with the calculations (Fig. 1a). In the Tohoku University Heliac, the experimental poloidal viscosity and the calculations were also compared and they showed good agreement (Fig. 1b). These results indicate that the Shaing model is appropriate for evaluation of the ion viscosity in helical devices, and show the possibility that the mechanism of the LH transition can be explained as the bifurcation phenomena originated from the ion viscosity.

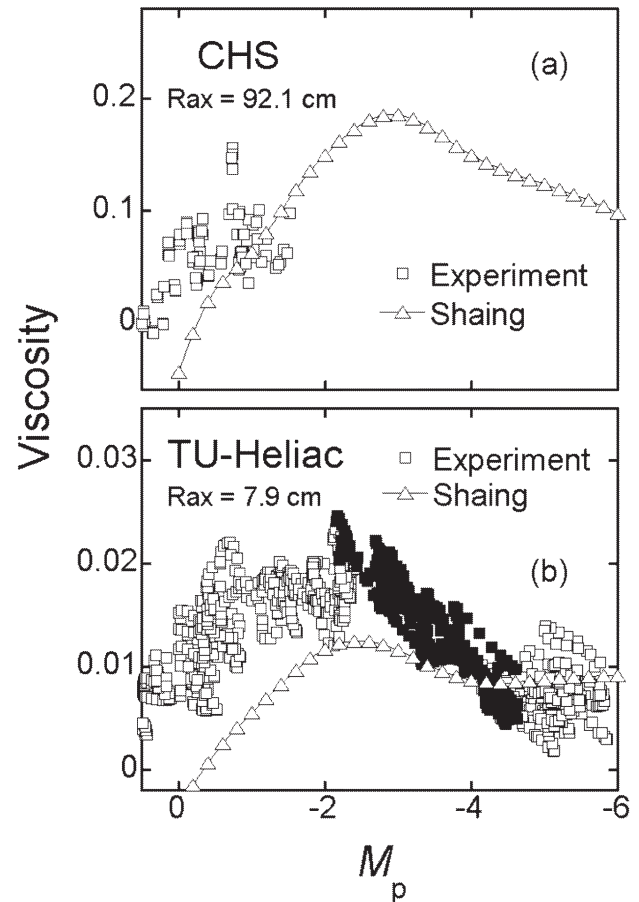


Fig. 1. The dependence of the poloidal ion viscosity on the poloidal Mach number in (a) the Compact Helical System and (b) the Tohoku University Heliac.

### References

- 1) Takahashi, H., *et al.*: J. Plasma Fusion Res. SERIES **6** 366-370 (2004).
- 2) Kitajima, S., *et al.*: Nucl. Fusion, **46**, 200-206 (2006).
- 3) Takahashi, H., *et al.*: Plasma Phys. Control. Fusion, **48**, 39-49 (2006).
- 4) Kitajima, S., *et al.*: Plasma Phys. Control. Fusion, **48**, A259-A267 (2006).
- 5) Takahashi, H., *et al.*: Fusion Sci. Technol., to be published.
- 6) Shaing K. C.: Phys Rev. Lett. **76**, 4364 (1996).

## §28. Study on the Mechanism of Collisionless Inward Penetration of Electrons via Stochastic Magnetic Region and Experimental Investigation of Energetic Electron Trap in Helical Magnetic Surface

Himura, H., Yamamoto, Y., Sanpei, A., Masamune, S. (KIT),  
Wakabayashi, H. (The Graduate Univ. for Advanced Studies),  
Fukao, M. (Osaka Electro-Communication Univ.),  
Isobe, M., Okamura, S., Matsuoka, K.

In the last year, we have verified the variation of  $\phi_s$  and  $n_e$  on magnetic surfaces of helical electron plasmas and the paper explaining the detail of it is now under reviewed<sup>1)</sup>.

Plotted data in Fig. 1 are  $\phi_s(z)$  measured by a probe with the high-impedance emissive method. Three profiles of  $\phi_s(z)$  are obtained for cases of  $V_{acc} = 300$  V, 600 V, and 1 kV, respectively. The horizontal axis is shown in  $\Psi^{1/2}$ . Here,  $\Psi^{1/2} = 0$  and 1 correspond to the  $R_{ax}$  and LCFS, respectively. In experiments,  $R_{ax}$  is fixed at  $R = 101.6$  cm. Thus, magnetic surfaces do not touch the grounded chamber wall. And, for this setting, the probe does not cross  $R_{ax}$ , being shifted about 4 cm inward from  $R_{ax}$ . Consequently, the lower limit of measurement points of  $\phi_s(z)$  is  $\Psi^{1/2} = 0.3$  on this cross-section. Substantial difference between two values of  $\phi_s$  (at  $z > 0$  and at  $z < 0$ ) at each magnetic surface (at same value of  $\Psi^{1/2}$ ) is observed in the region of  $0.3 < \Psi^{1/2} < 1$ . This means that  $\phi_s$  is never constant on magnetic surfaces. Also, as clearly recognized from the plotted data for  $V_{acc} = 1$  kV, the difference in  $\phi_s$  becomes larger in the outer region of magnetic surfaces. For example, at  $\Psi^{1/2} \sim 0.8$  the difference reaches about 200 V, while at  $\Psi^{1/2} \sim 0.3$  it almost disappears. Such a difference in  $\phi_s$  still appears even when  $V_{acc}$  is decreased, as shown with white ( $V_{acc} = 600$  V) and black triangles ( $V_{acc} = 300$  V). However, for these cases, the difference between the two values of  $\phi_s$  at each magnetic surface becomes smaller. Another significance is that despite  $V_{acc}$  is changed, measured  $\phi_s(z)$  in  $z > 0$  are always (negatively) larger than those in  $z < 0$ . Meanwhile, on this cross-section, helical magnetic surfaces are slightly shifted downward with respect to the center of the elliptic chamber wall. Considering contours of  $\phi_s$  (equi-potential surfaces) from the measured  $\phi_s(z)$ , the  $\phi_s$  contours are expected to shift upward with respect to the contours of constant  $\Psi$  (magnetic surfaces). We have so far obtained only two values of  $\phi_s$  at each magnetic surface, it suggests that equi-potential surfaces move away from the closest part of the grounded chamber wall.

In this research, the current-voltage ( $I_e$ - $V_p$ ) characteristics are also measured at each magnetic surface with the same emissive probe. For this measurement, the impedance of the probe is

changed to a low impedance (330  $\Omega$ ) so as to obtain  $I_e$  that flows out from the plasma through the probe. From the  $I_e$ - $V_p$  characteristic curve, we have determined the electron temperature  $T_e$ . Regarding with  $n_e$ , it is obtained from  $I_e$  ( $\sim en_e v_{th} S$ ) at  $V_p = \phi_s$ , where  $\phi_s$  has been pre-measured just before the  $I_e$  measurement, where  $v_{th}$  is electron thermal speed and  $S$  is the probe area. All other contributions to  $I_e$  except  $v_{th}$  are ignored, because  $v_{th}$  is much faster for the presented hot plasmas. Figure 2 shows  $n_e(z)$  for  $B = 0.9$  kG and  $V_{acc} = 600$  V. As can be seen from the plotted data,  $n_e$  is also non-constant on each magnetic surface. Significantly, unlike  $\phi_s$ , values of  $n_e$  near LCFS ( $\Psi^{1/2} = 1$ ) is larger in the  $z < 0$  region (white circles) than those in  $z > 0$  (black circles). This means that electrons tend to move towards the grounded chamber wall. This can be understood from the shift of  $\phi_s(z)$ . As explained, the envisioned contours of  $\phi_s$  have shifted upward with respect to the contours of constant  $\Psi$ . In that case, the corresponding (global) direction of  $E_{||}$  in the poloidal cross-section results in the upward direction as well. Therefore, electrons are forced toward the downward side ( $z < 0$ ) of the magnetic surfaces. In fact, this result seems also to be consistent with the stability analysis for nonneutral plasmas confined in magnetic surfaces.

<sup>1)</sup>H. Himura, H. Wakabayashi, Y. Yamamoto *et al.*, submitted to *Phys. Plasmas* (2006).

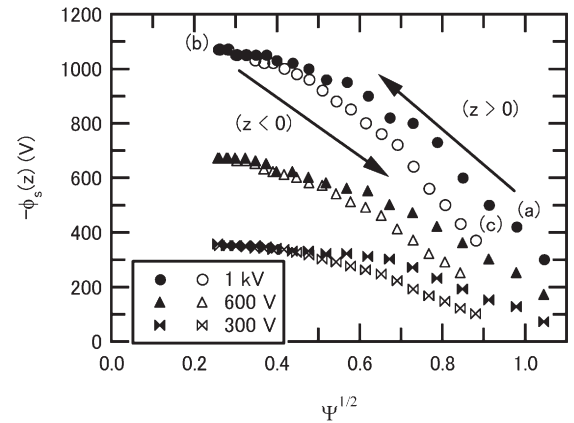


Fig. 1 Typical potential profile of CHS nonneutral plasma.

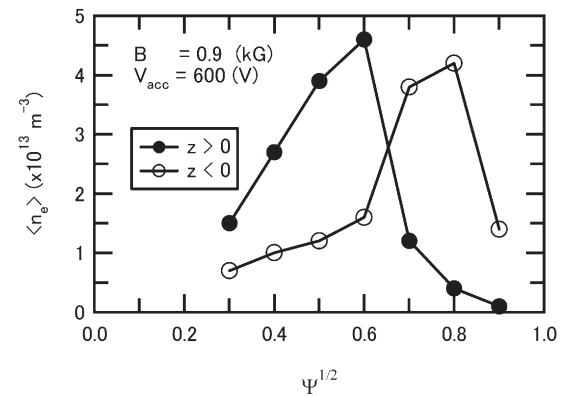


Fig. 2 Typical electron density profile of CHS nonneutral plasma.

## §29. Cotton-Mouton Polarimeter with the Use of HCN Laser

Akiyama, T., Kawahata, K., Itoh, Y., Okamura, S. (NIFS),  
Okajima, S., Nakayama, K. (Chubu Univ.)

A polarimeter for electron density measurements in magnetically confined plasmas is expected to be robust even in a high-density range. The reasons are as follows. It is free from fringe jump errors and is immune to the effects of mechanical vibrations, which degrade the reliability and resolution of an interferometer. There are two types of polarimeters, based on the Faraday and on the Cotton-Mouton effect, respectively. Although the Cotton-Mouton polarimeter is proposed for the international thermonuclear experiment reactor (ITER), its applications are fewer than those of Faraday polarimeters. We have developed a Cotton-Mouton polarimeter using an HCN laser (wavelength of  $337\ \mu\text{m}$ ) on CHS.

The method of measuring the Cotton-Mouton effect as a phase difference is adopted. It is insensitive to amplitude variations of detected signals due to oscillation instabilities of the laser and beam refraction in the plasma. Here, in order to assess the accuracy and measurement errors of the Cotton-Mouton polarimeter, it is combined with an interferometer that can operate simultaneously using the same probe beam. The schematic of the optical setup is shown in Fig. 1. The HCN laser beam is split into two beams the frequency of one is shifted with a super rotation grating. The frequency shift  $\omega_b$  is 1 MHz due to the high rotation speed (500 rps) of the rotating grating. After rotating the plane of polarization by  $\pi/2$ , two laser beams are combined. In this way an elliptically modulated beam is generated. The beam is split into probe and reference beams, and they are injected into the vacuum vessel. They are detected with Shottky barrier diodes (SBD, Farran Technology). After passing through an analog

band-pass filter and an amplifier, 1-MHz beat signals of the polarimeter's probe and reference are digitized. Then, complex demodulation is applied and the phase difference is extracted. For the interferometric measurement, the probe beam is split after passing through the plasma, and one polarization component (the O-mode) is selected with a polarizer. The transverse polarization component is selected from the reference beam and then they are combined. The 1-MHz beat signal is obtained in the same way. The phase shift of the signal firt corresponds to the phase shift of the O-mode component in the plasma. The phase shift is detected with a phase counter.

Figure 2 shows measurement results of the polarimeter and the interferometer along the plasma center chord. The result of the polarimeter is almost consistent with that of the interferometer. The response time of the polarimeter in Fig.4 is 0.32 ms. However, there are still slight differences between them. Possible reasons include changes in the magnetic field due to a finite  $\beta$  effect, changes in the electron density profile, and cross- and back-talk components.

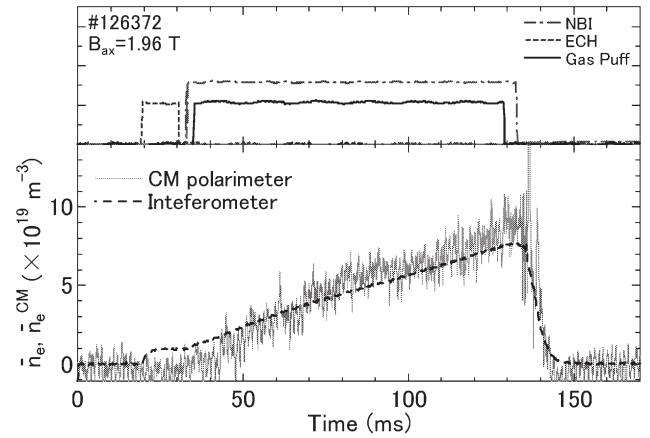


Fig. 2. Line averaged density evaluated from the interferometer and the Cotton-Mouton polarimeter. The response time is 0.32 ms

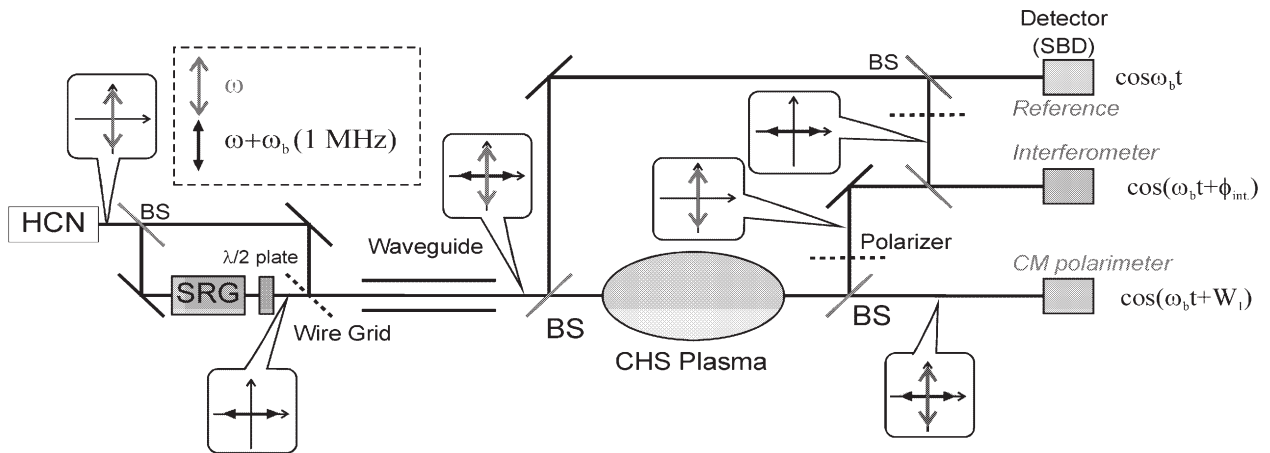


Fig. 1. Schematic of the optical arrangement of the Cotton-Mouton polarimeter combined with the interferometer on CHS.



### §30. Installation of New 54.5 GHz Gyrotron to ECH System in CHS

Yoshimura, Y., Akiyama, R., Matsuoka, K., Okamura, S., Kubo, S., Shimozuma, T., Igami, H., Notake, T., Mutoh, T.

Due to a big aging at the output window of previous 53.2 GHz gyrotron (430 kW output, 100 ms pulse length), the boron-nitride window surface was damaged. After that, the rough surface caused frequent arcings and prevented high power operation of the gyrotron. The maximum injection power to CHS vacuum vessel for 100 ms pulse length was limited less than 160 kW while the maximum power was formerly available up to 320 kW. Then installation of a new gyrotron was decided to perform CHS experiments with sufficient ECH power necessary for the experiments.

From a view point of early installation of a new gyrotron, a 54.5 GHz gyrotron of GYCOM (nominal output power of 450 kW) was selected because the company stored all the parts for it, neglecting the slight difference of operating frequency from the previous one. It was considered that the slight difference did not affect the quality of the EC-wave beams transmitted with the mirrors and polarizers designed for 53.2 GHz waves. Only an increase of power reflection at the sapphire disc used as a vacuum window on CHS was worried, but it was actually confirmed that the full power operation of the new gyrotron was available with the transmission line.

The installation was started at September 21st, 2005 with an engineer from GYCOM. At first, the gyrotron support rings on the super-conducting magnet vessel were aligned so that the gyrotron axis agreed with the center of the magnetic field distribution. The new gyrotron is a diode tube while the previous one is a triode. So the voltage dividing resistors connecting between cathode and anode, and anode and ground were removed from the gyrotron oil-tank. The new gyrotron needs gun-magnet which tailors the magnetic field around the cathode. The gun-magnet and current leads were set. After those installations and cablings, a water dummy load was set in front of the gyrotron output window, and the gyrotron operation was started.

Searching the optimum operating regime, the height of the gyrotron (that is, distance between the centers of the gyrotron cavity and the magnetic field distribution), the main magnetic field, the gun-magnet field, the beam voltage and the beam current were adjusted. Finally full performance of 470 kW, 100 ms was achieved with optimized operating parameters: the height of the gyrotron of 22 mm, the main magnet current of 32.86 A, the gun-magnet current of 0.55 A, the beam voltage of 65 kV and the beam current of 24.5 A.

To match the new gyrotron to the existing transmission line, the 11 cm lower position of the output window of the new gyrotron from the previous one was compensated by a stand with the height of about 10 cm and by a slight tilting of the gyrotron so that the output beam

aimed at the center of the 1st mirror of the transmission line. The 1st and 2nd mirrors were exchanged with the new ones which were designed to make the output beam from the new gyrotron to be transmitted by the other existing 10 mirrors of the transmission line.

After the beam alignment on the transmission line by adjusting mirror directions, the transmitted power was measured at just in front of the CHS vacuum window to evaluate the injection power and the transmission efficiency. The efficiency is 85 %, and that is reasonable value for the 9 mirrors transmission: the loss is theoretically evaluated as 1 to 2 % per one reflection.

At the practical operation for CHS experiment, the performance of the gyrotron was degraded. For long pulse operation, sometimes the output power drops before the pulse length setting probably due to the change of reflection to the gyrotron caused by the transmission line. Then the operation parameter search was partially performed, and finally new parameters: the height of the gyrotron of 22 mm, the main magnet current of 32.86 A, the gun-magnet current of 0 A, the beam voltage of 64 kV and the beam current of 25.0 A were found. With these parameters, the injection power of 415 kW with the pulse length of 100 ms was first achieved in the discharge #127735 on Jan. 11th, 2006.

Figure 1 shows the injection power as a function of the beam voltage. The injection power increases with the beam voltage up to 415 kW. With the beam voltage higher than 65 kV, the injection power decreases due to a mode jump, that is, the parameters go over the regime for adequate oscillation of designed TE<sub>8,15</sub> mode.

The high power, long pulse injection and the flexibility of injection power control contributed to the CHS experiments, especially to the ECH experiments such as ordinary – extraordinary – Bernstein mode conversion heating (O-X-B heating). The increment of the plasma stored energy by the obliquely injected O-mode waves increased with the injected power and reached over 30 % by the full power 415 kW injection to the plasmas sustained with 860 kW NBI.

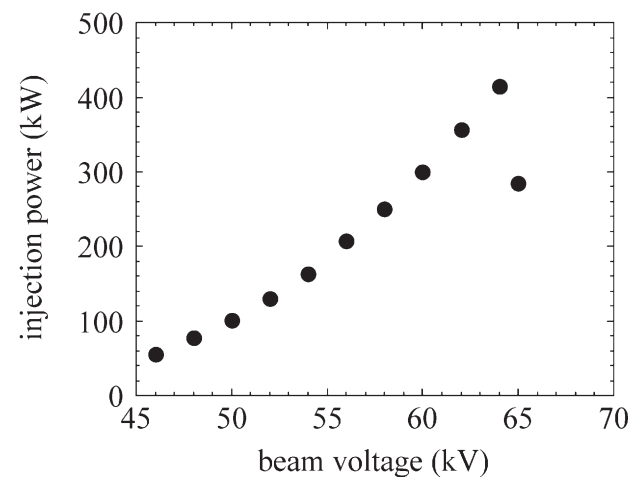


Fig. 1. ECH injection power to the CHS vacuum vessel as a function of the gyrotron beam voltage.



§31. Change of Effective Anode Area in Neutral Beam Injector for Compact Helical System

Chang, D.H. (Visiting Scientist, Korea Atomic Energy Research Institute), Nagaoka, K., Osakabe, M., Takeiri, Y.

Discharge properties of a neutral beam (NB) injector have to be characterized by the condition of plasma generation. The NB injector of Beamline-2 (BL-2) in Compact Helical System (CHS) consists of a magnetic bucket plasma generator, with multi-pole cusp fields, and a set of triode accelerators with multi-apertures. Discharge characteristics of BL-2 were investigated with the change of effective anode area between the bucket anode of plasma generator and the plasma grid (PG) of accelerator. Effective anode area of the NB injector should be reduced by the permanent magnets, distributed around the discharge bucket wall. The effective anode area, in general, affects the stability of discharge because the primary electron confinement, the plasma density, and the plasma potential were controlled by the anode area. The anode area was changed simply, in the experiments, by the connection of a resistor (200 ohms) to limit the arc current on plasma grid (PG) or by the direct connection (approximately 0.1 ohm) without the resistor. Magnetic field distribution has been also measured to define the arc plasma properties.

Accelerating power and neutral beam power of NB injector were typically 30 kV/ 60 A and 800 kW, respectively, and beam diameter is 300 mm. The injector plasmas were initialized with the help of 8 filaments (diameter of 1.6 mm), arranged symmetrically on the upper side of bucket chamber (cylindrical type with a diameter of 420 mm and a length of 232 mm). Arc discharges with the power of 60~62 kW have been produced for 0.6 sec pulse length by an operation of constant voltage (CV) mode. Discharge arc voltage and current were nominally 76 V, 820 A, respectively. Typical filament heating voltage and current were 12 V and 1000 A, respectively. Plasma density and electron temperature have been measured by using an electrostatic probe (diameter of 1 mm), which was a circular probe tip with facing the discharge plasmas.

Plasma densities have been decreased for the case of resistor connection, compared to the direct connection, as shown in Fig. 1. Two electron temperatures have been shown for the direct connection, but single temperature was obtained for the resistor connection. These results imply that primary electrons were abundant near the PG for the direct connection, and then plasma density could be increased by more frequent electron collisions to background neutral gases. Thus, the electron

temperature could be increased near the PG for the direct connection because of the rich population of primary electrons. The floating potential of direct connection was also lower than that of resistor connection. Otherwise, plasma potentials of direct connection were higher than the resistor connection even though the primary electrons were abundant. The arc efficiencies (ratio of beam current to arc power) of injector were not changed for two discharge cases. Therefore, more experimental studies should be required to confirm the discharge characteristic of the NB injector in the BL-2 of CHS.

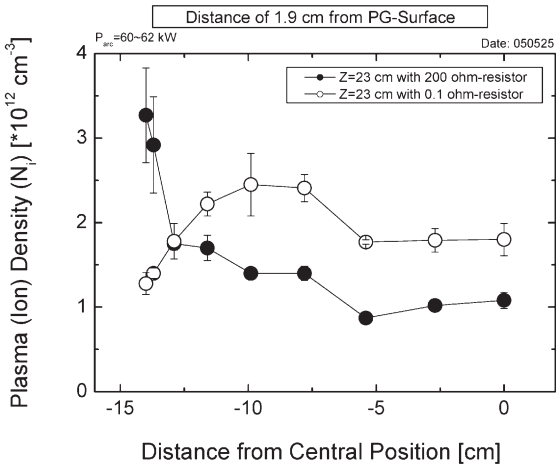


Fig.1 Radial distribution of plasma densities at 23 cm distance from the back plate of plasma generator and at 1.9 cm distance from the plasma grid. Closed circles represent the case of 200 ohms connection between the bucket anode and the PG. Open circles were the case of direct connection (approximately 0.1 ohm).

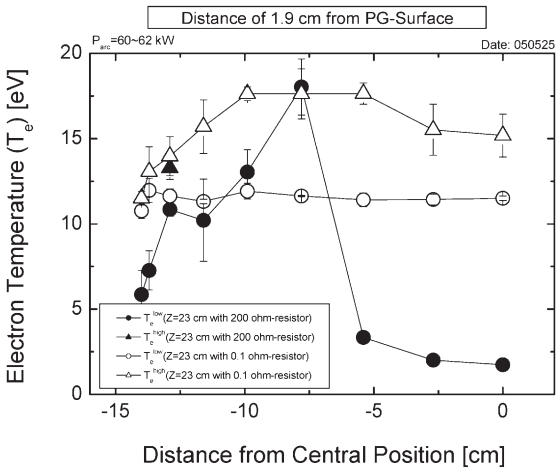


Fig.2 Radial distribution of electron temperatures at 23 cm distance from back plate of plasma generator and 1.9 cm distance from the PG. Superscripts of high and low in temperature symbol ( $T_e$ ) mean that the high and low temperatures in the results of two temperature measurement of electrostatic probe.

## §32. CHS Data Acquisition and Analysis System

Takahashi, C., Okamura, S., Iguchi, H., Ida, K., Fujisawa, A., Yoshimura, Y., Minami, T., Isobe, M., Nishimura, S., Suzuki, C., Nagaoka, K., Akiyama, T., Matsuoka, K.

The CHS data acquisition system utilizes two computer systems, namely, the Cinos system and the VAX system. Total amount of experimental data of 160 Gbytes have been acquired this year, which is 20 Mbytes/shot and 2 Gbytes/day in average. This number is larger than that of the last year by 15 %. The 85 % of the total data has been acquired by the Cinos system and the rest by the VAX system. No trouble occurred in the Cinos system throughout the year. While in the VAX system, troubles occurred five times in the magnetic disk and once in the power and terminal device. They are basically because the hardware is getting too old.

The number of unit (eleven) of the Cinos system and their fundamental structures are same as those in the last year. However, minor improvements have been continued. Three new modules are installed on one of the local units, which are used for the AUV spectroscopy. They are two AD/c modules and a Burst clock generator. The AD/c is a CAMAC module with 4-channel, 12 bit, 1 MHz sampling, 128 kbyte memory. The Burst clock generator is a CAMAC TTL level out put module with 6-channel, 10 MHz, and 16 Mega-count. The latter is used for the gate control of the CCD camera detector for the AUV spectrometer.

The shot number has been delivered from the main server computer to all the Cinos units through the local network. Therefore, the shot number transfer sometimes stops due to troubles within in the local network. In order to avoid this situation, a complementary system for the shot number delivery using an image processing is being developed. Since the Cinos system does not have the function of image processing so far, a new image-processing unit is prepared. It is composed of a TV camera, a RGB pedestal controller, a H-V Timing module, Fast 4ch AD/c. they are controlled by one of the Cinos units. Main characteristics of this image-processing unit are as follows. 1) Sampling can be started and terminated at an arbitrary H-positions of the scanning line of the TV camera. 2) Resolution of the video signal can be improved by changing the pedestal level of the signal out put. 3)  $\gamma$  correction for the color sensitivity is skipped, because one of the three color signals with best contrast is chosen automatically in the RGB signal. Those characteristics help

to compress data size of the image and enhance the processing speed. Pattern recognition is carried out through the comparison between the acquired image data and the reference image data about the image similarity.

Two new computers are introduced for data analysis. One uses the UNIX operating system and the other uses the VMS operating system. Two computers with different operating systems are necessary because the CHS data acquisition system has two different types of computers, namely, the Cinos system and the VAX system. Each computer has main memory of large capacity and is linked with its own RAID disk and DLT for mass data storage. Accessing old data set stored in these media from the new computers through the network has been successfully tested. After the CHS project is terminated, these new computer systems will be used as the main tools for the data analysis of an arbitrary shot in the past.



Figure.1. CHS new computer system for the old data analysis and storage system.

### Reference:

- [1] Takahashi, C. et al., Annual report of NIFS, April 2000-March 2001 298(2001)
- [2] Takahashi, C. et al., Annual report of NIFS, April 2001-March 2002 302(2002)
- [3] Takahashi, C. et al., Annual report of NIFS, April 2002-March 2003 285(2003)
- [4] Takahashi, C. et al., Annual report of NIFS, April 2003-March 2004 297(2004)
- [5] Takahashi, C. et al., Annual report of NIFS, April 2004-March 2005 300(2005)

## 4. Basic Research and Development

One of major plasma experiment devices for the basic plasma physics research in NIFS is HYPER-I, which has two powerful microwave source producing high density plasma close to  $n_e = 10^{19} \text{ m}^{-3}$ . It has basically a linear magnetic configuration adjustable for various physics research program. Important research topics in this experiment are (1) a plasma vortex structure with a central density hole (plasma hole), (2) a plasma with a high neutral density which rotates in the opposite direction of  $E \times B$  (anti- $E \times B$ ) and (3) development of a special type of probe to measure plasma flow direction.

For a plasma hole experiment, the radial force balance was analyzed with a term of strong centrifugal force. Two solutions of the radial profile of azimuthal velocity were obtained, which has a close relation to the observed plasma flow structure.

In the experiment of anti- $E \times B$  vortex, the information of the momentum exchange between the neutral gas flow and the ion flow is important. A diagnostic for 2-D flow pattern of the neutral gas using a tunable extended cavity diode laser (ECDL) was developed.

The absolute flow velocity measurement was made using the Doppler shift of laser induced fluorescence (LIF). The azimuthal velocity profiles were measured for both  $E \times B$  rotation plasma and anti- $E \times B$  plasma. The facing-double probe (FDP) was developed for the measurement of Mach number of plasma flow. The principle of FDP was verified by the particle-in-cell computer simulation. A comparison of the flow measurement with LIF and the directional Langmuir probe is scheduled for HYPER-I plasma.

Another new type of probe for the ion temperature measurement was developed. It consists of a central electrode and a guard electrode, which blocks the electrons from reaching the central electrode. Calibration experiment is planned using a HYPER-I plasma.

Basic research on the atomic and molecular processes is very important because it supplies fundamental data to understand physical processes in plasmas. A collision experiment of highly charged ions (HCIs) with rubidium atoms in the excited state was carried out using NICE device. The rubidium atom was excited with the diode laser and the charge exchange rate of iodine beam was compared for the ground state and the excited state of rubidium atom.

The research of excitation processes of electron-ion collisions was done with the exclusive high-density ion source and a tandem type electrostatic energy analyzer. The electron-Xe collisions were analyzed with various Xe ion beam current. It is necessary to cancel out the ion space charge effect to obtain the final spectroscopic information of ejected electron.

The isotope effect on the charge transfer cross section for charge exchange process of hydrogen ions ( $\text{H}^+$  or  $\text{D}^+$ ) and hydrogen molecules ( $\text{H}_2$ ,  $\text{HD}$  or  $\text{D}_2$ ) have been studied. In order to obtain more comprehensive understanding, the charge transfer cross section of  $\text{Li}^+$  ions with  $\text{H}_2$ ,  $\text{HD}$  and  $\text{D}_2$  molecules was measured.

In the basic research and development program, many small but important research programs have been running in addition to HYPER-I and NICE programs. Measurement of 200-750 nm spectra of laser produced Sn plasma has been done for the basic radiation data in the development of EUV light source for the lithography of LSI. In the non-neutral plasma physics study, a theoretical model based on the drift-kinetic equation has been developed for the radial transport induced by the rotating electric field.

Using a cylindrical plasma of 45 cm diameter produced by a RF wave of 7 MHz, the density transition phenomena along with plasma rotation and density profile modification was studied using ten concentric circular rings as biased electrodes. For the study of the ablation phenomena of solid hydrogen and plasma, an inductively coupled plasma was developed and its basic plasma parameters and profiles were measured. The negative hydrogen ion production was investigated using 915 MHz microwave, especially on the relationship among the microwave propagation, electron temperature and  $\text{H}^-$  production rate.

In the relation of divertor plasma, the plasma quenching phenomenon was studied using a pulse-modulated induction thermal plasma (PMITP). Argon plasma was used with the inclusion of molecular gas combination of  $\text{CO}_2 + \text{H}_2$  and  $\text{CO}_2 + \text{N}_2$ . For the study of atmospheric pressure plasma, a radio frequency inductively coupled plasma was produced. The thermal efficiency was estimated from equivalent circuit analysis of the induction coil circuit and calorimetric measurements of plasma heat load to the wall. For the current drive technique of low- $q$  toroidal confinement, a method using the Nernst effect is applicable. An EBW heating experiment was made on TS-4 at the University of Tokyo to confirm this new method. Particle reflection of low energy light ions from a polycrystalline W surface was studied. The energy and angular distribution of reflected H and O ions were measured. The Cherenkov instability in the azimuthal direction was investigated in a beam-plasma system in the TPD-II device.

Theoretical work has been continued on various physics topics related to the configuration design study of a quasi-axisymmetric stellarator. The effect of the ripple diffusion in the  $1/\nu$  regime was included in the neo-classical calculation of the parallel viscosity and bootstrap current.

(Okamura, S.)



## §1. High Density Plasma Experiment HYPER-I

Tanaka, M.Y. (Kyushu Univ.), Yoshimura, S., Tomida, A. (Nagoya Univ.), Yamaguchi, H. (Nagoya Univ.), Miyake, F. (Nagoya Univ.), Aramaki, M. (Nagoya Univ.), Okamoto, A. (Tohoku Univ.), Tsushima, A. (Yokohama National Univ.), Saitou, Y. (Utsunomiya Univ.)

High Density Plasma Experiment-I (HYPER-I) is a linear device with magnetic fields designed for various basic plasma experiments. Plasmas are produced and sustained by electron cyclotron resonance heating with an electron cyclotron wave (ECW), which is excited by a 2.45GHz microwave launched along the magnetic field line from an open end of the cylindrical chamber. Two microwave sources are available; one is a magnetron oscillator with 15 kW output, and is used for low power experiments. A klystron amplifier with 80 kW output (CW) is also available for high power and high density experiments.

The maximum plasma density is two orders of magnitude higher than the cutoff density of ordinary mode with the same frequency. The characteristic features of HYPER-I plasma are large diameter (30 cm) and high density ( $< 10^{13} \text{ cm}^{-3}$ ). A set of probe driving systems was installed in 2001 to measure the flow vector field on a plane perpendicular to the magnetic field. Velocity vector measurements are possible over 80% of the whole plasma cross-section. A tunable dye laser system was introduced in 2003 to develop a laser-induced fluorescence (LIF) Doppler spectroscopy system. The dye laser is excited by a pulsed Nd:YAG laser, and produces 30 pulses per second (max. 100 mJ /pulse ) in a range of wavelength 600-630nm. A tunable diode laser system for measuring the flow velocity of background

neutrals is under development in collaboration with Nagoya University. The research activities are mainly focused on vortex formation in plasmas, flow velocity measurement using LIF Doppler spectroscopy as well as velocity measurement with asymmetric probes.

### (i) vortex formation

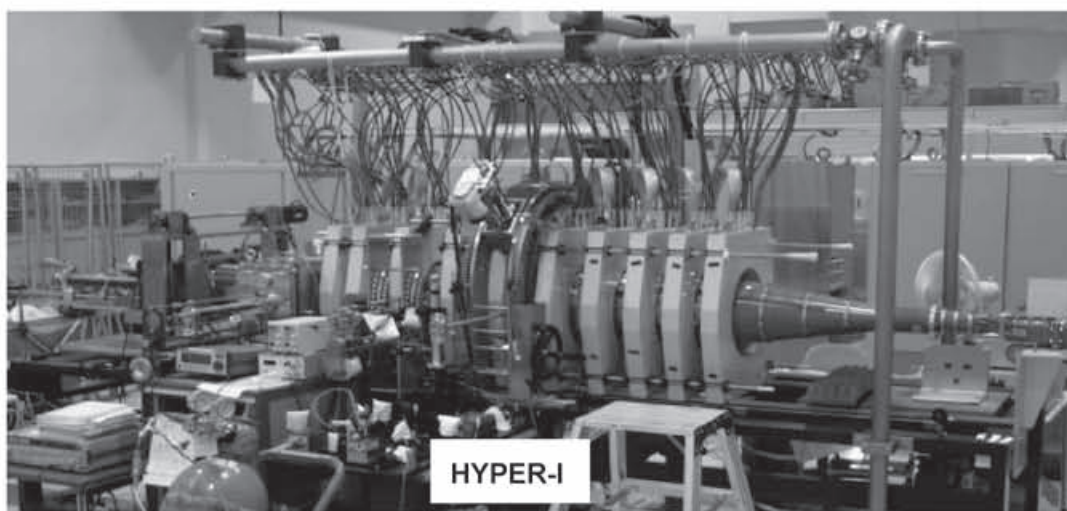
A vortex with a cylindrical density cavity in its core (referred to as plasma hole) has been observed, and identified as a viscous vortex such as Burgers vortex. The formation mechanism is studied with emphasis on radial force balance. It is found that in the core region, the centrifugal force dominates the radial electric force, resulting in rigid rotor equilibrium, while in the outer region the plasma rotates with  $\mathbf{E} \times \mathbf{B}$  drift. It is also found that the quasi-neutrality breaking takes place in the core region, which is quite exceptional in the sense that it occurs spontaneously over  $1000\lambda_D$  scale.

### (ii) anti- $\mathbf{E} \times \mathbf{B}$ vortex

Vortical motion in plasmas is usually driven by  $\mathbf{E} \times \mathbf{B}$  drift. We have observed a peculiar vortex, which rotates in the opposite direction to the  $\mathbf{E} \times \mathbf{B}$  drift. This means that an effective force is present and dominates the electric force. We expect that the effective force may be generated through charge exchange interaction between the plasma and the flow of background neutrals. The preliminary experiments on neutral flow measurement using a tunable diode laser has been started.

### (iii) velocity measurement using an asymmetric probe

For the simultaneous measurement of flow velocity, we are developing a new method using an asymmetric probe. This probe detects an unbalanced ion current between two electrodes and provides an easy-to-use method for flow velocity measurement. Development of LIF Doppler spectroscopy using two-photon pumping has also been started.





## §2. Radial Force Balance in Plasma Hole and Anomalous ExB Drift Solution

Yoshimura, S.,  
Yamaguchi, H., Tomida, A., Miyake, F. (Nagoya Univ.),  
Kono, M. (Chuo Univ.),  
Tanaka, M.Y. (Kyushu Univ.)

Spontaneous formation of a vortex structure with density hole around the central axis, *plasma hole*, has been observed in an ECR plasma produced in the HYPER-I device. The flow pattern of the plasma hole exhibits a monopole vortex with a sink at the center, and the rigid rotation observed in central region is a characteristic of the flow. So far we have considered that the flow pattern is explained by the ExB drift, however, we should note that the introduction of an effect of the centrifugal force is required when adopting the cylindrical coordinates.

Ion fluid equation in cylindrical coordinates is written as

$$\frac{\partial \mathbf{v}}{\partial t} + (\mathbf{v} \cdot \nabla) \mathbf{v} = -\frac{\nabla P_i}{m_i n_i} + \frac{e}{m_i} \left( -\nabla \phi + \frac{1}{c} \mathbf{v} \times \mathbf{B} \right) + \nu_{eff} \nabla^2 \mathbf{v},$$

where  $m_i$  is the ion mass,  $e$  the elementary electric charge,  $P_i = n_i T_i$  the ion pressure,  $\phi$  the electric potential,  $\nu_{eff}$  the effective viscosity coefficient. We normalize the velocity to ion sound speed and introduce the non-dimensional potential as follows:

$$\mathbf{v}/C_s \rightarrow \mathbf{v}, \quad e\phi/T_e \rightarrow \phi.$$

The force balance in the radial direction is given as

$$\frac{\partial}{\partial r} \left( \frac{v_r}{2} \right)^2 - \frac{v_\theta^2}{r} = -\frac{T_i}{T_e} \frac{\partial}{\partial r} \ln n_i - \frac{\partial \phi}{\partial r} + \frac{\Omega_i}{C_s} v_\theta, \quad (1)$$

where  $\Omega_{ci}$  is the ion cyclotron frequency. Here we use the steady state condition and assume the uniform temperature profile. Weak viscous force in the radial direction is neglected. From eq. (1) it can be seen that the radial force balance is determined by five forces: dynamic pressure gradient, centrifugal force, pressure gradient, electric force and Lorentz force. Defining the total potential by adding the dynamic pressure, electric potential and pressure, we can derive the following quadratic equation that determines the azimuthal flow velocity.

$$\left( \frac{C_s}{\Omega_i} \frac{v_\theta}{r} \right)^2 + \frac{C_s}{\Omega_i} \frac{v_\theta}{r} - \frac{C_s^2}{\Omega_i^2} \frac{1}{r} \frac{\partial \Phi}{\partial r} = 0 \quad (2)$$

$$\Phi = \phi + \frac{T_i}{T_e} \ln n_i + \frac{v_r^2}{2}.$$

Eq. (2) can be solved easily, and we have two solutions for the azimuthal flow velocity.

$$\frac{C_s}{\Omega_i} \frac{v_\theta}{r} = \frac{1}{2} \left[ -1 \pm \sqrt{1 + 4 \frac{C_s^2}{\Omega_i^2} \frac{1}{r} \frac{\partial \Phi}{\partial r}} \right] \quad (3)$$

In order to understand the physical meaning of this solution, we expand the second term on the right hand side by assuming the small potential gradient. The solution with the plus sign in front of the square root is rewritten as

$$v_\theta \approx \frac{C_s}{\Omega_i} \frac{\partial \Phi}{\partial r}. \quad (4)$$

This corresponds to an ordinary ExB drift. On the other hand, the solution with the minus sign is given by

$$v_\theta \approx -\frac{\Omega_i}{C_s} r - \frac{C_s}{\Omega_i} \frac{\partial \Phi}{\partial r}. \quad (5)$$

The principal term is the first term on the right hand side since we have assumed small potential gradient. This solution, which exhibits a rigid rotation even in the absence of an electric field, is referred to as the anomalous ExB solution. It represents the balance between centrifugal force and Lorentz force, whereas the ExB solution represents the balance between electric force and Lorentz force.

Figure 1 demonstrates the azimuthal flow velocity profile constructed from the connection of anomalous and ordinary ExB drift, where we use the total potential determined experimentally. Characteristic rigid rotation (-sqrt) is found in the central region, which suggests that the centrifugal force dominates the radial electric force. Meanwhile the ordinary ExB drift (+sqrt) is found in the outer region. In order to compare this result to the flow profile measured with directional Langmuir probe, a reliable calibration is required, which is our future work.

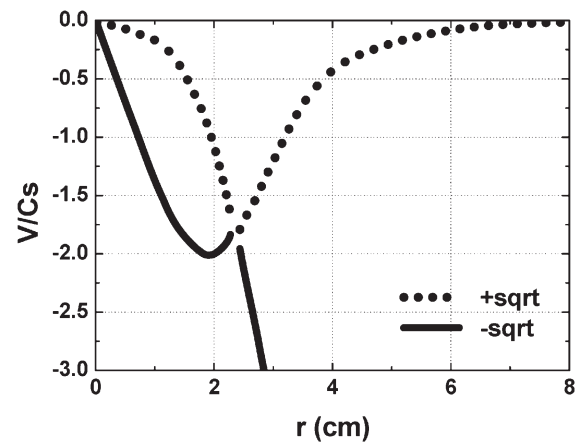


Fig. 1 Azimuthal flow velocity profile of plasma hole. (Calculation)

### §3. Measurements of Neutral-Gas Flow in High-Density Plasma Using a Tunable Laser Diode

Aramaki, M., Kono, A. (Dep. of Eng. Nagoya Univ.),  
Miyake, F. (Dep. of Phys. Nagoya Univ.),  
Tanaka, M.Y. (Kyushu Univ.),  
Yoshimura, S.

Both of the  $\mathbf{E} \times \mathbf{B}$  type and the anti- $\mathbf{E} \times \mathbf{B}$  type vortices have been found in the HYPER-I device. The information of the momentum exchange between the neutral gas flow and the ion flow is important to clarify the dynamics of the formation of the anti- $\mathbf{E} \times \mathbf{B}$  type vortex. The purpose of our collaboration is to get 2-D information of the neutral gas flow using a tunable extended cavity diode laser (ECDL). We performed both of Doppler laser absorption spectroscopy and laser induced fluorescence (LIF) spectroscopy of argon atoms. The neutral-gas flow will be estimated from the frequency shift of Doppler spectrum.

Figure 1 shows an experimental setup for laser absorption spectroscopy and laser induced fluorescence (LIF) spectroscopy using an ECDL. The wave length of the ECDL was tuned to 696.543 nm which excites the  $4s'[3/2]_2$  state of argon atom to the  $4p'[1/2]_1$  state. The frequency of laser light was swept more than 10 GHz to observe Doppler spectrum of argon atoms. An optical isolator was placed in front of the ECDL to avoid fluctuation by optical feedback. The spectrum of the ECDL was monitored using a Fabry-Perot interferometer (FP). The fringes of FP were used as a scale of the frequency variation of laser light. In the case of the absorption spectroscopy, the laser light was attenuated to less than 100  $\mu\text{W}$  using a neutral density (ND) filter and divided into three beam lines using beam splitters (BSs). Absorption spectra were detected by photo diodes and recorded by a computer. In the case of LIF spectroscopy, we used an optical chopper instead of the ND filter and the BSs. LIF signal was coupled to an optical fiber using a focusing lens and detected by a photomultiplier tube (PMT). An interference filter was inserted between the end of the optical fiber and the PMT. Signals from PMT were averaged by an oscilloscope before the data was transform to a computer.

Figure 2 shows an absorption spectrum of ArI metastable with a curve fitted Gaussian distribution. The temperature of the ArI is estimated as 770 K from this profile. Microwave power  $P_\mu$  and Ar pressure were 7.5 kW and  $4 \times 10^{-4}$  Torr, respectively. To discuss about the small deviation from Gaussian distribution, we need to improve S/N ratio and to consider about other broadening effect.

Figure 3 shows an oscillating component of LIF signal which was observed in low power discharge plasma ( $P_\mu \sim 40$  W). The exciting laser was modulated by an optical chopper at 1 kHz. The exciting wavelength was fixed at the center of Doppler absorption spectrum of  $4s'[3/2]_2 - 4p'[1/2]_1$  transition. The observed wavelength was 727.293 nm. LIF signal was clearly observed by averaging signal for 960 sweeps of the oscilloscope. The density of ArI

metastable in the low power discharge plasma was estimated by optical absorption spectra as about three times higher than the density in 7.5 kW discharge. The difference of the density was not so significant; however, we could not observe the LIF signal though signals were averaged for more than 10000 sweeps of the oscilloscope. One of the reasons of this result is fluctuation of optical emission from the high power discharge plasma. This result indicates the necessity of improvement of the ability of our LIF measurement system.

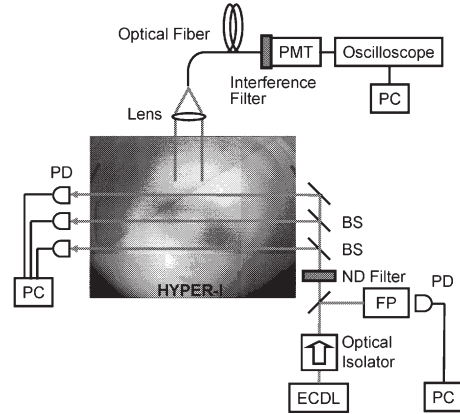


Fig. 1 Experimental setup for diode laser absorption spectroscopy and laser induced fluorescence spectroscopy.

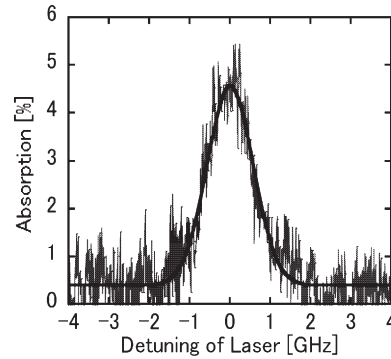


Fig. 2 Absorption spectrum of ArI metastable. The gray line is an observed Doppler spectrum, and the black line is a curve fitted Gaussian distribution.

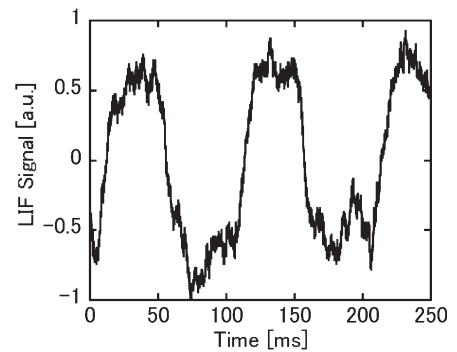


Fig. 3 Chopped LIF signals. Averaged for 960 sweeps.

#### §4. Measurement of Rotational Flow Velocity Using Laser-Induced Fluorescence Spectroscopy

Okamoto, A. (Tohoku Univ.), Tanaka, M.Y. (Kyushu Univ.),  
Yoshimura, S.

Local measurement of flow velocity is required for researches on plasma interaction with boundaries, transport physics, and non-linear plasma structure. A variety of vortical flow structures, for example, has been observed in an electron cyclotron resonance plasma,<sup>1)</sup> and is attracting much attention with respect to self-organization and transport. These vortices have eccentric feature; one has a supersonic rotation, the other has an anti- $E \times B$  rotation induced by neutral pressure gradient. Thus, a direct method of absolute velocity measurement, which complement to directional Langmuir probe (DLP)<sup>2)</sup> methods, is needed. Doppler-shifted fluorescence induced by a tunable laser (LIF) has the advantages of both spatial resolution and absolute velocity measurement.<sup>3)</sup>

The experiments were performed in the HYPER-I device at the National Institute for Fusion Science.<sup>4)</sup> In the present experiment, laser wavelength is tuned to 611.5 nm, which excites an Ar II metastable state ( $3d^2G_{9/2} - 4p^2F_{7/2}$ ). We observe de-excited spontaneous emission of wavelength, 461.0 nm ( $4s^2D_{5/2} - 4p^2F_{7/2}$ ). By changing injecting beam path of the laser, we can measure the rotation (azimuthal) velocity of argon plasmas.

Azimuthal velocity profile in an  $E \times B$  rotating plasma is shown in Fig. 1. The LIF Doppler spectrum was measured at five radial points, and the velocities were determined by shifts of the central wavelength of the line profile from that obtained at  $r = 0$ . The velocities quite well agree with the  $E \times B$  drift velocities determined by potential measurement. It is worth noting that these methods are completely independent, and therefore the consistency of the two results, as seen in Fig. 1, is very satisfactory. In addition, ambiguity of the DLP method in determining absolute velocity is removed by using LIF spectroscopy as a calibration standard.

Azimuthal velocity profile of a plasma, where the plasma rotation is dominated by neutral pressure induced  $F \times B$  drift, is shown in Fig. 2. The velocity determined by LIF spectroscopy and that determined by DLP show reversal of rotation around  $r = 40$  mm, while  $E \times B$  drift velocity

monotonically increase with radius indicating the flow in the center of the plasma is in anti- $E \times B$  direction.<sup>5)</sup>

These results show that LIF spectroscopy is a promising tool for local and absolute measurement of flow velocity. They also suggest that a combined system of DLP and LIF spectroscopy as a calibration standard resolves the ambiguity of absolute value in the DLP method and improves reliability even if the plasma flow is dominated by other than  $E \times B$  drift as well as in the supersonic region.<sup>6)</sup>

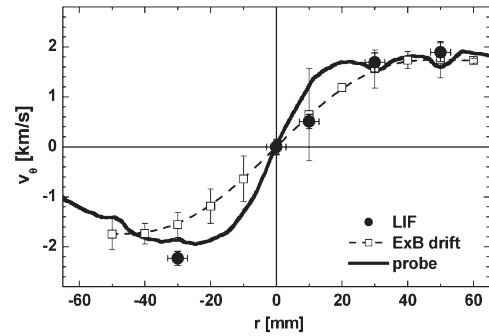


Fig. 1 Azimuthal velocity profile in an  $E \times B$  rotating plasma. The filled circle indicates the velocity determined by LIF spectroscopy, the open square by  $E \times B$  drift, and the solid line by DLP.

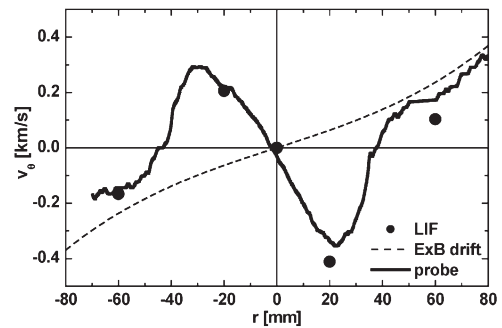


Fig. 2 Azimuthal velocity profile dominated by neutral pressure induced  $F \times B$  drift. The direction of rotation measured by LIF spectroscopy is the same as that measured by DLP and is opposite to that of the  $E \times B$  drift in the center of the plasma.

#### Reference

- 1) Okamoto, A. et al. : IEEE Trans. Plasma Sci., **33** (2005) 452, Tanaka, M.Y. et al. : *ibid.* 454
- 2) Nagaoka, K. et al. : J. Phys. Soc. Jpn. **70** (2001) 131
- 3) Okamoto, A. et al. : J. Plasma Fusion Res., **80** (2004) 1003
- 4) Tanaka, M. et al. : J. Phys. Soc. Jpn. **60** (1991) 1600
- 5) Okamoto, A. et al. : Phys. Plasmas, **10** (2003) 2211
- 6) Okamoto, A. et al. : J. Plasma Fusion Res. SERIES, **6** (2005) 606

## §5. Plasma Flow Measurement using Facing-Double Probe

Saitou, Y. (Utsunomiya Univ.),  
Tsushima, A. (Yokohama National Univ.),  
Yoshimura, S.,  
Tanaka, M.Y. (Kyushu Univ.)

A plasma flow is concerned in various phenomena observed in plasmas. Consequently, to measure the flow velocity is required in wide range of fields of plasma science, from basic investigation to applications. In this research, it is our purpose to establish a method how to determine a precise Mach number of a plasma flow using the Facing-Double probe (FDP). The observation method using the FDP is our new proposal for estimating the Mach number of the plasma flow<sup>1,2)</sup>. It is shown that the method is capable of determining the wide range of Mach number up to 2 by particle-in-cell (PIC) simulation and numerical calculations based on the fluid model. In addition, preliminary performed experiments have tended to support these numerical results. It is required for establishing the evaluating method of Mach number using FDP to compare Mach numbers obtained by other method such as the conventional Mach probe and/or Laser-Induced-Fluorescent method. The HIPER-I device in National Institute of Fusion Science (NIFS) has various methods for this propose.

Schematic drawing of the FDP for the present experiments is shown in Fig. 1. The gray parts are tungsten electrodes. In a conventional Mach probe, the electrodes are placed back-to-back putting an insulator between them. In case of FDP, it is a peculiarity that the electrodes are placed face-to-face. Because of such a shape of FDP, disturbance of plasmas due to a pre-sheath formed in front of the electrode is considered to be less than the disturbance in the case of the conventional Mach probe. At the same time, the shape of FDP has a new advantageous point in measuring the spatial profile of Mach number because the spatially limited pre-sheath expansion brings a relatively high spatial resolution and makes it possible to obtain a spatial Mach number distribution. Sizes of the electrodes and a distance between the electrodes are determined from a point of view that a plasma exists between the electrodes are regarded to be 1-dimensional. The electrodes are connected through a direct-current (dc) variable power supply and an ammeter.

When FDP is inserted into a flowing plasma, the dc voltage  $V_0$ , at which the ammeter shows no current, is related to Mach number  $M$ . That is, there is a following relation between  $V_0$

and  $M$ :

$$\frac{eV_0}{k_B T_e} \cong \left\{ 1 + \frac{\alpha}{\sqrt{1+\alpha}} \tan^{-1}(\sqrt{1+\alpha}) \right\} M \quad (1)$$

where  $e$  is the elementary electric charge,  $k_B$  the Boltzmann constant,  $T_e$  the electron temperature between the electrodes, and  $\alpha$  the normalized viscosity. When  $M$  is small, the value of  $M$  is proportional to the value of  $V_0$ . This suggests that the determination of Mach number using FDP is probably easier than using the conventional one.

The observed data from HIPER-I suggest that FDP seems possible to estimate Mach number though the results require us to refine the method at the same time. For example, the present electrodes of FDP have wide lateral areas and easily detect the charged particles plunged into them irrelevantly to the plasma flow. From this point of view, the shape of the electrode should be a plate with small lateral area. It is expected that FDP method is capable of measuring the spatial distribution of Mach number because of its shape. The measurement circuit is quite simple and easier to evaluate Mach number. It is expected that the method has wide range of application after the method is established.

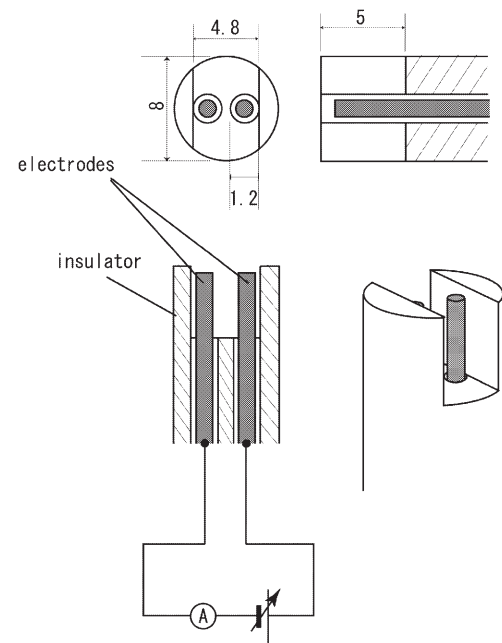


Fig. 1 Schematic drawing of the Facing-Double probe.

### References

- 1) Y. Saitou and A. Tsushima: Jpn. J. Appl. Phys., **40** (2001) L1387 - L1389.
- 2) Y. Saitou and A. Tsushima: J. Phys. Soc. Jpn., **70** (2001) 3201 - 3204.



## §6. Coefficient of Ion Sensitive Probe for Ion Temperature Measurement

Tsushima, A. (Yokohama National Univ.),  
Saitou, Y. (Utsunomiya Univ.),  
Yoshimura, Y., Tanaka, M.Y.

Electrostatic probes have been intensively used to measure plasma properties since the early study of plasma physics. Langmuir probes are the most widely used probes among them; they evaluate electron temperature,  $T_e$ , by fitting a simple function, analytically given by  $I \sim \exp(eV/k_B T_e)$  to measured V-I characteristics of the probes.<sup>1)</sup> Most electrostatic probes evaluate electron properties because the electron mass is much smaller than ion masses, and because the current to an electrode immersed in plasma is mainly dominated by electrons that reach the electrode.

To evaluate ion temperature, some modifications to electrostatic probes are required. An ion-sensitive probe that consists of a central electrode and a guard electrode, as shown in Fig. 1, is one of the examples.<sup>2)</sup> The central electrode is placed parallel to the magnetic field and the cylindrical guard electrode surrounds the central electrode to block electrons from reaching the central electrode, because the gyroradii of electrons are much smaller than those of ions. Thus, ion current flowing into the central electrode is measured with the bias voltage,  $V$ , applied to the central and guard electrodes against the ambient plasma. Ion temperature,  $T_i$ , is evaluated with the assumption that the measured V-I characteristics obey a simple function given by  $I \sim \exp(-eV/k_B T_i)$ .

However, a numerical study of the ion current of such ion-sensitive probes with various radii and heights of electron probes shows the need of a calibration coefficient,  $c$ , of each ion sensitive probe to evaluate ion temperature for a fitting function with the form:<sup>3)</sup>

$$I \sim \exp(-c eV/k_B T_i).$$

The coefficient,  $c$ , depends on the radius,  $R$ , and height,  $H$ , of an ion sensitive probe and Fig. 2 shows how the coefficient,  $c$ , depends of the normalized radius,  $R/\rho$ , and height,  $H/\rho$ , where,  $\rho$  is a characteristic ion gyroradius and given by  $\rho = [2mk_B T_i / (eB)]^{1/2}$ .

In the HYPER-1 device, ion temperatures estimated from the measured V-I characteristics of ion sensitive probes with the numerically obtained coefficient,  $c$ , will be compared with those estimated from Doppler broadening of the line of

laser induced fluorescence scattered by moving ions will be made.

### References

- 1) H. M. Mott-Smith and I. Langmuir: Phys. Rev. **28** (1926) 727-763.
- 2) I. Katsumata and M. Okazaki: Jpn. J. Appl. Phys. **6** (1967) 123-124.
- 3) A. Tsushima and Y. Tayama: Jpn. J. Appl. Phys., **44** (2005) 4128-4132.

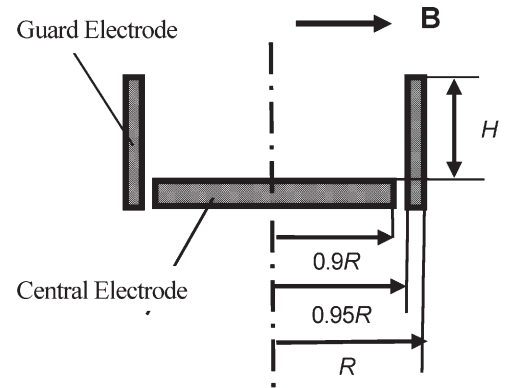


Fig. 1 Schematic drawing of ion sensitive probe.

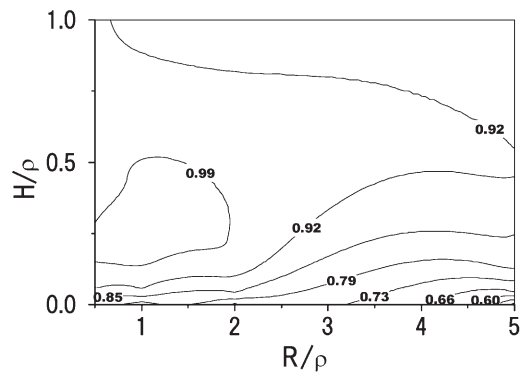


Fig. 2 Contour map of coefficient,  $c$ .

## §7. Excited Atomic Processes as Fundamental Researches for New Plasma Diagnostic

Iiyama, K., Matsuda, W., Sakai, Y., Jin, W.G., Takagi, S. (Dept. of Phys. Toho Univ.), Sakaue, H.A., Yamada, I.

The charge exchange spectroscopy (CXS) is widely used for a plasma diagnosis. Since collisions between highly charged ions (HCIs) and neutral species are dominant processes in charge exchange mechanism, we had carried out the HCI collision experiments with some atoms and molecules.<sup>1)</sup> In this work, we used the excited atoms as a target. When target species are excited, it is well known that charge exchange cross sections are resonantly increased under the classical overbarrier model. Using this mechanism, we can discuss the probability of the resonant charge exchange spectroscopy (RCXS). In order to propose the RCXS as a new method for a plasma diagnosis, we have carried out this study. On the other hand, since neutral atoms are usually excited in the fusion reactor, it is important for understanding the cooling mechanisms to measure the cross sections for the excited atomic processes like a charge exchange process.

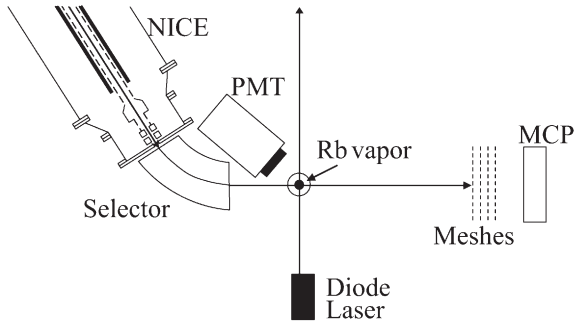


Figure 1: The experimental apparatus

The present experiments have been carried out as a series of a Naked Ion Collision Experiment (NICE) project in NIFS. The used apparatus which is based on the electron beam ion source (cryo-NICE) is shown in fig.1. The produced HCIs collide with the excited target beam after the charge selection. The iodine ions were used as the projectile. For the target we chose rubidium (Rb) atoms because it is easy to generate the atomic beam and excite to the resonant level. Rb atoms are excited with the diode laser from ground state to excited one after the Rb beam was generated through a thermal oven. The light from laser at the center wavelength 780 nm was delivered to the collision region, and operated on the  $5s \rightarrow 5p$  transition. The Rb target density was estimated with a surface ionizer and the excitation was confirmed with the photo-multiplier tube (PMT) combined with a band-pass filter. When the fluorescence light from the excited Rb was saturated, the 50% Rb atoms were excited in the beam. Both the charge exchange ions and no-exchange ions are detected

with micro-channel plate (MCP) after passing through the retarding meshes. We can select the charge of detect ions by applying the retarding voltage into the meshes and obtain the HCI intensity according to the initial charge of HCIs. The related voltage is easily decided by,

$$V_{q-i} = E_0 \times \frac{q}{q-i}, \quad (1)$$

where  $E_0$  is the energy of incident ions,  $q$  is the initial charge,  $i$  is the exchange charge.

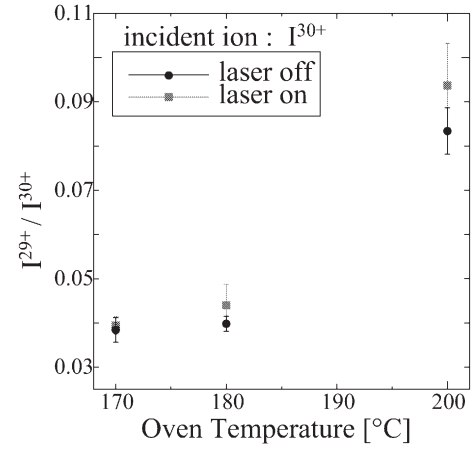


Figure 2: Ratio of  $I^{29+}/I^{30+}$  for  $I^{30+}$  - Rb and excited Rb collision experiments.

In this work, we succeeded in observing the signal from the HCI collision with the excited Rb. Figure 2 shows the experimental results of the ratio of  $I^{29+}/I^{30+}$  for  $I^{30+}$  - Rb and excited Rb collisions. As the oven temperature rises the ratio of  $I^{29+}/I^{30+}$  increases. This fact indicates that the target density depends on the oven temperature and the density is still low enough in the collision region for single collision. The character labeled "laser on" is for the ratio from the target including excited Rb. Thus although the absolute charge exchange cross sections for the excited Rb target have not determined yet, we confirmed the growth in charge exchange cross section for excited target. Using the absolute value of the charge exchange cross sections for  $I^{q+}$ -Rb collision that had been already measured<sup>2)</sup>, we can determine ones for  $I^{q+}$ -excited Rb collision by comparing our results, as follows.

$$\sigma_{ex} = \sigma_n \times \frac{2I_{ex} - I_n}{I_n}, \quad (2)$$

where  $\sigma_{ex}$  and  $\sigma_n$  mean total charge exchange cross sections, and  $I_{ex}$  and  $I_n$  are signal intensities, the subscript  $ex$  is for the excited target and  $n$  is for the no-excited one, respectively. In the near future, we will not only determine the charge exchange cross sections for excited Rb but also for excited cesium and potassium.

### References

- 1) M.Kimura et.al., J.Phys.B **28**, L643 (1995).
- 2) H.A.Sakaue et.al., Abstracts of Contributed Papers of 21st. ICPEAC **2**, 552 (1999).

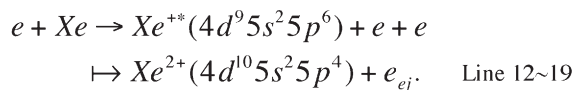
## §8. Study of the Excitation Processes in Electron-Ion Collisions

Sakaue, H.A., Yamada, I.,  
Hirayama, T. (Rikkyo Univ.),  
Ohtani, S. (Univ. Electro-Communications),  
Sakurai, M. (Kobe Univ.),  
Takayanagi, T. (Sophia Univ.)

The understanding of the interaction of electron-ion collision process is important not only for the control and diagnostic of plasma but also for the atomic physics at many atomic processes in high temperature plasma. The research of ionization process in the electron-ion collision have been done for a long time, and the data was offered to the plasma control, the diagnostics of plasma and so on. At present, however, there are few atomic data for the excitation processes of electron-ion collisions, because of its experimental difficulties such as a low signal-to-noise ratio due to a low target ion density and very small cross sections, etc.

We developed the exclusive high-density ion source for the collision experiments. Then, the original tandem type electrostatic energy analyzer was developed at the same time. We fine-tuned the electron energy analyzer using the Auger spectrum at the electron atom collisions.

In figure 1-(a), we show the NOO Auger spectrum in electron-Xe atom collisions. The collision energy is 500eV and the observation angle is 90 degree. These Auger electrons are emitted in following processes,



Then, Auger electrons of  $N_{4.5}O_{2.3}O_{2.3}$  are dominant. The line 7~11 are peaks of  $N_{4.5}O_1O_{2.3}$  Auger processes. In figure 1-(b), the Auger spectrum of B.S.Min et al.<sup>1)</sup> ( $E_c=500\text{eV}$ ,  $\theta=70^\circ$ ) is shown. The energy resolution of our spectrum is better than it. From these experiments, we ascertained that our energy analyzer was completed as the design.

In fig. 2, we show the ion beam current dependence of  $N_{4.5}O_{2.3}O_{2.3}$  Auger spectrum in electron-Xe collisions within the  $Xe^+$  ion beam. When the  $Xe^+$  ion beam current was 1.0  $\mu\text{A}$ , Auger spectrum peaks were separated respectively. But at 6.0  $\mu\text{A}$ , these Auger spectrum peaks are broadening and shifted to the low energy side. These phenomena are attributed to the electric field distribution of the location where Auger electrons are generated. Therefore we can

estimate the space charge effect for the  $Xe^+$  ion by analyzing this spectrum. We required canceling out this space charge at the ejected electron spectroscopy in electron-ion collision. Then we are doing the tests of canceling out the space charge at present. One is the direct electron supply method using electron shower and another is the electric field supply method using a tungsten coil. From now on, we will establish the most suitable method of canceling out the ion space charge and try the ejected electron spectroscopy in the electron-ion collisions.

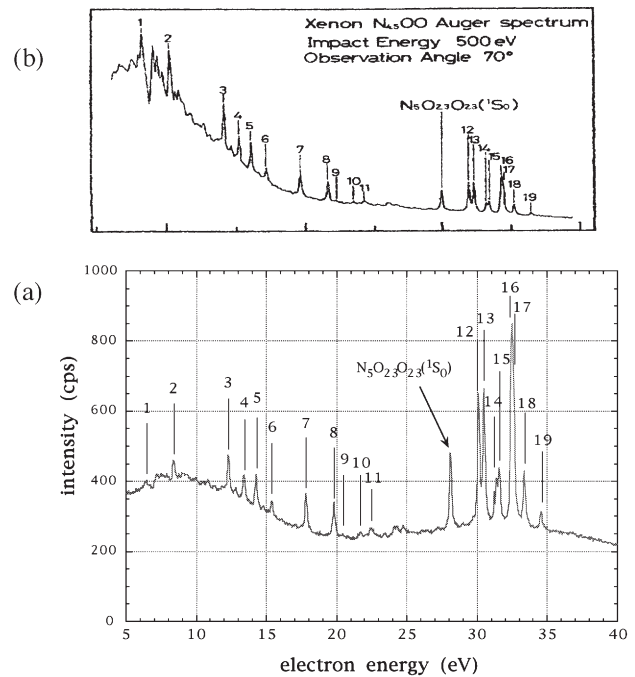


Fig. 1 Xe NOO Auger spectrum.

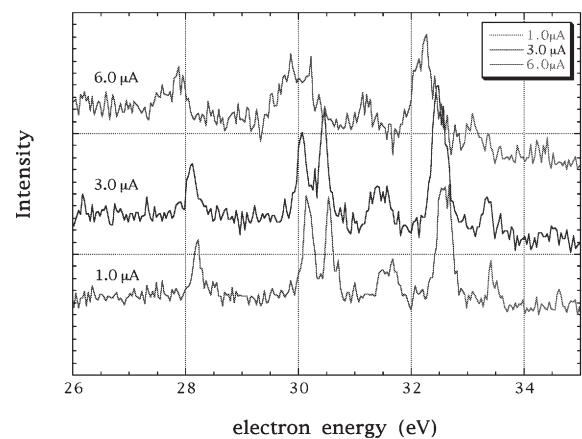


Fig. 2 The peak shift and broadening.

### Reference

1)B.S.Min et al., J.P.S.J.64 1183(1993)

## §9. Isotope Effect on Charge Transfer by Slow Lithium Ions from Hydrogen Molecules

Kusakabe, T. (Dept. Phys. Kinki Univ.),  
Kimura, M. (Kyushu Univ.),  
Pichl, L. (Div. Natural Sci., ICU),  
Sakaue, H.A.

We have recently investigated isotope effect on charge transfer by slow hydrogen ions ( $H^+$  and  $D^+$  ions) from hydrogen molecules ( $H_2$ , HD, and  $D_2$ ).<sup>1,2,3)</sup> The cross section ratios of  $\sigma(H^+ + D_2) / \sigma(H^+ + H_2)$  and  $\sigma(D^+ + D_2) / \sigma(H^+ + H_2)$  decrease to smaller value than unity below 1 keV/u, and reach a value of about 0.6 at the collision energy of 0.18 keV/u. Contrary to the case of  $H_2$  and  $D_2$ , the experimental  $\sigma(H^+ + HD) / \sigma(H^+ + H_2)$  and  $\sigma(D^+ + HD) / \sigma(H^+ + H_2)$  ratios are found to be almost unity in the entire energy region from 0.18 keV/u to 1.5 keV/u investigated. The theoretical analyses based on the molecular-orbital expansion method have been applied to these collisions taking into account the deference of the vibrational energy of the product hydrogen molecular ions and the Frank-Condon principle.

The above charge-transfer processes at low collision energies are known to be important in a number of applications, especially in the controlled thermonuclear fusion research. In order to get more comprehensive understanding about the isotope effect on charge transfer in ion-molecule collisions of the hydrogen family, we have measured the charge-transfer cross sections of  $^7Li^+$  ions colliding with the  $H_2$ , HD and  $D_2$  molecules in the energy range of 1.4 to 4.0 keV.

The  $^7Li^+$  ions were extracted from a surface ionization ion source. A platinum foil with the size of  $2 \times 2 \times 0.03$  mm spot-welded at a tungsten filament with 0.15 mm diameter was used as an anode for lithium ion emitter, which was coated with a mixed powder of  $Li_2CO_3$ ,  $Al_2O_3$  and  $SiO_2$ . The cross sections of charge transfer were determined by the initial growth rate

method with a position sensitive micro-channel plate detector.

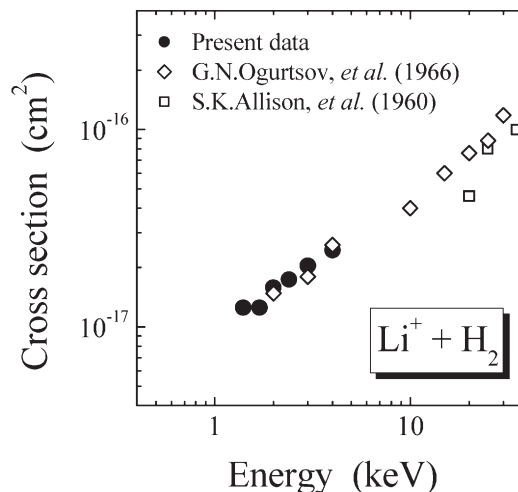


Fig. 1. Charge-transfer cross sections of  $Li^+$  ions in collisions with  $H_2$  molecules as a function of the collision energy.

Figure 1 shows the charge-transfer cross sections of  $Li^+$  ions colliding with  $H_2$  molecules. The present cross sections increase as the collision energy increases and are in good accordance with the previous data of Ogurtsov *et al.*<sup>4)</sup> We tried to measure the charge-transfer cross sections at energies below 1.4 keV. However, charge transferred lithium atoms are found to be heavily scattered at large angle, so that the most charge transferred lithium atoms could not be passed through the exit aperture of the collision cell.

Both the present charge-transfer cross sections of  $Li^+$  ions colliding with HD and  $D_2$  molecules are found to be about 15% smaller than those of  $H_2$  target.

The joint theoretical studies are now in progress for  $Li^+$  ions colliding with the hydrogen family to obtain clear conclusive evidence.

### Reference

- 1) Kusakabe, T. *et al.*: Phys. Rev. A **62** (2000) 062714.
- 2) Kusakabe, T. *et al.*: Phys. Rev. A **68** (2003) 050701(R).
- 3) Kusakabe, T. *et al.*: Phys. Rev. A **70** (2004) 052710.
- 4) Ogurtsov, G.N. *et al.*: Sov. Phys. - Tech. Phys. **11** (1966) 362.



## §10. Measurement of EUV Out-of-Band Spectra in Laser Produced Sn Plasmas

Namba, S. (Grad. School Eng. Hiroshima Univ.),  
Oda, T. (Fac. Eng. Hiroshima Kokusai Gakuin Univ.),  
Sato, K.

The hot dense plasmas created by intense laser pulses have been extensively studied for various applications, such as next generation extreme ultraviolet lithography (EUVL), x-ray microscopy, and absorption spectroscopy. Especially, in order to realize the next generation semiconductors with a node  $< 45$  nm, the development of EUV light source suitable for the lithography has been considered to be one of the urgent issues[1]. For the purpose of this, xenon and tin plasmas produced by a high-intensity laser and z-pinch have been used so far.

On the other hand, a Mo/Si multilayer mirror used for focusing and transmitting EUV light, which has maximum reflectivity around 13.5 nm in wavelength, suffers from heat load caused by intense emission radiated from high-density laser plasma, resulting in the deformation of the mirror surface. Moreover, since the Mo/Si mirror has also high reflectivity above 100 nm in wavelength, the unnecessary light for the lithography (out-of-band) as well as EUV emission could be transferred and exposed on the wafer. Consequently, the resolution of EUVL system becomes drastically worse. Therefore, the measurement of absolute emission intensity from UV to the infrared region provides essential information to enhance the miniaturization.

In this study, we measured the EUV out-of-band spectra in the wavelength region of 200-750 nm emitted from a laser produced Sn plasma to elucidate the spectral distribution.

The experiments were carried out by using a YAG laser (wavelength: 1064 or 355 nm). The target was tin plate (purity 99.9 %) mounted on the  $x$ - $z$  state to irradiate the fresh tin surface for each laser pulse. Spectroscopic investigations were performed using time- and spatial resolved optical system. For the measurement of spatial intensity distribution

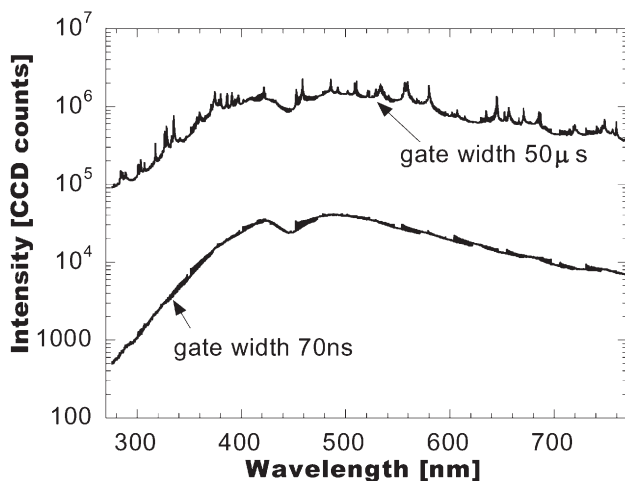


Fig.1. Out-of-band spectra for exposure times of 70 ns and 50  $\mu$ s.

along the direction parallel to the laser incidence, the emission was collected by a lens onto an optical fiber with 48 cores. The spatial resolved spectra were measured by a spectrometer coupled with a CCD camera with an image intensifier. The whole optical system was relatively calibrated by  $D_2$  and Xe lamps.

Figure 1 shows the spectral distribution between 280 and 780 nm under the experimental condition of 1064 nm, pulse width of 10 ns, and intensity of  $\sim 7 \times 10^{10}$  W/cm<sup>2</sup>. The exposure times for CCD camera were set to 70 ns and 50  $\mu$ s. As is clearly seen, the continuum emission dominates over the line emissions. The calibrated spectral intensity for 70-ns exposure is shown in FIG. 2 with solid curve. The dotted curve represents the Planck distribution corresponding to plasma temperature of 17 eV. The good agreement between experimental and Planckian curves was obtained. The out-of-band spectra, therefore, can approximately be regarded as the blackbody radiation.

The measurement of UV spectral region above 180 nm was also carried out using laser pulses with 355 nm,  $\sim 5$  ns pulse,  $\sim 7 \times 10^9$  W/cm<sup>2</sup>. The experimental curve can be reproduced by Planckian of  $\sim 10$  eV.

In general, the high Z atoms such as tin have many, complicated excited levels. Realistically, it is impossible to calculate the all optical transition which contributes to the out-of-band emission. However, the fact that the spectral distributions can approximately be expressed by Planckian with the certain plasma temperature makes the estimation of out-of-band spectra much simple, since we can neglect a great number of line emissions.

In future, we will measure the out-of-band spectrum in VUV region (100~200 nm). For calibration of optical system, the atomic branching ratio method will be employed to obtain the absolute intensity [2].

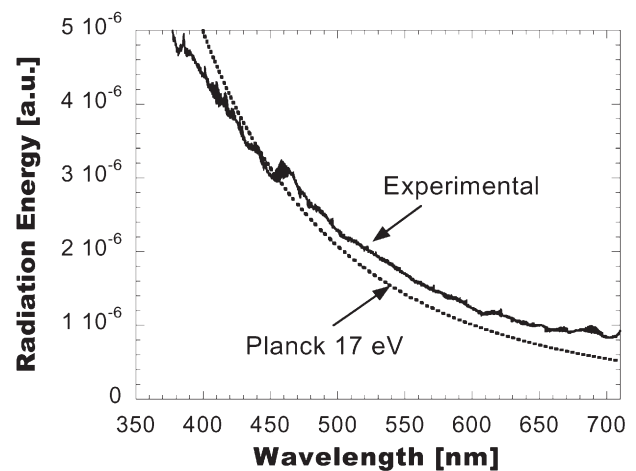


Fig. 2. Calibrated experimental spectrum. The Planckian curve with a plasma temperature of 17 eV is also shown.

### References

- [1] Namba, S., et al., Appl. Phys. Lett. **88**, 171503 (2006).
- [2] Sato, K., et al., Appl. Opt. **23**, 3336 (1984).

## §11. Theoretical and Experimental Studies on the Contribution of Wave-Particle Interactions to Radial Transport in a Strongly Magnetized Non-neutral Plasma

Kiwamoto, Y., Soga, Y., Aoki, J. (Grad. School of Human and Environmental Studies, Kyoto Univ.)

Rotating-wall technique has been commonly used for controlling the radial transport of particles in non-neutral plasmas in order to maintain a stationary density distribution against radial diffusion or to increase the on-axis density by compression.<sup>1)</sup> The purpose of the last aim is to increase the generation rate of anti-hydrogen from anti-protons and positrons trapped in a nested Penning trap<sup>2)</sup> The rotating wall stands for azimuthally rotating electric field driven by RF voltages applied to an azimuthal array of wall segments with a periodic phase shift. It worked quite well though the physical mechanism was not fully understood.

The purpose of our study was to explore the fundamental processes relevant to the radial transport induced by the rotating electric field. Combining preliminary experimental results in our laboratory and work reported in archives, we constructed a theoretical model in a closed form.<sup>3)</sup>

The model is based on a drift-kinetic equation of magnetized electrons radially bounded by a conducting wall via a vacuum region. The rotating electric field is assumed to belong to the Trivelpiece-Gould mode with non-zero mode numbers both in the azimuthal and axial directions. The radial flux is evaluated by the axial-velocity integration of the time-averaged product between the  $\mathbf{ExB}$  drift on fluctuating electric fields and the perturbation of the velocity distribution function. The net radial flux appears as a contribution of the particles axially resonant with the T-G mode wave. The concentration of the same-sign particles associated with the radial flux was found to increase the potential energy of the particle system with an increment exactly equal to the work exerted by the torque of the azimuthal components of the rotating electric field. The increment of the angular momentum of the particle system due to the radial transport was proved also to correspond to the wave torque.

The resonant particles responsible for the radial transport are subject also to the Landau-damping. The associated increment of the kinetic energy in the axial particle dynamics was found to be exactly equal to the decrement of the wave energy minus the increment of the potential energy associated with the radial transport at each radially sliced shell. This means within the framework of this theoretical model the Landau-damped energy of the wave is fully converted to the radial compression and the axial heating with a radially-varying branching ratio that is determined by the wave frequency and by the local frequency of equilibrium rotation.

Most of the features predicted by the model were confirmed in experimental examinations of the wave-driven

profiles of a pure electron plasma at least as long as the wave amplitude is much smaller than the electron temperature.<sup>4)</sup> Experimental confirmations were made on the dispersion relation of the waves driven by the phased RF voltages and propagating in the bulk plasma to belong to the T-G mode.

By combining the measured amplitude of the image current on the wall and the radial structure of the eigen-mode wave calculated on the basis of the observed density distribution, an evaluation is carried out for the absolute value of the wave amplitude propagating in the plasma. The quasi-linear radial flux evaluated by substituting the observed parameters into the model-derived equation was found to agree within a factor of three with the observed density distribution that is compressed by the wave as the time elapses. The compression rate was observed to be roughly proportional to the square of the observed wave-amplitude as the quasi-linear theory predicts.

An interesting observation that had not been predicted by the theoretical model was that the ratio of the wave frequency linearly ramped up with time to the on-axis plasma frequency is latched to a constant value around 0.2 during the period while the plasma is compressed efficiently.

The observation that a rapid expansion of the radial edge of a flattop distribution occurs when the sense of the rotation of the wave is reversed against the equilibrium  $\mathbf{ExB}$  rotation is what the model predicts and the observed parameters are also quantitatively consistent with the prediction of the model.<sup>4)</sup>

An novel and interesting parameter incorporated in the theoretical model is the momentum of the electro-magnetic field associated with the charge distribution and the homogenous magnetic field corresponding to the azimuthal  $\mathbf{ExB}$  flow. Though the electro-magnetic momentum appears only to belong to the basic concept of the theory of electromagnetism<sup>5)</sup> and not to be directly observable, the model indicates that the observed density distributions of magnetized electrons represent visually the distribution of the electro-magnetic angular momentum that changes in time absorbing the momentum of the plasma wave.

This work was supported by the Grant-in-Aid for Scientific Research of JSPS and by the collaborative program of NIFS. The authors deeply appreciate supports by Prof. M. Y. Tanaka and Dr. S. Yoshimura.

### References

- 1) F. A. Anderegg et al., Phys. Rev. Lett. **81**, 4875 (1998).
- 2) A. Mohri et al., J. Plasma Fusion Res. **80**, 1005 (2004).
- 3) Y. Kiwamoto, Y. Soga and J. Aoki, Phys. Plasmas **12**, 094501 (2005).
- 4) Y. Soga, Y. Kiwamoto and N. Hashizume, Plasmas **13**, 052105 (2006).
- 5) Koichi Ohta, *Introduction to Electrodynamics*, (Maruzen, 2000).

## §12. Study on Spatio-Temporal Structure of Bistable Density Transition

Shinohara, S., Kamataki, K., Nishijima, T. (Interdis. Grad. Sch. Eng. Sci., Kyushu Univ.),  
Fujisawa, A., Ida, K., Iguchi, H.

In the future nuclear fusion studies, understandings of transport barrier and its formation mechanism, which have been actively investigated in NIFS, are crucial. Plasma rotation driven by so-called  $\mathbf{E} \times \mathbf{B}$  drift has been also studied in relation to improvement of the magnetic confinement. Therefore, investigations of the dynamic process of the electric field and its effect on transition phenomena are very important.

We have been trying to control the density transition phenomena along with plasma rotation and density profile modification, using ten concentric circular rings as biased electrodes [1-3]. Here, dynamic changes of plasma performance including the electrode region were studied by applying the steady or pulsed bias voltages. Argon plasma at a pressure  $P$  of 0.1 - 10 mTorr in the cylindrical chamber, 45 cm in diameter and 170 cm in axial length, was produced by a RF wave of 7 MHz. Plasma parameters were measured by a developed 24 ch. Langmuir probe and a 3D scanning probe [3]. Data were stored with a data logger. Using this system, detailed spatio-temporal behavior was investigated. Typical plasma density  $n_e$  and electron temperature were  $4 \times 10^9$  -  $4 \times 10^{10} \text{ cm}^{-3}$ , 3 - 6 eV, respectively.

Comparing the two states, i.e., state I (high density) and state II (low density), as shown in Fig. 1, floating potential  $V_f$  in state II was higher than that in state I, which shows the easier trapping of electrons in state I. On the other hand, ion saturation current  $I_{is}$  was smaller in state I than that state II, which is the opposite character in the main plasma region. Applying a pulsed bias voltage from the low to the high voltages to satisfy the transition from state I to state II, fast change of bias current, as shown in Fig. 2, was found. Although the change of bias current  $I_b$  (bias voltage) was less than a few  $\mu\text{s}$  ( $\mu\text{s}$ ),  $I_{is}$  in the bulk plasma region changed slowly with less than ms. Here,  $V_f$  in the bulk region changed much slower on the order of ms. Note that, near the electrode region,  $I_{is}$  and  $V_f$  changed fast with less than a few tens of  $\mu\text{s}$  [4,5].

In conclusion, we have investigated the detailed spatio-temporal characteristics of density transitions by voltage biasing. Obtained results suggest that the plasma parameters near the electrode play an important role causing the transition, which may be interpreted from the particle behaviors. These understandings will be expected to contribute to the plasma confinement and stability control.

### References

- 1) S. Shinohara *et al.*, Trans. Fusion Technol. **39** (2001) 358; Phys. Plasma **8** (2001) 1154, **9** (2002) 1834.
- 2) S. Matsuyama and S. Shinohara, J. Nucl. Fusion Res.

4 (2002) 528.

3) S. Shinohara, Phys. Plasma **9** (2002) 4540; Rev. Sci. Instrum. **74** (2003) 2357.

4) S. Shinohara *et al.*, Thin Solid Films **506-507** (2006) 564.

5) S. Shinohara *et al.*, Eng. Sci. Rep. Kyushu Univ. **27** (2006) 355.

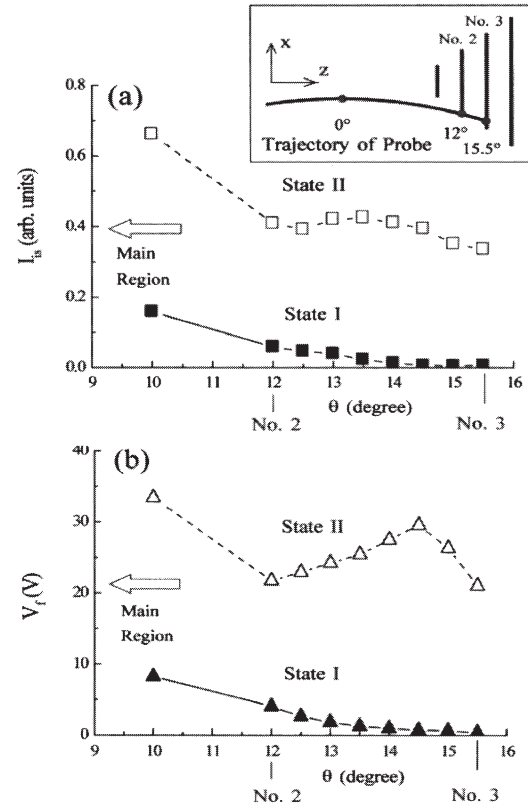


Fig. 1. Spatio-temporal behaviors of (a)  $I_{is}$  and (b)  $V_f$

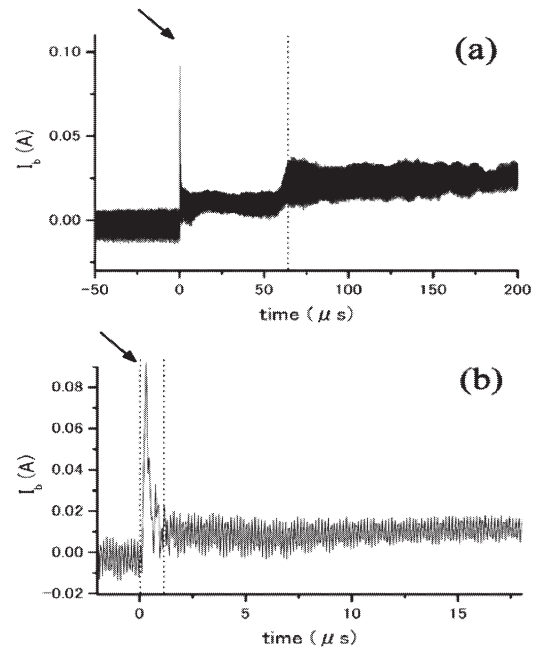


Fig. 2. Time evolution of  $I_b$  [(a) and (b) show different shots].

### §13. Basic Process of Solid Hydrogen Ablation by Means of Pellet Injection Apparatus with Changeable Size

Fujita, H., Ohtsu, Y., Misawa, T. (Saga Univ.),  
Sato, K.N. (Kyushu Univ.),  
Arimoto, H. (Nagoya Univ.),  
Yoshimura, S.

Interaction between plasma and solid is one of the important themes, which should be studied in the sense of plasma science. On the other hand, from the viewpoint of performance of nuclear fusion plasmas, pellet injection experiments have been actively carried out in many toroidal studies in the sense of the control of density profile, obtaining high density or improved confinement, and diagnostic purposes. However, it is, so far, an empirical scaling and the essential part of solid hydrogen ablation by plasmas, such as the interaction between pellet and plasma, have not been clarified. For instance, observation of so-called “Tail Mode”, which may be the result of charge exchange equilibrium state and the plasma rotation by the potential, might be affected by the density profile of the edge plasma. Thus, the study on pellet plasma interaction is one of the most interesting issues to be investigated as the fundamental plasma science.

In this research, an accumulation of data on the interaction between plasma and solid hydrogen is planned by measuring the fundamental process of pellet injection into inductively coupled plasma (ICP). ICP is possible to get high-density of  $10^{12}\text{cm}^{-3}$  and uniform density profile at low pressure of a few mTorr. This plasma is considered to be utilized as target plasmas to simulate edge plasmas. In this report, we present spatial distributions of plasma parameters in ICP.

The cylindrical vacuum chamber, made of stainless steel, has a diameter of 500 mm and a length of 1000 mm, in which one-turn helical antenna with a diameter of 200 mm is vertically set in the center of the chamber, having the same symmetry axis as the chamber. Pure argon is introduced into the vacuum chamber at a fixed pressure of 5 mTorr to examine the fundamental plasma characteristics. The helical antenna is connected to RF (13.56 MHz) power source through a matching box. The power is ranged from 50 to 500 W to generate ICP plasma. A tungsten cylindrical probe with 0.1 mm diameter and 2 mm length was used for measuring plasma parameters such as density and temperature of electrons. In order to reduce the effect of plasma potential oscillation to the probe measurement,

self-compensated LC filter was added. The center in the RF antenna is defined as  $r=0\text{cm}$  and  $z=0\text{cm}$ .

Figures 1(a) and (b) show two dimensional structures of density and temperature of electrons, respectively. Here, circle at  $r=10\text{ cm}$  in Fig.1 denotes the position of the loop antenna. These measurements were done at ranges of  $0 < r < 20\text{ cm}$  and  $0 < z < 20\text{ cm}$ . The electron density is about  $4 \times 10^{10}\text{ cm}^{-3}$  at  $r=0\text{ cm}$  and  $z=0\text{ cm}$  and decreases gradually with increasing a distance to radial direction. It is about  $3 \times 10^{10}\text{ cm}^{-3}$  at  $r=20\text{cm}$  and  $z=0\text{cm}$ . There is a depression of density at  $r=12\text{cm}$  and  $z=0\text{cm}$ . This is ascribed by the presence of RF sheath near the loop antenna. It is found that the density over  $10^{10}\text{ cm}^{-3}$  is performed at wide ranges of  $0 < r < 20\text{cm}$  and  $0 < z < 20\text{cm}$ .

On the other hand, the electron temperature is about 3 eV and its profile is almost uniform spacially at wide region of  $0 < r < 20\text{cm}$  and  $0 < z < 20\text{cm}$ . The temperature at  $r=7.5\text{cm}$  is about 4 eV. This is caused by the contribution of high energy electrons accelerated by the sheath near the antenna. As the results, it is revealed that inductively coupled plasma is effectively useful for the target plasma.

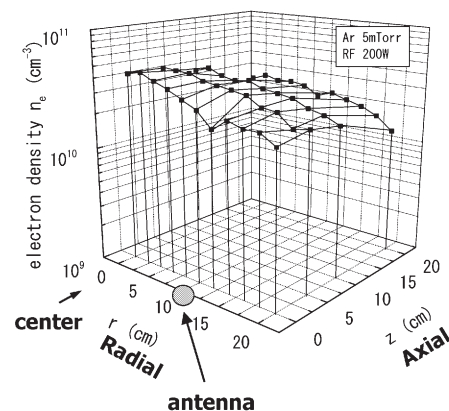


Fig.1 (a) Two dimension structure of electron density

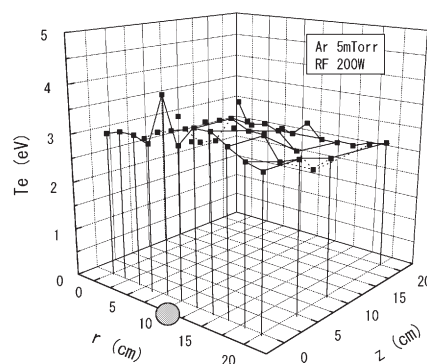


Fig.1 (b) Two dimension structure of electron temperature



## §14. Production of Ions and Radicals in H<sub>2</sub> ECR Plasma with Controlled Electron Temperature

Muta, H., Thang, D.H., Morino, K. (Interdisciplinary Graduate School of Engineering Sciences, Kyushu Univ.)

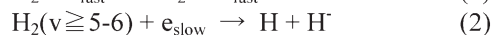
### 1. Introduction

Hydrogen (H<sub>2</sub>) plasma is widely used for scientific and industrial field. For instance, negative ions in H<sub>2</sub> plasma are used as a negative ion source for the NBI heating of fusion plasma. On the other hand, atomic hydrogen in the silane and methane plasma with a large amount of hydrogen dilution plays an important role for the thin film growth of silicon and carbon, respectively. In these applications, there are strong requirements for selective production, spatial profile control of the species in H<sub>2</sub> plasma.

In this paper, we focused on the negative ion H<sup>-</sup> and investigated the high production efficiency via 915 MHz microwave heating. Especially the relationships among the microwave propagation, electron temperature and H<sup>-</sup> production were examined experimentally.

### 2. Experimental

As is well known, the volume production and annihilation of H<sup>-</sup> mainly occur in the following reactions [1].



They indicate that two regions of electron temperature are necessary in the plasma in order to produce H<sup>-</sup> efficiently. In this study, 915 MHz ECR plasma were applied because the electron temperature can be controlled in a wide range. In addition, it is advantageous for long-time operation without filament. Using this system, we investigated the effect of microwave propagation on the electron temperature, continuously, relationship between the distribution of the electron temperature and production efficiency of H<sup>-</sup>. Experimental condition is the gas pressure of 10 mTorr, the microwave with TM<sub>01</sub> mode of 1-2 kW and almost uniform magnetic field of about 300 G. The electron temperature was separately measured as the component of parallel ( $T_{e\parallel}$ ) and perpendicular ( $T_{e\perp}$ ) to the magnetic field using Langmuir probe. Simultaneously, the microwave trace was measured by interferometry. In addition, the production efficiency of H<sup>-</sup> was estimated from the ratio of the electron saturation current to the ion saturation current.

### 3. Experimental results and discussion

Figure 1 and 2 show the axial distributions of the electron temperature and positive ion density, respectively. Then, the microwaves propagated until the ECR region ( $z \approx 350$  mm) and were absorbed completely. As seen in Fig. 1, the electron temperature was about 8-10 eV where the

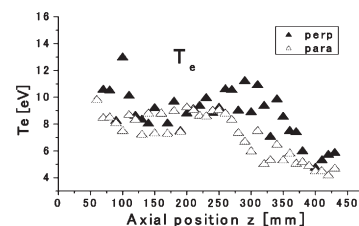


Fig. 1. The axial distribution of the electron temperature.

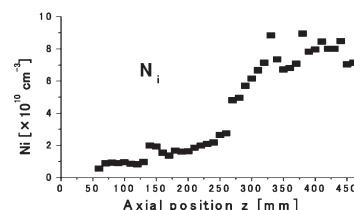


Fig. 2. The axial distribution of the positive ion density.

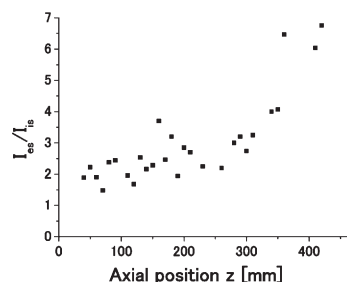


Fig. 3. The axial distribution of the saturation current ratio.

microwaves propagated. After the ECR region, the electron temperature was about 4 eV. Namely, two regions of electron temperature were successfully established. Figure 3 show the axial distribution of ratios of the electron saturation current to the ion saturation current. The ratio in the region of the high electron temperature was about a quarter of that of the low electron temperature. It seems that the negative ions produced much more in the region of the high electron temperature. In general, it is said that the optimal electron temperature for the high efficiency of H<sup>-</sup> production was below 1 eV. This experiment, however, shows the high production of H<sup>-</sup> at considerably high electron temperature. As one of the reasons, it is considered that reaction (1) and (2) were much promoted in comparison with reaction (3). These results should be confirmed using more precise measurement such as laser photo detachment method.

### Reference

1) Fukumasa, O. et. al., Contrib. Plasma Phys. **44**, No. 5-6, 516 – 522 (2004) / DOI 10.1002/ctpp.200410073.

# §15. Plasma-Quenching Efficiency of Molecular Gas Inclusion on Temperature of Ar Induction Thermal Plasmas

Tanaka, Y., Morishita, Y., Uesugi, Y. (Kanazawa Univ.), Ohno, N. (Nagoya Univ.)

In the tokamak fusion devises, the divertor is exposed to high-power density plasma. Thus, it is important to control heat flux from the high power-density plasma onto the divertor plate. Quenching of the high power-density plasma is deeply related with the plasma-quenching efficiency of gases surrounding the divertor plate. On the other hand, plasma-quenching efficiency of high power-density plasma is essential in the arc interruption phenomena in high-voltage circuit breakers, in which an arc formed between the electrodes is quenched by the molecular gas flow and by the ablated gas flow from the polymer nozzle. Thus, it is very important to investigate the quenching efficiency of molecular gases on the high-power density plasma fundamentally.

In our previous work, we used the inductively coupled plasma technique to investigate the plasma-quenching efficiency of various molecular gases for the purpose of finding arc quenching medium in a environmentally-friendly circuit breaker, and found that CO<sub>2</sub> has a high plasma-quenching efficiency compared with other natural environmental-friendly gases such as N<sub>2</sub>, O<sub>2</sub>, Air, Ar and He [1]. In this experiment, the CO<sub>2</sub> inclusion was found to decrease Ar excitation temperature and the diameter of the high-power plasma region.

The present work focuses CO<sub>2</sub> +H<sub>2</sub> and CO<sub>2</sub>+N<sub>2</sub> to see possible enhancement of the plasma-quenching efficiency of gas with additional molecular gas. Furthermore, we study effects of molecular gases on the dynamic behavior of thermal plasmas. For this study, we used pulse-modulated induction thermal plasma (PMITP) system. This system can produce a modulated coil-current sustaining the induction thermal plasma. The modulation of the coil current makes the induction thermal plasma under transient state. The experimental conditions are as follows: Input power to inverter power supply is 15 kW, pressure in the chamber is 230 torr, Ar gas flow rate is 98 L/min, and additional molecular gas flow rate is 2 L/min. Shimmer current level (SCL), which is a ratio of higher current level to lower current level in modulation current, is set to 100 to 50%. The gases CO<sub>2</sub>, H<sub>2</sub>, N<sub>2</sub>, and CO<sub>2</sub>+N<sub>2</sub>, CO<sub>2</sub>+H<sub>2</sub> were selected as additional molecular gases. Spectroscopic observation was carried out to find the transient behavior of the pulse-modulated induction thermal plasma with molecular gases. The measured wavelengths are 703 and 714 nm for Ar I lines and 709 nm for the neighbor continuum. Argon excitation temperature was estimated by the two-line method using the Ar I lines.

Fig. 1(a) shows the pulsing signal, (b) the radiation intensity of Ar I line at 714 nm, (c) and (d) the Ar excitation temperatures. The SCL is 80%. It is seen that the radiation intensity and Ar excitation temperature are modulated according to the modulation of the coil current. The maximum value of the radiation intensity in Ar-CO<sub>2</sub> plasma is lowest among the present gas condition. For Ar excitation temperature, particularly inclusion of CO<sub>2</sub> or

CO<sub>2</sub>+N<sub>2</sub> causes large decay in the minimum value of Ar excitation temperature in decaying process. However, we found in the experiment, Ar+CO<sub>2</sub>+H<sub>2</sub> PMITP cannot be sustained even for higher SCL.

Fig.2 shows the sustaining region of the PMITP with CO<sub>2</sub>, CO<sub>2</sub>+H<sub>2</sub> and CO<sub>2</sub>+N<sub>2</sub> versus duty factor and SCL. Duty factor is defined as a ratio of the time with higher current amplitude to a modulation cycle time. The curves indicate the boundaries between sustain and extinction of the PMITP. The right hand side of the curve indicates the sustaining region of the PMITP. From this figure, Ar+CO<sub>2</sub>+H<sub>2</sub> PMITP has a narrower sustaining region than Ar-CO<sub>2</sub> and Ar-CO<sub>2</sub>+N<sub>2</sub>, which may represent CO<sub>2</sub>+H<sub>2</sub> has a higher plasma-quenching efficiency than the others.

Reference  
[1] Tanaka, Y., Sakuta T., J.Phys.D:Appl.Phys. 35, (2002) 2149

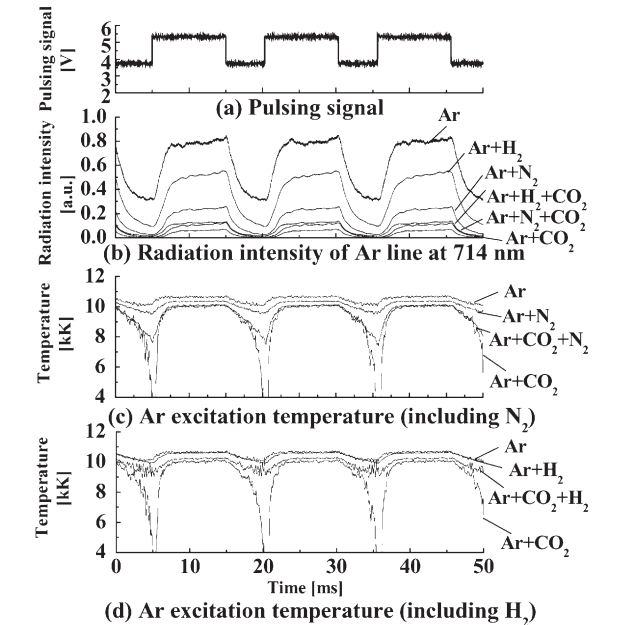


Fig.1 Time evolution of (a) pulsing signal, (b) radiation intensity of Ar line at 714 nm, (c) and (d) Ar excitation temperature.

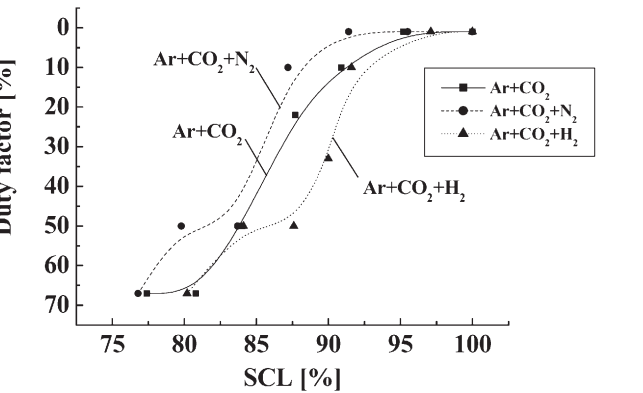


Fig.2 Sustaining region of pulse-modulated induction thermal plasmas with molecular gases.

§16. High Efficiency RF Induction Plasma Generation

Uesugi, Y., Hanaoka, E., Tanaka, Y. (Kanazawa Univ.), Ohno, N. (Nagoya Univ.), Tanaka, M. (Kyushu Univ.)

Radio frequency inductively coupled plasmas(ICPs) at atmospheric pressure have been applied to thermal decomposition of toxic materials, generation of functional nano particles using their high temperature and highly reactive properties. It is very important for industrial applications of high power ICPs to have a high thermal efficiency as well as well controlled plasma properties.

In this study thermal efficiency of high power ICPs at atmospheric pressure range is estimated from equivalent circuit analysis of the induction coil circuit[1] and calorimetric measurements of plasma heat load to the wall. In Fig. 1 an experimental setup for RF input power measurement and calorimetric measurement of the plasma heat load is shown schematically. From the loading impedance measurements of the induction coil it is shown that the conversion efficiency defined by plasma absorbed power( $P_{abs}$ )/RF fed power to the coil( $P_{inv}$ ) is 0.7~0.8 in Ar and Ar+H<sub>2</sub> plasmas at pressure range of 100~760 torr. Taking account that the conversion efficiency of the MOSFET inverter from AC power to 400~450 kHz RF power is about 0.95 total thermal efficiency of RF ICPs at atmospheric pressure range is 0.66~0.76 in the present experiments. This efficiency tends to decrease with gas pressure because the inductive coupling between induction coil and generated plasma becomes weak due to edge cooling of introduced cold gas.

In Fig. 2 plasma heat load to each part of the device obtained from calorimetric measurements is shown when Ar gas flow rate is changed keeping the gas pressure constant. At low Ar gas flow rate ~ 70 slpm about 60 % of the ab-

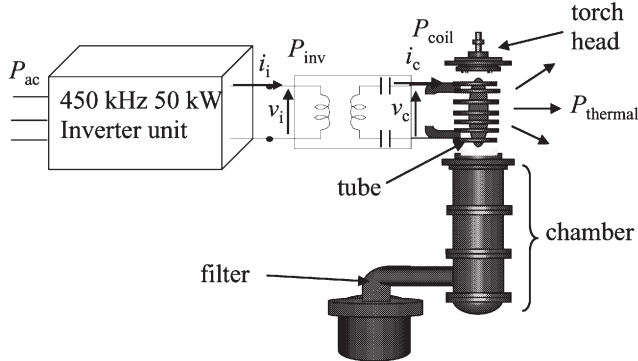


Fig. 1 Experimental setup of RF power and plasma heatload measurements.

sorbed power is delivered to quartz tube surrounding core inductively heated plasma and 35% to metal vacuum chambers in the downstream. When Ar gas flow rate is increased up to 100 slpm, the power flow pattern is drastically changed. Heat delivered to the quartz tube is reduced to ~30 % and that delivered to downstream chamber rises to 60 % as shown in Fig. 2. Cold sheath gas introduced from the top flange effectively cools the edge region of ICPs and reduces the thermal interaction between the edge plasma and tube. Consequently, most of the plasma thermal energy is delivered to the downstream region. These experimental observations agree well with those estimated from the electromagnetic fluid simulation. In Ar and H<sub>2</sub> mixture plasma, however, H<sub>2</sub> gas flow rate has little effects on the power flow pattern although simulations gives significant effects on it. This discrepancy might be related to the radiation losses. Some of the radiation losses is not measured in the present experiments. Now we are trying to measure the radiation losses from core plasmas.

Reference

[1]Uesugi, Y., Ukai, H., et al., IEEJ Trans., FM, 125(2005)749.

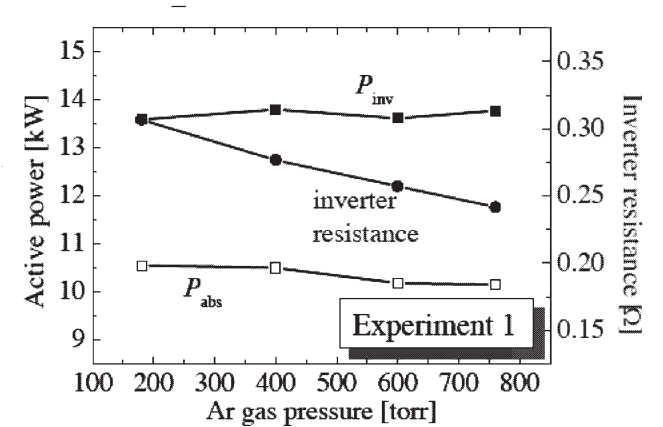


Fig. 2 Gas pressure dependence of the loading impedance of the induction coil including the matching circuit and plasma absorbed power.

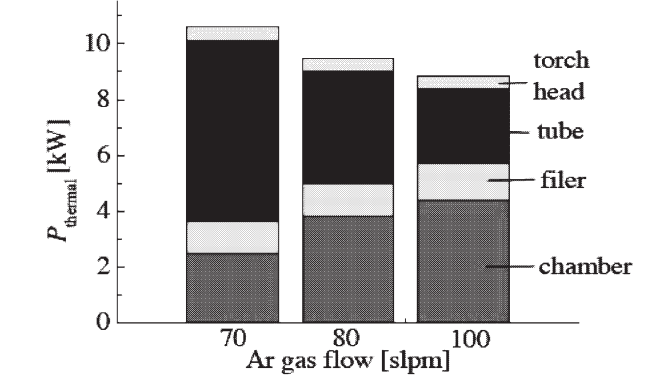


Fig. 3 Change of power flow distribution when Ar gas flow rate is changed. Total gas pressure is kept constant at 230 torr.

## §17. Experimental Study of Current Drive Using Nernst Effect

Kawamori, E. (High Temperature Plasma Center, The Univ. of Tokyo),  
Tokuzawa, T.

Development of current-drive technique is the most urgent issue in low- $q$  compact torus plasmas. A method of plasma current drive in a low- $q$  plasma using the Nernst effect is proposed by Hassam.<sup>[1]</sup> If a plasma has a steep temperature gradient in radial profile, the cross-field thermoelectric force is in the opposite direction to the usual resistive friction, thus maintaining the plasma current. In low- $q$  plasmas such as a Field Reversed Configuration (FRC), however, maintaining the electron temperature profile is difficult because of its high beta property. Electron Cyclotron resonance heating (ECRH) is a very powerful method to heat magnetically confined plasmas. However, the accessible plasma density is limited by a critical density. Electron Bernstein wave is considered as a possibility for overcoming the density limit. Therefore, we plan to employ an EBW in order to increase and maintain the electron temperature of a low- $q$  plasma in the TS-4 device. A 2.45 GHz magnetron with microwave power of 20kW for up to 200  $\mu$ s was installed to TS-4 at the

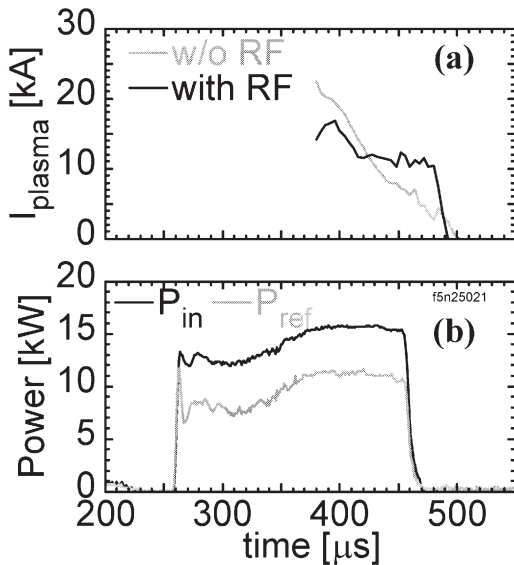


Fig. 1. Waveforms of (a) plasma current  $I_{\text{plasma}}$  of FRCs without and with RF injection, (b) incident ( $P_{\text{in}}$ ) and reflected ( $P_{\text{ref}}$ ) microwave powers in the case of the above shot with RF injection.

University of Tokyo. A launched O-mode (or X-mode) electromagnetic radiation will efficiently couple power to EBWs through a mode conversion process at the upper hybrid resonance UHR.

An electromagnetic wave injection experiment was carried out using O-mode. Electromagnetic wave was injected into FRC plasmas produced by counterhelicity

merging of two spheromaks. Figure 1 shows waveforms of (a) plasma current  $I_{\text{plasma}}$  of FRCs without and with RF injection, (b) incident ( $P_{\text{in}}$ ) and reflected ( $P_{\text{ref}}$ ) microwave powers in the case of the above shot with RF injection. The FRC formation was completed at  $t = 380 \mu$ s. The steady-phase of the plasma current was observed around  $t = 400$ - $480 \mu$ s in the FRC with RF injection while the plasma current of the FRC without RF injection was decreased with time. However, this difference was not clear because discharge conditions for both cases were slightly different. Another problem is the reflection of a large fraction of the launched microwave power under the present experimental condition as shown in Fig.1 (b). Optimization of the RF injection is needed. At the next stage, we are also planning an X-mode injection experiment.

In order to investigate the heating effect by EBW and a principle of the current drive by the Nernst effect, Two-Dimensional (2-D) Thomson scattering system for electron temperature measurement has been designed and constructing [2]. This new approach using multiple reflections and the time-flight of laser light enables us to measure the  $r$  (radial)- $z$  (axial) profiles of electron temperature and density: In this approach, (1) multiple

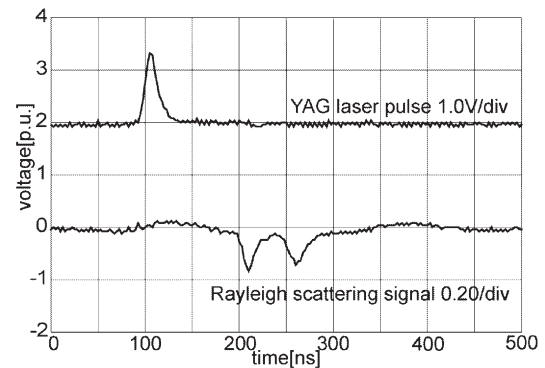


Fig. 2 Rayleigh scattering light from two adjacent measurement points.

reflections of YAG laser light are used to cover the whole  $r$ - $z$  plane of the CT plasma, and (2) the time delay of the scattered light along the laser beam is arbitrarily arranged by adjusting the multiply reflected laser light path in order to reduce the necessary number of detectors.

The two Rayleigh scattering signals were measured by the APD detectors as shown in Fig. 2. These data indicate that four sets of the preliminary results will constitute a new 2-D ( $3 \times 4$  points) measurement of the Rayleigh scattering and probably suggests that the basic principle of the 2-D TS system works reasonably well. We are now planning to perform full 2-D measurement of Thomson scattering light for 2-D Te and ne profiles.

### Reference

- [1]. Hassam, et.al., Phys. Rev. Lett, **83**, (1999) 2969.
- [2]. T. Sumikawa, et.al., Plasma Fusion Res. **1**, (2006) pp. 014-106.



## §18. Particle Reflections of Low Energy Light Ions from a Polycrystalline W Surface

Yamaoka, H. (RIKEN),  
Matsumoto, Y. (Tokushima Bunri Univ.),  
Tanaka, N., Takeuchi, S. (Tohoku Univ.),  
Sugawara, H., Shinto, K., Sasao, M. (Tohoku Univ.),  
Nishiura, M., Tsumori, K.,  
Wada, M. (Doshisha Univ.)

We have been developing an experimental system to study interactions of beams with solid surfaces. The system has successfully produced ion spectra reflected from Mo, carbon coated Mo, and W targets.<sup>1-3)</sup> Here we report the results of the study on particle reflections from a polycrystalline W surface, bombarded by low energy (1-2 keV) hydrogen and oxygen ions. Figure 1 shows examples of the contour plots of energy and angular resolved intensity profiles for H and O ions reflected from a room temperature W surface at an incident angle of  $20^\circ$  for a 2 keV  $H^+$  beam and a 0.8 keV  $O^+$  beam injection. The intensity of the reflected positive ions is higher than that of the negative ions in the case of hydrogen. We obtain similar results for  $H_2^+$  and  $H_3^+$  beam injections. The reflected  $H^-$  ions show an almost elastic scattering, while the  $H^+$  ions are reflected with energies smaller than the incident beam energies. There is no reflection angle dependence on the reflected beam energies for  $H^+$  beam injection. The width of the angular distribution of the reflected beam is of the order of  $10^\circ$  and it widens as the reflection angle increases. The reflected beam has a long tail at the higher reflection angle side. In the case of the  $O^+$  beam injection, the  $O^-$  ion production rate is much higher than the  $O^+$  ion production rate and this was common for the other tested materials such as a polycrystalline Mo and Si 100 crystal. The reflected oxygen ions show a strong dependence in angular distribution against the reflected beam energy. This is very different from the results for the  $H^+$  beam injection. These phenomena are also common for the other target materials. Figure 2 shows the angular distributions of the intensities of the reflected  $H^+$  and  $H^-$  ions for 2 keV  $H^+$  beam injection and those of  $O^+$  and  $O^-$  ions for 0.8 keV  $O^+$  beam injection. The intensity is the integral of the reflected beam energy profile at a given incident ( $\alpha$ ) and reflection ( $\beta$ ) angle. The components of the horizontal and vertical axes mean projections of the intensities to the horizontal and vertical axes. The total intensity is the root of the square of the sum of the horizontal and vertical components. Solid lines correspond mirror reflections. We can observe the mirror reflection in the lower incident angle. But the angle of the reflected ion beam is smaller than the mirror angle as the

incident angle increases.

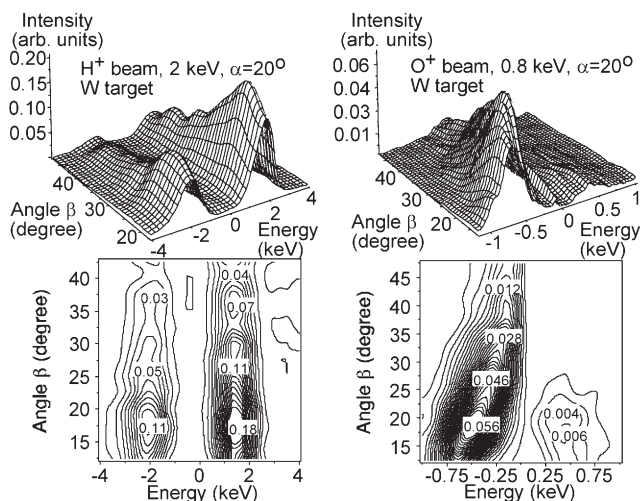


Fig. 1 Contour intensity plots of energy and angular resolved intensity profiles of H and O ions reflected from a W surface at the incident angle of  $20^\circ$  for  $H^+$  beam injection.

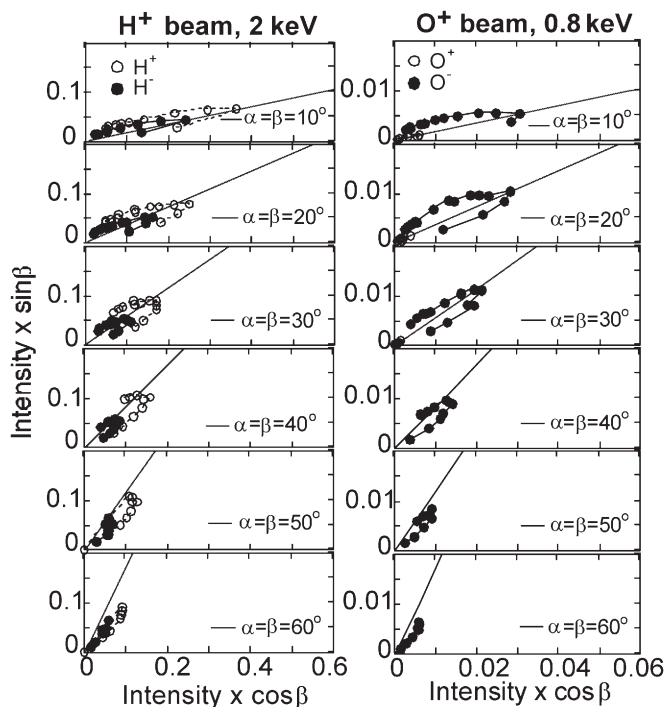


Fig. 2 Angular distributions of reflected  $H^+$  and  $H^-$  ion intensities for 2 keV  $H^+$  beam injection and those for  $O^+$  and  $O^-$  ions for 0.8 keV  $O^+$  beam injection.

### References

- 1) M. Wada, *et al.*, Rev. Sci. Instrum. **73** (2002) 955.
- 2) H. Yamaoka, *et al.*, J. Nucl. Mater. **337-339** (2005) 942.
- 3) H. Yamaoka, *et al.*, Rev. Sci. Instrum. **77** (2006) 03C301.

## §19. Experimental Study of Plasma Loaded Cyclotron Resonance Maser Using TPD-II Machine at NIFS

Minami, K. (Tokyo Denki Univ. Eng.),  
Sato, K.

Traditionally, cyclotron emission has been analyzed under the assumption that beam electrons are tenuous enough to neglect the effects of neutralizing ions. Previous researchers of cyclotron resonance maser (CRM) instability characterized by  $\omega > \tilde{\Omega}$  have followed this model applicable to tenuous beams such as  $\omega_b^2 \ll \tilde{\Omega}^2$ , where  $\omega$ ,  $\tilde{\Omega}$  and  $\omega_b$  are, respectively, radiation angular frequency, relativistic cyclotron frequency and relativistic beam plasma frequency. There can be another extreme model for the electron gyration. Free gyration may be prevented by a restoring force caused by the charge separation between dislocated electrons and localized immobile ions, if  $\omega_b^2 \gg \tilde{\Omega}^2$ . The free gyration model applicable for  $\omega_b^2 \ll \tilde{\Omega}^2$  results in the conventional understanding that the CRM instability is the unique principle of cyclotron emission from the electrons<sup>1)</sup>. On the other hand, the constrained electron model for  $\omega_b^2 \gg \tilde{\Omega}^2$  yields prediction that the Cherenkov instability in the azimuthal direction (CIAD) with  $\omega < \tilde{\Omega}$  can be another principle of cyclotron emission in addition to the CRM instability<sup>2,3)</sup>.

We are trying to detect experimentally CIAD in addition to CRM instability in a beam-plasma system produced by differential pumping of DC discharge plasma source called TPD-II machine<sup>4)</sup>. A TE<sub>011</sub> cylindrical cavity made of SUS with resonant frequency near 3.456 GHz is installed, and the beam plasma with radius 4 mm goes through the two end holes on the axis of the cavity. In front of the cavity, three SUS circular plates with a pin hole that selects electron beam with a particular pitch angle to enter.

In Fig. 1 is shown the microwave circuit including the cavity. Gunn oscillator with oscillation frequency 2-4 GHz and output power 20 mW is FM modulated 0.1 % by a saw tooth signal. An example of the input and output signals detected by loop antennas at the side wall displayed on a digital oscilloscope is shown in Fig. 2. Loaded Q values around 6900 are measured. The critical coupling condition is explored. Beam density and axial magnetic field are changed up to  $10^{13} \text{ cm}^{-3}$  and 1.0 T. Our final goal is to detect change in  $\omega$  of negative absorption from  $\omega > \tilde{\Omega}$  to  $\omega < \tilde{\Omega}$ , with increase in the beam density.

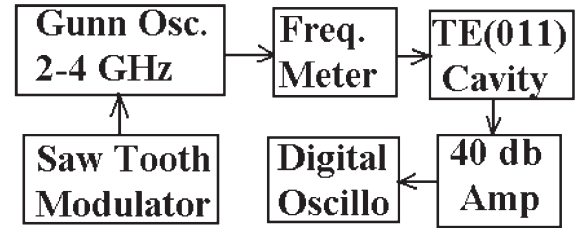


Fig. 1 Fabricated TE<sub>011</sub> mode cavity and circuit.

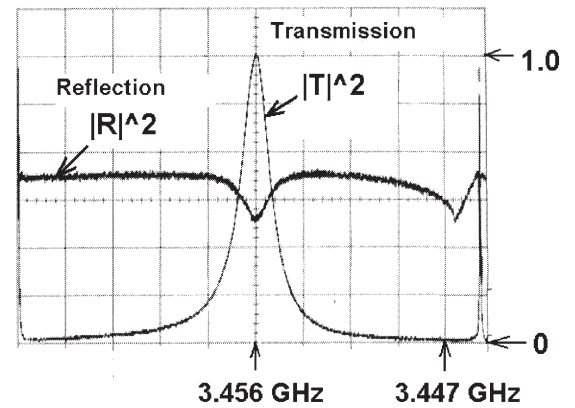


Fig. 2 Resonant curve of the TE<sub>011</sub> mode Cavity.

- 1) J. L. Hirshfield and J. M. Wachtel, *Phys. Rev. Lett.* vol. 12, no. 19, pp. 533-536, May 1964.
- 2) Y. Choyal, T. Watanabe, and K. Minami, *IEEE Trans. Plasma Sci.*, vol. 32, no. 3, pp. 1298-1309, June 2004.
- 3) K. Minami, Y. Choyal and T. Watanabe, *J. Plasma Phys.* 2006 (in press).
- 4) A. Matsubara, T. Watanabe, T. Sugimoto, S. Sudo, and K. Sato, *J. Nucl. Mater.* **337-339**, 181-185.

## §20. Effects of $1/\nu$ Ripple Diffusions on the Parallel Viscosity and Bootstrap Current

Nishimura, S., Sugama, H., Nakamura, Y. (Kyoto Univ.)

In recent studies for advanced helical devices, neoclassical plasma flows such as bootstrap currents due to the viscosity effects are attracting much attention as a new measure for configuration optimization. In many applications of the theory of the flows, a " $1/\nu$  regime" formula derived by Shaing, Carreras, et al.[1,2] in the Boozer coordinates has been often used. This representation was an extension of a previous theory developed in the Hamada coordinates [3]. As stated in Ref.[3], these existing formulas were obtained neglecting effects of  $1/\nu$  component of the perturbation at the ripple trapped pitch-angle range and the trapped/untrapped boundary layer in the phase space. In this sense, we may have to interpret the formulas derived by them rather as the expressions for the collisionless-detraping  $\nu$  regime [4]. Although this problem was already suggested in Ref.[3], the discussion was only qualitative. After our work in Ref.[5] to solve a problem on collisional momentum conservation, it was quantitatively confirmed that the analytical formulas express the viscosity in the collisionless limits of the  $\nu$  regime ( $E_s/\nu \neq 0$ ) [6]. Even if the mono-energetic viscosity coefficients  $N^*$  in the  $1/\nu$  regime can be obtained by using a direct numerical calculation of the linearized drift kinetic equation [5], this kind of numerical calculations cannot be incorporated in large scaled codes utilizing iterative processes. A MHD equilibrium calculation including the "self-consistent" bootstrap currents is an example of the iterative calculation. For this kind of application, a derivation of an analytical expression for the  $1/\nu$  regime ( $E_s/\nu \neq 0$ ) including the boundary layer effect is now the next theme. By combining our formulation and previous analytical theories for the boundary layer [8] and the ripple diffusions[9], we obtained the boundary layer correction  $N^*_{(\text{boundary})}$  in the  $1/\nu$  regime [6],

$$N^*_{(\text{boundary})} = -\frac{12}{\pi^3} \frac{\nu_D^a}{\nu} \frac{\langle B^2 \rangle}{\chi' \psi' f_c} \frac{V'}{4\pi^2} \times \int_0^\pi d\theta_B (2\delta_{\text{eff}})^{1/2} (\pi - 2\sin^{-1}\alpha^*) \theta_B \left( \frac{\partial \varepsilon_T}{\partial \theta_B} - \frac{2}{3} \sqrt{1-\alpha^{*2}} \frac{\partial \varepsilon_H}{\partial \theta_B} \right)$$

Here, we basically adopt the notations in Refs.[5,6], except that  $\delta_{\text{eff}}$  and  $\alpha^*$  are the effective ripple well depth and the effective ripple well length correction, respectively[7], and magnetic field strength is assumed to be  $B=B_0[1+\varepsilon_T(\theta)+\varepsilon_H(\theta)\cos\{L\theta-N\zeta+\gamma(\theta)\}]$  [8]. Figure 1 shows the analytical results given by an inter-regime connection between the  $n$  regime ( $N^*=N^{*(\nu)}$ ) and the  $1/\nu$  regime ( $N^*=N^{*(\nu)}+N^*_{(\text{boundary})}$ ), where  $N^{*(\nu)}$  is given by Refs.[1-3].

Following Refs.[5,6], the magnetic fields assumed here is  $B=B_0[1-\varepsilon_t \cos\theta_B + \varepsilon_h \cos(L\theta_B - N\zeta_B)]$  with  $L=2$ ,  $N=10$ ,  $B_0=1\text{T}$ ,  $\chi'=0.15\text{T}\cdot\text{m}$ ,  $\psi'=0.4\text{T}\cdot\text{m}$ ,  $B_\theta=0$ ,  $B_\zeta=4\text{T}\cdot\text{m}$ ,  $\varepsilon_t=0.1$  and  $\varepsilon_h=0.05$ , respectively. The radial electric field strength is changed in the range of  $1\times 10^{-6}\text{T} \leq E_s/\nu \leq 3\times 10^{-3}\text{T}$ , and the  $N^*$  becomes smaller with increasing the radial electric field strength. In viewpoint of practical applications, this strong radial electric field limit  $N^*=N^{*(\nu)}$  given by the previous analytical theory[1-3] may be appropriate for ions although, the boundary layer correction should be added for electrons with a large thermal velocity ( $E_s/\nu \neq 0$ ).

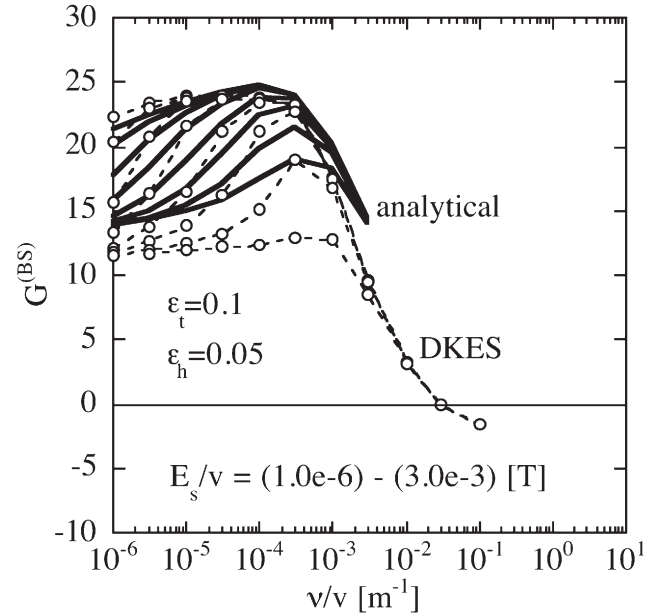


Figure 1 geometrical factor  $G^{(\text{BS})} = -\langle B^2 \rangle N^*/M^*$  defined in Refs.[5,6] as a function of the collisionality parameter  $\nu/\nu$  and the electric field parameter  $E_s/\nu$ . Both of the analytical (solid curve) and the numerical results using the DKES code (open circles) are shown.

### References

- [1] Shaing, K.C., Carreras, B.A., et al., Phys.Fluids **B1**, 1663 (1989)
- [2] Nishimura, S., et al., Ann.Pep of NIFS 2005 p.327, p.328
- [3] Shaing, K.C., et al., Phys.Fluids **29**, 2548 (1986); **B1**, 148 (1989)
- [4] Crume, Jr., E.C., et al, Phys.Fluids **31**, 11 (1988)
- [5] Sugama, H. and Nishimura, S., Phys.Plasmas **9**, 4637 (2002)
- [6] Nishimura, S., et al., to be published in Fusion Science & Technol.
- [7] Shaing, K.C. and Callen, J.D., Phys.Fluids **25**, 1012 (1982)
- [8] Shaing, K.C. and Hokin, S.A., Phys.Fluids **26**, 2136 (1983)

## 5. Theory and Computer Simulation Project

Various computer simulation researches have been pursued in the framework of the simulation science, which include simulations related to magnetic fusion plasma physics, laser fusion plasma physics, space plasma physics, basic plasma physics, physics of molecular dynamics and so on, and also related area supporting computer simulations such as numerical technique, visualization technique, virtual reality technique, and network technique. Some of them are originally initiated by NIFS, and the others are initiated through the NIFS collaboration program. The NIFS collaboration program is important in order to deepen physics understanding and extend the range of the simulation science. With the progress of the computer performance, the simulations based on the reduction to the elements or simulations in the mono-hierarchy are leading to the states that the simulations could explain and interpret the individual experimental phenomena. Thus, as a natural tendency, the paradigm shift is beginning from the simulations based on the reduction to the elements to those based on the integration of elements or simulations interconnecting various space-time scales or hierarchies in order to understand a whole structure of the natural phenomena.

From the realistic aspect, there are two approaches. One is an integrated model-based approach, where a so-called integrated simulation code applicable to the LHD is being developed through comparisons of the simulation results with the LHD experimental data. The other is a hierarchy model-based approach, where simulation models in each space-time hierarchy are intensively developed; then, the simulation models will be extended so as to include various physics and/or effects in adjacent hierarchies. The former activities are reported in the LHD project research collaboration, and the latter activities are reported hereafter.

Simulation codes in various space-time hierarchies are intensively developed from two ways; one way from macro to micro scales, and the other way from micro to macro scales. In the way from macro to micro scales, the properties of equilibria with micro-scale effects such as the Hall term, pressure anisotropy, electron inertia, and wave-particle interaction are being investigated, in order to understand the basis of the extended MHD and consider the closure problems of fluid equations. In order to understand the validity range of the MHD theory, the properties of ideal bal-

looning modes including the second stability and the nonlinear evolution of the interchange modes are investigated by comparing with LHD experimental results.

The interaction between MHD modes and energetic particles is considered to be one of interconnecting phenomena. The instabilities driven by energetic particles become important when Neutral Beam Injection (NBI) is introduced into thermal plasmas or  $\alpha$ -particles are produced by the thermonuclear fusion. The nonlinear properties of Toroidicity-induced shear Alfvén Eigenmode (TAE) modes in LHD are being investigated by using MEGA code extended into helical configurations, from which the important role of the low magnetic shear to drive TAE becomes clear. Nonlinear MHD effects on TAE observed in TFTR are also investigated by using MEGA code, where fully nonlinear effects of both the MHD fluid and energetic particles are contained, leading to the situation more consistent to the experimental results. Such MHD fluid parts are modified by using an extended Ohm's law in the simulations of TAE in ITER, which belongs to the extension into the drift model.

In order to extend the MHD fluid model into multi phases including gas, liquids, and solid phases, a CAP code is being developed in the general torus configurations, which is originally developed in order to investigate the pellet injection into plasmas. This will be applied to the analyses of the Super Dense Core (SDC) plasmas in LHD.

Resistive Wall Modes (RWM) are one of the key issues in ITPA MHD physics. The linear and nonlinear simulations are done in the equilibrium with poloidal rotation in the cylindrical geometry by using reduced-equations, in order to give the scenario to the small current quench observed in JT-60U.

Multi scale nonlinear interactions among micro turbulence, magnetic island, and zonal flows have been performed, where a set of reduced two-fluids equations is used. It is shown that the nonlinear interactions of micro and macro instabilities lead to fast breaking of magnetic surfaces, and then this breaking spreads the micro-turbulence over the plasma.

In order to understand the anomalous transport by toroidal Ion Temperature Gradient (ITG) modes in the helical configurations such as LHD, the gyrokinetic simulation code GKV with high velocity space resolution is extended into the non-axisymmetric toroidal flux tube geometry. By us-



ing the linearized version of GKV, the Geodesic Acoustic Mode (GAM) and the residual zonal flow are investigated. The results are quite consistent to the theoretical analyses.

To study peripheral (edge) plasmas near the separatrix or the last close flux surface, and SOL plasmas including divertor function is one of the key ingredients for understanding the plasma as a whole. As the first step, the plasma-wall interactions are investigated from the aspect of the generation of the conducting dust particles, the effects of Gravity on them, electrostatic potential due to the dust, the rate coefficient of electron impact ionization for electron truncated Maxwellian distribution, and radiation transfer. In order to treat the transport from core (peripheral) region, to SOL, and finally to Divertor, a Core-SOL-Divertor model is proposed based on the JT-60U recycling database, and applied to EAST operation space. A 3D electrostatic Particle-In-Cell (PIC) code has been developed in order to see Blob transport. Based on the stellarator-equivalent tokamak model, LHD plasma edge transport is investigated by using UEDGE code.

A Fast Ignition Interconnected Integrated (FI<sup>3</sup>) code is continuously being developed for transport of relativistic electrons in dense plasma. In FI<sup>3</sup> code, a radiation hydrodynamic simulation with PINOCO code has been combined with a collective PIC simulation with FISCOFI and a Fokker-Planck simulation with FIBMET by using the internet protocol DCCP. Integrated simulation for fast ignition with cone-guided targets has been done.

The dynamical evolution of collisionless driven reconnection, namely formation of non-Maxwellian distribution and its role in collisionless driven reconnection, is investigated by using a newly developed electromagnetic particle simulation code (PASMO) in a microscopic open system surrounded by macroscopic system. In this model the interaction between macro system and micro system is expressed by the plasma inflow and outflow through the system boundary. Improvement of the upstream boundary condition for PASMO has been done, in order to satisfy the frozen-in condition sufficiently. Simultaneously, 3D MHD simulation code with an open boundary is under developed for the macroscopic system on the basis of success under the periodic boundary condition. The mass ratio dependence of Drift Kink Instability (DKI) in the current sheet is investigated by using simulation, through which it is found that DKI is still unstable under the realistic mass ratio. A real-time earth magnetosphere simulator with 3D MHD code has been developed for forecasting space weather. Simulations of interplanetary shock wave caused by Coronal Mass Ejection

(CME) have been done, where Adapted Mesh Refinement (ARM) is used. 3D simulation study of flux rope dynamics in the solar corona has been done, in order to see the condition for the flux rope to be able to escape out of the arcade. Jet formation driven by magnetic bridges between ergosphere and disk around rapidly rotating black hole is examined by using 2D MHD simulation.

The energy transfer in Navier-Stokes and MHD turbulence simulations are performed in order to investigate which scaling appears, Iroshnikov-Kraichnan scaling or Kolmogorov scaling. It is reported that multifractal characters are present in both L- and H- and dithering H-mode data. A signature of wave collapse in the Generalized Nonlinear Schrödinger (GNLS) model of plasma turbulence is also being investigated. On the other hand, low-frequency instabilities due to flow velocity shear are examined by using PIC.

Molecular Dynamics simulations might become one of key simulations for NINS collaborations. Molecular dynamics simulations have been done to clarify, at the molecular level, the mechanisms of the structure formation of a single polymer chain in solution, from which it is shown that there is a prominent orientational correlation in the polymer chain. It is reported that there are three sort of elementary processes in the chemical reaction between the hydrogen atom and the graphene, namely absorption, reflection, and penetration. Moreover, the Nernst effect in the regime of the ballistic conduction is studied.

A complementary fluid method in  $\delta f$  particle simulation is developed, in order to improve the conservation properties of the  $\delta f$  particle simulation for collisionless Boltzmann equation. In multi-scale plasma dynamics, Equation-Free Projective Integration (EFPI) is reported. Orthonormal divergence-free wavelet analysis is used in order to investigate nonlinear interactions in a rolling-up vortex sheet, so that it is shown that the coherent structure is responsible to the energy transfer process, and that the energy transfer occurs locally in the sense of distance.

Construction of seamlessly integrated system between virtual environment and numerical simulation environment is reported. In this system, the researchers do not have to recognize these two computer system, and can perform the computer simulation and analyze the result interactively. A glassless Stereo-type visualization system for 3D MHD real-time earth's magnetosphere simulator has been developed, where the core of the system is the fast 3D-gridding methods simplifying the graphical rendering.

All those researches lead to the development of the simulation science.

(Sudo, S.)

## §1. Axisymmetric Toroidal Equilibrium with Flow in an Extended MHD Model

Ito, A., Nakajima, N., Ramos, J.J. (MIT)

Extended magnetohydrodynamic (MHD) models describe micro-scale effects on MHD and are used for multiscale nonlinear simulation. The micro-scale effects such as the Hall current, electron inertia, pressure anisotropy, and wave-particle interaction alter not only the time dependent phenomena but also the characteristics of equilibrium with flow. The strong flow is observed in the pressure pedestal in tokamaks where pressure has a steep profile and thus small scale effects may be significant. The goal of this study is to understand the effects of the micro-scale phenomena on axisymmetric toroidal MHD equilibrium with strong poloidal and toroidal flow. In MHD, the equilibrium equation can be both elliptic and hyperbolic partial differential equation depending on poloidal flow velocity  $V_p$  and velocities of MHD waves [1]. Since ellipticity and hyperbolicity are determined from the highest order derivative terms, their conditions are sensitive to the micro-scale effects. The equations have to be elliptic to be solved numerically in the same way as the Grad-Shafranov (GS) equation for static equilibria. While only one of the effects was treated in the literature for equilibrium studies [2-4], the Hall current and pressure anisotropy that arises from the kinetic treatment of collisionless magnetized plasma are considered simultaneously in the present study. We extend Hall MHD for the case of pressure anisotropy remaining the exact coincidence with kinetic theory in the linear dispersion relation for  $v_{Te} \gg \omega/|k_{\parallel}| \gg v_{Ti} \approx 0$  [5]. It is achieved by using the following pressure equations found from the fluid moment equations for heat fluxes [6] for mass-less electrons,

$$\mathbf{B} \cdot \nabla(p_{e\parallel}/n) = 0, \quad \mathbf{B} \cdot \nabla[(p_{e\parallel}/p_{e\perp} - 1)B] = 0, \quad (1)$$

instead of the Chew-Goldberger-Low double adiabatic equations. The ion pressures are ignored to neglect the ion finite Larmor radius effects for the finite ion skin depth  $d_i = \sqrt{M/\mu_0 n e^2}$ . The resulting dispersion relation for uniform plasma that has pressure anisotropy is

$$\begin{aligned} & (\omega^2 - k_{\parallel}^2 V_A^2 \tau) \left\{ \omega^4 - \left[ k_{\perp}^2 \left( 1 + \frac{2p_{e\parallel} - p_{e\perp}}{B^2/\mu_0} \frac{p_{e\perp}}{p_{e\parallel}} \right) + k_{\parallel}^2 \left( 1 + \frac{p_{e\perp}}{B^2/\mu_0} \right) \right] \right. \\ & \times V_A^2 \omega^2 + k_{\parallel}^2 C_{s\parallel}^2 (k_{\parallel}^2 \tau + k_{\perp}^2 \kappa) V_A^2 \left. \right\} = k_{\parallel}^2 d_i^2 V_A^2 \omega^2 \tau (k_{\parallel}^2 \tau + k_{\perp}^2 \sigma) \\ & \times [\omega^2 - k^2 C_{s\parallel}^2 (k_{\parallel}^2 \tau + k_{\perp}^2 \kappa) / (k_{\parallel}^2 \tau + k_{\perp}^2 \sigma)], \end{aligned} \quad (2)$$

where

$$\tau \equiv 1 - \frac{p_{e\parallel} - p_{e\perp}}{B^2/\mu_0}, \quad \kappa \equiv 1 + 2 \frac{p_{e\parallel} - p_{e\perp}}{B^2/\mu_0} \frac{p_{e\perp}}{p_{e\parallel}}, \quad \sigma \equiv 1 + \frac{p_{e\parallel} - p_{e\perp}}{B^2/\mu_0} \left( 1 + \frac{p_{e\perp}}{p_{e\parallel}} \right).$$

In the single fluid limit,  $d_i = 0$ , this dispersion relation

yields the condition for mirror stability  $\kappa > 0$  that is consistent with kinetic theory. The equilibrium equations take the form of the coupled GS equations for the ion stream function and the magnetic flux function as in the case of isotropic pressure [4]. While one of the GS equations is always elliptic for the isotropic case, pressure anisotropy makes the ellipticity condition for each equation fully coupled. The condition is identified as the nonexistence of real roots of a fourth-order algebraic equation. We have examined the condition for the following three cases. (i) For the isotropic pressure, the ellipticity condition reduces to the one obtained in Ref. 4:

$$V_p^2 < C_s^2, \quad \text{where } C_s \text{ is the sound velocity. (ii) For the}$$

anisotropic, static equilibrium,  $V_p = 0$ , the condition is

satisfied by the ellipticity condition for the static single fluid equilibrium:  $\tau > 0$  and  $\kappa > 0$ , which are also the stability conditions for the firehose and the mirror instability. (iii) For the anisotropic, flowing equilibrium

with  $V_p = C_{sp}$ , where

$$C_{sp}^2 = C_{s\parallel}^2 (B_p^2 \tau + B_{\phi}^2 \kappa) / (B_p^2 \tau + B_{\phi}^2 \sigma), \quad (3)$$

two of four roots of the algebraic equation are degenerated and the other two are complex. Hence  $C_{sp}$ ,

poloidal component of the sound velocity in the presence of pressure anisotropy found from Eq. (2) in the limit

$d_i \rightarrow \infty$ , could be the criterion for ellipticity.

## References

- [1] Hameiri, E.: Phys. Fluids 26 (1983) 230.
- [2] Iacono, R. et al.: Phys. Fluids B 2 (1990) 1798.
- [3] Yoshida, Z. et al.: Phys. Plasmas 11 (2004) 3660.
- [4] Ishida, A. et al.: Phys. Plasmas 11 (2004) 5297.
- [5] Ito, A. et al.: Phys. Plasmas 11 (2004) 5643.
- [6] Ramos, J. J.: Phys. Plasmas 10 (2003) 3601.

## §2. Properties of Ballooning Modes in the Planar Axis Heliotron Configurations with a Large Shafranov Shift

Nakajima, N., Hudson, R.S. (PPPL), Hegna, C.C. (Wisconsin U.)

The research on the ballooning modes in the planar axis heliotron configurations allowing a large Shafranov shift like LHD are summarized systematically, with particular attention given to the high- $\beta$  MHD equilibria in the inward-shifted LHD configurations. The relation of the quasi-modes to physical modes, the relation between ballooning modes and interchange modes, and also the effects of the boundary condition of the perturbations on the pressure-driven modes are clarified [1].

In the three-dimensional magnetic confinement configurations, the results of local mode analyses of the ballooning modes (quasi-modes) in the covering space along the magnetic field line can not be directly connected to those of the global mode analyses of the ballooning modes in the configuration space (physical modes), because the rule of superposition of the quasi-modes is not allowed because of the lack of symmetry. In other words, the eikonal  $S(\psi, \alpha)$ , where  $\psi$  and  $\alpha$  are the level of the flux surfaces and magnetic field lines, respectively, can not be determined, so that the phase relation of the quasi-modes with same eigenvalue is not established in superposing the quasi-modes. However, in planar axis heliotron configurations with a large Shafranov shift, a qualitative relation has been established that the quasi-ballooning modes in the covering space can be connected to physical ballooning modes in the configuration space. Such a relation comes from the topological structure of the level surfaces of the eigenvalues in the  $(\psi, \theta_k, \alpha)$  space, where  $\psi$ ,  $\theta_k$ , and  $\alpha$  are the label of the flux surfaces, the radial wave number, and the label of the magnetic field line on a flux surface, respectively. In the three-dimensional magnetic configurations, two types of level surfaces exist in the  $(\psi, \theta_k, \alpha)$  space. One is the topologically spheroidal level surfaces, and the other is topologically cylindrical level surfaces. The former's quasi-modes correspond to the three-dimensional ballooning modes inherent to three-dimensional configurations consisting of both relatively high poloidal and

toroidal mode numbers through strong poloidal and toroidal mode coupling. The latter's quasi-modes correspond to the two-dimensional ballooning modes with fairly weak toroidal mode couplings, which are similar to those in the axisymmetric configurations, and to interchange modes. In the Mercier stable MHD equilibria, only three-dimensional ballooning modes inherent to three-dimensional configurations might be excited. In the Mercier unstable MHD equilibria, not only three-dimensional ballooning modes as well as in the Mercier stable equilibria but also two-dimensional ballooning modes and/or interchange modes might be excited. Since the latter has the topologically cylindrical level surfaces of eigenvalues of quasi-modes in the  $(\psi, \theta_k, \alpha)$  space, the approximate quantization condition connecting the quasi-modes in the covering space to physical modes in the configuration space is applicable to them. Note that the quantization condition can be applicable to both two-dimensional ballooning modes and interchange modes. Two-dimensional ballooning modes and interchange modes have smaller growth rates than those of three-dimensional ballooning modes. There are two interesting points. By using the equilibrium profile variation method, it is shown that recently achieved high- $\beta$  MHD equilibria in the inward-shifted LHD configurations stay in the second stable state in the plasma core and stay near the marginally stable state in the plasma periphery. It should be clarified why the plasma core is easy to stay the second stability, and whether the experimentally suggested pressure profiles result from the ballooning instabilities or not.

Another interesting point is whether 3D ballooning modes are systematically distinguished or not. There is a case that the 3D ballooning mode has one radial node ( $N_r = 1$ ). Since 3D ballooning modes consist of the superposition of the 2D-like ballooning modes, if there is a rule in the superposition, then 3D ballooning modes might be systematically distinguished by the radial node numbers  $N_r$  and the behavior of the poloidal localization, for example, the number of the poloidal nodes created by the localization in the flux tubes. This point is associated with the integrability condition of the two degree of freedom Hamiltonian system related to the ray equations of the eikonal.

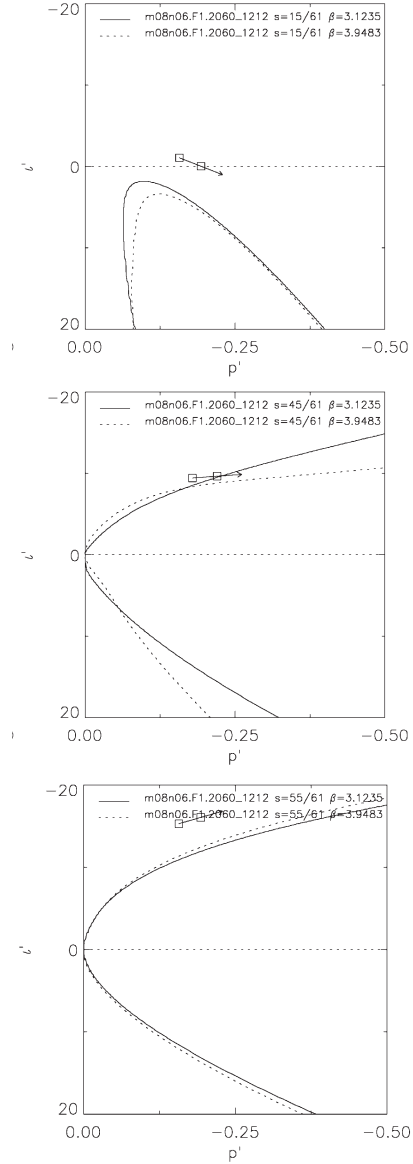
[1] N.NAKAJIMA, S.R.HUDSON, and C.C.HEGNA, Fusion Sci. and Tech. (accepted).

### §3. The 2nd Stability of Ballooning Modes in the Inward-shifted LHD Configurations

Nakajima, N., Hudson, R.S. (PPPL), Hegna, C.C. (Wisconsin U.)

MHD stability analyses of high- $\beta$  equilibria in the inward-shifted LHD configurations are performed [1], by using the currentless free boundary equilibria with pressure profile  $P(s) = P(0)(1 - s)(1 - s^9)$  where  $s$  is the normalized toroidal flux. The conditions for the MHD equilibria, namely the free boundary condition, the currentless condition, and the chosen pressure profile, reflect the experimental observations. The key points are that Mercier criterion is significantly improved by the magnetic well formation and that the dangerous  $\epsilon = 1/2$  rational surface disappears, as  $\beta$  increases. Those improvements are brought by the Shafranov shift of the whole plasma, leading to strong stabilization (self-stabilization) as  $\beta$  increases. In order to examine this situation in detail, the method of the equilibrium profile variations [2,3] has been applied to the MHD equilibria. This method of equilibrium profile variation is a very powerful means to investigate the stability margin of the equilibrium against high-mode-number ballooning modes, and gives the  $d\epsilon/d\psi - dP/d\psi$  stability diagram corresponding to the  $s - \alpha$  diagram in tokamaks. Typical examples are shown in Fig.1, where  $d\epsilon/d\psi - dP/d\psi$  stability diagram in the plasma core (first row), in the plasma periphery (second row), and in the plasma edge (third row) is drawn. The horizontal and vertical axes correspond to  $-s_q$  and  $\alpha$  in the  $s_q - \alpha$  diagram of tokamak plasmas. The solid (dashed) curves indicate the stability boundary of high-mode-number ballooning modes for  $\beta = 3\%$  ( $\beta = 4\%$ ). Two squares attached to the arrow in each graph indicate the positions of  $(\epsilon', P')$  corresponding MHD equilibria at  $\beta = 3\%$  and  $\beta = 4\%$ . The arrows denote the direction of the shift of  $(\epsilon', P')$  corresponding the MHD equilibrium as  $\beta$  increase from  $\beta = 3\%$  to  $\beta = 4\%$ . Judging from the direction of shift of MHD equilibrium according to  $\beta$  value and the relative position of MHD equilibria to the stability boundary, it might be concluded that the core region stays in the second stability state, the

peripheral region stays near the marginally stable state, and the edge region stays in the first stability state. Note that the pressure profiles used here have been experimentally obtained by using the gas puffing, so that the pressure gradient in the plasma periphery, where the high-mode-number ballooning modes are near the marginally stable state, is fairly stronger than that obtained by using pellet injection.



- [1] N. NAKAJIMA, S. R. HUDSON, C. C. HEGNA, and Y. NAKAMURA, Nucl. Fusion **46** 177 (2006).
- [2] C. C. HEGNA and N. NAKAJIMA, Physc. Plasmas **5** 1336 (1998).
- [3] S. R. HUDSON and C. C. Hegna, Physc. Plasmas **10** 4716 (2003).



## §4. Nonlinear Evolution of 3D MHD Instability in LHD

Miura, H., Nakajima, N., Hayashi, T.,<sup>1</sup> Okamoto, M.

We have been carrying out direct numerical simulations of fully three-dimensional, nonlinear MHD in the LHD. An initial condition with the  $\beta_0 = 4\%$  and  $R_{ax} = 3.6m$  has been provided by using the HINT code.<sup>1)</sup> The numbers of grid points are  $97 \times 97$  on a poloidal section and 640 in the toroidal direction. The parallel and perpendicular heat conductivity  $\kappa_{\parallel}$  are typically set to  $1 \times 10^{-3}$  and  $1 \times 10^{-6}$ , respectively. The viscosity and resistivity are  $2 \times 10^{-3}$  and  $1 \times 10^{-6}$ , respectively. The outline of our numerical results is that the parallel kinetic energy is as strong as the perpendicular kinetic energy. The parallel flow is excited as a part of the linear eigen-function.

In order to study the kinetic energy evolution in the view of the linear analysis, the velocity vector  $\mathbf{v}$  is decomposed into the parallel, normal and binormal components as

$$\mathbf{v} = v^b \mathbf{e}_b + v^{\nabla\psi} \mathbf{e}_{\nabla\psi} + v^{\nabla\psi \times b} \mathbf{e}_{\nabla\psi \times b}. \quad (1)$$

where  $\mathbf{e}_i (i = b, \nabla\psi, \nabla\psi \times b)$  are the unit vectors in the three directions. Then the Fourier-transform of the three components in the Boozer-coordinate system provides us the information about the time evolution of each Fourier modes of the three components. Typical observations on the Fourier modes are as follows.<sup>2)</sup>

In Fig.1(a), (b) and (c), time evolutions of the amplitudes of the Fourier modes  $m/n = 1/1$  and  $2/1$  of the normal, parallel and binormal components are shown, respectively, for the two values of  $\kappa_{\parallel}$ . The Fourier amplitudes of these modes grows exponentially because of the linear (pressure-driven) instability. It is observed that the Fourier modes of the three components are smaller in the simulation with the larger parallel heat conductivity  $\kappa_{\parallel} = 1 \times 10^{-3}$  than in the simulation with the smaller one,  $\kappa_{\parallel} = 1 \times 10^{-6}$ . A clear distinction among the three velocity components are found in their behaviors after the nonlinear saturations in the simulation of  $\kappa_{\parallel} = 1 \times 10^{-3}$ . While the Fourier modes of the normal and binormal component of the velocity are scattered away by the nonlinear interactions after the nonlinear saturations, their amplitudes being small, the Fourier modes of the parallel components keeps its amplitude till the end of the simulation ( $t = 1400\tau_A$ , beyond the time range in Fig.). The plasma appears to approach a near-equilibrium state keeping the parallel velocity relatively large, because the parallel velocity does not have direct relations with the interchange instability.

- 1) H. Harafuji, T. Hayashi and T. Sato, J. Comp. Phys., **81** (1989) 169.
- 2) H. Miura, N. Nakajima, T. Hayashi and M. Okamoto, to appear in Fusion Science and Technology.

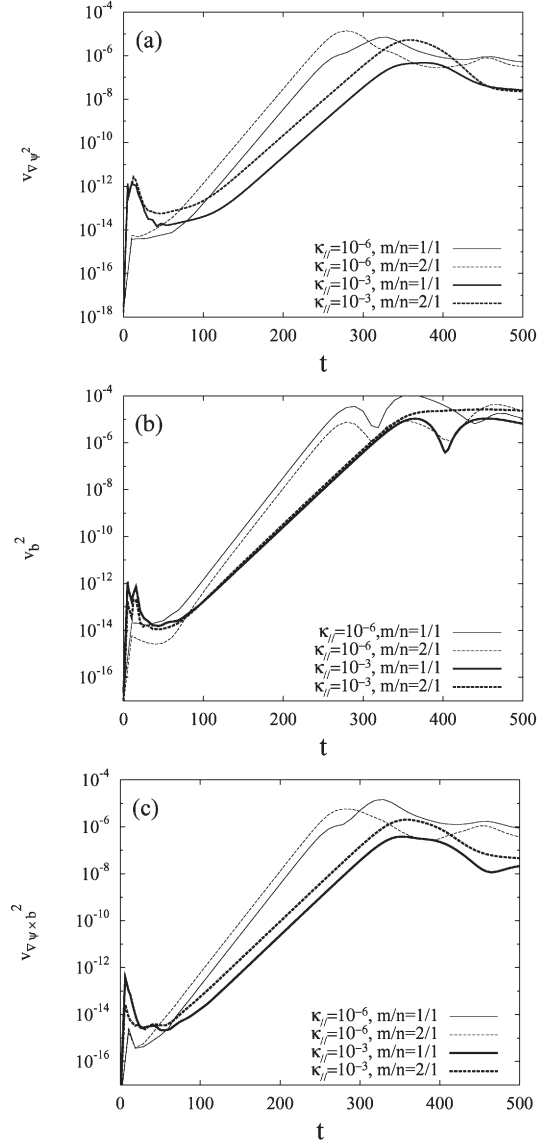


Fig. 1: Time evolutions of the amplitudes of the  $m/n = 1/1$  and  $2/1$  Fourier modes of (a)normal, (b)parallel and (c)binormal components of the velocity.

<sup>1</sup>Deceased April 2006

## §5. MPI Parallelization of MEGA Code for Helical Plasmas

Todo, Y., Nakajima, N.

The simulation code for magnetohydrodynamics (MHD) and energetic particles, MEGA [1], enables self-consistent simulations of the interaction between the MHD fluid and the energetic particles. In the MEGA code, the MHD equations are coupled with the energetic particles through the energetic particle current density perpendicular to the magnetic field  $\mathbf{j}_h$ , which does not contain the  $\mathbf{E} \times \mathbf{B}$  drift current.

$$\begin{aligned}\frac{\partial \rho}{\partial t} &= -\nabla \cdot (\rho \mathbf{v}) \\ \rho \frac{\partial}{\partial t} \mathbf{v} &= -\rho \bar{\omega} \times \mathbf{v} - \rho \nabla \left( \frac{v^2}{2} \right) - \nabla p + (\mathbf{j} - \mathbf{j}_h) \times \mathbf{B} \\ &\quad + \nu \rho \left[ \frac{4}{3} \nabla (\nabla \cdot \mathbf{v}) - \nabla \times \bar{\omega} \right] \\ \frac{\partial \mathbf{B}}{\partial t} &= -\nabla \times \mathbf{E} \\ \frac{\partial p}{\partial t} &= -\nabla \cdot (p \mathbf{v}) - (\gamma - 1) p \nabla \cdot \mathbf{v} \\ &\quad + (\gamma - 1) \left[ \nu \rho \omega^2 + \frac{4}{3} \nu \rho (\nabla \cdot \mathbf{v})^2 + \eta \mathbf{j} \cdot (\mathbf{j} - \mathbf{j}_{eq}) \right] \\ \mathbf{E} &= -\mathbf{v} \times \mathbf{B} + \eta (\mathbf{j} - \mathbf{j}_{eq}) \\ \mathbf{j} &= \frac{1}{\mu_0} \nabla \times \mathbf{B} \\ \bar{\omega} &= \nabla \times \mathbf{v}\end{aligned}$$

The energetic particles are described by the drift-kinetic equations.

The MEGA code has been extended to simulate helical plasmas [2] in the helical coordinate system  $(u^1, u^2, u^3)$  which is used in the MHD equilibrium code, HINT. The relations between the helical coordinates and the cylindrical coordinates  $(R, \varphi, z)$  for LHD are

$$\begin{aligned}h &= -1/2, \\ M &= 10, \\ R &= R_0 + u^1 \cos(hMu^3) + u^2 \sin(hMu^3), \\ z &= -[u^1 \sin(hMu^3) - u^2 \cos(hMu^3)], \\ \varphi &= -u^3.\end{aligned}$$

The numerical methods are the 4th order finite difference for the MHD equations and the 4th order Runge-Kutta method for the time integration. The numbers of grid points are (91, 115, 1000) for  $(u^1, u^2, u^3)$  coordinates. The  $\delta f$  particle simulation method is applied to the energetic ions. The number of marker particles is  $N=4 \times 10^6$ .

The vector calculations are expressed using the metric tensor as follows:

$$\begin{aligned}(\nabla \phi)^i &= g^{ik} \frac{\partial}{\partial x^k} \phi, \\ \nabla \cdot \mathbf{v} &= \frac{1}{\sqrt{g}} \frac{\partial}{\partial x^i} \sqrt{g} v^i, \\ \mathbf{j} \cdot \mathbf{E} &= g_{ik} j^i E^k, \\ (\mathbf{j} \times \mathbf{B})^i &= \sqrt{g} g^{ik} e_{klm} j^l B^m, \\ (\nabla \times \mathbf{B})^i &= \frac{1}{\sqrt{g}} e^{ikl} \frac{\partial}{\partial x^k} g_{lm} B^m.\end{aligned}$$

The MEGA code for helical plasmas has been parallelized using the Message Passing Interface (MPI). The domain decomposition in toroidal direction is employed for both the grid points and the marker particles. The MEGA code was run on the two nodes of the Plasma Simulator of NIFS (NEC SX-7). The MEGA code is accelerated with the three-step “parallelization”, vector process + automatic parallelization inside each node + MPI parallelization between nodes. It was found that 51.1Gflops is achieved using total 16 PE of two nodes (8PE + 8PE). This is comparable to the computation speed with 16 PE in one node, 53.3Gflops. These computation speeds are 36.3% and 37.9% of the peak performance of 16PE on the Plasma Simulator. The computational efficiency is so high that we can conclude the MEGA code is successfully parallelized on SX-7 using MPI. The time evolution of a toroidal Alfvén eigenmode (TAE) in an LHD plasma was investigated with the MEGA code. The toroidal electric field profile of the TAE is shown along with the outermost magnetic surface in Fig. 1.

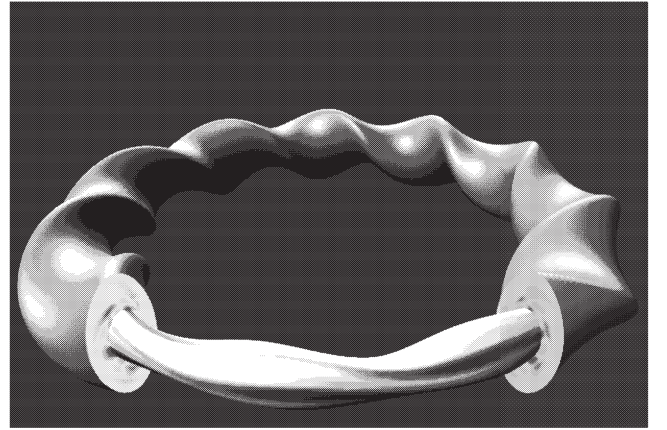


Fig. 1. Toroidal electric field profile of the TAE in the LHD plasma.

### References

- [1] Y. Todo *et al.*, Phys. Plasmas **12**, 012503 (2005).
- [2] Y. Todo *et al.*, in Fusion Energy 2004 (Proc. 20th Int. Conf. Vilamoura, 2004) IAEA, Vienna, TH/3-1Ra.

## §6. Nonlinear MHD Effects on the Alfvén Eigenmode Evolution

Todo, Y.,  
Berk, H.L., Breizman, B.N. (IFS, Univ. Texas at Austin)

For time evolution of Alfvén eigenmodes, an important nonlinearity arises from the dynamics of energetic particles that destabilize the Alfvén eigenmodes. It was demonstrated by computer simulations that the particle trapping cause the saturation of toroidal Alfvén eigenmodes (TAE). This enables reduced simulations of TAE, where spatial profiles and damping rates of TAEs are assumed to be independent of mode amplitude. TAE bursts at a Tokamak Fusion Test Reactor experiment were reproduced by a reduced simulation [1]. Many aspects of the TAE bursts were well reproduced, while only the saturation amplitude was  $\delta B/B \sim 2 \times 10^{-2}$  which is higher than the value  $\delta B/B \sim 10^{-3}$  inferred from the experimental plasma displacement. In another simulation run of TAE bursts, where the MHD nonlinear effects are taken account, the saturation level is lower than  $\delta B/B \sim 10^{-2}$  [2]. These simulation results motivate us to investigate the MHD nonlinear effects.

Two types of hybrid simulations of MHD fluid and energetic particles were carried out to investigate MHD nonlinear effects on Alfvén eigenmode evolution using MEGA code [3] and a linearized version of MEGA code. Fully nonlinear effects of both the MHD fluid and the energetic particles are contained in MEGA code. In the linearized version of MEGA code, the MHD equations are linearized while the nonlinear particle dynamics are followed.

The two types of simulation results were presented and compared [4]. A tokamak plasma, where a toroidal Alfvén eigenmode (TAE) with toroidal mode number  $n=4$  is the most unstable, was investigated. Comparison between the results of the two types of simulations clarified the MHD nonlinear effects. We found that the saturation level is  $\delta B/B \sim 8 \times 10^{-3}$  in the nonlinear MHD simulation results when the saturation level is  $\delta B/B \sim 2 \times 10^{-2}$  in the linear MHD simulation results. The MHD nonlinear effects suppress the saturation level of the TAE. The results shown in Figs. 1 and 2 indicate that the nonlinear suppression effect arises from the change in  $n=0$  harmonics of the magnetic field that is generated by the nonlinear electric field  $-\mathbf{v}_{TAE} \times \delta \mathbf{B}_{TAE}$ , a product of the velocity field and the magnetic field of the TAE. Axisymmetric velocity fields are also generated in the nonlinear run, although the change in the  $n=0$  magnetic field plays the dominant role in the suppression of TAE. The effect of the  $n=0$  harmonics of density variation will be investigated in the near future.

We have demonstrated that the MHD nonlinear effects suppress the TAE saturation level. It was also demonstrated by a computer simulation that the synchronized bursts of multiple TAEs take place with the MHD nonlinearity [2].

Thus, we can expect a simulation which reproduces the TAE bursts with saturation amplitude closer to that inferred from the experimental plasma displacement. On the other hand, energetic ion transport is also suppressed by the MHD nonlinearity. These results indicate that we need to focus on the feedback of the MHD fluid for the saturation level as well as beam ion transport in phase space when we try to simulate the TAE bursts.

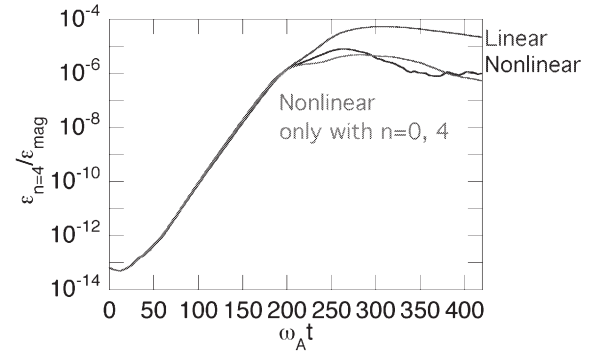


Fig. 1. Comparison of energy evolution of toroidal mode number  $n=4$  between the standard nonlinear MHD run, the linear MHD run, and the nonlinear MHD run where only  $n=0, 4$  modes are retained.

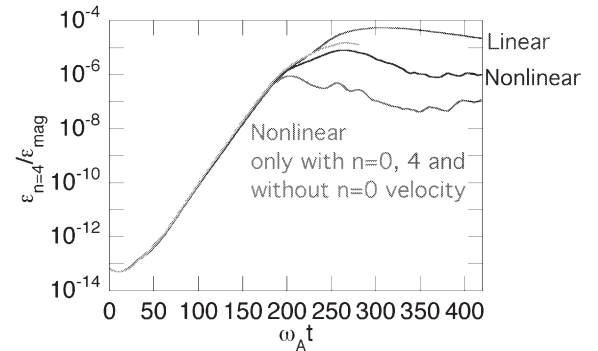


Fig. 2. Comparison of energy evolution of toroidal mode number  $n=4$  between the standard nonlinear MHD run, the linear MHD run, and the nonlinear MHD run where only  $n=0, 4$  modes are retained and the  $n=0$  velocity field is removed. The curve between the linear and the standard nonlinear runs represents a run where only  $n=0, 4$  modes are retained and the  $n=0$  magnetic field is removed.

### References

- [1] Y. Todo, H. L. Berk, and B. N. Breizman, *Phys. Plasmas* **10**, 2888 (2003).
- [2] Y. Todo, T.-H. Watanabe, Hyoung-Bin Park, and T. Sato, *Nuclear Fusion* **41**, 1153 (2001).
- [3] Y. Todo, K. Shinohara, M. Takechi, and M. Ishikawa, *Phys. Plasmas* **12**, 012503 (2005).
- [4] Y. Todo, H. L. Berk, and B. N. Breizman, "Nonlinear MHD Effects on the Alfvén Eigenmode Evolution", in *Proc. 9th IAEA Technical Meeting on Energetic Particles in Magnetic Confinement Systems* (Takayama, 2005) (NIFS-PROC-63, 2006), p. 79.

## §7. Simulations of Alfvén Eigenmodes with an Extended Ohm's Law

Todo, Y.

The drift model [1] is an extension of the magnetohydrodynamics (MHD) with the ion finite Larmor radius effects. The simulation code for MHD and energetic alpha particles, MEGA [2], has been extended with the drift model. In addition to the ion finite Larmor radius effects, the Ohm's law is extended with the effective resistivity where the electron Landau damping is taken account employing the Landau fluid model.

The extended MEGA code [3] is benchmarked with respect to the linear growth rate and the damping rate of the alpha-particle-driven  $n=4$  toroidal Alfvén eigenmode (TAE) in the TFTR D-T plasma shot #103101. The initial energetic particle distribution is similar to that of a previous particle simulation reported in Ref. 4, where an isotropic distribution for the energetic alpha particles is used in the velocity space. The number of marker particles used is  $5.2 \times 10^5$ . The number of grid points is  $101 \times 16 \times 101$  for the cylindrical coordinates ( $R, \phi, z$ ) where  $R$  is the major radius coordinate,  $\phi$  is the toroidal angle coordinate, and  $z$  is the vertical coordinate. The simulation domain in the toroidal angle coordinate is  $0 < \phi < \pi/2$  for this benchmark test of  $n=4$  TAE. First, the linear growth rate was investigated with the effective resistivity turned off. The destabilized mode has a TAE spatial profile which consists of two major harmonics  $m/n=6,7/4$  and frequency 215kHz. These results are consistent with the calculation with the NOVA-K code [5]. The linear growth rate obtained from this simulation, is  $8.7 \times 10^{-3}$  of the mode frequency. This linear growth rate is close to what is observed in the previous particle simulation [4] and calculated in the NOVA-K code [5]. Next, the damping rate was investigated with the alpha particle effects turned off and the effective resistivity turned on in the linear growth phase. The damping rate is  $\gamma_d/\omega = 4.8 \times 10^{-3}$ , while we found  $\gamma_d/\omega = 1.6 \times 10^{-3}$  with the conventional MHD model. The increase in damping rate with the drift model arises from the effective resistivity. The damping rate with the effective resistivity is roughly a half of the NOVA-K code results [5].

We investigated an ITER-like plasma with the extended MEGA code [3]. The plasma profile investigated is based on the non-inductive scenario reported in ITER Technical Basis [6]. The major and minor radii are  $R=6.35\text{m}$  and  $a=1.85\text{m}$ . The ellipticity and the triangularity are 1.85 and 0.4, respectively. The toroidal magnetic field at the plasma center is  $B=5.18\text{T}$ . The number density is assumed to be uniform  $6.7 \times 10^{19}\text{m}^{-3}$ . The safety factor is  $q_0=3.5$  at the plasma center,  $q_{\min}=2.2$  at  $r/a=0.7$ , and  $q_{\text{edge}}=5.3$  at  $r/a=1.0$ . The thermal pressure profile is assumed to be uniform to focus on the instabilities driven by the alpha particles. The beta value of the thermal plasma is  $\beta=2.5\%$ . The electron temperature is  $12.3\text{keV}$ , which is employed in the electron Landau damping model. The birth velocity of the alpha

particle corresponds to  $1.48v_A$ , where  $v_A$  is the Alfvén velocity at the plasma center. The spatial profile of the alpha particle beta value is calculated with the plasma profile of the non-inductive scenario taking account of the D-T reaction rate and the slowing-down of alpha particles. The alpha particle beta value at the plasma center is  $\beta_{\alpha 0}=2 \times 10^{-2}$ .

The nonlinear evolution of toroidal Alfvén eigenmodes (TAE) in the ITER-like plasma was investigated [3]. The number of marker particles used is  $2.1 \times 10^6$ . The number of grid points is  $101 \times 100 \times 101$  for the cylindrical coordinates. The TAEs with toroidal mode numbers  $n=2-5$  are destabilized. The TAEs peak around  $r/a \sim 0.3$ . The toroidal electric field profile of the  $n=3$  TAE is shown in Fig. 1. The saturation levels are  $\delta B_r/B \sim 10^{-3}$ . The redistribution of alpha particles leads to the change in alpha particle beta profile by  $\delta\beta_\alpha \sim 10^{-3}$ .

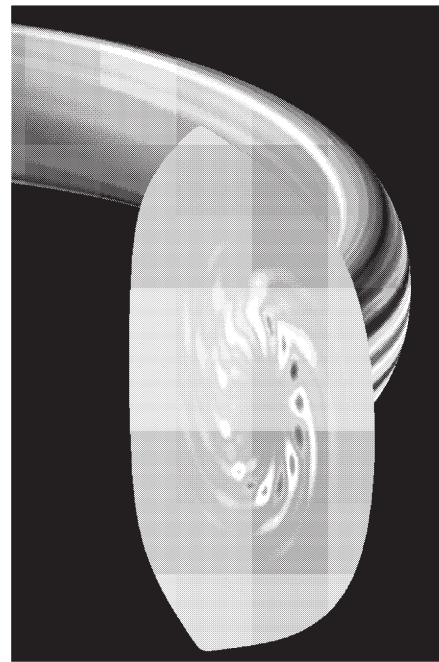


Fig. 1. Toroidal electric field profile of the  $n=3$  TAE in the ITER-like plasma.

### References

- [1] R. D. Hazeltine and J. D. Meiss, "Plasma Confinement" (Addison-Wesley Publishing Company, Redwood City, 1992) p. 222.
- [2] Y. Todo *et al.*, Phys. Plasmas **12**, 012503 (2005).
- [3] Y. Todo, "Simulations of Alfvén eigenmodes with an extended Ohm's law", to appear in Proc. 19th Int. Conf. Numerical Simulation of Plasmas (Nara, 2005), a special issue of J. Plasma Phys.
- [4] Y. Chen *et al.*, Phys. Plasmas **6**, 226 (1999).
- [5] G. Y. Fu *et al.*, Phys. Plasmas **5**, 4284 (1998).
- [6] <http://www.iter.org/reports.htm>



## §8. Motion of Ablation Cloud in Torus Plasmas

Ishizaki, R., Nakajima, N., Okamoto, M.

Motion of an ablation cloud is investigated in tokamak by using ideal MHD equations with ablation processes. The cloud quickly expands along the magnetic field and simultaneously drifts to the lower field side due to a tire tube force and  $1/R$  force. It is found that the acceleration of the cloud increases and subsequently decreases due to the energy deposit from the bulk plasma, and finally, the cloud is stopped due to the poloidal field.

The three dimensional MHD code including the ablation processes has been developed by extending the pellet ablation code (CAP) [1]. The cylindrical coordinate  $(R, \phi, Z)$  is used in the code.  $R$  and  $\phi$  are a major radius and toroidal angle, respectively, and  $R$ - $Z$  plane is a poloidal surface. The boundary is assumed to be a perfect conductor. The Cubic Interpolated Pseudoparticle (CIP) method is used in the code [2].

The MHD simulation has been carried out to clarify drift motion of the plasmoid in a tokamak plasma with  $\beta = 0.01$ ,  $R_0/a_0 = 2$  and  $\gamma = 5/3$ , where  $\beta$  and  $\gamma$  are the plasma beta and ratio of the specific heats.  $a_0$  and  $R_0$  are the minor radius and major radius at the center of the poloidal surface. In an initial condition, the plasmoid is stationary at  $R = R_0$ , and peak values of density and temperature of the plasmoid are 1000 times density and  $1/1000$  times temperature of the bulk plasma at the magnetic axis, respectively. The plasmoid, whose half width is  $0.03R_0$ , encounters the electrons with fixed temperature 2 keV and density  $10^{20} \text{ m}^{-3}$ . Figures 1(a) and (b) show density contours in the equatorial plane at  $t = 1.0\tau_A$  and  $6.0\tau_A$ , respectively. The plasmoid is found to expand in the toroidal direction and simultaneously drifts to the lower field side. Figure 2(a) shows temporal evolution of peak values of the plasmoid pressure and density. The pressure reaches more than 150 times the bulk plasma pressure due to heating. On the other hand, the density decreases because the plasmoid expands along the magnetic field. Since decrease in the density reduces the energy deposit to the plasmoid, the

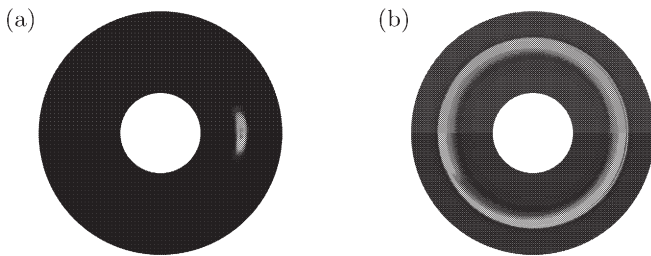


FIG. 1: Density contours in the equatorial plane in the tokamak plasma at (a)  $t = 1.0\tau_A$  and (b)  $t = 6.0\tau_A$ .

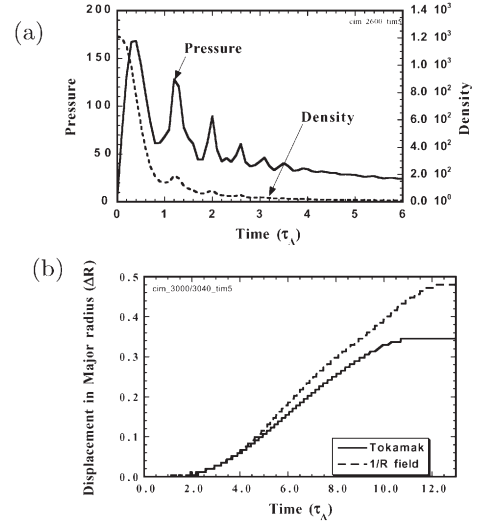


FIG. 2: (a) Peak values of pressure (solid line) and density (dashed line) of the plasmoid vs. time. (b) Displacements of the peak density of the plasmoid in tokamak plasma (solid line) and uniform plasma with the toroidal magnetic field (dashed line) vs. time.

pressure decreases after it reaches a peak value. In addition, the pressure and density have oscillation with a period of about  $1.0\tau_A$  induced by the fast compressional Alfvén wave. The drift motion is considered to be induced by a tire tube force coming from the plasmoid with an extremely large pressure disturbance and by a  $1/R$  force stemming from the toroidal magnetic field with a gradient and curvature. Figure 2(b) shows the temporal evolution of the displacement, of the peak density in the plasmoid from the initial position,  $\Delta R$ . Solid and dashed lines show  $\Delta R$  in the tokamak plasma and in a uniform plasma with the toroidal magnetic field, respectively. Although the plasmoid in the toroidal field can reach near the boundary;  $\Delta R = 0.5$ , one in tokamak plasma is stopped at  $\Delta R = 0.34$  because the poloidal field disturbs the motion of the plasmoid. Since the pressure increases and subsequently decreases as shown in Fig. 2(a), the acceleration also increases and subsequently decreases in both cases. The maximum drift speed in tokamak is about  $0.05v_A$  which is corresponding to  $10^5 \text{ m/s}$  in the parameters;  $B_0 = 1 \text{ T}$ ,  $\rho_0/m_p = 10^{20} \text{ m}^{-3}$  and  $R_0 = 1 \text{ m}$  where  $m_p$  is a proton mass. This value is fairly same order as experimental data [3].

A comprehensive simulation including the creation of the plasmoid with resistivity and atomic processes will be carried out as the future work.

## REFERENCES

- [1] R. Ishizaki et al., Phys. Plasmas **11**, 4064 (2004).
- [2] H. Takewaki et al., J. Comput. Phys. **61**, 261 (1985).
- [3] H. W. Muller et al., Nucl. Fusion **42**, 301 (2002).

## §9. Nonlinear Three Dimensional Simulation of Current-Driven Resistive Wall Mode

Sato, M., Nakajima, N.

In this study, we investigated the effect of nonlinear mode coupling of the RWM and other unstable modes by means of nonlinear three-dimensional simulation for a low beta cylindrical tokamak<sup>1)</sup>. The following reduced magnetohydrodynamic (MHD) equations are solved numerically in the cylindrical coordinates;

$$\begin{aligned}\frac{\partial \psi}{\partial t} &= -\mathbf{B} \cdot \nabla \phi + \eta J - E, \\ \frac{\partial U}{\partial t} &= \mathbf{v} \cdot \nabla U - \mathbf{B} \cdot \nabla J + \nu \nabla_{\perp}^2 U, \\ \frac{\partial T}{\partial t} &= \mathbf{v}_{\perp} \cdot \nabla T, \\ \mu_0 J &= \nabla_{\perp}^2 \psi, \quad U = \nabla_{\perp}^2 \phi,\end{aligned}$$

where  $\psi$  is the poloidal magnetic flux defined by  $\mathbf{B} = -\nabla \psi \times \mathbf{e}_z + B_0 \mathbf{e}_z$ ,  $\phi$  is the stream function defined by  $\mathbf{v}_{\perp} = \nabla \phi \times \mathbf{e}_z$ ,  $T$  is temperature, and Spitzer resistivity is assumed, i.e.,  $\eta \propto T^{-3/2}$ . For treating external MHD modes, a highly resistive plasma is introduced in the vacuum region to use the pseudo-vacuum model. The ratio of the resistivity in the highly resistive plasma  $\eta_v$  to one at the center  $\eta_0$  is chosen as  $\eta_v/\eta_0 = 10^7$ . The magnetic Reynolds number  $S = \tau_a/\tau_r$  is set to be  $S = 10^7$ , where  $\tau_a = R\sqrt{\mu_0 \rho_0}/B_0$ ,  $\tau_r = \mu_0 a^2/\eta_0$ ,  $\rho_0$  is density at  $r = 0$ ,  $R$  is major radius of the plasma and  $a$  is minor radius of the core plasma. It is assumed that a resistive wall and a perfect conducting wall are located at  $r_w = 1.2a$  and  $r_c = 2a$ , respectively.

For studying RWMs with  $(m, n) = (3, 1)$  mode, we use the equilibrium profile as shown in Fig.1. The resistivity profile is assumed to be proportional to  $1/J_{eq}(r)$  for  $r < r_w$ . For the equilibrium as shown in Fig.1, the linear growth rates of the RWM with  $(m, n) = (3, 1)$  and tearing modes with  $(m, n) = (5, 2)$  and  $(2, 1)$  are  $\gamma_{3,1} = 2.3 \times 10^{-3} \tau_a$ ,  $\gamma_{5,2} = 7.8 \times 10^{-3} \tau_a$ , and  $\gamma_{2,1} = 2.1 \times 10^{-4} \tau_a$ , respectively. Figure 2 shows numerical results of magnetic field line plots and a hot plasma region. In the linear phase ( $t = 260 \tau_a$ ), since the linear growth rate of the  $(m, n) = (3, 1)$  mode is largest, the  $(m, n) = (3, 1)$  mode is predominant. At  $t = 340 \tau_a$ , the

energy of the  $(m, n) = (5, 2)$  mode becomes comparable to one of the  $(m, n) = (3, 1)$  mode. Then, the magnetic field lines are stochastic around the plasma surface. The  $(m, n) = (3, 1)$  and  $(5, 2)$  modes are saturated for  $t \geq 380 \tau_a$ . Before the saturation, the  $(m, n) = (2, 1)$  mode rapidly grows by nonlinear mode coupling of  $(m, n) = (3, 1)$  and  $(5, 2)$  modes. However, the  $(m, n) = (2, 1)$  mode still grows after the saturation of  $(m, n) = (3, 1)$  and  $(5, 2)$  modes, and the energy of the  $(m, n) = (2, 1)$  mode becomes larger than one of the  $(m, n) = (3, 1)$  mode. The magnetic surfaces are elongated due to the  $(m, n) = (2, 1)$  mode at  $t = 390 \tau_a$ . In the last phase of the calculation, the stochastic region covers all plasma region.

In JT-60U, small current quench occurs at the plasma edge as a result of destabilization of the current-driven RWM with  $(m, n) = (3, 1)$  mode. After the RWM saturates, thermal quench propagates into the core region with large  $n = 1$  activity<sup>2)</sup>. It seems that our numerical result is one of the possible explanation for the major collapse following the current-driven RWM.

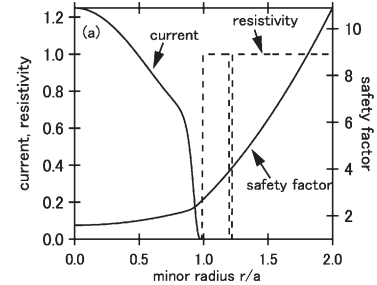


Figure 1: Equilibrium profiles for current, safety factor and resistivity.

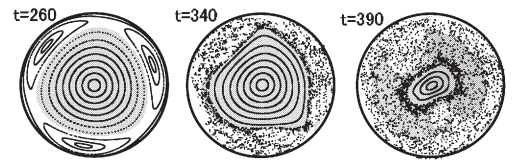


Figure 2: Magnetic field line plots at  $t = 260 \tau_a$ ,  $340 \tau_a$  and  $390 \tau_a$ . The gray region indicates the hot plasma.

### Reference

- 1) M.Sato and N.Nakajima, J. Plasma Phys. (accepted).
- 2) S.Takeji *et al.*, J. Plasma and Fusion Res., **78**, 447 (2001).

## §10. Multi-Scale-Nonlinear Interactions among Micro-Turbulence, Magnetic Islands, and Zonal Flows

Ishizawa, A., Nakajima, N., Okamoto, M., Ramos, J.J. (MIT)

We investigate multi-scale-nonlinear interactions among micro-instabilities, macro-scale tearing instabilities and zonal flows, by solving reduced two-fluid equations numerically. We find that the nonlinear interactions of these instabilities lead to fast breaking of magnetic surfaces then this breaking spreads the micro-turbulence over the plasma. These multi-scale-nonlinear interactions can explain complicated evolution of fluctuation observed in torus plasma experiments because micro-turbulence and MHD instabilities usually appear in the plasma at the same time, in spite of the fact that effects of micro-turbulence and MHD instabilities on plasma confinement have been investigated separately. For instance, MHD activities are observed in reversed shear plasmas with a transport barrier related to zonal flows and micro-turbulence (1), and micro-turbulence is observed in Large Helical Device plasmas that usually exhibit MHD activities (2).

We carry out three-dimensional simulations with a reduced set of two-fluid equations that extends the standard reduced two-fluid equations (3), by including temperature gradient effects. By solving this set of equations, we can describe the nonlinear evolution of tearing modes, interchange modes, ballooning modes and ion temperature gradient modes. We examine the multi-scale-nonlinear interaction among these instabilities in a reversed shear plasma with  $\beta=1\%$ ,  $a/R=0.25$ ,  $L_n=8a$ ,  $LT=a$  and  $q_{min}=2.2$ . In the linear phase, a ballooning structure of toroidal micro-instability appears in the bad curvature and positive shear region, as represented by the electric potential profile in the first frame of Fig.1. A tearing mode is also unstable, but its growth rate is small compared to that of the micro-instability. We start the nonlinear simulation at  $t=0$  by taking the result of the linear calculation as the initial condition.

We have found that the multi-scale nonlinear interaction among micro-turbulence, macro-scale tearing modes and zonal flows leads to fast breaking of magnetic surfaces, then this breaking spreads the micro-turbulence due to the micro-instability over the plasma. The mechanism of these interactions is as follows. The micro-instability induces zonal flows which attempt to suppress the tearing mode. However, the nonlinear-mode-coupling due to the micro-instability overcomes this suppression and accelerates the growth of the tearing mode. This tearing mode breaks the magnetic surfaces, and thus the tearing mode spreads the turbulence over the plasma. These nonlinear interactions can explain the evolution of  $n=1$  fluctuation observed before the disruption of reversed shear tokamak plasmas (1). These multi-scale-nonlinear simulations call to mind the importance of the choice of initial perturbations. To complement the simulation presented here, based on a linear mode initial condition, we will investigate the result

of a turbulent initial perturbation. Besides, the present simulation adopted an initial equilibrium without any flow. The effects of a flow due to a radial electric field in the initial equilibrium on the multi-scale-nonlinear interaction will be investigated as well.

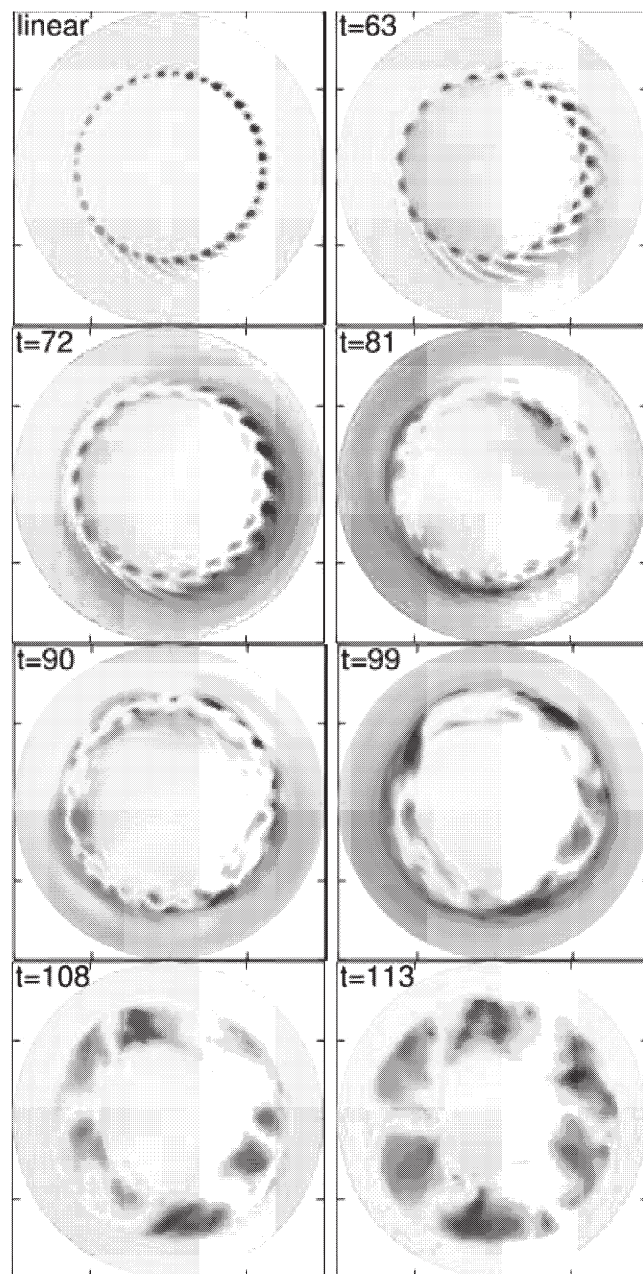


Fig.1. Time evolution of the electric potential on a poloidal section, where the time is normalized by the ion thermal transit time. The micro-instability dominates the linear evolution, then its ballooning structure is deformed by the zonal flow at  $t=72$  and the instability is suppressed by the flow. Next, the  $m=3$  tearing mode arises at  $t=99$ , finally the turbulence due to micro-instability expands over the plasma at  $t=113$ .

### Reference

- 1) S. Takeji, et al., Nuclear Fusion 42, 5 (2002).
- 2) K. Tanaka, et al., Nuclear Fusion 46, 110 (2006).
- 3) R. D. Hazeltine, et al, Phys. Fluids 30, 320 (1987).



## §11. Extension of Gyrokinetic-Vlasov Simulation for Helical Systems

Watanabe, T.-H., Sugama, H.

Gyrokinetic theory and simulation of plasma turbulence in magnetic confinement fusion have advanced physical understandings on the anomalous transport mechanism. Our gyrokinetic-Vlasov simulation code (GKV code) has confirmed the statistically steady state of the toroidal ion temperature gradient (ITG) turbulent transport in terms of detailed calculation of the entropy balance [1]. Recently, zonal flows have attracted many researcher's attention since they are a critical mechanism to suppress plasma turbulence and transport. Damping processes of zonal flows in ITG turbulence in helical systems are analytically investigated by Sugama and Watanabe [2, 3] based on the gyrokinetic theory as a generalization of the work by Rosenbluth and Hinton [4] for tokamaks. It turns out that helical ripples in the equilibrium field cause stronger damping of the geodesic acoustic mode (GAM) than the toroidal magnetic variation does, and that long-time responses of toroidally- and helically-trapped particles play a crucial role in determining the residual zonal flow amplitude. Analytical predictions about geometrical effects on GAM dispersion relation, the residual zonal flows, and the velocity-space structure of the distribution function are also verified by our gyrokinetic simulations which are recently extended to helical systems with keeping very-high resolution of the phase space.

Collisionless dynamics of zonal flows in tokamaks and helical systems are investigated by means of the helical version of the GKV code. A complete response of the zonal flow to given source terms has been analytically derived by taking account of the helical geometry and finite-orbit-width (FOW) effects. Analytical predictions about geometrical effects on the GAM dispersion relation, the residual zonal flows and the velocity-space structure of the distribution function are compared with the GKV simulation results. Results of the GKV simulations of the collisionless zonal flow damping in helical systems show that the initial potential given by the Maxwellian distribution with the poloidal and toroidal mode numbers,  $m = n = 0$ , is damped by the phase mixing and then reaches a finite constant amplitude. The period numbers of the helical field in the poloidal and toroidal directions are  $L = 2$  and  $M = 10$ , respectively. The amplitude of the flux-surface-averaged potential,  $\langle \phi_k(t) \rangle$ , oscillating with the GAM frequency asymptotically approaches the residual level predicted by our theory. The GAM damping rate is enhanced by the FOW effect and the helical ripples, both of which produce lower parallel phase velocity components of the GAM and accordingly a larger population of resonant ions than in the case of tokamaks with no orbit widths. Also, the frequency and the damping rate of the GAM oscillations observed in the GKV simulations are in good agreement with the GAM dispersion relation that is analytically derived from the short-time zonal-flow response kernel. The radial drift motions of particles

trapped in helical ripples yielding neoclassical transport in the weak collisional regime also influence the long-time behavior of the zonal flow.

Velocity-space structures of  $\delta f_{ik}$  with fine stripes along the  $v_{\perp}$ -direction are caused by parallel streaming motions of passing particles. A distinct hollow profile in the helical-ripple-trapped region is also produced by the radial drift motion, and its averaged profile shows a remarkable agreement with our theoretical analysis. Our analysis suggests that a higher-level zonal-flow response than in the tokamak case with the same aspect ratio can be maintained for a long time by reducing the radial drift velocity of the helical-ripple-trapped particles.

The obtained result encourages us to conduct the GKV simulation of turbulence in helical systems for further investigation into the zonal-flow regulation of the anomalous transport. For this purpose, we have first carried out the GKV simulation of the ITG instability. The obtained eigenfunction of the ITG mode in a helical configuration with  $L = 2$  and  $M = 10$  has a typical oscillating profile along the field line with helical ripples (see Fig.1) as predicted by the previous linear eigenmode analysis[5]. The GKV simulations of the ITG turbulent transport in helical systems will be performed in near future.

## References

- [1] T.-H. Watanabe and H. Sugama, Nucl. Fusion **46**, 24 (2006).
- [2] H. Sugama and T.-H. Watanabe, Phys. Rev. Lett. **94**, 115001 (2005).
- [3] H. Sugama and T.-H. Watanabe, Phys. Plasmas **13**, 012501 (2006).
- [4] R. M. Rosenbluth and F. L. Hinton, Phys. Rev. Lett. **80**, 724 (1998).
- [5] T. Kuroda et al., J. Phys. Soc. Jpn. **69**, 2485 (2000).

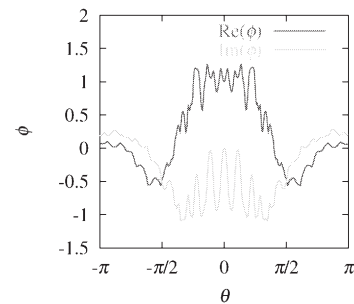


Figure 1: Field-aligned profiles for real (red) and imaginary (green) parts of the eigenfunction of the ITG mode obtained by the GKV simulation for a helical system with  $L = 2$  and  $M = 10$ .



## §12. Releasing of Spherical Conducting Dust Particle from Plasma-Facing Wall under Biased Potential

Smirnov, R. (UCSD),  
Tomita, Y.,  
Takizuka, T. (Naka Fusion Institute, JAEA)

The releasing conditions of a spherical conducting dust particle from a plasma-facing wall under biased potential is analyzed. A Debye sheath is formed near the wall with a strong electric field and a supersonic ion flow toward the wall, which create forces acting on the dust particle attached to the wall. The total force in our consideration includes the repulsive from the wall electrostatic force as well as the attractive drag force due to ion absorption and scattering, and electrostatic image force due to redistribution of charges on the wall. The ion drag force is obtained using the Orbital Motion Limited (OML) theory [1], which gives the absorption cross section of electrons and ions by the dust particle. The electric and the image force on the dust particle depend on the dust charge. The wall surface charge density and the dust radius  $R_d$  determine the charge of the dust particle as following

$$Q_d = -\xi_q \pi R_d^2 \varepsilon_0 E_w, \quad (1)$$

where  $E_w$  is the electric field at the wall surface and  $\xi_q$  is the form factor taking into account the effect of redistribution of the dust surface electric field. For the case of the conducting sphere placed on the wall in uniform external electric field, it was shown [2] that the value of the form factor is  $\xi_q \approx 6.58$ . The dust particle is capable to leave the wall when the total force acting on it is directed from the wall. All the forces are functions of the dust radius and the plasma parameters near the wall. Thus, if the plasma parameters are fixed then the releasing condition can be solved in respect to the dust radius. The solution is

$$R_{c1} = \frac{m_i u_{izw}^2}{\xi_q E_w q_i \ln A_d} \left[ -1 + \sqrt{1 + 4 \ln A_d (\alpha - 1)} \right], \quad (2)$$

where

$$\alpha \equiv \frac{\xi_q (1 - \xi_q / 16) \varepsilon_0 E_w^2}{m_i n_{iw} u_{izw}^2}, \quad (3)$$

$\ln A_d$  is the dust Coulomb logarithm,  $n_{iw}$  and  $u_{iw}$  are the ion density and flow velocity near the wall, respectively. The non-negative solution (2) exists when  $\alpha \geq 1$ . We called  $R_{c1}$  the first critical dust radius. If the dust particle radius  $R_d < R_{c1}$  then the particle will leave the wall, in the opposite case  $R_d \geq R_{c1}$ , the dust particle will be pinned to the wall. The values of the plasma parameters near the biased wall as functions of the sheath potential drop  $\varphi_{sh}$  are obtained using the Bohm sheath model, which assumes vanishing electric field and ion flow velocity equals to the

ion sound speed  $c_{s0} = \sqrt{T_e / m_i}$  at the sheath edge. The dependence of the  $\alpha$  parameter on the sheath potential drop is shown in Fig.1a. As we can see, the condition of the first critical dust radius existence is satisfied, when the sheath potential drop larger than the threshold value  $\varphi_{sh,th}$  corresponding to  $\alpha = 1$ . As shown in the Fig.1b, the first critical dust radius increases from zero at the threshold sheath potential drop to a few Debye lengths for deeper sheath potentials. For the potentials lower than the threshold one no physical solutions for the first critical dust radius exist and the dust particles of any size will be pinned against the wall with the ion drag forces. Thus, the region above the curve in the Fig.1b corresponds to the pinned dust particles, and the region below the curve corresponds to the particles sizes and the sheath potentials when the dust particles can be released from the wall.

The externally applied voltage to the wall allows to control the sheath potential drop. Therefore, the first critical dust radius and the threshold potential are the functions of the externally applied voltage. It shows the possibility to control the size of the released dust particles or even suppress the dust releasing from the wall when the wall potential is below the threshold value.

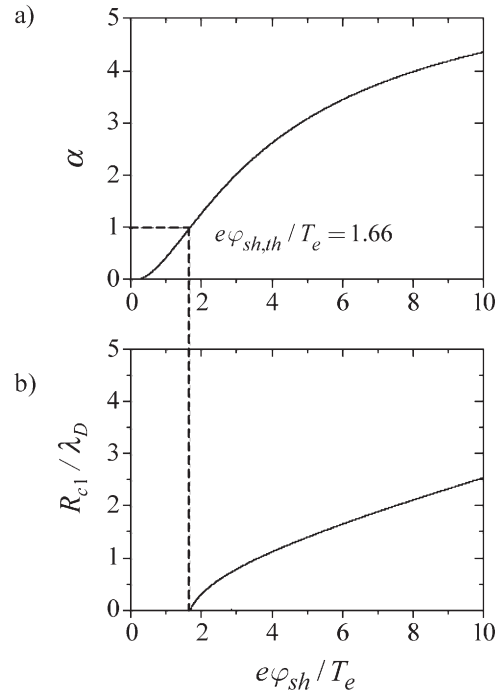


Fig. 1. The dependence of the parameter  $\alpha$  (a) and the first critical dust radius  $R_{c1}$  (b) on the sheath potential drop  $\varphi_{sh}$  in the Bohm sheath model. Here the parameters  $\xi_q = 6.58$  and  $\ln A_d = 3$ .

### Reference

- 1) Allen, J.E., Physica Scripta **45**, (1992) 497
- 2) Lebedev, N.N., and Skalskaya, I.P., Z. Tech. Phys. **32**, (1962) 375 (in russian)

### §13. Effect of Gravity on Releasing of Spherical Conductive Dust Particle from Plasma-Facing Wall

Smirnov, R. (UCSD),  
Tomita, Y.,  
Takizuka, T. (Naka Fusion Institute, JAEA)

The effect of the gravity on the first critical dust radius is clarified. The gravitational force acting on the dust particle can be arbitrary depending on the wall orientation to the horizontal. We consider two limiting cases: the bottom position of the horizontal wall and its upper position. Then the gravitational force acting on the solid spherical dust particle is  $F_g = \pm \frac{4}{3} \pi R_d^3 \rho_d g$ , where  $\rho_d$  is the mass density of the dust particle, and  $g$  is the free fall acceleration. The plus sign means the gravitational force directed toward the wall and the minus sign means from the wall direction. The solutions of the first critical radius accounting the gravitational force was found as

$$R_{c1} = \frac{m_i u_{izw}^2}{\xi_q E_w q_i \ln \Lambda_d} \left[ - (1 \pm \Delta_g) \pm \sqrt{(1 \pm \Delta_g)^2 + 4 \ln \Lambda_d (\alpha - 1)} \right] \quad (1)$$

where

$$\Delta_g = \frac{8}{3\sqrt{2} \xi_q} \left( \frac{1 + 2e\varphi_{sh}/T_e}{\sqrt{1 + 2e\varphi_{sh}/T_e} + e^{-e\varphi_{sh}/T_e} - 2} \right)^{1/2} \delta_g \quad (2)$$

and the dimensionless gravitational parameter  $\delta_g$  is defined as following

$$\delta_g \equiv \frac{\rho_d g \varepsilon_0^{1/2}}{e n_0^{3/2} T_e^{1/2}} \quad (3)$$

Here  $n_0$  is the plasma density and  $T_e$  is the electron temperature. As we can see from (1), the condition for the first critical dust radius existence,  $\alpha \geq 1$ , is not modified. Hence, the gravitational force does not affect the threshold sheath potential drop.

For the positive direction of the gravitational force, the first critical radius and the region of released dust particles decrease with increasing of the gravitational parameter. As shown in the Fig.1, when the gravitational parameter  $\delta_g < 1$  the first critical dust radius is practically unaffected by the gravity and for  $\delta_g > 10$  the first critical radius is inversely proportional to  $\delta_g$ .

In the case of the gravitational force directed from the wall the first critical radius (1) can have two positive solutions depending on the gravitational parameter. In this case, the released dust particles have radii in between the two solutions. In Fig.2a two regions of the released dust particles for the values of the gravitational

parameter  $\delta_g < 2.302$  are shown that are merged when  $\delta_g > 2.302$  (Fig.2c). For the specific value of the gravitational parameter  $\delta_g \approx 2.302$  the regions of released and pinned dust particles can be clearly seen (Fig.2b), where the indicated forces are dominant. Thus, the releasing of dust particles from the wall was described for any gravity conditions and wall potential values allowing to predict and control the size of released particles. The self-consistent effect of dust shielding in plasma will also be considered in future.

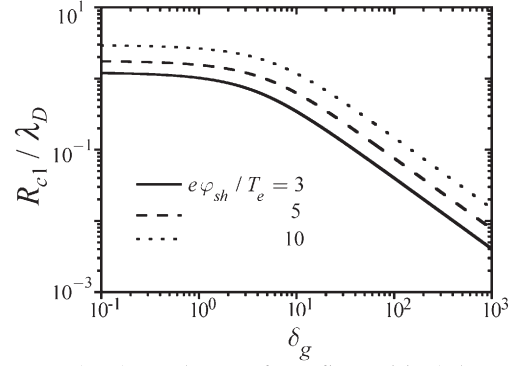


Fig. 1. The dependence of the first critical dust radius on the gravitational parameter  $\delta_g$  for the gravitational force directed toward the wall.

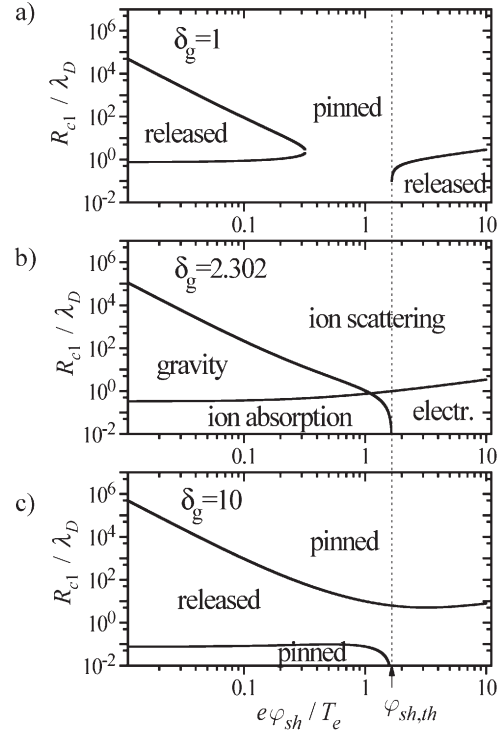


Fig. 2. The first critical dust radius  $R_{c1}$  as a function of the sheath potential drop  $\varphi_{sh}$  for the gravitational force directed from the wall.

## §14. Electrostatic Potential due to Induced Charge of Spherical Dust in Non-Uniform Electric Field

Tomita, Y.,  
Smirnov, R. (UCSD),  
Takizuka, T. (Naka Fusion Institute, JAEA),  
Tskhakaya, D. (Univ. of Innsbruck)

The induced charge on a spherical dust immersed in non-uniform electric field is studied theoretically. The spherical conducting dust with radius  $R_d$  is attached on the infinitely extended conducting plane wall. The potential  $\phi_{in}$  due to the induced charge satisfies the Laplace equation:

$$\left[ \frac{\partial}{\partial \alpha} \left( \frac{\alpha}{\alpha^2 + \beta^2} \frac{\partial}{\partial \alpha} \right) + \frac{\partial}{\partial \beta} \left( \frac{\alpha}{\alpha^2 + \beta^2} \frac{\partial}{\partial \beta} \right) \right] \phi_{in} = 0 \quad (1)$$

in  $(\alpha, \beta)$  space [1], where  $\alpha = R_d r / (r^2 + z^2)$ ,  $\beta = R_d z / (r^2 + z^2)$ , and the origin of the cylindrical coordinates  $r$  and  $z$  is the contact point of the dust on the wall. The plane  $z = 0$ , i.e.  $\beta = 0$ , corresponds to the wall surface and  $\beta = 1/2$  indicates the spherical dust surface, respectively. The external one-dimensional non-uniform electric field without the dust is approximated by the polynomial of the axial coordinate  $z$ :  $\phi_{ex}(z) = \sum_{k=1} h_k z^k$ . After taking into

account the boundary conditions at the dust surface, we can obtain the local electrostatic potentials  $\phi_{ex} + \phi_{in}$  in  $(\alpha, \beta)$  space. The induced charge  $Q_{din}$  is calculated from the electric field to the normal direction  $E_n$  at the dust surface ( $\beta = 1/2$ ):

$$\begin{aligned} Q_{din} &= \int_{S_d} \sigma_s dS = \varepsilon_0 \int_{S_d} E_n|_{\beta=1/2} dS \\ &= -2\pi\varepsilon_0 R_d^2 \int_{\alpha=0}^{\infty} \frac{\alpha}{(\alpha^2 + \beta^2)^2} \frac{\partial}{\partial \beta} (\phi_{ex} + \phi_{in})|_{\beta=1/2} d\alpha, \end{aligned} \quad (2)$$

where  $\sigma_s$  and  $S_d$  are the surface charge density and the dust surface area, respectively. Finally the induced charge  $Q_{din}$  is obtained as a function of the dust radius  $R_d$ :

$$Q_{din} = -2\pi\varepsilon_0 R_d^2 (c_1 h_1 + c_2 h_2 R_d + c_3 h_3 R_d^2 + \dots). \quad (3)$$

Here the coefficients  $c_k$ 's are the numerical constants, which are expressed by the Gamma and Rieman's Zeta functions. The first term of the RHS corresponds to the charge in the uniform electric field.

This result can be applied to the non-uniform potential in the Debye sheath. Our model of the Debye sheath formation is following: 1) Ions are monoenergetic, 2) Electrons have a truncated Maxwellian velocity distribution due to the absorption of high energy component by the wall, 3) The electric field is vanishing at the sheath entrance, and 4) The external electrostatic potential  $\phi_{ex}$  is expressed by the polynomial of degree three, where the coefficients  $h_k$ 's

are determined by the potential drop across the Debye sheath and the sheath width. The induced charge  $Q_{din}$  is shown as a function of the dust radius  $R_d$  in Fig.1 for the relatively shallower potential drop -  $e\phi_w/T_e = 3.5$  and deeper potential drop of 10.0, where the Debye sheath width is  $8.0 \lambda_{Dse}$ , where  $\lambda_{Dse}$  is the electron Debye length at the sheath entrance.

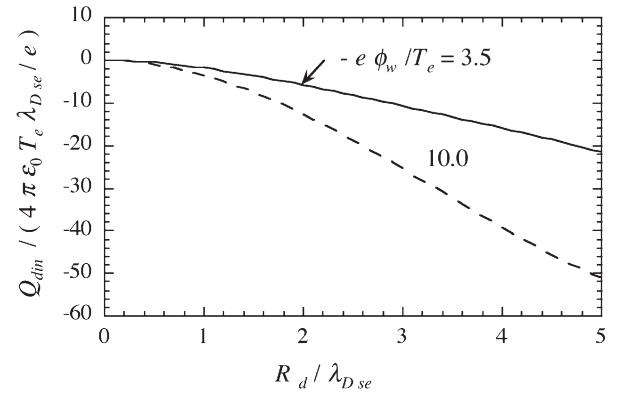


Fig.1 The induced dust charge as a function of the dust radius  $R_d$  for the cases of the potential drop -  $e\phi_w/T_e = 3.5$  and 10.0, where the Debye sheath width is  $8.0 \lambda_{Dse}$ .

The stronger electric field at the wall, which is made by the deeper wall potential, generates the higher induced charge. In case of the smaller dust than the Debye sheath width, the total charge approaches to the induced charge due to the non-uniform electric field, because the effect of plasma shielding is smaller than the effect of the induced electric field. These results can be compared to the results from the particle computer simulation [2], where the total charge includes both of effects, induced charge and plasma shielding. This theoretical analysis is important to understand the dust behavior in the boundary plasma [3].

### References

- 1) Levedev, N.N. and Skai'skaya, I.P., Z.Tech. Phys. **32** (1962) 375.
- 2) Smirnov, R., Tomita, Y., Takizuka, T. and Tskhakaya, D. to be appeared in Contr. Plasma Phys.
- 3) Krashenninnikov, S., Y. Tomita, Y., Smirnov, R., and Janev, R., Phys. Plasma, **11** (2004) 3141.

# §15. Rate Coefficient of Electron Impact Ionization for Electron Truncated Maxwellian Distribution – Single Electron Temperature –

Tomita, Y.,  
Smirnov, R. (UCSD),  
Takizuka, T. (Naka Fusion Institute, JAEA),  
Hatayama, A. (Keio Univ.),  
Matsuura, H. (Osaka Prefecture Univ.),  
Ohno, N. (Nagoya Univ.)

Around a floating wall, which is negatively charged because of lighter electrons, electrons with higher energy than a wall potential are absorbed to a target plate. Electron impact ionization for the electron truncated Maxwellian distribution was studied according to the Lotz formula [1]. A floating potential of a target wall  $\phi_f$  immersed in plasma is determined by the condition of the equal particle flux of ions and electrons,

$$e\phi_f / T_e = 0.5 \ln(2\pi m_e / Z_i m_i), \quad (1)$$

where  $e$ ,  $m_e$ ,  $m_i$ , and  $T_e$  is the unsigned charge on an electron, the electron mass, the ion mass, and the electron temperature at the sheath entrance, respectively. Here the low ion temperature is neglected compared to the electron one. The electrons with higher energy overcome this potential and are absorbed to the wall. On the other hand the slower electrons are repelled by this negative potential. These effects make the truncation of electron velocity distribution to the direction from the wall. The normalized truncated Maxwellian electron distribution function is expressed as:

$$f_e(\vec{v}) = \frac{2}{1 + \operatorname{erf}(\sqrt{\varepsilon_c} / T_e)} \left( \frac{m_e}{2\pi T_e} \right)^{3/2} \exp\left(-\frac{m_e}{2T_e} v^2\right), \quad (2)$$

where  $\operatorname{erf}$  is the error function.

The rate coefficient of electron impact ionization due to the truncated electron velocity distribution is calculated according to the Lotz formula [1]. The empirical formula of a cross-section is:

$$\sigma_{iz}^{LZ}(|\vec{v}|) = \sum_j a_j \zeta_j \frac{\ln(\varepsilon / \chi_j)}{\chi_j \varepsilon} \{1 - b_j \exp[-c_j(\varepsilon / \chi_j - 1)]\}, \quad (3)$$

where  $\varepsilon$ ,  $\chi_j$ , and  $\zeta_j$  are the energy of an impact electron, the binding energy of electrons in the  $j$ -th shell, the number of equivalent electrons in the  $j$ -th shell, and  $a_j$ ,  $b_j$ , and  $c_j$  denote the individual constants which have to be determined by a reasonable guess. This formula has good agreements with the experimental data.

In the case the truncated energy is larger than the binding energy of electrons in the  $j$ -th shell,

$\varepsilon_c = -e\phi_f \geq \chi_j$ , the rate coefficient is expressed as follows:

$$\langle \sigma v \rangle_{ic} = \sqrt{\frac{8}{\pi m_e}} \frac{2}{1 + \operatorname{erf}(\sqrt{\varepsilon_c} / T_e)} \frac{1}{T_e^{3/2}}$$

$$\begin{aligned} & \sum_j a_j \zeta_j \left\{ -\frac{T_e}{\chi_j} E_i\left(-\frac{\chi_j}{T_e}\right) + \frac{b_j \exp(-c_j)}{\chi_j / T_e + c_j} E_i[-(\chi_j / T_e + c_j)] \right. \\ & + \frac{T_e}{2\chi_j} E_i\left(-\frac{\varepsilon_c}{T_e}\right) - \frac{b_j \exp(-c_j)}{2(\chi_j / T_e + c_j)} E_i\left[-\frac{\varepsilon_c}{\chi_j} (\chi_j / T_e + c_j)\right] \\ & + \frac{1}{2} \sqrt{\frac{\varepsilon_c T_e}{\chi_j}} G\left(\frac{T_e}{\chi_j}, \frac{\varepsilon_c}{T_e}\right) - \frac{T_e \exp(-\frac{\varepsilon_c}{T_e}) \ln(\frac{\varepsilon_c}{\chi_j})}{2\chi_j} \\ & - \frac{b_j \exp(-c_j)}{2} \sqrt{\frac{\varepsilon_c}{\chi_j}} \frac{1}{\sqrt{\frac{\chi_j}{T_e} + c_j}} G\left[\frac{\chi_j}{T_e} + c_j, \frac{\varepsilon_c}{\chi_j} \left(\frac{\chi_j}{T_e} + c_j\right)\right] \\ & \left. - \frac{1}{\chi_j / T_e + c_j} \exp\left[-\frac{\varepsilon_c}{\chi_j} (\chi_j / T_e + c_j)\right] \ln\left(\frac{\varepsilon_c}{\chi_j}\right) \right\} \end{aligned} \quad (4)$$

where  $E_i$  is the exponential function and the function of  $G$  is defined as:

$$G(a, b) = \int_b^\infty dt \exp(-t) \ln(at) / \sqrt{t}. \quad (5)$$

On the other hand the truncated energy is lower than the binding energy of electrons in the  $j$ -th shell,

$\varepsilon_c = -e\phi_f < \chi_j$ , the rate coefficient is obtained as:

$$\begin{aligned} \langle \sigma v \rangle_{ic} &= \sqrt{\frac{8}{\pi m_e}} \frac{2}{1 + \operatorname{erf}(\sqrt{\varepsilon_c} / T_e)} \frac{1}{T_e^{3/2}} \\ & \sum_j a_j \zeta_j \left\{ -\frac{T_e}{\chi_j} E_i\left(-\frac{\chi_j}{T_e}\right) + \frac{b_j \exp(-c_j)}{\chi_j / T_e + c_j} E_i[-(\chi_j / T_e + c_j)] \right. \\ & + \sqrt{\frac{\varepsilon_c T_e}{\chi_j}} G\left(\frac{T_e}{\chi_j}, \frac{\varepsilon_c}{T_e}\right) - \frac{b_j \exp(-c_j)}{\sqrt{\frac{\chi_j}{T_e} + c_j}} G\left[\frac{1}{\frac{\chi_j}{T_e} + c_j}, \frac{\varepsilon_c}{\chi_j} \left(\frac{\chi_j}{T_e} + c_j\right)\right] \left. \right\} \end{aligned} \quad (6)$$

In case of the higher electron temperature, the difference is quite small; e.g. for  $T_e = 10$  eV the ratios are 0.97, 0.93, and 0.99 for hydrogen, helium, and argon plasma, respectively. On the other hand at the lower electron temperature the difference are appreciable, e.g. for  $T_e = 1$  eV these ratios are reduced to 0.72, 0.68, and 0.76, respectively. In the detached plasma condition at the divertor wall, where the plasma temperature is as low as few eV, this effect might be important to investigate the interaction between plasma and neutrals.

## References

1) Lotz, W., Zeitschrift Phys. **216** (1968) 241.



## §16. Rate Coefficient of Electron Impact Ionization for Electron Truncated Maxwellian Distribution – Double Electron Temperature –

Tomita, Y.,  
Smirnov, R. (UCSD),  
Takizuka, T. (Naka Fusion Institute, JAEA),  
Hatayama, A. (Keio Univ.),  
Matsuura, H. (Osaka Prefecture Univ.),  
Ohno, N. (Nagoya Univ.)

The rate coefficient of electron impact ionization for the case of plasma with higher-energy component is considered. The normalized velocity distribution function is expressed as:

$$f_e(\vec{v}) = n_e \left\{ \left(1 - \frac{n_{eh}}{n_e}\right) \frac{2}{1 + \operatorname{erf}\left(\sqrt{\frac{\varepsilon_c}{T_{el}}}\right)} \left(\frac{m_e}{2\pi T_{el}}\right)^{3/2} \exp\left(-\frac{m_e}{2T_{el}} v^2\right) + \frac{n_{eh}}{n_e} \frac{2}{1 + \operatorname{erf}\left(\sqrt{\varepsilon_c / T_{eh}}\right)} \left(\frac{m_e}{2\pi T_{eh}}\right)^{3/2} \exp\left(-\frac{m_e}{2T_{eh}} v^2\right) \right\}. \quad (1)$$

Here subscripts  $h$  and  $l$  denote the higher- and lower-energy components, respectively. The quantity  $n_e$  is the total electron density and  $\varepsilon_c$  is the truncated energy of electrons. In this case the floating wall potential  $\phi_f$  is given:

$$e\phi_f / T_e = \frac{\xi_{e1}}{2} \ln(2\pi m_e / Z_i m_i \xi_{e2}^2 \xi_{e3}) \quad (2)$$

Here the parameters  $\xi_{e1}$ ,  $\xi_{e2}$ , and  $\xi_{e3}$  are defined by the densities and temperatures of the higher- and lower-energy components:

$$\xi_{e1} \equiv 1 - \frac{n_{eh}}{n_e} + \frac{n_{eh}}{n_e} \frac{T_{eh}}{T_{el}}, \quad (3-1)$$

$$\xi_{e2} \equiv 1 - \frac{n_{eh}}{n_e} + \frac{n_{eh}}{n_e} \sqrt{\frac{T_{eh}}{T_{el}}}, \quad (3-2)$$

$$\xi_{e3} \equiv 1 - \frac{n_{eh}}{n_e} + \frac{n_{eh}}{n_e} \frac{T_{el}}{T_{eh}} \quad (3-3)$$

Here one can see the higher-energy component makes deepen the wall potential.

The effects of truncation of electron velocity distribution due to the floating wall potential is calculated. Fig.1 shows the ratio of the rate coefficient due to the truncation to the Maxwellian distribution for the hydrogen plasma; (a)  $T_{el} = 1.0$  eV,  $T_{eh} = 2.0$  eV and (b)  $T_{el} = 1.0$  eV,  $T_{eh} = 10.0$  eV. In Fig.3 the rate coefficients are shown for the case of helium plasma, respectively. In case of the higher temperature of high-energy component in hydrogen plasma, small amount of higher component changes appreciably the rate coefficient, Fig.2. On the other hand the effect of higher component in helium plasma is quite small, Fig.3.

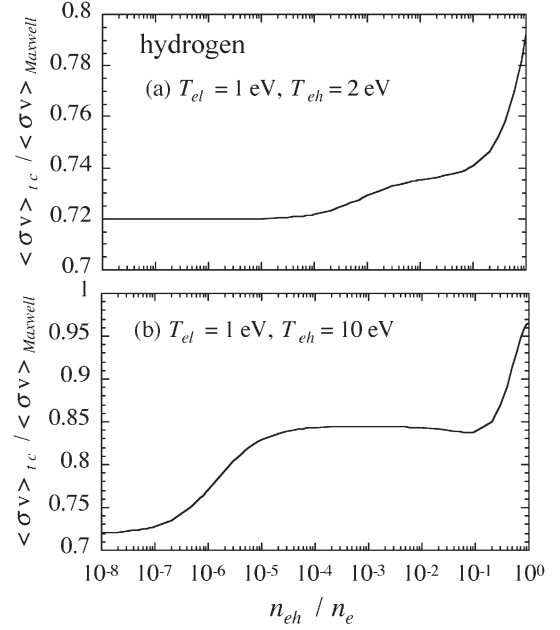


Fig. 1 Ratios of the rate coefficient of the truncated velocity distribution to the Maxwellian distribution for hydrogen plasma as a function of density fraction of the high-energy component: (a) )  $T_{el} = 1$  eV, )  $T_{eh} = 2$  eV and (b) )  $T_{el} = 1$  eV, )  $T_{eh} = 10$  eV.

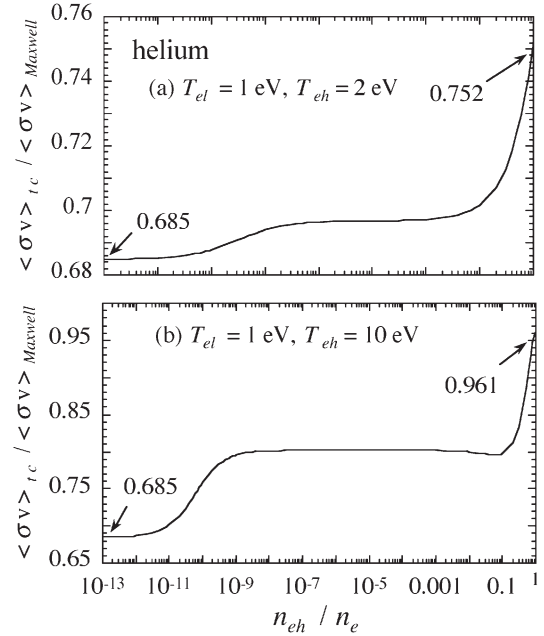


Fig. 2 Ratios of the rate coefficient of the truncated velocity distribution to the Maxwellian distribution for helium plasma as a function of density fraction of the high-energy component: (a) )  $T_{el} = 1$  eV, )  $T_{eh} = 2$  eV and (b) )  $T_{el} = 1$  eV, )  $T_{eh} = 10$  eV.

## §17. Core-SOL-Divertor Model Based on JT-60U Recycling Database and Application to EAST Operation Space

Hiwatari, R. (CRIEPI), Hatayama, A. (Keio Univ.), Takizuka, T. (JAEA), Zhu, S. (ASIPP), Tomita, Y.

The transport models applied to Core-SOL-Divertor (C-S-D) model are a 0D core plasma model based on ITER physics guidelines and a usual two-point model for SOL-divertor region. The key issue of this C-S-D model is how to combine the two-point model with the 0D core plasma model. In the C-S-D model, the particle balance for SOL-divertor region including the neutral transport is solved to evaluate the upstream SOL density  $n_s$ . The detail of C-S-D model was shown in the previous report<sup>1)</sup>. We assume that all neutral particles originate at the divertor plate at the rate proportional to the total particle flux to the divertor plate. Consequently, total neutral source rate at the edge region is as follows:

$$N_n = C_n \frac{1}{2} \left( 1 - \frac{1}{e^2} \right) n_d M_d C_s 2\pi R \Delta_n \sin(\psi) + N_{\text{puff}} \quad (1)$$

where  $\Delta_n$  is the density decay length and  $\psi$  is the angle of the magnetic field to the divertor plate. The coefficient  $C_n$  is a calibration factor.

To calibrate the factor  $C_n$ , the JT-60U divertor recycling database<sup>2)</sup> was utilized. The total ion flux on the plate and the total neutral flux from the divertor region are the key parameters in this simple neutral model, and their values were compared between the C-S-D model ( $P_{\text{NBI}}=0.5\sim 4.0\text{MW}$ ,  $B_t=4\text{T}$ ) and database ( $P_{\text{NBI}}=1\sim 12\text{MW}$ ,  $B_t=2\sim 4\text{T}$ ). The result from C-S-D model with  $C_n=1$  is quantitatively consistent with database, and it also reproduces the nonlinearity of total ion flux against the plasma density (Fig.1). It was found that  $C_n=0.5$  is preferable for a better agreement with the database. The

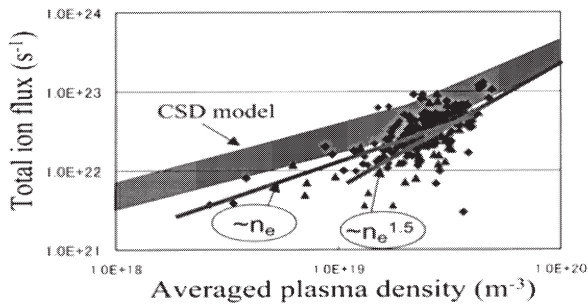


Fig.1 Total ion flux to divertor plates: C-S-D model (shaded region) and JT-60U recycling database<sup>2)</sup> (dots).

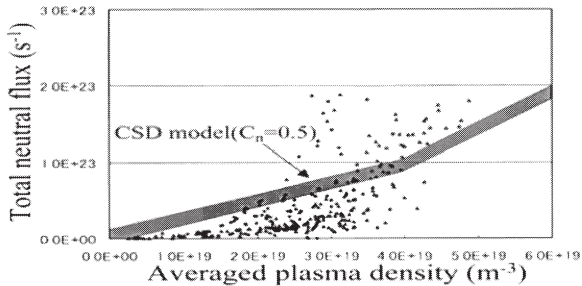


Fig. 2 Total neutral flux from divertor region.

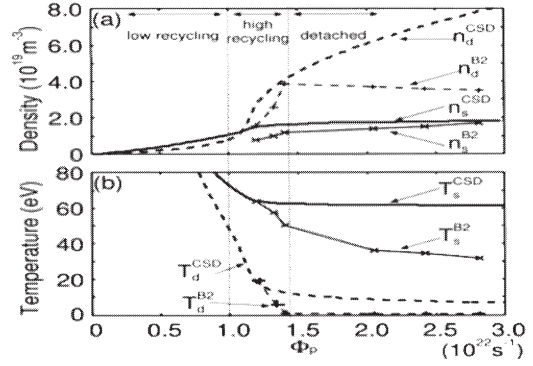


Fig.3 SOL-divertor parameters, (a) density and (b) temperature, v.s. particle flux from core plasma  $\Phi_p$ , obtained by the C-S-D model and the B2-EIRENE.

comparison of the total neutral flux is shown in Fig. 2, where  $C_n=0.5$  is chosen. Comparison with B2-EIRENE was carried out on the JT-60U plasma configuration (Fig.3), and it is shown that the calibration with the database ( $C_n=0.5$ ) improved the agreement for the high recycling regime in comparison with the previous result<sup>1)</sup>.

By using this C-S-D model, we explore the possible operation space of EAST in the space of the total particle flux  $\Phi_p$  and the total heat flux  $Q_{\text{in}}$  across the separatrix. The operational space is demonstrated in Fig. 4<sup>3)</sup>, and each boundary is the operation condition as for (1) max. heat load to the divertor  $q_{\text{div}} < 3.5\text{MW/m}^2$ , (2) LH transition condition  $Q_{\text{in}} > P_{\text{thr}}$ , (3) available LHCD power  $P_{\text{LHCD}} < 3.5\text{MW}$ , and (4) power balance condition  $P_{\text{LHCD}} < Q_{\text{in}}$ . The upper boundary of  $Q_{\text{in}}$  is limited to  $3.0\sim 3.5\text{MW}$  by  $q_{\text{div}} < 3.5\text{MW/m}^2$ . The boundary of  $q_{\text{div}} < 3.5\text{MW/m}^2$  for  $Q_{\text{in}} < 3.0\text{MW}$  region implies the low recycling state. The upper boundary of the particle flux  $\Phi_p$  is dominated by the power balance requirement for the low  $Q_{\text{in}}$  region, while it is limited by the available LHCD power for higher  $Q_{\text{in}}$ . In other words, the available power for the LHCD tends to be a key parameter to extend the operation density of the core plasma in this high  $Q_{\text{in}}$  regime.

This work was partly supported by JSPS-CAS Core-University Program on Plasma and Nuclear Fusion, and was also carried out as the joint research using nuclear fusion research facilities of JAEA.

### Reference

- 1) Hiwatari, R. et al., Annual report of NIFS Apr.2004-Mar.2005, p344, (2005)
- 2) Takizuka, T. et al., "Development of Database for the Divertor Recycling in JT-60U and Its Analysis" JAERI-Research 2003-010 (2003) (in Japanese)
- 3) Hiwatari, R. et al., Plasma Science and Technology 8, p114, (2006)

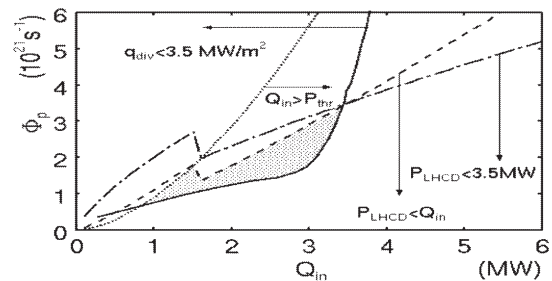


Fig. 4 Qualitative features of EAST operational space.

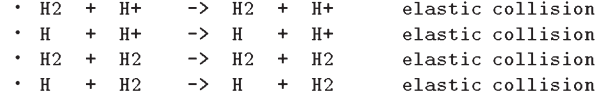
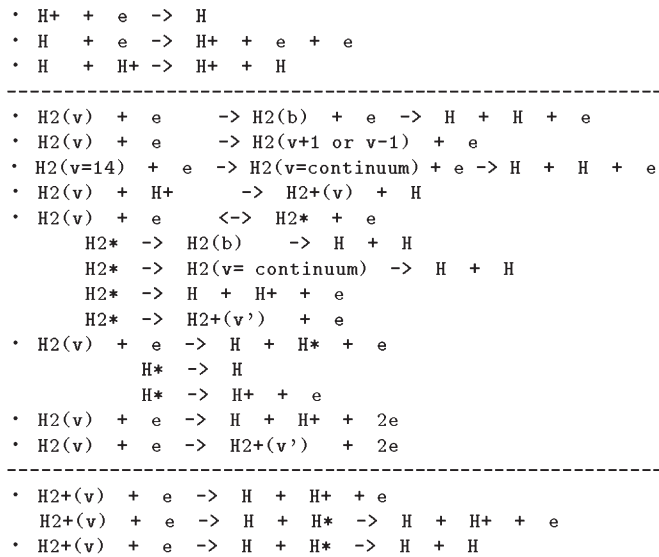
## §18. Self-Consistent Computation of Radiation Transfer in Edge Plasmas Based on Collisional Radiative Model and Neutral Transport Model

Sawada, K., Shiraki, K., Miyazawa, M., Tsujii, M. (Shinshu, Univ.), Iwamae, A., Atake, M., Sakaue, A. (Kyoto Univ.), Nakamura, H.

In divertor plasmas, radiation trapping is sometimes quite substantial. In applying the standard collisional-radiative model to such plasmas, we must properly include the effect of radiation trapping.

We have developed an iterative method which is based on the following algorithm: **(1)** Divide space into cubic cells of linear dimension  $\Delta l$ . **(2)** Give the ground state atom density  $n(1)$ , the ion density  $n_{H+}$ , the electron density  $n_e$ , the electron temperature  $T_e$ , and the line profile function  $g_{pq}(\nu)$  for the transition from upper level  $p$  to lower level  $q$  for each cell. Set the frequency interval  $\Delta\nu$  for the following calculation of emission and absorption. **(3)** Compute the population distribution of excited levels for each cell using the ordinal optically thin collisional-radiative model assuming no radiation trapping. **(4)** Compute the emission intensity radiated in each cell and the absorption in other cells using the population distributions obtained in step (3). **(5)** Compute the population distributions for each cell using the collisional-radiative model considering the absorption of photons. **(6)** Compute the emission intensity radiated in each cell and the absorption in other cells using the population distributions obtained in step (5). **(7)** Repeat steps (5)-(6). This iterative process is continued until the above values converge.

In order to calculate  $n(1)$  and the Doppler profile  $g_{pq}(\nu)$ , we have constructed a neutral transport code for hydrogen species which includes the following list of atomic and molecular processes.



We have applied our code to a RF cylindrical plasma ( $P_{rf} \leq 2.0\text{kW}$ ,  $f = 13.56\text{MHz}$ ) at Shinshu university. The gas pressure was  $0.005\text{Torr}$ . Figure 1 shows calculated densities of atom and molecule, and atom temperature.

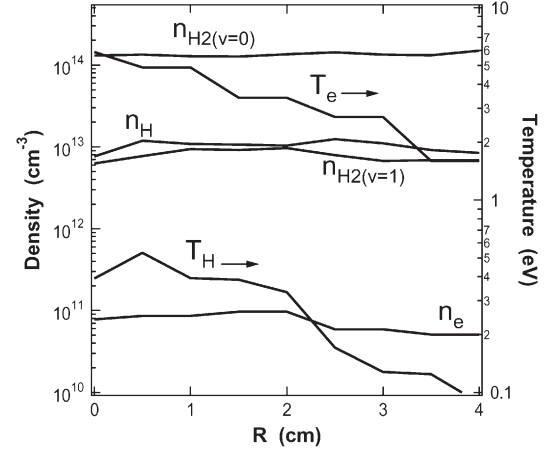


Fig.1. Calculated densities of atom and molecule, and atom temperature. Electron density and temperature measured by a double probe are also shown.

Figure 2 shows calculated populations of excited atom of the principal quantum number  $n = 3$ . Figure 2 also shows populations determined from measured intensities of the Balmer  $\alpha$ . The calculated values agree precisely with the measured ones.

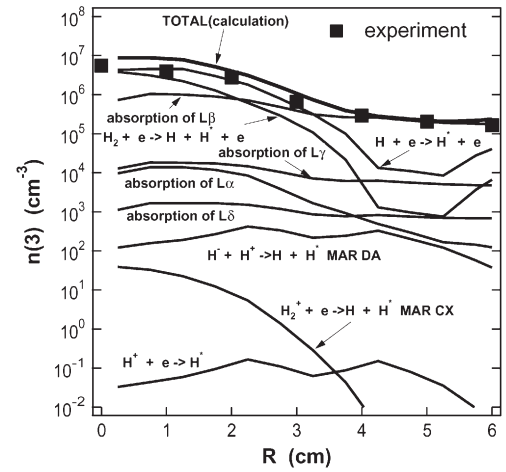


Fig.2. Calculated and measured populations of excited atom of the principal quantum number  $n = 3$ . The origins of the calculated populations of the excited atom are also shown.

## §19. Three-Dimensional Particle-in-Cell Simulation of Blob Transport

Ishiguro, S.

There is a growing interest in investigation of the kinetic effects of scrape off layer plasmas in magnetic fusion devices. For example, charged particle dynamics not only along a magnetic field but also across a magnetic field plays an important role in a blob transport across a magnetic field in a scrape off layer<sup>1-5)</sup>. Plasma behavior in the helical diverter in Large Helical Device (LHD) also may cast an importance of kinetic treatments in three dimensional configuration. Particle-in-Cell (PIC) simulation method is one of the candidates for kinetic treatment. Unfortunately, usual PIC simulation cannot treat a whole system of SOL because of large spatiotemporal scale in SOL plasma dynamics. However, some important physics, such as self-consistent potential structure formation and transport, can be presented by using a system with reduced space and time scale. In addition, PIC simulation takes an important part in multi-layer SOL simulation in which fluid type simulation and kinetic type simulation may be self-consistently connected. With these situations in mind we have been developing three dimensional PIC simulation code for investigation of dynamic plasma behavior in a SOL. By using this 3D bounded PIC code, we have demonstrated that a potential structure is self-consistently formed by the existence of a blob and the blob is transported across the magnetic field.

Configuration of our three dimensional PIC simulation code is followings. External magnetic field is pointing into the z-direction. Particle absorbing boundaries corresponding to diverter plates are placed in the both ends of z-axis. A particle absorbing plane corresponding to the first wall is also placed at one end of the x-axis. Particle reflecting plane is placed in the other end of the x-axis. In the y-direction, periodic boundary condition is applied. The system sizes  $L_x \times L_y \times L_z$  are  $256 \times 128 \times 2048$  and  $256 \times 128 \times 2048$  spatial grid system is used. The ion to electron mass ratio  $m_i/m_e$  is 100 and the ion to electron temperature ration  $T_i/T_e$  is 0.25. The time step width is 0.05 where the time is normalized by  $\omega_{pe}^{-1}$ . Initially plasma with density hump is placed in the system. The magnetic field along the z-axis has gradient in the x-direction and is given by  $B_z(x,y,z) = B_0(512/(768-x))$ . Figure 1 shows the potential profiles in x-z plane at  $y=64$  (a), in the z-direction at  $y=64$  and  $x=192$  (b), in x-y plane at  $z=1024$  (c), and in the y-direction at  $x=192$  and  $z=1024$  (d) at  $t=500$ , where each profile is averaged over the twice of the plasma period. Here the potential  $\phi$  is normalized by  $e/T_e$ . The potential profile in the z-direction sheathes are reasonably formed in

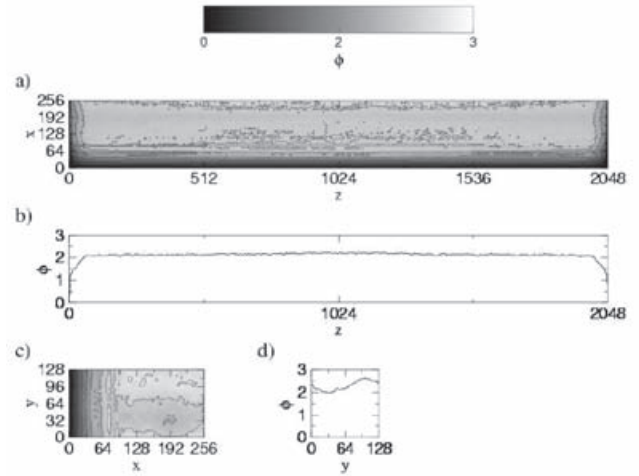


Fig. 1. Gray scale plot of potential in x-z plane at  $y=L_y/2$  (a), potential profile in the z direction at  $x=3L_x/4$  and  $y=L_y/2$  (b), gray scale plot of potential profile in x-y plane at  $z=L_z/2$  (c), and potential profile in the y direction at  $x=3L_x/4$  and  $z=L_z/2$  (d) at  $t=500$ .

the vicinity of the boundaries. In the y-direction a potential structure is created. The potential difference is  $\phi = 0.5$ . The ions move in the positive y-direction and electrons move in the negative y-direction due to grad-B drift. The positive edge of the density hump with  $y = 100$ , thereby, is positively charged and the negative edge of the density hump with  $y = 30$  is negatively charged. As a result, potential difference in the y-direction is self-consistently created. This self-consistent electric field pointing into the negative y-direction plays a role to push the density hump to the negative x-direction due to EXB drift. In the later time the density hump moves in the negative x-direction at the speed  $v = 0.1c_s$ , where  $c_s$  is the ion acoustic speed.

### References

- [1] Umansky, M et al.: Phys. Plasmas 5, (1998) 3373.
- [2] Schneider, R. et al., in: 17<sup>th</sup> International Conference on Plasma Physics and Controlled Fusion Research, Yokohama, Japan, 19-24 October, 1998, paper FI-CN-69/THP2/05.
- [3] Lipschultz, B. et al. in: 18<sup>th</sup> IAEA Fusion Energy Conference, Sorrento, Italy, 4-10 October, 2000, paper IAEA-CN-77/EX5/6.
- [4] Zweben, S. J. et al.: Nucl. Fusion 44, (2004)134.
- [5] Krasheninnikov, S. I. :Phys. Lett. A 283, 368 (2001) 368.



## §20. Edge Plasma Simulation for Stellarator System with 2D Transport Code UEDGE

Takayama, A., Tomita, Y., Ishiguro, S.,  
Pigarov, A.Yu., Krasheninnikov, S. (UCSD),  
Rognlien, T.D. (LLNL)

A new and simple approach for stellarator edge modeling is presented. This is based on averaging of edge plasma parameters and introducing effective 2-dimensional flux surfaces which allow to use UEDGE transport code, widely used for a tokamak edge plasma modeling. This approach is applied to edge modeling of Large Helical Device (LHD). It should be noted that our model is based on 2-dimensional configuration which is called as stellarator-equivalent tokamak (SET), while stellarator system is inherently 3-dimensional.

It is recognized that magnetic configuration at the edge of a stellarator system is very complicated and contains a mixture of closed flux surfaces and stochastic field lines. Because of its complexity, at present, there is no complete plasma transport code that fully accounts for all of the features of this highly complicated case. Moreover, it is even not very clear what kind of set of transport equations can be used for these purposes. At the same time, it is feasible that due to a strong anomalous cross-field plasma transport and convective plasma flows, rather detailed features of stellarator magnetic topology do not matter much for averaged plasma parameters. Therefore, it is worth to try a simple approach to the modeling of stellarator edge plasma based on “averaging” of edge plasma parameters along the magnetic axis and introducing effective two-dimensional flux surfaces. In this sense, we substitute the stellarator edge with what can be called a stellarator-equivalent tokamak (SET) edge. As a consequence 3-dimensional property of stellarator system cannot be investigated, but it is still possible to clarify the “averaged” 2-dimensional property of stellarator edge region and difference between stellarators and tokamaks in point of connections length of magnetic field lines and compression factor of a magnetic flux tube. We simulate the LHD-stellarator-equivalent tokamak with 2D multi-fluid edge plasma transport code UEDGE<sup>1)</sup>.

This method has following properties: Double null (bottom and top X-points) configuration; same large aspect ratio with LHD; same plasma cross-section elongation with the vertically elongated cross section of LHD; similar positions of X-points, strike points at divertor plates, and the magnetic axis; same radial gradient of magnetic flux in the core region adjacent to separatrix with LHD; and similar compression factor of a magnetic flux tube at the scrape-off layer (SOL) mid-plane and its width in the divertor near strike points.

In the LHD-SET configuration the characteristic connection length  $L_{\text{SOL}}$  of magnetic field lines from the SOL mid-plane to the

divertor plates is typically set equal to the characteristic connection length in the real stellarator configuration calculated with 3D magnetic field line tracing code and smoothened over a certain part of the SOL.

The UEDGE code solves the 2D multi-fluid plasma transport equations and reduced set of Navier-Stokes equations for neutral transport. The plasma sources are the ionization of recycling atoms from divertor plates and walls and flux from NBI-fuelled core plasma. Plasma is neutralized at divertor plates and walls and corresponding boundary conditions are similar to those in tokamaks<sup>1)</sup>. We assume the up-down symmetry with mid-plane and simulate only the bottom half domain. The constructed numerical mesh is non-orthogonal and non-uniform. The combined effect of small-scale magnetic islands, stochastic magnetic field layers as well as intermittency (infrequent but large-scale transport events) on cross-field plasma transport is modeled in UEDGE by prescribing the 2D profiles anomalous convective velocity  $V_{\text{conv}}$  and anomalous diffusivities  $(D_{\perp}, \chi_{\perp})$  and by adjusting these profiles in order to match the experimental plasma profiles and recycling data<sup>2)</sup>.

Figure shows a simulation result (ion velocity profile) of the case with the following conditions:  $B_t = 3$  [T],  $R_0 = 3.75$  [m],  $n_{\text{ec}} = 4.0 \times 10^{19}$  [m<sup>3</sup>],  $P_e = \gamma_{\text{ei}} W_0$ ,  $P_i = (1 - \gamma_{\text{ei}}) W_0$ ,  $\gamma_{\text{ei}} = 0.4$ ,  $W_0 = W_{\text{NBI}} - W_{\text{rad}}$ ,  $W_{\text{NBI}} = 3.5$  [MW],  $W_{\text{rad}} = 0.5$  [MW]. In the obtained steady-state solutions, the plasma flux through core interface is equal to the neutral flux plus the NBI fuelling rate  $F_{\text{NBI}}$ . Anomalous diffusivity for this case is  $D_{\perp} = 0.20$  [m<sup>2</sup>/s],  $\chi_{\perp} = 0.40$  [m<sup>2</sup>/s].



Figure Ion velocity profile

### References

- 1) Rognlien, T.D. *et al.*, J.Nucl.Mater. **196** (1992) 345.
- 2) Pigarov, A..Yu. *et al.*, J.Nucl.Mater. **313** (2003) 1076.

## §21. Integrated Simulations for Fast Ignition with Cone-Guided Targets

Sakagami, H.,  
Johzaki, T., Nagatomo, H., Mima, K. (Institute of  
Laser Engineering, Osaka Univ.)

It was reported that the fuel core was heated up to  $\sim 0.8$  keV in the fast ignition experiments with cone-guided targets at Osaka University, but efficient heating mechanisms and achievement of such high temperature have not been clarified yet. To estimate the scheme performance of the fast ignition, we must consider 1) overall fluid dynamics of the implosion, 2) laser-plasma interaction and fast electron generation, and 3) energy deposition of fast electrons within the core. It is, however, impossible to simulate all phenomena with a single simulation code due to divergence of both space and time scales, and we must simulate each phenomenon with individual codes and integrate them. To attack this challenging problem, we have been promoting the Fast Ignition Integrated Interconnecting code (FI) project.<sup>1,2)</sup> Under this project, the radiation-hydro code (PINOCO), the collective Particle-in-Cell code (FISCOF1), and the relativistic Fokker-Planck code (FIBMET) collaborate with each other by data transfer via the computer networks.

In the cone-guided target, there is a density gap between the cone tip and the imploded plasma, and fast electrons must across this boundary to reach the core. We model this density gap in FISCOF1 as follows: the preformed plasma is assumed to have exponential profile of the scale length  $5\text{ }\mu\text{m}$  with density from  $0.1n_c$  up to  $100n_c$ , where  $n_c$  is the critical density. Behind the preformed plasma, the cone tip is assumed as the plasma of  $10\text{ }\mu\text{m}$  width and  $100n_c$ , following the  $50\text{ }\mu\text{m}$  long imploded plasma with  $n_c$ ,  $2n_c$  or  $10n_c$ . Fast electrons are expected to lose their energy when they across the density gap. Simulations are performed with Gaussian laser pulse of  $\lambda_L = 1.06\text{ }\mu\text{m}$ ,  $\tau_{FWHM} = 150\text{ fs}$ ,  $I_L = 10^{20}\text{ W/cm}^2$  and immobile ions, and the energy of fast electrons is observed at  $10\text{ }\mu\text{m}$  rear of the density gap. The temporal profiles of the electron beam intensity are shown in Fig. 1 (a) and the time-averaged electron energy distributions are shown in Fig. 1 (b) for the density gap of  $10n_c$  (gray solid),  $2n_c$  (black solid) and  $n_c$  (black dash). Electron phase spaces at 350 fs are shown in Fig. 2 for the density gap of (a)  $10n_c$ , (b)  $2n_c$  and (c)  $n_c$ . The density gap is placed at the center of figures. In case of  $10n_c$ , the fast electron current is completely canceled by bulk electrons because the density of bulk electrons is much higher than that of fast electrons, and no micro-instability occurs. Thus fast electrons propagate through the imploded plasma without losing their energy, and they are too hot to heat the core. In case of  $2n_c$ , all of bulk electrons in the imploded plasma must flow with 70% of the light speed, and this stream of bulk electrons excites a strong two-stream instability, in which bulk electrons are heated up. An electrostatic field is built up at the gap, and a

relatively low energy part of fast electrons is confined inside the cone tip. On the other hand, the return currents are accelerated at the gap and injected into the cone tip. Therefore the cone tip is filled up with sloshing fast electrons, and some fractions of them are continuously released from there even after the laser pulse is dropped off, and expected to heat the core. The electron beam intensity does not drop off even after the laser pulse vanishes (see Fig.1(a)), and sub-MeV electrons that are very efficient for core heating are clearly observed much more (see Fig.1(b)). In case of  $n_c$ , the fast electron current is not neutralized any more even all of bulk electrons run with the light speed because the density of bulk electrons is only  $n_c$ , and a very strong electrostatic field is built up at the gap. Thus bulk electrons are also heated up by the two-stream instability, but sub-MeV electrons are reflected by this strong potential and confined inside the cone tip. The return currents are accelerated at the gap into the cone tip by this very strong electrostatic field and are sloshing inside the cone tip. Thus electrons with more than MeV energy are launched into the imploded plasma after laser irradiation.

If the density of the imploded plasma is large, the fast electron current can be easily neutralized without driving the instability. When it is small, the strong electrostatic potential is build up and disturb the propagation of sub-MeV electrons. Thus there would exist an optimal density of the imploded plasma for the core heating.

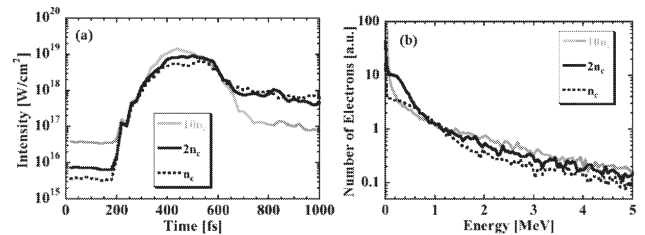


Fig.1. The temporal profiles of (a) the electron beam intensity and (b) the time-averaged electron energy distribution.

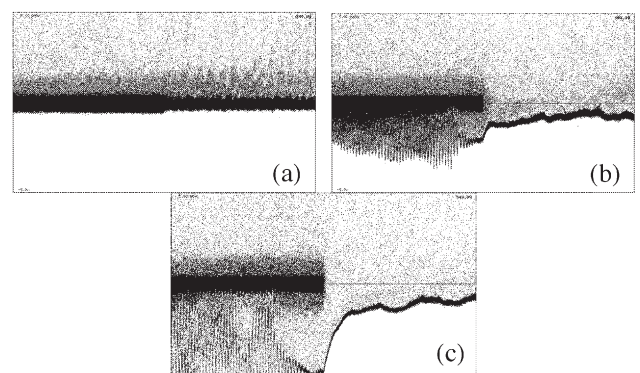


Fig.2. Electron phase spaces with the density gap of (a)  $10n_c$ , (b)  $2n_c$  and (c)  $n_c$ .

### References

- 1) Sakagami, H., and Mima, K. : Laser and Particle Beams **22** (2004) 41.
- 2) Sakagami, H., Johzaki, T., Nagatomo, H., and Mima, K. : Laser and Particle Beams **24** (2006) 191.

## §22. Formation of Non-Maxwellian Distribution and Its Role in Collisionless Driven Reconnection

Horiuchi, R., Ohtani, H.

The dynamical evolution of collisionless driven reconnection is investigated by using a newly developed electromagnetic particle simulation code in a microscopic open system ("PASMO") which is surrounded by macroscopic system [1,2,3]. In this model the interaction between macro system and micro system is expressed by the plasma inflow and outflow through the system boundary.

The plasma inflows can be symmetrically driven from two upstream boundaries by imposing the external electric field in the  $z$  direction. Because the frozen-in condition is satisfied at the upstream boundary, the particle distribution functions are given by the shifted Maxwellian there [1,2,3]. The plasma flows into the current sheet while modifying the current density profiles. Since charged particles are not magnetized near the neutral sheet, their motions change from magnetized gyration to unmagnetized thermal motion called meandering motion as they approach the neutral sheet. The inward electrostatic field is generated due to the charge separation in the edge region, where ions are unmagnetized, but electrons are still magnetized. This electrostatic field enhances the electric current by forming a strong electron  $\mathbf{E} \times \mathbf{B}$  drift motion, while it accelerates ions towards the neutral sheet, enhancing the ion meandering motion.

The existence of unmagnetized meandering motion in the current sheet modifies particle distribution function from the shifted Maxwellian to an anisotropic one. Figure 1 shows the ion distribution function in the phase space  $(y, v_y)$ , where the neutral sheet is located at the midpoint of the  $y$ -axis. The distribution satisfies the shifted Maxwellian near the upstream boundaries (left and right boundaries in this figure) as was expected. However, an ion hole appears at the center of current sheet, where distribution becomes two-peaked and no ions exist in low velocity region between two peaks. Thus, the strong anisotropic distribution is generated as result of unmagnetized meandering motion.

The strong modification of distribution function leads to the generation of off-diagonal components of pressure tensor term, which is one of major causes to violate frozen-in constraint and trigger collisionless reconnection [3,4]. Figure 2 demonstrates the spatial profiles of non-ideal terms for ions in two-fluid MHD as

$$n_j(\mathbf{E} + \mathbf{V}_j \times \mathbf{B}) = \frac{m_j}{q_j} \cdot n_j \left( \frac{\partial}{\partial t} \mathbf{V}_j + (\mathbf{V}_j \cdot \nabla) \mathbf{V}_j \right) + \frac{1}{q_j} \nabla \cdot \tilde{\mathbf{P}} + \frac{1}{q_j} \nabla p$$

The electric field becomes constant both in time and in space at the quasi-steady state, where magnetic

reconnection is constantly triggered by the electric field at the reconnection point. It is found from Fig. 2 that the reconnection electric field (solid line) is sustained by the ion pressure tensor originating from unmagnetized meandering motion (dashed line) in the ion current layer.

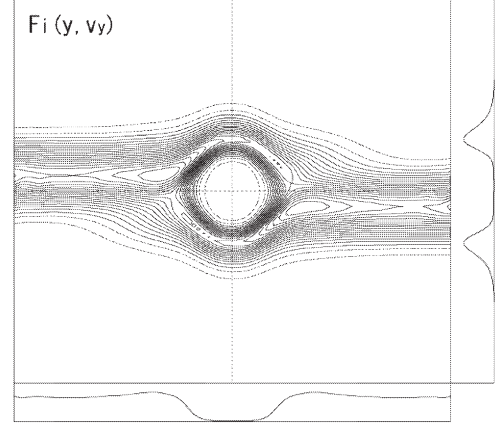


Fig. 1. Ion distribution function in phase space  $(y, v_y)$  at  $\omega_{ce}t=1343$ , where left and right boundaries correspond to the upstream boundaries.

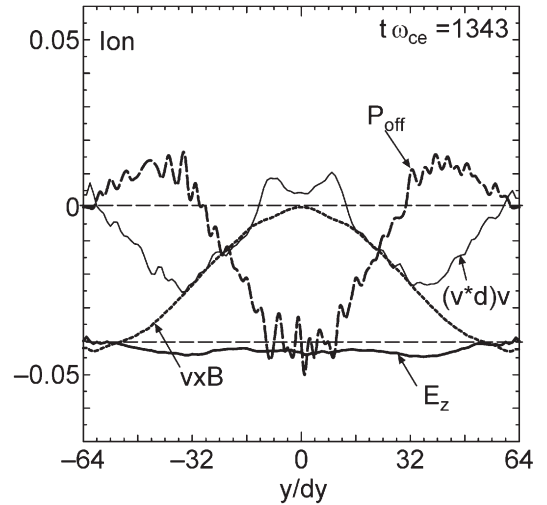


Fig. 2. Spatial profiles of non-ideal terms for ions at  $\omega_{ce}t=1343$ .

### Reference

- 1) W. Pei, R. Horiuchi and T. Sato, Phys. Rev. Lett., **87** (2001) 235003-1-235003-4.
- 2) R. Horiuchi, H. Ohtani, and A. Ishizawa, Comp. Phys. Comm., **164** (2004) 17-22.
- 3) R. Horiuchi, H. Ohtani, and A. Ishizawa, J. Plasma Phys., (2006) [in press].
- 4) A. Ishizawa, and R. Horiuchi, Phys. Rev. Lett., **95** (2005) 045003-1-045003-4.



## §23. Improved Upstream Boundary Condition for PASMO

Ohtani, H., Horiuchi, R.

Magnetic reconnection plays an important role in plasmas, and leads to the fast energy release from magnetic field to plasmas and the change of magnetic field topology [1]. To clarify the relationship between particle kinetic effects and anomalous resistivity due to plasma instabilities, we develop a three-dimensional Particle Simulation code for Magnetic reconnection in an Open system (PASMO), in which a distributed parallel algorithm is integrated for a distributed memory and multi-processor computer system using a programming paradigm, High Performance Fortran (HPF) [2]. Recently, we have improved a condition of the upstream boundary in order to satisfy the frozen-in condition sufficiently. In this paper, we show a properness of the improved condition.

The upstream boundary ( $y = \pm y_b$ ) is set in the ideal MHD region where ions and electrons are frozen into magnetic field. Thus plasma inflow is driven by  $\mathbf{E} \times \mathbf{B}$  drift due to a driving electric field applied in  $z$  direction. In the previous model, the particles are programmed to be supplied into the system through the boundary each time step. The number density at the input boundary is assumed to change according to the relation  $n_b = n_{b0} \frac{B_b}{B_{b0}}$ , where subscript  $b$  stands for the upstream boundary and subscript 0 for the initial time. We obtain the velocity distribution of the input particles from the shifted Maxwellian with the initial constant temperature under the assumption  $u_b \ll v_T$ , where  $u_b$  is the average velocity ( $u_b = \frac{\mathbf{E}_b \times \mathbf{B}_b}{B_b^2}$ ) and  $v_T$  is a thermal velocity. In the improved condition, on the other hand, the particles in the  $y$  boundary cells ( $0 < y < \Delta y$  and  $L_y - \Delta y < y < L_y$ , where  $\Delta y$  and  $L_y$  are the grid size and the simulation box size in  $y$  direction, respectively.) are removed every time step, and then, instead of them, the particles with the density  $n_b$  and the flow velocity  $u_b$  are newly loaded there based on quiet-start technique. The velocity distribution obeys a shifted Maxwellian with the initial constant temperature rigorously every time step.

Figures 1 and 2 show the contour plots of  $E_z + (\mathbf{v} \times \mathbf{B})_z$  for (a) electrons and (b) ions under the previous and improved conditions, respectively. When the frozen-in condition is satisfied, the quantity  $E_z + (\mathbf{v} \times \mathbf{B})_z$  vanishes.

In Fig. 1,  $E_z + (\mathbf{v} \times \mathbf{B})_z$  is zero near the  $y$  boundary for electrons but finite for ions. Because the flow velocity  $u_b$  becomes comparable to the ion thermal velocity  $v_{Ti}$  near the upstream boundary as the simulation advances, the assumption for the shifted Maxwellian ( $u_b \ll v_T$ ) is broken. This partly causes the numerical drawback in the previous model that the frozen-in condition is not satisfied for ions there.

In Fig. 2, on the other hand,  $E_z + (\mathbf{v} \times \mathbf{B})_z$  is zero near the upstream boundary both for electron and ion. This means that the improved condition for the upstream

boundary is more appropriate than the previous one, and then electrons and ions are frozen into magnetic field.

In concluding, we succeeded in improving the upstream boundary condition, and increasing the precision of the simulation.

### Reference

- 1) D. Biskamp: *Magnetic Reconnection in Plasmas* (Cambridge University Press, Cambridge, 2000).
- 2) H. Ohtani *et al*: accepted in LNCL.

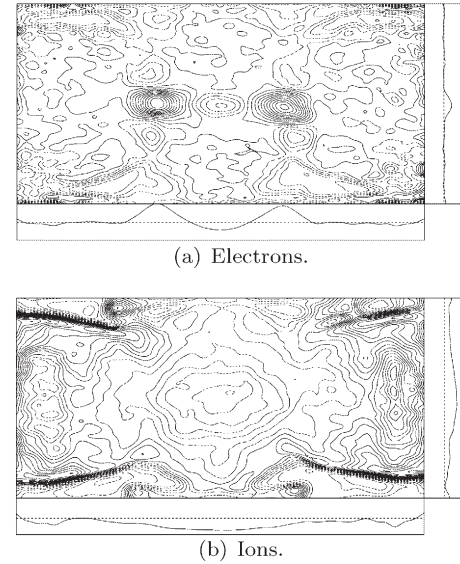


Fig. 1. Contour plot of  $E_z + (\mathbf{v} \times \mathbf{B})_z$  for (a) electrons and (b) ions in  $xy$  plane under the previous upstream boundary condition. Horizontal axis is  $x$ , and vertical axis is  $y$ . Right and bottom side panels show it along  $y$  direction at  $x = L_x/2$  and along  $x$  direction at  $y = L_y/2$ , respectively.  $L_x$  is the simulation box size.

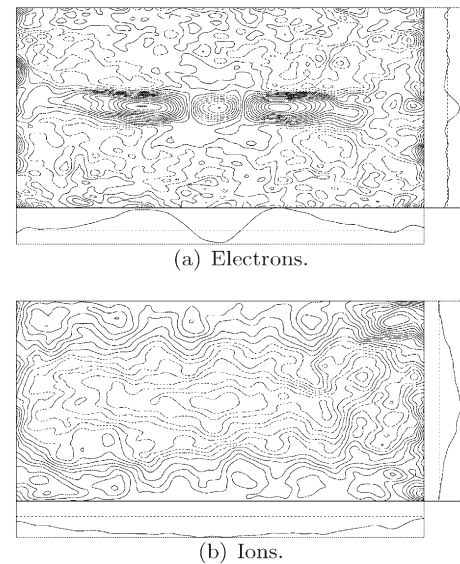


Fig. 2. The same figure as Fig. 1 but under the improved upstream boundary condition.



## §24. Mass Ratio Dependence of Drift Kink Instability in the Current Sheet

Moritaka, T. (Nagoya Univ), Horiuchi, R., Ohtani, H., Ishizawa, A.

Collisionless magnetic reconnection at the current sheet structure with the reversed magnetic field is one of the fundamental physical processes connect to dynamic plasma phenomena in high temperature and low density plasmas such as the solar corona, the geomagnetic tail and fusion plasma. Instead of binary collisions, microscopic nonideal effect can violate frozen-in condition and cause collisionless magnetic reconnection in such systems.

The current sheet can be unstable against a variety of microscopic plasma instabilities. The excitation of these instabilities and their relationship with magnetic reconnection are investigated by means of 2+1/2 dimensional explicit electromagnetic particle simulation. In the microscopic view of plasma, particle thermal motion with characteristic scale of larmor radius or meandering scale is important. Mass ratio is one of the parameters which determine these scales. The simulation is carried out for large mass ratio (mass ratio : 200,800) and the result is compared with previous case (small mass ratio : 25). Simulation with large mass ratio requires vast numerical costs to resolve spatial and temporal scale for both ions and electrons. We improve our simulation code by the optimal parallelization for SX7, to increase the speed of calculation about 20 times from previous simulation code. In addition, to prevent the effect of two-fluid stream instabilities for these instabilities, we set no background particles in the initial equilibrium by providing weak velocity shear near the boundary.

In each case, Lower Hybrid Drift Instability (LHDI)<sup>1)</sup> and Drift Kink Instability (DKI) are observed to grow at the periphery of current sheet and neutral sheet, respectively. Qualitatively, the generation of the nonideal term is similar to small mass ratio case (Fig.1). In the DKI growing phase after the saturation of LHDI, DC electric field consistent with total magnetic flux reduction is generated and current density dissipates at neutral sheet. The wavy coupling term, which stands for wave-particle interaction, balances this DC electric field term. The growth of DKI creates nonideal anomalous resistivity, and the growth rate of DKI can control the reconnection rate and time scale of them.

In the linear theory of DKI<sup>2)</sup> predicts that growth rate is reduced as mass ratio increases and DKI growth rate becomes quite small in realistic

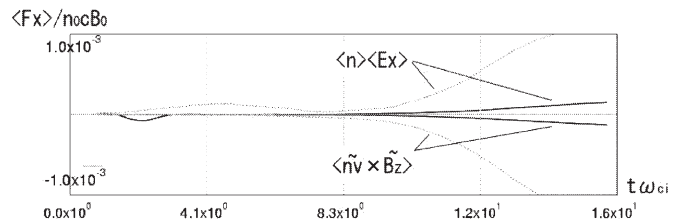


Figure 1: Time dependence of force balance between averaged electric field term and wavy component of magnetic force term ; mass ratio 25 (dashed lines) and mass ratio 200 (solid lines)

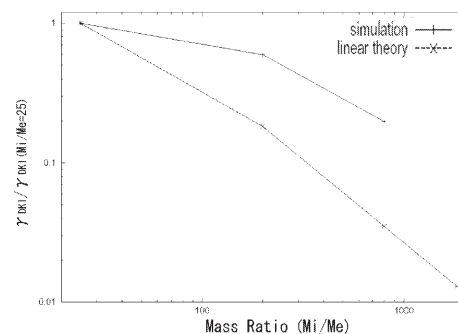


Figure 2: Mass ratio dependence of the growth rate of DKI in the simulation (+) and the theory calculated from 2)(x), where these rates are normalized by that for  $M_i/M_e = 25$

mass ratio. In the theory, the linear growth rate of DKI  $\gamma_{DKI}$  in the case of mass ratio  $M_i/M_e = 200$  is about a tenth of that for  $M_i/M_e = 25$ , and  $\gamma_{DKI}$  in the realistic mass ratio case is reduced to 0.01 of that for  $M_i/M_e = 25$ . However, this decrease of the growth rate according to the mass ratio increase is considerably less in the results of the simulation (Fig.2). In the case of  $M_i/M_e = 200$ , the growth rate of DKI is more than half in that for  $M_i/M_e = 25$ . And the relaxation rate of current density of this case also remains a third of the relaxation rate of  $M_i/M_e = 25$ . Even in the case of quite larger mass ratio case of  $M_i/M_e = 800$ , the growth rate is about one-fifth for that in the case of  $M_i/M_e = 25$ . This larger-than-expected growth of DKI is considered to be due to the current sheet deformation by the nonlinear effect of LHDI<sup>3)</sup>. These results suggest that the growth of DKI and the generation of anomalous resistivity can have a certain effect in triggering magnetic reconnection in realistic mass ratio case.

### References

- 1) R.C.Davidson et al, Phys.Fluids, **20**, 301(1977)
- 2) W.Daughton, Phys.Plasmas, **6**,1329(1999)
- 3) R.Horiuchi et al, Phys.Plasmas, **6**, 4565(1999)

## §25. Development of 3D MHD Simulation Code for Magnetic Reconnection in an Open System

Usami, S., Horiuchi, R.

Magnetic reconnection is a fundamental process to lead fast energy release. For instance, solar flares and geomagnetic substorms seem to be caused by magnetic reconnection. Because such high-temperature and low-density plasmas are collisionless, frozen-in condition holds macroscopically, and thus, reconnection can not take place. Collisionless reconnection requires microscopic processes which violate frozen-in condition. In order to clarify the mechanism of reconnection, we develop cross-hierarchy model to solve both microscopic and macroscopic physics consistently and simultaneously. Microscopic physics is described by particle simulation model, while macroscopic physics is expressed by MHD simulation model.

In this report, we explain the current situation of developing MHD code. We have developed the three-dimensional MHD code for a periodic boundary system, which is scheduled to be modified to one for an open boundary system. The basic equations to be solved are described in the dimensionless form, as follows:

$$\begin{aligned}\frac{\partial \hat{\rho}}{\partial \hat{t}} &= -\hat{\mathbf{v}} \cdot (\hat{\rho} \hat{\mathbf{v}}), \\ \frac{\partial (\hat{\rho} \hat{\mathbf{v}})}{\partial \hat{t}} &= -\hat{\mathbf{v}} \cdot (\hat{\rho} \hat{\mathbf{v}} \hat{\mathbf{v}}) - \hat{\mathbf{v}} \hat{P} + \hat{\mathbf{J}} \times \hat{\mathbf{B}} + \hat{\mu} \left( \hat{\Delta} \hat{\mathbf{v}} + \frac{1}{3} \hat{\nabla} (\hat{\nabla} \cdot \hat{\mathbf{v}}) \right), \\ \frac{\partial \hat{\mathbf{B}}}{\partial \hat{t}} &= -\hat{\mathbf{v}} \times (\hat{\mathbf{B}} \times \hat{\mathbf{v}}) - \hat{\eta} \hat{\nabla} \times \hat{\mathbf{J}}, \\ \frac{\partial \hat{P}}{\partial \hat{t}} &= -\hat{\mathbf{v}} \cdot (\hat{P} \hat{\mathbf{v}}) + (\gamma - 1) \left( -\hat{P} \hat{\nabla} \cdot \hat{\mathbf{v}} + \hat{\eta} \hat{\mathbf{J}}^2 + \hat{\mu} \left( \frac{\partial \hat{v}_i}{\partial \hat{x}_k} \left( \frac{\partial \hat{v}_i}{\partial \hat{x}_k} + \frac{\partial \hat{v}_k}{\partial \hat{x}_i} \right) - \frac{2}{3} \delta_{ik} \hat{\nabla} \cdot \hat{\mathbf{v}} \right) \right).\end{aligned}$$

We adopt fourth-order central difference scheme for a spatial derivative, while we use forth-order Runge-Kutta-Gill method for a time integral.

We examine the numerical accuracy of this MHD code by applying it to tearing instability. It is well known that the linear growth rate  $\gamma$  of tearing instability is proportional to  $\eta^{3/5}$  ( $\eta$  is electrical resistivity) [1]. In the first model, the initial magnetic field is assumed to be  $B_{x0}(y) = \cos(2\pi y/L_y)$ , where  $(L_x, L_y, L_z) = (516, 68, 6)$  ( $L_x$ ,  $L_y$ , and  $L_z$  are the mesh size for  $x$ ,  $y$ , and  $z$  directions.). Figure 1 shows the growth rate  $\gamma$  of tearing mode ( $m=2$ ) as a function of  $\eta$ . From the average slope of  $\log(\gamma)$  we have the relation  $\gamma \sim \eta^{0.50}$  and so the simulation results do not satisfy  $\gamma \sim \eta^{3/5}$ .

The reason may come from the fact that two current layers are very close to each other and so the growth rate is reduced by nonlinear coupling effect in the same way as double tearing modes [2]. In order to examine the nonlinear effect we simulate the tearing mode by using the initial magnetic field as

$$B_{x0}(y) = \begin{cases} \tanh[(y - L_y/4)/(L_y/32)] & \text{for } 0 < y < L_y/2, \\ \tanh[-(y - 3L_y/4)/(L_y/32)] & \text{for } L_y/2 < y < L_y, \end{cases}$$

Figure 2 displays the growth rate  $\gamma$  of tearing mode ( $m=2$ ) as a function of  $\eta$  in the case, where,  $(L_x, L_y, L_z) = (516, 132, 6)$  and two current layers are enough distant from each other. From Fig. 2, we find  $\gamma \sim \eta^{0.58}$ . The simulation results are consistent with the theory.

We have verified that our MHD code in a periodic boundary system is accurate. We are now developing MHD code for an open boundary system which is aimed to be connected with particle simulation code.

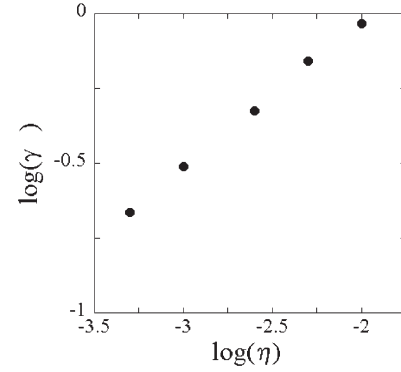


Fig. 1. Growth rate  $\gamma$  vs  $\eta$ . One current layer is very close to another one. We obtain  $\gamma \sim \eta^{0.50}$ .

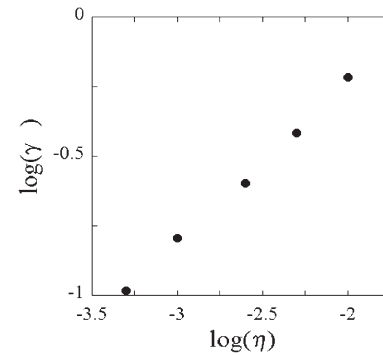


Fig. 2. Growth rate  $\gamma$  vs  $\eta$ . One current layer is distant from another one. We find  $\gamma \sim \eta^{0.58}$ .

### References

- [1] H. P. Furth and J. Killeen, Phys. Fluids **6**, 459 (1963).
- [2] P. L. Pritchett, Y. C. Lee, and J. F. Drake, Phys. Fluids **23**, 1368 (1980).

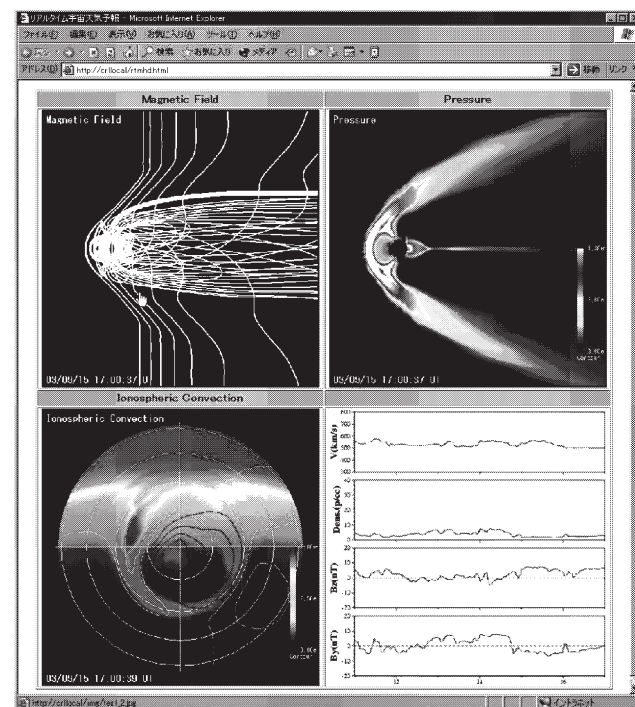
## §26. Real-Time Earth Magnetosphere Simulator with 3-Dimensional MHD Code

Den, M., Tanaka, T. (Kyushu Univ., CREST), Fujita, S. (Meteo. College, CREST), Obara, T., Shimazu, H. (NICT, CREST), Amo, H., Hayashi, Y., Nakano, E., Seo, Y., Suehiro, K., Takahara, H., Takei, T. (NEC)

We developed a real-time numerical simulator for the solar wind-space-magnetosphere-ionosphere coupling system, adopting the three-dimensional (3D) magneto-hydrodynamical (MHD) simulation code developed by Tanaka<sup>1)</sup>. By using the real-time solar wind data, which is available from the ACE spacecraft every minute, as the upstream boundary conditions for density, temperature, flow speed, and interplanetary magnetic field (IMF), our MHD simulation system can numerically reproduce the global response of the magnetosphere and ionosphere at the same time as in the real world. We achieved real-time 3D simulations of the solar wind-magnetosphere-ionosphere coupling system with a 44x56x60 mesh size by optimizing the parallelization and vectorization of code, and by adapting High Performance Fortran (HPF) language with eight CPUs on a super computer system located at the National Institute of Information and Communications Technology (NICT). We adopted observed ACE solar wind data as upstream boundary conditions to obtain simulation results close to the real-time magnetosphere. We visualized the simulation data at the same time as calculation using RVSLIB and the visualization data was renewed every minute. The main purpose of the Space Weather Forecast Project was to predict when and how disturbances in the space environment occur, how they develop, and to what extent they may cause damages to human systems. Our real-time MHD simulator can calculate the dynamical response of the magnetosphere and predict when geomagnetic disturbances occur and to what extent they develop. Fig.1 is a part of web page. Left top panel shows magnetic field lines, right top panels does the plasma pressure, left bottom panel does ionospheric convection (white and black line) and electrical potential, and right bottom panel does input solar wind data for most recent six hours. We showed AE indices obtained from real-time global MHD simulation ahead by about an hour from the actual time, indicating the activities of the magnetosphere about an

hour in advance. The plasma temperature and density in the geo-stationary orbit are plotted in about an hour advance as an index of magnetopause crossing and as input data for the simulation model of satellite charge. We expect to be able to predict the timing of sudden commencements and occurrences of the geomagnetically induced current associated with ground-based magnetic field disturbances for practical purposes. Furthermore, if electric field distribution in the ionosphere is obtained using our simulation output data, it can be used to predict GPS positioning errors, and might possibly be applied to a flight control system. Our real-time simulation is expected to become an essential approach to forecasting space weather. Our MHD simulation code<sup>1)</sup> could reproduce the magnetosphere activities with appropriate accuracy. We also confirmed that this code could continued running unless the solar wind conditions were intense, eg.,  $B_z < -20$  (nT). It should be noted that the intensity and region of the conductivity could be simulated qualitatively, but that they are not in agreement with ground based observation completely. The limited number of grids is one reason, and this is what should be overcome in future.

Figure1



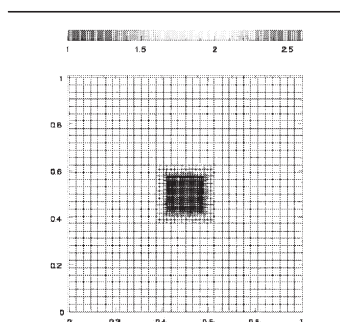
### References

- 1) Tanaka, T.: J. Comp. Phys., 111,(1994)381.
- 2)Den, M., et al.: Space Weather, 4, S06004 (2006) doi : 10.1029.

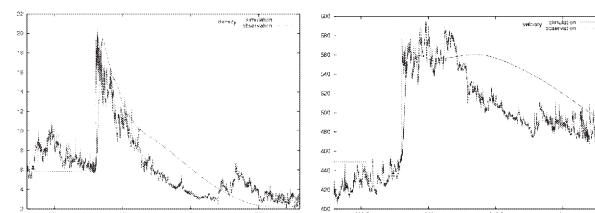
## §27. Simulation of Interplanetary Shock Wave Caused by CME on August 25, 2001

Den, M., Ogawa, T. (Kitazato Univ.), Tanaka, T. (Kyushu Univ., CREST), Yamashita, K. (Yamanashi Univ.)

We simulated propagation of an interplanetary shock wave caused by a coronal mass ejection (CME) on August 25, 2001. Prediction of shock passage time at Earth orbit is one of important subjects for space weather because interactions of the shock wave and CME with Earth magnetosphere causes disturbances such as magnetic storms or substorms and the shock wave itself can make high energy particles. Large dynamical scale makes three-dimensional (3D) simulations of shock wave propagations in an interplanetary space difficult. The distance between the sun and the earth is  $1.5 \times 10^{11} \text{m}$ , on the other hand the solar radius is  $7.0 \times 10^8 \text{m}$ . Furthermore, the shock surface is steep and the shock wave evolves with expansion which indicates that the region of the shock surface increases. We adopted an Adapted Mesh Refinement (AMR) method for grid formation. The AMR technique adapts dynamically the grids to suit the physical conditions and can monitor running structures by fine grids. Indeed we can set fine grids on the solar surface and the shock wave front and coarse grids are set the region where there is poor gradient in physical variables. Fig.1 shows the mesh structure at an initial time. The center region has fine grids and the sun is set here. In this code, a fully threaded tree<sup>1)</sup> is used. As for the flux part, the 3<sup>rd</sup> order accurate Roe-MUSCL algorithm is adopted for the space. The simulation box is a cube whose side length is  $(500R_s)^3 = (2.3\text{AU})^3$ . The inner boundary places at height of 0.15 $R_s$  above the solar surface. The cell size was



$(0.12R_s)^3$  near the sun and  $(7.8R_s)^3$  in the coarsest-mesh regions. The cell size on the shock front is  $(0.24R_s)^3$  at a beginning, and then it is enlarged to twice before the reserved cells are used up. The final cell size on the shock front is  $(0.98R_s)^3$ . We first obtain a steady-state solar wind and then input the model CME into the inner boundary. In our CME mode, maximum velocity ( $V_{\text{max}}$ ) of the CME plays an important role. This is a function of angle to the axis of a CME cone and has four parameters, angular radius of a CME, stand-up time, duration time, and attenuation time (see 2) and 3)). A CME occurred at 16:50 UT on August 25, 2001. The SOHO LASCO CME Catalog estimates that velocity of the CME is 1327 km/sec at 20 $R_s$  and we set  $V_{\text{max}} = 1772 \text{ km/sec}$  at the inner boundary. We assume that the CME occurs just above the X-ray flare which is detected at S17E34. The four parameters are set 50 degree, 0.1 hour, 0.1 hour, and 1 hour for angular radius, stand-up, duration, and attenuation time respectively. Simulation results are presented in Figs.2. We observed the solar wind by a virtual spacecraft at the L1 point in the simulation. Time plots of resulting density (left) and velocity (right) are displayed with the ACE's data in Figs.2. Observed



passage time of the shock wave is at 19:19 UT on August 27, and simulated one is 19:21 UT on that day. Degrees of jump at the shock front show good agreements with observations in both density and velocity. This indicates that our simulation can predict the shock passage time. For the future work, we will develop a realistic ambient solar wind model, introduce a magnetic field and will investigate an initiation of a CME for physics based model of CMEs.

### References

- 1) Khoklov, A.M.: J. Comp. Phys., 143(1998)519.
- 2) Odstrcil, D. et al.: J. Geophys. Res., 104(1999)483.
- 3) Ogawa, T. et al.: Adv. In Geosci., in press.



## §28. Three-Dimensional Simulation Study of Flux Rope Dynamics in the Solar Corona

Kusano, K. (The Earth Simulator Center, JAMSTEC),  
Inoue, S. (Solar Terrestrial Environment Laboratory,  
Nagoya University)

Solar flares and coronal mass ejections (CMEs) are the biggest explosion in our solar system, and greatly influence the electromagnetic condition around the earth, resulting magnetospheric storms, sub-storms, and the onset of aurora burst. Even though both flares and CMEs are widely believed to be related to magnetic energy liberation by magnetic reconnection, the physical relationship between flare and CMEs is not yet well understood.

On the other hand, it is often observed that many flares were associated with the eruption or the disappearance of dark filaments, which existed above magnetic neutral line until the onset of events. Therefore, it is also an important issue to understand whether there is some causality between the filament eruption and the onset of flares and CMEs. Various models have been proposed to explain the filament eruption mechanism.

However, the several important questions are not yet solved. Which in the loss-of-equilibrium or the loss-of-stability is more important for the launching of CME? What is the condition for filament eruption to develop to CME, and to be failed as a so-called confined eruption. In order to give the answers to them, the nonlinear 3D numerical simulation has been performed.<sup>1)</sup>

The simulation domain is a rectangle box,  $(0,0,0) < (x,y,z) < (L_x, L_y, L_z)$ , in which the magnetic neutral line is parallel to the  $x$  axis, and  $z$  denotes the altitude from the photospheric surface. The initial state consists of a magnetic arcade equilibrium, in which a force-free flux rope is embedded at  $z=h$ , plus a small perturbation that is given by the eigenfield of kink mode instability for the equilibrium. The equilibrium arcade is given by a dipole field for the magnetic dipole located at  $z=-d$  as same as the model proposed by Forbes and Priest.<sup>2)</sup> The horizontal boundaries for the  $x$  and  $y$  coordinate satisfy the periodic condition, and the top boundary ( $z=L_z$ ) is located far enough from the filament height ( $h \ll L_z$ ).

Several calculations have been carried out for various value of  $L_x$  that corresponds to the length of flux rope. As a result of them, it was found that there is a threshold of  $L_x$  for the flux rope to be able to escape out of the arcade. For instance, when  $L_x=7.5d$ , the flux rope can ascend continuously even after the growth phase of kink instability, as shown in Fig.1, whereas, for  $L_x=3d$ , the upward motion of the flux rope stops at a certain height.

Even for small  $L_x$ , however, we found that, if some external force is artificially applied onto the flux rope to help the upward motion only for a limited period before the ascending is saturated, the ascending of the flux rope can be continued. The result implies that there is some critical height, which has to be exceeded for the flux rope to escape from the confinement by magnetic arcade.

Also the variation of plasma density structure is investigated, and it was found that plasma density is depressed at the top of the magnetic rope during the ascending phase due to the cross-field expansion, as shown in Fig.2. The structure of the density depression is consistent with the observation of dimming in CMEs. The all results suggest the possibility that the kink instability is involved in the launching of CMEs.

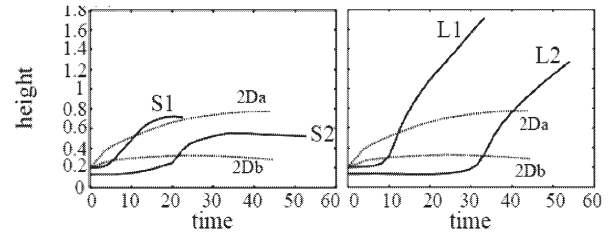


Fig. 1. The time history of the flux rope height for the various runs. Left and right panels show the result for  $L_x=3d$  and  $7.5d$ , respectively. For S1 and L1, the loss-of-equilibrium state is used as the initial state, and for S2 and L2 the dipole magnetic field is stronger than them. 2Da and 2Db are the results of the two-dimensional simulations, in which the translational symmetry for the  $x$  coordinate is applied.

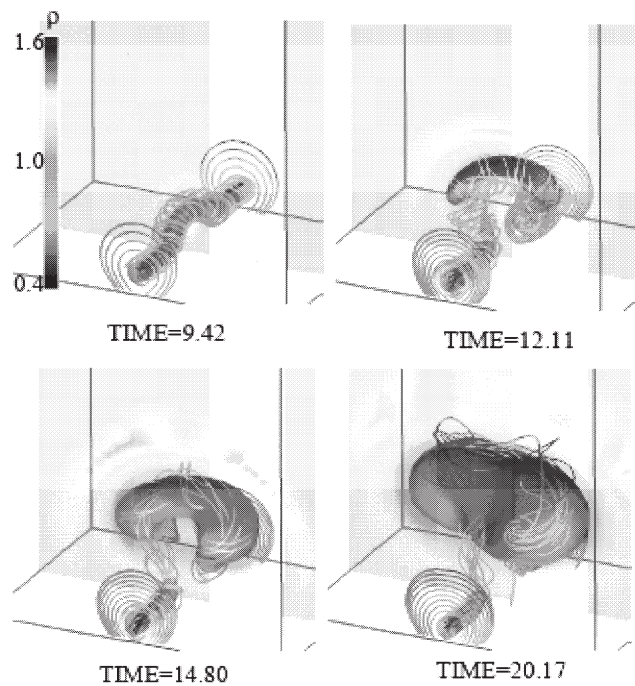


Fig. 2. The evolution of magnetic flux rope in case of  $L_x=7.5d$ . The gray surface is an iso-surface of density representing the density depression region.

### References

- 1) Inoue, S., Kusano, K., The Astrophys. J. **645**, (2006) 742
- 2) Forbes, T., Priest, E., The Astrophys. J. **446**, (1995) 377

## §29. Jet Formation Driven by Magnetic Bridges between Ergosphere and Disk Around Rapidly Rotating Black Hole

Koide, S. (Kumamoto Univ. Sci.)

Superluminal motions, which indicate relativistic motions of emission regions and observational evidence of relativistic jets, were observed around the quasars (QSOs) and active galactic nuclei (AGNs). In our Galaxy, superluminal motions were observed around the binary systems called micro-quasars ( $\mu$  QSOs). Recently, the observations of the afterglow of the long-duration gamma-ray bursts (GRBs) revealed that the long-duration GRBs also contain the relativistic jets. It is believed that these relativistic jets are formed due to violent phenomena around black holes. However, the distinct mechanism of their formation has not been revealed yet. We have performed the general relativistic magnetohydrodynamic (GRMHD) simulations to investigate the formation mechanism.<sup>1)</sup>

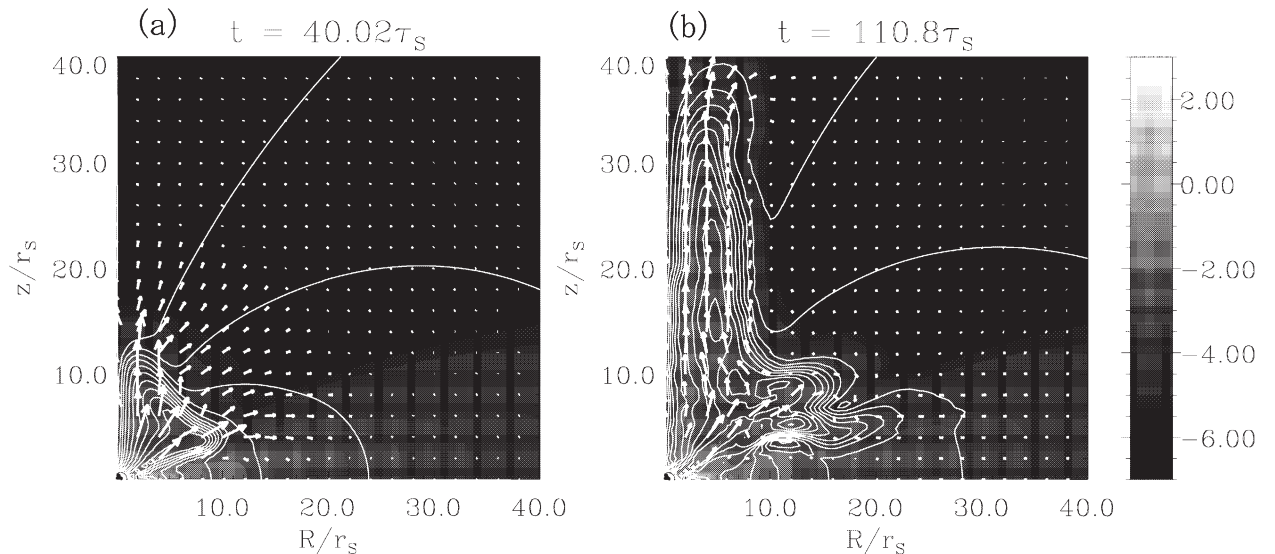
Here we report a two-dimensional numerical result of jet formation driven by magnetic field due to a current loop near a rapidly rotating black hole whose rotation parameter is 0.99995<sup>2)</sup>. We set the current loop along the intersection of the equatorial plane and the surface of the ergosphere around the black hole initially.

In such magnetic configuration, there are magnetic flux tubes which bridge the region between the ergosphere and the co-rotating disk. The magnetic flux tube, which we call 'magnetic bridge', is twisted rapidly by the plasma in the ergosphere due to the frame-dragging effect. The magnetic pressure of the magnetic flux tube increases and the strong magnetic pressure blows off the plasma near the ergosphere to form outflow (Fig. 1(a)). At  $t=40.02 \tau_s$ , the outflow begins to be collimated by the magnetic tension of the magnetic flux tube. Then, eventually, the jet is formed at  $t=110.8 \tau_s$  (Fig. (b)). The maximum velocity of the jet is  $0.46c$  at  $t=110.8 \tau_s$ . That is, the magnetic bridges can not be stationary and expand explosively to form a jet. Around the disk surface, part of the magnetic surface is elongated horizontally. This separation of the outflow to the jet along the axis and the horizontal flow is also seen in the nonrelativistic MHD simulations. The parameter survey of the background pressure shows that the radius of the collimated jet depends on the gas pressure of the corona. However, this does not mean the gas pressure collimates the jet. The gas pressure decelerates the jet and the pinch effect by the magnetic field becomes significant.

### References

- 1) Koide, S., Phys. Rev. D. **67**, (2003) 104010.
- 2) Koide, S., Shibata, K., & Kudoh, T. Phys. Rev. D, in press.

Fig.1 Time evolution of the system of the current loop, quasi-equilibrium coronal plasma, the corotating disk, and the rapidly rotating black hole at the origin. The gray-scale portion shows the logarithm of the mass density of the plasma. The arrows show the poloidal component of the plasma velocity. The white lines show the magnetic flux surfaces.



### §30. Analysis of the Energy Transfer in NS and MHD Turbulence by Using Massive DNS

Gotoh, T. (Nagoya Inst. of Tech.)

It has long been believed that the energy spectrum in the inertial range of MHD turbulence obeys Iroshnikov-Kraichnan scaling  $E(k) \propto k^{-3/2}$  [1]. Some of recent numerical simulations, however, have found that the Kolmogorov scaling of the energy spectrum holds also for the MHD turbulence. To the author's view, still it is far from the definite conclusion because the width of wavenumber range for the Kolmogorov scaling is not long enough. In order to get hints about this problem, on one hand avoiding the resolution limit of the numerical simulation, we have numerically studied the local or nonlocal nature of the energy transfer among the kinetic or magnetic components in the wavenumber space. Let us write the equations for the energy spectra as

$$\begin{aligned}\partial E^K(k, t)/\partial t &= T^K(k, t) - D^K(k, t) \\ &= \sum_q (T_{uu}(k, q, t) + T_{ub}(k, q, t)) - D^K(k, t), \\ \partial E^M(k, t)/\partial t &= T^M(k, t) - D^M(k, t) \\ &= \sum_q (T_{bu}(k, q, t) + T_{bb}(k, q, t)) - D^M(k, t),\end{aligned}$$

where  $D^\alpha(k, t)$ , ( $\alpha = K, M$ ) denotes the dissipation spectrum and  $T^\alpha(k, t)$  for the energy transfer due to the nonlinear interactions, in which the sum over the third wavenumber  $\mathbf{p}$  in the triad interaction ( $T^\alpha(\mathbf{k}, \mathbf{p}, \mathbf{q})$ ,  $\mathbf{k} = \mathbf{p} + \mathbf{q}$ ) is taken for easiness of analysis. For example  $T_{ub}(k, q)$  stands for contributions of  $\mathbf{b}(\mathbf{q})$  to  $\mathbf{u}(\mathbf{k})$ .

Direct numerical simulations were done for Elsässer variables  $\mathbf{z}^\pm = \mathbf{u} \pm \mathbf{b}$  with unit magnetic Prandtl number. Gaussian random fields with or without kinetic and/or magnetic helicity were initially generated and then evolved freely without any forcing. It was found that the magnetic helicity was important in the evolution of the energy spectrum. When  $H^M$  is finite, the energy cascades towards low wavenumbers. The energy decay is found to be  $E(t) \propto t^{-\beta}$ ,  $\beta = 1.2(H^M = 0)$ ,  $0.68(H^M \neq 0)$  and becomes slower when  $H^M \neq 0$ . Hatori has shown that  $\beta = 2/3$  for  $H^M \neq 0$  [2]. Figures 1 and 2 show comparison of  $T_{uu}(k, q)$  and  $T_{ub}(k, q)$  at  $q = 40$ .  $T_{uu}(k, q)$  is local in wavenumbers, in the sense that the transfer occurs at wavenumbers  $k$  nearby  $q$ . On the other hand  $T_{ub}(k, q)$  is nonlocal in that for almost all wavenumbers of  $k < q$ ,  $T_{ub}$  re-

mains uniformly constant and negative by reflecting the Lorentz force. Also it was found that the transfer in  $T_{bu}$  is nonlocal while that of  $T_{bb}$  is local. These facts suggest that the scaling exponent of the energy spectrum depends on relative strength between  $E^K$  and  $E^M$  and on the relative strength between  $(T_{uu}, T_{bb})$  and  $(T_{ub}, T_{bu})$ .

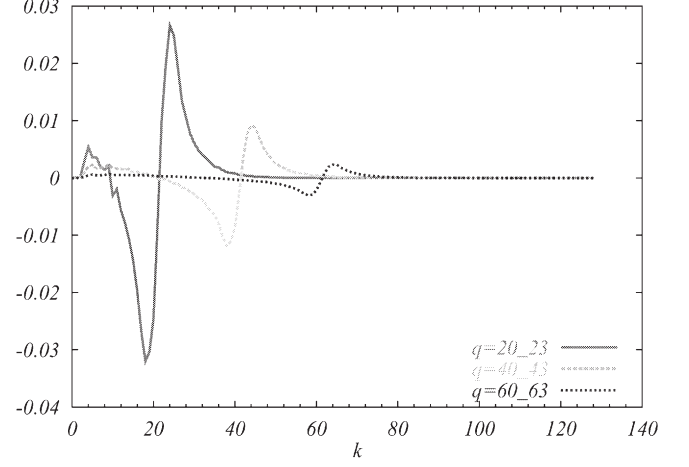


**Fig.1** Plot of  $T_{uu}(k, q)$  for  $q = 20-23, 40-43, 60-63$  when  $H^M = 0$  at  $t = 0$ . The energy is transferred locally.

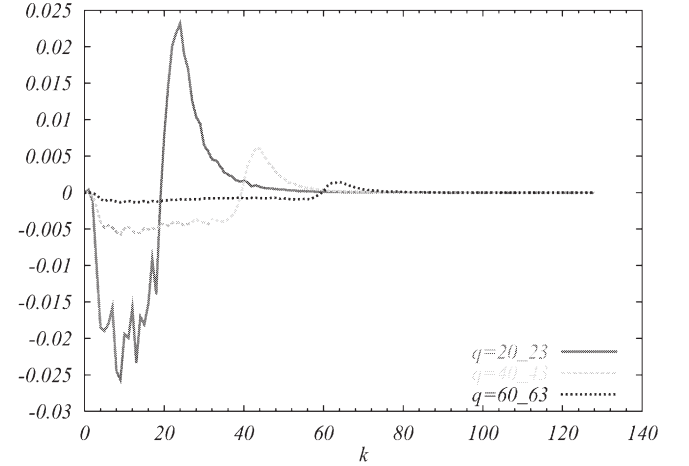


**Fig.2** Plot of  $T_{ub}(k, q)$  for  $q = 20-23, 40-43, 60-63$  when  $H^M = 0$  at  $t = 0$ . The energy is transferred nonlocally.

#### References

- 1) D. Biskamp, "Magnetohydrodynamic turbulence", Cambridge University Press, (2003).
- 2) T. Hatori, J. Phys. Soc. Jpn. **53**, 2539 (1984).
- 3) H. Kurosawa. *Energy transfer among wavenumbers in magnetohydrodynamic turbulence*, NIT Master Thesis (in Japanese) (2006).



### §31. Multifractal Characterization of L- and H-mode Plasma Edge Turbulence

Rajković, M. (Vinca, Serbia), Dendy, R.O. (UKAEA), Škorić, M.M.

Measurements of the edge plasma turbulence obtained by the reciprocating Langmuir probe are analyzed and tested for self-similarity, long-range dependence and multifractality. We provide evidence for the multifractal character present in both L- and dithering H-mode data and also provide support for the local self-similarity in the case of L-mode. Further, we claim that neither L-mode nor H-mode data seem to exhibit self-similarity in the global sense. Moreover, we use several fractal and multifractal measures in addition to some non-standard statistical techniques in order to characterize the L and H-mode fluctuations. Widely used methods [1] of characterization of plasma turbulence time series include probability distribution function (PDF), autocorrelation function (ACF) and power spectrum (PS), while recently several papers address the topic of possible long-range dependence in the edge turbulence of toroidal magnetic confinement devices. Upon getting a Hurst exponent in the range  $0.5 < H < 1$ , the authors often make conclusions concerning the global self-similar properties, particularly in relationship with the Self-organized criticality (SOC) models [1-2]. Still, self-similarity is a strong statistical property and the process  $X = \{X(t), t \in \mathbb{R}\}$  is self-similar with parameter  $H > 0$  (the so called H-ss process) if  $X(0) = 0$  and  $X(at) = a^H X(t)$ . We show that the datasets from two different confinement regimes in MAST (Mega Amp Spherical Tokamak, UKAEA, Culham) are locally self-similar (i.e. self-similar for sufficiently small time scales). We also show that the L-mode data, in agreement with the previous analysis [1], exhibit long range property in the sense that the spectral density  $S(\omega)$  satisfies the following relationship  $S(\omega) \sim C_f |\omega|^{-\alpha}$ , as  $\omega \rightarrow 0$ , ( $0 < \alpha < 1$ ,  $C_f \neq 0$ ). Again, consistently with [1], the particular H-mode does not show long range dependence property. However, we also give evidence that the processes under study in two datasets do not seem to be globally self-similar.

With the use of the wavelet analysis, we indicate that both the L- and H-mode regimes seem multifractal so that no single parameter (so called Hölder exponents) might be necessary to characterize the data [3-4], corresponding to various confinement conditions. Diagrams presented in Fig. 1, clearly illustrate that the confinement regimes under study are multifractal processes, and hence cannot be characterized by a single Hölder (Hurst) exponent. Specifically, none of the Linear multiscale diagrams have approximately constant  $h_q$  for positive  $q$  (a sign of global scaling). A Hölder exponent between 0 and 1 indicates that the signal is continuous but not differentiable at the considered point, and the lower the exponent the more irregular the signal is. Hence, all modes are characterized by continuous but not differentiable signals. The meaning

of the above mentioned analysis is as follows. Local exponents  $h$  are evaluated through the modulus of the maxima values of the wavelet transform at each point in the time series. Then, the scaling partition function  $Z_q(a)$  is defined as the sum of the  $q$ -th powers of the local maxima of the modulus of the wavelet transform coefficients at scale  $a$ . For small scales, the following relationship is expected  $Z_q(a) \sim a^{-\tau(q)}$ . For certain values of  $q$ , the exponents  $\tau(q)$  have familiar meanings. In particular  $\tau(2)$  is related to the scaling exponent of power spectra,  $S(f) \sim 1/f^\beta$ , as  $\beta = 2 - \tau(2)$ . For positive  $q$ ,  $Z_q(a)$  reflects the scaling of the large fluctuations and strong singularities, while for negative  $q$ ,  $Z_q(a)$  reflects the scaling of the small fluctuations and weak singularities [4]. Hence, the scaling exponent  $\tau(q)$  may reveal much about the underlying dynamics.

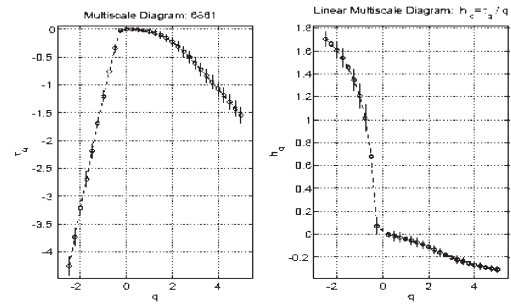


Fig. 1 Multiscale and Linear multiscale diagram for 6861 L- mode. No flatness, due to lack of global self-similarity.

Monofractal signals display linear  $\tau(q)$  spectrum,  $\tau(q) = qH - 1$ , where  $H$  is the global Hurst exponent. For multifractal signals  $\tau(q)$  is a nonlinear function  $\tau(q) = qh(q) - D(h)$ , where  $h(q) \equiv d\tau(q)/dq$  is not constant,  $D(h)$  is the fractal dimension  $D(h) = qh - \tau(q)$ . In order to distinguish between low and high confinement regimes we turn to the different multifractal properties such as regularization dimension, local Hölder exponents, various multifractal spectra etc. A typical example is pointwise Hölder exponents, measuring the scaling behavior at infinite resolution. The Large Deviation Spectrum; coarse grained Hölder exponents measuring scaling at finite resolution, points to discernible differences between the confinement regimes. Based on our results, it seems that two studied signals are the product of small-scale stochastic plasma turbulence, without large-scale events; consistent with Dudson et al [1]. Finally, we present a method based on the wavelet analysis which may characterize the long-range property, simultaneously with the intermittent property. In addition, it quantifies the degree of intermittency, enabling an efficient way of discerning between different intermittency regimes.

#### References

- 1) B. D. Dudson et al. PPCF 47 (2005) 901.
- 2) B. Ph. van Milligan, et al., Phys. Plasma, 5 (1998) 3632
- 3) A. Komori et al., Phys. Rev. Lett. 73 (1994) 660
- 4) M. Rajkovic, M.M. Skoric, NIFS Report No 833 (2006)



### §32. A Signature of Wave Collapse in the GNLS Model of Plasma Turbulence

Mančić, A., Maluckov, A. (University of Niš, Serbia),  
 Hadžievski, Lj. (Vinča Institute, Serbia),  
 Škorić, M.M., Kono, M. (Chuo University)

A term “wave collapse” is used to describe the formation of the singularity in a finite time in mathematical models describing nonlinear wave systems. It is one of the basic phenomena in nonlinear physics. The singularity also signals the limit of the model validity. It was predicted that the presence of the nonlocal nonlinearity eliminates collapse in the system governed by a nonlocal NLS equation.[1-5]

We discuss the wave collapse existence in the system described by the generalized nonlinear Schrödinger (GNLS) type of equation with two additional nonlocal nonlinear terms [2]:

$$i\frac{\partial A}{\partial t} + \frac{1}{2}A_{xx} + \frac{3}{16}|A|^2 A - \frac{1}{8}(|A|^2)_{xx}A + \frac{1}{48}(A^2)_{xx}A^* = 0, \quad (1)$$

where  $A$  is vector potential envelope. This equation models nonlinear coherent structures in, e.g.: ETG turbulence [5] and weakly relativistic laser-plasma interaction [2-4].

Localized stationary solution of (1) is found in a form of a moving soliton with 3 conserved quantities[3]:

$$A = \rho(u)\exp[i\theta(u) + i\lambda^2 t], \quad (2)$$

where  $u = x - vt$ , and  $v$  is the soliton velocity. After introducing the ansatz (2) in Eq.(1), first integration for localized boundary conditions ( $\rho(u), \rho(u)_u, \rho(u)_{uu} \rightarrow 0$  for  $u \rightarrow \pm\infty$ ) gives the soliton amplitude equation:

$$(\rho_u)^2 = \left(2\lambda^2 - v^2 - \left(\frac{3}{16} - \frac{v^2}{12}\right)\rho^2\right)\rho^2 \left/ \left(1 - \frac{5}{12}\rho^2\right) \right. \quad (3)$$

Singular point is  $\rho_c = \sqrt{12/5}$ , while region  $\rho < \rho_c$  corresponds to a bright soliton. Additional integration of (3) yields a moving soliton solution in implicit form, with the maximum soliton amplitude  $\rho_0^2 = (2\lambda^2 - v^2)/(3/16 - v^2/12)$ . For  $\rho_0 \ll \rho_c$  the soliton profile is secant hyperbolic, like the soliton of the standard cubic NLS equation. When  $\rho_0$  approaches the value of  $\rho_c$ , the soliton profile steepens and transits toward the pointed, cusp type of a profile (Fig.1).

Stability analysis by using Vakhitov-Kolokolov stability criterion shows that moving EM solitons are stable in the region  $\lambda < \lambda_s$ , where  $\lambda_s$  corresponds to the maximum value of photon number (wave energy) for a given velocity. A set of direct numerical simulations of the nonlinear model (1) has been performed in order to investigate soliton dynamics [3]. Initially perturbed stable solitons exhibit long lived oscillating behavior of the breather type, with the amplitude excursion from the initial value increasing as the level of perturbation grows, eventually leading to a rapid aperiodic growth of the amplitude. This continues up to the point when the amplitude reaches the critical value, creating a highly unstable cusp structure. Due to the coincidental break up of the numerical scheme, we were unable to follow the dynamics of this structure further.

The process above is similar to the initial stage of the collapse phenomenon, which is predicted in the case of the GNLS equation [4]. To conclude if the unstable cusp soliton structure in above model will collapse or break up, we have attempted some further analyses:

1) *Bifurcation analysis*: This approach is analogous to the one of Ref. [6]. Stability analysis shows that depending on parameters  $\lambda, v$  two types of bifurcation are possible: tangential bifurcation that corresponds to stable soliton solutions, and Hopf-Andronov (HA) bifurcation. The cascade of HA bifurcations can be the origin of complex behavior [7] of our system (collapse as one of possible scenarios). However the additional studies are needed to make a definite conclusion about the collapse.

2) *Linear stability analysis* around the cusp solution: Similar to Ref. [8], analysis of the simplified system (without the last term in Eq.(1)) is performed. It is shown that different families of solution are possible depending on the initial conditions and system parameters. One of them is the localized mode of a cusp type, as found in our model. This mode reminds of the so-called nonlinear explosion mode [8]. However, the strict conclusion about the collapse of the full system (1) is still missing.

3) *Virial theorem*: In the case of the NLS equation (first three terms in (1)), Virial theorem gives a sufficient condition for the collapse and an estimate of the collapse threshold [8]. However, we cannot reach that kind of conclusion, due to a singularity at the critical amplitude (3).

At present, the issue of wave collapse in GNLS model remains unresolved. One of the possible solutions is the inclusion of the thermal and higher order dissipative effects in the model. These effects will eventually saturate the system and remove a mathematical singularity to fill the gap in our understanding of its long time behavior. However turbulence model based on (1) may not be well founded [5]

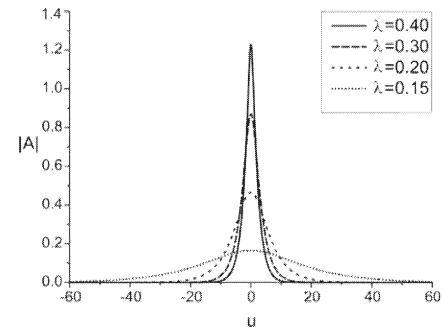


Fig.1. Soliton profile steepening ( $v=0.2$ )

#### References

- 1) Bang, O., et al, Phys. Rev. E **66**, (2002) 046619
- 2) Hadžievski, Lj., et, Phys. Plasmas **9**, (2002) 2569
- 3) Mančić, A., et al, Phys. Plasmas **13**, (2006) 052309
- 4) Maluckov, A., et al., in JPS meeting (Ehime, 2006)
- 5) Gürçan, O. D., et al, Phys. Plasmas **11**, (2004) 572
- 6) Pelinovsky, D., E., et al, Phys. Rev. E **53**, (1996)
- 7) Wiggins, S., “Introduction to Applied Nonlinear Dynamical Systems and Chaos”, (1990)
- 8) Yajima, N., et al, J. Phy. Soc. Japan **52**, (1983) 3414
- 9) Kuznetsov, E., A., Chaos **6**, (1996) 381

### §33. Low-Frequency Instabilities Due to Flow Velocity Shear in Magnetized Plasmas

Kaneko, T., Saito, H., Hatakeyama, R. (Dept. Electronic Eng., Tohoku Univ.),  
Ishiguro, S.

Sheared plasma flows parallel to magnetic field lines are recognized to play an important role in generation and suppression of low frequency plasma instabilities. According to the experimental results, it is demonstrated that the ion-acoustic, ion-cyclotron, and drift-wave instabilities are excited and suppressed by the parallel flow velocity shear, where the destabilizing and stabilizing mechanisms are well explained by the kinetic theory.<sup>1)</sup> In the experimental investigation, however, it is difficult to change the shape and the location of the velocity shear, and the plasma parameters such as the ratio of the ion to electron temperature, which are very effective in the growth rate of the shear driven instabilities.

In this sense, a particle simulation is very useful method to clarify the effects of the velocity shear, because the simulation can easily set these parameters. From the viewpoint of investigating the general properties of the velocity shear driven instabilities, the simulation should be performed in the three dimensional (3D) system because in most cases waves propagate obliquely or perpendicularly to the direction of the flow velocity gradient under the influence of the velocity shear.

In our work, a three dimensional electrostatic particle simulation with a periodic boundary model is performed,<sup>2)</sup> where an external uniform magnetic field points to the positive  $z$  direction. Electrons and ions are uniformly loaded in the system at  $t=0$ . The system sizes  $L_x$ ,  $L_y$  and  $L_z$  are  $128\lambda_{De}$ ,  $128\lambda_{De}$  and  $512\lambda_{De}$ , respectively. Here,  $\lambda_{De}$  is the Debye length. The number of electrons and ions per unit cell is 64. The ion to electron mass ratio  $m_i/m_e$  is fixed at 400. The ratio of the electron cyclotron to electron plasma frequency is  $\omega_{ce}/\omega_{pe} = 5$  and the ion to electron temperature ratio is  $T_i/T_e=0.5$ . The time step width  $\Delta t$  is  $0.1\omega_{pe}^{-1}$ . The parallel ion flow velocity shear is introduced by changing the ion flow velocity  $v_{di}$  spatially in the  $x$  direction as shown in Fig. 1, where  $v_{te}$  is the electron thermal speed. The strength of the velocity shear is changed by varying a spatial gradient of the ion flow velocity in the shear region (from the profile A to B) or the velocity difference between the central and peripheral regions (from the profile B to C).

Figure 2 shows time evolutions of the real (solid line) and the imaginary (dashed line) parts of the spatial Fourier mode of the ion density fluctuation  $\tilde{n}_i/\bar{n}_i$  as a function of the velocity shear strength, which is determined by the profiles of the ion flow velocity shown in Fig. 1. These modes are measured in the velocity shear region ( $32 < x/\lambda_{De} < 36$ ), which is indicated by dotted lines in Fig. 1.

According to the frequency spectra of these modes, the observed waves are identified as an obliquely propagating ion-acoustic instability. The fluctuation amplitude is found to increase with increasing the shear strength ( $A \rightarrow B$ ), but the instability is gradually stabilized when the shear strength exceeds a critical value ( $B \rightarrow C$ ), which is consistent with the experimentally obtained results.<sup>1)</sup>

In addition, these results clarify that the instability is characterized by the velocity shear strength independently of the velocity profile which is determined by the variation of the spatial velocity gradient or the velocity difference.

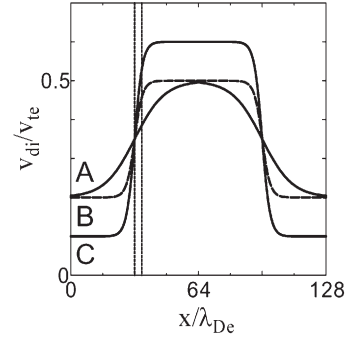


Fig. 1. Profile of ion flow velocity  $v_{di}$  in the  $x$  direction.

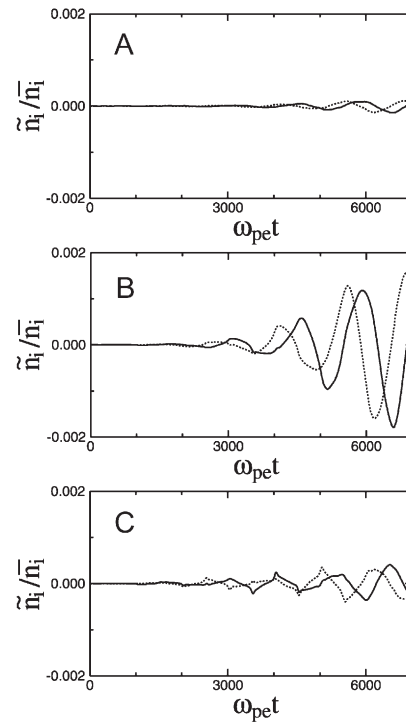


Fig. 2. Time evolutions of the real (solid line) and the imaginary (dashed line) parts of the spatial Fourier mode of the ion density fluctuation  $\tilde{n}_i/\bar{n}_i$  as a function of the velocity shear strength.

#### Reference

- 1) Kaneko, T. *et al.* : Phys. Rev. Lett. **90** (2003) 125001.
- 2) Matsumoto, N. *et al.* : J. Plasma Fusion Res. SERIES, **6** (2004) 707.

### §34. Molecular Dynamics Simulation for Structure Formation of a Single Polymer Chain in Solution: Local Orientational Correlation

Fujiwara, S., Hashimoto, M., Itoh, T. (Kyoto Inst. Tech.)

The structure formation of polymer chains such as polymer crystallization and microphase separation of block copolymers has so far been extensively studied. Since polymer chains have many internal degrees of freedom, they show diverse static and dynamical structures. Because of their structural diversity, polymeric materials have various physical properties. Over the last decade, many studies have been carried out in relation to the polymer crystallization by molecular dynamics (MD) simulation. However, owing to the large computational effort necessary, few MD works have been made on the structure formation of polymer chains immersed in a bath of solvent molecules. The purpose of this work is to clarify, at the molecular level, the mechanisms of the structure formation of a single polymer chain in solution. In particular, our concern is to investigate the effect of solvent molecules on the structure formation of a polymer chain. To this end, we carry out the MD simulations of a single polymer chain immersed in a bath of solvent molecules and analyze the formation process of the orientationally ordered structure during quenching.

The computational model is the same as that used in our previous works<sup>1),2)</sup>. We consider a linear polymer chain with 500 methylene (CH<sub>2</sub>) groups immersed in 3747 *n*-alkanes with six methylene groups. The methylene group is treated as a united atom. The united atoms interact via bonded potentials (bond-stretching, bond-bending and torsional potentials) and a non-bonded potential [12-6 Lennard-Jones (LJ) potential]. The atomic force field used here is the DREIDING potential<sup>3)</sup>. The equations of motion for all atoms are solved numerically using the velocity Verlet algorithm. We use the combination of a constant-temperature method ('ad hoc' velocity scaling method) and a constant-pressure method (Andersen's method). The external pressure is set to 0.1 MPa, which corresponds to atmospheric pressure. We apply the periodic boundary conditions. The MD simulations are performed as follows. At first, we provide a randomly distributed conformation of polymer solution in thermal equilibrium at high temperature ( $T = 550$  K). The system is then quenched to several lower temperatures ( $T = 300, 350, 400$  and  $450$  K). A simulation of 10 ns is carried out at each temperature.

We analyse the local orientational correlation to investigate the effect of solvent molecules on the structure formation of a polymer chain<sup>4)</sup>. The local orientational correlation functions are defined by

$$p_2^{\text{pp}}(r) = \langle [3 \cos^2 \psi(r) - 1]/2 \rangle_{\text{pp}} \quad (1)$$

for the correlation in the polymer chain,

$$p_2^{\text{ps}}(r) = \langle [3 \cos^2 \psi(r) - 1]/2 \rangle_{\text{ps}} \quad (2)$$

for that between the polymer chain and solvent molecules and

$$p_2^{\text{ss}}(r) = \langle [3 \cos^2 \psi(r) - 1]/2 \rangle_{\text{ss}} \quad (3)$$

for that between solvent molecules, where  $\psi(r)$  is the angle between two chord vectors separated by the distance  $r$ . The chord vector is defined as the vector formed by connecting centers of two adjacent bonds along chain molecules. The averages  $\langle \cdots \rangle_{\text{pp}}$ ,  $\langle \cdots \rangle_{\text{ps}}$  and  $\langle \cdots \rangle_{\text{ss}}$  are taken for pairs of chord vectors within the separation  $r \sim r + \Delta r$ . The subscripts 'pp', 'ps' and 'ss' respectively denote the average over pairs of chord vectors in the polymer chain, the average over pairs of the chord vector in the polymer chain and that in solvent molecules and the average over pairs of chord vectors in solvent molecules. Note that we impose the restriction  $|i - j| > 10$  for the two chord vectors  $i$  and  $j$  in the calculation of  $p_2^{\text{pp}}(r)$  to eliminate the correlation of the nearby chord vectors along the polymer chain. We show, in Fig. 1, the local orientational correlation functions  $p_2^{\text{pp}}(r)$ ,  $p_2^{\text{ps}}(r)$  and  $p_2^{\text{ss}}(r)$  at  $T = 300$  K. This figure indicates that there is a prominent orientational correlation in the polymer chain while there exists only a short-range orientational correlation between solvent molecules. It is also found from the correlation function  $p_2^{\text{ps}}(r)$  between the polymer chain and solvent molecules that the second and third peaks as well as the first peak can be observed although the intensity of the peaks decreases with the distance  $r$ .

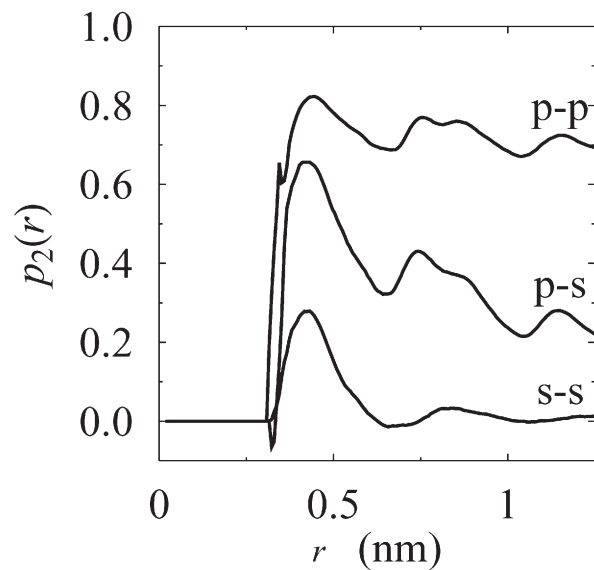


Fig. 1. The local orientational correlation function at  $T = 300$  K. p-p:  $p_2^{\text{pp}}(r)$ , p-s:  $p_2^{\text{ps}}(r)$  and s-s:  $p_2^{\text{ss}}(r)$ .

#### References

- 1) Fujiwara, S. and Sato, T., Comput. Phys. Commun. **147**, (2002) 342.
- 2) Fujiwara, S. and Sato, T., J. Macromol. Sci. - Phys. **B42**, (2003) 455.
- 3) Mayo, S.L. *et al.*, J. Phys. Chem. **94**, (1990) 8897.
- 4) Fujiwara, S. *et al.*, J. Phys. Soc. Jpn. **75**, (2006) 024605.

§35. Three Processes of the Reaction between a Hydrogen Atom and Graphene

Ito, A. (Nagoya Univ.),  
Nakamura, H.

The reaction among a hydrogen atom and graphite appears in various scenes, for example plasma and a carbon wall interaction on the divertor of a nuclear fusion device. When the hydrogen plasma do incident into the carbon wall,  $\text{CH}_x$ ,  $\text{C}_2\text{H}_x$  and  $\text{H}_2$  are generated by the chemical reaction. However their creation mechanism is not known because the chemical reaction is complicated. We studied the elementary process of the chemical reaction the hydrogen atom and the graphite.

For the elementary process, the minimal structure is selected in each. The one hydrogen atom is substituted for a hydrogen plasma ion at the request of the model potential. The carbon wall is replaced by a graphene. The graphene is minimal molecule in the graphite material. It has a two dimensional structure. We set the graphene which is size of  $2.13 \text{ nm} \times 1.97 \text{ nm}$  on the  $z = 0 \text{ \AA}$  plain formed by the x-axis and y-axis. The periodic boundary condition is imposed for the direction of the x-axis and y-axis. The carbon atoms of the graphene obey the Maxwell-Boltzmann distribution law at 300 K initially. After that, the hydrogen atom do incident from the position of  $z = 4 \text{ \AA}$ . The simulation is repeated with the change of the incident point randomly.

The classical molecular dynamics simulation was adopted in present work. We selected the Brenner's REBO potential<sup>1)</sup> as the model of the interaction between hydrogen atoms and carbon atoms. And, we modified the model potential to represent the chemical reaction. The second order symplectic integration was used.

We discovered that there are three sort of the reaction between the hydrogen atom and the graphene<sup>2)</sup>. One is an absorption process. The hydrogen atom creates a covalent bond with a nearest carbon atom and oscillates. The nearest carbon atom projects from the flat surface of the graphene (See Fig. 1). It is called overhang. The others are a reflection process and a penetration one. The former means that the incident hydrogen atom bounces off the graphene and leaves for  $z > 0$ . The latter is that the incident hydrogen atom goes through the hexagonal hole of the graphene toward  $z < 0$ . As a simulation result, Figure 2 shows the reaction rates of the three processes. The reactions depend on the incident energy of the hydrogen atom. When the incident energy is smaller then 1.0 eV, the hydrogen atom is reflected by the  $\pi$ -electron effect. When

the incident energy is greater than 1.0 eV, the potential energy in terms of the overhang classifies the reaction into the three processes.

Acknowledgments

The work is supported partly by the National Institutes of Natural Sciences undertaking for Forming Bases for Interdisciplinary and International Research through Cooperation Across Fields of Study, and partly by Grand-in Aid for Exploratory Research (C), 2006, No. 17540384 from the Ministry of Education, Culture, Sports, Science and Technology.

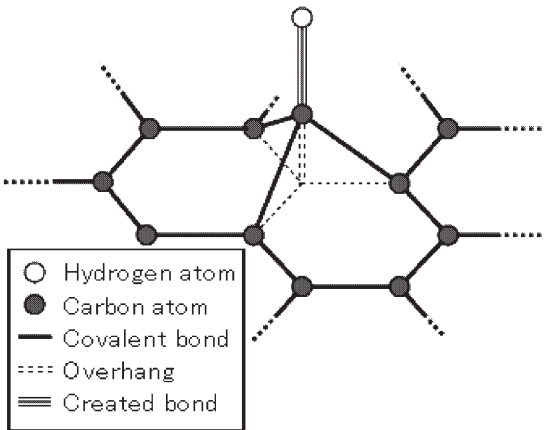


Fig. 1. The overhang of the nearest carbon atom by the hydrogen absorption.

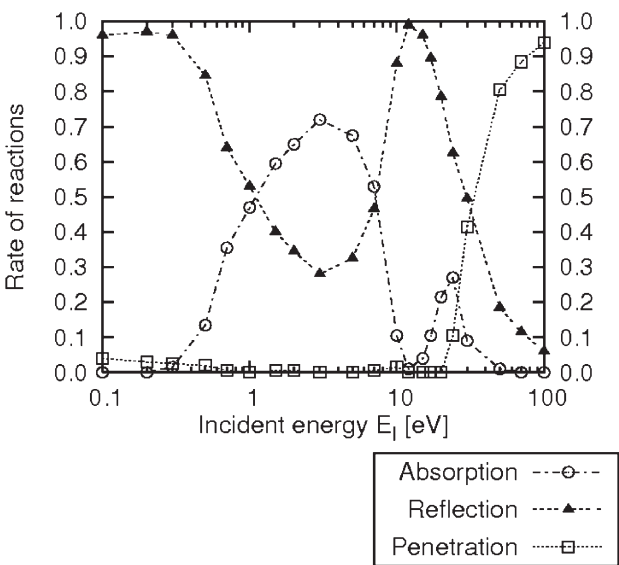


Fig. 2. The rates of the absorption, the reflection and the penetration.

Reference

1) Brenner, D. W. et al.: Phys. Rev. B **42** (1990) 9458.  
2) Ito, A. and Nakamura, H.: J. Plasma Phys., accepted.



### §36. Quantum Nernst Effect

Nakamura, H.,  
Hatano, N. (Univ. of Tokyo),  
Shirasaki, R. (Yokohama Nat'l Univ.)

We study the Nernst effect in the regime of the ballistic conduction. Using a simple argument based on edge currents, we predict that, when the chemical potential is located between a pair of Landau levels, (i) the Nernst coefficient is strongly suppressed and (ii) the thermal conductance is quantized with  $2(\pi k)^2 T/3h$ .

The Nernst effect in a bar of conductor is the generation of a voltage difference in the  $y$  direction under a magnetic field in the  $z$  direction and a temperature bias in the  $x$  direction. Each of the left and right ends of the conductor is attached to a heat bath with a different temperature,  $T_+$  on the left and  $T_-$  on the right. An electric insulator is inserted in between the conductor and each heat bath, so that only the heat transfer takes place at both ends. A constant magnetic field  $B$  is applied in the  $z$  direction. Then the Nernst voltage  $V_N$  is generated in the  $y$  direction.

Our basic idea is illustrated in Fig. 1. Because there is no input or output electric current, an edge current circulates around the Hall bar when the chemical potential is in between neighboring Landau levels. The edge current along the left end of the bar is in contact with the heat bath with the temperature  $T_+$  and equilibrated to the Fermi distribution  $f(T_+, \mu_+)$  while running from the corner C4 to the corner C1. The edge current along the upper edge runs ballistically, maintaining the Fermi distribution  $f(T_+, \mu_+)$  all the way from the corner C1 to the corner C2. It then encounters the other heat bath with the temperature  $T_-$  and equilibrated to the Fermi distribution  $f(T_-, \mu_-)$  while running from the corner C2 to the corner C3. The edge current along the lower edge runs ballistically likewise, maintaining the Fermi distribution  $f(T_-, \mu_-)$  all the way from the corner C3 to the corner C4. The Nernst voltage  $V_N = \Delta \mu / e \equiv (\mu_+ - \mu_-)/e$  is thus generated, where  $e$  ( $< 0$ ) denotes the charge of the electron.

First, the difference in the chemical potential,  $\Delta \mu$ , is of a higher order of the temperature bias  $f\epsilon T$ , because the number of the conduction electrons is conserved. The Nernst coefficient  $N = \Delta \mu / \Delta T \times L/(W|e|B)$  hence vanishes as a linear response. Second, the heat current  $I_Q$  in the  $x$  direction is carried ballistically by the edge current along the upper and lower edges. The edge current does not change much when we vary the magnetic field  $B$  as long as the chemical

potential stays between a pair of neighboring Landau levels. The thermal conductance  $G_Q = I_Q / \Delta T$  hence has quantized steps as a function of  $B$ .

We demonstrate the above under the confining potential  $V(y) = 0$  for  $|y| < w/2$  and  $V(y) = m\omega_0^2(|y| - w/2)^2/2$  for  $w/2 < |y| < W/2$  with the effective mass  $m = 0.067m_0$  with  $m_0$  being the bare electron mass, the sample size  $L = 20 \mu\text{m}$ , the potential width  $W = 20 \mu\text{m}$  with  $w = 16 \mu\text{m}$ , the potential height  $V(\pm W/2) = 5.0\text{eV}$ , and the chemical potential  $\mu = 15\text{meV}$ , or the carrier density  $n_s = 4.24 \times 10^{15}\text{m}^{-2}$ . Numerical calculation yields  $f(T, \mu)$  the Nernst coefficient and the thermal conductance as in Fig. 2. We see that our predictions are indeed realized at low temperatures. We also note that the Nernst coefficient is negative in the present case.

The precise forms of the peaks and the risers of the steps in Fig. 2 may be different from the reality. This is because our argument using the edge currents is not applicable when the chemical potential coincides with a Landau level, namely when  $\mu = (n+1/2)(\hbar/2\pi)\omega_c$ , or  $1/B = (n+1/2)(\hbar/2\pi)|e|/m\mu$ . There the heat current is carried by bulk states as well as the edge states. We then have to take account of impurities and possibly electron interactions.

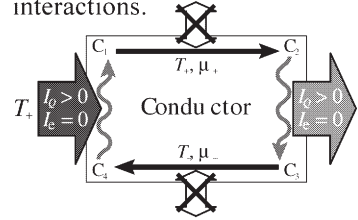


Fig. 1: A schematic view of the dynamics of  $T.$  electrons in a Hall bar under the setup for the Nernst effect.

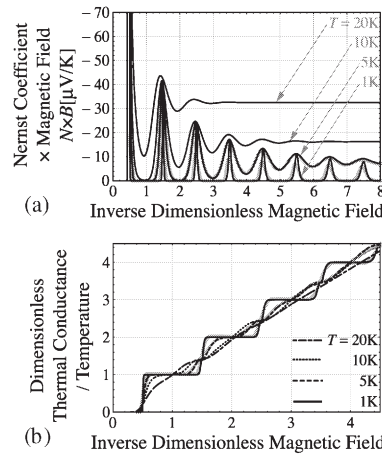


Fig. 2: Scaling plots of (a) the Nernst coefficient against the inverse magnetic field, and (b) the thermal conductance against the inverse magnetic field, at  $T = 1, 5, 10$  and  $20\text{K}$  for  $1\text{T} < B < 20\text{T}$ .

#### References

- [1] Nakamura, H., Hatano, N., Shirasaki, R.: Solid State Comm., 135 (2005)510.
- [2] Shirasaki, R., Nakamura, H., Hatano, N.: e-Journal of Surface Science and Nanotechnology, 3, (2005) 518.

### §37. A Complementary Fluid Method in $\delta f$ Particle Simulation

Todo, Y.

In  $\delta f$  particle simulation, the distribution function is represented by the sum of a reference distribution and a variation distribution, often represented by  $f_0$  and  $\delta f$ , respectively. In the  $\delta f$  method, Lagrangian markers (macro particles) are employed to estimate  $\delta f$ , but not the total distribution function  $f=f_0+\delta f$ . In particle simulations of plasmas, the number of Lagrangian markers is much smaller than that of real plasma particles. Thus, we cannot eliminate the errors in the Monte Carlo estimates with Lagrangian markers. The errors in the estimate lead to “numerical noise” in particle simulations. In the  $\delta f$  method, as contribution from  $f_0$  is calculated accurately, the errors in the estimate are in proportion to  $\delta f$ . If  $|\delta f/f_0| \ll 1$ , the  $\delta f$  method significantly reduces the numerical noise compared to the total  $f$  method.

A drawback of the  $\delta f$  method is that conservation properties, i.e., the conservation of particle, momentum, and energy, are not guaranteed, although a well-chosen initial distribution of Lagrangian markers improves them. When the distribution is divided into  $f_0$  and  $\delta f$ , the time evolution of  $\delta f$  is described by an advection term of  $\delta f$  and a linear source term associated with  $f_0$ . In the  $\delta f$  method,  $\delta f$  is approximated by the Klimontovich distribution function  $\delta f_K$  using Lagrangian markers. In the time evolution of  $\delta f_K$ , the advection term of  $\delta f_K$  can be written in conservative form and does not violate the conservation properties. On the other hand, the linear source term, which is a Monte Carlo estimate in the  $\delta f$  method, violates the conservation properties.

A new simulation method that improves the conservation properties of  $\delta f$  particle simulation for the collisionless Boltzmann equation was presented [1]. In the new simulation method, errors in the Monte Carlo estimate of the source term are corrected with a complementary fluid model. An example of the complementary fluid model was presented for bump-on-tail instability. The simulation results are compared with those of the conventional  $\delta f$  method in Figs. 1 and 2. We see good conservation properties in the complemented simulation results. The absolute value of the total energy variation is less than  $8 \times 10^{-5}$  in the units of Fig. 1 for the complemented simulation. The time evolutions of the variations in total number of particles are compared in Fig. 2. We see an excellent conservation of particles for the complemented simulation, where the absolute value of the variation is  $10^{-13}$  in the units of Fig. 2. Momentum is also well conserved for the complemented simulation. Thus, it has been demonstrated that particle, momentum, and energy are well conserved with the new simulation method.

The  $\delta f$  simulation contains the correct value of the distribution function only at the phase space position of each

marker particle. The new method provides a way to estimate the response of the rest part of the phase space. When no marker particles are used in the complementary fluid simulation code, it works as a fluid code. When the kinetic effects are important only in a part of plasma, the rest part may be treated as a fluid. The complementary fluid method will enable seamless simulations of such kinetic-fluid complex plasmas.

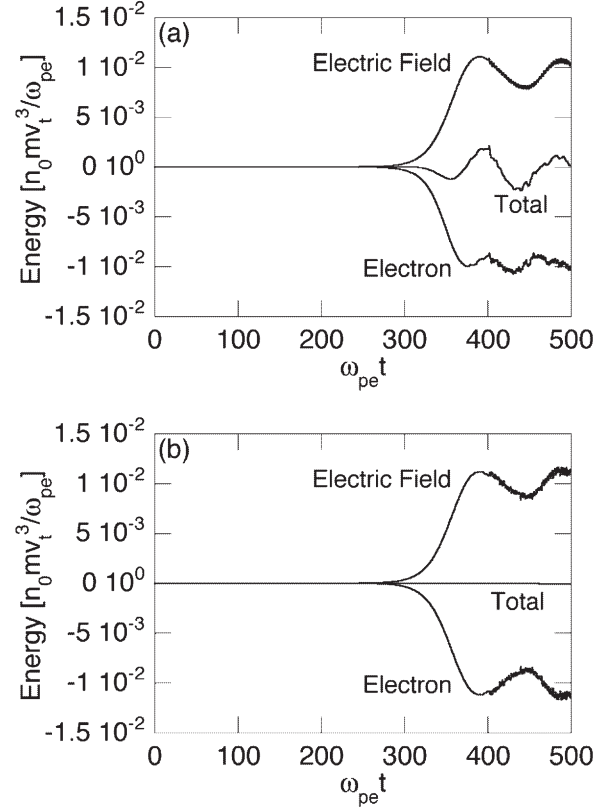


Fig. 1. Time evolution of the variations of electron kinetic energy, electric field energy and total energy in the simulation results (a) with the conventional  $\delta f$  method and (b) with the complementary fluid method.

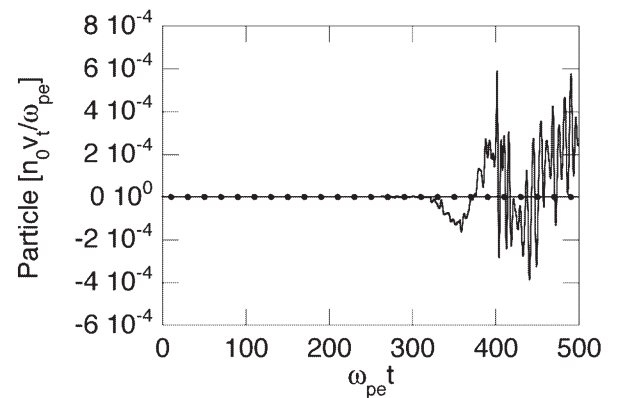


Fig. 2. Time evolution of the variations of total number of particles. The line with closed circles represents the simulation results with the complementary fluid method while the solid curve represents those with the conventional  $\delta f$  method.

[1] Y. Todo, J. Plasma Fusion Res. **81**, 944 (2005).

### §38. A Primal Coarse-Projective Integration Scheme in Multi-Scale Plasma Dynamics

Škorić, M.M., Maluckov, A. (University of Niš, Serbia),  
Ishiguro, S.

Multi-scale phenomena, such as, magnetic reconnection and turbulence are rather difficult to simulate because of the strongly interconnected physics of micro- and macro-scales. Over the past few years, a simulation framework called Equation-Free Projective Integration (EFPI) has been proposed and applied to a variety of multi-scale phenomena in engineering problems in which coarse-scale (macro) behavior can be obtained through short-time simulations within the fine-scale models (microscopic, stochastic, etc.) [1]. Recently, the first EPFI application to plasmas has been developed by Shay [2]. It studies propagation and steepening of a 1D ion acoustic wave with a particle in cell (PIC) code as a microscopic simulator in EPFI. Firstly, to initialize PIC, the macro variables are “lifted” to a fine microscopic representation. The PIC code is stepped forward for a short time, and the results are “restricted” or smoothed back to macro space. By numerical extrapolation, the time derivatives are estimated and coarse variable projected with a large step; the process is repeated.

Originally, the coarse-step forward in time was made by using only a small number of lower moments of the ion velocity probability density functions (PDF) [1]. It was found that the EFPI code can reproduce the PIC results. However, larger differences arise due to physics assumptions made in the lifting algorithm, specifically, that the ion PDF remains Maxwellian and that the plasma is quasi-neutral. More recent paper has discussed a generalization of Shay’s projective integration scheme [3] that estimates the joint  $x$ - $v$  phase space PDF using non-linear wavelet approximation.

As a rather simple alternative, we propose and implement a scheme based on a so-called, primal EPFI algorithm to simulate an ion acoustic wave paradigm including nonlinear plasma dynamics and kinetic effects. The micro-simulator is a standard version of 1D ES PIC code. The working hypothesis is that the ion motion could be assumed inherently coarse grained or “smoothed”, as compared to electron dynamics. Accordingly, we track individual ion orbits in time and simply extrapolate to project. A typical coarse projection time step, e.g. 100 times the micro-step, is still close to the intrinsic ion-time step. Moreover, we simply find a non-uniform ion density from projected ion orbits, and to lift ions, we actually just restart ion motion. Further, we track the electric potential and coarse grained average over the electron plasma period to extrapolate and project. We do not use any simplifying adiabatic approximation.

We perform a number of simulations within the same plasma variables range as in [2], also by varying the p-EFREE scheme parameters. Result for simulation snapshot at late time,  $t = 1.02$  (in ion periods) is given in Fig.1 for full PIC data and the p-EFREE code (black curve).

The smoothed variables, like particle density, PDF and even the ion phase space plots compare well. As expected, a discrepancy exists in the potential and electric field (not coarse) as a phase mismatch due to interruptive nature of the p-EFREE simulation cycle. Snapshots, provided at an earlier time, show better agreement. We also note that difference in particle densities, defies simple electron adiabatic approximation. Further, to check on conservation property of the scheme, in Fig. 2 we plot comparative time evolution of electron and ion kinetic energy and total energy for PIC and p-EFREE, in the total energy units. A phase mismatch-, time-lag in the ion kinetics, as compared to PIC, is now typically observed.

Some of preliminary results are already motivating. While the projection step was modest (20) the actual agreement with direct PIC is reasonable. We further point out that contrary to PIC simulations, which show standard numerical heating proportional to a number of time steps, in p-EFREE code the total energy remains fluctuating around the initial level; perhaps, an inherent potential of such methods in large-scale plasma simulation.

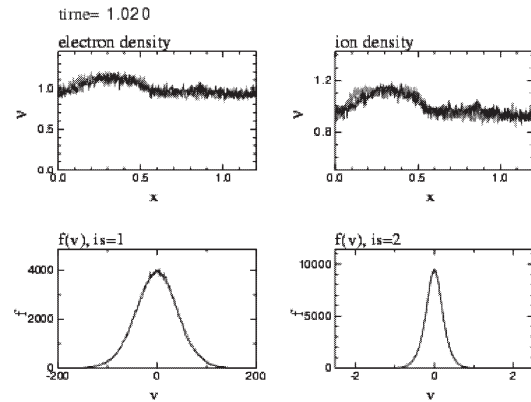


Fig.1. The snapshot at  $t=1.02$  for the electron and ion density and corresponding PDFs. Red / black lines are related to PIC and EPFI run, respectively.

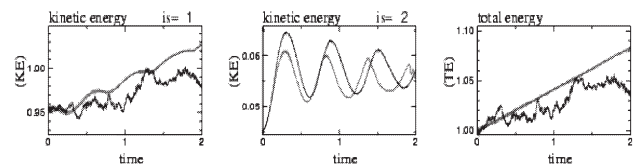


Fig.2. The kinetic energy of electrons (1) and ions (2) and total energy found from PIC (red) and EPFI (black).

#### References:

- 1) Kevrekidis, I., et al, Comm. Math. Sci. **1**, (2003) 715
- 2) Shay, M., Drake, J., Dorland W., J. Comp. Phys. (sub)
- 3) Maluckov, A., Stanchev, G, Drake, J., Dorland, W., Ishiguro, S., Škorić, M., in EPS Fusion (Rome, 2006)

§39. Orthonormal Divergence-Free Wavelet Analysis of Nonlinear Interactions in a Rolling-Up Vortex Sheet

Araki, K. (Okayama Univ. Sci.),  
Miura, H. (TCSC, NIFS)

Scale localness of nonlinear interactions in fully developed turbulence is one of the principal assumptions of Kolmogorov’s phenomenology[1]. We have developed orthonormal divergence-free wavelet basis[2] and applied it to the analysis of the dynamics of the Navier-Stokes equations

$$\frac{\partial \mathbf{u}}{\partial t} + (\mathbf{u} \cdot \nabla) \mathbf{u} = -\nabla P + \nu \Delta \mathbf{u}. \tag{1}$$

We have revealed that nonlinear inter-scale interactions supports the localness assumption[3]. Some analysis suggests that the nonlinear interaction may occur “locally” in the sense of spatial location[4],[5]. However the relation between the nonlinear interaction intensity and the coherent structure in turbulence was not so clearly understood. So we analyzed the nonlinear interaction in the definite vortical structures. We evaluate the nonlinear interaction defined by the formura

$$\langle j, \vec{l} | \mathbf{u} | k, \vec{l}' \rangle = \int \mathbf{u}_{j, \vec{l}} \cdot (\mathbf{u} \cdot \nabla) \mathbf{u}_{k, \vec{l}'} d^3 \vec{x} \tag{2}$$

where  $\mathbf{u}_{j, \vec{l}}$ ’s are wavelet decomposed velocity field and the indices  $j$  and  $\vec{l}$  imply the spatial scale and location of the analysing wavelet.

Numerical result is shown in Figure. We analyzed numerically the nonlinear interaction of rolling-up vortices which is generated by the instability of thin shear layer. We quantitatively verified the followings: (1) coherent structure is responsible for the energy transfer process; (2) both the forward and the backward tranfers are very active; (3) energy is transferred to the smaller scale as a whole, but the canceled amount is very large (see Table);

direction	amount	ratio to total
forward	$4.298 \times 10^{-5}$	8.6 times
backward	$3.796 \times 10^{-5}$	7.6 times
total (forward)	$5.025 \times 10^{-6}$	—

**Table:** the amount of nonlinear energy transfer between the scales  $j = 4$  and  $j = 5$ .

(4) energy transfer occurs “locally” in the sense of distance. 99% of energy transfer is due to nonlinear interaction within 2 grids of  $j = 4$  modes; (4’) interaction between distant wavelets are negligible (but much larger than the numerical errors); (5) wavelet energy intensity do not so well correspond to nonlinear transfer intensity.

[1]. U. Frisch, *Turbulence*, (Cambridge Univ. Press, Cambridge, 1995).

[2]. K. Araki *et al.*, NIFS-report NIFS-590 (1999);

[3]. K. Kishida, K. Araki, S. Kishiba, K. Suzuki, Phys. Rev. Lett., **83**, p.5487 (1999).

[4]. K. Kishida, K. Araki, "Orthonormal divergence-free wavelet analysis of spatial correlation between kinetic energy and nonlinear transfer in turbulence", in Y. Kaneda, T. Gotoh (Eds.), "Statistical Theories and Computational Approaches to Turbulence, Modern Perspectives and Applications to Global-Scale Flows", pp.248-259, (2002).

[5]. K. Araki, H. Miura, Ann. Rep. NIFS, April 2004-March 2005, p.362.

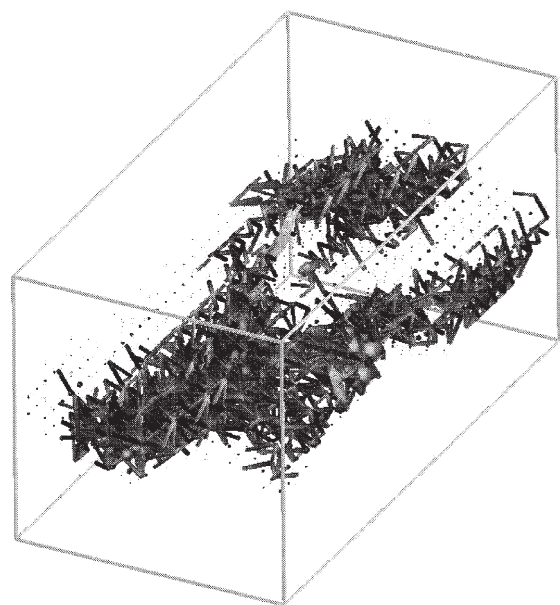


**Figure:** spatial distribution of “energy cascading” associated with the rolling-up of vortex layer.



#### §40. A Glassless Stereo-Type Visualization System for 3D MHD Real-Time Earth's Magnetosphere Simulator

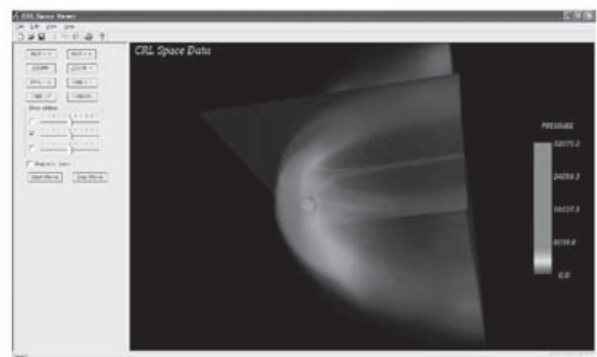
Den, M., Kuwabara, T. (Adv. Com.), Ogawa, T. (Kitazato Univ.), Tanaka, T. (Kyushu Uni.), Goncharenko, I. (3D inc.), Amo, H. (NEC)

We developed a 3D visualization system for our real-time Earth's magnetosphere simulator. On-line visualization of 3D magnetosphere data is still a challenge-able task in the community of researchers using numerical simulations because of relatively large simulation data sizes and high requirements imposed on processing and rendering time. The task is becoming more difficult if one takes into account the fact that the simulated data are non-uniformly distributed, while the standard graphical procedures require the data given in 3D rectilinear grids for fast rendering. We describe a 3D visualization system for volumetric rendering of magnetic pressure and magnetic field lines with output on standard and glassless stereo-displays. The core of the system is the fast 3D-gridding methods simplifying the graphical rendering.

There are three main steps in the dataflow scheme:\* original data transfer via the network;\* preprocessing (3D-gridding and smoothing);\* 3D scene rendering at the client sites. 3D rendering includes volume/iso-surface rendering, 3D magnetic field line rendering, layout and

annotation display. The whole rendering time depends on the selected methods of volume rendering (software-based ray casting or 2D-texturing done by OpenGL), density of magnetic field lines calculated by Runge-Kutta integration, and the size of preprocessed 3D-grids. Typically, with high-quality 3D-gridding, slight smoothing by fast 3D Gaussian filter, the usage of OpenGL-based volume rendering method gives sufficient visual quality. The whole OpenGL system is based on VTK 4.2 on top of OpenGL, with a thematic core graphical library developed especially for magnetosphere visualization. Other part of software includes network support, stereographic tools, preprocessing library, and GUI. All the rendering methods rely on fast 3D-gridding procedure described in our paper.

The partially cropped volume of the plasma pressure is shown in Figure 1.



With the system, it is possible to visualize high-quality graphical scenes including volumes, surfaces, and streamlines at a frequency rate sufficient for on-line monitoring through standard and glassless stereo-displays.

§41. Construction of Seamlessly Integrated System between Virtual Environment and Numerical Simulation Environment

Tamura, Y., Nakamura, H.,  
Kageyama, A. (Earth Simulator Center),  
Sato, S. (Earth Simulator Center)

In numerical simulation research, visualization is indispensable method now. Virtual reality technology is also very effective for visualizing numerical data, especially for visualizing complex and large-scale numerical simulation data. But virtual reality system is not friendly for simulation researchers, since computer for simulation is different from visualization computer in general. Especially in immersive virtual reality system (such as the CompleXcoope [1-2]) the researcher cannot simulate and analyze simulation result in one space, since they cannot use keyboard and sit before CRT.

So in this research, we propose seamless and interactive simulation environment by network communication. Under this environment, the researchers need not to recognize these two computers and can do computer simulation and analyze the result interactively.

i) Network Configuration

This seamless integrated system between the compute for numerical simulation and the computer for visualization is accomplished by socket communication (client-server model). In this system, not only numerical simulation result and simulation model, but also the position of observers and actions (e.g. drawing new isosurface, changing magnification) in remote sites, are shared. This system is very simple, but very effective since we cannot communicate with any researcher in any remote site without recognizing what he

looks at and is interested in.

At first, the simulation results are sent to the server process every output cycle, which is defined in the simulation program. If the observer, in the CompleXcoope system, changes some simulation parameters, these information is sent to the server and this server sends information to the calculating server. In the computer for the numerical simulation is restarted the numerical simulation by new parameters. By this system, the observer can simulate interactively without getting out.

ii) Estimation of data transfer rate

For estimating the data transfer rate of the system, we connected the computer for numerical simulation and the computer for the virtual reality system through 100Mbyte LAN. Fig.1 shows the result of estimation. This data shows that no data is lost if the transfer data size is under about 4000Kbyte/sec in this network environment. And the data packet size is not correlated with the success rate of data transfer. So by defining the packet size and total transfer data size per second from the computer for numerical simulation properly, the user can visualize in the CompleXcoope system smoothly.

(iii) Conclusion

We developed seamlessly integrated environment. This system enables user of virtual reality system to visualize in the immersive projection display (virtual reality system), calculating with remote computer.

In addition to this, the result of numerical simulation can be shared among remote sites, and the user can visualize and communicate in real time by network communication.

[1] A. Kageyama, Y. Tamura and T. Sato, Prog. Theo. Phys. Supplement 138 (2000).  
[2] Y. Tamura, et al},., Comput. Phys. Communications 142 (2001).

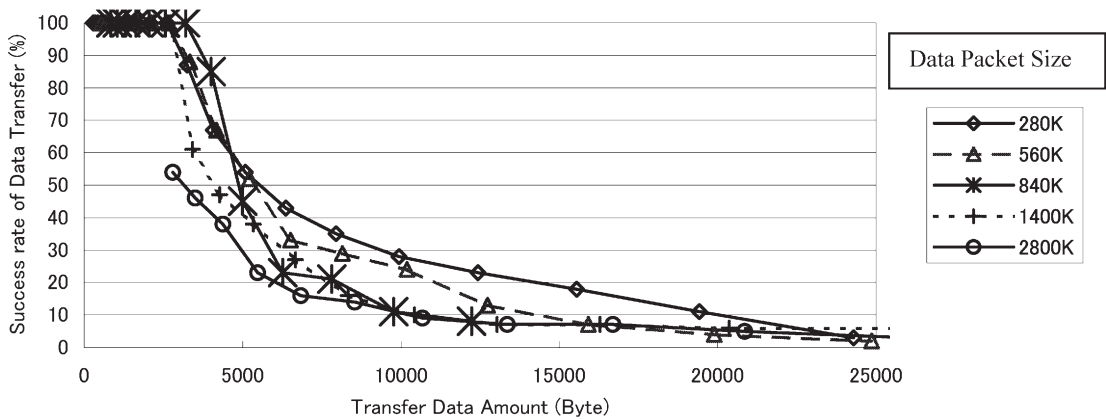


Fig. 1 Difference of success rate of data transfer in transfer data amount

## 6. Personal Interchange Joint Research Program

Although NIFS provides many types of joint research programs that cover a variety of researches on nuclear fusion or plasma physics, many original ideas and the extensive studies are also carried out in university laboratories and other institutes. Sometimes, they are complementary to the specific projects of NIFS, and worth to be supported by NIFS.

Personal interchange joint research program has been established for this purpose. Being different from other collaboration programs of NIFS, where the university researchers come and join the research activities held at NIFS, this program supports financially that the staff of NIFS goes out to join the collaboration research in universities. Two categories are prepared for collaboration; one is "project type" where the collaboration is made between two facilities; one is at NIFS and the other is at the university. A systematic research on the common subjects is done at both facilities by the researchers of both organizations to obtain a comprehensive knowledge on the subjects. The other is "detach type" where the researchers of NIFS take part in the study using the facility or experimental device at the university with a new idea or with an expert knowledge to explore a new field.

In this year, eight subjects were carried out as "project (P) type" and nine for "dispatch (D) type". All the programs have been done successfully, and brief summaries of each subject are listed below.

[P 1]: *"Electron Bernstein wave heating by long wavelength microwave in a spherical tokamak and a helical device"*

This program is the collaboration between Kyoto university LATE group and the NIFS CHS group on developing electron Bernstein wave (EBW) heating, which is crucial to produce high density plasma in both devices. In LATE spherical tokamak, plasma and toroidal current are initiated successfully by using ECH of two frequencies; 2.45GHz and 5GHz. In both cases plasma is considered to be heated by mode-converted EBW because the obtained density is higher than that for cut-off. In CHS, over-dense plasma is also routinely generated under different magnetic axis positions.

[P 2]: *"Assessment on fusion energy development from the socio-economic viewpoint"*

This subject was carried out between Univ. of Tokyo and NIFS on the assessment of nuclear fusion as a future energy source. This assessment was done from the view point of socio-economics. The evaluation was carried out on which characteristics people require for future energy source. Six items with two issues each have been chosen, and weight is inquired between two issues, for example, which should be cared much for environmental

load, CO<sub>2</sub> emission or waste disposal. Then the scientific score will be evaluated by specialists for several new energy sources including nuclear fusion.

[P 3]: *"Ion heating and acceleration in a supersonic plasma"*

This is a collaboration research program between NIFS HYPER-I group and Tohoku Univ. on studying fast plasma flow. The present study is on efficient heating of MPD arcjet plasma in HITOP device. When the RF of in the frequency range of 100kHz to 500kHz is applied by a right-handed helically-wound antenna, the perpendicular stored energy and ion temperature of plasma are clearly increased. This perpendicular energy is converted to parallel energy through diverging magnetic nozzle successfully, which is located downstream along plasma flow.

[P 4]: *"Higher-harmonic oscillation of Peniotron"*

This subject was carried out between NIFS ECH group and the group of Tohoku University on the development of high frequency microwave power source for plasma diagnostics. In order to develop a THz-range power source, they study a peniotron oscillator that has good conversion efficiency for higher harmonic waves. Then it is possible to produce high frequency wave using low magnetic field. A cavity with 18 vanes was designed for 17<sup>th</sup> harmonic oscillation, and an electron gun system was set up. Experiments are in progress.

[P 5]: *"Clarification on cooling mechanism of Stirling type pulse tube cryocooler"*

This collaboration was carried out between NIFS cryogenic group and the Institute of Quantum Science of Nihon University. The purpose of this project is to clarify the mechanism of Stirling type pulse tube cryocooler which is expected to be reliable due to its low level mechanical vibration. In this year, an influence of materials of the generator on a cooling power has been studied. They found that the regenerator with blackened mesh improve the performance compared with the one with non-blackened mesh.

[P 6]: *"Study on various atomic processes of impurity highly charged ions by versatile ion sources"*

This is a collaboration research program between NIFS NICE group and Tokyo-EBIT group of ILS (UEC). The aim of the research is collecting and evaluating relevant atomic data of highly-charged ions of heavy elements. In this year, the dielectric recombination (DR) has been investigated in Tokyo-EBIT. DR is the most important radiation energy-loss process of high temperature plasmas containing heavy impurity elements. The total cross section of He-like Bi ions have been measured successfully.

[P 7]: *"Study on purification and compatibility of structural materials with molten salt breeder"*

This is a collaboration research program between NIFS Fusion Engineering Center and Tokyu Univ. on studying compatibility of structural materials with Flibe (a mixture of LiF-BeF<sub>2</sub>) containing the corrosive species. In this year they have investigated the corrosion behavior by thermodynamic calculations, and preliminary dipping experiments. They found that some kinds of oxide layers could work as a protective scale. The soundness of this scale will be investigated.

[D 1]: *"Analysis of  $J_c$  properties in high magnetic fields for low activation superconducting wires"*

This is a program between NIFS and NIMS (National Institute for Material Science) on developing low activation superconducting materials. They adopted V-based alloys and MgB<sub>2</sub> compound as candidates, but their critical temperatures are lower than conventional Nb-based superconductors. Therefore improvement of critical temperature is important. They measured the critical temperature under the high magnetic field strength up to 18T, and V<sub>3</sub>Ga compound has good characteristics at high field.

[D 2]: *"Helium ash removal by moving-surface PFCs"*

In this program, a NIFS researcher carries out experiment using a unique test bed of plasma-material interaction (VECHILE-1) at Osaka University. In this year, they have shown that once the surface of copper was covered by lithium, the recycling of both hydrogen and helium reduced. This result is important because conventional cryopump does not have a good efficiency for pumping helium compared with hydrogen.

[D 3]: *"Experimental and theoretical studies of startup methods for Spherical Tokamak plasmas"*

This research program is on developing methods of current startup and sustainment in small spherical tokamak of university of Tokyo. A recent up-scaled device (UTST) has poloidal coils outside vessel to demonstrate double-null startup without central coil, and has accessibility for high power heating. A new finding of this year is that the ejection of current sheet or plasmoid causes high-speed merging as well as high-power heating. In the high compression case, the ion temperature increased right after the current sheet injection.

[D 4]: *"Advanced large-scale simulation on fusion plasmas by using the Earth Simulator"*

In this program, methods of advanced large-scale simulation have been developed by using high performance super computer of JAMSTEC: the Earth Simulator. In the study of strong turbulence in fusion plasma, the analysis of velocity distribution is important. For this sake, five-dimensional gyrokinetic-Vlasov simulation with high

velocity-space resolution is required. This code has run successfully on the Earth Simulator, and the steady state of ITG turbulence is obtained.

[D 5]: *"Heating and current drive experiments on the TST-2 Spherical Tokamak"*

This research program is to perform heating and current drive by RF wave on a spherical tokamak of university of Tokyo (TST-2). After moving TST-2 device to new Kashiwa campus, high power RF transmitters of 21MHz, 400kW used in JFT-2M were also moved from JAEA. An initial RF injection test has been carried out with new antennae in the condition of higher harmonic fast wave, and the soft-X ray measurement showed heating of plasma.

[D 6]: *"Degradation of Nb<sub>3</sub>Sn superconducting cable due to mechanical stress"*

This collaborative research program is carried out at Iwate University on development of a new test method for evaluating the property of superconducting cable. This test measured the induced voltage in the circuit of superconducting cable when the magnetic flux is changed at constant rate. The maximum magnetic field strength is 15T. The critical current of the cable can be evaluated by this method as a function of magnetic field strength. The sample can be applied mechanical compression externally, and the degradation of critical current was also measured.

[D 7]: *"magnetic island effect on radial particle flux in TU-heliac"*

This is a collaboration program that was carried out in the small helical axis stellarator of Tohoku University (TU-Heliac). The main objective is to study the effect of magnetic islands on transport. In TU-Heliac magnetic islands of  $m = 2$  and 3 can be produced by external vertical field coils. When the hot cathode is inserted into the plasma inside islands of  $m=3$ , and the current is induced (i.e. biased negatively), the improved mode appears. The threshold current for mode transition increased as the width of magnetic islands, which suggest that the ion viscosity increased with the width of magnetic islands.

[D 8]: *"ECH plasma experiments with an internal coil device Mini-RT"*

Mini-RT is a magnetically levitated internal coil device in university of Tokyo, where the magnetic dipole field is utilized for plasma confinement. For internal coil, an advanced high temperature super conducting wire is adopted. NIFS cryogenic group supported technically to realize this unique device. The plasma has been generated successfully by ECH. In this year, the possibility of electron Bernstein wave heating is discussed to produce more dense plasma. Magnetic configuration and plasma density profile (i.e., density gradient) can be changed by using levitation coil. Judging from the experimentally obtained density profiles, efficient mode conversion of 25% would be possible.



## LIST OF REPORT

- P 1. "Electron Bernstein wave heating by long wavelength microwave in a spherical tokamak and a helical device," Maekawa, T. (Kyoto Univ.), et al.
- P 2. "Assessment on fusion energy development from the socio-economic viewpoint," Ogawa, Y. (Univ. Tokyo), et al.
- P 3. "Ion heating and acceleration in a supersonic plasma," Ando, A. (Tohoku Univ), et al.
- P 4. "Higher-harmonic oscillation of Peniotron," Ando, A. (Tohoku Univ), et al.
- P 5. "Clarification on cooling mechanism of Stirling type pulse tube cryocooler," Yasohama, K. (Nihon Univ.), et al.
- P 6. "Study on various atomic processes of impurity highly charged ions by versatile ion sources," Ohtani, S. (Univ. Electro-Communications), et al.
- P 7. "Study on purification and compatibility of structural materials with molten salt breeder," Terai, T. (Univ. Tokyo), et al.

- D 1. "Analysis of  $J_c$  properties in high magnetic fields for low activation superconducting wires," Hishinuma, Y. (NIFS), et al.
- D 2. "Helium ash removal by moving-surface PFCs," Hirooka, Y. (NIFS), et al.
- D 3. "Experimental and theoretical studies of startup methods for Spherical Tokamak plasmas," Ono, Y. (Univ. Tokyo), et al.
- D 4. "Advanced large-scale simulation on fusion plasmas by using the Earth Simulator," Hayashi, T. (NIFS), et al.
- D 5. "Heating and current drive experiments on the TST-2 Spherical Tokamak," Takase, Y. (Univ. Tokyo), et al.
- D 6. "Degradation of  $NB_3Sn$  superconducting cable due to mechanical stress," Katagiri, K. (Iwate Univ.), et al.
- D 7. "magnetic island effect on radial particle flux in TU-heliac," Kitajima, S. (Tohoku Univ.), et al.
- D 8. "ECH plasma experiments with an internal coil device Mini-RT," Ogawa, Y. (Univ. Tokyo), et al.

(Kaneko, O.)

## §1. Electron Bernstein Wave Heating by Long Wavelength Microwave in a Spherical Tokamak and a Helical Device

Maekawa, T., Tanaka, H., Uchida, M., Yoshinaga, T. (Kyoto Univ.),  
Ikeda, R., Takeuchi, M., Shoji, T. (Nagoya Univ.),  
Toi, K., Suzuki, C.

On the LATE device at Kyoto University, formation of Spherical Tokamak by ECRH without center solenoid have been conducted [1,2], while on the CHS device at NIFS, experiments for transport study based on the “non-dimensionally similar approach” have been conducted to simulate various transport processes in high temperature plasmas[3]. In both cases, the plasmas are generated and maintained by ECRH in over-dense regime via mode-converted electron Bernstein waves (EBW) from long wavelength microwaves and efficient coupling from external microwaves to EBW is crucial for experiments.

Main objective of the LATE (Low Aspect ratio Torus Experiment) device is to demonstrate formation of ST plasmas by electron cyclotron heating (ECH) alone without center solenoid and establish its physical bases. By injecting a 2.45 GHz microwave pulse for 2 seconds, a plasma current of 2 kA is spontaneously initiated by  $\text{Prf}=15$  kW under a weak steady vertical field of  $B_v=17$  Gauss, and then ramped up with slow ramp-up of  $\text{Prf}$  and slow ramp-up of  $B_v$  for the equilibrium of the plasma loop and finally reaches 8 kA at  $B_v=90$  Gauss and  $\text{Prf}=35$  kW. In the case of a 5 GHz microwave pulse (130 kW, 60 ms), final plasma current reaches 12 kA at  $B_v=100$  Gauss. In both cases the plasma center locates near the second or third harmonic ECR layer as shown in Fig.1 and the line averaged electron density significantly exceeds the plasma cutoff density, suggesting that harmonic EC heating by the mode-converted EBW supports the plasma. The mode conversion rate is estimated based on the plasma slab model [4] and compared with the 5 GHz experiments. In 5 GHz case, the wavelength is relatively short compared with the plasma size and launcher diameter. Therefore, the conditions may meet the slab model. The slab theory predicts that oblique injection with left-handed circular polarization can give 90 % mode-conversion rate, while mode-conversion rate by the right-handed circular polarization is poor. However, there has been no appreciable difference observed between two polarizations.

In CHS, over-dense plasmas were routinely produced by 2.45 GHz microwaves which were launched perpendicularly or obliquely to the toroidal field, into hydrogen, helium or neon gas [5]. In these experiments, toroidal magnetic field was scanned from 1000 G to 600 G in the magnetic configurations of  $R_{ax}=97.4$ cm, 94.9cm, 101.6cm and 92.1cm, where  $R_{ax}$  denotes the magnetic axis position in the vacuum field. Radial profiles of electron temperature, electron density and plasma potential were measured with three sets of triple Langmuir probes placed on the top of the vertically elongated section, and on the inboard and outboard sides

of horizontally elongated sections. Fluctuation data of these plasma parameters were also taken by these probes. Two-dimensional electron density profile was obtained by a sheet-type Lithium beam probe developed by our group and successfully applied to LHD [6]. Radial profile of  $H\alpha$  emission profile was measured by a ten-channel visible spectrometer for evaluation of neutral atom density. In order to clarify mode conversion to EBW and absorption mechanism, experiments of ECH power-step and modulation were carried out. Higher modulation frequency of 7kHz or 9kHz was adopted to directly derive a power deposition profile. For these frequencies, time delay of response signals such as electron temperature and density perturbations by the modulated ECH power is almost no radial dependence. This indicates that radial profiles of these responses will correspond to the deposition profile of mode-converted EBW power. It is inferred from these data that EBW power is dominantly absorbed in interior region beyond the upper hybrid layer in over-dense plasmas.

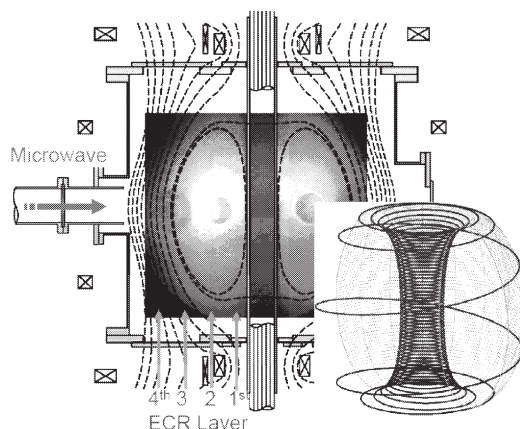


Fig. 1 The plasma encompasses the first to forth harmonic ECR layers (results from the LATE device)

### References

- [1] T. Maekawa *et al.* Nuclear Fusion, **45** (2005)1439.
- [2] T. Yoshinaga *et al.*, Phys. Rev. Lett., **96**(2006)125005
- [3] K. Toi *et al.*, 29<sup>th</sup> EPS on Plasma Physics and Controlled Fusion, Montereux, 2002, paper No.P4-06.
- [4] H. Igami *et al.*, Plasma Phys. and Control. Fusion, **46** (2004) 261
- [5] R. Ikeda *et al.*, J. Plasma Fusion Res., **81** (2005) 478.
- [6] Y. Takahashi *et al.*, Plasma and Fusion Res. :Rapid Communications, **1**(2006)013-1.

## §2. Assessment on Fusion Energy Development from the Socio-Economic Viewpoint

Ogawa, Y. (The University of Tokyo),  
Okano, K., Asaoka, Y., Hiwatari, R. (CRIEPI),  
Konishi, S. (Kyoto University),  
Tobita, K. (JAERI),  
Norimatsu, T. (Osaka University),  
Sagara, A.

In the 21 century global environment and energy issues becomes very important, and this is characterized by the long-term (in the scale of a few tens years) and world-wide issue. In addition, future prospect of these issues might be quite uncertain, and scientific prediction could be very difficult. For these issues vigorous researches and various efforts have been carried out from various aspects; e.g., world-wide discussion such as COP3 in Kyoto, promotion of the energy-saving technology and so on.

Development of environment-friendly energy has been promoted, and new innovative technologies are explored. Nuclear fusion is, of course, a promising candidate. While, there might be some criticism for nuclear fusion from the socio-economic aspect, because it would take long time and huge cost for the fusion reactor development. Here we have started to assess the fusion energy development, comparing with other innovative energy technologies.

At first, we have considered to evaluate the characteristics which the people require for future energy resources, based on questionnaire research from ordinary people. Several items are selected, and issues to be compared are defined. Here we have selected six items and related issues, as shown in Table 1.

Table 1. Items and issues to be compared.

Item	Issue
(A)Energy resource	1) total amount 2) distribution
(B)Environmental load	1) CO2 emission 2) waste disposal
(C)Economics	1) construction cost 2) operation cost
(D)Reliability and stability	1) natural vulnerability 2) social vulnerability
(E)Flexibility on operation	1) facility size 2) freedom on set-up
(F)Safety and security	1) hazard potential 2) military application

Here we have planned three questionnaires as follows;

- 1) Screening questionnaire for more than thousand ordinary people,
- 2) Evaluation of the social weight in each issue for more than one hundred ordinary people,
- 3) Evaluation of the scientific score in various energy technologies for a few tens specialists.

At the screening questionnaire, interest and recognition for environment and energy issues are inquired. Through the screening questionnaire, about one hundred people are

selected, where distribution on men-women, generation is paid much attention.

Next in the questionnaire research on the social weight, two issues for each item, shown in Table 1, are compared, and weight is inquired between two issues. For example in the case of the energy resource, the inquiry is as follows;

[ There are two energy resources A and B. The resource A has an inexhaustible amount, but is localized in the earth. The resource B is widely distributed in the earth, but the amount is limited. Which resource do you select?]

In the third questionnaires we are planning to evaluate a scientific score for several new energy technologies. Here we have selected following technologies;

- 1) Advanced coal technology with CO2 recovery system (abbr. CCT)
- 2) SOFC top combined cycle: natural gas (SOFC)
- 3) Solar power (Solar)
- 4) Wind power (Wind)
- 5) Space solar power station (SPS)
- 6) Advanced fission (Fission)
- 7) Fusion (Fusion)

At first we have compiled scientific data on each item listed in Table 1(i.e., energy resource, environmental load, economics, reliability and tolerance, and safety and security). A first version of the scientific data has been published from the CRIEPI group<sup>1)</sup>, and a preliminary questionnaire for evaluating scientific scores in Table 1 has been carried out.

Here we have carried out questionnaires for a few tens specialist, so as to evaluate a scientific score for each technology. In questionnaire the most superior technology is selected for each item-issue in Table 1. The total number of the top score is summarized in Table 2.

Table 2. A number of top score of various energy technologies for each item-issue.

Item-issue	CCT	SOFC	Solar	Wind	SPS	fission	Fusion
(A)-1	2	0	3	4	3	17	20
(A)-2	2	0	12	3	5	10	18
(B)-1	0	0	6	10	6	22	21
(B)-2	1	11	13	18	4	1	2
(C)-1	17	11	3	3	0	10	1
(C)-2	12	11	1	4	0	16	7
(D)-1	22	21	0	0	5	24	23
(D)-2	0	1	25	20	3	3	11
(E)-1	15	13	0	0	8	23	26
(E)-2	8	16	12	0	1	2	3
(F)-1	4	2	24	13	3	0	2
(F)-2	21	21	25	25	3	1	8

Based on results of questionnaires on social weight and scientific score, we will try to evaluate characteristics for each energy technology from the viewpoint of public acceptance.

### Reference

- 1) Hiwatari, R., CRIEPI internal report (2005).

### §3. Ion Heating and Acceleration in a Supersonic Plasma

Ando, A., Hattori, K., Inutake, M., Tobari, H., Shibata, M., Kasashima, Y. (Dept. Electrical Eng. Tohoku Univ.)

Recently a plasma flow has been recognized to play an important role in space and fusion plasmas. Intensive researches to develop a fast flowing plasma with high particle and heat fluxes are required for the purpose of basic plasma researches as well as various wall material researches and space applications.

An ion heating and magnetic nozzle acceleration in a fast flowing plasma attracts much attention in an advanced electric propulsion system. In the Variable Specific Impulse Magnetoplasma Rocket (VASIMR) project, it is proposed to control a ratio of specific impulse to thrust at constant power.[1] This is a combined system of an ion cyclotron heating and a magnetic nozzle, where a flowing plasma is heated by ICRF (ion cyclotron range of frequency) power and the plasma thermal energy is converted to flow energy by passing through a magnetic nozzle.

The purpose of this research is to investigate an ion heating and acceleration phenomena in a fast flowing plasma for the advanced plasma thruster and other applications.

We have performed an ion heating experiment using a right-handed helically-wound antenna in a supersonic plasma flow produced in the HITOP device.[2,3] RF waves in the frequency range of 100kHz to 500kHz are launched by the antenna set at  $Z=0.6\text{m}$  downstream of the magneto-plasma-dynamic arcjet (MPDA).

When RF waves excited in a flowing plasma with a density below  $1 \times 10^{12} \text{cm}^{-3}$ , we observed a strong increase of plasma stored energy  $W_{\perp}$  measured by a diamagnetic coil located at  $Z=2.23\text{m}$  shown in Fig.1. Ion temperature  $T_{i\perp}$  was measured by an electrostatic energy analyzer, of which collection surface faces to perpendicular direction to the plasma flow. Figure 2 shows dependences of  $T_{i\perp}$  on RF input power  $P_{\text{RF}}$ . It linearly increased with  $P_{\text{RF}}$ . When the diameter of the antenna was changed from 160mm to 130mm, larger increase of  $T_{i\perp}$  was observed as shown in Fig.2. It is caused by the improvement of plasma-antenna coupling, as the plasma diameter was about 100mm.

Ion acceleration in a magnetic nozzle is expected by energy conversion from  $W_{\perp}$  to  $W_{\parallel}$  in a diverging magnetic field. We have measured both  $T_{i\parallel}$  and  $T_{i\perp}$  by electrostatic energy analyzers set at  $Z=2.33\text{m}$  (before the nozzle) and  $Z=3.13\text{m}$  (after the nozzle). Figure 3 shows detected currents as a function of the retarding voltage. When a plasma flows in a diverging magnetic nozzle, increase of  $T_{i\parallel}$  and decrease of  $T_{i\perp}$  were clearly observed.

#### References

1) F.R.ChangDiaz, et al., Proc. of 36th Joint Propulsion Conf., (Huntsville,2000), AIAA-2000-3756.

2) A.Ando, Bull. Am. Phys., **50** (2005) 309. APS-invited (Denver, 2005).  
3) A.Ando, et.al., Proc. the 29th Int. Electric Propulsion Conf., IEPC- 2005-29 (2005).

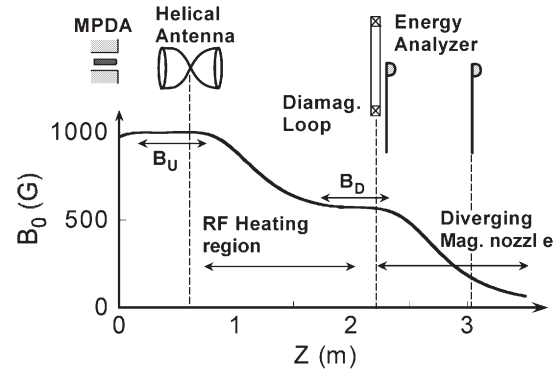


Fig.1 Magnetic field configurations and locations of the helical antenna, the diamagnetic loop coil and the electrostatic energy analyzer.

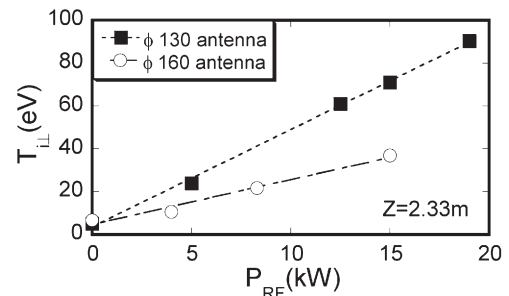


Fig.2 Dependence of ion temperature  $T_i$  as a function of input RF power.

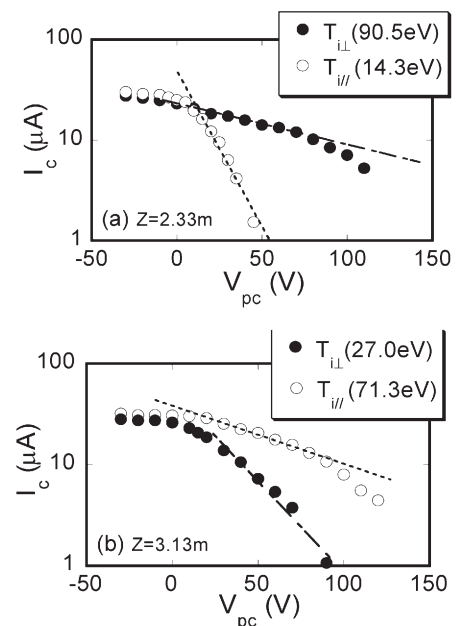


Fig.3 Electrostatic energy analyzer (EEA) signals measured at (a)  $Z=2.33\text{m}$  and (b)  $Z=3.13\text{m}$ .



#### §4. Higher-Harmonic Oscillation of Peniotron

Ando, A. (Dept. Electrical Eng. Tohoku Univ.),  
Sato, N. (RIEC, Tohoku Univ.), Shimozuma, T.,  
Inutake, M., Hattori, K. (Dept. Electrical Eng. Tohoku Univ.)

It is urgently required to develop a power source which can generate stably an electromagnetic wave in the frequency region of THz for the scattering diagnostics in large fusion devices. A gyrotron is a powerful source in the frequency region of millimeter and sub-millimeter and has been utilized in many devices not only for an electron cyclotron heating/current drive but for the scattering diagnostics. Though it can deliver a millimeter wave efficiently, a strong magnetic field is necessary in the high-frequency operation. As the oscillation frequency of this cyclotron maser device depends on an electron cyclotron frequency in a magnetic field, a strong magnetic field of more than 36Tesla is necessary to generate 1THz electromagnetic wave in a fundamental cyclotron harmonic oscillation. A higher-harmonic operation is feasible to reduce the strength of the magnetic field. However, gyrotrons are usually operated at 1st or 2nd harmonic condition because the efficiency becomes worse in a higher harmonic operation.

Peniotrons has been theoretically and experimentally recognized to generate an electromagnetic wave with very high conversion efficiency at cyclotron higher-harmonics, as well as cyclotron fundamental. Experiments of higher-harmonic operation with 3rd and 10th harmonic were successfully demonstrated in Tohoku University and 30GHz and 100GHz oscillations were obtained [1-3]. A slotted waveguide resonator was used for the peniotron interaction between an axis encircling electron beam and the space harmonic wave. An electron beam encircling with a large orbit interacts with the electromagnetic field near the resonator wall, where the vane structure enhances the intensity of electromagnetic field near the wall. The field intensity varies periodically along the beam orbit and electrons experience acceleration and deceleration during one Larmor motion. Owing to the peniotron interaction, electrons are gradually concentrated in the deceleration region, resulting that the electron kinetic energy converts to the electromagnetic wave energy. The  $n$ -th harmonic operation is possible by using  $(n+1)$ -vane slotted waveguide resonator.

In this research, we are going to develop a higher-harmonic peniotron power source, which can be utilized in the scattering diagnostics in larger fusion devices.

Resonators with a vane-number of 18 and 28 are designed and fabricated for 17th and 27th harmonic oscillation.

Figure 1 shows an electron gun which delivers large orbit electrons circulating near a cavity wall. The experimental tubes are demountable in an electron gun region. Electrons are emitted at side wall of the cathode and propagate to a cavity along an applied magnetic field. A cavity has 18 vanes at the wall as shown in Fig.2. When the emitted electrons reach the cavity, they rotate with an electron cyclotron frequency  $f_{ce} = eB/(2\pi m_e)$  in a magnetic field  $B$  with the radius of slightly smaller than the cavity radius. The electrons interact with electromagnetic field at the cavity. The magnetic field can be applied up to 0.5Tesla. When the 18-vane cavity is used, electrons can resonate with the electromagnetic field varying with 17th cyclotron harmonic ( $f = 17f_{ce}$ ) by the peniotron-like interaction. All of the sub-assemblies of the electron gun to the output circuit are aligned along the axis. Experiments of the peniotron oscillation are in progress.

#### References

- 1) N.Sato, et.al., IEEE Trans. Plasma Science, **30** (2002) 859.
- 2) K.Yokoo, Inst. Electronics, Inform. and comm. Eng., **ED2002-241** (2002) 43.
- 3) T.Ishihara, IEEE Trans. Electron Devices, **46** (1999) 798.

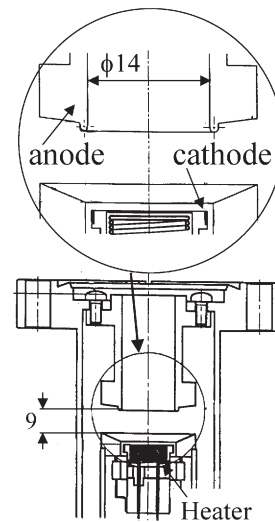


Fig.1 Schematic of large orbit electron gun.



Fig.2 Structure of resonant cavity with 18-vane.

## §5. Clarification on Cooling Mechanism of Stirling Type Pulse Tube Cryocooler

Yasohama, K. (Inst. of Quantum Sci., Nihon Univ.),  
Yamamoto, H. (Dept. of Elect. & Comp. Sci., Coll. of  
Sci. & Tech., Nihon Univ.),  
Matsubara, Y. (Musashi Inst. of Tech.),  
Mito, T., Iwamoto, A., Hamaguchi, S.,  
Maekawa, R.

The Stirling type pulse tube cryocooler has distinctive merits of low mechanical vibration and high reliability because it does not have a oscillating solid displacer in its low temperature part. A cooling power of this cryocooler is strongly depends on a structure of the regenerator and work-flow inside of the cryocooler. The work-flow is suitably adjusted by a phase control apparatus consisting of a inertance-tube and a buffer tank.

In the last year, we have carried an experimental study and numerical calculations on the properties of the phase control mechanism, and concluded that its performance can be predicted by the numerical calculations. In this year, much of the research has been focused on the properties of the regenerator, and an influence of materials of the regenerator on a cooling power has been studied.

In general Stirling type cryocoolers, the regenerator composed of many fine stainless steel mesh sheets laminated in the direction of the flow of a working fluid. This structure results from thermodynamic requirements. In this study, we adopted blackened stainless steel meshes in order to promote heat conduction between working fluid and the meshes. This blackening is a method that a thin blackened layer of thickness of about  $1\ \mu\text{m}$  is formed on the surface of weaving wires of meshes by a chemical treatment. In this experiment, two kinds of mesh, 150 and 250 in mesh number, were prepared, and 500 sheets for 150 mesh and 1000 sheets for 250 mesh were laminated, the laminated thickness for each mesh is 80mm. In addition, non-blackened meshes were also prepared for comparison of performances.

Pressure oscillation in working fluid is generated by a compressor made by CFIC, of which an exclusive volume is 400cc/cycle and oscillating frequencies are varied in range of 45 to 52Hz. The pulse tube has an inner diameter of 40mm and a length of 200 and 250mm. A length and inner diameter of the inertance tube are 1.4m and 10mm, respectively. The buffer tank has a volume of 3.75 liters. The working fluid is helium gas at a pressure of 2MPa.

Measurements were made on a electric input power and frequency for the compressor, temperature profiles along the regenerator and its lowest attained temperature, and pressure amplitudes at the input of the cryocooler and at the output of the pulse tube.

From a comparison in performances between the blackened and non-blackened meshes, the following results have been obtained. For the regenerator packed of 150 mesh, the lowest attained temperature is lower than the non-blackened mesh. Any differences in cooling power and PV input are not observed at a higher temperature of 80K. This indicates that the cooling power at lower temperatures can be increased by using blackened meshes. The temperature profiles in the regenerator were found to change linearly between lower and higher temperature parts in both of meshes. These properties are independent of lamination numbers of mesh sheets and of a length of pulse tube.

For the regenerator with 250 mesh, the lowest attained temperature is found to decrease with increasing a length of the pulse tube. The linear temperature profile is observed also in this case. However, the temperature difference between lower and higher temperature parts is larger for the blackened mesh than non-blackened one; the blackened mesh showed a higher temperature difference of 100K than the non-blackened one. This result indicates that the blackened mesh has higher thermal resistance in the direction of working fluid flow, which is preferable property required by thermodynamics for cryocoolers.

From those results, we have concluded that the blackened mesh improves the performance of the regenerator. In particular, obtainable materials of a mesh usable for a regenerator are limited at the present. Therefore, the introduction of blackened meshes is supposed to be an effective method to increase a cooling power of the present Stirling type pulse tube cryocooler. Furthermore, in other study, we have found mixed lamination of two or more kinds of mesh to be very effective. Thus, an adoption of blackened meshes for the mixed lamination is expected to make a more enhancement in cooling power. In this study, all measurements were made under the condition in which the inner diameter of the pulse tube and the dimensions (diameter and length) of the inertance tube were held to be constant. In future, we will perform an experiment to find an optimum operating point of the cryocooler by adjusting the dimensions of the pulse tube and inertance tube.

## §6. Study on Various Atomic Processes of Impurity Highly Charged Ions by Versatile Ion Sources

Ohtani, S., Nakamura, N. (ILS, UEC),  
Hirayama, T. (Rikkyo Univ.),  
Sakai, Y. (Toho Univ.),  
Sakurai, M. (Kobe Univ.),  
Tanuma, H. (Tokyo Metro. Univ.),  
Sakaue, H.A., Kato, D., Yamada, I.

Atomic processes of impurity ions of heavy elements in magnetically confined fusion plasmas have been issues of study concerning plasma radiation cooling, precise measurements of ion temperature and local magnetic field at core plasmas, secondary-particle emission in plasma-wall interaction, and so on. Our research aims at collecting and evaluating relevant atomic data of highly-charged ions of heavy elements. To this end, we promote a cooperative research at a high performance electron-beam-ion-trap (Tokyo-EBIT) of ILS (UEC) and an electron-beam-ion-source (NICE) of NIFS.

In 2005, we participated with measurements of dielectronic recombination (DR) at Tokyo-EBIT. In DR, an incident electron pushes electrons of a target ion up to excited levels, and is trapped by the target ion. The intermediate excited-state is unstable. It decays by releasing electrons, or is relaxed by emitting photons. DR is the latter case, and it becomes more probable for ions of higher charge-states. DR is therefore the most important radiation energy-loss process of high-temperature plasmas containing heavy impurity elements. At UEC, an experimental method was devised to measure total DR cross sections for ions of a certain charge-number. At ionization equilibrium of EBIT, number densities of ions ( $n$ ) are determined by cross sections ( $\sigma$ ) of electron-impact ionization (EI), radiative recombination (RR), DR and charge-exchange (CX) with surrounding neutral gas particles. Assuming the coronal model, ratio of

the ion number densities of neighboring charge state  $q$  and  $q-1$  is written as,

$$\frac{n_{q-1}}{n_q} = \frac{\sigma_q^{DR} + \sigma_q^{RR} + \langle \sigma_q^{CX} \rangle}{\sigma_{q-1}^{EI}} \quad (1),$$

where  $\langle \rangle$  stands for effective values at certain electron-beam currents. DR cross section would have peaks at certain incident electron energies which coincide with resonance energies of the intermediate excited states. Apart from the resonance energies, the cross section values would be zero. The other cross sections have smooth variation over electron-beam energies. Thus, DR cross sections can be isolated by subtracting rapidly varied component of the number density ratio from smooth component. The number density ratios of certain charge-states were obtained by measuring extracted ion intensities from EBIT using a position-sensitive detector placed after a charge-analyzing magnet.

At Tokyo-EBIT, the above method was used successfully to measure KLL-DR cross sections of He-like though B-like Bi ions. We are preparing the similar experiments at NICE in order to measure DR cross sections of Fe ions. Concentration of Fe ions and their radiation power at the core plasma of LHD have been issues of study. We will measure hitherto unknown chare-state specific DR cross sections of Fe ions to have an insight into mechanisms of radiation collapse and density limit of LHD plasma containing Fe ions. Also, the cross section data of Fe ions may be important for diagnostics of non-equilibrium high-temperature plasmas at the solar corona; our measurements will serve for precise EUV spectroscopy by the Solar-B satellite which will be launched in 2006.



## §7. Study on Purification and Compatibility of Structural Materials with Molten Salt Breeder

Terai, T., Suzuki, A., Nishimura, H. (Univ. of Tokyo), Nagasaka, T., Muroga, T., Sagara, A.

A mixture of  $\text{LiF-BeF}_2$ , Flibe, is considered as a candidate material for tritium breeding in a fusion liquid blanket. It has favorable characteristics such as high chemical stability and low electric conductivity. The liquid blanket system using Flibe is applied to the conceptual design for Force-Free Helical Reactor, FFHR. In this design, ferritic steel (*e.g.* Fe-9Cr-2W, JLF-1) and vanadium-based alloy (*e.g.* V-4Cr-4Ti) are candidate materials for the blanket structure.

Flibe itself has higher chemical stability as a fluoride than those of ordinary structural metals, which would be used for fusion reactors, and has almost no reactivity with structural materials. In the blanket operation condition, however, Flibe generates H (mainly as tritium), O, F, He, etc. by nuclear transmutation, and corrosive species such as HF should have a strong influence. Therefore, it is very important to investigate the compatibility of structural materials with Flibe containing the corrosive species. Up to the present, we have investigated the corrosion behavior by thermodynamic calculation and some preliminary experiments.

Recent thermodynamic data base systems enable us to calculate complex chemical equilibrium. In this work, a thermodynamic data base system, MALT2 and the *gem* code, which are attached to MALT2, were utilized for the calculation of chemical equilibrium for Flibe-structural material systems. By finding out the existing and emerging species and the phase equilibrium in the complex chemical systems at a certain temperature, we can estimate the possibility of the corrosion and get information for prevention of the corrosion. In this segment, corrosion behaviors of Fe-9Cr-2W in Flibe containing some amount of impurities are clarified by the thermodynamic calculations using the MALT2 code.

By this calculation, it was found that chromium was selectively attacked as is expected, and it is depleted under the condition of 10000ppm-T generation. Then, Fe is fluorinated to evaporate as  $\text{FeF}_3$ . On the other hand,  $\text{Cr}_2\text{O}_3$  can coexist in the system, and it might function as a protective layer. Hydrogen atmosphere simply results in reducing the attack on Fe, with decreasing the partial pressure of  $\text{FeF}_3$ . Addition of metallic Be has a positive effect of preventing corrosion.

To clarify the effect of the protective scale, some preliminary dipping tests were carried out. JLF-1 (Fe-9Cr-2W) specimen was used as dipping sample. The experiments were performed with Ar or Ar/1% $\text{O}_2$  or Ar/82ppmHF atmosphere. Nickel crucibles were used as containers, in each of which a test specimen was put with Flibe. The crucibles were kept at 823K for 30d after Flibe

was completely melted. After the specimen was taken out from Flibe, and cleansed in LiCl-KCl molten salt in order to remove the Flibe solidified on the surface. Then, LiCl-KCl sticking to the specimen was removed by ultrasonic washing in water, and finally the surface of the specimen was wiped with alcohol. In this experimental system, unknown but a very small amount of  $\text{H}_2\text{O}$  might react with  $\text{BeF}_2$  to give a trace of HF. The corrosion behavior was investigated by weight change measurement, SEM, XRD, RBS, etc. By visual observation, any destructive corrosion was not observed on each specimen. Fig.1 and Fig.2 are photos of specimens after dipping test.

From the thermodynamic analysis and the preliminary experiment on the corrosion against structural materials, it was suggested that some kinds of oxide layers could work as a protective scale for Fe-9Cr-2W. To evaluate soundness of protective scale and corrosion rate, we are planning to adapt electrochemical method for corrosion experiment. Anodic polarization on structural material specimen will show existence of the scale and soundness of it. Result that we will obtain from this experiment will help us to evaluate compatibility of the ferritic steel specimen with Flibe quantitatively.

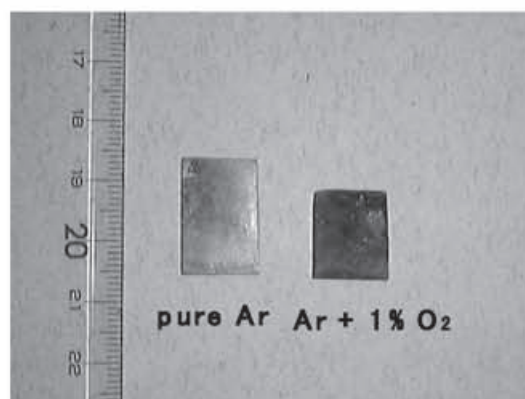


Fig.1. JLF-1 specimens after dipping tests under Ar and Ar/1% $\text{O}_2$  atmosphere.

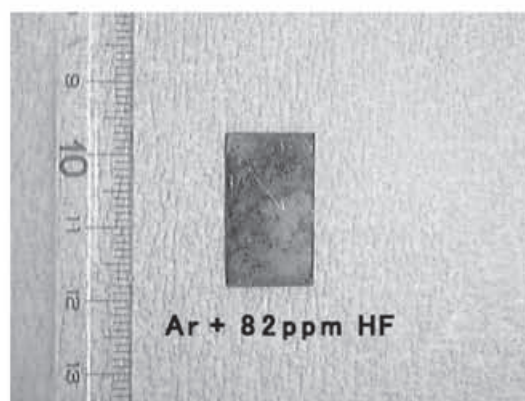


Fig.2. JLF-1 specimen after dipping test under Ar/82ppmHF atmosphere.



§8. Analysis of  $J_c$  Properties in High Magnetic Fields for Low Activation Superconducting Wires

Hishinuma, Y.,  
Takeuchi, T. (NIMS)

It is necessary to consider the neutron irradiation effect on superconducting magnets of an advanced fusion reactor. V-based alloys and  $MgB_2$  compound may be apply for a future fusion magnet because they have shorter decay time of induced radioactivity.

As the first trial to research V-based and  $MgB_2$  superconducting materials for fusion application, we selected Laves phase ( $V_2(Hf,Zr)$ ) and  $V_3Ga$  compounds as V-based low activation superconducting materials because they have high upper critical magnetic fields ( $H_{c2}$ ) above 20 T and better mechanical property than Nb-based compound. The mechanical property of superconducting wire is very important when large scaled magnet is constructed. The advantages of  $MgB_2$  compound for a future fusion application are not only low activation but also high  $T_c$  (39 K) and low cost. The wire fabrication process of  $MgB_2$  is very simple compared with the other superconducting materials. However, critical current density ( $J_c$ ) properties of V-based and  $MgB_2$  compound superconductors are lower than those of Nb-based superconductors such as  $Nb_3Sn$  and  $Nb_3Al$  at present,  $J_c$  properties of them must be improved in order to apply for fusion reactor.

We have studied the new wire fabrication process of  $V_2(Hf,Zr)$ ,  $V_3Ga$  and  $MgB_2$  compound wires having low activation sheath materials in order to improve  $J_c$  properties, and investigated the possibility of the application for a future fusion magnet based on  $J_c$  property under the high magnetic field.  $J_c$  measurements under the high magnetic field were carried out using 18T class High-Field Superconducting Magnet system in Tsukuba Magnet Laboratory of National Institute for Materials Science (TML-NIMS) shown in Fig.1.

The present status of  $J_c$ -B performances of V-based and  $MgB_2$  compound superconducting wires in our researches are shown in Fig. 2. Typical present  $J_c$  values of various Nb-based and  $MgB_2$  compound wires are also shown for the comparisons<sup>1)-3)</sup>.  $J_c$  properties of V-based compounds in our research are lower than those of Nb-based compounds at present, but  $J_c$  properties of new wire fabrication process in this study were improve compared with conventional process in each case. We thought that V-based superconducting materials had higher potential to  $J_c$  improvement though the progress of further process optimization and  $V_3Ga$  compound showed clear possibility of candidate materials for Nb-system superconductor, especially.

$J_c$  properties of  $MgB_2$  compounds in our research (Cu addition) are lower than SiC doped  $MgB_2$  compounds under the magnetic field above 10 T. However,  $J_c$  property of Cu addition  $MgB_2$  wire was higher than SiC doped

$MgB_2$  under the low and middle magnetic field below 6 T.  $MgB_2$  compound have possibility of alternative materials as Nb-Ti alloy wire for “Low activation superconducting magnet” by the progress of further  $J_c$  improvement.



Fig.1 18T class High-Field Superconducting Magnet in Tsukuba Magnet Laboratory of National Institute for Materials Science (TML-NIMS)

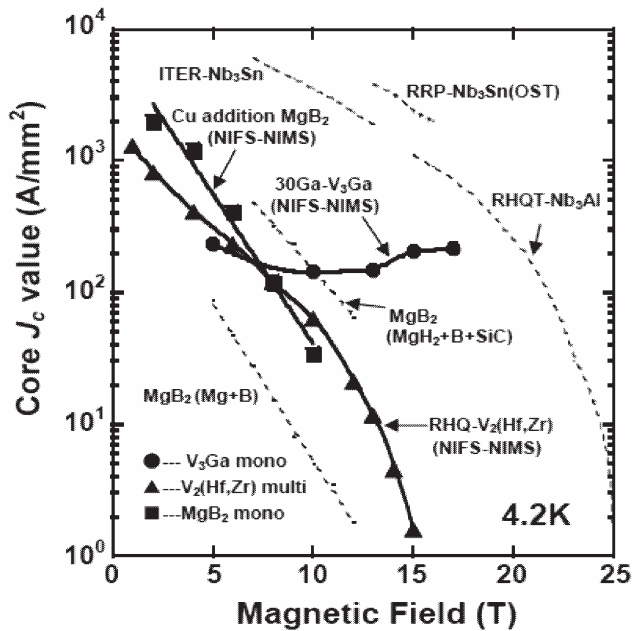


Fig.2 The present status of  $J_c$ -B performance on V-based and  $MgB_2$  compound wires in this study.

References

- 1) P. J. Lee et al: Microstructure, microchemistry and the development of very high  $Nb_3Sn$  layer critical current density, IEEE Trans. Appl. Supercond., 15, (2005), pp.3474-3477.
- 2) A. Kikuchi et al:  $Nb_3Al$  conductor fabricated by DRHQ (Double Rapidly-Heating/Quenching) process, IEEE Trans. Appl. Supercond., 11, (2001), p.3968-3971.
- 3) A. Matsumoto et al: Effect of  $SiO_2$  and SiC doping on the powder-in-tube processed  $MgB_2$  tapes, Supercond. Sci. and Tech., 16, (2003), p.926-930.

## §9. Experimental and Theoretical Studies of Startup Methods for Spherical Tokamak Plasmas

Ono, Y., Nagayama, Y., Takase, Y., Mekawa, T., Nishio, S., Nagata, M. (Univ. Tokyo, NIFS, Kyoto Univ., JAERI, Hyogo State Univ.)

A key issue for the spherical tokamak (ST) research is how effectively we can startup high-beta ST without using the center solenoid coil whose space is limited in the center of ST. The University of Tokyo has three key ST devices for ST startup but a few plasma diagnostics while NIFS has a variety of plasma diagnostics, especially high special resolution measurements of plasma temperature and density useful for the ST startup measurements but not ST device. We have been collaborating with the ST group in NIFS using ST committees in JSFS and IEEJ. In this program, we made the all-Japan joint study of ST startup based on collaboration not only with NFS but also with all ST groups in Japan: Kyoto Univ., Hyogo State Univ., Kyusyu Univ. and Kyusyu-Tokai University.

Our goal is to optimize the ST startup methods theoretically and experimentally. In 2005, the joint group made the high beta ST startup in TS-3 and 4, by combining PF coil induction and complete merging/ reconnection of two STs and also solenoid coil-less ST startup in TST-2, using RF and PF coil induction. We also made the corresponding Magnetohydrodynamic (MHD) simulation to verify these experimental results and started the first merging / reconnection experiment of NSTX.

At university of Tokyo, the merging techniques of TS-3 and 4 and also the RF heating/ current drive techniques of TST-2 were up-scaled to UTST device ( $R \sim 0.4m$ ) as shown in Figs. 1(a) and (b). In this device, all PF coils are located outside of the vacuum vessel to demonstrate (1) double-null startup of STs without CS coil, (2) their reactor-relevant reconnection heating for high-beta ST formation and (3) their sustainment by advanced RF and NBI techniques. The mega-watt heating power of reconnection is expected to transform the initial low-beta merging STs ( $\sim 5\%$ ) to the high-beta ST ( $\sim 30-50\%$ ) within short reconnection time. A new finding at Univ. Tokyo is that ejection of current sheet (or plasmoid) causes high-speed merging as well as high-power heating, respectively. In Fig. 2(b), the ion temperature  $T_i$  after the reconnection as well as the reconnection speed  $\gamma$ , increased

inversely with the toroidal field  $B_{t0}$  normalized by the constant poloidal field  $B_{p0}$ . It is because resistivity of the sheet as well as  $\gamma$  and  $T_i$  increase with ion gyroradius  $\rho_i$  ( $\propto B_{t0}^{-1}$ ) normalized by its thickness  $\delta$ [1]. In the high compression case,  $T_i$  increased right after the current sheet ejection[2], in sharp contrast with the low compression cases without sheet ejection. The increase in outflow was found to cause the ion heating. Based on this fact, the transient effects such as the flux pileup and ejection, enable us to have the high reconnection speed as well as the high-power reconnection heating, even if the merging high-q tokamaks have low current-sheet resistivity.

### References

- [1] E. Kawamori Y. Ono et al., Phys. Rev. Lett. **95**, 085003, (2005).
- [2] Y. Ono et al., to be published in Fusion Energy 2006.

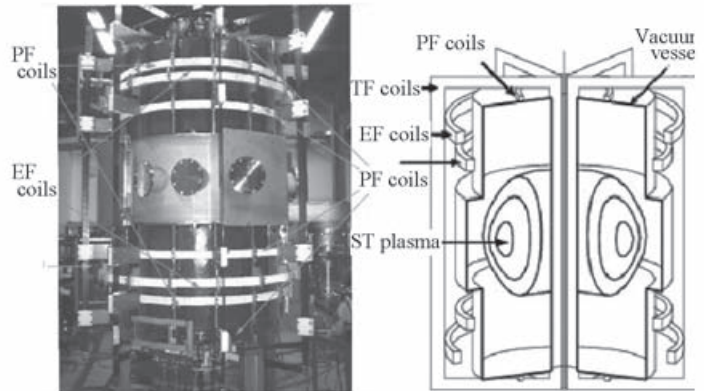


Fig. 1 Completed UTST Merging ST Device

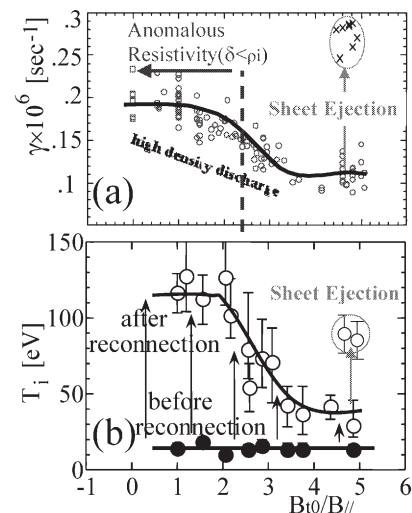


Fig. 2 The reconnection speeds  $\gamma$  (a) and ion temperatures  $T_i$  (b) as a function of toroidal field  $B_{t0}$  normalized by reconnecting poloidal field  $B_{p0}$  (constant). The transient  $\gamma$  and  $T_i$  right after ejection are also plotted.

## §10. Advanced Large-Scale Simulation on Fusion Plasmas by Using the Earth Simulator

Hayashi, T., Watanabe, T.-H.

In the project of utilizing Earth Simulator, it is aimed to clarify complex behaviors of fusion plasma, such as the anomalous transport, by means of advanced large-scale simulations. In high-temperature fusion plasma turbulence, the perturbed distribution function should be far from the Maxwellian because of the weak collisionality. In conventional gyrokinetic simulations of plasma turbulent transport, however, kinetic aspects of turbulence characterized by velocity-space structures of  $\delta f$  have hardly been investigated so far except in the limited works [1-3]. Then, it is expected that the gyrokinetic-Vlasov simulation code (GKV code) with high velocity-space resolution implemented on Earth Simulator can be a quite powerful tool for analyzing the anomalous transport, since applicability of the previous GKV simulations was restricted due to limited computer resources.

The five-dimensional gyrokinetic-Vlasov simulation code, GKV, can be successfully run on 192 computational nodes (1536 processor elements in total) of Earth Simulator. The maximum computation speed of 4.8 TFlops is achieved by hybrid implementation of automatic and MPI parallelization. In the full toroidal angle simulation of the ion temperature gradient (ITG) turbulence explained below, we have used (85, 169, 128, 128, 48) grid points (or mode numbers).

Saturation of the instability growth is given by a nonlinearly generated mean flow with sheared profile in the direction of the minor radius of the torus. As is widely recognized, the sheared flow called “zonal flow” plays the most important role in determining the transport level of the ITG turbulence. The elongated eddies found in the linear growth phase of the instability is suddenly broken by the nonlinearly excited zonal flows. Then, one finds the statistically steady state of the ITG turbulence (shown in Fig.1) with nearly constant transport flux. During the saturation of the ITG instability, we have found a new excitation process of the zonal flow with higher-order nonlinearity. Radial harmonics of the zonal flow components with shorter scale lengths are successively generated with higher growth rates, and effectively destroy the elongated eddy

structures. In the statistically steady state after saturation, however, the zonal flow with longest radial wavelength dominates and co-exists with turbulent eddies (see Fig.1), which may be related to behaviors of the geodesic acoustic mode (GAM) oscillations. The GAM is an oscillatory component of the zonal flow, and has a larger collisionless damping rate for a shorter radial wavelength because of the finite-orbit-width effects. It is also noteworthy that resolution in the poloidal wave number space in the present full toroidal angle simulation is largely improved in comparison to the conventional GKV simulations [1]. Thus, a fine structure of turbulent eddies can be clearly reproduced as seen in Fig.1.

In order to clarify a possible saturation mechanism, we have also performed the GKV simulation of the toroidal electron temperature gradient (ETG) turbulence. It is seen that the longer wavelength modes in the poloidal direction dominate after the saturation of the linear ETG instability, and that the radially elongated eddies are strongly modulated in the late phase of the simulation where nearly constant transport flux is successfully observed.

### References

- [1] T.-H. Watanabe and H. Sugama, *Nuclear Fusion*, **46**, 24 (2006).
- [2] T.-H. Watanabe and H. Sugama, *Phys. Plasmas*, **9**, 3659 (2002).
- [3] T.-H. Watanabe and H. Sugama, *Phys. Plasmas*, **11**, 1476 (2004).

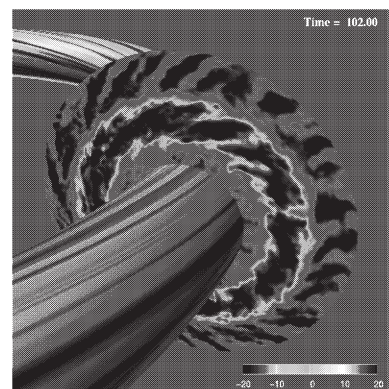


Fig.1: Results of gyrokinetic-Vlasov simulations of the ion temperature gradient turbulence in a tokamak configuration of the confinement magnetic field. Color contour maps represent electrostatic potential perturbations accompanying turbulence.

\* This work is carried out using Earth Simulator under the support by JAMSTEC.



## §11. Heating and Current Drive Experiments on the TST-2 Spherical Tokamak

Takase, Y., Ejiri, A. (Frontier Sci., U. Tokyo),  
Zushi, H., Hanada, K. (RIAM, Kyushu U.),  
Sasaki, K., Hoshika, H. (Eng. Sci., Kyushu U.),  
Mitarai, O. (IISTR, Kyushu Tokai U.),  
Nishino, N. (Eng., Hiroshima U.),  
Watari, T., Kumazawa, R., Seki, T., Shimpof, F.

This research is carried out as collaboration among several universities and NIFS. The purpose of this collaborative research is to perform heating and current drive experiments using radiofrequency (RF) waves on a spherical tokamak (ST) plasma, with the eventual objective of developing innovative methods for plasma start-up and steady-state sustainment.

The TST-2 spherical tokamak at the University of Tokyo is presently the largest ST device in Japan, with  $R = 0.38$  m and  $a = 0.25$  m (aspect ratio  $R/a = 1.5$ ). It has already achieved toroidal magnetic fields of up to 0.3 T and plasma currents of up to 0.14 MA. RF power of up to 400 kW in the frequency range 10–30 MHz is available for this experiment. In addition, transmitters at 200 MHz, previously used on the JFT-2M tokamak, have been transferred from JAEA.

During Fiscal Year 2005, two RF transmitters were brought to operation at a frequency of 21 MHz and an output power of 200 kW each. Heating experiments using the high harmonic fast wave (HHFW) have resumed after relocation of TST-2 to the Kashiwa Campus of the University of Tokyo, and initial results were obtained.

The preparation of RF transmitters for TST-2 was carried out by collaboration between the University of Tokyo RF group and the ICRF group of NIFS. Improvements and RF power testing were initiated in Fiscal Year 2004. During Fiscal Year 2005, full-power testing of the final power amplifiers, improvement of the control system (including the implementation of protection circuits), development of a tuning algorithm, adjustments of the matching circuits and transmission lines, and high power testing of the antenna were performed successfully.

Previously, while TST-2 was located on the Hongo Campus, only one transmitter was used for a short pulse (1ms or less). At the Kashiwa Campus, two transmitters were installed with a full set of power supplies. This has enabled operation at the full power of 400 kW using both transmitters, and for longer pulses (about 10 ms, sufficiently longer than the energy confinement time).

While TST-2 was at the Hongo Campus, an antenna consisting of two elements (current straps, each with width 10 cm, height 60 cm) was used to excite the HHFW. The RF currents flowing on the two current straps are out of phase. This antenna had a fixed spacing between the two current straps ( $18^\circ$  center to center), and the Faraday shield orientation was horizontal. The antenna was upgraded to enable excitation of different toroidal mode numbers (and therefore, the wavenumber parallel to the magnetic field,

which is important for determining wave absorption) by varying the distance between the two current straps. Since the excitation of the slow wave at the plasma periphery can lead to increased edge electric fields and RF sheath voltages, and consequently generation of impurities, the Faraday shield was modified to follow the average inclination of the magnetic field for typical operation (about  $30^\circ$  from horizontal) in order to short out the electric field parallel to the magnetic field lines. The separation between the two current straps can be adjusted so that the dominant toroidal mode number is 4, 6, or 10, which should be absorbed strongly by electrons with temperatures of around 70 eV to 400 eV.

In the HHFW heating experiments performed during Fiscal Year 2005, high power RF injection (greater than 300 kW) was achieved, and initial indications of electron heating, such as increased soft X-ray emission intensity, were observed.

In order to understand wave physics, it is very important to measure the wave excited in the plasma directly. A diagnostic to measure the wave in the plasma interior using microwave reflectometry is being developed on TST-2. It is indispensable to take diffraction effects into account in order to evaluate the experimental data quantitatively. Imaging optics have been designed and fabricated based on wave calculations taking this effect into account, and its performance was tested. The phase of the reflected wave from the plasma was measured when 100 kW of RF power was injected, and the density fluctuation amplitude obtained from its variation, and the RF electric field amplitude were evaluated. The upper limit on the RF electric field amplitude was about 1 kV/m, consistent with that obtained by an order estimate. An example of reflectometer data is shown in Fig. 1. The radial structure, obtained by sweeping the incident microwave frequency, is qualitatively consistent with the result of a full-wave calculation. However, a further noise reduction is required for a more quantitative comparison.

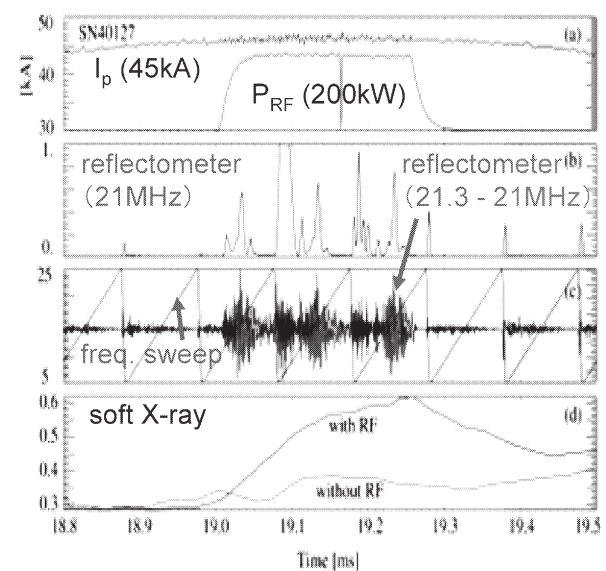


Fig. 1. Detection of the HHFW in the plasma by a reflectometer.



## §12. Degradation of Nb<sub>3</sub>Sn Superconducting Cable Due to Mechanical Stress

Katagiri, K. (Dept. of Mechanical Engineering, Iwate Univ.),  
 Seo, K., Hishinuma, Y., Nishimura, A.,  
 Nishijima, G., Watanabe, K. (Inst. for Materials Research, Tohoku Univ.),  
 Nakamura, K., Takao, T. (Dept. of Electrical and Electronics Engineering, Sophia University)

A new test method to evaluate the superconducting properties of multi-strand cable in high magnetic field under transverse compressive loading was developed. It is a kind of coil-test in high magnetic field with compressive load which simulated an electro-magnetic force in cable-in-conduit. When we look at the further fusion reactor, higher magnetic field will be required and larger electro-magnetic force will be generated. To develop new conductors for such an application, degradation because of the transverse compressive electro-magnetic force [1, 2] must be overcome.

A new test process was considered based on electro-magnetic induction by a back-up superconducting magnet [3], and the performance of the Nb<sub>3</sub>Sn cable was investigated [4]. By using the induction current, the test process can be made simple and safe. At the same time, joint performance and mechanical deformation behaviour are also able to be characterized. This report will present principle of our methods and test results of a multi-strand Nb<sub>3</sub>Sn cable.

Conceptual equivalent circuit is illustrated in Figure 1. The circuit is closed and circuit current,  $I$ , is induced by magnetic flux change,  $d\phi/dt$ . In eq. (1), the voltage of  $d\phi/dt$  is constant during the change rate in magnetic field is constant, and is balanced with sum of induction voltage of closed circuit,  $L(dI/dt)$ , joint voltage,  $R_J I$ , and superconducting cable voltage,  $R_{SC} I$ .

$$\frac{d\phi}{dt} = L \frac{dI}{dt} + R_J I + R_{SC} (I, B, T, \epsilon) I \quad (1)$$

$R_J$  is electric resistance of the soldered joint and supposed to be constant even in high magnetic field.  $R_{SC}$  is electric resistance of the superconducting cable. Since  $R_{SC}$  is given by  $V-I$  property of the superconducting cable, it is a function of current,  $I$ , magnetic field,  $B$ , temperature,  $T$ , and strain,  $\epsilon$ .  $I$  is regulated by both  $R_J$  and  $R_{SC}$ , basically. However, at high field,  $R_{SC} I$  is dominant because that  $R_J I$  decreases with magnetic field. Consequently, we obtain regulated current by  $R_{SC}$  with this experimental principle. In our method, flux flow voltage,  $R_{SC} I$  gradually changes during magnetic field change. In general, specific flux flow voltage is determined as a criterion to identify a critical current. Therefore, we call this regulated current in our study, quasi-critical current.

A sample fabricated with 18 + 9-Cu multi-strand Nb<sub>3</sub>Sn cable is shown in Figure 2. The bias magnetic field was applied in the horizontal direction in Figure 2 and compressive portion located at the centre of the bias magnetic field. The closed circuit of the cable was made on a round shape stainless mandrel and both



Fig. 1 Equivalent circuit of the sample

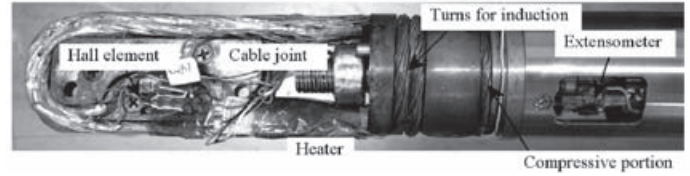


Fig. 2 Photograph of the sample. The Nb<sub>3</sub>Sn cable wound with 3 turns are jointed in both ends.

ends were soldered. Near the joint, a hall element was attached to measure the circuit current, and a heater was installed to break the persistent current. Three extensometers were installed to measure the relative displacement between upper plate, which was fixed to the supporting pipe, and lower plate, which is connecting to the main pull-rod running thorough the supporting pipe.

The quasi-critical current measurement was carried out using 15 T superconducting magnet at Tohoku Univ. The ramp rate of the bias field was changed to 0.58 T/min. The load was applied by a motor and gear system. The compressive load was applied up to 5 kN, 10 kN, 15 kN and 20 kN. Here, 20 kN corresponds to averaged stress of 29.3 MPa on the compressive plane. After the load reached the related compressive load, the gear was stopped and the bias magnetic field was ramped up and down. Results of the quasi-critical current measurement are shown in Figure 3. As described above, the quasi-critical current decreases as the magnetic field increases. This degradation becomes larger as an increase of the load, e.g. less than 50 % of virgin state in the case of 20 kN. Load-displacement curves were also obtained by three extensometers successfully.

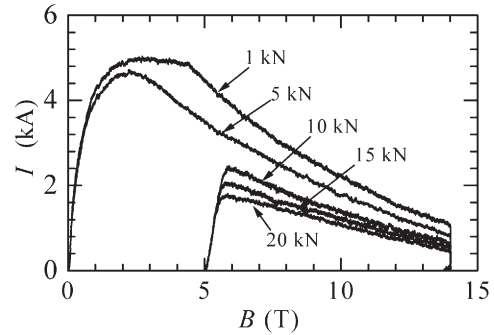


Fig. 3 Results of quasi-critical current measurement with compressive loading.

The degradation of quasi-critical current was observed by the new test procedure. With average stress of 29.3 MPa, the performance of the cable degraded less than half of virgin state.

### Reference

- 1) Mitchell, N., Cryogenics **43** (2003) 255.
- 2) Ulbricht, A. et al., Fusion Engineering and Design **73** (2005) 189.
- 3) Fabbriatore, P. et al., IEEE Trans. on Magn. **27** (1991) 1818.
- 4) Seo, K. et al., to be published on Fusion Engineering and Design (2006).

### §13. Magnetic Island Effect on Radial Particle Flux in TU-Heliac

Kitajima, S., Sasao, M., Shinto, K., Okamoto, A., Takahashi, H., Tanaka, Y., Utoh, H., Takenaga, M., Ogawa, M., Shinde, J., Aoyama, H., Iwazaki, K. (Dept. Eng. Tohoku Univ.), Takayama, M. (Akita Prefectural Univ.), Komori, A., Nishimura, K., Inagaki, S., Suzuki, Y.

The influence of the island width on the ion viscosity was studied in the Tohoku University Helic (TU-Heliac). It is important to study the effect of magnetic islands for the understanding of the transport mechanism and the research on the active control knob for helical reactors. Recently the healing of magnetic islands was observed experimentally, which provides good prospects in the design for helical reactors, and many ideas, in which magnetic islands are actively applied to control/improve confinement modes, are proposed. In LHD it is also important to study the  $m = 1$  island effect on the transport mechanism for the advanced control method of a plasma periphery. In TU-Heliac, a helical axis stellarator, the profile of a rotational angle can be changeable by selecting ratios of coil currents. TU-Heliac has local vertical field coils (auxiliary coils) which produce external perturbation fields to resonate the magnetic Fourier components of  $(n, m) = (3, 2), (5, 3)$  and to grow  $m = 2$  and 3 magnetic islands. The maximum island width was  $\sim 8$  mm in  $m = 3$  islands. Furthermore the improved mode transition has been triggered by the electrode biasing using a hot cathode made of  $\text{LaB}_6$ . The driving force  $\mathbf{J} \times \mathbf{B}$  for a plasma poloidal rotation was externally controlled and the poloidal viscosity was successfully estimated from the driving force<sup>1-4)</sup>. The purposes of our island experiments in TU-Heliac are, (1) to estimate the ion viscosity from the driving force in configurations containing magnetic islands, and (2) to study the magnetic island effect on the radial electric field and the radial particle flux.

The experimental set-up for the biasing experiments in configurations with magnetic islands is shown in Fig. 1. The  $\text{LaB}_6$  hot cathode (diameter, 10 mm; length, 17 mm) was inserted horizontally into the plasma inside the  $m = 3$  magnetic islands located along the plasma periphery. The hot cathode was heated by a floating power supply and negative current source was applied against the vacuum vessel (Fig. 1). The electrode current required for the improved mode transition increased with increasing width of magnetic islands located along the plasma periphery<sup>5)</sup>. This suggested that the ion viscosity increased with increases in the magnetic island width. The increase in the electrode current was equivalent to that in the driving

force for poloidal rotation, suggesting the possibility of an active viscosity control assisted by externally controlled island width and magnetic island rotation. The ratio of the radial electric field with islands to that without islands is shown in Fig. 2. Radial electric fields increased by  $\sim 20\%$  on the bulk plasma side of the magnetic islands. Thus, it seemed that the radial particle flux was enhanced by the magnetic islands in this region.

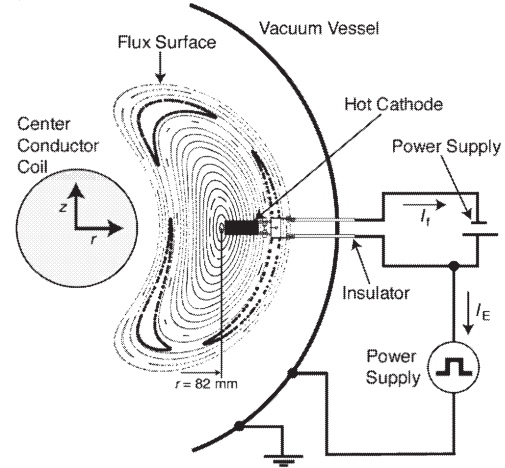


Fig. 1. The experimental set up of the hot cathode inserted horizontally into the plasma inside the  $m = 3$  magnetic islands.

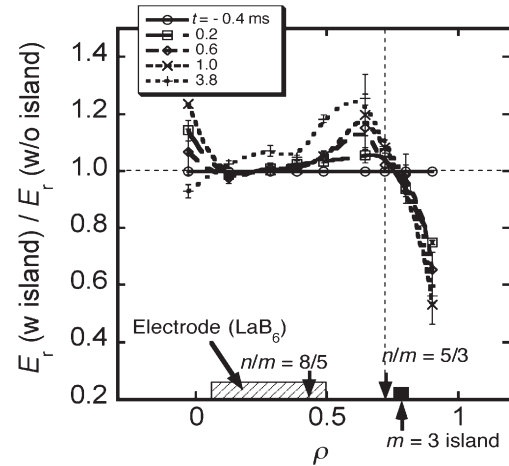


Fig. 2. Ratios of the radial electric field with islands to that without islands. The magnetic island was located at  $\rho = 0.7$  and  $t$  is the elapsed time after the supply of the perturbation fields.

#### References

- 1) Kitajima, S., *et al.*: Nucl. Fusion, **46**, 200-206 (2006).
- 2) Takahashi, H., *et al.*: Plasma Phys. Control. Fusion, **48**, 39-49 (2006).
- 3) Kitajima, S., *et al.*: Plasma Phys. Control. Fusion, **48**, A259-A267 (2006).
- 4) Tanaka, Y., *et al.*: Plasma Phys. Control. Fusion, **48**, A285-A293 (2006).
- 5) Kitajima, S., *et al.*: 15<sup>th</sup> International Stellarator Workshop [Madrid, Sep., 2005].

## §14. ECH Plasma Experiments with an Internal Coil Device Mini-RT

Ogawa, Y., Morikawa, J., Yatsuka, E. (The University of Tokyo),  
Yanagi, N., Mito, T.

In the internal coil device Mini-RT which has magnetically-levitated HTS coil, overdense plasma was observed. We considered about the possibility of heating by electron Bernstein wave (EBW) which enables us to heat overdense plasma.

Mini-RT has steep magnetic field gradient and it means that many harmonic electron cyclotron resonance (ECR) layers appear in the plasma confinement region. Figure 1 shows the cross section of Mini-RT.

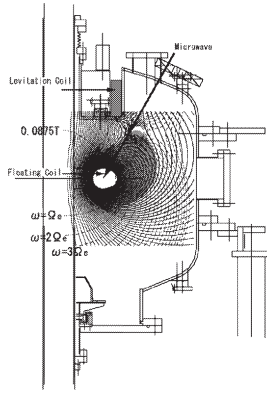


Fig. 1 Cross section of Mini-RT. Solid and dashed lines are contours of  $|B|$  and magnetic field line, respectively.

Experiments were carried out with F-coil supported. To control the plasma confinement region, we have applied a levitation coil current  $I_L$ . This enables us to change some important parameters for mode conversion, e.g. the characteristic scale length of density gradient. Examples of magnetic flux plot are shown in Fig. 2. Microwave with X-mode was injected from low field side and it was fed at a 30 degree to vertical. In this case, mode conversion efficiency  $C_B$  is given by

$$C_B = e^{-\pi\eta} (1 - e^{-\pi\eta}). \quad (1)$$

where  $\eta$  is called tunneling factor which is determined by the distance between R-cutoff and UHR locations. The frequency and power of microwave were 2.45GHz and 2.8kW c.w., respectively. Filling gas was hydrogen with

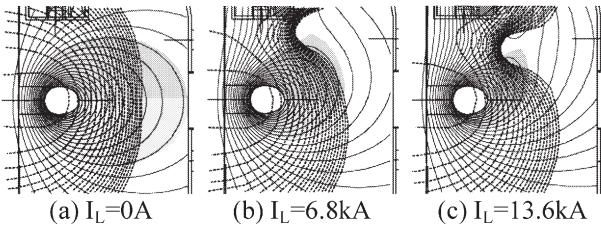


Fig. 2 Magnetic configuration and plasma confinement region on Mini-RT, where a floating coil current is fixed to be  $I_F=28\text{kA}$  in all three cases.

pressure of  $4 \times 10^{-2}$  Pa, and base pressure was  $1 \times 10^{-5}$  Pa.

Electron density and electron temperature on the midplane were measured by Langmuir probe. Line-integrated electron density was measured with 75GHz microwave interferometer, as well.

Figure 3 shows the profiles of electron density  $n_e$  and electron temperature  $T_e$ . Here we have compared three cases ( $I_L=0$  kA, 6.8 kA and 13.6 kA). The edge of electron density was determined by separatrix. Experiments were carried out with 2.8kW of microwave injection. For all three cases, electron density  $n_e$  has peak value comparable with 2.45GHz, O-mode cutoff density, i.e.  $7.6 \times 10^{16} \text{ m}^{-3}$ . For the cases of  $I_L=6.8, 13.6\text{kA}$ , steep density gradient at UHR location is expected. Therefore transport across evanescent region and mode conversion near the UHR may occur effectively.

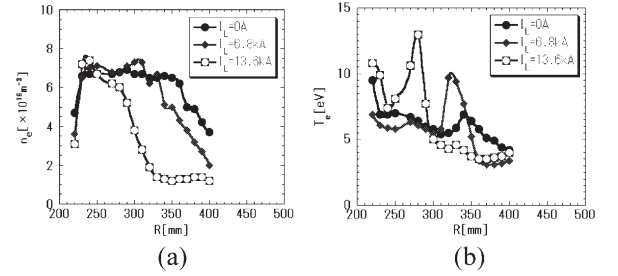


Fig. 3 Radial profile of (a)  $n_e$  and (b)  $T_e$ .

We estimated the conversion efficiencies by Eq. (1). Tunneling parameter  $\eta$  was written as

$$\eta = \frac{\Omega_e L_n}{c} \frac{\alpha}{\sqrt{\alpha^2 + 2L_n/L_B}} \left[ \frac{\sqrt{1+\alpha^2} - 1}{\alpha^2 + (L_n/L_B)\sqrt{1+\alpha^2}} \right]^{1/2} \quad (2)$$

where  $\alpha \equiv |\omega_{pe}/\Omega_e|_{UHR}$ ,  $L_n \equiv n/|\nabla n|_{UHR}$  and  $L_B \equiv B/|\nabla B|_{UHR}$ .

Table I shows the estimated mode conversion efficiencies.

TABLE I. Estimated Mode Conversion Efficiency

$I_L$ [kA]	$L_n$ [cm]	$L_B$ [cm]	$B_{UHR}$ [T]	$\alpha$	$C_B$ [%]
0	$\gg L_B$	6.9	0.029	2.9	1.5
6.8	6.5	3.0	0.021	4.0	24.8
13.6	3.9	4.3	0.032	2.6	24.4

We assumed  $n_e$  and  $T_e$  are the constant on flux surface and estimated  $L_n$  on the extended line of incident microwave. When the estimated conversion efficiency is large, electron temperature profile tends to have peak near the top of density slope. Thus heating by EBW due to the steep density gradient was expected. It is possible to achieve mode conversion more effectively due to reflection at L-cutoff. Generation of overdense plasma, e.g. by levitation of F-coil to avoid plasma energy loss, is one of the reasonable methods to attain effective mode conversion.

For the parameters in Mini-RT, absorption of cold waves is quite weak. Optical depths for fundamental O-mode and second harmonic X-mode are in the order of  $10^{-5}$ .

## 7. Collaborations Using Super SINET

The Super SINET is a fast network operated by National Institute of Information (NII) for scientific research. It consists of the 10 Gbps back-bone and 1 Gbps branches using an optical communication technology. The National Institute for Fusion Science (NIFS) has joined the Super SINET since 2001.

At first, isolated individual networks are made of the Super SINET. Each network connects a server computer at NIFS to a collaborator's computers. Since 2003, collaborator's computers have been directly connected to the LHD-LAN with the SuperSINET. Using the multi protocol label switching-virtual private network (MPLS-VPN) technology on SuperSINET, the LHD-LAN is extended to the remote stations. This extension is named "SNET". From a SNET remote station, collaborators can manipulate diagnostic devices in LHD. The SNET is managed by the "SNET task" and is operated by the Computer and

Information Network Center under the "SNET rules".

The SNET rules were established, when connecting SNET to the LHD-LAN in order to secure both LHD-LAN and SNET. The rules were renewed on 25<sup>th</sup> January 2006, when the NIFS super computer is connected to SNET. Main rules are as follows: (1) A remote station is prohibited to connect to the other network; (2) SNET is connected to the Internet passing through the firewall of NIFS-LAN; (3) a computer with a registered MAC address can be connected to SNET; (4) Servers in NIFS-LAN is connected after the SNET manager accepts the application; (5) SNET is taken care of by the SNET manager. SNET users can ask him by E-mail (snet@nifs.ac.jp) in order to solve problems on SNET.

Details of SNET are presented in the SNET home page (<http://snet.nifs.ac.jp/>), which has been established since 10<sup>th</sup> March 2006.

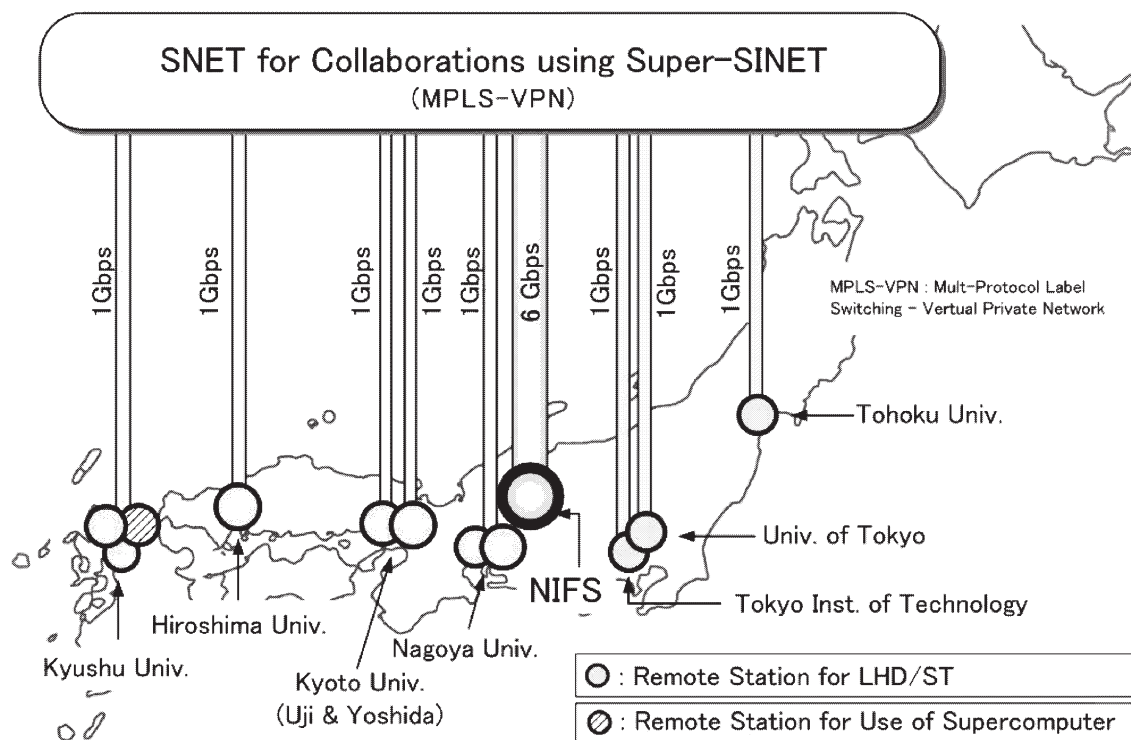


Fig.1 Remote stations of SNET in Japan.



A remote station is equivalent to the LHD control room. TV conference system is a useful item in the remote participation system. It is also connected to SNET. Since SNET is a fast local network, response is fast and no termination is caused when using TV conference system. Using the multi connection system, they can watch the LHD plasma in a remote station. Since LHD is continuous experiments and it lasts several hours in a day. The researches have to recognize how the experiment is going during the experiment. For this purpose, the TV conference system is also utilized in SNET.

In March 2006, two new items, such as super-computer collaboration and the Japan Spherical Tokamak (ST) Virtual Laboratory were adopted to SNET. Figure 1 shows present

SNET connection.

The Japan ST Virtual Laboratory is expected as a backbone of the Japan ST Research Program, which is promoted by the bi-directional collaboration at NIFS. QUEST, which is under construction at Kyushu University, is expected as a main experimental machine. Therefore, QUEST site was connected to SNET as a member of the Japan ST Virtual Laboratory. Since the most collaborators in the LHD remote stations are also members of the Japan ST Research Program, no difference has been adopted.

The super-computer collaboration is quite new. A new gateway server was newly installed as a SNET interface of NIFS super-computers. The first member of this collaboration is at Kyushu University.

(Nagayama, Y.)

§1. Reconstruction of the Network for Collaboration using Super-SINET

Tsuda, K., Nagayama, Y., Yamamoto, T., Ishiguro, S., Horiuchi, R., Hasegawa, H. (INTEC Solution Power Inc.)

The network for collaboration using Super-SINET was built on Super-SINET by MPLS-VPN since the 2001 fiscal year. A remote station for "superconductivity research", and eight remote stations for "LHD experiment remote participation" were installed by the 2004 fiscal year[1,2]. Those remote stations were; Univ. of Tokyo, Nagoya Univ., Kyoto Univ., Kyushu Univ., Tokyo Institute of Tech., Hiroshima Univ., Tohoku Univ., Kyoto Univ. and Univ. of Tokyo.

New subjects "remote use of supercomputer system" and "all Japan ST (Spherical Tokamak) research program" were added to the collaboration in the 2005 fiscal year. The "remote use of supercomputer system" is a project which uses the supercomputer system of NIFS efficiently from a remote station. The "all Japan ST research program" builds a virtual laboratory for ST research on Super-SINET and each laboratory communicates mutually and shares databases. To fill those needs, the network for collaboration using Super-SINET was reconstructed in the 2005 fiscal year.

The block diagram of the reconstructed network for collaboration using Super-SINET is shown in Fig. 1. The access place and the routing method from a remote station of each subjects are shown in Table 1. We adopted dynamic routing control for mutual communication between remote stations. RIP v2 was applied to all the routers linked to Super-SINET, and all the routers

- were defined as the same MPLS-VPN closed region.
- In NIFS side, we designed and constructed network as follows.
- For "LHD experiment remote participation" and "all Japan ST research program";
- 1) Five 1Gbps circuits were prepared from Super-SINET, and those were connected with three gateway routers.
  - 2) Three gateway routers adopted RIP v2 as routing control.
  - 3) The load balancing of five circuits from Super-SINET became possible by the function of RIP v2.
  - 4) The routing control between three gateway routers and a router of LHD-LAN adopted OSPF protocol.
  - 5) The load balancing between three gateway router and LHD-LAN become possible by ECMP function of OSPF.
- For the "remote use of supercomputer system";
- 1) One 1Gbps circuit was prepared from Super-SINET, and it was connected to a gateway route which was connected to a gateway server for Supercomputer system.
  - 2) The routing control adopted a static definition.

In the 2005 fiscal year, three remote stations were installed; Kyushu Univ. for the "remote use of supercomputer system" and the "all Japan ST research program", and Nagoya Univ. for the "LHD experiment remote participation".

The reconstructed network can perform mutual communication between remote stations, and can contribute to advance the collaboration for new subjects.

References

- 1) Tsuda, K., Nagayama, Y., Yamamoto, T., Hasegawa, H.: Ann. Rep. NIFS (2003-2004) 400.
- 2) Tsuda, K., Nagayama, Y., Yamamoto, T., Hasegawa, H.: Ann. Rep. NIFS (2004-2005) 383.

Table 1. Access and Routing for Subject

Subject	Access to	Static Routing	Dynamic Routing
Remote use of Supercomputer system	Supercomputer System	○	—
all Japan ST research program	another remote station	△	○
LHD Experiment Remote Participation	LHD-LAN, another remote station	△	○

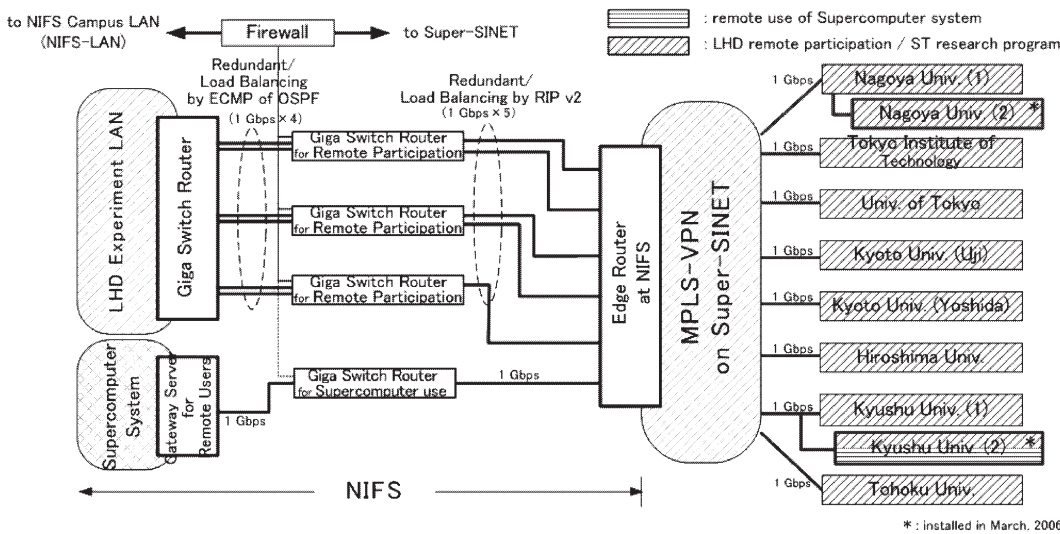


Fig. 1 The Block Diagram of Network for collaboration using Super-SINET

## 8. Fusion Science Archives

Archival activities have been extensively done since the foundation of Fusion Science Archives on Jan. 1, 2005.

Owing to the foundation the followings are pointed out as favorable aspects. A new office available also for meetings was set up with the area of 80 m<sup>2</sup>. The number of staff was increased from three to four, the storage space almost doubled with the total area of about 90 m<sup>2</sup> and the budget also increased. The circumstance surrounding Fusion Science Archives has been much improved than before. The increase in the number of staff helps make rapid the registration process of the data. The total number of database registered has amounted to more than 15,000. The category of collaboration research on Fusion Archives has been independent of any other research field and the number of research subjects on Fusion Archives was increased to six in comparison with that in the previous year as shown in the followings. The collaboration research contain 6 research subjects by which an essential part of fusion archives is covered: 1) Archival studies on nuclear fusion research, 2) Complementary studies of nuclear fusion research archiving by means of oral history, 3) The role of inter-university institute for nuclear fusion research in early period, 4) Studies on the problems related to information disclosure at nuclear fusion archives, 5) Historical research on fusion-plasma research devices, 6) Chronological studies on international collaboration of nuclear fusion research.

The regular meeting of Fusion Science Archives plays an important role in discussing the strategy of archival activities, where three professor emeriti usually take part in as collaborators, which is based on the idea that the strategy should be determined by taking account of collaborators' opinions as much as possible. The meeting is held usually every other week.

In registering database it is important to make indices of data appropriate for us to search by means of EAD (encoded archival description) that is the international standard. The idea of EAD was not so familiar to the member of the regular meeting because EAD has been primarily applied in the archives of social sciences. However, the member started to make efforts to understand EAD for improving the quality of the database. One of the staff participated in a one-week course of Archives College to augment the archival capability that was sponsored by NIJL (National Institute of Japanese Literature). The course was helpful to understand how

EAD could be applied in the fusion archives. On the other hand, the participation from the field of nuclear fusion science gave a strong and fresh impact to the sponsor because there have been very few participants from the field of natural sciences so far. It was pointed out in the course that it is important to inform the society of archival activities on fusion science on all occasions of physical society meetings and so on because archival activities on physics started early but now its activities have faded out. In this relation, the article on fusion archives was published in *Journal of Plasma and Fusion Research* No.5, 2005. Contents of the home page on Fusion Science Archives were improved towards opening to the public. Great effort was made by Sokendai (The Graduate University for Advanced Studies) on how to search the database on the home page.

The whole meeting was held twice, in September and in February, where the collaborators nationwide took part in to discuss the status and strategy of collaboration researches. The researchers were from Nihon Univ., Sokendai, KEK, NIJL, RIST (Research Organization for Information Science and Technology), Nagoya Univ., Kyoto Univ., Tohoku Univ., Univ. of Tsukuba, Osaka Univ., Kyushu Univ. Along with discussions on the six collaboration research subjects, the detailed discussion on EAD was made, and the status of fusion archives was introduced in Kyoto Univ. and in Univ. of Tsukuba.

Oral history was done with Professor Emeritus Yamamoto Kenzo as the interviewee. NIFS report was published on the oral history to Professor Emeritus Matsuura Kiyokata.

The activities on collaboration researches have been presented at the annual meetings of the Japan Society of Plasma Science and Nuclear Fusion Research in December 2005 and of the Physical Society of Japan in March 2006. In the former meeting, two posters were presented: "Establishment of Fusion Science Archives and Its Activities" and "Compilation of Chronology Based on Fusion Science Archives", in the latter one the oral presentation "An Oral History on the Involvement of Industries with Nuclear Fusion Research and Development in Japan" was made.

US-Japan workshop on Fusion Science Archives was held for the first time in UCLA and in PPPL in December 2005.

(Matsuoka, K.)

§1. NIFS Fusion Science Archives Database and Studies on the Problems Related to Its Disclosure

Namba, C., Matsuoka, K., Kimura, K., Hanaoka, S., Yamaguchi, T., Hotta, S. (Nagoya Univ.), Obayashi, H., Fujita, J. (NIFS, Professor Emeritus), Terashima, Y. (Nagoya Univ., Professor Emeritus), Abe, N. (Sokendai), Takaiwa, Y. (KEK), Gotoh, H. (NIJL), Nisio, S., Uematsu, E. (Sci. & Tech., Nihon Univ.)

NIFS Fusion Science Archives Database

Archival activities were continued during FY 2005. Much effort was made on registering the stored materials into NIFS Fusion Science Archives Database. By the end of FY 2005 the total number of registered materials amounted to more than 15,000. Table I shows the tags (fields) of the database.

Table I. Fields of Database

No.	Item	Description
1	Date registered	Date the material is registered in the database
2	Date checked	Date the material in the box is identified
3	ID number	5-digit number for each item; first three figures for the box-number and the rest for item identification
4	Date arranged	Date the material is put in the box
5	Document source	Person who offered the material
6	Title of the document	As remained on original material
7	Subtitle	As necessary
8	Year	19xx , 19xx-19xx
9	Brief description of the contents	Materials in detail
10	Author or organization	Document writer , letter sender, publisher
11	Date of issue	Date the material is issued, written
12	Appearance or form	Book, pamphlet, envelope, file, notebook, album
13	Box number	Box number in three figures: Bxxx
14	Reference ID No.	As necessary
15	Keyword 1 Organization	Author, publisher
16	Keyword 2 Classification	Scientific paper, meeting record, comment, news comment, letter, proposal, recommendation
17	Keyword 3 Committee	Name of committee, conference, study group
18	Keyword 4 Field or purpose	Research system, international collaboration, education, administration
19	Keyword 5 Research field	Plasma physics, reactor engineering, heating etc.
20	Keyword 6 Other information	As necessary
21	Remarks	

Features of the database:

- Each ID number, 033-03-01, for example, corresponds to the document stored in an envelope.
- Several documents are kept in a cardboard box; each box has its own box number: B033, for example.

- FileMaker Pro is used as database management system.
- Catalogue of registered documents will be available through INTERNET in the near future. Preparatory work to make the documents open to the public was performed and a preliminary version is now available from NIFS Homepage.
- In order to provide us with more convenient electronic finding aid, *Encoded Archives Description* (EAD) that is an international standard will be adopted. For this purpose, intensive collaboration with Sokendai, National Institute of Japanese Literature and KEK is now under way. It has been recognized that the database constructed on the basis of FileMaker Pro is easy to convert to EAD and is available online in XML data format.

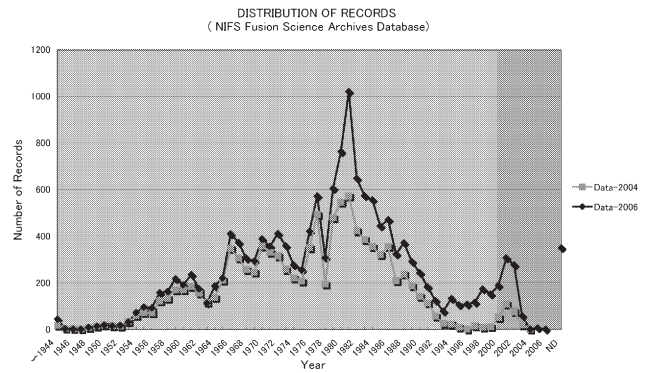


Fig. 1. Temporal distribution of registered documents

Some features of the registered documents:

- Temporal fluctuations are observed, being coincident with establishment of institutions or initiation of big projects. The reason why the number of the records around 1980 is at its maximum is that there have been a lot of events, such as deliberation on R-project, JT-60 operation and SCJ (Science Council of Japan) reformation (Fig. 1).
- Decrease in the number of recent records, especially after 1995.
- Sources are localized, being highly dependent on the contribution from individuals.
- Documents obtained through INTERNET are gradually increasing.

Problems related to information disclosure

We are planning to offer the documents and records collected and registered in NIFS Fusion Science Archives for public perusal. However some of them are inappropriate for disclosure to the public from the view point of protection of the personal data. An appropriate guideline for information disclosure is required. To establish the guideline we have surveyed the regulations for information disclosure at other organizations, such as National Archives of Japan and some universities. Those will be useful to establish the disclosure criteria on NIFS Fusion Science Archives.



## §2. Complementary Study of Nuclear Fusion Archiving by Means of Oral History

Fujita, J. (NIFS, Professor Emeritus),  
Terashima, Y. (Nagoya Univ., Professor Emeritus),  
Obayashi, H. (NIFS, Professor Emeritus),  
Matsuoka, K., Namba, C., Kimura, K.,  
Kato, N., Abe, N. (The Graduate Univ. Adv. Studies)

### *Introduction*

In carrying out archival studies on early days' nuclear fusion research in Japan through the collection of historical documents, it is noted that some of the documents are missing, and the underlying stories are not always clear due to the incompleteness of the materials. It is an urgent task to complement the archives through interviews with senior scientists who played important role in those days, by means of oral history, which is one of important methods in archival studies. So far interviews were conducted with Prof. Sekiguchi, T. on the topics of the nuclear fusion research in early days' Japan (NIFS-MEMO-33, NIFS-MEMO-40), Prof. Matsuura, K. on the initiation and the termination of Reacting Plasma Project (R-Project), (NIFS-MEMO-47) and Dr. Morino, N. on the participation of industries in the initial stage of fusion research in Japan.

### *Interviews*

In this fiscal year, an interview was conducted with Prof. Yamamoto, K., under the collaboration program with The Graduate University for Advanced Studies on "History and Archives of Inter-University Research Institute." The subject and other information concerning the interviews are listed below:

- (1) Interview with Prof. Yamamoto Kenzo
  - a. Interview subject: "On the "History of nuclear fusion research and development in Japan-1."
  - b. Interviewers: Fujita, J., Terashima, Y., Obayashi, H., Matsuoka, K., Namba, C., Kimura, K., Morino, N., Kitsunozaki, A, Kato, N.
  - c. Date and place: 2005.7.7, 2:00-5:00 pm, at the meeting room of National Institutes of Natural Sciences, Tokyo Branch.
- Interviews with Dr. Young, Kenneth M., and Prof. Yoshikawa, S. were also conducted on the occasion of US-Japan Workshop on Archiving of the Early Days' Nuclear Fusion Research in US and Japan:
- (2) Interview with Dr. Young, Kenneth M.
  - a. Interview subject: "Early days' nuclear fusion research at Plasma Physics Laboratory, Princeton University, and industrial involvement on nuclear fusion research in the United States."
  - b. Interviewers: Fujita, J., Matsuoka, K., Obayashi, H., Namba, C., Kimura, K., Tomita, Y, Mizuuchi, T, Abe, N.
  - c. Date and place: 2005.12.15, 9:15-12:15 am, at Furth Library, Princeton Plasma Physics Laboratory.
- (3) Interview with Prof. Yoshikawa Shoichi

- a. Interview subject: "History of nuclear fusion research at PPPL, especially of Prof. Yoshikawa's research."
- b. Interviewers: Matsuoka, K., Obayashi, H., Fujita, J., Namba, C., Kimura, K., Tomita, Y, Mizuuchi, T, Abe, N.
- c. Date and place: 2005.12.15, 2:00-4:30 pm, at Furth Library, Princeton Plasma Physics Laboratory.

### *Procedure of the Interview*

#### (1) Inquiries in advance

The questions from interviewers were first gathered and summarized as usual. The outline of the questions was handed to the interviewee in advance.

#### (2) Introduction of our archival activity

Before starting the interview, a brief summary of our archiving activity was introduced in order to help the interviewee to understand our intention of conducting the interview.

#### (3) Interview

No strict manner of oral history, which is an established technical method of the interview, was applied in our case, but a style of round-table talk was adopted because of its unfamiliarity and unsuitability in Japanese society. The agreement between interviewee and interviewers on video and voice recordings of the interview was orally confirmed in advance for each interview.

The talk by the interviewee, questions and answers, and discussions among all participants were altogether conducted under a moderator, Fujita, J. for interviews (1) and (2), and Matsuoka, K. for interview (3).

#### (4) Transcription and record making

After preparing a rough transcript, all the interviewers checked and edited it for accuracy and clarity. The response given in advance by the interviewee was also checked and confirmed for authenticity. The edited transcript then went on to the interviewee for corrections or additions.

#### (5) Publication

The interview records together with the outline of the questions will be published in a series of NIFS-MEMO after corrected by the interviewee.

### *Issues to be solved*

The interviews were very successful, mainly due to the cooperative manner of the interviewees. The issues, however, of exchanging written forms of agreement on recording the interviews and publishing the transcripts remained to be solved, taking various aspects into consideration.

### *Future plan*

We have a plan to extend the interviews toward more persons and subjects, especially focusing on the international collaborations before the formal collaboration program started. We have also an intention to conduct interviews with pioneering researchers on inertial confinement fusion.

We are making a continuing effort to edit and publish the reports of above-mentioned interviews in FY2006.

### §3. The Role of Inter-University Institute for Nuclear Fusion Research in Early Period

Obayashi, H., Fujita, J. (NIFS, Professor Emeritus), Terashima, Y. (Nagoya Univ., Professor Emeritus), Takaiwa, Y. (KEK), Uematsu, E. (Nihon Univ.), Kawakami, I. (Nihon Univ., Professor Emeritus), Matsuoka, K., Namba, C., Kimura, K., Hanaoka, S.

The idea of inter-university collaborating institute was produced in 1950s, when the scientific research activities in Japan had a very hard time in obtaining budget and other necessary supports. The Institute of Plasma Physics, Nagoya University (IPP, 1961-1989) belongs to this category and was established after the intensive discussions (AB-dispute, 1959) on the starting-up policies of fusion research in Japan. IPP was expected to be a center of collaborative work along A-plan, i.e., to promote the general studies of plasma physics and technology for fusion research. This line of activities was funded by Monbusho budget for university-based research. Although affiliated with Nagoya University, IPP was not always restricted within the host university, but kept its inter-university nature as to be operated substantially by the autonomy of the fusion researchers' community, Kakuyugo-Kondankai. This relation between the Institute and the University was often referred to as "Mutual Respect and Mutual Independence"

IPP had organized and carried out a number of collaborative activities with the nation-wide researchers, as well as its own programs. Compared with other collaborative institute, for instance, INS (Institute for Nuclear Study, Univ. Tokyo, 1954-1997) which was devoted mainly to the shared use of large accelerators, IPP paid more efforts to make collaboration works rather than simple use of some specified big facility. The principle was quite effective to bring university activities up.

After starting of IPP, the nation-wide strategy of nuclear fusion research was re-discussed by a Panel in SCJ (Science Council of Japan), in view of the next step of development. The report (1967) claimed the necessity of an approach along the line of comprehensive experimental device, where (i) projective planning, (ii) choice of machine type, and (iii) new institution for the program, were emphasized. This was a kind of restoration of B-plan, i.e., to introduce a sizable machine, and followed up by STA (Science and Technology Agency) budget for National Atomic Energy Research with an approval of JAEC (Japan Atomic Energy Commission). Then JAERI (Japan Atomic Energy Research Institute), ETL (Electro-technical Laboratory) and RIKEN

became in charge of the program, and Tokamak and other systems had come in the scope. It should be noted a new type of institute to conduct stepwise trials for fusion reactor goal with a target point defined on the  $(T - n\tau)$  diagram was first mentioned. As an actual system, JAERI became responsible for this new type of institution.

For the inter-university institute, IPP, the main target was to make systematic and basic research of plasma science and to give fundamental knowledge applicable to controlled fusion. Actually IPP at this period started keV-plasma confinement and multi-path approach for new regions of plasmas as its own program plans.

Due to the expanding areas of fusion science, SCM (Science Council of Monbusho) gave a new proposal for promotion of fusion researches in universities in 1975, to set up various research centers through 1980: Tokamak (Kyushu U.), Heliotron (Kyoto U.), Mirror (U. Tsukuba), Theory (Hiroshima U.), Laser (Osaka U.), Tritium (Toyama U.), etc. Developments in many directions induced somewhat different factors in the style of inter-university collaborations. As for IPP itself, possibility of a reacting plasma experiment (R-tokamak) had been considered.

On the JAEC-STA side, NFC (Nuclear Fusion Council) started in 1975, and the 2<sup>nd</sup> step of Comprehensive Fusion Research Program was set up to aim at break-even conditions in JT-60 machine. In this mission-oriented line JAERI, Naka Establishment, succeeded in attaining the aimed break-even plasma in JT-60U in 1996. The reactor technology development became much more important.

In 1980s SCM also reconsidered the way of promoting fusion research and development for universities, analyzing the general trends of research activities in the near future and gave the new propositions. Eventually the LHD project was given as the next step large program of university side. Among others the growing importance of inter-university scheme of collaborative activities was mentioned. The inter-university institute attached to a university should be up-scaled and to be independent of a particular university. Then IPP was reorganized jointly together with Plasma Physics Laboratory, Kyoto University and Institute for Fusion Theory, Hiroshima University, into a new organization for inter-university collaboration, NIFS (National Institute for Fusion Science) in 1989.

There were two different funding lines for fusion research promotion in Japan: Monbusho and STA. They were in a sense complementary and alternating in character. Since 2001 they have been reorganized into a single ministry MEXT.

We can follow these changes in the role of inter-university institute for fusion research by checking the materials preserved and indexed at NIFS Archives.

§4. Archival Studies on the Nuclear Fusion Research from Chronological Aspect

Kimura, K., Matsuoka, K., Namba, C., Hanaoka, S., Terashima, Y. (Nagoya Univ., Professor Emeritus), Obayashi, H. (NIFS, Professor Emeritus), Fujita, J. (NIFS, Professor Emeritus)

Introduction

It is essential for archival study to establish the dates and time sequences of past events. Based on NIFS Fusion Science Archives, the historical records have been registered for the database of fusion science chronology. Since there have been a lot of people, institutes, authorities concerned, and international relations in nuclear fusion research, the idea of multi-dimensional chronology is useful to survey the events and/or activities of organizations in the order of their occurrence at a glance.

Compilation of Multi-dimensional Chronology

Multi-dimensional chronology is compiled by gathering historical records, which are requisite for the research subject in archival study, from the chronological database. The subjects of the multi-dimensional chronology compiled in 2006 were (1) “Nuclear fusion research in 1960s in Japan,” (2) “The chronology of fusion researches in universities in comparison with industrial activities in 1950s,” (3) “Fusion research development at universities in Japan and visiting staff to IPP Nagoya Univ. from US,” and (4) “The chronology of the negotiation with the local residents on the site issue of NIFS to be founded.” At the end of 1970s Nagoya University entered into a preliminary negotiation with Toki municipal assembly about the site issue. The negotiation lasted for ten years until it was concluded in 1989.

A brief multi-dimensional chronology table was presented for reference, also on the occasion of an oral history interview. Table I shows a part of the chronology used on the oral history interview with Prof. Yamamoto Kenzo. He was involved in fusion research in different organizations, that is, Nagoya Univ., JAERI, and Japan Atomic Industrial Forum. Besides the activities in these organizations, those in Science Council of Japan, Atomic Energy Commission of Japan are also described in the table.

At the US-Japan Workshop on Fusion Science Archives held on Dec. 12-13, 2005, the contributions through personal exchanges between US and Japan were reported. Table II shows a part of the multi-dimensional chronology of fusion researches in universities in US and Japan and US researchers who visited the Institute of Plasma Physics, Nagoya University, before the Agreement on Treaty of Cooperation on Science between US and Japan was settled in 1979. Since there are few official documents preserved before the treaty, the steering committee records of IPP in NIFS Fusion Science Archives were surveyed for finding out US researchers who visited IPP in early days of

fusion research. The contribution by Japanese researchers in fusion study in early days in US remained to be surveyed for the future archival study.

Table I. An example of multi-dimensional chronology

Date	Classification					Event	ID of NIFS Archives
	SCJ	STA	Ind.	MOE	JAEC		
1940						Yamamoto Kenzo, Assistant Professor of Nagoya Univ., Dept. of Engineering	075-06
1956.1.1					*	Atomic Energy Commission of Japan established, 3 Laws on Atomic Energy enforced	411-01
1956.3.1			*			Japan Atomic Industrial Forum, Inc. established	511-33
1956.5.19		*				Science and Technology Agency established	510-46
1956.6.15		*				Japan Atomic Energy Research Institute founded	512-32
1957.2.6					*	1 <sup>st</sup> Kakuyugo Hannooh Kondankai (by JAEC)	301-04-02
1957.4.1		*				JAERI Tokai Research Institute founded	504-10
1958.4				*		Kakuyugo Kondankai (by Fusion researchers group)	301-04-09
1958.5.19					*	1 <sup>st</sup> Nuclear Fusion Special Committee of AEC (President: Hideki Yukawa)	301-11-03
1958.1	*					27 General Assembly "On the Promotion of Nuclear Fusion Research" (Recommendation)	308-17
1959.2.14				*		Atomic Energy Society of Japan established	504-07
1959.2.20					*	Plan A and Plan B on Nuclear Fusion Research in future proposed by Nuclear Fusion Special Committee of AEC	301-01-06
1959.4.22		*				JAERI Nuclear Fusion Research Committee started (Plan B) Chairperson: Kenzo Yamamoto	302-07-01
1959.5.14	*					Symposium on "How to develop nuclear fusion research in Japan" held by Genshiryoku Mondai Iinkai and Kakuyugo Tokubetsu Iinkai of SCJ	301-11-04

Table II. Fusion Research in US and Japan in Early Days

year	International events, conf.	Research at univ. in Japan	Personal exchange	Research in US
1955	The 1st United Nations Conf. on the Peaceful Uses of Atomic Energy (Geneva)			
1957	Lawson criterion IAEA established	Osaka(Ultra high temp.) Nagoya (Toroidal pinch) Kyoto (Helical ) Tokyo (Plasma β tron ) Nihon(Mirror)		DCX Stellarator Astron
1958	2 <sup>nd</sup> Geneva Conf.			
1961	1 <sup>st</sup> IAEA conference (Salzburg) minimum B	IPP Nagoya Univ. QP Project, TP		
1962		Kyoto Univ., Heliotron B	AL Gardner (UC Livermore Laboratory), guest staff of IPP Nagoya, QP Project (sponsor:JSPS Japan Society for the Promotion of Science) (1962.04 ~ 1962.06)	
1963		Osaka Univ., Cusp Plasma IPP Nagoya Univ., BSG Osaka Univ., Laser,		
1964	3 <sup>rd</sup> Geneva Conf. T-3, DC Octopole	Nagoya, Torus (Mark II) Kyoto, Heliotron C	J.M.Dawson( Princeton Univ.), theory group of IPP (Fulbright,1964.09~1965.07)	
1965	2 <sup>nd</sup> Culham Conference			Multipole(Ohkawa) Spherator(Yoshikawa)
1966	Int. Torus Symp. (PPPL)		C.K.Birdsall, (UC Berkeley) computer physics (invited by Osaka Univ.,1966)  R.T. Taussig, Columbia Univ. Theory group of IPP (sponsor:NSF,1966.10~1967.11) National Science Fund	

## §5. Research on History of Fusion and Plasma Research Devices

Kitsunozaki, A. (Research Organization for Information Science and Technology, RIST),  
Obayashi, H. (NIFS, Professor Emeritus),  
Kimura, K.

### Background and Purpose:

Plasma and fusion research in Japan has been started around 1950, almost the similar time as the systematic research was started in Europe, USSR at that time and the USA. Compared to other large-scale researches such as space research or nuclear fission research, the early start of research is one of special points of plasma and fusion researches in Japan. Fortunately, the present fusion research of Japan can be judged as one of leading forces of the world fusion research thanks to many efforts of research peoples during these 60 years.

These materials will be the proof how our research turned in one of the leading forces of the world which is very rare case in Japan. There is a big worry that those materials are being lost, particularly those before 1980.

This particular research focuses its work on the archiving of materials of the devices of plasma and fusion research and to make a set of summary documents for each device. Because those researches depend very much on devices, which means a special device needed to explore one research objective, the history of devices almost means the history of researches themselves.

The planned work here will make firm point data of devices which are basis to explore lines and planes of the history of plasma and fusion researches.

### Contents and Results:

The selected items in the set of summary documents for each device are: 1.Name of the device, 2.Name of organization, 3.Figures of the device, 4.Photos of the device, 5.Explanation of operation, 6.Major parameters of produced plasmas, 7.Original purpose of the research and changes, 8.Time table of conceptual design to construction and operation, 9.Major results (within 5 lines), 10.List of papers and presentations, 11.Names of all contributed persons, 12.Special points to be noted, 13.Importance experiences (Experience of failures are the most important.), 14.Source materials of above if any.

Most of devices have more than one name, and the popular name is usually different from the name on budgetary documents. Therefore, it is desirable that all of those names are shown and put on table of document search.

For name of organization, if name is changed, the new name will be shown in parenthesis. Scale is necessary in

drawings. Drawings and photos after attaching diagnostics are also desirable.

Some details of the device operation for each of the operation mode when there are several of operation modes are desirable as well as the typical plasma parameters for each operation mode.

As for the major results and the timetable, it is asked to persons to fill the formats to select results and events to avoid the table become too detailed. It is also requested to report about 'failures' because those experiences of unexpected outcome and how they managed to attain new results are very important example to younger researchers.

The amount of the set of summary documents is expected to be about 10 pages. If people wish to learn more detail, then he/she is requested to refer to papers and documents on the list of items 10 and 14.

As the work of the first year, summary of two devices has been made which will be examples of this work after the next year. The devices are RFX-XX / RFC-XX-M of former Institute of Plasma Physics, Nagoya University and JFT-2a of former Japan Atomic Energy Research Institute. Filling of the formats is asked to persons directly worked in the device, and a format to make addition and/or changes is prepared for future needs.

Thanks to the progress of electronic machines such as computers and scanners, it is now easy to get drawings and photos converted to electronic files. Those files will be accessible through electronic grids like internet in the near future. Those files are made using popular softwares such as Words and JPEG and all materials are prepared to be printed out to A4 sized papers.

This work has been conducted under NIFS research collaboration program: NIFS05KVXJ003



## §6. The Chronology on the International Exchange of Nuclear Fusion Study

Uematsu, E. (Sci. & Tech., Nihon Univ.),  
Kojima, C. (Commerce, Nihon Univ.),  
Nisio, S. (Nihon Univ., Professor Emeritus)

### 1. Background and purpose of the research.

Tomio Ariyasu of welding technology group of Osaka University attended the workshops on astrophysics at the Yukawa Institute for Theoretical Physics (Kiken) of Kyoto University in February and October of 1955. In the second workshop nuclear fusion on the Earth was discussed. He was interested in the nuclear fusion and participated in the Workshop on Ultra-High Temperature held in the Kiken in April of 1956. Ariyasu told the topics on ultra-high temperature to Minoru Okada (Welding Engineering Department, Osaka University) and Kōdō Husimi (Physics Department, Osaka University) with the help of Seikan Ishigai (Mechanical Engineering Department, Osaka University). Then in June of 1956 at Osaka University an open experiment of the high current discharge was carried out and the first nation-wide research group, the Handai Cho-koon Kenkyukai (Research Group of Ultra-High Temperature (Osaka University)) was organized. This was the first experiment with the aim of the nuclear fusion in Japan.

The Kiken Cho-Koon Kenkyukai was planned by Satio Hayakawa and Mitsuo Taketani. Hayakawa heard the Matterhorn Project of United States in the conference held in Mexico in 1955, and planned the Kiken Cho-Koon Kenkyukai after his homecoming. In Nagoya University, Kenzo Yamamoto had started the research of high-temperature plasma as a discharge phenomenon. The researchers of various fields had started research related to the nuclear fusion in Japan.

The Japanese Atomic Energy Commission (JAEC) organized the Kakuyugo Hannou Kondankai (the Assembly for Nuclear Fusion Reactions) in February 1957. Besides the background of this governmental movement, the Kakuyugo-Kondankai (Nuclear Fusion Research Group) of the researcher-initiated nation-wide organization was established in 1958. Nuclear Fusion Research Group published the transaction of the forum *Kakuyugo-Kenkyu* (*Nuclear fusion Research*) in July 1958, and the editorial office was placed at Nihon University. Literatures on the

nuclear fusion issued in foreign countries were collected by the editorial office. The research trend and the Japanese translation of papers were reported in *Nuclear Fusion Research*. It was the start of the international exchange to obtain the research information from foreign countries.

Kanji Honda of The University of Tokyo reported at the Kakuyugo-Kondankai meeting the researches on the ultrahigh-temperature plasma presented in the third international electric discharge conference held in Venice in 1957. The United Nations' Second International Conference on Peaceful Uses of Nuclear Energy was held in 1958, and information on the peaceful use of nuclear fusion was opened to the public. Goro Miyamoto of The University of Tokyo who attended the conference proposed the two projects of A and B in the Kakuyugo Senmonbukai (Special Panel on Nuclear Fusion Research (the First Stage Special Panel)) of JAEC in 1958. Shoichi Yoshikawa (PPPL) and Tihiro Ohkawa (GA), who were active fusion scientists abroad, reported the research trend of foreign countries in the Kakuyugokaigi (the Nuclear Fusion Council) of JAEC.

The historical investigation of the nuclear fusion had been carried out. However, the international exchange of nuclear fusion was not examined. It was our purpose to investigate the international exchange of nuclear fusion and to make the chronology.

### 2. Content and result of the research

Nuclear fusion research in Japan was discussed separately in different committees under the Ministry of Education, Science and Culture (MOE) and the Science and Technology Agency (STA). In each sectors, the international exchange has separately been carried out.

In this study, we examined international exchange of JAEC. We investigated the proceeding of the Kakuyugo Senmonbukai, the Kakuyugo Kenkyu Un-ei Kaigi (the Nuclear Fusion Research Management Council), and the Nuclear Fusion Council of JAEC, and made the chronology.

### 3. Material location and future planning

The proceeding of the Kakuyugo Senmonbukai, the Kakuyugo Kenkyu Un-ei Kaigi, and the Kakuyugokaigi has been arranged and preserved by Kenzo Yamamoto. The materials of the international exchange of JAEC preserved by Sigeru Mori were transferred in the Naka Fusion Institute of Japan Atomic Energy Agency (JAEA). As future planning, we want to investigate the materials of the international exchange stored in NIFS and to make the synthetic chronology.

## §7. US-Japan Workshop on Fusion Science Archives

Matsuoka, K., Namba, C., Kimura, K., Tomita, Y., Obayashi, H., Fujita, J. (NIFS, Professor Emeritus), Abe, N. (Sokendai), Mizuuchi, T. (Kyoto Univ.)

US-Japan workshop on Fusion Science Archives was held for the first time reflecting the fact that the US-Japan collaboration on the fusion science has played an important role on the development of nuclear fusion research in both countries and the internationalization of fusion science archives is to be commenced. The purpose of the workshop was for the participants to know the status of the activities each other, to know the difference in the circumstance on fusion science archives surrounding both countries, and to discuss the future direction. The topics were focused on the history before the Agreement between Japan and USA on Cooperation in Research and Development in Energy and Related Fields in 1979. The workshop consists of two parts: the former was on Dec. 12 -13 2005 in UCLA as a usual workshop and the latter on Dec. 15 -16 in PPPL to conduct interviews to two prominent scientists, Dr. Young Kenneth and Dr. Yoshikawa Shoichi, and to inspect archival activities in detail in PPPL and in Princeton University. UCLA has a plenty of scientists who specialize in archives as shown below and has a strong relation with Sokendai on this research field. Here, the workshop conducted in UCLA is primarily introduced.

Japanese participants are those shown as the authors of this report. Those from the US are as follows: Prof. Abdou M. (UCLA), Prof. Traweek S. (UCLA), Prof. Emeritus Chen F. F., Prof. Emeritus Fowler T. K., Prof. Meldrum M. (UCLA), Prof. Tamano T. (Formerly Univ. of Tsukuba and GA), Dr. Popescu A. (PPPL) et al.

Contents of presentations by Namba, C. Fujita J., Obayashi H., Kimura K. are described in this annual report. Dr. Abe N. introduced that Sokendai is composed of 18 Inter-University Research Institutes (IURI) and that archives are one of Sokendai's research projects. He explained the status of archives network of which final goal is to connect 18 IURIs on the basis of EAD and showed the NIFS digital finding aid as an example. Prof. Mizuuchi T. presented the history of experimental devices that originated in the Helicon project and succeeded by the Heliotrons for plasma confinement and presented photos showing that the devices are exhibited in good conditions.

Prof. Traweek S. expressed her opinion that the physics in the 20<sup>th</sup> century has shown a big change from at least four points of view; 1) how the research has been conducted, 2) how the budget has been allocated, 3) where

the research has been done, 4) who has done the research. The bilateral collaboration on nuclear fusion research should be a good example for us to investigate the change. However, it was pointed out that the documents registered are not many, so it is important to promote the archival activities for leaving on record the role played by the collaboration.

Prof. Emeritus Fowler T. K. talked about the history of plasma confinement as follows. In 1950s a variety of magnetic field configurations, e.g. mirrors, pinches, stellarators, were invented, however those suffered from instabilities, end losses, and complexity, respectively. In 1960s the energy principle that is a guiding principle for MHD stabilities was established, and the ideas of magnetic well and magnetic shear were verified to be effective theoretically and experimentally. While stellarators suffered from the Bohm diffusion, this was not the case for tokamaks. The era of tokamaks came in 1970s due to the epoch-making results in T-3, and C-Stellarator was converted to ST tokamak. In PLT the high ion temperature of 7 keV was achieved that was also an epoch-making result. Then three big tokamaks were constructed in US, in Europe and in Japan, which leads to ITER. Besides of tokamaks, he talked about the revival of stellarators, the advent of spheromak, and inertial fusion. Contributions of fusion sciences to natural sciences, for example, self-organization, application to astronomy, computer modeling, were introduced. Finally the attractive aspects of fusion energy were explained.

Prof. Emeritus Chen F. F. talked about the early phase of the Matterhorn Project in PPL including the staff, the students, and the status of researches in 1950s. A lot of photos on the so-called 2nd Geneva Conference in 1958 were impressive; the machines from USA, UK, and USSR, were reconstructed in the exhibition area of the conference hall and the researches were declassified.

Prof. Tamano T. talked about the US-Joint Safety Review Activities and history of fusion experimental devices primarily in GA (DC-Octopole, Doublets, OHTE) and in Univ. of Tsukuba (GAMMA 10).

Prof. Meldrum M. introduced on-going oral histories, for example, AIP activities including the interview to Prof. Koshiba M., activities in the space division of National Air and Space Museum, and History of Pain Collection in UCLA. She also explained the methodology and opening to the public of oral histories.

Dr. Popescu A. introduced the status of digitalization of MATT reports, Technical Memos, and PPPL reports.

It was pointed out by the participants that the archival activities on the fusion science in both countries still need more efforts including the activity of public relations.

## 9. Coordination Research Center

A major reorganization of former national laboratories was executed and a new institute, the National Institutes for Natural Sciences (NINS) was established in FY2004. These national institutes are the National Astronomical Observatory, the Institute for Molecular Science, the National Institute for Basic Biology, the National Institute for Physiological Sciences and NIFS. Along with this move formed at NIFS was a new Coordination Research Center, taking over from the Data and Planning Center, to promote coordinated research with external institutions, located in Japan and in foreign countries.

The new center consists of three divisions;

1. **Division of Academic Research Coordination**
2. **Division of Industry-Academia Research Coordination**
3. **Atomic and Molecular Data Research Center**

The functions of these divisions are summarized as follows:

1) The division of academic research coordination is intended to bridge between NIFS and external academic institutions, including universities and national laboratories. Currently, there are 4 working groups in this division. These are:

- 1-1. International Coordinated Research Group;
- 1-2. ITER Coordinated Research Group;
- 1-3. Laser Fusion Coordinated Research Group; and
- 1-4. Inter-Institutional Coordinated Research Group.

The international coordinated research group overlooks to at the international fusion research collaborations led by NIFS scientists and/or advises them to put together new initiatives on some of the areas which require immediate attention.

The ITER research coordinating group has formed a coordinating committee on some of the selected areas of collaboration in the ITER-related physics and technology fields. The idea behind this activity is to come up with new ideas though comprehensive understandings of toroidal plasmas confined in tokamaks and stellarators. To enhance direct interactions with ITER staff scientists, it has been promoted to attend the ITPA (International Tokamak Physics Activity) meetings. As a result, dozens of NIFS scientists attended ITPA meetings in FY2005.

The laser-fusion coordinated research group has been formed to establish a new link between magnetic and inertial

fusion research scientists. This is so that they can learn from each other through exchanging information and experiences in the areas of common interest. In FY2005, particular efforts were made to pursue the possibilities of using high-power lasers as plasma diagnostics for LHD.

The inter-institutional coordinated research group is to enhance interactions among the formally independent but now joint institutions under NINS. In FY2005, a number of meetings were held to solicit inputs from interested scientists. As a result, a NINS symposium is decided to be held in FY2006.

2) The division of Industry-Academia Research Coordination is to attract attention from industries, so that new areas of applications of existing technologies, developed originally for the sake of fusion research, can be explored. These technologies include microwaves and cryogenics. In FY2005, a major collaboration to develop new applications of high-power microwaves was executed in collaboration with the Gifu Prefecture Institute of Ceramics and Pennsylvania State University and will be continued in FY2006.

3) The Atomic and Molecular Data Research Center is to coordinate the efforts on the databases of atomic and molecular data for fusion and other plasma applications. These databases are summarized in Table 1. : AMDIS for cross-sections for electron collisions, CHART for heavy particle collisions and other related processes, as shown in Table 1. In FY2005, considerable attention was directed to the evaluation of C data and molecular targets such as  $H_2$ ,  $O_2$  and hydrocarbon molecules. These databases are used by more than 900 registered scientists all over the world. As a possible use of these database, the spectroscopy data taken in LHD have been analyzed. Also, a new initiative has been launched in collaboration with the National Astronomical Observatory, using a solar physics satellite: Solar-B. As for international collaboration, visited NIFS for an extended period (>30days) in FY2005 are: ① Igor Skobelev, Dr., Multi-charged Ions Spectra Data Center of All-Russian, Research Institute for Physical-technical and Radio-technical Measurements(VNIIFTRI), Russia, ② Zeqing WU, Dr., Institute of Applied Physics and Computational Mathematics, China, ③ Mitio Inokuti, Dr., Argonne National Laboratory (retired consultant), USA.

Table 1. Databases served through Web (<http://dbshino.nifs.ac.jp>)

Name	Records	Period	Contents
AMDIS	101,481	1961-2005	Excitation, Ionization and Recombination Data by Electron Impact
CHART	4,686	1957-2003	Numerical Data on Charge Exchange Cross Sections
MOL	3,175	1956-2004	(AMOL&CMOL) Numerical Data on Molecular Collision Processes
SPUTY	1,243	1931-2003	Numerical Data on Sputtering Yields for Mono-atomic Solids
BACKS	396	1976-1998	Numerical Data on Reflection Coefficients of Ions onto Surface
FUSION	1,269,374	1975-2004	Bibliography on Fusion Research extracted from INSPEC
PLASMA	80,032	1970-1986	Bibliography on Plasma Science extracted from INSPEC
AM	920,167	1970-2004	Bibliography on Atomic and Molecular Physics extracted from INSPEC
ORNL	75,625	1959-2003	Bibliography on Atomic Collisions collected at ORNL, USA

(Sato, M.)



## §1. Helium Ash Removal by Moving-Surface PFCs

Hirooka, Y. (NIFS), Nishikawa, M. (Osaka Univ.)

Ever since the discovery of the “Supershot” confinement regime in TFTR in late 1980’s, it has widely been recognized in the magnetic fusion energy research community that high-performance core plasmas often favor reduced wall recycling, i.e.,  $R \leq 1$ , where  $R$  is the particle recycling coefficient. To reduce particle recycling, wall conditioning techniques such as boronization have been applied to many plasma confinement experiments. Unfortunately, due to the surface saturation with trapped particles, the efficacy of wall conditioning has a finite lifetime, which necessitates the shutdown of plasma operation for re-conditioning. Clearly, this is not acceptable from the point of view of operating steady state fusion power reactors. It follows immediately from these arguments that enabling wall concepts R&D is necessary for the successful operation of steady state fusion devices beyond ITER.

Over the past decade, therefore, a variety of innovative plasma-facing component concepts have been proposed to provide a resolution for this steady state particle control issue. Essentially, all of these concepts employ moving-surface components, either made of a solid or liquid material, for in-line regeneration of particle trapping capabilities. One such concept proposed by Hirooka et al. [1] features a moving belt made of SiC-SiC fiber fabrics with an in-line getter film deposition system. In our previous work [2], proof-of-principle experiments were conducted on this concept with the moving belt simplified by titanium- or lithium-gettered rotating drums built in the laboratory-scale plasma facilities. Results indicate that hydrogen recycling can be reduced down to levels significantly lower than 100%, even at steady state, so long as gettering continues.

For the steady state operation of DT-fusion power reactors, not only unburned fuel but helium ash must be removed continuously so as to sustain the nuclear reaction. This means that a substantial pumping speed is necessary for helium ash removal. Given the edge helium partial pressure of the order of  $10^{-5}$  Torr, for example, the power output of 1GW would require a pumping speed as large as  $10^6$  liters/s. Although usually cryogenic pumps are employed for hydrogenic fuel particle control in existing large fusion devices, helium cannot be pumped at the same efficiency due to its extremely low boiling point of 4.2K. Unfortunately, the use of turbo-molecular pumps for helium ash removal is not quite realistic because of the conductance loss along the pumping ducts penetrating thick cryostat walls of superconducting magnets, essential for steady state fusion reactors. Nonetheless, helium ash removal has yet to be addressed as a critical issue in the magnetic fusion community.

In the present work, the use of moving-surface plasma-facing components (MS-PFCs) is proposed for the continuous removal of helium ash as well as hydrogenic

particles to maintain reduced recycling. It is of particular importance to investigate whether helium and hydrogen can simultaneously be incorporated in lithium deposits.

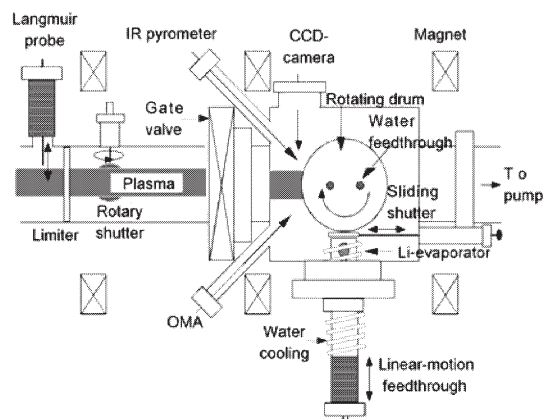


Fig. 1 A schematic diagram of the MS-PFC test unit.

Shown in Fig. 1 is a schematic diagram of the rotating drum MS-PFC test unit built in the VECHILE-1 facility [3]. The rotating drum is made of copper and is water-cooled. The rotation speed at the periphery is set at 10cm/s. The deposition of lithium is initiated after 100% steady respective state recycling was achieved. The deposition rate is set at about  $50 \text{ \AA/s}$ , adjusting the position and temperature of the evaporator.

Results of hydrogen and helium mixture plasma recycling measurements are shown in Fig. 2. Notice that, as soon as lithium deposition starts, steady state recycling of both hydrogen and helium, measured with  $H_\alpha$  and He-I spectroscopy, exhibits a noticeable decrease of about 20%. These data are suggestive of a multi-phase structure in the lithium-helium-hydrogen system, a hydride in the form of LiH and defect-trapped helium in lithium deposits [4].

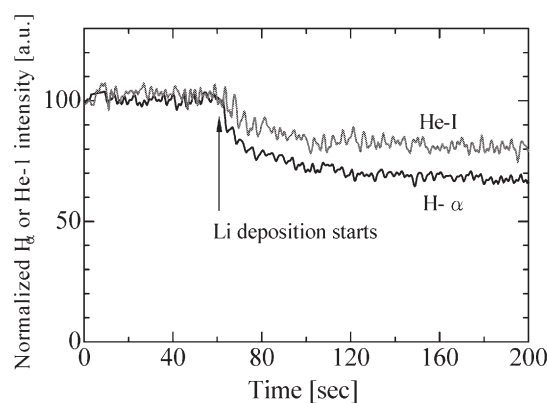


Fig. 2 Reduced steady-state recycling of hydrogen and helium from a lithium-deposited rotating drum.

### References

- 1) Hirooka, Y. et al, Proc. 17<sup>th</sup> SOFE, Oct 6-10<sup>th</sup>, 1997, San Diego, pp.906.
- 2) Hirooka, Y. et al., Fusion Sci. & Technol. **47**(2005)703.
- 3) Hirooka, Y. et al., J. Nucl. Mater. **337-339**(2005)585.
- 4) Hirooka, Y. et. al, paper presented at the 17<sup>th</sup> PSI-conf., May 22<sup>nd</sup>-26<sup>th</sup>, 2006, Hefei.

§2. How to Product, Use, and Export Photovoltaic Power in Developing Countries

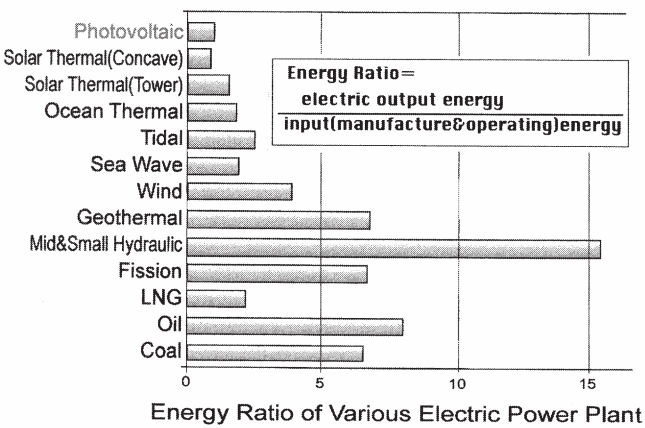
Tazima, T., Sato, M., Iguchi, H., Ikuta, K. (Tokyo Institute of Technology), Inutake, M. (Tohoku University)

In order to resolve the problems of energy and the environment of the world, We proposed a remarkable plan which is endorsed by Japan Committee for World Year of Physics as the Japanese Action Plan. This Action plan is presented in “The World Conference on Physics and Sustainable Development” which was held in Durban, South Africa on October 31-November 2, 2005.

This conference was a unique opportunity for the international physics community to come together and formulate a plan for tackling some of the large problems facing the world, and gave the physics community the chance to begin to focus on how we can work with colleagues in the developing world to bring more benefits to their world.

1.The sun brick as footstool of photovoltaic power plant.

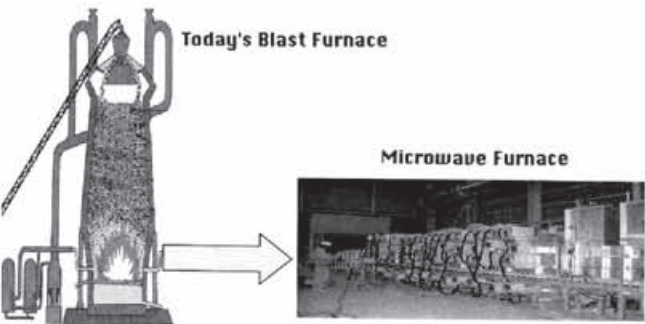
The major drawback of photovoltaic electric power plant is low energy ratio, because enormous footstool of solar cells requires extremely large production energy. We propose to employ the simple sun brick or the one of which surface is burnt by microwave. Then we can expect abundant photovoltaic power with reasonable energy ratio in many developing countries.



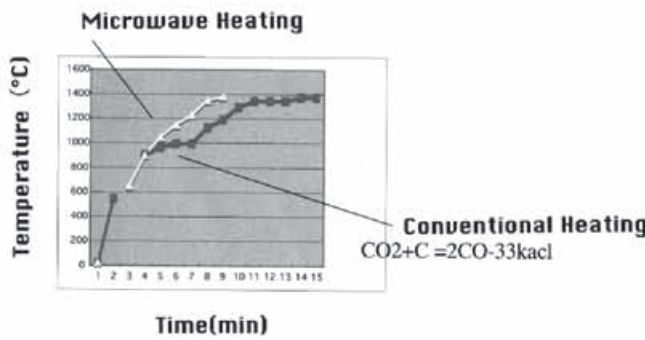
2.In-situ metal manufacture using microwave.

However, at present we have no method to store or export such abundant electric energy. Therefore we propose in-situ use of the electric power by converting it into microwave. Recent experiments suggest that the metal (e.g. Fe, Al, Ti)manufacture by microwave is possible, and this may have

many advantages , i.e. high efficiency, pulse operation, weak scale dependence, and excellent environmental safeguard characteristics.



Deoxidization of Iron Ore by Microwave Heating



3.Energy export in Mg

We also propose energy export by converting electric energy into chemical energy, i.e., Mg or Na manufacture by microwave. Recent experiments show that hydrogen gas and steam of high temperature and high pressure are produced, when Mg powder is burnt in the water within a boiler. The ash MgO or Na2O can be refined into Mg or Na by micro wave i.e. Mg or Na recycling is possible.



§3. Development of Cryogenic Foam Target with Guide Cone for FIREX-I

Norimatsu, T., Nakai, M., Nagai, K., Fujimura, T.  
(ILE, Osaka University),  
Iwamoto, A., Mito, T.

In FIREX-I (Fast Ignition Realization Experiment) project, heating of a compressed-DT plasma to an ignition temperature is the final goal of the project. Laser technologies to provide 10 kJ in a few pico-second and target fabrication technologies are the critical path toward the goal. Figure 1 shows the cryogenic foam target for FIREX-I that consists of a solid DT layer supported by a low density foam layer, a gas barrier, a guide cone, and the fuel feeder pipe. Fabrication of low density, low atomic number foam and control of the fuel amount is the critical path because the foam is an impurity for fusion plasma and the fuel amount directly influences the implosion timing.

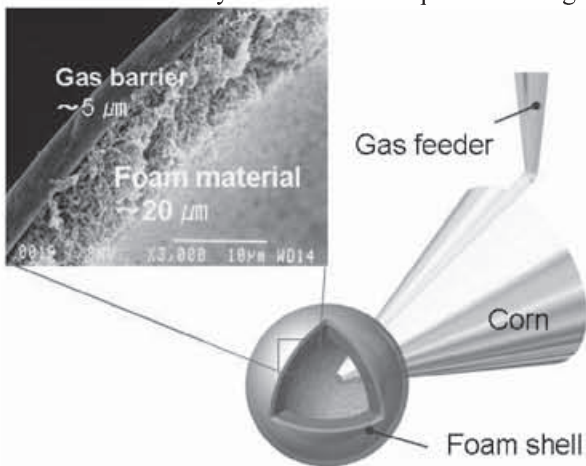


Fig. Cryogenic foam target with guide cone for FIREX-I

In 2005, the foam shell was developed at ILE under collaborative work with General Atomics, USA and the cryogenic experiment was carried out at NIFS.

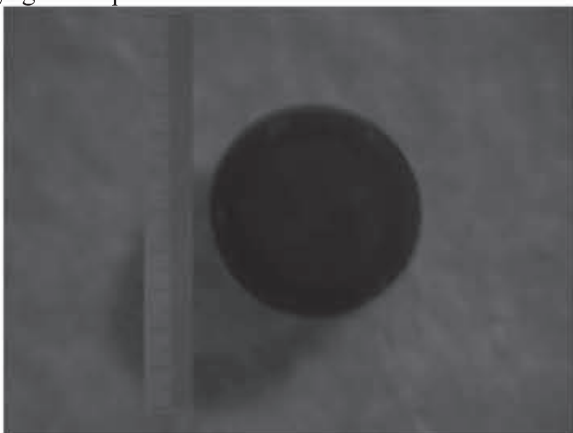


Fig. 2 Resorcinol-phloroglucinolcarboxylic acid /formaldehyde shell. Diameter 650 μm, the wall thickness 50 μm

Figure 2 shows a Resorcinol-phloroglucinolcarboxylic acid /formaldehyde shell whose material was newly developed at ILE this year. The thickness uniformity was much better than conventional RF foam and the control of thickness is more flexible because of the higher viscosity.

Current thickness uniformity was +/- 5% that should be reduced to +/- 2% and the density was 100mg/cc. We are now testing a new material to make foam shells with lower density.

At NIFS, control of fuel loading to the RF foam shell was examined in this year. Figure shows the first result for liquid hydrogen fill through the gas feeder pipe. Figure 3 shows experimental setup for interference observation of the foam shell.

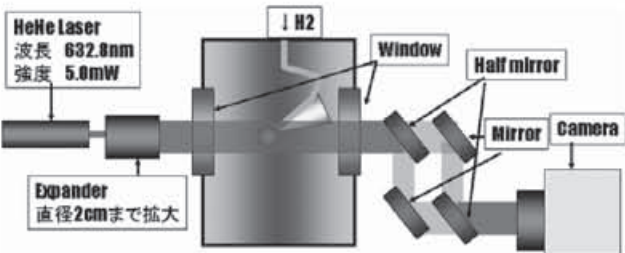


Fig. 3 Interference monitoring system for fuel control experiment.

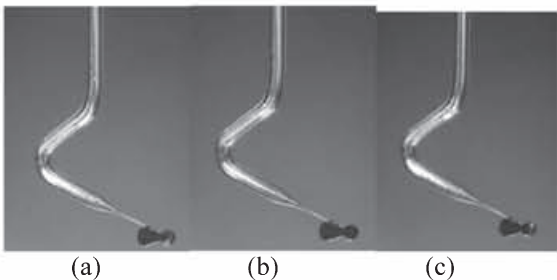


Fig. 4 Dry foam (a) and partially filled foam (b) and fully filled with liquid hydrogen (c), respectively.



Fig. 5 Interference pattern of foam shell filled with liquid hydrogen, indicating uniform distribution of liquid hydrogen.

The foam shell became dark when it is partially filled with liquid hydrogen as shown in Fig. 4. We are considering that the reason can be attributed to the increase of scattering in the foam.



§4. Activities on ITER Collaboration

Nakamura, Y., Todo, Y., Seo, K.

The ITER Research Coordinating Group (Division of Academic Research Coordination, Coordination Research Center) promotes research activities coordinated with the ITER project, cooperating with the ITER Collaboration Committee, which consists of NIFS specialists in various physics and technology fields including visiting professors from JAEA.

The International Tokamak Physics Activity (ITPA) aims at cooperation in development of the physics basis for burning tokamak plasmas. The ITPA continues the tokamak physics R&D activities that have been conducted on an international level for many years resulting in achievement of a broad physics basis useful for all fusion programs, for the ITER design, and for general tokamak research worldwide. The ITPA meetings, which are divided into seven groups (MHD, Disruption and Control; Confinement Database and Modeling; Transport Physics; Pedestal and Edge; SOL and Divertor; Steady State Operation; Diagnostics), are organized under the auspices of the ITPA Coordinating Committee. Each group meeting is scheduled to take place twice a year. We consider the ITPA meetings workshops on physics issues related to ITER and on comprehensive understanding of toroidal plasmas. We are strongly promoting NIFS scientists' participation and presentation in the ITPA meetings.

The numbers of participants and presentations from NIFS in the ITPA meetings held in the 2005 fiscal year (including one meeting held in March 2005) are summarized in Tables 1 and 2. The total participants amount to 29 persons and there were as many as 21 presentations. For example, the presentations on the first experimental demonstration of zonal flow in toroidal plasmas, on heating power threshold on electron transport barrier formation, and on computer simulation of toroidal Alfvén eigemodes drew much attention and contributed to the progress in understanding of the toroidal plasmas. Comparison between tokamak and helical plasmas is very important for the comprehensive understanding of toroidal plasmas.

In the 2005 fiscal year, the activity on ITER collaboration was newly budgeted. The travel expenses for six participants in the ITPA meetings held at the domestic locations and four participants in the ITPA meetings held abroad were supported with the budget.

To build up a closer connection with the Japan Participant Team for ITER Transitional Arrangements is one of the important works in our group. We held the periodical meeting with the domestic ITER team in 2005. We have been discussing the collaboration items and how to execute, taking into account each situation before the establishment of ITER organization. We are also closely

connecting with the Fusion Forum, which is promoting the nuclear fusion research including the ITER project in Japan. For the coordination with the university researchers, we attended the coordinating meetings of Fusion Network including fusion engineering and plasma science.

The ITER international team requested the collaboration with Dr. M. Kobayashi (Research Operations Division, Department of LHD Project) on "Power load analysis on the limiter configurations of ITER start-up phase". He visited Garching ITER Joint Work Site from Sept. 25, 2005 through Mar. 25, 2006. He applied the three dimensional transport analysis code EMC3-EIRENE to the ITER start-up phase and analyzed heat and particle load to the limiter. It was demonstrated that the three dimensional analysis for helical plasmas can make a great contribution to the ITER physics design.

Topical Group	Date (Place)	Participants (Presentations)
Diagnostics	14-18 Mar. (Culham)	2 (2)
Pedestal and Edge	18-21 Apr. (Kyoto)	5 (3)
Confinement Database and Modelling	18-21 Apr. (Kyoto)	2 (1)
Transport Physics	18-21 Apr. (Kyoto)	8 (6)
Steady State Operation	4-6 May (Como)	1 (1)
Coordinating Committee	6-7 June (Moscow)	1
MHD, Disruption and Control	4-6 July (Tarragona)	1 (1)
SOL and Divertor	4-7 July (Tarragona)	1 (1)
Pedestal and Edge	3-6 Oct. (St. Petersburg)	1 (1)
Transport Physics	3-6 Oct. (St. Petersburg)	1 (1)
Diagnostics	10-14 Oct. (Taejon)	2 (0)

Table 1. ITPA Meetings in 2005.

Topical Group	Date (Place)	Participants (Presentations)
SOL and Divertor	9-12 Jan. (Shanghai)	1 (1)
MHD, Disruption and Control	6-9 Feb. (Naka)	3 (3)

Table 2. ITPA Meetings in 2006.



## §5. 3D Edge Transport Analysis of ITER Start-Up Configuration for Limiter Power Load Assessment

Kobayashi, M. (NIFS),  
Feng, Y., Sardei, F. (MPI, IPP),  
Loarte, A. (EFDA),  
Federici, G., Strohmayer, G. (ITER),  
Reiter, D. (FZJ, IPP)

Two beryllium limiter modules, toroidally localized at the low field side (LFS), are foreseen to be used to sustain the plasma start-up phase in the current ITER design, as shown in Fig. 1. The 3D edge transport code, EMC3-EIRENE, has been implemented on the ITER start-up limiter configuration, in order to analyze 3D transport properties in geometry of the toroidally discrete limiter and to investigate the power load on the limiter surface. The main results of the analysis are summarized as follows:

1. Because of the finite shear in the edge, the interaction of the toroidally discrete limiters with flux surfaces of different  $q$ -values introduces a complex 3D pattern in the connection length profiles, where long and short flux tubes co-exist in the scrape-off layer (SOL), as shown in Fig. 2.

2. The severity of problems associated with very long flux tubes in the edge, which can bring a large amount of energy (proportional to  $\sqrt{L_C}$ , where  $L_C$  is the connection length), and cause a hot spot on the limiter, was mitigated and no significant localized power load was found. This is justified as follows: (i) For long flux tubes, at the region of  $s > 500$  m, (where  $s$  is a distance along flux tube measured from the limiter) the perpendicular energy transport time becomes shorter than the parallel energy transport time, resulting in no net energy input to the flux tube. (ii) Additionally, perpendicular transport was found to be very effective to smear out the difference in// energy flux conducted by the various flux tubes, if they interact within a perpendicular transport scale,  $\sim$  a few cm, which is usually the case in high plasma current ITER start-up configuration. These two effects significantly make weak dependence of energy deposition on  $\sqrt{L_C}$ .

3. The results presented are affected by the existing uncertainties of the transport coefficients,  $D_{\perp}$  and  $\chi_{\perp}$ . A parametric scan was carried out within a range estimated from the JET limiter discharge. At a smaller plasma current (e.g.  $I_p = 2.5$  MA), because of the larger  $D_{\perp}$  and  $\chi_{\perp}$ , the power decay length becomes longer and the power is deposited at the limiter edge, increasing the peak power load. Due to the low SOL input power in the smaller  $I_p$ , however, the peak power load is still far below the engineering limit. At higher plasma currents (e.g.,  $I_p = 6.5$  MA), the peak power load is found to be close to the engineering limit,  $8\text{MW/m}^2$ , especially for the lowest values  $D_{\perp}$  &  $\chi_{\perp}$  and highest SOL input power.

4. The radial decay of the power flux to the limiter obtained by the 3D modelling was found to be not a simple exponential decay. There exists also decay in the poloidal direction, which is not taken into account in a simple model.

The results of this assessment with those obtained by modelling with a simple model, it is found that by neglecting the 3D geometrical effects, the simple model overestimates peak power load by  $\sim 30\%$  for the same input power and  $\lambda_p$  (Fig. 3).

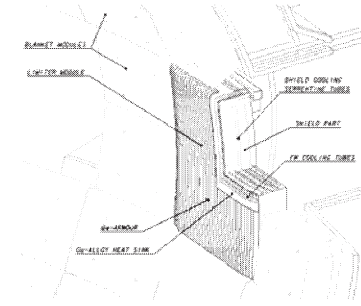


Fig. 1 ITER start-up limiter module.

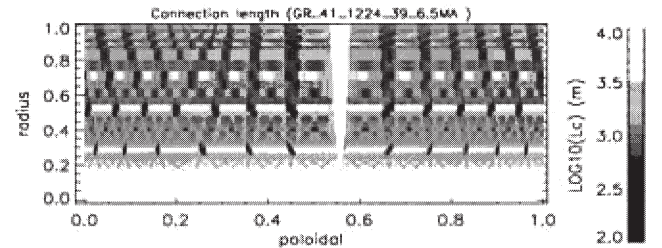


Fig. 2 Connection length profile (logarithmic scale) at  $I_p=6.5$  MA.

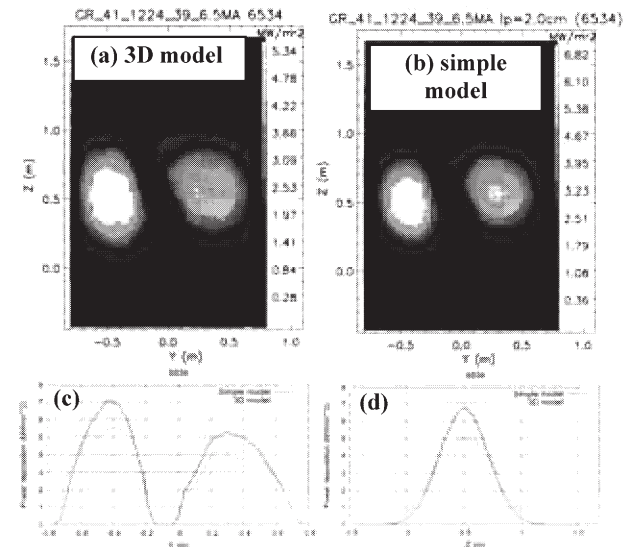


Fig. 3 Comparison of power deposition pattern (a & b) between 3D and simple exponential decay model. (c) & (d) horizontal & vertical cut.

§6. Microwave Heating of Water, Ice and Salt Solution: Molecular Dynamics Study

Tanaka, M., Sato, M.

It is well known that microwaves (300MHz - 300GHz range) can heat solid, liquid and gaseous matters such as daily or engineering materials, laboratory plasmas, and biological matters including living cells. A microwave oven used in daily food processing is one of such applications.

However, unlike laser lights whose photon energy is from several to tens of electronvolts, the photon energy of microwaves is as small as  $h\nu \sim 10^{-5}$  eV and their period is by orders of magnitude longer than the electronic processes (a few fs) occurring in molecules. Nevertheless, microwaves can control chemical reactions, synthesize organic and inorganic materials, and sinter metal oxides with high energy efficiency [1]. Thus, for the microwave-related heating and reactions to take place, non-resonant interactions between waves and materials that persist for many wave periods are expected.

In order to study the heating process of water by the microwaves of 2.5-20GHz frequencies, we have performed molecular dynamics simulations by adopting an explicit water model that uses point charges on rigid-body molecules [2]. All runs are started from the equilibrated states derived from the Ic ice of given density and temperature. In the presence of microwaves, the molecules of liquid water exhibit rotational motion whose average phase is delayed from the microwave electric field; a finite phase lag is required for absorption of the electromagnetic waves (dielectric loss). Microwave energy is transferred to the kinetic and inter-molecular energies of water, where one third of the absorbed microwave energy is stored as the inter-molecular energy [3].

The water in ice phase is hardly heated by microwaves. This is because water molecules are bound with adjacent molecules through the tight hydrogen-bonded network. The permanent electric dipoles do not respond to the microwave electric field.

Addition of small amount of salt to pure water, the typical salinity 1mol% (3wt%), substantially increases the heating rate of water because the water network is weakened at the sites where large-size salt ions are present.

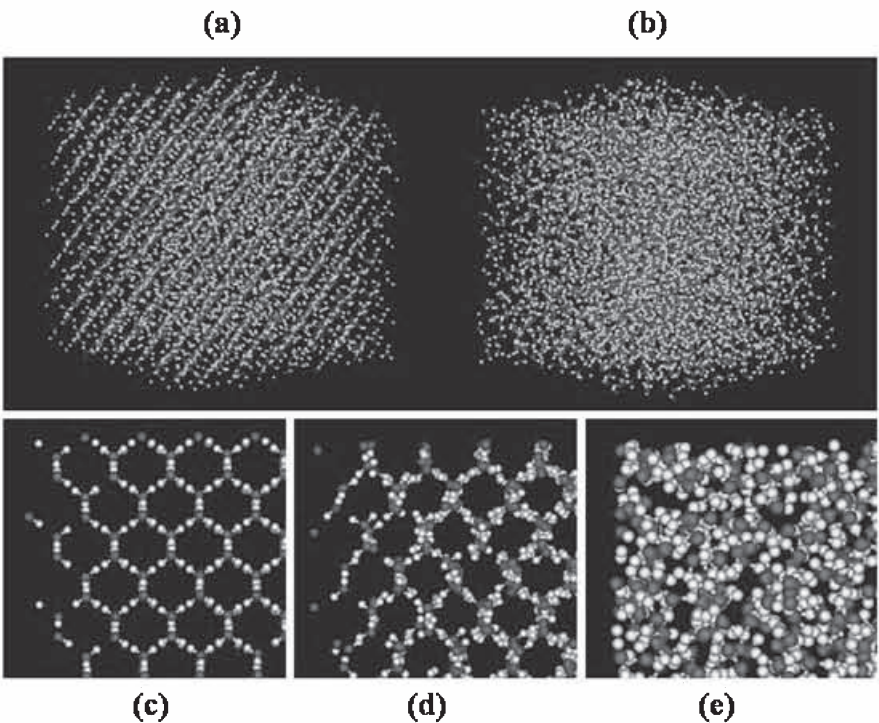


Fig.1 The bird's-eye view of water molecules at  $t=500\text{ps}$  after the microwave application, for (a) the ice at 230K, and (b) liquid water initially at 300K. Enlarged edge parts are shown for (c) the initial Ic ice, (d) the ice at 230K (edge part of (a)), and (e) liquid water (edge part of (b)). The microwave frequency is 10GHz and its strength is  $E_p/kT=0.42$ , where  $E$  is the AC electric field amplitude and  $p$  is the permanent electric dipole.

References

[1] R.D.Peelamedu, M.Fleming, D.K.Agrawal, and R.Roy, J .Am. Ceram. Soc., 85, 117 (2002).  
[2] H.C. Andersen, J.Comp.Phys., 52, 24 (1983).  
[3] M.Tanaka and M.Sato, Los Alamos Archive, cond-mat/0607766 (2006).

## §7. Destruction of an Intense Laser-Irradiated Fullerene Molecule: Ab initio (First-Principle) Molecular Dynamics Study

Tanaka, M., Kono, H. (Dept. Chemistry, Graduate School of Sci., Tohoku Univ.)

Recently, the competition between ionization and fragmentation of a large molecule in intense laser fields has attracted much attention. A spectacular production of a stable, highly charged fullerene molecule  $C_{60}$  by intense short laser pulses of the wavelength  $\lambda \sim 1600$  nm, reaching up to  $C_{60}^{12+}$  without any fragmentation, has been reported [1]. In a previous study, Kono and his collaborators theoretically examined the stability of selected  $C_{60}$  cations, ranging from  $C_{60}^+$  to  $C_{60}^{18+}$  using DFT/ B3LYP implemented in the Gaussian 03 suites program.

This year, we are interested in the dynamical behavior of the fullerene molecule when it is exposed to an intense laser pulse of  $\lambda \sim 1600$  nm and its intensity of the order of  $10^{15} \text{W/cm}^2$ . We use the first-principle molecular dynamics code SIESTA [2], which is based on the density functional theory of quantum mechanics and utilizes the atomic-basis set instead of the plane-wave one for much faster calculations.

First, we have prepared the initial fullerene molecule configuration of the  $I_h$  symmetry, through the geometry-optimization procedure. There we seeks for the energy minimum state by solving the SCF equation for electron density within the molecule and adjusting the position of carbon nuclei. After this procedure, we have applied the laser pulse of  $\lambda = 1600 \text{nm}$ ,  $6 \times 10^{14} \text{W/cm}^2$  and the pulse length 70fs, and have traced the dynamical state by SCF-Verlet algorithm in the time step of (1/3)fs.

Figure 1 shows the time history of the electronic energy, the sum of the electronic and nuclear kinetic energy, and the laser pulse, from top to bottom in this order, where the abscissa is the time in fs and the ordinate of the top two frames in eV. It is seen that, when the peak of the pulse has passed the molecule, the average electronic energy increases irreversibly by 35 eV, which is large but not enough to break the molecule. The envelope of the energy oscillation corresponds to the peak electric field which occurs in every 3fs. Carbon nuclei begin to vibrate in response to the sudden and large changes in the electron distribution, but the total

energy is conserved after the passage of the laser pulse even if the electronic and nuclei vibrations persist. Snapshots of the molecule at the initial and final times of the simulation are shown in Fig.2. In another run when the laser intensity approaches  $10^{15} \text{W/cm}^2$ , fragmentation of the fullerene molecule takes place in which carbon atoms are detached from the molecule symmetrically in a few pairs of two C atoms.

### References

- [1] J. Ohkubo, T. Kato, H. Kono, and Y. Fujimura, J. Chem. Phys. 120, 9123 (2004).
- [2] SIESTA <http://www.uam.es/departamentos/ciencias/fismateriac/siesta/>

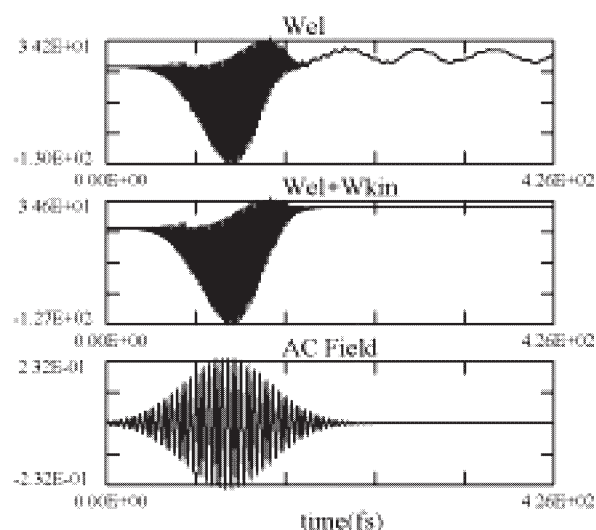


Fig.1 Time history that shows vibration of a fullerene molecule when an intense laser pulse is applied.

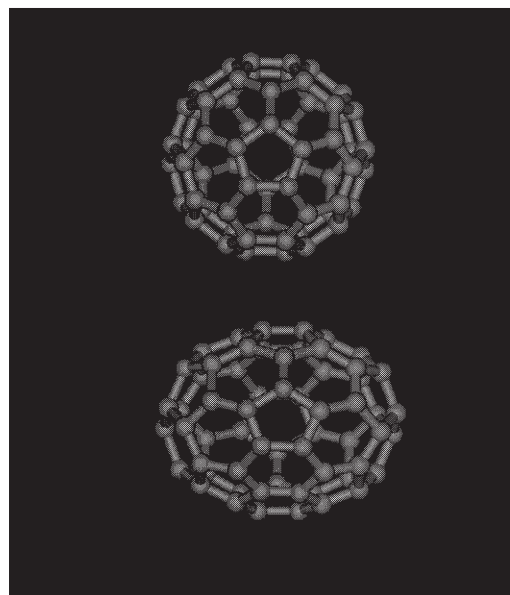


Fig.2 Bird's-eye view of  $C_{60}$  at the initial and final times of the simulation.



## §8. Ab initio Molecular Dynamics Study of Graphite Erosion and Formation of Hydrocarbon Molecules by Absorption of Many Hydrogen Atoms

Koga, T. (D3), Tanaka, M.

The most important and urgent thing for achievement of magnetically confined nuclear fusion may be to find suitable wall materials of a fusion reactor having both heat and radiation resistances. Researches show that the wall surface is damaged not only by the physical sputtering process but also through chemical reactions (sputtering), the latter of which is confirmed to have major influences on the damaging of the fusion reactor wall.

As a typical example of the chemical sputtering, we study the erosion process of graphite by means of the *ab initio* (first-principle) molecular dynamics (MD) simulation code SIESTA [1]. In the code, the electron distributions in materials are determined by solving the Kohn-Sham equation, which is based on the density functional theory of quantum mechanics. We use parallel computers (PC cluster) each consisting of four Pentium 4/64-bits to handle massive computations [2].

Previously we found by *ab initio* MD that hydrocarbon molecules  $\text{CH}_n$  with  $n > 1$  are not formed on a flat (undamaged) graphite because of strong attraction between H and C atoms [3]. Experimentally, on the other hand, hydrocarbon molecules are generated through the chemical sputtering when graphite absorbs large number of hydrogen atoms. Being enlightened by this experiment, we have started a new series of *ab initio* MD simulations.

The simulated system is made of five carbon layers of graphen sheets. Hydrogen atoms are added to the space around the specific layer of the graphite, and they are naturally adsorbed by the layer. When the number of adsorbed hydrogen atoms per graphite layer reaches about 50% that of carbon atoms, the graphite layer is deformed to a highly non-flat shape (hills and valleys) and hydrocarbon molecules such as  $\text{CH}_2$  and  $\text{CH}_3$  are formed by cutting the covalent bonds between carbon atoms. This has become possible due to the stretching of the specific C-C bonds.

Incidentally, in experiments the amount of the

hydrocarbon generation rate in the graphite increases at high temperature around 900K. We have shown by simulations that the already adsorbed hydrogen atoms are detached from the surface due to thermal vibrations at this temperature, thus the chemical sputtering is suppressed. Moreover, the  $\text{CH}_3$  molecules already formed on the graphite layer at low temperatures are detached from the graphite layer at high temperature. We find that a big hole is created on the graphite layer after a  $\text{CH}_3$  molecule has left, which facilitates further destruction of the layer.

As the applications of our research results, we propose to keep the wall material in high temperatures (around 1000K) to avoid its erosion by chemical sputtering. Also, a graphite-based material can be utilized as the hydrogen storage medium by controlling its temperature.

### References

- [1] SIESTA (Spanish initiative for electronic simulations with thousands of atoms): at <http://www.uam.es/departamentos/ciencias/fismateriac/siesta/>
- [2] M. Tanaka, Los Alamos Archive, physics/0407152 (2004).
- [3] Y. Zempo and M. Tanaka, Newsletter of National Institute for Fusion Science (February, 2004).
- [4] T. Koga and M. Tanaka, J. Korean Phys. Soc., in press (2006)

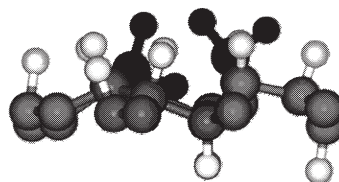


Fig.1 The molecular picture of the graphite layer after the absorption of many hydrogen atoms. White and gray balls denote hydrogen and carbon atoms, respectively, and a black molecule denotes  $\text{CH}_2$ .

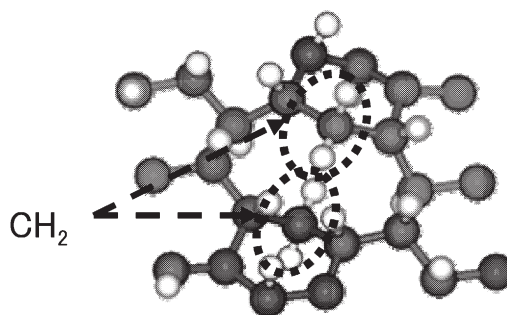


Fig.2 The eroded graphite with a created big hole after the formation of hydrocarbon molecules.



## §9. Experimental Analysis for Thermally Non-Equilibrium State Under Microwave Irradiations: A Greener Process for Steel Making

Sato, M., Matsubara, A., Takayama, S., Sudo, S., Motojima, O. (NIFS (National Institute for Fusion Science)), Nagata, K., Ishizaki, K. (Graduate School of Science and Engineering; Tokyo Institute Of Technology), Hayashi, T. (Research Institute of Industrial Products Gifu Prefectural Government), Dinesh Agrawal, Rustum Roy (Materials Research Institute, Penn State University)

Highly pure pig irons have been produced in a multimode microwave reactor from powdered iron ores with carbon as a reducing agent in a nitrogen atmosphere. Constituents in the compacted powder tend to absorb microwave energy selectively. Microwave-matter interactions create a thermal non-equilibrium state microscopically and enhance chemical reactions and phase mixing at the grain boundaries very rapidly.

Visible light spectroscopy is used to monitor the progress of these reactions. Before the temperature reaches 690°C, the heated powders radiate the continuous spectrum of blackbody emission. Small non-equilibrium hot spots first appear, move and finally burst to emit a brighter light from all over the surface. In the spectroscopic data, CN molecules and Fe (I) atoms have been identified. These bursts are similar to the “ignition propagation” normally observed in

chemical reactions.

The line spectra originated from CO molecules have not been detected yet. A solid-solid reaction is possible to occur between iron oxides and carbon to produce CO<sub>2</sub> directly. Sample weight loss was accelerated during the course of excess-emission. These is clear evidence that microwaves cause a thermally non-equilibrium state and accelerate the reduction process.

The reduction of iron ores is completed at 1380°C and relatively pure pig iron has been produced. It should be noted that the impurity levels of Mg, S, Si, P and Ti are only 5-10% of what has been found in the pig irons produced by modern conventional blast furnaces in the steel industries. The necessary amount of carbon needed is 1/2 compared to conventional blast furnace to produce the unit weight of steel, if we applied renewable energy or nuclear power for the microwave excitations.

## Reference

- [1] M.Sato, A.Matsubara, K.Kawahata, O.Motojima, T.Hayashi, S. Takayama, “Microscopically In-situ Investigation for Microwave” Processing of Metals by Visible Light Spectroscopy, Proc. 11<sup>th</sup> International Conference on Microwave and High Frequency Heating, O-24, Sep.11-15, 2005 Italy

## §10. Observation of the Temperature-Jump of the Sample during Microwave Iron Making

Matsubara, A., Takayama, S., Sato, M.

The microwave heating technology accumulated through the nuclear fusion research has contributed widely to the field of microwave processing. The fact that the microwave heating can be applied to powdered metals has paved the way for the development of the field of its science and application. [1] Highly pure pig irons can be produced in a microwave reactor from powdered iron ores with carbon as a reducing agent. [2] A typical chemical equation can be given as  $\text{Fe}_3\text{O}_4 + 2\text{C} \rightarrow 3\text{Fe} + 2\text{CO}_2 - 75.66 \text{ kcal/mol}$ , as magnetite ( $\text{Fe}_3\text{O}_4$ ) is employed. This reaction is endothermic, so that microwave energy sustains the reaction. In this report, we present a nature of the microwave heating in the iron making.

The hexagonal cross-section of the microwave furnace shown in Fig 1 reduces the microwave energy concentration to the center. The microwave (2.45 GHz, 2.5 - 5.0 kW) heating was performed in the nitrogen atmosphere. The infrared pyrometer monitored the surface temperature. UV-visible light emissions were observed with the spectrometer. The weight ratio of magnetite and graphite powders (these grain sizes were under  $50 \mu\text{m}$ ) was  $\text{Fe}_3\text{O}_4 : \text{C} = 89 : 11$ . The amount of carbon was equivalent to the mol concentration for de-oxidation of the magnetite to pig iron. Volume and total weight of the sample were 89 cc and 89.3g respectively.

Temporal evolution of the surface temperature is displayed in the Fig 2. For the period of  $t < 380 \text{ s}$  the system is low temperature ( $T < 690^\circ\text{C}$ ) state. Small hot spots due to the discharge spark, less than 1 mm in diameter, blink in the cracks of the sample. For the period of  $380 \text{ s} < t < 390 \text{ s}$ ,  $T$  jumps from  $690^\circ\text{C}$  to  $980^\circ\text{C}$  in a few second. Very bright discharge flashes, and then the bright flame bursts up. It should be mentioned that from this moment the temperature of the outside wall of the crucible begins to increase rapidly, indicating the sample-temperature monitored by the pyrometer detects indeed the  $T$ -jump without crucial overestimate by IR lines from both the sample and flame. Its UV-visible emission spectra consist mainly of carbon-nitride (CN) and Iron atoms (Fe I) [see Fig.2]. The Fe (I)'s continue, while the CN disappears in a few minutes. No emission lines of CO or  $\text{CO}_2$  are detected. After the burst ( $t > 390 \text{ s}$ ),  $T$  rises gradually from  $950^\circ\text{C}$ ; at  $T \approx 1350^\circ\text{C}$  molten metal appears in the crucible. Then, the

microwave power is turned off, and the emission and flame vanishes.

The  $T$ -jump indicates the change of energy balance of the sample. A possible interpretation is as follows. Before the jump, the sample is heated mainly by the microwave absorption of which channel is said (but still major open question) to be, e.g., Joule, dielectric, eddy-current, spin wave, multi photon, and etc. Just before the jump, the sample temperature reaches  $\sim 650^\circ\text{C}$  which is coincident with the critical value for the spontaneous chemical reaction, according to the comparison of Gibbs' free energies for iron oxide and carbon oxide. Under this condition, a discharge spark can ignite the burst and trigger the  $T$ -jump. The hot-spot temperature becomes much higher than the critical value of  $\sim 650^\circ\text{C}$ ; so that CO and  $\text{CO}_2$  are produced locally. Those particles are heated and excited by electrons that are multiplied with avalanche in the hot spot, resulting in molecule heat flux. The heat flux gives thermal energy to the surround of the hot spot, leads to the chain reaction and develops to the burst.

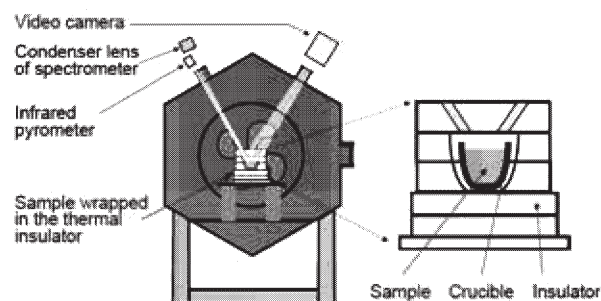


Fig.1. Schematic diagram of the microwave furnace.

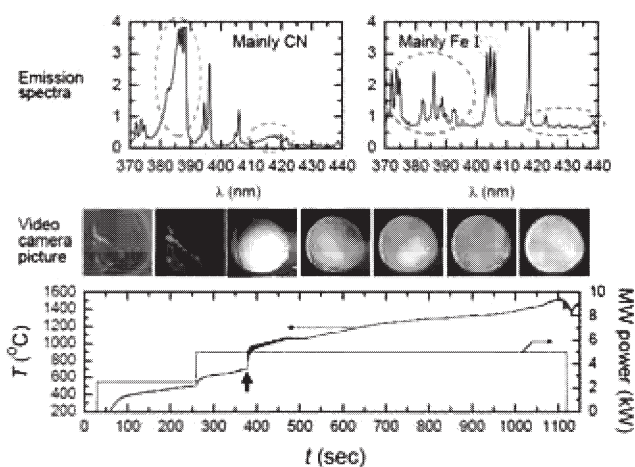


Fig.2. Emission spectra, video camera picture, and variation of the surface temperature of the sample.

- [1] Roy, R., et al., *Nature* **399**, 668 (1999).
- [2] Sato, M., et al., 11<sup>th</sup> *International Conference on Microwave and High Frequency Heating*, O-24, Sep.11-15, (2005).

## §11. Carbon Ion Emission Lines during Radiation Collapse in LHD

Kato, T., Sato, K., Funaba, H., Murakami, I., Peterson, B.

It is very important to understand radiation collapse for fusion research. It is reported that the density is limited by radiation collapse phenomena. Power balance between input power and radiation loss should be considered. In our case generally input power is much larger than the radiation power. This phenomenon indicates the power balance is broken locally. Generally it is considered that when the electron density is increased such as by gas puffing, the electron temperature is decreased and then the radiation loss increases. However these are not verified yet quantitatively. For radiation collapse the effect of electric field is reported as an alternative reason. In order to study the radiation loss quantitatively, we measured EUV spectra from carbon ions, CIII, CIV and CV for a shot with radiation collapse. We also measured hydrogen lines; Ly $\alpha$  and Ly $\beta$ .

We measured EUV spectra from carbon ions in two different wavelength regions using a SOXMOSS spectrometer; 200 – 346Å and 953 – 1232Å. We measured C V 227.18Å (1s2s<sup>3</sup>S - 1s3p<sup>3</sup>P), C V 248.6 (1s2p<sup>3</sup>P - 1s3d<sup>3</sup>D), C IV 312.4Å (2s - 3p), C IV 289.22 (2p - 4d) in the short wavelength range and CIII 977Å (2s<sup>2</sup> - 2s2p), CIII 1176Å (2s2p - 2p<sup>2</sup>), H Ly $\alpha$  (1s - 2p) and H Ly $\beta$  (1s - 3p) in the longer wavelength range. The spectra were taken every 20 ms. Time history of line intensities is shown in Fig.1. Line intensities of CIII, CIV and CV begin to increase at 0.94 sec when the gas puffing begins. CIII line intensities increase very rapidly more than CV lines.

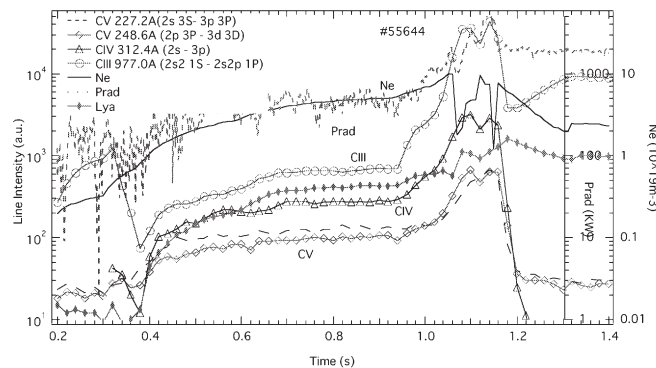


Fig.1 Time evolution of the observed carbon ion lines and hydrogen lines. The averaged electron density (solid line) and radiation power by bolometer (dotted line) are also shown.

Radiation power seen by bolometer increases about 8-9 times. Main part of the radiation might be CV or CIV

because the intensity time history looks like that of bolometric measurement.

We suited the time history of the intensity ratios of CV I(2p-3d)/I(2s-3p), CIV I(2p-4d)/I(2s-3p) and CIII I(2s2p<sup>3</sup>P - 2p<sup>2</sup>3P)/I(2s<sup>2</sup>1S - 2s2p<sup>1</sup>P). We also obtained the time dependence of the intensity ratio of I(Ly $\beta$ )/I(Ly $\alpha$ ). The intensity ratios of CV and CIII begin to increase at 0.94sec as shown in Fig.2, although the intensity ratios of CIV and H decrease from t = 0.94 and increase after 1 sec. We think that this deference comes from the difference of the transition energy of the two lines. We calculated the temperature dependence of intensities of CV lines for different plasma conditions with the use of collisional radiative model of He-like ions. According to our calculation the intensity ratio increases when the electron temperature become low and also increases when the recombination component increases. The increase by the recombination component is larger than by decrease of the temperature by our calculation. It is considered that the intensity ratio increases by the recombination component due to the decrease of the temperature after 0.94 s.

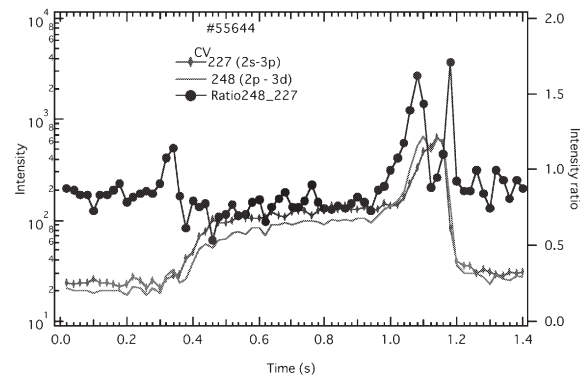


Fig.2. The time behaviour of the intensity ratio of CV lines (filled circle). The time evolution of the two lines are also plotted.

Since behaviour of carbon atom and ions in fusion plasma is important, the atomic data for these ions are important to analyze the spectra. We made an evaluation of atomic data for carbon atoms and ions C<sup>q+</sup> (q=1-5). We worked on data evaluation for the cross sections for electron impact excitation ionization and charge exchange between C<sup>q+</sup> (q=1-6) and hydrogen atoms. Recommended cross sections are represented by simple analytical formulae [1].

We would like to explain the rapid increase in time for CIII, CIV and CV lines. We also would like to explain the time dependence of bolometric measurement by carbon line emissions. The radiation power measured by bolometer is one order smaller than input power by neutral beam injection. Therefore it is considered that the energy balance is locally broken at periphery where carbon emission is dominant.

1) H. Suno and T. Kato, *Atomic Data Nucl. Data Tables*, **92**, 407 (2006).

## §12. EUV Spectra of Xe Ions Measured from LHD for Study of High Z Ion Emission

Kato, T., Kato, D., Sato, K., Funaba, H., Suzuki, C.,  
Yamamoto, N. (Nagoya Univ.),  
Nishimura, H., Nishihara, K. (Osaka Univ.),  
O'Sullivan, G. (Dublin City Univ., Ireland)

High Z materials such as Mo and W are expected to be used for fusion reactor. It is required to study the emission mechanism for high Z elements. EUV emission is studied extensively also for light sources for lithography. We measured EUV emission from Xe ions from LHD by Xe gas puffing for study of emission from high Z ions. EUV spectra from Xenon ions in LHD have been measured in the wavelength range 10 – 17 nm. Line identification is more difficult than C and Fe ions. We used the spectra before Xe gas puffing for wavelength calibration. We used mainly the lines from Fe ions for wavelength calibration.

We identify the lines of Xe ions in the spectra during the heating using the measurement by Berlin EBIT [1]. Spectral lines during the heating are identified from ions with outer 4s or 4p electrons ( $\text{Xe}^{23+}(4s^2 4p) - \text{Xe}^{25+}(4s)$ ) in 12 – 16 nm as shown in Fig.1. In Fig.1, the numbers 1, 3, 5, 7, 8, 11, 13, 14 indicate the lines of  $\text{Xe}^{23+}(4s^2 4p)$ ,  $\text{Xe}^{24+}(4s^2)$ ,  $\text{Xe}^{23+}$ ,  $\text{Xe}^{24+}$ ,  $\text{Xe}^{25+}(4s)$ ,  $\text{Xe}^{23+}$ ,  $\text{Xe}^{23+}$  and  $\text{Xe}^{24+}$ , respectively. These lines are 4p – 4d transitions for the lines of 3, 7 and 8 whereas 4s – 4p transitions for the lines of 11, 13 and 14. Spectral lines during the heating are identified with 4p - 4d and 4s – 4p transitions of  $\text{Xe}^{17+}(4d) - \text{Xe}^{25+}(4s)$  ions in 10 - 12nm as shown in Fig.2. The emission 4p – 4d transitions of  $\text{Xe}^{17+}$  ions in 10 – 12 nm is much stronger than those in 12 – 16nm. Therefore these emission is not measured in the longer wavelength range, 12 – 16nm during the heating. However emission  $\text{Xe}^{17+}$  ions is measured during radiation collapse as shown in Fig.3 in 12 – 16 nm. Spectra during radiation collapse are identified with  $\text{Xe}^{8+}(4d^{10})$  to  $\text{Xe}^{17+}(4d)$  (open 4d shell). The spectra during radiation collapse are very complicated and difficult to identify. However we could identify most of the lines as shown in Fig. 3. When we compare the charge exchange spectroscopy by Tanuma [2], the spectra during the radiation collapse looks like those from  $\text{Xe}^{17+}$  and  $\text{Xe}^{16+}$ . However it is difficult to identify these lines because these lines have not been studied yet. We made theoretical calculation using Cowan's code for  $\text{Xe}^{17+}$  ions. We are making a new identification for measured  $\text{Xe}^{17+} 4p - 4d$  transition lines with theoretical data by Cowan and Grant codes.

We can make a bench mark test of computer codes using the observed spectral lines. This is important because the theory has not been extensively tested for high- Z low charge ions. We will study plasma conditions which give the best EUV emission and will make a collisional radiative model for high-Z many-electron ions. We calculated the dielectronic recombination rate of  $\text{Xe}^{10+}$  ions[3] because they are necessary for our model..

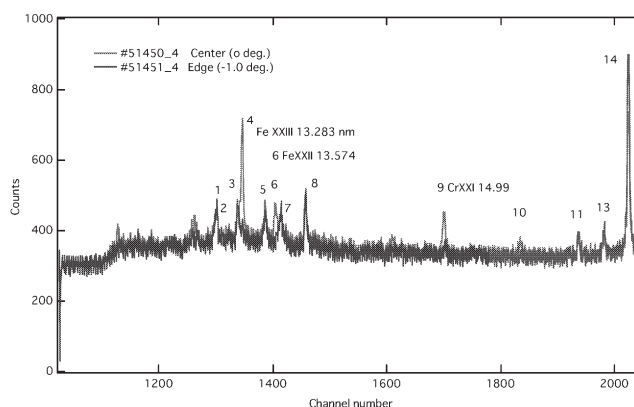


Fig.1 Spectral lines during the heating are identified from ions with outer 4s or 4p electrons ( $\text{Xe}^{23+}(4s^2 4p) - \text{Xe}^{25+}(4s)$ ) in 12 - 16nm.

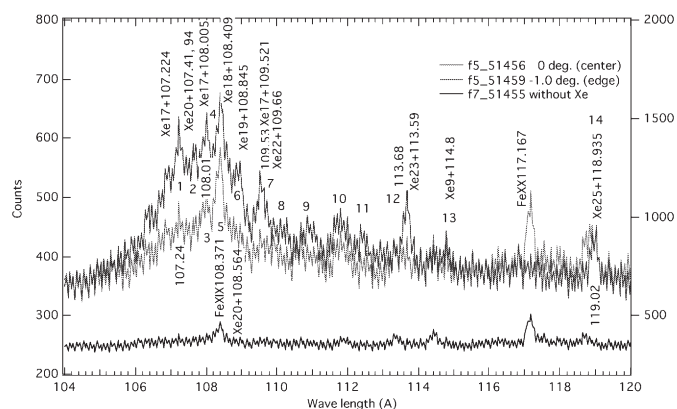


Fig.2 Spectral lines during the heating are identified with 4p - 4d transitions of  $\text{Xe}^{17+}$  (4d) -  $\text{Xe}^{25+}$  (4s) ions in 10 - 12nm

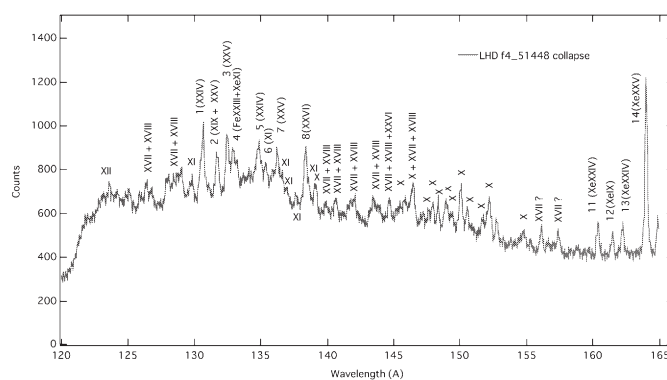


Fig.3 Spectral lines during radiation collapse are identified with  $\text{Xe}^{8+}(4d^{10})$  to  $\text{Xe}^{17+}(4d)$  (open 4d shell)

- 1) R. Radtke, C. Biedemann et al, PEARL conference (2005)
- 2) H. Tanuma, private communication (2004)
- 3) M.-Y. Song and T. Kato, NIFS-DATA-94 (2005)



### §13. Identification of Resonance Excitation Double-Autoionization of Li-like Iodine Ions

Kato, D., Sakaue, H.,  
Nakamura, N., Ohtani, S. (ILS, UEC)

Electron-impact ionization of highly-charged ions is important to understand energy balance and ionization balance of non-equilibrium high-temperature plasmas. Total ionization cross sections are substantially increased by the resonance excitation double-autoionization (REDA). In REDA, an incident electron pushes electrons of a target ion up to excited levels, and is trapped temporary by the target ion. The electron attached (excited) state is relaxed by releasing two electrons via two sequential autoionizations. As a result, the target ion loses one electron. The REDA cross section would have peaks at certain incident electron energies which coincide with resonance energies of the electron attached states. Apart from the resonance energies, the cross section values would be zero.

We identified the REDA peak of Li-like iodine ions by analyzing ion density ratios of He-like and Li-like ions in an electron beam ion trap (EBIT)<sup>1)</sup>. Ionization equilibrium in the EBIT is determined by balance among rates of electron-impact ionization which includes direct ionization (DI), excitation autoionization (EA) and REDA, recombination which includes radiative recombination (RR) and dielectronic recombination (DR), and ion loss due to ion escape from the trap or charge exchange with neutral particles. Denoting the DI+EA cross section by  $\sigma_{Li}^{DI+EA}$  [cm<sup>2</sup>], the REDA cross section by  $\sigma_{Li}^{REDA}$ , the RR+DR cross section by  $\sigma_{He}^{RR+DR}$  and the ion loss rate by  $1/\tau$  [s<sup>-1</sup>], ratios of the He-like ion density,  $n_{He}$ , to the Li-like ion density,  $n_{Li}$ , are written for a given electron beam current density,  $j$  [cm<sup>-2</sup>s<sup>-1</sup>], as,

$$\frac{n_{He}}{n_{Li}} = \frac{\sigma_{Li}^{DI+EA} + \sigma_{Li}^{REDA}}{1/j\tau + \sigma_{He}^{RR+DR}} \quad (1),$$

provided the electron beam energy is lower than the ionization energy of the He-like ion. To obtain eq. (1), the coronal model is assumed since the electron density is as low as 10<sup>-12</sup> cm<sup>-3</sup> in the EBIT. In conjunction with ion density ratios at off resonance energies,  $(n_{He}/n_{Li})_{NR}$ , the REDA cross sections are written as,

$$\sigma_{Li}^{REDA} = \sigma_{Li}^{DI+EA} \left[ \frac{(n_{He}/n_{Li})}{(n_{He}/n_{Li})_{NR}} - 1 \right] \quad (2).$$

Extracted ion intensities from the EBIT were measured by a position-sensitive detector placed after a charge-analyzing magnet. Figure 1 shows the REDA cross section determined by eq. (2) with the measured ion intensity ratios and theoretical values of  $\sigma_{Li}^{DI+EA}$ . Theoretical REDA cross section curve is also plotted for comparison. As seen in Fig. 1, the REDA peak is identified as composition of three electron attached states:  $(1s2s3s^2)_{J=1}$  and  $(1s2s3s3p)_{J=0,1}$ .

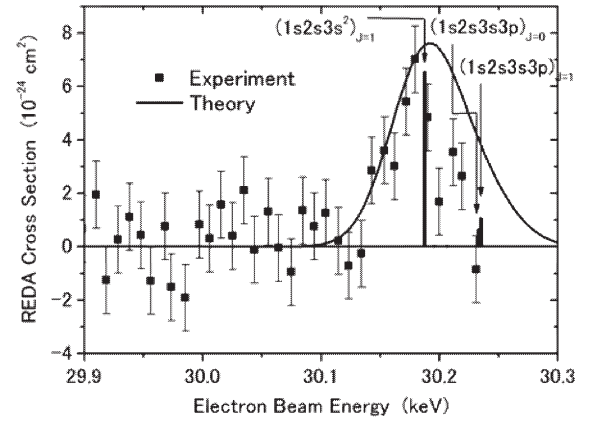


Fig. 1 Measured and theoretical REDA cross sections. The theoretical cross section is convoluted by a Gaussian function with electron energy width of 70 eV.

#### References

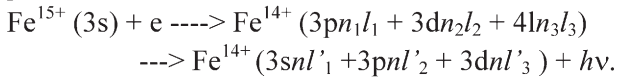
- 1) Nakamura, N., Tobiyama, H., Nohara, H., Kato, D., Watanabe, H., Currell, F.J. and Ohtani, S., Phys. Rev. A 74 (2006) 020705(R).

#### §14. Dielectronic Recombination Rate Coefficients to Excited States of Mg-like Fe and Dielectronic Satellite Lines

Murakami, I., Kato, T., Kato, D.,  
Safronova, U.I., Cowan, T.E. (Univ. of Nevada, Reno, USA),  
Ralchenko, Yu (NIST, USA)

Energy levels, radiative transition probabilities, and autoionization rates for Mg-like Fe ( $\text{Fe}^{14+}$ ) including  $1s^2 2s^2 2p^6 3l'nl$ , and  $1s^2 2s^2 2p^6 4l'nl$  ( $n=3-12$ ,  $l \leq n-1$ ) states are calculated by the Hartree-Fock-Relativistic method (Cowan code). Autoionizing levels above the thresholds  $1s^2 2s^2 2p^6 3l$  ( $l=s, p, d$ ) are considered. Configuration mixing [ $3sns + 3dnd$ ], [ $3snp + 3pns + 3pnd + 3dnp$ ] plays an important role for all atomic characteristics. Branching ratios relative to the first threshold and intensity factors are calculated for satellite lines, and dielectronic recombination (DR) rate coefficients are obtained for the excited 444 odd-parity and 419 even-parity states. It is found that the contribution of the highly excited states is very important for the DR rates. The contributions from the excited  $1s^2 2s^2 2p^6 3l'nl$  states with  $n \geq 12$  and  $1s^2 2s^2 2p^6 4l'nl$  states with  $n \geq 7$  to the DR rate coefficients are estimated by extrapolation of all atomic characteristics. The total DR rate coefficient is derived as a function of electron temperature. The state-selective DR rate coefficients to excited states of Mg-like Fe, which are useful for modeling Fe XV spectral lines in a recombining plasma, are calculated as well <sup>1)</sup>.

Dielectronic recombination from  $\text{Fe}^{15+}$  to the excited states of  $\text{Fe}^{14+}$  is defined by the following sequence of processes:



As the initial state we consider the ground state of  $\text{Fe}^{15+}$ ,  $3s$ . The doubly excited states,  $3pn_1l_1$  ( $n_1 \geq 10$ ),  $3dn_2l_2$  ( $n_2 \geq 7$ ), and  $4ln_3l_3$  ( $n_3 \geq 4$ ), are taken into account as autoionizing intermediate states.

The DR rate coefficients  $\alpha(j, i_0)$  to the excited state of  $\text{Fe}^{15+}$  are obtained by summing up the intensity factor  $Q_d(j, i, i_0)$  multiplied by the exponential factor, over

the autoionizing levels  $i$  as follows:

$$\alpha_d(j, i_0) = 3.3 \times 10^{-24} \left( \frac{I_H}{T_e} \right)^{3/2} \sum_i e^{-\frac{E_{i_0}}{T_e}} Q_d(j, i, i_0) / g(i_0)$$

where

$$Q_d(j, i, i_0) = g_i A_r(i, j) K(i, i_0),$$

$$K(i, i_0) = \frac{A_a(i, i_0)}{A_r(i) + A_a(i)},$$

$$A_r(i) = \sum_k A_r(k, i), \text{ and}$$

$$A_a(i) = \sum_{i_0'} A_a(i, i_0').$$

Here  $A_r(k, i)$  are radiative transition probabilities,  $A_a(i, i_0)$  are autoionization rates, and  $E_{i_0}$  is the level energy of autoionizing level  $i$  measured from the first ionization threshold.

The total DR rate coefficient is obtained by the summation of the rate coefficients of DR processes through all possible intermediate states (Fig.1). Our results are compared with the result by Gu (2004) <sup>2)</sup> and agree well for  $10\text{eV} < T_e < 100\text{eV}$ . The disagreement at high  $T_e$  could be explained by the inner-shell excitation of a  $2l$  electron. We could not comment on the disagreement at low  $T_e$  since Gu gave the DR rate only at  $T_e > 1\text{eV}$ .

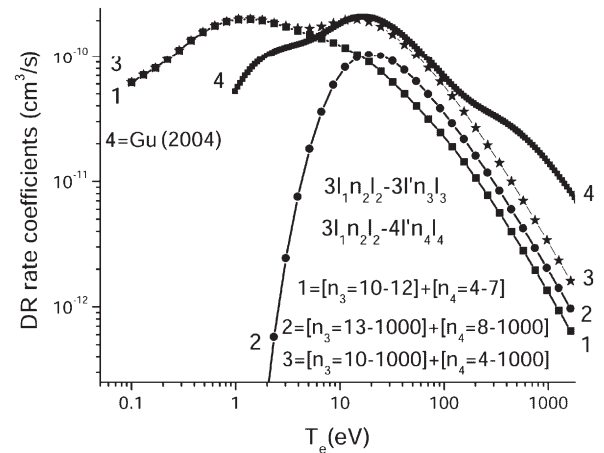


Fig.1 Total DR rate coefficient as a function of electron temperature (no. 3), compared with rate coefficient obtained by Gu <sup>2)</sup> (no.4). Line with no. 2 is the sum of the contributions from highly excited intermediate states.

#### References

- 1) I. Murakami et al, J. Phys. B, **39** (2006) 2917.
- 2) M. F. Gu, ApJ. Suppl., **153** (2004) 389.

# §15. Recommended Data on Proton-Ion Collision Rate Coefficients for Fe X – Fe XV and Fe XVII – Fe XXIII Ions

Skobelev, I. (Multicharged Ions Spectra Data Center of VNIIFTRI, Russia),  
Murakami, I., Kato, T.

Proton-ion collisions are important for excitation between fine structure levels of the ground states or metastable states of ions in high-temperature low density plasma. In the present work we evaluate atomic data for proton-induced excitation transitions in Fe X – Fe XV ions (M-shell ions)<sup>1)</sup> and Fe XVII – Fe XXIII ions (L-shell ions)<sup>2)</sup> with the help of different theoretical methods. For the most cases atomic data were obtained by semi-classical methods and quantum treatments were done for a few cases (FeXIII, FeXIV, and FeXXI). Evaluated data are fitted to a simple analytical formula with 7 parameters, which can describe dependency of the excitation rate coefficient on proton temperature in wide temperature range:

$$C_{ij}(T_p)[cm^3s^{-1}] = 10^{-10} p_1 \exp(-(p_2/T_p)^{p_3}) \frac{(T_p/p_6)^{p_7}}{1+(T_p/p_4)^{p_5}} \quad (1)$$

The values of the parameters are determined by fitting of the analytic formula to selected numerical data.

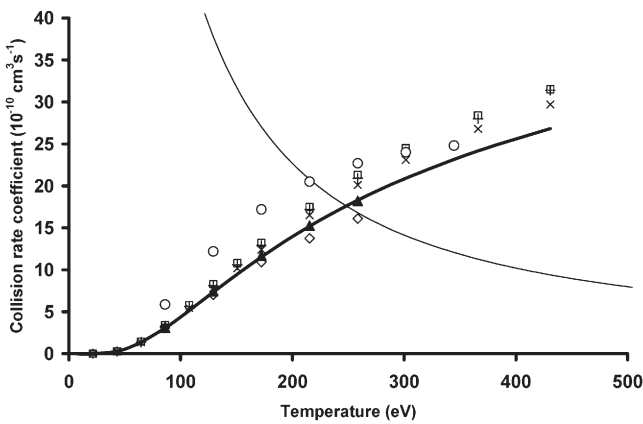


Fig. 1. Proton collision excitation rate coefficients for transition  $3s^2 3p^2 P_{1/2} - ^2P_{3/2}$  in Al-like Fe ions (Fe XIV): solid line – formula (1),  $\circ$  – data [3],  $\blacktriangle$  – data [4],  $+$  – data [5],  $\diamond$  – data [6],  $\square$  and  $\times$  – data [7] for different methods of consideration of small impact parameter region; thin solid line – electron rate coefficient of [8].

By comparing of proton collision excitation rates with electron ones it is shown that proton impact excitation processes may be important for Fe X, XI, XIII-XV ions and some transitions of Fe XVII – Fe XXIII ions at the higher temperature region. The results obtained can be used for plasma kinetics calculations and for the development of spectroscopy methods of plasma diagnostics.

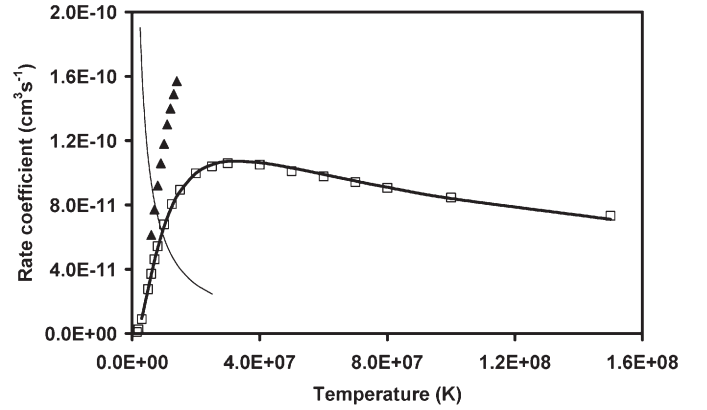


Fig.2 Collisional excitation rate coefficients for transition  $2s^2 2p^2 ^3P_1 - ^3P_2$  in C-like Fe ions (Fe XXI): solid thick line – formula (1) for protons, solid thin line – electrons [9],  $\blacktriangle$  data [10],  $\square$  - data [11].

## References

- 1) I. Skobelev, I. Murakami, and T. Kato, NIFS-DATA-95 (2006).
- 2) I. Skobelev, I. Murakami, and T. Kato, NIFS-DATA, in preparation.
- 3) S. O. Kastner and A. K. Bhatia, *Astron. Astrophys.*, **71**, 211 (1979)
- 4) D. A. Landman, *Astron. Astrophys.*, **43**, 285 (1975)
- 5) O. Bely and P. Faucher, *Astron. Astrophys.*, **6**, 88 (1970)
- 6) T. G. Heil, K. Kirby, A. Dalgarno, , *Phys. Rev. A*, **27**, 2826 (1983)
- 7) A. Burgess, J.A. Tully, *J. Phys. B.*, **38**, 2629 (2005)
- 8) P. J. Storey et al., *A&A*, **309** 677 (1996)
- 9) K. Butler and C. J. Zeippen, *A&AS*, **143**, 483 (2000)
- 10) P. Faucher, *A&A*, **54**, 589 (1977)
- 11) R. C. I. Ryans, V. J. Foster-Woods, F. P. Keenan, R. H. G. Reid, *ADNDT*, **73**, 1 (1999)

## §16. Evaluation of Electron Impact Excitation Rate Coefficients for Fe M-shell Ions

Murakami, I., Kato, T.,  
Skobelev, I. (Multicharged Ions Spectra Data Center of  
VNIIFTRI, Russia),  
Itikawa, Y. (ISAS/JAXA)

Spectroscopy is one of the most common diagnostic methods for various plasmas. Spectral line intensities and intensity ratios are used for diagnosing plasma temperature and density, or ion abundance. The relationship between line intensity and plasma temperature and density is usually given by a theoretical kinetic model in which line intensities are calculated from population densities of excited states. Electron impact excitation is one of the important processes which governs population densities. Reliable atomic data for electron impact excitation rates are necessary for plasma diagnostics.

Iron is one of the abundant elements in laboratory plasmas and in space. Iron abundance is often used as an index of heavy element abundance in space, such as intra-cluster medium, inter-galactic medium, hot gas in galaxies, inter-stellar medium, and the sun. Iron ions are one of major impurities in laboratory plasmas.

Iron M-shell ions are observed in transition region of the sun and planned to be measured by the EUV Imaging Spectrometer mounted on the SOLAR-B solar physics satellite which is scheduled for launch in 2006. In order to examine dynamics of the transition region, plasma diagnostics by the spectral lines are quite important and reliable theoretical model with reliable atomic data are necessary.

In this work we evaluate existing atomic data of electron impact excitation rate coefficients for M-shell Iron ions (Fe IX – Fe XVI) and give a set of recommended data. In case of Fe XIII we also make a fitting of the recommended data to an analytical form for easy use for plasma modeling and diagnostics<sup>1,2)</sup>.

Many theoretical studies on the excitation rate coefficients for Fe ions were done, but the experimental study is quite few. We examine the theoretical methods for calculating excitation rate coefficients with checking mainly the following points: (1) a number of levels included in the calculation, (2) treatment for configuration interaction, (3) a number of partial waves, (4) energy range, (5) relativity treatment, and (6) energy mesh for integrating cross sections to obtain rate coefficients. The R-matrix method is usually

better than the distorted-wave method because the former can take into account the resonance effect, which affect the rate coefficients at low temperature region largely. But the R-matrix method has limitation for high energy region of electron collision, so we need to pay attention to the valid temperature range of the rate coefficients. Considering all available data we select data as recommended data for each Fe ion. For Fe XIII we fit all the rate coefficients to analytic formulae for convenience of applications.

Figure 1 shows an example of excitation rate coefficients. Data calculated by using the full relativistic R-matrix code by Aggarwal and Keenan (2005) are the best for the case of Fe XIII ion.

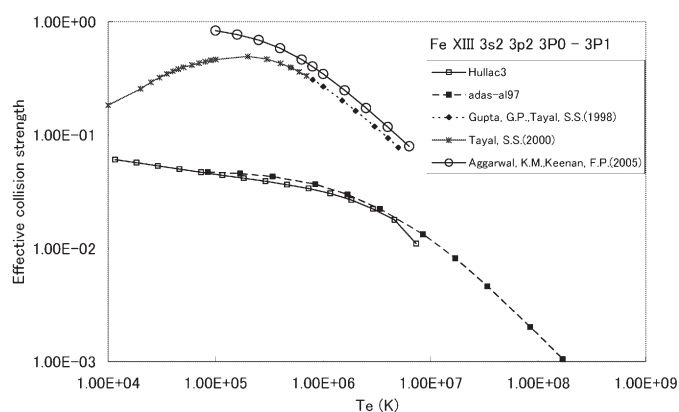


Fig.1 Excitation rate coefficient for  $3s^2 3p^2 \ ^3P_0 - \ ^3P_1$  transitions of Fe XIII ion as a function of electron temperature. Open circles are data calculated with full relativistic R-matrix code by Aggarwal and Keenan<sup>3)</sup>. Diamonds and stars are calculated by semi-relativistic R-matrix code<sup>4,5)</sup>. Solid squares are calculated by relativistic distorted wave method by Hullac code<sup>6)</sup>. Open squares are calculated by distorted wave method from the ADAS database<sup>7,8)</sup>.

### References

- 1) I. Skobelev, I. Murakami, and T. Kato, NIFS-DATA, in preparation.
- 2) I. Murakami, I. Skobelev, Y. Itikawa, and T. Kato, NIFS-DATA, in preparation.
- 3) K. Aggarwal and F. P. Keenan, *Astron. Astrophys.*, 429 (2005) 1117.
- 4) G. P. Gupta and S. S. Tayal, *Astrophys. J.*, 506 (1998) 464.
- 5) S. S. Tayal, *Astrophys. J.*, 544 (2000) 575.
- 6) A. Bar-Shalom, M. Klapisch, J. Oreg, *JQSRT*, 71 (2001) 169.
- 7) ADAS: <http://adas.phys.strath.ac.uk>
- 8) B. C. Fawcett and H. E. Mason, *ADNDT*, 43 (1989) 245.



# §17. Development of a Collisional-Radiative Model of Oxygen Ions for Plasma Diagnostics

Murakami, I., Kato, T., Goto, M., Morita, S., Safronova, U.I. (Univ. of Nevada, Reno, USA)

Oxygen ions are major impurities in laboratory plasmas. Spectral line intensity ratios can be used for diagnosing plasma temperature and density, or ion abundance. The relationship between line intensities and plasma temperature and density is usually given by a theoretical kinetic model. We are making a collisional-radiative model for oxygen ions for the purpose of plasma diagnostics. We make a detailed collisional-radiative model for Be-like oxygen ions (OV) including the effect of recombination from Li-like oxygen ions<sup>1)</sup> and inner-shell ionization from B-like oxygen ions. We also make a collisional-radiative model for ionizing plasma for all oxygen atoms and ions. The former model is applied to plasma diagnostics. The collisional-radiative models require a large set of atomic data. We calculate atomic data with Hullac code for excitation and inner-shell ionization rate coefficients and radiative transition probabilities. We calculated dielectronic recombination rate coefficients of OV ion with Cowan code<sup>2)</sup>.

The intensity ratio of OV(2s2p <sup>3</sup>P -2p<sup>2</sup> <sup>3</sup>P 76nm)/OV(2s<sup>2</sup> <sup>1</sup>S – 2s2p <sup>1</sup>P 63nm) is less than 1 if the population densities of OV excited states are dominated by the excitation from the ground state of OV (“ionizing component”). If plasma is in recombining phase, then the ratio becomes larger than 1<sup>1)</sup>. In our previous work<sup>1)</sup> we examined the measured ratio for the shot #15078 from the 3<sup>rd</sup> LHD experiment campaign and the ratio was 2.2 during the steady-state phase of plasma with nearly constant electron density and stored energy. Such a large ratio could not be explained with a simple collisional-radiative model with ionizing and recombining components, since it was difficult to expect the plasma was dominated by recombining component<sup>1)</sup>. Thus we next included the contribution of the inner-shell ionization from OIV to the excited states of OV. This inner-shell ionization component from OIV ions allowed us to explain the large ratio.

In this work we examine the same intensity ratio of the similar plasmas with long steady-state phase. In the 9<sup>th</sup> LHD experiment campaign we measured EUV spectra for LHD plasmas and observed OIII, OIV, OV, OVI lines as well as Ly series of hydrogen and CII and CIII lines.

The shot numbers and obtained ratios of OV(76nm)/OV(63nm) in steady—state phase are listed in

Table 1. Similarly to the previous work, the ratios are larger than 1 and we expect the inner-shell ionization component is important again. From the theoretical work, the dependence on the electron density of this intensity ratio is quite weak and the difference of the ratios from the three shots is difficult to explain with the different electron density. Figure 1 shows temperature dependence of the intensity ratio when n<sub>e</sub>=10<sup>19</sup>m<sup>-3</sup>. The measured ratios can be explained with a combination of electron temperature and ion abundance ratio n(OIV)/n(OV). More detailed analysis with OIV lines will be required to determine both parameters.

Table 1 Measured intensity ratio, OV(76nm)/OV(63nm) from the LHD experiments.

Shot number	OV(76nm)/OV(63n m)	Ne(max) (10 <sup>19</sup> m <sup>-3</sup> )	Wp(max) (kJ)
56839	1.53 ± 0.059	4.652	527.1
56840	1.30 ± 0.098	3.072	609.6
56841	1.13 ± 0.183	2.069	447.2

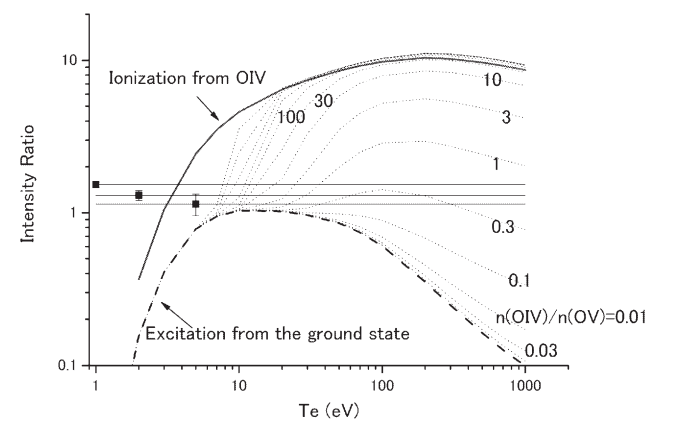


Fig.1 Intensity ratio of OV(76nm)/OV(63nm) as a function of electron temperature for electron density n<sub>e</sub>=10<sup>19</sup>m<sup>-3</sup>. Solid thick line is the ratio of inner-shell ionization component from OIV. Thick dashed line is for excitation component from the ground state of OV. Dotted lines are composed ratios of two components with different ion density ratios from 0.003 to 10000. Three horizontal lines with squares and error bars are measured ratio from LHD experiments in Table 1.

References  
1) I.Murakami et al., J. Plasma Fusion Res. SERIES, 5 (2002) 171.  
2) I.Murakami et al., Canadian J. Phys. 80 (2002) 1525.

## §18. Analysis of CV Spectral Lines and the Emitting Location in LHD Plasma

Murakami, I., Katai, R., Sugimoto, T., Kato, T., Sato, K., Shiraki, K., Tsujii, M. (Shinshu Univ.)

Carbon is one of major impurities in laboratory plasmas. We are interested in carbon ions which are expected to exist mainly in peripheral region of LHD plasmas. We obtained VUV spectra of LHD plasma by using the SOXMOS in the 8<sup>th</sup> campaign and examined two CV emission lines, the resonance line,  $1s^2\ ^1S - 1s2p\ ^1P$  (4.027nm), and the intercombination line,  $1s^2\ ^1S - 1s2p\ ^3P$  (4.073nm) (Fig.1). The spectral line intensity ratio can be used for plasma diagnostics.

The relationship between line intensities and plasma temperature and density is usually obtained by a theoretical kinetic model. We used a collisional-radiative model (CRM) for CV ions developed by Fujimoto and Kato<sup>1)</sup>. The calculated line ratio of the CV intercombination line and resonance line in ionizing plasma shows strong electron temperature dependence and weak electron density dependence for the density region of the LHD plasma. Thus we can use the line ratio as electron temperature diagnostics.

Comparing the measured line ratio with the calculated electron temperature dependence, we can estimate the electron temperature for the region where CV ions exist. Figure 2 shows the temporal evolution of the estimated electron temperature for 3 shots of the LHD plasma. During the steady state phase of the plasma after 1.6 sec, the obtained electron temperature is nearly constant at around 200eV. The plasma of the shots was continuously heated by NBI injection and showed nearly constant electron density and stored energy during the steady state phase.

Now we can compare the obtained temperature with the electron temperature radial profile measured by the Thompson scattering method in Figure 3. It indicates that CV ions exist at around  $r=2700\sim 2800\text{mm}$  ( $\rho = 0.96\sim 1.08$ ) region. This result confirms that the CV ions really exist in peripheral low temperature region in the LHD plasma.

This work was performed as a subject to educate graduate students who attended the 2<sup>nd</sup> Soukendai summer school at NIFS in 2005.

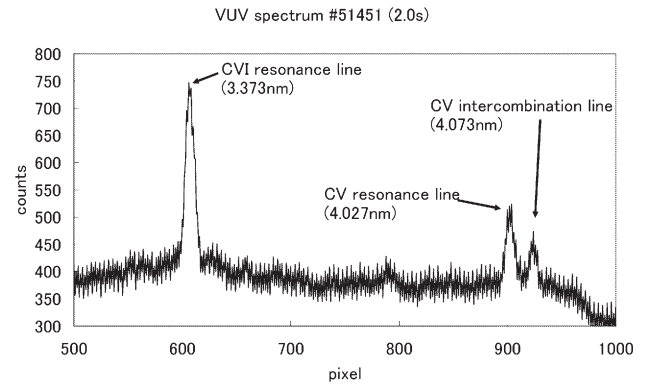


Fig.1 VUV spectrum for shot #51451 at 2.0sec.

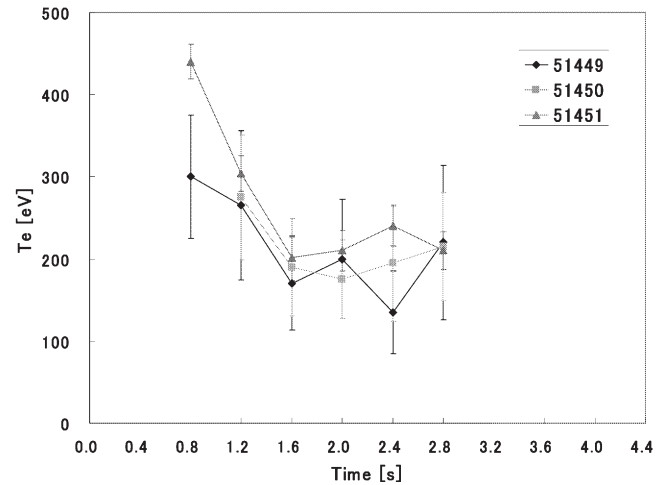


Fig.2 Temporary evolution of electron temperature estimated by using the CV line ratio with CRM calculation for the shots #51449~51451 of the LHD plasma.

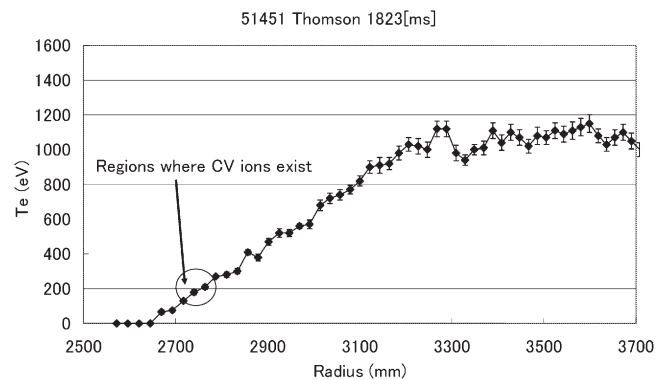


Fig.3 Electron temperature radial distribution measured by the Thompson scattering method for the shot #51451 at  $t=1823\text{msec}$ . Comparing with obtained electron temperature by using the CV line ratios, the region where CV ions exist is indicated.

## References

- 1) Fujimoto, T. and Kato, T., *Astrophys. J.* **246** (1981) 994; *Phys. Rev. A* **30** (1984) 379.

## §19. Cluster of Mono-Vacancy and Hydrogen Atoms in Ferritic Iron

Kato, D., Kato, T., Muroga, T., Noda, N.,  
Iwakiri, H. (Kyushu Univ.),  
Morishita, K. (Kyoto Univ.)

Atomic structure of vacancy-hydrogen clusters in metals is an issue of study concerning hydrogen retention in divertor materials. As the cluster may have substantially smaller formation energy than that of a mono-vacancy, it would have higher concentration at thermal equilibrium and increase hydrogen solubility. Strong enhancement of hydrogen retention in Mo under exposure to high pressure hydrogen gas has been observed. The enhancement may be associated with formation of the vacancy-hydrogen clusters.

We investigated the formation energies of the vacancy-hydrogen clusters in ferritic iron based upon *ab initio* calculations using the VASP code. Total energy for a super cell of the ferritic iron with hydrogen atoms was computed by means of Kohn-Sham density functional method. Perdew, Burk and Ernzerhof version of generalized-gradient approximation was used to evaluate the exchange-correlation energy. The cell shape and lattice configuration were relaxed until the lowest total energy was obtained for a given cell volume. By fitting Marnaghan's equation of state (EOS) to the so-obtained energy-volume curve, we determined values of the minimum total energy, the equilibrium volume and the elastic modulus of the cell.

Vacancy formation energy of 2.18 eV was obtained for a mono-vacancy created in a body-cubic-center super cell with 54 Fe atoms. The present value is consistent with experimental values measured by positron annihilation method (1.4-2.0 eV). By moving one interstitial hydrogen atom to an octahedral-site of the mono-vacancy, the total energy was decreased by 0.75 eV. Adding another hydrogen atom to the opposite octahedral-site decreased the total

energy by another 0.78 eV. Each value is approximation for a binding energy value of each hydrogen atom at the mono-vacancy. Since cluster formation energy is lower by the binding energies than that of a mono-vacancy, the present results tell us that vacancy concentration at thermal equilibrium is increased substantially by the cluster formation. Higher multiple trapping of hydrogen atoms in the cluster may cause enhancement of hydrogen solubility. It is quite intriguing to study the vacancy-hydrogen formation in tungsten that is considered to be the divertor material for the International Thermonuclear Experimental Reactor.

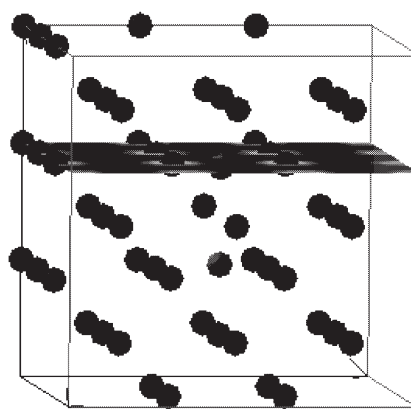


Fig. 1 An image for a super cell of ferritic iron (blue) with a mono-vacancy (center) and two hydrogen atoms (red). Locations of both hydrogen atoms are 0.22Å off from the octahedral-site toward to the center of the mono-vacancy.

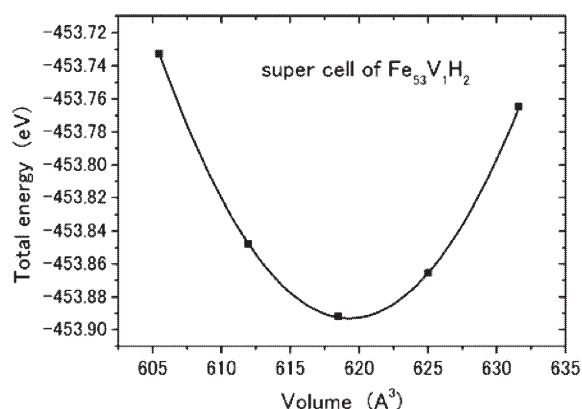


Fig. 2 Energy-volume curve for the super cell of Fig. 1. Solid squares stand for calculated values and solid line for Marnaghan's EOS.

## §20. Temperature Effect on Charge Transfer and Ionization in Collisions of $H^+$ Ions with Hydrocarbon Molecules

Kimura, M. (Kyushu Univ.),  
Kusakabe, T. (Kinki Univ.),  
Pichl, L. (Aizu Univ.),  
Watanabe, A. (Ochanomizu Univ.),  
Suzuki, R. (Hitotsubashi Univ.),  
Kato, D.

In research on controlled thermonuclear fusion, charge transfer processes of slow  $H^+$  ions in collisions with impurity molecular gases such as hydrocarbons and other fusion relevant molecules below a few-keV energies play a key role in low temperature edge plasmas of the current fusion devices which employ carbon-coated or graphite walls as plasma facing materials. Particularly, these impurity hydrocarbons have been detected near the divertor region in many experimental fusion reactors. Although many experimental studies have been performed on electron capture of  $H^+$  ions in collisions with various gas atoms and molecules, these investigations were concerned with vibrationally ground-state molecules. But experimental as well as theoretical studies from vibrationally excited targets are nearly non-existence. However under the usual operational condition where various gases are put under the room-temperature, non-negligible amount of gases is known to be in vibrationally excited state. Although collision cross-section data from these vibrationally excited species are urgently needed, very few studies have been carried out so far.

For this reason, we have been undertaking a joint experimental and theoretical investigation and determined charge-transfer cross-sections of  $H^+$ ,  $C^+$  and  $O^+$  ions colliding with vibrationally excited hydrocarbons (high temperature

molecules) and others such as  $H_2$ ,  $D_2$ ,  $CH$ ,  $NH$ ,  $H_2O$ ,  $NH_3$ , and  $C_mH_n$  ( $m < 4$ ) molecules in the energy range of 0.2 to 4.0 keV in collaboration with Prof. Buenker at U. Wuppertal. All collision processes which involve hydrocarbon molecules are exothermic with an appreciable energy difference, although it is relatively small for larger hydrocarbons. For some molecules, vibrationally excited molecules in the initial channel decrease the exothermicity, and hence, are expected to increase the electron capture cross section by an order of magnitude even when the target is in the first vibrational excited state. On the other hand, for other molecules, vibrational excited states are found to increase the exothermicity, which may lead to the smaller cross section. Hence, dynamics of electron capture from the vibrationally excited molecule varies from system to system, and needs to be considered carefully and systematically. In the present theory, the molecular - orbital expansion (MOCC) method is applied with both fully quantal and semiclassical formalisms.

We have observed strong evidence of *the temperature effect or vibrational effect*, in which the vibrational state of the target molecules significantly affects the charge transfer dynamics and cross sections in  $H^+ + C_mH_n$  collisions<sup>1, 2)</sup>. The observed cross sections of the charge transfer processes show a gradual increase as the collision energy decreases for all the present collision systems [ $H^+ + C_mH_n$ ] investigated. The observed cross sections at the present collision energies appear to have a linear-relationship with the ionization energy of the target molecules. This relationship will be discussed in more systematic manner elsewhere<sup>2)</sup>.

### References

- 1) Suno, H., Buenker, R.J., Kimura, M. and Janev, R., Phys. Rev. A. 70 (2004) 032703.
- 2) Suzuki, R., Li, Y., Liebermann, H-P., Buenker, R.J., Pichl, P. and Kimura, M., Phys. Rev. A 71 (2005) 032710.



## §21. LHD Simulated Experiment for Solar Non-Equilibrium Plasmas and Development of Its Spectroscopic Diagnostic Tools

Watanabe, T., Hara, H. (Nat. Astron. Obs., NINS),  
Kato, T., Murakami, I., Sato, K., Funaba, H., Morita,  
S., Goto, M., Muto, S. (Nat. Inst. for Fusion Sci.,  
NINS),  
Yamamoto, N. (Ecot. Cen., Nagoya U.)

Solar-B will be launched in summer 2006. EUV Imaging Spectrometer (EIS, 1) on board Solar-B

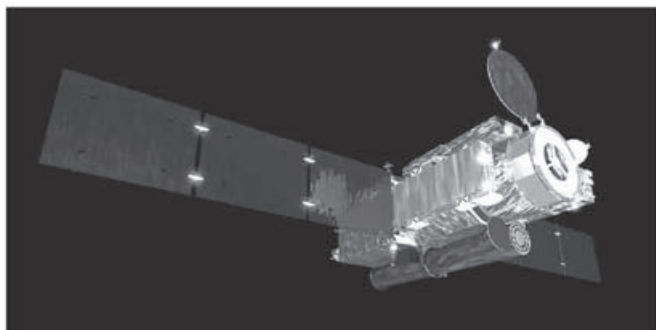


Fig. 1 Solar-B Spacecraft in orbit

accommodates the system of multilayer coated optics and back-illuminated CCD, and will be able to observe, for the first time in EUV observations, spectra and monochromatic images of non-ionization-equilibrium plasmas in the solar chromosphere, transition-region, and corona at two-wavelength bands of 170 – 210 Å and 250 - 290Å, with typical time-resolutions of 1 – 10 seconds.

Time-dependent collisional-radiative model will be developed to analyse the data taken by this EIS instrument, and to diagnose temperatures and densities of those plasmas in the outer atmospheres of the Sun. No systematic models yet exist for iron ions of L- and M-shells, which are very important for coronal plasma diagnostics. Atomic data 2) for iron ions of  $\text{Fe}^{9+}$  to  $\text{Fe}^{14+}$  are surveyed and evaluated, and most recommended data are determined. Parameters for analytical fitting functions are obtained and provided.

Possibility of getting the experimental data of ionization and recombination cross sections for iron ions with an instrument called NICE (Naked Ion Collision Experiment) is in consideration. EUV spectra in the wavelengths of 170 – 190 Å are taken by LHD, injecting iron TESPEL (tracer-encapsulated solid pellet). Data taken by this experiment has been analysed now. Temperatures at the center of LHD plasma reached almost 2keV,

similar to those of solar flares, and they are higher than those of coronal plasmas. Therefore, cooler surrounding plasmas in LHD should be observed more precisely at the next round.

Solar-B is currently scheduled to be launched on 23-Sep-06, and it will be put into a final sun-synchronous orbit in three week time after the launch. Scientific operation will start soon after the instrument commissioning phase. Prioritized “Initial Three Month Operation Plan” will be conducted, and the standard modes of scientific observations will be established. 3)

“Solar-B Science Center” was founded at NAOJ in 2005 to promote Solar-B sciences, constructing so called the “Level 2” database, that is a science-value added database. Solar-B Science Center will be able to provide three-dimensional photospheric magnetic field structures and movies of co-aligned images in X-ray, EUV, and optical wavelengths. Newly developed time-dependent collisional-radiative models in this study will be also included in the data-analysis software system in Solar-B Science Centre, and available for use of world-wide researchers, both of solar physics and plasma physics among others.

## References

- 1) Culhane, J. L. et al.: 2005, *Ad. Sp. Res.*, 36, 1491.
- 2) NIFS-DATA95, 2006
- 3) Watanabe, T. and the Solar-B Team: 2005, *Ad. Sp. Res.*, 36, 1478.
- 4) Landini, E. et al.: 2006, *Astrophys. J., Suppl.*, 162, 261.

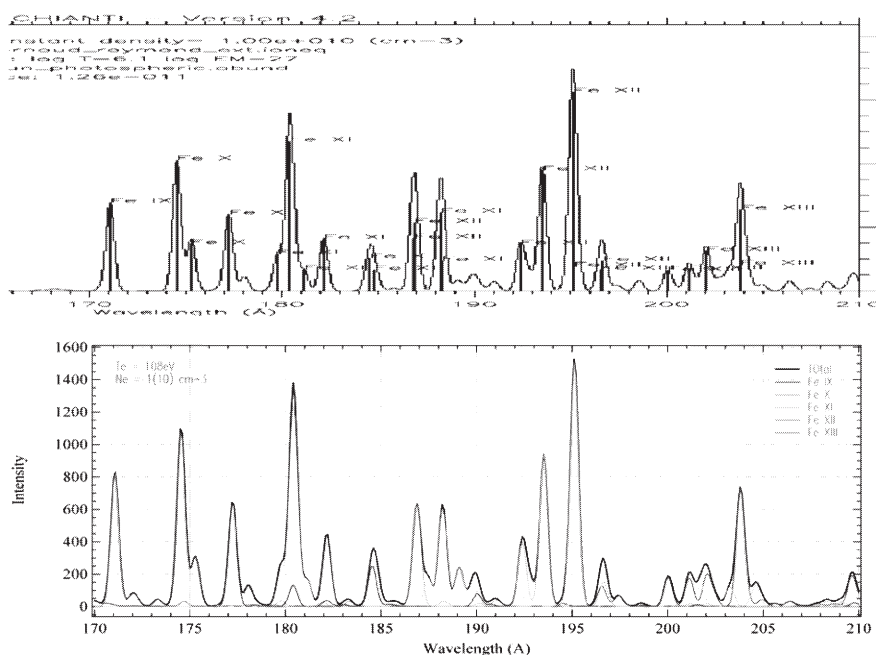


Fig. 2 Comparison of theoretical iron line spectra generated by an ionization-equilibrium model (CHIANTI 4); upper panel) and by currently developed time-dependent code at  $t = \infty$  (equilibrium state).

## §22. Plasma Diagnostics of Fe Ion Spectra for Solar-B and LHD

Yamamoto, N. (Nagoya Univ.),  
Kato, T., Murakami, I., Sato, K., Funaba, H., Tamura, N.,  
Watanabe, T. (Nat. Astron. Obs., NINS)

A satellite called Solar-B will be launched this September to study the Sun. It will observe the Sun to provide information about coronal heating. This satellite has a visible optical telescope (SOT), X ray telescope (XRT) and Extreme Ultra Violet Imaging System (EIS) to investigate the magnetic hydrodynamic phenomena totally in the Sun. Transition-coronal region has strong temperature and density gradient. In magnetic confined laboratory plasma, there are also strong spatial distribution of  $T_e$  and  $N_e$ . Time dependent atomic processes, non equilibrium model is necessary to investigate the behaviour of the ions in such conditions. In addition when an ion is moving in plasma, this ion is not in ionization equilibrium. Therefore it is necessary to study plasma diagnostics for non equilibrium ionization.

We construct a collisional-radiative model (CRM) for Fe ions. Atomic processes included are excitation/de-excitation by electron -impact, excitation/de-excitation by proton -impact, ionization and three-body recombination, radiative transition, radiative recombination and dielectronic recombination. The radiative recombination rate coefficients to excited states are included. However the dielectronic recombination to excited states are not included because these atomic data are not available yet. We need to investigate more how to include the dielectronic recombination in CRM.

We include the fine structure energy levels for  $2 \leq n \leq 5$  of Fe ions in our CRM (*about 10,000 levels*). The ions and configurations taken into account are as follows,

**K-shell ions;** Bare, H-like( $nl$ ), He-like( $1snl$ , 8828eV),  
**L-shell ions;** Li-like( $1s^2nl$ , 2024 eV), Be-like( $2l'nl$ ), B-like( $2s^2nl$ ,  $2s2pnl$ ,  $2p^2nl$ ), C-like( $2s^22pnl$ ,  $2s2p^2nl$ ,  $2p^3nl$ ), N-like( $2s^22p^2nl$ ,  $2s2p^3nl$ ,  $2p^4nl$ ), O-like( $2s^22p^3nl$ ,  $2s2p^4nl$ ,  $2p^5nl$ ), F-like( $2s^22p^4nl$ ,  $2s2p^5nl$ ,  $2p^6nl$ ), Ne-like( $2s^22p^5nl$ ,  $2s2p^6nl$ , 1266eV),

**M-shell ions;** Na-like ( $2s^2 2p^6 nl$ , 489eV), Mg-like ( $3l' nl$ ), Al-like ( $3s^2 nl, 3s 3p nl, 3s 3d nl, 3p^2 nl, 3p 3d nl$ ), Si-like ( $3s^2 3l' nl$ ), P-like ( $3s^2 3p 3l' nl$ ), S-like ( $3p^2 3l' nl$ ), Cl-like ( $3p^3 3l' nl$ ), Ar-like ( $3p^5 nl$ , 234eV),  
**N-shell ions;** K-like ( $3p^6 nl, 3p^5 3d nl$ , 151eV), Ca-like ( $3p^6 3d nl$ )

To make a reliable CRM we need reliable atomic data. It is found that sometimes proton collisions are important for excitation between fine structure transitions; for example, the proton excitation rate coefficients are larger than electron excitation rate coefficients for transition  $3s^23p\ ^2P_{1/2} - ^2P_{3/2}$  in Al-like Fe XIV ions, in the temperature region  $T_e > 200\text{ eV}$ .

The line intensity ratios are often used for plasma diagnostics. The intensity ratios of Fe ion lines have been used for density diagnostics in the Sun. The absolute values for intensity ratios are important to decide the

density. In order to know the difference of the calculated line intensity ratio by different atomic data we compared the intensity ratios of  $I(196.5\text{\AA } 3s^2 3p^2 \text{ } ^1D_2 - 3s^2 3p 3d \text{ } ^1F_3 / I(203.8\text{\AA } 3s^2 3p^2 \text{ } ^3P_2 - 3s^2 3p 3d \text{ } ^3D_3)$  using the two kinds of atomic data for Fe XIII. One is the data calculated by R-matrix method by Agarwal and another is one by distorted wave (DW) method by Hullac code. The density dependence of FeXIII line intensity ratio  $I(196.5\text{\AA})/I(203.8\text{\AA})$  is shown in Fig. 1. This intensity ratio is useful to diagnose the electron density in the region from  $10^9 \text{ cm}^{-3}$  to  $10^{11} \text{ cm}^{-3}$ . This ratio can be used for the Sun although the density of LHD is too high to use this ratio.

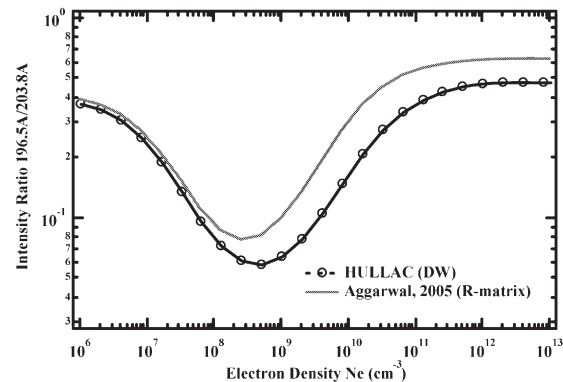


Fig.1. The calculated intensity ratios for Fe XIII  $I(196.5\text{\AA})/I(203.8\text{\AA})$ . The solid line indicates the ratio using the data by R-matrix and the dotted line by DW method.

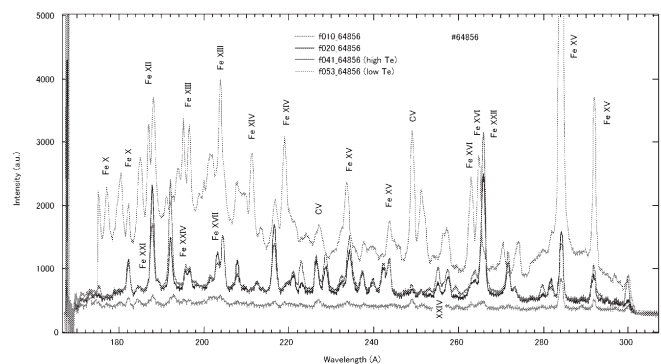


Fig.2 The observed Fe ion spectra from LHD by injecting Fe TESPEL pellet.

We have measured Fe ion line emissions in EUV regions (170 – 300 Å) by a SOXMOSS spectrometer from LHD injecting the Fe TESPEL. We obtained Fe ion spectra in both high temperature and low temperature cases. In Fig.2 the spectra for the shot 64856 are shown. In a high temperature case when neutral beam was on for heating, doublet lines from Fe XXIV (2s – 2p) were measured. In a case of low temperature when the heating beam was off, Fe X, XII, XIII, XIV, XV and XVI line pairs (3p – 3d) which can be used for diagnostics were measured. We are analyzing spectra observed on LHD. We will apply our model to SolarB/EIS spectra.

## §23. Network of Atomic and Molecular Database Related the Processing Plasmas

Iinuma, K., Ito, H. (Chiba Inst. Tech.), Sakai, Y. (Hokkaido Univ.), Samukawa, S. (Tohoku Univ.), Sugai, H. (Nagoya Univ.), Nakamura, Y. (Keio Univ.), Hatano, Y. (Tokyo Inst. Tech.), Kono, A. (Nagoya Univ.), Matsumi, Y. (Nagoya Univ.), Sato, T. (Muroran Int. Tech.), Tanaka, M. (Pegasasu Co.), Tanaka, H. (Sophia Univ.), Tsumori, K., Kato, T., Kato, D.

Following progress from the previous year, work on the **“Network of Atomic and Molecular Database related the Processing Plasmas”** project has conducted under the NIFS coordination. This project has included a number of application-related, i.e. plasma processing-including one company, atmospheric and radiological science research groups, and so on.

As a challenge for the 21<sup>st</sup> century compilation and evaluation of these databases, so invaluable for science development and the industry, needs to be enlarged to include data from other areas of science and engineering. This project aims at searching for reliable atomic and molecular databases for further development of the plasma processing technology (e.g. vertical integrated computer-aided design for device processing). In this fiscal year, atmospheric research area has been involved; one consultative meeting was held that discussed the following.

(1) Present status of the on-going issue for the linkage between the IEE Japan data-base and the NIFS data-base. The conclusions from the meeting were that (i) Through Profs. Ito and Nakamura (the IEE Japan), NIFS will keep to negotiate the linkage possibility of the IEE data-base via the NIFS home page, specifically, together with the issues on the data-base royalty and so on (ii) along this way, NIFS has started to extend the project to cover more comprehensive data-base net work system for the atmospheric discharge and upper atmospheric chemical reactions. (iii) Dr. K. Takahashi with Prof. Y. Matsumi reported the present status of the

atomic and molecular data base for the modeling of atmospheric process, emphasizing that the comprehensive net work for the data base and its exchanging the information.

(vi) Prof. T. Sato introduced new plasma application of the sterilization of bacteria in water by the corona discharge with the emphasis on the atomic and molecular database.

The debriefing session for the General Coordinated Researches was held and reported as follows.

(2) Since 2003, the product of three years of research was reviewed for the survey of the atomic and molecular data-base related to processing plasma, and for net work of atomic and molecular database related the processing plasma. Also, recent status of the atomic and molecular data needs demanded from new trends in processing plasma as well as from the international thermonuclear reactor design going at Cadarache, France were reported, emphasizing that activities at the Data Center is now expected to be important for research of these applications.

The four papers were invited: 1) Data Needs for Electron Interaction with Plasma Processing and Fusion Plasma Gases (H. Tanaka et al, 1<sup>st</sup> Korea-Japan Joint Seminar on Atomic and Molecular Data for Plasma, 8/31-9/1 2005 Jeju, Korea), 2) Electron Collision Data of C-H Compound Molecules for Plasma Modeling (H.Tanaka et al, 1<sup>st</sup> Research Coordination Meeting of the IAEA's Coordinated Research Program on Atomic and Molecular Data for Plasma Modeling IAEA, Vienna, Austria 26/9-28/9 2005), 3) Recent Trends in Low-energy Electron Collisions with Gaseous Molecules (H.Tanaka et al. 58<sup>th</sup> Annual Gaseous Electronics Conference 18/10, 2005 Sun Jose, US), 4) Low Energy Electron collision Data for Fluorocarbon Molecules (H. Tanaka et al. 6th International Workshop on Fluorocarbon Plasmas, 19-23 March 2006 Villard de Lans, France).

NIFS report has been arranged for the set of experimental electron-molecule collision cross sections data by H. Tanaka at the Sophia University.

The publications supported partially under this project are referred in each member's publication list.

## §24. Atomic and Molecular Data Compilation and Update of the NIFS Databases for Molecular Targets

Kimura, M. (Kyushu U.), Igarashi, A. (Miyazaki U.), Motohashi, M. (Tokyo U. Ag. and Tech.), Kusakabe, T. (Kinki U.), Morishita, T. (U. Elec-Comm.), Moribayashi, K. (JAEA), Kitajima, M. (Tokyo Inst. Tech.), Imai, M. (Kyoto U.), Pichl, L. (ICU.), Kato, D., Murakami, I., Kato, T.

Continuing and systematic efforts for making revision and update of NIFS databases have been carried out for electron and ion impacts on various atomic and some molecular targets by a few atomic and molecular collision physicists over the years by having obtained many participants. The original databases called AMIDIS for electron collisions and CHART for heavy-particle collisions, respectively, have been completed over decades ago, and from time to time, some efforts have been taken to update the databases by collecting those recently published, critically evaluating these data and implementing into these databases. Since the last revision made sometime ago, probably more reliable data for various atomic and molecular systems at different collision energy range are now available. Therefore, new and systematic effort to update these databases is considered to be not only important, but also indispensable to preserve human knowledge for future generations. In this contract year, we are concerned with molecular targets by electron and ionic impacts. For recent years, theoretically very extensive and accurate calculations have been performed routinely for inelastic processes for electronic and ionic impacts, while experimentally very elaborate beam experiments are also carried out, in combination with various types of lasers, so that one can determine different scattering parameters fairly accurately. Consequently,

significant progress for both areas has been made particularly since 1990. Therefore, we have felt it essential to reevaluate these new data critically and establish recommended values for electron and heavy-particle ionic impacts for molecular targets in the NIFS databases.

### **Electron impact:**

Compilation of the cross sections for the electron-impact excitation and ionization of various molecules such as hydrocarbons was attempted. With the close collaboration with specialists in the plasma-processing community, we have also undertaken the systematic effort to collect cross-section data for those molecular targets relevant to plasma processing such as  $C_mF_n$  and  $C_mCl_n$ . In addition, some attempts have been made to collect and evaluate cross-section data for ionic species. Extensive and systematic calculations based on the R-matrix method were performed recently for ionic targets by one of our members, and the cross section data from these studies were included in AMIDIS.

### **Ion impact:**

For ion impact, we have reviewed  $H^+$ ,  $B^{q+}$  (where  $q = 1-5$ ), and  $C^{q+}$  ( $q = 1-6$ ) impacts on hydrocarbons and other common molecules such as  $O_2$ ,  $H_2O$ , and  $CO_2$  from keV to meV collision energies, although very little investigation has been carried out for molecular targets. We have initiated a joint experimental and theoretical investigation to produce and evaluate cross section data for molecular targets by ion impact. This year, we have primarily been concerned with larger hydrocarbons such as  $C_mH_n$  where  $m > 2$  and  $n > 4$ .

Based on these investigations, we have completed a report of the progress of our activity which will be published as a NIFS report in 2006. Another report will be published as a regular article in Journal of Physical and Chemical Data.



§25. New System of Differential Cross Section Databases

Pichl, L. (International Christian Univ.),  
Kato, D., Murakami, I., Kato, T. (Nat. Inst. Fusion Sci.)

The numerical databases maintained at the NIFS Data Center are able to accommodate only single-variable numerical data [1]. Since the system is based on the ORACLE database management software, and outsourced to a professional company, its extension into multi-dimensional numerical data sets, such as the differential cross sections, would imply a substantial cost. Although the 1D data tables allow for various indexing, e.g. in the form of integer quantum numbers, it would not be practical to use the additional cross-section variables in the form of indices for the sake of data integration.

Instead, we have developed the first differential cross-section database in the Coordination Research Center as a free-software open-source solution. The main features of the online database system are shown in Fig. 1.

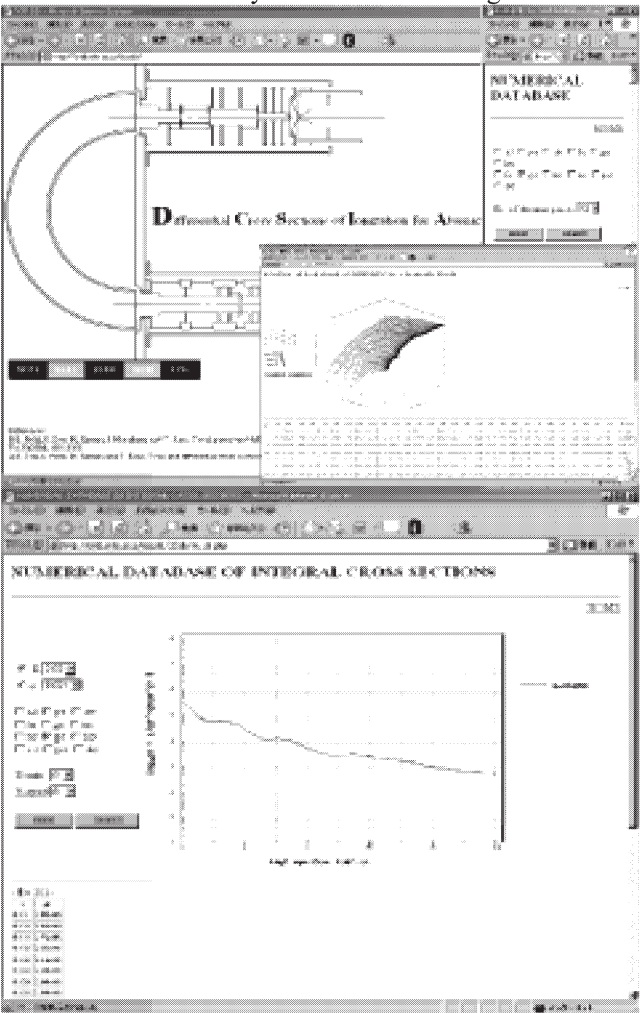


Fig. 1. Online database of differential cross sections at NIFS (<http://crdb.nifs.ac.jp/dcsdb/>) The upper panel shows the main page and a 3D plot GUI in the inset. The lower panel shows the GUI for 2D section plots.

The physical data contain energy-differential cross-sections of ionization of atomic hydrogen by proton impact, resolved with respect to the energy of impacting proton, energy of the ionized electron, and angular momentum quantum numbers, which were computed in our previous NIFS-based project [2]. The main features of the software system are: (1) seamless integration of all data in a hypercube and easy generation of 2D sections, and (2) graphical user interface (GUI) for 2D section plots and 3D data graphs, including multiple data sets in one graph. The 3D GUI also allows for selecting the range of data and manipulating the graph's viewpoint. All figures are generated on the fly, reducing the size of the database. The system is implemented on Fedora Core 3 SE Linux server (Apache server, PostgreSQL database, PHP logic layer).

In order to facilitate the design and deployment of new databases, we have also developed a prototype online database builder module, which allows for creation of database tables, online data input, data search and 2D plot generation. The interface is shown in Fig. 2.

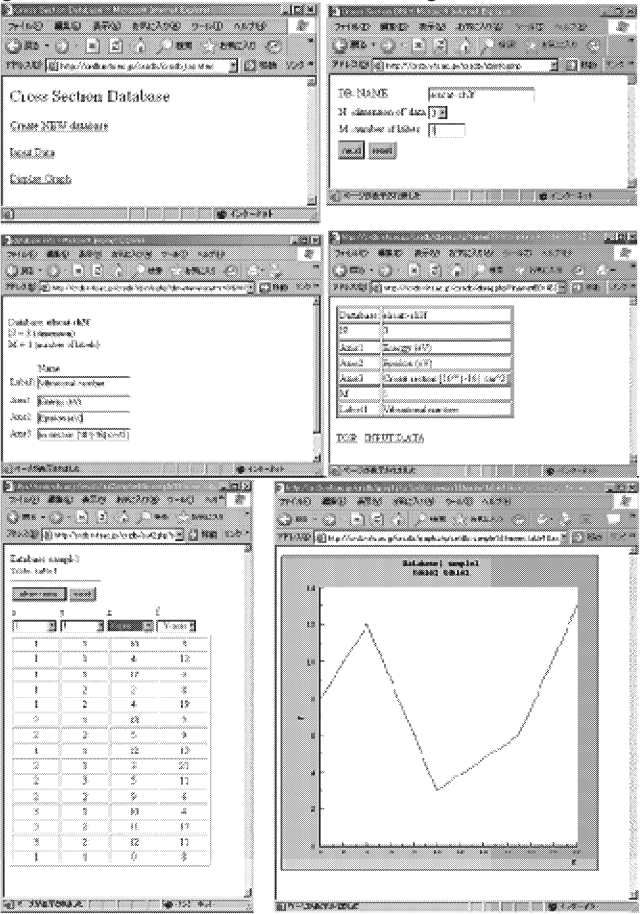


Fig. 2. Elements of the online database builder prototype.

Further research will include the integration of both modules.

References

[1] <http://dbshino.nifs.ac.jp/>  
[2] Pichl, L. et al., JPCRD **33** (2004) 1031.

## §26. Study of Evolutional Data Collecting System for the Atomic and Molecular Databases

Sasaki, A., Kubo, H. (Japan Atomic Energy Research Institute),  
Joe, K. (Nara Womens's University),  
Pichl, L. (The Aizu University),  
Ohishi, M. (National Astronomical Observatory),  
Kato, D., Kato, M., Murakami, I., Kato, T. (National Institute for Fusion Science)

We have been studying an evolutional atomic and molecular database based on computer and internet technology to collect and evaluate a large amount of data required for scientific as well as industrial applications since FY2003 [1]. We had working group meetings on 21-Jun-2005 and 27-Feb-2006, to understand the present status and direction of the project, and discuss about development and improvement of software to classify the papers on the atomic data.

We study the computational method to collect scientific articles, which contain atomic data, because this part can be realized using data mining methods and language processing technologies, and may relax a large amount of present effort of staff scientists in the data centers.

Firstly, we study a software program [2] which classify articles from the analysis of its abstract, based on a LVQ [3], a machine learning algorithm. We model abstracts using the term frequency and inverse term frequency (TF/IDF) of words in the abstracts. We use a set of papers concerning to the electron collisional ionization and excitation of atom and molecules collected by Itikawa [4] as the training samples, to decide the existence of the atomic data in unknown abstracts. Furthermore, we use approximately 300 abstracts from Phys. Rev. A-E, as well as 16000 abstracts from Phys. Rev. A as test examples to investigate characteristic feature of articles from a variety of fields of physics.

It is found that the possibility to find articles, which contain the atomic data, is approximately 1% in approximately  $10^4$  articles/year from Phys. Rev. A., which consists of the largest part of the source of the atomic data. That is, the accuracy and reproduction must be more than 90% to realize the application of the present software. Although, initial trial software shows almost sufficient reproduction >85%, the accuracy is found to be around 50%. Secondly, we study improvement of the accuracy of classification of articles by several ways. Initial classification software uses only independent words in the articles to characterize its content. The accuracy is expected to improve using better keywords as well as additional scientific and bibliographic information attached to the articles.

For instance, we investigate the PACS number in papers from American journals. It is found that 90% of the articles, which contains atomic data have a few common

PACS numbers. Information of authors may also be useful to specify their research area.

On the other hand, we investigate technical terms in the papers in two different ways. Firstly, we take technical terms from the scientific dictionary [6]. We find approximately 800 keywords in the papers concerning to the atomic data, from the total 26000 English keywords in the dictionary. Using these keywords, accuracy of the classification is found to improve slightly.

Secondly, we also use another software termex [7], to see number of technical terms specific to the papers on the atomic data is relatively small (<100). Moreover, it is found that the terms are sometimes represented by two or more consecutive words and form a graph structure, which consists of a stem and additional words such as "excitation", "impact excitation", and "excitation cross section". Extracted technical terms will be also applied to the classification software.

Furthermore, we develop a software to recognize and extract atomic and molecular symbols in the abstract [5]. Information of atoms, electron configurations, and spectral terms are represented in special forms in scientific articles such as, Al XI,  $1s^22s^22p^2$ , and  $^1S_0$ . In the electronic form of articles on the web sites, these expressions are represented using the syntax of HTML. We develop a rule-based software using perl regular expression to recognize description of atomic species.

Initial program classifies 5 categories, however, after investigation of articles from Phys. Rev. A-E, the characteristic feature of papers for atomic data would become clearer if we would increase the number of categories to 7, where atomic expression with left super script is classified as nuclear species, and repeated expression of atoms is classified as molecules. It is found that 90% of atomic data papers contain expressions of either ions, configurations, and spectral terms. Application of these scientific symbols will also be useful for the classification of the papers.

In summary, we develop and evaluate computer programs to retrieve papers concerning to the atomic data. In FY2006, we are planning to apply above techniques to find better keywords and specific physical expressions to the text classification software. We are also planning to apply the software to newly published papers to demonstrate the usefulness of the present programs for the development of the atomic and molecular database.

### References

- [1] M. Suzuki, et al., Proc. ITC-14 & ICAMDATA 2004, JPFR series, vol. 7 pp. 343 (2006).
- [2] A. Sasaki, et al., Proc. ITC-14 & ICAMDATA 2004, JPFR series, vol. 7 pp. 348 (2006).
- [3] Kohonen, T.; The Self-Organizing Maps (3rd edition), Springer, 2001.
- [4] Y.Itikawa, ADANDT, **63**, 315 (1996).
- [5] A. Sasaki, et al., J. Plasma Fusion Res. , **81**, 717 (2005).
- [6] 理化学事典第6版 (岩波書店) .
- [7] <http://gensen.dl.itc.u-tokyo.ac.jp/>

## §27. Private Tutoring Academy KENZAIJUKU Started

Yamada, M. (Guest Professor, NIFS)

The private tutoring academy of talented people raising for the employee of the managing staff candidate of the enterprise was held in the National Institute for Fusion Science. The name of the academy is KENZAIJUKU and the academy manager is Mr. Hiroaki Yanagida, professor emeritus of the University of Tokyo, and Mr. Tsurayuki Kado and I served as the coordinator.

This original trial was carried out under the auspices of Gifu Industries Association, and took the support of Gifu Prefecture and the Gifu Prefecture Research and Development Foundation. Main lecture themes are in such cases as bold plan of the business growth which started a change in the market and the training of the way of making use of the plan technique of the management strategy, a problem-solving ability and new material and new technology, the presentation technique of the new product.

The period was 5 days, from January 19 this year until the 21st and from January 28 until the 29th. Twenty people joined this academy with the minor pick form, by camping for training. The most part of this academy participant was the manager of new business industry or active as a backbone of the enterprise. Or, it participated on the second generation manager of the family partnership as well. In the distribution of the enterprise which participants belong to, though the most part was an enterprise in local Gifu Prefecture, there was participation in the managing staff of a leading company in Tokyo, and became the place of the training which is very rich in the stimulus.

As for the biggest characteristics, participants can associate with the lecturers of this academy at time out of regular class as well by camping for training.

This academy of the first has ever been popularity very much from the participants who attended, and it is decided that this academy of the second term is carried out this summer.

Main curriculum and lecturers at this academy of the first Contents are as the following.

### **i) The first-day**

[Kick off keynote lecture] Hiroaki Yanagida (professor emeritus of the University of Tokyo).[ 7 articles that creates 100% hit product], Noriaki Kanda (Meiji University Professor).[Computerized strategy in 2015],Kenji Kumasaka(Keio University Environment & Information Department manager).

### **ii) The second day**

[What is common to the president in the enterprise which continues the growth in the unfavorable wind],Michiaki Nishiura,Koichi Hayashi (Attax Group). [The know-how of the way of telling it Takako Kawamura(Gifu Broadcasting Corporation, announcer).[ Management strategic practice], [Case study group work](coordinators & lecturers).

### **iii) The third day**

[Hit products case research], Masao Yamada (Coordinator).[The verification of the core competence],Tsurayuki Kado(Coordinator).

### **vi) The fourth day**

[An ultimate presentation technique],Masao Yamada (Coordinator).[ As for the idea to make the articles to sell], Kuniharu Kondo(Chubu Economic Federation). [The manufacturing innovation of a period of computerization],Megumi Kuroiwa (Nagoya Institute of Technology, guest professor).

### **v) The fifth day**

[As for the project, from the idea of the reverse], Yoshie Komuro (Japan Anti-aging Laboratory director).[Core competence case study, presentation, evaluation], Masao Yamada (Coordinator)& Tsurayuki Kado (Coordinator).



## §28. EUV Spectra by $\text{Xe}^{q+} + \text{Xe}$ Charge Transfer

Yamamoto, N. (Nagoya Univ.), Kato, T., Kato, D.

Recently, Xe and Sn ion spectra produced by laser are studied as EUV light sources for lithograph for the wavelength 13.5nm, where reflection of multilayer mirror is high. In low-ionized Xe and Sn ions, many lines including satellite lines are emitted around 13.5nm. Atomic processes related to Xe or Sn ions should be studied to extract the radiation power efficiently from plasma.

For identification of complicated EUV spectra from these high Z ions, spectra by charge transfer  $\text{Xe}^{q+} + \text{Xe}$  [1] are useful. In these experiments, a Xe ion beam are taken out from an ECR ion source and injected to the neutral Xe gas target with kinetic energy of 20q keV. Spectra emitted by charge transfer were measured from vertical direction of the collisional crossing point.

Correct identification of spectral lines needs modeling to calculate line intensities by charge transfer processes. In this report, we constructed a collisional-radiative model including charge transfer processes, which assumed an intuitive function as equation (1) for charge transfer rates to an excited state  $i$ .

$$C_i^x \propto F_i \exp\left\{-\left[(E_i - E_c)/\sigma\right]^2\right\}, \quad (1)$$

where  $F_i$  is a coefficient to each energy level  $i$ ,  $E_i$  is an energy of  $i$  state,  $E_c$  is a captured energy measured from the ground state, and  $\sigma$  is captured energy width in Gaussian type distribution which we assumed for the energy dependence by electron transfer. If a charge transfer is a dominant process in collision system  $\text{Xe}^{q+} + \text{Xe}$  and collisional processes by electron impact are negligible, complicated rate equations are reduced to a simple equation as follows,

$$dN_i / dt = -\sum_j A_{ij}^r N_i + \sum_j A_{ji}^r N_j + C_i^x N_{\text{Xe}}, \quad (2)$$

where  $A_{ij}^r$  is a radiative transition rate from an  $i$  state to a  $j$  state, and  $N_i$  and  $N_{\text{Xe}}$  are population densities of an  $i$  state of  $\text{Xe}^{q+}$  ions and the ground states of neutral Xe atoms. The numbers of energy levels depend on ion species. For  $\text{Xe}^{8+} + \text{Xe}$  processes, energy levels  $4d^{10}nl$  and  $4d^9 4fnl$  of  $\text{Xe}^{7+}$  ions are included and the total number of the levels is 277. For  $\text{Xe}^{18+} + \text{Xe}$  processes, energy levels  $4s24p6nl$ ,  $4s^2 4p^5 4dnl$ ,  $4s4p64dnl$ ,  $4s^2 4p^4 4d^2 nl$ ,  $4s4p^5 4d^2 nl$ ,  $4s^2 4p^5 4f^2$  and  $4s4p^6 4f^2$  of  $\text{Xe}^{17+}$  ions are included, and the total number is 8831. A quasi-steady state solution of equation (2) is written as

$$N_i = r_i^{Xc} N_{\text{Xe}}. \quad (3)$$

Population densities are populated by charge transfer only.

Figure 1 shows the measured and theoretical spectra. A Gaussian type line profile is assumed in theoretical spectra. The measured spectra are emission spectra from

charge transfer of  $\text{Xe}^{8+} + \text{Xe}$ . The theoretical spectra are obtained from equation (1) - (3) with  $E_c = 79.5\text{eV}$  and  $\sigma = 1\text{eV}$ . These parameters in equation (1) are very sensitive to line spectra. The values  $F_i$  in equation (1) are assumed to be unity.

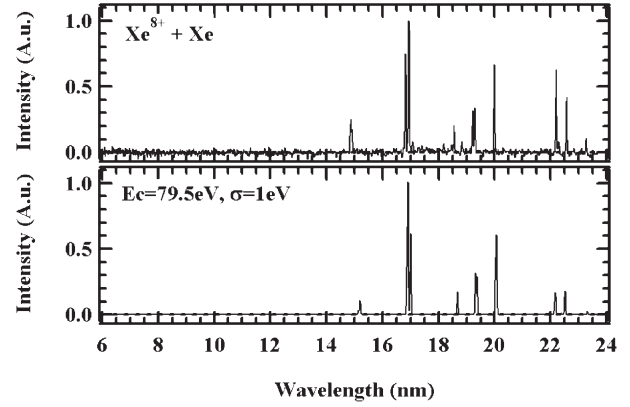


Figure 1 The measured spectra by  $\text{Xe}^{8+} + \text{Xe}$  processes (Top panel) and the theoretical spectra with  $E_c = 79.5\text{eV}$  and  $\sigma = 1\text{eV}$ , respectively.

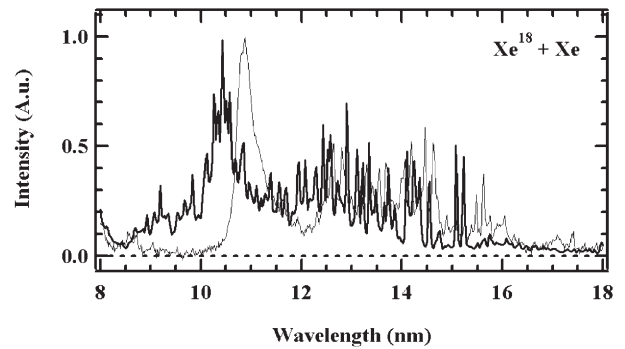


Figure 2 Comparison with the measured (thin line) and theoretical spectra (bold line) from charge transfer processes of  $\text{Xe}^{18+} + \text{Xe}$ . The theoretical spectra are calculated for  $E_c = 420\text{eV}$  and  $\sigma = 1\text{eV}$ , respectively.

Comparison with the measured and theoretical spectra by  $\text{Xe}^{18+} + \text{Xe}$  is shown in figure 2. The theoretical spectra roughly agree with the measured spectra if the wavelengths are shifted about 0.5nm to longer wavelength side. We found that a broad feature around 10.5-11.0 nm is produced by 4p-4d and 4d-4f transitions between various configurations and the comb-like spectra in 12.0-16.0 nm are produced by 4p-4d transitions of  $4s^2 4p^6 4d - 4s^2 4p^5 4d^2$ . Forbidden lines are generally strong in a case of charge transfer or recombining plasma where radiative cascade processes are dominant. However, we found that lines from metastable states are not measured in the spectra in ref [1]. It means that emissions from excited states with a long life time can not be measured in experiments. Measurable spectral lines from an ion beam are limited by a velocity of ions, an extension of target neutral Xe gas and a focal spot size of a spectrometer.

### References

[1] Tanuma, H. et al., NIMB 235 (2005) 331-336.



## 10. Fusion Engineering Research Center

The collaboration program on material irradiation test facility was completed in the last fiscal year, 2004-2005. Some of activities in this program were extended in the framework of the LHD Project Research Collaborations with newly settled plans. Then Activities in Fusion Engineering Research Center (FERC) are summarized as research and development for (1) advanced blanket systems, (2) advanced low activation materials, (3) advanced super conducting magnet systems.

One of the programs on blanket systems is closely related to design studies on Force-Free Helical Reactor, FFHR2m. Neutronics calculations were carried out to characterize self-cooled Li and Flibe blankets with vanadium alloy (V-4Cr-4Ti) structure, as advanced options for FFHR2m. The parameter dependence of Tritium Breeding Ratio (TBR) and neutron shield performance was examined for a Li blanket and a Flibe blanket. Calculations with a 1-d code suggest possible solutions in both type of blankets. For further understanding of the neutronics characteristics, detailed investigations with a 3-D helical geometry have been required. Construction of a 3-D neutron transport calculation system has been started. Preliminary results indicated necessity of an improvement in geometrical design. The blanket configuration has been modified to enhance the total TBRs and also improve the shielding performance for the coils. With a modified blanket configuration such as blanket dimensions, neutron reflectors *etc.*, both of the blanket systems would achieve adequate tritium breeding performance in the FFHR2m.

Discussion on a medium scale project aiming realization of an integrated blanket module has been started inside the FERC. Material corrosion in flowing Flibe would be studied in the first step of the project. Some types of loops have been under investigation as an experimental facility for these studies.

MHD (Magneto-hydrodynamics) pressure drop is one of critical issues in a Li/V blanket. Insulator coating has been developed with  $\text{Er}_2\text{O}_3$ . Coated specimens were exposed to liquid lithium at up to 973 K for 100 hours, and observed

their properties and corrosion behavior. In-situ coating is with  $\text{Er}_2\text{O}_3$  has been also investigated in Li doped with Er. It is suggested that thickness of the coated layer could be determined with choosing an appropriate operation time and temperature.

Irradiation experiments have been performed using the Fusion Neutronics Source (FNS) at JAEA. Specimens of Er, Teflon ( $\text{CF}_2=\text{CF}_2$ ) and NIFS-HEAT-2 (V-4Cr-4Ti) were selected in the experiments for simulating of Er in coating layers, F in Flibe and V, Cr, Ti in structural materials. Results are compared with those obtained with neutronics calculations.

Impurity behavior in V-4Cr-4Ti-Y alloys produced by levitation melting were investigated. Precipitates contributing to the hardening were identified as Ti-O type by microstructural observations. Small number density is considered to result in the smaller hardening in the Y-added alloy. Since O in solution interacts with irradiation defects, neutron irradiation hardening and embrittlement is expected to be improved by the Y addition.

Creep property of NIFS-HEAT-2 is investigated. It has been shown that hardened alloys have lower creep rate than the standard annealed alloy at high temperature and high stress level. Detail mechanisms have been discussed.

Tensile tests and microstructure analysis of the RAFM steel, JLF-1, were carried out from RT to 873 K at strain rate of 0.1%/s and 0.02%/s to investigate the material static deformation behavior. With strain hardening decreased, the difference between YS and UTS decreased significantly above 773 K; and the fracture mode was changed from shear fracture below 673 K to dimple fracture at 773 K and 873 K. It means that the potential to support the over loading decrease as the temperature rises, and much ductility appears.

Compatibility of the three kinds of materials, pure iron, Fe-9Cr and low activation ferritic steel JLF-1(Fe-9Cr-2W<sub>o</sub>), was investigated. Phase transition and Cr depletion resulted

in surface hardness reduction on JLF-1. The reduction of surface hardness also happened on the Fe-9Cr, probably due to the Cr dissolution. On the other hand, there was almost no change appeared on pure Fe.

Effects of 14 MeV neutron and gamma ray irradiation on interlaminar shear strength (ILSS) and fracture mode were investigated using G-10CR with FNS in JAEA. No clear difference in the ILSS at RT and 77K up to the neutron fluence of less than  $10^{20}$  n/m<sup>2</sup>. Irradiation test of gamma ray was carried out at Osaka University using Co<sup>60</sup> up to 1 MGy. The results tested at 77 K present the degradation of the ILSS after 1 MGy radiation, and RT tests did not show such degradation because of the lower ILSS.

Annealing effect was studied on microstructure and superconductivity of V-based Laves phase compound wires.

Average composition of Laves phase in the as-quenched and various post-annealed were investigated and the optimum RHQ condition and post-annealing temperature after RHQ was obtained.

A new test method to evaluate the superconducting properties of multi-strand cable in high magnetic field under transverse compressive loading was developed. It is a kind of coil-test in high magnetic field with compressive load which simulated an electro-magnetic force in cable-in-conduit. Quasi-critical current measurement was carried out using 15 T superconducting magnet at Tohoku University and their degradation were obtained as a function of compressive loading and field strength.

(Noda, N.)

§1. Neutronics for Li/Vanadium-alloy and Flibe/Vanadium-alloy Blanket Systems

Muroga, T., Tanaka, T., Sagara, A.

Neutronics calculations were carried out to characterize self-cooled Li and Flibe blankets with vanadium alloy (V-4Cr-4Ti) structure, as advanced options for the Force Free Helical Reactor (FFHR-2). In the present paper, the parameter dependence of Tritium Breeding Ratio (TBR) and neutron shield performance was examined for a Li blanket (FFHR-LV) and a Flibe blanket (FFHR-FV). Calculations of neutron transport and of nuclear reactions were performed for FFHR-LV and FFHR-FV blankets by using the MCNP-4C code and JENDL 3.2 nuclear data. The modified FFHR-2 design, FFHR2m1, has a plasma major radius of 14.0 m and a minor radius of 1.73 m. The neutron wall load is 1.5 MW/m<sup>2</sup>. In the present calculation, a simple torus was fully covered with uniform blanket layers consisting of self-cooled breeder channels and radiation shield.

The TBR was independent from the Flibe composition between 30 to 45 mol% of BeF<sub>2</sub> in the case of the FFHR-FV as shown in Fig. 1. Due to the increase in the temperature range of the coolant Flibe as a result of the change of the structural materials from JLF-1 (Low activation ferritic steel) to V-4Cr-4Ti, the fraction of BeF<sub>2</sub> can be changed from 43 mol% to 31 mol% without changing the margin to coagulation of Flibe and without changing TBR. The compositional change of Flibe resulted in a significant decrease in its viscosity as shown in Fig. 2.

The increase in the B<sub>4</sub>C in the shielding material resulted in the decrease in the fast neutron flux at the superconducting magnet by 60-70% in both FFHR-LV and FFHR-FV, as shown in Fig. 3.

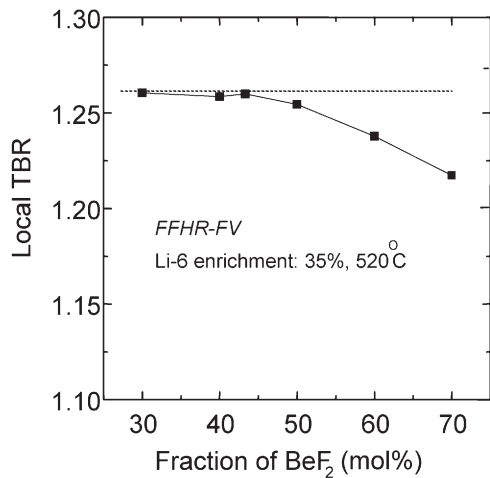


Fig.1 Local TBR as a function of the fraction of BeF<sub>2</sub> in Flibe for FFHR-FV. Blanket thickness : 60 cm, <sup>6</sup>Li enrichment : 35%, Temperature : 520 °C.

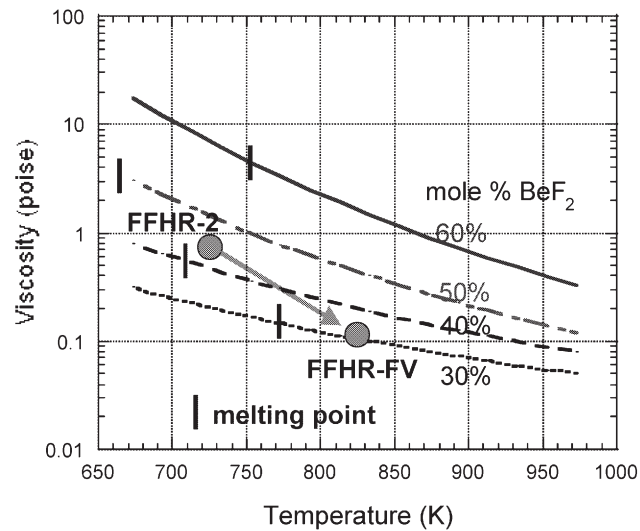


Fig.2 Viscosity of Flibe as a function of temperature and mole % of BeF<sub>2</sub>. The conditions for the minimum temperature region of the blankets of FFHR-2 and FFHR-FV are shown in the Figure.

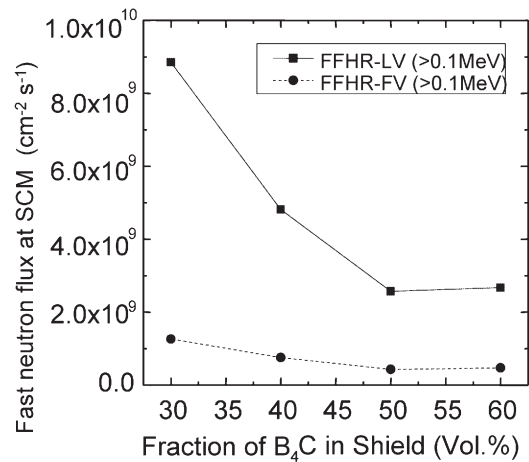


Fig.3 Fast neutron ( $E>0.1\text{MeV}$ ) flux at superconducting magnet as a function of the fraction of B<sub>4</sub>C in the shield for FFHR-LV and FFHR-FV. Blanket thickness : 54 cm for FFHR-LV and 60 cm for FFHR-FV, <sup>6</sup>Li enrichment : 35%, Temperature : 520 °C.

## §2. Development of 3-D Neutronics Calculation System for Helical Reactor Design

Tanaka, T., Sagara, A., Muroga, T.

Four types of advanced self-cooled liquid blanket systems (Flibe+Be/JLF-1, Flibe-cooled STB, Li/V-alloy and Flibe/V-alloy) have been studied in the design activity of the helical reactor FFHR2 [1-3]. Feasibilities of the blanket systems from the neutronics aspects have been investigated previously with a cylindrical or simple torus geometry assuming that the blanket layers completely covered DT core plasma, i.e. a geometry with no neutron leakage. Results of the investigations indicated that all of the four systems would achieve the compatibility between tritium self-sufficiency and neutron shielding ability within the limited blanket space of 1.2 m. However, for further understanding of the neutronics characteristics in the FFHR2, detailed investigations with a 3-D helical geometry have been required, since DT core plasma is covered with complicated blanket layers running helically in the toroidal direction. Construction of a 3-D neutron transport calculation system has been started in the present study.

The 3-D neutron transport calculation system is especially focusing on quick feedback between neutronics evaluations and design modifications of the blanket systems. Cross-sections of the helical blanket components are divided into quadrangular meshes on the design drawings as shown in Fig. 1 (a). The coordinates of the meshes are input data of the calculation system. Vertices of 3-D geometry data are calculated according to the coordinates of the meshes and numerical equations defining the helical structures as shown in Fig. 1 (b). The geometry data are converted to an input file for the Monte-Carlo neutron transport code MCNP-4C. After the Monte-Carlo transport calculation, the results and 3-D geometry data are processed and passed to post-process software for 3-D visualization.

Tritium breeding abilities of the Flibe+Be/JLF-1 and Li/V-alloy blanket systems in the FFHR2m design were investigated with the present calculations system. The cross-section of the geometry for the 3-D calculation is shown in Fig. 2 (a). The geometry data consisted of ~3,000 cells for simulation of the full torus. A uniform torus-shaped neutron source of 1.5 m in diameter was assumed in the investigation.

The total TBRs (Tritium Breeding Ratios) for the Flibe+Be/JLF-1 and Li/V-alloy blanket systems were 0.82 and 0.81, respectively. Comparison with the local TBRs calculated for a simple torus model indicated that the effective coverage of the original FFHR2m blanket configuration was 60-70% due to wide opening between the helical structures around the divertor pumping area. Based on the results, the blanket configuration has been modified to enhance the total TBRs and also improve the shielding performance for the coils as shown in Fig. 2 (b). For the modified blanket configuration, the effective coverage increased to ~80% and the total TBRs of 1.08 and 0.98 could be obtained. Both of the blanket systems would achieve

adequate tritium breeding performance in the FFHR2m by design optimization such as blanket dimensions, neutron reflectors etc.

Evaluation of tritium breeding ability for the Flibe-cooled STB system, which has a few more additional layers, has been underway by increasing the number of the cells. Import of geometry data from CAD system is also important function to be installed in the present calculation system for simulation of non-helical structures such as supporting structures, vacuum vessels etc. Plasma distribution will be simulated to examine the relation with neutronics performances. As to another important issue of neutron shielding performance for the superconducting coils, understanding of neutron flow through the helical structures is expected by division of the vacuum areas into small cells and 3-D visualization of the results.

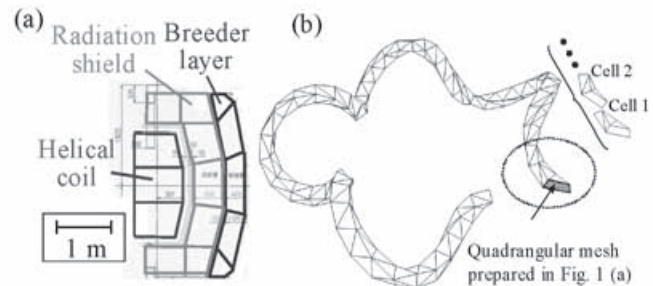


Fig. 1. (a) Division of cross-sections of helical structures into quadrangular meshes. (b) Generation of 3-D helical geometry data according to numerical equations.

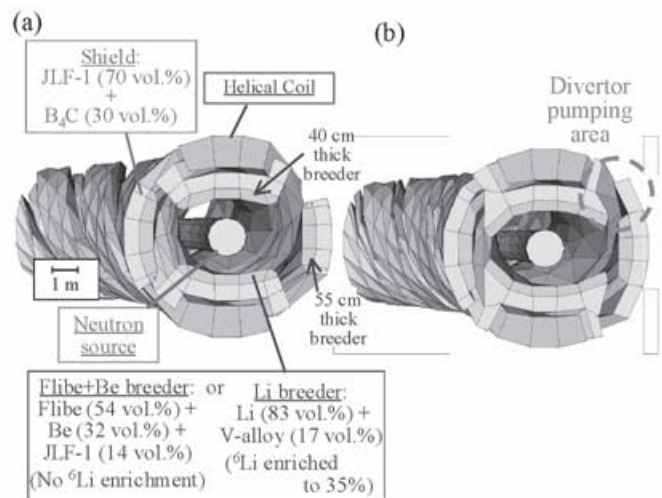


Fig. 2. (a) Cross-section of helical blanket geometry for neutron transport calculations. (b) Cross-section of modified blanket geometry. Breeding and shielding layers have been expanded around divertor pumping areas to improve tritium breeding and neutron shielding performances.

### References

- [1] A. Sagara *et al.*, Fusion Engineering and Design, 49-50(2000)661-666.
- [2] A. Sagara *et al.*, Nuclear Fusion, 45(2005)258-263.
- [3] T. Tanaka *et al.*, Fusion Science and Technology, 47(2005)530-534.
- [4] A. Sagara *et al.*, to be published in Fusion Engineering and Design.



### §3. Fabrication of Erbium Oxide Coatings by Arc-Source Plasma Deposition Device for Vanadium-Lithium Blanket System

Suzuki, A., Sawada, A. (Univ. of Tokyo),  
 Pint, B.A. (Oak Ridge National Laboratory),  
 Muroga, T.

A self cooled vanadium-lithium blanket is one of the most attractive blanket concepts for its continuous operation, low neutron reactivity and high operation temperature. However, there is a serious issue called MHD (Magneto-hydrodynamics) pressure drop, which is Lorentz force towards the opposite direction of liquid lithium flow caused by interaction of magnetic field and lithium. This Lorentz force ( $\vec{F}$ ) is described as;

$$\vec{F} = \frac{(2b)^2}{R} \bullet \vec{v} \times \vec{B} \times \vec{B} \quad (1)$$

Here, magnetic field ( $\vec{B}$ ), liquid lithium flow velocity ( $\vec{v}$ ) and length of pipe wall ( $2b$ ) can not be reduced extremely because of the reactors operation. It is considered to enlarge resistance of the pipe wall ( $R$ ) for reducing MHD pressure drop by establishing insulator coatings on inner pipe wall. Candidate materials of these insulator coatings are quite limited because liquid lithium has high reductivity and dissolves oxides or nitrides. From this viewpoint, candidates of the insulator coatings were chosen by means of exposure of bulk ceramics to liquid lithium. By the results of the experiment, erbium oxide ( $\text{Er}_2\text{O}_3$ ) is considered as one of the best candidate material for the coatings [1]. In this report, the coatings of erbium oxide were fabricated and exposed to liquid lithium at up to 973 K for 100 hours, and observed their properties and corrosion behavior.

In this study, coated specimens were fabricated by arc source plasma deposition [2]. The coatings were fabricated on room temperature substrates or on high temperature (which is above 849 K) substrates. The specimens were put into molybdenum capsules with lithium and the capsules were welded in argon atmosphere. The molybdenum capsule was put into a stainless steel 316 capsule and the stainless capsule was welded in the argon atmosphere. The capsules were heated up to 773 K, 873 K and 973 K for 100 hours. After the exposure, the capsules were opened in argon atmosphere, liquid lithium was melted and the specimens were taken out. The specimens were put into vacuum chamber to evaporate the residual lithium on the surface of the specimens.

For the exposure,  $\text{Er}_2\text{O}_3$  coated specimens fabricated with the substrate temperature of room temperature (room temperature specimen) and specimens fabricated with the substrate temperature of more than 850 K (high temperature specimen) were used. After the exposure, high temperature specimens showed better results, while the coatings of room temperature specimens were peeled off at 773 K and 873 K. Room temperature specimen exposed at 973 K had a good result as high temperature specimens. These results are shown in Fig. 1. From these results, it is considered that the crystal structure of room temperature specimens were

unstable to liquid lithium. These crystal structures were changed after the exposure to be stable to liquid lithium. Figure 2 shows the X-ray diffraction pattern of the samples. The crystal structure of the coatings was changed from room temperature's one to high temperature's one, but these change were promoted when temperature of the exposure becomes higher. Thus the coatings exposed at 773 K had worst result.

#### References

[1] B. A. Pint, J.H. Devan and J.R. DiStefano, J. Nucl. Mater. 307 (2002) 1344.  
 [2] A. Suzuki, T. Muroga, H. Maier and F. Koch, NIFS Annual Report 2004

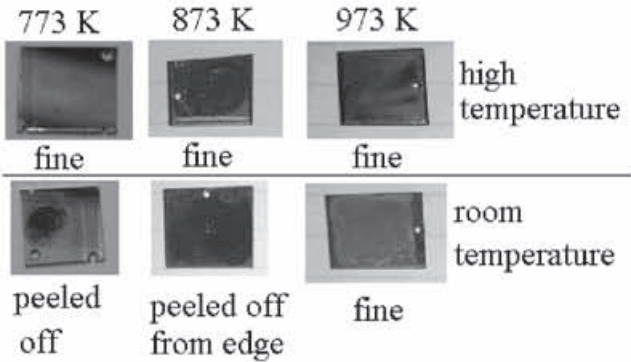


Fig. 1 Photos of specimens after 100 hours exposure

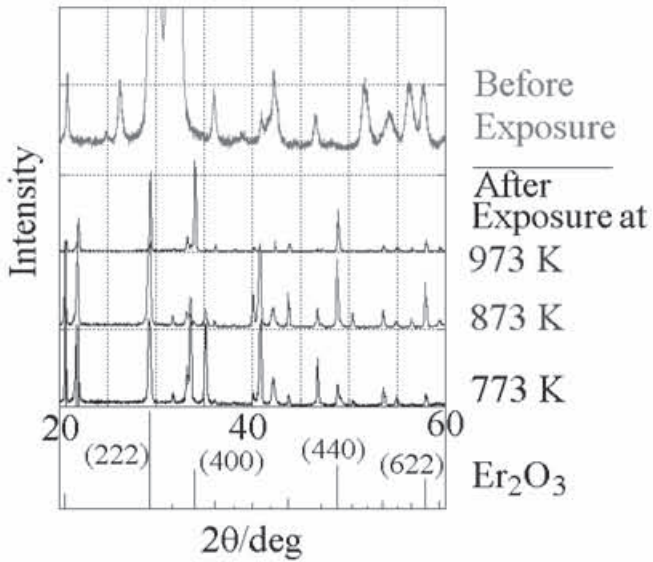


Fig. 2 Difference of crystal structure of the specimens after 100 hours exposure

§4. The Structural Stability and Growth Process of  $\text{Er}_2\text{O}_3$  In-situ Coating on V-4Cr-4Ti

Yao, Z., Muroga, T., Nagasaka, T., Tanaka, T., Suzuki, A. (Univ. Tokyo), Yeliseyeva, O. (KPMI, Ukraine)

Self-cooled Li/V-alloy blanket is thought to be a very attractive concept for fusion. One of the critical issues for this blanket concept is the large magneto-hydrodynamic (MHD) pressure drop when liquid Li flows in a metallic duct under a magnetic field. A promising solution is to apply an electrically insulating coating on the inner wall of metallic ducts. In the previous studies, the authors showed the feasibility, characteristics and growth kinetics of in-situ  $\text{Er}_2\text{O}_3$  coating by exposing V-4Cr-4Ti in liquid Li doped with Er. In this report, the structural stability and growth mechanism of  $\text{Er}_2\text{O}_3$  coating were shown.

One of the optional methods to make the in-situ coating is to form the coating in Li doped with Er in a factory after assembling of parts or in a reactor site before the operation. Doping of Er into the flowing Li is necessary for forming the  $\text{Er}_2\text{O}_3$  coating. After the formation of the coating, however, it may be preferred to remove both dissolved and undissolved Er from Li for the purpose of keeping the purity of Li for heat-transfer or tritium-recovery purposes, and of minimizing negative effects of Er on tritium breeding ratio (TBR) during the operation. In this case,  $\text{Er}_2\text{O}_3$  coating will face a pure Li environment. For verification of this option, the stability of the coating once formed in Li (Er) should be tested in pure Li. In this study, the re-exposure of the coating once formed in Li (Er) was carried out in pure Li to verify the potential stability of  $\text{Er}_2\text{O}_3$  coating without an Er supply. Fig. 1 shows the change of the coating thickness for the two cases of Li chemical histories. The re-exposure in pure Li at 973K for 300h did not influence the thickness of the coating once formed in Li (Er) at 973K for 100h.

Fig. 2 shows the effects of temperature change during Li exposure on the thickness of the coating. The thickness of the coating is quite different at 873K and 973K. With the stepwise increase in temperature from 873K to 973K, the growth rate increases but is smaller than that at the constant temperature of 973K. After long exposure the thickness for the case of stepwise temperature change is close to that of the constant temperature. This result may suggest the nucleation and pre-coating at 873K followed by the growth at 973K as a process for coating production.

Fig. 3 shows a general phenomenological model schematically on nucleation and growth processes of the surface layer on V-4Cr-4Ti in liquid Li doped with Er. Here  $\text{V}[\text{O}]+(\text{Ti}-\text{O})$  is the vanadium alloy charged by oxygen showing as both solid solution and titanium oxide, and  $\text{Li}[\text{Er}][\text{N},\text{O}]$  is Li doped with Er and containing the impurity of N and O. The ordinate  $d=0$  is the initial interface between solid and liquid metal. The model on formation of coating on V-alloys described that the growth of  $\text{Er}_2\text{O}_3$  coating after quick nucleation is controlled by

delivery of either oxygen from substrate or erbium from Li to the interface. The model also showed the formation mechanism of the observed intermediate layer.

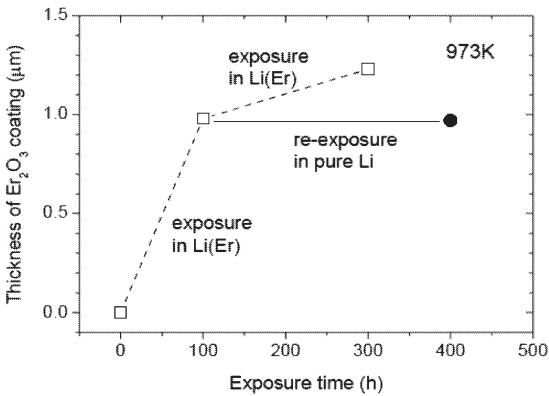


Fig.1 Change of coating thickness in two cases of Li chemical histories.

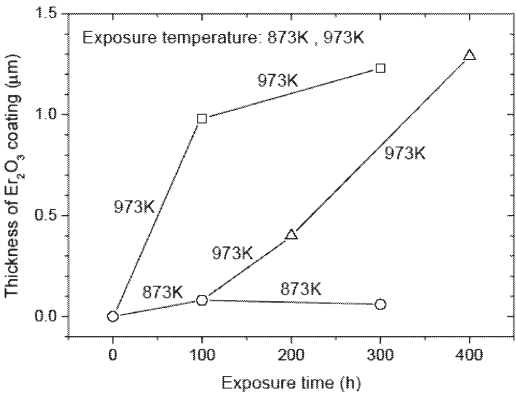


Fig.2 Effects of temperature change during exposure to Li (Er) on thickness of coating.

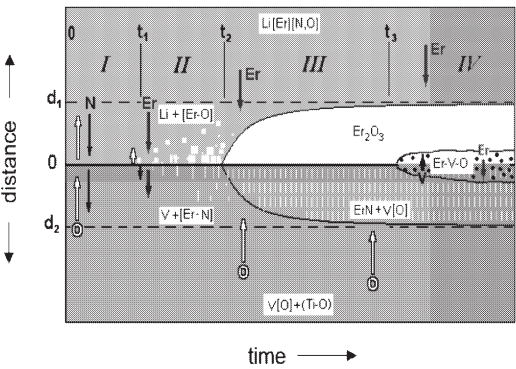


Fig.3 Scheme on nucleation and growth process of surface layers on V-4Cr-4Ti in liquid Li (Er).

§5. Activation Experiment with D-T Neutrons on Materials Relevant to Liquid Blankets

Li, Z.X. (Grad. Univ. Advanced Studies), Tanaka, T., Muroga, T., Sato, S. (JAEA), Nishitani, T. (JAEA)

In order to evaluate neutron activation of materials relevant to the liquid blankets such as Lithium/vanadium-alloy and Flibe/vanadium-alloy blankets, Irradiation experiments have been performed using the Fusion Neutronics Source (FNS) at JAEA. Specimens of Er, Teflon ( $\text{CF}_2=\text{CF}_2$ ) and NIFS-HEAT-2 (V-4Cr-4Ti) were selected in the experiments for the evaluations of the activation of Er in the MHD coating ( $\text{Er}_2\text{O}_3$ ), F in Flibe ( $\text{LiF}-\text{BeF}_2$ ) and V, Cr, Ti in the structural materials, respectively. The sizes of specimens were  $10 \times 10 \times 0.03 - 0.1 \text{ mm}^3$ . Nb foils with  $10 \times 10 \times 0.05 \text{ mm}^3$  were attached to the specimens to monitor the flux of fast neutrons. The irradiation with mono-energetic 14 MeV neutrons was conducted to examine the reactions with high energy neutrons. In addition, for the purpose of examining some important activation reactions with low energy neutrons, a Be mock-up was assembled to generate a neutron spectra with considerable low energy parts relevant to fusion blanket conditions. Fig. 1 shows the schematic cross-section of the Be mock-up.

The neutron spectra calculations were carried out using Monte Carlo transport codes MCNP-4C and JENDL3.3 files. A special routine was used in the calculations to represent generating D-T neutrons in the target [1]. The calculated spectra at the specimen location were shown in Fig. 2. The spectra without mock-up is a peak around 14 MeV while spectra at Position A and B in Be mock-up have considerable low energy parts.

After irradiation, the gamma-rays emitted from the irradiated specimens were measured with high purity Ge detectors. The activities of the nuclides were determined from the counts of the gamma-rays. The half life of the measured nuclides as followed ranges from 3.0 minutes to 43.7 hours:  $^{161}\text{Er}$ ,  $^{167}\text{Ho}$ ,  $^{168}\text{Ho}$ ,  $^{171}\text{Er}$ ,  $^{18}\text{F}$ ,  $^{51}\text{Ti}$ ,  $^{52}\text{V}$ ,  $^{48}\text{Sc}$ . The measured activities of nuclides have been compared with the ones calculated by FISPACT-2001 code and EAF-2001 file. The comparison was shown in Fig. 3. The results showed that the calculated activities of most of products are in agreement with the experiments within 20% uncertainty. Since the reaction generating  $^{168}\text{Ho}$  has a threshold near 14 MeV, potential source of discrepancy for  $^{168}\text{Ho}$  could be the uncertainties in spectrum estimation around 14 MeV and the cross section data of the energy group at around 14 MeV.

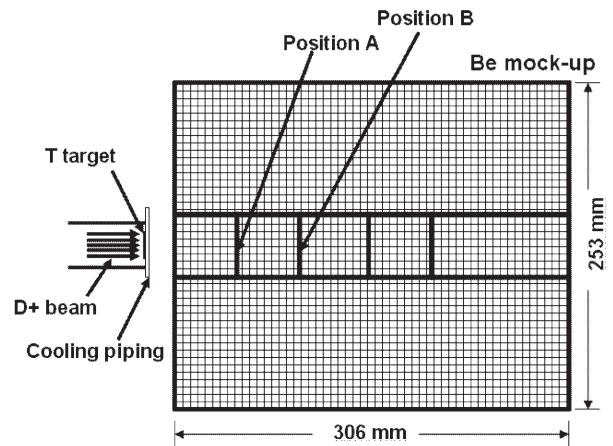


Fig. 1 Schematic cross-section view of the Be mock-up and the specimen locations

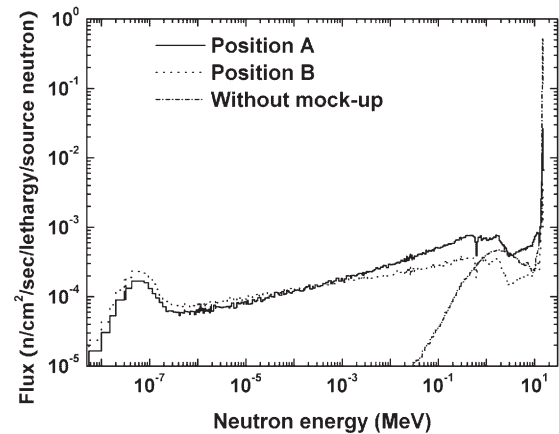


Fig. 2 Neutron spectra at locations without mock-up and Position A and Position B in Be mock-up

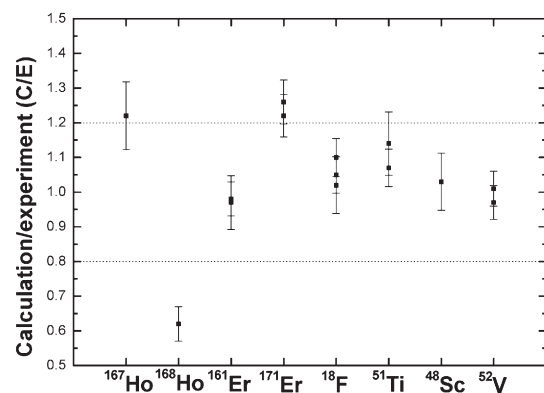


Fig. 3 Comparison of activities for nuclides between calculations and experiments

Reference

1)F. Maekawa, et al., Vol. II : Analysis, JAERI-Research 94-044, Japan Atomic Energy Research Institute, 1994.



§6. Impurity Behavior in V-4Cr-4Ti-Y Alloys Produced by Levitation Melting

Nagasaka, T., Muroga, T.,  
Hino, T., Satou, M., Abe, K., Chuto, T. (Tohoku Univ.),  
Ikubo, T. (Daido Bunseki Research, Inc.)

It has been clarified that reduction of oxygen level and control of Ti-C, N, O precipitate distribution are critical to improve workability, weldability and irradiation properties for V-4Cr-4Ti alloys. Yttrium (Y) addition is well known to be effective for reduction of oxygen level by oxide ( $Y_2O_3$ ) slug formation on the melting ingot surface. Because of the slug layer, the conventional large-scale melting processes, such as continuous arc-melting and electron beam melting, are not applicable to Y containing alloys. In the present paper, V-4Cr-4Ti-0.15Y alloy was fabricated by levitation melting.

Pure V, Cr and Ti used were the same grade as the reference high purity V-4Cr-4Ti alloy, NIFS-HEAT (NH). C, N and O impurity levels in Y were 210, 380 and 823 wppm, respectively. A 15 kg V-4Cr-4Ti-0.15Y ingot was melted under Ar gas ( $O_2$ : 0.62 ppm,  $N_2$ : 0.59 ppm) flowing in a levitation furnace. Fig. 1 shows a macrostructure of the cross section of the melted ingot. The alloyed part was chemically analyzed at the 10 cross points of the black lines. Chemical composition was very homogeneous except at the LS point, which is close to the fusion line between the melted part and the un-melted skull. No difference of composition was detected between the equiaxed and cylindrical crystal zones. The composition except the skull part was V- (4.50- 4.57)Cr- (4.56- 4.78)Ti- (0.09- 0.10)Y- (0.009- 0.013)C- (0.012- 0.015)N- (0.008- 0.013)O. Fig. 2 shows X-ray diffraction spectrum at the place pointed by arrows indicated in Fig. 1.  $Y_2O_3$  compound was clearly detected at the top and side skin of the ingot. A weak peak from  $Y_2O_3$  (circled) also detected at the inner surface of the void. The ingot was trimmed to remove the skin, the void containing  $Y_2O_3$  slug, and the un-alloyed skull, followed by cold rolling into sheets with 0.25-4 mm in thickness.

Fig. 3 shows hardness recovery by annealing (873-1373 K for 1 hr) and precipitation treatment (1373 K for 1 hr + 973 K for 1 hr) in the 1 mm-thick sheet. From 1073 K to 1273 K annealing, hardness of the Y-added alloy was similar to NIFS-HEAT (NH1). At 1373 K annealing, NH1 has shown hardening compared with 1273 K, whereas the Y-added alloy indicated no hardening. In the precipitation treatment, NH1 exhibited significant hardening. In contrast, the hardening in Y-added alloy was much smaller. The precipitates contributing the hardening were identified as Ti-O type by microstructural observations. Their size and number density was 20 nm and  $7.3 \times 10^{19} m^{-3}$  for NH1, while 35 nm and  $3.3 \times 10^{18} m^{-3}$  for the Y-added alloy. The small number density is considered to result in the smaller hardening in the Y-added alloy. As  $Y_2O_3$  precipitates were also detected in the Y-added alloy, O was thought to be stabilized as  $Y_2O_3$ , which can reduce oxygen amount in the Ti-O type precipitates and in solid solution state. Since O in solution interacts with irradiation defects, neutron irradiation hardening and embrittlement is expected to be improved by the Y addition.

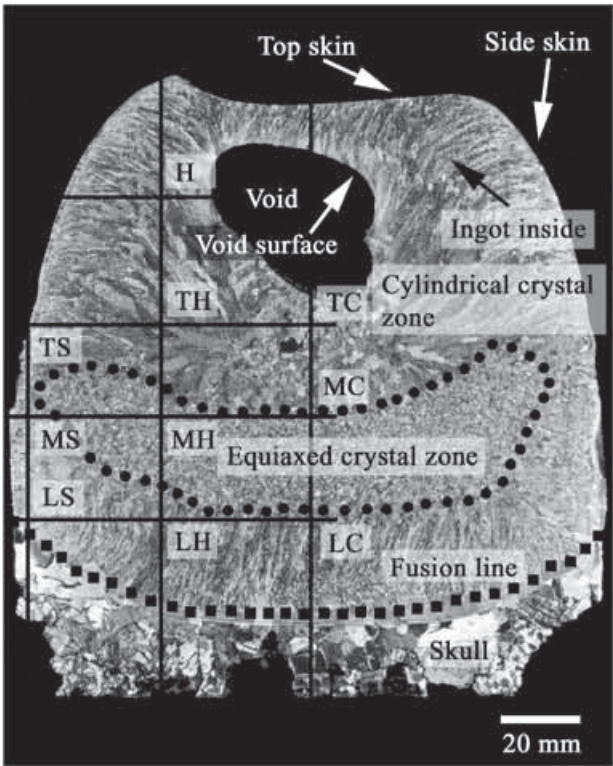


Fig. 1 Cross section of a V-4Cr-4Ti-0.15Y ingot fabricated by levitation melting.

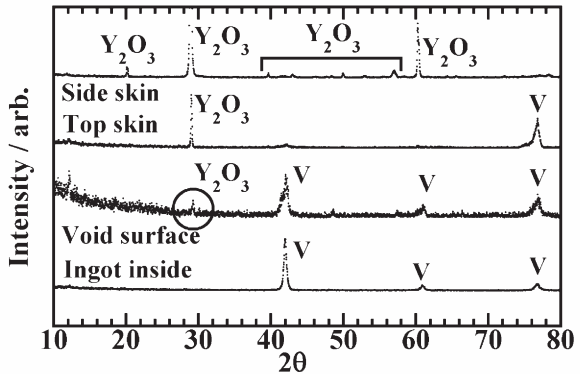


Fig. 2 XRD spectrum at the place pointed by arrows in Fig. 1.

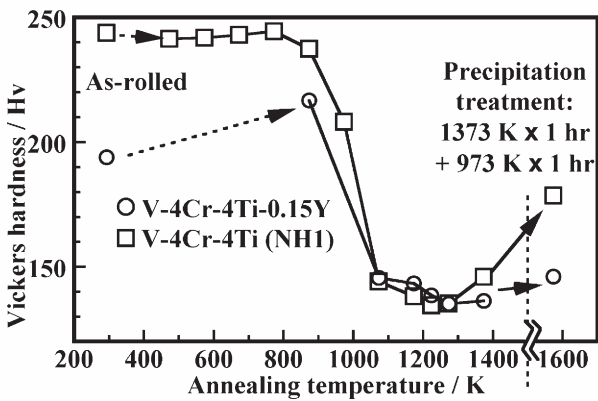


Fig. 3 Recovery of hardness by annealing (873-1373 K) and precipitation treatment (1373 K then 973 K) in the cold-rolled sheet.



§7. Creep Property of NIFS-Heat-2 Alloy Strengthened by Precipitation and Cold Rolling

Chen, J.M. (Southwestern Institute of Physics, China), Muroga, T., Nagasaka, T.

Creep resistance is a very important property for structural materials for fusion reactor. The creep strength will determine the upper temperature limit for the application in a blanket. V-4Cr-4Ti, such as NIFS-Heat-2, is taken as the leading V-base alloy for advanced fusion reactors. Some researches have been done to investigate the thermal creep and its mechanism. The alloy could be used at elevated temperature up to ~750°C at a designing stress level of ~100 MPa. Measures to improve the property were studied as well, mainly concentrated on adding more Cr to the alloy. Results showed the improvement was pronounced, but enhancing He or radiation embrittlement. This paper presents a thermo-mechanical process to strengthen the alloy with the expectation of better creep property at the same time.

V-4Cr-4Ti could be strengthened significantly by both precipitation and cold work [1]. An ageing at 600°C for 10 hrs could increase the hardness by a factor of ~21%, and an additional cold rolling with 20% reduction in thickness increases the hardness by ~18%. TEM observation showed extra high number density of ultra fine precipitates in the alloy after the ageing. However, since the precipitates are known to become unstable at temperatures above 600°C, the utilization of the strengthening for higher temperature application is questionable without other convincing technical supports. Therefore, creep and high temperature tensile properties of the alloy in the hardening state were examined.

The as-received NIFS-Heat-2 alloy plate was 0.5mm thick in cold rolling state (>90%CW). The plate was further cold rolled to ~0.31mm thick. Following a solid solution annealing (SA) at 1100°C for 1 hr, the plates were aged (SAA) at 600°C for 20 hrs in vacuum of <10<sup>-6</sup> torr. Finally cold rolling was conducted with a 20% reduction in thickness (SAACW). Miniature tensile specimens (gauge section dimension of 5x1.2x0.25mm), used in creep tests as well, were punched from the foils. To study the effects of high temperature annealing on tensile properties, some specimens were annealed at 750°C for 20 and 60 hrs, respectively.

Tensile tests were performed at room temperature and 600-800°C at strain rate of 6.67x10<sup>-4</sup>/s in vacuum of <10<sup>-6</sup> torr. Creep test was performed with a new machine designed with a manner of constant loading. The machine has a capability of 800°C and ultra high vacuum of less than 10<sup>-7</sup> torr during the test. To eliminate any contamination by the residual gas in the vacuum, Zr foil gas getter was used around the specimen.

Tensile test results indicated the strengthening by the aging, particularly the cold rolling, is very

significant. At room temperature, the standard annealed alloy (STD, annealing at 1000°C for 2hr) has yield strength (YS) of 328 MPa, while that for the SAACW alloy is more than 580 MPa. But its uniform elongation (UE) is fairly low, about 0.8%, indicating the heavy loss of strain hardening capability. Fig.1 shows the tensile properties of the alloy in various thermo-mechanical states at 750°C, here UTS is the ultimate tensile strength. The strengthening is also significant, but get smaller after the annealing at the temperature for 20-60 hrs, along with the recovery of the strain hardening capability.

Fig.2 shows the steady creep rate as a function of applied stress. It is obvious that the hardened alloy has lower creep rate than the STD alloy at high temperature and high stress level. It seems to be caused by the different deformation mechanisms. For SAACW alloy, even the highest applied stress was in the elastic deformation region. For the STD alloy, the stress is higher than the yield point; as a result, plastic deformation had happened before the creep. It produced high number density of dislocations in the alloy, leading to high creep rate.

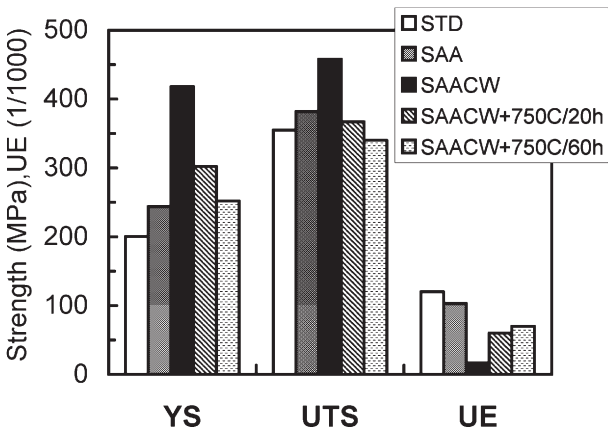


Figure 1. Tensile properties of NIFS-Heat-2 at 750°C.

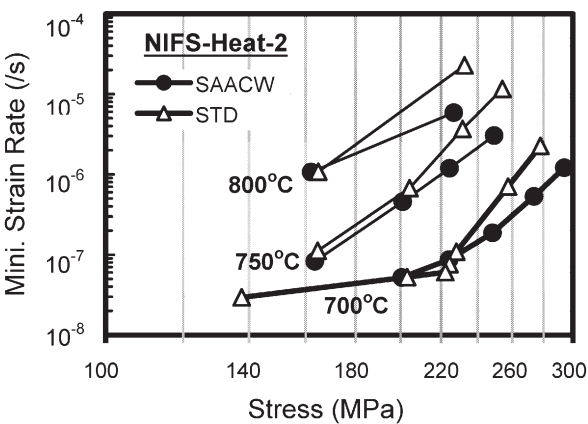


Fig.2 The steady state creep rate of the alloy at stresses.

Reference

[1] Chen JM, Muroga T. Nagasaka T. et al, "The mechanical properties of V-4Cr-4Ti in various thermo-mechanical states", ITC-15, Toki, Japan, Dec. 5-8.

§8. Temperature Effect on Strain Hardening and Fracture Mode of JLF-1 Steel under Static Plastic Deformation

Li, H. (Sokendai), Nishimura, A., Muroga, T., Nagasaka, T. (NIFS)

Development of structure materials for a blanket is one of critical issues for early realization of fusion energy. Material deformation behavior is the important information for the blanket design. Reduced activation ferritic/martensitic (RAF/M) steels are considered to be applied in potential fusion energy systems. Thus, it is necessary to study the temperature effect on strain hardening of RAF/M steels as the strain hardening shows the deformation resistance when the applied stress would exceed the yield stress.

In this work, the tensile tests and microstructure analysis of the RAFM steel, JLF-1, were carried out from RT to 873 K at strain rate of 0.1%/s and 0.02%/s to investigate the material static deformation behavior.

The yield stress (YS) and ultimate tensile strength (UTS) are the important data for design. The change in YS and UTS of JLF-1 steel against test temperature is shown in Fig. 1. The strain rate does not affect the YS and UTS significantly. The difference between YS and UTS decreases significantly above 773 K, which means strain hardening becomes smaller in this temperature region. Especially at 873 K, the UTS of JLF-1 drops to about 300 MPa, very close to the YS.

Fractography of the fracture surface of the tensile specimens was performed with scanning electron microscopy (SEM). Cup and cone fracture was observed in the specimens tested at high temperature. Fig. 2 shows the SEM image of fracture surface of the tensile specimen at 673 K. The dimple zone area was measured in Fig. 2, the change in ratio of dimple zone to fracture surface area is shown in Fig.3. Three regions could be defined according to the ratio change.

- 1) Region A: Around RT, the dimple zone was small.
- 2) Region B: Below 673 K, the change in ratio was independent on temperature, shear fracture was dominant.
- 3) Region C: At 773 K and 873 K, the change in ratio was very sensitive to temperature. Dimple fracture was dominant. Thus, little strain hardening was observed in Fig.1 in those temperature region.

From Fig.1 to Fig.3, with strain hardening decreased, the difference between YS and UTS decreased significantly above 773 K; and the fracture mode was changed from shear fracture below 673 K to dimple fracture at 773 K and 873 K. It means that the potential to support the over loading decrease as the temperature rises, and much ductility appears.

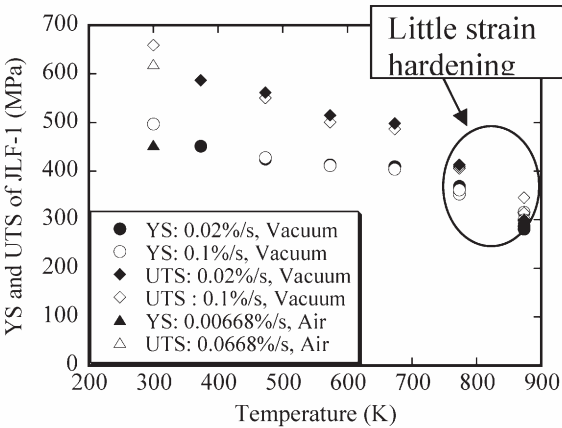


Fig.1 Change in YS and UTS against test temperature.

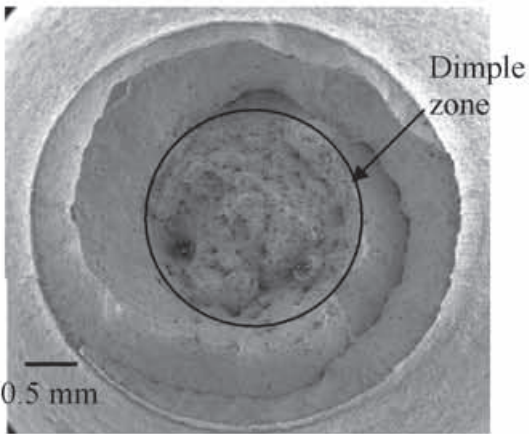


Fig. 2 SEM images of the fracture surfaces at 673 K.

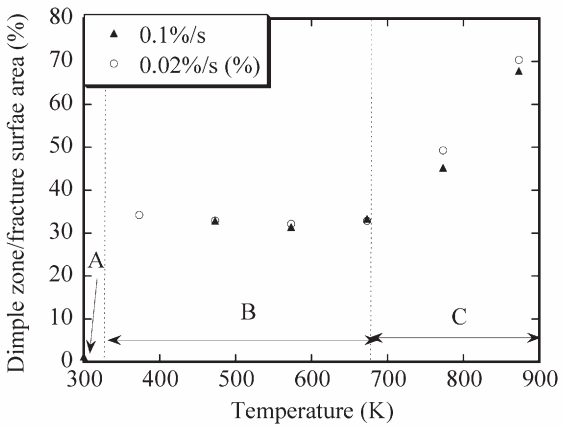


Fig 3 Change in the ratio of dimple zone to fracture surface area against temperature.

§9. Compatibility of Low Activation Ferritic Steels with Liquid Lithium

Xu, Q. (Grad. Univ. Advanced Studies), Nagasaka, T., Muroga, T.

One of the primary requirements for the development of fusion as an energy source is the qualification of materials for the first-wall/blanket system that will provide high performance and exhibit favorable safety and environmental features. Both economic competitiveness and the environmental attractiveness of fusion will be strongly influenced by the materials constraints. A key aspect is the development of a compatible combination of materials for the various functions of structure.

Fe-Cr-W base low activation ferritic steels (RAFM) have been identified as a leading candidate structural material for fusion blanket applications. Liquid lithium is an attractive breeding material. For the combination of RAFM and liquid lithium for the use as a breeding blanket, compatibility of the two materials could be the issue. However, since previous compatibility researches between ferritic steels and liquid lithium almost focused on the Fe-Cr-Mo steels, the data of compatibility of Fe-Cr-W low activation ferritic steels in lithium is quite limited.

In this study, compatibility of the three kinds of materials, pure iron, Fe-9Cr and low activation ferritic steel JLF-1(Fe-9Cr-2W), was investigated to elucidate the corrosion mechanism and find out the influence of different elements by means of exposure to static lithium at high temperature. Corrosion rate, microstructure and hardness change in the near-surface region were investigated after lithium exposure at 973K.

JLF-1 specimen was cut into 22×5×0.25mm from a block and grinded by sand papers and finally electro-polished. Fe-9Cr and pure iron was prepared by rolling to 0.25mm, cutting into the same size as JLF-1 specimen, followed by the same surface treatment as that for JLF-1 and annealing at 973K for 1hr. The purity of lithium was 99.99%, and during whole experiment, the lithium was isolated from air. All assembling work and preheat was done in glove box filled with Ar. The lithium exposure experiment was performed at 973K for 100hrs in molybdenum cup and the cup was heated in a stainless steel autoclave. After experiment, all specimens were cleaned by ammonia to remain the corrosion product.

After 100h lithium exposure at 973K, the etching appearance was observed on JLF-1, 9Cr and pure iron, some surface of specimen was covered by corrosion product. Normally there were three kinds of corrosion product on the surface of specimen after ammonia clean identified by their appearance, the big particle made up by Li<sub>2</sub>O, porous layer and Ni rich crystal attaching firmly on the surface. The Ni rich crystal didn't dissolve in ethanol or water when cleaning the specimen by ultrasonic.

EDS result indicated Cr dissolution on the surface of JLF-1 and 9Cr. The average composition of Cr on the

surface reduced from 9% to ~5% both for JLF-1 and Fe-9Cr. For pure iron, some Cr and Ni were detected on the surface.

The phase transition, from martensitic to single ferritic phase, was observed on the surface of JLF-1 specimen after lithium exposure, which was not observed in the specimen with identical heat history in vacuum. It seemed that the phase change was induced by carbon dissolution during the experiment. The phase transition and Cr depletion resulted in dramatic surface hardness reduction on JLF-1, dropping to 123Hv from 210Hv as shown in figure 1. The softening was observed to the depth of about 20μm. The reduction of surface hardness also happened on the Fe-9Cr, probably due to the Cr dissolution. On the other hand, there was almost no change appeared on pure Fe.

The dissolution rate of JLF-1 in liquid lithium was obtained by the weight loss for 100hrs. The average dissolution rate of JLF-1 was 0.012mm/yr at 973K.

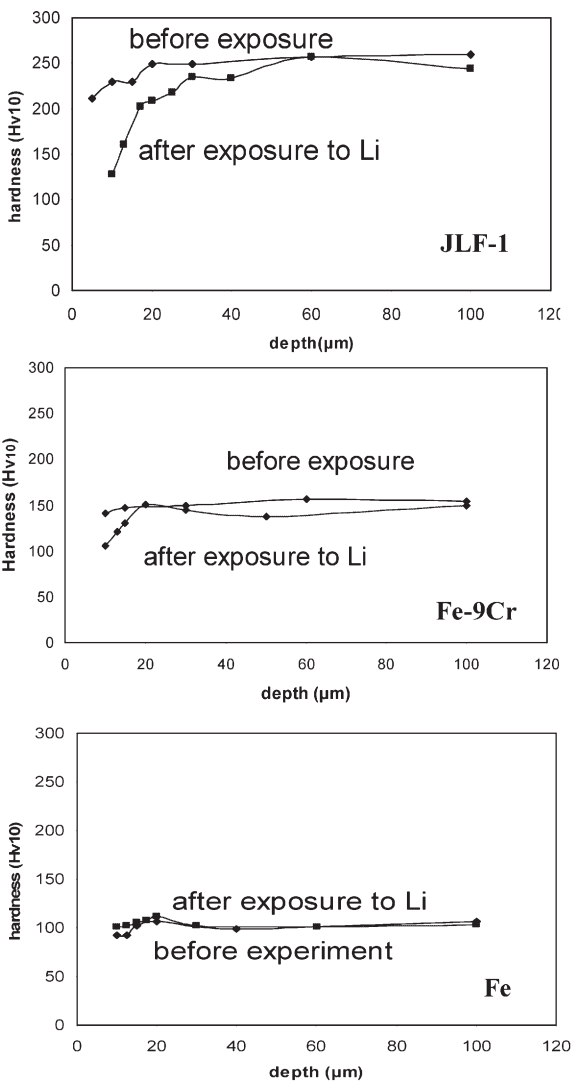


Fig.1 Depth dependence of hardness for JLF-1, Fe-9Cr and pure iron before and after lithium exposure for 100h at 973K



§10. Irradiation Effect of 14 MeV Neutron on Interlaminar Shear Strength of Glass Fiber Reinforced Plastics

Nishimura, A.

Intense neutron streaming from ports for neutral beam injectors is clarified by design activities for fusion reactors. Also, there is some neutron penetration through blankets, though blankets can reduce the fast neutron by the order of  $10^{-5}$  or  $10^{-6}$  n/m<sup>2</sup>. The streaming and penetration is very wide and 14 MeV neutron and gamma ray are the typical radiations. Epoxy resin type glass fiber reinforced plastics (GFRP) is used in a superconducting magnet system as an electric insulation material and a support structure. In this report, effects of 14 MeV neutron and gamma ray irradiation on interlaminar shear strength (ILSS) and fracture mode are investigated using G-10CR. A short beam test under three point bending was conducted at RT and 77 K.

The cryogenic target system for neutron irradiation was installed at Fusion Neutronics Sources (FNS) in Japan Atomic Energy Agency (JAEA). The small size specimens, which size was 2.5 mm thick, 10 mm wide and 15 mm long, were attached on the cryostat cap shown in Fig. 1. In the irradiation test, hall elements and superconducting wires were arranged at the same time. Neutron fluence of  $3.91 \times 10^{19}$  n/m<sup>2</sup> was irradiated. The irradiation test of gamma ray was carried out at Osaka University using Co<sup>60</sup> and up to 1 MGy of gamma ray was irradiated.

Two G-10CR plates were prepared. One is 2.5 mm thick plate and the specimen had original plate thickness. The other is 13 mm thick plate and the plate was sliced into two thinner plates of about 5 mm thick and 2.5 mm thick samples were machined out of these thinner plates.

After the irradiation, specimens were tested by three-point bending in air and in liquid nitrogen and the maximum bending load was recorded. The ILSS was obtained by the following equation:

$$\sigma_{ILSS} = (3 \times P_B) / (4 \times b \times h),$$

where  $P_B$  is the maximum bending load,  $b$  is specimen width (10 mm) and  $h$  is specimen thickness (2.5 mm).

Figure2 shows the ILSS test results after neutron irradiation. As far as the test results obtained here, there is no clear difference in the ILSS at RT and 77K. There is a report showing that neutron fluence of about  $10^{21}$  n/m<sup>2</sup> is corresponding to 1 MGy gamma ray irradiation. Neutron fluence of less than  $10^{20}$  n/m<sup>2</sup> would be too small irradiation to cause some degradation of strength.

Figure3 shows the effect of gamma ray on the ILSS. The results tested at 77 K present the degradation of the ILSS after 1 MGy radiation, and RT tests did not show such degradation because of the lower ILSS. Radiation of 10 MGy made the samples useless with delamination.

Most of the specimens showed both of interlaminar cracking and bending fracture, but some specimens were fractured with translaminar fracture which was the irregular shear occurred on the planes connecting the loading point and the supporting points. The translaminar shear fracture

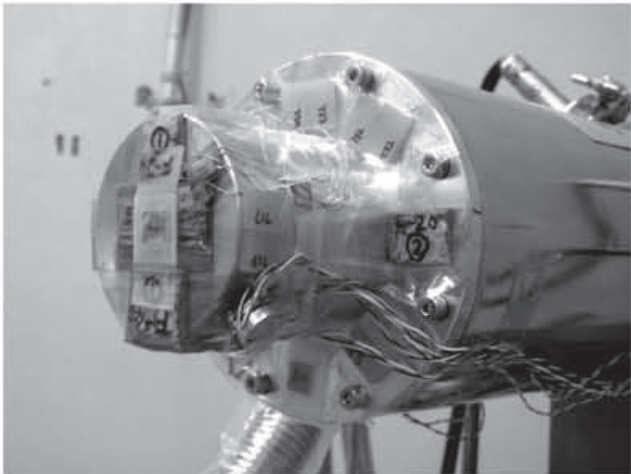


Fig. 1 Set up of cryogenic target with arrangement of GFRPs and other samples in RT space. (June 20, 2005)

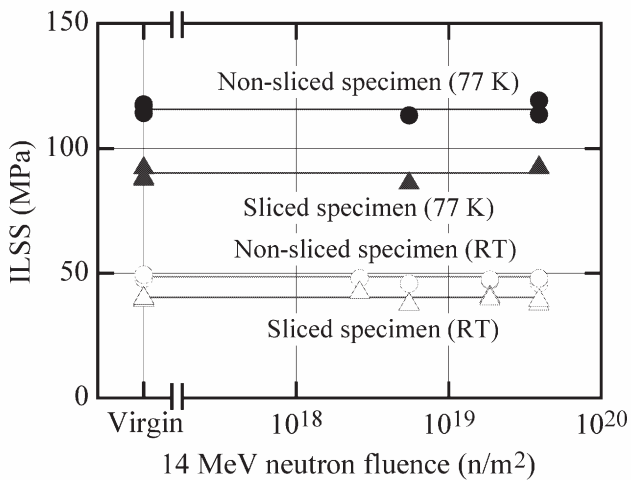


Fig. 2. Relation between interlaminar shear strength and 14 MeV neutron fluence.

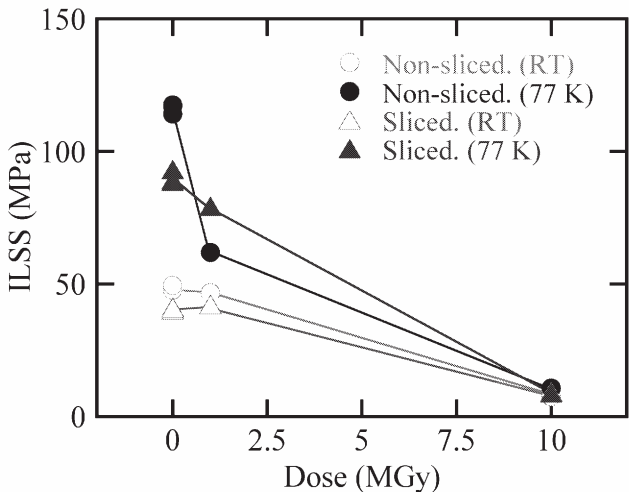


Fig. 3 Relation between interlaminar shear strength and gamma ray dose.

would be caused by special stress distribution formed in the sample by irregular restraint at the loading and the supporting points.



§11. Annealing Effect on Microstructure and Superconductivity of V-based Laves Phase Compound Wires through a RHQ Process

Hishinuma, Y., Nishimura, A., Kikuchi, A., Iijima, Y., Takeuchi, T. (NIMS), Inoue, K. (Univ. Tokushima)

V-based Laves phase compounds,  $V_2(\text{Hf,Zr})$ , show very attractive superconducting properties a maximum  $T_c = 10.1$  K, maximum  $H_{c2}$  above 20 T and a insensitivity to mechanical strain. V-based Laves phase compound shows much higher radiation resistance than that of Nb-based superconducting wires. Therefore we investigate that Laves phase compound superconductor is promising as low activation and high field conductors for advanced fusion reactors. However, Laves phase precursor (Hf-Zr alloy/V) is very hardness and lower workability, so that we fabricated the Laves phase multifilamentary wire by applying a rapidly-heating and quenching (RHQ) process to the PIT processed simple precursors (Hf-Zr metal mixed powder /V tube), and its microstructure and superconducting properties was investigated.

At first, high purity metal hafnium (Hf) and zirconium (Zr) powders were well ground by hand, the  $(\text{Hf}_{0.5}, \text{Zr}_{0.5})$  mixed metal powder was prepared and its powder was packed into V tubes. This composite  $((\text{Hf}_{0.5}, \text{Zr}_{0.5})/\text{V})$  was cold-rolled with a grooved roller and the wire drawn a diameter of about 1.20 mm. Intermediate annealing was carried out several times at 900°C for 1 hour to soften this composite during this deformation. This composite was cut into short pieces, and they were stacked into a Ta tube. The number of stacked  $(\text{Hf,Zr})/\text{V}$  composite was 55 pieces. This multifilamentary composite  $((\text{Hf,Zr})/\text{V}/\text{Ta})$  was cold-rolled with a grooved roller and drawing machine to wire of about 0.754 mm. This composite has good workability without breaking of wire during wire deformation. The precursor wire was set into RHQ apparatus, and it was applied to the RHQ treatment. Some of the as-RHQ wires were additionally post-annealed at 600°C in the vacuum.

We found that the optimum RHQ condition and post-annealing temperature after RHQ was 5.86 J/mm<sup>3</sup> and 600°C, respectively<sup>1)</sup>. The typical  $J_c$ -B curves of the samples of 5.86 J/mm<sup>3</sup> which post-annealed at 600 °C are shown to Fig.3. The post-annealing time conditions are 1, 10, 50 and 100 hours, respectively.  $J_c$  property on the 10 hours annealing sample was remarkably improved compared to that of as-RHQ sample. Furthermore, 50 and 100 hours annealing samples was lowered compared to 10 hours annealing sample. The average composition of Laves phase in the as-quenched and various post-annealed samples is shown to Fig.2. We confirmed that the average composition of Laves phase in as-RHQ sample was

obtained to be  $V_{1.58}(\text{Hf}_{0.68}, \text{Zr}_{0.32})$ , it was significantly the V-poor composition. The average composition of Laves phase when annealed for 10 h was changed to  $V_{2.18}(\text{Hf}_{0.58}, \text{Zr}_{0.42})$ , and its composition was almost similar stoichiometry of Laves phase. The other hands, the composition ratio between Hf and Zr of 50 and 100 hours annealed samples was changed to Zr-rich composition compared with 10 h annealed sample. We thought that  $J_c$  improvement by 10 h annealing was caused mainly by adjusting stoichiometric composition of Laves phase.

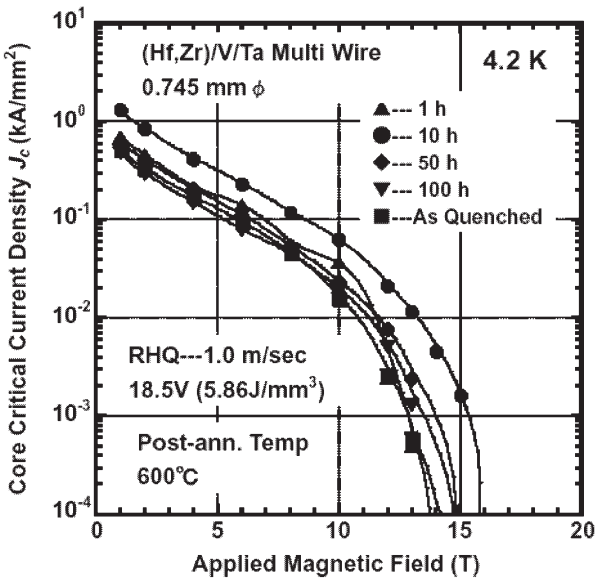


Fig. 1. The typical  $J_c$ -B curves of the as quenched and post-annealed samples for various annealing time

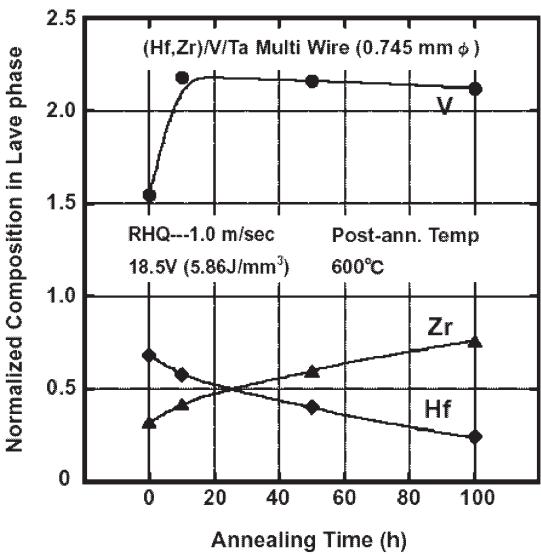


Fig.2. The average composition of Laves phase in the as-quenched and various post-annealed samples

Reference

1) Hishinuma et al: Fabrication of V-based Laves Phase Compound Multifilamentary Wires by Applying a Rapidly-Heating/Quenching Process to PIT Precursors and using V Tube, IEEE Transactions on Applied Superconductivity, 15, (2005), pp.3536-3539.

## 11. Safety and Environmental Research Center

The Safety and Environmental Research Center (SERC) has been studied to promote and to implement radiation safety issues in NIFS. The major mission of SERC is radiation safety management of X-ray emission devices which are LHD, CHS, and their plasma heating devices like NBI and ECH, and a Tandem type accelerator for plasma diagnostic device which is called as Heavy Ion Beam Probe (HIBP). For safety operation of LHD and relative devices, radiation management system and access-control system were well integrated. Radiation monitoring by the Radiation Monitoring System Applicable to Fusion Experiments (RMSAFE) has continued successfully. The other radiation safety issues are planning the safety management system and development of radiation safety equipments considering the deuterium (D) discharge plasma experiments, especially protection of neutron and tritium. The SERC is responsible to the research and development regarding fusion safety, so that variety of issues should be surveyed not only in the field of radiation safety management and radiation protection but also in the field of general safety science, health and environment. It would be pointed out that some of these scientific investigations have been successfully carried out as collaboration with researchers of many universities, research institutes and companies. Topics of the activities of the SERC during FY 2005 are summarized as follows:

### (i) Radiation management system

For the occupational workers in radiation control area, educational training and registration system have been established. The radiation management had been performed by radiation safety management office in the health and safety promoting division in NIFS and management issues have been discussed and proposed by the SERC. Major contributions are establishment of access control system and registration rule for the occupational radiation workers.

### (ii) Radiation monitoring system

It is required that the annual exposure dose caused by operation of some radiation emission devices should not exceed 50  $\mu$ Sv on the site boundary. To ensure the limit, a monitoring system RMSAFE has been installed. The RMSAFE is capable to detect burst X-ray and to discriminate the radiation caused by plasma experiment from the natural radiation and to accumulate the exposure dose. The annual radiation dose level caused by experiments of LHD and CHS at the site boundary was less than 1  $\mu$ Sv in FY 2005. Also the environmental radiation has been measured every three months using thermoluminescence dosimeter TLD and radiophoto-luminescence dosimeter RPLD. Also to apply to highly precise measurement, sensitivity of the TLD and RPLD to cosmic ray was measured in Ogoya tunnel. As the integrating dosimeter, an electronic integrating dosimeter has been applied to environmental radiation monitoring. In the present study measurement error has been clarified. To

develop a new integrating neutron dose monitor which is portable, good dose response and uniformly sensitive to all direction has been designed. The calculated dose response was well accorded in all energy range. It is expected to be useful for specifying the direction of a remote existing neutron source on great angular resolution.

### (iii) Environmental tritium measurements

It is important to grasp tendency of the environmental tritium concentration level in water and atmosphere before start out the DD experiment. Simple and accurate tritium measurement method in the environmental water with liquid scintillation counting system has been developed. Some water samples of extremely low level of tritium in the environmental have been measured. Also the atmospheric tritium gases have been measured with separating chemical forms of water, hydrogen and methane respectively. High sensitive tritium monitor has been developed using an improved proportional counter. These studies were performed as collaboration with Nagoya University, Kumamoto University and the other research organizations.

### (iv) Studies of tritium treatment system and safety

The tritium and neutron are key issues from view point of radiation safety for the DD experiment of LHD and for a future nuclear fusion facility. The specific technologies are extremely low level tritium monitoring and removing or separation of tritium from the vacuum pumping gas or exhausting air from the large plasma vacuum vessel. The main topics of research and developments are (a) measurement of tritium concentration in air by using gas chromatography, (b) direct immersion method to detect tritium in concrete, (c) study of chemical reaction of water vapor decomposition on Zr-Ni alloy, (d) safety tritium treatment system of exhaust gas and effluent liquid, (e) advanced honeycombs intend to high volumetric gas treatment under small flow resistance, (f) experimental analysis of activated dust behavior under the loss of vacuum event. These studies were performed as collaboration with Kyushu University, Shizuoka University and the other research organizations.

### (v) Non-ionizing radiation monitoring and management

Leakage of static magnetic field and variable frequencies of electromagnetic fields are concerned in a magnetic fusion plasma experimental facility. The static magnetic leakage has been measured continuously outside of the LHD hall, and its strength monitored was less than 1 mT. It began to monitor the electro magnetic field around the ICRF heating room. There are multiple electromagnetic fields around the LHD and related devices. To study about the safety issues of comprehensive frequencies of electromagnetic fields would be important in the large plasma experimental facility. It has been performed as collaboration with Utsunomiya University and Nagoya Institute of Technology.

(Uda, T.)

§1. Measurement Error of Radiation Monitoring by Means of an Electronic Dosimeter

Yamanishi, H.

Integrating dosimeters are applied to continuous environmental radiation measurement. It is general to use the thermo-luminescence dosimeter or the radiophotoluminescence dosimeter as the integrating dosimeter. On the other hand, in recent years electronic integrating dosimeter begins to be utilized for measuring individual dose and the ambient dose in radiation working area. In this study, the measurement error and the sensitivity difference between dosimeters were evaluated. Using these data, the reduction of the measurement error was discussed.

The electronic integrating dosimeter used in this study is able to record the time trend data of the dose. The minimum radiation dose unit is 1  $\mu\text{Sv}$ . Whenever 1  $\mu\text{Sv}$  is increased, the integrated dose is recorded the achieved time to secure memory of the dosimeter. When 1  $\mu\text{Sv}$  is divided by the time needed for the increase, the dose rate is provided. The smallest unit of the record time interval is two seconds. Data saved in the memory can be forwarded to a personal computer by the infrared communication.

The measurements were done in three kinds of dose rate environment, such as 55 nSv/h, 120 nSv/h and 1.2  $\mu\text{Sv/h}$ . Thirty two dosimeters were used in each measurement. The dosimeters were exposed more than 40  $\mu\text{Sv}$  as integrated dose. The dose rate that the integrated dose reached 40  $\mu\text{Sv}$  is different between the dosimeters. The dispersions were expressed in  $1\sigma$ . When the dose rate was 55 nSv/h, 123 nSv/h, 1.2  $\mu\text{Sv/h}$ , the dispersion was 2 nSv/h, 3 nSv/h, 20 nSv/h, respectively. As a result, the sensitivity difference between the dosimeters was less than 4 %. The systematic error was not recognized. In addition, 40 data were obtained for one dosimeter since every 1  $\mu\text{Sv}$  were recorded in the process of accumulating 40  $\mu\text{Sv}$ . The standard deviation  $1\sigma$  was 5 nSv/h, 10 nSv/h, 0.11  $\mu\text{Sv/h}$ , when the dose rate was 55 nSv/h, 123 nSv/h, 1.2  $\mu\text{Sv/h}$ , respectively. Consequently, the measurement error of the dosimeters was less than 10 %.

Figure 1 shows the example of the change in dose rate through integrating 40  $\mu\text{Sv}$ . The dose rate is 55 nSv/h. The dose rate at 40  $\mu\text{Sv}$  was normalized as 1 for each dosimeter. The measurement error is less than 20 %, even when the integrated dose is 1  $\mu\text{Sv}$ . Furthermore, when the integrated dose is 3  $\mu\text{Sv}$ , the measurement error is less than 10 %. When the integrated dose is 15  $\mu\text{Sv}$ , the measurement error is less than 5 %. When the sensitivity difference between dosimeters of 4 % is taken into account, the best measurement precision is provided at more than 15  $\mu\text{Sv}$  of integrated dose. In other words, in the environment of 50 nSv/h, highly precise measurement can be done on environmental monitoring by means of

integrating dose for 12.5 days.

Figure 2 shows the response irradiated on 1.05  $\mu\text{Sv/h}$  for two hours. The dose rate was measured correctly, the time delay of detection was 0.75 hour. The background dose rate was 0.12  $\mu\text{Sv/h}$ . The net dose 2.14  $\mu\text{Sv}$  was evaluated when the background dose was deducted.

The sensitivity difference between dosimeters was very small, and the systematic sensitivity difference was not recognized. Therefore, it was made clear that it was not necessary to manage the sensitivity of dosimeter individually, and the highly precise radiation monitoring was possible. The time when the dose rate would be changed can be grasped by using time trend data of the electronic integrating dosimeter. An accurate net dose can be evaluated with one dosimeter, because the background dose is recorded when the dosimeter is not irradiated by radiation sources. As a result, the electronic integrating dosimeter can be applied to environmental radiation monitoring.

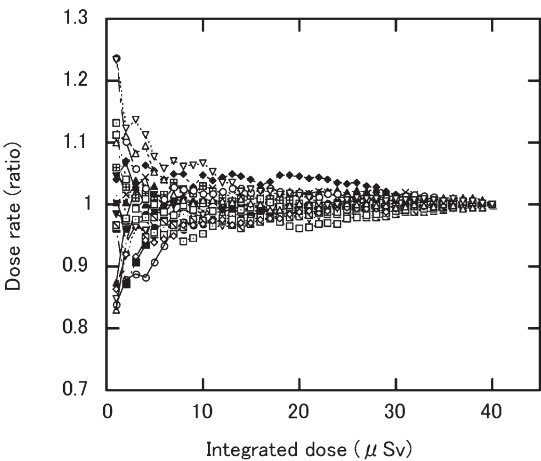


Fig. 1 Change in dose rate through integrating 40  $\mu\text{Sv}$ . The dose rate at 40  $\mu\text{Sv}$  was normalized as 1 for each dosimeter.

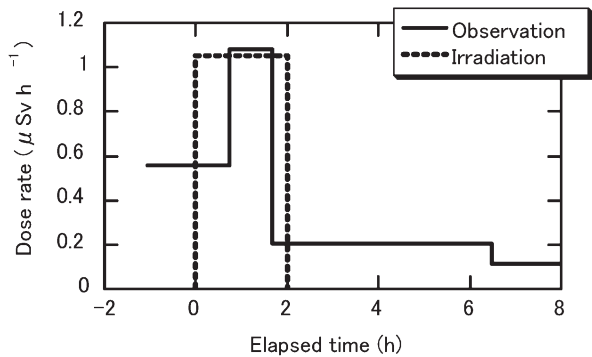


Fig. 2 Time variation of dose rate. The dosimeter was irradiated at 1.05  $\mu\text{Sv/h}$  for 2 hours.



§2. Design of an Integrating Type Neutron Dose Monitor

Yamanishi, H.

The radiation quality factors that ICRP recommends differ among neutron energies. In order to evaluate neutron dose precisely, it is expected that the neutron fluence of each energy group should be measured. REM counters are commonly used. However, these counters exhibit a large error for dose conversion in the intermediate energy range, since the fluence to dose conversion factor differs with the detector response, especially in this energy range. In several instruments developed prior to this study, multiple detectors were installed in a spherical polyethylene block. Those instruments are developed for measuring the energy spectrum and direction distribution of the neutron fluence. However, it is not suitable for radiation monitoring since the instrument needs complicated signal processing.

An integrating neutron dose monitor has been designed, which has lightweight and compact, good dose response, uniform sensitivity to all directions. In the instrument, the plural TLDs are arranged in the moderator at 3 levels of depth, in 12 directions. Although the TLDs were applied in this study, the other appropriate small detector may be adopted. The neutron dose can be measured correctly by the instrument with using three different energy response of the detectors. And the distribution of the value from the detectors may show a major incident direction of coming neutrons. The characteristic of the present monitor was discussed with the results of MCNP calculation.

The present designed instrument is spherical shape with 24 cm diameter, 9.1 kg. Because of its shape, the sensitivity of the instrument is almost uniform whatever direction neutrons come from. TLD was selected as neutron detector in this study. The constitute parts of the TLD are  $\text{CaSO}_4$  and  $^6\text{LiF}$ , and the size is 12 mm long and 2 mm diameter. The moderator of the instrument is composed of spherical shell. Figure 1 shows the layer structure of the instrument. The detectors are arranged between layers of the moderators. The order of the arrangement from outside to the center is 20 mm thick polyethylene (PE), TLD1, 40 mm thick boron nitrite (BN), TLD2, 45 mm thick PE and the center TLD3. The most outer TLD1 is for measuring neutrons of low energy, and TLD2 and TLD3 are sensitive to intermediate and high energy neutrons. The 12 sets of TLD1 and TLD2 are arranged 12 directions corresponding to the apexes of regular polyhedron with 20 sides. The total number of TLD is 25. The response of the TLD, the reaction rate of  $^6\text{Li}(n,\alpha)\text{T}$  was considered to be, was calculated using Monte Carlo calculation code MCNP-4B. The incident energies were chosen to less than 15 MeV.

The neutron dose is derived from the linear combination of 5 groups TLD value.

$$D = a_{F1}F1 + a_{F2}F2 + a_{S1}S1 + a_{S2}S2 + a_M M$$

F1 is the sum of the expected response of TLD1 in the 3 directions nearest to the neutron incident direction. S1 is the sum of the expected response of TLD1 in the 3 directions next to F-group. F2 and S2 correspond to TLD2. And M corresponds to the expected response of TLD3. The set of the dose conversion coefficient such as  $a_{F1}$ ,  $a_{F2}$  is selected to be good dose response by using the least-square method, comparing with the detector energy responses and the ideal dose curve. Figure 2 shows the calculated dose response from  $^{252}\text{Cf}$  spontaneous fission source in the center of a  $\text{D}_2\text{O}$  sphere with a radius of 150 mm. The calculated dose response was well accorded in all energy range with the expected  $H^*(10)$  which was derived from the fluence. In addition, the direction of coming neutrons can be found out from the distribution of the measured value TLD1. And, the rough constitution ratio of low energy to intermediate energy can be obtained by the measured value of TLD1 and TLD2.

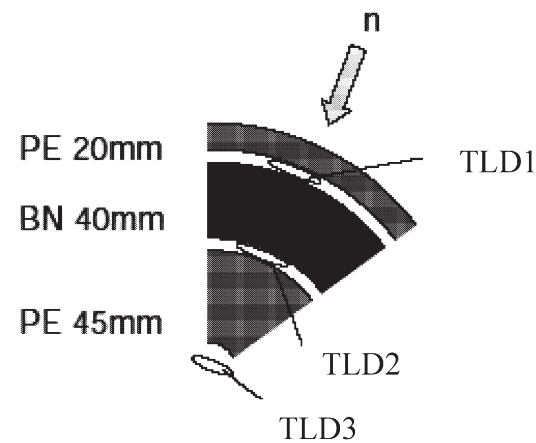


Fig. 1 Layer structure of the instrument. PE: Polyethylene, BN: Boron nitrate.

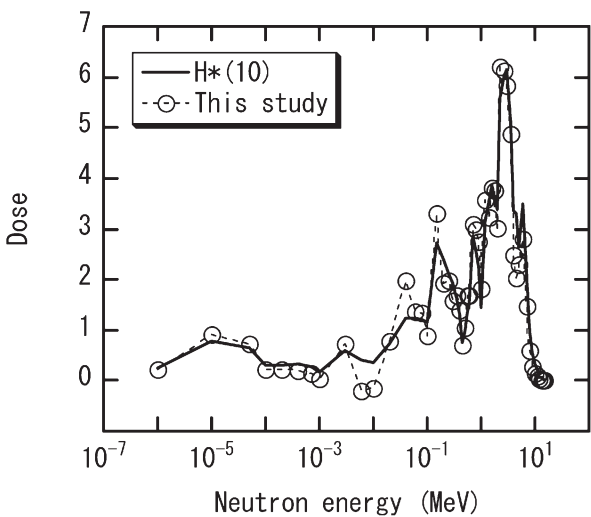


Fig. 2 Calculation result of the dose response to Cf-252( $\text{D}_2\text{O}$ ) moderated.



### §3. Sensitivity of TLD and RPLD to Cosmic Ray Hard Component Measured in Ogoya Tunnel

Yamanishi, H., Miyake, H.,  
Yamasaki, T. (Chubu Electric Power Company),  
Komura, K. (Kanazawa University)

Thermo-luminescence dosimeter (TLD) and radiophoto-luminescence glass dosimeter (RPLD) are used for environmental radiation monitoring. When these are applied to highly precise measurement, it is important to have evaluated the self dose and the sensitivity to cosmic rays. For the purpose of making clear these basic characteristics of TLD and RPLD, these dosimeters were set in several points in a tunnel, and were exposed for long period.

The measurement was done in the Ogoya tunnel which is located in Komatsu-shi, Ishikawa-prefecture. The overburden is 135 m at the point 300 m from the entrance of the tunnel, which corresponds to 270 m depth in water equivalent. Five sets of TLD and RPLD were set at the five points where were 20 m, 100 m, 200 m and 300m from the entrance of the tunnel, and the entrance of the tunnel. The dosimeters were installed in the lead box of 10 cm thickness because environmental gamma rays were shielded. The exposures were conducted as three series for 160 days, 266 days and 302 days. Since the dose due to cosmic rays is very small, the measurements were required high precision. In this study, lot control of the dosimeters, calibration of the readers, fading correction of TLD were paid attention to. The dose rates due to cosmic ray ionizing component at the measurement points were measured with NaI(Tl) scintillation detector. The relationship between the relative dose rate,  $X/X_0$ , and the count rate integrated in a pulse height region greater than 10 MeV,  $C/C_0$ , is empirically expressed by

$$X/X_0 = C/C_0 \quad (1)$$

where  $X_0$  and  $C_0$  are, respectively, the dose rate and the count rate measured in an outdoor environment at sea level where there is no influence from buildings. Values of 29.4 nGy/h and 1.18 cps were used as  $X_0$  and  $C_0$ , respectively. A discrimination level of 10 MeV was chosen to distinguish the cosmic-ray contribution of gamma rays from natural radionuclides. The energy calibration was conducted for each measurement using three points of 1.461 MeV from  $^{40}\text{K}$ , 2.614 MeV from  $^{208}\text{Tl}$  and 33 MeV from the interaction between muons and the detector.

Figure 1 and Fig. 2 show the relationship between measured dose rate by TLD or RPLD and intensity of cosmic ray hard component. The intensity of cosmic ray hard component in the horizontal axis was derived with consideration of the reduction effect by the 10 cm thick lead. From the tunnel entrance to the center of the tunnel, the dose rate measured by TLD or RPLD was decreased continually in correspondence with the decrease of the dose

rate due to cosmic rays. The intensity of cosmic ray at the center of the tunnel is about one  $100^{\text{th}}$  at the outside of the tunnel. The measured value of the dosimeters at the center of the tunnel corresponds to the self dose of the dosimeters. The self doses of the dosimeters were evaluated as 2 – 5 nGy/h as shown in Fig. 1 and Fig. 2. The sensitivity to cosmic ray hard component of TLD and RPLD is concluded to be 0.78-0.88 by the gradient of the regression line.

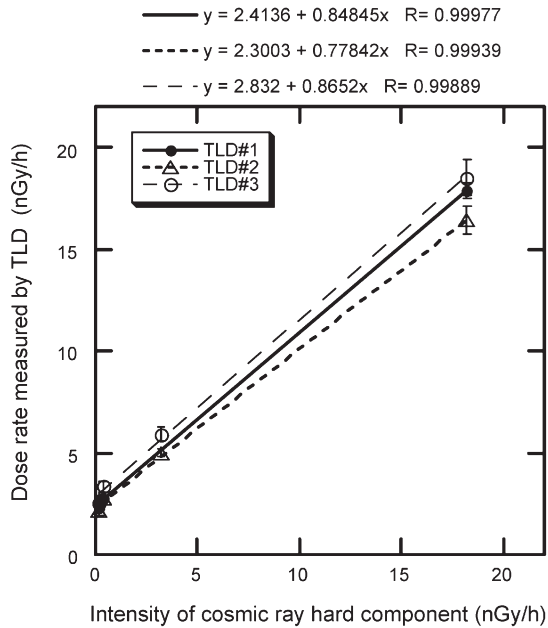


Fig. 1 Relationship between measured dose rate by TLD and intensity of cosmic ray hard component.

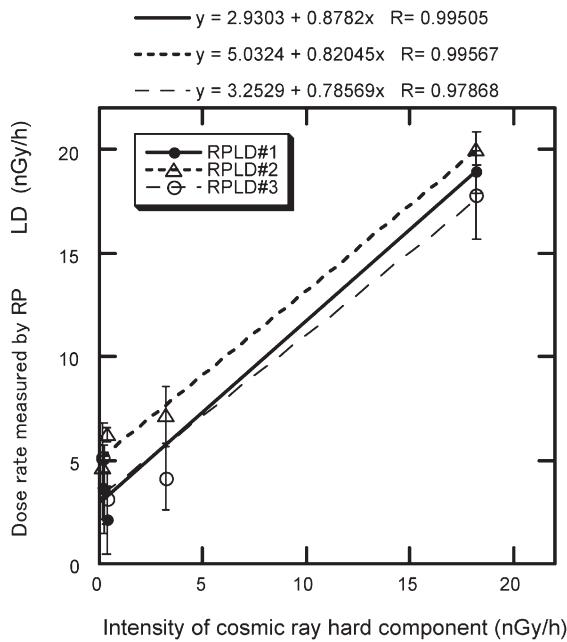


Fig. 2 Relationship between measured dose rate by RPLD and intensity of cosmic ray hard component.

§4. Consideration of Measuring Tritium Concentration in Air Using Gas Chromatograph

Kawano, T.

An analyzer previously developed for detecting extremely small concentrations of hydrogen in air was evaluated by using it to distinguish hydrogen isotopes. The analyzer utilizes the functions of a gas chromatograph and an atomic absorption spectrophotometer and is based on the reduction reaction of mercuric oxide with hydrogen. Three test samples were used: gas mixtures containing both protium and deuterium with almost equal concentrations of about 5, 20, or 50 cm<sup>3</sup>/1000 m<sup>3</sup> diluted in nitrogen. Each measurement was repeated more than 30 times, and chromatograms were obtained for each test sample. Examination of the chromatograms showed that the retention times for the protium and deuterium could be clearly distinguished. The retention times were virtually constant and indistinguishable, independent of the concentration and repetition time. The peak areas for the protium and deuterium were also stable, independent of the repetition time. Moreover, there was a clear linear relationship between the peak areas and concentrations for both elements. These results show that the analyzer can distinguish the two hydrogen isotopes and estimate concentrations of each as small as about 5 cm<sup>3</sup>/1000 m<sup>3</sup>. They also show that it may be possible to use the analyzer to monitor tritium concentrations in air.

In the present study, gas mixtures containing tritium itself was not used as test samples to avoid contaminating the analyzer with tritium during development. It can be, however, inferred the detection limit for tritium in air based on the results obtained using the mixtures of protium and deuterium without tritium.

The results of measurement of protium and deuterium shows that the analyzer should be able to detect concentration of tritium as small as about 5 cm<sup>3</sup>/1000 m<sup>3</sup> in air. Assuming that all tritiated compounds in air have the chemical form HT (H: protium, T: tritium), the concentration of 5 cm<sup>3</sup>/1000 m<sup>3</sup> corresponds to 240 Bq/cm<sup>3</sup>. Where, it have to be mentioned that a retention time of HT is assumed to be about 18 minutes that can be distinguished from both ones of HH and DD (about 15 and 21 minutes), using a low-temperature separation column (Hydro isopack).

The analyzer should thus be suitable for monitoring the level of tritium at radiation facilities. Japanese law requires regular monitoring of tritium levels in areas where tritium is handled, at the boundaries of controlled areas, and at the exhaust ports of the facilities. The detection limit of the analyzer and the required detection levels are summarized in Table 1. The right column shows the ratio of the detection level of the analyzer to the required level. The ratio shows the allowance of the detection level. For locations where the ratio is larger than unity, the analyzer's ability is sufficient.

Table 1. Detection limit and concentration limits at various locations.

	Concentration	Ratio
• Detection limit	240 Bq/cm <sup>3</sup>	1.00
• Work place	10000 Bq/cm <sup>3</sup>	41.6
• Boundary of controlled area	1000 Bq/cm <sup>3</sup>	4.16
• Exhaust port	70 Bq/cm <sup>3</sup>	0.29

The ratios for the work place and the boundary of a controlled area were 41.6 and 4.16 so the analyzer can be used at both locations instead of conventional radiation monitors like ionization chambers and proportional counters, to monitor tritium levels. However, the ratio was only 0.29 for the exhaust port, so it has to be improved its sensitivity to tritium before it can be used to monitor tritium concentration at port locations.

Finally, it need to continue considering furthermore because tritium may exist in the chemical form of HT (H: protium, T: tritium), as an extremely small part of all hydrogen isotopes (supposed major part of HH and small part of HT) in air samples. This is because air itself contains about 500 cm<sup>3</sup>/1000 m<sup>3</sup> of hydrogen in the form of HH naturally. For this case, a gas chromatogram obtained by the analyzer must be schematically drawn as shown in Fig. 1. That is, a peak for HT must appear on the tail of a peak for HH. It is very difficult to distinguish the peak of HT from the peak of HH because the peak of HH is huge compared with that of HT. Distinguishing HT from HH is thus a significant problem. As a consequence, a new method for distinguishing HT from HH should be developed.

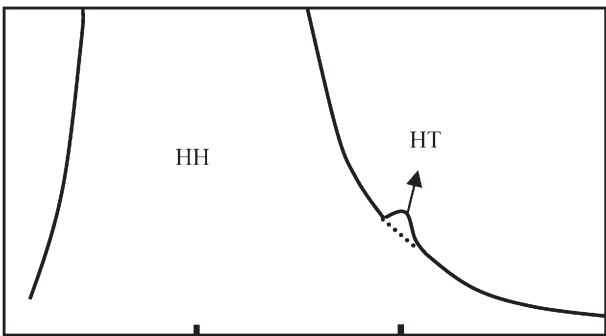


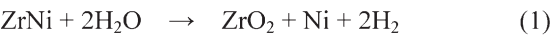
Fig. 1. Imagined hydrogen spectrum of sample gas containing a huge amount of protium and an extremely small amount of tritium.

§5. Chemical Reaction Equation of Water Vapor Decomposition on a Zirconium-Nickel Alloy

Kawano, T.

In the previous study, a series of experiments showed that a decomposition-processing vessel based on a ZrNi alloy could be used to effectively decompose methane and extract hydrogen in the chemical form of hydrogen molecules. Using the same vessel, a series of experiments was carried out under the same experimental conditions (temperature of 873 K; gas flow rate of 35 standard ml/min; material size of 70–200 meshes) by using water vapor instead of methane, because water vapor is also another one of the main tritiated compounds in an exhaust gas discharged from fusion-related facilities.

In the previous study, it could be assumed that Equation (1) described the chemical reaction producing the decomposition of water vapor and the generation of hydrogen gas.



This equation shows that one molecule of ZrNi should decompose two molecules of water vapor (H<sub>2</sub>O) and generate two molecules of hydrogen (H<sub>2</sub>). This equation was derived based on XRD spectra taken only before and after

water vapor decomposition experiment.

In the present report, the XRD spectra before starting the experiment, after 9.5, 20, 31 and 50 hours, and after the decomposition reaction ended were inspected. Obtained six typical spectra are shown in Fig. 1. Spectrum (A) was taken before starting the experiment (new ZrNi). As the experiment progressed, the pattern of the spectrum gradually changed from (A) → (B) → (C) → (D) → (E) and finally to (F), the spectrum obtained after the decomposition had completely finished (spent ZrNi).

The several peaks in (A) are all attributed to ZrNi, meaning that the breakdown materials of the ZrNi alloy were sufficiently pure for the experiment. Small, new peaks can clearly be seen in (B), and these new peaks, for example “P1” to “P4”, steadily grew from (B) to (F). These six spectra show that all the peaks of the pure ZrNi alloy in (A) were gradually replaced by new ones as the experiment progressed, and, by (F), they can all be attributed to ZrO<sub>2</sub> or pure Ni. None of the XRD spectra and gas chromatograms show any sign of an intermediate compound midway through decomposition. This confirms the previous result and means that after the decomposition of H<sub>2</sub>O, the Zr of the alloy was bound to oxygen, resulting in ZrO<sub>2</sub>, while the Ni was released as a simple substance.

To better understand the water vapor decomposition on ZrNi, the equation was validated by examining the relationships among the volume of decomposed water vapor, the volume of generated hydrogen, and the increase in weight of the breakdown material (ZrNi). It was found that all the experimental results were explained quite well using the proposed equation (1).

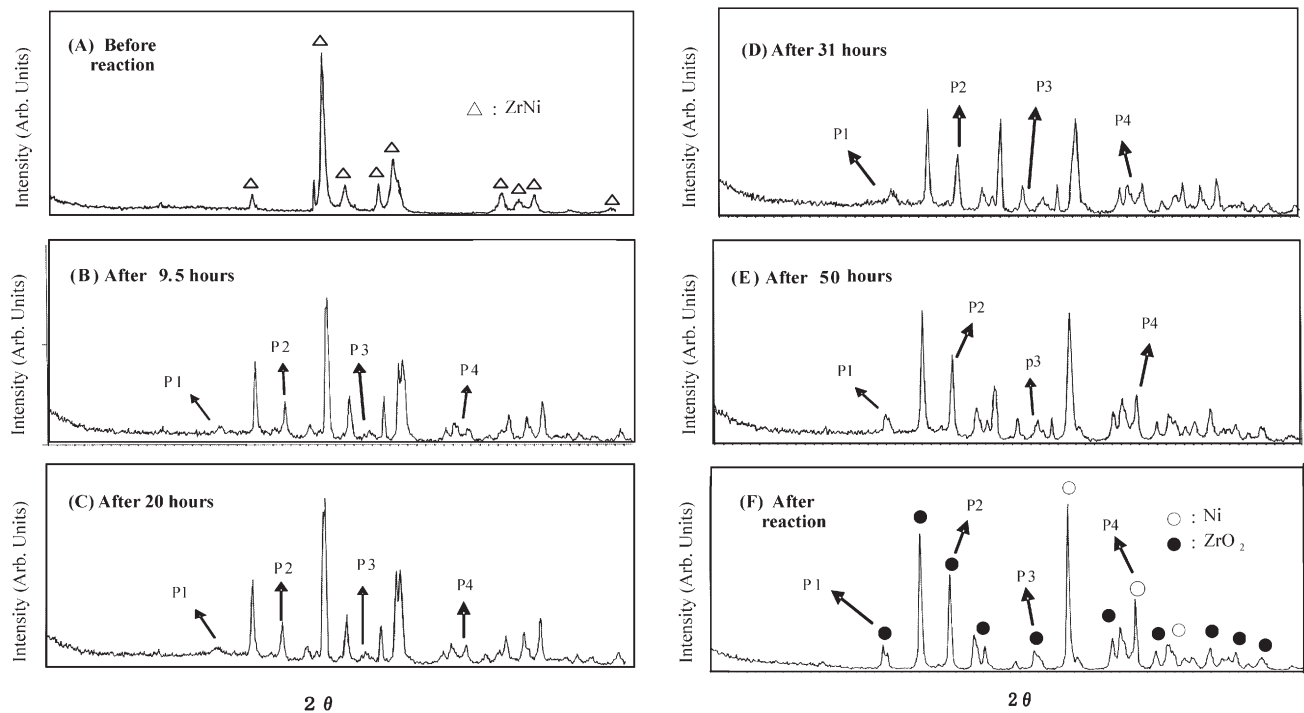


Fig. 1. Typical x-ray diffraction spectra of ZrNi samples taken before, during, and after reaction.

§6. Performance Test of Direct Immersion Method to Detect Tritium in Concrete

Kawano, T.

A tritium handling laboratory constructed at the National Institute for Fusion Science was characterized by the fact that tritium was the only radioisotope it handled. The main chemical forms were tritiated hydrogen gases (tritium gas) and tritiated water. The laboratory’s role, however, came to an end, and the necessary measures that were legally required at the discontinuation of radioisotope use were completed. During these measures, tritium contamination tests of all articles, fixtures, equipment, and the building itself including walls and floors was conducted. Aside from the necessary measures taken according to the law, the performance of a direct-immersion method (Appendix 1) was evaluated to detect tritium contamination in concrete.

There are several methods to measure tritium contamination in concrete. The heating-cooling method (Appendix 1) may be the most efficient way from the viewpoint of collecting tritium in concrete pieces. However, this method is not very practical when employed after the discontinuation of radioisotope use because of the inconvenience regarding time and ease of use. For this reason, the direct-immersion method may be used as a practical measure for evaluating tritium contamination of concrete walls and floors.

In this report, the direct-immersion method was compared with the heating-cooling method. An adequate quantity of concrete was chipped from the actual walls or floors, called a lot block, and used two 1-g pieces from the same lot block as samples. These samples was measured using both the direct-immersion and heating-cooling methods.

Table 1 shows contamination measured using both methods in the order of strength of tritium contamination. On the right, ratios are listed, which were obtained by dividing the contamination measured using the heating-cooling method with that measured using the direct-immersion method. The ratios are distributed from 2 to 3, and the averaged ratio is determined to be 2.54, with a standard deviation of 7.4%. The direct-immersion method may give an estimation that is 2.5 times smaller than the heating-cooling method, and that the ratios might be used as a collection factor to convert data obtained using the direct-immersion method to that of the heating-cooling method.

Appendix 1(direct-immersion method)

To measure tritium contamination in the concrete structure itself, a 1-g piece of concrete chipped from the wall or floor was placed into a dedicated vial, and 10 ml of scintillation cocktail (PerkinElmer Inc., Hionic-Fluor) was then added. The tritium in the concrete would gradually leach out into the scintillation cocktail. The amount of tritium in the cocktail saturated within several hours, which

Table 1 Comparison between heating-cooling method and direct immersion method

Position Number	Heating-cooling Method (Bq/g)	Direct Immersion Method (Bq/g)	Ratio
1	69.3	27.2	2.55
2	27.7	11.0	2.52
3	10.8	4.8	2.25
4	7.95	2.8	2.80
5	6.03	2.0	3.07
6	4.67	2.0	2.37
7	3.69	1.5	2.49
8	3.21	1.4	2.28
Average (except asterisked data)			2.54 (7.4%)

was certified in advance, so the vial containing the concrete piece was left for more than a day. The tritium was then measured using the liquid scintillation counter (Aloka LSC5100). This method makes it possible to directly measure tritium contamination in a piece of concrete.

Appendix 2 (heating-cooling method)

It is well known that the heating-cooling method is very effective for extracting tritium contained in concrete. In this method, a 1-g piece of concrete chipped from the concrete wall or floor was placed into a furnace and heated to 800 degrees centigrade for an hour in flowing dry air with a flow rate of 200 ml/min. The 800-degree temperature enables the extraction of not only free water but also bound water in concrete. With the heating of the concrete, tritium in the concrete was vaporized into the flowing dry air as water vapor. The air flowing out of the furnace was sent into a collection tube that was cooled in dry ice-ethanol (around -70 degrees centigrade). As a result, the water vapor including tritium in the flowing air condensed into drops of water in the cooled collection tube. After this collection procedure, about 0.5 ml of water was obtained. The collected water was put into a dedicated vial with 10 ml scintillation cocktail, and the tritium concentration was measured using the liquid scintillation counter.



## §7. Theoretical Expressions for Removing Tritium from Exhaust Gas

Kawano, T.

A tritium cleanup system for application to exhaust gases discharged from a large helical device has been developed. All the hydrogen including the tritium in the system is converted from its various chemical forms into molecules of hydrogen gas before removal. The system essentially consists of five components: a hydrogen separator, a decomposition-processing vessel, a hydrogen-absorbing vessel (Ti), a circular pump, and a buffer tank. The decomposition-processing vessel fulfills a very important role in decomposing various tritiated compounds and extracting tritium in the chemical form of hydrogen molecules.

In the previous study, the system's performance was tested based on computer simulations. In the simulations, the process gas was assumed to be made up of hydrogen and methane, where part of the hydrogen and methane had been tritiated. For expressing the removal of tritium in the simulations, two fundamental Eqs. (1) and (2) were used without any proof.

$$P_{Q2}(t + \Delta t) = P_{Q2}(t) + \frac{dP_{Q2}(t)}{dt} \Delta t - 2 \frac{dP_{CQ4}(t)}{dt} \Delta t \quad (1)$$

$$P_{CQ4}(t + \Delta t) = P_{CQ4}(t) + \frac{dP_{CQ4}(t)}{dt} \Delta t \quad (2)$$

Where,  $P_{Q2}(t)$ : Partial pressure of hydrogen [Pa] at time  $t$ ,  $P_{CQ4}(t)$ : Partial pressure of methane [Pa] at time  $t$ ,  $t$ : Stated time [hr], and  $\Delta t$ : Minimal elapsed time from stated time  $t$  [hr]. In this report, it will be shown how practical forms of both the differentiations in Eqs. (1) and (2) can be derived.

### (1) Differentiation: $dP_{Q2}(t)/dt$ :

The speed of hydrogen separation in a given volume is given by

$$\frac{dV_{Q2}}{dt} = K S [ (Pin)^{1/2} - (Pout)^{1/2} ] \quad (3)$$

Where,  $V_{Q2}$ : Volume of hydrogen in standard state (273 K, 0.1013 MPa) [ $Nm^3$ ],  $dV_{Q2}/dt$ : Speed of hydrogen separation [ $Nm^3/hr$ ],  $K$ : Rate constant [ $Nm^3/hr/Pa^{1/2}/cm^2$ ],  $S$ : Area of membrane for hydrogen separation [ $cm^2$ ],  $Pin$ : Absolute partial pressure of hydrogen at separator inlet [Pa], and  $Pout$ : Absolute pressure of hydrogen at separator outlet [Pa].

The residual volume of hydrogen at stated time  $t$  is  $V_{Q2}$  when the standard state applies. Then,  $P_0$  is the pressure of the standard state (0.1013 MPa).  $V_B$  and  $P_B$  are assumed to be the volume of the buffer tank regarded as the whole interior volume of the system and pressure when  $V_{Q2}$  has spread in the buffer tank at the stated time. Consequently, we obtain the following Eq. (4)

$$\frac{dP_B}{dt} = (P_0 / V_B) K S [ (Pin)^{1/2} - (Pout)^{1/2} ]. \quad (4)$$

This is the speed of hydrogen removal as a function of pressure. If we assume that the initial speed of separation is  $Q_0$ , we obtain the following Eq. (5)

$$\frac{dP_B}{dt} = \frac{Q_0 P_0}{V_B} \left[ \left( \frac{Pin}{Pin-0} \right)^{1/2} - \left( \frac{Pout}{Pin-0} \right)^{1/2} \right] \quad (5)$$

where,  $Pin-0$  and  $Pout-0$  are assumed to be initial partial pressures at the inlet and outlet of the separator.

Since  $P_{Q2}(0)$  and  $P_{Q2}(t)$  are partial pressures of hydrogen in the buffer tank for states at times 0 and  $t$ , Eq. (5) becomes

$$\frac{dP_{Q2}(t)}{dt} = - \frac{Q_0 P_0}{V_B} \left[ \left( \frac{P_{Q2}(t)}{P_{Q2}(0)} \right)^{1/2} - \left( \frac{P_{Ti}}{P_{Q2}(0)} \right)^{1/2} \right] \quad (6)$$

This gives us the differential  $dP_{Q2}(t)/dt$  in Eq. (1). Where  $P_{Ti}$  is about  $1 \times 10^{-4}$  Pa that is a practically attainable pressure in actual vacuum system using titanium as hydrogen-absorbing materials.

### (2) Differentiation: $dP_{CQ4}(t)/dt$

Suppose that the gas for processing was in the buffer tank at an overall pressure of  $P_T(t)$ , a part of which was methane at a partial pressure of  $P_{CQ4}(t)$ . That is, the gas for processing had a volume of  $V_B$  at  $P_T(t)$  and consisted of methane gas in  $V_B$  and at  $P_{CQ4}(t)$  and other gas components in  $V_B$  at  $(P_T(t) - P_{CQ4}(t))$ . The three volumes of the entire gas, methane, and other gas components should be same. The only difference is pressure. Therefore, the volume processed after circulation over a time interval of  $dt$  is also equal to the volume of methane processed over the same time interval. Assuming that the gas-flow rate is represented by  $F(P_T(t))$  [ $m^3/hr$ ] as a function of the total gas pressure, the volumes themselves processed after circulation over a time interval of  $dt$  are  $F(P_T(t))dt$  for the entire gas, methane, and the other gas components and decomposed methane is  $R_d \times F(P_T(t))dt$  ( $= dV$ ), where  $R_d$  is the rate of decomposition. As a result, methane with volume  $dV$  disappears, which leads to decrease  $dP_{CQ4}(t)$  in the partial pressure of methane in the buffer tank. This change is represented by:

$$P_{CQ4}(t) \times (V_B - dV) = (P_{CQ4}(t) - dP_{CQ4}(t)) \times V_B \quad (7)$$

$$P_{CQ4}(t) \times R_d \times F(P_T(t)) dt = dP_{CQ4}(t) \times V_B \text{ and}$$

$$\frac{dP_{CQ4}(t)}{dt} = - \frac{F(P_T(t))}{V_B} \times R_d \times P_{CQ4}(t) \quad (8)$$

Equation (8) represents the decreased speed that the partial pressure of methane drops to with the decomposition of methane.

Thus, we can estimate the respective partial pressures with Eqs. (1), (2), (6), and (8), if only definite values are assigned to  $Q_0$ ,  $P_0$ ,  $V_B$ ,  $P_{Q2}(0)$ ,  $P_{CH4}(0)$ ,  $P_{Ti}$ ,  $F(P_T(t))$  and  $R_d$ .

§8. Characteristics of Honeycomb Catalysts for Oxidation of Tritiated Hydrogen and Methane Gases

Uda, T., Tanaka, M.,  
Munakata, K. (Interdisciplinary Graduate School of  
Engineering Sciences Kyushu University)

To oxidize the isotopic hydrogen and its compound gases to water form by catalyst is a conventional method for removal of tritium from air in a tritium processing facility. If tritium release accident occurs in a fusion facility, large volumes of air would be processed by the air cleanup system. However high throughput of air would cause pressure drop in catalyst beds, it results in high load to the process gas pumping system. In this study, applicability of honeycomb catalysts to the tritium recovery system was examined. The honeycomb catalyst bed has an advantage in terms of pressure drop, which is estimated to be less than 1/10 of conventional particle-packed catalyst beds. Our previous studies revealed that honeycomb catalysts made of cordierite or Al-Cr-Fe metal alloy have preferable oxidizing performance. It was found that the platinum-deposited cordierite catalyst shows high oxidation rate for hydrogen gas, and the palladium-deposited metal honeycomb catalyst shows high oxidation rate for methane gas.

In this study, the properties of honeycomb catalysts were systematically studied by changing experimental parameters such as precious metal content, mesh density and so forth to obtain design data base for high performance honeycomb catalysts. As parameters the weighing rate of precious metal deposited on the honeycomb substances were varied from 1 g/L to 4 g/L and the mesh density of the honeycombs were changed from 260 to 400 CPSI as well. For operating conditions, the flow rate of the process gases, and the concentration of water vapor was varied.

Results of experimental study are as follows. The oxidation activity depends on weighing ratio of precious metal as shown in figure 1. But the mesh density CPSI has not been effective factor on oxidation. To avoid the pressure drop in the catalyst bed, lower CPSI would be preferable. The oxidation efficiency is large in small flow rate, namely small volume velocity. Of course large volume velocity is required in the catalytic oxidation process. In the next step, we examined affect of high moisture gas. Then oxidation efficiency for both hydrogen and methane gas decreases in case of including water vapor. Actually processing air by the cleanup system may be including some moisture element. So that the catalytic reactor should be designed by consider the loss of activity by moisture in air.

As conclusion, honeycomb catalysts are useful for the treatment of gases with high volumetric velocity in a fusion plant because of their low pressure drop in the catalyst reactor. The platinum catalysts were found to be suitable for oxidation of hydrogen gas, while the palladium catalysts exhibit better performance for oxidation of methane gas. With regard to hydrogen oxidization, the cordierite

honeycomb reveals a better oxidizing performance than the metal alloy honeycomb. It was also suggested that the oxidation rate depends on the amount of deposited precious metal but the mesh density does not strongly affects the oxidation rate. Experimental results indicate that the catalytic oxidization rate decreases with increasing moisture content in the experimental gases. It was found that the catalytic activity of palladium catalysts for hydrogen oxidization is substantially decreased under the condition of low temperature and high humidity. In conclusion, it can be said that the honeycomb catalysts are promising alternatives of conventional packed bed type of catalyst for the recovery of tritiated gas if proper precious metal is selected. Although the cordierite honeycomb possesses better oxidizing property than the metal honeycomb, the metal honeycomb has an advantage for oxidation of hydrogen gas under room temperature, because it does not have structural water molecule that would cause memory effects via tritium contamination.

We also obtained design data base for conventional particle catalyst. Based on the database, the catalyst volume can be estimated for large volumetric velocity for example 1000 Nm<sup>3</sup>/hour. It was found that these honeycomb catalysts can be used for the high-performance removal system of tritium from tritiated gases. These honeycomb catalyst are also applicable to the collection of tritiated gases for tritium measurement in atmospheric air around the fusion facility and the environment <sup>1)</sup>.

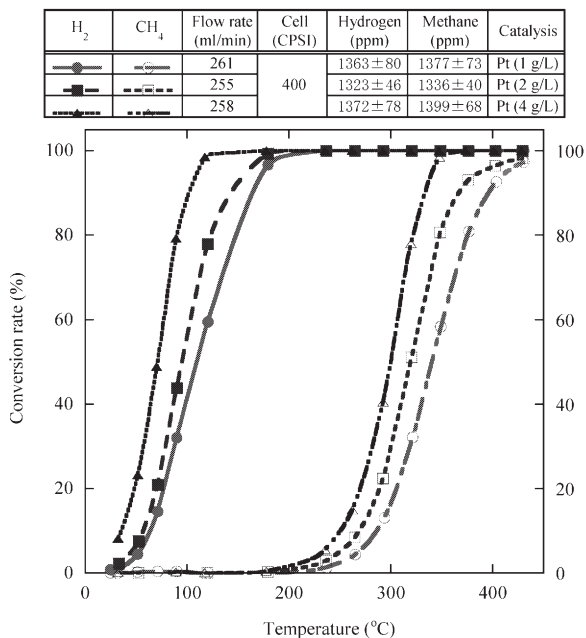


Fig. 1 Effect of precious metal weighing ratio on catalyst to oxidation.

1) . T. Uda, T. Sugiyama, K. Munakata, M. Tanaka and N. Momoshima, “Developments of gaseous water, hydrogen and methane sampling system for environmental tritium monitor”, Fusion Engineering and Design, 81 (2006) 1385.

§9. Entrainment Behavior of Activated Dust in Accidental Event

Ijiri, H., Ebara, S., Shimizu, A. (Kyushu Univ.), Kawano, T.

In fusion devices, there exist fine particles of hydrocarbon and/or metal, and these particles cause some troubles, absorption of tritium, radioactivation of constituent metal atoms, and so on. In case a vacuum vessel which is the first confinement barrier to radioactive materials in the fusion devices is broken by some sort of accident, these activated particles have possibilities to be released outside the vessel. From the viewpoint of safety, it is very important to make a prediction about the behavior of the activated particles and a lot of research has been done for this purpose. The behavior of particles under wet condition comes into the picture in the ICE/LOVA, the assumed accident events in ITER. Many of them, however, consider only dry condition and there is hardly any study that supposes wet condition where wet wall surface to capture particles exists. In this study, we focused attention on adhesion behavior of particles under the wet condition, especially on particle adhesion on wet wall surface, and quantitative estimates were performed experimentally.

Fig.1 shows the schematic diagram of experimental device. Gaseous nitrogen supplied from a compressed gas cylinder passes through a mass flowmeter and a particle feeding part, and then enters a straight duct with a dimension of 3000 mm length  $\times$  100 mm width  $\times$  10 mm height. A test section is located 2600 mm downstream from the entrance of the duct. A water pool with depth of 1 mm and width of 60 mm is installed in the test section and we regard this pool as the wet wall surface. In order to investigate the influence of length of the wet wall in the flow direction on particle adhesion, two kinds of water pool with the length of 150 and 300 mm are used. Graphite particles with average diameter of 30  $\mu\text{m}$  are used in the experiment. The particle adhesion to wall surface from suspension flow is expressed by using deposition velocity,  $V_d$  [m/s], which is the ratio of flux density of deposition particles at a sink surface,  $J$  [ $\text{g}/\text{m}^2/\text{s}$ ], to its concentration in the atmosphere,  $C$  [ $\text{g}/\text{m}^3$ ]. In this experiment, we examine the dependence of  $V_d$  upon Reynolds number of the suspension flow,  $Re$ , and  $C$ , and attempt to elucidate the difference of the deposition velocity on the wet wall from that on dry wall.

Fig.2 shows the relation between  $V_d$  and  $C$ . For all data,  $Re$  is the same at 1700. It is found from the figure that the deposition velocity is almost constant against the varying particle concentration. This result means that the amount of adhesion particles is proportional to the particle concentration, and this leads that interactions among particles have little influence on the adhesion in the concentration range used in the experiment. Fig.3 shows the relation between  $Re$  and  $V_d$  on both of wet and dry walls.

Any large difference of  $V_d$  cannot be found between both of the wet and dry walls while in the range of  $Re$  over about 3000  $V_d$  on the wet wall becomes discernibly larger than that on the dry wall. This is considered because the amount of particle entrainment from the dry wall becomes large as  $Re$  gets large.

In this study, we performed the experiment for adhesion of suspension particles to the wet wall surface. It was elucidated from this experiment that the deposition velocity was independent of the particle concentration. In addition there was no difference of particle adhesion between to the wet and dry wall surfaces while behavior of particle entrainment from the surface was different between them. This difference was responsible for the difference of the deposition velocity between the wet and dry walls, in other words, the deposition velocity on the wet wall became larger than that on the dry wall.

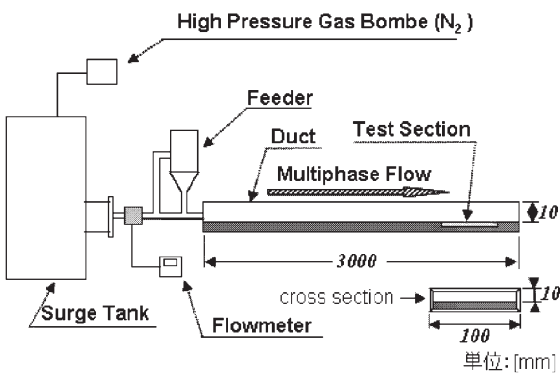


Fig.1 Schematic diagram of experimental device

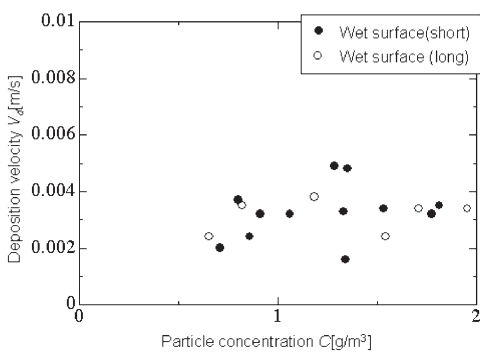


Fig.2 Relation between  $V_d$  and  $C$

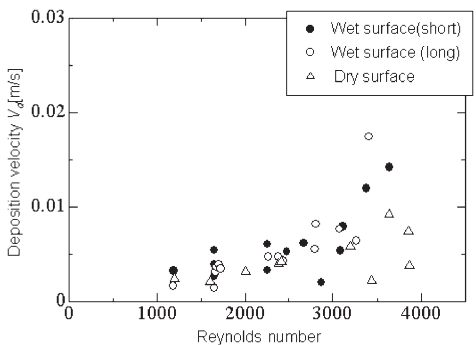


Fig.3 Relation between  $Re$  and  $V_d$

§10. Development of Exhaust Gas and Effluent Liquid Treatment System for LHD

Asakura, Y., Kawano, T., Sugiyama, T., Uda, T.

In order to carry out deuterium plasma experiments on the Large Helical Device (LHD), NIFS is planning to install a system for the recovery of tritium from exhaust gas and effluent liquid. As well as adopting proven conventional systems, NIFS is planning to apply the latest technologies. The following specific methods have been selected for final evaluation for actual applications.[1,2]

(A) Membrane Dehumidifier for Vacuum Vessel Purge Gas Treatment Unit

Oxidized tritium (tritiated water vapor) contained in the purge gas is usually removed using an absorbent column. However, if a dew point of less than -60 °C could be obtained using a polymer membrane dehumidifier, the equipment could be reduced in size and a more stable dehumidifying performance could be expected.

(B) High Sensitivity Tritium Monitor for Online Gas Phase Tritium Monitoring Unit

A real-time monitor has not been commercially available for concentrations under  $5 \times 10^{-4}$  Bq/cm<sup>3</sup>, which is 1/10 of the regulation value for tritiated water vapor in the exhaust gas. Using the hydrogen pump described, it is possible to lower the effective detection limit by greater than an order of magnitude, by concentrating the hydrogen-isotope gas (including tritium) and by removing the radon gas which is mixed in at the monitoring stage.

In order to make efficient developments, two collaborated researches have been carried out.

- 1) Development of hydrogen gas pumping apparatus applying proton conducting ceramics [TYK]
- 2) Study on polymer membrane type dehumidifier for tritium removal [Shizuoka Univ.]

Development status are summarized as follows.

① Membrane dehumidifier

In order to elucidate the performances under atmospheric pressure at the permeate side, we carried out experiments using a commercially available polyimide hollow-fiber filter module (Ube Industries, UM-XC5, O.D.: 90 mm, L: 710 mm) and the mock-up test dehumidifier, in which the permeated flow rate is kept to the constant value necessary to achieve the targeted dew point by regulating the purge gas flow rate automatically.

As shown in Fig.1, PID control of the purge gas flow rate is effective in keeping the targeted dew point during a long

time operation. The tritium recovery rate up to 99.9% (dew point of -90 °C) has been achieved under the present experimental conditions.

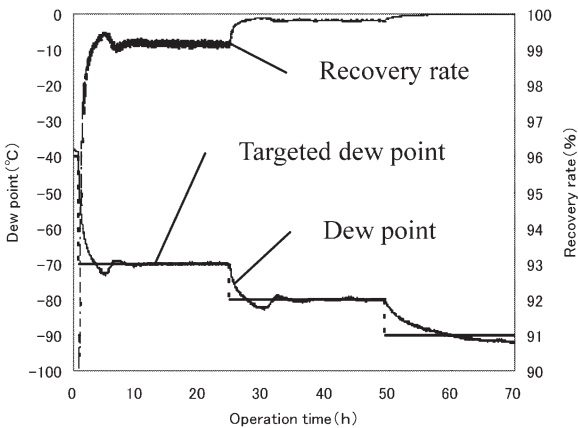


Fig1. Water-vapor separation performances

②High sensitivity tritium monitor

We have performed water-vapor electrolysis experiments in an atmosphere containing 20 % oxygen. In terms of stability during long-term operation, we have used a commercially available  $\text{CaZr}_{0.9}\text{In}_{0.1}\text{O}_{3-\alpha}$  tube with one end closed and with platinum electrodes (O.D.: 15 mm, I.D.: 12 mm, L: 200 mm, effective electrode area: 47 cm<sup>2</sup>). The hydrogen pump having the capacity of 1cc/min, which is necessary to the high sensitivity tritium monitor for concentration under  $5 \times 10^{-4}$  Bq/cm<sup>3</sup> has been made and under evaluations for a long time use. The new phenomena have been observed, in which hydrogen pump capacity gradually decreases with operation time and steeply increases with the a few minutes addition of the air to the cathode. As shown in Fig.2, periodical short time addition of the air to the cathode has been demonstrated to be effective to keep the hydrogen pump capacity during a long time operation.

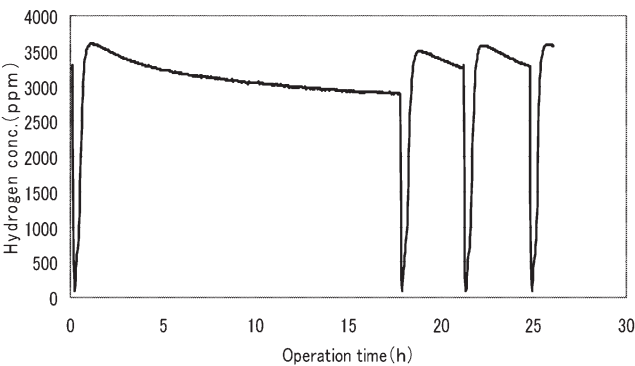


Fig.2 Hydrogen pump regeneration test results

References

[1] Y. Asakura, et al.,J.Nucl.Sci.Technol., **41** (2004) 863  
[2] Y. Asakura, et al.,Fusion Sci.Technol., **48** (2005) 401



## §11. Development of Proportional Counter to Measure Tritium in Atmospheric Air

Ogata, Y. (Nagoya Univ. School of Health Sciences),  
Sakuma, Y.

Tritium will be generated at the D-D plasma experiment, which will be one of the next projects of National Institute of Fusion Sciences. The D-D reaction includes  $D+D \rightarrow {}^3\text{He}+n$  and  $D+D \rightarrow T+p$ , which will generate tritium. The tritium concentration in the work place and the environment should be promptly monitored to guarantee safety of the experiments. Chemical species involving tritium in the atmospheric air are predominantly  $\text{H}_2\text{O}$ ,  $\text{H}_2$ , and  $\text{CH}_4$ . The sensitivity of conventional tritium gas monitors is too low to detect the legal tritium concentration. Alternative method is a liquid scintillation counting by measuring the trapped water vapor and trapped vapor of water oxidized hydrogen and methane. The method, however, requires lots of time and labor to collect the vapor, to exchange the chemical forms of hydrogen and methane gases, and to count the samples. The purpose of this study is to investigate a feasibility of a real-time monitoring of tritium on the water vapor in the atmospheric air.

The flow through type of proportional counter, 130-mm long, 29 mm in inner diameter was made of brass. The anode was made by a tungsten wire of  $50\ \mu\text{m}\phi$ . The block diagram is shown in Fig.1. PR gas, Ar, and hydrogen were used for counting gases at room temperature. The plateau characteristics were measured using an external  ${}^{137}\text{Cs}$  source. The change in the counts was collected via a multichannel scaler.

The experimental setup is illustrated in Fig.2. First, the remaining air in the system was purged by Ar, and the magnesium column was heated at  $550^\circ\text{C}$ . Then water in the evaporating flask was heated to generate water vapor. The water vapor was fed into the magnesium column, and was reduced to hydrogen gas<sup>1)</sup>. The gas was desiccated and was drawn into the proportional counter. At first step, water including natural tritium (natural water) was fed in the evaporating flask, and the generated hydrogen with Ar was counted. Next, water of which tritium concentration was  $12\ \text{kBq cm}^{-3}$  was put into the flask and the vapor was fed into the column. Finally, natural water was put into the flask again.

The plateau potentials were 2000-2300 V, 1450-1650 V, and 2530-2550 V, for PR gas, Ar, and hydrogen, respectively. The plateau for hydrogen was somewhat narrow than the previous counter constructed by us<sup>2)</sup>. Therefore, Ar was used for carrier of the water vapor and for counting gas.

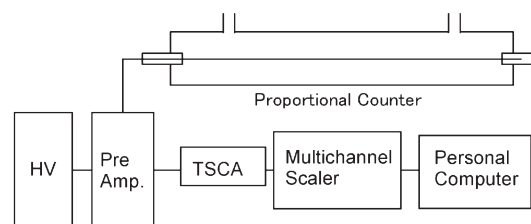


Fig.1 Block diagram of the system.

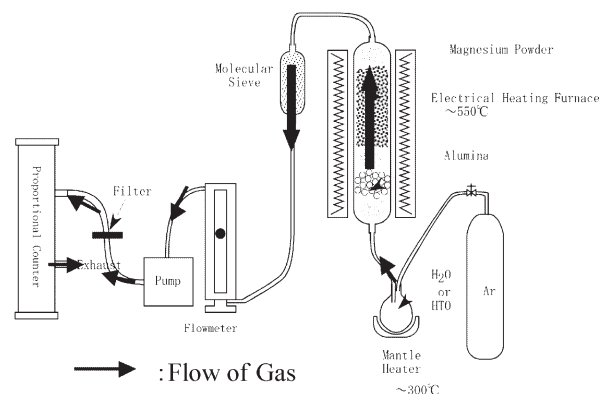


Fig.2. Experimental setup.

The count rate for the natural water was about 3 cps, which was the background count rate. After the tritiated water was put into the flask, the count rate was exponentially increased and was reached 12 cps. The count rate was gradually decreased after the natural water was put into the flask again.

The hydrogen concentration in the counting gas was 1.5%. Considering the hydrogen concentration, the background count rate, and the effective volume of the counter, the minimum detectable concentration (MDC) for 10 min counting was  $0.016\ \text{Bq cm}^{-3}$  at atmospheric temperature of  $20^\circ\text{C}$  and the relative humidity of 50%. The MDC was one-fiftieth of the legal limit of tritium concentration for work place, i.e.,  $0.8\ \text{Bq cm}^{-3}$ .

Tritium on the water vapor in the atmospheric air was measured using a proportional counter by reducing the water to hydrogen. Real-time tritium monitor is feasible by applying this method.

### References

- 1) W. W. Bowman and M. B. Hughes, Methods of Low-Level Counting and Spectrometry, IAEA, Vienna, (1981) 353.
- 2) Ogata, Y. et al.: Proc. 19<sup>th</sup> on Radiation Detectors and Their Uses. KEK (2005) 177.

## §12. Environmental Atmospheric Tritium Monitoring with Discriminate Sampling of Different Chemical Forms

Uda, T., Tanaka, M.,  
Sugiyama, T. (Nagoya Univ.),  
Momoshima, N. (Kumamoto Univ.)

As an environmental radiation safety issue, an atmospheric tritium monitoring system is necessary for the experiments of the LHD deuterium plasma discharges. The detailed variation of environmental tritium level at Toki site must be known before the experiments start and the tritium level must be monitored after the experiments start.

Atmospheric tritium mainly consists of three different chemical forms, that is, HTO, HT and  $\text{CH}_3\text{T}$ . Conventional technique of atmospheric tritium sampling is discriminate oxidization of tritiated species followed by collection of water with molecular sieve beds<sup>1)</sup>. For the practical use of this technique, we have developed the automatic system for the air sampling<sup>2)</sup>. We present the results of atmospheric tritium monitoring from April 2005 to March 2006.

### i) Sampling and radiation measurements

The air was collected about  $20 \text{ m}^3$  at a rate of 2 l/min once a month at NIFS Toki site. The sampling time spent to 168 hours. After collecting the air, water samples were recovered from the molecular sieves beds, which were regenerated at  $400^\circ\text{C}$ , passing  $\text{N}_2$  gas through it for 3.5 hours.

Radioactivity of tritium was counted by a low background liquid scintillation counter (LB-III, Aloka). The stocked water samples (65 g for HTO, 10 g for HT and  $\text{CH}_3\text{T}$ ) were mixed with the same amount of liquid scintillator (Ultima Gold LLT, PerkinElmer). Twenty ml of vials were used for counting the HT and  $\text{CH}_3\text{T}$  fractions while the HTO fractions were measured in 135 ml vials. Counting time was 1500 minutes for each sample, where measurements of 50 minutes were replicated for 15 times and the cycle was repeated twice. The detection limits of 20 ml and 135 ml vials were 1.6 Bq/L and 0.38 Bq/L, respectively.

### ii) Results of measurements

The measured values of tritium concentrations of the

water samples are shown in Fig. 1 with respect to each species. The measured values of HTO and  $\text{CH}_3\text{T}$  are near the detection limit, so that it is difficult to discuss the fluctuation of the tritium concentration as the seasonal change. On the other hands, the tritium concentration for HT is good enough values for the discussion of the seasonal fluctuation. The result is that it seems to be higher in autumn and spring, and the minimum lies in summer. The reason of the fluctuation might be influenced by an oceanic climate in summer and the westerly wind from the continent in spring and autumn. Thus we need to remark the fluctuation of tritium concentration by an environmental factor even after starting the deuterium plasma discharges.

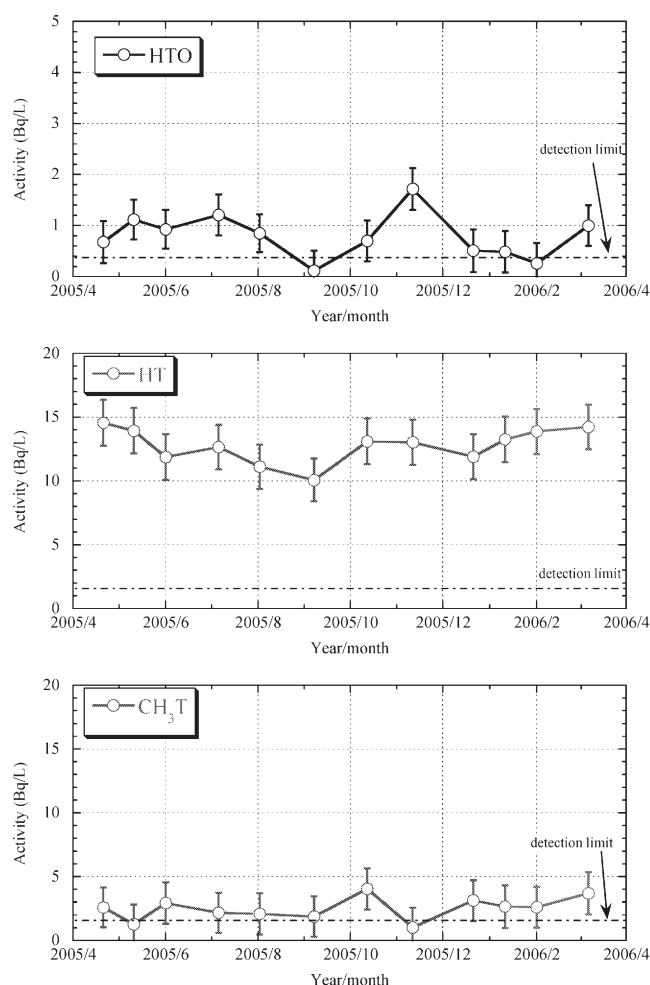


Fig. 1: Atmospheric tritium concentration in Toki area

### References

- 1) K. Shinotsuka, *et al.*, Journal of Radioanalytical and Nuclear Chemistry, **258**[2], (2003), 233
- 2) T. Uda, *et al.*, Fusion Engineering and Design, **81**, (2006), 1385

§13. A Simplified Method for Tritium Measurement in the Environmental Water Samples

Sakuma, Y.,  
Iida, T. (Graduate School of Eng., Nagoya Univ.),  
Ogata, Y. (School of Health Sciences, Nagoya Univ.),  
Kakiuchi, M. (Faculty of Science, Gakushuin Univ.),  
Torikai, Y. (HRC, Toyama-Univ.),  
Satake, H. (Faculty of Science, Toyama-Univ.)

1. Abstract

We have been studying the measurement of tritium concentration in the environmental water samples these several years. Liquid scintillation counting with the electrolyte enrichment is the most popular method to measure the low-level tritium samples. The conventional procedure was however very complicated and took a lot of time. Then, we have developed a simplified and accurate procedure with the electrolysis enrichment<sup>1)2)3)</sup>. By means of this procedure, we have been measuring tritium concentration of several samples for three years. Moreover, in order to shorten the required time keeping the accuracy, we have improved the procedure.

2. Experimental and Results

The measurement was carried out as follows;

**SAMPLING ⇒ RO FILTRATION ⇒ ENRICHMENT ⇒ LS COCKTAIL MIXING ⇒ LS COUNTING**

The measurement flow was the same with the previous one, but the enriching time and the LS counting time were shortened keeping the accuracy.

ENRICHMENT : 3 days → 2 days

LS COUNTING: 1,500 min → 1,000 min

To determine the tritium enrichment factor, the heavy water concentration was also measured before and after the enrichment using a very accurate density meter. The results were shown in Fig.

1. All most all of the measured values were between 0.05 and 0.5 Bq/kg. The values were always slightly decreasing.

3. Conclusion

(1) The measurement time were successfully shortened keeping the accuracy.

(2) The values were 0.05-0.5 Bq/kg-water except vapor samples.

The values were always slightly decreasing.

References

1) Y. SAKUMA et al., Proc. 10<sup>th</sup> ICRP, P-4a-248 (2000).  
2) Y. SAKUMA et al., J. Radioanalytical and Nuclear Chemistry, 255, No.2 (2003) 325.  
3) T. KOGANEZAWA et al., Radioisotopes, 53, No.5 (2004) 277.

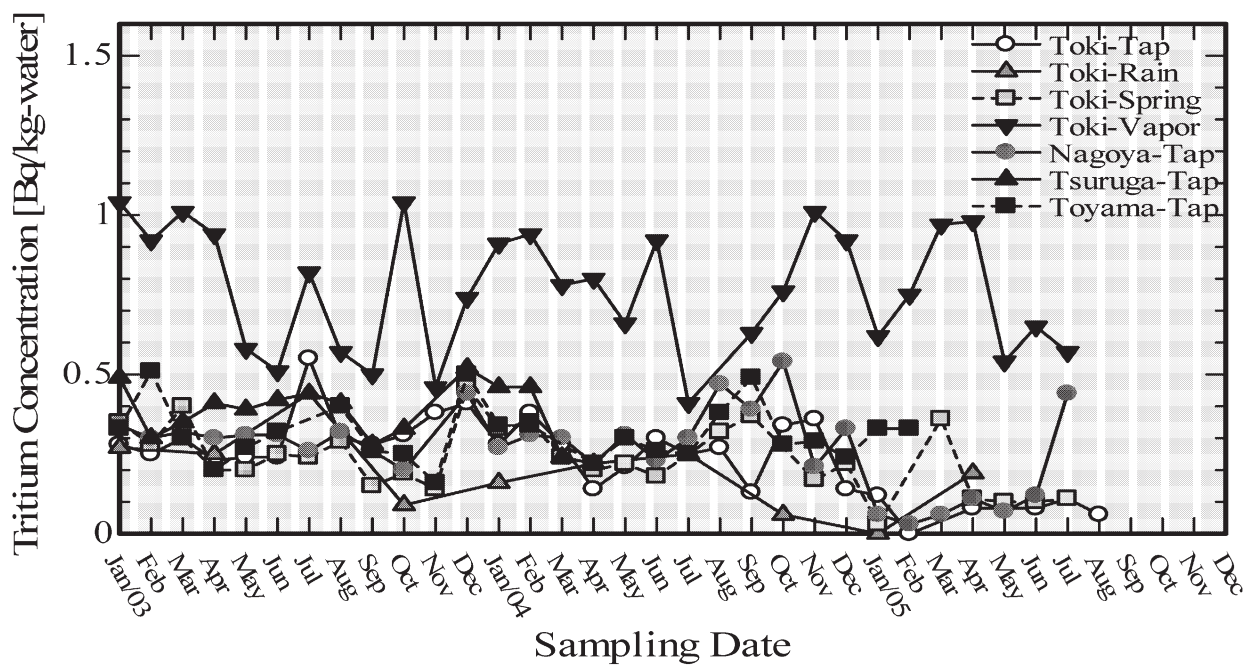


Fig. 1 Results of measurement.

## §14. Field Measurement in Hi-Level Multiple Source EM Environment

Kamimura, Y. (Dept. Engin., Utsunomiya Univ.)

In the nuclear fusion experiment facilities, there are the strong static magnetic fields, the ELF magnetic fields generated from the power supply equipments, and the leakage electromagnetic radiation such as various plasma heating devices of 10 MHz - 168 GHz. The electromagnetic radiations for the plasma heating are generated attended with the burst, and they show the spectra with wide frequency-range. These peculiar electromagnetic environment cause a potential error in the measurement result of the electromagnetic field measuring instrument. The purpose of this study is to establish the measurement technique whose reliability is higher than the employee's safety evaluations under such a special, high-level, electromagnetic environment. Moreover, the problem of an electromagnetic, environmental measurement is dug up, arranged, and the countermeasure method is examined.

### Method

Magnetic field strength is measured with two or more measuring instruments such as ELF-LF magnetic field meter (ELT-400), ELF-VLF electromagnetic field meter (EFA-3) and portable accumulative magnetic field meter (EMDEX-II). These results are compared mutually, and analyzed. For comparing ICNIRP guideline<sup>1)</sup> with the magnetic field environment of multifrequency or complex waveform direct, we have used the STD mode of ELT-400. To obtain the frequency spectrum of the observed magnetic field, the output of ELT-400 has been sent to a digital oscilloscope, and analyzed by its fast Fourier transform function.

### Result

As a result of the investigation, the maximum of the magnetic flux densities in the power supply room for the coils is 86.7  $\mu\text{T}$  in the vicinity of power-supply unit. It exceeds the occupational exposure restriction (about three times) considering the harmonic though it is a level that slightly exceeds public exposure restriction (83.3  $\mu\text{T}$ ) of the ICNIRP guideline if the waveform of the magnetic field is only fundamental harmonic. However, the magnetic flux density in the area that a general person enters does not exceed the public exposure restriction even if the harmonic is considered.

In the ELF magnetic field measurement in the motor-generator room for NBI, the magnetic flux densities during the acceleration are higher than that during the power generation. The magnetic flux density doesn't exceed the public exposure restriction even if approaching

motor-generator up to 120 cm. The harmonic of 60 Hz or more has not been generated.

The IC card reader of the entrance management system generates the magnetic field of 16.6 Hz for the power supply and of 125 kHz for the data communication. When we have probe approach the card reader most, the magnetic flux density exceeds the occupational exposure restriction. The electromagnetic interference to EMDEX-II that we worried before has no problem.

The effect on measured value of EMDEX-II with an electric carpet is examined, it is found as follows: [1] when laying it down on an electric carpet, the highest value is shown, [2] the maximum value on an electric carpet becomes about 80  $\mu\text{T}$ , [3] in the check experiment using ELT-400, the measured value decrease about 1/5 of EMDEX-II because the probe size is larger.

### Discussion

It is necessary to refer to the statement of ICNIRP in 2003 to evaluate the magnetic field exposure of a multifrequency in the frequency band up to 100 kHz.<sup>2)</sup> It is possible to execute it easily using the STD mode of ELT-400.

In the power supply room for the coils, though there is no problem in the general visitor route, the employees should carry the measuring instrument that has the STD mode when they enter the room for the check.

When the magnetic field is measured in the motor-generator room for NBI (5 Hz - 60 Hz), it is necessary to pay attention so as not to cut the frequency of 30Hz or less. An exact measurement cannot be expected with EMDEX-II.

EFA-3 and EMDEX-II are unsuitable to measuring the magnetic fields of the card reader of the entrance management system because the frequency range does not match. It is necessary to measure it paying attention to not cutting the frequency component of 30 Hz or less using ELT-400.

Note that the measured value can reach the public exposure restriction on an electric carpet when the employee carries about EMDEX-II and is monitoring the exposure to the magnetic field.

### Reference

- 1) ICNIRP: "Guidelines for limiting exposure to time-varying electric, magnetic and electromagnetic fields (up to 300 GHz)," Health Physics, **41**, 4 (1998) 449-522
- 2) ICNIRP Statement: "Guidance on determining compliance of exposure to pulsed and complex non-sinusoidal waveforms below 100 kHz with ICNIRP guidelines," Health Physics **84**, 3 (2003) 383-387



§15. Measurements of Static and Variable Magnetic Fields in a Large Plasma Experimental Facility

Uda, T., Takami, S., Obayashi, H., Kamimura, Y. (Utsunomiya University)

The safety guidelines for electromagnetic fields namely non-ionizing radiation has been proposed by the International Commission on Non-ionizing Radiation Protection (ICNIRP) and the other organizations. Although health affect of non-ionizing radiation is not clear it would be useful to measure electromagnetic fields around a large magnetic plasma experimental facility for development of nuclear fusion. The LHD is the largest super conductive plasma confinement device with strong static magnetic field and not less magnetic field is leak out around the device. Except the static magnetic fields caused by the superconducting magnetic systems, many electromagnetic devices are applied for fusion plasma experiments. Various frequencies of electromagnetic devices are used like NBI and its electric power source of a motor generator (60Hz), heating systems of ICRF (25-100 MHz), and ECH (84-168 GHz). Also for discharge cleaning, resonance frequency (2.45 GHz) system is used. As above mentioned, static magnetic field and wide spectrum of frequencies electromagnetic waves are concerned. Safety issues seem to be not only strong electromagnetic field but also complex of static magnetic field and variable frequencies of magnetic fields, which are from extremely low frequency (ELF) to high frequency. To establish the safety management system for workers in the plasma experimental facility, electromagnetic fields around the LHD and related devices have been measured. Leakage of static magnetic field strength has been measured since the first plasma experiment of the LHD in 1998. The fixed monitoring point is 23 m far from the center of the LHD in south direction. The measurement instrument is Gauss Meter 9900 (F.W. Bell Co) and three axial probe ZOA99-3208

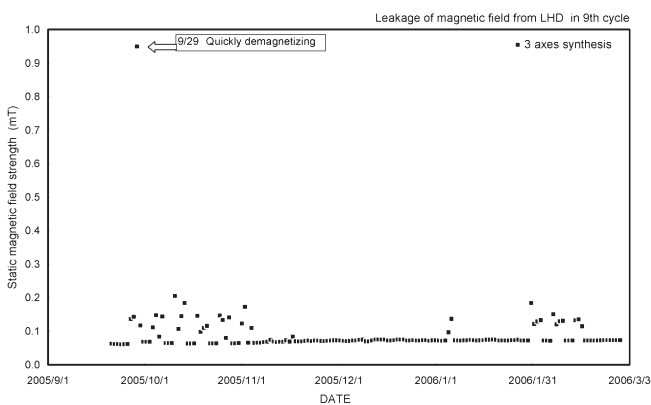


Fig.1 Leakage of static magnetic field measured outside of the LHD hall.

The leakage of magnetic field strength measured in the 9<sup>th</sup> cycle of the LHD experiment is shown in Fig.1. Background on not-operation period is about 0.06 mT, which is a double of terrestrial magnetic field. It is increased by magnetization of steel materials in the monitoring room. When the LHD plasma magnetic field is 3 T, it increased to 0.1 -0.2 mT. As major issues of the super conducting magnetic coil system, it decreases quickly for protection of the coil systems on quenching or on abnormal event occurrence. According to our experiences magnetic field strength at the fixed point was spontaneously increased to about 0.9 mT on such a coil protection mode. When looking at the measured data in detail, small variation of less than 0.01 mT was observed according to the local island divertor (LID) operation.

Except the coil systems of the LHD, there are some kinds of static magnetic field producing devices. Moreover there are many kinds of ELF related devices in the laboratory. Major devices are electric power source for super conducting magnetic coils system and a motor generator for power supply to the NBI device. The ELF magnetic field strength near the electric equipments in the laboratory was distributed around 0.2-40  $\mu$ T.

As previously mentioned there are many types of microwave generator for plasma heating such as ICRF and ECH and for discharge cleaning of plasma facing walls. We begin continuous monitoring around the ICRF wave generator using a data logging system. The measurement instrument is EMC-300 and three axes electric field probe Type 18 (Narda Co.). The logging time is 5 Hz, 0.2 sec, and mean value of 1 sec are shown in Fig. 2. The maximum electric field observed is 20 V/m, but the 6 minute mean value is less than that, of which maximum value is 10 V/m that is about 1/6 of the occupational regulation level proposed as guide line by the ICNIRP. Exposure dose measurement and evaluation considering such high frequencies of electromagnetic fields seems to be important safety management issues. To investigate the safety management system, we study in collaboration with Nagoya Institute of Technology and Utsunomiya University.

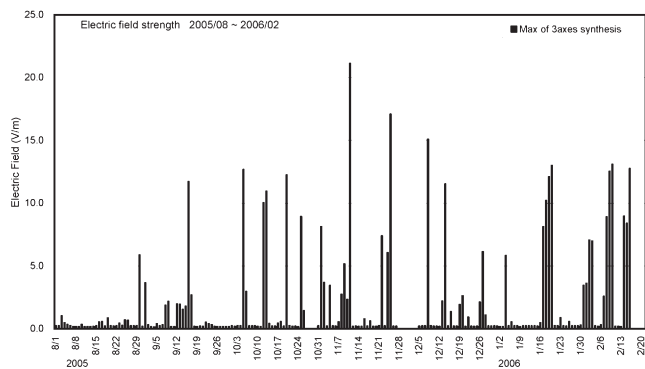


Fig.2 Electric field strength, mean of 1 sec, monitored around the ICRF electromagnetic wave generator in the period of 9th cycle.

## 12. Computer and Information Network Center

The Computer and Information Network Center was established in order to meet the various computational needs for numerical computations, simulation studies, data processing, and data access in the area of plasma physics, nuclear fusion research, and their related fields. Furthermore, the Center provides the network environment suitable for research life.

The Center has been mainly supporting the Large Helical Device (LHD) Experiment Project and its related Simulation Project, and the Research Collaboration with worldwide universities and institutes.

NIFS has two computer systems. One is “LHD Numerical Analysis System” which serves mainly for the LHD Experiment Project and is operated by the Center. The other is “Plasma Simulator”, NEC SX-7/160M5, which serves mainly for the Large-Scale Computer Simulation Research Project and is primarily operated by Theory and Computer Simulation Center.

The LHD Numerical Analysis System was replaced from NEC SX-5/6B with 6 CPUs to NEC SX-8/32M4 with 32 CPUs in January, 2006. The schematic view of the new

system is shown in Figure 1.

Since the establishment of NIFS, the Center has also made significant improvements in the LAN and WAN. And now, the campus information network of NIFS serves as an infrastructure of information, and is becoming indispensable to the research life.

### 1. LHD Numerical Analysis System

Our computer system was replaced in January, 2006. Table 1 presents performances of the previous and present systems. The amount of the memory and processing speed are 512GB and 512GFLOPS respectively, so that peak performance of the present computer system is more than 10 times faster than that of the previous one and distributed parallelized computations using multiple nodes are possible as well as auto-parallelized computations in one node at this system.

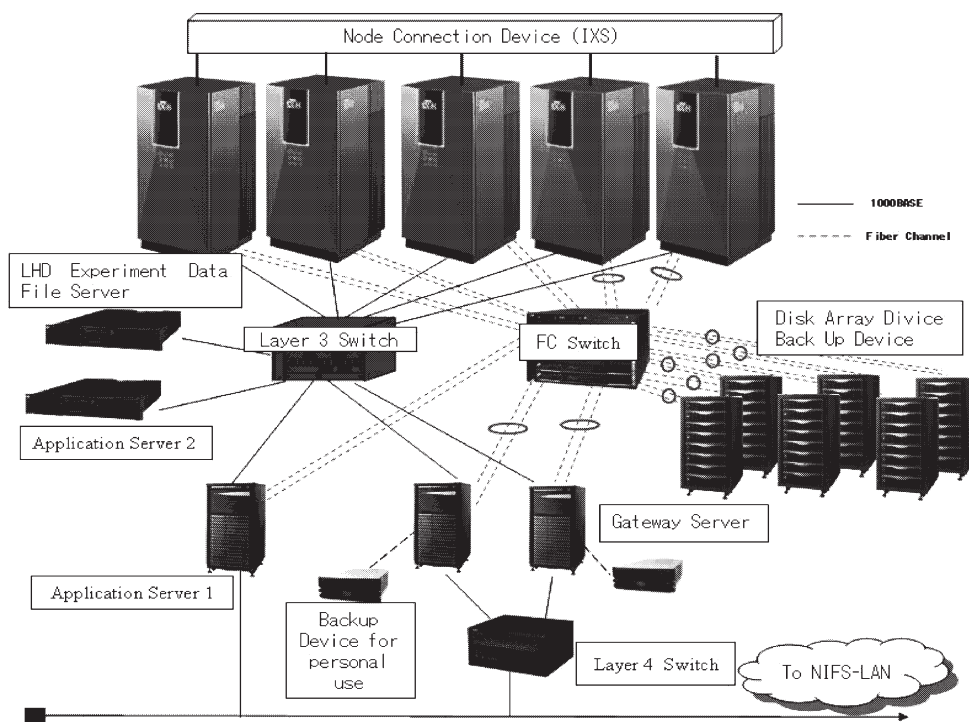


Fig. 1: Schematic View of LHD Numerical Analysis System

This architecture can provide a variety of que classes: 12 kinds of ques exist, in which users can use from 4GB and 1 CPU up to 512 GB and 32 CPUs using 4 nodes. The CPU server connected by Fiber Channel to the high-speed magnetic disk system (RAID) with 40TB storage. Two gateways as the front end processor are provided that the users can submit their batch jobs using NQSII through the NIFS-LAN from all over the world. The application servers and the LHD Experiment data file server are also provided for the analyses of the simulation results and for the data processing of LHD experiment, respectively. The local manual for the present computer system, FAQ (Frequently Asked Questions), and other any information associated with the system are presented on Web (<http://ccweb.nifs.ac.jp>).

The monthly used CPU time of the previous computer system from April to December 2005 are shown in Figure 2. The total operation time, the total used CPU time, the ratio of CPU time to the operation time, and the numbers of executed jobs for the same period with Figure 2 are summarized in Table 2. The number of registered users is 160 in 2005 and 171 in 2006. The averaged ratio of CPU time to the operation time is 46.5% in 2005 and 54.6% in

2006. It is noted that these ratios are not so high before and after the replace in general. Operation of the present system is almost stable, and hence it is expected that both the number of registered users and the averaged ratio of CPU time to the operation time increase.

Purpose	Previous System	Present System
Calculation Server	SX-5/6B (48GB) 6CPU Mem:64GB	SX-8/32M4 (512GF) 32CPU Mem:512GB (4 nodes) SX-8/8M1 (128GF) 8CPU Mem:128GB Node: IX connectionS (16GB/s one direction)
High Speed Disk Device	1.2TB (SX-5 direct connected)	10TB iStorage S2400 (SAN-GFS)
Large Volume Disk Device	NONE	10TB iStorage S2400 (SAN-GFS)
Backup Device	STK L700 10TB	20TB iStorage S2400 (SAN-GFS) 19.2TB (Uncompressed) iStorage T40A (2 systems)
Application Server 1 Application Server 2	TX-7/L1000 PA8500 (440MHz) 2CPU Mem:4GB	TX7/i6010 Itanium2 (1.6GHz) 2CPU Mem:16GB NX7000/rp3410-2 PA8800 (800MHz) 2CPU Mem:2GB
Gateway Server	TX7/L1000 PA-8500 (440MHz) Mem:1GB 3 systems	TX7/i6010 Itanium2 (1.6GHz) 2CPU Mem:4GB 2 systems

Table 1: Properties of the Previous and the Present LHD Numerical Analysis System

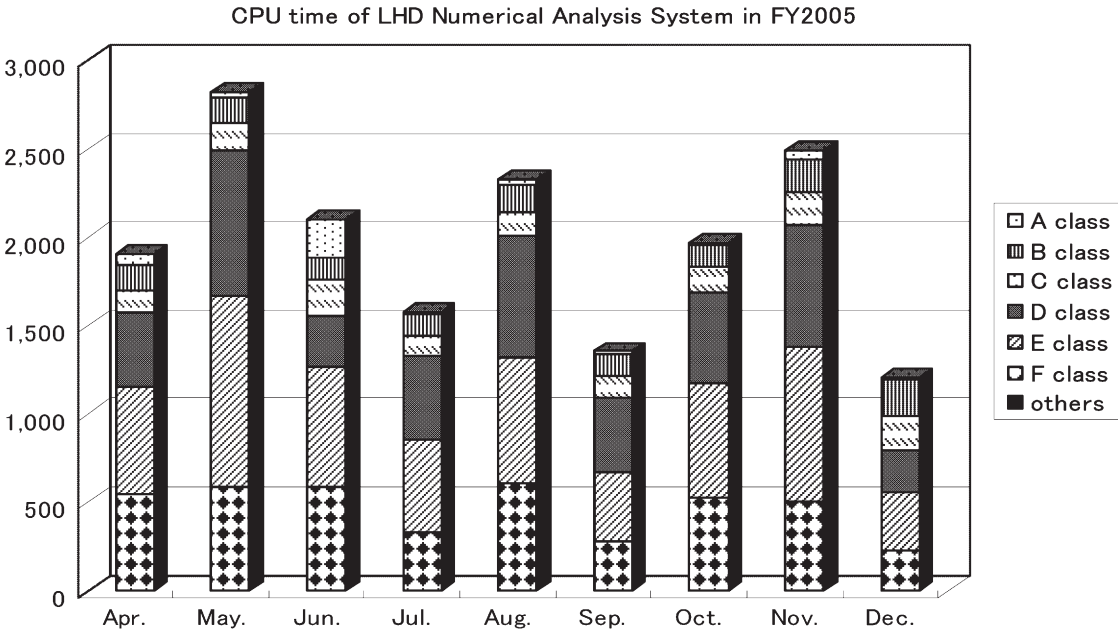


Fig.2: Operation Overview of SX-5 in FY 2005

A: operation	B: cpu time	Ratio: B/6A	Number of jobs
6,380:52	17,791:38	46.5%	41,634

Table 2: Summary of SX-5 Operation in FY 2005

## 2. NIFS Campus Information Network

The advanced NIFS campus information network called "NIFS-LAN" has been contributed to development of nuclear fusion research as the information infrastructure. NIFS-LAN consists of three autonomous clusters which have the different purpose and usage as follows;

- 1) Research Information Cluster is the network of general use, and covers the campus whole region.
- 2) LHD (Large Helical Device) Experiment Cluster is provided for LHD experiment, and covers the building relevant to LHD experiment.
- 3) Large-scale Computer Simulation Research Cluster is provided in order to do large-scale computer simulation research efficiently.

NIFS-LAN was built as ATM network using ATM (Asynchronous Mode) switches in the 1995 fiscal year, the 1996 fiscal year, and the 1998 fiscal year. Introducing the Gigabit network system in the 2001 fiscal year, NIFS-LAN was shifted to the Gigabit network system from ATM switching system. The gigabit network system has the speed of 1Gbps in the basic portion, and hosts for users are connected by 100Mbps, respectively.

NIFS-LAN is connected to Super-SINET (Super Science Information Network, managed by National Institute for Informatics), for the campus LAN and for the collaboration network using Super-SINET. In order to keep the security of NIFS-LAN, the highly efficient Firewall equipment is installed at the connection point of NIFS-LAN and Super-SINET. As shown below, NIFS-LAN with high-performance and high-security provides the user with comfortable and safe network environment.

### 1) Internet connection

NIFS-LAN is connected to Super-SINET by eight 1Gbps circuits. One circuit is used for Campus LAN and seven circuits are used for collaboration network using Super-SINET.

### 2) Improvement in security

In order to keep high-level security, NIFS-LAN introduced Firewall equipment, IDS (Intrusion Detection System), and VPN (Virtual Private Network). The One-time-password system is also worked, in order to make

LHD experiment data access from external researchers. Moreover, in order to protect of the attack from the outside, the mail server with an anti-computer virus function and a spam mail removal function works.

In the 2005 fiscal year, in order to raise a security level, the following things were performed.

- a) The schools and seminars about security were held several times.
  - b) The user was provided with security information by e-mail and Web.
  - c) The quarantine room for network security worked and support of quarantine processing of users was performed.
  - d) The network connected to the commercial ISP (internet service provider) for visitors of NIFS was built.
- 3) Reconstruction of Network for the collaboration using Super-SINET

The collaboration using Super-SINET was started in the 2001 fiscal year. The remote station for "LHD experiment remote participation" was installed in Tohoku University, University of Tokyo, Tokyo Institute of Technology, Nagoya University, Kyoto University, Hiroshima University and Kyushu University.

The subjects of "remote use of Supercomputer" and "all Japan ST (Spherical Tokamak) research program" were newly added to the collaboration using Super-SINET in the 2005 fiscal year. To fit with use of new subjects, the network for collaboration using Super-SINET was reconstructed. The users of the subjects "LHD experiment remote participation" and "all Japan ST research program" were provided the network environment which can be communicated mutually between remote stations. The users of the subject "remote use of Supercomputer" were provided with the network environment which can use the supercomputer system of NIFS efficiently from a remote place. This network was a closed VPN (Virtual Private Network) on Super-SINET, it is contributed to progress collaborations.

The connection between NIFS-LAN and the external networks is shown in Fig. 3. The block diagram of NIFS campus information network is shown in Fig. 4.

(Horiuchi, R.)



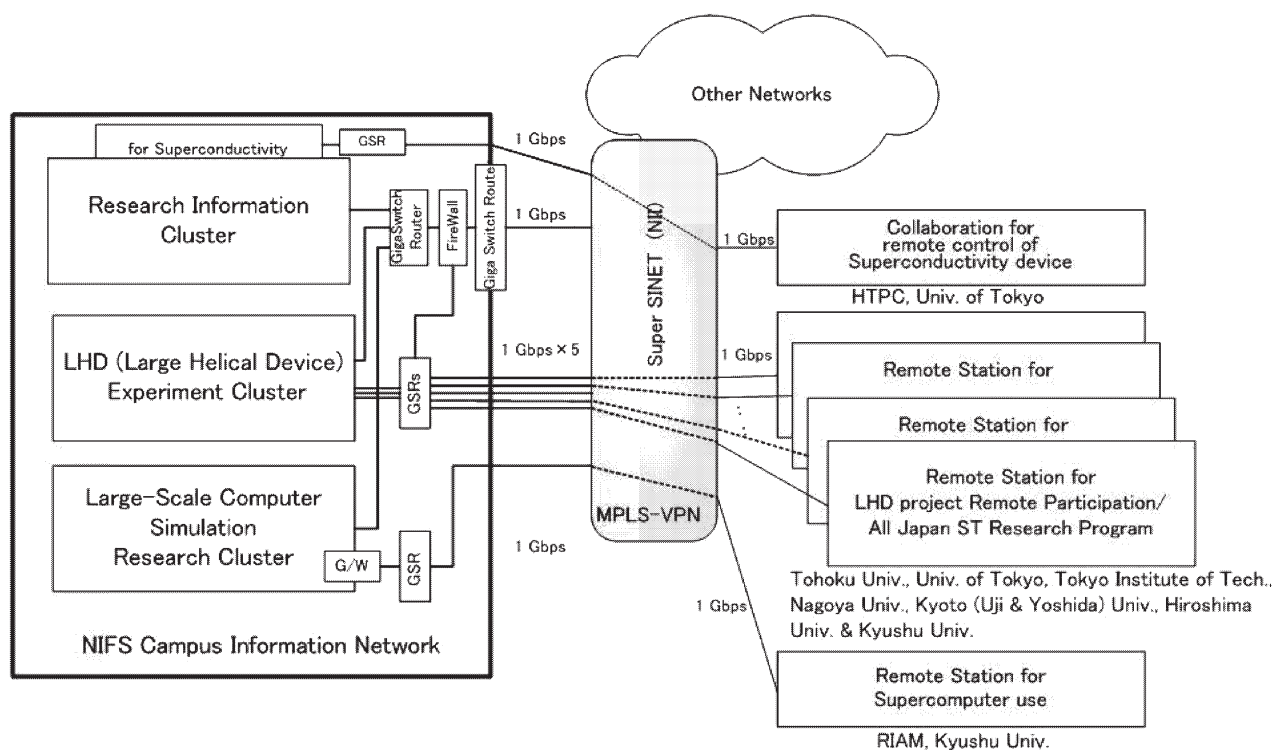


Fig. 3: External Connection of NIFS-LAN

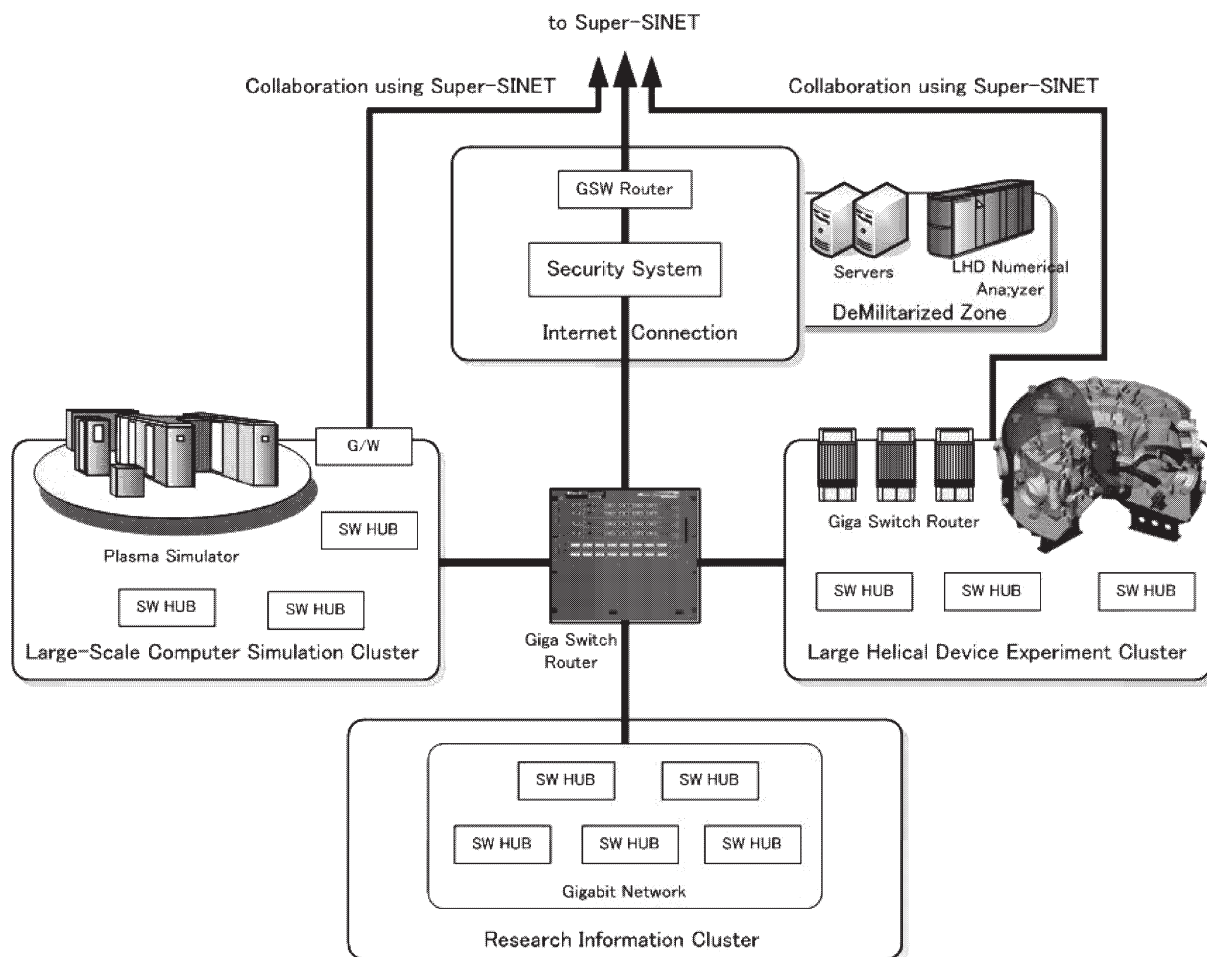


Fig.4: Block Diagram of NIFS Campus Information Network (NIFS-LAN)

## 13. Bidirectional Collaborative Research Program

This new collaborative research program started in 2004 under the support of the Ministry of Education, Culture, Sports and Technology to enforce the activities of nuclear fusion research in universities after the Committee of the Science Subdivision under the Council for Science and Technology required to execute their plan by promoting collaborative research. This new policy of the committee is summarized in the report “Policy for executing Japanese nuclear fusion research”, where it is pointed out that continuous scientific research activity is necessary for a comprehensive understanding of toroidal plasma physics under the parameters which can be extrapolated to the fusion reactor. Therefore the Large Helical Device (LHD) has been selected as one of four principal fusion research programs in Japan, and NIFS is expected to expedite collaborating research. It is also noted in the report that the universities must contribute to the study of important issues in nuclear fusion research, such as the function of electrostatic potential on plasma confinement, high beta plasma physics, optimum magnetic configuration for plasma transport, steady state plasma generation, and so on. NIFS is requested to play a leading role in the execution of these studies among universities as an inter-university research institute.

A bidirectional collaborative research program has been set up so as to accomplish the role of NIFS proposed above. In past collaborative programs, university researchers went to NIFS and joined the research activity at NIFS. But in this program, the opposite movement of researchers is enabled, so that NIFS researchers can go to the universities and join the activities at the universities. Hence a more efficient use of resources in both facilities becomes possible and the synergetic effect is expected. It involves four major university research centers; Plasma Research Center, University of Tsukuba / Laboratory of Complex Energy Process, Institute of Advanced Energy, Kyoto University / Institute of Laser Engineering, Osaka University / Advanced Fusion Research Center, Research Institute for Applied Mechanics, Kyushu University. In this collaborative program, the researchers of NIFS and of those four research centers can

move back and forth to each other to collaborate on the same research subject. In addition to this, each research center can have its own programs for using its major facility so that the researchers of other universities can come and join. It is unique and important that all these activities are supported financially as function of the NIFS bidirectional collaborative research program. The subjects of the bidirectional research program are subscribed from all over Japan every year as one of the three categories of the collaboration research program of NIFS, and the collaboration committee, which is organized under the administrative board of NIFS, adjudicates and selects the subjects.

One of the important roles of the collaboration committee is to make a plan for evolving the research activities in universities according to the guide line of “Policy for executing Japanese nuclear fusion research”. The change of the project of Kyushu University is the first result. It had been discussed through 2004-2005 including the way of sharing budget, and the conclusion was made. The main device TRIAM 1-M, which was a superconducting middle-size tokamak holding a record of long pulse operation among tokamaks in the world, was shut down. A new device QUEST, which is a normal conducting small spherical tokamak, has started its construction as a new program in Bidirectional Collaborative Research. The objective of QUEST is to study the high-beta long-pulse operation in spherical tokamak. The construction will be finished in 2007, and the experiments is planned to be conducted by the executing board which will include the researchers in Japanese universities other than Kyushu University.

In this year, fifty two subjects were adopted in this category, among which were 14 at Tsukuba University, 8 at Kyoto University, 14 at Osaka University, and 16 at Kyushu University. All of these collaborations were carried out successfully.

(Komori, A.)

## §1. Study of Potential Confinement Mechanism via Plasma Visualization Technology

Mase, A., Kogi, Y., Ignatenko, M., Kudo, K. (KASTEC, Kyushu Univ.),  
Yoshikawa, M., Nakahara, A., Itakura, A., Hojo, H.,  
Cho, T. (PRC, Univ. Tsukuba),  
Nagayama, Y.

In tandem mirrors, an electrostatic potential is created in order to improve axial confinement. The radial electric field due to this potential causes an  $\mathbf{E} \times \mathbf{B}$  plasma rotation in the direction of the ion diamagnetic drift velocity. The verification of the effect is one of the most critical issues to understand the physics basis for recent confinement improvement. Understanding the mechanism of this effect requires the use of sophisticated diagnostic tools for measurement of plasma profiles and their fluctuations. Significant advances in microwave and millimeter wave technology have enabled the development of a new generation of imaging diagnostics as visualization tool of plasma parameters. This report describes the development of millimeter wave imaging diagnostics (a phase imaging interferometer) applied to the GAMMA 10 tandem mirror.

The details of the phase imaging interferometer was described in elsewhere.<sup>1)</sup> The quadrature detection system provides the phase difference between two intermediate frequency (IF) signals obtained by mixing the transmitted signal (RF) and the local oscillator signal (LO). The phase difference is proportional to the line density of plasmas. In the last fiscal year, the quadrature phase detector is limited to 4, at least 4 plasma shots with good reproducibility are needed to obtain a full 2D profile. However, in FY2005, we have increased the number of phase detector to use all of the detector channels in one plasma shot.

The changes in the 2D line-density profiles for the case of high and low ECRH powers are shown in Fig. 1. The magnetic field strength is also shown in Fig. 1. Before the application of the ECRH power ( $t=164$  ms), the electron density is distributed along the magnetic field lines. When the ECRH power is applied at  $t=180$  ms, the plug potential is created near the position of  $z=961$  cm where the magnetic field strength equals to 1 T. It is noted that the density profile in the core region decreases during the injection of the ECRH power. At the outside of the plug potential ( $z>961$  cm), the plasma flow is disappeared due to the formation of the confining potential. When the ECRH power is high, the position is shifted. The position of the plug potential may be shifted for the case of high power ECRH. When the ECRH power is turned off at  $t=190$  ms, the confining potential disappears, and a short burst appears in the line-density signal corresponding to the axial drain of the plasmas. The variation of the profile in the axial direction is caused by the change in the magnetic field. The resolution of the interferometer is estimated to be less than 1/200 fringe.

The imaging array antennas and intermediate frequency (IF) systems, in the frequency range of  $f=70$  GHz and 1-4

GHz respectively, have been designed and fabricated by using microwave integrated circuit (MIC) technology to improve the spatial resolution and the signal to noise ratio of the imaging system.<sup>2)</sup>

We have also performed the numerical study of microwave imaging reflectometry (MIR) for the GAMMA 10 plasma.<sup>3)</sup> The main results are as follows. Depending on the cutoff curvature and spreading of reflected beam, the size of optics is the main limitation factor deteriorating MIR performance. Both conventional and imaging reflectometers can measure small amplitude and wave number fluctuations, however, only MIR system can measure density fluctuations with larger amplitude and wave number ( $\Delta n/n_0 > 0.04$ ,  $\Delta k/k_0 > 0.5$ , where  $n_0$  is the mean electron density,  $k_0$  is the incident wave number, and  $\Delta$  denotes those fluctuation components).

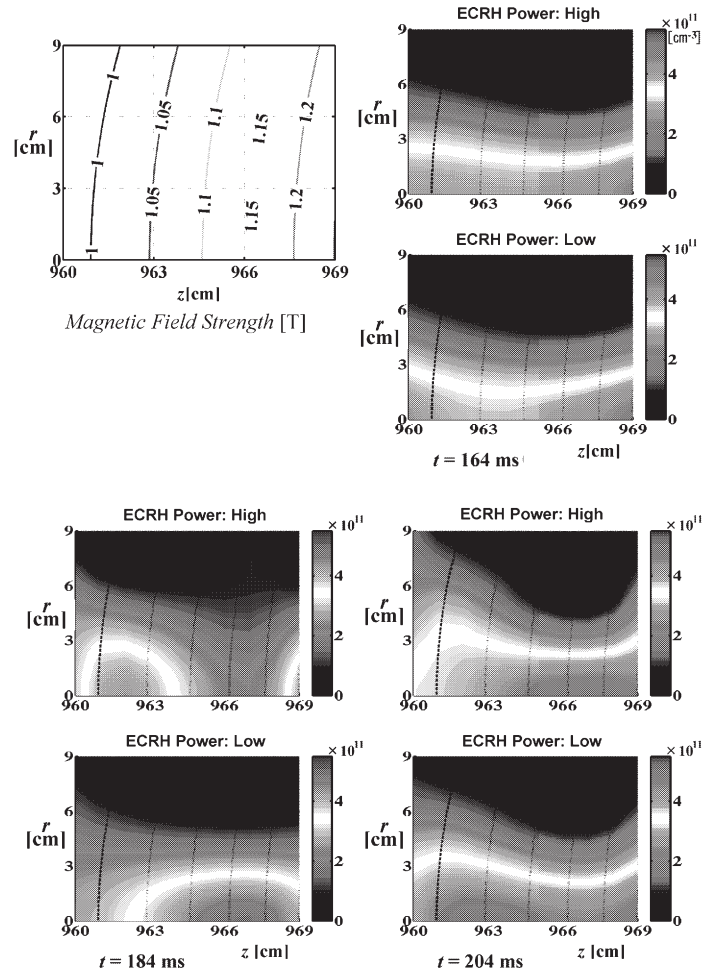


Fig.1. Time evolution of 2D line density profiles.

### References

- 1) Watabe, K. et al., Rev. Sci. Instrum. 73, 2282 (2002).
- 2) Kogi, Y. et al., Proc. Joint 30<sup>th</sup> Int. Conf. on Infrared and Millimeter Waves and 13<sup>th</sup> Int. Conf. on Terahertz Electronics, Williamsburg (2005) pp. 604-605.
- 3) Ignatenko, M., Mase, A., Bruskin, L. G., Kogi, Y., and Hojo, H., to be published in Nucl. Fusion.

## §2. Study of Impurity Ion Radiation Intensity in the GAMMA 10 Plasma

Yoshikawa, M., Kubota, Y., Kobayashi, T., Matama, K.  
(Univ. Tsukuba, PRC),  
Kato, T., Murakami, I.

Time- and space-resolved spectroscopic measurements of impurity ion radiation spectra give us a lot of important information, such as time and space variations of plasma density, electron and ion temperatures, etc. After comparing the collisional-radiative model (CR-model)<sup>1)</sup> calculation results for impurity ion line radiation intensities and those measured by spectroscopic method, we can obtain the impurity ion densities, electron density and temperatures. The aim of this study is to construct the database for plasma spectroscopic diagnostics in the fusion plasmas.

CR-model calculation codes for carbon and oxygen ions developed at NIFS were used in this study.<sup>1)</sup> These codes include the efficiencies for electron impact ionization, excitation, recombination and de-excitation. In the previous reports,<sup>2-4)</sup> we used CR-model calculation code for CII and CIII ions in order to obtain the time dependent CII and CIII ion density radial distributions. We calculated the CR-models for CIV and CV. Then we find that there must be  $C^{+3}$  and  $C^{+4}$  ions in the GAMMA 10 plasma in the core region. Then we set a VUV

spectrometer, which can observe the wavelength range from 50 to 450 nm, in GAMMA 10.

When we will develop the CR-model for each ion species, we have to include the energy levels and transition probabilities of collision cross sections. We used flexible atomic code (FAC) developed by M. F. Gu.<sup>5)</sup> FAC is free software. We calculated the electron impact excitation and ionization cross sections with FAC. We have to evaluate the results of FAC calculation to the database at NIST in order to use the results of FAC for CR-models. Figure 1 shows the comparison of energy levels between FAC calculation results and the NIST data in CII. Figure 2 shows the comparison of transition rates between FAC and NIST. These results show that the FAC is a good agreement with the NIST data within 10 % of error. Then we use the FAC calculation code in order to obtain the energy levels and transition probabilities of collision cross sections for CR-models.

### Reference

- 1) Kato, T., et al.: Fusion Eng. Des., **34-35** (1997) 789.
- 2) Yoshikawa, M., et al.: Annual Report of NIFS, April 2000-March 2001 (2001) 388.
- 3) Yoshikawa, M., et al.: Annual Report of NIFS, April 2001-March 2002 (2002) 374.
- 4) Yoshikawa, M., et al.: Annual Report of NIFS, April 2002-March 2003 (2003) 380.
- 5) M. F. Gu: ApJ., 582 (2003) 1241.

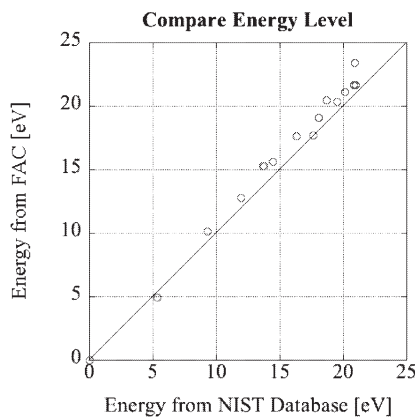


Fig. 1: Comparison between energy levels from NIST and FAC.

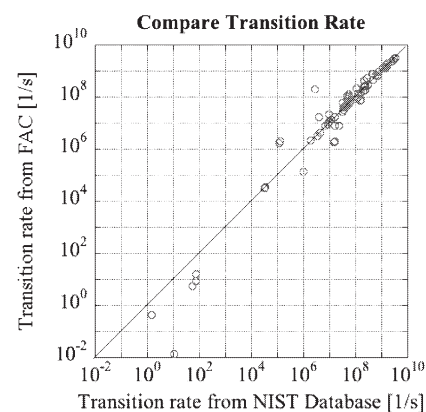


Fig. 2: Comparison between transition rates from NIST and FAC.



### §3. ICRF Wave Excitation and Propagation in the GAMMA 10 Tandem Mirror

Fukuyama, A. (Kyoto University),  
Yamaguchi, Y., Ichimura, M., Higaki, H. (University of Tsukuba)

The waves in the ion-cyclotron range of frequency (ICRF) are widely used for the plasma production, heating, and the stabilization of the magneto-hydrodynamic (MHD) instabilities. In the present tandem mirror experiments, the operation on the high density plasmas above  $10^{19} \text{ m}^{-3}$  is one of the most important subjects. Although the high ion temperature above 10 keV has been realized in GAMMA 10, the density is relatively low on such a high performance discharge [1]. The plasma production depends on the wave excitation in the plasma. In the present experimental conditions, the inhomogeneous scale length of the plasma and the magnetic field configuration is in the same order of the wavelength. Then, the wave excitation is strongly affected by the boundary conditions and the eigenmodes are formed in both radial and axial directions. The formation of the eigenmodes in GAMMA 10 has been studied computationally by using a full-wave code [2, 3].

Recently, a wide-band RF probe system is newly constructed in the GAMMA 10 tandem mirror for studying the eigenmode formations of excited waves experimentally [4]. A bar-type antenna is installed in the peripheral region in the anchor cell. The low power RF pulse is applied to the antenna via a wide-band impedance matching network. The applied frequency is swept between 8 and 20 MHz. The current on the antenna and the excited waves in the plasma are measured. The formation of eigenmodes is described by using the antenna-plasma and plasma-probe complex transfer function. The transfer function can be directly obtained from the complex amplitude of the excited wave by dividing that of the current on the antenna. The aim of this work is to establish experimental method for investigating the eigenmode formations, and to confirm the validity of the results from numerical studies.

In the experiment, the first experimental results are presented for the active diagnostic of the eigenmode formation in the minimum-B anchor cell of GAMMA 10. In this frequency range, several discrete peaks are clearly observed, which are indicating the large enhancement of the

excited wave fields. To confirm the resonant excitation of the eigenmodes, the real and imaginary parts of the complex transfer function are introduced. The frequency dependence of the real and the imaginary part of the complex transfer function are shown in Fig. 1. As shown in the figure, significant changes can be seen on the frequencies of each peak. In this region, launched waves are thought to be primarily on the fast wave branch in the cold plasma theory.

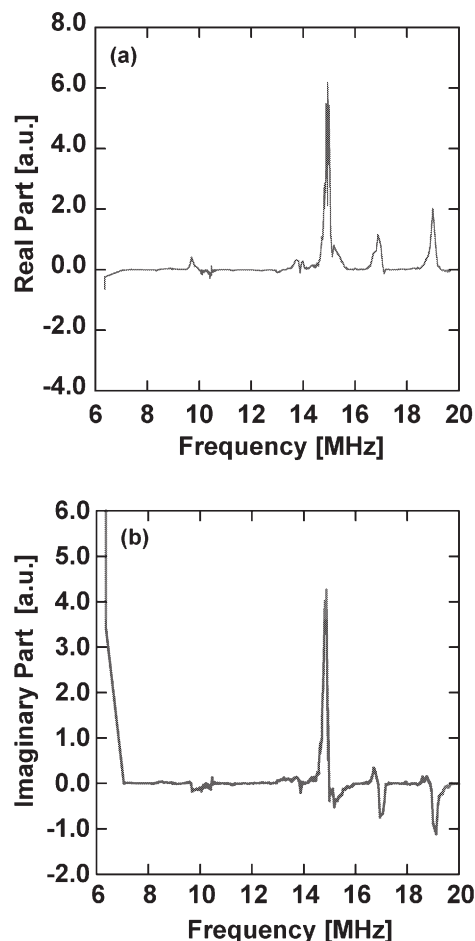


Fig.1 Real (a) and imaginary (b) parts of the complex transfer function between the antenna and the magnetic probe.

- [1] Ichimura, M., et al., Phys. Plasmas, **8**, 2066 (2001).
- [2] Fukuyama, A. and Ichida, A., Proc. of 1996 Int. Conf. on Plasma Phys., Vol.2, p.1342 (1997).
- [3] Yamaguchi, Y., et al., Trans. Fusion Sci. and Tech., **47**, 1536 (2005).
- [4] Y. Yamaguchi, et al., The 5th conference of Asia Plasma & Fusion Association (APFA 2005), TP11, August 29-31, 2005, Jeju (Korea),

#### §4. Development of High Performance Antennas for Electron Heating in GAMMA 10

Saito, T., Tatematsu, Y., Imai, T., Hojo, H. (Univ. Tsukuba, PRC),  
Kubo, S., Shimozuma, T., Yoshimura, Y.,  
Saigusa, M. (Faculty of Engineering, Ibaraki Univ.),  
Notake, T. (Graduate School of Engineering, Nagoya Univ.),  
Nagai, D., Nozaki, K., Machida, N. (Graduate School of Pure and Appl. Sci. Univ. Tsukuba)

##### I. Objectives

The role of electron cyclotron resonance heating (ECRH) in the GAMMA 10 tandem mirror is creating the plasma confining potential and heating of electrons in the central cell. The first objective of this subject is to confirm the performance of the antenna system designed and developed in the last year subject to increase the efficiency of power transmission to the resonance layer in the central cell. Second, this antenna is installed to heat electrons and improve the plasma quality. The third objective is the study of betterment of the antenna system for further high efficiency. For accurate evaluation of the antenna performance, a new apparatus for radiation measurement is started up.

##### II. Method and procedure

Second 500 kW gyrotron with higher power than the first gyrotron has been installed. Then, it is tried to generate high potential with strong electron heating at the East and West plugs. In the central cell, experiments of electron heating are carried out by installing the antenna fabricated last year. A test stand is constructed and the radiation pattern of the antenna is measured. A new antenna system with higher transmission efficiency is developed for central cell ECRH by changing the power transmission path.

##### III. Results

Experiments of high potential generation was done by using the new 28 GHz, 500 kW gyrotron and the plug antenna for an axisymmetric radiation profile on the resonance layer. An ion confining potential of 2.5 kV was obtained. This is a new record and 3.5 times as large as that of three years ago.

In the central cell, the microwave power in TE02 mode delivered from a 200 kW gyrotron was converted to TE11 mode and radiated onto the resonance layer. A clear increase in the diamagnetic signal and in the soft X-ray signal was observed during ECRH as plotted in Fig. 1. This shows that efficiency of ion heating is improved by reducing electron drag. This result is due to the optimization of radiation direction by using a new mirror attached just after the

waveguide and suppression of stray heating in the edge region. The highest bulk electron temperature of 290 eV was attained.

Calibration measurement was carried out by using the newly constructed test stand. The measured power transmission rate well agreed with the design value.

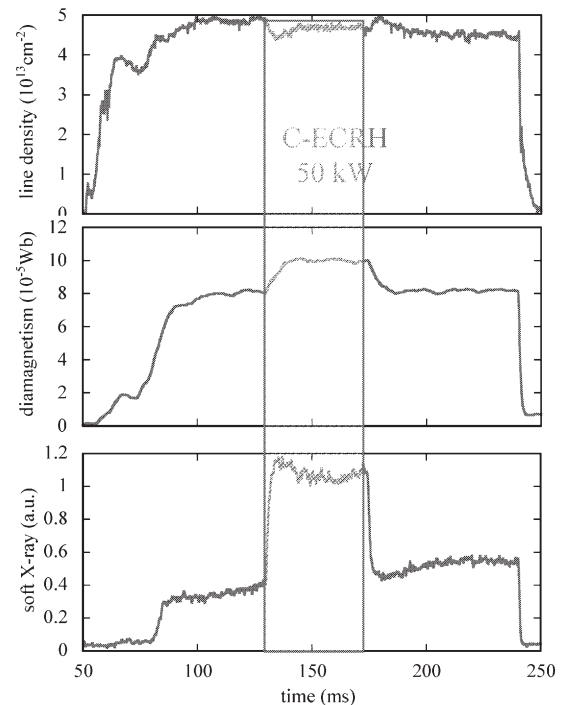


Fig. 1 Waveforms during central cell ECRH. The line density (upper trace), the diamagnetism (middle trace) and the soft X-ray signal (bottom trace).

##### References

- [1] Y. Tatematsu, T. Saito, H. Ikegami et al., Experiment of Fundamental ECRH in the GAMMA 10 Central Cell, *Trans. Fus. Sci. Tech.* **47**, No. 1T, (2005) 257.
- [2] Y. Tatematsu, K. Nozaki, T. Saito et al., Design of Reflecting Mirrors for Electron Cyclotron Wave Launching System in GAMMA 10, *Jpn. J. Appl. Phys.* **44**, No. 9A, 6791 (2005).
- [3] Y. Tatematsu, T. Saito, K. Nozai et al., Power up for ECRH in the GAMMA 10 Tandem Mirror, *EU-JA-US Workshop on RF Technology Exchange*.
- [4] Y. Tatematsu, T. Cho, H. Higaki, et al., High-Power ECRH Experiments in the GAMMA 10 Tandem Mirror, *5th General Scientific Assembly of Asia Plasma and Fusion Association*.

## §5. Propagation and Radiation of Cyclotron Waves and Excitation of Fluctuations Due to High Power Plug ECRH

Hatakeyama, R., Kaneko, T., Takahashi, K.  
(Dept. Electronic Eng., Tohoku Univ.),  
Saito, T., Tatematsu, Y., Yoshikawa, M.  
(Plasma Res. Center, Univ. Tsukuba)

An electron cyclotron wave (ECW) is an important plasma wave in the fields of basic plasma physics, thermonuclear fusion, and some applications. Especially, high power electron cyclotron resonance heating (ECRH) is hoped to be the most effective method for the formation of thermal transport barrier in tandem-mirror devices,<sup>1)</sup> where localized strong electron heating in the perpendicular direction against the magnetic-field lines is demanded. Although the localized wave absorption is necessary for efficient and strong electron heating as mentioned above, the Doppler shift effect by high energy electrons expands the cyclotron resonance region, namely, broadens the wave absorption region.

On the other hand, it was reported that a left-hand polarized wave (LHPW), which has been believed not to be related to ECR, is also unexpectedly and sharply absorbed near the ECR point through the mechanism of polarization reversal.<sup>2,3)</sup> In addition, the damping region of the LHPW is found to be more localized than that of the right-hand polarized wave (RHPW). When this new damping mechanism of the ECW is applied to the efficient electron heating in large fusion devices such as the tandem-mirror device using the high power ECRH, it is necessary to clarify the nonlinear effects of the strong wave field on the propagation and radiation of the ECW. Based on these backgrounds, the purpose of the present work is to clarify the propagation and radiation characteristics of the ECW, including the nonlinear effects such as parametric decay which can cause the degradation of the heating efficiency.

Experiments are carried out with a plasma in the west plug/barrier cell of the GAMMA10 tandem mirror. The plasma is produced in the central solenoid region by radio-frequency (RF) wave heating, and a potential barrier created by ECRH in the plug/barrier cells at the machine ends prevents the plasma from flowing out along the field lines. The ECRH power at 28 GHz is delivered to the fundamental resonance layer of 1 T for the plug and to the second harmonic layer of 0.5 T near the mid-plane for the thermal barrier. We have set up a measurement system for receiving and analyzing electromagnetic radiation in the electron cyclotron range of frequencies, which consists of a movable receiver antenna, a heterodyne circuit with a Gunn oscillator (27.9 GHz, 13 dBm), a balanced mixer, and a spectrum analyzer.

Figure 1 shows observed frequency  $\omega_{\text{rec}}/2\pi$  spectra of electromagnetic waves radiated from the plug region in the cases that (a) the plug ECRH ( $\omega_1/2\pi = 28.0$  GHz,  $P_1 = 240$  kW) or (b) the barrier ECRH ( $\omega_2/2\pi = 28.06$  GHz,  $P_2 = 100$  kW) is separately launched. A broadband radiation extending over several hundred MHz above 28 GHz in Fig.1(a) originates from electron cyclotron emission due to the high energy electrons produced by the plug ECRH. Sharp peaks detected at  $\omega_1/2\pi$  labeled by “P” [Fig.1(a)] and  $\omega_2/2\pi$  labeled by “B” [Fig.1(b)] indicate the launched plug and barrier ECRH, respectively.

When these plug and barrier ECRH are superimposed, on the other hand, several sharp peaks are observed around  $\omega_1/2\pi$  and  $\omega_2/2\pi$  at intervals of 20MHz as shown in Fig.1(c). Since this interval frequency is near the ion cyclotron frequency in the plug region, the sharp peaks are considered to be caused by nonlinear interaction between the strong electromagnetic wave for plug/barrier ECRH and an ion cyclotron wave excited in the plasma.

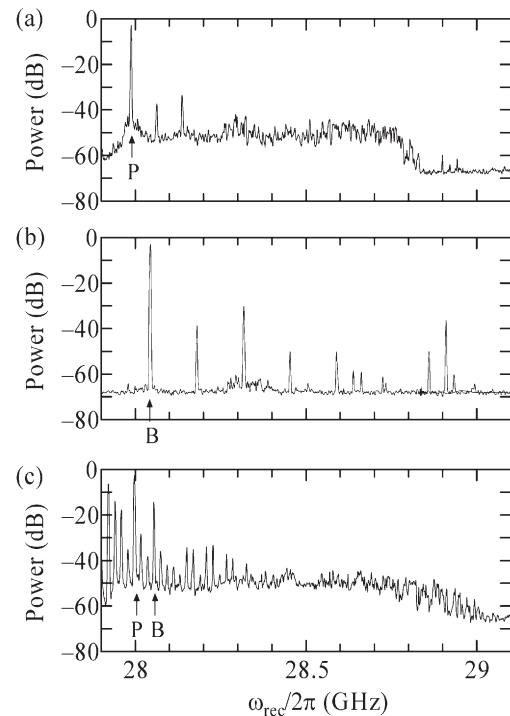


Fig. 1. Frequency spectra of electromagnetic waves radiated at the plug region in the cases that (a) plug ECRH ( $\omega_1/2\pi = 28.0$  GHz,  $P_1 = 240$  kW) or (b) barrier ECRH ( $\omega_2/2\pi = 28.06$  GHz,  $P_2 = 100$  kW) is separately launched, and (c) the plug and barrier ECRH are superimposed.

### Reference

- 1) Saito, T., Ishii, K., Itakura, A., Ichimura, M., Islam, M.K., *et al.* : J. Plasma Fusion. Res. **81** (2005) 288.
- 2) Kaneko, T., Murai, H., Hatakeyama, R., and Sato, N. : Phys. Plasmas **8** (2001) 1455.
- 3) Takahashi, K., Kaneko, T., and Hatakeyama, R. : Phys. Rev. Lett. **94** (2005) 215001.

## §6. ICRF Heating and Ion Acceleration at the Open End in GAMMA 10

Ando, A., Tobari, H., Shibata, M., Hattori, K., Inutake, M. (Dept. Electrical Eng. Tohoku Univ.),  
Ichimura, M., Higaki, H. (Plasma Research Center, Tsukuba Univ.)

Recently, it is expected that many plasma technologies developed in the long-running fusion researches should be utilized in other research fields. Near-future space exploration missions need further investigation of advanced electric propulsion systems which use high density plasma production and acceleration technique. A magnetic nozzle acceleration and ion heating in a fast flowing plasma attracts much attention in such an advanced electric propulsion system. In the Variable Specific Impulse Magnetoplasma Rocket (VASIMR) project, proceeded in NASA as a main engine in manned Mars missions, it is proposed to control a ratio of specific impulse to thrust at constant power.[1] This is a combined system of an ion cyclotron heating and a magnetic nozzle, where a flowing plasma is heated by ICRF (ion cyclotron range of frequency) power and the plasma thermal energy is converted to flow energy via a magnetic nozzle. ICRF heating and acceleration in a fast-flowing plasma has been firstly demonstrated in the HITOP device.[2] For the further development of the thruster, experimental investigation with higher RF power and higher magnetic field is inevitable.

The purpose of this research is to develop a high-power ion heating and ion acceleration technology using a large scale and open magnetic field device. The concept of the thruster well suites an open-ended mirror device, where intensive researches of plasma confinement and RF heating has been progressed. A well-organized large-scale linear magnetic device, GAMMA10, has a number of useful diagnostics and high power RF systems.

Firstly, we have performed experiments to measure ion Mach numbers in an open-end section. In the GAMMA10, there observed an increase of ion temperature in an open-end section under a high ion temperature mode operated with central ion beach heating. In order to investigate a relationship between central ion heating and an ion flow toward an open-end section, an ion Mach number was measured by up-down type Mach probe located at 30cm downstream from the central cell. Though the magnetic field at measurement position is 1Tesla, the Mach probe still under the unmagnetized condition because of the high ion temperature more than 100eV.

Here,  $M_i$  is represented as a ratio of ion flow velocity  $U$  to ion acoustic velocity  $C_s$ . It is related to a ratio of the plasma flow energy  $E$  to its thermal energy  $W$ .

$$M_i = \frac{U}{C_s} = \frac{U}{\sqrt{\frac{k_B(\gamma_e T_e + \gamma_i T_i)}{m_i}}} = \sqrt{\frac{\frac{1}{2} m_i U^2}{\frac{1}{2} k_B(\gamma_e T_e + \gamma_i T_i)}} = \sqrt{\frac{E}{W}}$$

Efficient plasma acceleration can be realized by converting plasma thermal energy to flow energy.  $M_i$  is one of the good indicators of plasma flow properties.

Figure 1 shows ion saturation currents detected by one of collection tips of the Mach probe. Mach number can be estimated from the ratio of the currents detected by facing the collection surface to different angles against the flow. The 0 degree corresponds to the case that the surface faces upstream of the flow direction, and 270 degree corresponds to perpendicular direction. These currents increase linearly with input RF power  $P_{RF}$ , which indicates that the ion Mach number is almost constant in various  $P_{RF}$ . Mach number attains to 2 at plasma center and nearly unity at peripheral region. This result suggests that ion flow velocity increases with the increase of ion temperature, as  $P_{RF}$  increases.

We also measured azimuthal rotation at the central cell region by the Mach probe. Mach number of the rotational flow also attains to nearly unity at the peripheral region.

Experimental researches on the effect of high-power RF heating on the plasma flow and energy conversion by a magnetic nozzle should be pursued further.

### References

- 1) F.R.ChangDiaz, et al., Proc. of 36th Joint Propulsion Conf., (Huntsville,2000), AIAA-2000-3756.
- 2) A.Ando, et al., Proc. the 7th APCST, (Fukuoka, 2004), A2 (2004) 45.

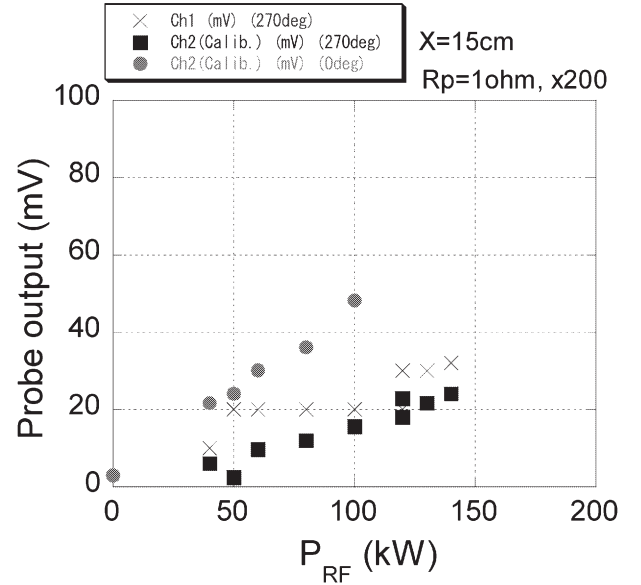


Fig.1 Ion saturation currents as a function of input RF power. The correction surface faces upstream of plasma flow (0 deg. : closed circles) and perpendicular (270 deg. : closed squares). Crosses are un-calibrated data.



## §7. Plasma Polarization Spectroscopy on GAMMA10 Tandem Mirror Plasma

Iwamae, A., Atake, M., Sakaue, A.  
(Dept. Mech. Eng. Sci. Kyoto Univ.),  
Kobayashi, T., Matama, K., Yoshikawa, M.  
(Plasma Research Center, Univ. of Tsukuba)

A departure from the Maxwellian velocity distribution of electron is observed. For example a plateau-shaped electron energy distribution function is observed in the plug region of GAMMA 10 tandem mirror, in the case the electron cyclotron resonance heating (ECRH) is adopted for formation of a plug potential with a thermal barrier<sup>1)</sup>. Since the electrons are accelerated in the direction perpendicular to the magnetic field, the non-Maxwell characteristics may indicate that the electron by ECR microwave in the plasma. When the EVDF is anisotropic, the emission from atoms and ions in the plasma may be polarized.

Emission lines from impurity ions in standard ICH plasma of hydrogen gas were observed in the central region of GAMMA10. Figure 1 shows the schematic drawing of the polarization observation. Three line-of-sights equipped polarization separation optics were located at the height  $y = 90, 0, -68$  mm. The orthogonal polarized components (extraordinary and ordinary rays) of the emission lines from the plasma were separated with a beam-splitting Glan-Thompson prism. Each of the e-ray and the o-ray was focused by a lens onto the entrance surface of an optical fiber having core diameter of 400  $\mu\text{m}$ . The plasma areas viewed by the both rays were confirmed to be identical with the He-Ne laser light. The optical fiber of 8-meter transmitted the light to a Czerny-Turner-type spectrograph. The entrance slit was 75  $\mu\text{m}$ . Spectra dispersed by the grating were recorded with an image intensifier coupled to a CCD (QImaging: Retiga1300R 1300x1030 of 7.4  $\mu\text{m}$  square pixels). The high voltage applied to the image intensifier was adjusted from 6.3 to 8.0 kV. Normally the voltage of 6.4 kV is applied. The repetition frequency of the CCD data acquisitions was 40 Hz. The emission profile was observed during 250 ms discharge duration. The electron line density was about  $1 \times 10^{13} \text{ cm}^{-2}$ .

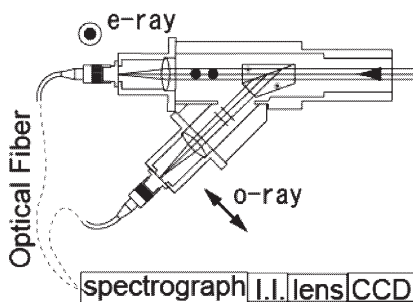


**Fig. 1.** Polarization separation optics used for the ion emission observation. Spectra dispersed by the grating were recorded with an image intensifier coupled a fast CCD

Figure 2 shows an example of the polarization resolved spectral profiles of O II  $2p^2 3s \ ^4P_{1/2, 3/2, 5/2} \leftarrow 2p^2 3s \ ^4D_{1/2, 3/2, 5/2, 7/2}$  and C III  $2s3s \ ^3S_1 \leftarrow 2s3p \ ^3P_{0, 1, 2}$  emission lines. For the purpose of reducing the noise of the image intensifier on the observed spectra, the time resolved spectra are averaged over seventeen discharges. Ten time-evolution spectra are obtained. In the first frame, 0-25 ms, the ion temperature is low and the lines are resolved. Nearby two emission lines from O II  $2p^2 3s \ ^4P_{1/2} \leftarrow 2p^2 3s \ ^4D_{1/2}$  and C III  $2s3s \ ^3S_1 \leftarrow 2s3p \ ^3P_0$  are never polarized. The sensitivity ratio is determined from these two line intensities. The uncertainty is, however, large owing to the low signal intensity of these two unpolarized lines.

The relative intensities of the  $\pi$  and  $\sigma$  components apparently change with the course of time. For example, for OII  $2p^2 3s \ ^4P_{3/2} \leftarrow 2p^2 3s \ ^4D_{5/2}$  at  $\lambda 464.18$  nm, the intensity of the  $\sigma$  component is higher than that of the  $\pi$  component at the time range of 125 – 150 ms. While at 175 – 200 ms, the intensity of the  $\pi$  component is higher than that of the  $\sigma$  component. We first discuss the possibility that this is due to the effect of statistical fluctuation of photons and electrons in the imaging intensifier. Since there is no correlation of the polarization separated spectra among the three different observed locations;  $z = 90, 0, -68$  mm, and no electron heating is applied in the observation time. We conclude that the apparent relative intensity variation is due to the statistical origin.

Various ECH (Plug ECH, Off-axis barrier ECH, central ECH) have been started in the GAMMA10 operation. We plan to observe the ECH overlapped plasmas.

### Reference

- <sup>1)</sup> T. Cho, *et. al.*, Phys. Rev. Lett. **64**, 1373 (1990).

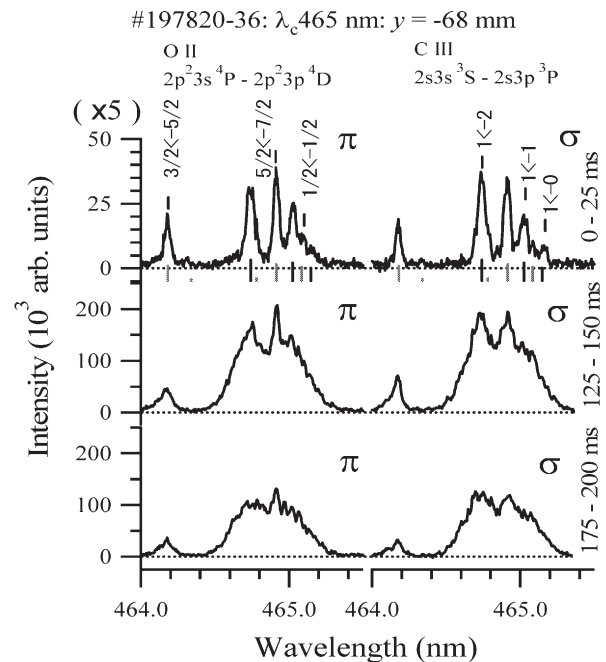


**Fig. 2.** The polarization separated line profiles: O II and C III emission. The  $\pi$  and  $\sigma$  components at different exposure times. Ten successive line profiles are obtained during 250 ms discharge. In the first frame intensity is scaled by a factor of 5.

## §8. Excitation of RF Waves in GAMMA 10 and in the Local Magnetic Mirror Configuration on LHD

Ichimura, M., Higaki, H., Kakimoto, S., Yamaguchi, Y. (University of Tsukuba),  
Watari, T., Kumazawa, R., Mutoh, T., Seki, T., Saito, K. (National Institute for Fusion Science)

In magnetically confined plasmas, fluctuations in the ion cyclotron range of frequency (ICRF) will be driven by the presence of non-thermal ion energy distribution. In a typical discharge on the GAMMA 10 tandem mirror, Alfvén-ion-cyclotron (AIC) modes are spontaneously excited due to strong temperature anisotropy [1]. On the while, in fusion-oriented devices with a toroidal configuration, the neutral beam (NB) injection and high power ICRF are commonly used to create high performance plasmas. Resultant high-energy ions are trapped in the local mirror configuration and will form the velocity distribution with the strong anisotropy. Especially in burning plasma experiments on JET and TFTR, fusion-product (FP) ions will form the non-thermal ion energy distribution in the bulk plasma and the ion cyclotron emissions (ICEs) have been observed [2,3]. To study the relation among the AIC-modes, beam-driven electrostatic instabilities and ICEs in the magnetically confined plasmas with non-thermal energy distribution is the main purpose of this work. In LHD, the measurement of fluctuations in the ion cyclotron frequency range has been started in the high power ICRF and the perpendicular NB injection experiments.

In GAMMA 10, plasmas with a strong temperature anisotropy are produced when the strong ICRF heating is applied. The temperature anisotropy is measured by using a diamagnetic loop array installed in the axial direction. Spontaneously excited modes in the fundamental ion cyclotron frequency and higher harmonic frequency range have been measured with magnetic probes. The AIC modes are excited as eigenmodes in the axial direction. Figure 1 shows the temporal evolution of the frequency spectrum of excited AIC-modes. The amplitude is represented by the brightness. The plasma parameters are

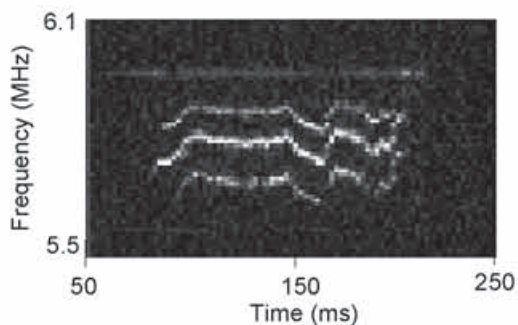


Fig.1 Temporal evolution of AIC-modes. The amplitude is represented by the brightness.

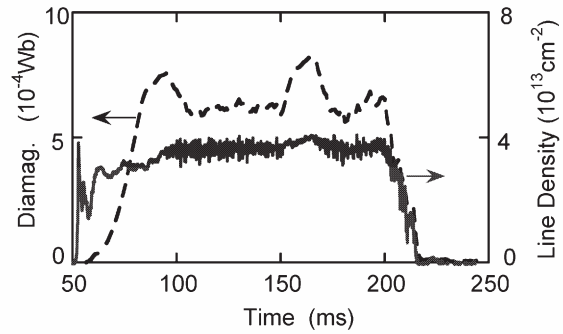


Fig.2 Temporal evolution of line density and diamagnetic signals on the same discharge in Fig.1.

indicated in Fig.2. It is clearly observed the frequency moves depending on the plasma parameters.

To evaluate the excitation of the higher harmonic waves, the dispersion relation of the electromagnetic waves in hot plasmas with the temperature anisotropy has been solved. It is verified the waves in the fast Alfvén wave branch become unstable due to the temperature anisotropy. Figure 3 shows the growth rate of the slow and fast Alfvén waves in plasmas with the temperature anisotropy. The growth rate is represented by the brightness. Near higher harmonic resonance layers, the fast Alfvén waves are destabilized in large perpendicular wave numbers and small parallel wave numbers. It is clearly shown the amplitude of the fundamental AIC-modes is extremely large compared with that of higher harmonic modes.

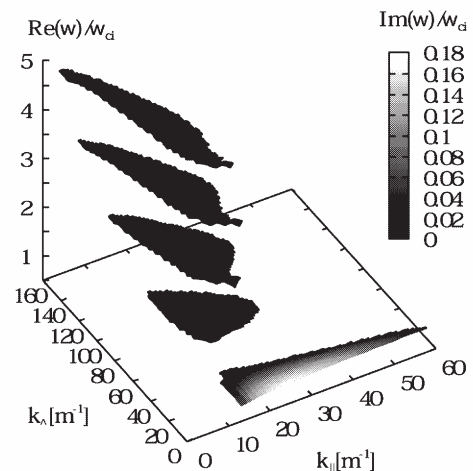


Fig.3 The growth rate of slow and fast Alfvén waves in the plasma with the temperature anisotropy.

## REFERENCES

- [1] Ichimura, M., et al., Phys. Rev. Lett. **70**, 2734 (1993).
- [2] Cottrell, G.A., et al., Nuclear Fusion, **33**, 1365 (1993).
- [3] Dendy, R.O., et al., Phys. Plasmas **1**, 1918 (1994).

## §9. Comprehensive Study of Relationship between Electron Distributions and Performances of Microwave and Mirror Devices

Ogura, K., Saito, H., Miyazawa, Y. (Niigata Univ.), Hirata, M., Cho, T., Kohagura, J., Numakura, T., Fukai, T., Yokoyama, N., Tokioka, S., Tomii, Y., Miyake, Y. (Plasma Research Center, University of Tsukuba)

We study oversized backward wave oscillator (BWO) driven by a weakly relativistic electron beam less than 100 kV and are operating in relatively high frequency region, above 10 GHz.<sup>1)</sup> The term “oversized” means that the diameter  $D$  of SWS is larger than free-space wavelength  $\lambda$  of output electromagnetic wave by several times or more. Note that high-power operations beyond 10 GHz are difficult for the conventional non-oversized slow-wave devices. It is important to study the relationship between the BWO performance and beam distributions.<sup>2)</sup>

The output powers of oversized BWO increase by increasing the beam voltage, i.e. by shifting the beam interacting point to the point of  $k_z z_0 = \pi$ . The quality factor  $Pf^2$  of oversized BWOs is about  $2 \times 10^4$  [kW·GHz<sup>2</sup>] in the range of 40-50 kV. This factor increases to about  $6 \times 10^4$  [kW·GHz<sup>2</sup>], by increasing the beam voltage above 70-80 kV. The power levels are about 100 kW or less. The output powers are not improved above  $6 \times 10^4$  [kW·GHz<sup>2</sup>], only by increasing beam voltage. To realize the higher output power, we need to change the beam configuration.<sup>2)</sup> By improving beam diode, the beam is distributed uniformly in a thin annular shape and propagates close to the waveguide wall. With the improved beam, the powers increase to about 500 kW (K-band BWO) and 200 kW (Q-Band BWO), with 90-100 kV beam voltage. The quality factor  $Pf^2$  is improved up to about  $3.5 \times 10^5$  [kW·GHz<sup>2</sup>], by controlling the beam configuration.

In tandem-mirror devices, the second-harmonic electron cyclotron heating (ECH) in the barrier region is utilized for the formation of a thermal-barrier potential, which reduces the electron heat flow between the central cell and the plug region. The fundamental ECH is employed for the formation of an ion-confining potential in the plug region. Scaling laws of potential formation and associated effects along with their physical interpretations are consolidated on the basis of experimental verification using the GAMMA10 tandem mirror. A proposal of extended consolidation and generalization of the two major theories—(i) Cohen’s strong ECH theory for the formation physics of plasma confining potentials and (ii) the generalized Pastukhov theory for the effectiveness of the produced potentials on plasma confinement is made through the use of the energy balance equation.

It is important to investigate electron-velocity distribution functions in these thermally isolated regions (the plug, the central-cell, and the barrier regions), since

these electron distribution functions are directly affected by electrostatic potentials in the kilovolt range. Several types of x-ray diagnostics, such as x-ray energy spectrum analyses, x-ray absorption methods, and x-ray tomographic reconstructions using various types of x-ray detectors have been employed for obtaining various shapes of electron-velocity distribution functions as well as their spatial profiles.<sup>3,4)</sup>

The progress in the confining potential leads to the remarkable effects of radially produced shear of electric fields on the suppression of intermittent vortex-like turbulent fluctuations. Such a shear effect is visually highlighted by x-ray tomography diagnostics. Spatially and temporally intermittent vortex-like fluctuated structures are observed as two-dimensionally reconstructed visual structures in kiloelectronvolt order ion-cyclotron heated plasmas having a weak shear. Such intermittent turbulent vortices disappear during the application of plug ECH. The potential rise due to ECH produces a stronger shear and improves the plasma confinement.<sup>5)</sup> The scaling data fit well to our proposed consolidated theory of the strong ECH theory with Pastukhov’s theory on energy confinement.

In this work, the electron distributions in both energy (or momentum) space and real space are examined. For the x-ray spectrum analyses, the relativistic Born approximation corrected by the Elwert factor is used for the values of the x-ray cross section. The numerical code for the x-ray analysis has been developed under this collaboration between Niigata Univ. and Plasma Research Center, University of Tsukuba. And the physics related to the electron distributions are examined. For the mirror device, phenomena are very complicated. In the case of the microwave device, the essential physics related to the electron distributions can be examined based on a very simplified model and system. For example, we propose a new version of self-consistent theory properly considering three dimensional beam motions and boundary conditions on the beam surface.<sup>2)</sup> It contains the essence of boundary problem for “moving plasmas”. Therefore, the comprehensive study of relationship between electron distributions and device performances is important to develop diagnostic methods of the various electron distribution functions and their spatial profiles.

### References

- 1) Ogura, K., *et. al.*: IEEJ Trans. FM. **125** (2005) 733.
- 2) Ogura, K., *et. al.*, *Joint Conference of 19th International Conference on Numerical Simulation of Plasmas and 7th Asia Pacific Plasma Theory Conference*, P1-19, Nara, Japan (July, 2005)
- 3) Hirata, M., *et. al.*: Trans. Fusion Sci. Technol. **47** (2005) 215.
- 4) Cho, T., *et. al.*: Phys. Rev. Lett. **94** (2005) 085002.
- 5) Cho, T., *et. al.*, Nucl. Fusion **45** (2005) 1650.



# §10. Study of Radial Transport of Bounce Ions by Use of a Lithium Beam Probe Method

Ishii, K., Saito, T., Katanuma, I., Yoshikawa, M., Kojima, A., Miyata, Y., Yamaguchi, T., Fujimoto, S. (Tsukuba Univ.), Iguchi, H., Nakamura, K.

Existence of the plug potential (PP) bounce ion which is bounced by the plug potential hill is essential to improve the axial confinement time in the tandem mirror GAMMA 10. The PP bounce ion and the inner mirror throat (IMT) bounce ion bounced by the IMT magnetic hill of the plug/barrier cell have been measured as neutral particles charge-exchanged from the bounce ions using a change exchange bounce ion analyzer (CX-BIA) located near the IMT.1,2) Radial profile measurements with high accuracy of the plasma and neutral particle density are required in order to estimate more quantitatively the bounce ions. We designed a diagnostic system composed of both radial profile measurements of electron density and neutral particle density. A neutral lithium beam probe (LiBP) method has already been used.3) It is useful for the profile measurement of the electron density over a wide range. Figure 1 shows the locations of the LiBP, the CX-BIA and H $\alpha$  detectors.

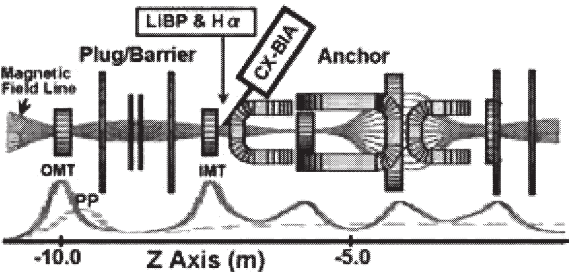


Fig.1 Locations of the diagnostic devices are shown with magnetic coils. Axial profiles of magnetic field strength and electrostatic potential are illustrated by a solid line and a dashed line, respectively.

We designed the LiBP system as shown in Fig.2.

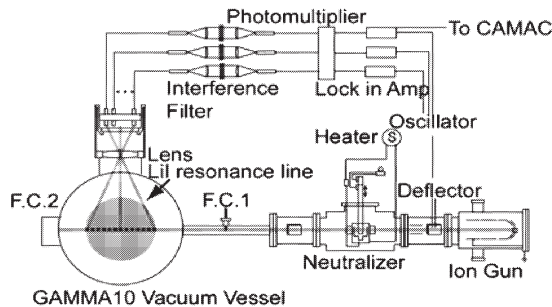


Fig.2 A LiBP system at the inner mirror throat.

In order to check the validity of the measurement by the LiBP method, we reconstructed the density profiles on the condition that the peak density was variable and the width was constant ( $r_{1/2}=2.5$  cm). The peak density was changed from  $1 \times 10^{12}$  cm $^{-3}$  up to  $1 \times 10^{14}$  cm $^{-3}$ . A Gaussian type of density profile was assumed as a good approximation. The calculated results are shown in Fig.3.

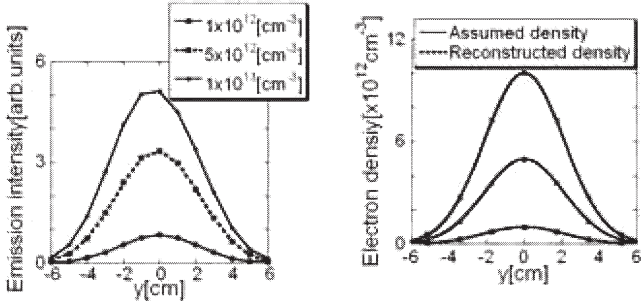


Fig.3 Intensity of light emitted from the lithium beam. Reconstruction of the electron density profiles. Solid lines are the initial density profiles. Dashed lines are the reconstructed profiles which coincide well with the initial profiles.

In the present experiment of the tandem mirror GAMMA10, the peak density is seemed to be usually several times  $10^{12}$  cm $^{-3}$  at the IMT. Therefore the attenuation of the neutral beam is not effective and the reconstruction of the density profiles is carried out quite well. In the range of more than  $6 \times 10^{13}$  cm $^{-3}$ , the reconstructed curves began to shift from the initial density profiles.

The outer mirror throat (OMT) bounce ion, together with the PP bounce ion, was also measured by the CX-BIA and the existence was confirmed as shown in Fig.4.

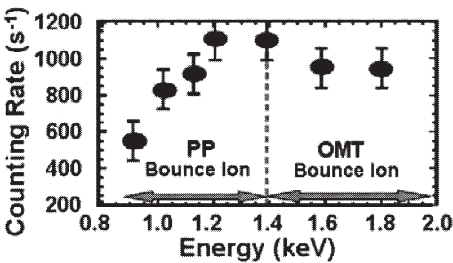


Fig.4 Detected counts of the PP and OMT bounce ions. Two kinds of bounce ions are separated at the energy of 1.4 keV.

Gold neutral beam probes were applied to measure the radial profiles of the plasma potential and the fluctuations excited in the plasma. We found the relation between the bounce ions and the potential profile.

## Reference

- 1) Ishii, K., et al., Rev. Sci. Instrum, **75**, (2004) 3619.
- 2) Miyata, Y., Master's Thesis, Graduate School of Pure and Applied Science, University of Tsukuba (2005).
- 3) Iguchi, H., et al., Rev. Sci. Instrum, **56**, (1985) 1050.



## §11. Cross Correlation Measurement between Density and Potential Fluctuations in a Tandem Mirror for the Purpose of Radial Transport Control

Takeno, H., Yasaka, Y. (Kobe Univ.),  
Hojo, H., Ichimura, M., Cho, T. (Univ. Tsukuba),  
Higaki, H. (Hiroshima Univ.)

Understanding physical mechanism between ICRF and DC electric field and/or flow shear might lead ICRF driven transport control irrespective of confinement magnetic configuration<sup>1)</sup>. As a basic study for this purpose, this report shows correlation measurement between density and potential fluctuations in GAMMA 10 following the previous study<sup>2)</sup>. In the HIEI tandem mirror, the mechanism of fluctuations were clarified from informations of relative phase difference between these fluctuations<sup>3)</sup>.

In the scrape-off layer plasma of GAMMA 10, low frequency fluctuation is observed by application of central cell ICRF. The frequency of the fluctuation is several kilo-hertz, and was identified as an electron drift wave.

Using an azimuthally aligned probe array on the limiter, correlation among signals obtained by the probes was measured. Fig. 1 shows correlation between density fluctuations measured by probes separated with azimuthal angle of 90 degrees. Time evolution of frequencies of high intensity is shown in Fig. 1(a) below a time sequence chart of RF application. There are fluctuations from first to fifth order with their fundamental frequencies of 17 kHz, and those frequencies decline on plug/barrier ECH application. The fundamental frequency is rather higher compared with the previous report as density gradient increases by setting movable limiter at inner position. The relation between frequency and relative phase difference is summarized in Fig. 1(b), showing proportional relation between both values.

Similar measurement was performed about correlation between density fluctuation and floating potential. In Fig. 2(a), time evolution of frequencies of high intensity is shown, and it is similar to that in Fig. 1(a). About the relation between frequency and relative phase difference, however, the results shown in Fig. 2(b) are quite different from that in Fig. 1(b).

According to the linear theory of stability, relative phase difference of fluctuations between density and potential is 0 for electron drift wave. In the present condition, by taking account of locations of probes, the relation between frequency and relative phase difference is expected to be those as Fig. 1(b). Analysis of this gap between theory and experimental results is under way.

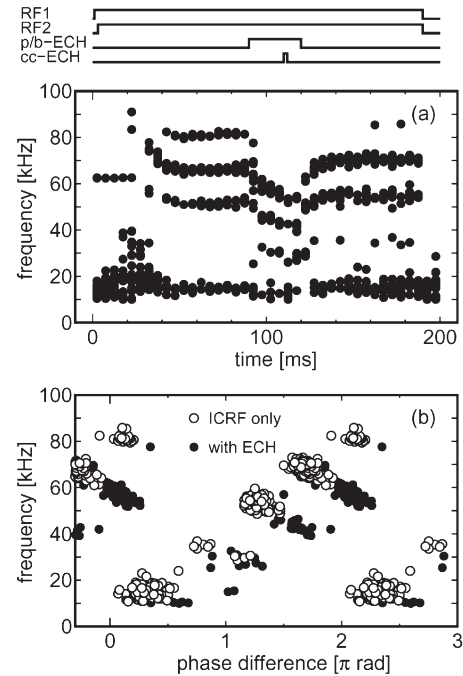


Fig. 1 Samples of correlation between density fluctuations. (a) high intensity frequency versus time and (b) relative phase difference.

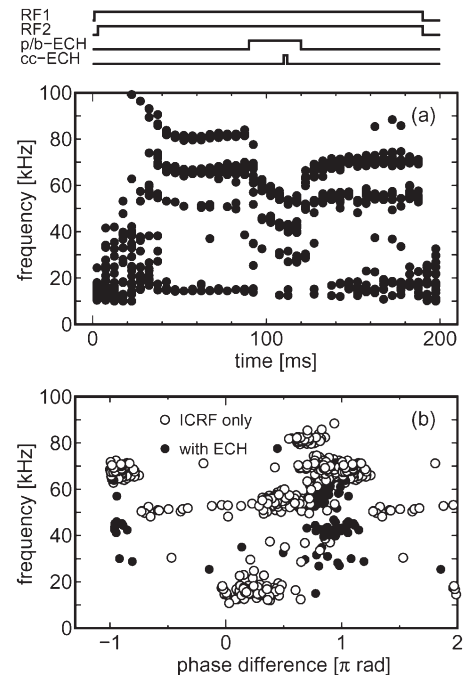


Fig. 2 Samples of correlation between density and potential fluctuations. (a) high intensity frequency versus time and (b) relative phase difference.

### Reference

- 1) O. Sakai and Y. Yasaka, Phys. Plasmas **2** (1995) 3249.
- 2) Takeno, H., *et al.*, Ann. Rep. NIFS April2004-March2005 (2005) 461.
- 3) Y. Yasaka, *et al.*, Trans. Fusion Sci. Technol. **43**(1T) (2003) 44.

## §12. Analysis of Neutral Particle Transport and Recycling Behavior in Open Magnetic Field Configuration Plasmas

Nakashima, Y., Yoshikawa, M., Islam, Md. K. (Univ. Tsukuba, P.R.C.),  
 Nishino, N. (Hiroshima Univ., Eng.),  
 Kobayashi, S. (Kyoto Univ., I.A.E.),  
 Sawada, K. (Shinshu Univ., Eng.),  
 Ishimoto, Y. (JAERI, Naka),  
 Kubota, Y., Higashizono, Y. (Univ. Tsukuba, Graduate School of Pure and Appl. Sci.),  
 Shoji, M., Sagara, A., Morisaki, T., Masuzaki, T.

Investigation of edge plasma behavior and neutral particle transport is important subject for open magnetic field configuration plasmas as well as toroidal configuration plasmas. Particularly in tandem mirror plasmas, penetration of neutrals into the core plasma region plays an important role in formation of the neutral density profile, since the plasma density is lower than that of tokamaks. Neutral particle transport simulations based on the Monte-Carlo methods have been widely used as a standard way to approach neutral behavior in the complicated systems of fusion devices. In this study, we develop three-dimensional neutral transport analyses in open magnetic field region such as in GAMMA 10 plasmas using the Monte-Carlo neutral particle code DEGAS. In order to investigate precise behavior of edge plasmas, a high-speed camera is applied to the GAMMA 10 central-cell for the first time.

In the last academic year, three-dimensional mesh model was structured. In this model, an up-down symmetry is introduced and the simulation space is divided into 11 segments radially and 8 segments azimuthally. In the axial direction, 69 segments are defined, which extend from the central midplane to the outer-transition of the anchor-cell. In order to apply the geometrical structure precisely into the simulation space, additional structures, "second wall", were successfully implemented. Figure 1 shows the comparison between the simulation result and the measured one in the central-cell. The open circles represent the results determined from the simulation in which only the central-cell is modeled and the simple exit is located at the outside of the mirror throat. In this case, it should be noted that the discrepancy is observed at the location of the gasbox ( $z = -240\text{cm}$ ). However, the triangles obtained from the present simulation, in which both central-cell and anchor-cell are combined into one structure, well reproduces the experimental results shown as filled circles. On the other hand, the data represented by cross are obtained from another simulation in which the size of the gasbox is artificially reduced. In this case, a noticeably higher intensity of calculated  $\text{H}\alpha$  emission is recognized. From these results, it is clarified that the neutral transport is much affected by a geometrical configuration.

In the GAMMA 10 central-cell, visible imaging measurement was carried out by using a fast camera

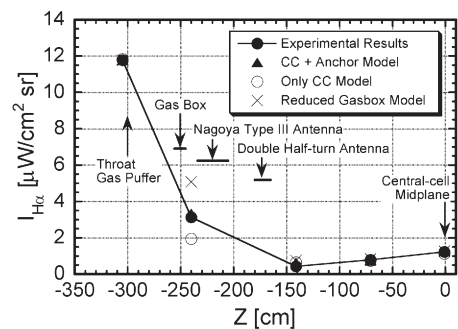


Fig. 1. Axial intensity profile of  $\text{H}\alpha$  line-emission. The solid circles are the experimental results. Triangles are the results of the present simulation. Open circles are determined from the simulation without the anchor-cell. Another simulation with reduced size of the gasbox model is shown in cross.

(Ultima-SE, Photron Inc.). Gas puff in the central region was used to visualize mainly plasma periphery and it is expected that plasma turbulence will be visualized. Figure 2 shows one of the digital video output images of gas puff imaging with 40500 FPS and 64x64 pixels (a), two-dimensional phase image distribution based on FFT analysis (b), a vertical profile obtained from the phase image analysis (d). As shown in Fig.2(a), the localization of plasma light and the vibration of plasma periphery were observed clearly by the fast camera. From FFT analysis, observed vibration with  $m = 1$  was speculated to be a fluctuation due to electron diamagnetic drift.

### Reference

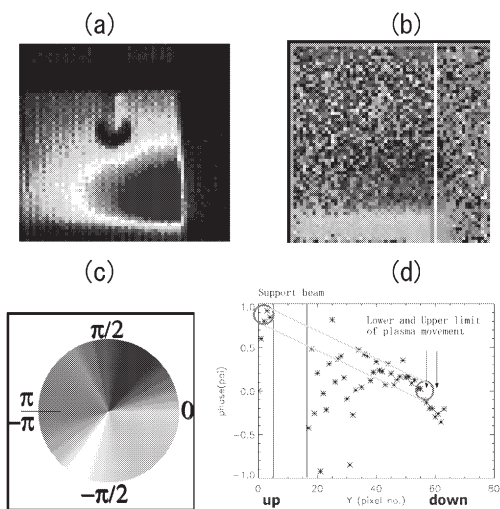


Fig. 2. Result of 2-dimensional image analysis

- 1) Nakashima, Y. *et al.*: J. Nucl. Mater. **337-339** (2005) 461.
- 2) Nakashima, Y. *et al.*: Proc.19th ICNSP and 7th APPTC (July 12-15, 2005, Nara, Japan)
- 3) Nishino, N., Nakashima, Y. *et al.*: to be published to J. Plasma and Fusion Research.

### §13. Progress in Potential Formation and Radial-Transport-Barrier Production for Turbulence Suppression and Improved Confinement in GAMMA 10

Cho, T., GAMMA 10 Group, Pastukhov, V.P.<sup>1</sup>,  
81 Collaborators from Japanese Universities and  
Institutes  
(Plasma Research Center, University of Tsukuba)  
(<sup>1</sup>Russian Research Center “Kurchatov Institute”,  
Russia)

(1) Four-time progress in ion-confining potentials  $\phi_c$  to 3.0 kV in comparison to  $\phi_c$  attained 1992-2002 is achieved in the hot-ion mode ( $T_i$ =several keV) [Fig. 1]. A scaling of  $\phi_c$ , which favorably increases with plug electron-cyclotron heating (ECH) powers ( $P_{PECH}$ ), is obtained.<sup>1)</sup>

(2) The advance in  $\phi_c$  leads to a finding of remarkable effects of radially sheared electric fields ( $dE_r/dr$ ) on turbulence suppression and transverse-loss reduction.<sup>2)</sup>

(3) A weak decrease in  $\phi_c$  with increasing  $n_c$  to  $\sim 10^{19} \text{ m}^{-3}$  with the recovery of  $\phi_c$  with increasing  $P_{PECH}$  is obtained.<sup>1)</sup>

(4) The first achievement of active control and formation of an internal transport barrier (ITB) has been carried out with the improvement of transverse energy confinement [Fig. 2]. Off-axis ECH in an axisymmetric barrier mirror produces a cylindrical layer with energetic electrons, which flow through the central cell and into the end region. The layer, which produces a localized bumped ambipolar potential  $\Phi_c$ , generates a strong  $E_r$  shear and peaked vorticity with the direction reversal of  $E_r \times B$  sheared flow near the  $\Phi_c$  peak. Intermittent vortex-like turbulent structures near the layer are suppressed in the central cell. This results in  $T_e$  and  $T_i$  rises surrounded by the layer. The phenomena are analogous to those in tokamaks with ITB.<sup>3)</sup>

(5) Preliminary central ECH (170 kW, 20 ms) in a standard tandem-mirror operation raises  $T_{e0}$  from 70 to 300 eV together with  $T_{i\perp 0}$  from 4.5 to 6.1 keV, and  $T_{i\parallel 0}$  from 0.5 to 1.2 keV with  $\tau_{p0}=95 \text{ ms}$  for  $\phi_c$  (=1.4 kV) trapped ions. The on-axis particle to energy confining ratio of  $\tau_{p0}/\tau_{E0}$  is observed to be 1.7 for  $\phi_c$  trapped ions (consistent with Pastukhov's theory) and 2.4 for central mirror-trapped ions with 240-kW plug ECH and 90-kW ICH ( $\eta_{ICH} \sim 0.3$ ;  $n_{lc}=4.5 \times 10^{17} \text{ m}^{-2}$ ).<sup>1)</sup>

(6) Recently, a 200 kW central ECH with 430 kW plug ECH produces stable central-cell plasmas ( $T_e=600 \text{ eV}$  and  $T_i=6.6 \text{ keV}$ ) with azimuthal  $E_r \times B$  sheared flow. However, in the absence of the shear flow, hot plasmas migrate unstably towards vacuum wall with plasma degradation.<sup>1)</sup>

### References

- 1) Cho, T. *et al.* Plenary Invited Talk in the 5th International Conference on Open Magnetic Systems for Plasma Confinement (Tsukuba, July 2006). [To be published in the American Nuclear Society Journal of Trans. Fusion Sci. Tech.]
- 2) Cho, T. *et al.* Phys. Rev. Lett. **94** (2005) 085002.
- 3) Cho, T. *et al.* Phys. Rev. Lett. **97**, No.5 (2006).

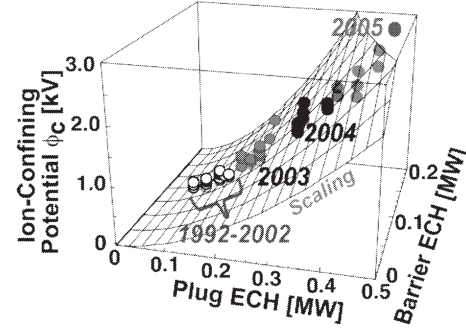


Fig. 1. Four-time progress in  $\phi_c$  including a new record of 3.0 kV for confining central-cell ions (filled symbols) [see  $\phi_c$  during 1992-2002 (open circles)] in accordance with a favorably rising scaling surface of  $\phi_c$  with plug ( $P_{PECH}$ ) and barrier ( $P_{BECH}$ ) ECH powers.  $T_i$ =several keV (the hot-ion mode).

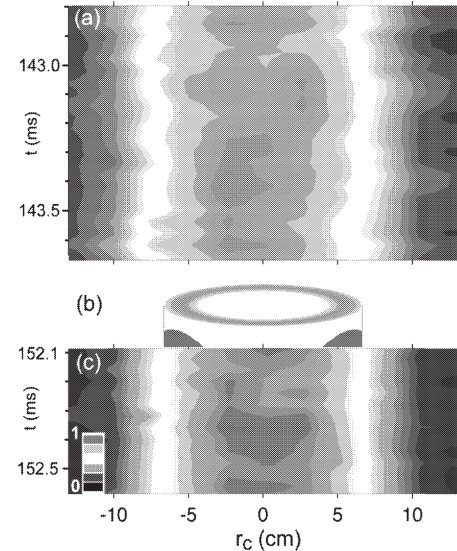


Fig. 2. Contours of central-cell x-ray brightness in (a) the absence and (c) presence of (b) cylindrically shaped energetic-electron-layer formation due to off-axis barrier-cell ECH. The hot-colored core region displays higher plasma-pressure locations. Strong turbulence with vortex-like structures continues to exist at  $r_c < 4 \text{ cm}$  in (a) and (c). However, a quietly suppressed region in (c) is observed in the energetic-electron layer [ $5 < r_c < 7 \text{ cm}$ ; see (b)] and the outer surrounding cylindrical layer ( $7 < r_c < 10 \text{ cm}$ ); ( $I \propto n_e n_i T_e^{2.3}$ ).



## §14. Initial Results of CUSPDEC Applied to the GAMMA 10 Tandem Mirror

Yasaka, Y., Takeno, H. (Kobe Univ.),  
Tomita, Y.,  
Ishikawa, M., Nakashima, Y., Hirata, M., Cho, T.  
(Univ. Tsukuba)

The cusp-type direct energy converter (CUSPDEC) is a device to recover kinetic energies of thermal ions produced in a D-<sup>3</sup>He fusion reactor. It utilizes a cusp magnetic field to separate ions from electrons, and a dc-biased plane collector to decelerate and collect ions as a one-stage direct energy converter. A small scale CUSPDEC device, called the Kobe\_Cusp DEC, was constructed and its characteristics have been investigated by using a low-energy plasma source. The CUSPDEC device consists of a plasma source, a guide field section, a cusp magnetic field section, and electron and ion collectors. The cusp field is created by two magnetic coils, A and B. By adjusting the current in the two coils,  $I_A$  and  $I_B$ , the field line curvature can be varied. Typical values are  $I_A = 30$  A and  $I_B = 40$  A. The Experimental results have revealed that the slanted cusp field has better capability of the charge separation than the normal cusp field. It is also found that the efficiency of energy conversion depends on the shape of the energy distribution function of incoming ions. Based on these experimental findings as well as theoretical and numerical studies, we now study the capability of the charge separation and ion energy conversion in the CUSPDEC device using GAMMA 10 plasmas as a source input.

Figure 1 shows the schematic diagram of the CUSPDEC device connected to the one end of the GAMMA

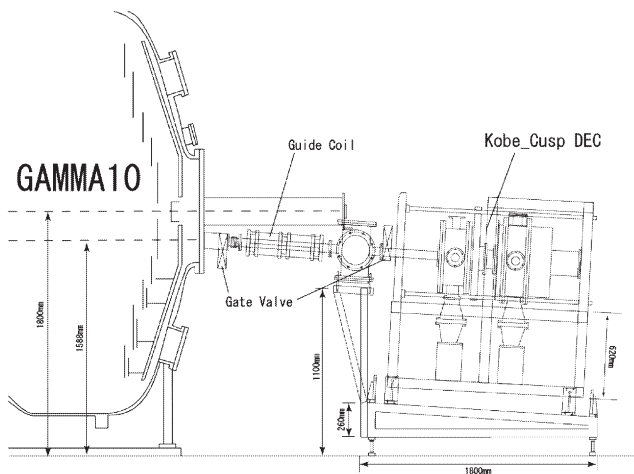


Fig. 1. Schematic diagram of CUSPDEC experimental device with GAMMA 10.

10 device through a guide section. The end loss flux of the GAMMA 10 plasma is introduced to the CUSPDEC. The data from an end loss analyzer show that the electron energy for the hot ion mode is up to 0.2 keV and that for the ECH phase is  $\sim 0.4$  keV or higher. The parallel ion temperature is

0.3–0.5 keV. When the end loss flux is introduced to the CUSPDEC device, it is expected that electrons are deflected toward the line cusp region along the field lines and ions pass through the null point flowing into the point cusp

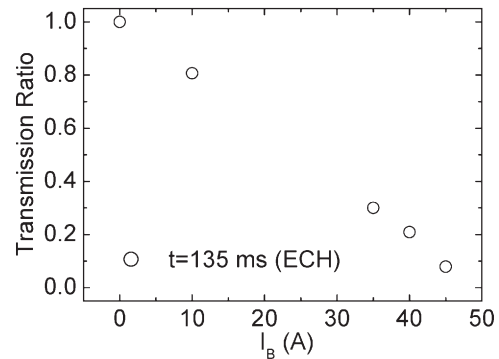


Fig. 2. Measured transmission ratio of electrons during the ECH phase with  $I_A = 40$  A.

region. We define the transmission ratio of electrons as the ratio of the electron flux at the point cusp with the cusp field to that without the cusp field. Figure 2 shows the transmission ratio as a function of  $I_B$  during the ECH phase. When the cusp field is formed ( $I_B > 10$  A), the electron flux tends to flow into the line cusp resulting in smaller transmission ratios. The larger the value of  $I_B$ , the smaller the transmission ratio. It means that the larger slant of the cusp fields leads to the better separation.

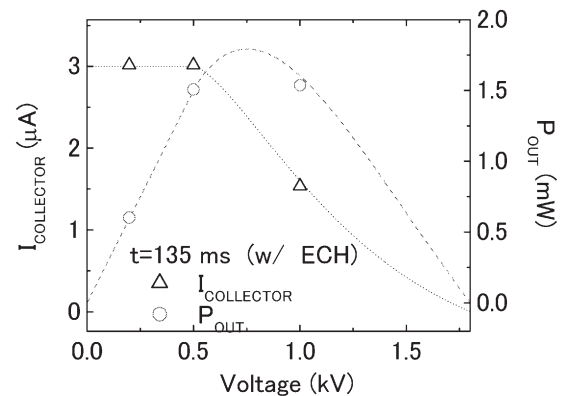


Fig. 3. Measured current-voltage characteristics of the ion collector (triangles) and estimated dc power output (circles).

The curve with triangles in Fig. 3 is the current-voltage characteristics of the ion collector operating as the one-stage direct energy converter, which is located at the point cusp region of the CUSPDEC device. The dotted line is drawn by assuming that the energy distribution function of ions is a shifted Maxwellian. The curve with circles shows the output dc power  $P_{\text{OUT}}$  available for an external load. Thus we have demonstrated that the basic functions of the CUSPDEC device are well operative for plasmas of the existing open magnetic confinement system.



## §15. Effects of Non-Axisymmetric Magnetic Field on Characteristics of Axisymmetric Cusp DEC

Tomita, Y.,  
Yasaka, Y., Takeno, H. (Kobe Univ.),  
Ishikawa, M., Nakashima, Y., Katanuma, I., Cho, T.  
(Univ. Tsukuba)

In order to investigate the characteristics of the cusp DEC, a single slant cusp configuration, which models the Kobe Cusp DEC, is considered. The oblique uniform magnetic field is applied to the axisymmetric field as a perturbation,

$$\vec{B}_1 = B_1 \sin \alpha \vec{x} - B_1 \cos \alpha \vec{z}, \quad (1)$$

where  $\alpha$  is the angle of the oblique magnetic field from the axisymmetric axis  $z$ . This magnetic field leads to the perturbed vector potential,

$$A_{1y} = B_1 \cos \alpha x - B_1 \sin \alpha z. \quad (2)$$

One of the indices to investigate the effect of the perturbed field to the axisymmetric DEC is Störmer potential  $V_{st}$  for  $j$ -th plasma species [1],

$$\begin{aligned} V_{st} &\equiv \frac{m_j}{2} r^2 \dot{\theta}^2 \\ &= \frac{1}{2m_j r^2} [P_\theta - q_j \psi - q_j \frac{\partial(v_y A_{1y})}{\partial \theta}]^2 \\ &\simeq V_{st0}(r, z) + V_{st1}(r, \theta, z). \end{aligned} \quad (3)$$

Here  $P_\theta$  and  $\psi$  are the canonical angular momentum and the flux function, respectively. The perturbed and unperturbed Störmer potentials are expressed as

$$\begin{aligned} V_{st0}(r, z) &= \frac{1}{2m_j r^2} (P_{\theta 0} - q_j \psi)^2, \text{ and} \\ V_{st1}(r, \theta, z) &= -\frac{q_j B_1 (P_{\theta 0} - q_j \psi) r \cos \theta}{m_j r^2} \\ &\quad \times (r \cos \theta \cos \alpha - z \sin \alpha), \end{aligned} \quad (4)$$

respectively.  $P_{\theta 0}$  is the unperturbed canonical angular momentum, which is one of the constant of motions. The contour lines of the unperturbed Störmer potentials  $V_{st0}$  for ions are shown in Fig.1 for the case of the canonical angular momentum  $P_\theta / (e\mu_0 I_{c,in} R_{in} / \pi) = 0.5$ , where  $I_{c,in}$  and  $R_{in}$  are the coil current and radius of the inlet single cusp coil, respectively. In Fig.1 the radius and current of the outlet coil are double of the inlet one, which makes the slant cusp field. The labels in Fig.1 indicate the values of  $V_{st0} / [(e\mu_0 I_{c,in} / \pi)^2 / 2m_i]$ . The stagnation point

$(\partial V_{st0}(r, z; P_\theta) / \partial r = \partial V_{st0}(r, z; P_\theta) / \partial z = 0)$  of the Störmer potential in  $(r, z)$  space give classification between trapped charged particles in the line cusp region and those which are passed through the single cusp field to the point cusp region. The value of Störmer potential at the

stagnation in Fig.1 is 1.55. The perturbation of the non-axisymmetric field changes the distribution of the Störmer potential. The azimuthal dependence of the perturbed Störmer potential is shown in Fig. 2, where the perturbed magnetic field  $B_1 / (\mu_0 I_{c,in} / \pi R_{in}) = 1.0$  and  $\alpha = 10$  degree. One can see the non-axisymmetric magnetic field deforms the barrier of potential, where the ions with lower energy cannot pass through the enhanced potential to the point cusp. Roughly speaking, one percent perturbation of the magnetic field changes the potential by one percent at the most.

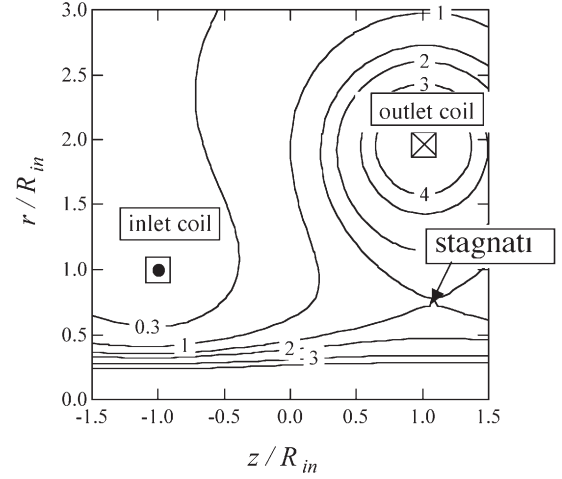


Fig. 1. Contour lines of the unperturbed Störmer potentials for ions. The normalized potential at the stagnation point is 1.55.

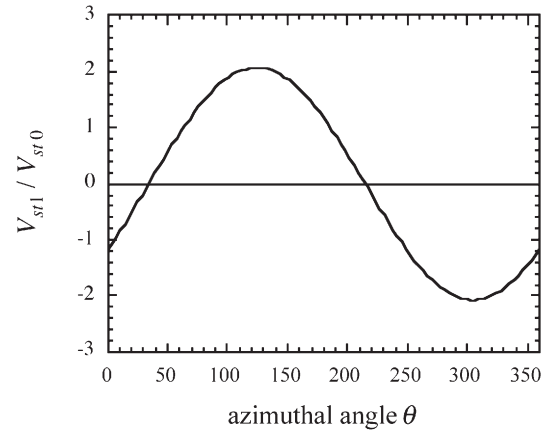


Fig.2. Azimuthal dependence of the perturbed Störmer potential.

### Reference

- 1) W. Schuurman and H. de Kluiver, Plasma Phys., 7, (1965) 245.

## §16. The Observation of the Negative Toroidal Current in Heliotron-J

Watanabe, K.Y.,  
Motojima, G., Okada, H., Nakamura, Y., Sano, F.  
(Kyoto Univ.)

In helical devices, net toroidal currents are not required to produce magnetic field for plasma confinement, while theoretical prediction suggests that there are several kinds of net toroidal currents, that is, bootstrap current, beam driven current and microwave driven current. Even if these toroidal currents are sufficiently small to activate current driven instabilities, they can affect the characteristics of the magnetic configurations. The Heliotron-J device (H-J) is quite suitable to study the driving mechanism of toroidal current in helical devices because there we can make the operation with various magnetic configurations more easily comparing with other helical devices. Here we show an experimental result on the bootstrap current in H-J.

Figure 1 shows the dependence of the observed toroidal current and the plasma stored energy on the electron density in H-J ECH plasmas. Various symbols in Fig.1 correspond to the various bumpiness configurations. The bumpiness increases in the order of circles, squares and triangles. In the all configurations, the toroidal currents decreases with the plasma stored energy. The fact is consistent with the BS current behavior. However, for the smallest bumpiness configuration, the observed toroidal current flow in the negative direction (to reduce the rotational transform) and the amplitude of the toroidal current increases with the density decrease in the low density region with  $n_e < 0.6 \times 10^{19} \text{ m}^{-3}$ . Figure 2 shows the observed toroidal current and the prediction of BS current

by SPBSC code [1] under the assumption of  $E_r=0$  in a density range with  $n_e \sim 0.6 \times 10^{19} \text{ m}^{-3}$ . In the calculation, the electron and the ion temperature are assumed  $T_e=600\text{--}700\text{eV}(1-\rho^2)^2$ ,  $T_i=150\text{--}200\text{eV}(1-\rho^2)^2$ , respectively. The electron density is assumed as  $n_e \sim (1-\rho^6)$ . Here is a normalized minor radius.  $B_{04}/B_{00}$  denotes the amplitude of the bumpy component. In a large bumpiness configuration, the predicted BS current with  $E_r=0$  is almost consistent with the observation in both the direction and the amplitude. In a small bumpiness configuration, the predicted BS current with  $E_r=0$  is inconsistent with the observation in the direction. In the higher density case, even in a small bumpiness configuration, the predicted BS current with  $E_r=0$  is almost consistent with the observation. In Fig.2, the radial electric field is assumed as  $E_r=0$ . However, in the plasma with different collisionalities between electrons and ions, it is pointed out that the BS current proportional to the radial electric field in the helical systems because the geometric factors depend on the collisionalities in helical systems [2]. In the low-density ECH discharges, the positive electric field is expected [3], which suggests that a cause of the negative current in Figs.1 and 2 would be radial electric field. In Fig.3, the theoretical prediction of BS current under an assumption of  $E_r$  is shown. Here the electric potential profile is assumed proportional to the electron temperature. As the central electric potential increases, the prediction of BS current decreases and the sign becomes negative. In the case that the central electric potential is larger by 3 times than the electron temperature, the prediction of BS current would be as large as the observed toroidal current. According to the calculation with some density profile, the density profile effect on the BS current is not so large in the discharge condition in Fig.2.

In order to confirm the above-mentioned cause of the observed negative toroidal current, ECCD effects and super-thermal effects should be eliminated. This is one of the future subjects.

### Reference

- [1] K.Y.Watanabe et al, Nucl.Fusion 35(1995)335.
- [2] N.Nakajima et al, J.Phys.Soc.Jpn 61(1992)833.
- [3] H.Idei et al., Phys.Rev.Lett. 71, 2220 (1993).

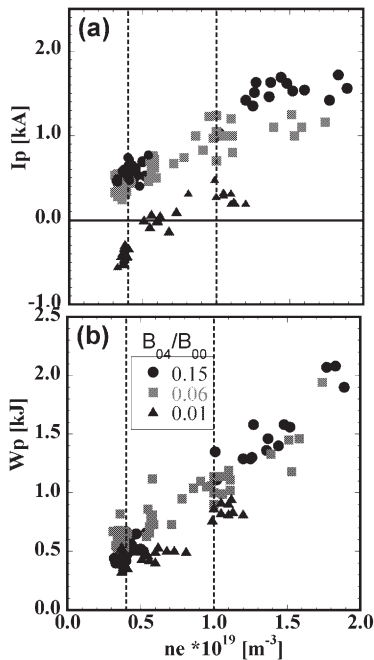


Fig.1 The observed toroidal current (a) and the plasma stored energy vs. the electron density.

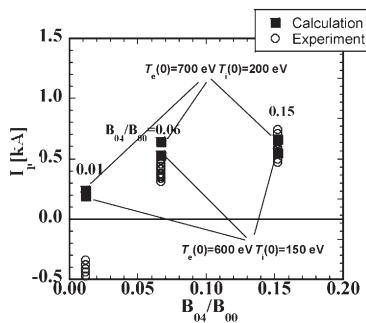


Fig.2 Comparison between the observed toroidal current and the predicted BS current with  $E_r = 0$  in  $n_e \sim 0.4 \times 10^{19} \text{ m}^{-3}$ .

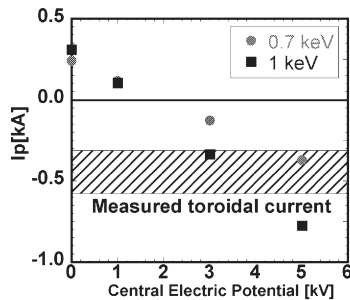


Fig.3 The dependence of the predicted BS current on  $E_r$  ( $B_{04}/B_{00}=0.01$ ).

## §17. ICRF Heating Experiment in Heliotron J

Mutoh, T., Kumazawa, R., Seki, T., Saito, K., Okada, H., Torii, Y., Sano, F., Hanatani, K., Mizuuchi, T., Kobayashi, S., Nagasaki, K. (IAE, Kyoto Univ.), Kondo, K., Nakamura, Y. (Grad. School, Energy Sc., Kyoto Univ.)

The formation and confinement experiment for fast ions is performed using the ICRF minority heating scheme with a proton minority and a deuteron majority in Heliotron J, a low-shear helical-axis heliotron ( $R_0 = 1.2$  m,  $a = 0.1$ - $0.2$  m,  $B_0 \leq 1.5$  T). The effect of the magnetic configuration on the fast ion confinement is one of the most important issues in helical devices. In this report, the effect of the bumpiness on the trapped fast ion confinement is clarified by using ICRF minority-heating. The role of one of the Fourier components, the bumpiness, is a key issue for the design principle of the magnetic field of Heliotron J, where the particle confinement is controlled by the bumpiness. The proper bumpiness causes deeply trapped particles to be confined in the small grad-B region. The fast ion confinement was studied using tangentially injected fast ions by using NBI in the previous work. However, trapped particles were not sufficiently investigated in the NBI experiment.

The ICRF loop antennas are installed on the low-field side of the corner section of the Heliotron J. The high energy ions are produced up to 10 keV by injecting an ICRF pulse into an ECH target plasma where  $T_i(0) = 0.2$  keV,  $T_e(0) = 0.8$  keV and  $\bar{n}_e = 0.4 \times 10^{19} \text{ m}^{-3}$ . Figure 1 shows the time

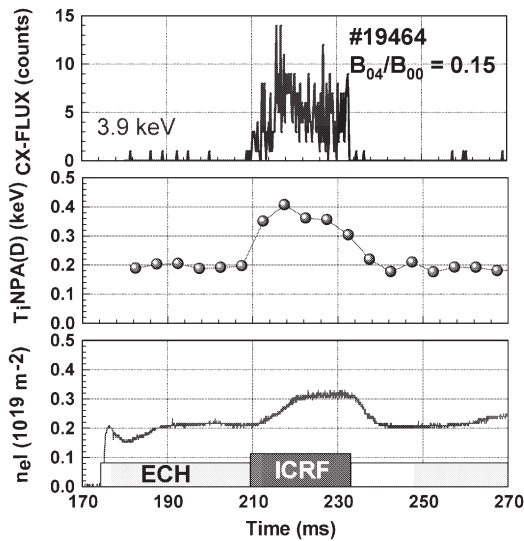


Fig. 1 Time traces of the charge-exchange flux (H), the ion temperature and the electron density.

traces of the line integrated density, the ion temperature and the hydrogen flux of 3.9 keV. Hydrogen and deuterium fluxes are measured by a charge-exchange neutral energy analyzer (CX-NPA). During the ICRF pulse, the ion temperature measured by the CX-NPA is almost doubled and the fast neutral flux is observed.

The amplitude modulation of the ICRF power is also performed for estimating the confinement of the fast ions. The injection power is modulated with the frequency of 100 Hz, and then the CX flux is modulated as well. The phase delay of the CX flux to the injection power is caused through the acceleration by RF wave and collision damping. Fokker-Plank equation with the loss term is used for estimation of the fast ion confinement. From this experiment, the confinement of the fast ions for the high bumpy ripple is longer than that for the medium. It is considered that the bumpy control is effective for the fast ion confinement in Heliotron J as expected from the calculation using the DKES code and the discussion of the field structure that the grad-B drift is smallest in the configuration with the largest bumpy ripple.

The ion temperature increases with  $P_{\text{ICRF}}/n_e l$  in this power range for two cases as shown in Fig. 2. Here,  $P_{\text{ICRF}}$  is the injected ICRF power and  $n_e l$  is the line integrated density. The increment of the ion temperature in the high bumpy case is larger than that in the case of  $B_{04}/B_{00} = 0.06$ . Therefore, the heating efficiency is better in the high bumpy case. The bulk ion heating in this heating scheme is caused through the Coulomb collisions with the high energy minority ions produced by the ICRF heating. It is considered that the energy transfer from the minority ions is larger in the high bumpy case since the high energy tail is larger. The global energy confinement time in target ECH plasmas is almost same for three configurations except the improved confinement mode.

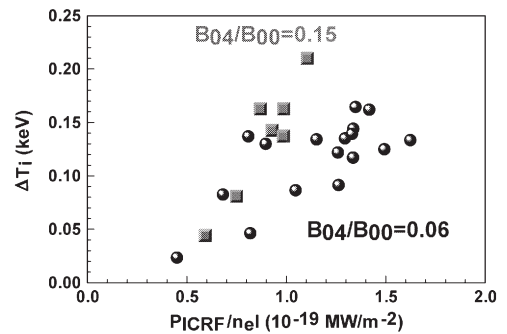


Fig. 2 Increase of the bulk ion temperature vs. the injected ICRF power for two cases of the bumpy ripples.

## §18. Hard X-Ray Diagnostic by Use of CdTe Detector in Heliotron J

Isobe, M., Okamura, S., Yoshimura, Y. (NIFS),  
Kobayashi, S., Sano, F. (Kyoto Univ.)

### 1. Introduction

The Heliotron J device is designed to provide quasi-omnigenous (QO) property on magnetic field configuration. In a Heliotron J type configuration, the non-axisymmetric bumpy ripples play an important role to obtain good neoclassical confinement [1,2]. Because of this reason, the Heliotron J is flexible in changing the magnetic field configuration to explore optimized configuration experimentally. The primary purpose of this work is to study dependence of confinement property on magnetic field configuration through measuring pulse height spectra of X-rays, i.e. energy distribution of electrons in low-density ECRH plasmas.

### 2. Hard X-ray detector and electronics

Aiming at detection of X-rays originating from energetic electrons generated by ECRH, a hard X-ray detector based on a cadmium telluride (CdTe) diode (Amptek inc. /XR-100T-CdTe[3]) is chosen because a silicon (Si) semiconductor detector suitable for measuring relatively low energy X-rays is being employed in the Heliotron J. Because the atomic number  $Z$  of the CdTe detector is much higher than that of the Si detector, the CdTe detector is more suitable for high energy X-ray measurement. The detection volume of CdTe is  $3 \times 3 \times 1 \text{ m}^3$ . The thickness of beryllium (Be) window installed in front is 4 mil. The electronic circuit used in this system and a typical output pulse from a shaping amplifier due to X-ray irradiation are shown in Figure 1. This system is operated in pulse height analysis (PHA) mode. We employ a tungsten aperture system variable in its size ( $50 \mu\text{m} \sim 200 \mu\text{m}$ ) from the outside of vacuum. This allows us to operate the system under appropriate counting rate.

### 3. Experimental setup

After the energy calibration of the system was carried out by use of  $\gamma$ -ray sources ( $^{133}\text{Ba}$  : 384 keV, 356 keV, 303 keV, 274 keV and  $^{241}\text{Am}$  : 59.5 keV), we installed this detector on the Compact Helical System (CHS) to make sure whether the system can work well as a whole. In this test, X-rays up to 10 keV was successfully detected in a low density ( $n_e \sim 0.23 \times 10^{19} \text{ m}^{-3}$ ) ECRH plasma at magnetic field strength  $B_t$  of 0.95 T. In a higher  $n_e$  plasma ( $n_e \sim 0.5 \times 10^{19} \text{ m}^{-3}$ ), the maximum photon energy became lower than that in  $n_e \sim 0.23 \times 10^{19} \text{ m}^{-3}$  and was 6~7 keV. After we made sure that the system could work correctly in NIFS, the detector and electronics have been moved to the Heliotron J site. Figure 2 shows the location of Heliotron-J diagnostic port where the detector was installed. We have set the whole system in this fiscal year. In 2006,

dependence of confinement property on magnetic field configuration is going to be investigated through measuring

pulse height spectra of X-rays in low-density ECRH plasmas.

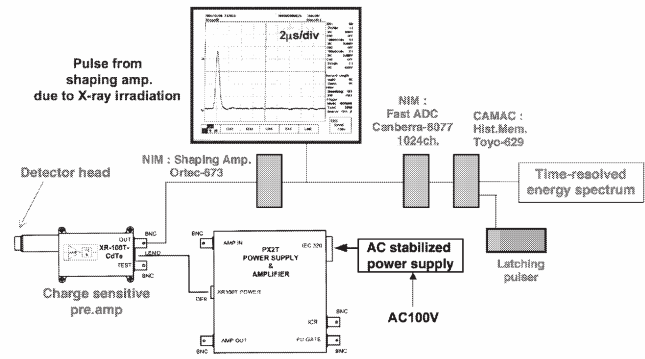


Figure 1 Electronic circuit for X-ray diagnostic by use of CdTe detector. Typical output pulse from shaping amplifier due to X-ray irradiation is also shown.

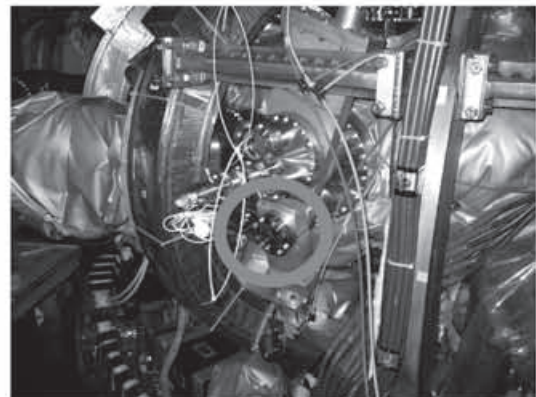


Figure 2 Diagnostic port on Heliotron-J where the CdTe X-ray detector was installed.

### References

- 1) Obiki, T. *et al.*, Nuclear Fusion **41**, (2001)833.
- 2) Mizuuchi, T. *et al.*, Plasma Science & Technology **6**, (2004)2372.



## §19. Evaluation of Boozer Coordinates Based on the Field Line Tracing Approach

Yokoyama, M., Suzuki, Y.,  
Nakamura, Y., Mizuuchi, T., Sano, F., Heliotron J  
Experimental Team (Kyoto Univ.)

The dependence of the confinement quality of H-mode on magnetic configuration found in Heliotron J (HJ) has been attempted to understand based on the poloidal viscosity 1) depending on the magnetic structure 2). However, the VMEC2000 equilibrium calculations have been limited to rather smooth magnetic surfaces. This has excluded the corrugated magnetic surfaces located at the peripheral region, where the poloidal viscosity is expected to become larger. Thus, the evaluation of poloidal viscosity in such a region with corrugated magnetic surfaces is important to investigate the configuration dependence of H-mode quality in more detail.

For this purpose, Boozer coordinate 3) construction has been attempted based on the magnetic field line tracing 4). Since this approach does not depend on the Fourier representation of magnetic surface shape essential for VMEC2000 calculations, it is anticipated to enlarge the plasma volume where Boozer coordinates can be evaluated.

Several representative magnetic configurations in HJ have been used as test cases to validate this approach. The magnetic field lines are launched from the equatorial plane with the interval of 7 mm. The information for the trajectory in the real space and the magnetic field strength variation along that trajectory on magnetic field lines (only lines which can do 200 or more toroidal turns) are exploited to construct the Boozer coordinates.

Figure 1 shows the magnetic surfaces in the “standard” configuration where Boozer coordinates are successfully evaluated based on this field line tracing approach. As for reference, the outermost magnetic surface from

VMEC2000 calculation is shown with the solid curve in a plasma region. It is recognized the corrugated magnetic surfaces are now included compared to the VMEC2000 boundary. This “enlargement of plasma radius” is the important result to promote the poloidal viscosity evaluation, which might enhance the understanding of the configuration dependence of H-mode quality in HJ.

The coordinate transformation from Boozer to Hamada 5) is required to evaluate the poloidal viscous damping coefficient in Ref. 1). In this regard, Fourier spectral decomposition for the real coordinates in Boozer coordinates is essential, which is now underway.

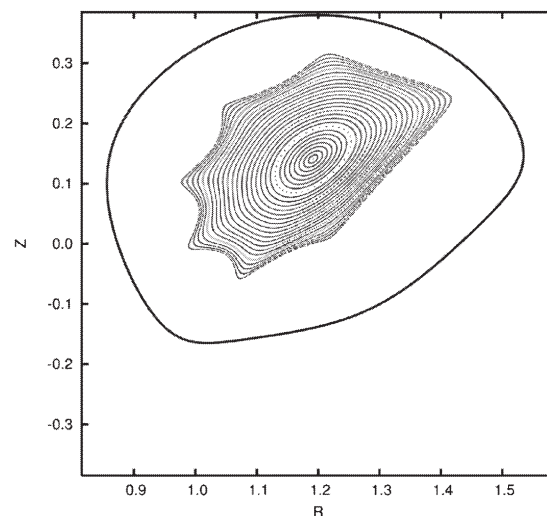


Fig. 1 The magnetic surfaces in the “standard” configuration in HJ, where the Boozer coordinates are successfully evaluated with the field line tracing approach. The solid curve denotes the outermost magnetic surfaces treated in VMEC2000.

### References

- 1) H.Wobig et al., Plasma Phys. Controll. Fusion, **37** (1995) 893.
- 2) F.Sano et al., Nucl. Fusion **45** (2005) 1557.
- 3) A.H.Boozer, Phys. Fluids **23** (1980) 904.
- 4) J.A.Rome et al., J.Comput. Phys. **82** (1989) 348.
- 5) S.Hamada, Nucl. Fusion **2** (1962) 23.

§20. Study of Neutral Hydrogen Atom and Impurity Behaviors in Heliotron J III-2

Kondo, K. (Graduate School of Energy Science, Kyoto University),  
Sano, F. (IAE, Kyoto University)

The main object is to make clear the magnetic configuration dependence of heating efficiency by ICRF and NBI for Heliotron J plasmas. In order to obtain high heating efficiency the reduction of impurities is necessary. The impurity behavior is investigated with a vacuum ultraviolet spectrometer in the wavelength region from 5 to 40 nm in ICRF and NBI heated plasmas.

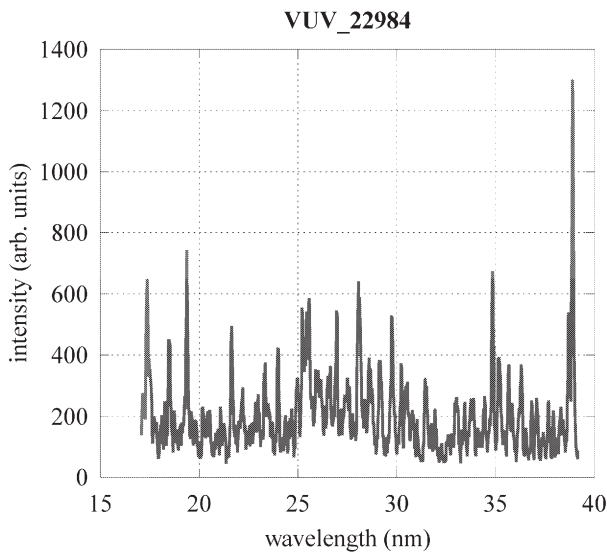


Fig. 1

Figure 1 shows a typical VUV spectrum observed in ICRF heated plasma. The most prominent spectra are Fe, Ti, Cr, C and O ions. In particularly, titanium is dropped into plasmas accidentally and many spectral lines are identified. They are Ti XI(38.61), Ti X(36.01, 28.96), Ti IX(29.63, 27.87, 26.79), Ti VIII(26.36, 25.86), Ti VII(26.48, 25.47) and Ti VI(25.53, 25.11).

Figure 2 show the dependence of Ti XI line intensity on the ICRF power. The magnetic configuration is the standard one in Heliotron J confining magnetic field. The distinguished character of the magnetic configuration in Heliotron J is controllability of the bumpiness.

The dependence of the impurity behavior on the bumpiness is investigated.

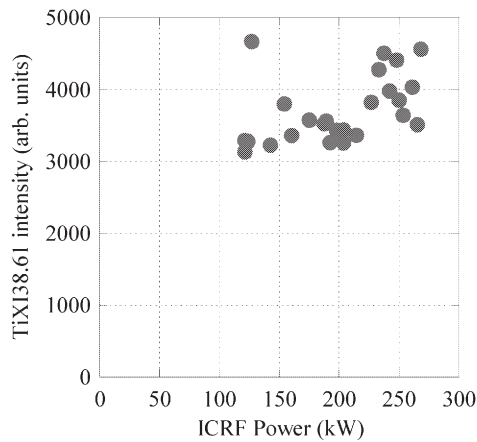


Fig. 2

As for neutral hydrogen atoms, the Doppler-shifted H $\alpha$  spectral intensity is measured in order to estimate beam energy fraction and beam decay. Figure 3 shows an example of the Doppler-shifted H $\alpha$  spectral profiles of E, E/2 and E/3. The injection energy E is 25 keV. The sightlines are provided for three toroidal and ten for poloidal directions. The decay length of the injected beam is estimated from the intensities with three toroidal positions.

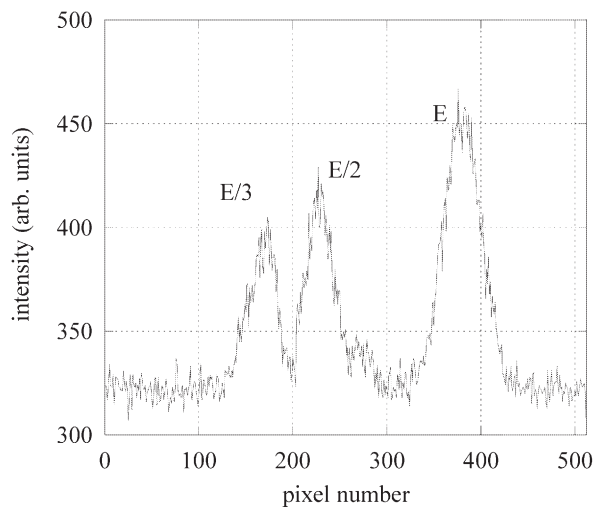


Fig.3

The capability for estimating the density ratio of C<sup>6+</sup> ion to the electron is also investigated.

## §21. Optimization of Helical System Concept

Sano, F. (Institute of Advanced Energy, Kyoto University)

The collaboration research between the Heliotron J group and other experimental groups such as the CHS group has been continued to understand machine-independent torus plasma confinement physics through the systematic study using the data obtained in this collaboration. The main purpose of this research is to promote experimental and theoretical studies based on the data of the improved confinement in Heliotron J and CHS for the optimization of helical confinement field aiming the control of the transport in the helical plasmas [1].

The five themes for the collaboration research has been selected; (1) the database construction for plasma confinement [2], (2) the structure formation accompanying with the confinement transition [3], (3) ECCD, EBW Heating [4], (4) the production and confinement of high energy particles and (5) the theoretical analysis of helical configuration optimization. Each group joined the plasma experiment for one week in the first and second term of this fiscal year, and we have been using fast internet for data exchange and analysis. For the collaboration of this year, we have put emphasis on the themes of the database construction, the production and confinement of high energy particles, and EBW physics.

### Database construction

Construction of a database (ISS04) progressing, the contribution of the effective helical ripple  $\epsilon_{\text{eff}}$  on the confinement for L-mode and H-mode in Heliotron J plasmas (particularly, ECH plasmas) is becoming clear. For example, energy confinement time normalized by the ISS04 scaling-law (L-mode) increases as the effective ripple,  $\epsilon_{\text{eff}}$ , decreases and the enhancement factor reaches 1.5 at the maximum in H-mode. However, the dependence of the high energy particle confinement in ICRF and NBI experiments is different from that for energy confinement. It is left as a future problem.

### High energy particle generation

Formation mechanism of observed ion tail having energy of several times of ion temperature of bulk under a certain condition in ECH/ECCD plasmas does not yet become clear although there are some suggestions such as the mode conversion of EC wave into LH wave, the influence of asymmetric Maxwell distribution, and so on. A fast ion tail is measured by a low density range than  $1.0 \times 10^{19} \text{m}^{-3}$  in Heliotron J. It is also observed that the high energy flux

increases as the electron density decreases. Data analysis about the density dependence of tail generation in CHS has been continued since last year. It is noted that the data analysis of the potential (HIBP) and the magnetic fluctuation in the frequency range from 50 to 300 kHz in low density has been carried out, which is considered to appear at the beginning of the tail formation.

### EBW experiments

ECH and ECCD are used for generation of currentless plasmas, electron temperature distribution control, MHD instability suppression and so on. Usually the electromagnetic wave mode such as O-mode and X-mode is selected because of the effectiveness of one-pass absorption. However, it is very difficult to apply this method to high density plasmas so that there is a density limit called cut-off density. To resolve this problem, mode conversion from an electromagnetic wave to an electrostatic wave can be utilized. The electron Bernstein wave (EBW) does not have the density limit for its propagation, and have an advantage that it is absorbed efficiently in the electron cyclotron resonance layer.

The optimization of the O-X mode conversion has been tried in CHS by injecting the 53.5-GHz ECH beam of 350 kW into NBI plasma, then, controlling the injection angle and polarization. In OXB heating, the injection of the beam is oblique against the torus. A Sniffer probe on the opposite side to the injection is used for the estimation of the leaked micro wave since it measures the wave which is not absorbed at the first passage of the resonance layer. From the dependence of the probe signal intensity on the ECH injection angle, there is a minimum point of the signal when the injection angle is -11 deg in the toroidal angle and the beam goes near the axis. This incidence condition somehow deviates from the O-X mode conversion most suitable point calculated from a vacuum magnetic field a little. It is supposed that it could come from an effect of refraction by a plasma. It is considered for heating that the optimization of the density profile for the improvement of the O-X mode conversion ratio or the field control for centralization of ECH power absorption is required since no increase of the stored energy is observed.

### References

- [1] F. Sano, et al., Nucl. Fusion **45**, 1557(2005).
- [2] H. Yamada, et al., Nucl. Fusion **45**, 1684 (2005).
- [3] T. Mizuuchi, et al., J.P.F.R., 81, 949(2005).
- [4] K. Nagasaki, et al., Nucl. Fusion **45**, 13(2005).

§22. Study of Peripheral Plasma in Heliotron J  
Using Fast Camera

Nishino, N., Fukuyama, Y., Kondo, E., Fukamizu, T.,  
Abe, T. (Hiroshima Univ.),  
Kondoh, K., Mizuuchi, T., Sano, F. (Kyoto Univ.)

2-d imaging technology using a fast camera is applied in Heliotron J plasma to study peripheral turbulence. Langmuir probe and fast camera measurement are the powerful methods in the research field of plasma turbulence [1, 2]. We have been using a fast camera as an imaging tool since 2004, and we were already successful to find harmonic oscillation just after L-H transition [3] using a combination of carbon limiter and a fast camera. This year we demonstrated a new fast camera, which is capable to take a picture with 160,000 frames per second (FPS). The local gas puff was used to brighten the plasma for spontaneous emission due to the electron impact collision. The radius of Heliotron J plasma is about 20cm, and neutral atoms can penetrate to the plasma core. However, the results show that only the adjacent area from the local gas puff is brightened. Therefore, we believe peripheral plasma is mainly brightened by the local gas puff. Figure 1 shows the filamentary structure in Heliotron J plasma with local gas puff. Without gas puff the same phenomena are seen by fast camera, but SN ratio is not sufficient.

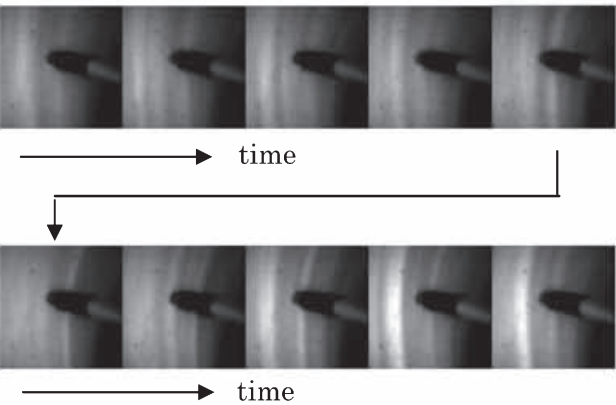


Fig.1 Filamentary structure in Heliotron J plasma  
Speed of record is 105,000 FPS  
These filamentary structures are frequently observed in

ST/Tokamak plasmas. However, it is first time to find these phenomena in Heliotron J plasma. It may suggest that these phenomena are the basic physics of plasma in the magnetic field. Recently these peripheral turbulences might be related to the energy/particle confinement. In this serious study of Heliotron J the ion saturation current of the probe are coincidence of the bright emission region of the images. It is suggested that the bright emission region of the filamentary structure is relative high density/temperature region. These filamentary structure moves across the magnetic field. The direction of the motion is the electron diamagnetic direction, and it is opposite to the negative ExB direction. The results of the density scan experiment show the motion of the filamentary structure was very fast in low electron density plasmas and it was insufficient to catch the precise movement of them even with the speed of 105,000 FPS. However, in very high density plasma ( $n_e > 3 \times 10^{19} \text{ m}^{-3}$ ), the motion was slower and the movement of them was seen clearly (see Fig.2). Typical lifetime of them in high density plasma is 500-700 microseconds. These results are presented in the international meeting [4]. Physics models of the filamentary structure are proposed by several theoretical groups. Therefore, the further study is necessary to investigate the peripheral turbulence, and it is needed to compare the theories and the experiments.

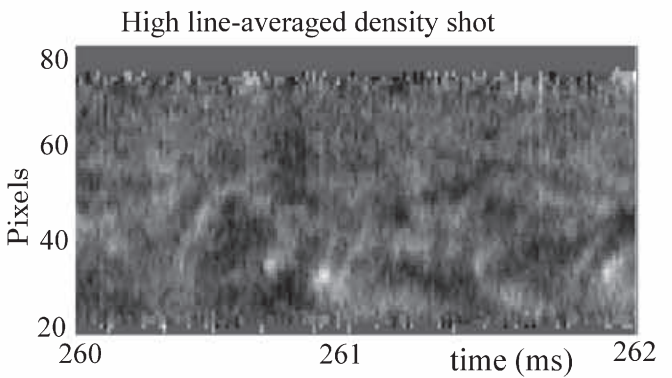


Fig.2 Time slice image along the line shown in Fig.1  
References

- 1). T.Mizuuchi, et al.: J Nucl. Mater. **337-339** 332(2005)
- 2). N.Nishino, et al.: J. Plasma Fusion Res. **1278** 179 (2004)
- 3). N. Nishino, et al.: J Nucl. Mater. **337-339** 1073(2005)
- 4). Nishino, N., et.al.: 17<sup>th</sup> Plasma-Surface Interaction



### §23. Study on Neutral Particle Transport in Non-Axisymmetric Helical Plasmas

Nakashima, Y., Islam, Md. K. (Univ. Tsukuba, P.R.C.),  
 Mizuuchi, T., Kobayashi, S. (Kyoto Univ., I.A.E.),  
 Kubota, Y., Higashizono, Y. (Univ. Tsukuba, Graduate School of Pure and Appl. Sci.),  
 Yabutani, H. (Kyoto Univ., Graduate School of Energy Sci.),  
 Shoji, M.

In magnetically confining plasma devices, investigation of neutral transport is an important subject for understanding edge plasma behavior and for the estimation of particle confinement characteristics. In non-axisymmetric plasmas, such as helical devices, the analysis of neutral transport becomes complex due to the three-dimensional configuration of the system. The objective of this study is focused on the neutral transport in the above three-dimensional non-axisymmetric plasma and leads to the understanding of its edge plasma and the plasma-wall interactions with such plasmas. In this research, a fully three-dimensional Monte-Carlo simulation code DEGAS<sup>1,2)</sup> is applied to Heliotron-J device<sup>3,4)</sup>, which utilizes a helical-axis heliotron configuration and examine the neutral particle behavior in a carbon-target experiment of Heliotron-J.

Figure 1 shows the schematic view of the plasma cross-section and the carbon-target. The material of the target is CFC and an electrostatic probe is installed on the top of the target. In a 70 GHz second-harmonic electron cyclotron heating (ECH) plasma, a number of measurements such as two-dimensional image measurement with a camera and high time-resolving  $D\alpha$  line-emission profile detector and spectroscopic measurements were carried out under the condition of changing the insertion length of the carbon-target. In this experiment, the target was inserted from 15 mm outside of the outer-most magnetic surface (-15 mm) to 10 mm inside of the surface (+10 mm).

Figure 2(a) shows the 2-D image of the target obtained with the camera in the case of the insertion length of +10 mm. A strong light emission area is observed in the left side of the target except for its top. In this viewing angle, the magnetic surface is raised up from the left to the right of this figure. Therefore the contact between the

carbon-target and the plasma is concentrated on the left side. Such localization of light emission shown in Fig.2(a) is thought to be ascribed to the above geometrical reason.

Figure 3 shows the preliminary mesh model for the DEGAS simulation of the carbon-target experiment. At present improvement of the mesh is in progress.

#### Reference

- 1) Heifetz, D. *et al.*, J. Comput. Phys. **46** (1982) 309.
- 2) Nakashima, Y. *et al.* J. Nucl. Mater. **196-198** (1992) 493.
- 3) Kobayashi, S. *et al.* 31st EPS Conf. Plasma Phys. London, ECA **Vol.28G**, P-5.097 (2004).
- 4) Sano, F. *et al.*, Nucl. Fusion **45** (2005) 1557.

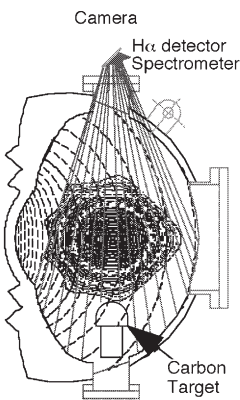


Fig. 1 Schematic view of Heliotron-J cross-section and the carbon target

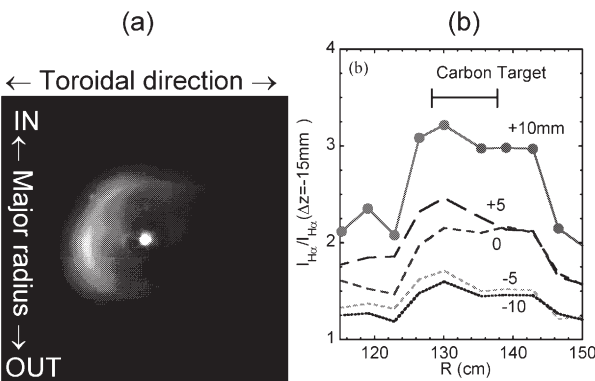


Fig.2 (a) 2-dimensional image of  $H\alpha$ ,  $D\alpha$  line-emission, (b) profile of the intensity ratio in different insertion length of the carbon limiter.

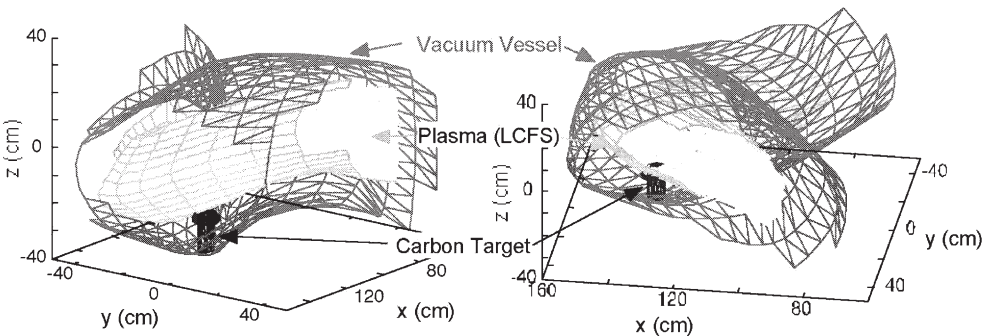


Fig.3 Plasma mesh model simulating the carbon-target experiment used in DEGAS Monte-Carlo simulation.

# §24. Study on Tritium Behavior in Liquid Blanket System of Laser Inertial Fusion Reactor

Nishikawa, M. (Graduate School of Eng. Sci., Kyushu U.),  
 Fukada, S. (Graduate School of Eng., Kyushu U.),  
 Katayama, K. (Graduate School of Eng. Sci., Kyushu U.)

In designing of the liquid blanket system for a laser inertial fusion reactor, it is necessary to have the effective tritium recovery system for assurance of tritium self-supply and to have the tritium safety confinement system for certification of tritium radiation safety. Then, It is required to know the tritium transfer properties in liquid breeder materials because the wetted wall system is considered to protect the first wall in design of the inertial fusion reactor of Osaka University. At present, use of Lithium Lead is considered as the breeder material though only a small amount of reports have been made on tritium transfer properties. It is anticipated that a large part of the bred tritium may permeate to the outer circumstances because the solubility of hydrogen in lithium lead is considered to be so small. Accordingly, the object of the present researchers is to make the measurement of tritium diffusivity and solubility in lithium lead and lithium as a part of the cooperative research program lead by the Institute of Laser Engineering, Osaka University.

The following advancements are made in this year.

- (1) Neutronics calculation estimated using the ANISN code shows that thickness of 1m is enough to obtain the effective tritium breeding ratio when LiPb is chosen as the blanket material as shown in Fig. 1.
- (2) The solubility of hydrogen into LiPb obtained in this study is compared in Fig. 2 with solubility from other researchers. It is necessary to have more data because no good agreement of data of

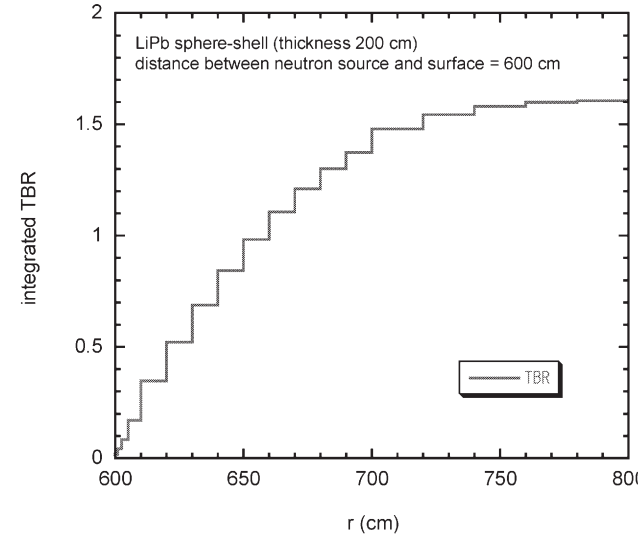


Figure 1 Tritium breeding ratio estimated for LiPb blanket

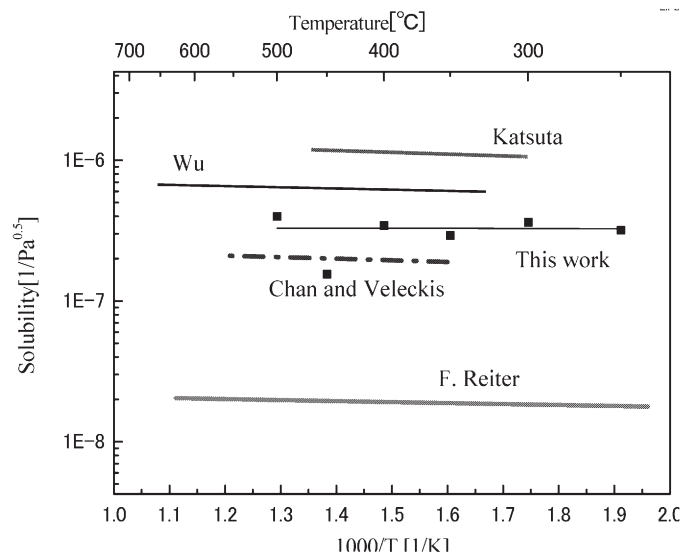


Figure 2 Solubility of hydrogen in LiPb

- each study is obtained as can be seen from Fig. 2.
- (3) The tritium release behavior from solid breeder blanket materials are also performed in this cooperative research works. It is assured in this study that the model constructed by the present authors can predict the tritium release behavior from solid breeder materials. Almost all parameters required to estimate the tritium behavior using this code have been quantified in the series of experiment by the present authors.

[Reports published in 2005 related to this study]

- 1) Study of tritium behavior in cement paste, H. Takata, T. Motoshima, S. Satake and M. Nishikawa, Fusion Sci. and Tech., vol. 48, 589-592(2005).
- 2) Transfer phenomena of tritiated water from air to water, M. Nishikawa, H. Takata, T. Takeishi, and K. Kamimae, Fusion Sci. and Tech., vol. 48, 386-389(2005).
- 3) Recovery of retained tritium from graphite tiles of JT-60U, T. Takeishi, K. Katayama, M. Nishikawa, N. Miya and K. Masaki, Fusion Sci. and Tech., vol. 48, 565-568(2005).
- 4) Release behavior of bred tritium from irradiated Li<sub>4</sub>SiO<sub>4</sub>, T. Kinjyo, M. Nishikawa, K. Katayama, T. Tanifuji, M. Enoda and S. Beloglazov, Fusion Sci. and Tech., vol. 48, 646-649(2005).
- 5) Study on water uptake of proton exchange membrane by using tritiated water sorption method, H. Takata, M. Nishikawa, Y. Arimura, T. Egawa, S. Fukada and M. Yoshitake, J. Hydrogen Energy, vol. 30, 1017-1025(2005).
- 6) Diffusion coefficient of tritium through molten salt flibe and rate of tritium leak from fusion reactor system, S. Fukada, R.A. Anderl, A. Sagara and M. Nishikawa, Fusion Sci. and Tech., Vol.48, 666-669(2005).

§25. Aerosol Formation and its Effects on the Chamber Wall Lifetime and Operation of IFE Power Reactors

Hirooka, Y. (NIFS),  
Tanaka, K.A. (Osaka Univ.)

It is well known that along with DT-pellet implosions, IFE reactor chamber wall components will be exposed to repeated short-pulses of 14 MeV neutrons, intense X-rays, high-energy unburned fuel particles and pellet debris such as CD complex ions. As a result, wall materials will be subject to ablation, but re-deposition of ejected materials may occur at the same time. These processes will directly affect the lifetime of wall components and perhaps the implosion pulse frequency, i.e. reactor power output, as well for the reason to be mentioned next.

Whether the wall surface material is a solid or liquid, one predicts some aerosol formation in the chamber periphery region where ejected material flows cross over each other, leading to local density maxima. In addition to this, aerosol formation is also possible at the center of symmetry of a reactor chamber if it is in the form of sphere or cylinder.

Depending up on the collision conditions of ejected materials, the size of aerosol particles to be formed at the center may increase by coalescence, but can decrease by disintegration. As such, aerosol formation will occur in a yet-to-be explored manner. Importantly, either way the air-borne time can be orders of magnitude longer, compared with that for direct re-deposition, due to the loss of momentum.

These air-borne aerosol particles are likely to absorb or reflect the subsequent laser beams intended for implosion, affecting directly the reactor power output. It follows from these arguments that the pellet implosion frequency must be controlled to avoid the aerosol effects. Despite its critical importance, this technical issue has not yet been clearly addressed in the IFE research community.

The present work is intended to investigate the behavior of aerosol formation from ablated materials in the center of symmetry of an IFE reactor chamber. As shown in Fig. 1-(a) and (b), a laboratory experimental setup has been put together for this purpose. A high-power (~1J) pulse-operation (~50ns, 10Hz) YAG laser beam is employed for the primary materials ablation. This laser beam is first split and then reshaped to have a rectangular cross-section to radiate two targets, as shown in Fig. 2. Selected as the target materials are lithium, lead, and their alloys. Currently, this dual-target laser ablation setup is being installed with a turbo-molecular pump system to prepare for actual experiments.

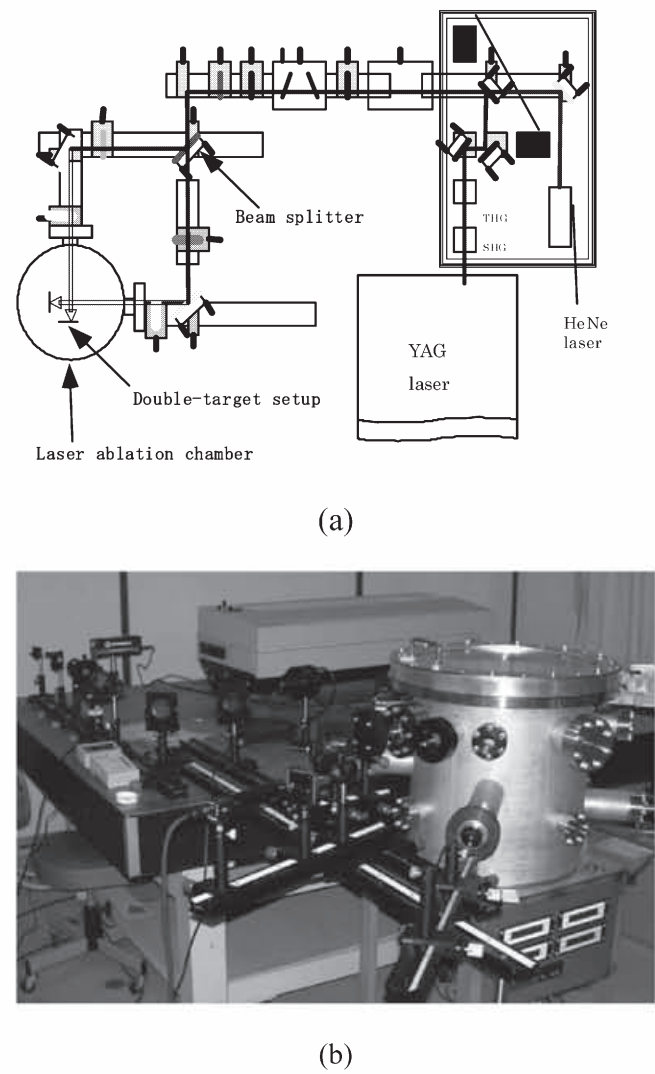


Fig. 1 A schematic diagram of the laser-ablation experimental setup (a), and a close-up on the ablation chamber (b).

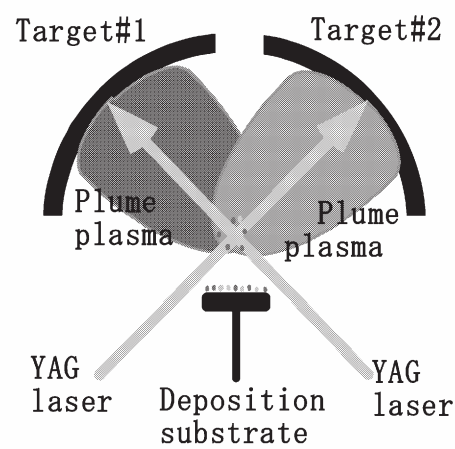


Fig. 2 A schematic diagram of the dual-target experimental setup for aerosol formation due to ablation plume-to-plume interactions.

## §26. Surface Wave Structure of Vertical Liquid Film Flow with Artificial Oscillation

Kunugi, T., Kino, C. (Kyoto Univ.),  
Norimatsu, T. (Osak Univ.),  
Sagara, A.

In order to produce the electricity from a inertia confinement fusion reactor, it is necessary to protect the wall of the reactor chamber from high heat flux and high energy particles. One of the possible ideas for the chamber wall protection scheme is a liquid wall concept. The authors have been developing the direct numerical procedure so-called MARS (Multi-interface Advection and Reconstruction Solver) method [1] for tracking the free-surface behavior and studying the active control of the falling film flow along the vertical wall [2]. In this study, the MARS simulation has been carried out for investigating the surface wave structure of vertical liquid film flow with artificial oscillation.

### NUMERICAL PROCEDURES

The governing equations are the continuity equation for multi-phase flows, momentum equation based on a one-field model and the energy equations:

$$\frac{\partial F_m}{\partial t} + \nabla(F_m V) - F_m \nabla V = 0 \quad (1)$$

$$\frac{\partial V}{\partial t} + \nabla(VV) = G - \frac{1}{\langle \rho \rangle} (\nabla P + \nabla \tau - F_V) \quad (2)$$

$$\frac{\partial V}{\partial t} \langle \rho C_V \rangle_M T + \nabla \langle \rho C_V \rangle_M TV = \nabla \langle \lambda \rangle_M \nabla T + Q \quad (3)$$

here,  $F$  is the volume fraction of fluid and the suffix  $m$  denotes the  $m$ -th fluid or phase,  $\langle \rangle$  denotes a material average and  $F_V$  is a body force due to a surface tension based on the CSF (Continuum Surface Force) model[3].  $\tau$  shows a viscous shear stress.  $\rho$  is the density,  $\lambda$  is the thermal conductivity and  $C_v$  is the specific heat at constant volume. The surface volume-tracking technique is based on the MARS.

Figure 1 shows the computational domain and Table 1 shows the fluid properties used in this study.  $\delta_0$  is the equilibrium film thickness. The mesh sizes are used as  $(\Delta x, \Delta y) = (0.4\delta_0, 0.1\delta_0)$ . Here,  $\delta_0$  is an equilibrium liquid film thickness derived by the Nusselt theory. The inlet mean velocity,  $U_0$  derived by the Nusselt theory can be controlled with an external forcing as expressed:

$$U = [1 + \varepsilon \sin(2\pi ft)]U_0 \quad (4)$$

controlled with an external forcing as expressed: here, the forcing frequencies:  $f=20\text{Hz}$ ,  $30\text{Hz}$  and  $45\text{Hz}$  are considered in the present study.

Figure 2 shows the surface wave structures. There are three groups of wave pattern such as (a) Solitary-shaped wave, (b) large solitary wave with several capillary waves and (c) solitary wave merged with capillary wave.

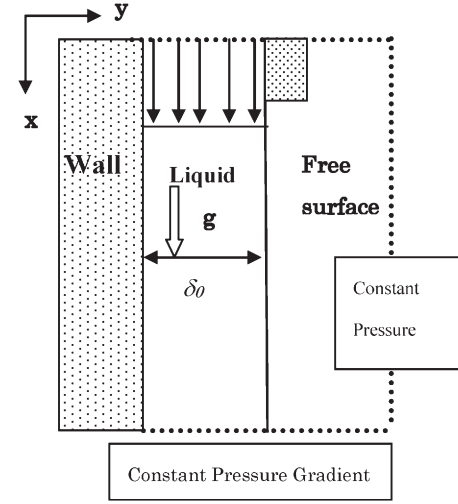


Fig. 1. Computational domain

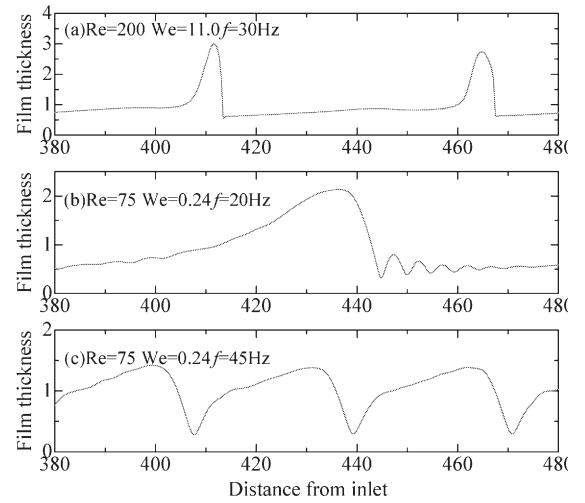


Fig. 2. Wave structure

In order to investigate the flow condition of the wave patterns, we introduce a new non-dimensional parameter,  $We/Ka$  (Kapitza number  $Ka = \sigma \rho^{1/3} / g^{1/3} \mu^{4/3}$ ). The wave pattern can be classified based on  $We/Ka$  as shown in Fig. 3.

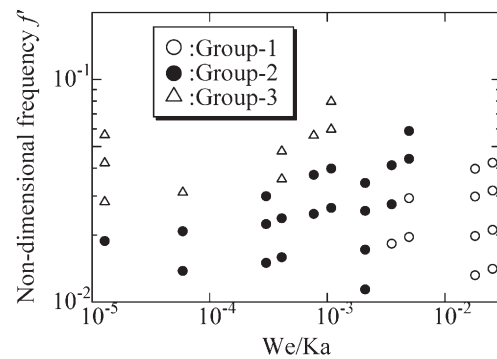


Fig. 3 Wave pattern mapping

### REFERENCES

- [1] Kunugi, T., CFD J., **9**, 563 (2001)
- [2] Kunugi, T& Kino, C. Fus. Eng. Des., **65**, 387 (2003)
- [3] Brackbill, J. U. et. al., JCP, **100**, 335 (1992)



## §27. X-ray Penumbra Imaging for Laser-Produced Plasma –Uniformly Redundant Penumbra Array–

Chen, Y.-W. (Ritsumeikan Univ.)

Penumbra imaging is a technique which uses the fact that spatial information can be recovered from the shadow or penumbra that an unknown source casts through a simple large circular aperture. Since such an aperture can be “drilled” through a substrate of almost any thickness, the technique can be easily applied to highly penetrating radiation such as neutrons and  $\gamma$  rays. The limitation of penumbra imaging is that the straightforward deconvolution is very sensitive to noise contained in the penumbra image. In this paper, in order to increase the SN ratio of the penumbra image, we propose a new imaging technique of uniformly redundant penumbra array (URPA), which combines the advantages of URA to the penumbra imaging. In URPA, multi penumbra apertures are used instead of single penumbra aperture, which are arranged in *m*-sequence as shown in Fig.1(b). The reconstruction process contains two steps: one is to use a decoding operator to obtain the real penumbra image and the second step is to use a wiener filter to reconstruct the source image like conventional penumbra imaging.

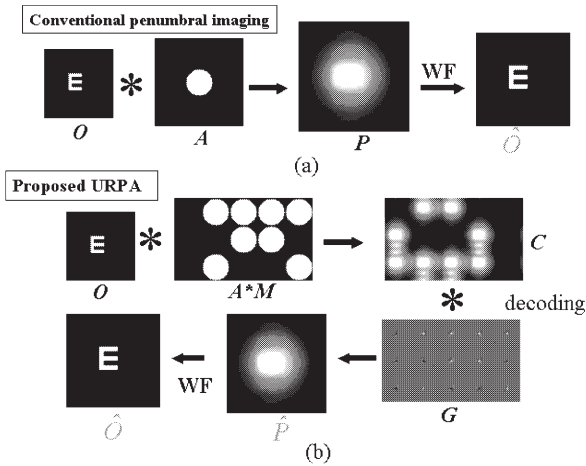


**Fig.1 The basic concept of URPA; (a) conventional penumbra imaging; (b) URPA**

The aperture function of URPA can be expressed as  $A*M$ , where  $A$  is the penumbra aperture function and  $M$  is the two-dimensional *m*-sequence with an array of  $r \times s$ . Thus the image ( $C$ ) obtained on the detector is given as

$$C = O * A * M = P * M \quad (1)$$

As shown in Eq.(1), the image ( $C$ ) on the detector is a coded penumbra image.

The decoded penumbra image is given by

$$P' = C * G = P * (M * G) \quad (2)$$

Where  $G$  is a decoding operator. In order to obtain a perfect penumbra image,  $M * G$  must be a delta function. The key point is that the autocorrelation  $\rho$  of *m*-sequence with an array of  $r \times s$  is given by

$$\rho = M * M = \begin{cases} (r \times s) / 2; & \text{mod}(i, r) = 0 \text{ and } \text{mod}(j, s) = 0 \\ (r \times s) / 4; & \text{otherwise} \end{cases} \quad (3)$$

The cycle autocorrelation is a single value with a nonzero background. Furthermore, by defining a balanced operator

$$G(i, j) = \begin{cases} 1 & \text{if } M(i, j) = 1 \\ -1 & \text{if } M(i, j) = 0 \end{cases} \quad (4)$$

We can get a perfect delta function of  $M * G$  as

$$\rho = M * G = \begin{cases} (r \times s) / 2; & \text{mod}(i, r) = 0 \text{ and } \text{mod}(j, s) = 0 \\ 0; & \text{otherwise} \end{cases} \quad (5)$$

Thus we can obtain a perfect penumbra image with a  $(r \times s + 1)/2$  times flux. It means that the proposed URPA can provide a penumbra image with a high SN ratio.

The simulation results are shown in Fig.2. It can be seen that The SNR of penumbra images can be significantly improved by URPA. The larger the URPA size, the higher the SNR. By using a penumbra image with higher SNR, we can easily obtain a reconstructed image with high resolution and high SNR. The SNR of the reconstructed image using  $15 \times 17$  URPA is improved by a factor of 500 compared with the conventional penumbra imaging for the case of  $\sigma^2 = 13.8$ .

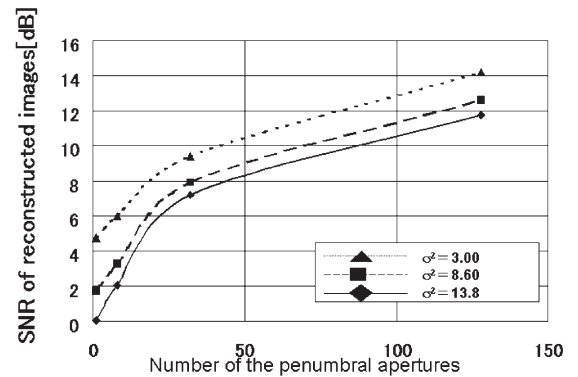


**Fig.2 Simulation results**

## §28. Design Study on Foam-Cryogenic Targets by Integrated Simulations

Nakao, Y. (Kyushu Univ.),  
Mima, K., Nagatomo, H., Johzaki, T., Sunahara, A. (Osaka Univ.),  
Sakagami, H. (Univ. of Hyogo),  
Taguchi, T. (Setsunan Univ.),  
Nishiguchi, A. (Osaka Inst. Technol.),  
Okamoto, M., Horiuchi, R., Ishiguro, S.

The purpose of this study is to analyze the recent fast ignition experiments with cone-guiding targets<sup>1)</sup> and carry forwards a design of form-cryogenic targets. To simulate overall physics phenomena and identify the crucial issues involved in the core plasma heating, an integrated code system, "Fast Ignition Integrated Interconnecting code" (FI<sup>3</sup> code)<sup>2)</sup>, was developed. In this code system, the implosion dynamics is simulated by an ALE-CIP radiation hydro-code "PINOCO"<sup>3)</sup>. A collective PIC code "FISCOF"<sup>4)</sup> simulates laser-plasma interactions to evaluate the time-dependent energy distribution of relativistic electron beam (REB). The core heating process is simulated using a relativistic Fokker-Planck (RFP) code<sup>5)</sup> coupled with a hydro-based burn simulation code "FIBMET"<sup>6)</sup>.

### Integrated Simulation

Using the FI<sup>3</sup> code system we analyzed the core heating properties of a cone-guiding shell target. First, an implosion simulation was carried out for a polystyrene target (1.06 g/cm<sup>3</sup>, 8μm-thickness, 250μm inner radius) which is attached with an Au cone having an opening angle of 30 degree. At the maximum compression, the optical size of the core,  $\int \rho(r=0)dz$ , reached 0.14 g/cm<sup>2</sup>.

The profiles of fast electrons generated by laser-plasma interaction were then evaluated with FISCOF. The Au cone tip was modeled by the 10μm-thickness plasma with  $n_e = 100 n_c$ , where  $n_c$  is the critical density. The 60μm-thickness imploded plasma was putted behind the cone tip. The simulation was carried out by assuming that the electron density in the rear of the cone tip is  $n_{e, rear} = 100 n_c$ ,  $10 n_c$  and  $2 n_c$ . A 750 fs Gaussian pulse ( $\lambda_L = 1.06\mu\text{m}$ ,  $I_L = 10^{20} \text{W/cm}^2$ ) was assumed as a heating laser. The forward-directed fast electrons were observed behind the cone tip.

Using the imploded core profile at the maximum compression and the time-dependent momentum profiles of REB obtained for the cases of  $n_{e, rear} = 100 n_c$ ,  $10 n_c$  and  $2 n_c$ , we simulated the core plasma heating with FIBMET. The REB source was injected behind the cone tip by assuming a super-Gaussian profile with 30μm width. **Figure 1** shows the temporal evolutions of bulk electron and ion temperatures averaged over the core region ( $\rho > 10 \text{g/cm}^3$ ).

In the low density plasmas located between cone tip and dense core, a static field is built up owing to a strong micro-instability, which moderates the fast electrons and reserves the energy around the cone tip for a long time. Due to this density gap effect, in the case of  $n_{e, rear} = 10 n_c$ , the core heating rate and the resultant temperature rising rate are

low in the early stage of core heating ( $t < 2 \text{ps}$ ) compared with the case of  $n_{e, rear} = 100 n_c$ . The core heating duration, however, is long since the sloshing fast electrons in the cone tip continue to be released from the cone tip after the laser irradiation. Thus, in the case of  $n_{e, rear} = 10 n_c$ , the core temperature reaches  $\sim 0.5 \text{keV}$ ; the temperature increment is 0.20 keV, which is a higher increment than that (0.17 keV) in the case neglecting the density gap between the cone tip and the dense core.

The core size is smaller than the range of MeV electrons, so that most of the fast electrons penetrate the core. The energy coupling from the REB to the core was estimated to be 22% in the case of  $n_{e, rear} = 10 n_c$ ; the coupling from the heating laser to the core was only 6.5%.

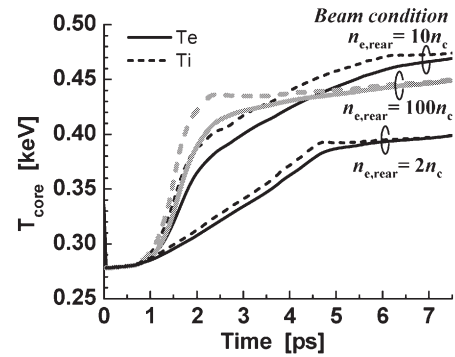


Fig.1 Temporal evolution of core plasma temperatures for three different electron densities in the rear of cone tip.

### Discussion

The integrated simulations assuming long duration (750 fs) for the heating laser showed that the density gap effect is more pronounced than in the previous simulations assuming short pulse (150 fs). However, we could not obtain core heating as observed in the experiments. In the simulation the core was heated up to 0.5keV, which is still lower than the temperatures measured in the experiments. In the above simulations, the heating laser-plasma interactions were treated by 1D-PIC, which resulted in underestimating the energy coupling from laser to fast electrons. For further study, in addition to inclusion of collisions in the cone and the geometrical effects in laser-plasma interactions, we should consider additional heating mechanisms such as fast ion heating.

### References

- 1) R. Kodama et al., Nature, **412** (2001) 798; **418** (2002) 933.
- 2) H. Sakagami, K. Mima, Laser Part. Beams, **22** (2004) 41.
- 3) H. Nagatomo et al., Proc. of 2<sup>nd</sup> IFSA (Kyoto, 2001), Elsevier, 140 (2002).
- 4) H. Sakagami et al., Proc. of 3<sup>rd</sup> IFSA (Monterey, 2003), ANS, 434 (2004).
- 5) T. Yokota et al, Phys. Plasmas, **13** (2006) 022702.
- 6) T. Johzaki et al, J. Plasma Fusion Res. SERIES, **6** (2004) 341.

§29. Natural Diamond Detector for Neutron and  $\gamma$ -ray Measurements in Laser Fusion Experiments

Isobe, M. (NIFS),  
Azechi, H. (I.L.E., Osaka Univ.),  
Krasilnikov, A.V. (TRINITI, Russia)

In the GEKKO XII laser facility, a neutron time-of-flight detector called MANDALA has been employed to measure energy spectrum of neutrons produced by fusion reactions [1]. The neutron detection by use of the MANDALA is restricted in the fast ignition experiment due to huge flux of prompt X-rays. Because of this reason, an examination of different neutron detection method is required. Natural diamond detectors (NDD) have been applied to the Large Helical Device (LHD) to diagnose energy distribution of fast neutral particles originating from neutral beam heating and ion cyclotron resonance heating [2,3]. Because the diamond itself is known to be fast in time response, neutron and  $\gamma$ -ray may be detected separately in laser fusion experiments.

NDD with ohmic Au contacts and a DC bias can work as a radiation detector. Three NDDs having different area( $\phi 2$  mm,  $2\text{ mm} \times 2\text{ mm}$ ) and thickness (0.1 mm and 0.2 mm) have been prepared for this purpose. The signal generation process is basically similar to that of a Si semiconductor detector. In the case of the high energy photons such as X-rays and  $\gamma$ -rays, electron-hole pairs are generated by photoelectric events inside the NDD. In the case of neutrons, a variety of nuclear processes such as elastic and inelastic scattering  $^{12}\text{C}(n,n')^{12}\text{C}$ , nuclear reaction  $^{12}\text{C}(n,\alpha)^9\text{Be}$  and so on are involved [4]. In comparison with a Si detector, the primary advantages of NDD include a high band gap of 5.5 eV, short mean free drift time of  $\sim 10$  ns, large saturation carrier velocity of  $2.2 \times 10^7$  cm/s for  $E$  of  $10^4$  V/cm, high breakdown voltage of  $10^7$  V/cm. Further detailed descriptions of NDD's properties are available in Ref. 4 and 5.

Because the time response of GHz range is required in the laser fusion experiment, the circuit used in LHD, so-called PHA, can not be used for this purpose. In order to improve time response as much as possible, a circuit shown in Figure 1 is used. A high voltage bias-T (Picoseconds Pulse Lab./Model : 5531) resistively couples the signal cable to a high voltage power supply and capacitively couples the signal cable to a GHz sampling oscilloscope. The total bandwidth is expected to be  $\sim 1$  GHz by use of this electronics. As for photons and neutrons, a time to reach NDD from the target as a function of distance between target and NDD is shown in Figure 2. Since the total system bandwidth is about 1 GHz, NDD should be more than 15 cm away from the target to separate neutron signal from  $\gamma$ -ray signal. Figure 3 shows the diagnostic port on the target chamber where NDD is installed. In next fiscal year, we are going to apply NDD

to fast ignition experiment to make sure of NDD's performance.

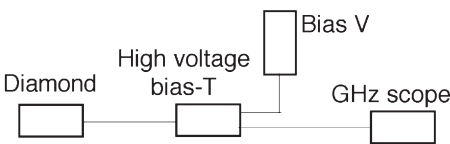


Fig.1 Electric circuit used for NDD in laser fusion experiment.

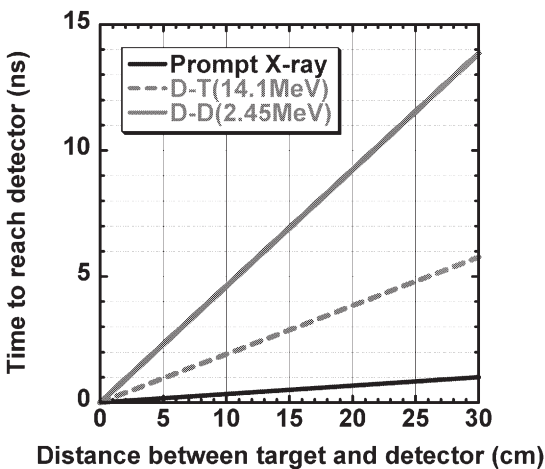


Fig.2 Time to reach NDD as a function of distance between target and detector.

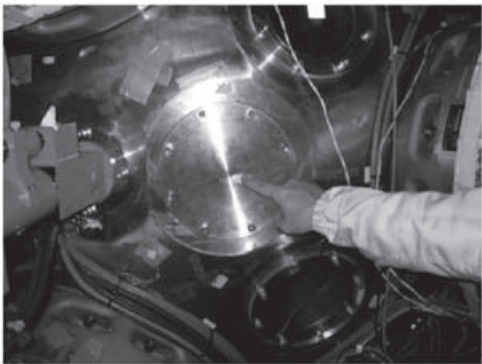


Fig.3 Diagnostic port on the target chamber for NDD installation.

References  
1) Izumi, N., *et al.*, Rev. Sci. Instrum. **70**(1999)1221.  
2) Isobe, M., *et al.*, Rev. Sci. Instrum. **72**, (2001) 611.  
3) Saida, T., *et al.*, Nucl. Fusion, **44**, (2002) 488.  
4) Pillon, M., *et al.*, Nucl. Instrum. Methods **B101**, (1995) 473.  
5) Krasilnikov, A.V., *et al.*, Rev. Sci. Instrum. **68**, (1997) 1721.

§30. Development of Gas Gun for Target Injection in Laser-Fusion Reactor

Endo, T. (Hiroshima Univ.)

The conceptual design of the target injector for a laser-fusion reactor was studied by a working group, the leader of which was Prof. T. Norimatsu (ILE, Osaka Univ.), in FY 2004-2005. In that study, we discussed a system, in which a set of target and sabot was firstly accelerated by a gas gun up to a certain speed, and subsequently its speed was finely adjusted by a coil gun. The gas gun for the target injector is under development at Hiroshima University in these years. From the past studies on the gas gun, it was found that it was easy to accelerate a projectile up to the required speed, which was about 300 m/s, but it was not so easy to stabilize the attitude of the flying projectile. In FY

2004, in order to stabilize the attitude of the flying projectile, we prototyped an acceleration tube with rifling, where the tube had a twisted line of guide pins and the projectile had a tilted groove, but it did not work well.

In FY 2005, we added the shooting stabilizer shown in Fig. 1 at the end of the acceleration tube, by which we intended to reduce the disturbance on the projectile exiting the gas gun. The shooting stabilizer consisted of the pressure reducing device and the fine adjuster. The pressure reducing device was basically a vacuum chamber containing an inner tube. The inner tube was 520 mm in length and 9.8 mm in inner diameter. The side wall of the inner tube had 100 holes of 3.75 mm in diameter for pressure release of the accelerating gas behind the projectile. In the fine adjuster, the side wall of the projectile was held by three plates of 90 mm in length, two of which were pressed to the projectile by springs.

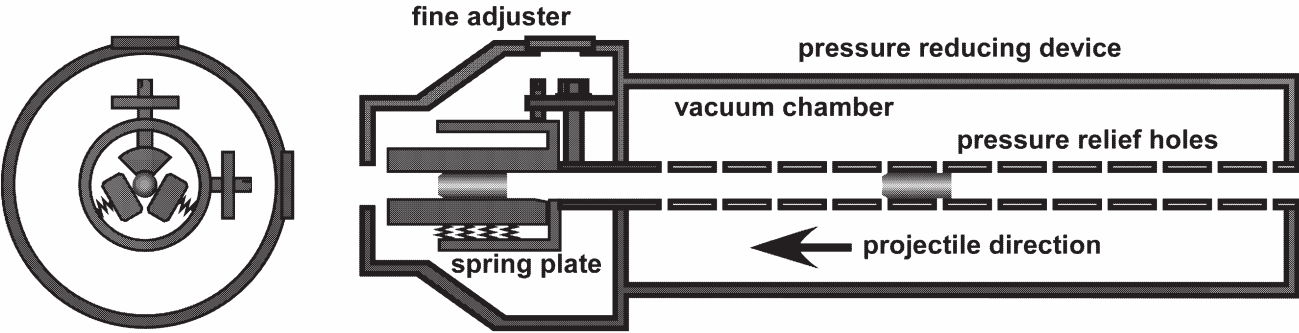


Fig. 1 Shooting Stabilizer

The projectiles used in the shooting experiments were made of Duracon acetal copolymer (a kind of polyoxymethylene resin). The projectile was a cylinder, which was 28 mm in length and 9.7 mm in diameter. For the guide-pin-type rifling in the acceleration tube, the side wall of the projectile had a tilted groove, which was 2.1 mm in both of the width and depth.

The shooting experiments were carried out at the accelerating gas pressure of 0.3 MPa. The projectile speed was about 55 m/s in the present experiments, although it was about 80 m/s before adding the shooting stabilizer. That is, the shooting stabilizer lowered the projectile speed by about 30%. However, the lowering of the projectile speed due to the shooting stabilizer is not so important because the projectile speed can be raised easily by higher gas pressure and longer acceleration tube.

In the present stage of the gas-gun development, the controllabilities of the flight direction and projectile attitude are more important. The controllability of the flight direction was 5.1 mrad (standard deviation) in the present experiments, although it was 7.9 mrad (standard deviation) before adding the shooting stabilizer. Indeed, the controllability of the flight direction was improved. But the required controllability of the flight direction is higher than the present status by one order at least.

Figure 2 shows the observed attitude of an in-flight

projectile. This picture was taken at 1.7 m from the exit of the gas gun with the light source of pulsed LEDs (duration: 7  $\mu$ s, interval: 0.7 ms). As shown in Fig. 2, the attitude of the flying projectile was not controlled. We need much more research and development.

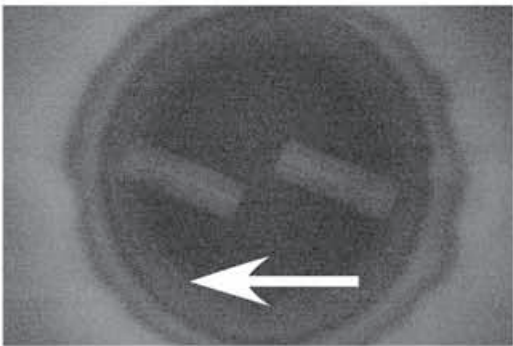


Fig. 2 Flying Projectile



### §31. Preliminary Study of Chamber Engineering for Fast Ignition Laser Fusion Reactor

Konishi, S., Yamamoto, Y., Takeuchi, Y., Hinoki, T. (Kyoto Univ.),  
Nishimura, H., Norimatsu, T., Fujioka, S., Azuchi, H., Kozaki, Y. (ILE, Osaka Univ.),  
Sagara, A.

One of the major problems in the technological feasibility of the inertial confinement fusion reactor is the chamber that should accept pulsed load of radiation, ion particles and debris and be pumped out in the repeated pulsed operation cycle of several Hz. Especially in a fast ignition scenario, lead (or lithium lead) cones attached to the target fuel pellets add specific material transfer issues such as deposition on the chamber wall, ablation, and formation of clusters that are suspected to affect the pumping characteristics (Fig.1). Ablated metal particles from the wall are suspected to form various sizes of clusters that fly slower and more difficult to evacuate. This collaborative research will investigate the basic behavior of the ablated particles from the surface simulating laser fusion chamber.

Figure 2 illustrates the setup of the experimental apparatus using the EUV database laser and the target chamber at ILE, Osaka Univ. Thomson parabola is used for ion energy and charge state measurements, the quadrupole mass spectrometer is for detection of polymer particle, and the charge collector is for ion current of ablated particle along the time.

The fiscal year 2005, we used the QMS with SEM, and tried to measure time variation of specific mass number synchronized to the laser pulse, as the mass scanning time of a QMS is not fast enough compared with decay time of ablated particles in the chamber. Two experimental campaigns of 2 weeks each were performed in the fiscal year 2005.

With Pb target, Thomson parabola detected lead ions of 1 to 7 charges with high energy (several keV). Figure 3 shows the example of the time variation of mass number 27, 54 with Al target. As the variation curves show almost same, the 54 amu particles are estimated to be dimer of Al.

In the fiscal year 2006, we plan to investigate time variation of emitted particles synchronized to laser pulse and identify the source of them (the chamber surface, primary target, and secondary target), and also try to improve measurement method.

#### Acknowledgement

The authors appreciate Prof. Sakawa of Nagoya University for their supports on the experiments.

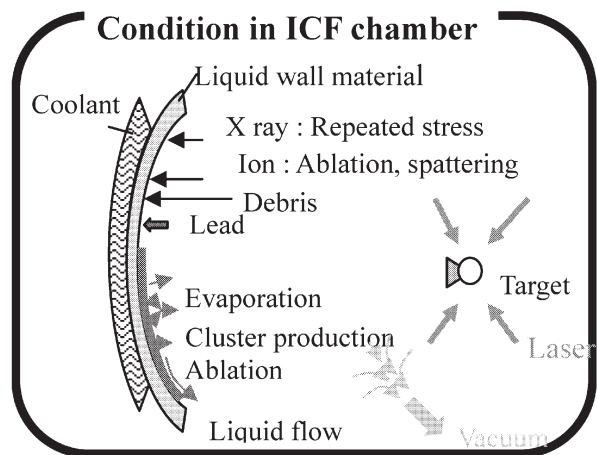


Fig. 1 Schematics of particle flow in ICF chamber

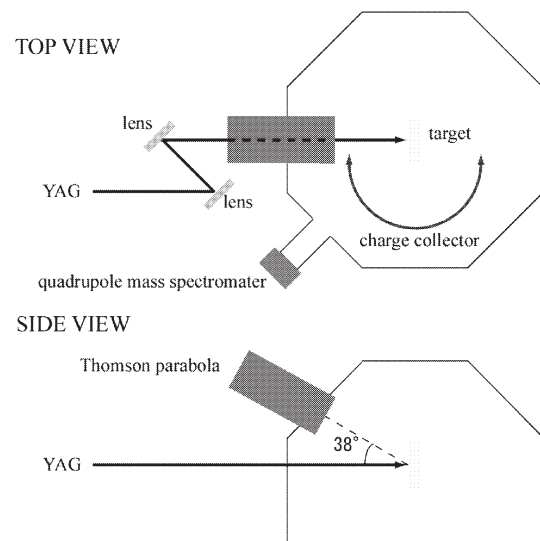


Fig.2 Experimental Apparatus

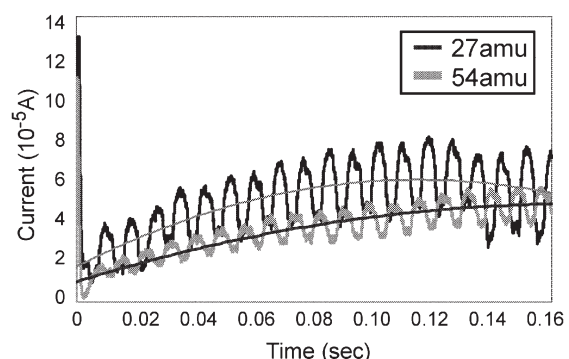


Fig.3 Time variation of 27, 54 amu with Al target

## §32. IFE Reactor Chamber Wall Ablations with Intense Particle and Laser Beams

Kasuya, K., Kuzuu, S., Kobayashi, T., Ozawa, S. (Tokyo Inst. Tech.), Norimatsu, T., Nakai, M., Nagai, K. (Osaka Univ.), Miyamaoto, S. (Himeji Inst. Tech.), Sato, M., Shimoda, K. (Gunma Univ.), Mroz, W., Prokopiuk, A. (M. Univ. Tech)

The IFE reactor chamber walls are ablated with the high flux pulsed radiations of various kinds including photons and particles. It is very important to know the conditions in the IFE reactor chambers after these ablations. In the worst case, the produced mists of the wall materials remain at the chamber center and prevent the survival of the injected fuel targets. So that, in this article, we investigated how the candidate wall materials respond to (1) such intense particle beams (which are produced with the fusion implosions) and (2) such intense laser lights (which leak from the main laser driver lights to irradiate the fuel targets).

An intense pulsed proton source and an ArF laser were used to ablate various sample materials. The surface analyses after the beam irradiations were performed with various diagnostic tools in Institute of Laser Engineering, Osaka University and Department of Energy Sciences, Tokyo Institute of Technology.

The most recent results concerning these research works were published in the references [1-6]. The reference [5] was an invited paper, while [3] and [4] were reports as one of the members of the corresponding IAEA sub-committee.

Because of a super COE project (proposed by the other group in Tokyo Institute of Technology and accepted by the Ministry of Education, Culture, Science and Technology during this fiscal year, we evacuated from our co-use large facility area of about 300m<sup>2</sup> before the end of this fiscal year. During this evacuation, we tried to reorganize our experimental facilities associated with our research subjects, and our pulsed power apparatuses were re-designed. We also discussed our future plan, under which our big machines are moved from Yokohama to NIFS (Toki), and a new five-year project is started to investigate the IFE chamber wall responses. Although this plan could not be realized, one of our medium size pulsed power system (pulsed ion beam machine called as "PICA-3") was decided to be moved from Yokohama to Faculty of Engineering, Gunma University in the coming fiscal year.

Cryogenic pulsed ion diode was re-designed to produce intense He beam. Together with the proton beam, the He ion beam is useful to simulate the interaction between the beam and the chamber wall surfaces after the IFE implosion. Helium

adsorption with an Ar or SF<sub>6</sub> surface over a cryogenic panel may become useful in our future works.

For the first time in this paper, the first author proposed a new type of Marx generator, as follows. The insulator oils for the conventional Marx generators up to now were mineral oils, which were more flammable and regulated under the law of fire-brigade stations. Under the present day law in Japan, oils with the flash points lower than 250 degree by Celsius are strictly regulated. If we use more than 2000 liter of oils, the facility space must have special restrictions under the law. In some case, we must prepare halon fire extinguisher systems. On the contrary, if we can use plant oils (which are not so flammable as the mineral oils and the flash points are higher than 250 degree by Celsius), the Marx generators can be installed in wider ranges of experimental site areas without such difficulties.

To realize a Marx generator with easier oil handling with plant oil, we investigated the electric breakdown voltage as a function of the electrode gap length, at first. One of our emerging results is shown elsewhere because of the page limitation, here. The insulation endurance is enough high for this oil to be used as the insulating oil of a new Marx generator.

We are now preparing to operate a new pulsed-power system with this kind of new Marx generator. To suppress the oil degradation by the bulk oxidation, a new small inert gas supply system with a slightly higher pressure than the atmospheric pressure is also added to the new Marx generator.

### References

- 1) Kasuya, K., Norimatsu, T., Nakai, S., Renk T.J., and Mroz, W.: Proc. 8th Japan-China Sympo. Materials for Advanced Energy Systems and Fission & Fusion Engineering, (2005) 47
- 2) Kasuya, K., Norimatsu, T., and Nagai, K.: Proc. 15th Int. Sympo. Gas Flow and Chemical Lasers & High Power Laser Conference SPIE-5777, (2005) 961
- 3) Kasuya, K., Kishi, A., and Funatsu, M.: Proc. 3rd Research Co-ordination Meeting of the IAEA Coordinated Research Project on Elements of Power Plant Design for Inertial Fusion Energy, IAEA-TECDOC-1466, (2005) 111
- 4) Kasuya, K., Kishi, A., Funatsu, M., and Kasamatsu, A.: Proc. 3rd Technical Meeting on Physics and Technology of Inertial Fusion Energy Targets and Chambers, (2005) 39
- 5) Kasuya, K., Mroz, W., Prokopiuk, A., and Norimatsu, T.: Proc. SPIE Int. Congress on Optics and Optoelectronics, Conf. on Laser and Application, SPIE-5958, (2005) 1T1
- 6) Kasuya, K., Kinoshita, Y., Norimatsu, T., Nakai, S., Mroz, W., and Prokopiuk, A.: Fusion Engineering and Design, 81, (2006) 1653

### §33. Establishment of Material Database Including High Temperature Irradiation Effect and Material Design of SiC/SiC Composites for Inertial Fusion Dry Wall Chamber

Kohyama, A., Hinoki, T., Ikeda, S. (Institute of Advanced Energy, Kyoto University),  
Norimatsu, T. (Institute of Laser Engineering, Osaka University)

The first wall of an Inertial Fusion Energy (IFE) chamber will suffer serious damage from intense pulsed neutrons and other energetic particles. In particular, a dry wall chamber demands extremely severe conditions for the first wall material, although a dry wall chamber has the advantage of simplicity for design. Due to excellent mechanical properties at high temperatures, chemical stability and low activation following neutron irradiation, SiC/SiC composites is attractive both for Magnetic Fusion Energy and IFE. Irradiation experiment for SiC and SiC/SiC composites over 1500 °C had not been carried out due to technical difficulty, although the knowledge about irradiation resistance at high temperature over 1500 °C is indispensable, in particular for designing dry wall chamber of IFE. Up to now, irradiation effect on swelling behavior of SiC fabricated by chemical vapor deposition (CVD) process have been evaluated up to 1600 °C using the DuET facility at Kyoto University. It was found that the magnitude of swelling of the CVD SiC was limited to very low level. The objective of this work is to understand the stability of SiC/SiC composites to high temperature irradiation over 1500 °C including mechanical properties to establish design window for IFE dry wall chamber.

A high purity polycrystalline 3C-SiC produced through CVD process were irradiated with 5.1MeV Si<sup>2+</sup> for inducing displacement damage at DuET facility, Kyoto University. The damage level was up to 2.1 dpa ( $2.1 \times 10^{25}$  n/m<sup>2</sup>, E>0.1 MeV) at surface of the material, and irradiation temperature was up to 1600 °C. Microstructure including fracture surfaces of the irradiated materials were examined by optical microscopy and scanning electron microscopy (SEM) at MUSTER (multi-scale testing and evaluation research) facility. In case of ion-irradiation, irradiated region in the material is limited to a few μm. Nano-indentation and three-point flexural tests, where tensile stress was applied for the irradiated region, were carried out to evaluate mechanical properties. The evaluation by three-point flexural test is based on the fact that strength of dense ceramics is determined by the defect at surface and adjacent to surface.

Hardness and elastic modulus obtained by nano-indentation and flexural strength of non-irradiated and irradiated CVD SiC are summarized in Table 1. Following irradiation, hardness increased and elastic modulus decreased, although the values at 1600 °C irradiation were close to those for a non-irradiated material. Evaluation of ion-irradiation effect on mechanical properties by flexural test is novel method. From observation of fracture surface

Table 1: Summary of hardness and elastic modulus obtained by nano-indentation and flexural strength of non-irradiated and irradiated CVD SiC

	Hardness (GPa)	Elastic modulus (Gpa)	Flexural strength (MPa)
Non-irradiated	789	35.9	410
2.1dpa, 600 °C	1251	40.8	381
2.1dpa, 800 °C	1092	41.4	395
2.1dpa, 1600 °C	1421	37.0	407

by SEM, it was found that crack initiation and propagation of both non-irradiated and irradiated materials concentrated on the region within a few μm from surface, where mostly corresponded to irradiated region. Obvious irradiation effects on flexural strength were obtained, although the magnitude of the strength seems too large. Figure 1 shows a Weibull plot of flexural strength of non-irradiated and irradiated CVD SiC. Flexural strength increased significantly with irradiation at all conditions in this work. Weibull modulus, which shows distribution of data, of materials irradiated at 600 °C and 800 °C decreased following irradiation, where Weibull modulus of materials irradiated at 1600 °C was larger than that of non-irradiated material. The results for materials irradiated at 600 °C and 800 °C were consistent with previous neutron irradiation results. It is said that the novel evaluation method of three-point flexural for ion-irradiated materials can be used to evaluate irradiation effect on mechanical properties of SiC ceramics. Although the results for materials irradiated at 1600 °C require more analysis and discussion, it can be concluded with the swelling results obtained previously that CVD SiC doesn't degrade following irradiation at up to 1600 °C.

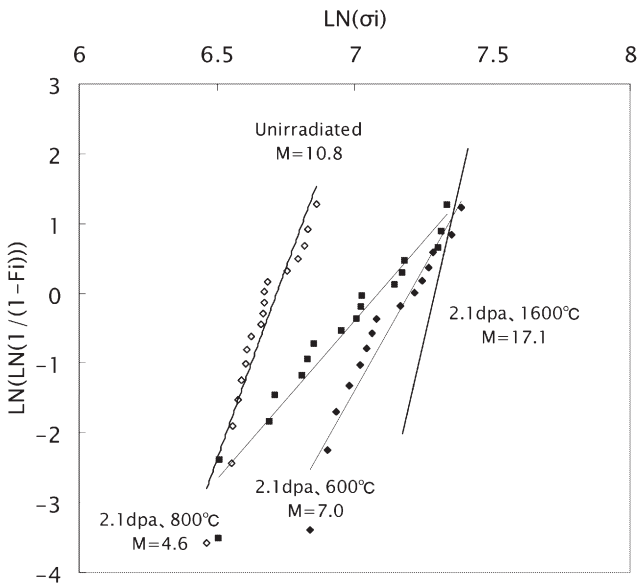


Figure 1: Weibull plot of flexural strength of non-irradiated and irradiated CVD SiC

### §34. Development of Coil Gun for Fast Ignition

Yoshida, H. (Gifu Univ.)

Laser-fusion reactor is filled with vapor and droplets of liquid-wall metal and debris of target. Injected targets must be tracked and irradiated by laser beams. We are developing a coil gun and target detector. In order to improve the injection speed and accuracy of the coil gun, functional analysis and optimization were done. Target detection accuracy is affected by scattering and extinction of probe beam by metal vapor and droplet in the reactor. An optical correlation method is applied to target detection experiment.

### Improvement of injection speed and accuracy

The coil gun is composed of the barrel coil and pulse power supply. The first stage of it is shown in the Fig. 1. The traveling magnetic wave is generated by sequentially regulated pulse currents of barrel coils. The magnetic wave induces induction current in the sabot. Interaction between the magnetic wave and the induction current accelerates the sabot along the barrel axis. By the optimization of sabot configuration and timing of pulse currents, the acceleration reached to 580G which is the required maximum value of ice capsule strength. The final speed of sabot was 7.8 m/s in the first section of coil gun.

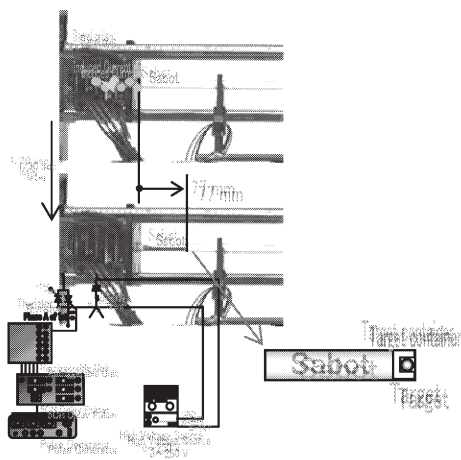
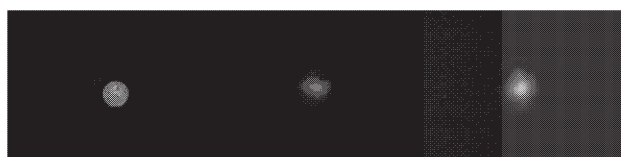


Fig. 1 Coil gun and injected sabot.

Tumbling of sabot is measured during acceleration for evaluation of injection stability and accuracy. The coaxial positioning of sabot to the barrel axis decreases the tumbling angle down to 0.3deg.

## Target detection experiment by optical correlation method

The matched filter recorded the interference image of the circular target was utilized for optical correlation method. It was positioned at the distance of 5m from the target. The detected optical image without the matched filter is shown in Fig. 2(a). A white paint cell was inserted in the optical path as scattering and extinction material. The size of distributed particle in the cell was 30um typ, The concentration was turned to be the extinction of 10%. The target image through the cell was degraded as shown in Fig.2 (b). The optical correlation image is shown in Fig.2(c). The position accuracy was estimated 90 um from the correlation peak of the image. The accuracy of the optical correlation method was not affected by the extinction cell in this experiment.



(a)Optical image    (b)Optical image    (c)Correlation image  
with extinction    with extinction.

Fig. 2 Detected circular target images.

## Reference

- 1) T. Norimatsu, D. Harding, R. Stephens , A. Nikroo , R. Petzoldt, H. Yoshida, K. Nagai, and Y. Izawa: Fusion Sci. Technol. (2006)483.



### §35. Researches on Compression and Heating of Cryogenic Target and Related Physics

Mima, K. (ILE, Osaka Univ.), et al.

#### **FIREX project**

In the April of 2003, the construction of heating laser of 10 kJ/10 ps/1.06  $\mu\text{m}$  (Laser for Fusion Experiment; LFEX), for FIREX-I (Fast Ignition Realization Experiment) has started. [1] The present outlook of the LFEX laser is shown in Fig.1. Target fabrication and irradiation system of foam cryogenic target are developed as the collaboration program between Osaka University and NIFS (National Institute for Fusion Science), see Figure 2. After the completion of LFEX, we will irradiate a foam cryogenic cone shell target with LFEX in late 2007. The target fabrication technology is further developed to reduce the foam density to less than 20mg/cc by the end of FY2006.

#### **Plasma experiment**

In order to investigate implosion dynamics, planer cryogenic foam layer targets are irradiated with GEKKO XII laser. As a result, we found that a deuterium layer is compressed and accelerated by ablation pressure as expected in simulations. We also irradiated a foam cryogenic deuterium layer with the peta watt laser to find that the fast electron is strongly shielded by self generated E-M fields on the plastic-cryogenic layer interface. As an alternative fast heating scheme, the impact of a highly accelerated foil has been proposed and the ablative acceleration to  $6.5 \times 10^7$  cm/sec was achieved.

#### **Integrated simulation of fast**

The cone target implosion and heating processes are studied by using the Fast Ignition Integrated Interconnected code (FI<sup>3</sup> code) which connects a radiation hydro code (PINOCO), a collective PIC code, and a Fokker Planck code. The FI<sup>3</sup> code has been used to analyze cone target experiments. 2D hydro simulations for cone-shell target implosion by PINOCO well reproduce experimental results.

#### **Summary**

Toward FIREX-I experiment, laser construction, target fabrication, plasma experiment for preparation, and

integrated simulation studies are in advance. In the test operation of LFEX, out put of 3kJ/beam/1.06  $\mu\text{m}$  was achieved recently. A conceptual reactor design is completed which discloses future issues of fast ignition research. [2]



Fig.1 Present outlook of LFEX (heating laser for FIREX-I).

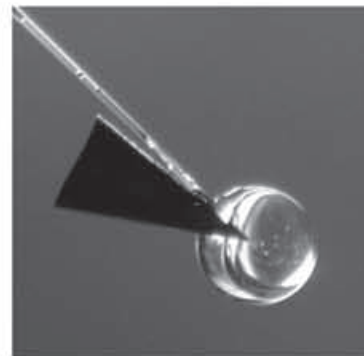


Fig. 2, liquid H<sub>2</sub> filed plastic shell with cone  
This is developed by the collaboration with NIFS

[1] K. Mima, *et al*, Proceedings of Inertial Fusion Science and Applications 2005

[2] K. Tomabechi *et al.*, Proceedings of Inertial Fusion Science and Applications 2005

### S36. X-ray Imaging in Fast Ignition Fusion Experiments –An ICA based Poisson-Noise Reduction Algorithm–

Chen, Y.-W. (Ritsumeikan Univ.),  
Han, X. (Univ. of the Ryukyus)

Penumbra imaging is a technique which uses the fact that spatial information can be recovered from the shadow or penumbra that an unknown source casts through a simple large circular aperture.<sup>1</sup> Since such an aperture can be “drilled” through a substrate of almost any thickness, the technique can be easily applied to highly penetrating radiation such as neutrons and  $\gamma$  rays. To date, the penumbra imaging technique has been successfully applied to image the high-energy x rays, protons, and neutrons in laser fusion experiments. The limitation of penumbra imaging is that the straightforward deconvolution is very sensitive to noise contained in the penumbra image. The penumbra images are always degraded by Poisson noise.

In this paper, we proposed a Poisson noise filtering method based on independent component analysis (ICA) for penumbra imaging. The goal of ICA is to perform a linear transformation which makes the resulting variables as statistically independent from each other as possible. In image decomposition by ICA, most independent components have super-Gaussian distribution and the corresponding basis functions are similar to localized and oriented human visual response (receptive field). In the proposed filtering, the penumbra image is first transformed by using ICA basis functions and then the noise components are removed by a soft thresholding technique, which is known as Shrinkage. Compared with other methods such as wavelet-based filtering, the ICA-based filtering is determined by data alone and adaptive to the data. The filter is used as a preprocessing of reconstructions of penumbra images.

A penumbra image  $\mathbf{x}$  can be represented by a linear combination of basis functions as Eq.(1), where  $\mathbf{A}_i$  is the basis function and  $s_i$  is the coefficient, which can be used as image features or image coding. Unlike Fourier transform or wavelet-based method, in our proposed ICA based method, the basis functions are learned from similar images by ICA. The advantage of the ICA based method is that we can obtain a set of adaptive basis functions based on data or images alone.

$$\mathbf{x} = \sum_{i=0}^{N-1} s_i \mathbf{A}_i = s_0 \mathbf{A}_0 + s_1 \mathbf{A}_1 + s_2 \mathbf{A}_2 + \cdots + s_{N-1} \mathbf{A}_{N-1} \quad (1)$$

The Eq. (1) can be rewritten as

$$\mathbf{x} = \mathbf{A} \mathbf{s} \quad (2)$$

Since we must obtain the  $\mathbf{A}$  from sample images  $\mathbf{x}$  alone, the solution of Eq.(2) can be viewed as a blind source separation problem, which can be solved by ICA. The goal of ICA is to find a matrix  $\mathbf{W}$  that results in the estimates of coefficient  $\mathbf{s}$  being statistically as independent as possible

over a set of data ( $\mathbf{x}$ ) as shown in Eq. (3)

$$\mathbf{s} = \mathbf{W} \mathbf{x} \quad (3)$$

The estimates or independent components  $\mathbf{y}$  may possibly be permuted and rescaled. The rows of  $\mathbf{W}$  respond to the columns of  $\mathbf{A}$  (basis function  $\mathbf{A}_i$ ).

Bell & Sejnowski proposed a neural learning algorithm for ICA [9]. The approach is to maximize the joint entropy by stochastic gradient ascent. The updating formula for  $\mathbf{W}$  is:

$$\Delta \mathbf{W} = (\mathbf{I} + g(\mathbf{s}) \mathbf{s}^T) \mathbf{W} \quad (4)$$

where  $\mathbf{s} = \mathbf{W} \mathbf{x}$ , and  $g(\mathbf{y}) = 1 - 2/(1 + e^{-\mathbf{y}})$  is calculated for each component of  $\mathbf{s}$ . Before the learning procedure,  $\mathbf{x}$  is sphered by subtracting the mean  $\mathbf{m}_x$  and multiplying by a whitening filter.

The basic idea of the proposed filtering is that we first remove the DC component of scattered X ray which is estimated from Monte Carlo simulations from the first component and then we use a soft thresholding (shrinkage) to smooth out the noise components and obtain noise-free components  $\hat{\mathbf{s}}$ .

$$\hat{\mathbf{s}} = g(\mathbf{s}) \quad (5)$$

where  $g(\mathbf{s})$  is a shrinkage function, which is defined as Eq.(6):

$$g(\mathbf{s}) = \mathbf{s} \frac{\mathbf{s}^2 - \delta^2}{\mathbf{s}^2} \quad (6)$$

where  $\delta^2$  is the power of Poisson noise. The noise power of  $i$ -th component. Thus, we can obtain the noise power for each component in ICA-domain and the estimate of noise power can adapt to local variations in the signal or noise. The filtering is performed as:

$$\hat{\mathbf{x}} = \sum_{i=0}^{N-1} \hat{s}_i \mathbf{A}_i = \hat{s}_0 \mathbf{A}_0 + \hat{s}_1 \mathbf{A}_1 + \hat{s}_2 \mathbf{A}_2 + \cdots + \hat{s}_{N-1} \mathbf{A}_{N-1} \quad (7)$$

The experimental results are shown in Fig.1. Figure 1(a) is the result without filtering and Fig.1(b) is the result with ICA-filtering. As shown in Fig.1, the source image has been reconstructed with a high SNR, while if we do not use the filter, the reconstructed image is not clear.

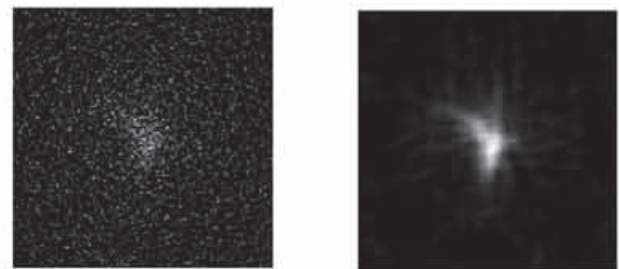


Fig.1 (a) without filtering; (b) with ICA filtering .

Y.W. Chen, X.Han and S.Nozaiki, *Rev. Sci. Instrum.*, Vol.75, pp.3977-3878(2004)

### §37. Neutral Particle Behavior in the Edge Plasma of TRIAM-1M Tokamak Measured Using Zeeman Spectroscopy (NIFS04KUTR001)

Kado, S., Shikama, T. (The Univ. of Tokyo),  
Zushi, H. (RIAM, Kyushu Univ.)

Standard passive spectroscopy yields only a line-integrated emission along the viewing chord. In order to obtain the local plasma parameters, active methods such as the charge exchange spectroscopy, which makes use of a neutral beam injection, have been applied for highly-charged (usually hydrogenic) ions in core region. We have been developed a method in which local information can be obtained from the Zeeman patterns even in the device without NBI [1]. In principle, this method can be applied both to the core and the boundary region. We have shown that the radial position of emission, temperature and the flow velocity in the position can be determined from the best-fit of the spectral line shape calculated by taking into account the Zeeman profile, the Doppler broadening and the Doppler shift [2]. In the present report, we have applied this method to the flow measurement of neutral atoms in the edge region [3].

The experiments were performed in the TRIAM-1M super-conducting tokamak under the condition of 8.2 GHz lower hybrid current driven discharge. The magnetic field strength of about 7 T at the plasma center was generated using sixteen Nb<sub>3</sub>Sn super-conducting toroidal field coils. The plasma boundary shape was restricted by three D-shaped poloidal limiters and one vertically movable limiter installed in the upper port of the vacuum vessel. All plasma-facing components were made of molybdenum.

The emission from the atoms was observed using fan-shaped 25 viewing chords in the poloidal section. In front of the objective lenses, a linear polarizer was attached with its polarization axis perpendicular to the toroidal field direction for the observation of the  $\sigma$  components. The collected emission was dispersed using a spectrometer (Acton Research AM-510) having a focal length of 1 m and equipped with a 1800 grooves/mm ruled grating. The dispersed image was detected by an electrically cooled back-illuminated CCD (Andor DU440-BU2). The dimension of the CCD chip is 2048 x 512 pixels and each pixel size is 13.5 x 13.5  $\mu\text{m}^2$ .

The flow velocity of hydrogen and helium atoms were measured based on the Doppler shift of the separated spectra. Figure 1 shows the measured flow velocity profiles for the cold temperature components (< 1eV) of the hydrogen and helium atoms. The velocities were measured as projections on the viewing chords. A positive value of the velocity denotes a red-shift of the spectrum directing towards the inboard side, while a negative value shows the opposite. One can see that the obtained flow profiles indicate an inward neutral flow in both the hydrogen and helium cases. The reason for the inward neutral flow can be explained from the initial velocity and the momentum balance in the radial direction. With the neutral pressure gradient and ion-neutral friction forces, the neutral momentum balance equation in the radial direction can be written as

$$m_0 n_0 \frac{dv_{r0}}{dt} = -\nabla_r p_0 + m_0 (v_{ri} - v_{r0}) n_0 n_i \langle \sigma v \rangle_{i0(ela,cx)},$$

where  $m_0$ ,  $n_0$ ,  $v_0$  and  $p_0$  are the neutral mass, density, drift velocity, and pressure, respectively.  $v_i$  and  $n_i$  are the ion velocity and density, and  $\langle \sigma v \rangle_{i0(ela,cx)}$  is the reaction rate of ion-neutral elastic and charge exchange collisions. The source and sink terms due to the recombination and ionization processes in the continuum equation are included as  $v_{r0} \nabla_r n_0 = S$ , namely the  $\nabla_r p_0$  term, where  $v_{r0}$  is assumed to be constant and  $S$  represents the summation of the source and sink terms. The ratio of the pressure gradient force (inward) to the ion neutral friction force (outward) in the above equation can be written with the thermal velocity  $v_{th0}$  and scale length  $L_{n0}$  of the neutrals as

$$R \approx -v_{th0} / L_{n0} n_i \langle \sigma v \rangle_{i0(ela,cx)}.$$

Under the achievable experimental condition of TRIAM-1M, the ratio  $R$  becomes larger than unity, that is to say the pressure gradient force is at least several times larger than the friction force. Moreover, one should bear in mind that the initial velocity when the neutrals are released from the wall is directed inward. It can be concluded, therefore, that the neutral dynamics is mainly dominated by the radial neutral pressure gradient. In addition, in the figure, the observed inward flow velocity is higher in the case of hydrogen than helium. This fact also suggests that the flow is driven by the pressure gradient in which the velocity is inversely proportional to the mass.

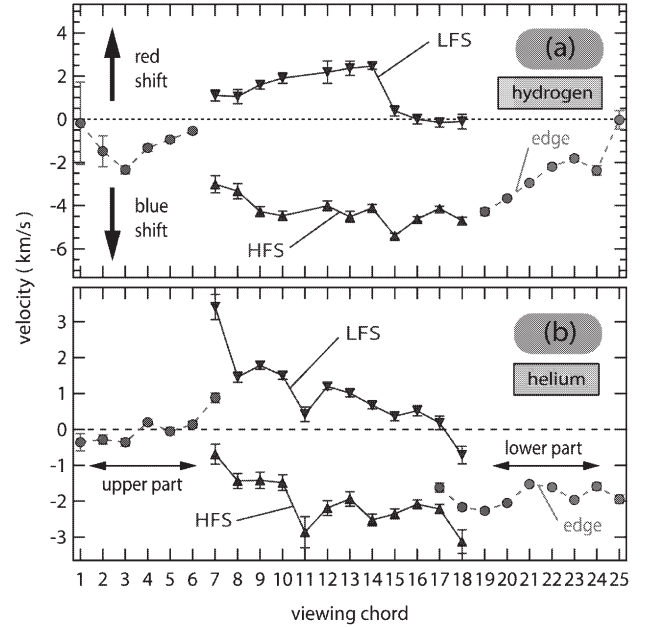


Figure 1: The measured flow velocities of the cold temperature components of hydrogen and helium atoms.

#### References

- 1) J. Weaver, *et al. Rev. Sci. Instrum.* **71** (2001) 1664.
- 2) T. Shikama, *et al. Phys. Plasmas* **11** (2004) 4701.
- 3) T. Shikama, *et al. Plasma Phys. Control. Fusion* **48** (2006) 1125.



### §38. Start-Up and Sustainment of Spherical Tokamak by ECH/ECCD

Maekawa, T., Tanaka, H., Uchida, M., Iwamae, A., Yoshinaga, T. (Kyoto Univ.), Hanada, K., Zushi, H., Idei, H., Hasegawa, M. (Kyushu Univ.)

Spherical Tokamak (ST) concept is attractive since it maintains high beta plasmas in a compact shape of low aspect ratio. Without central Ohmic solenoid, structure of ST reactor is greatly simplified. We need a non-inductive method for plasma initiation and current start up. The electron cyclotron heating and current drive (ECH/ECCD) is potentially an attractive candidate for this purpose since plasma initiation and current start-up might be realized simultaneously by microwaves launched far from the plasma with a simple launcher. We have attempted ECH experiments in the Low Aspect ratio Toru Experiment (LATE) device [1, 2] and found that low aspect ratio equilibria with the toroidal currents up to 12 kA are obtained as shown in Figure 1. In near future ECH/ECCD start-up will also be investigated in the QUEST device.

LATE is a tiny device with a vacuum chamber made of stainless steel in the shape of a cylinder with the diameter of 1.0 m and the height of 1.0 m [1]. The center post is a stainless steel cylinder with the outer diameter of 11.4 cm, enclosing 60 turns of conductors for the toroidal field. The return conductors are grouped into 6 limbs and go around far from the vacuum vessel, which allows good accessibility to the vacuum chamber and suppresses toroidal field ripple at a low level (1.5 % at  $R=50$  cm and 0.07% at  $R=30$  cm). There are four sets of poloidal field coils. One is for feedback control of vertical position of the plasma loop, and the rest are for the vertical field for equilibrium and their currents are preprogrammed. There is no central solenoid for inductive current drive. Three 2.45 GHz magnetrons, including two 5kW CW tubes and a 20 kW 2 seconds tube, and a 5 GHz klystrons (130kW, 60msec) are used for ECH. In all cases, microwaves are injected from radial ports with injection angles slightly deviate (about 15 degrees) from normal to the toroidal field.

In the case of a 2.45 GHz microwave pulse for 2 seconds, a plasma current of 2 kA has been spontaneously initiated by  $P_{rf}=15$  kW under a weak steady vertical field of  $B_v=17$  Gauss, and then ramped up with slow ramp-up of  $P_{rf}$  and slow ramp-up of  $B_v$  for the equilibrium of the plasma loop and finally reaches 8 kA at  $B_v=90$  Gauss and  $P_{rf}=35$  kW. In the case of a 5 GHz microwave pulse (130 kW, 60 ms), a plasma current of 6 kA has been spontaneously initiated under a steady field of  $B_v=56$  Gauss, and then ramped-up with a ramp of  $B_v$  and reached 12 kA at  $B_v=100$  Gauss. In both cases the plasma center locates near the second or third harmonic ECR resonance layer and the line averaged electron density significantly exceeds the plasma cutoff density, suggesting that harmonic EC heating by the mode-converted EBW supports the plasma.

Spontaneous current generation (current jump) has been observed for a wide range of  $B_v$ . This bridges the gap between the open field equilibrium maintained by the pressure driven current in the external field and the closed field equilibrium at a larger current. Experimental results and the theoretical analyses suggest a current jump model that is based on the asymmetric electron confinement along the field line appearing upon simultaneous transitions of field topology and equilibrium [2].

Once a closed field is formed, EC current drive may become effective, since EC-driven current carrying passing electrons are confined as far as the plasma loop is in equilibrium by an appropriate ramp of  $B_v$  field. In the experiments, significant hard X-ray emissions have been observed. Their intensity increases as the plasma current increases, suggesting that current carrying fast electron tail is formed.

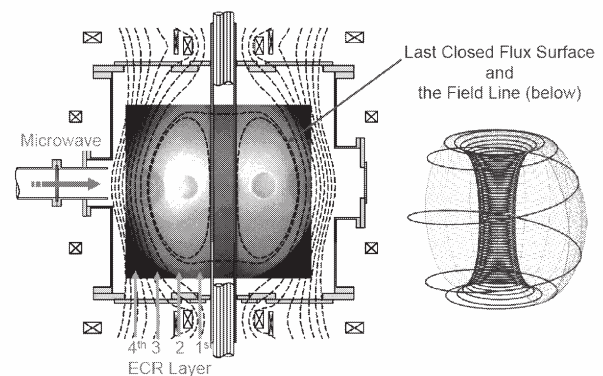


Fig. 1 Microwave Spherical Torus produced in the LATE device ( $I_p=12$  kA,  $B_v=100$  Gauss,  $B_t=720$  Gauss)

In CPD, an 8.2 GHz microwave was injected by eight horn type antennas as shown in Fig. 2. Four horn antennas were adjusted to O-mode injection and the others to X-mode. Two flat mirrors to control the injection angle in the case of O-mode injection were installed.

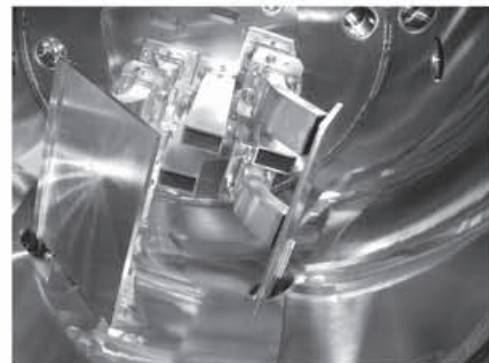


Fig. 2 A photograph of the antenna system for an 8.2 GHz microwave installed on CPD.

#### References

- [1] T. Maekawa *et al.* Nuclear Fusion, **45** (2005)1439.
- [2] T. Yoshinaga *et al.*, Phys. Rev. Lett., **96**(2006)125005



### §39. Experimental Study of Compact Plasma Wall Interaction Experimental Device (CPD)

Hanada, K., Sato, K.N., Zushi, H., Yoshida, N., Nakamura, K., Sakamoto, M., Idei, H., Hasegawa, M., Sasaki, K. (Kyushu University), Mitarai, O. (Kyushu Tokai University), Nisino, N. (Hiroshima University), Nagata, M., Fukumoto, N. (University of Hyogo), Maekawa, T., Tanaka, H. (Kyoto University), Takase, Y., Ejiri, A. (University of Tokyo), Nagayama, Y., Hirooka, Y.

#### 1. Introduction

Spherical tokamak (ST) is a candidate for cost-effective fusion reactor and the improvement of the plasma performance of ST has been tried in many institutes. University of Tokyo has been executed the RF heating experiments on TST-2. The plasma start up without ohmic heating coil by RF current drive has been developed on LATE constructed by the experimental group of Kyoto University. One of the effective ways to provide fuel into plasma is compact toroid (CT) injection, which has been proceeded in University of Hyogo. Steady state operation is also a key issue to realize a fusion reactor. In the research of tokamaks, steady state operation will become crucial point and the trials to do long pulse operations in a large tokamak, JT-60U started. The experimental group of Kyushu University has many experiences to sustain the plasma current by use of RF current drive.

The cooperation of these experimental groups under the assistance with NIFS had the possibility to make a new way to realize the fusion reactor using steady state operation of ST. In 2003, we executed the collaboration, which TST-2 moved tentatively to Kyushu University and the RF injection experiment to TST-2 were done successfully (TST-2@K project) [1-5]. A compact ST called compact plasma wall interaction experimental device (CPD) was constructed on the site of TST@K under the framework in by-directional collaboration program organized by NIFS and the collaborated program in the experiments are started in 2005. The purposes of CPD are 1) confirmation of the effect of EBWCD, 2) investigation of the effect of wall temperature to PWI, 3) CT injection to ST, 4) study of the active control of PWI, 5) confinement study of energetic particles in ST, 6) role in the platform of innovative concept. In 2005, the system of compact toroid (CT) injection produced by the group of Hyogo University is installed.

#### 2. Installation of the CT injection system

The CT injection system was developed by the experimental group of Hyogo University and it was installed on JFT-2M site in JAERI. The power supply of the system was provided by the JAERI group in JFT-2M. The experiments on JFT-2M had been shut-down and the CT injection system was consigned to the group of Hyogo University. In JFT-2M, the high applied voltage for plasma acceleration is required to inject CT to the plasma because of high magnetic field. In CPD, the operated magnetic field

will be one-fourth of one in JFT-2M and the applied voltage become to be mild. Therefore the operation region of the CT will be wide, which is effective to understand the physical mechanism of CT injection. A photograph after the installation of the CT system is shown in Fig. 1.

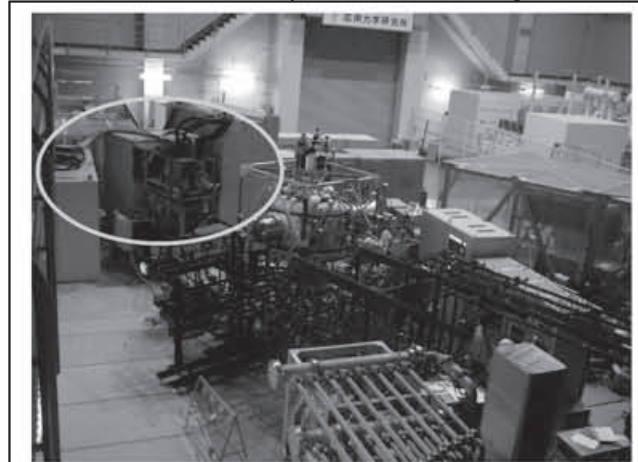


Fig. 1 A photograph around CPD. Blue circle shows the compact toroid (CT) injection system installed on CPD.

#### 3. Installation of the antenna system of an 8.2 GHz microwave

To develop a current drive method by use of electron Bernstein wave (EBW), an antenna system is installed on CPD as shown in Fig. 2. The system is composed of eight horn antennas. Four horns will be used as X-mode antennas and the others as O-mode ones. As in the case of O-mode injection, the injection angle to the magnetic field is a key to excite EBW in the plasma, two mirrors are installed to control the injection angle.



Fig. 2 The photograph of the CPD during vacuum leak check at the experimental hall of TRIAM-1M.

#### References

- [1] Mitarai, O., et al., Rapid communication J. Plasma and Fusion res. Vol. 80, No.7 (2004)
- [2] Kasahara, H., et al., Proc. the 31th EPS meeting (London) (2004).
- [3] Shiraiwa, S. et al., PRL in press.
- [4] Ejiri, A., et al., Nuclear Fusion in press.
- [5] Sasaki, K., Proc. the 33th EPS meeting (Roma) (2006).

## §40. Modeling of Global Particle Balance and Plasma-Surface Interactions in TRIAM-1M

Hirooka, Y. (NIFS),  
Sakamoto, M. (Kyushu Univ.)

Because Cadarache has been selected as the construction site for ITER (the International Thermonuclear Experimental Reactor), the magnetic fusion research community may be considered to have reached one of the milestones to be achieved for fusion power utilization. However, the execution of the 20 year long ITER program does not necessarily mean that all the technical issues will be resolved. On the contrary, issues to remain unresolved after ITER will be most critical in proceeding to the final step, i.e., the construction of a DEMO followed by commercial fusion power reactors. Among these post-ITER issues, particle control has recently been receiving considerable attention as being a key to sustain true steady state operation of fusion devices. Particle control can bring about multiple effects on the overall reactor performance as to core plasma density stability, tritium economy and radiation safety, and impurity generation and related lifetime of PFCs (plasma-facing components), etc.

Although ITER is planned to operate in the long pulse mode, the pulse duration is limited to ~500 seconds due to the OH capacity. Interestingly, recent operation experiences with the TRIAM-1M tokamak have demonstrated that it takes hours of continuous plasma interactions for wall components to reach their respective steady state temperatures [2]. Therefore, one predicts that the ITER pulse length is not long enough to address the steady state particle control issue. This means that the core plasma density will be affected by the gas desorption from PFCs during the course of discharge.

In the present work, the effect of gas desorption from PFCs on the core plasma density has been analyzed, using the zero-dimensional, 4-reservoir particle balance model [1]. This model is modified to take into account the effect of gas desorption from the limiter along with the temperature evolution shown in Fig. 1.

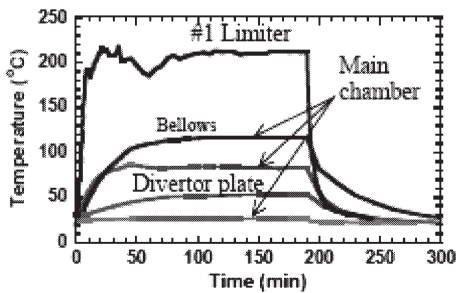


Fig. 1 Temperature evolutions of PFCs during the course of plasma discharge in TRIAM-1M [2].

Here, for simplicity, it is assumed that thermal desorption of hydrogen occurs exponentially along with the temperature evolutions. The thermally desorbed gas is taken as a secondary fueling source in such a way that:

$$\frac{dN_{arv}}{dt} = \frac{N_{arv}}{\tau_{arv}} + \alpha_1 \frac{\langle \sigma v \rangle_{cl}}{2V_{gs}} N_{gs} N_{sl} - \alpha_2 \frac{\langle \sigma v \rangle_{cl}}{V_{gs}} N_{gs} N_{arv} + \left( \frac{N_{sl}}{\tau_{sl}} + \alpha_1 \frac{\langle \sigma v \rangle_{cl}}{2V_{gs}} N_{gs} N_{sl} + \alpha_2 \frac{\langle \sigma v \rangle_{cl}}{V_{gs}} N_{gs} N_{arv} \right) (R_e^v f_{arv} + R_y^v f_{arv}) + f_{arv} (\Phi_{cl} + \Phi_{il}) \quad (1)$$

$$\frac{dN_{sl}}{dt} = \frac{N_{sl}}{\tau_{sl}} + \frac{N_{arv}}{\tau_{arv}} - \alpha_1 \frac{\langle \sigma v \rangle_{cl}}{V_{gs}} N_{gs} N_{sl} + \beta \frac{\langle \sigma v \rangle_{cl}}{V_{sl}} N_{gs} N_{sl} + \left( \frac{N_{sl}}{\tau_{sl}} + \alpha_1 \frac{\langle \sigma v \rangle_{cl}}{2V_{gs}} N_{gs} N_{sl} + \alpha_2 \frac{\langle \sigma v \rangle_{cl}}{V_{gs}} N_{gs} N_{arv} \right) (R_e^v f_{sl} + R_y^v (1 - f_{arv})) + f_{sl} (\Phi_{cl} + \Phi_{il}) \quad (2)$$

$$\frac{dN_{gs}}{dt} = -S_{imp} N_{gs} - \beta \frac{\langle \sigma v \rangle_{cl}}{V_{sl}} N_{gs} N_{sl} + \left( \frac{N_{sl}}{\tau_{sl}} + \alpha_1 \frac{\langle \sigma v \rangle_{cl}}{2V_{gs}} N_{gs} N_{sl} + \alpha_2 \frac{\langle \sigma v \rangle_{cl}}{V_{gs}} N_{gs} N_{arv} \right) (R_e^v (1 - f_{sl} - f_{arv}) - \gamma Y_{qu} \frac{N_{sl}}{\tau_{sl}} + Y_{qu-1} \alpha_1 \frac{\langle \sigma v \rangle_{cl}}{2V_{gs}} N_{gs} N_{sl} + Y_{qu-2} \alpha_2 \frac{\langle \sigma v \rangle_{cl}}{V_{gs}} N_{gs} N_{arv}) + (1 - f_{arv} - f_{sl}) (\Phi_{cl} + \Phi_{il}) \quad (3)$$

$$\frac{dN_{wall}}{dt} = \left( \frac{N_{sl}}{\tau_{sl}} + \alpha_1 \frac{\langle \sigma v \rangle_{cl}}{2V_{gs}} N_{gs} N_{sl} + \alpha_2 \frac{\langle \sigma v \rangle_{cl}}{V_{gs}} N_{gs} N_{arv} \right) (1 - R_e - R_y) + \gamma Y_{qu} \frac{N_{sl}}{\tau_{sl}} + Y_{qu-1} \alpha_1 \frac{\langle \sigma v \rangle_{cl}}{2V_{gs}} N_{gs} N_{sl} + Y_{qu-2} \alpha_2 \frac{\langle \sigma v \rangle_{cl}}{V_{gs}} N_{gs} N_{arv} - \Phi_{il} \quad (4)$$

where  $N_{core}$ ,  $N_{SOL}$ ,  $N_{gas}$ ,  $N_{wall}$  are the particle inventories in the core, SOL, gas, and wall, respectively,  $\alpha_1$ ,  $\alpha_2$ ,  $\beta$ , are adjusting parameters to express degrees of separation between the SOL and gas regions. All other symbols have their usual meanings. The secondary gas fueling is indicated by  $\Phi_{int}$  in red. Results obtained are in good agreement, as shown in Fig. 2, with the experimental data.

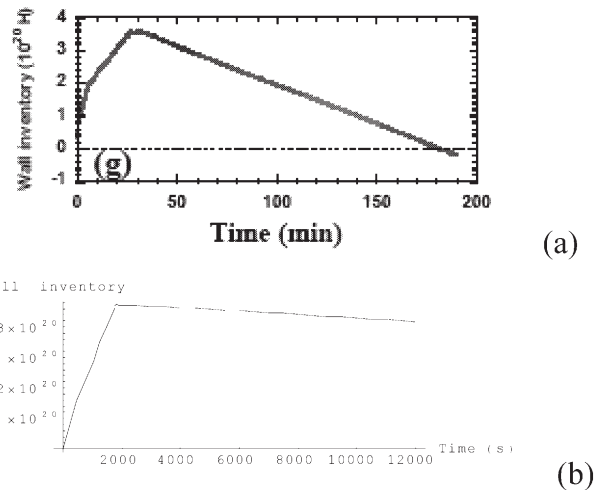


Fig. 2 A comparison between (a) the experimental data [2], and (b) the model prediction on the wall inventory.

## References

- [1] Y. Hirooka et al., Nucl. Mater. 313-316(2006)588.
- [2] M. Sakamoto et al., IAEA-FEC(2002), Exp4-07.

§41. Active Control Over Wall Recycling in a Spherical Tokamak: CPD by a Moving-Surface PFC

Hirooka, Y. (NIFS),  
Zushi, H. (Kyushu Univ.)

Ever since the discovery of the “Supershot” confinement regime in TFTR experiments in late 1980’s, it has widely been recognized in the magnetic fusion community that high performance core plasmas often favor reduced wall recycling. To reduce edge recycling, wall conditioning techniques such as boronization have been applied for many plasma confinement experiments. However, by nature, due to the surface saturation with trapped particles, the efficacy of wall conditioning has a finite lifetime, necessitating the shutdown of plasma operation for re-conditioning. Clearly, this is not acceptable from the point of view of operating steady state fusion power reactors. It is clear from these arguments that enabling wall concepts R&D is necessary for the successful operation of steady state fusion devices beyond ITER.

Over the past decade, therefore, a variety of innovative plasma-facing component concepts have been proposed to provide a resolution for this particle control issue. These concepts typically employ either a solid or liquid plasma-facing material, but both are continuously circulating for in-line regeneration of particle trapping capabilities. One such concept proposed by Hirooka et al. [1] employs a moving belt of SiC-SiC fiber fabrics with an in-line getter film deposition system.

In our previous work [2], proof-of-principle experiments on this concept with the moving belt, simplified by a belt of lithium deposited on a water-cooled rotating drum (see Fig. 1-(a)), were conducted at bombarding plasma densities of the order of  $10^{10-11}\text{cm}^{-3}$  and electron temperatures around 5eV. As shown in Fig. 1-(b) [2], spectroscopic data on  $H_{\alpha}$  have indicated that steady state hydrogen recycling is reduced by 14% and 24%, respectively, at the lithium deposition rates of  $9.5\text{Å/s}$  and  $7.3\text{Å/s}$  due to the chemical codeposition effect, forming LiH.

In the present work, a compact spherical tokamak: CPD, located at the Kyushu Univ., will be installed with a similar rotating drum as the limiter head to investigate if the concept of MS-PFC can be used for active control over edge recycling in a confinement device, leading to an improvement of core plasma performance. A schematic diagram of the experimental setup is shown in Fig. 2-(a). For this purpose, a prototype rotating limiter made of tungsten-coated copper has been put together and is currently at the final stage before actual installation.

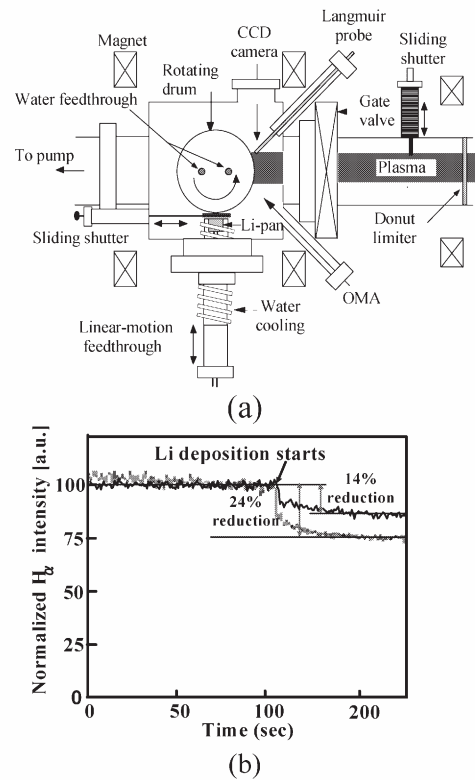


Fig. 1 A schematic diagram of the off-line rotating drum setup (a), and reduced steady-state hydrogen recycling from a lithium-gettered rotating drum [2].

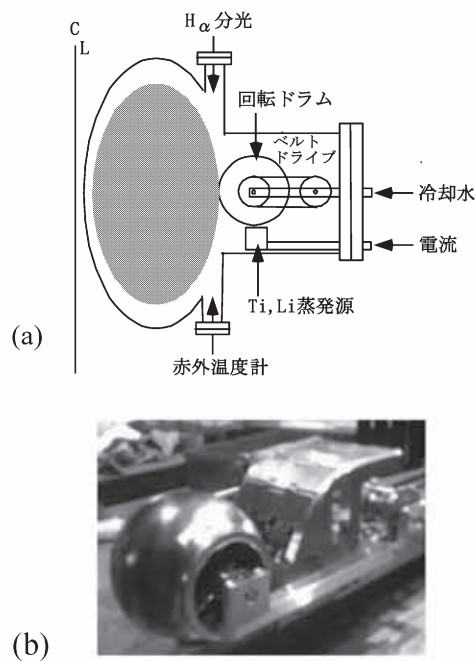


Fig. 2 A schematic diagram of the rotating drum limiter on the CPD spherical tokamak (a), and a close-up on the water-cooled rotating drum head made of copper.

**References:**  
[1] Hirooka, Y. et al., Proc. 17<sup>th</sup> IEEE-SOFE, San Diego, Oct. 6<sup>th</sup> -10<sup>th</sup>, 1997, pp.906.  
[2]Hirooka, Y. et al., Fusion Sci. & Technol. **47**(2005)703.



## §42. Compact Toroid Injection into Spherical Tokamak Plasmas in the Small PWI Device

Nagata, M., Fukumoto, N. (Univ. Hyogo),  
Masamune, S., Sanpei, A. (Kyoto Inst. Tech.),  
Asai, T. (Nihon Univ.),  
Kanki, T. (Japan Coast Guard Academy),  
Hanada, K. (Kyushu Univ.)

One of important issues on fusion programs is to develop a reliable fuelling technology for fusion reactor. Conventional particle fuelling schemes such as continuous gas puffing and pellet injection have been sufficient to fuel the existing fusion devices. However, they may be inadequate for central fuelling in fusion reactors. A large portion of fuel deposited in the edge will not reach the core region and accumulate on the vessel walls of the reactor. The central deposition is required to reduce the tritium accumulation and maximize a fuelling efficiency. Compact toroid (CT) injection appears to be capable of this task as the advanced particle fuelling methods for fusion plasmas. So far, several CT injectors were constructed and tested on various tokamaks including TdeV, STOR-M, TEXT-U, etc. in Canada and U.S.A. In Japan, CT injection programs were carried out in the JFT-2M tokamak at JAERI by our group at Himeji Institute of Technology (now University of Hyogo) [1-4]. In a series of CT injection experiments (1998 – 2004) on JFT-2M, we achieved significant progress. At present, a test of CT injection on a relatively large fusion device is strongly desirable, but it is unfortunately difficult to realize it soon. Before doing the test on large devices, there are several key issues that need to be resolved. First one of them is to identify fuelling mechanism of CT particle. Such a basic research is applicable for even a small-size fusion device. Finding a complex mechanism of CT fuelling process becomes a pioneering work as laboratory reconnection experiments also. The long term objective is to make CT injection a fuelling technology applicable for ITER. From this year, we have started the collaboration on CT injection experiments into spherical tokamak (ST) plasmas in the CPD device which was built at Kyushu university. This research is connected with developing the SPICA injector for fuelling LHD at NIFS.

The main objectives of this research collaboration are as follows; (1) Detailed understandings of complicate interactions involving magnetic reconnection process between the injected CT and ST plasmas. (2) Testing of CT injection into the ST plasma including deep fuelling, plasma rotation and control of plasma pressure profile (3) Demonstration of non-inductive current start-up of ST plasmas by CT injection. (4) Studies of two-fluid effects of the ST plasma in which a toroidal flow is driven by a tangential CT injection. CT injector and its power supply are used the same as on JFT-2M. Note that it becomes much easier to do precision control of CT particle inventory and velocity as compared to experiments on JFT-2M because the toroidal magnetic field energy of the

ST is much smaller than that of a conventional tokamak as shown by Fig. 1.

The main work in the starting year is to move the total CT injection system to Kyusyu university from JAERI. It has been successfully completed at the beginning of November 2007. The power supplies consist of fast capacitor banks of formation (20kV, 144μF) and acceleration (40kV, 92.4μF) of CT plasma and slow capacitor banks of bias coils (2.4kV, 34mF) and 4 gas puff valves (5kV, 4x320μF). After the set-up of the CT injector and those capacitor banks and a vacuum pumping system around the CPD device (see Fig. 2), we checked if the performance of CT injector keeps the same high level as in the experiments on JFT-2M. After replacement of several ignitlons, we confirmed that it can be still operated with the best condition (the acceleration current 260 kA at 20 kV, the formation current 200 kA at 10 kV).

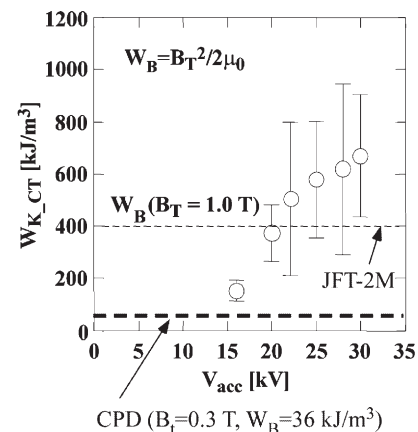


Fig.1 Performance of the CT injector used on JFT-2M [4]. Kinetic energy  $W_{K-CT}$  of CT is as a function of the acceleration bank voltage  $V_{acc}$ . For a deep penetration,  $W_{K-CT}$  must be larger than the magnetic energy of the toroidal field  $B_T$ . The condition is satisfied enough for CPD.

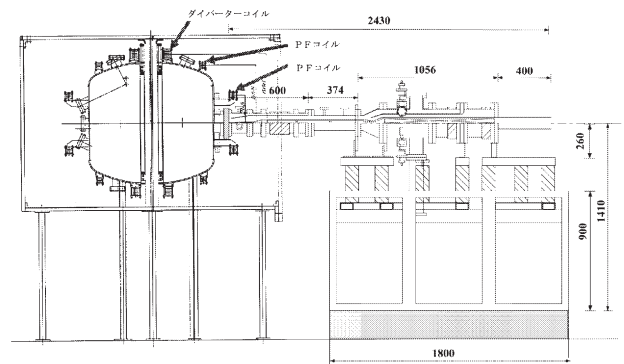


Fig.2 Schematic drawing of the CT injector and the CPD device.

### References

- [1] M. Nagata, et al., Nuclear Fusion **41**, 1687 (2001).
- [2] N. Fukumoto, et al., Nuclear Fusion **43**, 982-986 (2004).
- [3] N. Fukumoto, et al., Fusion Engineering and Design, **70**, 289-297 (2004).
- [4] M. Nagata, et al., Nuclear Fusion **45**, 1056-1060 (2005).



#### §43. Generation of Runaway Electrons by Electron Cyclotron Wave Heating during Current Disruption of TRIAM-1M Tokamak

Toi, K., Ohdachi, S., Isobe, M.,  
Idei, H., Nakamura, K. (Res. Institute for Appl. Mech.,  
Kyusyu Univ.),  
TRIAM-1M Group

A serious concern in a tokamak fusion reactor is impacts of current disruption on a tokamak system. This was already recognized in the initial phase of tokamak researches started in USSR. Impact of current disruption will be more severe in a large sized tokamak with non-circular cross section. Disruption would lead to huge energy and particle losses to plasma facing components, vacuum vessel and superconducting magnets. Moreover, current disruption often induces generation of large amount of runaway electrons (REs) through induced large loop voltage and magnetic reconnection process. In ITER, the runaway electron energy would reach around 15 MeV and carry about two thirds of plasma current ( $\sim 10$  MA)[1]. Loss of these REs to the wall in short time scale is also serious concern. Recently, mitigation techniques of disruption effects such as noble gas jet achieve a satisfactory success.

It should be noted that thus produced runaway current tends to be peaked [2]. If most of plasma current is replaced by the runaway current and properly maintained by a certain method, the disruption effects can be minimized. On the other hand, this process would lead to an interesting magnetic configuration realized in a tokamak plasma with relativistic electron beam. This is very similar to the Astron-Spherator configuration as shown in Fig.1 [3], where the REs would realize a peaked current density profile and deepen the magnetic well due to large Shafranov shift. These characters are very attractive for achieving high beta tokamak plasma having improved confinement.

In order to investigate this possibility, we tried a preparatory experiment for effective RE production by application of electron cyclotron heating (ECH) and/or current drive (ECCD) during disruption phase. Combined effect of ECH/ECCD and large loop voltage induced by current quench may generate REs very effectively. The experiment was carried out on the following conditions in a small sized tokamak TRIAM-1M: the toroidal field  $B_t=6.38$ T. When the horizontal position of plasma column was forcedly outward-shifted, disruption occurred at the plasma current  $I_p \sim 80$ kA, as shown in Fig.2. In this shot, ECH power of  $\sim 130$  kW was applied to the plasma about 10 ms before the disruption. Hard X-ray

emission was obviously enhanced, but the runaway current was not induced. Main reason is that the position of the plasma current channel is not maintained in an optimum position and the runaway current does not build up. This trial is planned to extend in a large tokamak such as JT-60U. In JT-60, about 0.8 MA runaway current was generated spontaneously by disruption and sustained for a long time ( $>1$ s)[4]. ECH/ECCD application to such plasma may lead to more effective replacement of the plasma current to runaway one. NBI heating of the tokamak plasma driven by runaway current will provide an opportunity to test the above-mentioned idea.

#### References

- [1] ITER Physics Basis, Nucl. Fusion **39**, 2251 (1999).
- [2] L.G. Eriksson et al., Phys. Rev. Lett. **92**, 205004-1 (2004)
- [3] S. Yoshikawa et al., Phys. Rev. Lett. **26**, 295 (1971).
- [4] R. Yoshino and S. Tokuda, Nucl. Fusion **40**, 1293 (2000).

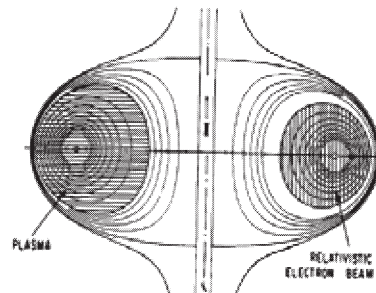


Fig.1 Astron-Spherator configuration cited from ref.3.

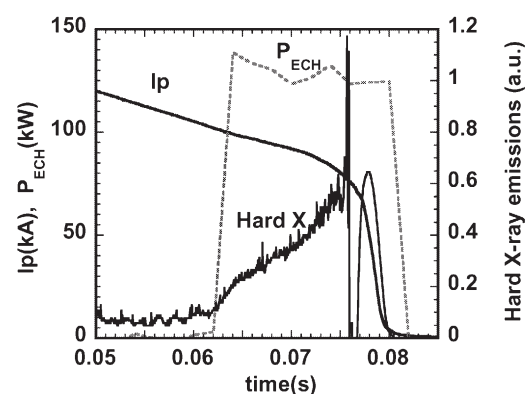


Fig.2 Time evolution of hard X-ray emission enhanced by applied ECH pulse during current disruption on TRIAM-1M tokamak.

§44. Design Study of Long-Pulse NBI  
for the Plasma Boundary Dynamics  
Experimental Device

Takeiri, Y., Nagaoka, K., Osakabe, M.,  
Zushi, H. (Kyushu Univ.)

The plasma boundary dynamics experimental device (QUEST), which is being designed in Kyushu University, is a spherical tokamak (ST) with a low aspect ratio. The objectives of the QUEST are to realize long-pulse and/or steady-state plasmas and to investigate their plasma properties including the related engineering aspects. In order to sustain high-density plasmas in steady state, the plasma heating and current drive by NBI are required. The conceptual design for a steady-state NBI system, which is suitable to the CREST plasmas, was carried out.

The reference design is a 40keV-1MW NBI system. To realize the steady-state injection, a steady-state ion source is required. For that, cooling ability for the grids of the ion source should be enhanced by attaching cooling channels in the vicinity of the beam apertures. However, the transparency of the fully cooled grids is degraded due to the cooling channels. Therefore, the dimensions of a steady-state ion source become larger compared with those of a short-pulse one producing the same beam current.



Fig. 1. Photograph of the plasma grid of the test positive-ion source. The lower half area is used for the beam extraction.

The fully cooled grid is thicker due to the cooling channels, and, then, the diameter of the beam aperture should be larger according to the grid thickness to extract

high-density beams. The grid gap length should be also enlarged according to the aperture diameter for formation of a non-distorted beam emission surface. On the other hand, since the specified beam energy is as low as 40keV, the gap length should be kept short for preventing the beam current from being lowered.

To optimize the design of the grid system in the low-energy and steady-state ion source, we tested a fully cooled grid system with a test positive-ion source. Figure 1 shows the plasma grid of the test source, a lower half of which delivers positive ion beams. As shown in the figure, the grid is designed as fully water-cooled for steady-state operation, in which the cooling channels are silver-brazed in the vicinity of every aperture row.

In the ion source test, high-current ion beams of 40A are delivered from the half grid-area with a current density of 200mA/cm<sup>2</sup> in a short-pulse operation below 1sec. The beam duration is limited by heat load of the calorimeter. Since the heat load of the plasma grid is due to the arc plasma, grid distortion due to the heat load in the long-pulse operation can be verified by extending the arc duration prior to the beam extraction.

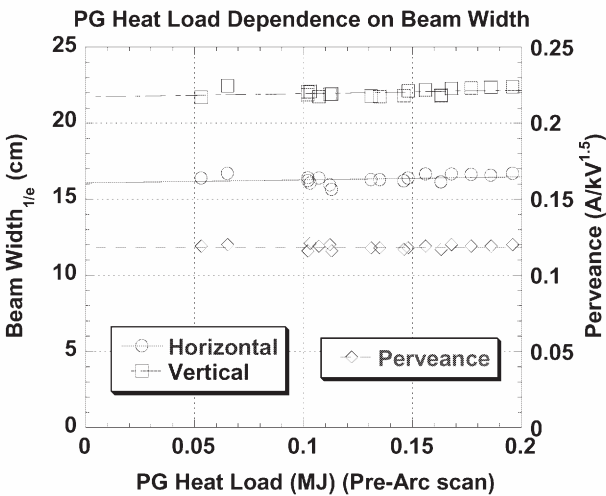


Fig. 2. Variations of the horizontal and the vertical beam widths as a function of the heat load of the plasma grid.

Figure 2 shows the variations of the beam widths in both the horizontal and the vertical directions as a function of the heat load of the plasma grid, which is scanned by extending the arc duration prior to the beam extraction. The maximum heat load corresponds to 10-sec beam extraction. The beam widths are not changed against the increase in the heat load of the plasma grid, as shown in the figure. This result shows that no heat distortion should be observed in the steady-state operation.

The further optimization to the design of the steady-state ion source will be carried out for the QUEST-NBI system.

#### §45. Development of Two-Dimensional Lithium Beam Probe for Edge Density Measurement in CPD

Morisaki, T.,  
Tsuchiya, H. (Grad. Univ. for Advanced Studies),  
Zushi, H. (RIAM, Kyushu Univ.),  
Inada, Y. (Interdisciplinary Grad. School of Eng. Sci.)

Detailed measurement of the edge plasma is essential to promote studies of edge physics and edge control. In that sense, imaging diagnostics is quite useful to acquire an overall picture and a comprehensive knowledge of the phenomenon. Recently a two-dimensional lithium beam probe (2D-LiBP) has been developed in NIFS for the edge plasma measurement on LHD, and has started to provide 2D-density profiles on the poloidal plane. 1)

The 2D density profiles are obtained by observing 2D Li I (670.8 nm) emission profiles due to the Li-electron impact excitation. The sheet shaped Li beam is injected to the plasma through two rectangular apertures of which width is 6 mm. The beam flux profile was measured by an absolutely calibrated quartz crystal monitor on the test stand, and compared with a result from the Monte Carlo simulation, as shown in Fig. 1. It was found that a high quality beam with radial uniformity within  $\pm 15\%$  and toroidal FWHM of 35 mm is achieved as expected by the simulation, and its maximum flux at the center is  $\sim 2 \times 10^{14} \text{ cm}^{-2} \text{ s}^{-1}$ .

The 2D-LiBP was installed in CPD which is a compact ST device with the divertor configuration. The sheet shaped 2D-beam is injected to the plasma from the bottom port through the X-point, as depicted in Fig. 2 (a). The 2D-image of Li I emission ( $0.3 \text{ m} \times 0.5 \text{ m}$ ) is detected by a CCD camera coupled with an interference filter (670.8  $\pm 5 \text{ nm}$ ). The time and spatial resolutions of the optical system are 1 ms and 1 mm, respectively.

Preliminary results were obtained in the first plasma experiment on CPD. Since CPD had not fixed its operational conditions to achieve the ST configuration at that time, no flux surface to confine the plasma existed during the discharges. The plasmas was initially produced by 8.2 GHz ECH on the resonance layer then spread over around the vacuum vessel. Figure 2 (b) shows a 2-D emission profile obtained after the plasma diffused out to the vessel wall. It is found that the beam attenuation due to relatively high electron density is taken place at the region.

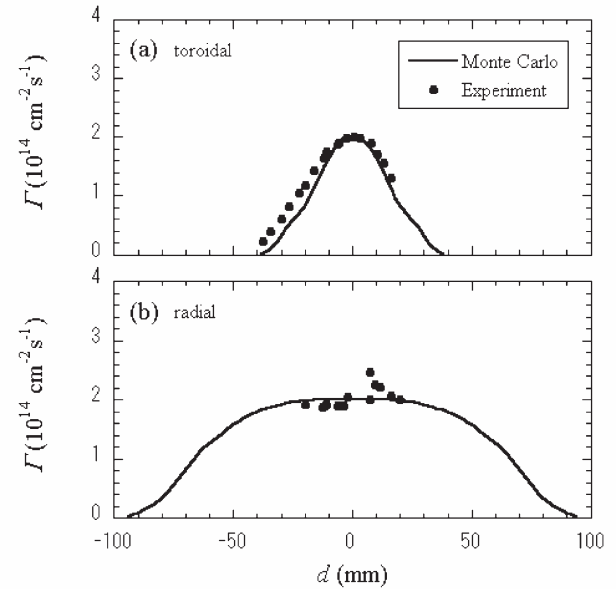


Fig. 1. (a) Toroidal and (b) radial flux profiles of sheet-shaped Li beam.

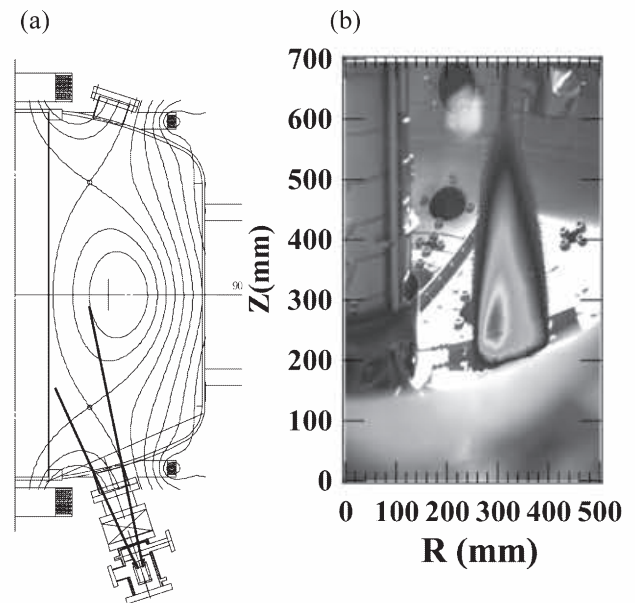


Fig. 2. (a) Schematic of 2D-LiBP diagnostics installed in CPD. (b) Observed 2D Li I emission profile superimposed on a normal camera view from the window port.

#### References

- 1) Takahashi, Y., Morisaki, T., Toi, K., LHD Experimental Group, Plasma and Fusion Res. 1, (2006) 013.



## §46. Integration of PWI Experiments, Diagnostics, Simulation and Modeling in Steady State Plasma

Sakamoto, M. (RIAM, Kyushu Univ.) on behalf of collaborators

Understanding of phenomena of plasma-wall interaction is one of the most critical issues from the viewpoints of the steady state operation of fusion plasma. It is necessary to investigate comprehensively from macroscopic and microscopic viewpoints. In this study, we have utilized the superconducting tokamak TRIAM-1M, in which a long pulse operation can be carried out, as a platform of the study under Interactive Coordinated Researches of NIFS.

In this year, we carried out the plasma experiments for six and half weeks. Many collaborators joined the experiments and multi-directional studies could be promoted [1-11]. As the macroscopic approach, the following measurements have been carried out; the recycling structure of the long duration discharges with profile measurements of  $H_\alpha$  intensity, DEGAS simulation, spectroscopic measurement of the boundary plasma, Langmuir probe measurement of the scrape of layer (SOL), heat load profile on the plasma facing components, global particle balance, development of the particle balance modelling including the change in the wall temperature and plasma flow measurement. As the microscopic approach, the following measurements have been carried out; analysis of the radiation damage process using the surface probe system, analysis of the structure of the deposition layer, quantitative estimation of the retention inside the deposits, real time measurement of the growth of the deposition layer using the optical method and dust measurement.

In order to study the transport of neutral hydrogen in the torus, a toroidal profile of  $I_{H\alpha}$  has been measured at 7 sections in the toroidal direction. The poloidal limiter (PL) and the movable limiter (ML) are strong sources of the recycling flux. The recycling neutrals travel to the toroidal direction and its amount decays with a characteristic length  $\lambda$ . The value of  $\lambda$  decreases not inversely but gradually with increase in  $\bar{n}_e$ , i.e.  $\lambda \propto \bar{n}_e^{-0.2}$ . The density dependence of  $\lambda$  can be well reproduced by DEGAS simulation using a cylindrical model.

The global particle balance in the vacuum chamber has been studied using a simple gas balance model. In the initial phase of the long duration discharge, the global wall pumping rate seems to correlate with OII line intensity. The oxygen impurity affects the physicochemical properties of the deposits and then the capability of hydrogen retention of the deposits increases significantly. The result may suggest the impact of codeposition of hydrogen with oxygen and molybdenum on the global wall pumping.

The dust observations were carried out using a high speed camera in the long duration discharges. The

dust velocity was in the range of 10 to 50 m/s. The number of dusts which were observed in a unit time increased with the discharge duration.

In order to study the deposition property during the long duration discharge, an in situ measurement system of erosion and deposition has been developed which is based on the interference of light on a thin semi-transparent layer of deposited material. A sapphire window at the viewing port is used as a substrate and is located at about 75 mm away from the LCFS. The net erosion/deposition rate on the window depends on the discharge conditions and is in the range of  $-2 \times 10^{-3}$  nm/s to  $2 \times 10^{-3}$  nm/s for the long duration discharges ( $0.1 \times 10^{19} \text{m}^{-3} \leq \bar{n}_e \leq 1 \times 10^{19} \text{m}^{-3}$ ), where plus and minus signs indicate deposition and erosion, respectively. In the high density and long duration discharge ( $\bar{n}_e \sim 1 \times 10^{19} \text{m}^{-3}$ ,  $P_{rf} \sim 60 \text{kW}$ ), It is found that OII line intensity is higher during the erosion phase although  $H_\alpha$  line intensity keeps constant. It seems that the oxygen impurity strongly affects the property of erosion and deposition rather than hydrogen. In practice, a codeposited layer was found in the material probe experiments. The probe head was inserted in the SOL and at 5mm behind the limiter surface in the high density discharges ( $\bar{n}_e \sim 1 \times 10^{19} \text{m}^{-3}$ ). It was exposed for 407 s which is cumulative discharge time of 186 shots. The microstructure of the deposits is bcc polycrystalline and the grain size is 10-20 nm. The Mo deposition rate is about  $2 \times 10^{18} \text{Mo/m}^2\text{s}$  and the hydrogen retention rate of the codeposited layer is about  $3 \times 10^{17} \text{H/m}^2\text{s}$  [3]. It is consistent with the wall pumping rate, i.e.  $\sim 4 \times 10^{17} \text{H/m}^2\text{s}$ , estimated using the gas balance model. Thus, the codeposition plays an important role in the global wall pumping and the bridge between the microscopic and macroscopic phenomena.

### References

- 1) Zushi, H. et al., Nuclear Fusion, Vol.45, No.10 (2005) S142.
- 2) Sakamoto, M. et al., Proc. of 32nd EPS Conference on Plasma Physics (Tarragona, 2005) P5-005.
- 3) Tokitani, M. et al., Proc. of 12nd ICFRM International Conference (Santababara, 2005) 04-35.
- 4) Nakashima, K. et al., Proc. of conference on JSPF (2005) 30aA26P.
- 5) Ogawa, M. et al., Proc. of conference on JSPF (2005) 30aA27P.
- 6) Takaki, K. et al., Proc. of conference on JSPF (2005) 30aA28P.
- 7) Sakaki, K. et al., Proc. of conference on JSPF (2005) 30aA29P.
- 8) Sakamoto, M. et al., Proc. of conference of JSP (2005) 20aWG-1.
- 9) Sakamoto, M. et al., Proc. of 61st conference of JSP (2006) 28pUD-5.
- 10) Noxaki, Y. et al., Proc. of 61st conference of JSP (2006) 28pUD-4.
- 11) Zushi, H. et al., Proc. of 61st conference of JSP (2006) 30pUD-10.



## §47. Current Drive and Heating Experiments using RF/mm-Waves on the TRIAM-1M Tokamak

Idei, H. (Kyushu Univ.) for the TRIAM Experimental Group

The power dependence on density and current drive efficiency in the Lower Hybrid Current Drive (LHCD) plasma was investigated in wide ranges of line-averaged electron density of  $\bar{n}_e = 0.1 \sim 4.7 \times 10^{19} m^{-3}$ , and plasma current of  $I_p = 15 \sim 100 kA$ . The high power RF-wave of the frequency of 8.2GHz was generated at the klystron system, and the net power up to 0.24MW was injected to the plasma. The generated power was almost maximum of the system. The highest current achieved ever, of 100kA, that corresponded to a safety factor  $q \leq 4$ , was achieved in series of the high power experiments. The highest density achieved ever, of  $4.7 \times 10^{19} m^{-3}$ , was also achieved in the series of the experiments. The power dependence was studied in the wide ranges of the plasma parameters. Figure 1 shows the typical waveforms at the high density operation. The density increased with the net injected power  $P_{LH}$ , and the maximum density was attained by the high power and the strong gas-puffing. The current drive efficiency  $\eta_{CD}$  gradually decreased with the increase of the density. The plasma discharge was terminated at the maximum density, but the achieved density was far from the density limit predicted by Sverdrup and Wegrowe models based on the wave propagation characteristics. The  $\eta_{CD}$  scaling has a dependence on both the density and the electron temperature. The observed decrease of  $\eta_{CD}$  was due to the decrease of the electron temperature by the density increase. The driven current decreased, and the plasma confinement became worse. The ion temperature  $T_i$  gradually decreased with the decrease of the current, as shown in Fig.1. The electron temperature also decreased by the degradation of the plasma confinement. The power dependence on density and current drive efficiency has been studied in the link with the plasma confinement. The observed improved- $\eta_{CD}$  (Enhanced CD: ECD) mode has been also modeled in association with the electron temperature.

In order to investigate the spectrum gap problem and controllability for the current profile by means of counter current drive (ctr-CD) in the LHCD plasma, combination experiments with the backward (BW) propagating LH wave and/or Electron Cyclotron (EC) wave were performed in LHCD plasmas sustained by the forward (FW) propagating wave. Figure 2 shows time evolutions of the plasma current change  $\Delta I_p$  and the Shafranov shift  $\Delta$  when the ratio  $P_{BW}/P_{FW}$  of the BW

and FW injected power was scanned. The current decreased due to the peaking of the current profile  $j(r)$  for the BW injection at  $P_{BW}/P_{FW} < 0.8$ , and the current rapidly increased due to the broadening of  $j(r)$  at  $P_{BW}/P_{FW} > 0.8$ . A large Shafranov shift was observed in the hard X-ray radial profile, which suggests that a high poloidal beta plasma was achieved via the contribution of tail electrons. The ctr-ECCD decreased the current at a larger ratio of  $P_{BW}/P_{FW} \sim 1.3$ , when the EC resonance position was inboard side for the magnetic-axis of the plasma. The effects of the ctr-CD with the BW propagating LH- and EC-waves have been studied.

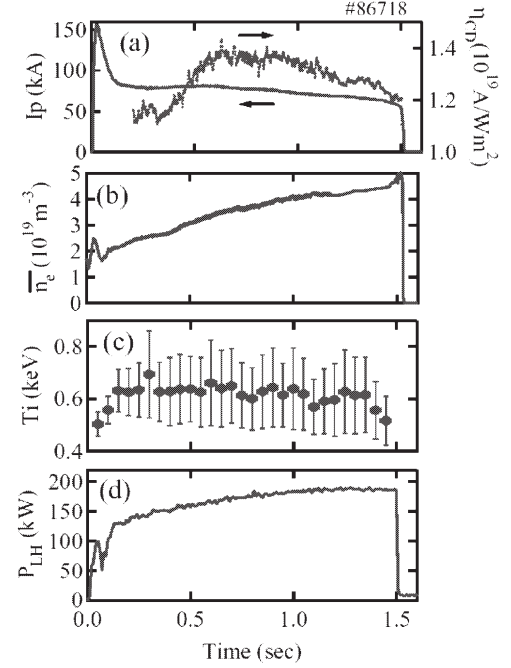


Fig. 1: Typical waveforms at the high density operation.

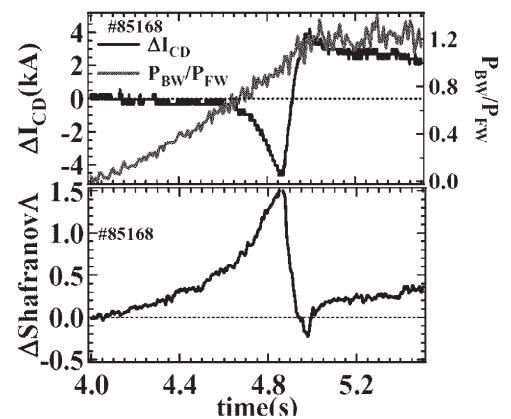


Fig. 2: Plasma current change  $\Delta I_p$  and Shafranov shift  $\Delta$  when the ratio  $P_{BW}/P_{FW}$  of the BW and FW injected power was scanned.

This work was realized in the bi-directional collaboration (NIFS06KUTR016) organized by NIFS.

§48. Dust Measurement in TRIAM-1M using Fast Camera

Nishino, N., Fukuyama, Y., Kondo, E., Fukamizu, T., Abe, T. (Hiroshima Univ.), Sasaki, K., Hanada, K. (Kyushu Univ.)

Dust in plasma is very popular problem in nuclear fusion reactor due to tritium inventory and impurity source. The candidate of dust should be the wall and/or limiter. It is natural thought that the process of dust formation relates temperature of the wall/limiter. Triam-1M can afford to have long time discharges and it is very suitable machine to research this dust formation. In this study to investigate the dust source and the behavior of dust in plasma two coherent fiber bundles and one fast camera are provided, and it is tried to get the information of dust position with 3-dimension. The length of the port duct is long (>2m) due to the super conductor machine. Therefore, two long tubes for coherent fiber bundles are installed in Triam-1M (see Fig.1). Also, a telecentric optical system is designed to get two ends of both fiber bundles together to make an image on the camera sensor (see Fig.2).

It was obtained by fast camera measurement at previous our work [1] that dust particle motion in a plasma was about a few m/s to a few hundreds m/s, and also dust formation relates temperature of the limiter in Triam-1M. The velocity ambiguity is due to one eye measurement. Therefore, 3-d dust measurement is very important for comparison with dust theory and experimental results. Unfortunately one fiber bundle was damaged by hard X-ray due to run away discharges during test season. Therefore, it is impossible to get the accurate dust position at this time. Figure 3 shows typical image of dust particle in Triam-1M limiter plasma. In this image dust is generated on Mo limiter, and the source area of dust on the limiter is heated up and brightened by plasma contact. Camera images show dust motion in plasma was very complicated. Dust particle was accelerated sometimes and decelerated in another moment.

These motions are thought to be caused by charge up of dust particle due to electron attachment. After plasma experiment dust collection plan will be performed and dust composition will be analyzed by EPMA. The results will be presented to the international meeting [2].

Triam-1M is shut down at 2005. Therefore, it is decided that the fast camera will be installed to the next device ‘QUEST’ at Kyushu University, and dust measurement will be continued

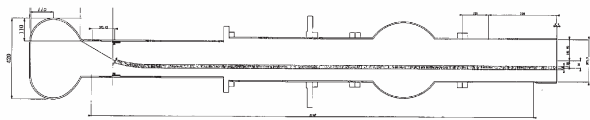


Fig.1

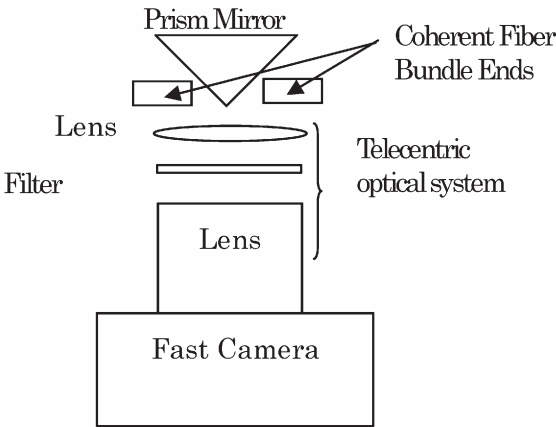


Fig.2

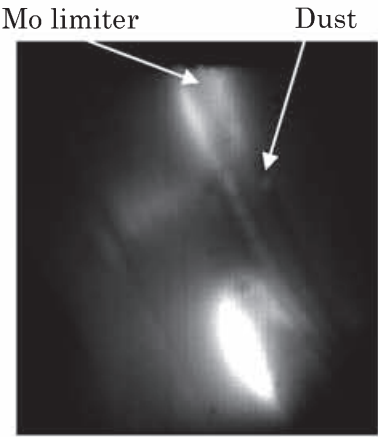


Fig.3

- 1). Sasaki, K., et.al.: JPFS meeting
- 2). Sasaki, K., et.al.: 17<sup>th</sup> Plasma-Surface Interaction

## §49. Neutral Particle Transport in Steady-State Torus Plasmas

Nakashima, Y., Yoshikawa, M., Islam, Md. K. (Univ. Tsukuba, P.R.C.),  
 Kobayashi, S. (Kyoto Univ., I.A.E.),  
 Sakamoto, M., Zushi, H. (Kyush Univ., RIAM),  
 Kubota, Y., Higashizono, Y. (Univ. Tsukuba, Graduate School of Pure and Appl. Sci.),  
 Ogawa, M., Takagi, K. (Kyushu Univ., Inter disciplinary Graduate School of Eng. Sci.),  
 Shoji, M.

It is an important subject to investigate the behavior of neutral particles in order to evaluate the particle and energy confinement properties in the plasmas. Particularly in long duration and steady-state plasmas, the neutral behavior is though to contain much interesting feature, since the time constant of plasma-wall interactions has longer characteristic time than other time constants such as particle and energy confinement times<sup>1)</sup>. In this study, a neutral transport simulation code is applied to TRIAM-1M tokamak, which produces long duration plasmas, in order to estimate the spatial profile of neutral density and neutral temperature in the plasma.  $H\alpha$  and its spatial profile measurements are also carried out in the several positions in TRIAM-1M. The ultimate goal of this study is a comprehensive understanding of the significant behavior of neutral particles in steady-state torus plasmas.

In TRIAM-1M, totally 14  $H\alpha$  line-emission detectors are install in major radial direction and toroidal one. By using these detector arrays, detailed spatial profiles of  $H\alpha$  line intensity has been measured and neutral particle behavior was investigated from the neutral transport simulation with the DEGAS Monte-Carlo code<sup>2,3)</sup>. In the previous research, the spatial profile of the  $H\alpha$  intensity in poloidal cross-section showed a good agreement with the Monte-Carlo simulation. On the other hand, the toroidal profiles obtained from the experiments do not explain its density dependence estimated from the mean-free-path length based on the experimental data. In order to solve this discrepancy, a neutral transport analysis along the toroidal direction has been performed by using a cylindrical mesh model.

Figure 1 shows the mesh model used in the DEGAS simulation. In a cylindrical geometry, a plasma column and scrape-off layer (SOL) region surrounding the plasma are defined. a neutral particle source is given near the midplane of the cylinder and gas is injected uniformly

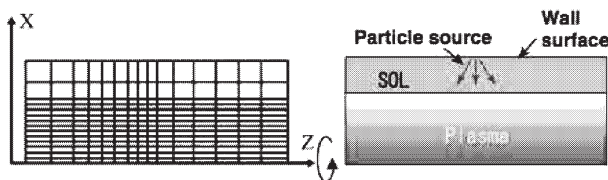


Fig. 1 Toroidal mesh model used in the simulation.

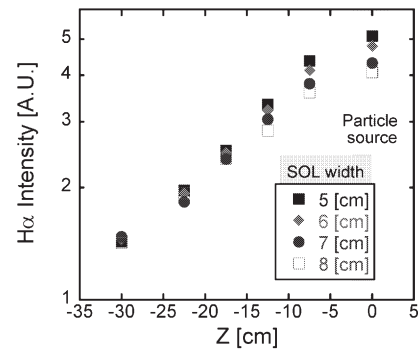


Fig. 2. Simulation result of  $H\alpha$  line intensity obtained by the DEGAS simulation.

in azimuthal direction. In Fig. 2, the simulation results of the  $H\alpha$  line intensity are plotted along the toroidal direction (Z-axis) As shown in the figure, the decay length of the intensity depends on the SOL width. This result indicates that the geometry of the vacuum vessel and plasma is strongly affects the neutral behavior.

Figure 3 shows the 2-dimensional profiles of atomic hydrogen temperature calculated in both low-density and high-density plasmas. It is found that a significant difference is clearly revealed between the two density cases. From this result, the decay length of the neutral particle density in the plasma is affected by not only the plasma density but also the temperature of the neutrals. More detailed and systematic study using DEGAS simulation will be performed in near future.

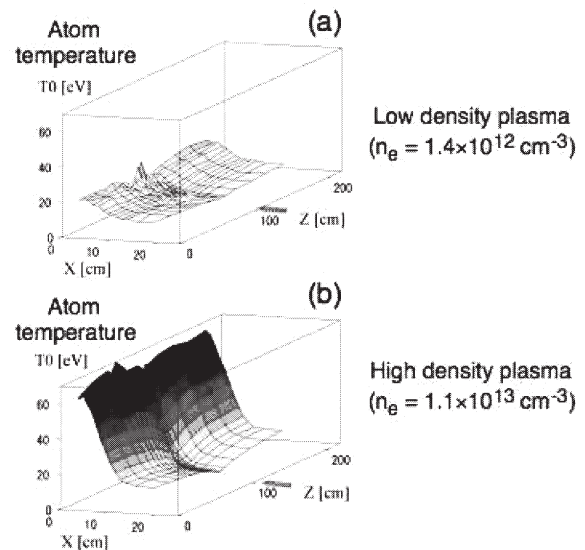


Fig. 3. Spatial profile of hydrogen atom temperature calculated from DEGAS.

### Reference

- 1) Sakamoto, M. *et al.*, Nucl. Fusion. **44** (2004) 639.
- 2) Heifetz, D. *et al.*, J. Comput. Phys. **46** (1982) 309.
- 3) Nakashima, Y. *et al.* J. Nucl. Mater. **196-198** (1992) 493.

## §50. Construction and Development of Long Term Sustained Spherical Tokamak “QUEST” in Kyushu University

Sato, K.N., Zushi, H., Hanada, K., Nakamura, K., Sakamoto, M., Idei, H., Hasegawa, M., Kawasaki, S., Nakashima, H., Higashijima, A., Yoshida, N., Tokunaga, H. (RIAM, Kyushu Univ.),  
 Takase, Y., Ono, Y., Ogawa, Y. (Univ. of Tokyo),  
 Ando, A. (Tohoku Univ.),  
 Oono, T. (Nagoya Univ.),  
 Maekawa, T., Kishimoto, Y. (Kyoto Univ.),  
 Ishida, A. (Niigata Univ.),  
 Nagata, M. (Univ. of Hyogo),  
 Nishino, N. (Hiroshima Univ.),  
 Mitarai, O. (Kyushu Tokai Univ.),  
 Asakura, N., Matsukawa, M., Shimizu, K.,  
 Nishio, S. (JAEA),  
 Nakamura, Y., Nagayama, Y., Hirooka, T.,  
 Muto, T., Takeiri, Y., Kaneko, O., Yamada, H.,  
 Komori, A.

Steady state operation (SSO) is one of the critical issues for the future fusion reactor, and understanding of the global wall recycling is quite important from the viewpoint of density control for the SSO, since the wall plays significant roles as the particle sink and source.

In TRIAM-1M, the ultra-long discharge with the duration of 5 h 16 min has been achieved using a local movable limiter with good cooling capability. Moreover, effects of the movable limiter on the global wall recycling have been studied. Due to insertion of the movable limiter to the plasma edge, SOL parameters, the toroidal profile of the neutral particle density and the heat load on the wall are changed to influence the global wall recycling. In 5 h 16 min discharge, the temperature increase in the plasma facing components could be successfully suppressed by the insertion of the movable limiter. Long time global wall saturation (i.e. global balance

between particle absorption and release of the wall) was not observed.

A new project of long term sustained spherical tokamak “QUEST” in Kyushu University has been proposed and the device construction has been started as the three years plan (FY2005-2007).

Main objectives of the project are to investigate the following issues:

- i) Development of current start-up and long-term current driving in an ST
- ii) Integrated studies of plasma performance and recycling of long-term sustained ST with the advanced PWI handling by active wall-temperature control and a divertor system with intensive pumping.

The device parameters are decided to be as a major radius of  $R = 0.68$  m, a minor radius of  $a = 0.40$  m, and a magnetic field strength of  $B = 0.25$  T in order to carry out the issues above. A plasma current of 100 kA with the density of  $0.4 \times 10^{19} \text{ m}^{-3}$  at a heating power level of 1 MW is expected to be obtained in the quasi-steady state operation. The side view of the device is shown in Fig.1.

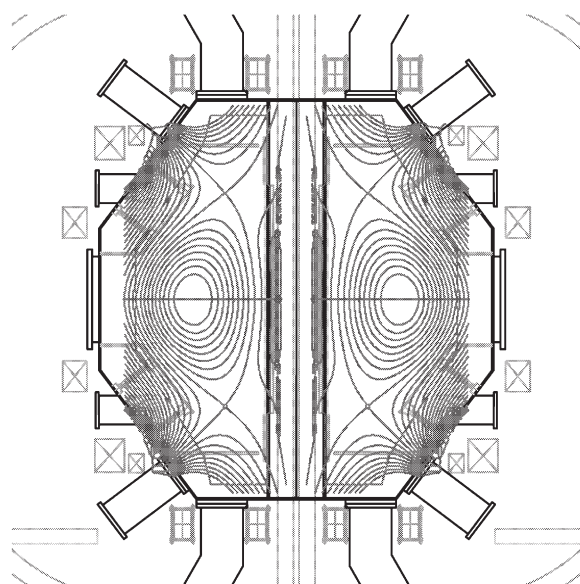


Fig.1 Side view of the new ST device “QUEST” in Kyushu University.



### §51. Development of an Ion Beam Source for a Low Voltage / High Current Neutral Beam Injector

Ono, Y., Takase, Y., Zushi, H., Ejiri, A., Kawamori, E., Itagaki, T. (Univ. Tokyo, Department of Frontier Sciences), Asai, T., Takahashi, T. (Nihon Univ.)

The Low-voltage and high-current neutral beam injector (NBI) is essential to sustainment of ultra-high beta STs at UTST device, which is one of core experiments for the all-Japan ST research project. The requested properties for the NBI are its beam energy <25kV, its beam current >20A, and low-beam divergence, while its pulse length can be as short as 10msec. We organized a new research team composed of Univ. Tokyo, Nihon Univ., Osaka Univ. and Kyusyu Univ. to develop the compact and maintenance-free ion beam source for NBI by combining the washer-gun plasma source techniques at Univ. Tokyo with the electrode design technique at Nihon Univ. and Osaka Univ. We will optimize the plasma source and the electrode system to complete the compact and cost-effective low-voltage/ high-current NBI.

In 2005, we developed (1) the plasma source by washer gun, and (2) the electrode system for ion acceleration and deceleration. Figure 1 shows the final design of our NBI system under development, which is composed of the washer gun plasma source, the plasma source chamber, the electrode system and the neutral cell. We completed the washer gun plasma source and most of the plasma source chamber, leading us to studying the properties of the washer gun plasma source. Figures 2(a) and (b) show the time evolutions of the gun current and the electron density averaged over 1m from the gun, respectively. The CO<sub>2</sub> laser interferometer result clearly shows that the electron density inside the plasma source chamber is  $10^{18}$ - $10^{19}$ [m<sup>-3</sup>]. Unlike the conventional filament method, high-density plasma over  $10^{18}$  [m<sup>-3</sup>] was obtained economically by the combination of the washer gun and the source chamber. The plasma duration time ~ 100μsec is limited by the capacitor bank and gas puff. Based on these results, we will complete the test module of ion beam source around

Jan. 2007, and will start optimizing the electrode system for ion acceleration and deceleration.

### References

[1] E. Kawamori and Y. Ono, Physical Review Letters, 95, (2005), 085003..

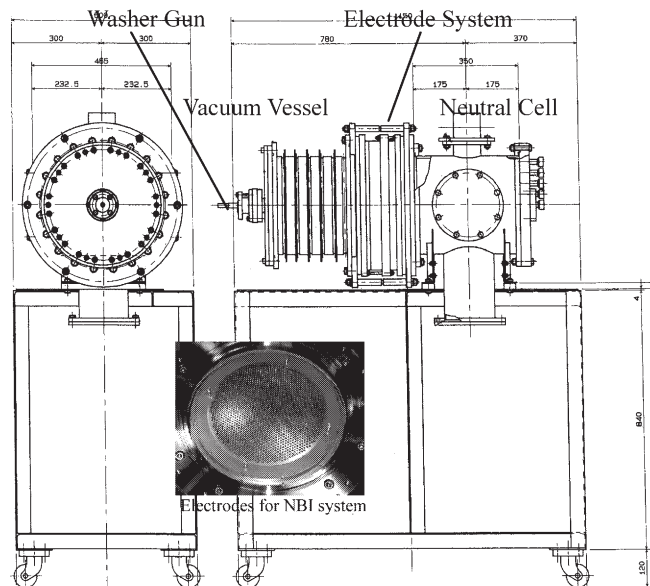


Fig. 1 Low-voltage/ high-current NBI device with washer gun under development.

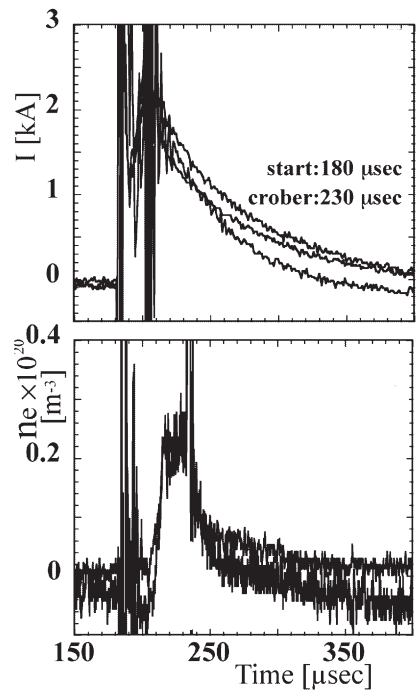


Fig. 2 Time evolutions of discharge current of the washer gun current I (a) and electron density (b).

## §52. Organization of the All-Japan ST Research Group

Takase, Y., Ono, Y., Ogawa, Y. (Frontier Sci. and High Temp. Plasma Ctr., U. Tokyo), Sato, K., Zushi, H., Hanada, K., Yoshida, N. (RIAM, Kyushu U.), Kishimoto, Y., Maekawa, T. (Energy, Kyoto U.), Nagata, M. (Eng., Hyogo U.), Ishida, A. (Nat. Sci., Niigata U.), Nishino, N. (Eng., Hiroshima U.), Mitarai, O. (Eng., Kyushu Tokai U.), Asakura, N., Matsukawa, M., Nishio, S. (Fusion Res. Dev., JAEA), Komori, A., Nagayama, Y., Hayashi, T.

Based on the conclusions of the “Kyushu University Plasma Boundary Dynamics Experimental Device Review Committee”, a formal proposal was made to reorganize spherical tokamak (ST) research in Japan as the All-Japan ST Research Program, and to build a new ST device at Kyushu University to fulfill one of the missions of this program, steady state operation. This proposal was officially approved by the NIFS Collaboration Committee.

The All-Japan ST Research Program is organized under Bi-Directional Collaboration of NIFS, and promotes creative and innovative research at universities and other institutions. To maintain international competitiveness and to make significant contributions internationally, it is crucial to integrate all resources, including experimental research using existing devices in addition to the new ST, as well as theoretical and computational research. The purpose of this collaborative research is to organize the All-Japan ST Research Group to carry out this program, and to initiate its activity. It will also form the All-Japan ST Research Program Steering Committee to coordinate activities and to establish priorities within the All-Japan ST Research Program.

Three meetings were held, and the All-Japan ST Research Group and the All-Japan ST Research Program Steering were organized. The All-Japan ST Research Group consists of all researchers interested in ST research, and carries out research. The All-Japan ST Research Program Steering Committee consists of leaders of experimental and theory/simulation groups, with the members of the Kyushu University Plasma Boundary Dynamics Experimental Device Review Committee as core members, and this group coordinates the All-Japan ST Research Program.

The first of the three meetings (April 21 at Kyoto University, attended by 16 researchers) was a joint meeting of the All-Japan ST Research Group and the fifth meeting of the Kyushu University Plasma Boundary Dynamics Experimental Device Review Committee. At this meeting a resolution was made to form the All-Japan ST Research Program Steering Committee. The second meeting (Aug. 5 at the University of Tokyo, attended by 11 researchers) and the third meeting (Dec. 7 at NIFS, attended by 12 researchers) were meetings of the All-Japan ST Research Program Steering Committee. Through these meetings, a common understanding of the objectives, mission, and

basic strategy of the All-Japan ST Research Program was developed.

In particular, the All-Japan ST Research Program aims at establishing the scientific basis and contributing to broadening the options for fusion power plants. These are accomplished by creative and innovative research, focused in the two major research elements of “ultra-high beta” and “ultra-long pulse.” Plasma start-up, current drive, heat and particle control, and plasma-wall interaction are important enabling research elements necessary to support the main objectives of the program. High quality research on these elements will be realized by collaboration on the all-Japan scale. Research which cannot be pursued on ST devices in Japan, such as the sustainment of very high beta plasmas, will be performed utilizing international collaborations.

The All-Japan ST Research Group was established as a result of this activity. Prof. Takase of the University of Tokyo has been selected as the coordinator of the program. In addition, the All-Japan ST Research Program Steering Committee was established provisionally, and has started its activity. Preparations are in progress to establish new rules that would make the All-Japan ST Research Program Steering Committee an officially authorized committee under the NIFS Bi-Directional Collaboration Committee. The All-Japan ST Research Program Steering Committee is expected to replace the functions of the Kyushu University Plasma Boundary Dynamics Experimental Device Review Committee.

ST research in Japan, including the activities of the All-Japan ST Research Program Steering Committee, will continue to be supported by Bi-Directional Collaboration of NIFS. The Steering Committee will lay down the research plan for the All-Japan ST Research Program, including formation of research strategy, establishment of priorities of research elements, coordination of roles of different groups, utilization of experimental devices, and enhancement of collaborations. In addition, a plan is being developed to make the All-Japan ST Research Program function as a virtual research center, making full use of remote conferences and remote experimental participation via the Super SINET.

This collaboration has also contributed greatly to the improvement of the QUEST device design.

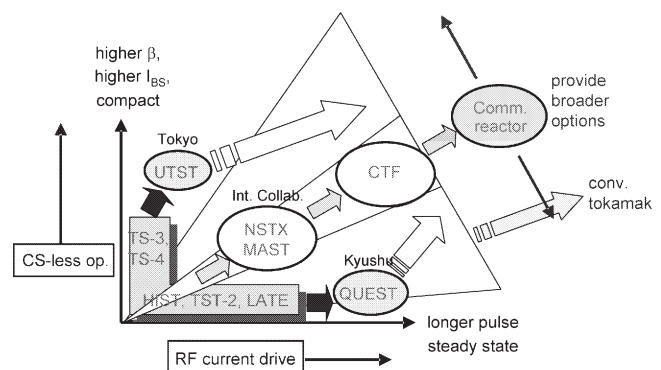


Fig. 1. Strategy of the All-Japan ST Research Program.

## 14. Public Relations Office

### 1. *Introduction*

The Public Relations Office (hereinafter referred to as the PR Office) was established in the end of July 2003 for the following purposes: 1) to guide the ordinary visitors around the institute (NIFS Tour); 2) to create the institute web side as well as to operate and manage various servers used for the PR purposes; 3) to work on the efficiency improvement as an Inter-Operational institute; and 4) to translate documents into foreign languages. Throughout the above activities, the PR Office is to fulfill its major responsibility, informing the public or the society of the necessity of nuclear fusion research as well as reporting research activities in a simple and concise manner.

### 2. *PR activities*

In the year 2005, the institute had 3,000 visitors for the NIFS tour. The PR Office distributed brochures, explained plasmas and the institute's Large Helical Device (LHD), and toured the institute facilities. Also in the annual open house taken place in August, the PR Office offered a quiz show, asking questions about the nuclear fusion and plasma as well as the science in general, hosted by the institute mascot character 'Plasma-kun'. The quiz show received much popularity among the visitors. Furthermore, as a part of promotional activities, the PR Office dispatched to the science museums located in Fukuoka and Osaka and academic institutions like elementary schools and high schools in the neighboring prefectures, giving various types of scientific exhibitions and demonstrations. Besides, the office gave a series of assistance in the events called "SSH (Super Science High school)" by showing students around the institute. In the future, the PR Office hopes to further deepen the understanding of the NIFS visitors regarding nuclear fusion and plasmas. Therefore, diversification of the NIFS tour courses, improvement of their contents, refurbishment as well as expansion of the scientific exhibitions, foundation of a closer liaison between the tour and scientific experiments, and so many more activities should be planned then carried out.

### 3. *Web sites management*

Continuing from the last year, the PR Office carried out the maintenance and improvements of the institute web pages and built some new contents in addition to the existing ones. In the FY 2005, the office focused on developing the contents entitled "What's Nuclear Fusion?" mainly targeted for children.

The NIFS top page (<http://www.nifs.ac.jp/index-j.html>) is to be remodeled into a new design, such that the general visitors, collaborative researchers, students, or corporate visitors could easily find information they need, by the end of this year. The office is also revising existing pages so

that they will be optimized for various Internet search engines. In the future, such contents that they introduce facilities in the institute and explain the plasma property and its confinement method in a simple manner need to be created. Combining those activities introduced herein, the PR Office is challenging to expand the number of accesses to the NIFS top page for the 10 times as much as it is now. Simultaneously, the Office will conduct a detail access analysis to find the viewer's needs and revise existing pages in such style that meets the demand.

### 4. *Efficiency improvement as an Inter-Operational Institute*

In order to improve the convenience of collaborative researchers visiting NIFS, the PR Office placed a public display at the entrance of the Library building to provide various meeting information. Also, the office carried out a series of assisting operations to hold a videoconference with a remote partner. Furthermore, it is also the responsibility of the PR Office to maintain, operate, and manage mailing lists that are inevitable to provide the collaborative researchers and the general public with information. In the future, web pages that are specifically focused on the collaborative research related subjects should be created in a close association and cooperation with the Collaborative Research Committee members.

### 5. *Document translation*

The PR Office translated major contents including the NIFS web page as well as scientific reports and brochures in English. Also, the office provided translation supports for some other contents, namely several manuals like the method of LHD experiment data acquisition. In the future, translations of such information concerning the NIFS research accomplishments as well as the detail of various experiment devices then the active transmission of those information to the foreign nations will be necessary.

All of the activities introduced above were carried out in close correspondence with the NIFS General Affairs Division, Public Relations Committee, Open House Committee, Video Production Committee, and some others.

(Takahata, K.)



## 15. Research Information Office

### 1. Introduction

The function of the research information office is indicated as follows:

- Accumulation of research activity information related to fusion science and construction of a useful evaluation data base system for improvement of level of research and education.
- Information disclosure of the latest study results by publication of research reports such as an annual report, a NIFS report, etc.

### 2. Construction of research activity database

We have been constructing the database by accumulating research activity information of the National Institute for Fusion Science including activities of collaboration research. It aims at the construction of a useful data base for the improvement of the level of the education and research. Accurate data of the articles presented by researchers and students has been required as a database that indicates the activity of the collaboration research. Therefore, "NIFS article information system" has been constructed as the research activity database. Moreover, this system plans to accumulate and offer data to the international society by linking with the "University information database" of National Institution for Academic Degrees and University Evaluation.

The counting of the presented papers and the extraction of the statistical data can be done by using the "NIFS article information system". Once the article is registered in the "NIFS article information system", the researcher need not submit again the article list at each counting for different evaluation, because reuse of the data base is possible. Moreover, an individual author is recognized in the "NIFS paper information system". Therefore, even if the name of the author on the article is the same (the same first name and the same family name), it is possible to distinguish them. It expands not only to an accurate accounting but also to the possibility of an article information system. For instance, the researcher who logs in can make the latest article list of himself. The article can be retrieved and can be inspected. It is expected that the article before presentation can be inspected internally, which contributes to the transparency of the publication of the article.

DOI (Digital Object Identifier) link is offered to the published article. DOI is a system that specifies the article by the identification number to an individual article, which is an electronic version of ISBN that is attached to a book. This DOI was developed by the United States publication society, and opened to the public in 1997, and is being managed by the international DOI foundation. The article can be referred to only by clicking DOI links of articles in "NIFS article information system". "NIFS article information system" can be also used for various procedures in the institute. Labor savings in the evaluation can be attempted by integrating an input and various procedures to "NIFS article information system".

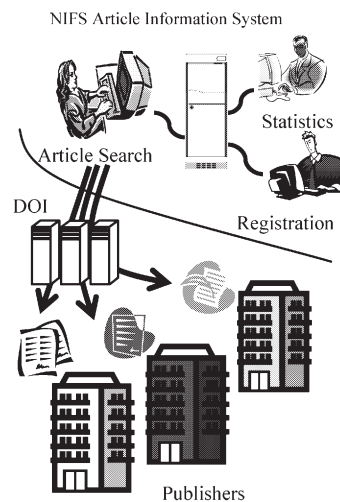


Fig.1. Function of NIFS article information system.

### 3. Publication of NIFS reports and Collection of Reports

Publication of the annual report and the series NIFS Research Report is also an important task of the Research Information Office. NIFS series are the preprints for presenting promptly the results of collaboration research work of NIFS.

#### NIFS Research Report

Present the results of research work for nuclear fusion, plasma physics and theory & simulation and experiments in related fields.

#### NIFS-PROC

Proceedings of international conferences or symposia organized by NIFS and the reports of the meetings for the collaboration research work of NIFS.

#### NIFS-TECH

Present the results of technical research development related to nuclear fusion and plasma physics.

#### NIFS-DATA

Data series compiling the evaluated basic data for fusion science and related fields.

#### NIFS-MEMO

Technical data and reference for newly developed devices, databases, hardware and software of computer codes.

Table 1 Number of published NIFS reports

	FY 1989-2004	FY 2005	TOTAL
NIFS	811	20	831
NIFS-DATA	92	4	96
NIFS-TECH	12	1	13
NIFS-PROC	59	2	61
NIFS-MEMO	45	2	47
Annual Report	16	1	17

The office also collects laboratory reports and other literatures concerning nuclear fusion and related fields from foreign institutions. The total number of collected reports in this fiscal year was about 500 and approximately 35,600 reports have been collected so far.

(Mito, T.)



### III. International Collaboration

The international collaboration is one of major activities of the institute. The collaboration covers multilateral institutional collaborations, bilateral ones, other governmental or inter-institutional agreements and personal exchanges. Those are mostly supported by Grant-in-Aid of Scientific Research of Ministry of Education, Culture, Sports, Science and Technology (MEXT), or JSPS (Japan Society for Promotion of Science) program. A detailed description of activities is given in the following tables. The multilateral collaborations are those under the US-Japan Fusion Cooperation Program, the IEA TEXTOR Collaboration and IEA Stellarator Agreement. In order to promote scientific exchanges between NIFS and foreign leading institutes, the following agreements on academic exchange and cooperation shown in Table I have been

signed up. Grant-in Aid for International Scientific Research programs and individual travel grants for participating overseas international symposia (both being supported by MEXT) have effectively functioned to promote international activities of NIFS. Guest professors (supported by MEXT), who stayed for more than three months, and research fellows (JSPS research fellowship) are listed in Tables II and III, respectively. The 15<sup>th</sup> International Toki Conference on Plasma Physics and Controlled Nuclear Controlled Fusion was held in December 2005, NIFS being as the host institute. Statistics of visitors and visit by NIFS staff in FY 2005 are as follows; foreign scientists from 26 countries visited NIFS 175 person-times and NIFS staff went abroad 213 person-times (to more than 11 countries).

(Matsuoka, K.)

Table I. List of Academic Exchange and Cooperation Agreement with NIFS

<i>Organization</i>	<i>Country</i>	<i>Effective from</i>
UCLA, Plasma and Fusion C.	USA	3 July '90
Institute of Plasma Physics, Academia Sinica	China	27 June '92
Max-Planck Institute for Plasmaphysics	Germany	11 May '93
Kurchatov Institute of Nuclear Fusion	Russia	15 May '93
Kharkov Institute of Physics and Technology	Ukraine	7 Oct. '94
The Australian National University	Australia	8 May '95
Korea Basic Science Institute	Korea	6 March '96
Forschungszentrum Karlsruhe GmbH	Germany	6 Oct. '05
Princeton Plasma Physics Laboratory	USA	3 March '06
Institute for Fusion Studies, The University of Texas at Austin	USA	6 March '06

**Table II** List of guest professors in FY 2005

Name	Organization	Country	Term
WELLER Arthur	Max-Planck Institute for Plasmaphysics	Germany	Jan.5 '05 ~ Apr.4 '05
TSKHAKAYA David	Institute of Theoretical Physics, University of Innsbruck	Austria	Jan.6 '05 ~ Apr.15 '05
VYACHESLAVOV Leonid Nikolaevich	Budker Institute of Nuclear Physics	Russia	Jan.10 '05 ~ May10 '05
IGITKHANOV Juri Levanovic	Max-Planck Institute for Plasmaphysics	Germany	Apr.7 '05 ~ Sept.7 '05
RAMOS Alcazar Jesus	Plasma Science and Fusion Center, Massachusetts Institute of Technology	USA	Jun.10 '05 ~ Sept.9 '05
VINYAR Igor	St.Petersburg State Technical University	Russia	Jun.27 '05 ~ Sept.26 '05
SKOBELEV Igor	Multicharged Ions Spectra Data Center of VNIIFTRI	Russia	Sept.15 '05 ~ Jan.15 '06
PETROSKY Tomio Yamakoshi	Ilya Pligogine Center for Studies in Statistical Mechanics and Complex Systems,The University of Texas at Austin	USA	Oct.20 '05 ~ Jan.19 '06
VLADMIROV Serguei	Research Center for Theoretical Astrophysics, School of Physics, University of Sydney	Australia	Jan.5 '06 ~ Apr.7 '06
VOYTSENYA Volodymyr	Kharkov Institute of Physics and Technology	Ukraine	Jan.10 '06 ~ Apr.10 '06
CHEN Jiming	Southwestern Institute of Physics	China	Feb.24'06 ~ Jul.23'06
SERGEY Neudachin	Russian Research Center "Kurchatov Institute"	Russia	Jan.11'05 ~ Apr.14'05

**Table III** List of JSPS invited fellows for NIFS in FY 2005

○Postdoctoral Fellowships for Foreign Researchers			
Name	Organization	Country	Term
Clive Alvin Michael	Australian National University	Australia	1 Apr. '05 ~ 31 Mar. '07
Sergi Ferrando I Margalet	Swiss Federal Institute of Technology	Switzerland	28 Nov. '05 ~ 27Nov. '07
Liu Yi	Southwestern Institute of Physics	China	20 Nov.'05 ~ 19 Nov. '07
○Invitation Fellowship Programs for Research in Japan			
Name	Organization	Country	Term
None			

## 1. US – Japan (Universities) Fusion Cooperation Program

The term of the agreement of the US-Japan Joint Activity in the area of fusion research has expired in October 2005. However, both sides agreed the usefulness and necessity of the continuation of the US-Japan Joint Activity. So, the new scheme for the US-Japan Joint Activity is being pursued.

NIFS as a member of "Inter-University Research Institute, National Institutes of Natural Sciences" conducted quite successfully the LHD experiments as well as theory and simulation together with collaborators from Universities, JAEA and the international institutions.

One of the main activities of the Japanese university researchers participating in the US-Japan collaboration is the research in the national spherical torus experiment (NSTX) in Princeton University, while many US researchers participated in the LHD experiments just as in the last year.

The international efforts for establishing the ITER project are going well among parties: Japan, Europe, USA, Russia, China Korea, and India. In addition to this, the ITER Broader Approach (ITER-BA) activity started between Japan and Europe. The location for the ITER-BA activity is Rokkasho village of Aomori prefecture in Japan.

### **Fusion Physics Planning Committee (FPPC)**

In the area of fusion physics, out of 59 exchanges 46 were completed. This completion number is almost the same as in the previous year. The workshops were successfully held, and the exchanges continue to be productive and beneficial to both sides. The annual meeting of the FPPC was held by a televideo communication on June 15, 2006. Participants were from Universities, NIFS, JAEA, and DOE to summarize the 2005 activities and formulate the 2006 activities. They agreed to re-organize category areas considering the change of the research area distribution. The result is as follows: 1) Planning, 2) Steady-state Operation (including Current drive and Heating, Plasma-surface Interactions, Heat and Particle Control in Divertor and SOL), 3) MHD and High Beta (including Disruption and Equilibrium), 4) Confinement (including New confinement schemes), 5) Diagnostics, 6) High Energy

Density Science (including Inertial Fusion Research with Laser, Heavy ion beam and Z pinch)

### **Joint Institute for Fusion Theory (JIFT)**

Almost all of the activities in the three categories - workshops, personal exchanges, and joint computational projects were carried out during the past year, although more U.S. scientists are encouraged to visit Japan.

All four workshops were successfully held, in addition to the JIFT Steering Committee meeting. In the category of personal exchanges, two Visiting Professors and three Visiting Scientists made exchange visits, while one exchange visit was cancelled. The JIFT joint computational projects were also active.

### **Fusion Technology Planning Committee**

The US/Japan collaboration on fusion technology completed another productive and successful year in FY 2005. Of the 31 planned cooperative items related to the JUPITER-II, 22 were completed as follows: 1 committee meeting, 16 personnel exchanges, and 5 workshops/technical meetings. Of the 18 planned cooperative items related to the general technology joint planning categories, 12 were completed as follows: 7 workshops/technical meetings and 5 personnel exchanges. Activities of the 5th year of the JUPITER-II collaboration are developing. Programs are subdivided to 9 tasks and significant results have been obtained.

The 24th Executive Secretary Meeting (ESM) was held simultaneously by a televideo communication on August 31, 2006. It was noted that both sides have developed a significant and mutually valuable collaboration involving all technical elements of the fusion energy sciences program.

General Secretary for US-Japan  
Collaboration Planning Committee  
Shigeru Sudo

# STATISTICAL REVIEW OF FUY 2005 EXCHANGE PROGRAM (NIFS)

## Grand Total

		US → J	J → US	Total
Proposed	Man	99	164	263
	Item	39	86	125
Performed	Man	78	129	207
	Item	30	64	94

## Personnal Exchange Program

(Including Overall Planning)

		US → J	J → US	Total
Proposed	Man	2	11	13
	Item	3	2	5
Performed	Man	0	11	11
	Item	3	2	5

## Fusion Technology

### (1) Superconducting Magnets

		US → J	J → US	Total
Proposed	Man	6	0	6
	Item	1	0	1
Performed	Man	4	0	4
	Item	1	0	1

### (2) Structural Materials

		US → J	J → US	Total
Proposed	Man	1	6	7
	Item	1	2	3
Performed	Man	1	1	2
	Item	1	1	2

### (3) Plasma Heating Related Technologies

		US → J	J → US	Total
Proposed	Man	3	9	12
	Item	3	3	6
Performed	Man	0	8	8
	Item	1	2	3

### (4) Blankets

		US → J	J → US	Total
Proposed	Man	1	1	2
	Item	1	1	2
Performed	Man	0	0	0
	Item	0	0	0

### (5) In-Vessel/High Flux Materials and Components

		US → J	J → US	Total
Proposed	Man	11	0	11
	Item	3	0	3
Performed	Man	10	0	10
	Item	2	0	2

### (6) Others

		US → J	J → US	Total
Proposed	Man	0	12	12
	Item	0	4	4
Performed	Man	0	11	11
	Item	0	3	3



Fusion Physics

(1) Planning

		US → J	J → US	Total
Proposed	Man	0	8	8
	Item	0	4	4
Performed	Man	0	8	8
	Item	0	4	4

(2) Plasma Core Phenomena

		US → J	J → US	Total
Proposed	Man	13	14	27
	Item	3	10	13
Performed	Man	11	12	23
	Item	3	8	11

(3) Plasma Edge Behavior and Control

		US → J	J → US	Total
Proposed	Man	0	10	10
	Item	0	7	7
Performed	Man	0	8	8
	Item	0	5	5

(4) Heating and Current Drive

		US → J	J → US	Total
Proposed	Man	1	8	9
	Item	1	5	6
Performed	Man	1	7	8
	Item	1	4	5

(5) New Approach and Diagnostics

		US → J	J → US	Total
Proposed	Man	28	26	54
	Item	11	18	29
Performed	Man	24	21	45
	Item	7	14	21

Joint Institute of Fusion Theory

		US → J	J → US	Total
Proposed	Man	18	14	32
	Item	5	6	11
Performed	Man	15	14	29
	Item	4	6	10

DOE/MEXT Materials (Annex I)

		US → J	J → US	Total
Proposed	Man	15	45	60
	Item	7	24	31
Performed	Man	12	28	40
	Item	7	15	22

(Sudo, S.)

## 2. TEXTOR Collaboration

It has been recognized that plasma-surface interactions (PSI) are still a big issue in ITER. From this viewpoint, the work under the TEXTOR Implementing Agreement is gradually widened and more intimate cooperation to the ITPA topics group has been requested. Coordination among the different tokamak Implementing Agreements is discussed on board. On the other hand, the PSI issues are widely common between tokamaks and helical systems. Moreover, the PSI in steady state operations has particular importance at present and near future. Possible ways of extension/rearrangements of the IEA agreements are under discussion in some of the collaboration groups. In any case, works not limited to TEXTOR but coordinated with joint multi-machine experiments are pursued from now on.

### DED experiments

In this fiscal year, collaboration experiments with Dynamic Ergodic Divertor (DED), modified schemes with  $m/n=3/1$ ,  $12/4$ ,  $6/2$  have been applied. Either static modification or dynamic application were investigated.

The Japanese team has proposed Excitation of Alfvén eigenmodes (AEs) and impedance measurement by

### Japanese Participation in 2005 – 2006

using the DED coil. RF current (100kHz-1MHz) were

superimposed on the DED coil to excite the AEs. Characteristics of the AEs, damping, stability of TAE were studied. The goal of this study is to demonstrate possibility of the suppression of TAE by the field modification by superimposing DC DED current. The coil impedance and excited RF magnetic fields were measured by Mirnov coil for various parameters of density,  $B_t$  and DC DED current. Analysis and Calculation are going on for the DED coil impedance spectrum to identify the AEs excitations conditions.

### PSI studies related with test limiters

The new roof limiter made by isotropic graphite is being assembled. The most important feature of it is local heating capability. In this limiter, small thin plate heater (BN plate heater, Tectra co.) is embedded. By using this limiter head it is possible to expose two samples with different temperature to TEXTOR edge plasmas in the same drift side (ion drift side or electron drift side).

A modeling work has performed for erosion and deposition patterns on W and Ta limiters exposed to the TEXTOR edge plasma. The erosion and deposition patterns on W and Ta test limiters exposed to the TEXTOR deuterium plasma containing a small amount of C impurity are simulated with the modified EDDY code. The EDDY

Subjects	Participants	Term	Key Persons <i>etc.</i>
1. PSI studies with test limiters	K. Sugiyama (Kyushu Univ.) Y. Sakawa (Osaka Univ.) Y. Ueda (Osaka Univ.)	06. 3. 5 - 3. 19 06. 3. 6 - 3. 19 06. 3.13 - 3.19	T. Tanabe / V. Philipps
2. Tangential X-ray Camera			K. Toi / G. Fuchs
3. Tritium Measurement		04. 9.11 – 9.19	M. Matsuyama / V. Philipps
4. DED experiments	T. Shoji (Nagoya Univ.) T. Shoji (Nagoya Univ.) T. Shoji (Nagoya Univ.)	05. 6. 11 - 6. 19 05. 10. 3 - 10.17 06. 2. 26 - 3.21	T. Shoji / K. H. Finken
5. Millimeter-Wave Imaging			A. Mase/ A. J. H. Donne
6. H recycling	K. Sawada (Shinshu U.) M. Sakamoto (Kyushu Univ.)	05. 9.12 - 9. 24 06. 3. 4 – 3.12	M. Sakamoto/ K. H. Finken
7. Edge Plasma Diagnostics	A. Tsushima A. Tsushima (Yokohama National Univ.)	05. 6. 16 - 6. 25 06. 2. 21 - 3. 3	A. Tsushima / S. Jachmich
8. He measurement in LHD			H. Funaba/M. Lehnen
9. PSI with ferritic steel			Joint work with item 1 (Key person from JAERI Y. Kusama)

code was modified to be able to simulate erosion and deposition pattern under actual test limiter conditions. In addition, ionization and dissociation processes of hydrocarbon molecules other than methane were included in the codes.

Pure W and K doped W were exposed to TEXTOR edge plasma to examine whether blistering takes place or not. Sample temperature was carefully controlled less than 500 deg C, in which blistering was observed in ion beam experiments. The samples were exposed to 12 OH shots and 8 NBI shots. Total fluence was an order of  $10^{24} \text{ m}^{-2}$ , enough fluence for blistering to appear in ion beam experiments. But no blistering was observed. The reason is under investigation.

In the previous W and Ta twin limiter experiments, carbon deposition pattern was different between Ta and W. But in this case, W and Ta sides were not exposed in the same edge plasmas, so the experimental results were unreliable. In 2004, W and Ta were placed on the same side of a graphite roof limiter to expose the same plasma. After exposure to 12 OH shots and 8 NBI shots, different carbon deposition pattern was observed. Detailed analysis will be done in future.

### X-Ray Tangential Camera

In order to study the images, e.g., those we obtained at DED experiments, tomographic reconstruction codes have been developed. From one tangential view of the plasma, it is not possible to reconstruct a three-dimensional (3D) radiation profile. We assume that radiation along the magnetic field lines is constant and try to reconstruct a two-dimensional (2D) profile on a poloidal plane. First, video image is decomposed to one stationary component and fluctuating components using singular value decomposition method (SVD). Then, equilibrium magnetic field is determined by the stationary image; we select an equilibrium by which the best reconstruction can be made. Using this equilibrium magnetic field, the lines of sights are interpreted as the curved lines on the target poloidal plane. Thereby, 3D-reconstruction problem is reduced to the well-known 2D problem. It is found that a method based on the truncated least square method using orthogonal components generated also by SVD are suitable for this kind of reconstruction. We have, therefore, successfully reconstructed 2D images on a poloidal plane. We have extended this code using flux coordinate so that we can use in the 3D equilibrium field, e.g., of the Large Helical Device (LHD).

### Other Collaborations

Modeling is an important approach to understanding of recycling processes. A Jülich group has developed a comprehensive neutral transport code EIRENE. A Japanese atomic data group has contributed in this fiscal year to improve the code by implementing recent reliable cross sections of atomic and molecular processes into collisional radiative model. Effective reaction rate coefficients have been calculated using recent cross sections, including initial vibrational level resolved MAR (molecular assisted

recombination) rate coefficients. Velocity distribution of hydrogen atoms which are produced from various molecular processes have been also calculated for EIRENE.

Notch filter with rejection frequency of 140 GHz has been designed at UC Davis (UCD), and fabricated using electro fine forming (EF2) technique in Kyushu Hitachi Maxell, Ltd. The rejection of  $-32.5 \text{ dB}$  at  $f=140 \text{ GHz}$  and less than 1 dB transmission loss at the pass band are obtained, which are better than those values fabricated by conventional etching process. The filter has been attached to the microwave imaging reflectometer (MIR) system in TEXTOR-94 tokamak operated by UCD-PPPL and FOM group.

Simulation study of microwave imaging reflectometry has been performed. For the particular amplitude of fluctuations, the imaging reflectometer is found to be able to measure parameters of the fluctuations accurately if the width of wavenumber spectrum  $\Delta k_{\text{fluct}} \leq 0.2 k_0$ , where  $k_0$  is the wavenumber of an incident wave. While the conventional reflectometer is able to measure accurately if  $\Delta k_{\text{fluct}} \leq 0.1 k_0$ . Therefore imaging reflectometer demonstrates wider range of measurable parameters in comparison with the conventional system.

Partial pressure measurement with penning gauges has been prepared and applied to LHD collaborating with a Jülich group for hydrogen (H), helium (He) or noble gases (Ne, Ar etc.) in the vacuum vessel of the Large Helical Device (LHD). The penning gauge spectroscopy was operated during the main discharges of LHD, which are aimed for the high density, high stored energy, LID (Local Island Divertor), ICRF or the long pulse experiments and so on. In the high density cases, the signal could be acquired with the time resolution of 5ms. As the peripheral pressure during the long pulse discharges was quite low, no signals of lines could be obtained even when the exposure time was up to 20 seconds. However, temporal development of the intensity of H $\alpha$  and He I lines was obtained after the end of the long pulse discharges. H $\alpha$  appeared later than the He I lines since the main gas in the long pulse experiments was helium.

Reduced activation ferritic steel is one of the candidates for structure materials of a fusion demonstration reactor. Compatibility of the ferritic steel with the fusion plasma is one of the critical issues. The experimental results were presented at 7th International Symposium on Fusion Nuclear Technology (ISFNT-7, May 22-27, 2005, Tokyo). Main contents are as follows

- Sputtering of the constituent elements from the ferritic steel (F82H) was comparable to that from a stainless steel (SUS304).
- The limiter melted slightly. A droplet of  $\sim 1 \text{ mm}$  in diameter was formed from the material and released from the limiter, and it returned to the limiter. Although the mechanism was discussed, it was not fully understood

(Noda, N.)

### 3. International Collaboration on Helical Fusion Research — IEA Stellarator Agreement —

#### 1. Background and overview

Since 1985 the world stellarator research community has been continuing to promote international collaborations under the IEA Implementing Agreement referred to as “Cooperation in Development of the Stellarator Concept”. Based on the approval by the FPCC, this agreement has been extended for the next four years till July 2010. Participating countries in this agreement are Japan, U.S.A., Australia, Germany, Spain, Ukraine, and Russia.

In order to discuss technical and administrative issues associated with the collaborations, the Stellarator Executive Committee was put together in 1985 under the IEA implementing agreement and has been playing the key role in the world stellarator research community. The first Chairman of the committee was Dr. G. Greiger, former Director of IPP-Garching. Prof. A. Iiyoshi of Chubu Univ. served as the second Chairman from 1998 to 2004. In 2004, Dr. C. Alejaldre of CIEMAT in Spain took over from Prof. Iiyoshi as the third Chairman, and at the same time, Prof. O. Motojima, Director General of NIFS, became the vice-Chairman of the committee.

The Stellarator Executive Committee meeting was held on October 4th, 2005, during the 15th International Stellarator Workshop in Ciemat, Madrid, Spain, in October 3rd – 7th, 2005. In this meeting, C. Alejaldre gave a brief summary of recent progress in the fusion programme (ITER) and its impact on the stellarator community. He reported that the 42nd meeting of CERT would be held at IAE headquarters on 18th October. The agenda of the meeting includes a presentation of co-operation in the development of the stellarator concept. At the June 2005 CERT meeting, the term of this agreement was extended, provisionally, for six months to January 2006. Extension is now sought for a longer period. C. Alejaldre showed the draft of the presentation. F. Wagner, J. Lyon, M. Zarnstorff, J. Harris and O. Motojima suggested up-dating the presentation with more emphasis on the importance of stellarators to push relevant technologies for ITER and the contribution of stellarators both to physics understanding and reactor studies. It was agreed that the draft of the presentation will be distributed (by C. Hidalgo) and suggested modifications in the presentation will be sent by E-mail.

Prof. O. Motojima pointed out the National Institute for Fusion Science (NIFS) was recently reorganized (2004) as an agency independent of the Japanese Government into the National Institutes of Natural

Sciences (NIFS). As a consequence, the Japanese Government admits NIFS as the representative organization in Japan to execute the IEA Stellarator Agreement. This means that NIFS is now able to take full responsibility for all of its own activities, independent of the Japanese Government. Therefore, the Japanese Government is ready to transfer the responsibility for taking part in the IEA Stellarator Agreement directly to NIFS. To complete this process smoothly, Prof. O. Motojima asks for the approval of the Stellarator Executive Committee. The whole committee supported unanimously this proposal.

The next meeting will be held in conjunction with the 21st IAEA Fusion Energy Conference in Chengdu, China, in October 16th – 22nd, 2006.

#### 2. Japan

##### 2-1. LHD team at NIFS.

##### 2-1-1. International collaborations by the LHD team at NIFS

##### Collaboration with EU

1) M. Yokoyama (NIFS) has proceeded the international collaboration on Internal Transport Barrier Physics in helical systems such as LHD, CHS, TJ-II (CIEMAT, Spain) and W7-AS (Germany) based on the framework of the International Stellarator Profile DataBase (approved by IEA, Stellarator Executive Committee). The significance of electron root (helical-specific physics) in low collisional helical plasmas has been commonly recognized, which was reviewed in the 15th International Stellarator Workshop (Madrid, October 2005).

2) M. Kobayashi visited the ITER site in Garching (Germany) from September 27th, 2005 to March 25th, 2006 to conduct the power load analysis of the ITER start-up limiter modules with Dr. G. Federici and Dr. A. Loarte. He also visited Dr. Y. Feng at Max-Planck institute in Greifswald (Germany) for implementing the 3D edge transport code for the ITER limiter configuration.

3) Dr. Arthur Weller, IPP Greifswald stayed at NIFS from January 5th to April 4th, 2005. He and K. Toi made comparison study on MHD stability and production of high beta plasmas in LHD and W7-AS in order to improve performance of these high beta plasmas further. We focused on differences and similarities in both plasmas.

4) Dr. Yuri Igitchkanov from the Max-Planck-Institut für



Plasmaphysik in Greifswald, Germany visited NIFS (B. J. Peterson and N. Ohyabu) from April 7th to September 7th, 2005 as a NIFS Guest Professor to work on the topic of "Modelling of impurity transport in helical devices". He attended and presented his results at the 19th International Conference on Numerical Simulation of Plasmas and 7th Asia Plasma Theory Conference in Nara.

5) Dr. Schubert (Max-Planck-Institut für Plasmaphysik) visited NIFS (K. Tanaka) from December 10th to 21st, 2005 attended Japan Australian workshop for plasma diagnostics and joined LHD experiments.

6) M. Goto visited Forschungszentrum Jülich and joined the development study of an image X-ray spectrometer in collaboration with Dr. Günter Bertschinger. The spectrometer makes use of a spherically cut crystal with which the measurement of radial distribution of spectrum becomes possible. A preliminary measurement for the helium-like argon ion has been carried out in TEXTOR and the results were presented at the 37th conference of EGAS (European Group on Atomic Systems) in 2005.

#### **Collaboration with USA**

1) T. H. Watanabe and H. Sugama (NIFS) visited Institute for Fusion Studies, The University of Texas at Austin from January 29th to February 4th in order to collaborate with Dr. W. Horton and Dr. J. W. Van Dam on Application of the Fusion Theory to Space Plasmas.

2) K. Ichiguchi (NIFS) visited Oak Ridge National Laboratory from June 8th to 29th under the JIFT program. He collaborated with Dr. B. A. Carreras for the numerical study of the nonlinear MHD behavior of LHD plasmas.

3) H. Funaba and N. Tamura (NIFS) visited PPPL from July 11th to 15th in order to discuss about the plan of Tracer-Encapsulated Cryogenic Pellet (TESPEL) injection into NSTX and impurity transport with Dr. Kugel (PPPL) and Dr. Stutman (John Hopkins Univ.).

4) L. Grisham (PPPL) visited NIFS (Y. Oka) from January 10th to 15th to join the Doppler shift measurements experiment in order to study the stripping spectrum and related phenomena in LHD accelerator.

5) J. Ramos (MIT) visited NIFS (T. H. Watanabe) from June 10th to Sep. 9th as a NIFS guest researcher as well as a JIFT exchange researcher in order to advance a collaboration research on the extended MHD and generalized two-fluid equations for magnetized plasmas.

6) Tomio Y. Petrosky (Texas Univ. at Austin) stayed at NIFS from October 20th to January 19th as a NIFS Guest professor for collaboration research on "Dissipation structure and self-organization in plasmas".

#### **Collaboration with Russia**

1) V. Sergeev (St. Petersburg Technical University,

Russia) visited NIFS (S. Sudo and N. Tamura) for one month, studied the configuration of the pellet ablated cloud by measuring Stark broadening with spatial resolution on LHD.

2) I. Vinyar (St. Petersburg Technical University, Russia) visited NIFS (S. Sudo) from November 6th to December for the collaboration of the first TECPEL operation on LHD. It was successful, and the TECPEL was injected into the LHD plasma for the first time.

3) A. V. Krasilnikov (Troitsk Institute for Innovating and Fusion Research, Russia) visited NIFS (M. Isobe) from January 4th to 24th, 2005. He has studied confinement properties of co-going and counter-going beam ions measured with natural diamond detectors and made a comparison between the two cases. The results were presented in the 9th IAEA Technical Meeting on Energetic Particles in Magnetic Confinement Systems (Takayama, Nov. 2005).

4) A. Pshechnikov (General Physics Institute, Russian Academy of Science) visited NIFS (S. Kubo) for two weeks and made the experiment and analysis of density fluctuations using gyrotron scattering in LHD.

5) L. N. Vyacheslavov (Budker Institute of Nuclear Physics) visited NIFS (K. Tanaka) from January 10th to February 12th, 2006 and continued developing CO<sub>2</sub> laser imaging interferometer for density profile and fluctuation measurements on LHD.

6) Dr. Sarksyian, Dr. Arkasyan, Dr. Skvortsova, and Dr. Kharchev (General Physics Institute) visited NIFS (K. Tanaka, S. Inagaki, H. Yamada) from February 4th to 18th, 2006 and discussed the collaboration on microwave scattering experiments.

7) Dr. Neudatchin Sergey (Russian Science Center, Moscow) has visited NIFS as a guest professor and collaborated on the problem of transient transport in LHD plasmas. By applying his detailed analysis code on the observation of the electron cyclotron emission, he and collaborators have identified the very rapid propagation of the change of effective thermal transport coefficient. In addition to it, a new transport barrier after the onset of RF heating was identified. These findings were published in a couple of scientific articles, and were reported at the H-mode workshop as well as at other international conferences.

#### **Collaboration with Australia**

1) M. Yokoyama (NIFS) visited Plasma Research Laboratory (PRL) at Australian National University (ANU) as the Visiting Academic to investigate the helical-specific features on mean zonal flow - GAM oscillation properties. The significant impact of the geodesic curvature (i.e., poloidal variation of magnetic field strength) on the energy transfer from mean zonal flow to GAM oscillation has been revealed for H1-NF

Heliac, which can be extended to other helical systems where the geodesic curvature effect is controllable through the three dimensionality of magnetic field. The experimental proposal has been drawn for LHD based on this finding.

2) S. Vladimirov (Univ. Sydney) visited NIFS (Y. Tomita) from January 10th to April 11th, 2006 for the collaboration research on the theoretical and simulation study of generation and growth of dust particles in divertor plasma.

## **2-1-2. Plans for 2006**

1) M. Yokoyama (NIFS) will continuously proceed International Stellarator Profile DataBase activity in collaboration with TJ-II and W7-AS. Quantitative understanding for ITB shot properties, such as the dependence of ECH power threshold on effective helicity and ripple trapped fraction, will be investigated based on a wide range of ITB discharges from LHD, CHS, TJ-II and W7-AS.

2) V. Sergeev (St. Petersburg Technical University, Russia) will visit NIFS (S. Sudo and N. Tamura) for about one month, in order to continue the configuration study of the pellet ablated cloud by measuring Stark broadening with spatial resolution on LHD for the basis of high energy particle measurements with the pellet charge exchange.

3) L. Grisham (PPPL) will join the NB injection experiments and discuss the improvement on negative ion system on LHD and the spectrometry.

4) A. V. Krasilnikov (Troitsk Institute for Innovating and Fusion Research, Russia) will visit NIFS (M. Isobe) for 3 weeks on January 2006 and work on fast neutral particle measurements by using natural diamond detectors in LHD.

5) Yu. Wei (Prof. Shanghai Institute of Optics and Fine Mechanism) will visit NIFS (host: R. Horiuchi) from September 15th to December 20th, 2006 for studying Microscopic self-organization in laser plasma.

## **2-2. CHS team at NIFS.**

### **Collaborations with US**

1) T. Akiyama (NIFS) visited PPPL (Drs. H.K. Park and E. Mazzucato) from March 20th to 23rd to discuss on FIR laser scattering measurement system on CHS.

2) D. A. Spong (ORNL) visited NIFS (M. Isobe) from November 14th to 18th to discuss the particle orbit simulation study for the experimental research of fast ion loss with MHD activities.

3) S. Okamura (NIFS) visited PPPL from February 23rd to March 3rd for the discussion of future collaboration in NCSX for electron heating experiment with high power gyrotrons. He also discuss with NCSX design team for

the stellarator configuration optimization work.

### **Collaborations with Germany**

S. Okamura (NIFS) visited Max-Planck-Institut in Greifswald (Dr. Hartfuss) on October 10th and discussed the advanced diagnostics for stellarator experiments.

### **Collaborations with Spain**

A. Fujisawa visited CIMAT from June to September, 2005 and cooperated with F. Castejon in order to write the invited paper to EPS conference, which was on the internal transport barrier formation in helical devices.

## **2-3. Heliotron-J team at Kyoto University**

### **2-3-1. International collaborations by the Heliotron-J team at Kyoto University**

1) The workshop on “Multi-Channel Measurements and its Tomographic Analyses in Toroidal Plasma Diagnostics” was held on January 25th. A. Weller (IPP, Greifswald), B. Blackwell (ANU) and Liu Yi (South-western Institute of Physics, China) participated on the workshop.

2) B. Blackwell (ANU) visited Kyoto Univ. for two weeks on January 12th to 29th to participate in the Heliotron J experiments. The MHD analysis by using such as SVD method, tomographic technique, ECH system and data acquisition were collaborated.

3) N. Kharchev (GPI, Russia) visited Kyoto Univ. on February 21st to discuss the scattering diagnostics using strong microwaves.

4) K. Nagasaki (Kyoto) visited CIEMAT for two weeks on March 5th to 18th to collaborate in the plasma breakdown and ECCD experiments with A. Fernandes, A. Cappa, V. Tribaldos, F. Castejon and F. Tabares. The experimental results on plasma breakdown were compared with the Heliotron-J and CHS data. The results were presented in APFA2005, and published in the proceedings of Korean Physical Society.

5) B. Zurro (CIEMAT) visited Kyoto Univ. as a guest professor from July 4th to October 3rd. He joined the Heliotron J experiment related to charge exchange spectroscopy, and had lectures of plasma physics for graduate students.

6) H. Laqua visited Kyoto Univ. on October 31st for discussion about ECRH system and ECRH physics on Heliotron J, WEGA and W7-X.

7) A. Baciero (CIEMAT) visited Kyoto Univ. from December 3rd to 16th in order to participate in the Heliotron J experiments. The data analysis software developed for TJ-II was applied to the charge exchange spectroscopy in Heliotron J.

8) Boyd Blackwell (ANU) joined the Heliotron J experiment from December 14th to 16th. He applied his

MHD analysis code by using data mining technique to Heliotron J magnetic probe data.

9) H. Punzmann (ANU) visited Kyoto Univ. on December 19th for discussion about ECH system for Heliotron J and H-1 Heliac.

10) The ray tracing calculation code, “TRECE” for ECH/ECCD for Heliotron J configuration was extended to some configurations under the collaboration with V. Tribaldos (CIEMAT).

## **2-3-2. Plans for 2006**

1) The US-Japan workshop on “New approaches to advanced plasma confinement in helical system” will be held at Auburn University. S. Knowlton (Auburn Univ.), D. Anderson (U. Wisconsin), J. Talmadge, (U. Wisconsin), G. Neilson (PPPL) and J. Lyon (ORNL) will participate in the workshop.

2) B. Blackwell (ANU) will visit Kyoto Univ. for three weeks to participate in the Heliotron J experiment. His MHD analysis code by using data mining technique will be applied to Heliotron J magnetic probe data.

3) A. Cappa (CIEMAT) will visit Kyoto Univ. for two weeks to participate in the Heliotron J experiment. The plasma breakdown and ECCD will be analyzed.

## **3. EU**

### **3-1. GERMANY**

#### **3-1-1. International collaborations in 2005**

##### **Collaborations with EU**

1) Roman Zagorsky, Włodzimierz Stepniowski (IPPLMF Warsaw), to IPP Greifswald, Apr. 17 - May 22, 2005, Plasma edge modelling for ergodic configurations

2) Guenther Eibl (Uni. Innsbruck), to IPP Greifswald, April 18 - May 13, 2005, Plasma edge modelling

3) Xavier Bonnin (CNRS U. of Paris), to IPP Greifswald, May 2 - 14, 2005, Modelling of plasma edge transport

4) Xavier Bonnin (CNRS U. of Paris), to IPP Greifswald, Sep. 25 - Oct. 7, 2005, Modelling of plasma edge transport

5) Carolin Nührenberg (IPP Greifswald), to CIEMAT, Oct. 10 - 11, 2005, ITG turbulence TORB BSC simulations

6) Heinrich Laqua (IPP Greifswald), 2 weeks, to CIEMAT, ECRH experiments

7) WEGA: “Electron Cyclotron Waves Heating Experiments” with CIEMAT, Regular exchange, via Video

8) Dr. McCarthy (CIEMAT), to IPP Greifswald, Sep. 7 - 8, 2005, Preparation of an ACORD-24 analyser for its later use in the TJ-II stellarator

9) V. Tribaldos (CIEMAT), to IPP Greifswald, 2 weeks, Discussions of aspects of stellarator optimisation

10) C.D. Beidler, H. Maassberg (IPP Greifswald), to

CIEMAT, International Collaboration on Neoclassical Transport (IEA implementing agreement) and preparation of the International Stellarator Profile Data Base activity

## **Collaborations with Japan**

1) Yasuhiro Suzuki (NIFS), to IPP Greifswald, Oct. 10, 2005 - Mar. 31, 2006, 3D MHD equilibrium code benchmarking

2) Axel Koenies (IPP Greifswald), to NIFS, Nov. 7 - 20, 2005, Kinetic MHD modes in stellarators

3) M. Kobayashi (NIFS), to IPP Greifswald, 6 weeks, Edge plasma modelling with the EMC3-EIRENE code

4) Y. Suzuki (NIFS), to IPP Greifswald, 3 months, Implementation and benchmarking of the HINT equilibrium code

5) C.D. Beidler, A. Dinklage (IPP Greifswald), to NIFS, 2, Energy confinement time scaling

## **Collaborations with Russia**

1) Alexey Subbotin (Kurchatov Institute), to IPP Greifswald, Mar. 1 - 28, 2005, Investigations on ballooning modes in stellarators

2) Vitaly Shafranov (Kurchatov Institute), to IPP Greifswald, May 22 - 28, 2005, Theory of optimized stellarators

3) Mikhail Mikhailov (Kurchatov Institute), to IPP Greifswald, May 22 - Jun. 19, 2005, Integrated optimization of stellarators

4) Alexander Zvonkov (Kurchatov Institute), to IPP Greifswald, Sep. 4 - Oct. 2, 2005, Investigations on toroidal mirror confinement

5) Jürgen Nührenberg (IPP Greifswald), to Kurchatov Institute, Apr. 6 - 8, 2005 and Nov. 29 - Dec. 2, 2005, Theory of optimized stellarators

6) Prof. Anatoly Kislyakov (Ioffe Physical-Technical Institute), to IPP Greifswald, Jan. 16 - Feb. 12, 2005, Testing of W7-AS neutral particle analysers/use for W7-X diagnostics

7) Dr. Mikhail Tournianski (UKAEA, Culham Science Centre), to IPP Greifswald, Mar. 29 - 31, 2005, Checking of the possibilities of testing a compact neutral particle analyser on MAST

## **Collaborations with Ukraine**

1) Ljudmilla Krupnik (1 week), Alexander Chmyga (7 weeks), Alexander Zhezhera (5 weeks) (IPP Kharkov), to IPP Greifswald, Setting up HIBP diagnostic

2) Alexander Chmyga and Alexander Zhezhera (IPP-Kharkov), to IPP-Greifswald, 2 months, Setting up HIBP diagnostic

## **Collaborations with USA**

1) Bas Braams (Emory Uni. Atlanta), to IPP Greifswald,

Sep. 4 – 16, 2005, Plasma edge modelling

2) Ilon Joseph (UCSD), to IPP Greifswald, Sep. 4 – 25, 2005, Plasma edge modelling of ergodic configurations

3) Rick Moyer (UCSD), to IPP Greifswald, from Sep. 22 - 27, 2005, Plasma edge modelling of ergodic configurations

4) Tom Rognlien (LLNL), to IPP Greifswald, October 6 - 14, 2005, Plasma edge modelling

5) D. Mikkelsen (PPPL), to IPP Greifswald, 2 weeks, Preparation of a predictive transport code development for stellarators

### **3-1-2. Conference participation**

1) J. Nührenberg (IPP Greifswald), ISW 2005 Madrid, Oct. 3 - 7, 2005

2) C. Nührenberg (IPP Greifswald), IAEA TM Madrid, Oct. 10 - 11, 2005

3) J. Nührenberg (IPP Greifswald), IAEA TM Madrid, Oct. 10 - 11, 2005

4) Y. Feng, R. Preuss, D. Sharma (IPP Greifswald), EPS in Tarragona (Spain), Jun. 27 - July 1, 2005

5) Y. Feng, F. Sardei (IPP Greifswald), PET, Jülich (Germany), Oct. 16 - 19, 2005

6) R. Preuss (IPP Greifswald), MaxEnt05, San Jose (USA), Aug. 7 - 12, 2005

7) A. Kus (IPP Greifswald), 25th European Meeting of Statisticians, Oslo (Norway), Jul. 24 - 28, 2005

8) A. Dinklage (IPP Greifswald), IAEA-TM, Budapest (Hungary), Jul. 12 - 15, 2005

9) C.D. Beidler, A. Dinklage, H. Maassberg, N. Marushchenko, F. Sardei, Y. Turkin (IPP Greifswald), ISW 2005, Madrid, Oct. 3 - 7, 2005

10) C.D. Beidler, H. Maassberg, N. Marushchenko, Y. Turkin (IPP Greifswald), IAEA-TM Madrid, Oct. 10 - 11, 2005

### **3-1-3. Participation in joint projects**

#### **International Stellarator Confinement Data Base**

Contributions from C.D. Beidler, A. Dinklage, A. Kus, R. Preuss (IPP Greifswald),

#### **International Stellarator Profile Data Base**

Contributions from C.D. Beidler, H. Maassberg (IPP Greifswald)

#### **International Collaboration on Neoclassical Transport**

Contributions from C.D. Beidler and H. Maassberg (IPP Greifswald)

### **3-1-4. Planning 2006**

#### **Planning Stellarator Theory**

The planning for 2006 has not yet been detailed but the collaborations will comprise a similar extent with many

of the researchers of the above list.

#### **Neutral Particle Diagnostics**

W. Schneider will take part in the initial operation of the ACORD -24 analyser at TJ-II for about a week and later for a period of about one month, during an experimental campaign

#### **International Stellarator Confinement Data Base**

1) R. Preuss (IPP Greifswald) plans to visit scaling studies at CIEMAT

2) C.D. Beidler, R. Preuss (IPP Greifswald) will visit NIFS/U-Kyoto

3) J.H. Harris, H. Yamada (NIFS) are expected to visit IPP Greifswald for scaling studies.

R. Preuss plans visits at U- Stuttgart for scaling studies

#### **International Stellarator Profile Data Base and International Collaboration on Neoclassical Transport**

1) C.D. Beidler, H. Maassberg, R. Preuss will visit NIFS/U-Kyoto Stellarator Transport Code development:

2) Y. Turkin will visit NIFS/U-Kyoto

#### **EMC3-EIRENE code for edge plasma modelling**

Y. Feng will visit NIFS for 3 months

#### **Collaboration on ECRH, ECCD and ECE**

N. Marushchenko will visit NIFS/U-Kyoto

#### **International Collaboration on Data Validation**

A. Dinklage, J. Geiger, Joint organisation of the VALIDATION workshop at FZ Jülich

#### **Implementation of the HINT equilibrium code**

Y. Suzuki (NIFS) is visiting IPP Greifswald for 3 months

#### **Teaching, general cooperation**

F. Wagner (IPP Greifswald) will visit Kyushu University for a month

#### **VALIDATION workshop**

Collaboration with FZ Jülich /FOM: A. Dinklage, J. Geiger are going to visit Jülich for joint organization of the workshop

#### **Conference participation**

1) R. Burhenn, A. Dinklage, P. Kornejew, R. König, E. Pasch, A. Werner (IPP Greifswald), 16. Conference on High Temperature Plasma Diagnostics, Williamsburg, USA, May 7 – 11, 2006

2) V. Erckmann, H. Laqua, N. Marushchenko (IPP Greifswald), 14. Joint Workshop on Electron Cyclotron Emission and Electron Cyclotron Heating, Santorini



Islands, Greece, May 9 – 12, 2006

3) Y. Feng (IPP Greifswald), 17. Plasma Surface Interactions in Controlled Fusion Devices (PSI), Hefei, China, May 22 – 26, 2006

4) J. Geiger, R. König, G. Kühner, R. Preuss, A. Werner (IPP Greifswald), Data Validation Workshop, Jülich, Germany, May 29 – 31, 2006

5) T. Klinger, M. Schubert, Y. Turkin, F. Wagner, G. Warr (IPP Greifswald), 33. EPS Conference Plasma Physics, Rome, Italy, Jun. 19 – 23, 2006

6) H. Braune, J. Schacht, H. Laqua (IPP Greifswald), 24. Symposium on Fusion Technology (SOFT), Warsaw, Poland, Sep. 11 – 15, 2006

7) F. Wagner (IPP Greifswald), 2nd International Conference on Plasma Physics and Controlled Fusion, Alushta, Crimea, Sep. 11 – 16, 2006

8) G. Michel, IRMMW THz 2006 (IPP Greifswald), Shanghai, China, Sep. 18 – 22, 2006

9) V. Erckmann (IPP Greifswald), 21st IAEA Fusion Energy Conference, Chengdu, China, Oct. 16 – 22, 2005

### **3-2. SPAIN**

#### **3-2-1. International collaborations in 2005 using TJ-II at CIEMAT**

##### **Collaboration with Russia**

K. Sarkisyan (and the ECRH IOFAN team) participated in the operation of the ECRH system of TJ-II and in the Bernstein Waves heating project. N. Matveev (and the GUP-VEI institute team) was involved in the power supply for Bernstein modes heating system.

M. Tereshchenko (from IOFAN) visited CIEMAT and collaborated in the EBW theoretical calculations involving relativistic ray tracing and Fokker Plank calculations (October – December 2005).

S. Petrov (IOFFE) visited CIEMAT (May – November 2005) to participate in the final installation a new neutral particle analyzer in TJ-II.

N. Skvortsova (IOFAN) participated in experiments with 2 mm scattering in TJ-II (November 2005).

Dr. S. Shchepetov visited CIEMAT and was involved in modelling of edge instabilities and Alfvén modes studies (October – November 2005).

Melnikov and L. Eliseev (Kurchatov Institute) visited CIEMAT to investigate the structure of plasma potential in ECRH and NBI plasmas in the TJ-II stellarator.

##### **Collaborations in Europe Germany**

IPP (Stuttgart). G. Müller participated in the improvement of some components of the ECRH system in 2005 (six months stay). Holtzauer was involved in reflectometry and Bernstein wave simulations (May and September 2005).

IPP-Greifswald. A. Weller visited CIEMAT (October 2005) being involved in RX studies (IONEQ code).

G. Pereverzev (IPP-Garching) visited CIEMAT in February 2005 to work on the effect of geometry and electric field on transport in TJ-II plasmas, using ASTRA code.

##### **Portugal**

C. Silva visited CIEMAT to continue our collaboration on edge studies (biasing experiments) during 2005. Horacio Fernandes participated (November 2005) in the definition of control and software requirements for JET-EP2 diagnostic enhancement and test in TJ-II facilities (fast camera).

##### **Hungary**

G. Kocsis visited CIEMAT (November 2005) to define the JET-EP2 diagnostic enhancement project scope and test in TJ-II facilities.

##### **Czech Republic**

M. Horn and I. Duran were visiting CIEMAT to participate in the development of TJ-II edge plasma diagnostics (electromagnetic probes)

##### **Collaboration with USA**

D. Rasmussen (ORNL), P. Ryan, J. Tsai and D. Schechter visited to CIEMAT. Discussions were focused on three topics: NBI, Electron Bernstein waves and Pellet injection. The NBI activities were organized around the general status of NBI into TJ-II, NBI Electrical System, Ion Source and beam transmission. Physics issues and hardware required to install a (ORNL) pellet diagnostic in the TJ-II were discussed.

M. Murakami was visiting CIEMAT (Mayo) to discuss TJ-II NBI operation issues.

G. Barber and S. Combs (ORNL) visited CIEMAT to check NBI tetrode behavior and to discuss upgrades of NBI system.

PPPL: S. Zweben visited CIEMAT in December 2005 to discuss recent 2-D visualization experiments (influence of electric fields on turbulent blobs) in the TJ-II stellarator and possible collaboration in JET tokamaks.

B. Carreras visited CIMAT in November 2005 to continue our long-standing collaboration between the CIEMAT, the University of Carlos III and Oak Ridge National Laboratory in the statistical description of turbulent transport in fusion plasmas.

D. Rapisarda was visiting UCSD to continue our collaboration on spectroscopy.

D. Spong was collaborating in the investigation of Alfvén modes appearing NBI heated plasmas in TJ-II stellarator.

#### **Collaboration with Ukraine**

The Heavy Ion Beam Probe team (headed by L. Krupnik, Institute of Plasma Physics, National Science Center “Kharkov Institute of Physics and Technology”, Kharkov) has been fully involved in the characterization of radial electric fields in ECRH and NBI plasmas in the TJ-II stellarator during 2005 experimental campaign. In addition, an upgrade of existing HIBP system was agreed.

S. S. Pavlov (from “Kharkov Institute of Physics and Technology”, Kharkov) IOFAN) visited CIMAT to work on relativistic ECRH calculations (October – December 2005).

#### **Collaboration with Japan**

K. Nagasaki stayed in CIEMAT (February 2005), being involved in TJ-II operation and discussing comparative ECR studies in Heliotron J and TJ-II.

Dr. B. Zurro (July – September) and A. Baciero (December) stayed in Heliotron J, being involved in spectroscopy studies

#### **International collaborations: Stellarator Implementing agreement**

During 2005 we continued with the participation in the “International Collaboration on Neoclassical Transport” (ICNT), whose main goal is to provide a comprehensive description of the neoclassical transport processes relevant to plasma performance in stellarator experiments.

#### **International Stellarator Confinement Database and profile database**

During 2005, CIEMAT has continued participating in the activities of the International Stellarator Confinement Database and in the recent group on profile database.

#### **3-2-2. Plans for 2006**

The TJ-II stellarator physics programme will be based on

Phase I (ECRH: 300-600 kW) and Phase II (NBI) heating scenarios during 2006 with studies supporting international stellarator data-base, plasma –wall (including a Li-coating technique to improve density control), heating, transport and modelling

In addition, we will continue and extend our physics studies in tokamaks (in particular in JET), looking for common clues as a fundamental way to investigate basic properties of magnetic confinement including studies in plasma-wall, ELMs physics, equilibrium, transport and diagnostic development.

Activities to design a new stellarator based on magnetic configurations with reduced neoclassical transport and using the experience based on TJ-II results, showing the advantages of stellarator magnetic topology via rational surfaces and magnetic shear to improve confinement properties, will be initiated during 2006.

Research activities in the TJ-II stellarator will be focussed in the following topics:

- **Equilibrium windows and operational limit of TJ-II.**

Further investigation of the empirical confinement scaling laws in ECRH and NBI heated plasmas. The database will be extended to cover a broad range of rotational transforms and plasma volume (ripple). Continue with the international collaboration on neoclassical transport and international stellarator data –base.

- **Magnetic topology, transitions and confinement.**

Further investigation of the role of low order rational surfaces and magnetic shear on radial electric fields and transport will be done. The impact of island sizes on e-ITB will be addressed.

- **Plasma –wall.**

Due to the effect of Lithium on wall conditioning (e.g. suppression of H recycling) Li coating is an attractive tool for density control in the TJ-II stellarator. The impact of Li coating on density control and TJ-II confinement will be investigated.

- **Transport, MHD and modelling.**

Further characterization of effective transport coefficients (bulk and impurities) in ECRH and NBI heated plasmas including parametric evolution with magnetic configuration and investigation of the statistical description of transport processes. The impact of magnetic topology (magnetic ripple) as a tool to control ELMs-like events will be addressed. Massive orbit calculations in presence of collisions and electric field are performed to elucidate the influence of kinetic processes on confinement. ECRH pump-out is being simulated to be compared with the

experimental results.

#### •Momentum transport.

Investigation of rotation of core and edge plasmas in ECRH and NBI plasmas. Study of the relaxation of flows and electric fields in plasma regimes with different magnetic ripple with and without rational surfaces.

The following collaborations are planned:

#### **Collaboration with Russia**

IOFAN: ECRH group (K. Sarkisyan) participation in ECRH system operation and the Bernstein Waves heating project. E. Bolshakov and A. Dorofeyuk will participate in the development of a power measurement system for the EBWH project. GUP-VEI (Moscow): Power supply for Bernstein modes heating system.

M. Tereshchenko will stay in CIEMAT to collaborate in further improvement of TRUBA: including a relativistic current drive module able for EBW. He will collaborate in the developments of kinetic theory that are foreseen in CIEMAT. The important point is to deal with 3D geometry using models as exact as possible.

N. Skvortsova (IOFAN) will continue her involvement in experiments with 2 mm scattering in TJ-II.

A. Melnikov and L. Eliseev (Kurchatov Institute) will visit Ciemat to participate in the characterization of radial electric fields in the TJ-II stellarator and comparative studies with T-10 tokamak.

#### **Collaborations in Europe**

IPP-Greifswald: H. Laqua might participate in ECRH experiments in the TJ-II stellarator during 2006.

IPF (Stuttgart): G. Müller will collaborate in the development of a low pass filter for the high voltage power supply of the ECRH system during 2006. E. Holzhauser will visit CIEMAT in 2006 for reflectometry and studies of EBW Heating in the TJ-II stellarator.

E. Blanco will visit IPF (Stuttgart) being involved in reflectometry simulations.

Czech Republic: M. Horn and I. Duran will participate in the test and development of TJ-II edge plasma diagnostics (electromagnetic probes).

IST-Portugal: C.Silva and IST team will visit Ciemat to continue our collaboration on edge studies during 2005. Continuing the collaboration in design and development of reflectometry in TJ-II, M. E. Manso, L. Cupido and IST team.

During 2006 the TJ-II ECRH group will collaborate with FOM Association in some ITER tasks related with ECRH Upper port measurements.

Continuing with the collaboration on neoclassical transport, V. Tribaldos will visit IPP-Greifswald to analyze recent results and propose future works.

A one-month visit, scheduled for April, of a member from the Institut für Theoretische Physik, Technische Universität Graz, Graz, AUSTRIA to seek for optimized configurations of TJ-II based on a method jointly developed with CIEMAT.

A. Cooper (CRPP-Lausanne) will visit CIEMAT in March to implement a bootstrap current model that works in the low collisionality regime (March).

#### **Collaboration with USA**

D. Rasmussen (ORNL) will visit CIEMAT to continue with NBI, Bernstein and pellet experiments collaboration.

J. Tsai (ORNL) will stay in CIEMAT in 2006 for beam conditioning at second NBI injector and to discuss beam transmission properties.

S. Zweben (PPPL-USA) will be involved on the characterization of turbulence in the TJ-II stellarator using high-speed imaging. Comparative studies TJ-II NSCX (using similar analysis tools) are planned. In addition, a joint effort to investigate instabilities in JET is in progress.

B. A. Carreras (ORNL) will visit CIEMAT to investigate statistical properties of turbulent transport.

J. Harris will visit CIEMAT to discuss joint research activities on stellarator database studies and momentum transport and ballooning stability.

#### **Collaboration with Ukraine**

Further investigation of the structure of radial electric fields using HIBP diagnostic (Institute of Plasma Physics, National Science Center “Kharkov Institute of Physics and Technology”) will be done.

The relativistic effects study will be extended to the case of ICRH in reactor-like plasmas as well as to waves with imaginary frequency in collaboration with S. S. Pavlov (Institute of Plasma Physics, National Science Center “Kharkov Institute of Physics and Technology”).

#### **Collaboration with Japan**

K. Nagasaki (Institute of Advanced Energy, Kyoto University) will participate in some ECRH experiments in the TJ-II stellarator and comparative studies of electron cyclotron resonance (ECR) in Heliotron J and TJ-II.

Dr. Masaki Osakabe, a member of LHD experimental group, will visit CIEMAT to discuss an international collaboration of energetic particle transport in stellarators.

#### **International Stellarator Confinement Database**

Activities will continue with further analysis and presentations in the major conferences. Emphasis will be paid to investigate the role of plasma volume (ripple) on

iota scaling.

#### **4. Russia**

##### **International collaboration in 2005**

##### **Collaboration between General Physics Institute (GPI) and CIEMAT (Spain)**

- 1) Five persons participated in the exploitation and modernisation of the TJ-II gyrotron complex (total duration of visits: 7 months-person).
- 2) 13 persons participated in development of the numerical code and preparation of the system for plasma heating by Bernstein mode (total duration of visits: 18 person-months).
- 3) One person participated on 2mm scattering diagnostic (duration: 2 months).

##### **Collaboration between Kurchatov Institute and IPP**

- 1) Three person visited IPP to continue the numerical calculation on stellarators optimization (3 persons-months).
- 2) Two persons visited NIFS to study the turbulence of near-wall plasma (3 persons-months).
- 3) As a result of this collaboration 9 papers were published.

##### **Collaboration between GPI and NIFS (Japan)**

Three persons participated in the analysis of experimental data of plasma fluctuation in LHD with the aide of the new statistical method (total duration of visits: 5 months).

##### **Research plans for 2006**

- 1) Close collaboration between GPI and CIEMAT (Spain) will be continued along the same line as in 2005.
- 2) The collaboration GPI and NIFS (Japan) will be continued on analysis of experimental data of plasma fluctuation in LHD
- 3) The collaboration between Kurchatov Institute and IPP (Greifswald, Germany) will be continued on development of the numerical optimization of advanced stellarators, and to study quasi-isodynamic stellarators with large number of periods and calculations of real winding for the same optimized configurations
- 4) In GPI work on the L-V project will be continued in order to optimize the magnetic field configuration. The problems of plasma equilibrium and stability will be studied by using currently available computer codes (in collaboration with Kurchatov institute and IPP (Greifswald, Germany))
- 5) In GPI one will continue experiments on studying how modifications to the stellarator magnetic topology that are achieved by generating ohmic currents influence confinement of ECRH plasma in L-2M.
- 6) Fabrication of the power supply system for a new

ECR heating system for L-2M (GPI).

#### **5. Ukraine**

##### **5-1. Institute of Plasma Physics of the National Science Center “Kharkov Institute of Physics and Technology” of the NAS of Ukraine (IPP NSC KIPT)**

##### **5-1-1. International collaboration of the NSC KIPT in 2005**

##### **5-1-1-1. International collaborations of the plasma theory division**

##### **Collaboration with Technische universität Graz, Austria**

- 1) Optimization of stored energy for URAGAN-2M is carried out in the  $1/\nu$  regime with applying the fast field line tracing NEO code (V.V.Nemov, S.V.Kasilov and V.N.Kalyuzhnyj in collaboration with B. Seiwald and W.Kernbichler (Institut für Theoretische Physik, Technische universität Graz, Austria)).
- 2) New target functions which are related to collision-less  $\alpha$ -particle confinement are introduced. They are based on specific averages of the bounce averaged VB drift velocity of trapped particles across magnetic surfaces (V.V.Nemov and S.V.Kasilov visited Institut für Theoretische Physik, Technische universität Graz, Austria, and worked with W. Kernbichler and G.O.Leitold)
- 3) The electron cyclotron heating in a stellarator has been modelled using the Monte Carlo method and taking into account the nonlinear wave-particle interaction effects and non-Maxwellian distribution function of electrons. These effects are shown to cause broadening of radial power deposition profiles at low plasma densities in the heating scenario using the second harmonic resonance for the extraordinary wave (S.V.Kasilov in collaboration with W.Kernbichler, R.Kamendje and M.F.Heyn (Institut für Theoretische Physik, Technische universität Graz, Austria)).

##### **Collaboration with NIFS, Japan**

- 1) Neoclassical transport for LHD in the  $1/\nu$  regime was analyzed by the NEO code (mainly for inward shifted configurations). The results are benchmarked with the corresponding results obtained recently with the GIOTA code as well as with Monte-Carlo calculations from the DCOM code. (V. V. Nemov and S. V. Kasilov in collaboration with W. Kernbichler (Institut für Theoretische Physik, Technische universität Graz, Austria), M. Isobe, M. Matsuoka and S. Okamura (National Institute for Fusion Science, Japan)).
- 2) Removal of Cold  $\alpha$ -Particles from Fusion Helical Reactor. The conditions when He ions can escape from the confinement volume of the helical reactor due to the drift of the drift island, while D and T ions are confined.



(Prof. Alexander Shishkin (NSC KIPT), O. Antufyev (Kharkov V. N. Karazin National University) in collaboration with Prof. O. Motojima and Prof. A. Sagara (NIFS, Japan). Two joint reports (PS 2-24 and PS 2-25) were presented at 15th International Toki Conference "Fusion and Advanced Technology", 2005, Japan, with the following submission to Fusion Engineering and Design.

#### **Collaboration with PPPL, USA**

V. A. Rudakov continued collaboration with A. V. Georgiyevskiy, E. Fredrickson and M. Zarnstorff (Princeton Plasma Physics Laboratory, USA). E-beam mapping simulation program on the NCSX stellarator was studied.

#### **Collaboration with Uppsala University, Sweden**

V. E. Moiseenko continued collaboration with O. Agren, N. Savenko and S. Jonansson from Uppsala University, Sweden. The study of fundamental properties of the charged particle motion in stationary magnetic and electric fields is carried out. The study relates both for open-ended and toroidal magnetic traps.

### **5-1-1-2. International collaborations by the plasma experiment divisions**

#### **Collaboration with NIFS (Japan)**

- 1) Investigation of the transport barrier formation in the core and edge plasmas (V. Chechkin and E. Volkov in collaboration with S. Masuzaki and K. Yamazaki).
- 2) The study of the behavior of fast ions during formation of transport barriers (V. Chechkin and E. Volkov in collaboration with S. Masuzaki, K. Yamazaki and T. Mizuuchi).
- 3) Investigations of electrostatic turbulence in the edge and divertor plasmas (V. Chechkin and E. Sorokovoy in collaboration with S. Masuzaki and T. Mizuuchi).

#### **Collaboration with Cadarache, France**

Problems of in-vessel mirrors in ITER (V. Voitsenya and V. Konovalov in collaboration with NIFS (Japan), Cadarache (France), RNC "Kurchatov Institute" (Russia)).

#### **Collaboration with Argonne National Laboratory, USA**

The use of W-Pd bimetallic systems for hydrogen recycling control (G. Glazunov in collaboration with A. Hassanein and R. Causey (USA)).

#### **Collaboration with CIEMAT, Madrid, Spain**

- 1) Modernisation of the HIBP secondary beam detection system in TJ-II (Dr. L. I. Krupnik et al (IPP NSC KIPT) I collaboration with Dr. C. Hidalgo and TJ-II team

(CIEMAT)).

- 2) Studies of the radial electric fields end confinement in the TJ-II stellarator with NBI heating in variety of magnetic configurations (Dr. L. I. Krupnik and HIBP team in collaboration with C. Hidalgo and TJ-II team).

#### **Collaboration with IPP, Greifswald, Germany**

- 1) Development and manufacturing the system of the Heavy Ion Beam Probe (HIBP) diagnostic for WEGA Stellarator (Dr. L. I. Krupnik and HIBP team (IPP NSC KIPT) in collaboration with Dr. M. Otte and WEGA team.
- 2) Delivery and integration of the HIBP diagnostic system in IPP Greifswald (Dr. L. I. Krupnik and HIBP team in collaboration with Dr. M. Otte and WEGA team).

#### **Collaboration with Kurchatov Institute, Moscow, Russia**

Study of the radial electric field end GAM during ECR heating by HIBP diagnostic in T-10 tokamak in comparative regimes with TJ-II stellarator (Dr. L. I. Krupnik and HIBP team (IPP NSC KIPT in collaboration with Dr. A. V. Melnikov and T-10 team (Kurchatov Institute)

### **5-1-2. Plans for 2006 of the IPP NSC KIPT**

#### **5-1-2-1. Plans for 2006 of the plasma theory division**

##### **Collaboration with Austria (Institut für Theoretische Physik, Technische Universität Graz)**

- 1) Continuation of optimization of stored energy for URAGAN-2M for the 1/v regime.
- 2) Using worked out new target functions which are related to collision-less  $\alpha$ -particle confinement. A number of optimized stellarator configurations will be analyzed with respect to trapped particle confinement.
- 3) A numerical method will be developed for fast evaluation with the help of integration along the magnetic field lines of the bootstrap current and current drive efficiency in stellarators with arbitrary collisionality.

#### **Collaboration with Japan (National Institute for Fusion Studies)**

New physics mechanisms for removal of cold  $\alpha$ -particles from fusion helical reactor with simultaneous confinement of the main plasma, which appropriate the constructive advantages of Force Free Helical Reactor, will be studied.

#### **Collaboration with USA (Princeton Plasma Physics Laboratory)**

Numerical studies of the NCSX stellarator vacuum magnetic configuration will be continued.

### **Collaboration with Sweden (Uppsala University)**

The investigation of the charged particle motion in stationary magnetic and electric fields will be continued.

### **The tasks to be solved at IPP NSC KIPT**

- 1) Using KIPT code for calculating the magnetic surfaces of URAGAN-2M with taking into account the current-feeds and detachable joints of the helical winding. The base of coil data will be transformed to a new form which will be valid for the NEO code runs for URAGAN-2M with taking into account the current-feeds and detachable joints of the helical winding.
- 2) Using the developed numerical model. The study of Alfvén resonance heating in the URAGAN-2M will be carried out.
- 3) Further development of the reactor concept on the basis of the stellarator system.

### **5-1-2-2. Plans for 2006 of the plasma experiment divisions**

#### **Collaboration with NIFS (Japan)**

- 1) The study of the role of stochastic magnetic field line layers near rational surfaces on a formation of inferior and edge transport barriers (E. Volkov, V. Chechkin and A. Skibenko in collaboration with S. Masuzaki and T. Mizuuchi).
- 2) The influence of losses of fast ions on a formation of edge transport barriers (V. Chechkin and A. Slavnyj in collaboration with S. Masuzaki and T. Mizuuchi).
- 3) V. Voitsenya's visit to NIFS (90 days) with aims: 1) Optimization of wall conditioning procedure (V. Voitsenya and D. Naidenkova in collaboration with J. Kubota, Masuzaki and A. Sagara); 2) Environment effect on in-vessel mirrors (V. Voitsenya and Konovalov in collaboration with A. Sagara).

#### **Collaboration with ANL, USA**

Hydrogen permeability and erosion behaviour of the W-Pd bimetallic systems (G. Glazunov in collaboration with R. Causey and A. Hassanein (USA)).

#### **Collaboration with Spain (CIEMAT, Madrid)**

- 1) Development and creation of the upgrading high voltage power supply system for HIBP diagnostic in TJ-II stellarator.
- 2) Study of the plasma potential and density and their fluctuations in combined ECR and NBI heating regimes in TJ-II stellarator. Comparative study of the electric fields behavior in TJ-II stellarator (Spain) and T-10 tokamak. (Russia).

#### **Collaboration with Germany (IPP, Greifswald)**

- 1) Development and manufacturing of the control and

data acquisition systems for Heavy Ion Beam Probe (HIBP) diagnostic in WEGA Stellarator.

- 2) Installation and launching of the HIBP diagnostic in WEGA stellarator.
- 3) Starting up of the experiments on electric potential measurements in WEGA stellarator

### **Collaboration with Russia (Kurchatov Institute, Moscow)**

- 1) Modernization of the HIBP hard ware system for T-10 tokamak
- 2) Calibration of the new electrostatic energy analyzer developed for T-10.
- 3) Comparative study of the plasma electric fields behavior in the T-10 tokamak and TJ-II stellarator during ECR heating.

### **The tasks to be solved at IPP NSC KIPT**

- 1) Works in support of putting into operation of the Uragan-2M torsatron during 2005-2007. The manufacture of the systems (central desk, ICRH system, vacuum system) for the Uragan-2M torsatron.
- 2) Starting of works on development of the new stage of the HIBP diagnostic for stellarator Uragan-2M (IPP NSC KIPT, Kharkov). Calculations and optimization of the HIBP implementation for the Uragan-2M device. Development of the HIBP hard ware structure for the Uragan-2M.
- 3) Development and designing of the new probing beam injectors for HIBP diagnostic in stellarators. Study of the Ti and Cs ion emitters of the high intensity. Development of the Li injector with current intensity of up to 10 mA.

### **5-2. Karazin National University, Kharkov**

#### **5-2-1. International collaboration in 2005**

#### **Collaboration with Max-Planck-Institut für Plasmaphysik, Germany**

- 1) Impurity transport and electromagnetic waves in the plasma periphery of a HELIAS reactor configuration and WENDELSTEIN 7-X (Prof. Dr. I. Girka (University) and Prof. Dr. A. Shishkin (NSC KIPT) in collaboration with Prof. Dr. F. Wagner, Dr. H. Wobig, Dr. R. Schneider, Dr. Yu. Igitkhanov and Dr. C. Beidler (MPIPP)).
- 2) Sandwich Fellowship Program was established between the University and MPIPP since 2001. In brief it means education of PhD students from the University by both supervisors from the University and MPIPP with the following PhD thesis defense at the University. The first PhD thesis [Stochasticity of impurity ion trajectories and particles flows in high temperature plasma of stellarators was defended by former Sandwich PhD student O. Shyshkin (University) on December, 2005 (supervisor from MPIPP side was Dr. R. Schneider).

- 3) Erosion of tungsten layers by deuterium bombardment (Sandwich PhD student I. Bizyukov under the supervision of Dr. K. Krieger (MPIPP)).
- 4) The experiments on the pulsed plasma diagnostics, proofing the RF plasma source design and improving the data analysis in the plasma diagnostic methods (Dr. K. Polozhiy (University), who occupied the Postdoctoral position at the IPP under the supervision of Prof. Dr. h.c. V. Dose).
- 5) Designing the new diagnostic methods in area of the plasma reactive processes at the plasma-wall interaction (during the visit of Dr. Th. Schwarz-Selinger (MPIPP) to the University, November, 2005).
- 6) Testing the ICRF antenna of new geometry (junior researcher A. Onyshchenko, University) during his visit to MPIPP in collaboration with Dr. J.-M. Noterdaeme, Dr. Vl. Bobkov, W. Becker (MPIPP)).
- 7) University graduate O. Mishchenko defended PhD thesis carried out at the Stellarator Theory Division MPIPP under the supervision of Dr. A. Koenis, academic supervisor was Prof. Dr. J. Nührenberg.

#### **Collaboration with National Institute for Fusion Studies, Japan:**

- 1) Dynamics of D+D fusion products in LHD geometry (Prof. Dr. A. Shishkin, A. Eremin, A. Moskvitin and Yu. Moskvitina (University) in collaboration with Prof. Dr. O. Motojima and Dr. S. Sudo (NIFS)).
- 2) The conditions when  $42\text{He}$  ions can escape from the confinement volume due to the drift of the drift island, while  $21\text{D}$  and  $31\text{T}$  ions are confined are found by Prof. Dr. A. Shishkin, O. Antufyev (University), and Prof. Dr. O. Motojima, Dr. A. Sagara (NIFS).

#### **Collaboration with Los Alamos National Laboratory, USA:**

The development and investigation of radiation resistant materials for optical windows in devices of plasma diagnostics. Research was carried out by University group (Dr. V. Gritsyna, Dr. V. Kobayakov, Yu. Kazarinov (University) and Dr. K. Sickafus (LANL)).

#### **5-2-2. Plans of National University for 2006**

- 1) The new numerical tool: 3-D Impurity Transport Code will be developed by O. Shyshkin on the base of the 1-D Impurity Transport Code. This numerical tool will allow studying the impurity ions transport in different plasma configurations of modern drift optimized stellarators such as Wendelstein 7-X and HELIAS reactor. In the new version of the code, the treatment of the plasma configurations with the magnetic islands, which are the part of the divertor islands configurations, where the stochastic behavior of the magnetic field lines is observed, would be emphasized. That would be the

principal new feature of the code.

- 2) Excitation of the second chain of the islands, overlapping of adjacent island chains and stochastization of the magnetic field lines as the result of finite plasma pressure in the magnetic field configuration of the stellarator Wendelstein 7-X.
- 3) New physics mechanisms for removal of cold  $\alpha$ -particles from fusion helical reactor with simultaneous confinement of the main plasma, which appropriate the constructive advantages of Force Free Helical Reactor, Japan, will be studied. Namely the small magnetic islands at the plasma periphery will be proposed to make use of.
- 4) Sputtering of tungsten, accumulation of deuterium in tungsten, blistering and growth of a carbonic film at irradiation of tungsten by ions of carbon and deuterium. Simulation of sputtering and growth of a film in a zone of the implantation by Monte-Carlo method (code TRIDYN). The next Sandwich PhD student I. Bizyukov (University) will defend his thesis (supervisor from MPIPP is Dr. K. Krieger).
- 5) Coating technologies related to plasma facing materials and components. Operation testing of the coatings (including multilayer) aimed for protection of the ICRF antennas. New Sandwich PhD student A. Onyschenko (University) will start his research "Influence of the coating on the dielectric rigidity of the ICRF antenna at Technology Division" (MPIPP).
- 6) Erosion of the carbon surfaces under effect of the hydrogen (neutral and charged) species from plasma: designing the bright plasma sources with the high density plasma fluxes for an experimental modeling of the conditions at the wall and for testing of the materials for the fusion applications; diagnostics of pulsed low-temperature plasmas; investigation of basic deposition mechanisms of hydrocarbon coatings; determination of time-resolved data for the electrical characteristics, such as the resulting mass- and energy-resolved ion fluxes to the wall as well as plasma potential, floating potential, and electron density and temperature; improving the data analysis in the existing diagnostic methods at using Bayesian probability theory.
- 7) Collaboration with Colorado School of Mines (Colorado, USA) on the development, fabrication and characterization of optical magnesium aluminate spinel ceramics transparent in the wide range of spectral region for RF heating and optical diagnostics of plasma.

#### **5-3. Kyiv Institute for Nuclear Research (Ukraine)**

##### **5-3-1. International collaboration in 2005**

##### **Collaboration with Germany**

A collaboration between the Kyiv Institute for Nuclear Research (KINR) and Max-Planck-Institut für Plasmaphysik (IPP) was continued. The main research



topics were the following. (i) Equilibrium features and transport of the energetic ions produced during NBI and ICRH in Wendelstein 7-X. (ii) Alfvén instabilities driven by the energetic ions in Wendelstein 7-X, including a study of theoretical aspects of Alfvén instabilities in stellarators and modeling Alfvén instabilities in Wendelstein-line stellarators. The main results were as follows.

A new Alfvén mode called “non-conventional global Alfvén eigenmode” (NGAE) is predicted. It is shown that NGAE can be transformed to a kinetic Alfvén wave (KAW), which results in enhancement of the thermal conductivity of the plasma. The enhancement is shown to be strongest when the electron collision frequency exceeds the particle transit frequency in the wave field. The developed theory is applied to explaining experimental observations of thermal crashes during bursting Alfvénic activity in Wendelstein 7-AS.

An invariant of the motion of well-circulating particles in stellarators with a large number of the field periods is derived. The mode structure in weak-shear systems is determined by solving an eigenmode equation analytically. The results were used in the development of a theory of Alfvén instabilities driven by fast ions with finite orbit width.

A general expression for the growth rate of Alfvén instabilities driven by circulating and semi-trapped energetic ions in stellarators is derived, which generalizes that obtained in a recent work (Ya.I. Kolesnichenko et al., *Phys. Plasmas* 11 (2004) 158) by taking into account the finite orbit width of the energetic ions. It is found that the finite orbits typically reduce the growth rate, but in some cases they enhance instabilities, leading to additional resonances. The developed theory is applied to a particular shot in Wendelstein 7-AS, where Alfvénic activity had a bursting character, being strongest at the end of each burst. It is concluded that finite orbits in the mentioned shot are actually a trigger of instability bursts; on the other hand, they weaken a strong instability at the burst end, which justifies the perturbative approach used. A detailed analysis of destabilized Alfvén eigenmodes in W7-AS precedes the stability analysis. An explanation of the frequency chirping observed is suggested.

Effects of the radial electric field, on the confinement of trapped fast ions in the Wendelstein-line stellarators are studied. It is shown that negative electric field improves the confinement; in particular, a radially localized field can play the role of a transport barrier for ions escaping from the plasma when. In contrast to this, a positive

electric field can deteriorate the ion confinement. Such a field accompanied by the plasma rotation with the frequency around a certain magnitude, which we refer to as the resonance rotation frequency, leads to a quick particle loss. A possibility to use the plasma rotation with the resonance frequency for the ash removal in a Helias reactor is considered. The mentioned results are obtained analytically and numerically. The analytical consideration was done on the basis of the derived bounce-averaged equations of the particle motion. The numerical calculations were carried out for Wendelstein 7-X and a Helias reactor by the guiding centre code ORBIS (ORBits In Stellarators) developed in this work.

The properties of the Alfvén continuum (AC) and the Alfvén eigenmodes (AE) in stellarators in the high-frequency range (that of the helicity-induced and mirror-induced gaps) are elucidated. With this aim the AC in the vicinity of two close gaps is studied, including the case when the gaps cross at a certain radial point. It is shown that the gaps “annihilate” at the crossing point, i.e., the width of the joint gap at the crossing point is the difference of the widths of the two separate gaps. The AC wave functions are shown to be trapped in narrow bands of the flux surfaces, which are located on either the inner or the outer circumference of the torus. To investigate the structure of AEs of the discrete spectrum in this frequency range, the ballooning formalism is employed. It is shown that the high-frequency AEs are also localized in narrow poloidal sectors.

Publications that resulted from the collaboration in 2005:

- [1] Ya.I. Kolesnichenko, Yu.V. Yakovenko, A. Weller, A. Werner, J. Geiger, V.V. Lutsenko, and S. Zegenhagen, “Novel mechanism of anomalous electron heat conductivity and thermal crashes during Alfvénic activity in Wendelstein 7-AS”, *Phys. Rev. Lett.* 94 (2005) 165004.
- [2] Ya.I. Kolesnichenko, V.V. Lutsenko, A. Weller, A. Werner, H. Wobig, Yu.V. Yakovenko, J. Geiger, and S. Zegenhagen, “Effects of fast-ion-orbit width on Alfvén instabilities in stellarators: a general theory and its application to a W7-AS experiment”, submitted to *Nucl. Fusion*.
- [3] Ya.I. Kolesnichenko, V.V. Lutsenko, A.V. Tykhyy, A. Weller, A. Werner, H. Wobig, “Confinement of fast ions in Wendelstein 7-X in the presence of the radial electric field”, submitted to *Nucl. Fusion*.
- [4] Ya.I. Kolesnichenko, V.V. Lutsenko, A. Weller, A. Werner, Yu.V. Yakovenko, J. Geiger, A.V. Tykhyy, and S. Zegenhagen, “Analysis and interpretation of observations of Alfvénic activity in Wendelstein 7-AS”, 32<sup>nd</sup> EPS Conf. on Plasma Physics, Tarragona, 2005, Abstracts, Rep. P2.125,



[http://eps2005.ciemat.es/database/abstracts/contributed/P2\\_125.pdf](http://eps2005.ciemat.es/database/abstracts/contributed/P2_125.pdf).

[5] Ya. I. Kolesnichenko, V. V. Lutsenko, A. Weller, A. Werner, H. Wobig, Yu. V. Yakovenko, J. Geiger, A. V. Tykhyy, and S. Zegenhagen, "Novel physics involved in interpretation of Alfvénic activity accompanied by thermal crashes in W7-AS", Report at the 15<sup>th</sup> International Stellarator Workshop, Madrid, October 2005; 15<sup>th</sup> Int. Stellarator Workshop, Madrid, 2005, IAEA Tech. Comm. Mtg, 2005 (CIEMAT, Madrid, 2005), p.15;

[http://www-fusion.ciemat.org/cgi-bin/sw05/dir\\_talks.cgi](http://www-fusion.ciemat.org/cgi-bin/sw05/dir_talks.cgi).

[6] Ya. I. Kolesnichenko, V. V. Lutsenko, A. Weller, A. Werner, H. Wobig, Yu. V. Yakovenko, J. Geiger, and S. Zegenhagen, "Effects of fast-ion-orbit width on Alfvén instabilities in stellarators: a general theory and its application to a W7-AS experiment", Report at the IAEA Technical Meeting on Innovative Concepts and Theory of Stellarators, Madrid, October 2005; 15<sup>th</sup> Int. Stellarator Workshop, Madrid, 2005, IAEA Tech. Comm. Mtg, 2005 (CIEMAT, Madrid, 2005), p. 163.

[7] Yu. V. Yakovenko, Ya. I. Kolesnichenko, A. Weller, H. Wobig, and O. P. Fesenyuk, "Properties of the high-frequency part of the Alfvén continuum and eigenmodes in stellarators", Ibid., p. 162.

## **6. United States**

### **6-1. International collaborations in 2005**

#### **Collaborations with Australia**

S. Hudson (PPPL) visited Bob Dewar (ANU) to collaborate on developing a new 3D equilibrium code.

#### **Collaborations with Japan**

1) C. Hegna (U. Wis.) attended the US/Japan JIFT Workshop on Stellarator Theory - Jan 26-28, 2005 Kyoto, Japan - gave talk "Finite Larmor Radius Stabilization of Ballooning Instabilities in 3-D Plasmas". He also collaborated with N. Nakajima (NIFS) and DY. Nakamura (Kyoto) on ideal stability calculations relevant to LHD plasmas - this directly lead to parts of two papers: S. R. Hudson, C. C. Hegna and N. Nakajima "Influence of pressure-gradient and shear on ballooning stability in stellarators," Nuclear Fusion 45, 271 (2005), and N. Nakajima, S. R. Hudson, C. C. Hegna and Y. Nakamura, "Boundary modulation effects on MHD instabilities in heliotrons," Nuclear Fusion 46, 177 (2006).

2) J. Lyon (ORNL) visited NIFS to discuss results from the ORNL neutral particle analyzer on LHD and to repair one of the detector channels.

3) D. Mikkelsen (PPPL) visited Sadayoshi Murakami at Kyoto University discuss modelling of neutral beam orbits in stellarators. He also visited NIFS to discuss recent experimental turbulence results, and the further

collaborations with PPPL to model results CHS and JIPP-TII.

4) D. Spong (ORNL) presented a talk at the 9th IAEA Technical Meeting on "Energetic Particles in Magnetic Confinement Systems" in Takayama, Japan and gave a talk at the mini-conference on "Energetic ion driven MHD modes in CHS and LHD" at NIFS. He also visited NIFS to collaborate on modelling fast ion losses associated with frequency sweeping Alfvén modes in the CHS stellarator.

5) Prof. H. Himura (Kyoto) visited the CNT experiment (Columbia) in September and participated in experiments investigating the stability of electron plasmas with a significant ion fraction, inspired by non-neutral experiments on the CHS.

6) K. Ichiguchi (NIFS) visited ORNL to work on a multi-scale code that combines the slow increase in plasma beta by heating with the stellarator equilibrium developing stable path to high beta. This led to a paper "Multi-scale approach to the solution of the nonlinear MHD evolution of Heliotron plasmas" by K. Ichiguchi and B. A. Carreras that was accepted for publication in J. Plasma Physics.

7) Prof. S. Okamura (NIFS) visited PPPL in February to work on optimization codes and discuss future plans for collaboration on NCSX. NIFS, the University of Tokyo, PPPL, and other collaborating institutions proposed a long term collaboration on ECH for NCSX.

#### **Collaborations with Germany**

1) I. Joseph (UCSD) visited MPI-Greifswald to develop a coupled TRIP3D/E3D numerical model for the boundary of the DIII-D tokamak in the presence of error fields and externally applied magnetic perturbations.

2) D. Mikkelsen (PPPL) visited MPI-Greifswald to discuss simulation of neutral beam heating and discuss benchmarks against the tokamak code TRANSP.

An analytic representation of neoclassical mono-energetic diffusion coefficients appropriate for NCSX was developed, and plans made for testing the adequacy of this approximation. Plans were discussed for future collaboration on comprehensive modelling and hybrid analysis of Alfvénic modes.

3) M. Zarnstorff (PPPL) visited MPI-Greifswald and collaborated with A. Weller (IPP) and the W7AS group to continue the analysis of parametric scans of W7AS high-beta data. This resulted in three conference papers.

4) V. Erckmann (IPP) visited PPPL to discuss possible collaborations on NCSX.

#### **Collaborations with Spain**

1) G. Barber and S. Combs (ORNL) visited CIEMAT to improve the performance of the TJ-II NBI and to discuss the design of a pellet injector for TJ-II. Improvements

were made to the NBI electrical system and the modulator vacuum tubes were conditioned to 45 kV. Decisions were made on the ORNL/CIEMAT interfaces and design for the pellet injection system.

2) B. Carreras (ORNL) visited TJ-II to continue work on analysis of experiments at TJ-II to study a possible transition at the plasma edge that is responsible for the creation of the edge shear flow layer, and new experiments were planned. Work was done on a transport model in collaboration with B. van Milligen and R. Sanchez. A paper was completed and published in European Journal of Physics. During a separate visit, he worked on the development of a two-equation version of the model based on continuous time random walk (CTRW) and critical gradients and on application of an approach based on the CTRW to neoclassical stellarator transport.

3) M. Murakami (ORNL) visited CIEMAT to participate in NBI experiments in TJ-II and make suggestions for experiments based on the experience from the Advanced Toroidal Facility stellarator results.

4) D. Rasmussen (ORNL) visited CIEMAT and participated in discussions on the status and plans for the two ORNL NBI systems (one operating and one to be installed on TJ-II in 2006), an ORNL pellet injection system (to be installed in the fall of 2006), and an electron Bernstein wave emission diagnostic (to be installed in the spring of 2006).

5) P. Ryan and C-C. Tsai (ORNL) visited Culham Laboratory and CIEMAT to decide on the eventual disposition of ORNL NBI equipment that is on loan to Culham and to improve the performance of NBI #1 prior to the start of the TJ-II 2006 campaign. Improvements to the electrical system and repair of the beam line #2 bending magnet were discussed.

6) D. Schechter and C-C. Tsai (ORNL) visited CIEMAT to enhance the performance of the TJ-II NBI and to transfer NBI assembly, maintenance, conditioning and repair skills to CIEMAT staff. The ion source was reassembled with appropriate gap spacing and aperture alignment of the grids of the ion accelerator and the vacuum leak of the ion source for NBI #2 was repaired.

7) D. Spong gave a talk at the IAEA Technical Meeting on Innovative Concepts and Theory of Stellarators at CIEMAT.

8) S. Zweben (PPPL) visited TJ-II to continue the collaboration on gas-puff imaging of edge turbulence, analyzing past data and preparing for the coming run period. This collaboration is being broadened to include JET.

#### **International Stellarator Workshop**

A. Boozer (Columbia U.), J. Canik (U. Wisconsin), K. L. Ku (PPPL), J. Lyon (ORNL), D. Spong (ORNL), and W.

Reiersen (PPPL) gave invited talks at the 15th International Stellarator Workshop at CIEMAT in Madrid, Spain, and a total of twelve contributed papers were presented from all the US stellarator groups.

#### **6-2. Program Plans for 2006**

##### **CNT**

Full characterization of pure electron plasma equilibria. Further investigations of instabilities and waves driven by a finite ion fraction. Installation of external mesh probes and retractable emitter and operation without internal probes.

##### **CTH**

The key activities for 2006 include:

- Diagnostic commissioning
- Field-mapping and correction of vacuum field errors with full equilibrium coil set. The 15-coil error correction system has not yet been fully proven.
- Measurement of edge islands & stochasticity in plasma with emphasis on edge temperature and density gradients measured by probes
- Experimental equilibrium determination and 3-D reconstruction attempts with magnetic measurements from external probes and loops, and later with input from SX arrays

Initial characterization of stability of current driven stellarator plasmas

The Compact Toroidal Hybrid laboratory plans to host a US/Japan workshop in November 2006 at Auburn University. An official request has been submitted to OFES by Prof. F. Sano of Kyoto University and PI of the Heliotron J experiment. The proposed title of the workshop is "New approaches to advanced plasma confinement in helical systems".

##### **HSX**

HSX activities for CY2006 emphasize increased heating power through installation of a new transmission line (in progress) and increasing the operating magnetic field to the designed  $B=1.0$  T level. Modifications needed for these goals should be completed by April 2006. Fundamental heating will double the attainable plasma density and reduce the non-thermal electron population. A DNB is being installed to measure plasma flows and infer the radial electric field for transport studies. Physics studies will emphasize differences in electron thermal conductivity between symmetric/non-symmetric operation, the influence of magnetic islands on plasma flow, bootstrap current measurements and modeling, fluctuation-induced/anomalous transport, and further clarification of observed MHD activity which appears

Alfvénic in nature. Expanded collaborations with the TJ-II group will be pursued.

#### **NCSX**

Construction of the National Compact Stellarator Experiment (NCSX) will continue during 2006. The three vacuum vessel sectors will be delivered to PPPL and assembly operations begun. Delivery of modular coil winding form deliveries will continue throughout the year, supplying the coil winding operations at PPPL.

A contract will be placed for fabrication of the planar TF coils. The physics design of the external trim coils, magnetic alignment, and plasma-facing component will be developed.

PPPL will host an US/Japan workshop on US/Japan JIFT Workshop on March 14-16, 2006 titled "Issues in the theoretical analysis of three dimensional configuration". The workshop is being organized by N. Nakajima (NIFS), S. Hudson and D. Monticello (PPPL).

#### **QPS**

A test coil will be wound with the internally cooled cable conductor to test the winding, vacuum canning and potting techniques for larger, more complex shaped coils. Additional test coils will be wound to determine their thermal, mechanical and fatigue properties. The prototype casting of the modular coil winding form will be machined to the needed tolerance prior to winding the full-size prototype coil with the internally cooled cable conductor.

(Komori, A.)

## 4. JSPS-CAS Core-University Program on Plasma and Nuclear Fusion

A bilateral international collaboration program “JSPS-CAS Core-University Program (CUP) on Plasma and Nuclear Fusion” was started from FY 2001 as a ten-year collaboration program. This program is supported by the Japan Society for the Promotion of Science (JSPS) for Japanese side and by the Chinese Academy of Science (CAS) for Chinese side. National Institute for Fusion Science (NIFS) and Institute of Plasma Physics, Chinese Academy of Science (ASIPP) serve as the core institutes for this program in each country and assist the collaborations between all participating institutes and universities in Japan and China. It has been implemented for the past five years including this fiscal year. At this mid-point of a ten-year program, results of CUP in the first half have been evaluated by JSPS. This collaboration program has been rated as the top rank “Excellent”, with some encouraging comments.

### General review of collaboration in FY 2005

In this fiscal year, construction of the EAST tokamak device was almost completed with toroidal and poloidal coils superconducting. Following the scheduled completion in March 2006, the first cooling down of all superconducting coils will begin in early next fiscal year.

After examinations on the cryogenic system, the vacuum vessel is scheduled to be open for installations of diagnostics. In Japan, LHD device has been used for collaborating researches: There was a large progress in long pulse experiment, achieving a new record of one-hour discharge injecting 1.6 GJ of ICRF power. Understanding in the transport physics of torus was also deepened.

The advance in nuclear fusion research in China is remarkable and is appreciated by nuclear fusion society in Japan. Xie Jikang and Zheng Wanguo were invited for talks in the JSPF meeting to report the status of researches in magnetic and laser fusions in China. In this fiscal year, the seminar entitled as “Production and steady state confinement of high performance plasma in magnetic confinement systems” was organized, so that a comprehensive view of the results under CUP was obtained. The papers presented there were published in a series of papers in the international journal “Plasma Science and Technology”.

The researcher exchanges conducted in FY 2005 are summarized as follows in order of Category. The whole collaboration programs implemented in FY2005 are summarized in Table 1.

**Table 1 STATISTICAL REVIEW OF CUP collaborations in FY2005**

	Title	J→C person (person·day)	C→J person (person·day)	Total person (person·day)
I-1A	Development of Advanced Plasma Heating for High-Performance Plasma Confinement	2 (11)	2 (56)	4 (67)
I-1B	Development of Diagnostic and Control Methods for High-Performance Plasma Confinement	3 (23)	4 (56)	7 (79)
I-2A	Study on Plasma-Surface Interactions and Plasma Facing Materials	3(18)	2 (75)	5 (93)
I-3A	Atomic and molecular processes in plasma	4 (26)	4 (108)	8 (134)
I-4C	Development of High Pressure Plasmas for Environmental Application and Materials Processing	2 (18)	2 (27)	4 (45)
I-4D	Heating Behavior of Blast Furnace Slag Bearing High Ti Under Microwave	1 (6)	1 (5)	2 (11)
I-5A	Study of Ultrahigh Density Plasma (Inertial Confinement Fusion)	4 (31)	3 (20)	7 (51)
I-5B	Theory and simulation on Inertial Fusion Plasmas	3 (21)	4 (40)	7 (61)
II-A	Study on Reduced Activation Materials for Fusion	2 (11)	3 (44)	5 (55)
II-B	Study on CTR Blanket and Tritium	2 (8)	2 (22)	4 (30)
II-C	Design integration of advanced reactors and key technology evaluation	2 (10)	1 (48)	3 (58)
II-D	Development of Superconducting key technology for advanced fusion reactor	4 (26)	3 (40)	7 (66)
III-A	Study on Theoretical Analysis of MHD and Microinstabilities in Plasmas	2 (14)	2 (42)	4 (56)
III-B	Study on Transport Theory: Code Development of Numerical Analysis and Confinement Improved Mode in Torus Plasmas	1 (7)	1 (21)	2 (28)
III-C	Physics of self-organization in Complex plasmas	1 (8)	2 (28)	3 (36)
III-D	Modeling of edge and divertor plasma and control of impurities and recycling particles	1 (5)	1 (10)	2 (15)
	Scientist Exchange	3 (16)	5 (26)	8 (42)
	JSPS-CAS Core University Program Seminar on Production and steady state confinement of high performance plasmas in magnetic confinement systems	12 (61)	0 (0)	12 (61)
	Grand Total	52 (320)	42 (668)	94 (988)



### **I-1A Development of advanced plasma heating for high performance plasma**

M. Ichimura (Univ. of Tsukuba) visited ASIPP for the discussion of Alfvén cyclotron mode which is detected in GAMMA-10 device and its application to tokamaks.

K. Saito (NIFS) visited ASIPP hosted by Zhao Yanping and worked on the tuning method which is under collaboration between NIFS and ASIPP. A new algorithm of liquid stub tuner control was proposed as well as the need of correct measurements in reflected RF waves.

Gao Xiang (ASIPP) visited Kyushu Univ. to work on steady state sustainment of plasmas. He focused on comparison of the long time scale events observed in 240sec long pulse shots attained in HT-7 experiments and 5-hour shots attained in TRIUM-1M device.

Ding Bojiang (ASIPP) visited JAEA (Japan Atomic Energy Agency, former JAERI) and joined JT-60 experiments. He analyzed the diagnosed plasma rotation in JT-60 to clarify the internal transport barrier formed with LHCD.

### **I-1B Development of diagnostics and control method for high performance plasma**

T. Mizuuchi (Kyoto Univ.) visited SWIP hosted by Ding Xuan Tong. He gave a talk “Effects of configuration control on the plasma performance in Heliotron-J” and discussed optimization of gas feeding method. SWIP had developed SMBI and the discussion was useful for both institutes.

T. Maekawa (Kyoto Univ.) visited ASIPP hosted by Wan Baonian and He Yexi. He discussed the collaborations in spherical tokamaks LATE and SUNIST based on the non-inductive current start-up and maintenance achieved in the latter.

K. Nakamura (Kyushu Univ.) visited ASIPP hosted by Luo Jiarong and carried out an experiment on sensor-less sensing plasma control. This experiment was carried out on HT-7 device under CUP and promising result was obtained. A new idea was proposed to further improve the one in the previous year and examined in experiments.

Wan Baonian (ASIPP); see the description in the category I-3A.

Wang Huazhong (ASIPP) and Shen Biao (ASIPP) visited NIFS hosted by T. Morisaki and S. Sakakibara. They worked on magnetic measurements and determination of magnetic configurations in coming EAST device referencing those of LHD. They also worked on improvement of the data acquisition systems from points of

view of easy access.

Zhou Yan (SWIP) visited NIFS hosted by K. Tanaka. He studied particle transport using the data of FIR measurement and applied the code developed by K. Tanaka. He also attended “seventh Australia-Japan workshop on Plasma Diagnostics” and “15th Int. Toki conf. on fusion and advanced technology” presenting the results of CUP.

Duan Xuru (SWIP) visited NIFS hosted by K. Ida, S. Yoshimura and K. Toi. He studied the components of CXS including new techniques for MSE application.

### **I-2A Study on plasma surface interactions and plasma facing materials**

M. Matsuyama (Toyama Univ.) and K. Okuno (Shizuoka Univ.) visited SWIP hosted by Feng Kaiming and ASIPP hosted by Xiao Bingjia. They discussed the behavior of hydrogen isotopes in plasma facing components and exchanged opinions on application to ITER.

N. Ashikawa (NIFS) visited Donghua Univ. (in Shanghai) and ASIPP hosted by Hu Jiansheng. She presented a paper in the ITPA meeting on the results of the experiments carried out in the previous year aiming at hydrogen recovery from plasma facing wall. Uses of RF discharge for this specific purpose have been examined in HT-7, LHD, and TEXTOR.

Hu Jiansheng (ASIPP) visited NIFS hosted by N. Ashikawa and investigated Oxidization of the wall for the specific purposes of removal of hydrogen and deposited materials. The effects of two methods O-ICR and O-GDC were compared.

Liu Xiang (SWIP) visited Toyama Univ. hosted by M. Matsuyama and studied the tritium distribution in the surface layer by use of the beta-ray induced X-ray spectroscopy. In this collaborative experiment, properties of V-4Cr-Ti, which one of the candidates for advanced reactor, were investigated.

### **I-3A Atomic and molecular processes in plasma**

S. Ohtani (Univ. Electro-communications) visited Fudan University hosted by Zou Yaming to discuss key subjects on the Shanghai EBIT device. He also gave a seminar on physics achievements on Tokyo EBIT device.

F. Koike visited South-West Normal Univ. hosted by Dong Chenzhong. Through discussions in his laboratory, drafts of four papers were born which will be submitted after revisions via E-mail communications.

M. Kimura (Kyushu Univ.) visited Institute of Physics, CAS hosted by Wang Jianguo. He gave a seminar on

“Atomic Collision Physics: Bases for High-Tech” and discussed about application for China - Japan International collaboration of Science and Technology.

I. Shimamura visited Shanghai Jiaotong University hosted by Li Jiaming and Qu Yizhi. He gave a seminar on “Quasi-bound states in positron scattering processes”. He discussed with many Chinese scientists about their work and his work in a broad area of atomic molecular physics.

Wan Baonian (ASIPP) visited NIFS hosted by T. Kato and S. Morita and worked for spectroscopy: He engaged in designing diagnostics for EAST device referencing those of LHD device. He focused on the use of these diagnostics for investigation of plasma wall interaction, clarifying the physics that are contained in the spectral line profiles of atoms and molecules. He also attended the CUP coordinator meeting and KOSEF meeting.

Wu Zeqing (Inst. of Appl. Physics and Comp. Mathematics) visited NIFS hosted by T. Kato and I. Murakami and worked on the intensity ratio of 2s-3p and 2p-4d for CIV and improved the codes in order to account for the recommended data set.

Xiao Bingjia (ASIPP) visited NIFS hosted by T. Kato and studied effects of the vibration of molecules on the recombination processes of hydrogen which may play an important role in the dynamics in front of the diverter target.

Zhu Linfan (Univ. Sci. Technol. China) visited Univ. of Electro-Communications hosted by S. Ohtani and investigated inner shell excitation process of rare gas atoms.

#### **I-4C Development of high pressure plasmas for environmental application and material processing**

H. Sugai (Nagoya Univ.) visited Fudan Univ. hosted by Liang Rongqing. He also visited Huazhong Univ. of Science and Technology hosted by Liu Minghai and Wuhan Institute of Technology. He made influencing lectures in each place followed by intense discussions.

T. Oda (Univ. of Tokyo) visited (Dalian Univ. Tech.) hosted by Wu Yan. He introduced his own work on removal of environmentally harmful gas. He also visited (Dalian Maritime Univ.) and discussed many practical problems in researches under development in China.

Qiu Jieshan (USTD) visited Tohoku Univ. hosted by R. Hatakeyama. During his stay, he worked on creating double walled nano-tubes as well as Y-branched double wall nano-tubes. He reported these results at “International Conference on Reactive Plasmas”.

Meng Yuedong (ASIPP) visited Tohoku Univ. hosted

by R. Hatakeyama. He succeeded to create  $C_{60}$ -encapsulated double walled carbon nano-tubes finding coulomb blockage phenomena.

#### **I-4D Heating behaviors of blast furnace slag bearing high Ti under microwave**

N. Yoshikawa (Tohoku Univ.) visited Tsinghua Univ. hosted by Bai Chenguang. He attended a symposium “Second electro magnetic processing meeting” held at Northeastern Univ. and presented results of the collaborative research on selective extraction of Ti from steel making slag. He also discussed at Tsinghua Univ. with Li Jin Feng and Pan Wei.

Wang Haichuan (Anhui Univ. Tech.) visited Hiroshima Univ. and NIFS hosted by N. Yoshikawa. He attended the “2005 autumn meeting of Japan Institute of metals” and presented a paper “Development of application research of Microwave Heating in metallurgy”. He discussed at NIFS how to extract Ti and V from steel making slag.

#### **I-5A Study of ultra-high density plasma (Inertial confinement fusion)**

K. Tanaka (Osaka Univ.), K. Nagai (Osaka Univ.), H. Yoneda (Univ. of Electro-Communication) and N. Yugami (Utsunomiya Univ.) attended the 2005 Workshop on Ultra high Density Plasma Production held at JiuZhai Gou and presented their papers: “Fast Ignition Relate Basic to Integrated Experiments & Status of FIREX project”, “Japan China collaboration research on new porous materials”, and “Study of warm dense matter with ultra-short pulse lasers”, “Experimental observations of radiations from laser and plasma interaction”. The host at Research Center of Laser Fusion is Feng Jin and the host at Shanghai Institute of Fine Mechanics is Lin Zunqi

Zheng Wanguo (RCLF, Mianyang), Ding Yongkun (Research center of Laser Fusion, CAEP), and Li Yutong (Institute of Physics, CAS) visited Osaka Univ. hosted by K. Tanaka. The attended 2005 JSPF meeting: Zheng Wanguo gave an invited talk “Recent Experiment Progress of TIL at CAEP” reporting the status of laser fusion in China. Ding Yongkun gave an oral presentation “Recent Progress of ICF Experimental Investigations on Shenguang II Laser Facility”.

#### **I-5B Theory and simulation on inertial fusion plasmas**

S. Nakai (Osaka Univ.), H. Sakagami (NIFS), and K. Mima (Osaka Univ.) attended the “2005 Workshop on Ultra

high Density Plasma Production, application and Theory for Laser Fusion” held at JiuZhaiGou and presented papers: “IFE Power Plant Development”, “Holistic simulations for core-heating of fast ignition”, and “Recent results and future prospects on laser fusion research at ILE”.

Sheng Zhengming (Inst. Physics) and Chen Min (Inst. Physics) visited Osaka Univ. hosted by K. Mima and attended “19th international Conference on Numerical Simulation of Plasma” and “7th Asia Pacific Plasma Theory Conference” and presented papers.

Sheng Zhengming (Inst. Physics) and Chen Min (Inst. Physics) visited Osaka Univ. hosted by K. Mima. On their second visit, they had a workshop in which the following subjects have been discussed: “Electron injection and trapping in a plasma wake field using ionization of highly charged states of atoms”, “Simulation of electron emission and acceleration along a solid surface”, and “High energy density physics in peta-watt lasers”.

Zheng Jun and discussed “creation of hot electrons and protons in the interaction of ultra-short laser pulse with micro droplet”. He also attended the 7th Asia Pacific Plasma theory conference and presented a paper.

#### **II-A Study on reduced activation for fusion**

A. Kohyama (Kyoto Univ.) visited ASIPP and Shanghai Institute of Ceramics hosted by Wu Yican and Dong Shaoming. He discussed the progress of the SiC/SiC composite under CUP and considered its application to ITER.

K. Abe (Tohoku Univ.) visited SWIP hosted by Feng Kaiming. He reported “the activities in Japan towards development of blanket and its materials” followed by a talk by Feng Kaiming “Conceptual design activation for fusion reactor and ITER TBM (Test Blanket Module Design) at SWIP”.

Jiang Dongliang (Shanghai Institute of Ceramics) visited Kyoto Univ. hosted by A. Kohyama and discussed Optimization of SiC Chemistry.

Zhang Chonghong (Institute of Modern Physics) visited Hokkaido Univ. hosted by T. Shibayama. He worked on the following three subjects: 1) Defects formation in silicon carbide irradiated with heavy inert-gas ions. 2) Micro-structural evolution in silicon implanted with chlorine ions. 3) Cavity formation in alumina implanted with helium and trapping of Au in the cavities.

Xu Yongdong (North-Western Polytechnic Univ.) visited Kyoto Univ. hosted by A. Kohyama. Mechanical properties of SiC/SiC were discussed.

#### **II-B Study on CTR blanket and tritium**

S. Tanaka (Univ. of Tokyo) and Y. Ohya (Univ. of Tokyo) visited SWIP and CAEP hosted by Feng Kaiming and Zhang Guoshu. Tanaka discussed recent experimental results on hydrogen behavior in  $\text{Li}_2\text{O}$ . Ohya discussed recovery of tritium by use of laser irradiation. These two institutes are linked through ITER oriented development; the collaborations with these institutes will become more important.

Xue Xiaogang (CIAE) and Zheng Jianping (CIAE) visited NIFS and Univ. of Tokyo hosted by Muroga. They discussed “Enhancing Fission-Fusion common technology”.

#### **II-C Design integration of advanced reactors and key technology evaluation**

M. Sato (Tohoku Univ.) visited SWIP hosted by Feng Kaiming. He attended the discussion with K. Abe (II-A). He gave a talk “Fundamental research on MHD coating for V-Li System” followed by a talk by Chen Jiming “Fusion Materials & Technology research in SWIP”.

H. Takahashi (Hokkaido Univ.) visited UST, Beijing hosted by Hu Benfu. Database for low activation austenite materials was discussed.

Li Yanfen (ASIPP) visited NIFS hosted by Muroga. He discussed reduced activation martensitic steel, which is a candidate structure material for DEMO, comparing the test piece developed in China with JLF-1 in mechanical properties.

#### **II-D Development of superconducting key technology for advanced fusion reactor**

N. Amemiya (Yokohama National Univ.) visited North-West Institute of Non-ferrous Metal Research in Xi'an and Inst. Electrical Engineering, CAS in Beijing hosted by Zhang Pingxiao and Xiao Liye. He discussed “Experimental & numerical approaches to AC-loss characteristics of next generation high-Tc superconductor and related technology”.

A. Nishimura (NIFS), S. Nishijima (Osaka Univ.), and T. Takeuchi (NIMS) visited; 1) Technical Institute of Phys. & Chemistry in Beijing hosted by Li Laifeng at Cryogenic Laboratory, 2) Xi'an Jiatong Univ. hosted by Li Yanzhong, 3) North-West Institute of Non-ferrous Metal Research hosted by Liu Xianghong, and 4) ASIPP hosted by Wu Songtao. They investigated the generally the competences of academic institutes and in industry in Japan and China to the superconductor engineering for ITER and discussed

fringe benefits to other industrial applications.

Xu Liuwei (ASIPP) and Wu Yu (ASIPP) visited NIFS hosted by S. Yamada. They attended the 15th international Toki-conference “Fusion and advanced technology” and presented papers. In NIFS, they introduced, in a seminar, the test facility for EAST in ASIPP and discussed its application to ITER with obtained initial data. Wu Yu visited JAEA and discussed for future collaborations.

### **III-A Study on theoretical analyses of MHD and micro-instability in plasmas**

H. Sanuki (NIFS) visited ASIPP and SWIP hosted by Li Jiangang, Pan Chuanhong, and Wang Shaojie. He had with K. Itoh a seminar for each of the two institutes and gave influencing lectures. He gave a lecture “Review of Mathematical Tools for Nonlinear Phenomena” followed by discussions of the direction of the investigation (see also III-B below).

M. Furukawa (Tokyo Univ.) visited ASIPP and SWIP hosted by Wang Shaojie and Li Jiquan. He gave a lecture “Stabilization of ballooning modes by toroidal rotation in tokamaks” and discussed with Dong Jiaqi and Li Jiquan for new results on the effects of streamer on ETG mode. At ASIPP he discussed with Wang Shaojie and Deng Zhou on kinetic effects on sawtooth stabilization.

Li Jiquan (SWIP) visited NIFS hosted by H. Sanuki and Y. Kishimoto. He began investigation on convective cell formation in electro magnetic drift wave turbulence as well as the ITG/ETG dynamics of large-scale structure.

Gao Zhe (Tsinghua Univ.) visited NIFS hosted by H. Sanuki. He investigated on “critical threshold of short wave length ion temperature instability in toroidal plasmas” in which he addressed the cause of electron transport anomaly.

### **III-B Study on transport theory code development of numerical analysis and confinement improvement**

K. Itoh visited ASIPP and SWIP hosted by Li Jiangang, Pan Chuanhong, and Wang Shaojie. He made with H. Sanuki a seminar for each of the two institutes and gave influencing lectures (see above III-A). He gave a lecture “Physics of collapse event in toroidal plasmas”, and discussed from the points of views of 1) statistical natures of collapse phenomena, 2) zonal flow, and 3) various problems in their current experimental investigations.

Wang Shaojie (ASIPP) visited NIFS hosted by H. Sanuki. He introduced his work using Grad-Shafranov-Helmholtz model equation trying to give an

account for equilibriums including current hole.

### **III-C Physics of self- organization in complex plasmas**

R. Horiuchi (NIFS) visited IAPCM hosted by Zhu Shaoping. He also attended the 2005 Workshop on Ultra high Density Plasma Production held at JiuZhaiGou.

Li Baiwen (IAPCM) visited NIFS hosted by R. Horiuchi. He discussed in NIFS on relativistic electromagnetic soliton and well collimated return relativistic electron beam. He also attended 19th ICNSP & APPTC and presented a paper.

Li Long (IAPCM) visited NIFS hosted by R. Horiuchi. He also attended 19th ICNSP & APPTC and presented a paper.

### **III-D Modeling of edge and Diverter plasma and control of impurities and recycling particles**

Y. Tomita (NIFS) visited ASIPP hosted by Zhu Sizheng. He attended the seminar “Production and steady state confinement of high performance plasma in magnetic confinement systems”. He presented a paper “Dust particle behavior in boundary plasma”. Other collaborative works in this category were also presented there, including 1) Prediction for ITER diverter performance by Zhu Sizheng and 2) Over all feature of EAST operation space by using simple Core-SOL-diverter model by R. Hiwatari.

Xu Guosheng (ASIPP) visited NIFS hosted by Y. Tomita and H. Sanuki. He worked on understanding turbulence placing emphases on possible coupling of drift waves with Alfvén waves and creation of large-scale low frequency wave packets. He gave a talk “Turbulence in HT-7 tokamak”.

### **Symposium**

The JSPS-CAS seminar in FY2005 is titled as “Production and steady state confinement of high performance plasma in magnetic confinement systems” focusing on Category-I.

The seminar was held in ASIPP with program leaders Wan Baonian at ASIPP and K. Toi at NIFS. There were totally 32 attendees from Japan and China: In China, there were 6 presentations from ASIPP, 6 from SWIP, 1 from Tsinghua Univ., and 3 from USTC. There were 16 attendees from Japan including 8 presentations from NIFS, 3 from JAERI, 1 from Tsukuba Univ., 1 from Kyoto Univ., and 2 from Kyushu Univ., and 1 from CRIEPI.

As titled, this seminar impressed the attendees with the experimental progresses made in the past 5-years under CUP,



deepening in the understanding of the physics of torus. The devices HT-7, HL-2A, LHD, JT-60U, and TRIAM-1M were efficiently used and many significant results have been obtained. The devices in different concepts, LATE, Heliotron-J, and GAMMA-10, provided with them valuable complementary data to facilitate a comprehensive understanding. There were also some theoretical papers assisting understanding of the experimentally observed

phenomena.

The papers presented there were published in a series of papers in Chinese magazine "Plasma Science and Technology" and as NIFS-PROC-60.

(Watari, T., Namba, C., Toi, K., Yamada, S.)

## IV. Department of Engineering and Technical Services

The Department of Engineering and Technical Services is involved in all kinds of work in the design, fabrication, construction and operation of experimental devices in the fields of software and hardware.

This department is composed of engineers, and their tasks fall under the following five goals:

To develop advanced and systematic engineering capabilities on the basis of basic engineering results which have been obtained thus far.

To educate excellent engineers with responsible administration.

To cultivate creative engineering abilities.

To improve the documentation of and the transfer of engineering knowledge to the next generation.

To perform tasks with a systematic responsibility.

The department consists of the following five divisions: the Fabrication Technology Division takes care of the construction of small devices and the quality control of parts for all Divisions. The Device Technology Division is responsible for LHD and LHD peripheral devices except for the heating devices and the diagnostic devices. The Plasma Heating Technology Division has responsibility for the ECH system, ICRF system and NBI system. The Diagnostic Technology Division develops, operates and maintains all diagnostic devices and the Control Technology Division has responsibility for the central control system, the current control system and the LHD network. The number of staff is 46 engineers and several part-time workers. We take care of the development, the operation and the maintenance of LHD and the LHD peripheral devices with about 47 operators.

### 1. Fabrication Technology Division

The main tasks are the fabrication of experimental equipment, technical consultation, research and development of apparatus, technical cooperation and supply of experimental parts and materials. The division also administers all office work of the department. The staff of our division is mainly working in the central workshop. In our division, we received about 400 jobs for the fabrication of devices in this fiscal year. 95% of them could be fabricated in our central workshop. We support the construction of the devices and their control systems as requested from each research division.

#### (1) Phase detection circuit

The circuit (Fig.1) was designed and manufactured for the FIR heterodyne laser interferometer system on LHD. The 3-channel phase comparison part of this circuit is integrated on a FPGA (Field Programmable Gate Array). With the FPGA, it is possible to program the inner logic circuit flexibly and the size of this circuit can be downsized.

We manufactured 10 circuits, which supplied LHD(5 units), CHS(1), Kyoto University(2) and Chubu University(2). An Automatic Fringe Jump Corrector (AFJC) was added to the circuits for LHD use.

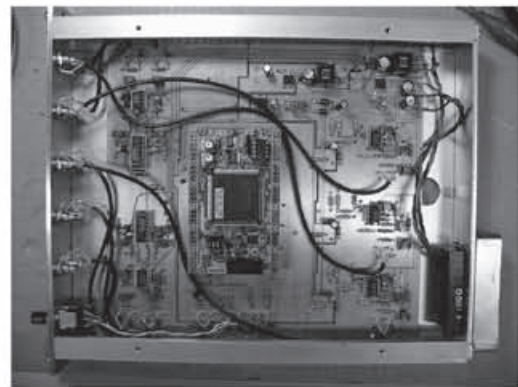


Fig .1 Phase detection circuit

#### (2) Timing demodulator prototype

The circuit (Fig.2) receives experiment timing signal from the LHD central control system through optical fibers and de-modulates it. The control data for the circuit is detected from the optical signal, the trigger for synchronization with the experiment sequence and clock signal are sent to plasma diagnostics instruments. The circuit is constructed from a timing de-modulator and Linux computer to control the de-modulator, which are integrated in a one-chip FPGA. We will manufacture the 10 circuits for practical use after the proto -typing phase.

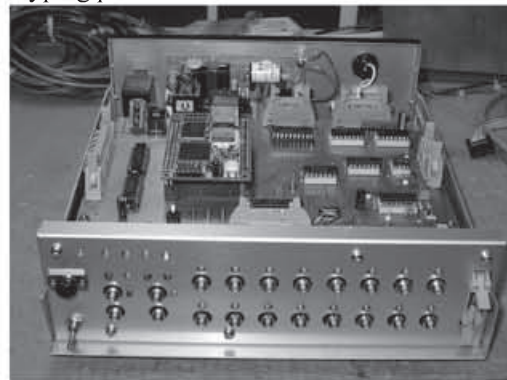


Fig.2 Prototype of the timing de-modulator

#### (3) A concave mirror for the Microwave Imaging Reflectometer (MIR).

An MIR is developed in order to visualize electron density fluctuations in LHD. (Fig.3) In an MIR system, to focus the reflected microwave from the plasma to the detectors, it is necessary that we manufactured a large elliptical concave mirror. The material of the mirror is an aluminum alloy; the size is 500mm in the major axis, 450mm in the minor axis and a thickness of 40mm.

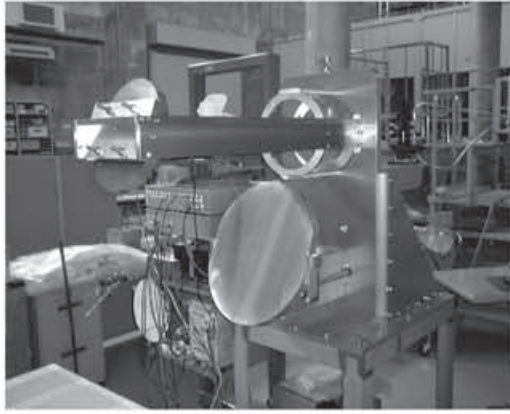


Fig.3 Microwave Imaging Reflectometer (MIR)

The mirror material is annealed before cutting it is cut. Annealing of the material aims to modify the crystal structure, and to remove the residual stress in the material. It takes about 192 hours to cut the material, because the cutting speed is slow to minimize the roughness of the mirror surface. The mirror is installed in the vacuum vessel, and is operated by remote control. In order to prevent perturbation to the magnetic field on LHD, non-magnetic materials must be used. Examples these are, the carbonized titanium sliding bearing, the SUS304 ball bearings and the ultrasonic motor. (Fig.4)



Fig.4 Sliding bearing

## 2. Device Technology Division

The Division supports the operation, the improvement and the maintenance of LHD, the peripheral devices, the cryogenic system for LHD and the super conducting R&D devices at SC magnet Laboratory.

### (1) Operation and Maintenance of LHD

LHD operation started on August 8 in the ninth-experimental campaign, the cryostat was evacuated as usual. The evacuation of the plasma vacuum vessel began on August 9. We found ten vacuum leaks; five CF-flanges of the plasma vacuum vessel, four helico-flex gaskets and a gate-valve had a seat leak. The vacuum leaks were fixed on Aug. 23, and the coil cool-down was started at Aug. 31. The cooling down was completed on Sep. 26.

The first energizing of LHD in the ninth-campaign was on Sep. 27. The number of operation days of the SC-coils was 66 days. The number of days of the plasma experimental period was 142 days. The warm up of the S.C.-coils was started on Feb. 17.

During this period, the interruption of commercial power occurred seven times due to thunderstorms. They were on July 20, 27, Aug. 7 and Aug.26.

The LHD water-cooling system had an accident during the 9th operation.

### (2) Measurement of pumping speed of the vacuum pumping system for LHD

We measured the pumping speed of the vacuum pumping system for LHD. Hydrogen gas with a constant gas flow rate  $Q(\text{Pam}^3/\text{s})$  was injected into the LHD by the gas puff device, and we measured the pressure  $P(\text{Pa})$  at that time. The result is shown in Figure 5. The pumping speed corresponds to the gradient of the  $P$ - $Q$  graph. We know that (1)the pumping speed of vacuum pumping system for LHD was 273  $\text{m}^3/\text{s}$ , (2)the pumping speed of LID device was 242  $\text{m}^3/\text{s}$ , and (3)the pumping speed of Vacuum pumping system + LID was 407  $\text{m}^3/\text{s}$ . The theoretical pumping speed derived by simple calculation is (1) 244  $\text{m}^3/\text{s}$  and (2) 204  $\text{m}^3/\text{s}$ , and there was no big difference between the experimental value and the theoretical value. We showed that we could measure the pumping speed even through the vacuum vessel has a big volume like as in LHD.

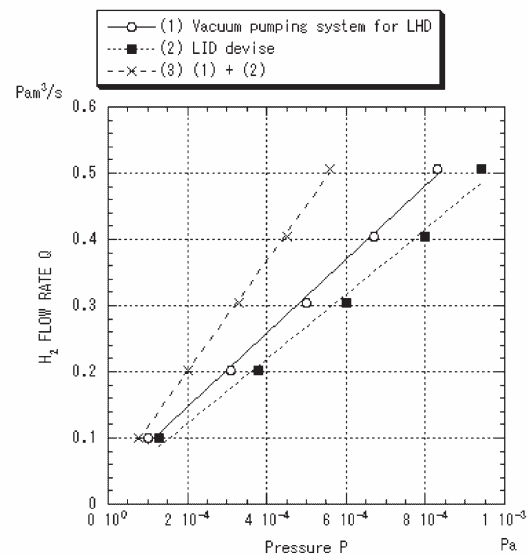


Fig.5 Pumping speed of the vacuum pumping systems  
(3) Elasto-plasticity analysis of hook.

The 30 ton crane hook the guide rail of a large shielding door due to operator error. The hook was deformed by 20mm due to this accident. The influence on the guide rail of the large shielding door and on this hook were examined through analysis using the CAE program ANSYS. This residual displacement of 20.5mm was caused by a load of 68.5ton. Figure 6 shows the stress on the hook by

elasto-plasticity analysis.

This result shows that the accident stress was more than 68 ton. After that we found that the inter-lock for the over load of this 30 ton crane was 80 ton. We will have to change this inter-lock value soon.

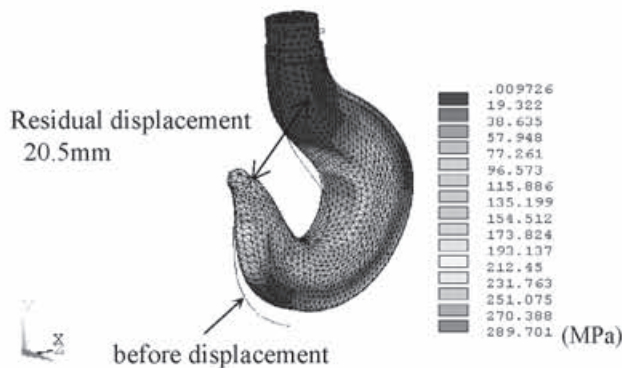


Fig. 6 Stress on hook at 68.5ton  
(3) Water-cooling system stopped by accident.

At midnight on December 2, 2005, an accident occurred with a check valve of a load pump of the cooling water system (the 4th line, # 2). Because supply of cooling water stopped temporarily due to this accident, the LHD refrigerator system was emergency stopped by this accident.

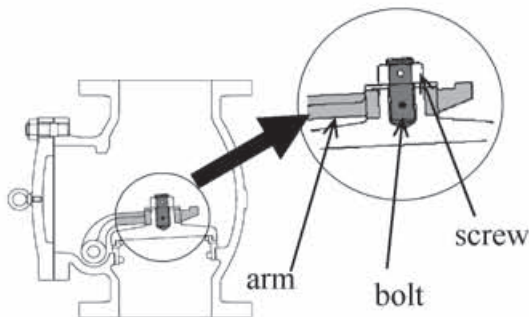


Fig. 7 Cross section of the check valve  
Regarding the condition of the damaged valve, a bolt that linked an arm to a valve disc was left out of the valve disc (in figure 7), and the valve disc came off from the arm as shown in figure 8.



Fig. 8 Inside of damaged valve  
After this experimental period, when we checked the other

check valves of the same model as the damaged valve (the 4th water-line, # 3pump-line, #4pump-line), we found that there was a wobble in a bolt that linked the arm to the valve disc in the #4pump-line. After a result of dismantling the valve to examine it in detail, we found that a spring pin to fix the bolt was broken. This phenomenon says that a spring pin of the # 2 check valve was broken by vibration, and the threads of the bolt and the valve disc wore down little by little.

In addition, the operation time of the #2pump-line was about 40,000 hours and about 13,000 hours for the #3 and #4 pump-lines. Therefore it is thought that a spring pin may break before its operation time exceeds 10,000 hours, so we replaced all of these check valves with new ones this time. And in the future, we will carry out periodical checks of the check valves each 10,000 hours.

(4) Recover operation of the Helium Refrigerator/Liquefier  
The helium refrigerator for LHD has an equivalent refrigeration capacity of 9.1 kW at 4.4K, it includes eight sets of the oil injected screw-type compressors. The total consumed electric power is 3.49 MW with 1100 g/s mass flow rate.

During the steady-state cooling phase, the water cooling system was stop by an accident. The water flow late interlock system stopped the turbines and the helium compressors. An emergency stop program stopped the LHD Helium Refrigerator/Liquefier system in safely. But 6000m3 of Helium gas was lost in this accident. The water cooling system was fixed less than two hours after the accident, and we could turn on the compressors and the turbines by the end of that night.

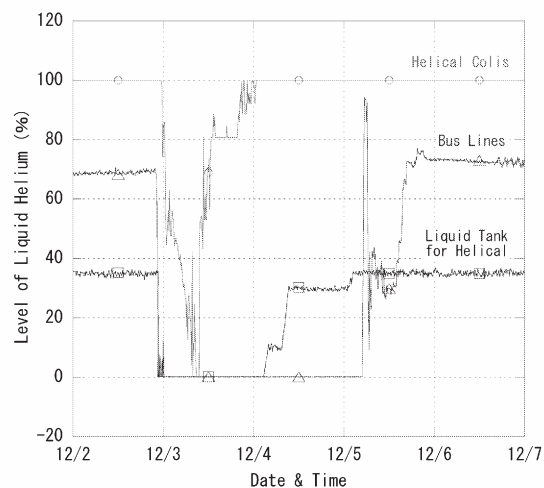


Fig. 9 Liquid helium level behavior during accident

Figure 9 shows the liquid helium level behavior of the helical coil, the helical liquid tank and the bus line. The helical coil liquid helium level was recovered in less than 1day. The liquid helium level of the bus-lines had took 3days.

The reason is that we worried about the variation in the



temperature of the inside of the cryostat. We must charge lots of helium gas and purify the charged helium gas before the liquefy operation, after that we recovered the bus line liquid helium level.

#### (5) Technical Support for SC magnet Laboratory

A cryogenic system with a capacity of 200 l/h (500 W at 4.2 K) and a high dc current supply of 75 kA at 21 V, including a cooling water system with an 800 kW heat exchanger, was installed at the CSL. Operation of these test facilities and daily inspection of them are carried out by the members of the Device Technology Division. In particular, we are responsible for the annual duty inspection of the cryogenic system, regular maintenance of the cooling water system and preparation for the experiments.

### 3. Plasma Heating Technology Division

The main works of this division are the operation and the maintenance of plasma heating devices and common facilities. We have also provided technical support for the improvement and the development of these devices, and the installation of new devices.

Steady state plasma experiments by the ICRF system with a power level of more than 1MW have been proposed as one of the main targets of the mission experiment. Though the power level of the ICRF system was below 1MW, the total injection energy of all the heating devices was about 1.6 GJ exceeding last year's record for this mission. Other than this effort, NBI(#4) which has a positive ion source and a pulsed high power gyrotron(#8) connected with evacuated transmission lines have been newly installed in order to upgrade the plasma performance. The details of these activities are as follows.

#### (1) ECH

##### (a) Gyrotron Operation & LHD experiment

During the 9th experimental campaign, we could inject millimeter waves with a total power level of over 2MW into LHD by using 8 gyrotrons for pulsed operation. The reliability of the ECH operation for the experimental shots was 90%. The average of the transmission efficiency of all waveguide lines was about 68%. A continuous wave (CW) gyrotron worked stably without any trouble and assisted steady state mission experiments by ICRF as a main heating source. We have newly installed a pulsed 800 kW output gyrotron(#8) at 84GHz instead of the gyrotron(#7) at 168GHz in order to increase the power level of the fundamental frequency. At the same time, we have modified the transmission line for this gyrotron from air tight to vacuum type in order to reduce the risk of arcing that had limited the power level of transmission so far. In the evacuated transmission line using two pumps the vacuum level reached down to  $1\sim 1\times 10^{-2}$  Pa. The operation of the newly installed gyrotron(#8) started in November, the power level of the injected millimeter waves from this gyrotron into LHD was 500kW.

##### (b) Compact gyrotron stand with insulating oil jacket.

We installed a new 84GHz gyrotron for the 9th experimental campaign. Since all existing gyrotron tanks were occupied, we needed to make a new one. Due limited setting space, and furthermore in order to reduce the volume of insulation oil, we decided to make a compact ( $1\times 2\text{ m}^2$ ) gyrotron stand which supports the gyrotron, super conducting magnet (SCM), matching optics unit (MOU) with an insulating oil jacket for introducing high voltage. The whole view of this stand after the gyrotron installation is shown in Fig. 10. The

advantages of the jacket structure are the conciseness of the maintenance and the compactness of the insulating oil volume. This oil jacket has two high voltage (cathode/heater and body) inputs, two sets of cooling water inlet and outlet and a view port. We installed this stand in a new area, and enabled up to 500 kW injection power to via an evacuated corrugated waveguide with an inner diameter of 88.9mm.

#### (c) Measurement of the beam pattern in the LHD vacuum vessel.

We confirmed the transmitted millimeter wave beam position in the vacuum vessel by the setting a Kapton sheet on the mid plane of LHD. We injected a gyrotron output beam and observed the temperature rise of the sheet by a thermal imaging camera. Table 1 shows the results obtained from such a measurement. Measured spot size, shape and position are generally in good agreement with the designed ones. Large discrepancies in the spot position between designed and measured one are found in the 1.5Lin antenna. These discrepancies are reproduced by a cross check using a He-Ne laser. It can be explained by the deviation of the steering plane mirror angle of 1 degree. This deviation might be caused by some external forces acting on the steering mechanism during the maintenance or cleaning process done after the final check using He-Ne laser at the initial setting. The other large deviation is found at the 2O antennas. Unlike other antennas, the drive of the 2O antennas was carried out by push and pull of a wire and a pulley. We checked antennas in the air, the movements of mirrors were smooth, and the reproducibility did not have any problem. A wire was driven without skidding. This deviation might be caused by a slight stretch of a wire. All of these deviations are corrected by the adjustment of the offset parameters in a control program.

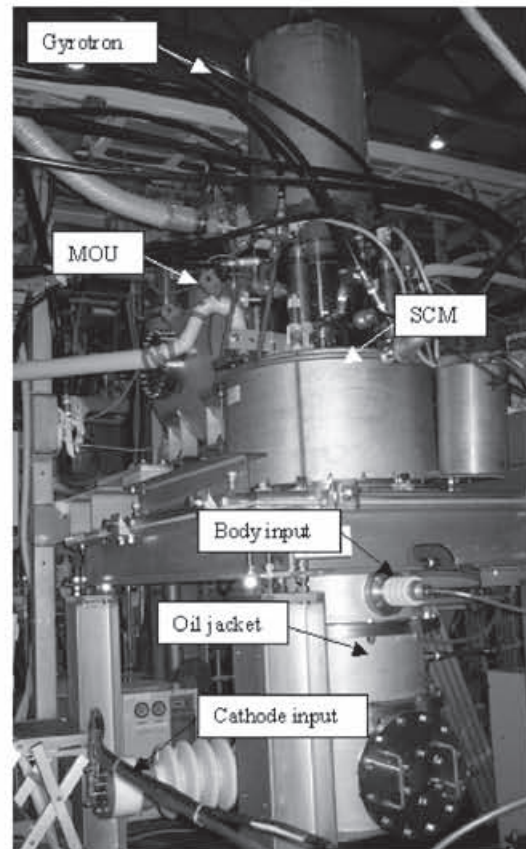


Fig.10. New gyrotron tank arrangement

antennas	1.5L in	1.5L out	2O left	2O right	5.5U out	9.5 in	9.5U out
radius direction (m)	-0.1	-0.015	—	—	0.01	0.01	0.03
toroidal direction (m)	-0.03	0.03	> 0.1	> 0.1	0.01	0.01	0.01
poloidal direction (m)	—	—	> 0.1	> 0.1	—	—	—

Table.1. Measurement of beam position

(2) ICRF

(a) ECH camphor injection

In the eighth experimental campaign the long pulse plasma discharge of about a half hour was achieved but was terminated by a sudden increase in the radiated power and the subsequent decrease in the electron temperature. This phenomenon occurred just after the impurity (eg., Fe) injection following sparking on the vacuum surface. An instantaneous injection of ECH (Electron cyclotron heating) power was tried just before the plasma collapse using a sudden increase in the electron density as a trigger. The triggering electric circuit is shown in Fig.11.

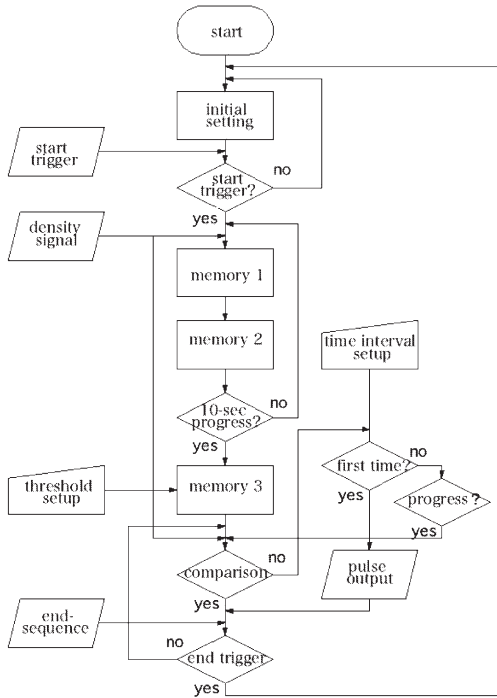


Fig. 11 Time evolutions of plasma parameters and heating power in the long-pulse plasma discharge of 1905seconds.

The electron density measured by FIR interferometer was employed to judge whether the ECH power was injected or not. The threshold setup can be change from 1.2 to 2.0 times that averaged electron density for 10 s before the event occurs. A time interval circuit is also employed in order to maintain the ECH power duty cycle, i.e., 1/150. The time is variable from 10s to 990s. In the ninth experimental

campaign trials were carried out of the long pulse discharge with more than 1MW of ICRF heating. A trial of the instantaneous ECH power injection (which we call ECH camphor injection) was carried out to restore the electron temperature using the sudden increase in the density as a trigger, as shown in Fig.12, where the plasma of  $n_e=1 \times 10^{19} \text{ m}^{-3}$ ,  $T_e \sim T_{i0}=1.2 \sim 1.3 \text{ keV}$  was sustained for 285 s with an applied RF heating power,  $P_{\text{ICH}}(1.33 \text{ MW}) + P_{\text{ECH}}(0.11 \text{ MW})$ . A small amount of heavy metal penetrated at 178.2 s, but the subsequent density increase was less than 25% (the level set to launch ECH power injection as the trigger threshold) and was not enough to trigger such ECH power injection. Heavier metal penetrated at 178.4 s. accompanied by a sudden increase in the electron density and a reduction of the electron temperature. Then the ECH power was simultaneously injected as shown in Fig.2; the electron temperature was increased to 2.1keV and the electron density was decreased to  $0.9 \times 10^{19} \text{ m}^{-3}$ , as often observed in the high electron temperature plasma discharge.

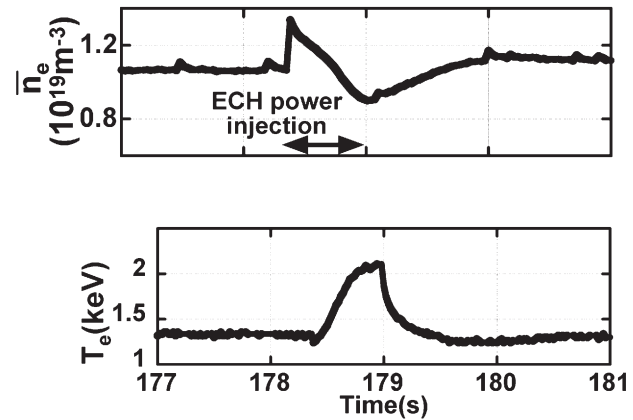


Fig.12. Total heating energy vs. average magnetic axis with the swing width

(b) Route change of the transmission line for 3.5U antenna

We had to change the route of the transmission lines for 3.5U and 4.5U antennas, since the newly installed LHD-NBI#4 at the southeast part of the LHD main hall interfered with them. Therefore, we removed the transmission lines and cables for the 3.5U and 4.5U antennas that had been installed until the eighth experimental campaign. We removed and transferred the stages for the transmission lines. Made a new route for the transmission line for the 3.5U antenna which was narrower in space and had more bends as compared with the former route. So, we need many corner components (L type coaxial tube) for the transmission line. As a result the number of the coaxial tubes used between the antenna and the stub for the 3.5U antenna increased from 19 to 24 pieces. The construction of the new stage for the transmission lines was completed at the space between C1 stage and C2 stage, thanks to the united efforts of the staff from the Device Technology Division.

(3) NBI

(a) The construction and operation of BL4

We constructed the fourth beam line for LHD (BL4) and operated it. (Fig.13) Although BL4 is a positive-NBI system, almost the same design concept as BL1-3, which are negative-NBI systems, was applied for the cost reduction.

The main specifications of BL-4 are as follows.

- Beam Energy : 40keV ( $H^0$ )
- Beam Power : 3MW(with two ion sources)



: 6MW(with four ion sources / upgrade)

Two years ago, the BL4 construction plan with two ion sources was approved. The construction began in March last year, and finished in October last year. We constructed the positive-ion sources for BL4 in May last year, and tested them at the NBI test bed. These ion sources are world's largest ones as a positive-NBI system (Size: 93cm x 47cm x 49cm, Weight: about 640kg). The maximum ion beam current recorded over 100A with one-ion source. At the beginning of the ninth experimental campaign, the beam injection into the LHD with a port-through power of 0.7MW (the beam energy of 27keV and the ion acceleration current of 50A) was successfully performed. About a month later, the design values of beam energy (40keV) and beam current (150A) were simultaneously achieved, and port through power is beyond 3MW. But in this campaign, long pulse operation was impossible, because of beam concentration on the residual ion beam dump. The improvement of the residual ion beam dump is necessary for 10sec beam operation, which is the specification. Although an NBI system with this specification is not new any longer, this quick achievement of the specification and the reliable operation were brought by our NBI group's activity and the high technical capabilities of the manufacturers. After the last experimental campaign, BL4 has been modified for upgrading the performance with four ion sources. We will inject over 6MW of neutral beam from BL4 into LHD in the next experimental campaign.

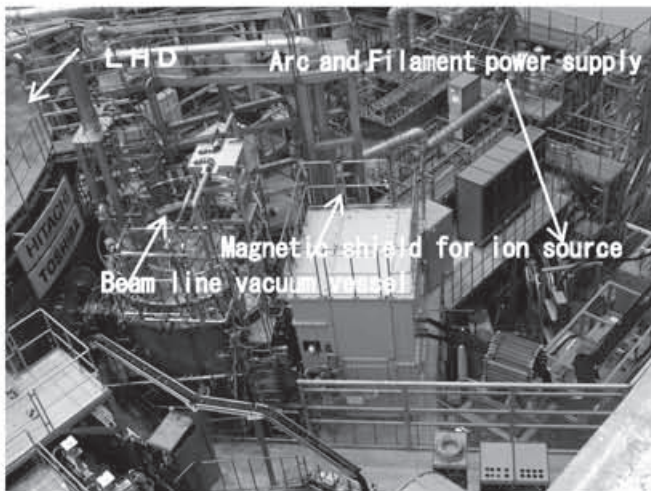


Fig.13. Over View Photograph of BL-4

#### (b) TV monitoring system for LHD-NBI#4 device

The fourth neutral beam injector(NBI#4) has been newly installed in the LHD Hall. This is a positive-ion-based NBI and is utilized for plasma-ion heating and the measurement of the ion temperature profile. NBI#4 has a power supply which generates 40kV. Ion sources are electrically floated at that high voltage against the beam-line stage when a positive ion beam is produced. Therefore, it is important for the NBI system to work normally with no electrical breakdown. Since we operate remotely the sequence controls for the beam conditioning and the beam injection at the Control Room outside the LHD Hall, a TV monitor system was constructed with CCD cameras to monitor the main facilities during operation. The viewed targets are the NBI device area fenced from the public, two ion sources located vertically up and down, the acceleration power supply facilities and the working area around the NBI injection port. These cameras

are connected with optical cables to the adaptors in a cabinet rack which is in the Control Room. This system is the same as the NBI#3 monitor system in which fine pictures are monitored with the optical cable transmission. In a rotating camera controlled remotely, image signals and camera control signals are multiplexed and transmitted. Higher-performance products were introduced into this system. 1) A rotating camera combines a color CCD camera with a zoom lens and a pan/tilt/zoom function, and all are in a compact package. 2) High sensitivity cameras are mounted for monitoring the ion sources because the ion sources are in dark environments, enclosed with the shield. As an image is darkened, the camera switches from a color mode to a B&W mode automatically by a function to maintain optimized sensitivity (minimum illumination: 0.8lux for color / 0.07lux for B&W). 3) A monitoring display is a 20-inch LCD panel in place of a CRT display. The displays monitoring the NBI#4 device are lined along with the other NBI monitors and remote-camera controllers on a table for the NBI operation. So all NBI device can be watched there.

#### (c) Data acquisition system in NBI

In NBI, PC-based measurement instruments "WE7000" are utilized to acquire various kinds of data such as output voltage and current of the power supplies, temperatures of the beam-line components, and cooling water temperatures and water flow rates of the electrodes. The data acquisition system consists of a PC and WE7000 stations, which programs are linked with network cables. Although a control program is attached to the WE7000 system, we coded some original programs in order to have the flexibility to respond to special situations in our experiments. There are four beam-lines for LHD, and some parts of the acquisition programs are common. There, however, are particular parts in the programs for individual beam-lines. The program consists of various subroutines connected to each other, and users can adopt some routines for their own purpose. Acquisition data are displayed in text form and graphical plots on a computer screen, and users can understand easily the present situation of each beam-line. So, this acquisition system is very useful for the proper operation of the beam-line.

#### (4) Motor-Generator (MG)

The MG is used to supply the pulsed power to the NBI for LHD and the CHS magnetic coils. The MG had generated 40,991 shots in this fiscal year and 343,368 shots since its construction. The operation time counted 1,945 hours in this fiscal year and 15,627 hours, in total.

Under the annual inspection in this fiscal year, the following components were checked: oil in the MG, a rectifier for excitation, a circuit breaker, two air-break switches, an air compressor, 35 protective relays and 14 vacuum circuit-breakers. Besides the annual inspection, the two switches of the air compressor indicated in with the units of Pascal, fifty-four batteries of the UPS for the MG control computer and heaters for antifreeze that exist in the cooling tower were renewed. During the next LHD experimental campaign, the length of the brushes would be worn below the critical level. So, new brushes should be installed before the start of the next LHD experiment. As for a human safety, a monitor for deficiency of oxygen was set up in the basement of the MG building.

## 4. Diagnostics Technology Division

This division supports utility construction and the device

installation work for the LHD diagnostics, and the development, operation and maintenance of the diagnostic devices and of the data acquisition system for LHD and the plasma experiment. For the ninth experimental campaign, some diagnostics were newly installed and reconstructed on the LHD: the PSD (Position Sensitive Detector), some diagnostics removed from the 5O ports of LHD for the new NBI construction after the eighth experimental campaign etc.

In this experimental campaign, the diagnostic data of LHD plasma by the HIBP was clearer than those of the eighth one by the modification of the beam alignment and improvement of the signal detectors. A new data acquisition system was developed for calibration of the Thomson Scattering Diagnostics system, which can collect all channels (~1000) calibration data at the same time. Some troubles were caused by some diagnostic systems, for example, by the ECE system, by the Thomson data acquisition system, and so on, but the plasma experiment was not stopped by those troubles in this experimental campaign.

Our principal tasks in this fiscal year are described in the following.

#### (1) Development, Operation and Maintenance of the Radiation Monitoring System

A radiation warning information system using e-mail messages was developed and installed in the radiation monitoring system of the NIFS site. In this system, when a radiation warning occurs, the e-mail message will be sent to the manager’s portable telephone in the radiation control office of NIFS.

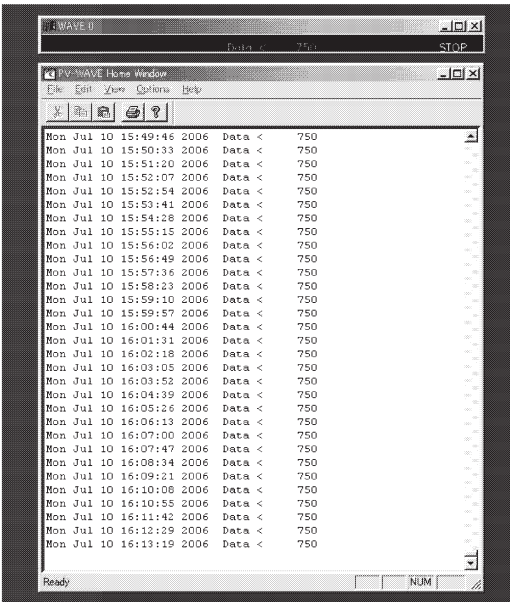


Fig.14 Display of the application program for the radiation warning information system.

#### (2) Thomson Scattering Diagnostics

In the LHD Thomson scattering diagnostic, calibration data has to be acquired for all of the about 100 polychrometers

regularly. Thus, the connection was changed to each polychromator to get calibration data. In this fiscal year, the data acquisition system for calibration was constructed, which can collect all channels (~1000) of data at the same time. It is constructed with 13 PXI-6225 ADC’s (National Instrument) that have 13x80 inputs. The schematic view is shown in below. The control application was developed with LabVIEW.

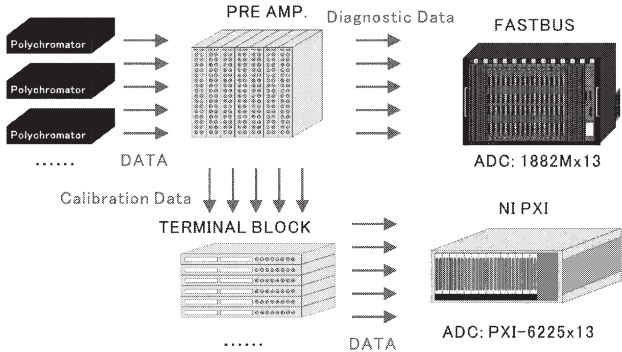


Fig. 15 The schematic view of the calibration and diagnostic data acquisition system

#### (3) Operation and Maintenance of FIR Diagnostics and Microwave reflectometer

The operation and the maintenance (for example, high voltage power supply, vacuum system, supplied gas system, phase detection circuit, dehydrator, water cooling system etc.) were responsibly executed. Therefore in this ninth experimental campaign, in almost all shots, electron density data was taken completely. So it contributed widely to the LHD plasma experiment.

#### (4) Improvement Designs for the HIBP Ionization Source

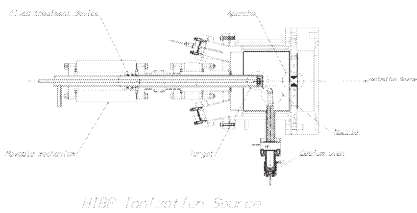


Fig. 16 HIBP ionization source

Three improved designs were made for the HIBP ionization source. (1)The center part in the aperture electrode opening was squeezed and the shape was optimized. (2)The center part of the target electrode was cut down spherically in the improved design so that the distance from the aperture opening would be uniform. The target position was improved to be continuously changeable. The quartz pipe, which covers the target and the prop, was also



improved to be fixable at an arbitrary position. Moreover, the target electrode was cooled by water so that cesium may adhere easily. (3) Heaters were installed directly on the cesium oven and the cesium nozzle in the improved design so that the entire cesium steam could reach the target. In addition, the top of the cesium nozzle was bent towards for the target for the efficient supply of cesium.

(5) Vacuum Leak Test with the Test Chamber in the Plasma Diagnostics Laboratories

Preliminary vacuum leak tests were carried out on diagnostic devices to be used for the LHD plasma experiment and the parts to be used in these diagnostic devices by using the leak test chamber in the Plasma Diagnostic Laboratories.

For example, a BaF2 window used for an interferometer and the vacuum parts used for the soft x ray diagnostic system, the Li beam probe diagnostic system, the MLM spectrometer, and the laser blow off system, the special flange used for the MIR diagnostic system and etc. We carefully tested the vacuum components. Therefore, in this 9th experimental campaign, the plasma experiment was not stopped because of diagnostic device vacuum leakage.



Fig. 17 Snap shot of the vacuum leak test in the Plasma Diagnostic Laboratories

(6) Trouble of ECE device and the correspondence  
In the LHD plasma, the measurement of the electron temperature from the ECE (electron cyclotron emission) device has been a useful diagnostic tool. Trouble occurred in the ECE device including the Michelson interferometer in the latter half of the ninth experimental campaign. The cause of the trouble was an abnormal signal in value reading part of a linear scale for the detection of the mirror position in the spectroscop of the Michelson interferometer device. The linear scale and the photo-coupler make a pair function, from which a standard pulse signal is generated. A mechanical small scratch occurred on the linear scale surface. It made the reading abnormal and the accurate mirror position was not able to be detected. This time we exchanged the full set of the relevant section for a new one and confirmed that it passed the basic running test. We will be able to offer the new physical measurement data through this maintenance in the tenth experimental campaign as in

the previous campaigns.

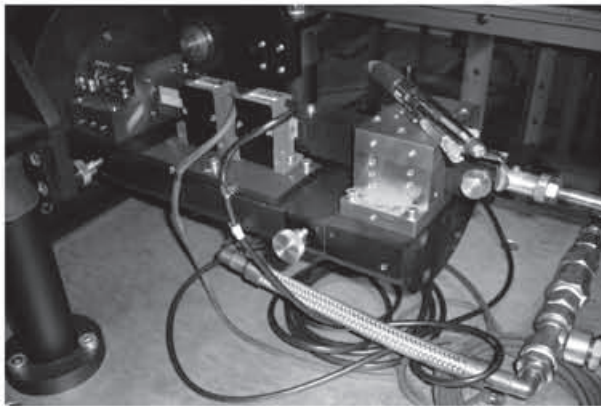


Fig. 18 View of the one pair position sensor device to linear scale and photo- coupler

(7) Development of Data Acquisition System  
To support the steady-state plasma experiments in LHD, new functions have been developed for the LABCOM data acquisition system. Using new WE7000 and PXI digitizers for continuous ultra-wideband data acquisition at 80 MB/s, the system is now able to perform data acquisition, storage, and server-to-client transfer fully in real-time. To manage the high amount of data for long-pulse experiments, the system has been modified to use 64-bit integer values for the number of samples, to segment the compressed data into multiple blocks by using the “titz” library, and to use the JPEG-LS algorithm for compressing image data. Its merit as a complete solution for the next generation of fusion experiments has been demonstrated by faultlessly recording an 84 GB shot.

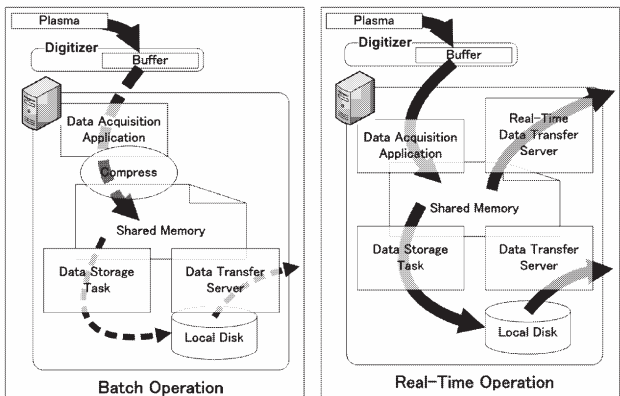


Fig. 18 Summary of LHD Data Management System

### 5. Control Technology Division

The Control Technology Division has contributed important technological parts in the system management and system development for the fusion research in this institute. The works of system management are as follows; the LHD

central control system, the LHD super-conducting coil power supply system, the LHD-LAN system, the LHD numerical analysis system, the NIFS campus LAN system, the CHS data acquisition system, etc. The works of system development in this year are as follows; an improvement of the LHD coil current calculation program for the LHD operator, a development of readout electronics for the neutron detector, a development of a coil winding machine for 1 MJ class SMES, an improvement of the ICRF stub tuner controller, a numerical simulation of the pulse tube refrigerator and the thermo-acoustic generator, etc. The activities in detail of this division are as follows.

### (1) Improvement of the LHD coil current calculation program for the LHD operator

Setting the helical and the poloidal coil currents is one of the most important operations in terms of the safety of LHD. At the setting of those coil currents, care must be taken that each current value is under the maximum value for the magnetic field condition, and the necessity and the current values for the pre-stressing of those coils must be decided. It is necessary to not only confirm the setting to an accurate value but also to set it according to some decided operation rules. Until the eighth experimental campaign, we were applying the rule manually when we calculated the coil current. We have developed the automatic calculation program to avoid the operation mistakes. Besides, we reviewed the vague rules. In the next experimental campaign, we will develop the program to included it in the transmission of the coil current to SC coil control system.

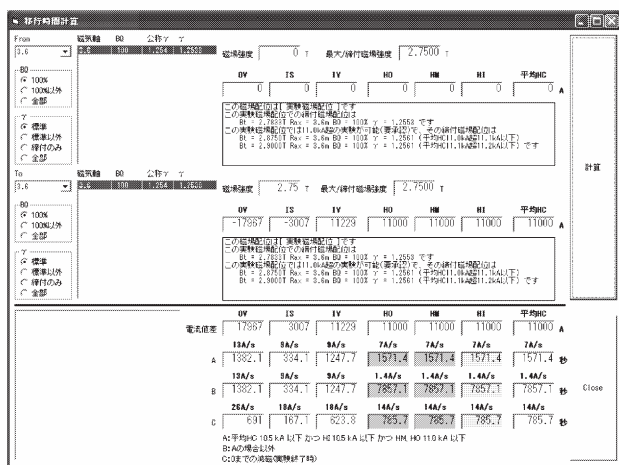


Fig.19 Console window of the LHD coil current calculation

### (2) Liquid stub tuner controlled by multi computer system

The world record input heating energy of 1.6GJ was achieved in the long-pulse plasma discharge in the 9th experimental campaign of LHD. We have continued improving the feedback control of an ICRF liquid stub tuner since the eighth experimental campaign. It was one of the keys to achieve the long-pulse plasma discharge. The liquid

stub tuner control system is composed of a pulsed motor controller, AD/C, Digital I/O Multi-computer system of VME, Owner LAN and Unix server. This system controls the start/stop and CCW/CW directions of the pulse-motors of 10 liquid stub tuners monitoring the reflected and forward RF powers.

The LAN control line was not used in this fiscal year to employ other control methods. Therefore, we suffered noise troubles arising from employing this modification. The cause depends on a CW/CCW pulse inducing the electric current between the pulsed motor control board and motor driver. A CW/CCW pulse flowed into other power supplies in the control box and influenced the next motor. We rewired the control box to improve it. Figure 20 shows the control box, which could reduce the influences of electric noise. As a result, the ratio of the reflected to the forward RF power could be kept less than 1% during the long-pulse plasma discharge.



Fig. 20 Control box of the liquid stub tuner

### (3) Development of Readout Electronics for a Neutron Detector

The readout system for the neutron detector of the heavy hydrogen experiment has been developed. The output signal of the neutron detector is generated from the electrolytic dissociation chamber. In order to measure accurately for the burst mode events of the neutrons, the signal processing system will use the pulse counter together with the current integrator. The proto-type readout electronics were designed and manufactured in this year.

The proto-type amplifier for the pulse counter is constructed a CS-510 and a MA-405. The CS-510 of a hybrid charge sensitive pre-amplifier and the MA-405 of a hybrid pulse-shaping amplifier with pole-zero cancellation for use with a wide range of the detectors was adopted. These hybrid amplifiers were developed and used at the TRISTAN project, High Energy Accelerator Research Organization (KEK) in 1990.<sup>[\*]</sup> Figure 21 shows the block diagram of the amplifier circuits for the pulse counter. Assuming the input capacitance of 1pF, the output voltage at the pre-amplifier ( $V_{CS-510}$ ) is proportional to the number of signal electrons. In the case of an input for a CS-510 expected to be  $2.5 \times 10^5$  electrons, the output will be as follows.

$$V_{CS-510}=Q/C=(1.6 \times 10^{-19}) \cdot (2.5 \times 10^5)/(1 \times 10^{-12})=40 \text{ [mV]}$$

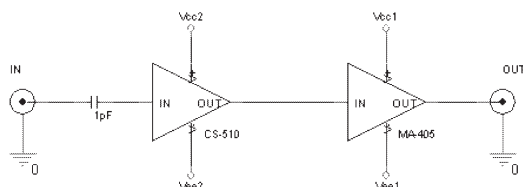


Fig. 21 The Schematic of the proto-type amplifier for the pulse counter. This circuit consists of a CS-510 and a MA-405.

The circuit characteristics of the proto-type pulse counter are as follows. The total gain (charge to volt conversion coefficient) and inverting rise time is measured to be 0.8 V/2.5x10<sup>5</sup> electrons and 5 ns, respectively. A picture of the amplifier output is shown in figure 22. The inverting amplification factor of the MA-405 stage is found to be 20.

The other side, the proto-type amplifier for the current integrator was made of three AD845(operational amplifier, Analog Device) and a MAX4278(unity voltage gain buffer, Maxim). The 1st stage of this circuit is constructed as a current to voltage conversion integrator with a time constant of 10 μs. The 2nd and 3rd stages are constructed as gain and buffer drivers with an amplification factor of 1000. Figure 23 shows the block diagram of the amplifier circuits for the current integrator.

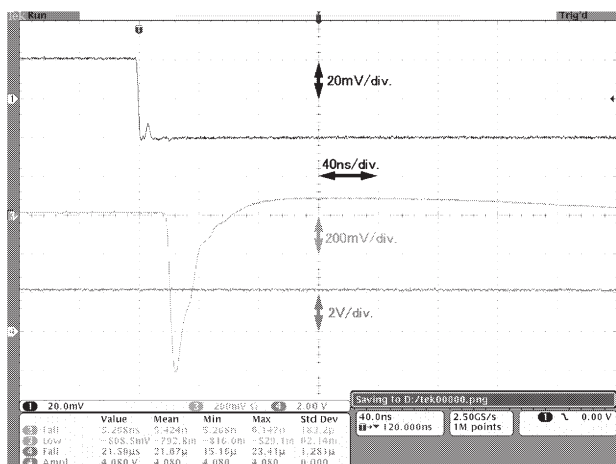


Fig. 22 The Picture of the proto-type amplifier for the pulse counter output (middle) when a square pulse of 40 mV (top) was fed into the test-pulse input of the CS-510.

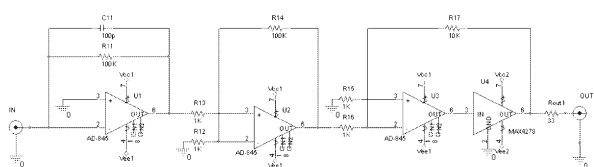


Fig. 23 The Schematic of the proto-type amplifier for the current integrator. This circuit consists of three AD845 and a

MAX4278.

The circuit characteristics of the proto-type current integrator are follows. The total gain (current to volt conversion coefficient) and inverting rise time is measured to be 0.1 V/nA and 20 μs, respectively. A picture of the amplifier output is shown in Figure 24.

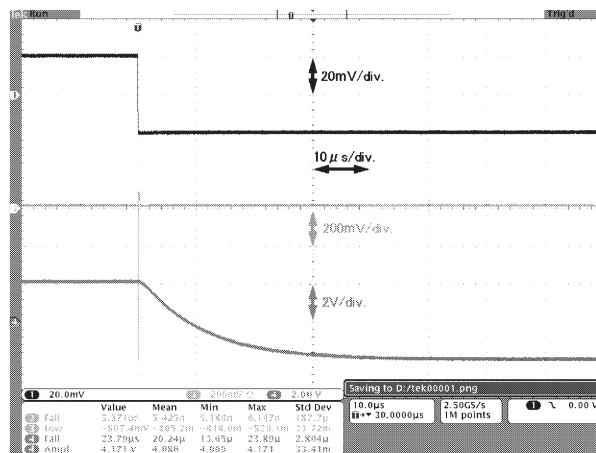


Fig. 24 Picture of the proto-type amplifier for the current integrator output (bottom) when a square pulse of 40 mV (top) converted for 40 nA with a 1 MΩ was fed into the input of the AD845

In the next steps, we will test the connection to the test chamber with a real signal input as a realistic operating condition for the application.

#### Reference

[\*] K. Tsukada et al., “Readout electronics for the vertex chamber of the TOPAZ detector at TRISTAN, KEK” Nuclear Instruments and Methods in Physics Research A300 (1991) pp.575-580.

#### (4) Development of coil winding machine for 1 MJ class SMES

We have developed a coil winding machine for a 1MJ class Super Conducting Magnetic Energy Storage (SMES) coil since 2002.

In the winding control it is necessary to control the twist angle of the conductor with an accuracy of plus or minus five degrees to suppress AC losses which are created while energizing. Therefore, the conductor angles have been collected with plural proximity sensors and they are analyzed for twist control with a personal computer.

In the 2004 fiscal year, a 100kJ class coil has been built as a proof of principle model and its excitation test was carried out successfully. This fiscal year, we modified the control program to cope with the 1MJ coil winding. The major modified points are as follows.

(a) The number of proximity sensor was increased from two to five, to research the detailed conductor behavior.



(b) A reflective photo-interrupter was placed near the coil bobbin. Its compactness enables it to rotate around the conductor to measure the actual conductor angle as close to the coil bobbin as possible. Consequently, it achieved an accuracy of  $\pm 1$  degree.

(c) A proportional control method was implemented to improve the following characteristic in case of a large error.

(d) The network communication method has been upgraded from UDP/IP with 10Base-T to TCP/IP with 100Base-T and the data collection code in the control program has been modified. As a result, the winding time was shortened by half and we were able to complete the 1 MJ coil within 90 days.

(e) The confirmation of the next twist angle and the tension control parameter which were judged manually has been completely automated.

The 1 MW class super-conducting pulse coil will be fabricated, adapting this new detecting technique. For the future step, we are planning to use the image data processing to improve the accuracy of twisted angle and the quality inspection of the conductor surface.



Fig. 25 The twist angle detector utilizing a reflective photo-interrupter

#### (5) Data Acquisition and Analysis system for CHS

The CHS data acquisition system (Cinos) consists of 10 similar sub-units. Each unit has a VME computer and various types of modules depending on their purposes. The total operating time of the Cinos computer system was about 2000 hours in this fiscal year. There was no shutdown time originating from troubles in the hardware or the software for the last two years. The Cinos was upgraded this year by adding peripheral modules and soft-ware resources. The added modules are a reflection memory module and AD/c modules. The purpose of this improvement is to keep the data acquisition time short even with an increase in the size of the experiment data. Main improvements are as follows:

(a) We replaced an old computer with a high-speed computer in one of the Cinos units last year, where the memory size was also increased from 768Mbyte to 1Gbyte. However, writing time into this 1Gbyte memory became

longer than before because the memory controller writes the data in turn. Some data related to the machine operation need to be displayed quickly after the shot. Therefore, we decided to add a VME reflected memory of 16Mbyte specially for such kind of data. Those data will be able to be referred more quickly than before. Since this memory is connected to the other Cinos units by 1.2 Gbaud speed fiber-optic, those data in this memory can be referred to from any other Cinos unit easily. This new memory system is still under development but will start to run soon.

(b) Five CAMAC fast AD/C modules (1MHz, 12 bit, 6 CH) have been installed on the 5 different Cinos units to meet with increasing data size.

#### (6) LHD-LAN Management

LHD-LAN has been provided for the LHD experiment since 1996. As the LHD experiment progresses, a larger number of computers has been connected to the LHD-LAN. They store a large amount of data, and therefore, require high-performance data transferring environments. Thus the Gigabit Ethernet (GbE) system has been installed in the LHD-LAN since FY 2000. In addition to regular management works, our new contributions for FY 2005 were as follows;

(a) Increase of L2 and L3 switches for LHD data acquisition server LAN.

(b) Upgrade of file server system for LHD domain users.

(c) Upgrade of NIFS-LAN gateway router for the LHD control building.

(d) Increase of SNET nodes.

(a) Due to the increase of data acquisition system, the high-performance GbE ports for them had become insufficient. The LAN upgrade has been carried out by two steps: Before the beginning of the 9th LHD experimental campaign, two Layer-2 switching hubs with 24 GbE ports were installed at first. After the campaigns, a new VLAN (Virtual LAN) was established using a Layer-3 switching hub (48 GbE ports) that was installed in LHD data acquisition server LAN.

(b) The file server system for the LHD domain, Microsoft Windows 2000 and Windows Server 2003 Active Directory domain, has been upgraded to provide a wider home directory area for each user. The new server system consists of a computer and a disk array system which has a pair of mirrored RAID 5 with a hot standby disk. Its total capacity is 1.5 TB. As a result, the disk quota for each user has been extended from 10 GB to 100 GB. Monthly backup to the tape library is also scheduled automatically for all the user files..

(c) The NIFS-LAN gateway router for the LHD control building has been replaced. The new equipment is a Layer-3 switch which consists of 2 GbE ports and 24 Fast Ethernet ports, providing two VLANs of NIFS DHCP-LAN and the operator's subnet.

(d) The LHD's remote participation system via Super SINET, namely, SNET was initiated in FY 2000. By FY 2004, nine nodes of SNET were established at University of Tokyo (Depart. of Technology and High Temperature



plasma Center), Nagoya University, Kyoto University (Uji and Yoshida Campus), Kyushu University, Tohoku University, Tokyo Institute of Technology and Hiroshima University. In this FY 2005, two additional nodes have been installed at Nagoya University (Yamazaki Laboratory) and Kyushu University (Research Institute for Applied Mechanics). The latest block diagram of LHD-LAN is shown in figure 26.

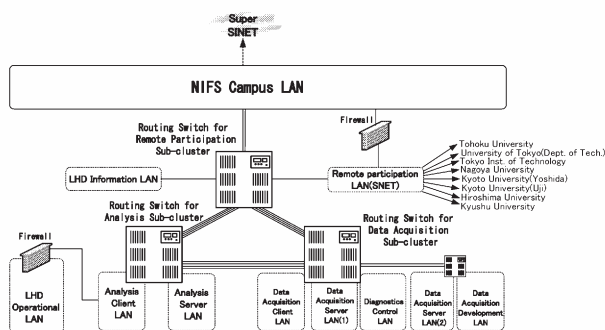


Fig. 26 The latest block diagram of LHD-LAN

#### (7) Renewal of a mailing list server with “Mailman”

The NIFS mailing list server was renewed in this fiscal year, because the warranty of the present mail server was expired. The old mailing list server had employed a mailing software “Majordomo” for seven years. However, there were some problems in “Majordomo” regarding the change of members, and the setting of sub-lists. In addition, version-up has been canceled for the past several years. We decided to use the free software “Mailman”, which doesn't have these problems. Since the “Mailman” has the web interface, we can access the server via the Web browser to perform management of the list. We chose the Solaris 9 operating system for the new server and installed necessary free software Mailman (mailman-2.1.6), Sendmail (sendmail-8.13.4), Python (python-2.3.3), and Apatch (httpd-2.0.53) etc. Switching from the old server to the new server was done without any trouble with both systems running. After having shifted to the new mailing list server, some part of the work for making lists are left to the list manager of the software. The duties for the server manager were decreased. Those results were as we expected.

#### (8) Introduction of SSL-VPN

It is an important issue to improve the security level in the network system. There was a demand that the staff of this institute be able to access a server from outside of the institute, a VPN (Virtual Private Network) server was used for this purpose until now. The VPN system had to be installed as exclusive software in the PC of a user because the VPN required the use of exclusive client software so far. An SSL-VPN system has been prepared newly to be introduced instead of the conventional VPN.

So the SSL-VPN system works on a browser so that the user need not install some client software, and it will offer

secure service. We set up the new server that introduced Free-RADIUS for network authentication and accounting. As the result of the test operation, it is clear that we can use the system with no trouble. This system will operate after the decision to adopt it by the institute.

## 6. Symposium on Technology and Technical Exchange

### (1) The Symposium on Technology

The Symposium on Technology was held on March 2 and 3, 2006 at the Institute for Molecular Science. There were about 400 participants from many Japanese universities, national laboratories, technical colleges and some industries. In this symposium 109 papers were presented in 5 oral sessions and a poster session. Technical experience and new techniques were reported and discussed. On the other hand, the Symposium on Technology of the practice or experiment for students was held with the same schedule at Tottori University. Seven papers were presented from our department; one of them was presented at the Tottori University. The titles of the presentations were as follows; The measures against the Dual System for Japan, Unification of Ultra-Wideband Data Acquisition and Real-Time Monitoring in LHD Steady-State Experiments, Approach of Department of Engineering and Technical Services in maintenance of peripherals for the Large Helical Device, Development of a Rotatable Mirror in Vacuum for Microwave Imaging Reflectometry in the Large Helical Device, Construction of a mailing list server by Mailman, One hour operation of a 84GHz gyrotron in LHD, Data acquisition system in NBI.

In the steering committee held during the symposium, Nagoya University was adopted as the next host organization and we exchanged our views frankly about the symposium as it ought to be. Figure 27 shows a snapshot of the poster session.

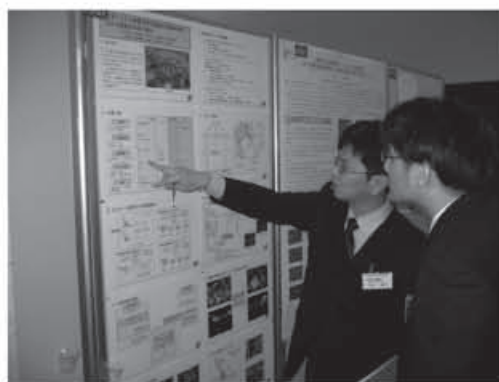


Fig.27 Snapshot of the poster session

### (2) The technical exchanges

The technical exchanges between our department and other institutes or universities were held in order to improve the technical skill of the staff.

Forty-six technical officials of other laboratories

participated in our 6 exchange programs in this fiscal year. The program names and participants were as follows; "Symposium on Safety and Health Management in a Laboratory" from 8 universities and 4 institutes, "Three-dimensional CAD simulation" from Kagoshima University and Kumamoto University, "Application of a multitasking machining center" from Ishikawa Technical College, "Safety sanitation management" and "Measurement and control technique using a PC" from the High Energy Accelerator Research Organization.

## V. Department of Administration

The Department of Administration principally handles general affairs and accounting work. In the very first fiscal year of the new institute, the effort has been made on the establishment of its organization and the preparation of facilities. Especially, intensive work has been done for the planning of construction in the new site which is urgently needed for promoting the Large Helical Device Project.

The Department consists of 4 divisions, namely, General Affairs, Joint Research, Financial Affairs, and Facilities, details of which will be described in the following.

### *General Affairs Division*

The General Affairs Division consists of 5 units: General Affairs, Documents and Public Relations, Personnel, Employee Relations and Science Information and Library. Major responsibilities of this division are to provide administrative support for the activities of the Board of Councilors and the Advisory Council for Research and Management, preparation of various ceremonies and events, documents and public information services, enactment of rules and regulations, general personnel administration and library services.

### *Staff Members*

(2005 Fiscal Year)

Director-General	1
Professors	41
Associate Professors	36
Research Associates	56
Administrative Staff	44
Technical & Engineering Staff	46
Visiting Scientists	24
Total	248

### *Books and Journals*

(2005 Fiscal Year)

Japanese Books	13,499
Books in Other Languages	44,110
Total (vols)	57,609
Japanese Journals	272
Journals in Other Languages	775
Total (titles)	1,047

### *Financial Affairs Division*

The Financial Affairs Division has 3 sections and 2 special members: Financial Affairs, Accounting, Contract, and 2 expert staff members in charge of Budget and Government Procurement. The sections and expert staff members are responsible for the financial management relating to budget, revenue/expenditure, corporate property, and supply of articles.

### *Settlement*

(2005 Fiscal Year)  
(in million of Yen)

Salaried Wages	2,111
Operating Cost	8,905
Equipment	0
Site & Buildings	12
Grant-in-Aid for Scientific Research	187
Total	11,215

### *Facilities Division*

The Facilities Division consists of 4 units: General Affairs Section of Facilities Division, Planning Section of Facilities Division, Control and Maintenance Section of Facilities Division and The Building and Repairs Section of Facilities Division. They are responsible for the office work relating to the budget, planning and designing, contract, supervision of the work of construction and maintenance for office building, campus road, equipment of lighting, telephone, power station, air conditioning, water service, gas service, elevator, crane etc. Recently, they have promoted Facility Management. (Facility Management combines proven management practices with most current technical knowledge to provide human and effective work environments. It is the business practice of planning, providing and managing productive work environments.)

Research stuff Building, Administration Building, the Library, the Guest House, the Central Work-shops, and six main laboratories; Cryogenics and Superconductivity Laboratories, the Plasma Heating Laboratories, the Plasma Diagnostics Laboratories, the Computer Center and Simulation Laboratories, the R & D Laboratories and Large Helical Devices Building, were constructed from 1990 to 2000.

### *Site and Buildings*

(2005 Fiscal Year)

Toki	
Site	464,445 m <sup>2</sup>
Buildings	
Total Building Area	39,235 m <sup>2</sup>
Total Floor Space	69,759 m <sup>2</sup>



### *Joint Research Division*

The Joint Research Division consists of four units, Research Planning Section, Research Promotion Section, International Academic Section, and Policy Planning Evaluation Section, which are in charge of arranging international cooperation, and inter university coordination, respectively. The latter deals with subsidy for scientific research and support the graduate school program.

### *Joint Research*

(2005 Fiscal Year)

LHD Joint Planning Research			Joint Research			Joint Research Using Computer			Workshop			Total		
Applications	Applications Accepted	Researchers Accepted	Applications	Applications Accepted	Researchers Accepted	Applications	Applications Accepted	Researchers Accepted	Applications	Applications Accepted	Researchers Accepted	Applications	Applications Accepted	Researchers Accepted
37	33	278	243	239	1,674	46	46	127	19	19	555	345	337	2634

### *Number of Graduate School Students*

(Research Students)

(2005 Fiscal Year)

Degree/Year	Master's Course	Doctor' s Course	Total
Affiliation			
Nagoya Univ. Graduate School	2	0	2
Tokyo Univ. Graduate School	0	3	3
Others	12	5	17
Total	14	8	22

(The Graduate University for Advanced Studies Students)

(2005 Fiscal Year)

Doctor's Course			
Grade 1	Grade 2	Grade 3	Total
7	7	11	25

### *International Exchange*

Number of Foreign Researchers

(2005 Fiscal Year)

Invited by Ministry of Education,Culture, Sports, Sciences and Technology	Joint Research	Workshop Participants	Visitors	Invited by Japan Society for the Promotion of Science	Others	Total
15	39	106	0	5	10	175

Foreign Researchers to NIFS

(2005 Fiscal Year)

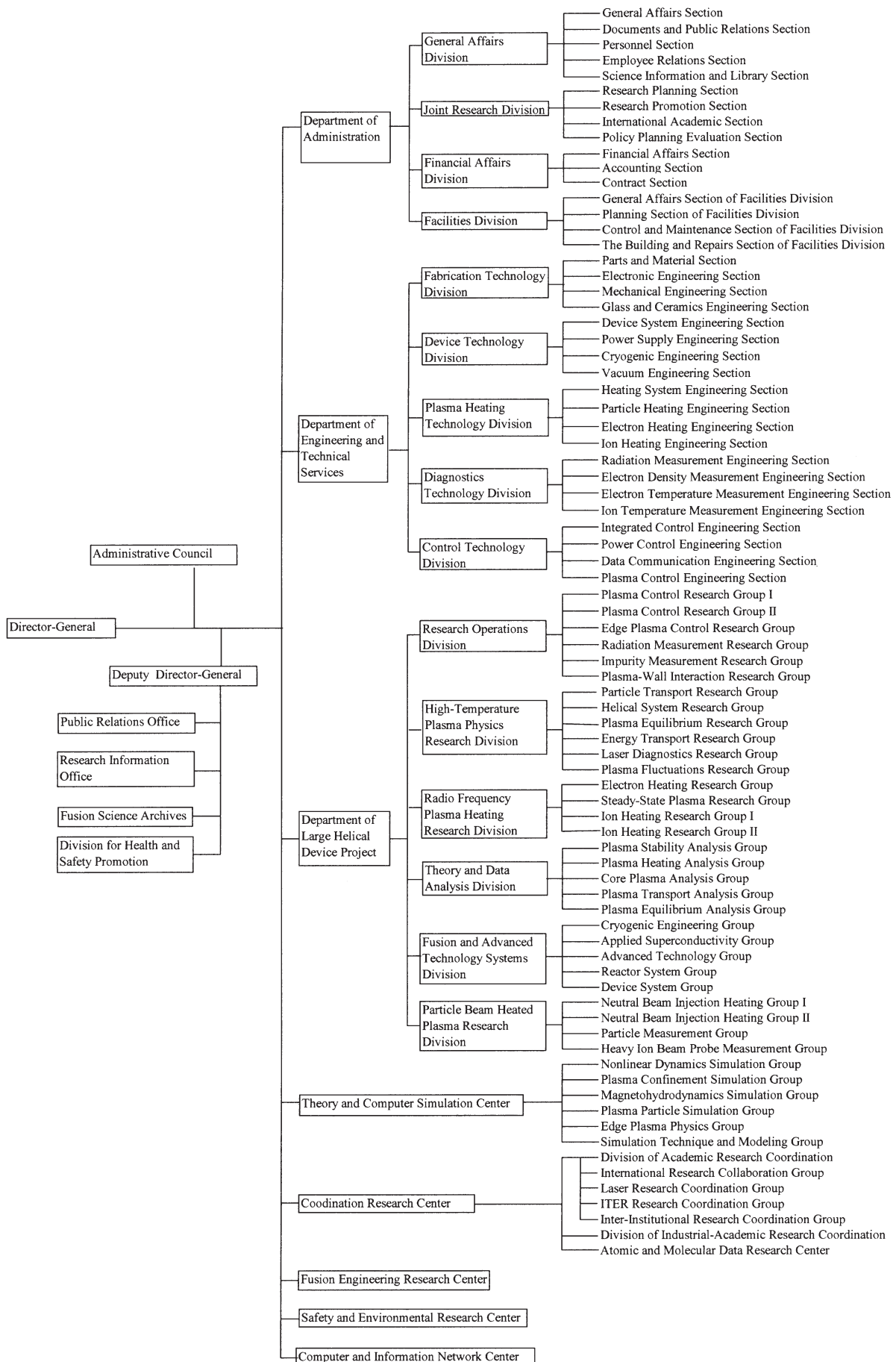
P.R.China	U.S.A.	Russia	India	F.R.G.	Ukraine	R.Korea	Spain	Others	Total
29	39	18	6	15	3	16	3	46	175

NIFS Researchers to Overseas

(2005 Fiscal Year)

U.S.A.	F.R.G	P.R.China	Russia	France	R.Korea	Italy	Spain	Austria.	Others	Total
69	21	18	9	9	38	8	23	8	10	213

# APPENDIX 1. Organization of the Institute



## APPENDIX 2. Members of Committees

### Advisory Council for Research and Management

OHSAWA, Yukiharu	Professor, Graduate School of Science, Nagoya University	UDA, Tatsuhiko	Director of Safety and Environmental Research Center, NIFS
OKAJIMA, Shigeki	Professor, School of Engineering, Chubu University		
OGAWA, Yuichi	Director, High Temperature Plasma Center, University of Tokyo		
SASAO, Mamiko	Professor, Graduate School of Engineering, Tohoku University		
SANO, Fumimichi	Director, Laboratory for Complex Energy Processes, Institute of Advanced Energy, Kyoto University		
CHO, Teruji	Director, Plasma Research Center, University of Tsukuba		
HINO, Tomoaki	Professor, Graduate School of Engineering, Hokkaido University		
MATSUDA, Shinzaburo	Executive Director for ITER promotion, Japan Atomic Energy Agency		
MIMA, Kunioki	Director, Institute of Laser Engineering, Osaka University		
YOSHIDA, Naoaki	Professor, Research Institute for Applied Mechanics, Kyusyu University		
SUDO, Shigeru	Deputy Director-General, NIFS		
KOMORI, Akio	Director of Department of Large Helical Device Project, NIFS		
OKAMOTO, Masao	Director of Theory and Computer Simulation Center, NIFS		
OHYABU, Nobuyoshi	Director of Research Operations Division, NIFS		
KAWAHATA, Kazuo	Director of High-Temperature Plasma Physics Research Division, NIFS		
MUTO, Takashi	Director of Radio Frequency Plasma Heating Research Division, NIFS		
HAYASHI, Takaya	Director of Theory and Data Analysis Division, NIFS		
MITO, Toshiyuki	Director of Fusion and Advanced Technology Systems Division, NIFS		
SATO, Motoyasu	Director of Coordination Research Center, NIFS		
NODA, Nobuaki	Director of Fusion Engineering Research Center, NIFS		

## APPENDIX 3. List of Staff

### Director-General

MOTOJIMA, Osamu

### Deputy Director-General

SUDO, Shigeru

### Department of Large Helical Device Project

Prof. KOMORI, Akio (Executive Director)

#### (Research Operations Division)

Prof. OHYABU, Nobuyoshi (Director)

Prof. KOMORI, Akio

Prof. MORITA, Shigeru

Prof. OKAMURA, Shoichi

Prof. NAGAYAMA, Yoshio

Assoc. Prof. IGUCHI, Harukazu

Assoc. Prof. PETERSON, Byron Jay

Assoc. Prof. MORISAKI, Tomohiro

Assoc. Prof. MASUZAKI, Suguru

Res. Assoc. SAKAMOTO, Ryuichi

Res. Assoc. ISOBE, Mitsutaka

Res. Assoc. YOSHIMURA, Shinji

Res. Assoc. KOBAYASHI, Masahiro

Res. Assoc. SHOJI, Mamoru

Res. Assoc. GOTO, Motoshi

Res. Assoc. MIYAZAWA, Jun-ichi

Res. Assoc. SUZUKI, Chihiro

Res. Assoc. ASHIKAWA, Naoko

Res. Assoc. INAGAKI, Shigeru

#### ( High-Temperature Plasma Physics Research Division )

Prof. KAWAHATA, Kazuo (Director)

Prof. SUDO, Shigeru

Prof. YAMADA, Hiroshi

Prof. NARIHARA, Kazumichi

Prof. TOI, Kazuo

Assoc. Prof. TANAKA, Kenji

Assoc. Prof. SAKAKIBARA, Satoru

Assoc. Prof. WATANABE, Kiyomasa

Assoc. Prof. SATO, Kuninori

Res. Assoc. TOKUZAWA, Tokihiko

Res. Assoc. AKIYAMA, Tsuyoshi

Res. Assoc. EMOTO, Masahiko

Res. Assoc. NARUSHIMA, Yoshiro

Res. Assoc. NAKANISHI, Hideya

Res. Assoc. NISHIMURA, Shin

Res. Assoc. MUTO, Sadatsugu

Res. Assoc. TAMURA, Naoki

Res. Assoc. YAMADA, Ichihiko

Res. Assoc. MINAMI, Takashi

Res. Assoc. FUNABA, Hisamichi

Res. Assoc. OHDACHI, Satoshi

#### (Radio Frequency Plasma Heating Research Division)

Prof. MUTOH, Takashi (Director)

Prof. NAKAMURA, Yukio

Prof. KUMAZAWA, Ryuhei

Assoc. Prof. KUBO, Shin

Assoc. Prof. SIMOZUMA, Takashi

Assoc. Prof. SEKI, Tetsuo

Res. Assoc. YOSHIMURA, Yasuo

Res. Assoc. IGAMI, Hiroe

Res. Assoc. NISHIURA, Masaki

Res. Assoc. SAITO, Kenji

#### (Theory and Data Analysis Division)

Prof. HAYASHI, Takaya (Director)

Prof. SANUKI, Heiji

Prof. ITOH, Kimitaka

Prof. SUGAMA, Hideo

Prof. NAKAJIMA, Noriyoshi (Additional Post)

Assoc. Prof. KANNO, Ryutaro

Assoc. Prof. ICHIGUCHI, Katsuji

Res. Assoc. YOKOYAMA, Masayuki

Res. Assoc. MIZUGUCHI, Naoki

Res. Assoc. SATAKE, Shinsuke

Res. Assoc. SUZUKI, Yasuhiro

Res. Assoc. TODA, Shin-ichiro

Res. Assoc. YAMAGISHI, Osamu

---

※ This list was made up as of March 31, 2006.



**(Fusion and Advanced Technology Systems Division)**

Prof. MITO, Toshiyuki (Director)  
Prof. SATO, Motoyasu  
Prof. IMAGAWA, Shinsaku  
Prof. SAGARA, Akio  
Prof. NODA, Nobuaki (Additional Post)  
Assoc. Prof. TAKAHATA, Kazuya  
Assoc. Prof. YANAGI, Nagato

Assoc. Prof. CHIKARAISHI, Hirotaka  
Assoc. Prof. YAMADA, Syuichi  
Assoc. Prof. MAEKAWA, Ryuji  
Res. Assoc. HAMAGUCHI, Shinji  
Res. Assoc. TAMURA, Hitoshi  
Res. Assoc. IWAMOTO, Akifumi

**(Particle Beam Heated Plasma Research Division)**

Prof. KANEKO, Osamu (Director)  
Prof. IDA, Katsumi  
Prof. TAKEIRI, Yasuhiko  
Prof. HAMADA, Yasuji  
Assoc. Prof. OKA, Yoshihide  
Assoc. Prof. OZAKI, Tetsuo  
Assoc. Prof. FUJISAWA, Akihito  
Res. Assoc. OSAKABE, Masaki

Res. Assoc. NAGAOKA, Ken-ichi  
Res. Assoc. TSUMORI, Katsuyoshi  
Res. Assoc. YOSHINUMA, Mikirou  
Res. Assoc. IKEDA, Katsunori  
Res. Assoc. SHIMIZU, Akihiro  
Res. Assoc. NISHIZAWA, Akimitsu  
Res. Assoc. IDO, Takeshi

**Theory and Computer Simulation Center**

Prof. OKAMOTO, Masao (Director)  
Prof. HORIUCHI, Ritoku  
Prof. NAKAJIMA, Noriyoshi  
Prof. ISHIGURO, Seiji  
Prof. SAKAGAMI, Hitoshi  
Prof. SKORIC, Milos  
Assoc. Prof. TODO, Yasushi  
Assoc. Prof. TOMITA, Yukihiro  
Assoc. Prof. WATANABE, Tomohiko

Assoc. Prof. NAKAMURA, Hiroaki  
Assoc. Prof. MIURA, Hideaki  
Res. Assoc. ISHIZAWA, Akihiro  
Res. Assoc. OHTANI, Hiroaki  
Res. Assoc. ITO, Atsushi  
Res. Assoc. TAKAYAMA, Arimichi  
Res. Assoc. ISHIZAKI, Ryuichi  
Res. Assoc. TAMURA, Yuichi

**Coordination Research Center**

Prof. SATO, Motoyasu (Director, Additional Post)

**( Division of Academic Research Coordination )**

Prof. SUDO, Shigeru (Chief, Additional Post)

**[International Research Collaboration Group]**

Prof. MATSUOKA, Keisuke (Group Chief )  
Prof. WATARI, Tetsuo

Prof. NODA, Nobuaki (Additional Post )  
Assoc. Prof. HIROOKA, Yoshihiko

**[Laser Research Coordination Group]**

Prof. OKAMOTO, Masao (Group Chief, Additional Post)  
Prof. SAKAGAMI, Hitoshi (Additional Post )  
Assoc. Prof. TAJIMA, Teruhiko

Assoc. Prof. OZAKI, Tetsuo (Additional Post )  
Res. Assoc. IWAMOTO, Akifumi  
(Additional Post )

**[ITER Research Coordination Group]**

Prof. NAKAMURA, Yukio (Group Chief, Additional Post)  
Assoc. Prof. TODO, Yasushi (Additional Post )  
Res. Assoc. SEO, Kazutaka (Additional Post )

**[Inter-Institutional Research Coordination Group]**

Prof. YAMADA, Hiroshi (Group Chief, Additional Post)  
Prof. SUGAMA, Hideo (Additional Post )  
Assoc. Prof. TANAKA, Motohiko

**( Division of Industrial-Academic Research Coordination )**

Prof. SATO, Motoyasu (Director, Additional Post)  
Prof. MITO, Toshiyuki (Additional Post)  
Assoc. Prof. YANAGI, Nagato (Additional Post)  
Assoc. Prof. SHIMOZUMA, Takashi (Additional Post)

Assoc. Prof. CHIKARAISHI, Hirotaka  
(Additional Post)  
Assoc. Prof. YAMADA, Shuichi (Additional Post)  
Assoc. Prof. MAEKAWA, Ryuji (Additional Post)

**( Atomic and Molecular Data Research Center )**

Prof. KATO, Takako (Chief)  
Prof. MORE, Richard  
Assoc. Prof. MURAKAMI, Izumi

Res. Assoc. SAKAUE, Hiroyuki  
Res. Assoc. KATO, Daiji

**Fusion Engineering Research Center**

Prof. NODA, Nobuaki (Director)  
Prof. NISHIMURA, Arata  
Prof. MUROGA, Takeo  
Prof. SAGARA, Akio (Additional Post)  
Prof. IMAGAWA, Shinsaku (Additional Post)

Assoc. Prof. NAGASAKA, Takuya  
Res. Assoc. SEO, Kazutaka  
Res. Assoc. HISHINUMA, Yoshimitsu  
Res. Assoc. TANAKA, Teruya  
Res. Assoc. KATO, Daiji (Additional Post)

**Safety and Environmental Research Center**

Prof. UDA, Tatsuhiko (Director)  
Prof. ASAKURA, Yamato  
Prof. NISHIMURA, Kiyohiko  
Assoc. Prof. SAKUMA, Yoichi

Assoc. Prof. KAWANO, Takao  
Res. Assoc. YAMANISHI, Hirokuni  
Res. Assoc. SUGIYAMA, Takahiko

**Computer and Information Network Center**

Prof. HORIUCHI, Ritoku (Director, Additional Post)  
Prof. DEN, Mitsue  
Assoc. Prof. TSUDA, Kenzo

Res. Assoc. YAMAMOTO, Takashi  
Res. Assoc. USAMI, Shunsuke

**Guest Professor**

Prof. KUSAMA, Yoshinori (Japan Atomic Energy Agency (JAEA))	(Apr. 1, '05–Mar. 31, '06)
Prof. YAMAZAKI, Kozo (Nagoya University)	(Apr. 1, '05–Mar. 31, '06)
Prof. MATSUBARA, Youichi (Musashi Institute of Technology)	(Apr. 1, '05–Mar. 31, '06)
Prof. MATSUOKA, Mamoru (Mie University)	(Apr. 1, '05–Mar. 31, '06)
Prof. OKUMURA, Haruhiko (Mie University )	(Apr. 1, '05–Mar. 31, '06)
Prof. SAKAMOTO, Keishi (Japan Atomic Energy Agency (JAEA))	(Apr. 1, '05–Mar. 31, '06)
Prof. WATANABE, Kunihiro (Japan Agency for Marine - Earth Science and Technology )	(Apr. 1, '05–Mar. 31, '06)
Prof. YOSHIDA, Zensyo (The University of Tokyo)	(Apr. 1, '05–Mar. 31, '06)
Prof. NISHIHARA, Motohisa (Hitach Ltd.(retired))	(Apr. 1, '05–Mar. 31, '06)
Prof. IKEDA, Tetsuo (Nagoya Institute of Technology)	(Apr. 1, '05–Mar. 31, '06)
Prof. OKAMOTO, Yukou (Nagoya University)	(Apr. 1, '05–Mar. 31, '06)
Prof. NORIMATSU, Takayoshi (Osaka University )	(Apr. 1, '05–Mar. 31, '06)
Prof. TAKEUCHI, Takao (Superconducting Materials Center, National Institute for Materials Science)	(Apr. 1, '05–Mar. 31, '06)
Prof. MOMOSHIMA, Noriyuki (Kumamoto University)	(Apr. 1, '05–Mar. 31, '06)
Prof. YAMADA, Masao (Yamada Masao Urban Design Network Ltd.)	(Jul. 1, '05–Mar. 31, '06)
Prof. SAITO, Teruo (University of Tsukuba )	(Apr. 1, '05–Mar. 31, '06)
Prof. TANAKA, Masayoshi (Kyusyu University)	(Jan. 1, '06–Mar. 31, '06)
Assoc. Prof. MURAKAMI, Sadayoshi (Kyoto University)	(Apr. 1, '05–Mar. 31, '06)
Assoc. Prof. HOUJYU, Hitoshi (University of Tsukuba )	(Apr. 1, '05–Mar. 31, '06)

Assoc. Prof. HAYAKAWA, Naoki (Nagoya University)	(Apr. 1, '05–Mar. 31, '06)
Assoc. Prof. MURAKAMI, Masakatsu (Osaka University )	(Apr. 1, '05–Mar. 31, '06)
Assoc. Prof. NAMBA, Chusei (NIFS(retired))	(Apr. 1, '05–Mar. 31, '06)
Assoc. Prof. TAKAMARU, Hisanori (Chubu University)	(Apr. 1, '05–Mar. 31, '06)
Assoc. Prof. SUZUKI, Akihiro (The University of Tokyo)	(Apr. 1, '05–Mar. 31, '06)
Prof. WELLER, Arthur (Max-Planck-Institute for Plasma Physics)	(Jan. 5, '05–Apr. 4, '05)
Prof. TSKHAKAYA, David (Institute of Theoretical Physics,University of Innsbruck)	(Jan. 6, '05–Apr. 15, '05)
Prof. VYACHESLAVOV, Leonid Nikolaevich (Budker Institute of Nuclear Physics)	(Jan. 10, '05–May.10, '05)
Prof. IGITKHANOV, Juri Levanovic (Max-Planck-Institute for Plasma Pyhsics)	(Apr. 7, '05–Sept. 7, '05)
Prof. RAMOS, Alcazar Jesus (Plasma Science and Fusion Center,Massachusetts Institute of Technology)	(Jun. 10, '05–Sept. 9, 05)
Prof. VINYAR, Igor (St.Petersburg State Technical University)	(Jun. 27, '05–Sept.26, 05)
Prof. SKOBELEV, Igor (Multicharged Ions Spectra Data Center of VNIIFTRI)	(Sept 15, '05–Jan. 15, '06)
Prof. PETROSKY, Tomio Yamakoshi (Ilya Prigogine Center for Studies in Statistical Mechanics and Complex Systems,The University of Texas at Austin)	(Oct 20, '05–Jan. 19, '06)
Prof. VLADMIROV, Serguei (Research Center for Theoretical Astrophysics,School of Physics,University of Sydney)	(Jan. 5, '06–Apr. 7, '06)
Prof. VOYTSENYA, Volodymyr (Kharkov Institute of Physics and Technology)	(Jan. 10, '06–Apr.10, '06)
Prof. CHEN, Jiming (Southwestern Institute of Physics)	(Feb. 24, '06–Jul. 23, '06)
Assoc.Prof. NEUDACHIN, Sergey (Kurchatov Institute)	(Jan. 11, '05–Apr.14, '05)

**COE Research Fellow**

HASEGAWA, Hiroki	(Apr. 1, '05–Jun. 20, '05)
JINBO, Shigeaki	(Apr. 1, '05–Nov. 15, '05)
GONCHAROV, Pavel	(Apr. 1, '05–Oct. 31, '05)
NOTAKE, Takashi	(Apr. 1, '05–Mar. 31, '06)
MATSUMOTO, Yoshikatsu	(Apr. 1, '05–Mar. 31, '06)
YAMAGUCHI, So-ichiro	(Jul. 1, '05–Mar. 31, '06)
HEMMI, Tsutomu	(Oct. 1, '05–Mar. 31, '06)
KALINIA, Diana	(Oct. 1, '05–Mar. 31, '06)
SONG, Mi-young	(Apr. 1, '05–Mar. 31, '06)
NAKAMURA, Ki-ichiro	(Apr. 1, '05–Mar. 31, '06)
NUNAMI, Masanori	(Apr. 1, '05–Mar. 31, '06)

**Research Fellow (Science research)**

PARCHAMY, Araghy Homaira	(Apr. 1, '05–Mar. 31, '06)
KOBUCHI, Takashi	(Apr. 1, '05–Mar. 31, '06)
ESMAEIL, Farshi Haghro	(Apr. 1, '05–Dec. 31, '05)
PAVLICHENCO, Rostislav Olegorich	(Apr. 1, '05–Mar. 31, '06)
YAMAGUCHI, So-ichiro	(May.16, '05–Jun. 30, '05)
YAO, Zhenyu	(Oct. 1, '05–Mar. 31, '06)
GONCHAROV, Pavel	(Nov. 1, '05–Mar. 31, '06)
YAKOVLEV, Mykhaylo	(Dec. 16, '05–Mar.15, '06)

**Research Fellow (Industrial-Academic coordination)**

SUNO, Hiroya	(Apr. 1, '05–Apr. 30, '05)
MATSUBARA, Akihiro	(Apr. 1, '05–Mar. 31, '06)
SEKI, Ichiro	(May.16, '05–May. 31, '05)

**Specialist Research Fellow**

KOZAKI, Yasuji	(Mar.1, '06–Mar. 31, '06)
----------------	---------------------------

**JSPS Research Fellow**

SATO, Masahiko	(Apr. 1, '04–Mar. 31, '07)
KASUYA, Naohiro	(Apr. 1, '05–Mar. 31, '06)
<i>(Postdoctoral Fellowships for Foreign Researchers)</i>	
CLIVE, Alvin Michael.	(Apr. 1, '05–Mar. 31, '07)
FERRANDO=MARGALET, Sergi	(Nov. 28, '05–Nov. 27, '07)
LIU, Yi	(Nov. 20, '05–Nov. 19, '07)
<i>(Invitation Fellowship Programs for Research in Japan)</i>	

**Department of Administration**

SATO, Yukinori	(Department Director)
----------------	-----------------------

**General Affairs Division**

YAMAMOTO, Hiroshi	Director
DEGUCHI, Hidenori	Deputy Director
General Affairs Section	
ICHIOKA, Akihiro	Chief
Documents and Public Relations Section	Chief
Personnel Section	
KAWAI, Tohru	Chief
Employee Relations Section	
KAWAI, Tohru	Chief
Science Information and Library Section	Additional Post
	Chief

**Financial Affairs Division**

FUJINAMI, Toyohiko	Director
TAKEDA, Minoru	Deputy Director
DOHMAE, Hiroki	Chief
SHIROSHIMA, Toshiaki	Chief
Financial Affairs Section	
SAKAGUCHI, Toshihiro	Chief
Accounting Section	
YAMADA, Kenji	Chief
Contract Section	
IKEDA, Katsumi	Chief

**Joint Research Division**

TAKEUCHI, Masao	Director
MORITA, Yasuo	Deputy Director
Research Planning Section	
IDO, Satoshi	Chief
Research Promotion Section	
KOBAYASHI, Toshinari	Chief



International Academic Section  
MATSUURA, Katsunori      Chief  
Policy Planning Evaluation Section  
AKAGAWA, Yasuhiro      Chief

**Facilities Division**

HOSOKI, Tsutomu      Director  
WATANABE, Yasuo      Deputy Director  
General Affairs Section of Facilities Division  
WATANABE, Yasuo      Chief  
Additional Post  
Planning Section of Facilities Division  
NAKAGAWA, Shin-ichi      Chief  
Control and Maintenance Section of Facilities  
Division  
HAYASHI, Hidenori      Chief  
The Building and Repairs Section of Facilities  
Division  
NITTA, Haruki      Chief

**Department of Engineering and Technical Services**

YAMAUCHI, Kenji                      Department Director  
IIMA, Masashi                      Deputy Department Director

**(Fabrication Technology Division)**

TANIGUCHI, Yoshiyuki              Director  
Parts and Material Section  
    BABA, Tomosumi              Chief  
Electronic Engineering Section  
    ITO, Yasuhiko              Chief  
Mechanical Engineering Section  
    SUGITO, Syoji              Chief  
Glass and Ceramics Engineering Section  
    OKADA, Kohji              Chief

**(Plasma Heating Technology Division)**

TAKITA, Yasuyuki              Director  
Heating System Engineering Section  
    KATOH, Akemi              Chief  
Particle Heating Engineering Section  
    ASANO, Eiji              Chief  
Electron Heating Engineering Section  
    KOBAYASHI, Sakuji              Chief  
Ion Heating Engineering Section  
    SHIMPO, Fujio              Chief

**(Control Technology Division)**

KODAIRA, Jun-ichi              Director  
Integrated Control Technology Section  
    TSUKADA, Kiwamu              Chief  
Power Control Engineering Section  
    TAKAHASHI, Chihiro              Chief  
Data Communication Engineering Section  
    YOKOTA, Mitsuhiro              Chief  
Plasma Control Engineering Section  
    KATOH, Takeo              Chief

**(Device Technology Division)**

IIMA, Masashi                      Director  
Device System Engineering Section  
    YONEZU, Hiroaki              Chief  
Power Supply Engineering Section  
    YASUI, Koji              Chief  
Cryogenic Engineering Section  
    MORIUCHI, Sadatomo              Chief  
Vacuum Engineering Section  
    HAYASHI, Hiromi              Chief

**(Diagnostics Technology Division)**

MIYAKE, Hitoshi                      Director  
Radiation Measurement Engineering Section  
    KONDO, Tomoki              Chief  
Electron Density Measurement Engineering  
Section  
    KATOH, Shinji              Chief  
Electron Temperature Measurement Engineering  
Section  
    KOJIMA, Mamoru              Chief  
Ion Temperature Measurement Engineering  
Section  
    KOMOTO, Toshikazu              Chief

---

This list was made up as of March 31, 2006

## APPENDIX 4. List of Publications I (NIFS Series)

- NIFS-812 M.S. Chu, K. Ichiguchi  
Effect of the Resistive Wall on the Growth Rate of Weakly Unstable External Kink Mode in General 3D Configurations  
May 2005
- NIFS-813 J. García, K. Yamazaki, J. Dies, J. Izquierdo  
Internal Transport Barrier Simulation in LHD  
June 2005
- NIFS-814 T. Watari, Y. Hamada, T. Notake, N. Takeuchi and K. Itoh  
Geodesic Acoustic Mode Oscillation in the Low Frequency Range  
Sep. 2005
- NIFS-815 T. Watari, Y. Hamada, A. Nishizawa, J. Todoroki and K. Itoh  
Unified Linear Response Function for the Stationary Zonal Flow and the Geodesic Acoustic Mode  
Sep. 2005
- NIFS-816 A. Fujisawa, A. Shimizu, S. Ohshima and H. Nakano  
A Recipe to Make Zeolite Ion Source for Plasma Diagnostics Beam  
Sep. 2005
- NIFS-817 A. Fujisawa, K. Itoh, A. Shimizu, H. Nakano, S. Ohshima, H. Iguchi, K. Matsuoka, S. Okamura, S.-I. Itoh and P. H. Diamond  
Spectrograph of Electric Field Fluctuation in Toroidal Helical Plasma  
Sep. 2005
- NIFS-818 H. Wakabayashi, H. Himura, M. Isobe, S. Okamura and K. Matsuoka  
Observation of Non-Uniformity of Space Potential on Magnetic Surfaces in Helical Nonneutral Plasmas  
Sep. 2005
- NIFS-819 H. Sugama and T.-H. Watanabe  
Collisionless Damping of Zonal Flows in Helical Systems  
Sep. 2005
- NIFS-820 T. Tanaka, R. Nagayasu, F. Sato, T. Muroga, T. Ikeda, T. Iida  
Comparison of Electrical Properties of Ceramic Insulators under Gamma Ray and Ion Irradiation  
Oct. 2005
- NIFS-821 S.-I. Itoh, K. Itoh, P.H. Diamond and A. Yoshizawa  
Possible Global Magneto-fluid Structure of the Solar Convection Zone  
Oct. 2005
- NIFS-822 K. Itoh, Y. Nagashima, S.-I. Itoh, P.H. Diamond, A. Fujisawa, M. Yagi and A. Fukuyama  
On the Bicoherence Analysis of Plasma Turbulence  
Oct. 2005
- NIFS-823 T. Nagasaka, T. Muroga, M. Li, D.T. Hoelzer, S. J. Zinkle, M.L. Grossbeck and H. Matsui  
Tensile Property of Low Activation Vanadium Alloy after Liquid Lithium Exposure  
Oct. 2005
- NIFS-824 A. Fujisawa, A. Shimizu, H. Nakano, S. Ohshima, K. Itoh, H. Iguchi, K. Matsuoka, S. Okamura, S.-I. Itoh and P.H. Diamond  
Properties of Turbulence and Stationary Zonal Flow on Transport Barrier in CHS  
Oct. 2005
- NIFS-825 A. Fujisawa, A. Shimizu, H. Nakano, S. Ohshima, K. Itoh, H. Iguchi, Y. Yoshimura, T. Minami, K. Nagaoka, C. Takahashi, M. Kojima, S. Nishimura, M. Isobe, C. Suzuki, T. Akiyama, Y. Nagashima, K. Ida, K. Toi, T. Ido, S.-I. Itoh, K. Matsuoka, and S. Okamura  
Turbulence and Transport Characteristics of a Barrier in a Toroidal Plasma  
Oct. 2005

- NIFS-826 S. Ohshima, A. Fujisawa, A. Shimizu and H. Nakano  
Development of Zeolite Ion Source for Beam Probe Measurements of High Temperature Plasma  
Oct. 2005
- NIFS-827 S. Satake, M. Okamoto, N. Nakajima, H. Sugama and M. Yokoyama  
Non-local Simulation of the Formation of Neoclassical Ambipolar Electric Field in Non-axisymmetric Configurations  
Nov. 2005
- NIFS-828 S. Satake, M. Okamoto, N. Nakajima and H. Takamaru  
Development of Three-Dimensional Neoclassical Transport Simulation Code with High Performance Fortran on a Vector-Parallel Computer  
Nov. 2005
- NIFS-829 R. Shirasaki, H. Nakamura, N. Hatano  
Impurity Effect in the Quantum Nernst Effect  
Nov. 2005
- NIFS-830 K. Itoh, S.-I. Itoh, P.H. Diamond, T.S. Hahm, A. Fujisawa, G.R. Tynan, M. Yagi and Y. Nagashima  
Physics of Zonal Flows  
Jan. 2006
- NIFS-831 M. Nunami, R. Kanno, S. Satake, H. Takamaru and T. Hayashi  
Development of Computational Technique for Labeling Magnetic Flux-surfaces  
Mar. 2006
- NIFS-DATA-93 U.I. Safronova, I. Murakami, T. Kato, D. Kato, Yu. Ralchenko  
Dielectronic Recombination Rate Coefficients to Excited States of O III from O IV and Dielectronic Satellite Lines  
Apr. 2005
- NIFS-DATA-94 M.-Y. Song and T. Kato  
Dielectronic Recombination of  $\text{Xe}^{10+}$  Ions and Satellite line of  $\text{Xe}^{9+}$  Ions  
Oct. 2005
- NIFS-DATA-95 I. Skobelev, I. Murakami, T. Kato  
Recommended Data on Proton-Ion Collision Rate Coefficients for Fe X - Fe XV Ions  
Jan. 2006
- NIFS-DATA-96 I. Murakami, T. Kato, D. Kato, U.I. Safronova, T.E. Cowan and Yu. Ralchenko  
Atomic Data for Dielectronic Recombination into Mg-like Fe  
Mar. 2006
- NIFS-MEMO-46 Safety and Environmental Research Center National Institute for Fusion Science  
Report on Administrative Work at Radiation Safety Center in fiscal year 2003  
June 2005
- NIFS-MEMO-47 Y. Terashima, H. Obayashi, J. Fujita, C. Namba, K. Kimura, K. Matsuoka, S. Hanaoka,  
An Archival Study on the Reacting Plasma Project (R-Project) at the Institute of Plasma Physics, Nagoya University - An Interview with MATSUURA Kiyokata, Professor Emeritus at Nagoya University -  
Jan. 2006
- NIFS-PROC-60 B. Wan and K. Toi (Eds.)  
Proceedings of JSPS-CAS Core University Program Seminar on Production and Steady State Confinement of High Performance Plasmas in Magnetic Confinement Systems, 27-29 July, 2005, Hefei, China  
Sep. 2005
- NIFS-PROC-61 Edited by E. Hotta  
New Aspects of High Energy Density Plasma, Mar. 7-8, 2005, NIFS  
Oct 2005
- NIFS-TECH-13 R. Sakamoto, H. Yamada  
Pellet Injector Systems for Plasma Refueling on LHD  
Apr. 2005



## APPENDIX 5. List of Publications II (Journals, etc.)

- (1) Aramaki,M., Okumura,Y., Goto,M., Muto,S., Morita,S., Sasaki,K.  
Measurements of Gas Temperature in High-Density Helicon-Wave H<sub>2</sub> Plasmas by Diode Laser Absorption Spectroscopy  
Japanese Journal of Applied Physics Vol.44, No.9A (2005) 6759-6763
- (2) Asakura,Y., Sugiyama,T., Kawano,T., Uda,T., Tanaka,M., Tsuji,N., Katahira,K., Iwahara,H.  
Application of New Technologies for Gaseous Tritium Recovery and Monitoring  
Fusion Science and Technology Vol.48, No.1 (2005) 401-404
- (3) Bacal,M., Hatayama,A., Matsumiya,T., Hamabe,M., Kuroda,T., Oka,Y.  
Extraction Physics in Volume H- ion Sources  
Review of Scientific Instruments Vol.77, No.3 (2006) 03A502-1-03A502-3
- (4) Chiba,S., Omae,M., Yuki,K., Hashizume,H., Toda,S., Sagara,A.  
Experimental Research on Heat Transfer Enhancement for High Prandtl-Number Fluid  
Fusion Science and Technology Vol.47, No.3 (2005) 569-573
- (5) Chiba,S., Yuki,K., Hashizume,H., Toda,S., Sagara,A.  
Numerical Research on Heat Transfer Enhancement for High Prandtl-number Fluid  
Fusion Engineering and Design Vol.81, No.1-7 (2006) 513-517
- (6) Chu,M.S., Ichiguchi,K.  
Effect of the Resistive Wall on the Growth Rate of Weakly Unstable External Kink Mode in General 3D Configurations  
Nuclear Fusion Vol.45, No.8 (2005) 804-813
- (7) Diamond,P.H., Itoh,S. -I., Itoh,K., Hahm, T.S.  
Zonal Flows in a Plasma-a Review  
Plasma Physics and Controlled Fusion Vol.47, No.5 (2005) R35-R161
- (8) Ebara,S., Nagata,S., Irida,H., Yokomine,T., Shimizu,A.  
Feasibly Study on Cast-like IFMIF High Flux Test Module  
Fusion Engineering and Design Vol.81, No.8-14 (2006) 887-891
- (9) Enoda,M., Akiba,M., Tanaka,S., Shimizu,A., Hasegawa,, Konishi,S., Kimura,A., Kohyama,A., Sagara,A., Muroga,T.  
Overview of Design and R&D of Test Blankets in Japan  
Fusion Engineering and Design Vol.81, No.1-7 (2006) 415-424
- (10) Fujiwara,S., Hashimoto,M., Itoh,T., Nakamura,H.  
Molecular Dynamics Simulation for Structure Formation of a Single Polymer Chain in Solution  
Journal of the Physical Society of Japan Vol.75, No.2 (2006) 024605-1-024605-8
- (11) Fukada,S., Anderl, R.A., Sagara,A., Nishikawa,M.  
Diffusion Coefficient of Tritium Through Molten Salt Flibe and Rate of Tritium Leak from Fusion Reactor System  
Fusion Science and Technology Vol.48, No.1 (2005) 666-669
- (12) Fukada,S., Morisaki,A., Sagara,A., Terai,T.  
Control of Tritium in FFHR-2 Self-cooled Flibe Blanket  
Fusion Engineering and Design Vol.81, No.1-7 (2006) 477-483
- (13) Fukumoto,K., Takahashi,S., Kurtz,R. J., Smith,D. L., Matsui,H.  
Microstructural Examination of V  
Journal of Nuclear Materials Vol.341, No.1 (2005) 83-89
- (14) Gotoh,T., Watanabe,T.  
Statistics of Transfer Fluxes of the Kinetic Energy and Scalar Variance  
Journal of Turbulence Vol.6, No.33 (2005) 1-18
- (15) Hameiri,E., Ishizawa,A., Ishida,A.  
Waves in the Hall-magnetohydrodynamics Model  
Physics of Plasmas Vol.12, No.7 (2005) 072109-1-072109-13

- (16) Hara,M., Maeda,Y., Nakagawa,Y., Suehiro,J., Yamada,S.  
DC Breakdown Voltage Characteristics in the Presence of Metallic Particles in Saturated Liquid Helium  
IEEE Transaction Dielectrics and Electrical Insulation Vol.26, No. (2005) 373-376
- (17) Hasegawa,H., Kato,K., Ohsawa,Y.  
Persistent Acceleration of Positrons in a Nonstationary Shock Wave  
Physics of Plasmas Vol.12, No.8 (2005) 082306-1-082306-6
- (18) Hashizume,H., Ito,S., Takami,S., Sagara,A.  
Joint Performance of HTc Superconductor for Remountable Magnet System  
Fusion Science and Technology Vol.47, No.4 (2005) 901-905
- (19) Hayakawa,N., Nagino,M., Kojima,H., Goto,M., Takahashi,T., Yasuda,K., Okubo,H.  
Dielectric Characteristics of HTS Cables Based on Partial Discharge Measurement  
IEEE Transactions on Applied Superconductivity Vol.15, No.2 (2005) 1802-1805
- (20) Hemmi,T., Yanagi,N., Seo,K., Maekawa,R., Takahata,K., Mito,T.  
Experimental Evaluation of Loss Generation in HTS Coils Under Various Conditions  
IEEE Transactions on Applied Superconductivity Vol.15, No.2 (2005) 1711-1714
- (21) Hino,T., Hashiba, Y., Yamauchi,Y., Hirohata,Y., Nishimura,K., Ashikawa,N., Masuzaki,S., Sagara,A., Noda,N.,  
Ohyabu,N., Komori,A., Motojima,O.  
Deuterium Retention and Desorption Behavior of Boron  
Fusion Engineering and Design Vol.81, No.1-7 (2006) 127-131
- (22) Hino,T., Hayashishita,E., Yamada,T., Liu,X., Kohyama,A., Yamauchi,Y., Hirohata,Y., Nobuta,Y.  
Progress of Plasma Surface Interaction Study on Low Activation Materials  
Fusion Engineering and Design Vol.81, No.1-7 (2005) 181-186
- (23) Hirooka,Y., Ohgaki,H., Hosaka,S., Ohtsuka,Y., Nishikawa,M.  
Lithium-Gettered Moving Surface Plasma-Facing Components for Particle Control in Steady State Magnetic Fusion  
Devices  
Fusion Science and Technology Vol.47, No.3 (2005) 703-707
- (24) Hiwatari,R., Hatayama,A., Zhu,S., Takizuka,T., Tomita,Y.  
Overall Features of EAST Operation Space by Using Simple Core-SOL-Divertor Model  
Plasma Science & Technology (China) Vol.8, No.1 (2006) 114-117
- (25) Ichimasa,Y., Sasajima,E., Makiyama,H., Tauchi,H., Uda,T., Ichimasa,M.  
Uptake of Heavy Water and Loss by Tangerine in the Heavy Water Vapor Release Experiment in a Greenhouse as a  
Substitute for Tritiated Water  
Fusion Science and Technology Vol.48, No.1 (2005) 775-778
- (26) Ida,K., Inagaki,S., Sakamoto,R., Tanaka,K., Funaba,H., Takeiri,Y., Ikeda,K., Michael,C., Tokuzawa,T., Yamada,H.,  
Nagayama,Y., Itoh,K., Kaneko,O., Komori,A., Motojima,O., LHD experimental group  
Slow Transition of Energy Transport in High-Temperature Plasmas  
Physical Review Letters Vol.96, No.12 (2006) 125006-1-125006-4
- (27) Ida,K., Miura,Y., Ido,T., Nagashima,Y., Shinohara,K.  
Studies of Radial Electric Field Formation and its Effect on Fluctuations and Transport Barriers in the JFT-2M Tokamak  
Fusion Science and Technology Vol.49, No. 2 (2006) 122-138
- (28) Ida,K., Yoshinuma,M., Nagaoka,K.  
Increasing Rate of Water Temperature Due to an Ekman Layer Flow in a Heated Pot  
American Journal of Physics Vol.73, No.7 (2005) 635-638
- (29) Ida,K., Yoshinuma,M., Watanabe,K., Kobuchi,T., Nagaoka,K.  
Measurements of Rotational Transform Due to Noninductive Toroidal Current Using Motional Stark Effect  
Spectroscopy in the Large Helical Device  
Review of Scientific Instruments Vol.76, No.5 (2005) 053505-1-053505-5
- (30) Ida,K., Yoshinuma,M., Yokoyama,M., Inagaki,S., Tamura,N., Peterson,B. J., Morisaki,T., Masuzaki,S., Komori,A.,  
Nagayama,Y., Tanaka,K., Narihara,K., Watanabe,K. Y., Beidler,C. D., LHD experimental group  
Control of the Radial electric field shear by modification of the magnetic field configuration in LHD  
Nuclear Fusion Vol.45, No.5 (2005) 391-398

- (31) Ido,T., Miura,Y., Hoshino,K., Kamiya,K., Hamada,Y., Nishizawa,A., Kawasumi,Y., Ogawa,H., Nagashima,Y., Shinohara,K., Kusama,Y., JFT-2M group  
Observation of the Interaction between the Geodesic Acoustic Mode and Ambient Fluctuation in the JFT-2M Tokamak Nuclear Fusion Vol.46, No.5 (2006) 512-520
- (32) Ikeda,R., Takeuchi,M., Ito,T., Toi,K., Suzuki,C., Matsunaga,G., Shoji,T., Matsuoka,K., Okamura,S., CHS Eexperimental Group  
Production of Over-Dense Plasmas by Launching of 2.45GHz Electron Cyclotron Waves on the Compact Helical System Journal of Plasma and Fusion Research Vol.81, No.7 (2005) 478-479
- (33) Ikeda,R., Takeuchi,M., Ito,T., Toi,K., Suzuki,C., Matsunaga,G., Shoji,T., Matsuoka,K., Okamura,S., CHS experimental Group  
Production of Over-Dense Plasmas by Launching of 2.45 GHz Electron Cyclotron Waves on the Compact Helical System Journal of Plasma and Fusion Research Vol.81, No.7 (2005) 478-481
- (34) Imagawa,S., Takahata,K., Yanagi,N., Mito,T.  
Measurement of Residual Magnetic Field by Superconducting Magnets of The LHD IEEE Transactions on Applied Superconductivity Vol.15, No.2 (2005) 1419-1422
- (35) Inagaki,S., Takenaga,H., Ida,K., Isayama,A., Tamura,N., Takizuka,T., Shimozuma,T., Kamada,Y., Kubo,S., Miura,Y., Nagayama,Y., Kawahata,K., Sudo,S., Ohkubo,K.  
Comparison of Transient Electron Heat Transport in LHD Helical and JT-60U Tokamak Plasmas Nuclear Fusion Vol.46, No.1 (2006) 133-141
- (36) Ishigohka,T., Tsuchiya,T., Adachi,Y., Ninomiya,A., Yanagi,N., Seo,K., Sekiguchi,H., Yamada,S., Imagawa,S., Mito,T.  
AE Measurement of the LHD Helical Coils IEEE Transactions on Applied Superconductivity Vol.15, No.2 (2005) 1423-1426
- (37) Ishikawa,M., Horita,K., Yasaka,Y., Takeno,H., Tomita,Y.  
Performance Analysis of Experimental Device of Travelling Wave Direct Energy Converter Fusion Engineering and Design Vol.81, No.0 (2006) 1689-1694
- (38) Ishizawa,A., Horiuchi,R.  
Suppression of Hall-term Effects by Gyroviscous Cancellation in Steady Collisionless Magnetic Reconnection Physical Review Letters Vol.95, No.4 (2005) 045003-1-045003-4
- (39) Itoh,K., Hallatschek,K., Itoh,S-I., Diamond,P. H., Toda,S.  
Coherent Structure of Zonal Flow and Onset of Turbulent Transport Physics of Plasmas Vol.12, No.6 (2005) 062303-1-062303-14
- (40) Itoh,K., Itoh,S. -I., Hahm,T. S., Diamond,P. H.  
Effect of Turbulence Spreading on Subcritical Turbulence in Inhomogeneous Plasmas Journal of the Physical Society of Japan Vol.74, No.7 (2005) 2001-2006
- (41) Itoh,K., Itoh,S. -I., Yagi,M.  
Self-sustained Annihilation of Magnetic Islands in Helical Plasmas Physics of Plasmas Vol.12, No.7 (2005) 072512-1-072512-6
- (42) Itoh,K., Nagashima,Y., Itoh,S-I., Diamond,P. H., Fujisawa,A., Yagi,M., Fukuyama,A.  
On the Bicoherence Analysis of Plasma Turbulence Physics of Plasmas Vol.12, No.10 (2005) 102301-1-102301-9
- (43) Kaneko,T., Reynolds,E. W., Hatakeyama,R., Koepke,M. E.  
Velocity-Shear-Driven Drift Waves with Simultaneous Azimuthal Modes in a Barium-Ion Q-machine Plasma Physics of Plasmas Vol.12, No.10 (2005) 102106-1-102106-6
- (44) Kanno,R., Hayashi,T., Okamoto,M.  
Formation and Healing of n=1 Magnetic Islands in LHD Equilibrium Nuclear Fusion Vol.45, No.7 (2005) 588-594
- (45) Kanno,R., Satake,S., Nunami,M.  
Stochastic Approach to Modeling Fluctuating Flow Plasma and Fusion Research Vol.1, No.0 (2006) 012-1-012-4

- (46) Kasai,S., Kamiya,K., Shinohara,K., Kawashima,H., Ogawa,H., Uehara,K., Miura,Y., Okano,F., Suzuki,S., Hoshino,K., Tsuzuki,K., Sato,M., Oasa,K., Kusama,Y., Yamauchi,T., Nagashima,Y., Ida,K., Hidekuma,S., Ido,T., Hamada,Y., Nishizawa,A., Kawasumi,Y., Uesugi,Y., Okajima,S., Kawahata,K., Ejiri,A., Amemiya,H., Sadamoto,Y.  
Plasma Diagnostics in JFT-2M  
Fusion Science and Technology Vol.49, No.2 (2006) 225-240
- (47) Kasuya,K., Kinoshita, Y., Norimatsu,T., Nakai,S., Mroz,W., Prokopiuk,A.  
First Wall Ablations with High-Flux Pulsed Proton Beams and UV Laser Lights for IFE Reactor Design Base  
Fusion Engineering and Design Vol.81, No.8-14 (2005) 1653-1659
- (48) Kasuya,N., Itoh,K.  
Convective Particle Transport Arising from Poloidal Inhomogeneity in Tokamak H Mode  
Physics of Plasmas Vol.12, No.9 (2005) 090905-1-090905-8
- (49) Kasuya,N., Itoh,K.  
Multi-Dimensional Structure of the Electric Field in Tokamak H-Mode  
Journal of Plasma and Fusion Research Vol.81, No.7 (2005) 553-562
- (50) Kasuya,N., Itoh,K.  
Two-Dimensional Structure and Particle Pinch in Tokamak H Mode  
Physical Review Letters Vol.94, No.19 (2005) 195002-1-195002-4
- (51) Kawagoe,A., Sumiyoshi,F., Mito,T., Chikaraishi,H., Maekawa,R., Seo,K., Baba,T., Hemmi,T., Okumura,K., Iwakuma,M., Hayashi,K., Abe,R.  
Stability Evaluation of a Conduction-Cooled Prototype LTS Pulse Coil for UPS-SMES  
IEEE Transactions on Applied Superconductivity Vol.15, No.2 (2005) 1891-1894
- (52) Kawano,T.  
Theoretical Expressions for Removing Tritium from Exhaust Gas  
Fusion Engineering and Design Vol.73, No.2-4 (2005) 127-134
- (53) Kawano,T., Tsuboi,N., Tsujii,H., Asakura,Y., Uda,T.  
Isotopic Separation Analysis of Infinitesimal Concentrations of Hydrogen Using Trace Reduction Detector  
Fusion Engineering and Design Vol.48, No.1 (2005) 405-408
- (54) Kimura,A., Kasada,R., Kohyama,A., Konishi,S., Enoda,M., Akiba,M., Jitsukawa,S., Ukai,S., Terai,T., Sagara,A.  
Ferritic Steel-blanket Systems Integration R&D  
Fusion Engineering and Design Vol.81, No.8-14 (2006) 909-916
- (55) Kiwamoto,Y., Aoki,J., Soga,Y., Sanpei,A.  
Controlled Experiments on Self-organization of Ordered Structures in a Pure Electron Plasma  
Plasma Physics and Controlled Fusion Vol.47, No.5A (2005) A41-A51
- (56) Kobayashi,M., Miyazawa,J., Masuzaki,S., Igitkhanov,Y., Sakamoto,R., Ashikawa,N., Morisaki,T., Ohyaabu,N., Yamada,H., Funaba,H., Komori,A., Motojima,O., The LHD Experimental group  
Analysis for Hydrogen Particle Balance of Plasma-wall System in the Large Helical Device  
Journal of Nuclear Materials Vol.350, No.1 (2006) 40-46
- (57) Kodama,H., Oyaidzu,M., Yoshikawa,A., Kimura,H., Oya,Y., Matsuyama,M., Sagara,A., Noda,N., Okuno,K.  
Helium Irradiation Effects on Retention Behavior of Deuterium Implanted into Boron Coating Film by PCVD  
Journal of Nuclear Materials Vol.337-339, No.0 (2005) 649-653
- (58) Kohyama,A., Abe,K., Kimura,A., Muroga,T., Jitsukawa,S.  
Recent Accomplishments and Future Prospects of Materials R & D in Japan  
Fusion Science and Technology Vol.47, No.4 (2005) 836-843
- (59) Kojima,H., Noguchi,S., Kurupakorn,C., Hayakawa,N., Goto,M., Hirano,N., Nagaya,S., Okubo,H.  
Temperature Dependence of Critical Current at 4.2K  
IEEE Transactions on Applied Superconductivity Vol.15, No.2 (2005) 2550-2553



- (60) Komori,A., Morisaki,T., Masuzaki,S., Kobayashi,M., Feng,Y., Shoji,M., Ohyabu,N., Ida,K., Tanaka,K., Kawahata,K., Narihara,K., Morita,S., Peterson,B. J., Sakamoto,R., Sakakibara,S., Yamada,H., Ikeda,K., Kaneko,O., Kubo,S., Miyazawa,J., Nagaoka,K., Nakanishi,H., Ohkubo,K., Oka,Y., Osakabe,M., Reiter,D., Sardei,F., Shimozuma,T., Takeiri,Y., Tsumori,K., Watanabe,K. Y., Yamada,I., Yoshimura,Y., Yoshinuma,M., Motojima,O., LHD Experimental Group
- Edge Plasma Control by Local Island Divertor in LHD  
Nuclear Fusion Vol.45, No.8 (2005) 837-842
- (61) Komori,A., Sakakibara,S., Morisaki,T., Watanabe,K. Y., Narushima,Y., Toi,K., Ohdachi,S., Masuzaki,S., Kobayashi,M., Shoji,M., Ohyabu,N., Ida,K., Tanaka,K., Kawahata,K., Narihara,K., Morita,S., Peterson,B. J., Sakamoto,R., Yamada,H., Ikeda,K., Kaneko,O., Kubo,S., Miyazawa,J., Nagaoka,K., Nakanishi,H., Ohkubo,K., Oka,Y., Osakabe,M., Shimozuma,T., Takeiri,Y., Tsumori,K., Yamada,I., Yoshimura,Y., Yoshinuma,M., Motojima,O., LHD Experimental Group
- Characteristics of Confinement and Stability in Large Helical Device Edge Plasmas  
Physics of Plasmas Vol.12, No.5 (2005) 056122-1-056122-8
- (62) Kondo,S., Hinoki,T., Kohyama,A.
- Synergistic Effects of Heavy Ion and Helium Irradiation on Microstructural and Dimensional Change in  $\beta$ -SiC  
Materials Transactions Vol.46, No.6 (2005) 1388-1392
- (63) Kubo,S., Shimozuma,T., Yoshimura,Y., Notake,T., Idei,H., Inagaki,S., Yokoyama,M., Ohkubo,K., Kumazawa,R., Saito,K., Seki,T., Mutoh,T., Watari,T., Narihara,K., Yamada,I., Ida,K., Takeiri,Y., Funaba,H., Ohyabu,N., Kawahata,K., Kaneko,O., Yamada,H., Itoh,K., Ashikawa,N., Emoto,M., Goto,M., Hamada,Y., Ido,T., Ikeda,K., Isobe,M., Khlopenkov,K., Kobuchi,T., Masuzaki,S., Minami,T., Miyazawa,J., Morisaki,T., Morita,S., Murakami,S., Muto,S., Nagaoka,K., Nagayama,Y., Nakanishi,H., Narushima,Y., Nishimura,K., Nishiura,M., Noda,N., Ohdachi,S., Oka,Y., Osakabe,M., Ozaki,T., Peterson,B. J., Sagara,A., Sakakibara,S., Sakamoto,R., Shoji,M., Sudo,S., Takeuchi,N., Tamura,N., Tanaka,K., Toi,K., Tokuzawa,T., Tsumori,K., Watanabe,K..
- Extension and Characteristics of an ECRH Plasma in LHD  
Plasma Physics and Controlled Fusion Vol.47, No.5A (2005) A81-A90
- (64) Kumazawa,R., Mutoh,T., Saito,K., Seki,T., Nakamura,Y., Kubo,S., Shimozuma,T., Yoshimura,Y., Igami,H., Ohkubo,K., Takeiri,Y., Oka,Y., Tsumori,K., Osakabe,M., Ikeda,K., Nagaoka,K., Kaneko,O., Miyazawa,J., Morita,S., Narihara,K., Shoji,M., Masuzaki,S., Kobayashi,M., Ogawa,H., Goto,M., Morisaki,T., Peterson,B. J., Sato,K., Tokuzawa,T., Ashikawa,N., Nishimura,K., Funaba,H., Chikaraishi,H., Watari,T., Watanabe,T., Sakamoto,M., Ichimura,M., Takase,Y., Notake,T., Takeuchi,N., Torii,Y., Shimpo,F., Nomura,G., Takahashi,C., Yokota,M., Kato,A., Zhao,Y., Kwak,J. G., Yoon,J. S., Yamada,H., Kawahata,K., Ohyabu,N., Ida,K., Nagayama,Y., Noda,N., Komori,A., Sudo,S., Motojima,O., LHD experimental group
- Long-pulse Plasma Discharge on the Large Helical Device  
Nuclear Fusion Vol.46, No.0 (2006) S13-S21
- (65) Kurupakorn,C., Kojima,H., Hayakawa,N., Goto,M., Kashima,N., Nagaya,S., Noe,M., Juengst,K. -P., Okubo,H.
- Recovery Characteristics after Current Limitation of High Temperature Superconducting Fault Current Limiting Transformer (HTc-SFCLT)  
IEEE Transactions on Applied Superconductivity Vol.15, No.2 (2005) 1859-1862
- (66) Kusano,K.
- Simulation Study of the Formation Mechanism of Sigmoidal Structure in the Solar Corona  
Astrophysical Journal Vol.631, No.2 (2005) 1260-1269
- (67) Li,B., Ishiguro,S., Skoric,M. M., Song,M., Sato,T.
- Stimulated Raman Cascade and Photon Condensation in Intense Laser Plasma Interaction  
Physics of Plasmas Vol.12, No.10 (2005) 103103-1-103103-8
- (68) Matsumoto,Y., Nishiura,M., Matsuoka,K., Wada,M., Sasao,M., Yamaoka,H.
- Density and Velocity of H<sup>-</sup> in the Extraction Region of a Negative Ion Source Using the Perturbation of H<sup>-</sup> beam Current by a Pulse Laser Injection  
Review of Scientific Instruments Vol.77, No.3 (2006) 03B705-1-03B705-3
- (69) Matsunaga,G., Toi,K., Kawada,S., Kotani,J., Suzuki,C., Matsuoka,K., CHS Group
- Excitation of Toroidicity-Induced Alfvén Eigenmodes by the Electrodes Inserted in a Heliotron/Torsatron Plasma  
Physical Review Letters Vol.94, No.22 (2005) 225005-1-225005-4

- (70) Mima,K., Tanaka,K., Miyanaga,N., Kodama,R., Nagatomo,H., Jhozaki,T., Kitagawa,Y., Nishimura,H., Sakagami,H., Taguchi,T.  
New Frontier of Fast Ignition Laser Fusion  
Journal of Plasma and Fusion Research Vol.81, No.Suppl. (2005) 42-47
- (71) Mito,T., Kawagoe,A., Chikaraishi,H., Okumura,K., Abe,R., Hemmi,T., Maekawa,R., Seo,K., Baba,T., Yokota,M., Morita,Y., Ogawa,H., Yamauchi,K., Iwakuma,M., Sumiyoshi,F.  
Prototype Development of a Conduction-Cooled LTS Pulse Coil for UPS-SMES  
IEEE Transactions on Applied Superconductivity Vol.15, No.2 (2005) 1935-1938
- (72) Miura,Y., Mori,M., Shoji,T., Matsumoto,H., Kamiya,K., Ida,K., Kasai,S.  
Studies of Improved Confinement in JFT-2M  
Fusion Science and Technology Vol.49, No.2 (2006) 96-121
- (73) Miyazawa,J., Masuzaki,S., Sakamoto,R., Arimoto,H., Kondo,K., Tamura,N., Shoji,M., Nishiura,M., Murakami,S., Funaba,H., Peterson,B. J., Sakakibara,S., Kobayashi,M., Tanaka,K., Narihara,K., Yamada,I., Morita,S., Goto,M., Osakabe,M., Ashikawa,N., Morisaki,T., Nishimura,K., Yamada,H., Ohyabu,N., Komori,A., Motojima,O.  
Self-sustained Detachment in the Large Helical Device  
Nuclear Fusion Vol.46, No.5 (2006) 532-540
- (74) Miyazawa,J., Masuzaki,S., Sakamoto,R., Peterson,B. J., Sakakibara,S., Ohyabu,N., Komori,A., Motojima,O., LHD Experimental Group  
Sustained Detachment with the Self-Regulated Plasma Edge beneath the Last Closed Flux Surface in LHD  
Journal of Plasma and Fusion Research Vol.81, No.5 (2005) 331-332
- (75) Miyazawa,J., Yamada,H., Murakami,S., Funaba,H., Inagaki,S., Ohyabu,N., Komori,A., Motojima,O., LHD experimental group  
Global Confinement Scaling for High-density Plasmas in the Large Helical Device  
Plasma Physics and Controlled Fusion Vol.48, No.2 (2006) 325-337
- (76) Miyazawa,J., Yamada,H., Murakami,S., Funaba,H., Peterson,B. J., Osakabe,M., Tanaka,K., Sakakibara,S., Inagaki,S., LHD Experimental Group  
Temperature Dependence of the Thermal Diffusivity in High-collisionality Regimes in the Large Helical Device  
Plasma Physics and Controlled Fusion Vol.47, No.6 (2005) 801-813
- (77) Miyazawa,J., Yamada,H., Peterson,B. J., Murakami,S., Funaba,H., Osakabe,M., Tanaka,K., Sakakibara,S., LHD Experimental Group  
Electron Pressure Profiles in High-Density Neutral Beam Heated Plasmas in the Large Helical Device  
Journal of Plasma and Fusion Research Vol.81, No.4 (2005) 302-311
- (78) Mizuguchi,N., Khan,R., Hayashi,T.  
Nonlinear Simulation of Edge-Localized Mode in Spherical Tokamak  
IEEJ Transactions on Fundamentals and Materials Vol.125, No.11 (2005) 934-937
- (79) Momoshima,N., Matsushita,R., Nagao,Y., Okai,T.  
Uptake of Deuterium by Dead Leaves Exposed to Deuterated Water Vapor in a Greenhouse at Daytime and Nighttime  
Journal of Environmental Radioactivity Vol.88, No.1 (2006) 90-100
- (80) Momoshima,N., Nagao,Y., Toyoshima,T.  
Electrolytic Enrichment of Tritium with Solid Polymer Electrolyte for Application to Environmental Measurements  
Fusion Science and Technology Vol.48, No.1 (2005) 520-523
- (81) Morisaki,T., Masuzaki,S., Komori,A., Ohyabu,N., Kobayashi,M., Miyazawa,J., Shoji,M., Gao,X., Ida,K., Ikeda,K., Kaneko,O., Kawahata,K., Kubo,S., Morita,S., Nagaoka,K., Nakanishi,H., Narihara,K., Oka,Y., Osakabe,M., Peterson,B. J., Sakakibara,S., Sakamoto,R., Shimozuma,T., Takeiri,Y., Tanaka,K., Toi,K., Tsumori,K., Watababe,K. Y., Watari,T., Yamada,H., Yamada,I., Yan,L., Yang,Q., Yang,Y., Yoshimura,Y., Yoshinuma,M., Motojima,O., LHD., Experimental Group  
  
Review of Divertor Studies in LHD  
Plasma Science & Technology (China) Vol.8, No.1 (2006) 14-18
- (82) Morita,S., Goto,M., Muto,S., Katai,R., Yamazaki,H., Nozato,H., Iwamae,A., Atake,M., Fujimoto,T., Sakaue,A., Nishimura,H., Sakurai,I., Matsumoto,C., Furuzawa,A., Tawara,Y., Aramaki,M., Okumura,Y., Sasaki,K., Gong,X., Li,J., Wan,B., Cui,Z.  
Spectroscopic Studies on Impurity Transport of Core and Edge Plasmas in LHD  
Plasma Science & Technology (China) Vol.8, No.1 (2006) 55-60

- (83) Motojima,O., Ida,K., Watanabe,K. Y., Nagayama,Y., Komori,A., Morisaki,T., Peterson,B. J., Takeiri,Y., Ohkubo,K., Tanaka,K., Shimozuma,T., Inagaki,S., Kobuchi,T., Sakakibara,S., Miyazawa,J., Yamada,H., Ohyabu,N., Narihara,K., Nishimura,K., Yoshinuma,M., Morita,S., Akiyama,T., Ashikawa,N., Beidler,C. D., Emoto,M., Fujita,T., Fukuda,T., Funaba,H., Goncharov,P., Goto,M., Ido,T., Ikeda,K., Isayama,A., Isobe,M., Igami,H., Ishii,K., Itoh,K., Kaneko,O., Kawahata,K., Kawazome,H., Kubo,S., Kumazawa,R., Masuzaki,S., Matsuoka,K., Minami,T., Murakami,S., Muto,S., Mutoh,T., Nakamura,Y., Nakanishi,H., Narushima,Y., Nishiura,M., Nishizawa,A., Noda,N., Notake,T., Nozato,H., Ohdachi,S., Oka,Y., Okaiima,S., Osakabe,M., Ozaki,T., Sagara,A., Saida,T., Saito,K.,  
Overview of Confinement and MHD Stability in the Large Helical Device  
Nuclear Fusion Vol.45, No.10 (2005) S255-S265
- (84) Murakami,I., Safronova,U. I., Vasilyev,A. A., Kato,T.  
Excitation Energies, Radiative and Autoionization Rates, Dielectronic Satellite Lines, and Dielectronic Recombination Rates to Excited States for B-like Oxygen  
Atomic Data and Nuclear Data Tables Vol.90, No.1 (2005) 1-74
- (85) Muroga,T., Tanaka,T.  
Neutronics Investigation into Lithium/Vanadium Test Blanket Modules  
Fusion Science and Technology Vol.47, No.3 (2005) 540-543
- (86) Muroga,T., Tanaka,T., Sagara,A.  
Blanket Neutronics of Li/Vanadium-alloy and Flibe/Vanadium-alloy Systems for FFHR  
Fusion Engineering and Design Vol.81, No.8-14 (2006) 1203-1209
- (87) Mutoh,T., Kumazawa,R., Seki,T., Saito,K., Nakamura,Y., Kubo,S., Takeiri,Y., Shimozuma,T., Yoshimura,Y., Igami,H., Ohkubo,K., Miyazawa,J., Masuzaki,S., Shoji,M., Watanabe,T., Ashikawa,N., Nishimura,K., Sakamoto,M., Osakabe,M., Tsumori,K., Ikeda,K., Chikaraishi,H., Funaba,H., Morita,S., Goto,M., Tokuzawa,T., Takeuchi,N., Ogawa,H., Shimpo,F., Nomura,G., Takahashi,C., Yokota,M., Zhao,Y. -P., Kwak,J. -G., Yamada,H., Kawahata,K., Ohyabu,N., Kaneko,O., Ida,K., Nagayama,Y., Noda,N., Komori,A., Sudo,S., Motojima,O., LHD Experimental Group  
  
Thirty-Minute Plasma Sustainment by ICRF, EC and NBI Heating in the Large Helical Device  
Journal of Plasma and Fusion Research Vol.81, No.4 (2005) 229-230
- (88) Nagaoka,K., Isobe,M., Shinohara,K., Osakabe,M., Shimizu,A., Okamura,S.  
Energetic Ion Measurements Using a Directional Probe  
Plasma and Fusion Research Vol.1, (2006) 005-1-005-2
- (89) Nagasaka,T., Muroga,T., Noda,N., Kawamura,M., Ise,H., Kurishita,H.  
Tungsten Coating on Low Activation Vanadium Alloy by Plasma Spray Process  
Fusion Science and Technology Vol.47, (2005) 876-880
- (90) Nagayama,Y., Katsurai,M.  
Proposal of Steady State Superconducting Spherical Tokamak Experiment  
IEEJ Transactions on Fundamentals and Materials Vol.125, No.11 (2005) 964-965
- (91) Nagayama,Y., Narihara,K., Narushima,Y., Ohyabu,N., Hayashi,T., Ida,K., Inagaki,S., Kalinina,D., Kanno,R., Komori,A., Morisaki,T., Sakamoto,R., Sudo,S., Tamura,N., Tokuzawa,T., Yamada,H., Yoshinuma,M., LHD Experimental Group  
Experiment of Magnetic Island Formation in Large Helical Device  
Nuclear Fusion Vol.45, No.8 (2005) 888-893
- (92) Nagayama,Y., Tomita,Y.  
Steady Burning Criteria for D-3He Spherical Torus Reactor with Internal Transport Barrier  
IEEJ Transactions on Fundamentals and Materials Vol.125, No.11 (2005) 947-952
- (93) Nakajima,N., Hudson,S. R., Hegna,C. C., Nakamura,Y.  
Boundary Modulation Effects on MHD Instabilities in Heliotrons  
Nuclear Fusion Vol.46, (2006) 177-199
- (94) Nakamura,H., Hatano,N., Shirasaki,R.  
Quantum Nernst Effect  
Solid State Communications Vol.135, No.8 (2005) 510-514
- (95) Nakamura,H., Tamura,Y.  
Phase Diagram for Self-assembly of Amphiphilic Molecule  $C_{12}E_6$  by Dissipative Particle Dynamics Simulation  
Computer Physics Communications Vol.169, No.1-3 (2005) 139-143

- (96) Nakamura,N., Tobiyama,H., Nohara,H., Kato,D., Watanabe,H., Currell,F. J., Ohtani,S.  
Observation of Resonant-excitation Double Autoionization in Electron- $I^{50+}$  Collisions  
Physical Review A Vol.73, No.2 (2006) 020705-1-020705-4
- (97) Nakanishi,H., Ohsuna,M., Kojima,M., Imazu,S., Nonomura,M., Emoto,M., Okumura,H., Nagayama,Y.,  
Kawahata,K., LHD Experimental Group  
Ultra-Wideband Real-Time Data Acquisition in Steady-State Experiments  
Journal of Plasma and Fusion Research Vol.82, No.3 (2006) 171-177
- (98) Narushima,Y., Sakakibara,S., Watanabe,K. Y., Ida,K., Narihara,K., Ohdachi,S., Inagaki,S., Yoshinuma,M.,  
Yamada,I., Cooper,W. A., Yamada,H., Yamaguchi,T., Takeiri,Y., LHD Experimental Group  
Effect of Plasma Current on  $m = 1$  Mode in LHD  
Journal of Plasma and Fusion Research Vol.1, (2006) 004-1-004-3
- (99) Nishimura,A., Hishinuma,Y., Seo,K., Tanaka,T., Muroga,T., Nishijima,S., Katagiri,K., Takeuchi,T., Shindo,Y.,  
Ochiai,K., Nishitani,T., Okuno,K.  
14 MeV Neutron Irradiation Effect on Superconducting Magnet Materials for Fusion Device  
Advances in Cryogenic Engineering Vol.824, (2006) 208-215
- (100) Nishimura,A., Hishinuma,Y., Seo,K., Tanaka,T., Muroga,T., Nishijima,S., Katagiri,K., Takeuchi,T., Shindo,Y.,  
Ochiai,K., Nishitani,T., Okuno,K.  
Irradiation Effect of 14 MeV Neutron on Interlaminar Shear Strength of Glass Fiber Reinforced Plastics  
Advances in Cryogenic Engineering Vol.824, (2006) 241-248
- (101) Nishimura,A., Hishinuma,Y., Tanaka,T., Muroga,T., Nishijima,S., Shindo,Y., Takeuchi,T., Ochiai,K., Nishitani,T.,  
Okuno,K.  
Design, Fabrication and Installation of Cryogenic Target System for 14 MeV Neutron Irradiation  
Fusion Engineering and Design Vol.75-79, (2005) 173-177
- (102) Nishimura,A., Muroga,T., Takeuchi,T., Nishitani,T., Morioka,A.  
Nuclear Technology and Potential Ripple Effect of Superconducting Magnets for Fusion Power Plant  
Fusion Engineering and Design Vol.81, No.8-14 (2006) 1675-1681
- (103) Nishiura,M., Ido,T., Shimizu,A., Kato,S., Tsukada,K., Nishizawa,A., Hamada,Y., Matsumoto,Y., Mendenilla,A.,  
Wada,M.  
Optimization of Negative Ion Sources for a Heavy Ion Beam probe  
Review of Scientific Instruments Vol.77, No.3 (2006) 03A537-1-03A537-3
- (104) Nobuta,Y., Ashikawa,N., Hino,T., Yamauchi,Y., Hirohata,Y., Nishimura,K., Sagara,A., Masuzaki,S., Noda,N.,  
Ohyabu,N., Komori,A., Motojima,O.  
Material Probe Analysis of Boronized Wall in LHD  
Fusion Engineering and Design Vol.81, No.1-7 (2006) 187-192
- (105) Noe,M., Juengst,K. -P., Elschner,S., Bock,J., Breuer,F., Kreutz,R., Kleimaier,M., Weck,K. -H., Hayakawa,N.  
High Voltage Design, Requirements and Tests of a 10 MVA Superconducting Fault Current Limiter  
IEEE Transactions on Applied Superconductivity Vol.15, No.2 (2005) 2082-2085
- (106) Notake, T., Idei, H., Shimozuma, T., Sato, M., Kubo, S., Ito,S., Takita, Y., Ohkubo, K., Yoshimura, Y., Kobayashi,  
S., Mizuno, Y., Watari, T., Kumazawa, R., Shapiro, M.A., Temkin, R.J.,  
Evaluation of Phase Correcting Mirrors for an 84 GHz Gyrotron Based on Direct Phase Measurements at Low Power  
Level  
Fusion Engineering and Design Vol.73, Issue1(2005)p9-18
- (107) Nozato,H., Morita,S., Goto,M., LHD Experimental Group  
A New Method on Recycling Coefficient Measurement Using Impurity Pellet Injection in a Large Helical Device  
Review of Scientific Instruments Vol.76, No.7 (2005) 073503-1-073503-5
- (108) Ohya,M., Shigemasu,S., Shirai,Y., Shiotsu,M., Imagawa,S.  
Stability of Superconducting Wire With Various Surface Conditions in Pressurized He II (1)-Experimental Results  
IEEE Transactions on Applied Superconductivity Vol.15, No.2 (2005) 1703-1706
- (109) Ohyabu,N., Narushima,Y., Nagayama,Y., Narihara,K., Morisaki,T., Komori,A.  
Bifurcation of Equilibria between with and without a Large Island in the Large Helical Device  
Plasma Physics and Controlled Fusion Vol.47, No.9 (2005) 1437-1431



- (110) Oka, Y., Ikeda, K., Takeiri, Y., Tsumori, K., Kaneko, O., Nagaoka, K., Osakabe, M., Asano, E., Kondo, T., Sato, M., Shibuya, M., Grisham, L., Umeda, N., Honda, A., Ikeda, Y., Yamamoto, T.  
Doppler-shift Spectra of Ha Lines from Negative-ion-based Neutral Beams for Large Helical Device Neutral Beam Injection  
Review of Scientific Instruments Vol.77, No.3 (2006) 03A538-1-03A538-4
- (111) Oka, Y., Shoji, T., Ikeda, K., Kaneko, O., Nagaoka, K., Osakabe, M., Takeiri, Y., Tsumori, K., Asano, E., Kondo, T., Sato, M., Shibuya, M.  
Ion-beam Extraction with Single Hole Extractor from Multiantenna rf Ion Source in NIFS  
Review of Scientific Instruments Vol.77, No.3 (2006) 03B506-1-03B506-3
- (112) Okamoto, A., Nagaoka, K., Yoshimura, S., Vranjes, J., Kado, S., Kono, M., Tanaka, M. Y.  
Tripolar Vortex in a Plasma  
IEEE Transactions on Plasma Sciences Vol.33, No.2 (2005) 452-453
- (113) Okamura, S., Minami, T., Akiyama, T., Oishi, T., Fujisawa, A., Ida, K., Iguchi, H., Isobe, M., Kado, S., Nagaoka, K., Nakamura, K., Nishimura, S., Matsuoka, K., Matsushita, H., Nakano, H., Nishiura, M., Ohshima, S., Shimizu, A., Suzuki, C., Takahashi, C., Toi, K., Yoshimura, Y., Yoshinuma, M.  
Edge and Internal Transport Barrier Formations in CHS  
Nuclear Fusion Vol.45, No.8 (2005) 863-870
- (114) Okubo, H., Hayakawa, N.  
A Novel Technique for Partial Discharge and Breakdown Investigation Based on Current Pulse Waveform Analysis  
IEEE Transaction Dielectrics and Electrical Insulation Vol.12, No.4 (2005) 736-744
- (115) Okumura, M., Yuki, K., Hashizume, H., Sagara, A.  
Evaluation of Flow Structure in Packed-bed Tube by Visualization Experiment  
Fusion Science and Technology Vol.47, No.4 (2005) 1089-1093
- (116) Oya, Y., Onishi, Y., Okuno, K., Kawano, T., Asakura, Y., Uda, T., Tanaka, S.  
Hydrogen Isotope Behavior in Type 316 Stainless Steel Sorbed by Various Methanods  
Fusion Science and Technology Vol.48, No.1 (2005) 597-600
- (117) Rabin, Y., Tanaka, M.  
DNA in Nanopore: Counterion Condensation and Coion Depletion  
Physical Review Letters Vol.94, No.14 (2005) 148103-1-148103-4
- (118) Reynolds, E. W., Kaneko, T., Koepke, M. E., Hatakeyama, R.  
Laser-Induced-Fluorescence Characterization of Velocity Shear in a Magnetized Plasma Column Produced by a Segmented Q-machine Source  
Physics of Plasmas Vol.12, No.7 (2005) 072103-1-072103-6
- (119) Safronova, U. I., Ralchenko, Yu., Murakami, I., Kato, T., Kato, D.  
Atomic Data for Dielectronic Recombination into C-like Oxygen  
Physica Scripta Vol.73, No.2 (2006) 143-159
- (120) Sagara, A., Imagawa, S., Mitarai, O., Dolan, T., Tanaka, T., Kubota, Y., Yamazaki, K., Watanabe, K. Y., Mizuguchi, N., Muroga, T., Noda, N., Kaneko, O., Yamada, H., Ohyabu, N., Uda, T., Komori, A., Sudo, S., Motojima, O.  
Improved Structure and Long-life Blanket Concepts for Heliotron Reactors  
Nuclear Fusion Vol.45, No.4 (2005) 258-263
- (121) Sagara, A., Imagawa, S., Tanaka, T., Muroga, T., Kubota, Y., Dolan, T., Hashizume, H., Kunugi, T., Fukada, S., Shimizu, A., Terai, T., Mitarai, O.  
Carbon tiles as spectral-shifter for long-life liquid blanket in LHD-type reactor FFHR  
Fusion Engineering and Design Vol.81, No.8-14 (2006) 1299-1304
- (122) Sagara, A., Tanaka, T., Muroga, T., Hashizume, H., Kunugi, T., Fukada, S., Shimizu, A.  
Innovative Liquid Breeder Blanket Design Activities in JAPAN  
Fusion Science and Technology Vol.47, No.3 (2005) 524-529
- (123) Sakagami, H., Kishimoto, Y., Sentoku, Y., Taguchi, T.  
Progress of Laser-Plasma Interaction Simulations with the Particle-In-Cell Code  
Journal of Plasma and Fusion Research Vol.81, (2005) 64-75
- (124) Sakamoto, R., Yamada, H.  
Three-dimensional Observation System for Pellet Ablation Traveling in the High Temperature Plasmas  
Review of Scientific Instruments Vol.76, No.10 (2005) 103502-1-103502-4

- (125) Sano, F., Mizuuchi, T., Kondo, K., Nagasaki, K., Okada, H., Kobayashi, S., Hanatani, K., Nakamura, Y., Yamamoto, S., Torii, Y., Suzuki, Y., Shidara, H., Kaneko, M., Arimoto, H., Azuma, T., Arakawa, J., Ohashi, K., Kikutake, M., Shimazaki, N., Hamagami, T., Motojima, G., Yamazaki, H., Yamada, M., Kitagawa, H., Tsuji, T., Nakamura, H., Watanabe, S., Murakami, S., Nishino, N., Yokoyama, M., Ijiri, Y., Senju, T., Yaguchi, K., Sakamoto, K., Tohshi, K., Shibano, M.
- H-mode confinement of Heliotron J  
Nuclear Fusion Vol.45, No.12 (2005) 1557-1570
- (126) Sano, F., Mizuuchi, T., Kondo, K., Nagasaki, K., Okada, H., Kobayashi, S., Hanatani, K., Nakamura, Y., Yamamoto, S., Torii, Y., Suzuki, Y., Shidara, H., Kaneko, M., Arimoto, H., Azuma, T., Arakawa, J., Ohashi, K., Kikutake, M., Shimazaki, N., Hamagami, T., Motojima, G., Yamazaki, H., Yamada, M., Kitagawa, H., Tsuji, T., Nakamura, H., Watanabe, S., Murakami, S., Nishino, N., Yokoyama, M., Ijiri, Y., Senju, T., Yaguchi, K., Sakamoto, K., Tohshi, K., Shibano, M.
- H-mode Confinement Studies of Heliotron J  
Nucl. Fusion 45, No.12(Dec.2005)1557-1570
- (127) Sasaki, A., Murata, M., Kanamaru, T., Shirado, T., Isahara, H., Ueshima, Y., Yamagiwa, M.
- Methods to Extract Information on the Atomic and Molecular States from Scientific Abstracts  
Journal of Plasma and Fusion Research Vol.81, No.9 (2005) 717-722
- (128) Sasaki, K., Maeda, T., Takada, N., Aramaki, M., Goto, M., Muto, S., Morita, S.
- Production of Radicals and Particulates by Interaction between High-Density Hydrogen Plasma and Graphite Plate  
Japanese Journal of Applied Physics Vol.44, No.10 (2005) 7614-7618
- (129) Sasao, M., Connor, K. A., Ida, K., Iguchi, H., Ivanov, A. A., Nishiura, M., Thomas, D. M., Wada, M., Yoshinuma, M.
- Ion Sources for Fusion Plasma Diagnostics  
IEEE Transactions on Plasma Sciences Vol.33, No.6 (2005) 1872-1910
- (130) Satake, S., Kunugi, T., Naito, N., Sagara, A.
- Direct Numerical Simulation of MHD Flow with Electrically Conducting Wall  
Fusion Engineering and Design Vol.81, No.1-7 (2006) 367-374
- (131) Satake, S., Okamoto, M., Nakajima, N., Sugama, H., Yokoyama, M., Beidler, C. D.
- Non-local Neoclassical Transport Simulation of Geodesic Acoustic Mode  
Nuclear Fusion Vol.45, No.11 (2005) 1362-1368
- (132) Seki, M., Yamamoto, I., Sagara, A.
- Overview of Recent Japanese Activities in Fusion Technology  
Fusion Science and Technology Vol.47, No.3 (2005) 300-307
- (133) Seo, K., Mito, T., Miller, J. R., Kawabata, S., Ichihara, T., Hasegawa, M.
- Analysis of Joint-Resistance-Induced Non-Uniform Current Distribution  
IEEE Transactions on Applied Superconductivity Vol.15, No.2 (2005) 1595-1598
- (134) Seo, K., Takahata, K., Mito, T., Hayashi, H., Terazono, K., Semba, T., Miyashita, K.
- Calibration on Inductive Heater for Stability Test of Cable in Conduit Conductor  
IEEE Transactions on Applied Superconductivity Vol.15, No.2 (2005) 1695-1698
- (135) Sharpe, J. P., Humrickhouse, P. W., Skinner, C. H., the NSTX Team, Tanabe, T., Masaki, K., Miya, N., the JT-60U Team, Sagara, A.
- Characterization of Dust Collected from NSTX and JT-60U  
Journal of Nuclear Materials Vol.337-339, No.0 (2005) 1000-1004
- (136) Shigemasa, S., Ohya, M., Shirai, Y., Shiotsu, M., Imagawa, S.
- Stability of Superconducting Wire With Various Surface Conditions in Pressurized He II (2)-Numerical Analysis  
IEEE Transactions on Applied Superconductivity Vol.15, No.2 (2005) 1707-1710
- (137) Shimizu, A., Fujisawa, A., Ohshima, S., Nakano, H.
- Consideration of Magnetic Field Fluctuation Measurements in Torus Plasma with a Heavy Ion Beam Probe  
Review of Scientific Instruments Vol.76, No.4 (2005) 043504-1-043504-6

- (138)Shimozuma,T., Kubo,S., Idei,H., Inagaki,S., Tamura,N., Tokuzawa,T., Morisaki,T., Watanabe,K. Y., Ida,K., Yamada,I., Narihara,K., Muto,S., Yokoyama,M., Yoshimura,Y., Notake,T., Ohkubo,K., Seki,T., Saito,K., Kumazawa,R., Mutoh,T., Watari,T., Komori,A.  
Transition Phenomena and Thermal Transport Properties in LHD Plasmas with an Electron Internal Transport Barrier  
Nuclear Fusion Vol.45, No.11 (2005) 1396-1403
- (139)Shinohara,K., Ishikawa,M., Takechi,M., Kusama,Y., Todo,Y., Gorelenkov,N., Cheng,C., Fukuyama,A., Kramer,G., Nazikian,R., Matsunaga,G., Ozeki,T.  
Instability in the Frequency-Range of Alfvén Eigenmodes Driven by Negative-Ion-Based Neutral Beams in JT-60U  
Journal of Plasma and Fusion Research Vol.81, No.7 (2005) 547-552
- (140)Shinohara,S., Mizokoshi,H.  
Development of a Strong Field Helicon Plasma Source  
Review of Scientific Instruments Vol.77, No.3 (2006) 036108-1-036108-4
- (141)Shinto,K., Sugawara,H., Takenaga,M., Takeuchi,S., Tanaka,N., Okamoto,A., Kitajima,S., Sasao,M., Nishiura,M., Wada,M.  
Optimization of a Compact Multicusp He<sup>+</sup> Ion Source for Double Charge Exchanged He<sup>-</sup> Beam  
Review of Scientific Instruments Vol.77, No.3 (2006) 03B512-1-03B512-4
- (142)Shoji,M., Watanabe,T., LHD Experimental Group  
Production of Hot Spot on a Vertically Installed Divertor Plate by ICRF Heating in the Large Helical Device  
IEEE Transactions on Plasma Sciences Vol.33, No.2 (2005) 440-441
- (143)Shoji,T., Oka,Y., NBI group  
Characteristics of Multiantenna rf Ion Source  
Review of Scientific Instruments Vol.77, No.3 (2006) 03B513-1-03B513-4
- (144)Sudo,S., Viniar,I., Lukin,A., Reznichenko,P., Umov,A.  
Trace-encapsulated Pellet Injector for Plasma Diagnostics  
Review of Scientific Instruments Vol.76, No.5 (2005) 053507-1-053507-7
- (145)Sugama,H., Watanabe,T. -H.  
Collisionless Damping of Zonal Flows in Helical Systems  
Physics of Plasmas Vol.13, No.1 (2006) 012501-1-012501-18
- (146)Sugiyama,T., Asakura,Y., Uda,T., Abe,Y., Shiozaki,T., Enokida,Y., Yamamoto,I.  
Hydrogen Isotope Separation by Combined Electrolysis Catalytic Exchange under Reduced Pressure  
Fusion Science and Technology Vol.48, No.1 (2005) 132-135
- (147)Sugiyama,T., Asakura,Y., Uda,T., Kotoh,K.  
Measurement of Breakthrough Curves on Pressure Swing Adsorption for Hydrogen Isotope Separation  
Fusion Science and Technology Vol.48, No.1 (2005) 163-166
- (148)Suzuki,C., Nishimura,H., Ochiai,M., Kato,T., Okamura,S., More,R. M., Nishihara,K., Nakai,M., Shigemori,K., Fujioka,S., Ogawa,H.  
Temperature-Dependent EUV Spectra of Xenon Plasmas Observed in the Compact Helical System  
Journal of Plasma and Fusion Research Vol.81, No.7 (2005) 480-481
- (149)Suzuki,E., Nakano,T., Takahashi,N., Gotoh,T.  
Energy Transfer and Intermittency in 4-Dimensional Turbulence  
Physics of Fluids Vol.17, No.8 (2005) 081702-1-081702-4
- (150)Suzuki,R., Rai,N. S., Liebermann,H. -P., Buenker,R. J., Pichl,L., Kimura,M.  
Elastic and Electron-capture Processes in H<sup>+</sup> + C<sub>2</sub>H<sub>4</sub> Collisions Below the 10-keV Regime  
Physical Review A Vol.71, No.3 (2005) 032710-1-032710-10
- (151)Tachikawa,K.  
The History and Future A15s in Japan  
IEEE Transactions on Applied Superconductivity Vol.15, No.3 (2005) 2443-2449
- (152)Tachikawa,K., Ikeda,Y., Koyata,T., Nakaze,T., Takeuchi,T.  
High-Field Performance of (Nb,Ta)<sub>3</sub>Sn Wires Prepared from Sn-Ta Matrix  
IEEE Transactions on Applied Superconductivity Vol.15, No.3 (2005) 3486-3489

- (153) Tachikawa, K., Ikeda, Y., Koyata, Y., Takeuchi, T.  
Structure and Performance of (Nb,Ta)<sub>3</sub>Sn Superconducting Wires Fabricated from Sn-Ta Sheet  
Journal of the Japan Institute of Metals Vol.68, No.9 (2005) 624-628
- (154) Tachikawa, K., Kato, H., Zaitu, K., Miyatake, T., Hamada, M., Takeuchi, T.  
Nb<sub>3</sub>Sn Multi-filamentary Superconducting Wires Prepared by Ta-Sn Powder in Tube Process  
IEEE Transactions on Applied Superconductivity Vol.15, No.3 (2005) 3490-3493
- (155) Takahashi, H., Yokoyama, M., Kitajima, S., Tanaka, Y., Utoh, H., Sasao, M.  
Hysteresis during Transition into Improved Mode on Biasing Experiment under the Electrode Current Control in  
Tohoku University Heliac  
Plasma Physics and Controlled Fusion Vol.48, No.1 (2006) 39-49
- (156) Takahashi, K., Kaneko, T., Hatakeyama, R.  
Effects of Polarization Reversal on Localized-Absorption Characteristics of Electron Cyclotron Wave in Bounded  
Plasmas  
Physics of Plasmas Vol.12, No.10 (2005) 102107-1-102107-7
- (157) Takahashi, K., Kaneko, T., Hatakeyama, R.  
Polarization-Reversal Induced Damping of Left-Hand Polarized Wave on Electron Cyclotron Resonance  
Physical Review Letters Vol.94, No.21 (2005) 215001-1-215001-4
- (158) Takahashi, T., Hirano, Y., Asai, T., Tomita, Y., Mizuguchi, N., Kondoh, Y.  
Beam Ion Loss due to Charge Exchange Process in the Open Field Region of a Field-Reversed Configuration  
Journal of Plasma and Fusion Research Vol.81, No.6 (2005) 421-422
- (159) Takahashi, Y., Morisaki, T., Toi, K., LHD Experimental group  
Two-Dimensional Measurement of Electron Density Profile in the Edge Region of the Large Helical Device Plasma by  
a Sheet-Shaped Thermal Lithium Beam  
Journal of Plasma and Fusion Research Vol.1, No.013 (2006) 013-1-013-2
- (160) Takamatsu, T., Masuda, K., Kyunai, T., Toku, H., Yoshikawa, K.  
Inertial Electrostatic Confinement Fusion Device with an Ion Source Using a Magnetron Discharge  
Nuclear Fusion Vol.46, No.1 (2006) 142-148
- (161) Takamatsu, T., Masuda, K., Yoshikawa, K., Toku, H., Nagasaki, K., Kyunai, T.  
Magnetron-Discharge-Based Ion Source for Improvement of an Inertial Electrostatic Confinement Fusion Device  
Fusion Science and Technology Vol.47, No.4 (2005) 1290-1294
- (162) Takeda, T., Yoshikawa, A., Oyaidzu, M., Nakahata, T., Nishikawa, Y., Kimura, H., Onishi, Y., Miyauchi, H., Oya, Y.,  
Sagara, A., Noda, N., Okuno, K.  
Helium Irradiation Effects for Deuterium Retention in Boron Coating Films  
Fusion Engineering and Design Vol.81, No.1-7 (2006) 301-306
- (163) Takeiri, Y., Ikeda, K., Oka, Y., Tsumori, K., Osakabe, M., Nagaoka, K., Kaneko, O., Asano, E., Kondo, T., Sato, M.,  
Shibuya, M., Komada, S.  
Characteristics of Long-pulse Negative-ion Source in the Neutral Beam Injector of Large Helical Device  
Review of Scientific Instruments Vol.77, No.3 (2006) 03A523-1-03A523-4
- (164) Takeiri, Y., Morita, S., Tsumori, K., Ikeda, K., Oka, Y., Osakabe, M., Nagaoka, K., Goto, M., Miyazawa, J., Masuzaki, S.,  
Ashikawa, N., Yokoyama, M., Murakami, S., Narihara, K., Yamada, I., Kubo, S., Shimozuma, T., Inagaki, S., Tanaka, K.,  
Peterson, B. J., Ida, K., Kaneko, O., Komori, A., LHD Experimental group  
High-ion Temperature Experiments with Negative-ion-based Neutral beam injection heating in Large Helical Device  
Nuclear Fusion Vol.45, No.7 (2005) 565-573
- (165) Takeno, H., Kiriya, Y., Yasaka, Y.  
Experiments to Improve Power Conversion Parameters in a Traveling Wave Direct Energy Converter Simulator  
Fusion Science and Technology Vol.47, No.3 (2005) 450-454
- (166) Tamura, N., Inagaki, S., Ida, K., Shimozuma, T., Kubo, S., Tokuzawa, T., Tanaka, K., Neudatchin, S. V., Itoh, K.,  
Kalinina, D., Sudo, S., Nagayama, Y., Ohkubo, K., Kawahata, K., Komori, A., LHD Experimental group  
Observation of Core Electron Temperature Rise in Response to an Edge Cooling in Toroidal Helical Plasmas  
Physics of Plasmas Vol.12, No.11 (2005) 110705-1-110705-4



- (167) Tanaka, K., Michael, C., Sanin, A., Vyacheslavov, L. N., Kawahata, K., Murakami, S., Wakasa, A., Okajima, S., Yamada, H., Shoji, M., Miyazawa, J., Morita, S., Tokuzawa, T., Akiyama, T., Goto, M., Ida, K., Yoshinuma, M., Yamada, I., Yokoyama, M. Y., Masuzaki, S., Morisaki, T., Sakamoto, R., Funaba, H., Inagaki, S., Kobayashi, M., Komori, A., LHD Experimental group  
Experimental Study of Particle Transport and Density Fluctuations in LHD  
Nuclear Fusion Vol.46, No.1 (2006) 110-122
- (168) Tanaka, M., Asakura, Y., Uda, T., Katahira, K., Iwahara, H., Tsuji, N., Yamamoto, I.  
Studies on Hydrogen Extraction Characteristics of Proton-conducting Ceramics and Their Applications to a Tritium Recovery System and Tritium Monitor  
Fusion Science and Technology Vol.48, No.1 (2005) 51-54
- (169) Tanaka, M. Y., Nagaoka, K., Okamoto, A., Yoshimura, S., Kono, M.  
Plasma Hole  
IEEE Transactions on Plasma Sciences Vol.33, No.2 (2005) 454-455
- (170) Tanaka, T., Muroga, T., Sagara, A.  
Tritium Self-Sufficiency and Neutron Shielding Performance of Self-Cooled Liquid Blanket System for Helical Reactor  
Fusion Science and Technology 47, No.3 (Apr.2005) pp.530-534.
- (171) Tanaka, Y., Arita, K. -I., Nagayama, Y., Kiyota, S.  
Transmutation of High-level Wastes in a Spherical-tokamak Reactor  
IEEE Transactions on Fundamentals and Materials Vol.125, No.11 (2005) 953-957
- (172) Toda, S., Itoh, K.  
Test of the Theoretical Model for the Improved Confinement in Helical Plasmas  
Journal of the Physical Society of Japan Vol.74, No.11 (2005) 2987-2989
- (173) Todo, Y.  
A Complementary Fluid Method in delta-f Particle Simulation  
Journal of Plasma and Fusion Research Vol.81, No.11 (2005) 944-948
- (174) Toi, K., Ohdachi, S., Watanabe, F., Narihara, K., Morisaki, T., Gao, X., Goto, M., Ida, K., Masuzaki, S., Miyazawa, J., Morita, S., Sakakibara, S., Tanaka, K., Tokuzawa, T., Watanabe, K. W., Yan, L., Yoshinuma, M., LHD Experimental group  
Formation of Edge Transport Barrier by L-H Transition and Large Reversed Plasma Current on LHD  
Plasma Science & Technology (China) Vol.8, No.1 (2006) 5-9
- (175) Tokitani, M., Miyamoto, M., Tokunaga, K., Fujiwara, T., Yoshida, N., Komori, A., Masuzaki, S., Ashikawa, N., Inagaki, S., Kobuchi, T., Goto, M., Miyazawa, J., Nishimura, K., Noda, N., Peterson, B. J., Sagara, A.  
Microscopic Modification of Wall Surface by Glow Discharge Cleaning and its Impact on Vacuum Properties of LHD  
Nuclear Fusion Vol.45, No.12 (2005) 1544-1549
- (176) Tomita, Y., Smirnov, R., Zhu, S.  
Induced Charge of Spherical Dust Particle on Plasma-Facing Wall in Non-uniform Electric Field  
Plasma Science & Technology (China) Vol.8, No.1 (2006) 122-124
- (177) Uda, T., Sugiyama, T., Asakura, Y., Munakata, K., Tanaka, M.  
Development of High Performance Catalyst for Oxidation of Tritiated Hydrogen and Methane Gases  
Fusion Science and Technology Vol.48, No.1 (2005) 480-483
- (178) Vlad, M., Spineanu, F., Itoh, S-I., Yagi, M., Itoh, K.  
Turbulent Transport of Ions with Large Larmor Radii  
Plasma Phys. Control. Fusion Vol. 47, No.7 (2005) 1015-1029
- (179) Vyacheslavov, L. N., Tanaka, K., Sanin, A. L., Kawahata, K., Michael, C., Akiyama, T.  
2-D Phase Contrast Imaging of Turbulence Structure on LHD  
IEEE Transactions on Plasma Sciences Vol.33, No.2 (2005) 464-465
- (180) Wang, J., Fujiwara, O., Uda, T.  
New Approach to Safety Evaluation of Human Exposure to Stochastically-varying Electromagnetic Fields  
IEEE Transaction Dielectrics and Electrical Insulation Vol.47, No.4 (2005) 971-976

- (181) Watanabe,F., Ohdachi,S., Takagi,S., Toi,K., Sakakibara,S., Watanabe,K. Y., Morita,S., Narihara,K., Tanaka,K., Yamazaki,K., LHD Experimental group  
Observation of Internal Structure of Edge MHD Modes in High Beta Plasmas on the Large Helical Device  
Journal of Plasma and Fusion Research Vol.81, No.12 (2005) 967-968
- (182) Watanabe,K., Sakakibara,S., Narushima,Y., Funaba,H., Narihara,K., Tanaka,K., Yamaguchi,T., Toi,K., Ohdachi,S., Kaneko,O., Yamada,H., Suzuki,Y., Cooper,W. A., Murakami,S., Nakajima,N., Yamada,I., Kawahata,K., Tokuzawa,T., Komori,A., LHD Experimental group  
Effects of Global MHD Instability on Operational High Beta-regime in LHD  
Nuclear Fusion Vol.45, No.11 (2005) 1247-1254
- (183) Watanabe,T. -H., Sugama,H.  
Velocity-space Structures of Distribution Function in Toroidal Ion Temperature Gradient Turbulence  
Nuclear Fusion Vol.46, No.1 (2006) 24-32
- (184) Watanabe,T. -H., Sugama,H.  
Vlasov and Drift Kinetic Simulation Methods Based on the Symplectic Integrator  
Transport Theory and Statistical Physics Vol.34, No.3-5 (2005) 287-309
- (185) Watanabe,T., Matsumoto,Y., Hishiki,M., Oikawa,S., Hojo,H., Shoji,M., Masuzaki,S., Kumazawa,R., Saito,K., Seki,T., Mutoh,T., Komori,A., LHD Experimental group  
Magnetic Field Structure and Confinement of Energetic Particles in the LHD  
Nuclear Fusion Vol.46, No.2 (2006) 291-305
- (186) Watari,T., Hamada,Y., Fujisawa,A., Toi,K., Itoh,K.  
Extension of Geometric Acoustic Mode Theory to Helical Systems  
Physics of Plasmas Vol.12, No.6 (2005) 062304-1-062304-8
- (187) Yagi,M., Yoshida,S., Itoh,S.-I., Naitou,H., Nagahara,H., Leboeuf,J. -N., Itoh,K., Matsumoto,T., Tokuda,S., Azumi,M.  
Nonlinear Simulation of Tearing Mode Based on 4-field RMHD Model  
Nuclear Fusion Vol.45, No.8 (2005) 900-906
- (188) Yakovlev,M., Inagaki,S., Shimozuma,T., Kubo,S., Morisaki,T., Nagayama,Y., Kawahata,K., Komori,A.  
Heat Pulse Propagation Across the Rational Surface in a Large Helical Device Plasma with Counter-neutral Beam Injection  
Physics of Plasmas Vol.12, No.9 (2005) 0925061-1-092506-6
- (189) Yamada,H., Harris,J. H., Dinklage,A., Ascasibar,E., Sano,F., Okamura,S., Talmadge,J., Stroth,U., Kus,A., Murakami,S., Yokoyama,M., Beidler,C. D., Tribaldos,V., Watanabe,K. Y., Suzuki,Y.  
Characterization of Energy Confinement in Net-current Free Plasmas Using the Extended International Stellarator Database  
Nuclear Fusion Vol.45, No.12 (2005) 1684-1693
- (190) Yamada,S., Nakanishi,Y., Kojima,H., Hiue,H., Uede,T., Mito,T.  
Elimination of Variable Harmonics on Motor Generator Circuit for Experimental Fusion Facility  
Fusion Engineering and Design Vol.75, No.0 (2005) 93-97
- (191) Yamaguchi,T., Watanabe,K., Sakakibara,S., Narushima,Y., Narihara,K., Tokuzawa,T., Tanaka,K., Yamada,I., Osakabe,M., Yamada,H., Kawahata,K., Yamazaki,K., LHD Experimental group  
Measurement of Anisotropic Pressure Using Magnetic Measurements in LHD  
Nuclear Fusion Vol.45, No.11 (2005) 133-136
- (192) Yamamoto,S., Toi,K., Ohdachi,S., Nakajima,N., Sakakibara,S., Nuehrenberg,C., Watanabe,K. Y., Murakami,S., Osakabe,M., Goto,M., Kawahata,K., Masuzaki,S., Morita,S., Narihara,K., Narushima,Y., Ohyabu,N., Takeiri,Y., Tanaka,K., Tokuzawa,T., Yamada,H., Yamada,I., Yamazaki,K., LHD Experimental group  
Experimental Studies of Energetic-Ion-Driven MHD Instabilities in Large Helical Device Plasmas  
Nuclear Fusion Vol.45, No.5 (2005) 326-336
- (193) Yamanishi,H.  
Design of a Portable Directional Neutron Source Finder  
Nuclear Instruments and Methods in Physics Research Section A Vol.544, No.3 (2005) 643-648
- (194) Yamanishi,H.  
Measurement error of radiation monitoring by means of an electronic dosimeter  
Japanese Journal of Health Physics Vol.40, No.4 (2005) 372-375

- (195) Yamaoka, H., Matsumoto, Y., Nishiura, M., Tsumori, K., Sugawara, H., Takeuchi, S., Shinto, K., Sasao, M., Wada, M.  
Development of an Angular-resolved Momentum Analyzer System to Study Particle Reflections from Solid Surfaces  
Review of Scientific Instruments Vol.77, No.3 (2006) 03C301-1-03C301-3
- (196) Yanagi, N., Mito, T., Hemmi, T., Seo, K., Morikawa, J., Ogawa, Y., Iwakuma, M.  
Effective Resistance of the HTS Floating Coil in the Mini-RT Project  
IEEE Transactions on Applied Superconductivity Vol.15, No.2 (2005) 1399-1402
- (197) Yao, Z., Suzuki, A., Muroga, T., Katahira, K.  
In Situ Formation and Chemical Stability of Er<sub>2</sub>O<sub>3</sub> Coating on V-4Cr-4Ti in Liquid Lithium  
Fusion Engineering and Design Vol.75-79, No.1 (2005) 1015-1019
- (198) Yasaka, Y., Kiriya, Y., Yamamoto, T., Takeno, H., Ishikawa, M.  
Particle Discrimination Experiment for Direct Energy Conversion  
Fusion Science and Technology Vol.47, No.3 (2005) 455-459
- (199) Yatsuyanagi, Y., Kiwamoto, Y., Tomita, H., Sano, M. M., Yoshida, T., Ebisuzaki, T.  
Dynamics of Two-Sign Point Vortices in Positive and Negative Temperature States  
Phys. Rev. Lett. Vol.94, No.5 (2005) pp.054502 (1-4)
- (200) Yokoyama, M., Watanabe, K.  
The Role of the Bumpy Field for the Ripple Diffusion in Strongly Inward Shifted Configurations in LHD  
Nuclear Fusion Vol.45, No.12 (2005) 1600-1607
- (201) Yu, W., Li, B. W., Yu, M. Y., He, F., Ishiguro, S., Horiuchi, R.  
Laser-field synchrotron radiation  
Physics of Plasmas Vol.12, No.10 (2005) 103101-1-103101-5
- (202) Yu, W., Xu, H., He, F., Yu, M. Y., Ishiguro, S., Zhang, J., Wong, Y.  
Direct acceleration of solid-density plasma bunch by ultraintense laser  
Physical Review E Vol.72, No.10 (2005) 046401-1-046401-6

# Author Index

## A

Abe, K.	264, 454
Abe, N.	410, 411, 416
Abe, R.	111, 115
Abe, T.	502, 528
Adachi, Y.	215
Aizu, K.	207
Akao, H.	62
Akiyama, R.	160, 322
Akiyama, T.	161, 162, 222, 293, 294, 295, 296, 297, 298, 299, 300, 302, 307, 321, 324
Amano, H.	239
Amo, H.	373, 387
Ando, A.	394, 395, 486, 530
Ando, K.	116
Ando, T.	230
Anma, Y.	251
Aoki, J.	336
Aoki, K.	106
Aoyama, H.	319, 404
Araki, K.	386
Aramaki, M.	326, 328
Arimoto, H.	40, 338
Arimoto, K.	172
Asai, T.	92, 208, 522, 531
Asakura, N.	530, 532
Asakura, Y.	286, 287, 288, 289, 290, 291, 470
Asano, E.	135, 136
Asaoka, Y.	393
Ashikawa, N.	42, 63, 64, 65, 66, 67, 68, 93, 233, 235
Atake, M.	57, 365, 487
Atarashi, M.	239
Azechi, H.	509
Azuchi, H.	511
Azumi, M.	188, 189

## B

Baba, T.	111, 248
Balandin, A.L.	172
Bansal, G.	114, 120, 121, 122, 123
Baudouy, B.	119
Beidler, C.D.	20
Berk, H.L.	353
Breizman, B.N.	353

## C

Carreras, B.A.	178, 179
Castejon, F.	20
Chang, D.H.	323
Chen, J.M.	455
Chen, Y.-W.	507, 516
Chikada, T.	260
Chikaraishi, H.	88, 99, 104, 111, 115, 283
Chikaraishi, N.	100
Cho, T.	211, 214, 227, 481, 489, 491, 493, 494, 495

CHS Experimental Group	294, 299, 305, 306, 307, 309, 312, 315, 316
Chuto, T.	454
Cowan, T.E.	432

## D

Dantsuka, T.	106
Darrow, D.S.	130
Den, M.	373, 374, 387
Dendy, R.O.	378
Diamond, P.H.	200, 201, 202, 203, 204
Dinesh Agrawal	427
Dinklage, A.	20
Dong, J.Q.	190, 191, 192

## E

Ebara, S.	242, 279, 469
Eiza, N.	255
Ejiri, A.	402, 519, 531
Emoto, M.	163
Endo, T.	510
Enokida, Y.	288
Estrada, T.	20

## F

Federici, G.	423
Feng, Y.	54, 423
Ferrando i Margalet, S.	196
FFHR Design Group	283
Fujimoto, S.	490
Fujimura, T.	421
Fujino, T.	208
Fujioka, S.	511
Fujisawa, A.	20, 200, 300, 305, 306, 307, 308, 309, 310, 319, 324, 337
Fujita, H.	338
Fujita, J.	410, 411, 412, 413, 416
Fujita, S.	373
Fujita, T.	16
Fujiwara, S.	381
Fukada, S.	241, 278, 504
Fukai, T.	489
Fukamizu, T.	502, 528
Fukao, M.	320
Fukumasa, O.	219
Fukumoto, K.	252
Fukumoto, N.	92, 519, 522
Fukuyama, A.	79, 200, 215, 229, 483
Fukuyama, Y.	502, 528
Funaba, H.	17, 36, 145, 229, 429, 430, 439, 440
Furukawa, H.	284
Furuzawa, A.	225

## G

GAMMA 10 Group	493
Gao Zhe	190, 191, 192



Goncharenko, I. ....	387
Goncharov, P.R. ....	82, 159
Goto, K. ....	220, 313, 314
Goto, M. ....	15, 39, 40, 41, 42, 69, 223, 225, 435, 439
Goto, S. ....	173
Goto, T. ....	276
Gotoh, H. ....	410
Gotoh, T. ....	205, 377
Grisham, L. ....	136

## H

Hadžievski, Lj. ....	379
Hahm, T.S. ....	202, 204
Hallatschek, K. ....	201, 203
Hamabe, M. ....	219
Hamada, Y. ....	149, 150, 151
Hamaguchi, S. ....	86, 90, 106, 112, 119, 396
Hamajima, T. ....	101, 105
Hamasaki, S. ....	245
Han, X. ....	516
Hanada, K. ....	218, 402, 518, 519, 522, 528, 530, 532
Hanaoka, E. ....	341
Hanaoka, S. ....	410, 412, 413
Hanatani, K. ....	497
Hara, H. ....	439
Hara, M. ....	93, 102, 103, 235
Haruyama, T. ....	106
Hasegawa, A. ....	242
Hasegawa, H. ....	408
Hasegawa, M. ....	518, 519, 530
Hashiba, Y. ....	233
Hashimoto, M. ....	381
Hashizume, H. ....	236, 263, 280
Hashizume, K. ....	235
Hata, K. ....	106, 259
Hatakeyama, R. ....	380, 485
Hatano, N. ....	383
Hatano, Y. ....	93, 235, 441
Hatayama, A. ....	362, 363, 364
Hattori, K. ....	394, 395, 486
Hayakawa, N. ....	110
Hayashi, H. ....	145
Hayashi, T. ....	176, 177, 182, 186, 351, 401, 427, 532
Hayashi, Y. ....	373
Hegna, C.C. ....	349, 350
Heliotron J Experimental Team ....	499
Heller, R. ....	117
Hemmi, T. ....	111, 114, 115, 120, 121, 122, 123
Higaki, H. ....	75, 483, 486, 488, 491
Higashijima, A. ....	530
Higashizono, Y. ....	492, 503, 529
High-Density Group ....	52, 53
Himura, H. ....	320
Hino, T. ....	66, 233, 264, 454
Hinoki, T. ....	255, 511, 513
Hirano, Y. ....	143, 208
Hirata, M. ....	227, 489, 494
Hirayama, T. ....	333, 397
Hirohata, Y. ....	235
Hirooka, T. ....	530
Hirooka, Y. ....	419, 505, 519, 520, 521
Hisamichi, Y. ....	41
Hishinuma, Y. ....	230, 231, 268, 399, 403, 459

Hiwatari, R. ....	364, 393
Hochin, T. ....	165
Hojo, H. ....	147, 148, 227, 481, 484, 491
Homma, H. ....	235
Honda, A. ....	136
Horiguchi, K. ....	265
Horiike, H. ....	240
Horiuchi, R. ....	369, 370, 371, 372, 408, 476, 508
Hoshika, H. ....	402
Hoshino, M. ....	9, 58
Hotta, S. ....	410
Hozumi, N. ....	102
Hudson, R.S. ....	349, 350

## I

Ichiguchi, K. ....	178, 179
Ichimasa, Y. ....	238
Ichimura, M. ....	75, 227, 483, 486, 488, 491
Ida, K. ....	10, 12, 13, 20, 25, 33, 35, 36, 40, 69, 70, 155, 158, 229, 298, 300, 301, 304, 310, 324, 337
Ida, M. ....	240
Idei, H. ....	76, 79, 128, 167, 218, 518, 519, 523, 527, 530
Ido, T. ....	149, 150, 151
Igami, H. ....	19, 51, 76, 77, 78, 80, 81, 82, 83, 126, 127, 128, 129, 294, 322
Igarashi, A. ....	442
Igitkhanov, Y. ....	54
Ignatenko, M. ....	169, 481
Iguchi, H. ....	307, 311, 312, 319, 324, 337, 420, 490
Iida, T. ....	240, 261, 473
Iijima, Y. ....	268, 459
Ikubo, T. ....	454
Iinuma, K. ....	441
Iiyama, K. ....	332
Ijiri, H. ....	469
Ikeda, K. ....	69, 70, 72, 135, 136
Ikeda, R. ....	315, 316, 318, 319, 392
Ikeda, S. ....	513
Ikeda, Y. ....	136
Ikuta, K. ....	420
Imagawa, S. ....	84, 86, 87, 90, 112, 273, 274, 275, 276, 277, 279
Imai, M. ....	442
Imai, T. ....	227, 484
Imamura, Y. ....	257
Imazawa, R. ....	172
Imazu, S. ....	166
Inada, Y. ....	525
Inagaki, S. ....	10, 19, 23, 24, 28, 36, 51, 76, 77, 78, 83, 167, 216, 404
Inoue, K. ....	267, 459
Inoue, S. ....	240, 375
Inoue, T. ....	88, 149, 150
Inutake, M. ....	394, 395, 420, 486
Irie, M. ....	92
Isayama, A. ....	36, 76
Ise, T. ....	88
Ishibashi, K. ....	245
Ishida, A. ....	530, 532
Ishida, M. ....	104
Ishigohka, T. ....	87
Ishiguro, E. ....	168
Ishiguro, S. ....	366, 367, 380, 385, 408, 508
Ishii, K. ....	490

Ishikawa, M. ....211, 212, 213, 214, 494, 495  
 Ishimoto, Y. ....65, 492  
 Ishiyama, A. ....105  
 Ishizaki, K. ....427  
 Ishizaki, R. ....355  
 Ishizawa, A. ....357, 371  
 Islam, Md. K. ....492, 503, 529  
 Isobe, M. ....82, 130, 216, 293, 294, 295,  
 296, 298, 299, 300, 305, 307, 313,  
 314, 319, 320, 324, 498, 509, 523  
 Itagaki, M. ....37  
 Itagaki, T. ....172, 531  
 Itakura, A. ....481  
 Itikawa, Y. ....434  
 Ito, A. ....348, 382  
 Ito, H. ....441  
 Ito, S. ....51, 80, 81, 126, 127, 128, 129  
 Ito, Y. ....222  
 Itoh, K. ....10, 24, 181, 183, 184, 188, 189, 191, 192,  
 199, 200, 201, 202, 203, 204, 305, 306, 310  
 Itoh, S.-I. ....181, 183, 188, 189, 199, 200,  
 201, 202, 203, 204, 310  
 Itoh, T. ....381  
 Itoh, Y. ....321  
 Iwakiri, H. ....248, 437  
 Iwakuma, M. ....108, 111, 243  
 Iwama, N. ....59  
 Iwamae, A. ....57, 223, 365, 487, 518  
 Iwamoto, A. ....96, 105, 106, 118, 245, 396, 421  
 Iwazaki, K. ....319, 404  
 Izumi, Y. ....231

## J

Jin, W.G. ....332  
 Jinguji, Y. ....315  
 Joe, K. ....444  
 Johzaki, T. ....368, 508

## K

Kado, S. ....226, 301, 517  
 Kageyama, A. ....388  
 Kakimoto, S. ....75, 488  
 Kakiuchi, M. ....473  
 Kalinina, D.V. ....24, 154  
 Kamataki, K. ....141, 337  
 Kamimura, Y. ....474, 475  
 Kamiya, K. ....238  
 Kaneko, O. ....69, 70, 134, 135, 136,  
 141, 143, 389, 530  
 Kaneko, T. ....380, 485  
 Kanki, T. ....522  
 Kanno, R. ....186, 187  
 Kasaba, K. ....96, 247  
 Kasada, R. ....250  
 Kasahara, H. ....215  
 Kasashima, Y. ....394  
 Kasuya, K. ....512  
 Kasuya, N. ....184, 188, 189  
 Katagiri, K. ....96, 247, 403  
 Katai, R. ....436  
 Katanuma, I. ....214, 490, 495  
 Katayama, K. ....504  
 Kato, A. ....109

Kato, D. ....248, 397, 430, 431, 432, 437,  
 438, 441, 442, 443, 444, 446  
 Kato, H. ....243  
 Kato, M. ....444  
 Kato, N. ....411  
 Kato, S. ....149, 150, 151, 154  
 Kato, T. ....429, 430, 432, 433, 434, 435,  
 436, 437, 439, 440, 441,  
 442, 443, 444, 446, 482  
 Kawabata, S. ....107  
 Kawagoe, A. ....107, 111  
 Kawahara, Z. ....282  
 Kawahata, K. ....22, 23, 24, 26, 27, 36,  
 144, 146, 147, 148, 155, 160, 161,  
 162, 167, 169, 170, 222, 302, 321  
 Kawai, Y. ....221  
 Kawakami, I. ....412  
 Kawakami, M. ....248  
 Kawamitsu, S. ....168  
 Kawamori, E. ....172, 342, 531  
 Kawamura, K. ....234  
 Kawana, R. ....213  
 Kawano, T. ....287, 290, 464, 465,  
 466, 467, 469, 470  
 Kawara, Z. ....236  
 Kawasaki, S. ....220, 530  
 Khan, R. ....182  
 Khilchenko, A.D. ....156  
 Kikuchi, A. ....268, 459  
 Kim, S.W. ....249  
 Kimura, A. ....250  
 Kimura, K. ....410, 411, 412, 413, 414, 416  
 Kimura, M. ....334, 438, 442  
 Kimura, N. ....106  
 Kino, C. ....506  
 Kiridoshi, S. ....63  
 Kishimoto, Y. ....530, 532  
 Kitajima, M. ....442  
 Kitajima, S. ....143, 216, 319, 404  
 Kitsunozaki, A. ....414  
 Kiwamoto, Y. ....336  
 Kiyama, S. ....143  
 Kizu, K. ....65, 230  
 Kobayashi, H. ....98  
 Kobayashi, M. ....5, 6, 7, 54, 423  
 Kobayashi, S. ....51, 76, 80, 81, 82, 126,  
 127, 128, 129, 254, 492,  
 497, 498, 503, 529  
 Kobayashi, T. ....217, 263, 482, 487, 512  
 Kobuchi, T. ....33, 35  
 Koga, K. ....63  
 Koga, T. ....426  
 Kogi, Y. ....28, 147, 169, 481  
 Kogoshi, S. ....220  
 Kohagura, J. ....227, 489  
 Kohyama, A. ....249, 513  
 Koide, S. ....376  
 Koizumi, N. ....230  
 Kojima, A. ....490  
 Kojima, C. ....415  
 Kojima, M. ....165, 166  
 Komada, S. ....135, 136  
 Komatsu, K. ....238  
 Komori, A. ....3, 5, 6, 7, 36, 54, 55, 66,  
 233, 404, 480, 530, 532, 542  
 Komura, K. ....463  
 Kondo, E. ....502, 528  
 Kondo, H. ....240

Kondo, K. ....	40, 261, 497, 500
Kondo, T. ....	135, 136
Kondoh, K. ....	502
Konishi, S. ....	393, 511
Kono, A. ....	328, 441
Kono, H. ....	425
Kono, M. ....	327, 379
Konoshima, S. ....	61
Kosaki, M. ....	102
Kotoh, K. ....	290
Kozaki, Y. ....	511
Krashennnikov, S. ....	367
Krasilnikov, A.V. ....	509
Kubo, H. ....	444
Kubo, N. ....	130
Kubo, S. ....	19, 24, 50, 51, 76, 77, 78, 79, 80, 81, 82, 83, 126, 127, 128, 129, 218, 227, 294, 322, 484
Kubota, Y. ....	217, 482, 492, 503, 529
Kudo, K. ....	169, 290, 481
Kuge, A. ....	111
Kukita, Y. ....	240
Kumazawa, R. ....	44, 47, 49, 50, 58, 69, 75, 215, 402, 488, 497
Kunugi, T. ....	236, 282, 506
Kurishita, H. ....	254, 257, 258
Kuroda, N. ....	166
Kurumada, A. ....	257
Kusakabe, T. ....	334, 438, 442
Kusano, K. ....	375
Kuwabara, T. ....	387
Kuzuu, S. ....	512

## L

LABCOM Group .....	166
Laqua, H.P. ....	77, 83
LHD Experimental Group .....	12, 13, 17, 21, 36, 47, 49, 54, 66, 88, 145, 154
Li, H. ....	456
Li, Z.X. ....	453
Liu, Y. ....	59, 60
Loarte, A. ....	423

## M

Maaßberg, H. ....	20
Machida, N. ....	484
Maeda, M. ....	106
Maehata, K. ....	245
Maekawa, R. ....	86, 106, 109, 111, 116, 118, 119, 245, 396
Maekawa, T. ....	76, 133, 392, 518, 519, 530, 532
Maluckov, A. ....	379, 385
Mančić, A. ....	379
Masamune, S. ....	92, 320, 522
Mase, A. ....	28, 147, 148, 169, 481
Masuda, K. ....	171
Masuzaki, S. ....	5, 6, 7, 8, 12, 13, 15, 40, 46, 54, 64, 66, 68, 228, 233, 244
Masuzaki, T. ....	42, 234, 492
Matama, K. ....	217, 482, 487
Matsubara, A. ....	427, 428
Matsubara, Y. ....	109, 396
Matsuda, W. ....	332
Matsui, H. ....	240, 242, 251, 252, 256

Matsukawa, M. ....	230, 530, 532
Matsukawa, T. ....	104
Matsumi, Y. ....	441
Matsumoto, C. ....	225
Matsumoto, Y. ....	37, 151, 275, 343
Matsuo, K. ....	242, 311
Matsuoka, K. ....	294, 298, 299, 300, 305, 306, 307, 310, 311, 320, 322, 324, 409, 410, 411, 412, 413, 416, 535
Matsuura, H. ....	303, 362, 363
Matsuzawa, Y. ....	208
Mekawa, T. ....	400
Mendenilla, A. ....	151, 152
Michael, C.A. ....	22, 24, 26, 155, 156, 198
Mima, K. ....	284, 368, 508, 515
Minami, K. ....	344
Minami, T. ....	20, 293, 294, 295, 296, 297, 298, 299, 300, 304, 305, 307, 324
Minoda, A. ....	102
Misawa, T. ....	338
Mitarai, O. ....	42, 273, 275, 402, 519, 530, 532
Mito, T. ....	87, 90, 94, 96, 97, 105, 106, 107, 108, 111, 112, 115, 116, 117, 118, 120, 121, 122, 123, 124, 232, 243, 245, 277, 396, 405, 421, 534
Miura, H. ....	351, 386
Miura, Y.M. ....	230
Miya, N. ....	65
Miyake, F. ....	326, 327, 328
Miyake, H. ....	463
Miyake, Y. ....	489
Miyamaoto, S. ....	512
Miyamoto, K. ....	239
Miyamoto, M. ....	64, 248, 248
Miyamoto, S. ....	240
Miyata, Y. ....	490
Miyauchi, H. ....	287
Miyazawa, J. ....	52, 53, 54, 92
Miyazawa, K. ....	12, 13
Miyazawa, M. ....	365
Miyazawa, Y. ....	489
Mizuguchi, N. ....	182, 208, 209
Mizuno, Y. ....	51, 80, 81, 102, 126, 127, 128, 129
Mizuuchi, T. ....	76, 416, 497, 499, 502, 503
Momoshima, N. ....	239, 472
Mori, H. ....	199
Mori, S. ....	219
Moribayashi, K. ....	442
Morikawa, J. ....	243, 405
Morino, K. ....	339
Morisaki, T. ....	5, 6, 7, 12, 13, 15, 42, 54, 55, 492, 525
Morishita, K. ....	248, 437
Morishita, T. ....	442
Morishita, Y. ....	340
Morita, S. ....	12, 13, 14, 15, 39, 40, 41, 69, 70, 153, 173, 223, 225, 435, 439
Morita, Y. ....	111
Moritaka, T. ....	371
Moriuchi, S. ....	113
Motohashi, M. ....	442
Motojima, G. ....	496
Motojima, O. ....	1, 36, 54, 66, 118, 427
Mroz, W. ....	512
Munakata, K. ....	289, 468
Murakami, I. ....	429, 432, 433, 434, 435, 436, 439, 440, 442, 443, 444, 482
Murakami, M. ....	76

Murakami, S. ....	11, 20, 82, 130, 229
Murakami, Y. ....	102
Muramoto, Y. ....	102
Muraoka, K. ....	16
Murata, I. ....	261
Murata, Y. ....	172
Muroga, T. ....	93, 231, 235, 240, 241, 242, 248, 249, 252, 253, 254, 255, 256, 260, 261, 262, 263, 264, 398, 437, 449, 450, 451, 452, 453, 454, 455, 456, 457
Muta, H. ....	339
Muto, S. ....	27, 82, 153, 439
Mutoh, T. ....	19, 47, 51, 69, 75, 77, 78, 83, 125, 127, 130, 210, 215, 294, 322, 488, 497, 530

## N

Nagai, D. ....	484
Nagai, K. ....	118, 421, 512
Nagakura, Y. ....	86
Nagao, M. ....	102
Nagaoka, K. ....	35, 38, 69, 70, 71, 72, 135, 136, 137, 138, 139, 140, 293, 294, 298, 299, 300, 307, 310, 313, 314, 323, 324, 524
Nagasaka, T. ....	93, 235, 251, 252, 253, 254, 264, 398, 452, 454, 455, 456, 457
Nagasaki, K. ....	76, 77, 78, 82, 83, 294, 497
Nagashima, Y. ....	200, 310
Nagata, K. ....	427
Nagata, M. ....	92, 400, 519, 522, 530, 532
Nagata, S. ....	262
Nagatomo, H. ....	368, 508
Nagayama, Y. ....	18, 23, 24, 28, 36, 163, 167, 169, 172, 216, 271, 285, 400, 406, 408, 481, 519, 530, 532
Naitou, H. ....	219
Nakahara, A. ....	481
Nakahata, T. ....	287
Nakai, H. ....	106
Nakai, K. ....	254
Nakai, M. ....	118, 421, 512
Nakajima, N. ....	174, 176, 177, 180, 182, 185, 198, 229, 348, 349, 350, 351, 352, 355, 356, 357
Nakamura, A. ....	111
Nakamura, H. ....	242, 365, 382, 383, 388
Nakamura, Hideo ....	240
Nakamura, Hiroo ....	240
Nakamura, K. ....	266, 298, 312, 403, 490, 519, 523, 530
Nakamura, N. ....	397, 431
Nakamura, Y. ....	46, 47, 49, 69, 176, 177, 229, 235, 345, 422, 441, 496, 497, 499, 530
Nakanishi, H. ....	164, 165, 166
Nakano, E. ....	373
Nakano, H. ....	150, 306, 307, 308, 309
Nakano, T. ....	65
Nakao, Y. ....	508
Nakasaki, Y. ....	228
Nakashima, H. ....	530
Nakashima, Y. ....	211, 214, 217, 492, 494, 495, 503, 529
Nakayama, K. ....	160, 162, 222, 321
Namba, C. ....	410, 411, 412, 413, 416, 558
Namba, S. ....	335
Narihara, K. ....	12, 13, 14, 18, 21, 31, 51, 145

Narita, F. ....	265
Narui, M. ....	252
Narushima, Y. ....	34, 36, 37, 38, 71, 172
NBI Group ....	72, 137, 138, 139
Nejoh, Y.N. ....	206
Nemoto, T. ....	213
Ninomiya, A. ....	87
Nishida, T. ....	290
Nishiguchi, A. ....	508
Nishihara, K. ....	430
Nishijima, G. ....	403
Nishijima, S. ....	231
Nishijima, T. ....	141, 337
Nishikawa, M. ....	244, 419, 504
Nishimura, A. ....	89, 230, 231, 247, 265, 268, 270, 403, 456, 458, 459
Nishimura, H. ....	216, 224, 398, 430, 511
Nishimura, K. ....	63, 65, 66, 67, 68, 216, 233, 404
Nishimura, S. ....	294, 298, 299, 300, 324, 345
Nishino, N. ....	402, 492, 502, 528, 530, 532
Nishio, S. ....	400, 530, 532
Nishitani, T. ....	231, 261, 453
Nishiura, M. ....	130, 143, 149, 150, 151, 152, 216, 343
Nishizawa, A. ....	149, 150, 151
Nisino, N. ....	519
Nisio, S. ....	410, 415
Nita, N. ....	251
Nobuta, Y. ....	66
Noda, N. ....	40, 49, 66, 67, 233, 242, 246, 254, 257, 258, 259, 437, 447, 540
Noguchi, S. ....	105
Nomura, S. ....	99
Nonomura, M. ....	166
Norimatsu, T. ....	118, 284, 393, 421, 506, 511, 512, 513
Norimura, T. ....	238
Notake, T. ....	19, 51, 76, 77, 78, 79, 80, 81, 83, 126, 127, 128, 129, 218, 294, 322, 484
Nozaki, K. ....	484
Nuga, H. ....	215
Numakura, T. ....	227, 489
Nunami, M. ....	186, 187

## O

O'Sullivan, G. ....	430
Oakberg, T. ....	162
Obara, T. ....	373
Obayashi, H. ....	410, 411, 412, 413, 414, 416, 475
Ochiai, K. ....	231, 261
Oda, A. ....	275
Oda, T. ....	40, 335
Ogata, Y. ....	471, 473
Ogawa, H. ....	111, 149, 150, 216
Ogawa, M. ....	319, 404, 529
Ogawa, T. ....	374, 387
Ogawa, Y. ....	243, 276, 393, 405, 530, 532
Ogiwara, H. ....	249
Ogura, K. ....	489
Ohdachi, S. ....	12, 13, 14, 32, 523
Ohishi, M. ....	444
Ohishi, T. ....	298
Ohkubo, J. ....	97
Ohkubo, K. ....	218
Ohnishi, M. ....	211
Ohno, N. ....	228, 244, 317, 340, 341, 362, 363



Ohshima, S. ....	306, 308, 309
Ohsuna, M. ....	166
Ohta, K. ....	228
Ohtani, H. ....	369, 370, 371
Ohtani, S. ....	333, 397, 431
Ohtsu, Y. ....	338
Ohtsuka, Y. ....	244
Ohyabu, N. ....	5, 6, 7, 40, 54, 66, 91, 233, 234
Oikawa, S. ....	37
Oishi, T. ....	301
Oka, Y. ....	69, 70, 135, 136, 142
Okada, H. ....	496, 497
Okai, T. ....	239
Okajima, S. ....	160, 162, 222, 302, 321
Okamoto, A. ....	143, 319, 326, 329, 404
Okamoto, M. ....	185, 187, 216, 351, 355, 357, 508
Okamoto, Y. ....	236
Okamura, S. ....	292, 293, 294, 295, 296, 297, 298, 299, 300, 301, 302, 303, 305, 306, 307, 310, 311, 313, 319, 320, 321, 322, 324, 325, 498
Okamura, T. ....	86, 119
Okano, K. ....	393
Okayama, S. ....	213
Okumura, H. ....	164
Okumura, K. ....	111
Okuno, K. ....	67, 230, 287, 291
Ono, H. ....	250
Ono, K. ....	64
Ono, T. ....	238
Ono, Y. ....	172, 400, 530, 531, 532
Ooba, K. ....	116
Oono, T. ....	530
Oosako, T. ....	215
Osakabe, M. ....	27, 70, 72, 82, 130, 135, 136, 137, 138, 139, 216, 314, 323, 524
Oshima, S. ....	307
Oya, Y. ....	67, 287, 291
Oyaidzu, M. ....	67, 287, 291
Ozaki, T. ....	82, 159
Ozawa, S. ....	512

## P

Parchamy, H. ....	61
Pastukhov, V.P. ....	493
Pavlichenko, R. ....	28, 170
Pavlichenko, T. ....	160
Peterson, B.J. ....	59, 60, 61, 300, 429
Pichl, L. ....	334, 438, 442, 443, 444
Pigarov, A.Yu. ....	367
Pint, B.A. ....	451
Prokopiuk, A. ....	512

## R

Rajković, M. ....	378
Ralchenko, Yu ....	432
Ramos, J.J. ....	348, 357
Rego, I. ....	220
Reiter, D. ....	54, 423
Rognlien, T.D. ....	367
Rustum Roy ....	427

## S

Saeki, K. ....	207
Safronova, U.I. ....	432, 435
Sagara, A. ....	63, 65, 66, 67, 68, 93, 209, 210, 233, 234, 235, 236, 242, 244, 261, 263, 272, 273, 274, 275, 276, 277, 278, 279, 280, 281, 282, 283, 284, 393, 398, 449, 450, 492, 506, 511
Saigusa, M. ....	227, 484
Saito, H. ....	380, 489
Saito, K. ....	68, 73, 74, 75, 131, 132, 215, 488, 497
Saito, T. ....	227, 484, 485, 490
Saitoh, H. ....	235
Saitou, Y. ....	326, 330, 331
Sakagami, H. ....	368, 508
Sakai, Y. ....	332, 397, 441
Sakakibara, S. ....	12, 13, 14, 15, 17, 24, 27, 29, 30, 34, 36, 37, 51, 157, 158, 229
Sakakita, H. ....	143, 220
Sakamoto, K. ....	227
Sakamoto, M. ....	42, 49, 220, 519, 520, 526, 529, 530
Sakamoto, R. ....	9, 10, 18, 52, 53, 58, 154, 217, 220
Sakamoto, T. ....	254
Sakaue, A. ....	57, 223, 365, 487
Sakaue, H. ....	431
Sakaue, H.A. ....	332, 333, 334, 397
Sakaue, M. ....	223
Sakuma, Y. ....	239, 471, 473
Sakurai, I. ....	225
Sakurai, M. ....	333, 397
Samukawa, S. ....	441
Sanada, K. ....	265
Sanin, A.L. ....	26, 155, 156
Sano, F. ....	496, 497, 498, 499, 500, 501, 502
Sanpei, A. ....	92, 320, 522
Sanuki, H. ....	190, 191, 192, 206, 207
Sardei, F. ....	54, 423
Sarkar, B. ....	122
Sasaki, A. ....	444
Sasaki, K. ....	173, 402, 519, 528
Sasaki, M. ....	215
Sasao, M. ....	130, 143, 152, 216, 319, 343, 404
Satake, H. ....	473
Satake, M. ....	263
Satake, S. ....	185, 186, 187, 236, 282
Sato, A. ....	106
Sato, F. ....	262
Sato, H. ....	101
Sato, K. ....	40, 168, 172, 211, 335, 344, 429, 430, 436, 439, 440, 532
Sato, K.N. ....	220, 338, 519, 530
Sato, M. ....	135, 136, 137, 138, 139, 356, 417, 420, 424, 427, 428, 512
Sato, N. ....	395
Sato, S. ....	261, 388, 453
Sato, T. ....	441
Sato, Y. ....	104
Satou, M. ....	264, 454
Sawada, A. ....	262, 451
Sawada, K. ....	219, 223, 288, 365, 492
Saxena, Y.C. ....	122
Seki, R. ....	37
Seki, T. ....	43, 45, 48, 68, 75, 215, 402, 488, 497
Sekiguchi, H. ....	87
Seo, K. ....	120, 122, 230, 231, 281, 403, 422
Seo, Y. ....	373
Shats, M.G. ....	197

Shibahara, M. ....	236
Shibata, M. ....	394, 486
Shibuya, M. ....	135, 136, 138, 139
Shibuya, T. ....	234
Shikama, T. ....	226, 262, 517
Shimada, K. ....	230
Shimada, R. ....	99, 302
Shimada, Y. ....	215
Shimazu, H. ....	373
Shimizu, A. ....	149, 150, 151, 242, 275, 279, 294, 299, 300, 306, 307, 308, 309, 469
Shimizu, K. ....	530
Shimizu, N. ....	37
Shimizu, Y. ....	102
Shimoda, H. ....	37
Shimoda, K. ....	512
Shimohiro, T. ....	97
Shimozuma, T. ....	19, 20, 24, 27, 51, 76, 77, 78, 79, 80, 81, 82, 83, 126, 127, 128, 129, 133, 167, 218, 227, 294, 322, 395, 484
Shimpo, F. ....	50, 402
Shinde, J. ....	319, 404
Shindo, Y. ....	265
Shinohara, S. ....	141, 337
Shinozaki, T. ....	289
Shinto, K. ....	143, 152, 216, 319, 343, 404
Shintomi, T. ....	106
Shiotsu, M. ....	106, 259
Shirai, Y. ....	106
Shiraki, K. ....	365, 436
Shirasaki, R. ....	383
Shiratani, M. ....	63
Shoji, M. ....	40, 54, 56, 57, 492, 503, 529
Shoji, T. ....	142, 318, 392
Shoji, Y. ....	96, 247
Skobelev, I. ....	433, 434
Škorić, M.M. ....	378, 379, 385
Smirnov, R. ....	359, 360, 361, 362, 363
Soga, Y. ....	336
Strohmayer, G. ....	423
Sudo, S. ....	24, 40, 154, 171, 346, 427, 537
Suehiro, J. ....	102, 103
Suehiro, K. ....	373
Sugai, H. ....	441
Sugama, H. ....	185, 186, 193, 194, 195, 196, 345, 358
Sugawara, H. ....	143, 343
Sugihara, S. ....	239
Sugimoto, M. ....	256
Sugimoto, T. ....	436
Sugiyama, K. ....	289
Sugiyama, T. ....	239, 288, 290, 470, 472
Sumitomo, N. ....	215
Sumiyoshi, F. ....	107, 111
Sunahara, A. ....	508
Suzuki, A. ....	235, 240, 241, 260, 262, 398, 451, 452
Suzuki, C. ....	293, 294, 298, 299, 300, 303, 307, 315, 316, 318, 319, 324, 392, 430
Suzuki, Ch. ....	196
Suzuki, R. ....	438
Suzuki, Y. ....	31, 33, 37, 157, 176, 177, 229, 404, 499

## T

Tachikawa, K. ....	97, 117, 232
Taguchi, T. ....	508
Takagi, K. ....	529
Takagi, S. ....	332
Takahara, H. ....	373
Takahashi, C. ....	132, 294, 299, 300, 307, 324
Takahashi, H. ....	216, 319, 404
Takahashi, K. ....	485
Takahashi, T. ....	92, 208, 208, 239, 531
Takahata, K. ....	85, 101, 120, 122, 123, 230, 277, 533
Takaiwa, Y. ....	410, 412
Takamaru, H. ....	186, 187
Takamatsu, T. ....	171
Takami, S. ....	88, 109, 475
Takamura, S. ....	317
Takao, T. ....	266, 403
Takase, Y. ....	215, 400, 402, 519, 530, 531, 532
Takayama, A. ....	367
Takayama, M. ....	216, 319, 404
Takayama, S. ....	427, 428
Takayanagi, T. ....	333
Takeda, H. ....	238
Takeda, S. ....	231
Takei, T. ....	373
Takeiri, Y. ....	20, 49, 69, 70, 135, 136, 137, 138, 139, 219, 323, 524, 530
Takenaga, H. ....	16
Takenaga, M. ....	143, 319, 404
Takeno, H. ....	211, 212, 213, 214, 491, 494, 495
Takeo, M. ....	245
Takeuchi, M. ....	299, 315, 316, 318, 319, 392
Takeuchi, S. ....	143, 343
Takeuchi, T. ....	231, 268, 399, 459
Takeuchi, Y. ....	511
Takita, Y. ....	51, 80, 81, 126, 127, 128, 129
Takiyama, K. ....	40
Takizuka, T. ....	359, 360, 361, 362, 363, 364
Tamai, H. ....	230
Tamura, H. ....	97, 117, 245, 265, 277
Tamura, N. ....	24, 59, 60, 154, 440
Tamura, Y. ....	209, 388
Tanabe, T. ....	237, 258
Tanaka, H. ....	37, 76, 392, 441, 518, 519
Tanaka, K. ....	10, 12, 13, 14, 15, 16, 22, 24, 26, 31, 33, 42, 49, 51, 155, 156, 160, 198, 222, 302
Tanaka, K.A. ....	505
Tanaka, M. ....	341, 424, 425, 426, 441, 468, 472
Tanaka, M.Y. ....	326, 327, 328, 329, 330, 331
Tanaka, N. ....	143, 343
Tanaka, S. ....	241, 287
Tanaka, T. ....	231, 240, 261, 262, 373, 374, 387, 449, 450, 452, 453
Tanaka, Y. ....	216, 228, 271, 319, 340, 341, 404
Tani, M. ....	248
Tanuma, H. ....	397
Tatematsu, Y. ....	227, 484, 485
Tauchi, H. ....	238
Tauchi, Y. ....	219
Tawara, T. ....	172
Tawara, Y. ....	225
Tazima, T. ....	420
Terai, T. ....	260, 398
Terashima, Y. ....	410, 411, 412, 413
Thang, D. ....	220

Thang, D.H. ....	339
Timura, T. ....	172
Tobari, H. ....	394, 486
Tobita, K. ....	393
Toda, S. ....	183, 201, 203
Todo, Y. ....	352, 353, 354, 384, 422
Toh, K. ....	262
Toi, K. ....	12, 13, 14, 27, 32, 82, 298, 299, 300, 313, 314, 315, 316, 317, 318, 319, 392, 523, 558
Tojo, H. ....	215
Tokioka, S. ....	489
Tokitani, M. ....	64, 248
Toku, H. ....	171
Tokunaga, H. ....	530
Tokunaga, K. ....	244
Tokuzawa, T. ....	12, 13, 24, 27, 51, 146, 147, 161, 222, 342
Tomida, A. ....	326, 327
Tomii, Y. ....	489
Tomita, N. ....	302
Tomita, Y. ....	171, 208, 211, 212, 213, 214, 275, 285, 359, 360, 361, 362, 363, 364, 367, 416, 494, 495
Tomota, Y. ....	257
Tonegawa, A. ....	234
Torii, Y. ....	497
Torikai, Y. ....	473
TRIAM Experimental Group ....	220, 527
TRIAM-IM Group ....	523
Tribaldos, V. ....	20
Tskhakaya, D. ....	361
Tsuchiya, B. ....	262
Tsuchiya, H. ....	55, 525
Tsuchiya, K. ....	230
Tsuda, K. ....	408
Tsuda, M. ....	101, 105
Tsuji, T. ....	76
Tsuji, M. ....	365, 436
Tsuji-Iio, S. ....	99, 302
Tsujimura, J. ....	215
Tsukada, K. ....	149, 150, 151
Tsumori, K. ....	69, 70, 135, 136, 138, 139, 141, 219, 343, 441
Tsushima, A. ....	207, 326, 330, 331
Tsutsui, H. ....	99, 302
Tsuzuki, K. ....	65

## U

Uchida, K. ....	147
Uchida, M. ....	76, 392, 518
Uda, T. ....	238, 239, 278, 287, 288, 289, 290, 460, 468, 470, 472, 475
Ueda, Y. ....	244
Uematsu, E. ....	410, 412, 415
Uesugi, Y. ....	228, 340, 341
Umeda, N. ....	136
Unno, H. ....	207
Urano, H. ....	16
Uriu, Y. ....	87
Usami, S. ....	372
Utoh, H. ....	216, 319, 404

## V

Vinyar, I. ....	154
-----------------	-----

Vyacheslavov, L.N. ....	26, 155, 156
-------------------------	--------------

## W

Wada, M. ....	143, 151, 152, 343
Wakabayashi, H. ....	320
Watanabe, A. ....	266, 438
Watanabe, F. ....	12, 13, 14
Watanabe, H. ....	253
Watanabe, K. ....	37, 275, 403
Watanabe, K.W. ....	12, 13
Watanabe, K.Y. ....	14, 15, 17, 29, 30, 31, 33, 34, 35, 36, 38, 71, 157, 158, 177, 229, 496
Watanabe, S. ....	76
Watanabe, T. ....	46, 62, 163, 275, 439, 440
Watanabe, T.-H. ....	193, 194, 195, 196, 358, 401
Watari, T. ....	58, 75, 215, 402, 488, 558
Wataya, Y. ....	167

## X

Xia, H. ....	197
Xu, Q. ....	457

## Y

Yabutani, H. ....	503
Yagai, T. ....	101
Yagi, M. ....	181, 183, 188, 189, 200, 310
Yagi, Y. ....	143
Yagy, J. ....	65
Yamada, H. ....	9, 11, 16, 20, 29, 30, 33, 36, 58, 92, 177, 217, 220, 229, 530
Yamada, I. ....	145, 332, 333, 397
Yamada, M. ....	445
Yamada, S. ....	87, 102, 103, 113, 230, 558
Yamada, Y. ....	97, 117
Yamagishi, O. ....	26, 155, 193, 198
Yamaguchi, H. ....	326, 327
Yamaguchi, S. ....	28
Yamaguchi, T. ....	31, 37, 157, 158, 410, 490
Yamaguchi, Y. ....	75, 483, 488
Yamamoto, H. ....	396
Yamamoto, I. ....	288
Yamamoto, N. ....	430, 439, 440, 446
Yamamoto, S. ....	82
Yamamoto, T. ....	136, 408
Yamamoto, Y. ....	171, 320, 511
Yamanaka, S. ....	240
Yamanishi, H. ....	239, 461, 462, 463
Yamanoue, T. ....	172
Yamaoka, H. ....	343
Yamaoka, N. ....	240
Yamasaki, K. ....	253
Yamasaki, T. ....	463
Yamashita, K. ....	374
Yamauchi, K. ....	111
Yamazaki, K. ....	14, 121, 172, 275, 276
Yanagi, N. ....	76, 86, 87, 90, 105, 106, 112, 114, 120, 121, 122, 123, 243, 405
Yao, Z. ....	260, 452
Yasaka, Y. ....	211, 212, 213, 214, 491, 494, 495
Yasohama, K. ....	396
Yatsuka, E. ....	405

Yelisseyeva, O. ....	452
Yokomine, T. ....	242, 279, 281, 282
Yokota, M. ....	111, 132, 149, 150
Yokota, Y. ....	147
Yokoyama, M. ....	11, 20, 185, 197, 198, 216, 229, 319, 499
Yokoyama, N. ....	489
Yoshida, H. ....	514
Yoshida, M. ....	163
Yoshida, N. ....	64, 242, 244, 248, 253, 258, 519, 530, 532
Yoshikawa, A. ....	67, 287, 291
Yoshikawa, K. ....	171
Yoshikawa, M. ....	217, 481, 482, 485, 487, 490, 492, 529
Yoshimura, M. ....	33
Yoshimura, S. ....	326, 327, 328, 329, 330, 338
Yoshimura, Y. ....	19, 51, 76, 77, 78, 80, 81, 82, 83, 126, 127, 128, 129, 196, 293, 294, 298, 299, 300, 305, 307, 322, 324, 331, 484, 498
Yoshinaga, T. ....	392, 518
Yoshinuma, M. ....	12, 13, 25, 35, 155, 301, 304
Yoshizawa, S. ....	269
Yuki, K. ....	236, 263, 280, 282
Yutani, S. ....	242
Yuyama, M. ....	106

## Z

Zhu, S. ....	364
Zubarev, P.V. ....	156
Zushi, H. ....	402, 517, 518, 519, 521, 524, 525, 529, 530, 531, 532



# How to Reach National Institute for Fusion Science



## ACCESS

### When you use the public transportation facility

#### ◇ from Centrair

• **Centrair** — (μ-sky) — **Meitetsu Kanayama Sta.** (36km)

about 25min

**JR Kanayama Sta.** — (JR Chuo Line) — **JR Tajimi Sta.** (33km)

about 33min (express)

**JR Tajimi Sta.** — (Toutetu Bus) — **Kenkyuugakuentoshi** (7km)

about 15min

#### ◇ from JR Nagoya Sta.

• **JR Nagoya Sta.** — (JR Chuo Line) — **JR Tajimi Sta.** (36km)

about 22min (super express)

about 30min (express)

about 40min (local)

**JR Tajimi Sta.** — (Toutetu Bus) — **Kenkyuugakuentoshi** (7km)

about 15min

#### ◇ from Nagoya Airport (Obihiro-Akita-Yamagata-Niigata-Kouchi-Matsuyama-Kumamoto)

• **Nagoya Airport** — (taxi) — **JR Kachigawa Sta.** (4km)

about 10min

• **Nagoya Airport** — (Meitetsu Bus) — **JR Kachigawa Sta.** (4km)

about 19min

**JR Kachigawa Sta.** — (JR Chuo Line) — **JR Tajimi Sta.** (21km)

about 20min

**JR Tajimi Sta.** — (Toutetu Bus) — **Kenkyuugakuentoshi** (7km)

about 15min

### When you use a car

• from **Chuo Expressway Toki I.C. or Tajimi I.C.** (8km)

about 20min

• from **Tokai-Kanjo Expressway Tokiminami Tajimi I.C.** (2km)

about 5min

# National Institute for Fusion Science

## Building Arrangement



### NIFS plot plan

- |   |                                    |
|---|------------------------------------|
| ① Cryogenics and Superconductivity Laboratories | ⑮ Guest Housing                    |
| ② Large Helical Device Building                 | ⑯ High-Voltage Transformer Station |
| ③ Computer Center and Simulation Laboratories   | ⑰ Cooling Water Pump House         |
| ④ Heating Power Supply Building                 | ⑱ Helium Compressor House          |
| ⑤ LHD Control Building                          | ⑲ Cooling Tower                    |
| ⑥ Plasma Heating Laboratories                   | ⑳ Warehouse                        |
| ⑦ Plasma Diagnostics Laboratories               | ㉑ Helium Tank Yard                 |
| ⑧ R & D Laboratories                            | ㉒ Power Station                    |
| ⑨ Motor-Generator Building                      | ㉓ Recreation Facilities            |
| ⑩ Central Workshops                             | ㉔ Gymnasium                        |
| ⑪ Research Staff Building                       | ㉕ Club House                       |
| ⑫ Library                                       | ㉖ Guard Office                     |
| ⑬ Administration Building                       | ㉗ Power Station                    |
| ⑭ Auditorium                                    |                                    |